SECOND EDITION

Oral and Maxillofacial Radiology

A DIAGNOSTIC APPROACH

DAVID MACDONALD
Editor



WILEY Blackwell

ORAL AND MAXILLOFACIAL RADIOLOGY

ORAL AND MAXILLOFACIAL RADIOLOGY

A DIAGNOSTIC APPROACH

Second Edition

Edited by

David MacDonald BDS, BSc (Hons.), LLB (Hons.), MSc(Lond.), DDS (Edin.), DDRRCR, FDSRCPS, FRCDC

Professor & Chair, Oral and Maxillofacial Radiology
University of British Columbia
British Columbia, Canada

WILEY Blackwell

This edition first published 2020
© 2020 John Wiley & Sons, Inc.

Edition History
John Wiley and Sons (1e, 2011)

All rights reserved. No part of this publication may be reproduced, stored in a retrieval system, or transmitted, in any form or by any means, electronic, mechanical, photocopying, recording or otherwise, except as permitted by law. Advice on how to obtain permission to reuse material from this title is available at http://www.wiley.com/go/permissions.

The right of David MacDonald to be identified as the author of the editorial material in this work has been asserted in accordance with law.

Registered Office
John Wiley & Sons, Inc., 111 River Street, Hoboken, NJ 07030, USA

Editorial Office
111 River Street, Hoboken, NJ 07030, USA

For details of our global editorial offices, customer services, and more information about Wiley products visit us at www.wiley.com.

Wiley also publishes its books in a variety of electronic formats and by print-on-demand. Some content that appears in standard print versions of this book may not be available in other formats.

Limit of Liability/Disclaimer of Warranty
The contents of this work are intended to further general scientific research, understanding, and discussion only and are not intended and should not be relied upon as recommending or promoting scientific method, diagnosis, or treatment by physicians for any particular patient. In view of ongoing research, equipment modifications, changes in governmental regulations, and the constant flow of information relating to the use of medicines, equipment, and devices, the reader is urged to review and evaluate the information provided in the package insert or instructions for each medicine, equipment, or device for, among other things, any changes in the instructions or indication of usage and for added warnings and precautions. While the publisher and authors have used their best efforts in preparing this work, they make no representations or warranties with respect to the accuracy or completeness of the contents of this work and specifically disclaim all warranties, including without limitation any implied warranties of merchantability or fitness for a particular purpose. No warranty may be created or extended by sales representatives, written sales materials or promotional statements for this work. The fact that an organization, website, or product is referred to in this work as a citation and/or potential source of further information does not mean that the publisher and authors endorse the information or services the organization, website, or product may provide or recommendations it may make. This work is sold with the understanding that the publisher is not engaged in rendering professional services. The advice and strategies contained herein may not be suitable for your situation. You should consult with a specialist where appropriate. Further, readers should be aware that websites listed in this work may have changed or disappeared between when this work was written and when it is read. Neither the publisher nor authors shall be liable for any loss of profit or any other commercial damages, including but not limited to special, incidental, consequential, or other damages.

Library of Congress Cataloging-in-Publication Data
Names: MacDonald, David, 1955– author.
Title: Oral and maxillofacial radiology : a diagnostic approach / David MacDonald.
Description: Second edition. | Hoboken, NJ : Wiley-Blackwell, 2020. |
Includes bibliographical references and index. |
Identifiers: LCCN 2019006680 (print) | LCCN 2019007237 (ebook) | ISBN 9781119218715 (Adobe PDF) |
ISBN 9781119218722 (ePub) | ISBN 9781119218708 (hardback)
Subjects: | MESH: Diagnostic Imaging | Stomatognathic System–pathology | Diagnosis, Oral
Classification: LCC RC78.7.D53 (ebook) | LCC RC78.7.D53 (print) | NLM WN 230 | DDC 616.07/54–dc23
LC record available at https://lccn.loc.gov/2019006680

Cover image: © Babak Chehroudi
Cover design: Wiley

10.5/12.5pt Slimbach by SPi Global, Pondicherry, India

10 9 8 7 6 5 4 3 2 1

To my parents, my daughters, Amy and Alicia, and my wife

Contents

List of contributors ix

Preface xi

Part 1 Introduction 1

Chapter 1 Basics of radiological diagnosis 3

Chapter 2 Viewing conditions and physiological phenomena and radiological interpretation 47

Chapter 3 Evidence-based radiology 63

Part 2 Advanced imaging modalities 73

Chapter 4 Computed tomography 75

Chapter 5 Cone-beam computed tomography 89

Chapter 6 Magnetic resonance imaging 111

Chapter 7 Positron emission tomography 135

Chapter 8 Basics of ultrasound 151

Part 3 Radiological pathology of the jaws 159

Chapter 9 Radiolucencies 161

Chapter 10 Radiopacities 273

Chapter 11 Maxillary sinus 341

Chapter 12 Lesions within the soft tissues 387

Chapter 13 Imaging of the salivary glands 415

Chapter 14 Oral and maxillofacial vascular lesions 447

Chapter 15 Fractures of the face and jaws 473

Chapter 16 Temporomandibular joint diseases 493

Part 4 Extragnathic lesions **517**

Chapter 17 Introduction to extragnathic lesions 519

Chapter 18 Benign lesions 529

Chapter 19 Malignant lesions 555

Part 5 Osseointegrated implants **611**

Chapter 20 Osseointegrated implants 613

Index 631

List of contributors

Jackie Brown
BDS, MSc (Lond.), FDSRCPS, DDRRCR
Senior Lecturer, Dental and Maxillofacial Radiologist, King's College London, London, UK

Manraj Heran
MD, FRCPC
President, Society for Pediatric Interventional Radiology
Associate Professor, Diagnostic & Therapeutic Neuroradiology, Vancouver General Hospital
Pediatric and Interventional Radiology, British Columbia's Children's Hospital, University of British Columbia, Canada

Pedro Lourenco
MD, FRCPC
Interventional Radiology Fellow, Department of Radiology, University of British Columbia and McGill University, Canada

David MacDonald
BDS, BSc(Hons.), LLB(Hons.), MSc (Lond.), DDS(Edin.), DDRRCR, FDSRCPS, FRCDC
Professor & Chair, Oral & Maxillofacial Radiology, University of British Columbia, British Columbia, Canada
Senator, University of British Columbia
Consultant, British Columbia Cancer Agency
Regional Director (North America), International Association of Dento-Maxillo-Facial Radiology

Montgomery Martin
MD, FRCPC
Medical Director & Provincial Lead, Radiology, British Columbia Cancer Agency, Clinical Assistant Professor, University of British Columbia, British Columbia, Canada

Savvas Nicolaou
MD, FRCPC
Professor of Radiology, Vancouver General Hospital, University of British Columbia, British Columbia, Canada
Vice Chair of CPD & Education Director of Emergency Trauma Imaging
Diplomate of the American Board of Radiology
Fellow of American College of Emergency Radiology
Fellow of the Royal College of Surgeons and Physicians of Canada

Michael O'Keeffe
MB Bch BAO, MRCSI, FFRRCSI
Assistant Professor of Radiology, University of Toronto
Staff Radiologist in Emergency and Trauma Radiology, Sunnybrook Health Sciences Center, Toronto, Ontario, Canada.

LI Ka Lun Thomas
BDS(HK), MSc(London), DDRRCR, DGDP(UK), FCDSHK, FHKAM(DS), Private Practitioner
Honorary Clinical Associate Professor, Faculty of Dentistry, The University of Hong Kong, Hong Kong

Donald Wilson
BSc, MD, FRCPC
Provincial Lead, Functional Imaging, British Columbia Cancer Agency, Vancouver Centre
Clinical Assistant Professor, Department of Surgery, University of British Columbia, British Columbia, Canada

Jonn Wu
BMSc, MD, FRCPC
Fellow of the Royal College of Physicians and Surgeons, Canada
Chair, Provincial Head and Neck Tumour Group, British Columbia Cancer Agency
Radiation Oncologist, British Columbia Cancer Agency,
Clinical Associate Professor, Faculty of Medicine, University of British Columbia, British Columbia, Canada

Preface

The primary purpose of this second edition follows that of the first. Although now written to address the medical radiologists' needs in addition to those of dental, oral, and maxillofacial clinicians, some excerpts of reviews of the first edition reveal the core around which this edition has been built: "The purpose of this textbook is to guide diagnosticians of all skill levels in generating a diagnosis of lesions affecting the face and jaws" and it has been "thoroughly accomplished. [1]" Furthermore, "All chapters include high-quality illustrations with concise, readable legends, along with excellent decision-making flow charts to help guide the reader through the interpretive process" [1]. "The superb image quality and succinct texts make it easy to recommend to dental practitioners, maxillofacial specialists and residents embarking on their careers" [2]. This edition has increased the number of diagnostic flowcharts. Moreover, "Each topic is well referenced with current evidence-based studies and epidemiological data that can be useful in identifying radiographic lesions and developing differential diagnoses" [2].

Importantly, "This is not a traditional textbook in [oral and maxillofacial] radiology since there is an emphasis on description of high-tech imaging techniques such as CT scanning, magnetic resonance, positron emission tomography and ultrasound" [3]. This edition has not only expanded its coverage of these cross-sectional imaging modalities, but has included interventional radiography, which here has made a substantial debut in the oral and maxillofacial textbook literature.

These developments have been accompanied by expanding the co-authorship to include leading specialists in trauma, interventional radiology, salivary gland radiology, functional imaging, and radiation oncology. The last two emphasize the continued role of the radiologist in the management and follow-up of head and neck cancers. All these innovations allow this edition to dovetail better with other texts that the dental or medical reader is likely to be familiar with, bridging the gaps between them.

This second edition also supports the continuing transition of dentists, with their traditional focus on the oral cavity, to oral physicians, who are more fully integrated into general health-care provision and enhancement of wellness. The new chapter on soft-tissue calcifications reinforces the dentists' role in the detection of possible carotid artery atheromas and details the radiologists' role in their management.

This new edition continues the first edition's harmonization of terminology between the specialities that operate in and around the face and jaws.

In conclusion, this textbook will enable quick and accurate pattern recognition using up-to-date flowcharts, written by experts, and will translate both into the clinic and into the undergraduate's, the graduate's, and the resident's examination halls.

References

1. Danforth, R.A. and Mah, J. (2012). Book review: Oral & Maxillofacial Radiology: A Diagnostic Approach. *J. Clin. Orthod.* 46: 506.
2. Tong, A. (2012). Book review: Oral & Maxillofacial Radiology: A Diagnostic Approach. *J. Oral Maxillofac. Surg.* 41: 1451.
3. Wenzel, A. (2011). A fresh innovative approach to radiology disorders. *Tandlaegebladet* Oct 6. (Danish).

Part 1
Introduction



Chapter 1

Basics of radiological diagnosis

1.1 Introduction

Although lesions that primarily affect the face and jaws may not hitherto have substantially impacted the practice of most radiologists save that of the head and neck specialist, the recent advent of *cone-beam computed tomography* (CBCT) and its increasingly widespread use in dentistry have begun to change this. As noted elsewhere, "The main downside of this technology's widespread availability is that the radiological knowledge of many of the dentists who own and operate these units may not yet be adequate enough for interpretation of a CBCT dataset. Therefore, until dental education catches up, medical radiologists may be approached to interpret some datasets, particularly where the availability of oral and maxillofacial radiologists is sparse or nonexistent" [1]. Therefore, it is the primary aim of this textbook to enhance the radiological knowledge of both the radiologist and oral clinician (all dentists and oral and maxillofacial specialists), so that the former may be able to optimally assist and the latter in turn to minimize the already heavy workload of most radiologists, by referring only those cases that need a radiologist's expertise.

Although the medical reader of this textbook, particularly the radiologist, will find much that is familiar, such as the imaging of malignancies and those lesions immediately adjacent to the jaws, the reader will equally find that there is much that is different. This difference goes beyond simply the pre-eminence of conventional radiography in imaging disease of the face and jaws owing to the fact that much of the pathology that affects them is unique to the jaws. The three main reasons for this are set out in Table 1.1. One purpose of this textbook is to attempt to harmonize the medical and dental terminologies so as to enhance the quality of communication between clinicians to optimize patient care. To this end two new chapters have been added, one addressing vascular anomalies and the other calcifications occurring in the soft tissues. In the course of writing this second edition, the World Health Organization's (WHO) 2017 edition on the *Classification of Head and Neck Tumours* was published [2]. Although this publication is very welcome, as it brings our understanding of lesions affecting the maxillofacial region up to date, unfortunately it has taken a step backward with regard to some important lesions peculiar to the jaws. These will be discussed at appropriate junctures, beginning later in this chapter. This edition will now be referred to as the "WHO's 2017 edition" throughout.

Conventional radiography (CR) of the face and jaws, despite the recent advent of CBCT, is still central to diagnosis of the

Oral and Maxillofacial Radiology: A Diagnostic Approach, Second Edition. Edited by David MacDonald.
© 2020 John Wiley & Sons, Inc. Published 2020 by John Wiley & Sons, Inc.

Table 1.1 The three main differences that underline the most important and/or frequent lesions that affect the face and jaws in comparison to those in the extragnathic skeleton.

	Difference	Implications
1	Bones of the face and jaws come from a different origin to the extragnathic skeleton.	The bones of the face and jaws are derived from **membrane ossification** rather from **endochondrial ossification** in the extragnathic skeleton. *This difference may explain why fibrous dysplasia occurring in the jaws is different to that of the extragnathic skeleton*.
2	Epithelium is buried with the jaw bones. It is derived from two sources.	First, from the **ectoderm-covering prominences which form the face**. Failure of these prominences to fuse results in facial clefts, including that of the palate. *Epithelial rests remaining after successful fusion may result in the nasapalatine cyst, the only nonodontogenic cyst of the jaws*.
		Second, from the **dental lamina from which the teeth originate.** From these rests are derived the odontogenic neoplasms and cysts. *The odontogenic neoplasms have, as observed by their higher placement in the scale of severity of outcomes in Table* 1.3*, an enhanced likelihood of recurrence after primary surgery*.
3	The jaw bones have a unique capacity to resist infection.	If this were not so, nearly every dental infection that extended into the bone would result in osteomyelitis.

face and jaws. Nevertheless, as exhibited in Figure 1.1, almost every imaging modality available to the medical radiologist can play its part in the diagnosis and further evaluation of a particular lesion or a patient's complaint. The radiologist can influence the selection of the appropriate modality. The radiologist will find the oral clinician appreciative, as knowledge of most advanced modalities is still limited in most dental programs. Nevertheless, the clinician, regardless of training, should have at least a basic understanding of how the image is made and the normal anatomy and its variants in order to be able to identify artifacts, particularly those that can mimic the appearance of disease. This enhances medical–dental communication. Figure 1.1 outlines the main attributes of the imaging modalities that are featured in this textbook. These imaging modalities have been broadly divided into conventional radiography and advanced imaging.

Diagnosis in oral and maxillofacial radiology is most frequently based both on the clinical findings (including presenting complaint and history) and on the features observed on conventional radiographs. A definitive diagnosis is possible for a large proportion of lesion types that present to the primary care dentist. These lesions do not include just those lesions of inflammatory origin, mainly the sequelae of dental caries, that present as periapical radiolucencies (histologically periapical granulomas, cysts, and abscesses) or radiopacities (*condensing osteitis*), but also *dentigerous cysts* and *dense bone islands* (DBIs, also known as idiopathic osteosclerosis [IOS]). They are not only the most

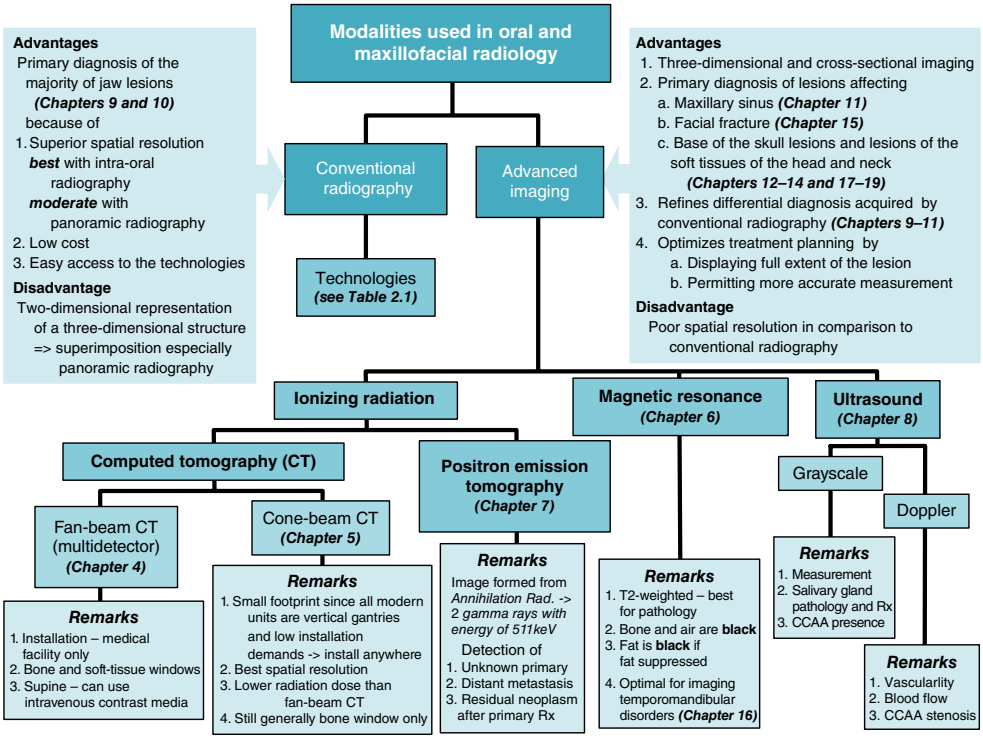


Figure 1.1 The modalities used in oral and maxillofacial radiology. This is an overview of the main imaging modalities, including remarks concerning their clearest clinical uses, relative advantages over other modalities, and limitations of use. CCAA, calcified carotid artery atheroma; keV, kiloelectron volts; Rx, recipe!, treatment.

frequently occurring lesions affecting the jaws, but a majority of them also have distinctive clinical and radiological presentations. Some other lesions such as *florid osseous dysplasia*, the *cementoblastoma*, the *compound odontoma*, and some cases of *odontogenic myxoma* can be definitively diagnosed solely on their radiological appearance. In those situations where a definitive diagnosis is not possible, a differential diagnosis should be developed. This will consist of two or more lesions. Such cases are frequently referred to a specialist as much for a diagnosis as for treatment. In order to assist readers in their diagnosis, this textbook is illustrated throughout with diagnostic flowcharts.

There is an expectation that the images created should adequately display the area of clinical interest, with the purpose of addressing those clinical questions that indicated the need for the investigations. Thus, the image or images should display the entire area of pathology and be free of artifacts. Therefore, an unerupted third molar should not only include the entire tooth and its follicle, but also at least a clear margin of 1 mm around them. This would allow the clinician to determine whether it is close to the mandibular canal or any other adjacent structure.

An example of inadequacy of radiography resulted in a Canadian dental malpractice case that continued for 12 years through at least five courts before it was concluded, presumably settled [3]. The only positive result of this failure to include only 98 % of a third molar was its not insignificant contribution to Canadian law specifically and common law in general. From reading the case, it is abundantly clear that if an adequate radiograph or radiographs had been taken in the first instance, this case would have had little ground upon which to proceed, and the spilling of so much legal ink and personal and professional distress would have been avoided.

Radiographs are prescribed for three reasons: diagnosis, presurgical planning, and follow-up. Those prescribed for the purpose of diagnosis and/or presurgical planning should be made prior to biopsy, because this can change the radiology of the lesion appreciably. This is particularly so with regard to advanced imaging such as *fan-beam computed tomography* (CT, installed in most medical hospitals) and *magnetic resonance imaging* (MRI). Two cases demonstrate the effects of biopsy prior to CT.

The biopsy of an odontogenic myxoma, a locally invasive benign neoplasm, prior to CT, provoked an inflammatory response within the depth of the lesion, which was enhanced by the intravenous contrast (Figure 1.2). Contrast is recommended for lesions which include a neoplasm or a vascular lesion in their differential diagnosis. With regard to neoplasms, this is important to determine local invasion of adjacent soft tissues, which would need to be resected along with the rest of the neoplasm.

Figure 1.3 displays a case of *fibrous dysplasia*, which caused a substantial expansion of the affected mandible. When it was first seen by general surgeons unfamiliar with its manifestation in the jaws, they performed multiple biopsies. These biopsies created their own artifacts on a subsequent CT. These artifacts were loss of cortex and dysplastic tissue exuding through a biopsy site.

1.2 Introduction to Conventional Radiography

All prescriptions for a radiological investigation must be based upon a thorough clinical examination. CR will be the first

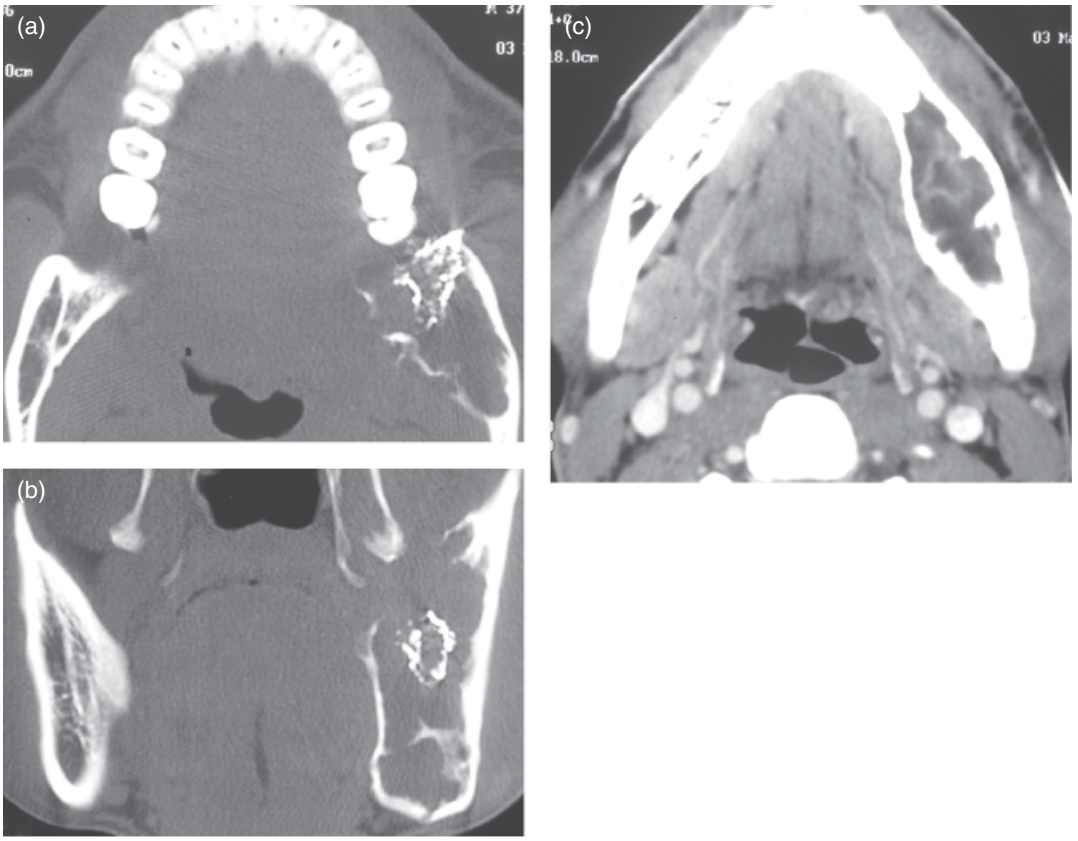


Figure 1.2 Computed tomography of an odontogenic myxoma carried out after the lesion had been biopsied. The biopsy site still has its dressing in place (a and b). As a result there was enhancement (c) by the intravenous contrast at the site biopsied that is more likely to reflect hyperemia in response to the trauma of surgery. Note: All the major blood vessels including the facial and lingual arteries are enhanced in Figure 1.2c. Source: Reproduced with permission from MacDonald-Jankowski, D.S., Yeung, R., Li, T.K., and Lee, K.M. (2004). Computed tomography of odontogenic myxoma. *Clin. Radiol.* 59: 281–287.

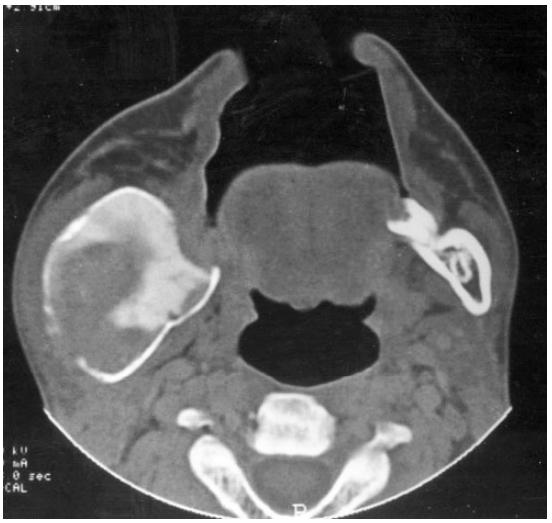


Figure 1.3 Bone-window axial computed tomography of fibrous dysplasia affecting the vertical ramus of the mandible. The cortical defects are the result of several biopsies performed prior to referral for computed tomography. Such operations can largely invalidate any clinically important radiological findings because these, if erroneous, could lead to a wrong diagnosis and inappropriate treatment. Note: Radiology is very central to the diagnosis of specific fibro-osseous lesions, discussed later.

imaging modality to be prescribed to investigate further a lesion occurring within the bony jaws obvious to or suspected by the clinical history and/or examination. For the majority of lesions affecting the jaws, CR is likely to be the sole imaging modality deemed clinically necessary. The principal advantages of CR are its superior spatial resolution (especially of the intraoral technologies), low radiation dose, and low cost. It is also available in the dental office or surgery. It is most likely that this prescription will include a panoramic radiograph that may be accompanied by intraoral radiographs. These images may be in either analog (film) or digital format. An overview of the various conventional radiographic technologies is set out in Table 2.1. The panoramic radiograph permits an overview of the jaws from condyle to condyle. It also permits comparison between sides. These premises can be valid only if the patient is properly positioned within the panoramic radiographic unit, exposed by the most appropriate exposure factors, and the image is properly developed. Finally, it is also expected that the resultant image is properly reviewed (read) under optimal viewing conditions (see Chapter 2).

Although there is little, if no, place for routine radiographic screening in the modern practice of dentistry, every image should be carefully reviewed to identify any pathology that may be incidental to the patient's complaint and the results of the clinical examination. The fairly widespread practice of prescribing panoramic radiographs prior to the fabrication of complete removable prostheses in the completely edentulous patient was again recently questioned [4].

The panoramic radiograph, in addition to permitting determination of the specific features of the lesion or suspected lesion that prompted its making, can also reveal macroscopic abnormalities such as size differences and changes in a specific anatomical location (Figure 1.4). Macroscopic anomalies (Table 1.2), such as craniofacial anomalies with or without cleft lip and palate, are now investigated by cross-sectional imaging modalities *multidetector computed tomography* (MDCT) (Figure 1.5) or CBCT (Figure 1.6). Although the use of CBCT for assessments for orthodontic reasons has so far no evidence basis, it may be called upon in the case of severe symmetry in order to facilitate optimal treatment planning. Figure 1.7 displays the results of such a case.

Medical readers will be aware that their dental colleagues will to a substantial degree be concerned with those diseases that principally affect the teeth and oral mucosa. In addition to caries and periodontal disease, some of the other important disease and radiological features the dentist will consider are set out in Figure 1.8. The reader should be aware that taurodontism, which is the increase in the vertical height of the pulp, like that observed in ungulates rather than the usual cynodont pattern of the typical human dentition, has been reported normally in some East Asian communities and is not wholly reliable as a marker of disruption in dental development [5].

Furthermore, CR can complement the clinical examination by confirming defects in the dental development, such as the number, eruption, size (Figure 1.9), and even structure of the teeth (Figure 1.10). Because these features have been fully addressed in other basic texts and are generally well understood, space constraints preclude offering images of them here.

The various lesions occurring within the face and jaws often present with similar features at certain stages. Most will at some stage present as a radiolucency as they

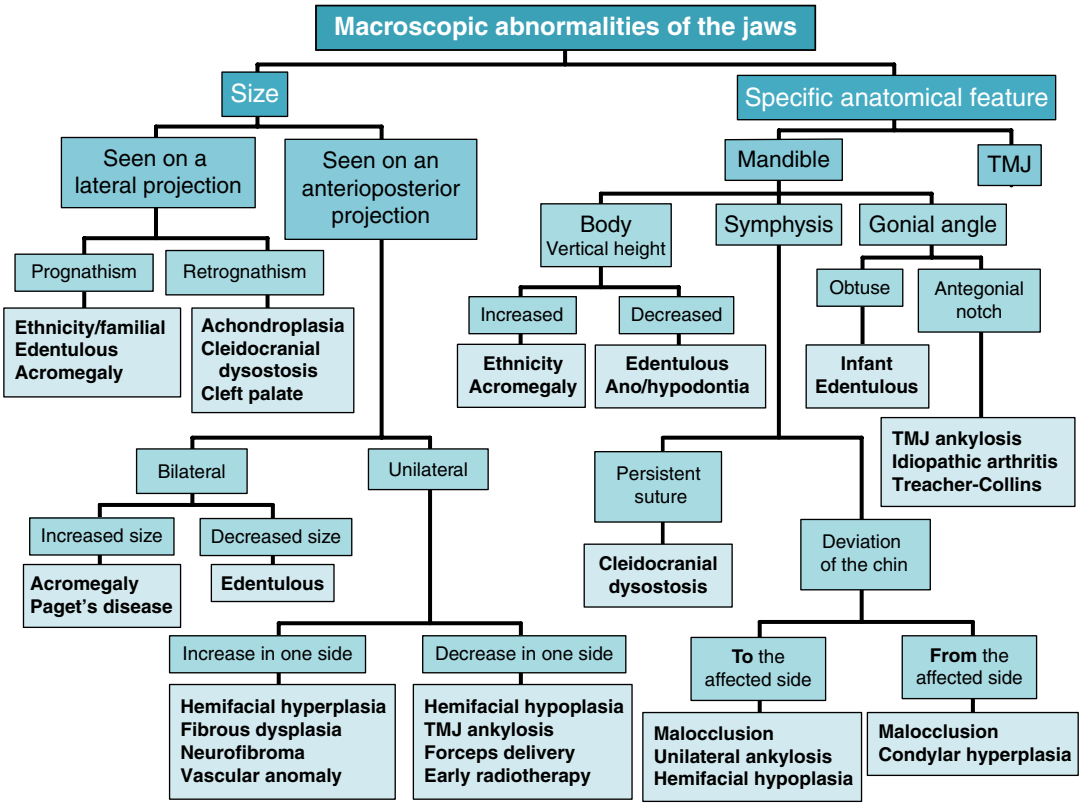


Figure 1.4 Classification of macroscopic abnormalities. TMJ, temporomandibular joint.

Table 1.2 Classification of the main developmental syndromes that cleft or deform the face and the jaws.

		Specific feature/syndrome
Cleft lip and palate	Nonsyndromic	Bilateral cleft lip and palate
		Isolated cleft lip and palate
		Incomplete cleft lip
		Subcutaneous cleft palate
	Syndromic	22 deletion syndrome
		Stickler syndrome
		Pierre Robin syndrome
		Nevoid basal cell carcinoma syndrome
Craniofacial anomalies	Craniosynostosis	Apert syndrome
		Crouzon syndrome
		Pfeiffer syndrome
	Face and jaws alone	Hemifacial microstomia
		Facial clefting
		Moebius syndrome
		Treacher-Collins syndrome

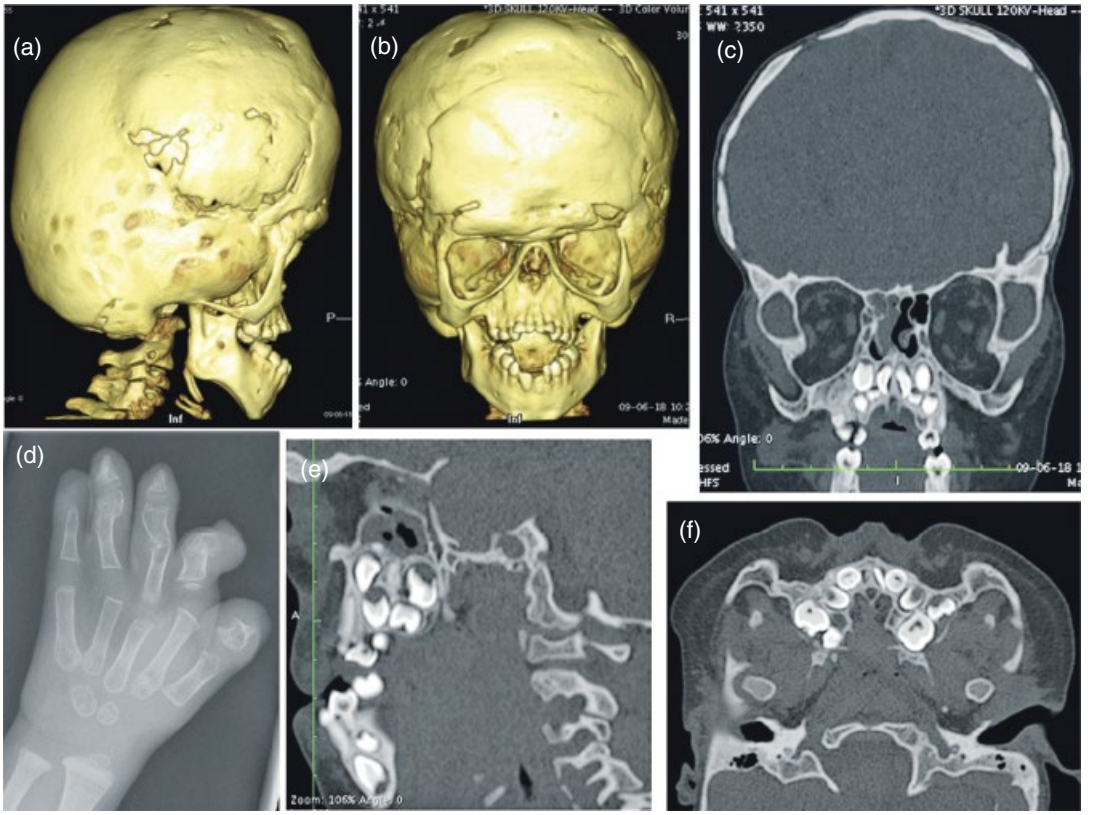


Figure 1.5 Multidetector computed tomography and plane film of the hand of a patient with Apert's syndrome, an acrocephalosyndactyly characterized by malformations of the skull, face, hands, and feet. The first three are displayed in this figure. The coronal sutures of the skull in this case are prematurely closed, resulting in a brachycephalic skull which is short, but high (a and b). This shape is termed acrocephaly. The growing brain, though markedly constrained, is causing variable thinning of the skull (c). (d) Displays deformity of the hand. The mandible and maxilla are hypoplastic because the first brachial arch from which they develop is affected (a and b). The hypoplastic maxilla results in overcrowding of the developing teeth (c–f).



Figure 1.6 Large field-of-view cone-beam computed tomography (CBCT) displaying cleft palates. (a) Coronal reconstruction of the CBCT dataset displaying a cleft on the left side. This reconstruction is at the level of the first molar. The nasal septum has fused normally with the normal part of the hard palate (HP). The patient is wearing an orthodontic appliance. Its metal clasps have created a metal artifact at the level of the crowns of the maxillary teeth. (b) Coronal reconstruction of the CBCT dataset through the apex of the orbit, displaying a bilateral cleft which has created a large defect in the middle of the HP. (c) The axial reconstruction of the same dataset as (b) exhibits the bilateral clefts passing through the alveolar ridge in the lateral incisor position. The shape of the soft tissue denoting the upper lip reveals a repaired bilateral cleft lip.

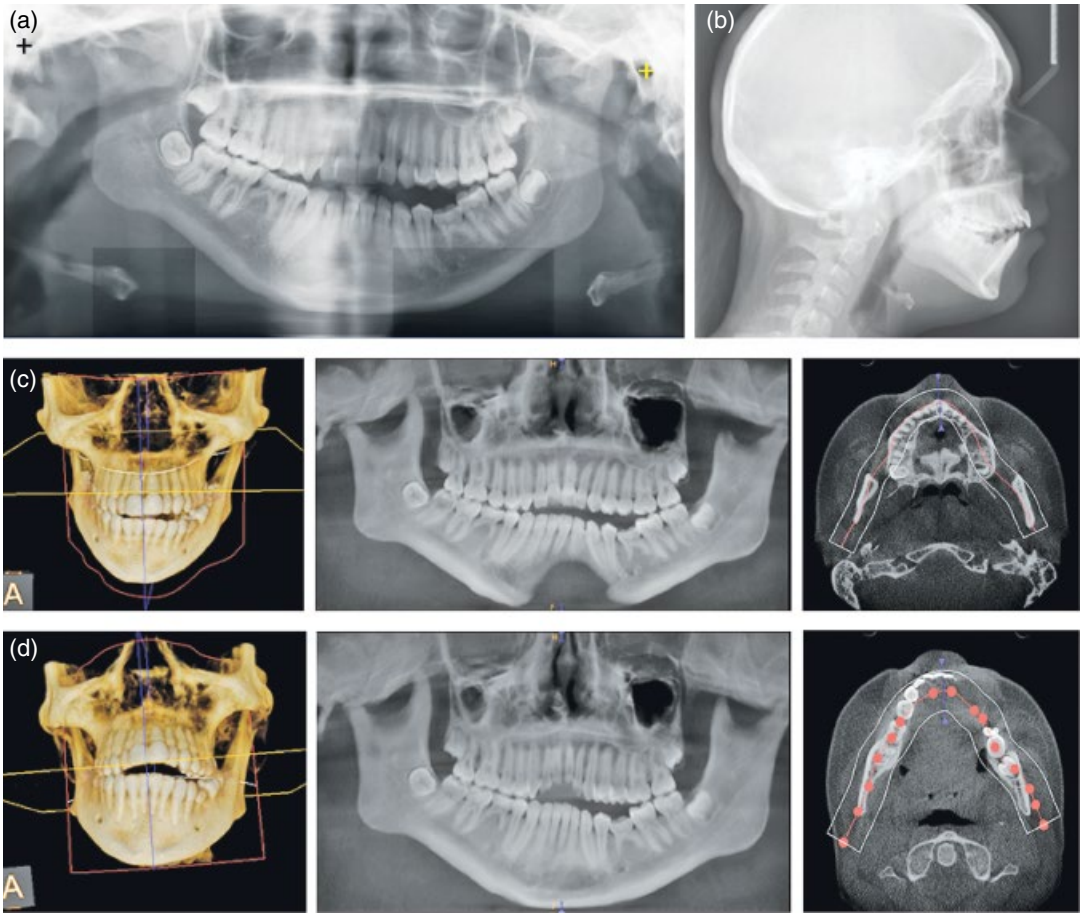


Figure 1.7 Investigation of marked asymmetry of the jaws using conventional panoramic radiography, lateral cephalometry, and large field-of-view cone-beam computed tomography. (a) The marked asymmetry of the jaws on the panoramic radiograph is real and not due to defective technique. The crosses mark the position of the external acoustic meatus (a black cross on the right side and a yellow cross on the left side). (b) A lateral cephalogram displaying the lateral soft-tissue profile of the face in addition to that of the facial skeleton. The top of the skull has been cropped, reflecting the current protocol recently approved by the American Board of Orthodontics in order to reduce the radiation to children. (Credit to the University of British Columbia's Dr. David Kennedy, deputy director of the Graduate Orthodontic program, and Ms. Sabina Reitzik, Oral and Maxillofacial Radiology faculty, for driving this issue forward.) The line of images at (c) represent the three-dimensional (3D) reconstruction, the panoramic reconstruction, and the axial reconstruction of the maxilla at the level of the hard palate, displaying asymmetry. The "defect" in the anterior mandible is due to the thickness chosen for the panoramic reconstruction of the maxilla not including that part of the mandible. The line of images at (d) represent the 3D reconstruction, the panoramic reconstruction, and the axial reconstruction of the mandible at the level of the atlantoaxial joint. The "absent" crowns of the maxillary incisors reflect the narrow thickness of this panoramic reconstruction of the mandible. The whole examination reveals hypoplasia of both the maxilla and the mandible on the right side.

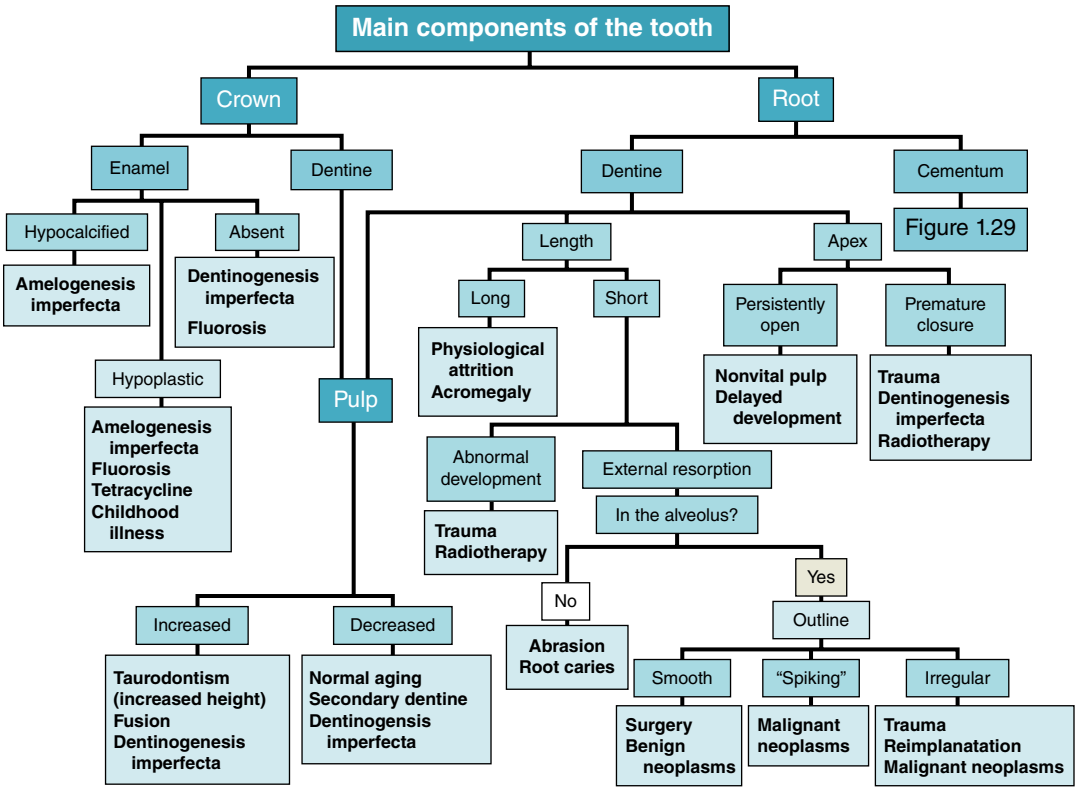


Figure 1.8 Those lesions other than caries which affect the main components of the tooth, namely the enamel, dentine, and pulp. Some important radiological features such a root resorption are also displayed.

create space for further growth within the bony jaws. The borders of this radiolucency give a further clue to their intrinsic behavior. Encapsulated benign neoplasms and many uninfected cysts grow at a moderate pace and are generally well defined. They may even have a cortex. Infected lesions and malignancies are generally associated with a poorly defined margin, reflecting their more aggressive infiltrative expansion into previously normal bone. Sometimes, if the infected lesion becomes less virulent, the adjacent bone may respond by laying down more bone on the trabeculae, thickening them, thus resulting in sclerosis.

Slow-growing lesions, such as most cysts and encapsulated neoplasms, can displace teeth and adjacent structures such as the mandibular canal and cortices. More aggressive lesions are more likely to resorb them. Some malignancies, such as a *squamous cell carcinoma*, will destroy structures with very little displacement, whereas others will provoke a periosteal reaction, such as the onion layer typical of *osteogenic sarcoma* or *Ewing's tumor*. Such a periosteal reaction can also occur in *chronic osteomyelitis*. These periosteal reactions are frequently seen in the extragnathic skeleton [6], but are infrequently seen in the jaws.

After the lesion has been properly imaged and reviewed, clinicians reach the point at which they want to identify the lesion. Because the aim at this stage is to achieve, if possible, a definitive diagnosis,

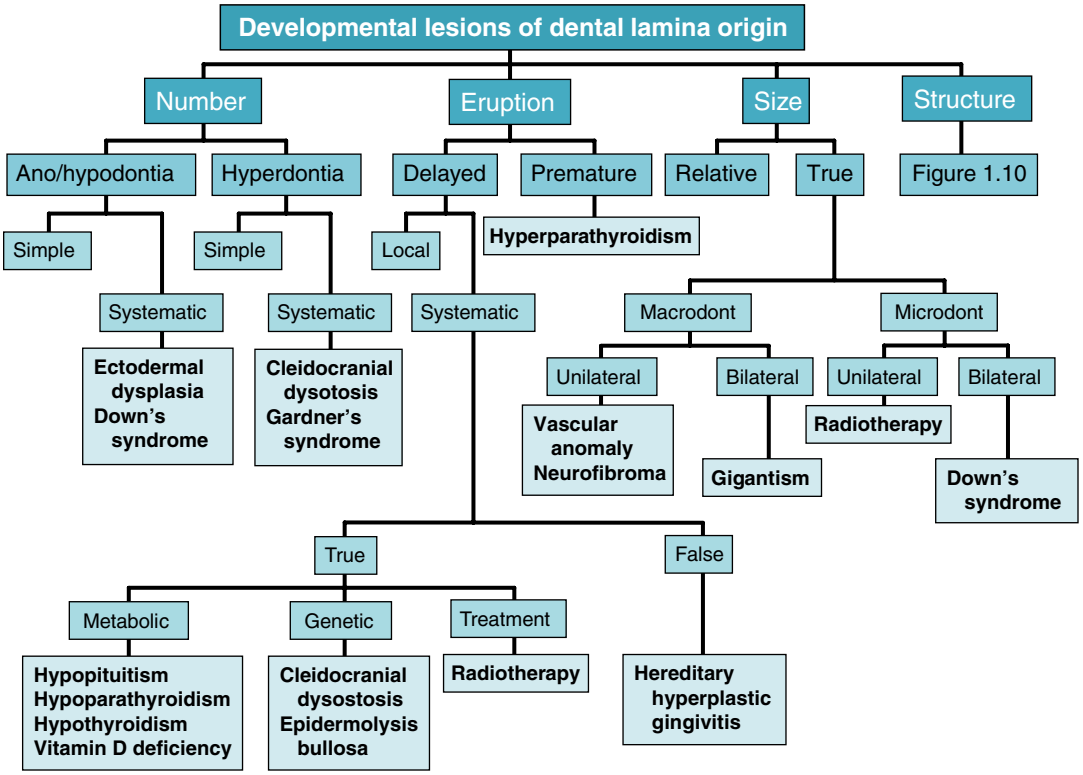


Figure 1.9 Classification of developmental lesions of dental lamina origin – number and size of teeth and their eruption.

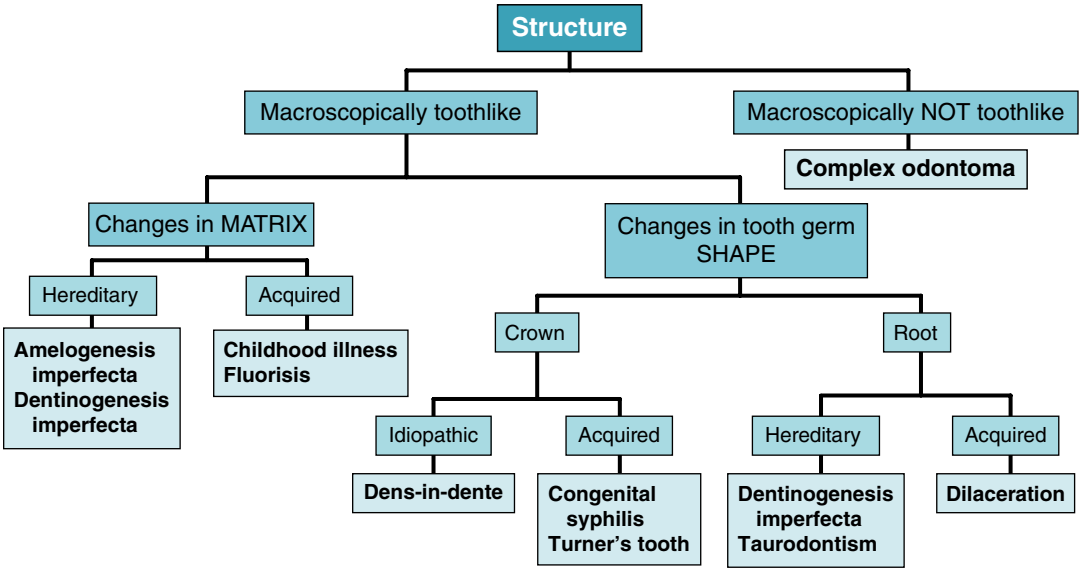


Figure 1.10 Classification of developmental lesions of dental lamina origin – structure.

it follows that this is best accomplished if the images of the lesion have been scrupulously reviewed. To this end, I developed the rule of the "Five Ss" (shade, shape, site, size, and surroundings) and its ancillary "Three Ds" (diameter, density, and displacement). There are many lesions that can be definitively diagnosed at this stage, but some require further investigation, which could include advanced imaging. Although a radiological feature as distinctive as the 'tennis-racket' pattern (Figure 1.32) has a high specificity for the odontogenic myxoma, not all myxomas display it. Predictive values (sensitivity, specificity, positive predictive value and negative predictive value) [7] will be considered later in Chapter 3. Therefore, most lesions require two or more radiological and/or clinical features for a provisional diagnosis.

In order to ensure that the most appropriate investigations are applied, the provisional diagnosis should be restricted to no more than three lesions if possible, placing the most likely in the first position so that the most appropriate investigation can be performed to determine whether it is that lesion. An important exception to this "most likely" rule is the potential seriousness of outcome of the lesions. Table 1.3 compares clinical outcomes according to a 10-step (0 through 9) hierarchy of seriousness of outcomes. The higher-placed lesions have the more serious outcomes.

The selection of lesions can vary among clinicians, depending upon that particular lesion's presentation and frequency within a particular clinician's patient pool. The age, gender, and ethnic origin of the individual patient and site of predilection are perhaps overemphasized in most teaching programs. The main problem with this is that many lesions frequently present first outside their expected age ranges. Occasionally, this expected age range may simply be out of date. An example is fibrous dysplasia: the majority in a recent systematic review first presented in the third decade and older.

The *relative period prevalence* (RPP) [8] was developed to indicate better to the clinician reader of a report the likelihood of a particular lesion presenting within the reported community per year of that report. This has been set out for the most frequent lesions registered in the pathology files of a major center in the United Kingdom in Table 9.1. This is an average for that particular report, depending upon the total number reported and the number of years covered by the report. The RPP of most of the most important and/or frequent lesions affecting the face and jaws in this textbook is included in all accompanying tables more descriptively as "mean number per year per report."

Another source of inaccuracy is that lesions are often superficially reported not only dependent upon their RPP, but on the proportion or percentages of the other lesions within the same group of lesions, such as odontogenic neoplasms [9]. The latter is substantially dependent upon the edition of the WHO classification of odontogenic neoplasms used. Many previously classified odontogenic neoplasms are no longer formally considered as such. An example is the cementifying fibroma (then later combined with the "ossifying fibroma," previously considered to be a separate lesion, as the *cemento-ossifying fibroma*), once considered by the WHO's 1971 edition [10] to be an odontogenic neoplasm, is now considered to be a wholly osseous neoplasm, the ossifying fibroma. Some other lesions have since been reclassified as neoplasms, only to subsequently again be classified as cysts. The *parakeratotic variant of the odontogenic keratocyst*, a cyst according to the

Table 1.3 Scale of severity of outcomes/potential severity of outcomes of oral maxillofacial radiology.[a]

9	***Resection, but high likelihood of recurrence or metastasis***
	Poorly differentiated squamous cell carcinoma
	Osteosarcoma
	Fibrosarcoma
	Adenoid cystic carcinoma (neural spread)
8	***Resection and lower likelihood of recurrence or metastasis***
	Well-differentiated squamous cell carcinoma (qualified by site)
	Chondrosarcoma
	Ameloblastic carcinoma
	Mucoepidermoid carcinoma
7	***Resection and likelihood of recurrence or metastasis rare***
	Verrucous carcinoma
	Solid ameloblastoma
	Odontogenic myxoma
	Dentinogenic ghost cell tumor (DGCT)
6	***Enucleation and cytotoxic treatment (Carnoy's solution)***
	Unicystic ameloblastoma (provided not affecting posterior maxilla)
	Keratocystic odontogenic tumor (KCOT)
5	***Simple enucleation and high chance of recurrence (recurrence rate of 10% and over)***
	Aneurysmal bone cyst (ABC)
	Ameloblastic fibroma
	Ossifying fibroma (OF)
	Glandular odontogenic cyst (GOC)
	Cementoblastoma
	Pleomorphic (salivary) adenoma (PSA)
	Calcifying epithelial odontogenic tumor (CEOT)
	Calcifying odontogenic cyst (COC)
4	***Simple enucleation and little chance of recurrence***
	Adenomatoid odontogenic tumor (AOT)
	Osteoblastoma/osteoid osteoma
	Orthokeratinized odontogenic cyst (OOC)
	Giant cell lesions (large ones may need resection)
	Complex odontoma, including ameloblastic fibro-odontoma (AFO)
	Squamous odontogenic tumor (SOC)
	Primordial odontogenic tumor (POT)
	Warthin's tumor
3	***Simple enucleation and no chance of recurrence (in a neoplastic fashion)***
	Periapical radiolucencies of inflammatory origin (PRIO)
	Nasopalatine duct cyst (NDC)
	Dentigerous cyst
	Compound odontoma
2	***Conservative surgery may be required only to improve esthetics***
	Fibrous dysplasia (surgery not indicated unless compelled by esthetics or by risk of blindness)
	Cherubism
	Condensing/sclerosing osteitis (treatment of the affected tooth may result in regression)
1	***No treatment generally required***
	Linqual bone defect (LBD)
	Osseous dysplasia (florid and focal, but *not* expanding forms, which require treatment)
	Mucosal antral pseudocyst
	Osteoma – solitary, nonsyndromal (ivory type could be surgically difficult)
	Simple bone cyst (SBC)
	Idiopathic osteosclerosis/dense bone island

[a] This table was inspired by the Richter scale for earthquakes. The scale is based on the general current treatment paradigms for each lesion.

WHO's 2005 edition [11], became the *keratocystic odontogenic tumor* (KCOT), a neoplasm. The same has also happened to the *calcifying odontogenic cyst*, which is now according to the WHO's 2005 edition the *calcifying cystic odontogenic tumor* (CCOT) [11]. The WHO's 2017 edition changed both KCOT and CCOT back to their old names and their cystic rather than neoplastic status [2]. Such changes render reliance on proportions or percentages increasingly unreliable. Since the RRP remains unaffected by these continual reclassifications, it will be retained and given for every lesion upon which a systematic review has been performed.

The nomenclature used throughout will be, as far as possible, that used by the WHO's 2017 edition [2], excepting those lesions where there are strong grounds for preservation of that in the WHO's 2005 edition [11]. Common synonyms will appear in parentheses with the first appearance of each term in each chapter. As far as possible, the morphology code of the International Classification of Diseases for Oncology (ICD-O) will be provided, along with the invaluable behavior codes (/0 for benign; /3 for malignant, and /2 for uncertain). Although the vast majority of lesions are diagnosed and treated in oral and dental practice solely on clinical and radiological criteria, the overwhelming majority of such lesions are sequelae of dental caries. There are many other lesions, such as cysts and neoplasms, in which a definitive diagnosis based on their histopathology is necessary.

After a diagnosis has been made, the clinician has a choice of three broad approaches to the lesion's management. These have been summarized in the rule of the Three Rs. *Refer* (to an appropriate colleague) and *review* are obvious, whereas *recipe* (treatment) requires an explanation. This is derived from the apothecary's "barred R," now often reduced to *Rx*, derived from the Latin imperative *Recipe!* meaning *Take!* or *Receive!* This is still printed at the top-left corner of prescriptions for pharmaceuticals and/or other treatment.

In dentistry, the treatment delivered will vary with the specialty. The bulk of treatment performed by general or family dentists will be to prevent or address the sequelae of dental caries and periodontal bone loss, assisted by implantologists. Orthodontists will address misplaced teeth and developmental disorders of the jaws. Surgeons assist their colleagues with implant placement, removal of unerupted teeth, and removal of lesions, mainly cysts and neoplasms. Although some chapters or sections will review the technology that may assist dental colleagues in these tasks, it is the diagnosis, management, and follow-up of lesions that this textbook has set out to address.

1.3 Radiological Features

The radiological features central to the diagnosis of oral and maxillofacial lesions are encapsulated as the Five Ss and Three Ds.

1.3.1 SHADE

Shade reflects the presentation of a lesion or feature on a particular imaging modality and the terminology used is peculiar to each modality: for example, hypo/hyper-echoic, -attentuating, -intense, and -avid for *ultrasound*, CT, MRI, and *positron emission tomography* (PET), respectively. On CR, shade reflects the *radiodensity* of the lesion or feature under consideration and is its most obvious radiological attribute.

The radiodensity of a lesion observed by CR is usually described as one of three manifestations: *radiolucency*, *radiopaque*, and *mixed*. The radiolucency appears

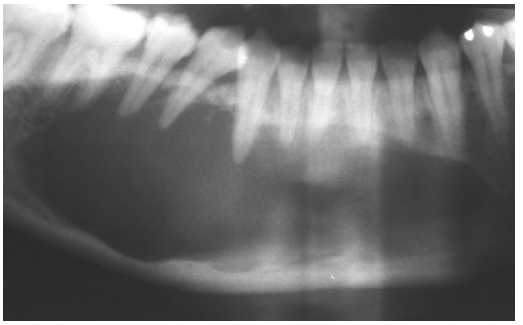


Figure 1.11 Panoramic radiograph displaying a well-defined unilocular radiolucency within the mandible, extending from the right first molar's distal root to the junction between the contralateral canine and first premolar. The right lower border of the mandible has been eroded and displaced downward. The root of the right first premolar has been displaced distally. The root of the second premolar displays resorption. This is a unicystic ameloblastoma. Note 1: This panoramic radiograph had not been made using the optimal technique. It is in the head-down position. Note 2: The apparent root resorption or shortening of the teeth in the anterior sextant is most likely to be an artifact, due to its appearing outside the focal trough of the panoramic radiography. This happens particularly in the anterior sextant. Note 3: The horizontal band superimposed upon the roots of the right molars is the secondary image of the contralateral lower border of the mandible. Source: MacDonald-Jankowski, D.S., Yeung, R., Lee, K.M., and Li, T.K. (2004). Ameloblastoma in the Hong Kong Chinese. Part 2: systematic review and radiological presentation. *Dentomaxillofac. Radiol.* 33: 141–151.

black and represents an absence of the bone type normal for that site (Figure 1.11).

The radiopacity appears *white* and represents an excess of mineralized tissue – frequently abnormal mineralized tissue (Figure 1.12). This abnormal tissue is usually laid down by cells (almost invariably abnormal bone cells and their variants) due

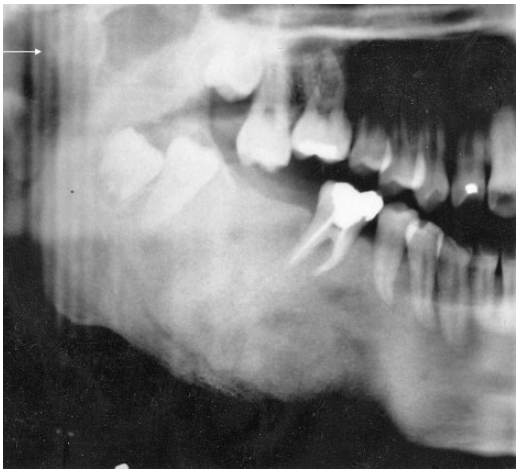


Figure 1.12 Panoramic radiograph displaying a generalized radiopacity of the posterior sextant. The mandibular canal has been reduced in thickness and displaced to the lower border of the mandible. Two unerupted molars are embedded within the vertical ramus. The lesion has expanded the body of the mandible vertically. This is fibrous dysplasia. Note 1: The mandibular canal is very obvious here as a radiolucent structure set against a background of abnormal (in this case dysplastic) bone. It has not only been displaced downward in this instance, but also reduced in diameter and with a slightly irregular course. Note 2: The radiolucent presentation of the maxillary alveolus is a result of the superimposition of the air-filled oral cavity upon it. It may be prevented by instructing the patient to raise the tip of his/her tongue to contact the hard palate. Note 3: The secondary image of the contralateral mandible is superimposed upon the upper two-thirds of the vertical ramus. Note 4: The soft-tissue images of the soft palate and dorsum of the tongue are superimposed upon the upper third of the vertical ramus. The air space of the residual oral cavity between them presents as a radiolucent line, which has been mistaken to represent a fracture of the vertical ramus in other cases. Source: MacDonald-Jankowski, D.S. (1999). Fibrous dysplasia in the jaws of a Hong Kong population: radiographic presentation and systematic review. *Dentomaxillofac. Radiol.* 28: 195–202.

to dysplastic or neoplastic processes and may show some sort of structure. It is not always possible to determine the process by histopathology, as three clinically and radiologically very different lesions, fibrous dysplasia (Figure 1.12), ossifying fibroma (Figure 1.13), and osseous dysplasia (formerly known as cemento-osseous dysplasia; Figure 1.14), display similar histopathological appearances, those of *fibro-osseous lesions*. This is discussed in detail in Chapter 10. Sometimes the bone is not per se abnormal, but merely thickened trabeculae, as found for DBIs (Figures 1.15 and 1.16).

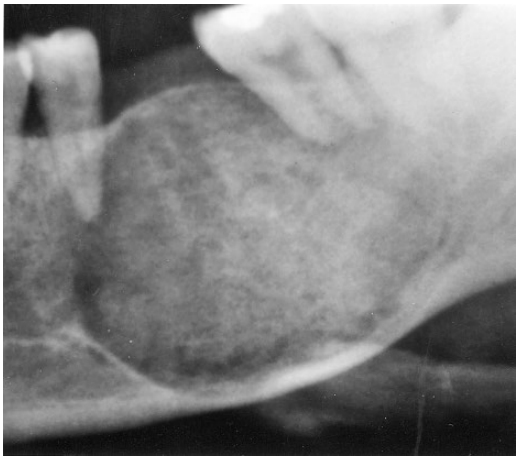


Figure 1.13 Panoramic radiograph displaying an ossifying fibroma. The lesion is well defined. It has a capsule of varying thickness. It has displaced downward the lower border of the mandible and displaced upward the alveolar crest. It has also displaced the mandibular canal toward the lower border of the mandible. It has displaced the root of the premolar forward and the roots of the molar distally. Its central radiodensity has a cotton-wool pattern. Note 1: The partial superimposition of the hyoid bone on the lower border of the mandible is an indicator that the exposure had been made in the chin-down position. Note 2: The soft tissue of the gingival mucosa is observed in the edentulous space. Source: MacDonald-Jankowski, D.S. (1998). Cemento-ossifying fibromas in the jaws of the Hong Kong Chinese. *Dentomaxillofac. Radiol.* 27: 298–304.



Figure 1.14 Panoramic radiograph exhibiting radiopacities in all four posterior sextants. The mandibular lesions are confined to the alveolar process; that is, they are found above the mandibular canal, which can be seen in places. This is a case of florid osseous dysplasia. Note: The relative radiolucency of the anterior sextant of the maxilla is due to the superimposition of the residual oral cavity.

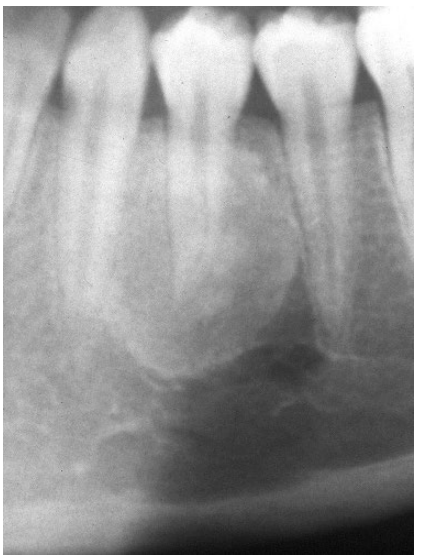


Figure 1.15 Panoramic radiograph displaying a well-defined radiopacity associated with the root of the first premolar. The periodontal ligament space is intact and of regular thickness, separating it from the radiodense bone. This tooth displays an intact crown; there is no caries or restoration. There is also no periodontal bone loss. The radiopacity is in direct contact with the adjacent normal bone; there is no radiolucency space between them. This dense bone island is also known as idiopathic osteosclerosis.

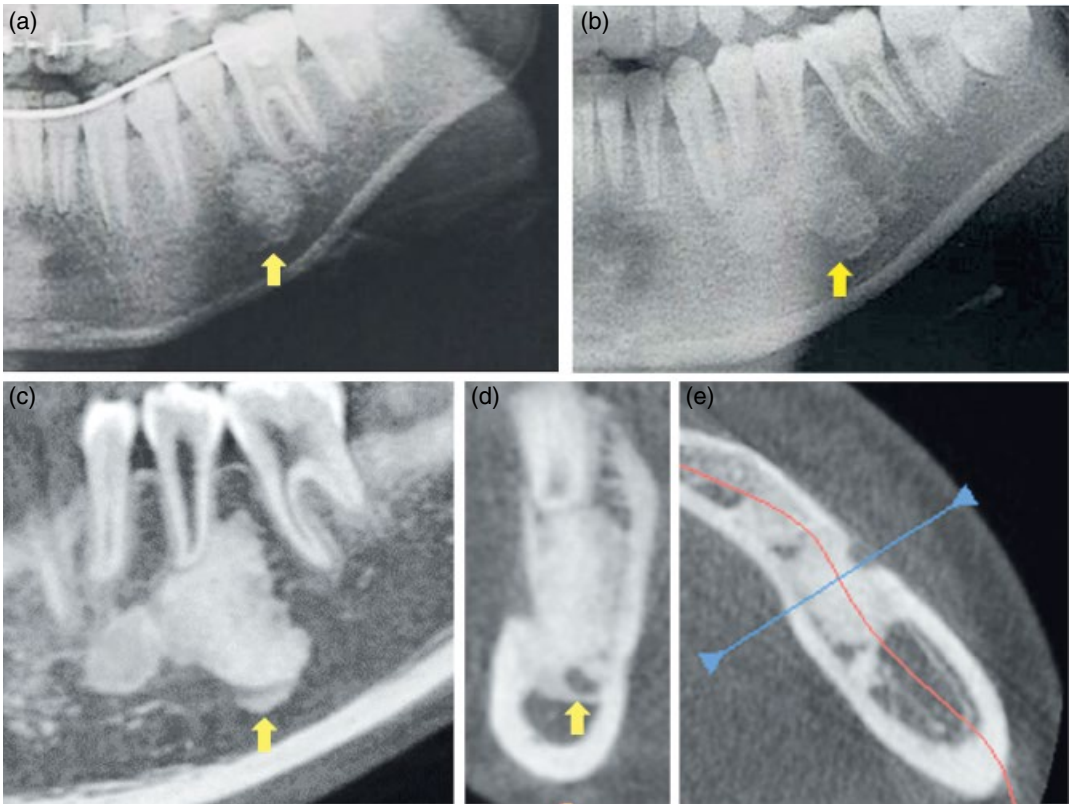


Figure 1.16 Conventional panoramic radiographs (a and b) and cone-beam computed tomography (CBCT) (c–e) of a dense bone island (DBI). The DBI (also called idiopathic osteosclerosis) is the most frequently observed radiopaque lesion of the jaws. Clinically it is distinguished from (periapical) condensing sclerosis by a positive pulp vitality test. It classically is observed in the alveolus/alveolar process (wholly or substantially above the mandibular canal in the mandible). It arises within the alveolus. It does not cause expansion, displacement, or resorption of roots. Nevertheless, it can interfere with orthodontic treatment. (a) Displays a round DBI between the apices of the lower left second premolar and the mesial root of the first molar teeth. The radiolucent band around it is the Mach band effect (see Chapter 2). The DBI has reached the mandibular canal (yellow arrows). Three years later (orthodontic treatment has been completed) its relationship to the mandibular canal is unchanged, but it has no relationship to the first molar. It is larger and has a separate, but not contiguous, DBI. (c) A panoramic radiographic reconstruction of the CBCT dataset. It reveals that the lesion is continuous with the trabeculae, as expected of a DBI. It is separated from the premolar root by a normal periodontal space. (d) An axial reconstruction. This is a view from below. The red line represents the clinician's selected line of the arch from which the transaxial reconstruction in (e) is formatted. The DBI is seen in continuity with the buccal and lingual cortices. (e) The transaxial reconstruction through the mental foramen reveals that the DBI has partially encompassed the mandibular canal. Source: Dr. David Yang, Oral & Maxillofacial Surgeon, Vancouver, Canada.

Occasionally mineralization can also be dystrophic; this is a deposition of mineral in soft-tissue lesions, such as calcification of lymph nodes (Figure 1.17), tonsils (Figure 1.17), sialoliths, antroliths, acne scars, and so on. This is not laid down by bone cells, but still may display some structure, usually as concentric layers of accretion.

Radiopacities can arise from variants of anatomy such as mineralization of the stylohyoid complex (Figure 1.18). The normal (not mineralized) soft-tissue structures, of which the easiest to recognize are the tongue and soft palate, can be present on panoramic radiographs and lateral cephalograms (Figure 1.18) by virtue of their being silhouetted against an air-filled space. Similarly, the ear lobe (Figures 1.18 and 1.19b) is also very frequently apparent. Fractures can result in opacities if the fractured ends overlap (Figure 1.18). Incorrect panoramic radiographic technique (head down) can result in the superimposition of the body of the hyoid on the body of the mandible, resulting in a radiopacity (Figure 1.19a).



Figure 1.17 Panoramic radiograph displaying a number of normal and abnormal radiopacities. Structures, which are normally composed of soft tissue, can present as radiopacities either by being silhouetted against air, as already seen for the soft palate and tongue, or becoming calcified. The latter can occur secondary to an infection. Classically this infection was tuberculosis. The calcified structures are the lymph nodes (cervical jugulodigastric and submandibular nodes) and the palatine tonsil (small opacities superimposed upon the mandibular foramen). This calcification is dystrophic. Another calcified, but almost always normal, structure is the styloid process. Note 1: The soft palate and tongue are clearly visible. Note 2: The horizontal band of smeared radiopacity occupying the superior two-thirds of this image represents the contralateral mandible.



Figure 1.18 Panoramic radiograph displaying a normal-sized styloid process (it extends no lower than the mandibular foramen; see Chapter 10 for more details) and a calcified stylohyoid ligament reaching the hyoid bone. The lesser horn is presented as a round radiopacity superimposed upon the superior margin of the hyoid bone. These are also normal features. Note 1: The pinna of the ear is superimposed upon the styoid process. Note 2: The condyle is fractured and displaced anteriorly. As it overlaps the superior vertical ramus, an increased radiopacity occurs at the site of this overlap. Note 3: The black line delineating the line of the fractured condyle represents the Mach band effect and is discussed further in Chapter 2. Note 4: The soft palate and dorsum of the tongue are in contact and the radiolucent line observed in Figure 1.12 is substantially absent. Note 5: The superior half of the image is occupied by the secondary image of the contralateral mandible.

In a properly performed panoramic radiograph, the hyoid bone is usually observed below the mandible (Figure 1.19b).

Mixed radiodensity describes a lesion presenting as a white area/s within a black area (Figure 1.20). This generally represents the deposition of mineralized tissue in an area where the bone type normal for that area had been previously removed to create space for the lesion, which subsequently undergoes mineralization.

Those lesions that substantially present as radiolucencies are considered in Chapter 9, whereas those that most frequently present as either complete radiopacities or mixed lesions will be considered in Chapter 10.

1.3.2 SITE

A solitary localized or single lesion suggests a local cause, whereas multiple lesions – particularly those affecting several sextants – suggest a systemic cause that could have general health implications. Although generally if enough cases of a lesion are reported they divide evenly between right and left, it is nevertheless important to record this feature correctly to avoid inappropriate investigations or treatment for that particular patient. It is also clearly important to record the jaw and sextants properly, not only for the above reason, but because some lesions have particular dispositions for a particular jaw and sextant.

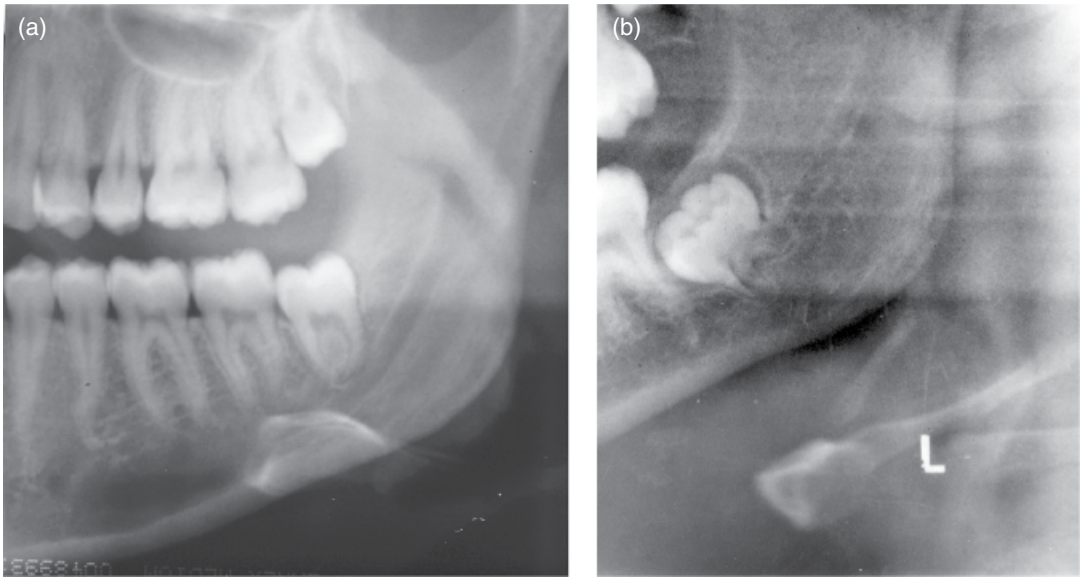


Figure 1.19 Panoramic radiographs displaying the hyoid bone. (a) Although this panoramic radiograph is correctly taken, the hyoid bone is superimposed upon the lower body of the mandible. This may be misinterpreted as a radiopaque lesion within the mandible. It is well defined and delineated by the black line of the Mach band effect. (b) The components of the hyoid bone, which are frequently apparent on panoramic radiographs and lateral cephalograms. The body and lesser and greater horns are observed as distinct entities. There are two depictions of the greater horn: the smaller and better detailed is the ipsilateral, whereas the longer and poorer detailed is the contralateral. The radiolucent area between the contralateral greater horn and the body represents the joint between them, which is frequently patent. Note 1: The secondary images of the contralateral mandible appear in both (a) and (b). Note 2: There is a small air-filled space between the soft palate and the dorsum of the tongue, which is superimposed upon the mandibular foramen in (a). Note 3: The pinna of the ear in (b).

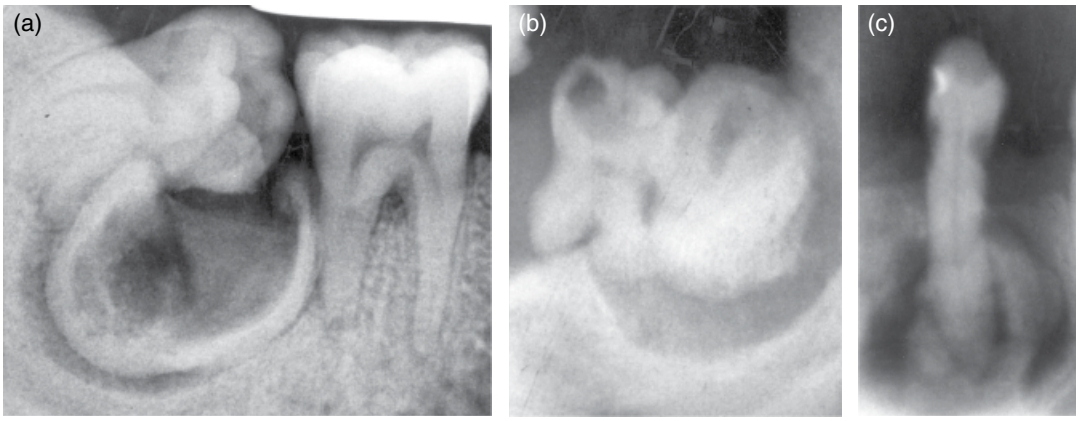


Figure 1.20 Panoramic radiographs displaying radiopaque lesions. (a) A well-defined radiolucency within which there is an annular (ringlike) radiopacity. This is an annular odontoma, which is a subset of the complex odontoma. (b) A well-defined radiolucency, associated with an almost wholly extruded molar tooth. Within the radiolucency and associated with the molar tooth is a well-defined radiopacity. This is a complex odontoma. (c) A radiolucency at the apex of an incisor. Within the radiolucency are several radiopacities. This is a case of osseous dysplasia. Source: (b) Reproduced with permission from MacDonald-Jankowski, D.S. (1996). Odontomas in a Chinese population. *Dentomaxillofac. Radiol.* 25: 186–192.

Identify the affected jaw as the maxilla or mandible and the sextants as either anterior or posterior. The junction between the anterior (incisors and canines) and posterior (premolars and molars) sextants is arbitrarily defined by a vertical line passing between the canine and first premolar tooth. In a medical report the teeth are usually identified by their expanded name, such as "right maxillary canine" or "left third molar," whereas in dental reports they are identified by their dental notation. Of the several notations in use, the most frequently used are the Fédération Dentaire International (FDI) or American (also called universal) systems. These are set out in Figure 1.21.

Those lesions primarily affecting the maxillary antrum often present quite differently radiologically than they do in the mandible and anterior sextant of the maxilla (Figure 1.22). The lesions that affect the maxillary antrum will be considered separately in Chapter 11.

In order to differentiate between the alveolar and basal portions of the mandible, the relationship of the lesion to the mandibular canal should be reviewed (Figures 1.16 and 1.23). The equivalent feature for the maxilla is the hard palate (HP; Figure 1.22). This is readily observed on panoramic radiographs or lateral cephalograms.

A lesion arising above the mandibular canal is in the alveolus and is therefore likely to be an *odontogenic* lesion (see Figures 1.13 and 1.23), whereas a lesion below the mandibular canal is likely to be a *nonodontogenic* lesion (Figure 1.24). Note: the term "odontogenic" as used in this context refers both to those lesions which are derived directly from the tissues which give rise to the teeth, and also to those lesions whose development is in some essential way influenced by these tissues. The term "nonodontogenic" in this context refers to those lesions which are observed elsewhere in the skeleton outside the jaws (viz. extragnathic) and whose development is not likely to have been influenced by the aforementioned tissues. Although the *simple bone cyst* (SBC) has been reported elsewhere in the skeleton, its presentation predominantly in the alveolus (whose presence is dependent on the presence of teeth) indicates that it has a relationship to the dental tissues (Figure 1.25). In some cases SBC arises

FEDERATION DENTAIRE INTERNATIONAL NOTATION (FDI)																
Maxilla	**Right Posterior Sextant**					**Anterior Sextant**						**Left Posterior Sextant**				
	Molars			Premolars		Can.	Incisors				Can.	Premolars		Molars		
	8	7	6	5	4	3	2	1	1	2	3	4	5	6	7	8
	18	**17**	**16**	**15**	**14**	**13**	**12**	**11**	**21**	**22**	**23**	**24**	**25**	**26**	**27**	**28**
Mandible	**48**	**47**	**46**	**45**	**44**	**43**	**42**	**41**	**31**	**32**	**33**	**34**	**35**	**36**	**37**	**38**
	8	7	6	5	4	3	2	1	1	2	3	4	5	6	7	8
	Right Posterior Sextant					**Anterior Sextant**						**Left Posterior Sextant**				

AMERICAN TOOTH NOTATION OR "UNIVERSAL" SYSTEM																
Maxilla	**Right Posterior Sextant**						**Anterior Sextant**					**Left Posterior Sextant**				
	8	7	6	5	4	3	2	1	1	2	3	4	5	6	7	8
	1	**2**	**3**	**4**	**5**	**6**	**7**	**8**	**9**	**10**	**11**	**12**	**13**	**14**	**15**	**16**
Mandible	**32**	**31**	**30**	**29**	**28**	**27**	**26**	**25**	**24**	**23**	**22**	**21**	**20**	**19**	**18**	**17**
	8	7	6	5	4	3	2	1	1	2	3	4	5	6	7	8
	Right Posterior Sextant					**Anterior Sextant**						**Left Posterior Sextant**				

Figure 1.21 Two of the most commonly used dental notations. Can., canine.

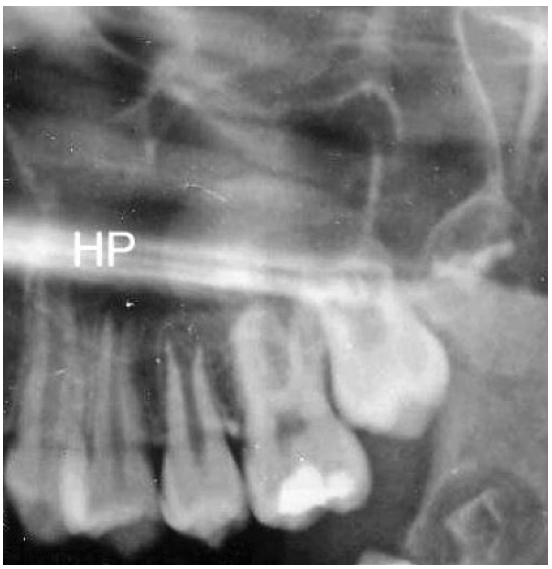


Figure 1.22 Panoramic radiograph displaying a soft-tissue opacity within the maxillary antrum. It is not associated with a carious or heavily restored tooth, which may suggest that the tooth's vitality has been compromised. This lesion is a mucosal antral cyst, also called a pseudocyst. Note 1: The hard palate (HP) presents as two images. The lower is its junction with the ipsilateral alveolus and the upper that with the contralateral alveolus. Note 2: The soft tissue is visualized on a radiograph because it is silhouetted against the air-filled space of the maxillary antrum. This silhouetting is further enhanced by a black line around the mucosal antral cyst, representing the Mach band effect. The same phenomena are associated with the visualization of the tongue, soft palate, and pharynx. Note 3: The root of the second premolar is still developing, as evidenced by the presence of two "inverted chisels." Source: Reproduced with permission from MacDonald-Jankowski, D.S. (2004). Fibro-osseous lesions of the face and jaws. *Clin. Radiol.* 59: 11–25.

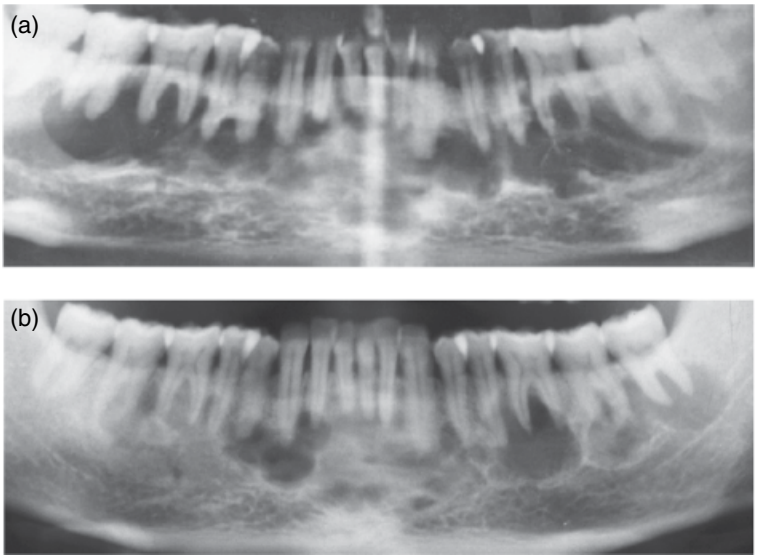


Figure 1.23 (a) Panoramic radiograph exhibiting a well-defined radiolucency, which occupies the entire length of the alveolus. This was a simple bone cyst, which arose from the four original discrete lesions (b). Each of these original lesions recurred after surgery and eventually coalesced into one lesion in (a). Source: (a) Reproduced with permission from MacDonald-Jankowski, D.S. (1995). Traumatic bone cysts in the jaws of a Hong Kong Chinese population. *Clin. Radiol.* 50: 787–791.

in association with osseous dysplasia, an odontogenic lesion (Figure 1.26).

A lesion below the HP (especially on panoramic radiographs) is likely to be an odontogenic lesion, whereas that arising above the HP is likely to be a nonodontogenic lesion (Figure 1.22).

A lesion arising within the mandibular canal is likely to be a neural or vascular lesion.

If the lesion is in the alveolus, its relationship not only to teeth but to a certain part of the tooth or teeth is important to refine further the differential diagnosis. If it is related to the crown of an unerupted tooth, this could suggest its origin within the follicle, whereas its relationship to the root of an erupted tooth with evidence of caries or periodontal disease could suggest an inflammatory cause, and should provoke a testing of the pulp vitality of that tooth. Note: pulp vitality testing is generally recommended for any tooth/teeth that is/are adjacent to a lesion. This clearly becomes less likely if the lesion is separated from the apex by a periodontal ligament space, which is represented by a near uniformly wide (0.2 mm) radiolucent line (Figure 1.27). The precise location of the lesion in relation to the root is important: most inflammatory lesions are associated with the root apex, whereas this is less so if it is associated with the side of the root (Figure 1.28).

The *periodontium* is the overarching term for all tissues that surround and support the tooth. The *periodontal ligament space* (also called *periodontal ligament membrane*) is one of the three components of the periodontium. The other two radiologically apparent components are the *lamina dura of the alveolar bone* and the *cementum of the root*. The main lesions that affect the periodontium have been set out in the flowchart in Figure 1.29. The length of the tooth directly affects the quality of the periodontium by determining the surface area available for periodontal fiber attachment.

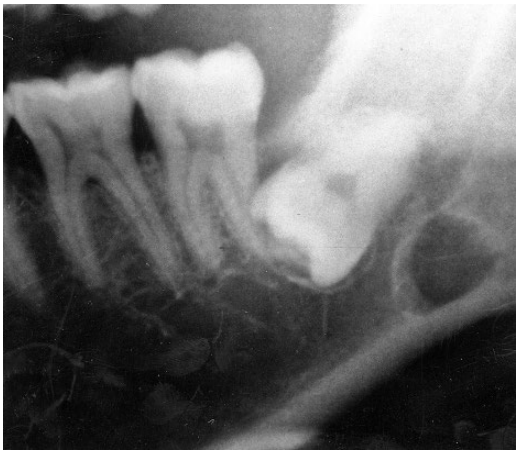


Figure 1.24 Panoramic radiograph exhibiting a well-defined radiolucency between the mandibular canal and the lower border of the mandible. This is the classical presentation of the lingual bone defect. The more radiolucent center represents the ostium on the lingual cortex, which is narrower than the larger defect mushrooming out within the basal process of the posterior mandible. Note 1: The semi-inverted unerupted third molar tooth has a normal follicle. Note 2: It is likely that there is no root resorption of the distal root immediately adjacent to the unerupted tooth. Persuasive evidence for this contention is derived from observation of the periodontal margin on the distal aspect of this root, through the crown of the third molar. Note 3: The horizontal "break" in the lower border of the mandible is caused by the Mach band effect enhancement of the superimposition of the hyoid body upon it.



Figure 1.25 Standard anterior occlusal projection (of the anterior sextant) of the mandible displaying a well-defined radiolucency, which exhibits scalloping between the roots of the anterior teeth. Their lamina dura is intact and they do not exhibit root resorption. The superior portion of the lesion appears to be more translucent than the inferior portion, because of the superimposition of the menton. This is a simple bone cyst. Source: Reproduced with permission from MacDonald-Jankowski, D.S. (1995). Traumatic bone cysts in the jaws of a Hong Kong Chinese population. *Clin. Radiol.* 50: 787–791.



Figure 1.26 Periapical radiolucency of the mandibular molars, displaying a well-defined radiolucency associated with the apices of all three molars and the second premolar tooth. The alveolar-facing margin appears scalloped, whereas there is a septum on the inferior margin. As a result, this lesion is now considered to be multilocular. At the apex of the second molar tooth is a radiopacity. This appears to be dysplastic. This is a simple bone cyst containing an area of osseous dysplasia. Note: The more translucent area in the center of the lesion represents perforation or at least significant erosion of either the buccal or lingual cortex or both. Source: Reproduced with permission from MacDonald-Jankowski, D.S. (1995). Traumatic bone cysts in the jaws of a Hong Kong Chinese population. *Clin. Radiol.* 50: 787–791.



Figure 1.27 Standard anterior occlusal projection displaying an endodontically treated incisor. At its apex is a mature osseous dysplastic lesion. It may be surmised that the lesion presenting to the original clinician was that of a radiolucency. Note: It is not unusual to see such apical lesions associated with root-treated incisors. This suggests that the early radiolucent stage of this lesion had been mistaken for a periapical radiolucency of inflammatory origin. Pulp vitality is an essential investigation when the vitality of a tooth is questioned.

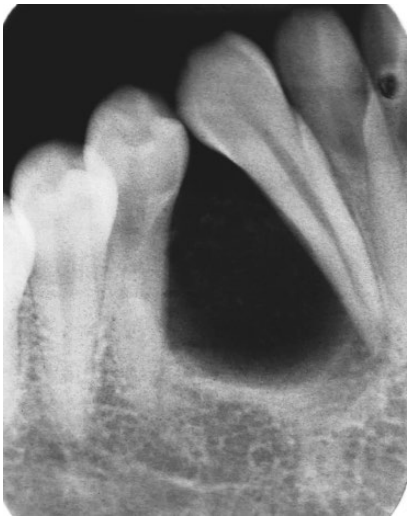


Figure 1.28 Periapical radiograph displaying a well-defined radiolucency between the noncarious and pristine canine and first premolar tooth. A positive pulp vitality test ruled out a lateral radicular cyst. Other lesions that may give this presentation are the lateral periodontal cyst, and the keratocystic odontogenic tumor. At histopathology it was found to be the latter.

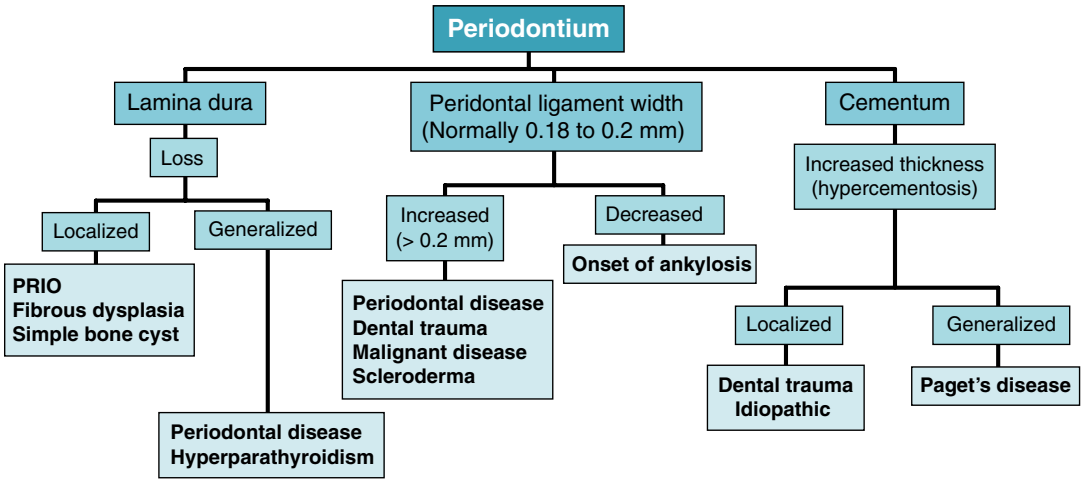


Figure 1.29 Classification of lesions affecting the periodontium. PRIO, periapical radiolucencies of inflammatory origin.

1.3.3 SHAPE

The shape of a lesion may give a clue to its broad behavior. If it has a smooth, rounded shape, it is *unilocular*. Although this shape is typical of less serious lesions such as inflammatory cysts and dentigerous cysts, which can be readily enucleated with a minimal tendency to recur, it is frequently seen in *unicystic ameloblastomas* (Figure 1.30). Sometimes a generally rounded shape may present with an undulating or scalloped periphery (Figure 1.25) typical of SBCs.

Those lesions whose outline has been broken into loculi by "septae" are *multilocular*. This shape is indicative of more serious lesions, which require more radical treatment, even resection, because of their marked propensity to recur. Such lesions are the *solid ameloblastoma*, KCOT, and odontogenic myxoma. The multilocular radiolucency can present with three basic patterns: soap bubble, honeycomb (Figure 1.31), and tennis racket (Figure 1.32). With the exception of the tennis racket pattern, which is virtually pathognomic for odontogenic myxoma, the other two patterns have so far not shown a particular predilection for any specific lesion.

The clinician should not confuse multilocular with scalloping (Figure 1.25)!

It should be noted that some KCOTs, particularly those observed in the younger and small in size patient (who thus may themselves be at an early stage in their life history), are generally unilocular, whereas those cases observed in the older and larger patient may appear multilocular. This is particularly so in sporadic/nonsyndromic KCOTs. Although multilocularity may represent the maturity of a lesion [12] rather than its tendency to recur if inadequately treated, the multilocular shape may complicate attempts at conservative treatment, making enucleation



Figure 1.30 Panoramic radiograph displaying a well-defined radiolucency within the posterior sextant of the body of the mandible. Although there are two unerupted molars about its periphery, it is more intimately associated with the second molar, which has been displaced to the lower border of the mandible. The horizontally inclined third molar's follicular space is partially evident and is less likely to be contiguous with the larger lesion. The lesion almost wholly surrounds the second molar tooth, including its root. The absence of an attachment of the lesion at or within 1 mm of the cementoenamel junction and root resorption of the distal root of the first molar tooth suggest that the lesion is very unlikely to be a dentigerous cyst. This is a unicystic ameloblastoma. Note 1: The secondary image of the lower border of the mandible is partially superimposed upon the radiolucency. The inferior third displays the radiodensity that would have been obvious throughout the lesion if superimposition did not occur. The superior two-thirds display a radiodensity, which is similar to the ground-glass appearance classically observed of fibrous dysplasia. This superimposition of the secondary image of the contralateral anatomy can be obviated on the panoramic reconstructions of computed tomography imaging. Note 2: The slightly more radiolucent superior third represents the substantial erosion or penetration of the cortex of the alveolar crest. The lesion immediately distal to the first molar is likely to be fluctuant.

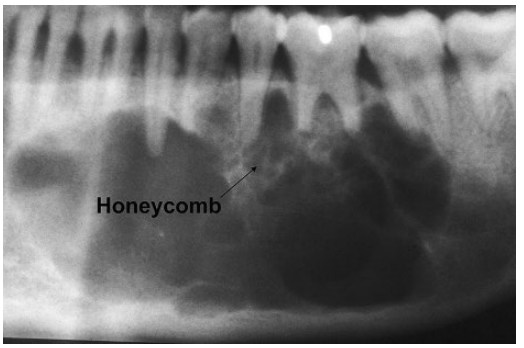


Figure 1.31 Panoramic radiograph showing a well-defined multilocular radiolucency extending from between the second molar and the junction between the contralateral canine and lateral incisor of the mandible. Many of the roots, particularly those of the first molar, display resorption, and those of the second molar are displaced distally. The lower border of the mandible has been both eroded and downwardly displaced. There are two multilocular patterns: the majority is of the soap-bubble pattern and a small area about the apex of the second premolar is of the honeycomb pattern. The latter is made up of multiple continuous cells of similar size, which together recall the appearance of a bee's honeycomb. This is a solid ameloblastoma. Source: MacDonald-Jankowski, D.S., Yeung, R., Lee, K.M., and Li, T.K. (2004). Ameloblastoma in the Hong Kong Chinese. Part 2: systematic review and radiological presentation. *Dentomaxillofac. Radiol.* 33: 141–151.

even with curettage or adjuvant treatment less effective in the removal of the entire lesion. Such lesions may prompt resection, but such a decision should be made on a case-by-case basis.

Most cysts and a few neoplasms display expansion in all directions to assume a round (spherical in *three dimensions* [3D]) or oval shape, whereas others may assume a fusiform (or spindle) shape. Although the fusiform shape is classically associated with fibrous dysplasia (Figures 1.33 and 1.34), it can be observed for some neoplasms, such as odontogenic myxoma and KCOT. These two lesions primarily extend through the marrow spaces between the trabeculae mesiodistally, effecting some buccolingual expansion only once they have achieved four or more dental units mesiodistally. This minimal expansion in the body of the mandible is also a function of its thicker cortex. The thinner cortex elsewhere in the jaws is less effective in constraining the lesion's expansion.

1.3.4 SIZE

The size of a lesion can be rendered in metric units (imperial units are still used, but increasing less so) or according to its anatomical boundaries (Figure 1.35). The latter is particularly necessary if the lesion is displayed on a panoramic radiograph. This modality is subject to not only substantial magnification but also distortion, particularly in the horizontal plane [13].

Another method for determining size from a panoramic radiograph is using the "dental unit." This is set out in Figure 1.35 [12]. Each tooth and the mesiodistal width of bone it spans is one unit, except for each lower incisor, which counts for a half a unit. This can be extended into the ramus: each of the retromolar to the mandibular foramen, the mandibular foramen to the base of the condyle and coronoid processes, and the condyle and coronoid accounts for one dental unit [12]. This was recently used to compare the sizes of KCOTs as they appeared on a panoramic radiograph [12]. These give a reasonable estimate of the lesion's size, which may reflect an approach to surgery based on

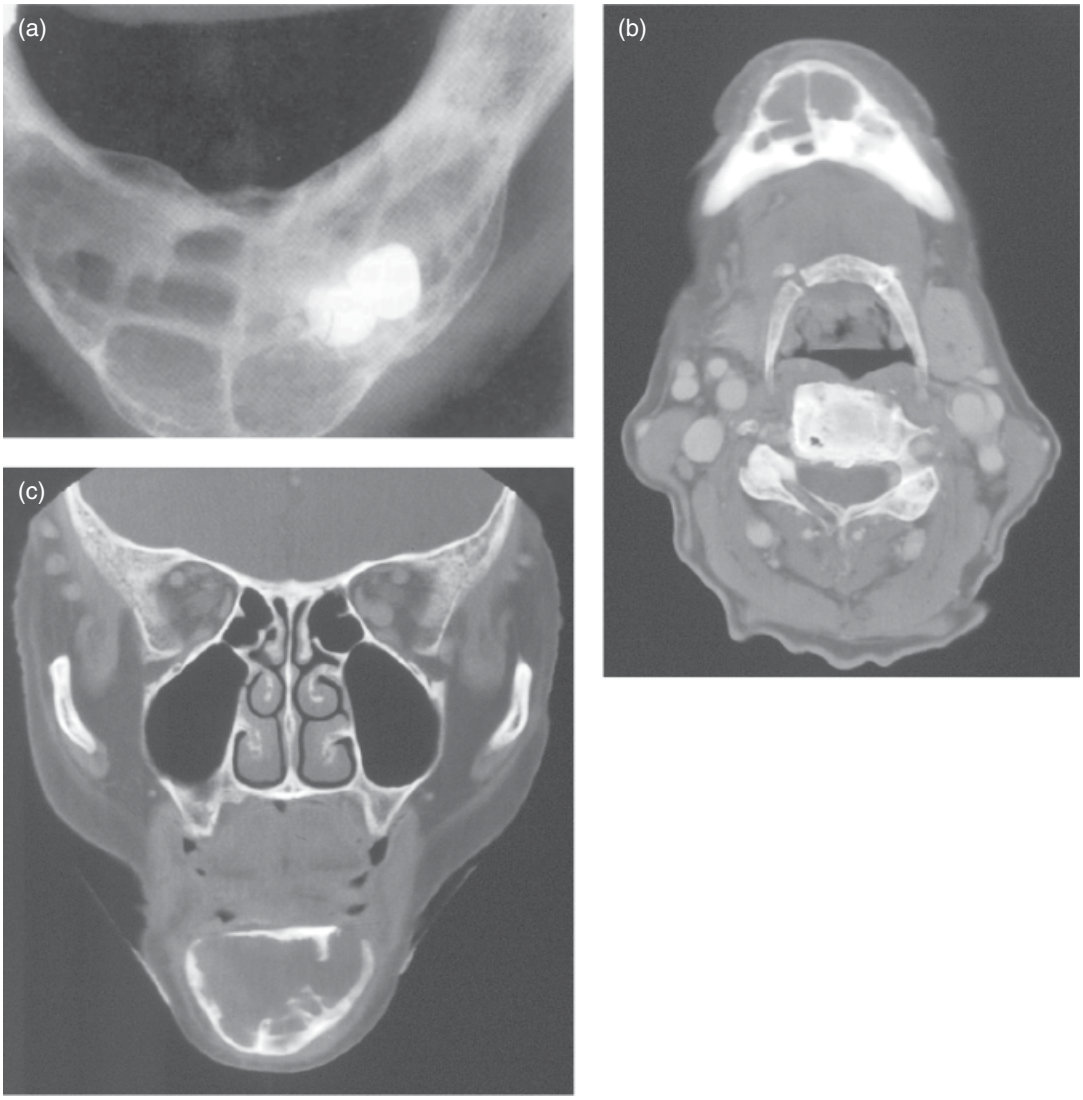


Figure 1.32 True occlusal projection of the anterior sextant of the mandible (a) and the axial (b) and coronal (c) computed tomographic sections (bone window) displaying the tennis-racket multilocular pattern, which is virtually pathognomonic of the odontogenic myxoma. (a) The "strings" of the tennis racket appear to completely transverse the entire anterior sextant. Images (b) and (c) instead display the septae confined to the periphery of the lesion, leaving a central "atrium" completely free of septae. Note 1: The shape of the lesion recalls the fusiform shape typically observed in fibrous dysplasia affecting the jaws. Note 2: In (b) the patency of the synovial joint of the hyoid bone with the lesser horn immediately adjacent to it is readily displayed. Note 3: Also in (b) there is enhancement of the major blood vessels, but none of the lesion. Source: Reproduced with permission from MacDonald-Jankowski, D.S., Yeung, R., Li, T.K., and Lee, K.M. (2004). Computed tomography of odontogenic myxoma. *Clin. Radiol.* 59: 281–287.

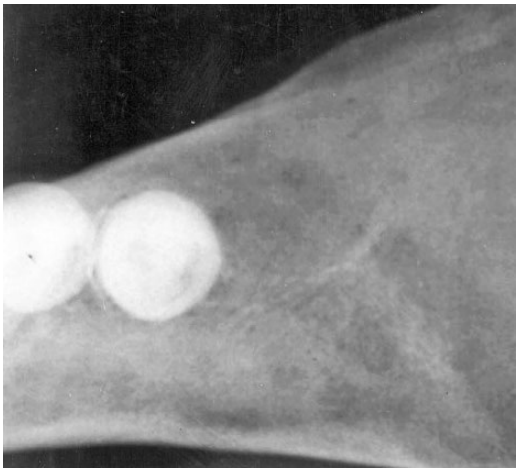


Figure 1.33 True occlusal projection of the mandible displaying fibrous dysplasia. A well-defined margin between the dysplastic and adjacent normal bone is absent. The gradual expansion of the lesion from the adjacent normal bone is apparent. This pattern of expansion recalls the shape of a spindle, hence fusiform. Both the buccal and lingual cortices are greatly reduced in thickness in comparison to the normal cortex anteriorly. The reduction in cortical thickness is gradual and reflects the broad zone of transition typical of fibrous dysplasia. The radiodensity can be observed to vary in pattern, from ground glass to peau d'orange and cotton wool. The first two are apparent here. Source: MacDonald-Jankowski, D.S. (2004). Fibro-osseous lesions of the face and jaws. *Clin. Radiol.* 59: 11–25.

such units. Nevertheless, if surgery of a substantial lesion is contemplated, the use of advanced imaging, such as CT and MRI, permits very accurate measurements of lesions (Figure 1.36).

1.3.5 SURROUNDINGS

The lesion's effect on its surroundings is twofold: the degree of marginal definition and the impact on adjacent structures.

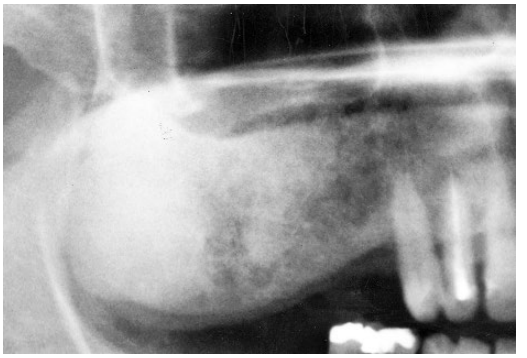


Figure 1.34 Panoramic radiograph displaying fibrous dysplasia affecting the right hemimaxilla. It exhibits similar fusiform expansion to that apparent in Figure 1.33. The dysplasia has involved the lower part of the posterior antral wall.

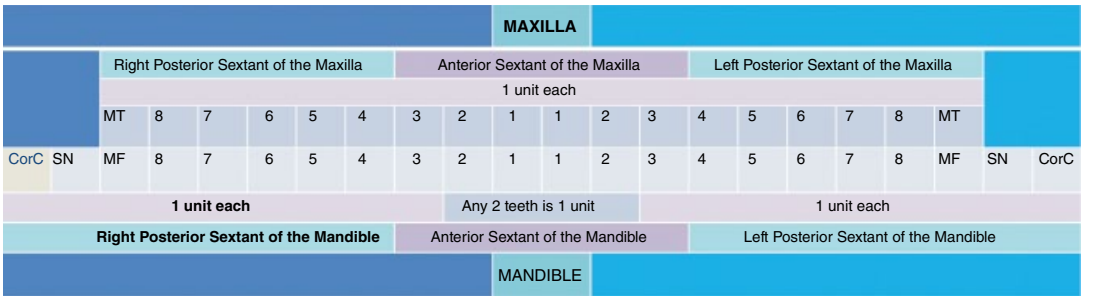


Figure 1.35 Dental units. As an alternative to reporting the size of a lesion observed on a conventional panoramic radiograph by reference to its position within the dental arch and its other adjacent anatomy, size may be reported as dental units. This figure expresses diagrammatically the text in Section 1.3.4. CorC, condyle and/or coronoid process; MF, mandibular foramen; MT, maxillary tuberosity; SN, sigmoid notch. Source: MacDonald, D., Gu, Y., Zhang, L., Poh, C. (2013). Can clinical and radiological features predict recurrence in solitary keratocystic odontogenic tumors?. *Oral Surg. Oral Med. Oral Pathol. Oral Radiol.* 115: 263–271. Reproduced with permission of Elsevier.

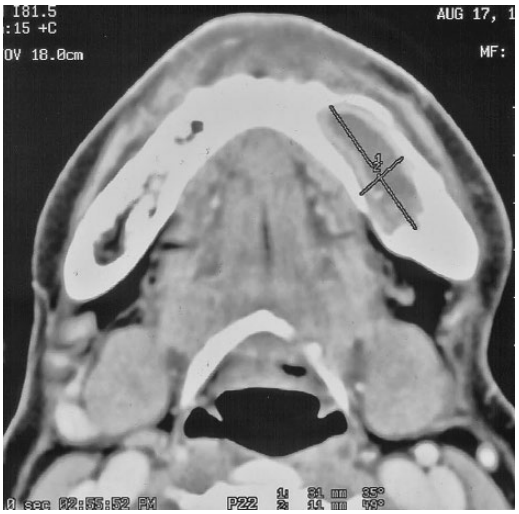


Figure 1.36 Axial computed tomography (soft-tissue window) displaying a radiolucency within the mandible. The digital measurements are set out at the bottom of the frame. Note: Intravenous contrast media has enhanced the blood vessels. The tortuous outline of the lingual artery is observed near the midline anteriorly.



Figure 1.37 Periapical radiograph displaying a radiolucency with a well-defined periphery. The lesion, a solid ameloblastoma, has resorbed the roots in line with its bony outline.

The degree of definition of the normal adjacent tissue-lesion zone of transition should be, as far as possible, objectively assessed. This is important, because marginal definition is the most important radiological feature after radiodensity. Failure to use a standard objective parameter can result in significant differences of opinion between clinicians, affecting the differential diagnosis. One such objective definition of margin definition was proposed by Slootweg and Müller [14]. If the normal adjacent tissue-lesion zone of transition is less than 1 mm, the lesion can be described as well defined and thus is more representative of an uninfected cyst or benign neoplasm (Figure 1.37), whereas that which exceeds 1 mm is poorly defined, suggestive of an inflamed lesion or a malignant neoplasm (Figure 1.38). This can be appreciated by running a 0.5 point pen around the periphery of the lesion displayed in an analog format (film). If this



Figure 1.38 Panoramic radiograph displaying a poorly defined radiolucency occupying the posterior body of the mandible. There is almost no lamina dura associated with the first molar tooth. There appears to be a thick soft-tissue mass anterior to the vertical ramus. This is a squamous cell carcinoma. Note 1: The secondary image of the contralateral mandible is superimposed upon the vertical ramus. Note 2: The radiolucent region above the tongue represents the residual air-filled space of the oral cavity.

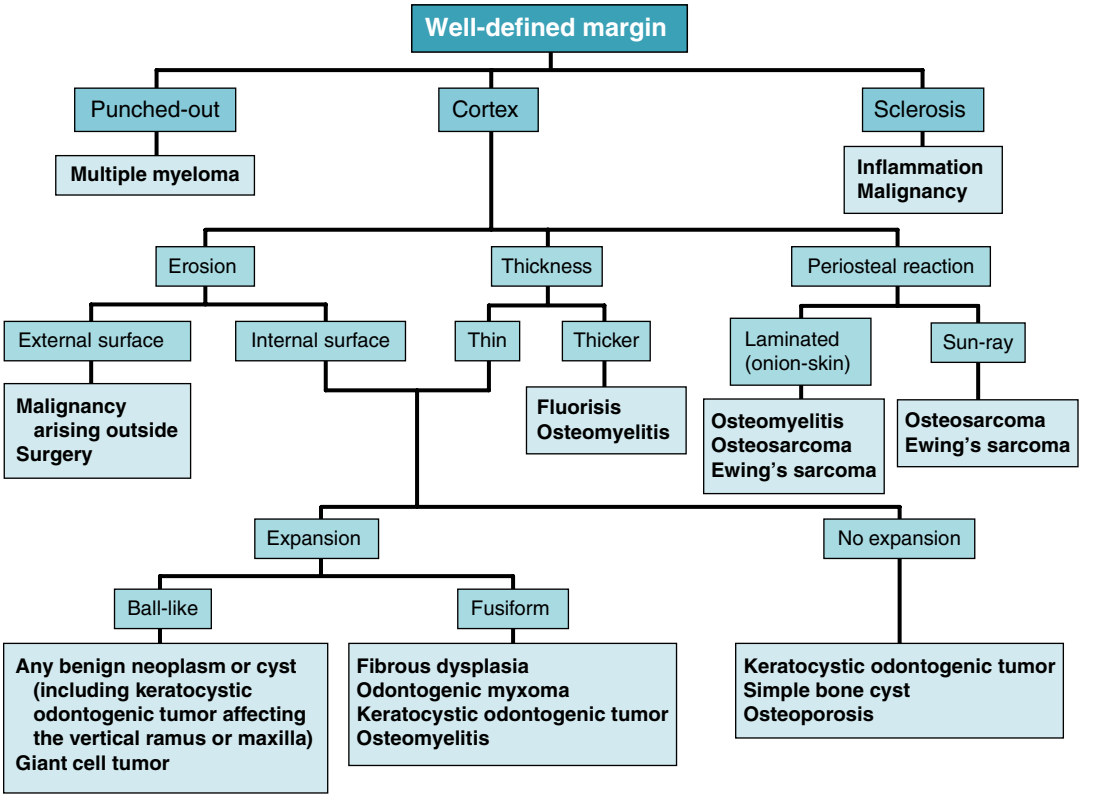


Figure 1.39 Assessing the cortex for refinement of the differential diagnosis.

can be achieved with ease, then the margin is well defined.

Well-defined lesions may or may not have a cortex, which may assist in further refinement of the differential diagnosis (Figure 1.39). Although a cortex is, in the majority of cases, strongly suggestive of a benign lesion, be aware that multiple cortices resembling the layers of an onion (Figure 10.6) may suggest not only chronic inflammation, but also some malignancies.

A cortex should be distinguished from sclerosis. A cortex is well defined with regard to both the lesion and the normal adjacent bone, whereas the sclerosis is poorly defined with regard to the latter (Figure 1.40).

The effect of the lesion on adjacent structures is expressed by the rule of the Three Ds: diameter, density, and displacement. Structures such as the mandibular canal can be affected by all three, whereas the cortex and the lamina dura are affected by only density and displacement.

1.3.6 DIAMETER

Changes in diameter are best seen in hollow structures such as the mandibular canal and mental and mandibular foramina. If their diameters are increased, this suggests that there is a lesion within the structure, whereas if it is decreased the lesion is outside. See Figure 1.12, which displays a narrow mandibular canal invested by fibrous dysplasia.

1.3.7 DENSITY

Changes in density can be observed on teeth, cortices, and hollow structures. A reduction of density on part of a tooth root may suggest resorption, either by the

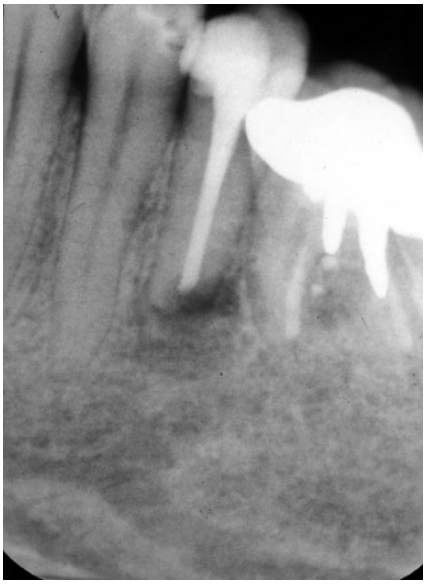


Figure 1.40 Periapical radiograph of the mandibular premolar region. The mental foramen, mandibular canal, and incisive canal are clearly obvious. Note the upward and backward bend of the canal toward the mental foramen. Note 1: The periapical radiolucency associated with the endodontically treated tooth displays root resorption. The radiolucency is well defined, but is not corticated. Note 2: The molar, which had also been endodontically treated, exhibits a radiolucency at the furcation. Within this radiolucency are radiopacities with a similar radiodensity to that of the root-filling material. Therefore, the former are likely to represent extrusion of cement though a perforation of the furcation into the tissues. The well-defined margin of the radiolucency has been enhanced by a zone of sclerosis apical to it.



Figure 1.41 Oblique lateral projection of the posterior body of the mandible. Note the obliquely superimposed hyoid bone on the mandible and the contralateral angle of the mandible in the top right corner. The radiolucency is well defined with a thin cortex. It is unilocular. Although the lesion is associated with the cementoenamel junction of the unerupted third molar, suggestive of a dentigerous cyst, the root resorption of the first and second molars is substantial. The latter is more indicative of an ameloblastoma. This is a unicystic ameloblastoma. Note: The two vertical curved lines in the anterior half of the lesion arise from marked erosions or perforations of either the buccal or lingual cortex. Source: Reprinted with permission from MacDonald-Jankowski, D.S., Yeung, R., Lee, K.M., and Li, T.K. (2004). Ameloblastoma in the Hong Kong Chinese. Part 2: systematic review and radiological presentation. *Dentomaxillofac. Radiol.* 33: 141–151.

lesion or by an anatomical structure such as the mandibular canal. Reduction in density of the cortices suggests erosion or even full perforation by the lesion (Figure 1.41). It should be appreciated that much of the radiolucency of a lesion is not derived from the absence of cancellous bone but also from erosion, even perforation, of either buccal or lingual cortex or both. When the last occurs, the lesion's degree of radiolucency is higher and is usually associated with appreciable buccolingual expansion. Perforations of the cortex can occur in several places in the same lesion; if very large, these can give the illusion of multiloculation (Figure 1.42). Always look again for septae before arriving at this conclusion.

Changes in density of the mandibular canal (an increase in translucency or blackening) in association with a lesion or tooth suggest an intimate relationship between them, urging caution during surgery to minimize the risk of damage

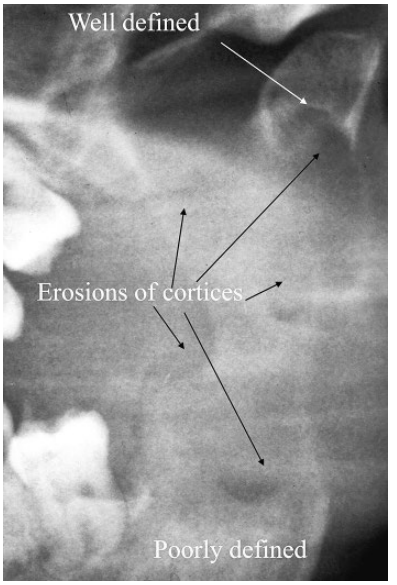


Figure 1.42 Panoramic radiograph displaying a radiolucency occupying the vertical ramus. The superior margin at the condyle is well defined, whereas that inferiorly appears poorly defined. The latter was caused by the superimposition of the secondary image of the lower border of the contralateral margin upon the lower margin. The Swiss-cheese presentation of the affected vertical ramus reflects the occurrence of more erosions or perforations at certain sites rather than at others. This is a unicystic ameloblastoma.

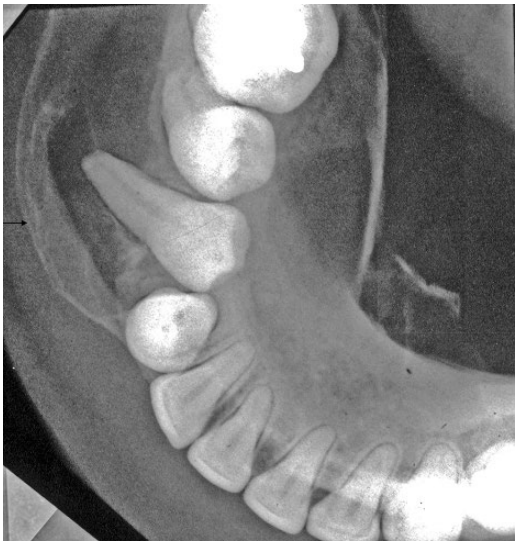


Figure 1.43 True occlusal projection of the mandible already reviewed in Figure 1.11. There is substantial buccolingual expansion. Both the buccal and the lingual cortex are very thin, particularly buccally, in addition to the distal displacement observed in Figure 1.11. The root of the first premolar has also been displaced buccally. This is a unicystic ameloblastoma. Source: MacDonald-Jankowski, D.S., Yeung, R., Lee, K.M., and Li, T.K. (2004). Ameloblastoma in the Hong Kong Chinese. Part 2: systematic review and radiological presentation. *Dentomaxillofac. Radiol.* 33: 141–151.

to the neurovascular bundle it contains. The mandibular canal can appear more translucent (blacker) and thus more conspicuous if the bone is abnormal, as is evident in the case of fibrous dysplasia in Figure 1.12.

Air-filled spaces such as the maxillary sinus (Figure 1.22) and the pharynx (Figures 1.17–1.19) are visible as radiolucent structures by virtue of the absence of any tissue that could attenuate the X-ray beam; in other words, much of the beam passing though these structures is relatively unattenuated in comparison to the patient being imaged. Density changes within normally air-filled spaces are invariably increased densities. In the maxillary sinus, this represents both discrete lesions and complete opacification by inflammatory fluid.

1.3.8 DISPLACEMENT

The lesion can displace teeth, buccal and lingual cortices (Figure 1.43), the lower border of the mandible (Figure 1.44) and the antral floor, and the mandibular canal (see Figure 1.13). The types of lesions that most frequently displace adjacent structures

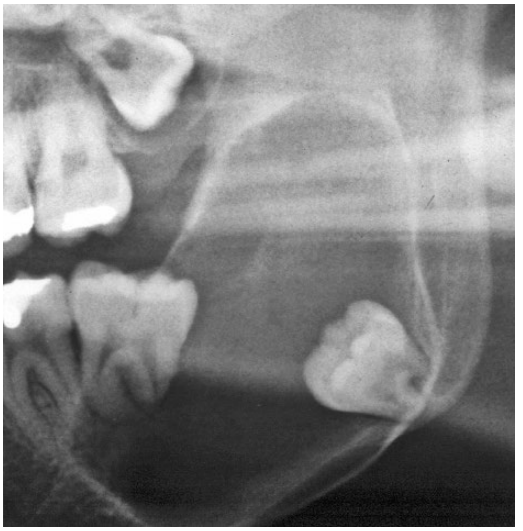


Figure 1.44 Panoramic radiograph displaying a unicystic ameloblastoma associated with the third molar (this attachment is apical to the cementoenamel junction). The second molar's roots appear to have been displaced anteriorly. The lowest border of the lesion has expanded down past the still undisplaced and largely intact lower border of the mandible. Although this phenomenon is generally a feature of the ameloblastoma, it has also been observed for orthokeratinized odontogenic cysts. Note 1: The secondary image of the contralateral mandible has conferred a ground-glasslike appearance on the upper two-thirds of the lesion. The lower third displays a truer degree of radiodensity. Note 2: The erupting maxillary third molar exhibits an enlarged follicular space. Source: Reprinted with permission from MacDonald-Jankowski, D.S., Yeung, R., Lee, K.M., and Li, T.K. (2004). Ameloblastoma in the Hong Kong Chinese. Part 2: systematic review and radiological presentation. *Dentomaxillofac. Radiol.* 33: 141–151.

are most benign neoplasms, particularly those with a capsule, and cysts.

The buccolingual expansion (Figure 1.43) in conjunction with vertical expansion (Figure 1.11) can confer an overall ball-like shape in 3D.

1.4 Ultimate Purposes of Radiological Diagnosis

For the large majority of patients, radiology is central in the treatment planning for caries, periodontal disease, and dentofacial disharmony (orthodontics and orthognathic surgery). In addition, radiology is important for the following reasons:

1. Distinguishing between a malignant and a benign lesion, because early diagnosis enhances survival of the former.
2. Prompt consideration of locally invasive benign neoplasms, so that the most appropriate treatment can be provided to minimize recurrence.
3. Prompt consideration of a vascular lesion, so that the most appropriate treatment plan can be formulated to avoid potentially fatal exsanguination.
4. A thorough review of the entire conventional radiograph, particularly panoramic radiographs, lateral cephalograms, and other face and skull views, since they display not only larger areas of the patient, but also those areas that are normally considered to be outside the normal practice of dentistry. Nevertheless, the dentist who prescribed them is held responsible for detecting any incidental findings and subsequent referral to an appropriate clinician, who could simply be the patient's personal or family medical practitioner or a dental or medical specialist. With the advent of CBCT, prescribing dentists are further responsible for the review of the entire dataset, either by themselves or by referral to a radiologist.

1.5 Incidental Findings

Incidental findings (IFs) are those findings which are discovered secondarily to an investigation made for another purpose. Once identified, many such findings, such as unerupted teeth, DBIs, SBCs, and lingual bone defects, though relatively common, may have little impact on that particular patient's treatment plan. The patient in such cases is informed and reassured and a note made in the record. Other lesions such as cysts and neoplasms require further evaluation, leading to their treatment. All these lesions occur within the jaws. There are other lesions which, though outside the jaws, can be visualized on panoramic radiographs, lateral cephalograms, and large, and occasionally small, *field-of view* (FOV) CBCTs. The most likely one is a *calcified carotid artery atheroma* (CCAA) and its differential diagnosis. These are found in the soft tissues of the neck, to which Chapter 12 is wholly dedicated. Other areas in which IFs may be found are the nose and sinuses, eyes, base of the skull, vertebrae, and airways of the nasopharynx and oropharynx.

Lopes et al. recently showed that 92% of their CBCTs, of which 67% were medium-sized FOVs confined to the jaws, revealed IFs [15]. Furthermore, 29% required further imaging and 28% needed treatment or referral. Therefore, the active search for IFs on images and identifying them are required clinical activities.

1.6 The Need to Report

The need to report every radiographic image is required by most jurisdictions [16–18]. While a sentence or two has in the past sufficed for most conventional radiographs, this is inadequate for most CBCT datasets. A major problem is that most dentists have had little or no training in the review of these datasets, and oftentimes have little understanding of what they are looking at and whether it is clinically significant. One of the aims of this textbook is to reveal many of the most frequent and/or important lesions that may present in a CBCT dataset. The foregoing Five Ss and Three Ds allow the clinician to describe the lesion/s. Chapters 9–11 will explore the main clinical and radiological manifestations and outcomes of treatment of the most frequent and/or important lesions affecting the face and jaws. Although these chapters to a substantial degree address the conventional radiology of these lesions, images of advanced modalities are also introduced when and where appropriate. These are separately considered in Chapters 4–8.

1.7 System of Evidence Used in This Textbook

Systematic review (SR) was developed to sift the enormous body of literature on a specific topic in an objective fashion, presenting clinicians with a conclusion or answer which they can apply to a particular patient or problem. Sackett et al. [19] defined a "systematic review as a summary of the medical literature that uses explicit methods to search systematically, appraise critically, and synthesize the world literature on a specific issue." This means that unlike a traditional literature review, the SR, like any other form of primary research, will have a "materials and methods" section and a "results" section [20]. Although SR has generally been applied to treatment and drug trials, following MacDonald-Jankowski and Dozier's [20] approach it has also become a powerful tool when adapted to reveal the clinical, demographic, and radiological

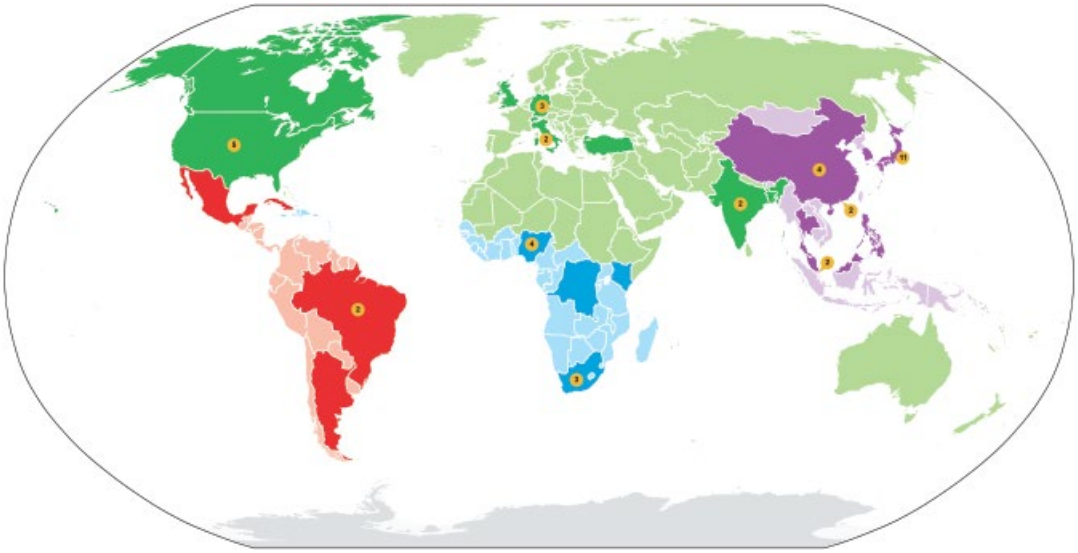


Figure 1.45 Ameloblastoma: global distribution of those reports included in the systematic review. Green is for Western or predominantly Caucasian communities, blue for sub-Saharan African communities, violet for East Asian communities, and red for Latin American communities. The lighter shades denote each of the four global groups or regions, whereas the darker shades denote a systematic review–included report for a particular state. If more than one such report exists, the number over one is inserted for that state. Source: James Pagnotta, Media Support Analyst, Faculty of Dentistry, University of British Columbia.

features, and the outcomes of follow-up after primary treatment, of the most frequent and/or important lesions of the face and jaws.

An essential element of MacDonald-Jankowski and Dozier's approach to SR is meta-analysis [20]. Meta-analysis, as defined by the *Dictionary of Epidemiology*, is "the process of using statistical methods to combine the results of different studies" [21].

The SRs that are central to this textbook, following the procedure set out by MacDonald and Dozier [20], have been performed on the ameloblastoma (Figure 1.45) [22, 23], odontogenic myxoma (Figure 1.46) [7], KCOT (Figure 1.47) [24], dentigerous cyst (Figure 1.48) [25], orthokeratinized odontogenic cyst (Figure 1.49) [26], glandular odontogenic cyst (Figure 1.50) [27], fibrous dysplasia (Figure 1.51) [28], ossifying fibroma (Figure 1.52) [29], florid osseous dysplasia (Figure 1.53) [30], focal osseous dysplasia (Figure 1.54) [31], idiopathic osteosclerosis (Figure 1.55) [32], central giant cell granuloma [33], cleidocranial dysostosis [34], nevoid basal cell carcinoma syndrome (Figure 1.56) [35], and extranodal non-Hodgkin lymphoma (Figure 1.57) [36].

In order to ensure that the entire world literature on a particular lesion was captured in the literature search, each SR authored by MacDonald-Jankowski or MacDonald in all non-English-language journals and the *Literature Index for Latin-America and the Caribbean* (LILACS) and *Biblioteca Regional de Medicina* (BIREME) databases was included. The PubMed interface of MEDLINE (maintained by the United States National Library of Medicine

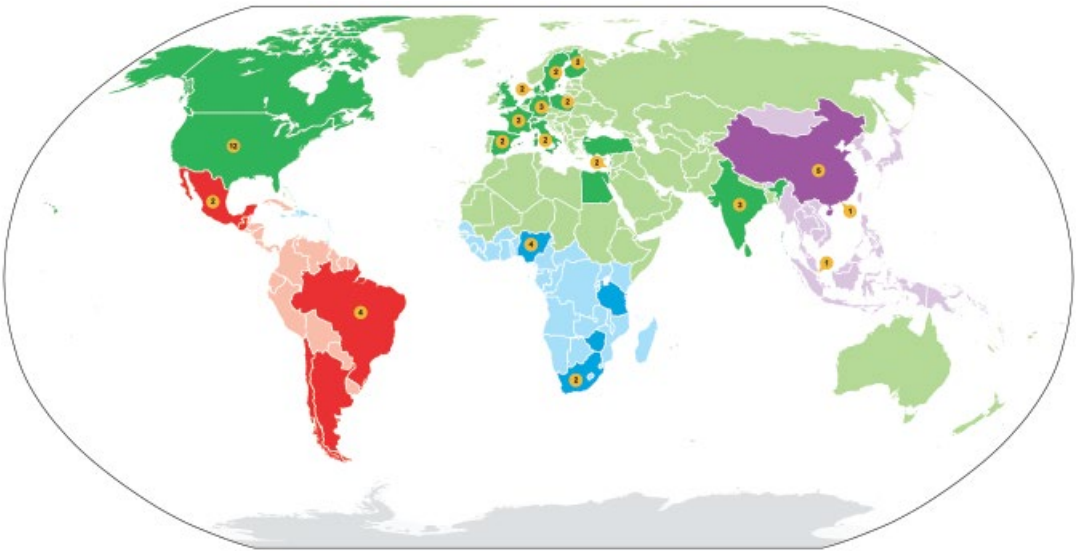


Figure 1.46 Odontogenic myxoma: global distribution of those reports included in the systematic review. Note that both Swedish reports are binational: one with Denmark and one with Finland. Green is for predominantly Caucasian communities, blue for sub-Saharan African communities, violet for East Asian communities, and red for Latin American communities. The lighter shades denote each of the four global groups or regions, whereas the darker shades denote a systematic review–included report for a particular state. If more than one such report exists, the number over one is inserted for that state. Source: James Pagnotta, Media Support Analyst, Faculty of Dentistry, University of British Columbia.

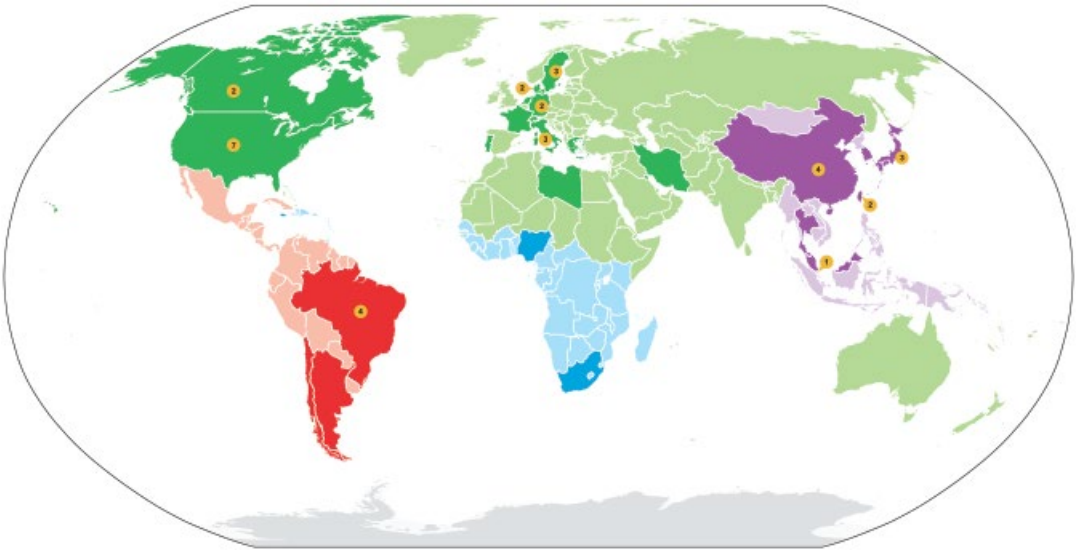


Figure 1.47 Keratocystic odontogenic tumor: global distribution of those reports included in the systematic review. Green is for predominantly Caucasian communities, blue for sub-Saharan African communities, violet for East Asian communities, and red for Latin American communities. The lighter shades denote each of the four global groups or regions, whereas the darker shades denote a systematic review–included report for a particular state. If more than one such report exists, the number over one is inserted for that state. Source: James Pagnotta, Media Support Analyst, Faculty of Dentistry, University of British Columbia.

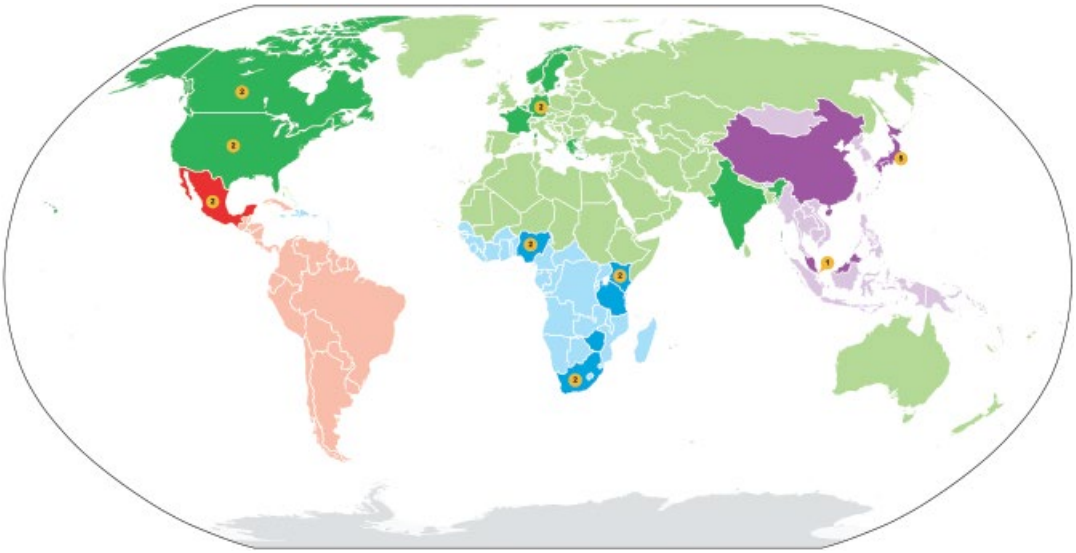


Figure 1.48 Dentigerous cyst: global distribution of those reports included in the systematic review. Green is for predominantly Caucasian communities, blue for sub-Saharan African communities, violet for East Asian communities, and red for Latin American communities. The lighter shades denote each of the four global groups or regions, whereas the darker shades denote a systematic review–included report for a particular state. If more than one such report exists, the number over one is inserted for that state. Source: James Pagnotta, Media Support Analyst, Faculty of Dentistry, University of British Columbia.

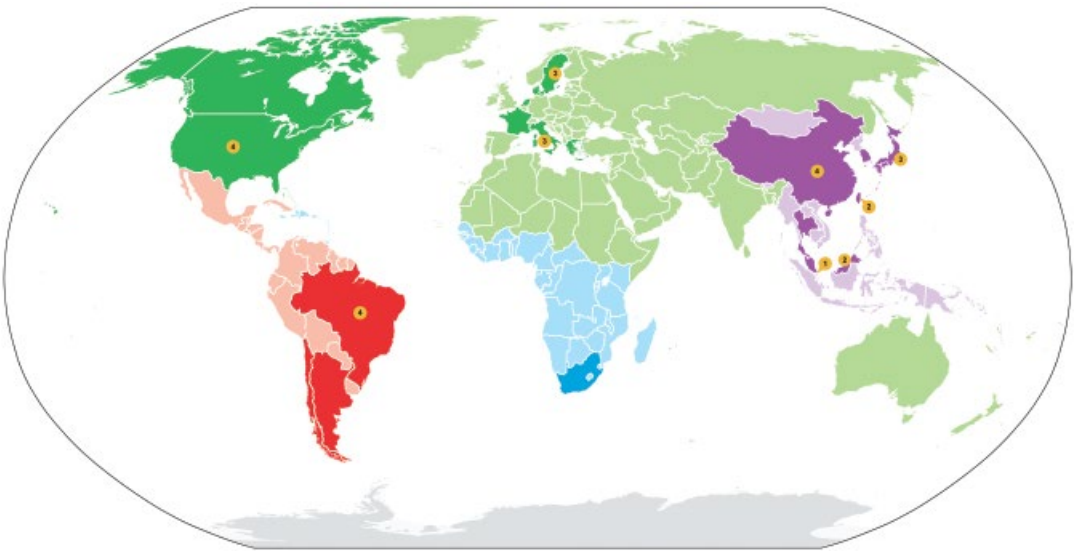


Figure 1.49 Orthokeratinized odontogenic cyst: global distribution of those reports included in the systematic review. Green is for predominantly Caucasian communities, blue for sub-Saharan African communities, violet for East Asian communities, and red for Latin American communities. The lighter shades denote each of the four global groups or regions, whereas the darker shades denote a systematic review–included report for a particular state. If more than one such report exists, the number over one is inserted for that state. Source: James Pagnotta, Media Support Analyst, Faculty of Dentistry, University of British Columbia.

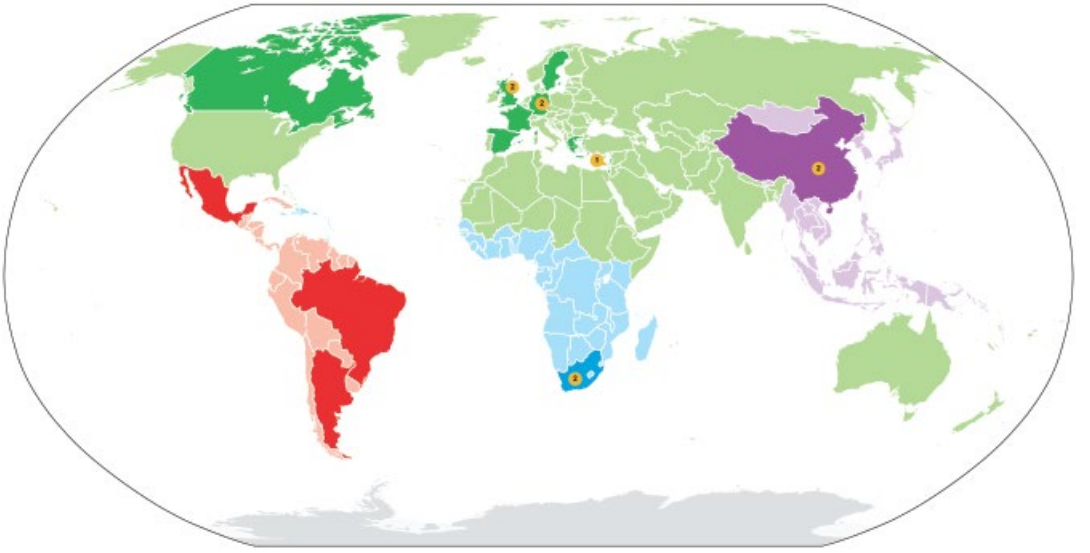


Figure 1.50 Glandular odontogenic cyst: global distribution of those reports included in the systematic review. Green is for predominantly Caucasian communities, blue for sub-Saharan African communities, violet for East Asian communities, and red for Latin American communities. The lighter shades denote each of the four global groups or regions, whereas the darker shades denote a systematic review–included report for a particular state. If more than one such report exists, the number over one is inserted for that state. Source: James Pagnotta, Media Support Analyst, Faculty of Dentistry, University of British Columbia.

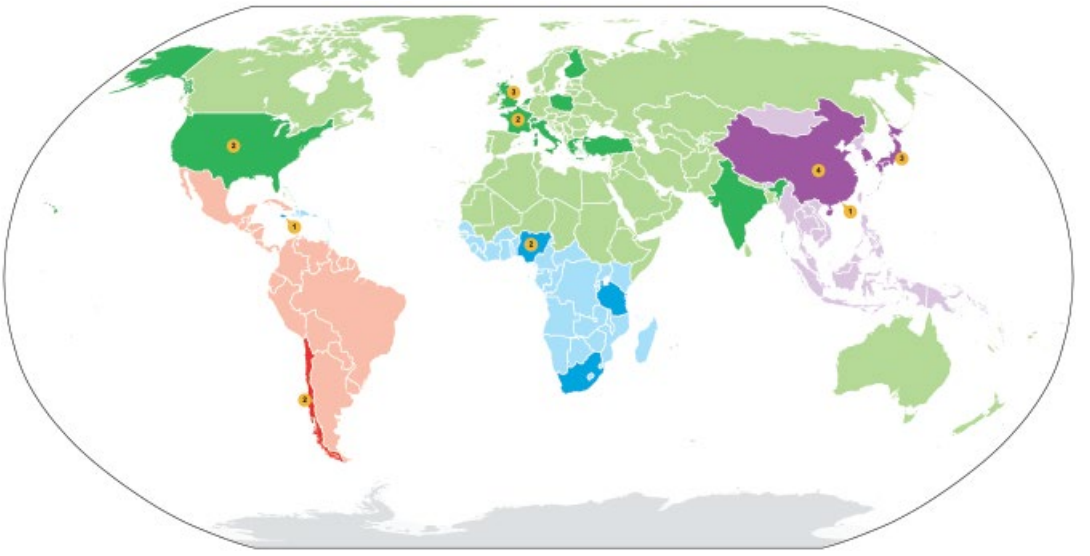


Figure 1.51 Fibrous dysplasia: global distribution of those reports included in the systematic review. Green is for predominantly Caucasian communities, blue for sub-Saharan African communities, violet for East Asian communities, and red for Latin American communities. The lighter shades denote each of the four global groups or regions, whereas the darker shades denote a systematic review–included report for a particular state. If more than one such report exists, the number over one is inserted for that state. Source: James Pagnotta, Media Support Analyst, Faculty of Dentistry, University of British Columbia.

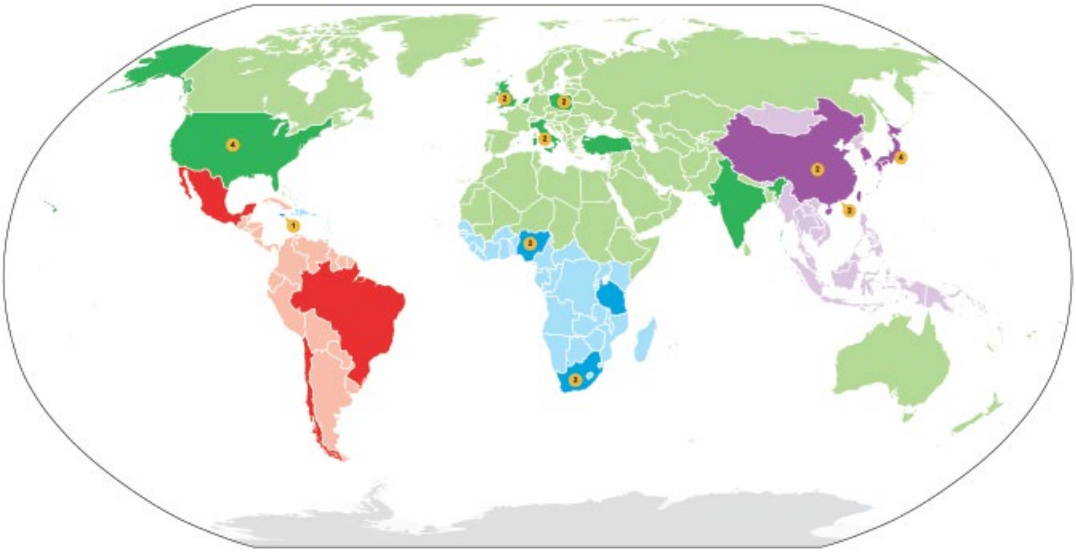


Figure 1.52 Ossifying fibroma: global distribution of those reports included in the systematic review. Green is for predominantly Caucasian communities, blue for sub-Saharan African communities, violet for East Asian communities, and red for Latin American communities. The lighter shades denote each of the four global groups or regions, whereas the darker shades denote a systematic review–included report for a particular state. If more than one such report exists, the number over one is inserted for that state. Source: James Pagnotta, Media Support Analyst, Faculty of Dentistry, University of British Columbia.

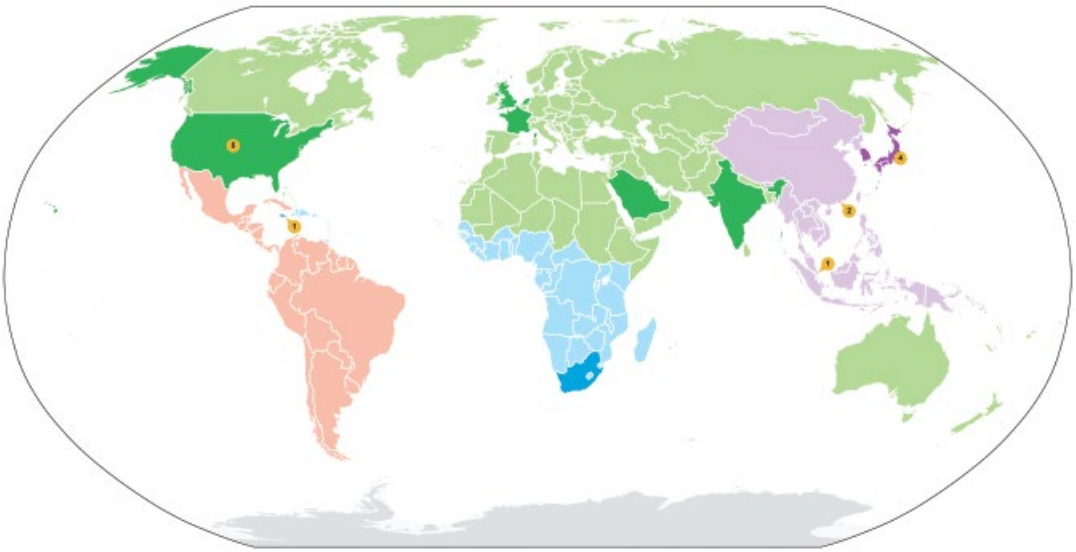


Figure 1.53 Florid osseous dysplasia: global distribution of those reports included in the systematic review. Green is for predominantly Caucasian communities, blue for sub-Saharan African communities, violet for East Asian communities, and red for Latin American communities. The lighter shades denote each of the four global groups or regions, whereas the darker shades denote a systematic review–included report for a particular state. If more than one such report exists, the number over one is inserted for that state. Source: James Pagnotta, Media Support Analyst, Faculty of Dentistry, University of British Columbia.

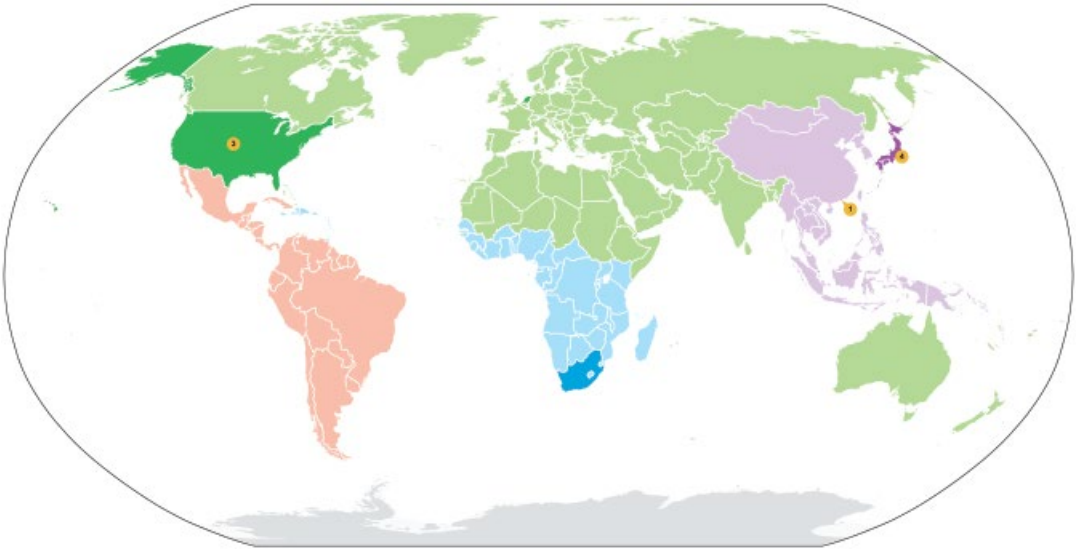


Figure 1.54 Focal osseous dysplasia: global distribution of those reports included in the systematic review. Green is for predominantly Caucasian communities, blue for sub-Saharan African communities, violet for East Asian communities, and red for Latin American communities. The lighter shades denote each of the four global groups or regions, whereas the darker shades denote a systematic review–included report for a particular state. If more than one such report exists, the number over one is inserted for that state. Source: James Pagnotta, Media Support Analyst, Faculty of Dentistry, University of British Columbia.

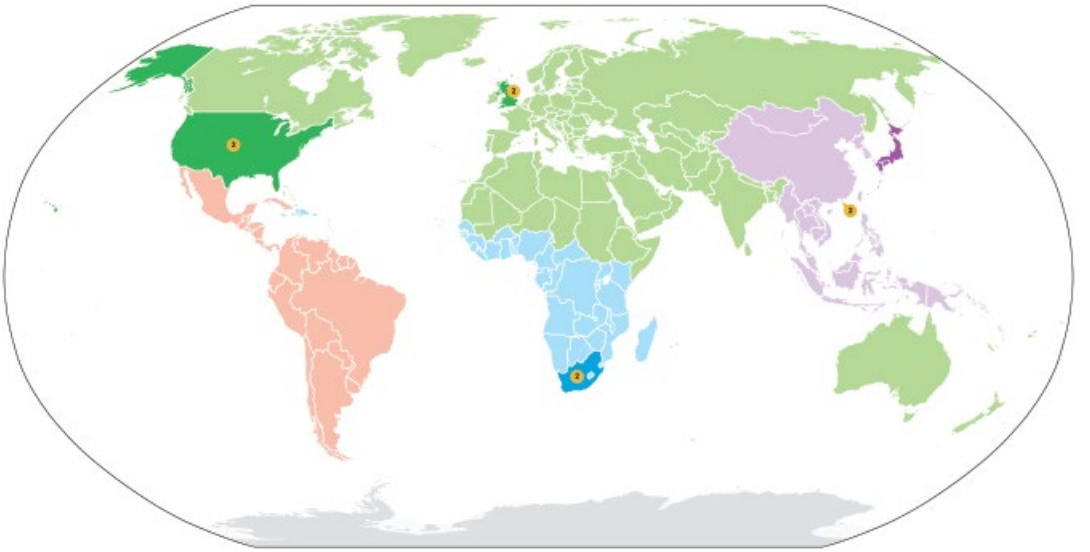


Figure 1.55 Idiopathic osteosclerosis: global distribution of those reports included in the systematic review. Green is for predominantly Caucasian communities, blue for sub-Saharan African communities, violet for East Asian communities, and red for Latin American communities. The lighter shades denote each of the four global groups or regions, whereas the darker shades denote a systematic review–included report for a particular state. If more than one such report exists, the number over one is inserted for that state. Source: James Pagnotta, Media Support Analyst, Faculty of Dentistry, University of British Columbia.

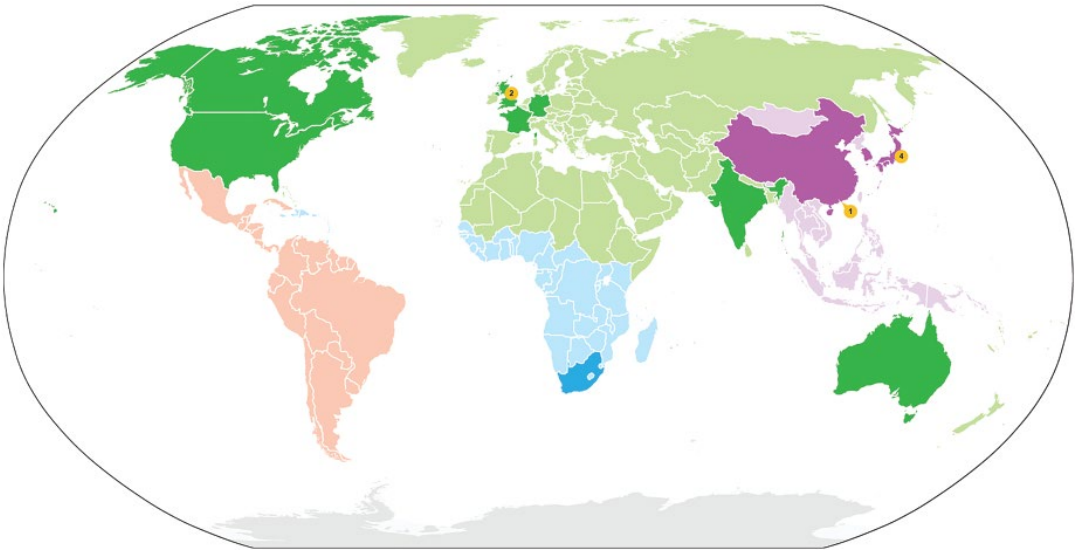


Figure 1.56 Nevoid basal cell carcinoma syndrome: global distribution of those reports included in the systematic review. Green is for predominantly Caucasian communities, blue for sub-Saharan African communities, violet for East Asian communities, and red for Latin American communities. The lighter shades denote each of the four global groups or regions, whereas the darker shades denote a systematic review–included report for a particular state. If more than one such report exists, the number over one is inserted for that state. Source: James Pagnotta, Media Support Analyst, Faculty of Dentistry, University of British Columbia.

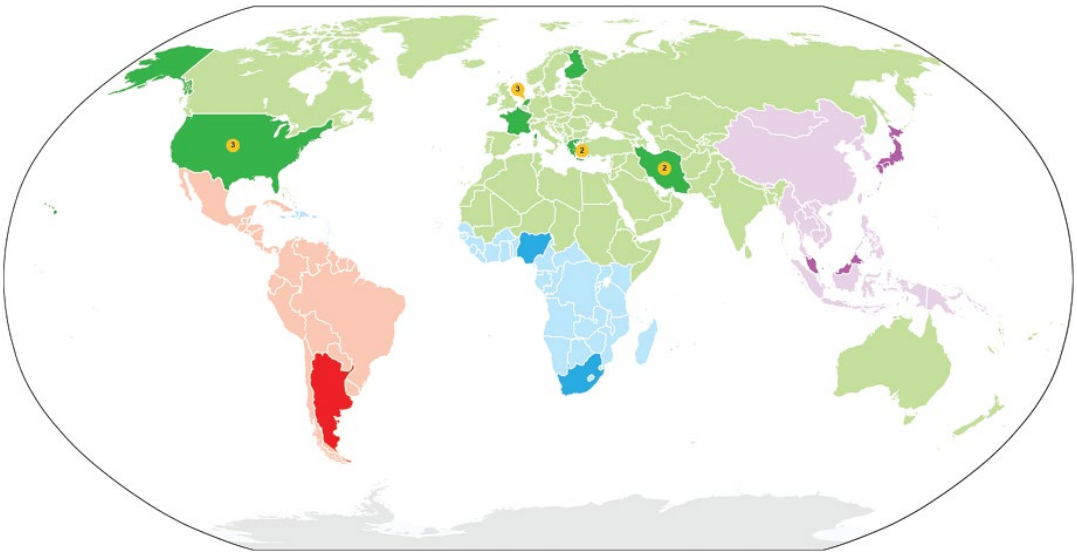


Figure 1.57 Non-Hodgkin lymphoma, extranodal, arising in the alveolus of the jaws: global distribution of those reports included in the systematic review. Green is for predominantly Caucasian communities, blue for sub-Saharan African communities, violet for East Asian communities, and red for Latin American communities. The lighter shades denote each of the four global groups or regions, whereas the darker shades denote a systematic review–included report for a particular state. If more than one such report exists, the number over one is inserted for that state. Source: James Pagnotta, Media Support Analyst, Faculty of Dentistry, University of British Columbia.

[NLM] at the National Institutes of Health [NIH]) was the principal search engine. In addition, relevant journals were hand searched and the reference lists of publications were harvested (mined) to include literature that may have not been captured by the database searches.

1.8 Global Groups

In order to determine deeper patterns within the SR, its reports are divided into four global groups based broadly on ethnicity: these are East Asian (predominantly represented in the SR by Chinese and Japanese authors), sub-Saharan African (predominantly Black Africa, including Jamaica), Caucasian (North America and Europe, Middle East, North Africa, and India), and Latin American (including Cuba). The "White alone," "black alone," and "Hispanic or Latino" populations of the United States were at the 2010 census 72.4%, 12.6%, and 16.3%, respectively [37]. Although all three displayed an increase in percentage since the 2000 census, the "Hispanic or Latino" displayed the largest increase. Note: 100% was exceeded when all three were added up and without consideration for "American Indian or Alaska Native, Asian, and Native Hawaiian or Other Pacific Islanders." Reports from the Indian subcontinent are included in the Caucasian group, because 95% of Indians are Caucasian (Indo-Aryans and Dravidians). Although these four global groups are cartographically represented by four almost discrete regions, they are not primarily regional, because variable socioeconomic and other ethnocultural factors also play important roles that affect the availability and provision of diagnostic and therapeutic services. For example, the South Asian nations, including India, although largely Caucasian, are still developing their economies, along with many of those of sub-Saharan Africa. Although Africa itself is divided between a Caucasian North and a substantially Black sub-Saharan South, it is the latter that constitutes the bulk of the population of both the African continent and the African diaspora (Jamaica is 90% sub-Saharan African origin). Although the global distribution for each lesion is largely determined by the number, size, and quality of the reports included in the SR, the lesions for some communities are likely to be underreported. These are discussed in Chapters 9 and 10.

References

1. MacDonald, D.S. (2016). Lesions of the jaws presenting as radiolucencies on cone-beam computed tomography. *Clin. Radiol.* 71: 972–985.
2. El-Naggar, A.K., Chan, J.C., Grandis, J.R. et al. (2017). *WHO Classification of Head and Neck Tumours*, WHO Classification of Tumours. No. 9, 4e. Lyon: IARC Press.
3. *Holsten v. Card and Wu*. Supreme Court of British Columbia. https://www.courts.gov.bc.ca/jdb-txt/sc/99/18/s99-1804.html (Accessed December 27, 2018).
4. Kratz, R.J., Walton, J.N., MacEntee, M.I. et al. (2017). Panoramic radiographs made before complete removable dental prostheses fabrication: a retrospective study of clinical significance. *J. Prosthet. Dent.* 118: 26–30.
5. MacDonald-Jankowski, D.S. and Li, T.K. (1993). Taurodontism in a young adult Chinese population. *Dentomaxillofac. Radiol.* 22: 140–144.
6. Wenig, B.M., Mafee, M.F., and Ghosh, L. (1998). Fibro-osseous, osseous, and cartilaginous lesions of the orbit and paraorbital region. Correlative clinicopathologic and radiographic features, including the diagnostic role of CT and MR imaging. *Radiol. Clin. N. Am.* 36: 1241–1259.

7. Pretty, I.A. and Maupomé, G. (2004). A closer look at diagnosis in clinical dental practice: part 2. Using predictive values and receiver operating characteristics in assessing diagnostic accuracy. *J. Can. Dent. Assoc.* 70: 313–316.
8. MacDonald-Jankowski, D.S., Yeung, R., Lee, K.M., and Li, T.K. (2002). Odontogenic myxomas in the Hong Kong Chinese: clinicoradiological presentation and systematic review. *Dentomaxillofac. Radiol.* 31: 71–83.
9. Lu, Y., Xuan, M., Takata, T. et al. (1998). Odontogenic tumors. A demographic study of 759 cases in a Chinese population. *Oral Surg. Oral Med. Oral Pathol. Oral Radiol. Endod.* 86: 707–714.
10. Pindborg, J.J., Kramer, I.R.H., and Torloni, H. (1971). *Histological Typing of Odontogenic Tumours, Jaw Cysts, and Allied Lesions*. Geneva: World Health Organization.
11. Barnes, L., Eveson, J.W., Reichert, P., and Sidransky, D. (2005). *Pathology and Genetics of Head and Neck Tumours*, WHO Classification of Tumours. No. 9, 3e, 284–327. Lyon: IARC Press.
12. MacDonald, D., Gu, Y., Zhang, L., and Poh, C. (2013). Can clinical and radiological features predict recurrence in solitary keratocystic odontogenic tumors? *Oral Surg. Oral Med. Oral Pathol. Oral Radiol.* 115: 263–271.
13. Langland, O.E., Langlais, R.P., McDavid, W.D., and DelBalso, A.M. (1989). *Panoramic Radiography*, 2e, 52–57. Philadelphia: Lea and Febiger.
14. Slootweg, P.J. and Müller, H. (1990). Differential diagnosis of fibro-osseous jaw lesions. A histological investigation on 30 cases. *J. Craniomaxillofac. Surg.* 18: 210–214.
15. Lopes, I.A., Tucunduva, R.M., Handem, R.H., and Capelozza, A.L. (2017). Study of the frequency and location of incidental findings of the maxillofacial region in different fields of view in CBCT scans. *Dentomaxillofac. Radiol.* 46: 20160215.
16. Miles, D.A. and Danforth, R.A. (2014). Cone beam computed tomography: from capture to reporting. *Dent. Clin. N. Am.* 58: ix–x.
17. Miles, D.A. and Danforth, R.A. (2014). Reporting findings in the cone beam computed tomography volume. *Dent. Clin. N. Am.* 58: 687–709.
18. Friedland, B. and Miles, D.A. (2014). Liabilities and risks of using cone beam computed tomography. *Dent. Clin. N. Am.* 58: 671–685.
19. Sackett, D.L., Strauss, S.E., Richardson, W.S. et al. (2000). *Evidence-based Medicine: How to Practice and Teach EBM*, 2e, 133–136. Edinburgh: Churchill-Livingstone.
20. MacDonald-Jankowski, D.S. and Dozier, M.F. (2001). Systematic review in diagnostic radiology. *Dentomaxillofac. Radiol.* 30: 78–83.
21. Clarkson, J.E., Bonner, B.C., Deery, C., and Grimshaw, J. (2003). *Evidence-Based Dentistry for Effective Practice*, 68–75. Martin Dunitz.
22. MacDonald-Jankowski, D.S., Yeung, R., Lee, K.M., and Li, T.K. (2004). Ameloblastoma in the Hong Kong Chinese. Part 1: systematic review and clinical presentation. *Dentomaxillofac. Radiol.* 33: 71–82.
23. MacDonald-Jankowski, D.S., Yeung, R., Lee, K.M., and Li, T.K. (2004). Ameloblastoma in the Hong Kong Chinese. Part 2: systematic review and radiological presentation. *Dentomaxillofac. Radiol.* 1: 141–151.
24. MacDonald-Jankowski, D.S. (2011). Keratocystic odontogenic tumour: a systematic review. *Dentomaxillofac. Radiol.* 40: 1–23.
25. MacDonald-Jankowski, D.S. and Chan, K.C. (2005). Clinical presentation of dentigerous cysts: systematic review. *Asian J. Oral Maxillofac. Surg.* 15: 109–120.
26. MacDonald-Jankowski, D.S. (2009). Orthokeratinized odontogenic cyst: a systematic review. *Dentomaxillofac. Radiol.* 39: 455–467.
27. MacDonald-Jankowski, D.S. (2010). Glandular odontogenic cyst: a systematic review. *Dentomaxillofac. Radiol.* 39: 127–139.
28. MacDonald-Jankowski, D.S. (2009). Fibrous dysplasia: a systematic review. *Dentomaxillofac. Radiol.* 38: 196–215.
29. MacDonald-Jankowski, D.S. (2009). Ossifying fibroma: a systematic review. *Dentomaxillofac. Radiol.* 38: 495–513.
30. MacDonald-Jankowski, D.S. (2003). Florid cemento-osseous dysplasia: a systematic review. *Dentomaxillofac. Radiol.* 32: 141–149.
31. MacDonald-Jankowski, D.S. (2008). Focal cemento-osseous dysplasia: a systematic review. *Dentomaxillofac. Radiol.* 37: 350–360.
32. MacDonald-Jankowski, D.S. (1999). Idiopathic osteosclerosis in the jaws of Britons and of the Hong Kong Chinese: radiology and systematic review. *Dentomaxillofac. Radiol.* 28: 357–363.

33. Stavropoulos, F. and Katz, J. (2002). Central giant cell granulomas: a systematic review of the radiographic characteristics with the addition of 20 new cases. *Dentomaxillofac. Radiol.* 31: 213–217. Erratum in *Dentomaxillofac. Radiol*. 2002; 31:394.
34. Golan, I., Baumert, U., Hrala, B.P., and Müssig, D. (2003). Dentomaxillofacial variability of cleidocranial dysplasia: clinico-radiological presentation and systematic review. *Dentomaxillofac. Radiol.* 32: 347–354. Erratum in *Dentomaxillofac. Radiol*. 2004;33:422.
35. MacDonald, D., Li, T., Leung, S.F. et al. (2017). Non-Hodgkin lymphoma arising within the alveolus of the maxilla. *Oral Surg. Oral Med. Oral Pathol. Oral Radiol* 124: e233–e238. https://doi.org/10.1016/j.oooo.2017.04.015.
36. MacDonald, D. and Lim, S. (2018). Extranodal lymphoma arising within the maxillary alveolus: a systematic review. *Oral Radiol.* 34 (2): 113–126.
37. United States Census Bureau. United States 2010 Decennial Census. https://www.census.gov/programs-surveys/decennial-census/decade.2010.html. (Accessed November 29, 2018).

Chapter 2

Viewing conditions and physiological phenomena and radiological interpretation

2.1 Introduction

Conventional imaging is represented by both digital and analog technologies, whose main features are outlined and compared in Table 2.1. Conventional imaging almost invariably precedes advanced imaging, because it imparts a lower dose of radiation, is generally cheaper, is more widely available, and – particularly in regard to intraoral technology – affords the best spatial resolution. This last feature has so far not been remotely achieved by the enormous advances in *cone-beam computed tomography* (CBCT). Table 2.1 reveals that digital imaging systems facilitate integration into an electronic patient record and transmission of images to colleagues, as well as the ability for clinicians to withstand a catastrophic loss of their office by off-site electronic record storage. Furthermore, the phosphor plate system is forgiving in errors in exposure settings, thus minimizing the need for retakes. Nevertheless, all intraoral digital systems have an Achilles' heel: they pose an infection control problem, because the intraoral detectors cannot be sterilized, but merely decontaminated. Although one study reported that they could be sealed in bags prior to insertion, the seals were occasionally defective [3]. An outbreak of a serious infection, recently experienced with Ebola, could prompt a return to analog, since the entire film packaging is disposed of in the darkroom.

Once the image has been captured, it needs to be displayed and then interpreted. The quality of image display should as closely as possible reflect the quality of the image captured. Display is dependent upon both the quality of the monitor and the ambient lighting. The roles of the monitors in *oral and maxillofacial radiology* (OMFR) are set out in Figure 2.1, the monitor technologies in Figure 2.2, and an overview of the most important features of image quality on monitors in Figure 2.3.

Although the optimal viewing conditions of the images produced by conventional radiography employed by specialist radiologists may differ markedly from those used by many other clinicians, in medicine in North America those clinicians who perform primary interpretation of radiographic images are held to the same standard of care as radiologists [4]. This is important, in that the former are generally likely to review their radiographic imaging in brightly lit clinical areas. While this bright lighting assists in the proper clinical/physical evaluation of the

Oral and Maxillofacial Radiology: A Diagnostic Approach, Second Edition. Edited by David MacDonald.
© 2020 John Wiley & Sons, Inc. Published 2020 by John Wiley & Sons, Inc.

Table 2.1 Comparison between the imaging technologies available to dentists for conventional radiography

Feature	Radiographic film (analog)	Solid state detectors		Phosphor plate detector
		CCD	CMOS	
Brief description partly provided by Parks [1]	Silver bromide developed to silver, the density of which provides the grayscale image	X-rays cause emitted electrons to collect in electron wells converted to grayscale image	Array of field effect transmitters with a polysilicon gate	Scanned by red light laser and emit blue light
Vulnerability to damage?	No, unless poorly stored – heat fogs it	Yes, by dropping and autoclaving	Yes, by dropping and autoclaving	Yes, frequently unusable after 50 uses
Immediate image?	No, chemical development of latent image	Yes	Yes	No, needs to be scanned into the patient record
Likelihood of image degradation if delayed?	No, unless reexposed before developed	N/A	N/A	Yes, deteriorates with delay before scanned
Special room required?	Yes, dark room	No	No	Yes, dim room
Noxious chemicals?	Yes	No	No	No
Whole surface available for image capture?	Yes	No	No	Yes
Spatial resolution (detail) in line pairs per millimeter (lp/mm)?	Kodak InSight 20 lp/mm	Kodak RVG-ui 20 lp/mm	Kodak RVG 6000 20 lp/mm	Planmeca Dixi 16 lp/mm
	All above are from Farman and Farman's 2005 report [2], which compared 17 detectors.			
Dynamic range?	Narrow	Narrow	As wide as the phosphor plate	Wide
Shorter exposure time?	Yes, if E and F speed	Same as E and F speed	Same as E and F speed	Yes, potential to be shorter
More exposures required for full-mouth survey?	No, optimum	Yes, smaller area available for image capture	Yes, smaller area available for image capture	No, same area available for image capture as film

Retakes more likely?	No	Yes, cone cuts more likely	Yes—cone cuts more likely	No
Patient comfort?	Yes	No, bulky and inflexible	No, bulky and inflexible	Yes, same as film
Permit taking of vertical bitewings?	Yes	No, bulky and inflexible	No, bulky and inflexible	Yes, same as film
Occlusal size available?	Yes	No	No	Yes
Panoramic radiograph?	Yes	Yes	Not yet available	Yes
Lateral cephalogram?	Yes	Yes	Not yet available	Yes
Infection control challenges?	No, disposal after single use	Yes	Yes	Yes
Integration with an electronic patient record (EPR)?	No, also scanned image contains a fraction of the information	Yes	Yes	Yes
Image display	Bright, light viewing box	All three digital technologies under high-brightness medical diagnostic-grade grayscale monitor		
Optimal viewing conditions?	All viewed under reduced ambient lighting			
Ease of image enhancement?	No, brightness only	Yes	Yes	Yes
Integrity of original image (vulnerability to fraud)?	No	No, almost all modern systems preserve original image; any subsequent amendments are preserved as date-stamped editions. Although no system is impervious to fraud, forensic engineers are aware of common processes.		
Long-term storage?	Yes, if properly developed	Unknown	Unknown	Unknown
Vulnerability of data in the image to loss?	Not if properly developed and stored, but will be destroyed in case of surgery destruction	If the data is backed up to a remote facility it can survive destruction of the surgery		
Telemedicine?	No	Yes	Yes	Yes

Source: Adapted from MacDonald, D.S. (2009). Factors to consider in the transition to digital radiological imaging. *J. Irish Dental Assoc.* 55: 26–34.
CCD, charge-coupled device; CMOS, complementary metal oxide semiconductor; N/A, not applicable.

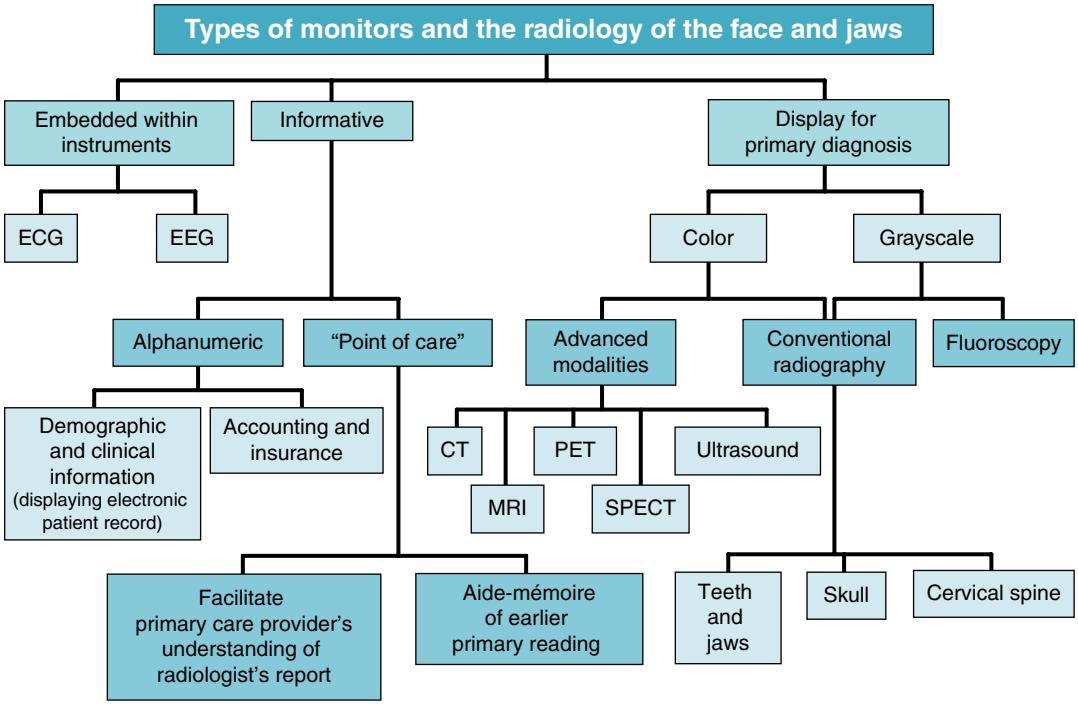


Figure 2.1 Types of monitors and their clinical roles. CT, computed tomography; ECG, electrocardiogram; EEG, electroencephalogram; MRI, magnetic resonance imaging; PET, positron emission tomography; SPECT, single positron emission computed tomography.

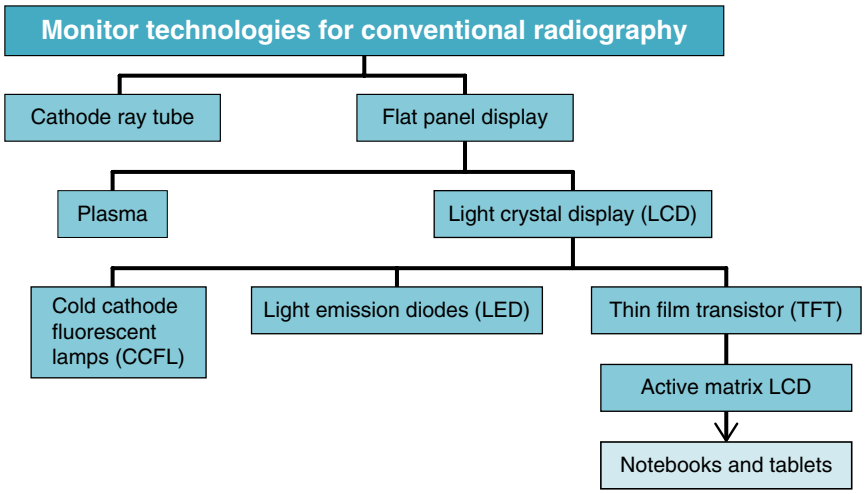


Figure 2.2 Monitor technologies for conventional radiography. Note: The plasma flat panel display has been included for completeness. Although it has been used in conference rooms where its large size was an advantage, it has not been considered as a technology for primary interpretation.

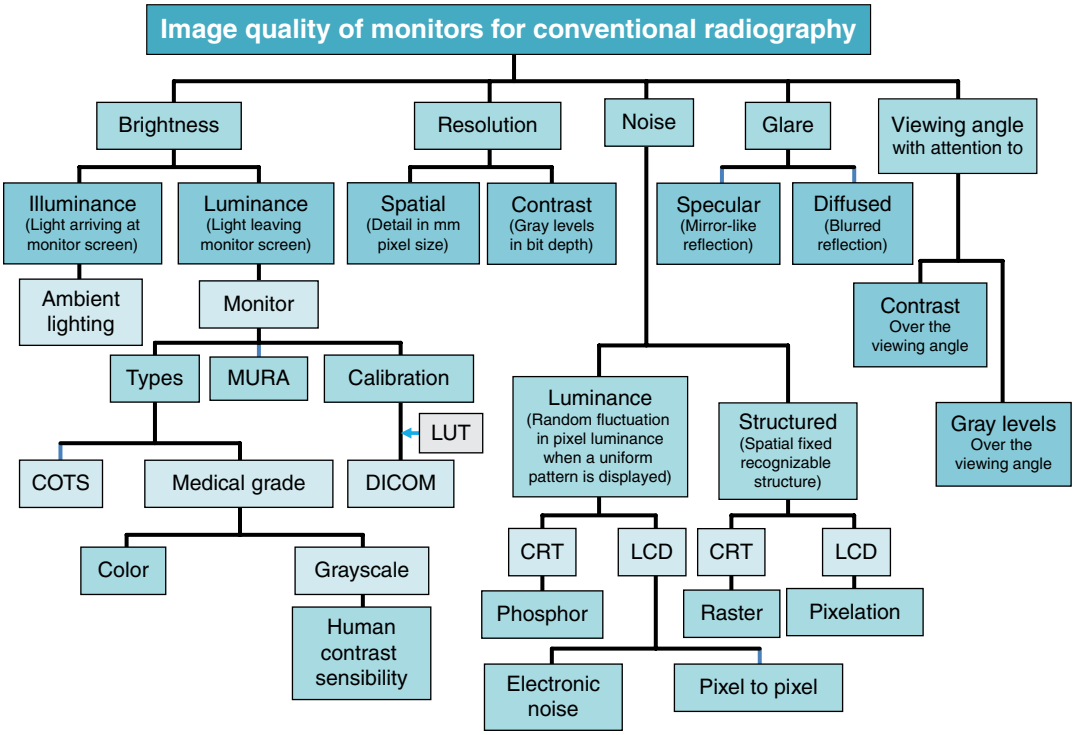


Figure 2.3 Image quality of monitors for conventional radiography. COTS, commercial off-the-shelf; CRT, cathode ray tube; LCD, liquid crystal display; LUT, look-up table; MURA, nonuniformity of brightness.

patient, it can catastrophically degrade the displayed radiographic image. Furthermore, the monitors used in the former are most likely to be *commercial off-the-shelf* (COTS) monitors. The image quality of such monitors is inferior to those displayed on the radiologist's *medical-grade diagnostic* (MGD) monitors. MGD monitors conform to *Digital Imaging and Communications in Medicine Part 14: Greyscale Standard Display Function* (*DICOM Part 14; GSDF*) [5]. For brevity this will be abbreviated to DICOM 14. DICOM calibration is assisted by a *look-up table* (LUT). As most dentists and oral and maxillofacial specialists are their own radiologists, for the foregoing reasons they should use the same viewing conditions as specialist radiologists for primary readings (radiological diagnosis) of their patients' images. The first attempt to inform the dental profession of Canada [6] of the need for MGD monitors as part of a choice to adopt digital radiography has since been extended to the British [7–9] and Australian [10] dental professions.

Despite the widespread adoption by dentists and dental institutions of the digital modalities for conventional radiography, this has not been accompanied by appropriate quality in image display. Butt and Savage's study of 29 COTS monitors derived from 12 general dental offices revealed that not one passed the American Association of Physicists in Medicine's Task Group 18's (AAPM TG18) acceptance criteria [10]. This study underlines the need for properly calibrated display monitors to be available for all dentists who

use digital radiography. In addition to a lack of understanding by many dentists and oral and maxillofacial specialists as to why viewing conditions are important, another significant point is the fact that MGD monitors are considerably more expensive than COTS monitors. Nevertheless, recently the display of a DICOM 14–calibrated COTS monitor was judged equivalent to an MGD monitor [11].

It is first necessary to explore the factors that contribute to the displayed image perceived by the clinician.

2.2 Image Display

Although Krupinski et al. found no difference between the performance of radiologists using monitors of differing luminance, the dwell time (time spent reviewing the image prior to diagnosis) was significantly longer when the viewing conditions were suboptimal [12]. The two factors affecting display are the quality of the monitor and the ambient lighting at the time of the review of the image displayed on that monitor.

2.2.1 MONITORS

In medicine three broad types of monitors are used: those embedded in instruments, such as in electrocardiogram (ECG) and electroencephalogram (EEG) instruments; those that are informative (electronic patient record etc.); and those for primary diagnosis (Figure 2.1). All medical (clinical) images regardless of modality are generally read by the radiologist on MGD monitors, where those used solely for informative purposes are COTS monitors. Although color monitors are used for reading cross-sectional or three-dimensional images created by in computed tomography (CT), magnetic resonance imaging (MRI), ultrasound (US), and positron emission tomography (PET), planar images (which include dental images: intraoral and panoramic images) have to be read on high-spatial-resolution, high-brightness grayscale (monochromatic) monitors. MGD is the "standard" monitor type for primary interpretation of most medical images. The main advantage of MGD monitors is their high luminance, which makes it easier to see the entire grayscale from black to white. This advantage is further enhanced by performing the primary interpretation of these images under reduced ambient lighting.

The radiologist produces a report, which accompanies the images. The referring clinician, using a "point-of-care" monitor (usually a COTS monitor), has the radiologist's report as a guide. These point-of-care monitors can be sited in the operating room, be desk mounted at the chairside in the dental office, or be a handheld tablet (smartphone, iPad etc.) at the bedside. Furthermore, smartphones and tablets can carry a library of ebooks and decision support applications [13] that may improve the quality of care. Because of the reduced luminance of COTS monitors, and the essential high brightness of the point-of-care venues, any other technical advantage of the monitor is nullified, however. Nevertheless, recently the display of 20 cases for each of nine radiology subspecialties on an iPad 3 and a 2 megapixel *light-emission diode* (LED) monitor were reviewed by the American Board of Radiology (ABR) examiners [14]. The "relevant image features were rated more visible" on the iPad 3 than on the LED monitor overall. Furthermore, a large majority of the ABR examiners considered the iPad 3 to be adequate for image display for examination of almost all specialty areas, including conventional projection or plane radiographs [14]. Although this report enhances the use of the iPad 3 and its successors and other makes

which use *Retina Display* or equivalent technology in the clinical situation, their definitive adoption for formal primary interpretation would require extensive and rigorous testing. Araki et al. reported that tablets "showed lower diagnostic accuracy, especially for superficial caries" [15]. Another important limitation of smartphone and tablet devices is that any patient-identifiable information on them cannot be carried out of the hospital because of patient confidentiality protection reasons. Furthermore, the clinician must be aware that the visibility of the touch screen is reduced by multiple fingerprints. In addition, the clinician may not perceive the image the reporting radiologist saw due to poorly selected display settings and the brightness of the ambient light [16].

Important features of an MGD monitor are optimal spatial resolution (image detail, measured in line pairs per millimeter [lp/mm]), contrast resolution (discerning the difference between two adjacent densities, commonly expressed in bit depth or gray levels), high brightness, adjustment for the human eye's nonlinear perception, and self-calibration.

The displayed image should fully represent all the data captured by the detector. Ideally, the display of each pixel of the image captured by the detector should be represented by a corresponding pixel on the monitor display, in order to optimize the detector's spatial resolution. This is a 1-to-1 or 1 : 1 display. Therefore, information contained within the captured image may not be displayed on the monitor if the display is not 1 : 1. Haak et al. reported that ratios of 1 : 1 and 2 : 1 were significantly better for the detection of approximal caries than a ratio of 7 : 1 [17].

As indicated by the multitude of features in Figure 2.3, MGD monitors, particularly those for conventional radiography, are technologically complex. Since a discussion of all of these features is outside the remit of this textbook, only the main features will be detailed in this chapter. A variety of technologies have been reflected in monitor design (Figure 2.2). The *cathode ray tube* (CRT) is now effectively obsolete and will not be considered further. There are various *liquid crystal display* (LCD) technologies, which differ with regard to their backlighting technologies. Although some *cold cathode fluorescent light* (CCFL) backlit LCD monitors are still in service, newer ones are backlit by LED. Other LCD technologies are *thin film transistor* (TFT) and *in-plane switching* (IPS). Apple's Retina Display uses IPS. Although TFT LCDs have very high resolutions and are used in monitors, they, like Retina Display, are also used in notebooks, smartphones, and tablets, which are, as already mentioned, increasingly commonplace in point-of-care situations. IPS LCDs, in contrast to older LCDs, allow a wide viewing angle. The advantage is that not only do viewers no longer need to sit directly in front of the monitor, as they did for earlier LCD monitors, but more than one viewer can view a particular monitor at the same time, thus enhancing training and communication with colleagues.

The increased availability of touchscreen monitors introduces another variable, since fingerprints may interfere with the quality of the display [16]. Furthermore, both reflective protective screens and highly reflective monitor screens should be avoided [16].

The MGD monitor's *grayscale standard-display function* (GSDF) is based on a phenomenon called *human-contrast sensitivity* (HCS), which takes the human eye's nonlinear perception into account. The human eye more easily sees relatively small changes in brighter areas than in darker areas. The GSDF adjusts the brightness so that all areas have the same level of perceptibility [5].

Although the monitors employed for medical diagnosis use at least a 12-bit–depth technology, if they operate within an *operating system* such as Windows, they will resolve to only 8-bit depth (or the 256 gray level used by COTS monitors). Note: some current color monitors can resolve over 32-bit depth. Despite this, medical monitors do require 12-bit-depth technology for accurate self-calibration, which is performed to DICOM 14 standards. An LUT is a precalculated array-indexing operation which can make a significant saving on processing time. A LUT is used to conform the monitor's self-calibration to the DICOM 14 curve.

Seto et al.'s results "indicate that medical display systems must be carefully … calibrated to ensure adequate image quality" [18]. Self-calibration of the monitor's luminance (brightness) ensures that every time dentists, in their essential role as radiologists, review an image it is of optimal quality. Furthermore, the performance of the monitor should be repeatable [5]. Although MGD monitors are exceptionally bright, most at 500 candles per square meter (cd/m^2) or above, New York City guidelines require the minimal luminance to be 350 cd/m^2 [19]. As all monitors fade with time, self-calibration ensures optimal and standardized brightness, until the backlight brightness falls below the threshold and needs to be replaced. Nevertheless, the results from photometers incorporated into self-calibrating MGD monitors older than five years should be compared with those from an externally calibrated photometer [19].

The aforementioned clinical reports on monitors for the display of medical images have had to be performed on those technologies already in service. Therefore they cannot encompass those technologies which have emerged most recently. Two such technologies are Adobe's RGB (red, green, and blue) and Digital Cinema Initiatives' DCI/P3, both renowned for their wide-gamut colorspace. They differ substantially from the current monitor technologies, which to a large degree use white LED backlights, for which blue light predominates. Adobe and DCI/P3 both use a wide gamut which includes reds and greens. Although currently these are in service with photographers and other imaging professionals, they are yet to make substantial inroads into imaging medicine. Nevertheless, this has already begun to some degree: Apple has adopted DCI/P3 for its most recent desktop and iMac Pro models, which are used by some clinicians for clinical purposes. Although Adobe RGB is DICOM 14 compliant, DCI/P3 is not yet (personal communication, Edison Wrzosek, Technical Support, Faculty of Dentistry, University of British Columbia).

2.2.2 AMBIENT LIGHTING (ILLUMINANCE)

Illuminance (reduced ambient lighting) essentially goes in tandem with monitor brightness. Recommendations for reduced ambient lighting in diagnostic reading stations for conventional analog (and digital) radiographs are 2–10 lx (illuminance is commonly expressed in *lux* or more simply lx), in comparison with 200–250 lx in clinical viewing stations in hospitals [20]. The evidence for the need for reduced ambient lighting for dentistry is provided by Haak et al. [21]. They found that differences in monochromatic intensity were detected significantly earlier if the ambient lighting was reduced (70 lx versus the 1000 lx recommended for the dental operatory) [21]. Hellen-Halme et al. demonstrated that when the reduced ambient lighting is less than 50 lx there is a significant increase in the accuracy of diagnosing approximal caries in comparison to above 1000 lx [22]. A DICOM 14–calibrated COTS monitor improves the detection of dentinal caries on lower molars on bitewings (intraoral radiographs) in dim lighting and

the detection of enamel caries in upper molars in bright lighting [23].

2.3 Image Enhancement

Image enhancement of the captured image is clearly an advantage that digital technologies have over film. Parks displayed and discussed several enhancements: density (brightness), contrast, measurement, image inversion, magnification, flashlight, and pseudocolor [1]. Although altering the brightness can lighten overexposed images, underexposed images should be retaken. Therefore, the need to optimally expose a solid-state detector is just as important as it is for film. As indicated earlier, images should be reviewed at a 1 : 1 ratio. This may not be always possible, particularly for detectors with very high spatial resolutions or for large images such as panoramic radiographs. In such cases a 1 : 1 ratio will magnify (*magnification*) the image, requiring the clinician to scroll or pan through the image. Haak et al. demonstrated that review of radiographic images at higher magnification improves accuracy [22]. Perhaps one of the most desired features of digital radiology is measurement; nevertheless, Kal et al. found that all processing algorithms provided significantly shorter measurements of the endodontic file lengths than their true length [24].

Koob et al. compared different image processing modes or filters on the reproducibility and accuracy of the assessment of approximal caries viewed in charge-coupled devices (CCDs) [25]. Although they found there were no significant differences in reproducibility, the exposure time influences the overall accuracy of the central depth measurement of the approximal carious lesion. Haiter-Neto et al. found that the accuracy of the detection of non-cavitated approximal caries among seven solid-state detectors was not significant [26].

2.4 Storage and Compression of Images

The need to review (read) the primary images under optimal conditions also requires that these images must be faithfully preserved and stored so that they can be reaccessed and reread later. This may be necessary as part of the continued management of the patient not only by the primary clinician, but also for referral to another. These images may also be required by clinicians to defend themselves in a legal case like the one overviewed in Chapter 1.

Adopting digital technology does not alleviate the problem of long-term storage of all existing films (analog images). Fundamentally, the storage of electronic dental records must accurately preserve the original content of the record (e.g. text, image, or chart) [27]. The record must include complete information about the creation of any modification of the record (author, date, time, and exact source of the record, such as the workstation). The format must be "read only" and protected from unauthorized alteration, loss, damage, or any other event that might make the patient information it contains inaccessible. Many jurisdictions require that digital clinical data be backed up to a remote server. The advantage of this is that this data is preserved if the surgery has been destroyed by fire or natural catastrophe. The advantage to both dentists and their patients is that the data can be retrieved and treatment quickly recommenced at an alternative venue. This is particularly important as the value of a practice is still based in part on the goodwill represented by active patient records.

Many jurisdictions require retention of dental records for at least 10 years. Dentists considering adopting digital radiography need to consider this, as it is likely that during that period, at least for some of their patients, they may need to convert to

a different system at least once. It is a common experience that *information technology* (IT) changes rapidly with time, with a risk that different generations of technology may become incompatible with each other. Therefore, in order to ensure that data survives transfer from one system to another, dentists must ensure not only that the systems are DICOM 14 compatible, but also that all digital images are transferred into the new record system without loss of data. So far there does not appear to be a report to confirm that this can actually be achieved in dentistry.

Although not much of an issue for a single practitioner, the storage of images may present a much greater challenge for a large group practice that uses CBCT data for implants and orthodontic cephalometry. Intraoral images account for only hundreds of bytes of storage and panoramic radiographs for just a few thousand. The very large image files required for CBCT data quickly exhaust even a very generous storage capacity.

Compression of image files is an alternative to increasing storage. Two systems are used for compression: *lossless* and *lossy*. Lossless compression does not result in a loss of data. Lossy compression, however, involves an irrevocable loss of data. Although Eraso et al. reported that loss of image quality is not a factor unless the file size is reduced to 4% or less [28], Fidler et al., who systematically reviewed the literature on lossy compression, reported that the amount of information lost is difficult to express and standardize [29]. Therefore, until lossy compression has been definitively tested, all data contained in a clinical image file must be preserved. Furthermore, the format of the image at the time of creation remains the original [30]. Therefore, scanning a film, even on a medical-grade scanner, only creates a copy; the film is the original image and must be preserved. Furthermore, images created digitally remain the original images, although they may have been printed onto the appropriate quality of paper or transparencies by medical-grade printers. These printouts are just copies. It also follows that any modification of the original image can only be an edition of the original, which must remain unaltered. The later edition should be automatically date-stamped with the date of its later creation.

Dentists must understand that the image they view on their monitor is not the original image captured by the detector, This captured image is in itself not the raw image captured by the detector, but instead an image which has been automatically preprocessed so as to compensate for defects such as nonfunctioning pixels. The programs which perform this preprocessing cannot be accessed and modified by the dentist. It is this preprocessed or "presented" image that constitutes the "original" image from a legal perspective.

All referred digital images should ideally be delivered on a *compact disc* (CD), *digital video disc* (DVD), or *Universal Serial Bus* (USB) flash drive rather than emailed if a *local area network* (LAN) is not available. Email is not only not secure, but often requires lossy compression of the original images. All image files should be saved and stored as *Tagged Image File Format* (TIFF) rather than as *Joint Photographic Experts Group* (JPEG) images on a LAN. JPEG is prone to further lossy compression each time it is opened.

2.5 Physiological Phenomena and Radiological Interpretation

Once the optimally made image is viewed under optimal conditions by the trained and experienced clinician, that image should be optimally interpreted. The quality of image

capture and of image display avails clinicians or their patients little unless supported by clinicians' prior knowledge of the radiological pathology, the artifacts associated with each particular modality, and the physiological phenomena that may interfere with proper interpretation. Unfortunately, physiological phenomena within each clinician may influence the diagnosis [31]. As an educator and practitioner in OMFR, I have observed two such phenomena that are particularly important, certainly with regard to student and general clinicians. These are *reversible (or ambiguous) figures* and the *Mach band effect*.

Perhaps the best known reversible (or ambiguous) figure is the "two faces or vase" image. When such a figure is viewed, only one orientation can be perceived. This phenomenon is believed to arise from the transmission of sensory data to the visual cortex by way of at least two alternate pathways. The clinical importance of this phenomenon is that the clinician's perception of a particular image may change due to fatigue that occurs in one pathway, compelling the image data to be transmitted by the other pathway. Figure 2.4 shows this phenomenon with some of my undergraduate students in formal examinations. Although it is expected that the clinician's experience of this phenomenon will decline with further training and practice, fatigue will always be a problem when the workload increases. Examination-induced fatigue may have contributed to these students' response to this type of image.

The Mach band effect is ubiquitous in radiology and occurs at the junction of two regions of differing radiodensity (Figure 2.5), particularly where there are superimposed structures [32]. Although in dentistry this phenomenon is most noticeable on the panoramic radiograph, it also is frequently experienced upon reviewing the *enamel-dentinal junction*



Figure 2.4 Panoramic radiograph of florid osseous dysplasia (FOD). Some students and general dental clinicians report the subjacent radiolucency rather than left mandibular FOD. Source: Reproduced with permission from MacDonald-Jankowski, D.S. (1992). Gigantiform cementoma occurring in two populations; London and Hong Kong. *Clin. Radiol.* 45: 316–318.

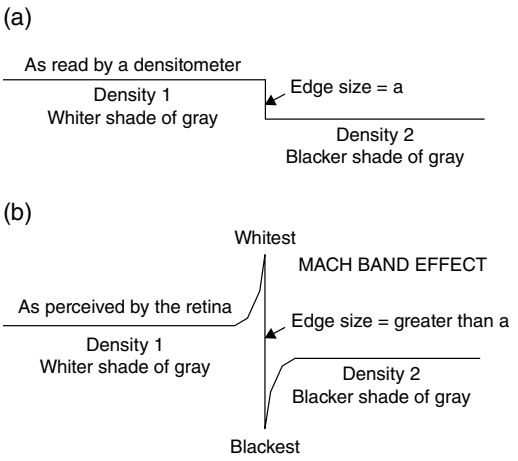


Figure 2.5 Mach band effect. Schematic diagram of (a) two adjacent radiodensities as read by a densitometer and (b) two adjacent radiodensities as perceived by the human retina. The size of the step (a) is now greater, accentuating the difference between the two densities and making the step easier to perceive.

(EDJ) of teeth on all conventional images. In the latter, the enamel margin immediately adjacent to the EDJ is white, whereas the dentine trends to black. The Mach band effect arises within the retina and results from the physiological process of lateral inhibition. With stimulation of a receptor (either a rod or a cone) in addition to initiating the transmission of an impulse toward the visual cortex, inhibitory impulses are being transmitted to neighboring receptors, preventing them from also discharging an impulse back to the visual cortex.

The Mach band effect can be observed in any panoramic radiograph, particularly in relation to the secondary image of the contralateral lower border of the mandible (Figure 2.6). The Mach band effect is a two-edged sword. Although it is invaluable in assisting the clinician to perceive otherwise small differences between adjacent densities, it can create artifacts, particularly "fracture lines" (Figure 2.6). In addition, on occasion it may create the illusion of a capsule around a radiopacity that may mislead the clinician to consider an incorrect diagnosis; Figure 2.7 is such a case. A biopsy and subsequent radiology, including CBCT, confirmed that this was not a lesion that required surgery.



Figure 2.6 Panoramic radiograph displaying the Mach band effect. It accentuates the soft-tissue shadows created by the soft palate, dorsum of the tongue, and palatine tonsil to mimic a fracture through the angle of the mandible. Note 1: The secondary image of the contralateral lower border of the mandible is delineated by the Mach band effect. Note 2: The white fingerprint marks are most likely to arise from the fixer-contaminated fingers of the person taking the film out of the cassette and placing it into the processor.

2.6 Avoidance of Visual Fatigue

Kagadis et al. addressed features of an optimum radiologist image-reading environment and routine that may contribute to a reduction in errors and fatigue [16]. This would be of interest to dentists who with the advent of CBCT may find themselves in front of a monitor reviewing images for a larger part of their work day. Visual fatigue may be reduced or even eliminated by the 20–20–20 rule: every 20 minutes look 20 feet away for 20 seconds. This helps to reduce eye strain by allowing eye muscles to relax. In addition, avoidance of abrupt and frequent changes between light and dark can be achieved, as mentioned earlier, by maintaining a low level of ambient lighting. The use of zoom and pan functions instead of moving the head closer to the monitor to see fine details also contributes to an optimal viewing distance [16]. Furthermore, these and a comfortable chair and appropriate desk height also enhance good posture and avoid back strain.



Figure 2.7 Conventional panoramic radiograph (a) displaying a well-defined radiolucency substantially in the alveolus around the roots of the lower right second and third molars. This was observed as an incidental finding. There is no appreciable displacement or root resorption. Nor do the affected teeth exhibit caries or large restorations; they are vital. This excluded consideration of sclerosing osteomyelitis. The well-defined radiopacity appears to be surrounded by a well-defined radiolucency suggestive of a capsule. Since there was no clinically obvious buccolingual expansion, a periapical (b) was prescribed. This revealed trabeculae "crossing" through the radiolucent "capsule." Cone-beam computed tomography was performed (c–e). Trabeculae link the radiopacity with adjacent normal bone. This is a dense bone island, which was confirmed histopathologically. The well-defined radiolucent capsule perceived on the panoramic radiograph (a) was therefore determined to be due to the Mach band effect, i.e. trabeculae.

References

1. Parks, E.T. (2008). Digital radiographic imaging: is the dental practice ready? *J. Am. Dent. Assoc.* 139: 477–481.
2. Farman, A.G. and Farman, T.T. (2005). A comparison of 18 different x-ray detectors currently used in dentistry. *Oral. Surg. Oral. Med. Oral. Pathol. Oral. Radiol. Endod.* 99: 485–489.
3. MacDonald, D.S. and Waterfield, J.D. (2011). Infection control in digital intraoral radiography: evaluation of microbiological contamination of photostimulable phosphor plates in barrier envelopes. *J. Can. Dent. Assoc.* 77: b93.
4. Berlin, L. (2015). Medicolegal—malpractice and ethical issues in radiology. Must all monitors meet DICOM standards? *AJR Am. J. Roentgenol.* 204: W492.

5. National Electrical Manufacturers Association (NEMA). Digital imaging and communications in medicine (DICOM). Part 145: Grayscale Standard Function. 2006. http://dicom.nema.org/dicom/2006/06_14pu.pdf (Accessed December 29, 2018).
6. MacDonald-Jankowski, D.S. and Orpe, E.C. (2007). Some current legal issues that may affect oral and maxillofacial radiology. Part 2: digital monitors and cone-beam computed tomography. *J. Can. Dent. Assoc.* 73: 507–511.
7. McIlgorm, D.J., Lawinski, C., Ng, S., and McNulty, J.P. (2013). Could standardizing "commercial off-the-shelf" (COTS) monitors to the DICOM part 14: GSDF improve the presentation of dental images? A visual grading characteristics analysis. *Dentomaxillofac. Radiol.* 42: 20130121.
8. McIlgorm, D.J., Lawinski, C., Ng, S., and McNulty, J.P. (2013). Quality of "commercial-off-the-shelf" (COTS) monitors displaying dental radiographs. *Br. Dent. J.* 215: E22.
9. McIlgorm, D. (2016). Viewing your digital radiographs: which monitor is best? *Br. Dent. J.* 220 (8): 393–397.
10. Butt, A. and Savage, N.W. (2015). Digital display monitor performance in general dental practice. *Aust. Dent. J.* 60: 240–246.
11. McIlgorm, D.J. and McNulty, J.P. (2015). DICOM part 14: GSDF-calibrated medical grade monitor vs a DICOM part 14: GSDF-calibrated "commercial off-the-shelf" (COTS) monitor for viewing 8-bit dental images. *Dentomaxillofac. Radiol.* 44: 20140148.
12. Krupinski, E., Roehrig, H., and Furukawa, T. (1999). Influence of film and monitor display luminance on observer performance and visual search. *Acad. Radiol.* 6: 411–418.
13. Székely, A., Talanow, R., and Bágyi, P. (2013). Smartphones, tablets and mobile applications for radiology. *Eur. J. Radiol.* 82: 829–836.
14. Toomey, R.J., Rainford, L.A., Leong, D.L. et al. (2014). Is the iPad suitable for image display at American Board of Radiology examinations? *AJR Am. J. Roentgenol.* 203: 1028–1033.
15. Araki, K., Fujikura, M., and Sano, T. (2015). Effect of display monitor devices on intraoral radiographic caries diagnosis. *Clin. Oral Investig.* 19: 1875–1879.
16. Kagadis, G.C., Walz-Flannigan, A., Krupinski, E.A. et al. (2013). Medical imaging displays and their use in image interpretation. *Radiographics* 33: 275–290.
17. Haak, R., Wicht, M.J., Nowak, G., and Heilmich, M. (2003). Influence of displayed image size on radiographic detection of approximal caries. *Dentomaxillofac. Radiol.* 32: 242–246.
18. Seto, E., Ursani, A., Cafazzo, J.A. et al. (2005). Image quality assurance of soft copy display systems. *J. Digit. Imaging* 18: 280–286.
19. Ruuge, A., Erdi, Y., and Mahmood, U. (2016). SU-F-I-61: assessment and characterization of the built-in internal photometer of primary diagnostic monitors. *Med. Phys.* 43: 3400–3401.
20. Samei, E., Badano, A., Chakraborty, D. et al. (2005). Assessment of display performance for medical imaging systems: executive summary of AAPM TG18 report. *Med. Phys.* 32: 1205–1225.
21. Haak, R., Wicht, M.J., Heilmich, M. et al. (2002). Influence of room lighting on grey-scale perception with a CRT and a TFT monitor display. *Dentomaxillofac. Radiol.* 31: 193–197.
22. Hellén-Halme, K. and Lith, A. (2012). Effect of ambient light level at the monitor surface on digital radiographic evaluation of approximal carious lesions: an in vitro study. *Dentomaxillofac. Radiol.* 41: 192–196.
23. Kallio-Pulkkinen, S., Huumonen, S., Haapea, M. et al. (2016). Effect of display type, DICOM calibration and room illuminance in bitewing radiographs. *Dentomaxillofac. Radiol.* 45: 20150129.
24. Kal, B.I., Baksi, B.G., Dündar, N., and Sen, B.H. (2007). Effect of various digital processing algorithms on the measurement accuracy of endodontic file length. *Oral Surg. Oral Med. Oral Pathol. Oral Radiol. Endod.* 103: 280–284.
25. Koob, A., Sanden, E., Hassfeld, S. et al. (2004). Effect of digital filtering on the measurement of the depth of proximal caries under different exposure conditions. *Am. J. Dent.* 17: 388–393.
26. Haiter-Neto, F., dos Anjos Pontual, A., Frydenberg, M., and Wenzel, A. (2008). Detection of non-cavitated approximal caries lesions in digital images from seven solid-state receptors with particular focus on task-specific enhancement filters. An ex vivo study in human teeth. *Clin. Oral Investig.* 12: 217–223.

27. Fefergrad, I. (2004). Recordkeeping in dentistry. In: *Dental Law in Canada* (ed. J. Downie, K. McEwen and W. MacInnes), 271–278. Markham, ON: Butterworths LexisNexis Canada.
28. Eraso, F.E., Anaioui, M., Watson, A.B., and Rebeschini, R. (2002). Impact of lossy compression on diagnostic accuracy of radiographs for periapical lesions. *Oral Surg. Oral Med. Oral Pathol. Oral Radiol. Endod.* 93: 621–625.
29. Fidler, A., Likar, B., and Skaleric, U. (2006). Lossy JPEG compression: easy to compress, hard to compare. *Dentomaxillofac. Radiol.* 35: 67–73.
30. Goga, R., Chandler, N.P., and Love, R.M. (2004). Clarity and diagnostic quality of digitized conventional intraoral radiographs. *Dentomaxillofac. Radiol.* 33: 103–107.
31. Daffner, R.H. (1989). Visual illusions in the interpretation of the radiographic images. *Curr. Probl. Diagn. Radiol.* 18: 62–87.
32. Wallis, S.A. and Georgeson, M.A. (2012). Mach bands and multiscale models of spatial vision: the role of first, second, and third derivative operators in encoding bars and edges. *J. Vis.* 12: 18. https://doi.org/10.1167/12.13.18.

Chapter 3

Evidence-based radiology

3.1 Introduction

Although the specialties of dentistry and radiology are both technology driven, the former is composed of generalists, who, like their physician counterparts, are more preoccupied with enhancing "wellness," which returns the majority of their patients to society with restored or improved esthetics and function (physical and/or mental) than just diagnosis and treatment of dental caries, as was the case only a few decades ago. In addition to this is a movement from solo to group practices [1], and the development of a more holistic oral physician working within an ethnically diverse community, moving from the traditional "extension for prevention" to a "minimally invasive" and biomedical approach to the treatment of dental diseases with an increased use of three-dimensional technology, including cross-sectional imaging [2]. Furthermore, Atchison et al. advocated an "integration of dental and medical care [which] increased access to and coordination of patient care by means of offering health care services traditionally provided by the other profession" [3]. This textbook has set out not only to address some of the imaging challenges of this integration facing the modern dentist, but also to meet the needs of the medical radiologist, whose increased interest and involvement in the diagnosis of jaw lesions are indicated by the increasing publication of papers in a leading medical radiology journal [4–6]. The services of radiologists, on the other hand, are called upon to assist in the diagnosis and assessment of patients who the clinical specialists and generalists have determined may have a disease that requires treatment upon diagnosis. Following Rontgen's discovery of X-rays in 1895, *conventional radiography* (CR) was quickly developed and held sway, until the cross-sectional imaging modalities of diagnostic ultrasound, *computed tomography* (CT), and *magnetic resonance imaging* (MRI) became commonplace in medicine in the 1960s, 1970s, and 1980s, respectively. Dentistry almost wholly relied on CR (including panoramic radiography) until the advent of *cone-beam computed tomography* (CBCT) for the discipline only two decades ago.

In the United States, it has been suggested that radiological practice is moving from volume-based performance and interpretation of a large number of examinations to a higher-quality service centered on patient outcomes [7]. The last is based on *evidence-based practice* (EBP), which in turn has been incorporated into "practice-based learning and improvement" and "systems-based practice," which are two of the six core competencies of the Accreditation Council for Graduate Medical Education (ACGME) and two of the twelve American

Oral and Maxillofacial Radiology: A Diagnostic Approach, Second Edition. Edited by David MacDonald.
© 2020 John Wiley & Sons, Inc. Published 2020 by John Wiley & Sons, Inc.

Board of Radiology (ABR) "milestones" for diagnostic radiology. Systems-based practice requires the resident to "demonstrate effective use of resources to provide optimal health care, work effectively and coordinate patient care in various healthcare settings and systems, and advocate for quality patient care and patient care outcomes" [8].

The term radiology was first used in 1900 and is defined by *Merriam-Webster* as "a branch of medicine concerned with the use of radiant energy (such as X-rays) or radioactive material in the diagnosis and treatment of disease" [9]; by the *Oxford British and World English Dictionary* as "the science dealing with X-rays and other high-energy radiation, especially the use of such radiation for the diagnosis and treatment of disease" [10]; and by the *Farlex Partner Medical Dictionary* as "the scientific discipline of medical imaging using ionizing radiation, radionuclides, nuclear magnetic resonance, and ultrasound. Synonym(s): diagnostic radiology" [11]. Although the last of the three precisely describes the remit of the modern medical radiologist, the first two reflect the original twin pillars of medical radiology, diagnosis and treatment, which are reflected in today's separate specialties of diagnostic radiology and radiation oncology. The role of the latter and the contribution that diagnostic radiology (CT and MRI) makes to the radiation oncologist are revealed in Chapter 19. Diagnostic radiologists are also increasingly involved in interventional radiology, such as in the treatment, not only the diagnosis, of salivary gland duct obstructions (Chapter 13) and vascular lesions (Chapter 14).

3.2 Interaction of the Radiologist with Other Clinicians

The radiologist reports directly back to the referring clinician. The degree of interaction between them varies widely according to country and the particular institution. At cancer centers, such as the British Columbia Cancer Agency (BCCA), radiologists work very closely with their colleagues who deliver actual clinical care to the patient not only to achieve the diagnosis, but in conjunction with them to formulate the optimal treatment plan. Because of their generally broad clinical experience prior to specialty training, radiologists are well placed to further assist clinicians in considering other tests that may confirm the diagnosis or optimize treatment planning. One such area is the renewed interest in *keratocystic odontogenic tumors* (KCOTs), particularly the solitary/sporadic/nonsyndromic type, regarding whether they are true neoplasms or cysts, or either, as discussed in Chapter 9. The WHO 2005 edition emphasized the importance of *protein patched homolog 1* (PTCH1) in the diagnosis of KCOTs [12]. The value of such genetic markers was emphasized by the Human Genome Project. This had earlier excited considerable hope in a future of personalized medicine and dentistry [13]. These issues will be discussed later in this chapter, after a review of the scientific basis of radiology.

3.3 The Scientific Basis of Radiology

Radiology, as the suffix "-ology" implies, is a science. The *Oxford British and World English Dictionary*'s definition of a science is "The intellectual and practical activity encompassing the systematic study of the structure and behaviour of the physical and natural world through observation and experiment" [14]. Part of this systematic study in the analysis of results is the statistical method. The *Oxford British and World English Dictionary*'s definition of

statistics is "The practice or science of collecting and analyzing numerical data in large quantities, especially for the purpose of inferring proportions in a whole from those in a representative sample" [15]. In order to generate these "large quantities" in an objective way, "systematic review" was developed in the late 1980s [16]. The application of systematic review to the most frequent and/or important lesions of the face and jaws has already been discussed. Integral to systematic review is the meta-analysis, an essential element of MacDonald-Jankowski and Dozier's approach [17]. Meta-analysis, as defined by the *Dictionary of Epidemiology*, is "the process of using statistical methods to combine the results of different studies" [18]. The basics of these statistical methods have already been addressed in many excellent texts [19–21]. Table 3.1 defines the more important statistical characteristics of a diagnostic system. Others are defined and discussed by Lavelle et al. [7]

Table 3.1 Definitions of the most used terms applicable to radiology.

Term	Definition
Sensitivity	The proportion of patients with the disease who have a *positive* test.
Specificity	The proportion of patients with*out* the disease who have a *negative* test.
Positive predictive value	The probability that patients with a positive test truly have the disease.
Negative predictive value	The probability that patients with a negative test truly *do not* have the disease.

Source: Adapted from Lavelle, L.P., Dunne, R.M., Carroll, A.G., and Malone, D.E. (2015). Evidence-based practice of radiology. *Radiographics* 35: 1802–1813.

3.4 Systematic Review

Systematic review was developed several decades ago to provide clinicians quickly with answers to their clinical questions. Fundamental to systematic review was the research question, which was composed of four standard elements known as PICO: the **P**roblem to be addressed, the **I**ntervention to be assessed, its **C**omparison with the current and/or established intervention or "gold standard," and its **O**utcomes. From this were formulated the search terms, the databases to be searched, and then the inclusion and exclusion criteria. In the process of their formulation, the developer of a particular systematic review had to be careful not only to avoid the introduction of bias, but to minimize that already intrinsic to all the databases. Foremost among these biases is *publication bias*: studies with positive outcomes are more likely to be published and thus will skew any systematic review toward that outcome.

Until recently only a fraction of the world's medical literature was indexed, namely that published in major journals and preferably in English. This has since changed markedly. Many leading European, Japanese, and Chinese national journals now publish either exclusively in English or issue an English edition to accompany that in the national language. Most journals require that submitting authors identify and list the major topics relevant to their manuscript. These are invariably Medical Subject Heading (MeSH) or "entry terms" (MeSH synonyms) as used by PubMed. The titles and abstracts of indexed papers are also electronically searched when "textword" or a free-written term is used [17]. Furthermore, PubMed has also indexed many online-only journals, many of recent origin. Many Romance-language journals (mainly Spanish and Portuguese) are

indexed in LILACS, an index of scientific and technical literature based at BIREME, the Latin American and Caribbean Center on Health Sciences Information, based in São Paulo. Clark and Castro recommend that LILACS should be searched to improve the quality of a systematic review [22]. Although many LILACS journals are now also indexed in PubMed, at least their non-English abstracts should be reviewed by a native Spanish or Portuguese speaker to determine whether they may be compliant with the inclusion criteria. Only then will a translation of the full paper become necessary. As Spanish is the second most frequently spoken language after Chinese and Portuguese the sixth, finding a medically and/dentally qualified colleague who is a native Spanish or Portuguese speaker is not very difficult. Both PubMed and LILACS, due to the generosity of the governments of the USA and Brazil, respectively, are accessible free of charge [17]. Unless there is a very good reason, all relevant papers published in languages other than English which otherwise comply with the inclusion criteria should be incorporated in a systematic review and their content evaluated according to the exclusion criteria. This was done for the systematic reviews on the most frequent and/or important lesions of the face and jaws detailed in Chapter 1. The outcome of this was a unique display of the demographic, clinical, and radiological details of each systematic review according to the four global groups representing all humanity, which are cartographically displayed in Figures 1.45–1.57. Recently, for instance, marked differences were revealed in the presentations of nevoid basal cell carcinoma between Northern Europeans and East Asians [23].

As already stated, an important element of the systematic review is meta-analyses, which "are excellent for providing higher levels of evidence in medical science" [24]. Park et al. reviewed the meta-analyses and systematic reviews published between 2007 and 2015 in the 10 leading international medical radiological journals [24]. Nearly a third were published by Chinese teams; American teams constituted only a sixth and British a tenth [24]. The lower proportions by the two principal nations with English as a first language may reflect the fact that the increase in the number of radiologists has not kept up with the substantial increase annually in the radiologist's clinical workload, particularly with regard to CT and MRI [25, 26]. In a Canadian report in an academic setting, 88% of the radiologist's time was taken up with clinical activities, most of which had a direct effect on patient management [27]. This imbalance not surprisingly reduces the time available to perform quality research in these countries. A further imposition is the dearth internationally of oral and maxillofacial radiologists against the increasing availability of CBCT, particularly large field-of-view datasets that should be reviewed by a radiologist [5] simply because they include extragnathic regions that are outside the competence of dentists in most jurisdictions.

A large systematic review commissioned by the American Academy of Osseointegration (AAO) addressed the survival of dental implants at 5, 10, and 15 years post-implantation [28]. The results of this study have been set out in Table 20.1. This systematic review from the outset clearly declared that it would only consider English-language literature. This could be justified, since the topic was the survival of case series of osseointegrated implants. For such an important topic, publication bias was less likely. Most of this research was published in the higher-impact dental journals. Around 3500 English-language publications were captured. Furthermore,

the authors had to defend their systematic reviews before an international board of experts [28, p. 136], who were able to amend the systematic review as appropriate. In this case they included two more studies. The board chairman's consensus report was published with the revised systematic review [28, pp. 137–139]. The success of this systematic review was due to the fact that content experts and statisticians set it up and performed the analysis. It was very different to many systematic reviews which had been performed in dentistry at the same time. In most of these the formulation of the systematic review was driven by the informationist (usually a database librarian) and not the content expert. However, Sardanelli et al. reported that 38% of systematic reviews on medical imaging included an imaging specialist (a radiologist or nuclear/functional imaging doctor), whose presence did significantly increase the scientific quality of the systematic review [29].

Furthermore, due to the lack of involvement of a statistician, most of these dental systematic reviews were bad on heterogeneity, which frequently resulted in no difference being observed between the intervention and the gold standard. A systematic review comparing interdental brushing to flossing with regard to reducing periodontitis was anticipated to be at high risk of heterogeneity [30]. Therefore, a statistician was recruited. Although interdental brushing was significantly more effective, the differences between the studies were displayed with a flowchart, which enhanced the value of the systematic review to the clinician [30].

BOB CAT, another systematic review that generated multiple consensus statements for the management of Barrett's esophagus with no dysplasia, indefinite for, or low-grade dysplasia from a large-scale evidence review and a Delphi process, is perhaps the largest systematic review to date [31]. It has been adopted by the British National Health Service (NHS), which awarded it National Institute for Health and Care Excellence (NICE) accreditation.

While the oral and maxillofacial field is itself small, it shares in the diagnosis and management of oral and oropharyngeal cancers with many medical specialties. The eighth American Joint Committee on Cancer (AJCC) edition of the *Cancer Staging Manual* has introduced a number of changes in how these cancers are to be interpreted, reported, and managed [32].

Systems-based practice requires the resident to "demonstrate effective use of resources to provide optimal health care, work effectively and coordinate patient care in various healthcare settings and systems, and advocate for quality patient care and patient care outcomes" [8]. Leddy et al.'s own institution uses a continuous *quality improvement* (QI) process called IMPROVE. This stands for **I**dentify the problem, **M**easure the impact, **P**roblem analysis, **R**emedy the critical issues, **O**perationalize the solutions, **V**alidate the improvement, and **E**valuate over time [8].

3.5 Gene Markers and Markers of Gene Mutations

One of the "trends and developments shaping the future of diagnostic medical imaging is personalized medicine" [33]. Personalized medicine is based upon both the sequencing of the human genome and improvements in the current clinical methods of characterizing disease [33]: "Since the completion of the Human Genome project in 2003… it has become evident that many, if not all, human diseases are influenced by the variation and function of genes" [34]. A major factor that has emerged in our understanding

of some important lesions affecting the face and jaws is gene mutations. They are important to the dentist and to the radiologist, as some understanding of them is necessary to the developing discussion about their classification and behavior. Some of the most important genes and mutations will be discussed later in this section.

Although the human genomic code has been sequenced, future work on this will not solely lead to a complete understanding of the make-up of the human body or phenotype. According to Thrall, "the majority of medical practice is still guided by information about phenotype rather than genotype and the International Classification of disease system is based primarily on descriptors of disease phenotypes – even for diseases with known genotype associations" [33]. In addition to the genotype, epigenetics will need to be considered. Epigenetics is the study of inheritable changes in gene expression, without actual change in the genes. Although epigenetic change is a natural process that directs the differentiation of cells, it can be brought about, for example, by aging of the individual, or exposure to environmental and lifestyle factors. It acts generally by *deoxyribonucleic acid* (DNA) methylation, histone modification, or by preventing protein production by non-coding *ribonucleic acid* (RNA) [35].

Solomon drew some similarities and then indicated differences between the identification of incidentalomas in genomics and radiology [36], and Park et al. likened whole-genome sequencing to whole-body CT [37]. The main difference is that radiology can only display changes in the phenotype. Any significant gene mutation detected by the gene marker for it will otherwise remain undetected on clinical and/or radiological examination until it is expressed in the phenotype. The phenotype has been compared to a symphony produced by an orchestra. The individual performers and their instruments are likened to the individual genes, the sheet music to the epigenetic code, and the conductor to the epigenetic machinery that controls the expression of the genes [32]. Although literature has reported on genes associated with odontogenesis and oncogenesis for decades, it is relatively recently that genes such as PTCH1 and its mutations (see next section), and the *sonic hedgehog* (SHH) pathway of which it is part, have become noteworthy [38]. The SHH signaling pathway is essential to embryonic and postnatal development in addition to adult organ homeostasis [39]. SHH signaling is implicated in many diseases, including cancer [39].

3.6 Protein Patched Homolog 1

PTCH1 is a transmembrane protein which assists in the regulation of cell proliferation and differentiation. PTCH1 gene mutations have been associated with *nevoid basal cell carcinoma syndrome* (NBCCS), sporadic and syndromic KCOTs, basal cell carcinomas, and medulloblastomas.

Table 3.2 sets out the 2 × 2 contingency table from which sensitivity and specificity have been calculated for PTCH1 and syndromic KCOT [40]. PTCH1 mutation positivity is a "major criterion" for NBCCS, a multisystem syndrome which affects the skin, eyes, jaws, ovaries, skeleton, and nervous system (with the occasional medulloblastoma, a rare brain tumor). It is particularly important in the determination of whether early-onset KCOT in an East Asian child or adolescent patient is the early manifestation of NBCCS [41]. This is particularly important since the dermatological markers such as basal cell carcinomas and palmer/plantar pitting are much less frequent in this

Table 3.2 A 2×2 contingency table illustrating the outcomes of the test for the identification of mutations of protein patched homolog-1 (PTCH1) and syndromic versus nonsyndromic (sporadic/spontaneous/solitary) keratocystic odontogenic tumors (KCOTs) to calculate sensitivity, specificity, positive predictive value (PPV), and negative predictive value (NPV).

		Syndromic KCOTs			
		Syndromic	Sporadic	Total	
PTCH1 Mutations	Identified	11(TP)	13(FP)	24	PPV [TP/(TP+FP)] = 11/24 = **46%**
	Not identified	3(FN)	16(TN)	19	NPV [FN/(FN+TN)] = 3/19 = **16%**
	Total	14	29	**43**	
		Sensitivity [TP/ (TP+FN)] = 11/14 **= 79%**	**Specificity** [TN/(FP+TN)] = 13/29 **= 45%**		

Source: Computation of raw results derived from Guo, Y.Y., Zhang, J.Y., Li, X.F., et al. (2013). PTCH1 gene mutations in keratocystic odontogenic tumors: a study of 43 Chinese patients and a systematic review. *PLoS One* 8: e77305.
Key: FN, false negative; FP, false positive; TN, true negative; TP, true positive.

community. Furthermore, East Asians are significantly more likely to present with multiple KCOTs which are not syndromic. This is developed further in Chapter 9. The two groups of KCOTs, one for which mutations of the PTCH1 gene were identified and the other for which no mutations were identified, gives an insight into the current controversy over whether KCOT is a neoplasm or a cyst. Although this discussion will be developed further in Chapter 9, the literature surrounding this topic revealed the shortcomings of relying to a substantial degree on the outcome of such tests.

Nagao et al. revealed that one reason for failure to identify PTCH1 mutations in a number of Japanese NBCCS families was the fact that the entire PTCH1 gene has been deleted [42]. Karagozoglu et al.'s report of detecting no PTCH1 mutations in sporadic cases of KCOT may have been in the mind of the present author as a result of a limited number of mutations searched for [43]. Guo et al.'s study, published a few years later, found considerably more [38]. Regardless of the possibility that Karagozoglu et al.'s study was based on fewer PTCH1 mutations, their study is important in that not a single case of PTCH1 mutations–negative KCOT recurred after over four years of follow-up [43]. This may serve as the foundation of the present author's contention in Chapter 9 that sporadic KCOTs may be two separate lesions, one neoplastic with a tendency to recur and the other purely a developmental cyst. Park et al. reported that 16 out of 141 patients tested for 40 genes in addition to BRCA1/2, who had a personal or family history of breast cancer, had pathological variants in 9 non-BRCA1/2 genes [37]. Their report reveals the complexity of current testing, as only a minority of the genes are well understood [37].

In addition to the PTCH1 gene mutations or deletions, there may be other genetic defects that may contribute to KCOTs. The KCOT has a higher stromal *microvascular density* (MVD) than the dentigerous cyst,

the most common developmental cyst (discussed in Chapter 9), and the normal oral mucosa [44]. This refocuses on the KCOT's stroma. Jiang et al. were only able to identify abnormal expression of the *lysyl oxidase-like 4* (LOXL4) gene in both the KCOT's stromal tissues and fibroblasts [44]. This may enhance angiogenesis in KCOT, which may thereby in turn promote the locally invasive behavior of KCOTs [44]. LOXL4 expression has also been shown to be important in many malignancies, including head and neck cancer [45]. Recently a large-scale meta-analysis of genome- wide association studies doubled the number of new risk loci for Barrett's esophagus and esophageal adenocarcinoma and "revealed new insights into the causes of these disease" [46].

The importance of an awareness of relevant though nonradiological phenomena and tests, such as the tests for PTCH1 mutations and for LOXL4 expression, as ancillary diagnostic information is well known to the medical radiologist, in the same way that the oral and maxillofacial clinician integrates clinical, radiological, and where necessary histopathological and/or hematological information into the definitive diagnosis. The AJCC's eighth edition's new category on *extranodal extension* (ENE) and its particular relevance to that edition's equally new advice to radiologists with regard to *human papilloma virus* (HPV) p16–positive *oropharyngeal squamous cell carcinoma* (OPSCC) [32] is discussed at the end of Chapter 19.

3.7 Concluding Remarks

1. As technical developments and improvements in diagnostic knowledge proceed, practicing clinicians need to keep their practice updated. Although only a small number of clinicians have the time and/or facility to participate in research that embodies this knowledge, a mindfulness of the need to convey the essential message, namely significant findings, to their busy colleagues is desired.
2. Systematic reviews should, whenever possible, include a meta-analysis.
3. Systematic reviews, as emphasized in Chapter 1 and displayed in the tables in Chapters 9 and 10, should, whenever possible, present results that take account of ethnicity.

References

1. Bailit, H.L. (2017). The oral health care delivery system in 2040: executive summary. *J. Dent. Educ.* 81: 1124–1129.
2. Weintraub, J.A. (2017). What should oral health professionals know in 2040: executive summary. *J. Dent. Educ.* 81: 1024–1032.
3. Atchison, K.A., Weintraub, J.A., and Rozier, R.G. (2018). Bridging the dental-medical divide: case studies integrating oral health care and primary health care. *J. Am. Dent. Assoc.* 149: 850–858.
4. MacDonald, D.S. (2015). Maxillofacial fibro-osseous lesions. *Clin. Radiol.* 70: 25–36.
5. MacDonald, D.S. (2016). Lesions of the jaws presenting as radiolucencies on cone-beam computed tomography. *Clin. Radiol.* 71: 972–985.
6. Boeddinghaus, R. and Whyte, A. (2018). Trends in maxillofacial imaging. *Clin. Radiol.* 73: 4–18.
7. Lavelle, L.P., Dunne, R.M., Carroll, A.G., and Malone, D.E. (2015). Evidence-based practice of radiology. *Radiographics* 35: 1802–1813.
8. Leddy, R., Lewis, M., Ackerman, S. et al. (2017). Practical implications for an effective radiology residency quality improvement program for milestone assessment. *Acad. Radiol.* 24: 95–104.
9. Merriam-Webster. Radiology. 2018. https://www.merriam-webster.com/dictionary/radiology (Accessed November 15, 2018)
10. Oxford British and World English Dictionary. Radiology. 2018. https://en.oxforddictionaries.com/definition/radiology (Accessed November 15, 2018)

11. Farlex Partner Medical Dictionary. Radiology. 2012.https://medical-dictionary.thefreedictionary.com/radiology (Accessed November 15, 2018)
12. Philipsen, H.P. (2005). Keratocystic odontogenic tumour. In: *WHO Classification of Tumours, Pathology and Genetics of Tumours of the Head and Neck* (ed. L. Barnes, J. Eveson, P. Reichert and D. Sidransky), 306–307. Lyon: International Agency for Research on Cancer (IARC).
13. Slavkin, H.C. (2001). The human genome, implications for oral health and diseases, and dental education. *J. Dent. Educ.* 65: 463–479.
14. Oxford British and World English Dictionary. Science. 2018.https://en.oxforddictionaries.com/definition/science (Accessed November 15, 2018)
15. Oxford British and World English Dictionary. Statistics. 2018. https://en.oxforddictionaries.com/definition/statistics (Accessed November 15, 2018)
16. Egger, M., Smith, G.D., and Altman, D.G. (eds.) (2001). *Systematic Reviews in Health Care: Meta-analysis in Context*, 2e. London: BMJ Books.
17. MacDonald-Jankowski, D.S. and Dozier, M.F. (2001). Systematic review in diagnostic radiology. *Dentomaxillofac. Radiol.* 30: 78–83.
18. Clarkson, J.E., Bonner, B.C., Deery, C., and Grimshaw, J. (2003). *Evidence-Based Dentistry for Effective Practice*, 68–75. Martin Dunitz.
19. Brunette, D.M. (2007). *Critical Thinking: Understanding and Evaluating Dental Research*, 2e. USA: Quintessence.
20. Anvari, A., Halpern, E.F., and Samir, A.E. (2015). Statistics 101 for radiologists. *Radiographics* 35: 1789–1801.
21. Pretty, I.A. and Maupomé, G. (2004). A closer look at diagnosis in clinical dental practice: part 3. Effectiveness of radiographic diagnostic procedures. *J. Can. Dent. Assoc.* 70: 388–394.
22. Clark, O.A. and Castro, A.A. (2002). Searching the Literatura Latino Americana e do Caribe em Ciências da Saúde (LILACS) database improves systematic reviews. *Int. J. Epidemiol.* 31: 112–114.
23. MacDonald, D.S. (2015). A systematic review of the literature of nevoid basal cell carcinoma syndrome affecting East Asians and North Europeans. *Oral Surg. Oral Med. Oral Pathol. Oral Radiol.* 120: 408–415.
24. Park, J.Y., Lee, K.H., Ku, Y.J. et al. (2017). Characteristics, trends, and quality of systematic review and meta-analysis in general radiology between 2007 and 2015. *Acad. Radiol.* 24: 1013–1022.
25. Rosenkrantz, A.B., Hughes, D.R., and Duszak, R. Jr. (2016). The U.S. radiologist workforce: an analysis of temporal and geographic variation by using large national datasets. *Radiology* 279: 175–184.
26. Royal College of Radiologists. Clinical radiology: UK workforce census 2016 report. https://www.rcr.ac.uk/system/files/publication/field_publication_files/cr_workforce_census_2016_report_0.pdf (Accessed November 15, 2018).
27. Dhanoa, D., Dhesi, T.S., Burton, K.R. et al. (2013). The evolving role of the radiologist: the Vancouver workload utilization evaluation study. *J. Am. Coll. Radiol.* 10: 764–769.
28. Bryant, R., MacDonald-Jankowski, D.S., and Kim, K. (2007). Does the type of implant prosthesis affect outcomes for the completely edentulous arch? *Int. J. Oral Maxillofac. Implants* 22 (suppl): 117–139.
29. Sardanelli, F., Bashir, H., Berzaczy, D. et al. (2014). The role of imaging specialists as authors of systematic reviews on diagnostic and interventional imaging and its impact on scientific quality: report from the EuroAIM evidence-based radiology working group. *Radiology* 272: 533–540.
30. Imai, P., MacDonald, D.S., and Li, X. (2012). Comparison of interdental brush to dental floss for reduction of clinical parameters of periodontal disease; a systematic review. *Can. J. Dent. Hygiene* 46: 68–78.
31. Bennett, C., Moayyedi, P., Corley, D.A., DeCaestecker, J., Falck-Ytter, Y., Falk G., Vakil, N., Sanders, S., Vieth, M., Inadomi, J., Aldulaimi, D., Ho, K.Y., Odze, R., Meltzer, S.J., Quigley, E., Gittens, S., Watson, P., Zaninotto, G., Iyer, P.G., Alexandre, L., Ang, Y., Callaghan, J., Harrison, R., Singh, R., Bhandari, P., Bisschops, R., Geramizadeh, B., Kaye, P., Krishnadath, S., Fennerty, M.B., Manner, H., Nason, K.S., Pech, O., Konda, V., Ragunath, K., Rahman, I., Romero, Y., Sampliner, R., Siersema, P.D., Tack, J., Tham, T.C., Trudgill, N., Weinberg, D.S.,

Wang, J., Wang, K., Wong, J.Y., Attwood, S., Malfertheiner, P., MacDonald, D., Barr, H., Ferguson, M.K., Jankowski, J. BOB CAT Consortium. (2015). BOB CAT, a large-scale evidence review and consensus statements for management of Barrett's esophagus with no dysplasia, indefinite for, or low grade dysplasia, based on a Delphi process. *Am. J. Gastroenterol.* 110: 662–682.

32. Glastonbury, C.M., Mukherji, S.K., O'Sullivan, B., and Lydiatt, W.M. (2017). Setting the stage for 2018: how the changes in the American Joint Committee on Cancer/Union for International Cancer Control Cancer Staging Manual eighth edition impact radiologists. *AJNR Am. J. Neuroradiol.* 38: 2231–2237.
33. Thrall, J.H. (2016). Trends and developments shaping the future of diagnostic medical imaging: 2015 annual oration in diagnostic radiology. *Radiology* 279: 660–666.
34. Eng, G., Chen, A., Vess, T., and Ginsburg, G.S. (2012). Genome technologies and personalized dental medicine. *Oral Dis.* 18: 223–235.
35. Williams, S.D., Hughes, T.E., Adler, C.J. et al. (2014). Epigenetics: a new frontier in dentistry. *Aust. Dent. J.* 59 (Suppl 1): 23–33.
36. Solomon, B.D. (2014). Incidentalomas in genomics and radiology. *N. Engl. J. Med.* 370: 988–990.
37. Park, J.Y., Kricka, L.J., Clark, P. et al. (2014). Clinical genomics: when whole genome sequencing is like a whole-body CT scan. *Clin. Chem.* 60: 1390–1392.
38. Amm, H.M. and MacDougall, M. (2016). Molecular signaling in benign odontogenic neoplasia pathogenesis. *Curr. Oral Health Rep.* 3: 82–92.
39. Zhang, X., Tian, Y., Yang, Y., and Hao, J. (2017). Development of anticancer agents targeting the hedgehog signaling. *Cell. Mol. Life Sci.* 74: 2773–2782.
40. Guo, Y.Y., Zhang, J.Y., Li, X.F. et al. (2013). PTCH1 gene mutations in keratocystic odontogenic tumors: a study of 43 Chinese patients and a systematic review. *PLoS One* 8: e77305.
41. MacDonald, D.S. (2015). A systematic review of the literature of nevoid basal cell carcinoma syndrome affecting East Asians and North Europeans. *Oral Sug. Oral Med. Oral Pathol. Oral Radiol.* 120: 408–415.
42. Nagao, K., Fujii, K., Saito, K. et al. (2011). Entire PTCH1 deletion is a common event in point mutation-negative cases with nevoid basal cell carcinoma syndrome in Japan. *Clin. Genet.* 79: 196–198.
43. Karagozoglu, K.H., Van Hagen, J.M., Baart, J.A., and Van Der Waal, I. (2011). Genetic screening for nevoid basal cell carcinoma syndrome in patients with a solitary keratocystic odontogenic tumour is not useful. *Minerva Stomatol.* 60: 1–4.
44. Jiang, W.P., Sima, Z.H., Wang, H.C. et al. (2014). Identification of the involvement of LOXL4 in generation of keratocystic odontogenic tumors by RNA-Seq analysis. *Int. J. Oral Sci.* 6: 31–38.
45. Görögh, T., Quabius, E.S., Meyer, P., and Hoffmann, M. (2015). Characterisation of seven newly established head and neck squamous cell carcinoma cell lines. *Eur. Arch. Otorhinolaryngol.* 272: 1251–1258.
46. Gharahkhani, P., Fitzgerald, R.C., Vaughan, T.L., Palles, C., Gockel, I., Tomlinson, I., Buas, M.F., May, A., Gerges, C., Anders, M., Becker, J., Kreuser, N., Noder, T., Venerito, M., Veits, L., Schmidt, T., Manner, H., Schmidt, C., Hess, T., Böhmer, A.C,, Izbicki, J.R., Hölscher, A.H., Lang, H., Lorenz, D., Schumacher, B., Hackelsberger, A., Mayershofer, R., Pech, O., Vashist, Y., Ott, K., Vieth, M., Weismüller. J,, Nöthen, M.M.; Barrett's and Esophageal Adenocarcinoma Consortium (BEACON); Esophageal Adenocarcinoma GenEtics Consortium (EAGLE); Wellcome Trust Case Control Consortium 2 (WTCCC2), Attwood, S., Barr, H., Chegwidden, L., de Caestecker, J., Harrison, R., Love, S.B., MacDonald, D., Moayyedi, P., Prenen, H., Watson, R.G.P., Iyer, P.G., Anderson, L.A., Bernstein, L., Chow, W.H., Hardie, L.J., Lagergren, J., Liu, G., Risch, H.A., Wu, A.H., Ye, W., Bird, N.C., Shaheen, N.J., Gammon, M.D., Corley, D.A., Caldas, C., Moebus, S., Knapp, M., Peters, W.H.M., Neuhaus, H., Rösch, T., Ell, C., MacGregor, S., Pharoah, P., Whiteman, D.C., Jankowski, J., Schumacher, J. (2016). Genome-wide association studies in oesophageal adenocarcinoma and Barrett's oesophagus: a large-scale meta-analysis. Lancet Oncol. 17: 1363–1373.

Part 2

Advanced imaging modalities



Chapter 4

Computed tomography

4.1 Introduction

Computed tomography (CT) can be divided broadly into fan-beam CT – including helical computed tomography and its subset *multidetector computed tomography* (MDCT) – and *cone-beam computed tomography* (CBCT) [1] (Figure 4.1); the latter is addressed in Chapter 5.

CT, particularly MDCT, is increasingly available for the investigation of face and jaw lesions. This chapter introduces the various types of CT, while concentrating on MDCT, and covers window level and width, *three-dimensional* (3D) reformatting, and the limitations of CT. The indications for an increased need for CT are discussed.

4.2 Why Do We Need Computed Tomography?

Formerly, clinicians relied on a clinical examination and "conventional radiography" (traditional *two-dimensional* [2D] imaging) to assess and diagnose lesions affecting the jawbones. Unfortunately, conventional radiography generally reveals images that lack the sensitivity to display small changes in the bone. Conventional radiography also presents only as a 2D image the superimposition of all structures within the 3D volume of the region examined.

In addition to displaying the skeleton of the face and jaws in 3D and multiplanar reconstructions (axial, coronal, and sagittal), CT also allows display of the soft tissue with sufficient contrast resolution to differentiate between muscle, fat, lymph nodes, glands, and the vasculature.

The blood vessels of the head and neck and the vasculature of the various structures both in health and disease are enhanced (made more obvious) by the use of intravenous iodinated contrast media. This is required to diagnose and to stage carcinoma. The latter is achieved by identification of lymph node involvement and is assisted by intravenous contrast media. This also allows determination of whether there is extracapsular spread.

4.3 What Are the Basic Construction and Principles of Computed Tomography?

The CT unit has three main components, as shown in Figure 4.2. The CT unit itself consists of the gantry (some of which may be angled up to 30°) and the patient table (or bed or couch) that moves the patient through the aperture in the gantry (Figure 4.2a), and the control console (Figure 4.2b). There are two types of CT unit available: third- and fourth-generation units (Figure 4.3).

Oral and Maxillofacial Radiology: A Diagnostic Approach, Second Edition. Edited by David MacDonald.
© 2020 John Wiley & Sons, Inc. Published 2020 by John Wiley & Sons, Inc.

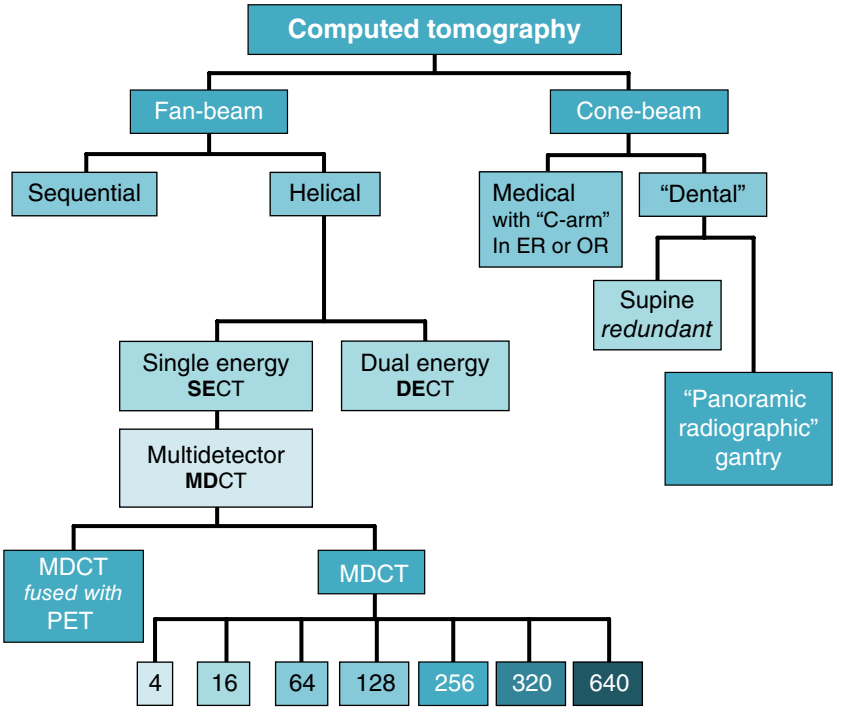


Figure 4.1 Classification and nomenclature of computed tomography. Key: DECT, dual energy computed tomography; ER, emergency room; MDCT, multidetector computed tomography; OR, operating room; PET, positron emission tomography; SECT, single energy computed tomography.

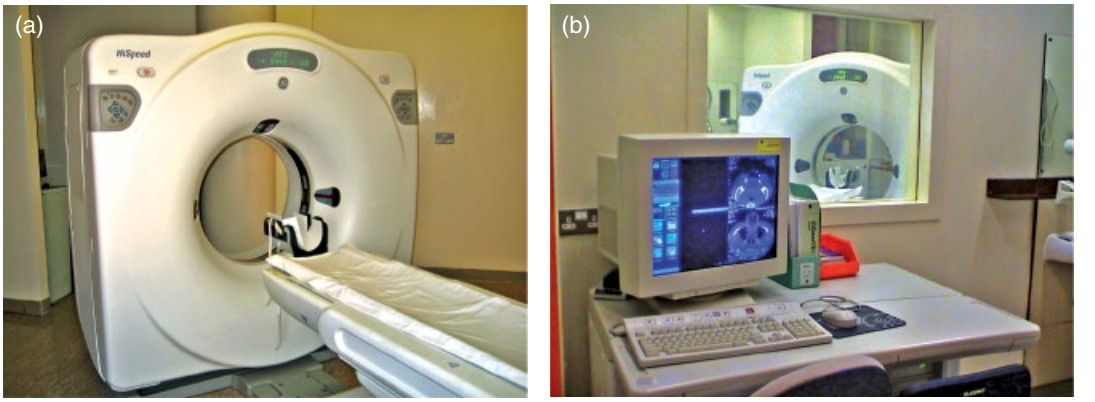


Figure 4.2 Three components of the computed tomography (CT) unit: (a) the gantry, containing the X-ray tube and detectors, and the table upon which the patient lies and is progressively advanced through the gantry; and (b) the control console with monitor. This is separated from the CT unit by a lead wall, including a lead glass window. It is crucial to observe the patient and gantry throughout the entire exposure, in case the exposure needs to be terminated. Source: Reproduced with permission from MacDonald-Jankowski, D.S. and Li, T.K. (2006). Computed tomography for oral and maxillofacial surgeons. Part 1: spiral computed tomography. *Asian J. Oral Maxillofac. Surg*. 18: 68–77.

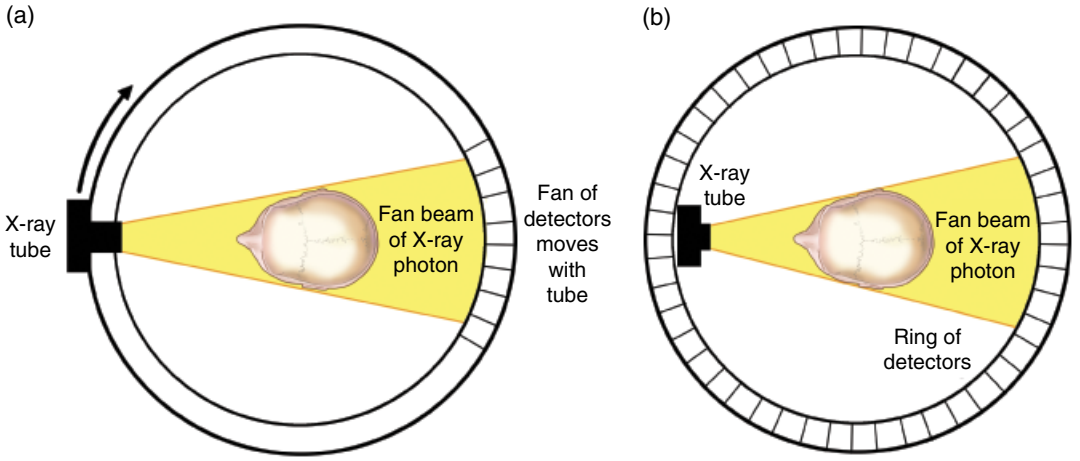


Figure 4.3 The two types of computed tomography (CT) units currently available. (a) The third-generation CT unit permits a fan array of detectors to rotate around the patient in tandem with the rotating X-ray tube – the X-ray beam is fan shaped; and (b) the fourth-generation CT unit only permits rotation of the X-ray tube within the continuous, but stationary, array of detectors – the X-ray beam is fan shaped. Source: Reproduced with permission from MacDonald-Jankowski, D.S. and Li, T.K. (2006). Computed tomography for oral and maxillofacial surgeons. Part 1: spiral computed tomography. *Asian J. Oral Maxillofac. Surg*. 18: 68–77.

The former constitutes the vast majority of CT equipment. For the third-generation CT, called "rotate-rotate," the X-ray tube and the detectors, which occupy an arc, are fixed in opposing positions within the gantry and rotate as a unit around the patient when in operation (Figure 4.3a), whereas for the fourth-generation unit, called "rotate-stationary," the X-ray tube alone rotates within a complete stationary ring of detectors (Figure 4.3b). Although the advantage of the fourth-generation unit is that the detectors have time to recover before being irradiated again, it has been substantially displaced from the market by the third-generation unit, particularly when it became the basic vehicle for helical and then MDCT.

4.4 How Is the Computed Tomographic Image Displayed?

The display is a digital image reconstructed by the computer as pixels (picture elements), which represent a 3D block of tissue. The voxel is the pixel size multiplied by the slice thickness (the voxel's length is from as low as 1 mm in some units to 20 mm). Each pixel is assigned a CT number (see later), representing tissue density. This density is proportional to the degree to which the material within the voxel has attenuated the X-ray beam. The resultant *attenuation coefficient* of a particular voxel reflects the mean of all tissues within it, the proportion of hard to soft tissues, and the voxel length (slice thickness).

There are three planes: X, Y, and Z. X and Y together represent the axial plane, a transverse plane through the patient. The Z plane represents the head-to-toe long axis of the patient. Upon inspection of an axial section, the pixels are represented by 2D squares in the axial (XY) plane of a 3D section of a thickness of the patient in the Z plane.

As the CT unit is almost always sited in a medical facility, the dataset will be reviewed and then reported by a medical radiologist. Referring/prescribing clinicians

will review the datasets transferred to them on a *digital video disc* (DVD), *compact disc* (CD), or *universal serial bus* (USB) flash drive with the appropriate software. This should be read in conjunction with the radiologist's report.

4.5 What Is Helical Computed Tomography?

HCT is also known as *volume acquisition CT*. As Hounsfield's genius introduced and developed the concept of CT in 1968, that of Kalender introduced HCT. HCT violates a previous firm tenet of radiology: the patient should not move during the exposure. Instead, HCT requires that the patient, who still remains motionless, be moved through the aperture of the gantry during the generation of X-rays by the rotating X-ray head (Figure 4.4a), creating a helix or spiral of data. This is in contrast to the separate incremental slices, stacked like coins, of the conventional sequential slice CT (the original technology of the 1970s and 1980s), now frequently called "sequential CT" (Figure 4.4b). Because there is a continuous string of data encompassing a volume of the patient with HCT, this data can be readily reconstructed to give 3D images. To achieve the same for sequential CT, the patient would need to undergo a second exposure overlapping with the first, thus doubling the radiation dose. As sequential CT has long been redundant, HCT has become the basis of all subsequent developments in fan-beam CT.

4.5.1 WHAT DOES THE DATA FOUND ON THE IMAGE REPRESENT?

Reviewers of HCT images should understand the terms bone and soft-tissue windows, *window width* (WW), and *window level* (WL).

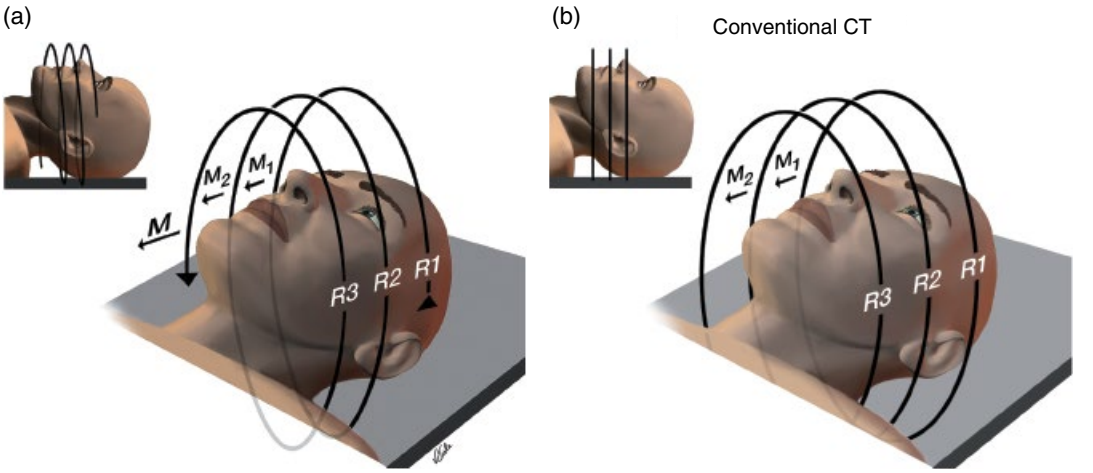


Figure 4.4 Helical computed tomography (HCT) and sequential computed tomography (CT). (a) In HCT, the rotating X-ray tube describes a helix or spiral as it exposes the patient on the bed continuously moving through the gantry; and (b) in sequential CT, the rotating X-ray tube can only describe complete loops between incremental movements of the patient's table through the gantry. M, movement; R, rotation. Source: Reproduced with permission from MacDonald-Jankowski DS, Li TK. Computed tomography for oral and maxillofacial surgeons. Part 1: Spiral computed tomography. *Asian J. Oral Maxillofac. Surg*. 2006;18:68–77.

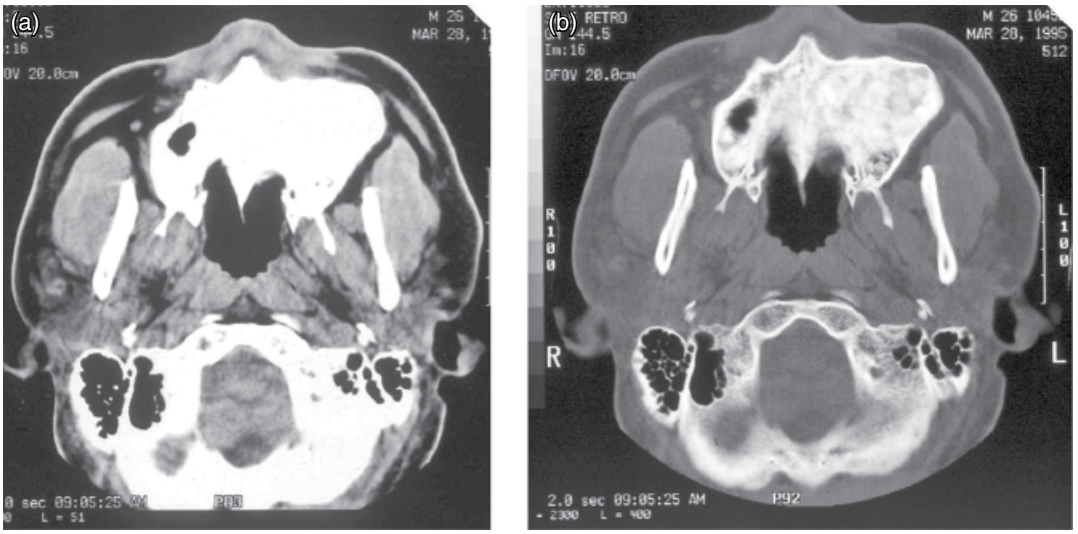


Figure 4.5 Soft-tissue and bone windows. The soft-tissue window (a) displays cell-rich structures such as the muscles, skin, salivary glands, brainstem, and blood vessels as "gray" structures, whereas the fatty subcutaneous tissues and fascia appear almost as black as the air-filled pharynx and mastoid air cells; the bony structures appear as homogeneous white areas. The bone window (b) displays the bony structures in such detail that trabeculae could be discerned. Note that bony structures appear slightly smaller in area than they do in the soft-tissue window. The bony window displays soft tissue, but fat is appreciated as a darker gray shape in comparison to the nonfatty structures. Note: It can be noticed that, with the same slice thickness, the area covered by the bone image on the soft-tissue window appears larger than that on the bone window. This is due to differences in windowing and leveling as well as the sharpness of the edges as defined by the spatial filter. Source: Reproduced with permission from MacDonald-Jankowski, D.S. and Li, T.K. (2006). Computed tomography for oral and maxillofacial surgeons. Part 1: spiral computed tomography. *Asian J. Oral Maxillofac. Surg*. 18: 68–77.

Bone and soft-tissue windows and their widths and levels are expressed in *Hounsfield units* (HU), which are also called "CT numbers." These range from a minimum of −1000 HU representing air (fixed point), through 0 HU representing water (fixed point), up to 3000 HU representing dense metal or bone. Bone and soft-tissue windows (Figure 4.5) are two of the three standard protocols for viewing the data captured by CT; the air window is the third protocol and is used mainly by respiratory physicians. Each of these protocols optimizes viewing of tissue types by appropriately adjusting the WL and WW. The soft-tissue window for face and jaw lesions is sited close to that of water (0 HU), WL at 40–60 HU, and WW at 250 HU, whereas the bone windows for such lesions are WL at 250–500 HU and WW at 1000–2000 HU or greater. The *level* may be defined as equivalent to tuning a radio to the desired frequency, whereas the *width* is equivalent to a filter. It is now almost routine for the complete dataset to be reviewed by referring clinicians. With the appropriate software, they can handle the data to suit their own requirements. The accompanying radiologist's reports should be referred to while reviewing the images.

4.6 What Is Multidetector Computed Tomography?

MDCT, sometimes referred to as *multislice computed tomography* (MSCT), is a subset of HCT. It can use from 4 up to 640 detector arrays. This means that the time needed to acquire data from a given volume of the patient is correspondingly reduced. MDCT has substantially replaced the original single-slice HCT units. As time passes, MDCT units with a lower number of detector arrays are being replaced with those with high numbers. Lin et al., using a 320 MDCT on an anthropomorphic head phantom, finally reported that a protocol using a 135 kVp tube voltage (rather than 120 kVP or 80 kVp), an 80 mA tube current, and the volume-scanning mode (rather than 64- or 80-slice detectors) offers adequate visualization of both soft-tissue and bone structures, while keeping the radiation dose as low as possible [2].

4.7 Dual-Energy Computed Tomography

The term *dual-energy computed tomography* (DECT) refers to CT that uses two photon spectra rather than two distinct energies [3]. Therefore, the DECT X-ray tube produces the usual polychromatic bremsstrahlung radiation just like *single-energy computed tomography* (SECT), the usual CT unit, rather than the almost monochromatic beam derived from a molybdenum target and filter system used in mammography. As Johnson reports, "The settings of 80 and 140 *kilovolts* (kV) are commonly used because they provide the maximum difference and least overlap between the spectra with standard tubes" [3]. A large proportion of photon energies below 80 kV will have little chance of penetrating through to reach the detector. These photons will simply be absorbed by the patient's tissues, contributing only to the radiation dose. Those photon energies above 140 kV are too high for soft-tissue contrast, but will merely contribute to the dose to the patient [4]. Three of the current technical solutions for DECT are set out schematically in Figure 4.6. Although the fourth method, "sequential acquisition," requires the minimum of special hardware, the time gap between the two exposures using different spectra could be problematic in many clinical situations. It is indicated for *metal artifact reduction* (MAR) and is required in cases where contrast media has not been used.

DECT differs from SECT in another important way. DECT relies on the *photelectric effect* (PEE) rather than on Compton scatter, which accounts for the greatest attenuation of the primary beam (beams in MDCT) in SECT. Therefore, the residual primary beam captured by DECT will reflect the "K-edges" of the elements within the irradiated tissue and how close the beam's energy was to them. The closer the incident photon energy is to the binding electron energy in the K-shell electron, the better the PEE. The binding electron energy increases with the atomic number (Z). Therefore, a kVp of 80 will resonant better with the K-edges of the atoms of hydrogen, carbon, nitrogen, and oxygen, which have low atomic numbers (Z = 1, 6, 7, and 8, respectively), these atoms of which the soft tissues are composed, whereas a kVp of 140 will resonant better with atoms of higher atomic numbers, such as calcium (Z = 20) and iodine (Z = 56; used in contrast media).

Before DECT can be feasibly applied clinically, its image quality must be at least equal to that of SECT and its radiation dose equal to if not lower than SECT. At the outset, a major disadvantage of DECT

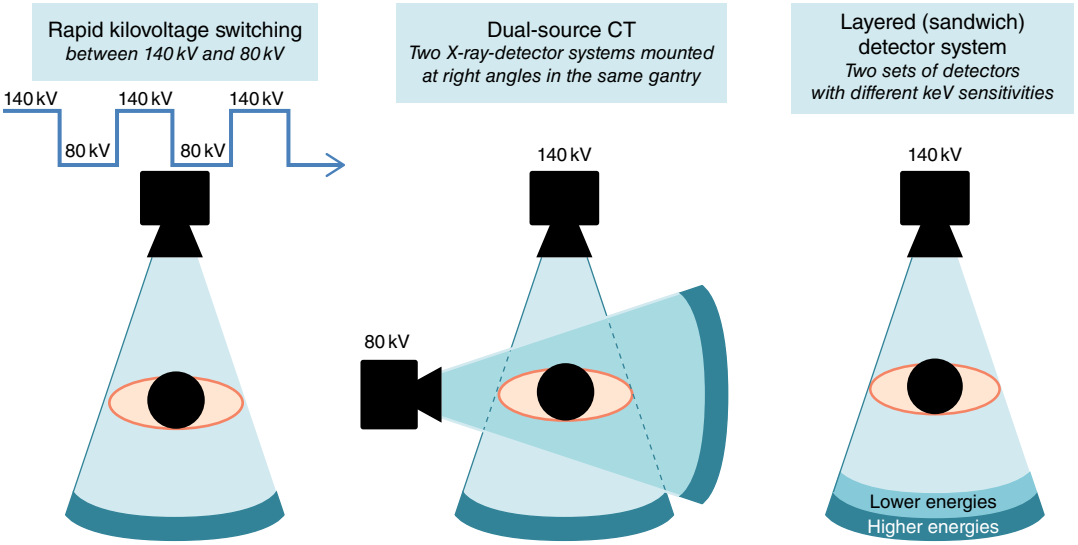


Figure 4.6 Dual-energy computed tomography (DECT). Schematic diagrams of three technical solutions. The patient is represented by the pink shoulders and the black head. Source: Adapted from Figure 2 of Johnson, T.R. (2012). Dual-energy CT: general principles. *Am. J. Roentgen*. 199: S3–S8.

was that it required more radiation than a SECT scan [3]. Forghani and Mukherji note: "The balance of diagnostic quality versus dose also depends on patient-specific factors… a pediatric patient would be different from an adult head and neck cancer patient receiving radiation therapy as part of their therapeutic regimen" [4]. In addition to minimizing the area to be investigated by DECT, alteration of exposure factors, such as kV, can be used, provided that a potential decrease in image quality is taken into consideration beforehand. This may result in more artifacts, particularly in the lower neck/thoracic inlet. Furthermore, alteration of either or both DECT energies, especially if this increases the overlap of their spectra, may diminish the advantage of DECT and make DECT acquisition more like SECT [4].

The datasets of each of the two DECT energies can be combined in a number of ways according to clinical need. These are *virtual monochromatic image* (VIM), *weighted average* (WA or "blended images" for dual-source units), or material decomposition maps [4].

In addition to the investigation of osteoporosis (see Figure 9.19), DECT has been used to investigate *head and neck squamous cell carcinoma* (HNSCC) cancer. Low-energy VIMs have displayed early cancers. Standard WA images have revealed the invasion of the noncalcified thyroid cartilage by HNSCC. Furthermore, DECT has been used to effect dental artifact reduction [4].

4.8 Artifacts Observed on Computed Tomography

Table 4.1 lists many of the causes of artifacts observed on CT. As only a few important causes will be discussed in this chapter, the reader is referred to Kalender [5] and to Barrett and Keat [6]. Patient-based causes arise from insufficient immobilization of the patient, causing movement artifacts, and the presence of metal dental restorations (Figure 4.7), fixed orthodon-

Table 4.1 Main causes of artifact on computed tomography (CT).

Groups	Subclasses	Cause
Patient-based artifacts	Motion artifacts	Tongue* *swallowing*
	Metal artifact*	*Beam hardening**
		Photon starvation
Physics-based artifacts	Beam hardening*	Cupping artifact
		Streaks and dark bands
	Partial volume averaging	Pixel size
	Quantum mottle (noise)	
	Photon starvation	Obese (subcutaneous fat), shoulder
	Aliasing in CT	
Hardware-based artifacts	Ring artifact	If a detector is defective or not calibrated
	Out-of-field artifact	Lower neck if large/obese upper thorax
Multidetector artifacts	Cone-beam effect	Worsens with more detectors.

Note: *denote features that are particularly important causes of artifacts and are discussed further in the text.

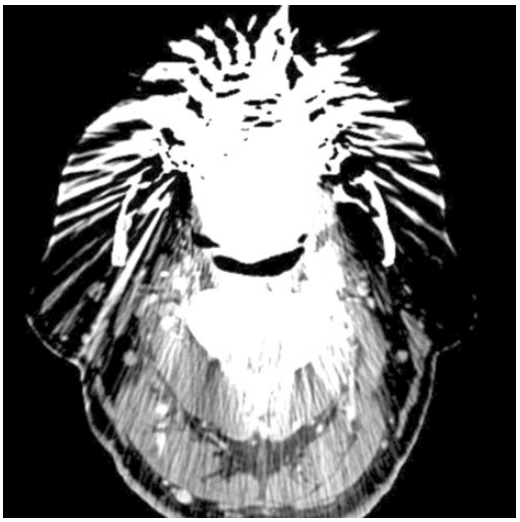


Figure 4.7 Axial computed tomographic section displaying substantial metallic spraying arising from extensive metal restorations. Source: Courtesy of Dr. Montgomery Martin, British Columbia Cancer Agency.

tic appliances and surgical plates, or screws and wires which are in or close to the area of interest. The metal structures also interact with the physics-based parameters of CT, which are fundamental to all CT units. Dependent on the particular manufacturer and model, hardwear-based artifacts also play a role. These in turn could interact with a patient-based cause such as the patient's size. Obese patients may not only be too heavy for that particular unit, their shoulders may exceed the field of measurement, which is smaller than the gantry aperture (Figure 4.8). Excessive subcutaneous fat can cause photon starvation artifacts generally observed in CT of the abdomen [7]. Although this may not affect the imaging of the head, which does not increase substantially in size even in a very obese patient, a fat upper thorax and shoulders

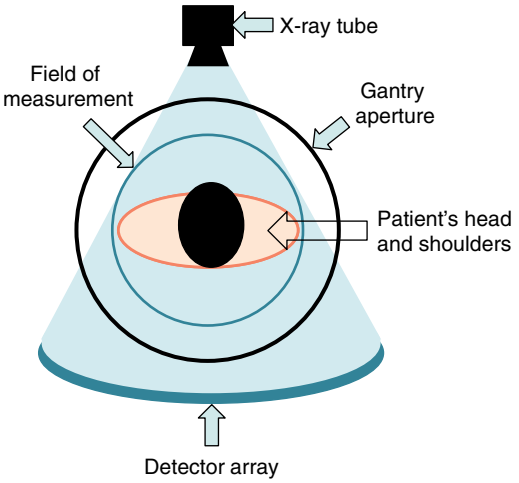


Figure 4.8 Schematic diagram displaying the need for the patient to be wholly contained within the field of measurement rather than simply within the gantry aperture.

may affect the lower neck and thoracic inlet, both by exceeding the field of measurement and/or by photon starvation.

A major cause of patient movement artifact in a CT of the head and neck is swallowing, which can nullify the value of a CT investigation for oral cancer.

4.8.1 DENTAL ARTIFACT REDUCTION

The extensive use of metals in dental restoration, ranging from amalgams to crowns and bridges, has long compromised the CT evaluation of lesions within or close to the jaws. This is substantially due to the high atomic number of the elements used for dental restoration. Dental amalgam is largely composed of silver (Z = 47) and mercury (Z = 80). Gold (Z = 79) is still routinely used for crowns and bridges. Although titanium has a lower atomic number (Z = 22), it causes artifacts if a low kVp is used. Zirconium has been recently introduced in the production of dental crowns, and although its atomic number (Z = 40) is half that of gold it is still high.

The main causes of metal artifacts are beam hardening and photon starvation [8, 9]. Beam hardening occurs when the low-energy photons in the polychromatic X-ray beam are attenuated by high atomic number material [9, 10]. This results in an increase in the average energy of the beam, leading to dark/black streaks on the image [10]. Beam hardening was frequently observed in earlier head CT, transecting the midbrain in the coronal plane between the petrous (from Latin *petra*, meaning rock) apices. Photon starvation occurs when almost all the primary beam has been absorbed. This results in the arrival of very few photons getting through to the detector. As a result, the image is usually noisy. Also many of these photons are scattered by the Compton effect to produce streaks. Almost from the first introduction of CT into clinical practice, radiologists and medical physicists and engineers have endeavored to minimize if not remove these artifacts. These approaches to MAR are briefly summarized in Table 4.2.

In addition to metal implant optimization and acquisition improvement, which are largely selected and performed by radiographic technicians and radiologists, there are four separate approaches to creating MAR software. Most of the studies on MAR are *in vitro* or phantom studies and very few are actual clinical studies. Therefore, despite the plethora of reports on this topic, many radiologists prefer not use MAR, other than for metal implant optimization. There is a real risk that the MAR software may "erase" any pathology, thus resulting in a false negative. This is particularly a consideration in the mouth, where nearly 5000 new squamous cell cancers occur among 35 million Canadians annually [11]. De Crop et al. reinforced this sentiment, stating that "MARs reconstruction in CT images of the oral cavity to reduce dental hardware metallic artifacts

Table 4.2 Methods for metal artifact reduction in computed tomography.

Group	Subclasses	Brief description	Comment
Metal implant optimization	Angulation of primary beam	Adjust gantry by about 20°	Still widely used
	Remove metal from FOV	Remove amalgams. Extract metal-restored teeth	Drastic action! Only acceptable in preradiation treatment planning
	Do not use barium or iodine as contrast medium	Tantalum, tungsten, and bismuth best for DECT, not SECT	
	Use low-attenuating metals (current or near future)	Titanium (Z = 22) implants and magnesium (Z = 12) screws and carbon fiber nails	Magnesium screws disappear eventually – need further studies
Acquisition improvement	Parameter adjustment	↑ kVp results in ↓ beam hardening and noise ↑ mA or ↓ pitch results in ↓ noise	Increases radiation dose
	DECT	130 keV optimal for MAR	50% artifact reduction in one study
	Photon-counting CT	50 to 80 keV range gave best MAR	Good for teeth and implants
Physics-based preprocessing	Noise suppression	↓ streaks by algebraic reconstruction (ART)	
	Scatter and beam hardening correction	Beam hardening correction	For low Z implants – titanium
Projection completion	Interpolation	MAR for CBCT must deal with three-dimensional reconstruction	
	Reproduction	Replace metal artifacts with HU for water	
	Normalization	Normalized original projection data to prior image projection data	Normalized MAR
Iterative reconstruction	Corruption avoidance	Use data outside metal trace to replace it	Omits the metal trace
	Statistical compensation	Statistically down-weighs the metal data	No omission of metal trace
	Knowledge utilization	Uses compressed sensing and known component models	This makes use of existing huge database of a particular population
Image post processing (Perhaps the least popular approach)	Direct	Simple normalization of rows and columns to a gray value	Not effective
	Hybrid	Integrated with other categories of MAR, such as projection completion	Better than direct

Source: Extracted from Gjesteby L, De Man B, Jin YN, Paganetti H, Verburg J, Giantsoudi D, Wang G. Metal artifact reduction in CT: where are we after four decades? *IEEE Access.* 2016; 4: 5826–5849.
Note: upward-pointing arrows = increase; downward-pointing arrows = decrease.
ART, algebraic reconstruction technique; CBCT, cone-beam computed tomography; DECT, dual-energy computed tomography; FOV, field of view; HU, Hounsfield units; MAR, metal artifact reduction; SECT, single-energy computed tomography.

is not sufficient and may adversely influence the image quality" [8]. They went on to state that in their study "clinical images showed an over smoothening of the image resulting in loss of essential image information, although less streaking artifacts are visible around the metal instertions in the MARs reconstructed image" [8].

Cha et al. combined DECT and MAR software [9]. Although they reported that this markedly reduced metallic dental artifacts and significantly improved image quality in the tongue, it did not do so in the adjacent parotid. Furthermore, they reported MAR software artifacts in the deep center of the neck.

The MAR issue will only become more prevalent as concern about radiation dose delivered by CT is addressed by reducing exposure factors [10].

4.9 What Is Three-dimensional Reformatting and Why Is It Required?

Each original voxel is divided into cubes, called *cuberilles*, by interpolation; each cuberille has the same mean attenuation coefficient of the original voxel (Figure 4.9). The need for this interpolation arises because the original voxel's resolution is best in the axial plane, where the density of pixels is greatest. Only those cuberilles that represent the surface of the *object of interest* are projected onto the monitor. The 3D reconstructions are capable of being rotated to display the reconstruction from any point of view (Figure 4.9).

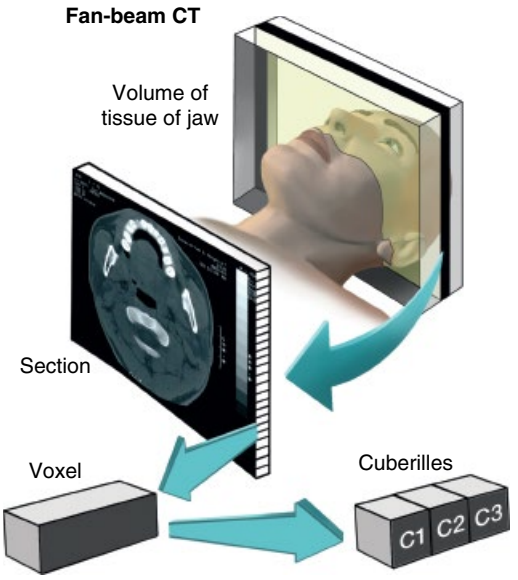


Figure 4.9 Fan-beam (medical) computed tomography (CT) achieved three-dimensional reconstruction by slicing the voxel into cuberilles, each with the same attenuation coefficient as the original voxel. As these cuberilles are arrayed in the Z axis (patient's long axis), then the spatial resolution would be, as a result, poorer in that axis. Source: Reproduced with permission from MacDonald-Jankowski DS, Li TK. Computed tomography for oral and maxillofacial surgeons. *Part 1: Spiral computed tomography. Asian J. Oral Maxillofac. Surg. 2006;18: 68–77*.

4.10 Intravenous Contrast

Intravenous contrast medium (IVCM) enhances blood vessels. Figure 4.10 reveals *enhancement* of the normal blood vessels of the face. IVCM for CT is iodinated and



Figure 4.10 Axial computed tomographic section (bone window) displaying enhancement of the normal blood vessels of the face.

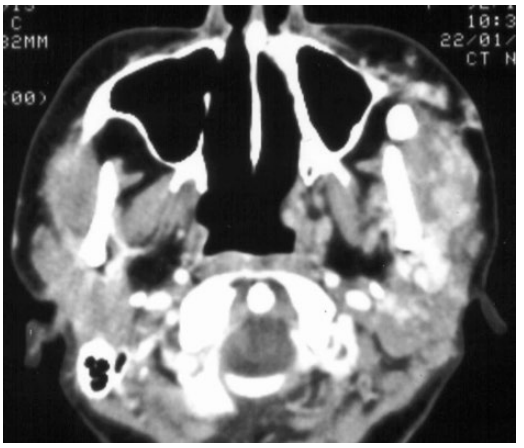


Figure 4.11 Axial computed tomographic section (soft-tissue) displaying enhancement of a large vascular malformation affecting the face, particularly the left side. The large blood vessels are also enhanced. There is a large phlebolith between the left vertical ramus of the mandible and the inferior aspect of the malar buttress.

occurs in an ionic or nonionic form. The term enhancement represents an increase in HU for that area or structure after delivery of the IVCM. This enhancement is dependent upon the degree of vascularization of that area or lesion. Vascularization is increased in inflamed (traumatized and/or infected) tissue and in neoplastic lesions or vascular anomalies. Figure 4.11, in the case of the last, displays the use of IVCM rendering obvious a large *anteriovenous malformation* (AVM). For optimal vascular and tissue contrast, Baum et al. recommend that 150 ml of contrast medium (CM) be delivered at a 2.5 ml/s flow rate with a start delay of 80 seconds [12]. CM has also been found to assist in the identification of malignancies, their primaries and their metastases. Enhanced metastatic lymph nodes may display enhancement at the node's periphery, but none in its center, because of central necrosis. This is pathenomic of a metastatic node.

The World Health Organization's definition of an *adverse drug reaction* (ADR) is "A response to a drug which is noxious and unintended, and which occurs at doses normally used in man for the prophylaxis, diagnosis, or therapy of disease, or for the modifications of physiological function" [13]. The American College of Radiology has further organized ADRs according to their severity [14]. Such reactions to CM can be allergic [15] or some other reaction [16], for example associated with thyroid disease, kidney damage, or amplification of deoxyribonucleic acid (DNA) damage in CT investigations.

Kornelius et al. reported that IVCM "was associated with a higher risk of thyroid dysfunction, including hyperthyroidism and hypothyroidism" [17]. Do stated that the risks of *contrast-induced nephropathy* (CIN) in the general population may be overestimated [18]. CIN risk may be higher in high-risk populations such as those with *chronic kidney disease* (CKD). In such populations, CM should be used with caution and the lowest possible amount used, but only after the patient's hemodynamic status has been optimized [18]. Riley's commentary concluded that although there is an association between DNA *double-strand breaks* (DSBs) and IVCM, so far no direct causal link has been made between these DSBs and cancer induction [19]. Gould et al. reported a 19% increase in DSBs when 19 mg/ml of IVCM was employed in pediatric cardiac catheterization [20].

Although globally the IVCMs that most institutions use are *nonionic iodinated contrast media* (NICMs), mild hypersensitivity reactions occur in up to 12.7% of patients with ionic CM and 3.1% with the lower osmolar nonionic CM, but the death rates for both are equal, at 1 per 100 000 investigations [21]. While a careful history of prior experiences can indicate a patient at risk [22], this is not helpful for those without such a history. Therefore, a high level of vigilance for all patients is required and the

procedure should be performed in a hospital setting, where emergency teams are on stand-by. Fortunately, as most MDCTs are so sited, this is not an issue. On the other hand, a German team commented that the imprecise term "iodine allergy," without further and timely investigation as to the true cause of the reaction (i.e. testing for antibodies etc.), may subsequently subject the patient to unnecessary prophylactic regimes, or even deprive the patient of an otherwise clinically indicated enhanced scan [23]. They discuss the myths and misconceptions about CMs [24]. Contradicting an earlier assertion that females were more likely to experience CM-related ADRs, Lee et al. reported that there was no significant difference between sexes [25].

Whenever contrast is used, regardless of modality, precontrast images should be taken first.

4.11 Overall Risk of Harm to Patients Visiting a Computed Tomographic Suite

Mansouri et al. reported that 0.22% of patients visiting a large American academic hospital for a CT experienced some form of harm [26]. The three leading causes were 34% from adverse drug interactions, 30% from the delivery of intravenous medication, and 11% from diagnostic test order errors (such as the wrong patient in the initial requisition).

4.12 Concluding Remarks

It is all too well known that CT imparts a high radiation dose to the patient. Therefore, all clinicians must seek to ensure that CT is the optimal investigation at that particular moment of the patient management process, and whether another modality not using ionizing radiation would be more appropriate, such as ultrasonography or magnetic resonance. Such decisions can be assisted by reference to the radiologist, to a pre-existing agreed protocol, or to a widely available reference such as the Royal College of Radiologists' "Making the Best Use of Clinical Radiology" [27]. While an appropriately indicated CT prescribed and undertaken in good time may lead to the enhancement both of life itself and of the quality of life of the patient, this presupposes that the dataset is interpreted by a radiologist who is aware of the limitations of the investigation, the artifacts, variants of normal anatomy, and incidental findings (also called incidentalomas) [27]. The last are important to identify, as they if are not recognized as such they may in turn lead to further and unnecessary investigations.

References

1. MacDonald-Jankowski, D.S. and Li, T.K. (2006). Computed tomography for oral and maxillofacial surgeons. Part 1: spiral computed tomography. *Asian J. Oral Maxillofac. Surg.* 18: 68–77.
2. Lin, W.C., Wang, H.H., Hsu, W.L. et al. (2017). Investigation of an optimized scanning protocol for the dentomaxillofacial region using 320-slice multidetector computed tomography. *Dentomaxillofac. Radiol.* 7: 20160395.
3. Johnson, T.R. (2012). Dual-energy CT: general principles. *Am. J. Roentgen.* 199: S3–S8.
4. Forghani, R. and Mukherji, S.K. (2018). Advanced dual-energy CT applications for the evaluation of the soft tissues of the neck. *Clin. Radiol.* 73: 70–80.
5. Kalender, W.A. (2000). *Computed Tomography*. Munich: Publicis MCD Verlag.
6. Barrett, J.F. and Keat, N. (2004). Artifacts in CT: recognition and avoidance. *Radiographics* 24: 1679–1691.

7. Modica, M.J., Kanal, K.M., and Gunn, M.L. (2011). The obese emergency patient: imaging challenges and solutions. *Radiographics* 31: 811–823.
8. De Crop, A., Casselman, J., Van Hoof, T. et al. (2015). Analysis of metal artifact reduction tools for dental hardware in CT scans of the oral cavity: kVp, iterative reconstruction, dual-energy CT, metal artifact reduction software: does it make a difference? *Neuroradiology* 57: 841–849.
9. Cha, J., Kim, H.J., Kim, S.T. et al. (2017). Dual-energy CT with virtual monochromatic images and metal artifact reduction software for reducing metallic dental artifacts. *Acta Radiol.* 58: 1312–1319.
10. Gjesteby, L., De Man, B., Jin, Y.N. et al. (2016). Metal artifact reduction in CT: where are we after four decades? *IEEE Access.* 4: 5826–5849.
11. Canadian Cancer Society. Oral cavity cancer statistics. 2018. http://www.cancer.ca/en/cancer-information/cancer-type/oral/statistics/?region=on (Accessed November 14, 2018)
12. Baum, U., Greess, H., Lell, M. et al. (2000). Imaging of head and neck tumors—methods: CT, spiral-CT, multislice-spiral-CT. *Eur. J. Radiol.* 33: 153–160.
13. World Health Organization. 2018. http://www.who.int/medicines/areas/quality_safety/safety_efficacy/trainingcourses/definitions.pdf (Accessed November 14, 2018.)
14. ACR Committee on Drugs and Contrast Media (2017). *ACR Manual on Contrast Media*, 10.3e. Reston, VA: American College of Radiology https://www.acr.org/Clinical-Resources/Contrast-Manual (Accessed November 14, 2018.
15. Schopp, J.G., Iyer, R.S., Wang, C.L. et al. (2013). Allergic reactions to iodinated contrast media: premedication considerations for patients at risk. *Emerg. Radiol.* 20: 299–306.
16. Iyer, R.S., Schopp, J.G., Swanson, J.O. et al. (2013). Safety essentials: acute reactions to iodinated contrast media. *Can. Assoc. Radiol. J.* 64: 193–199.
17. Kornelius, E., Chiou, J.Y., Yang, Y.S. et al. (2015). Iodinated contrast media increased the risk of thyroid dysfunction: a 6-year retrospective cohort study. *J. Clin. Endocrinol. Metab.* 100: 3372–3379.
18. Do, C. (2017). Intravenous contrast: friend or foe? A review on contrast-induced nephropathy. *Adv. Chronic Kidney Dis.* 24: 147–149.
19. Riley, P. (2015). Does iodinated contrast medium amplify DNA damage during exposure to radiation. *Br. J. Radiol.* 88 (1055): 20150474.
20. Gould, R., McFadden, S.L., Horn, S. et al. (2016). Assessment of DNA double-strand breaks induced by intravascular iodinated contrast media following in vitro irradiation and in vivo, during paediatric cardiac catheterization. *Contrast Media Mol. Imaging* 11: 122–129.
21. Brockow, K., Christiansen, C., Kanny, G. et al. (2005). Management of hypersensitivity reactions to iodinated contrast media. *Allergy* 60: 150–158.
22. Li, X., Liu, H., Zhao, L. et al. (2017). Clinical observation of adverse drug reactions to nonionic iodinated contrast media in population with underlying diseases and risk factors. *Br. J. Radiol.* 90: 20160729.
23. Böhm, I., Nairz, K., Morelli, J.N. et al. (2017). Iodinated contrast media and the alleged "iodine allergy": an inexact diagnosis leading to inferior radiologic management and adverse drug reactions. *Rofo* 189: 326–332.
24. Böhm, I., Morelli, J., Nairz, K. et al. (2017). Myths and misconceptions concerning contrast media-induced anaphylaxis: a narrative review. *Postgrad. Med.* 129: 259–266.
25. Lee, H., Song, S., Oh, Y.K. et al. (2017). Is gender still a predisposing factor in contrast-media associated adverse drug reactions? A systematic review and meta-analysis of randomized trials and observational studies. *Eur. J. Radiol.* 89: 81–89.
26. Mansouri, M., Aran, S., Shaqdan, K.W., and Abujudeh, H.H. (2016). How often are patients harmed when they visit the computed tomography suite? A multi-year experience, in incident reporting, in a large academic medical center. *Eur. Radiol.* 26: 2064–2072.
27. Royal College of Radiologists (2017). *iRefer: Making the Best Use of Clinical Radiology*, 8e. London: Royal College of Radiologists https://www.rcr.ac.uk/publication/irefer-making-best-use-clinical-radiology-eighth-edition (Accessed November 30, 2018.

Chapter 5

Cone-beam computed tomography

5.1 Introduction

Although cone-beam computed tomography (CBCT), also called *volumetric computed tomography* (VCT), is nearly two decades old, it has revolutionized the practice of dentistry, so much so that there is hardly a dental specialty which it has not affected [1]. CBCT's cross-sectional images reveal a new insight into the most frequent and/or important lesions of the face and jaws [2, 3]. The cross-sectional images are actually reconstructions from a volume of data. Figure 5.1 displays the cross-sectional or *multiplanar reformation* (MPR) in the axial (a), sagittal (b), and coronal (c) planes and the *three-dimensional* (3D) reconstruction (d) representing the dataset volume. The second most frequently used reconstruction is "curved," which is virtually identical to the Dentoscan program most medical radiologists are familiar with. Figure 5.2 displays a case in which curved reformatting or reconstruction has been employed. "Reconstruction" appears to be the preferred term. The panoramic image reconstructed from a CBCT dataset is called a "synthetic panoramic image" by some authorities [5]. Although reconstructed panoramic images can appear similar to a conventional panoramic radiograph (Figure 5.3), if the "slice" thickness is too narrow or it does not pass simultaneously through the greatest height of both jaws, parts may be excluded (compare the three reconstructed panoramic images in Figures 1.7 and 5.2).

The advantages and disadvantages of CBCT as compared to fan-beam CT are set out in Table 5.1. CBCT's small footprint (the surface area it occupies is similar to that of a conventional panoramic radiographic unit), light weight (no strengthening of the floor is required), moderately low exposure factors (particularly tube voltage), low cost of purchase and installation, and relative ease of use have seen its appearance even in many dental offices in addition to specialist practices. Unfortunately, this ubiquity of availability has not always been matched by the appropriate knowledge of the risks CBCT poses to the patient in addition to the real benefits to that patient. This deficiency in knowledge directs the activities of dental regulatory bodies, dental education providers, governments, and not least the medical radiologist (for the reasons set out at the end of this chapter). Readers are expected to have an understanding of the risks as well as the benefits of ionizing radiation and how its use is governed by their jurisdiction. This chapter will raise and discuss those technical issues that are of central importance to the clinician who either is prescribing CBCT investigations and/or is a CBCT unit owner. Those who wish to know more about the technical details of CBCT are directed to Pauwels

Oral and Maxillofacial Radiology: A Diagnostic Approach, Second Edition. Edited by David MacDonald.
© 2020 John Wiley & Sons, Inc. Published 2020 by John Wiley & Sons, Inc.

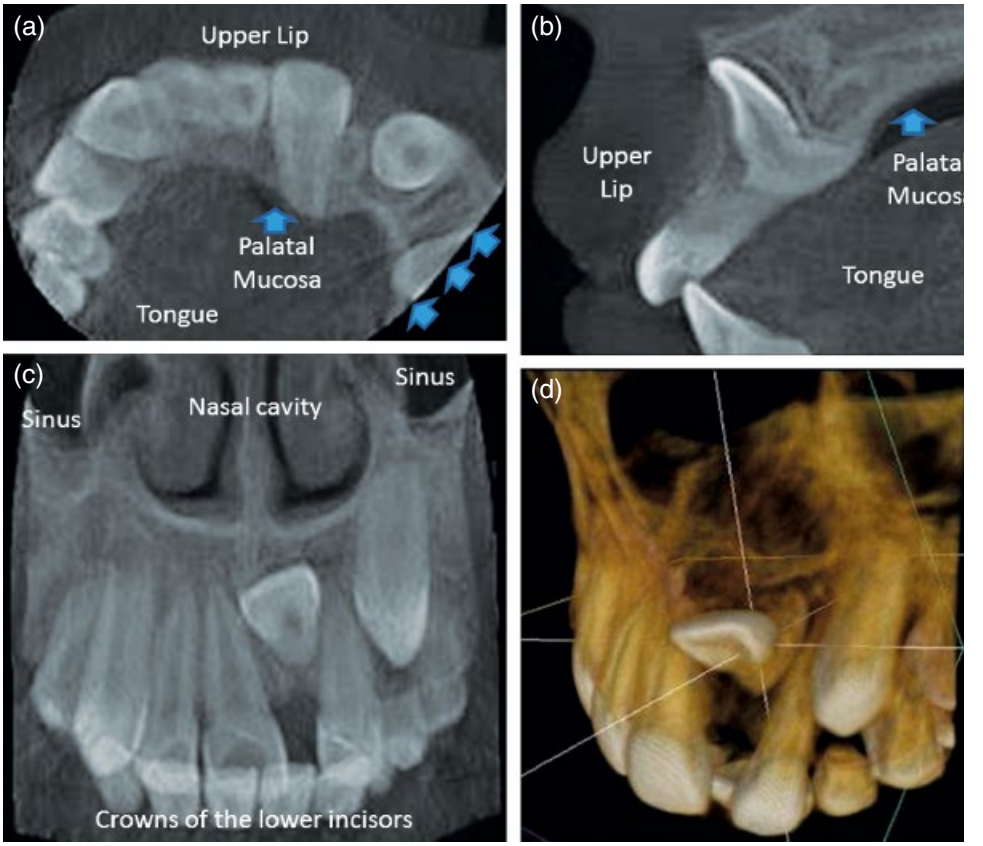


Figure 5.1 Small (5 × 5) field-of-view (FOV) cone-beam computed tomography (CBCT) displaying a dilacerated left central incisor. The cross-sectional or multiplanar reformations (MPR) are in the axial (a), sagittal (b), and coronal (c) planes, and the three-dimensional (3D) reconstruction (d) represents the dataset volume. The three planes are centered on the dilacerated tooth as obvious "cross-hairs" in (d). The three blue arrows in (a) define part of the 5 cm diameter and (c) and (d) denote the 5 cm height of the 5 × 5 FOV made on a Carestream 9300 CBCT. The dataset has also captured the crowns of the lower incisors. The tongue substantially obturates the oral cavity (which appears as black); compare with that in Figure 5.8. The palatal mucosa is thinner; compare with that in Figure 5.8. The contour of the upper lip is silhouetted by the air surrounding the patient. Note: the erupting left maxillary canine is eroding the root of the preceding deciduous maxillary canine. This resorption is normal and desired.

et al.'s overview [5]. The clinical process leading to the optimal use of CBCT is set out in Figure 5.4 [1].

5.2 What Is Cone-Beam Computed Tomography?

Unlike multidetector computed tomography (MDCT; the now standard CT unit used in medicine), CBCT uses a cone beam instead of a fan beam (Figure 5.5) [6]. This means that since the cone irradiates a larger volume in a single rotation (nowadays this rotation may be as little as 180°), the radiation dose imparted is much lower than that by a fan beam. The fan-beam CT needs many rotations to cover the same volume of patient that is of interest to the clinician. This introduces another feature of CBCT, *field of view* (FOV), which will be developed later in the chapter. In CBCT

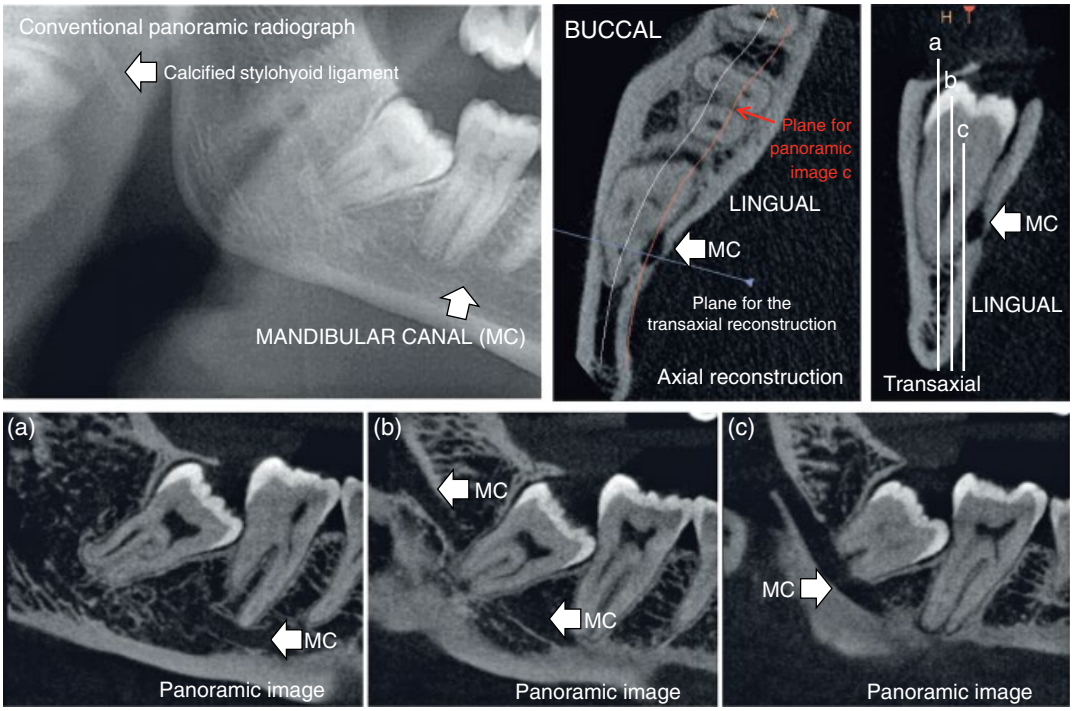


Figure 5.2 Part of the conventional panoramic radiograph and small (5 × 5) field-of-view (FOV) cone-beam computed tomography (CBCT) of an impacted right third molar (wisdom tooth). The images in the top row are part of a conventional panoramic radiograph, axial and transaxial reconstructions of a CBCT dataset, with the operator manually drawn white line on the axial denoting the line of the dental arc from which the reconstructed panoramic view that (a) in the bottow row represents. This tooth has an intimate relationship with the mandibular canal (MC), being grooved by the MC, which in turn has compressed it against the lingual cortex in the transaxial, which the MC has then markedly eroded. Note also that the apex of the distal root of the impacted right third molar in (a) is very slightly hooked; this may complicate the ease of removal of that root. The white line on the axial reconstruction is the manually drawn line that determines the central panoramic reconstruction. This can be moved buccally or lingually. The reconstructed panoramic images (b) and (c) (red line in the axial reconstruction) represent reconstructions more lingual to reconstructed panoramic image (a). Note how the mandible shape changes between the three reconstructed images. The blue line on the axial reconstruction perpendicular to the white line represents a transaxial reconstruction, which is the third of the top-row images. It displays the vertical planes of the three panoramic reconstructions (a–c).

the radiation can be reduced by reducing the size of the volume to be investigated, i.e. the jaws rather than the whole head. When fan-beam CT has been applied for purely dental purposes, such as preimplant planning, prior to the advent of CBCT then at least a substantial part of the head was irradiated.

Hitherto casually used terms such as "medical" CT instead of MDCT and "dental" CT for CBCT should be discontinued, as both technologies can be and are validly applied to any part of the body. Otorhinolaryngology surgeons have also been using CBCT for almost as long as have oral clinicians, not only for petrous temporal disease [7] but for other head and neck lesions [8]. Other recent medical applications have been in orthopedics [9], osteoporosis [10], and balloon-pulmonary angioplasty guided by CBCT in patients with chronic thromboembolic pulmonary hypertension [11].

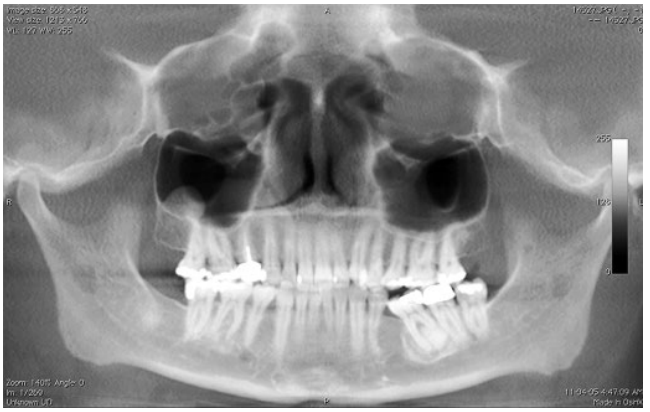


Figure 5.3 Reconstructed panoramic image (RPI) of large field-of-view (FOV) cone-beam computed tomography (CBCT). It extends above the base of the skull. Unlike the conventional panoramic radiograph, the RPI displays all structures within its selected thickness, thus excluding the secondary images and superimpositions (vertebral column) observed on the former. The bilateral radiolucencies in the maxilla are sections through the air-filled spaces of the malar/zygomatic buttress. There are two lesions. The mixed lesion on the mandibular left first molar presents osseous dysplasia. The radiopacity in the right maxillary sinus arising from its floor is a wholly soft-tissue lesion, the mucosal antral pseudocyst. Note: The vertical grayscale bar on the left indicates that this image presents with 256 (255 plus 1) gray levels or 8 bits. The right–left scale conventions for reconstructed panoramic radiographs are the same as those for conventional panoramic radiographs.

Although the original CBCT unit, the New Tom, required the patient to be supine, almost every other CBCT manufactured today for dental uses a gantry similar to the fixed horizontal C-arm that is already common for panoramic radiography. The patient is either seated or standing within it during the exposure.

The machine itself is relatively simple. Only one center of rotation is needed for CBCT, compared to the complex rotational geometry required for the modern panoramic radiographic unit. CBCT basically consists of an X-ray generator on one end and a *flat panel detector* (FPD; see later) on the other end. The simple single rotational movement minimizes the need for repair and maintenance, thereby improving reliability. CBCT usually operates at a higher kV than the panoramic radiographic unit. The range is from 75 to 120 kV. Some machines use a pulsed X-ray beam and/or a shorter arc of rotation (as low as 180°) for further dose reduction.

5.3 Why Is Cone-Beam Computed Tomography Desirable?

The advantage of CBCT is its superior spatial resolution (the ability to identify separately two minute points very close together), relative to fan-beam CT, of structures with high-contrast mineralized tissue such as teeth and bone.

Some current CBCT units, by their restriction of the pre-exposure selection of the highest spatial resolution only to the smallest FOV, thereby restrict the amount of radiation that can be delivered by a larger FOV. It should be noted that the lowest or default spatial resolution of a CBCT in the most modern units is still superior to the best

Table 5.1 Summary comparison of the main features of cone-beam computed tomography and fan-beam computed tomography.

Feature	Cone-beam CT	Fan-beam CT
Ease of access for dental patients?	Yes; fairly ubiquitous	No; hospital/medical facility
Patient tolerance	Similar to panoramic unit	Some patient preparation
Patient positioning	Similar to panoramic unit – sit or stand	Supine only
Footprint	Similar to panoramic unit	Requires its own room
Radiography technician required?	No, but much training is required, particularly when small FOVs are used	Yes
Floor strengthening?	No – similar to panoramic unit	Yes
Special electrical requirements?	No – similar to panoramic unit	Yes, high-tension supply
Spatial resolution/ bone detail	Best at 0.076 mm/voxel –especially important for endodontics	Best at 0.35 mm/voxel
Spatial resolution in three dimensions	Best	MDCT cuberilles are getting more CBCT-like, but are still not cuboidal
Contrast resolution/ soft-tissue detail	Up to 16-bit depth so far	Best at 16-bit depth and higher
Radiation dose	Less – particularly if a small FOV is used	Higher – whole head
Cost to the North American patient	For a dental reason CBCT is 4–8 times cheaper; the patient invariably pays	For a “medical-like” disease the patient’s health insurance may pay
Intravenous contrast medium use?	No, unless the patient is supine with a medical doctor present to administer	Yes
Who is responsible for reporting?	Prescribing clinician, who should at least ensure that a report was made	Medical radiologist

Note: FBCT is extensively used in medicine. The most current and widely available manifestation of FBCT technology is MDCT (see Figure 4.1). The features in the table are discussed in detail in the text.
CBCT, cone-beam computed tomography; FBCT, fan-beam computed tomography; FOV, field of view; MDCT, multidetector computed tomography.

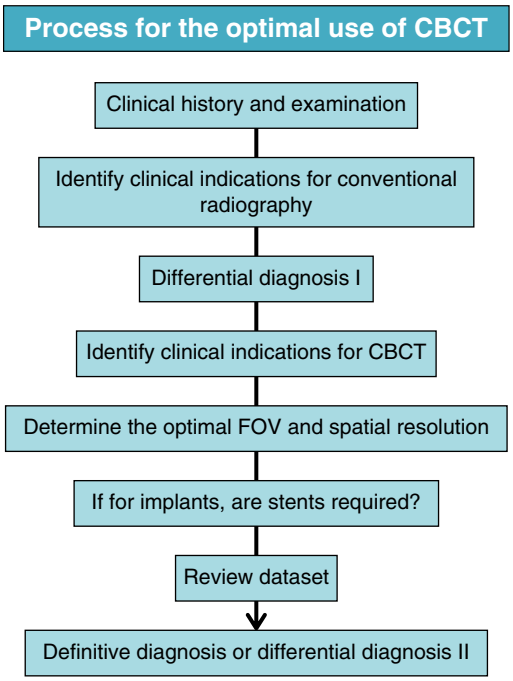


Figure 5.4 Process for the optimal use of cone-beam computed tomography (CBCT). Conventional radiography (CR), in addition to producing images of the best spatial resolution (image detail), imparts a significantly lower radiation dose to the patient, especially important for child patients due to their greater vulnerability to radiation-induced injury. The requirement that the entire image be reviewed, well established for CR, is just as relevant for a CBCT dataset. Key: FOV, field of view. Source: MacDonald, D. (2017). Cone-beam computed tomography and the dentist. *J. Investig. Clin. Dent.* 8 (1): 85–92. doi: https://doi.org/10.1111/jicd.12178. Reproduced with permission of Wiley.

spatial resolution of fan-beam CT (namely MDCT using hundreds of detectors).

Although CBCT is an improvement on *conventional radiography* (CR) with regard to elimination of superimposition and 3D reconstruction, its spatial resolution is still inadequate, particularly in comparison to intraoral radiography. Brullman and Schulze reported that the difference in spatial resolution between CBCT (Accuitomo, Morita) and intraoral

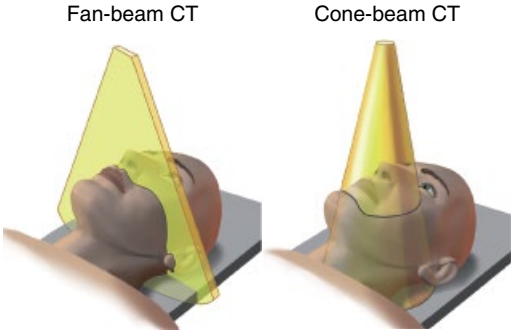


Figure 5.5 The fan beam upon which medical hospital-based computed tomography is based interrogates only a slice of tissue, whereas the cone beam of cone-beam computed tomography (CBCT) interrogates a three-dimensional region within a single 360° rotation (now often less). Source: Reproduced with permission from MacDonald-Jankowski, D.S., and Orpe, E. (2006). Computed tomography for oral and maxillofacial surgeons. Part 2: Cone-beam computed tomography. *Asian J. Oral Maxillofac. Surg.* 18: 85–92.

CR is one order of magnitude [12]. They suggested that a CBCT scan of a real patient is more realistically just above 1 line pair per mm. Therefore, intraoral images will continue to display fine features such as the "ground-glass" and "peau d'orange" (orange peel) appearance of bone, the poorer-defined margins associated with fibrous dysplasia, and the fine cortices of other lesions. On the other hand, CBCT's reconstructed panoramic image (Figure 5.3) is superior to that of a conventional panoramic X-ray because it displays no superimposed secondary images and is geometrically more accurate.

CBCT reconstructs 3D images by generating cuberilles directly, each with its own attenuation coefficient (Figure 5.6 compared to Figure 4.9). This allows 3D reconstructions with better spatial resolution in the Z plane (the patient's long axis), in addition to the axial (XY) plane. Except perhaps for the most modern MDCT units with a high number of

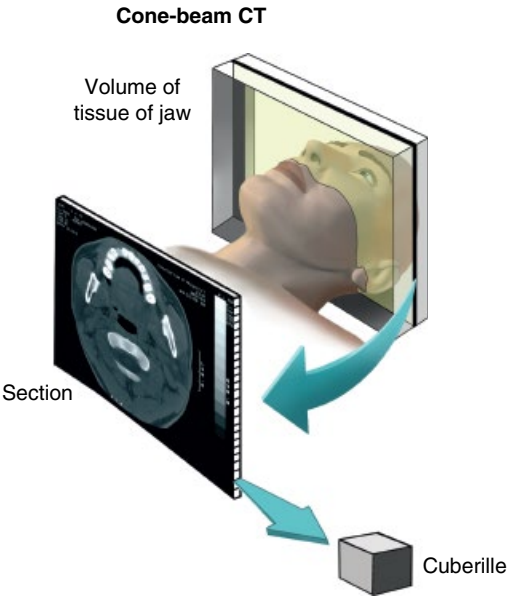


Figure 5.6 Cone-beam computed tomography (CBCT) reformats three-dimensional (3D) images by generating cuberilles directly, each with its own attenuation coefficient. This allows 3D reformations with better spatial resolution in the Z axis (in comparison to the fan bean in Figure 4.9), in addition to the axial (XY) plane. Source: Reproduced with permission from MacDonald-Jankowski, D.S., and Orpe, E. (2006). Computed tomography for oral and maxillofacial surgeons. Part 2: Cone-beam computed tomography. *Asian J. Oral Maxillofac. Surg.* 18: 85–92.

detectors, most standard fan-beam MDCT can only produce cuberilles secondarily from voxels (see Figure 4.9). These cuberilles have the same attenuation coefficient (seen as a particular shade of gray) as the parent voxel. On the other hand, the attenuation coefficient of each of CBCT's cuberilles represents a specific cube of tissue. This and the generally higher spatial resolution of CBCT result in highly detailed 3D images (Figure 5.1d).

Most CBCT now makes use of FPDs constructed of amorphous silicon, rather than the image intensifiers frequently used in fan-beam CT. FPDs have the advantage of not producing the geometric distortion that occurs with image intensifiers [13]. In addition, FPDs have a wider dynamic range, better *signal-to-noise ratio* (SNR), and better spatial resolution [14].

CBCT's spatial resolution is many times superior to that of MDCT. The best spatial resolution for CBCT is 0.076 mm voxel size, in comparison to 0.35 mm voxel size for the best MDCT.

The dataset of an MDCT of the head will capture the entire head, from which 3D or multiplanar reconstructions can be made. The dataset for a CBCT will depend on the FOV selected. The FOV is usually given in the format 8 × 8, which means an FOV of 8 cm in diameter and 8 cm in height. An 8 × 8 FOV will adequately capture the dentition and alveolus of both jaws and is ideal for multiple implant planning. The range of FOVs available for a particular unit will vary with each individual model. Figure 5.7 reveals the smaller FOVs available for one unit, the Carestream 9300, and their clinical indications. The figure only includes those FOVs which are most applicable to dental practice, such as implant placement, endodontics, the removal of impacted teeth, and a more detailed evaluation of some jaw lesions [1, 2]. With regard to impacted maxillary canines, Eslami et al. reported that "CBCT is more effective than CR (conventional radiography) in evaluating cases that are difficult to diagnose in the initial evaluation with CR" [15]. Figure 5.8 displays such an example. Prescriptions for the larger FOVs would only be made for craniofacial anomaly cases, which include those with cleft lip and palate (Figure 1.6) and where craniofacial surgery was being contemplated. Otherwise these should not be prescribed, particularly for routine orthodontics. Recent research reaffirmed that the outcomes of conventional and CBCT cephalometry exhibited no significant difference, despite the latter imparting a higher radiation dose to the patient [16].

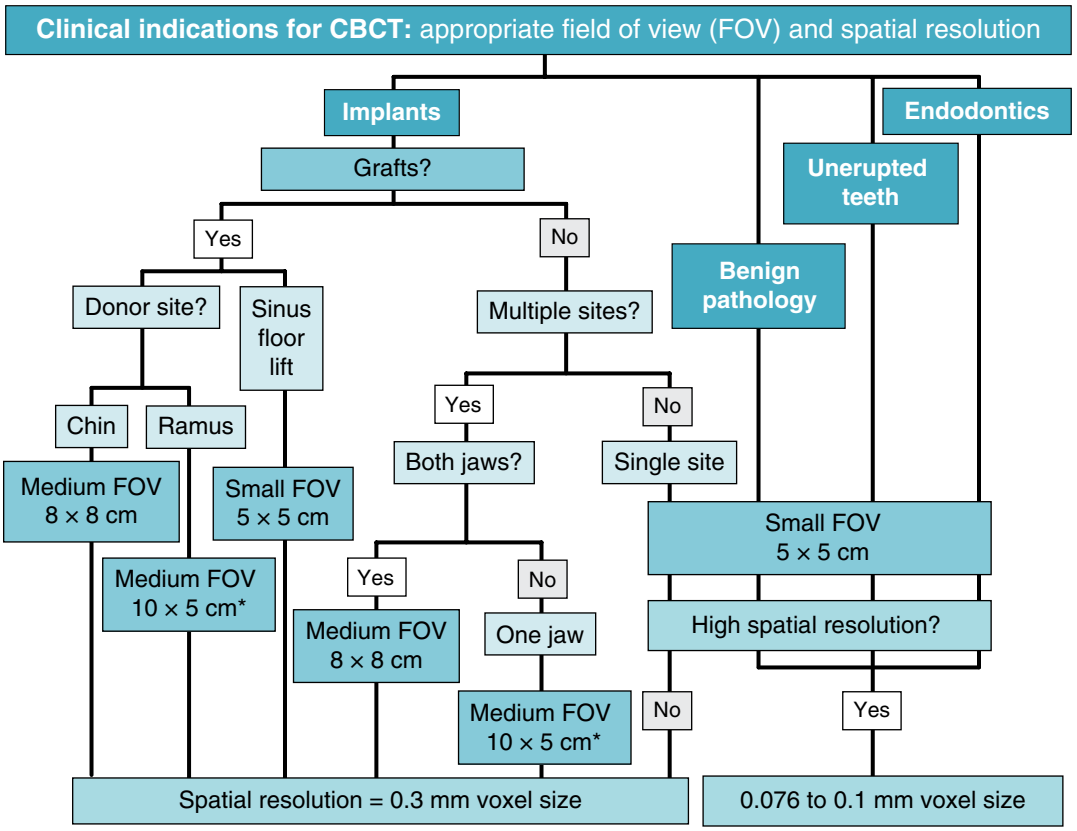


Figure 5.7 A balance must be struck between minimizing the risk of radiation-induced harm and the need to obtain images of diagnostic quality appropriate for the clinical procedure that is being contemplated. The flowchart reveals that the spatial resolution (degree of detail seen) and the size of the field of view (FOV) vary with clinical indications. Note: The FOVs selected for the flowchart are those available on a Carestream 9300 cone-beam computed tomography (CBCT) unit; other units may offer different FOVs. Nevertheless, use the smallest FOV possible to reduce the radiation dose. The conventional radiological features that suggest "benign pathology" are set out in [4]. Any lesions that cannot be fully displayed within a small FOV (with better spatial resolution) should be referred to an oral and maxillofacial surgeon or radiologist, or to a medical clinic or hospital for multidetector computed tomography (MDCT), as intravenous contrast (media) may be required. The asterisk cautions the reader that due to the more posterior positioning of this FOV, lesions of medical interest such as calcification of the carotid arteries may be observed. Source: MacDonald, D. (2017). Cone-beam computed tomography and the dentist. *J. Investig. Clin. Dent.* 8 (1): 85–92. doi: https://doi.org/10.1111/jicd.12178. Reproduced with permission of Wiley.

5.4 When Does Cone-Beam Computed Tomography Properly Complement the Work of the Dentist?

Osseointegrated implants were first developed by Brånemark and his team half a century ago [17]. Since then they have completely transformed prosthodontics. In addition to excellent technical skills, careful assessment of the patient is necessary to ensure that the implant/s and subsequent restoration have the best chance of success. Although implants have achieved considerable long-term success, as evidenced by an American Academy of Osseointegration (AAO) systematic review

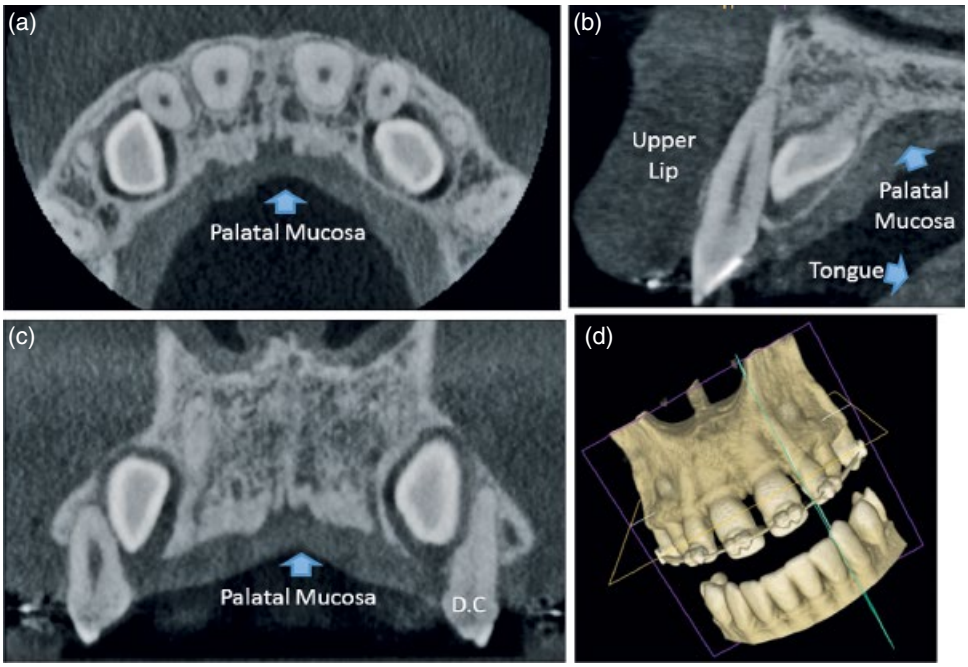


Figure 5.8 Small (5 × 5) field-of-view multiplanar reformatted cone-beam computed tomography of impacted maxillary canines prescribed after parallax using conventional intraoral radiographs was equivocal. Axial (a), sagittal (b), and coronal (c) reconstructions were made of the dataset represented by the three-dimensional reconstruction (d). The position of each plane is clearly displayed in (d). Note: The lower (mandibular) teeth were cropped out in order to compile this figure. (a) and (b) reveal that the crown of the maxillary canine is in intimate contact with the roots of the erupted permanent lateral incisors, but is not resorbing them at this moment; (c) displays the left maxillary canine resorbing the root of the deciduous canine. This kind of resorption is expected and desirable.

[18], the need for good preimplant cross-sectional imaging has generally come to be viewed as essential for successful implants. Table 5.2 shows that substantial literature on the value of CBCT to the implantologist is only recent. Hatcher and co-workers [19] first published on CBCT and implants in 2003. As Table 5.2 demonstrates, this was soon followed by a deluge of publications.

CBCT assists dentists or prosthodontists and their surgeons not only to place implants in sites which allow optimum restoration, but also identifies those at risk of a complication. Wanner and co-authors reported in their systematic review that the five most frequent complications were permanent nerve injury, damage to teeth adjacent to the implant, excessive bleeding in the floor of the mouth, mandibular fracture, and displacement of implants into the maxillary sinus [20]. Such inadvertent injury can be minimized by CBCT, which allows accurate measurement to determine the safe parameters within which the implant can be placed.

The advent of CBCT units with smaller FOVs and even better spatial resolutions has transformed endodontics. Now the endodontist can determine the degree of calcification of a pulp canal (Figure 5.9) or the site and angulation of a root fracture

Table 5.2 Publications on cone-beam computed tomography and dental implants.

Year of publication[a]	Number of publications that year
2003	1
2004	0
2005	0
2006	1
2007	6
2008	14
2009	15
2010	33
2011	44
2012	65
2013	46
2014	70

[a] Year of first publication, which could have been online.
Note: This search was undertaken in PubMed and was for <"CBCT" and "Dental implants">.
Source: MacDonald, D. (2017). Cone-beam computed tomography and the dentist. *J. Investig. Clin. Dent.*. 8 (1): 85–92. doi: https://doi.org/10.1111/jicd.12178. Reproduced with permission of Wiley. Note: This table had been updated as far as 2014.

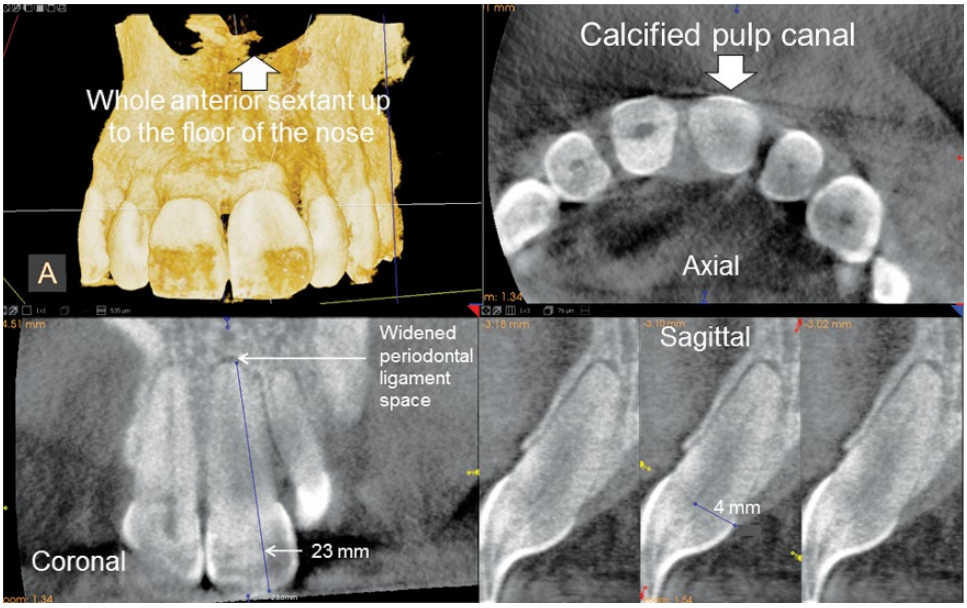


Figure 5.9 Small field-of-view multiplanar reformatted cone-beam computed tomography of the anterior sextant of the maxilla (including the floor of the nose and inferior aspect of the nasal cavity), displaying a calcified pulp canal in the right central incisor. The calcified canal displays a residual canal on the sagittal reconstructions. The widening of the apical periodontal ligament space on the coronal reconstruction appears to be an early periapical lesion in the sagittal reconstructions. Accurate measurements of the tooth can enhance the quality of the subsequent treatment planning and treatment provided. Source: Courtesy of Dr. David Gane, Founder and Managing Director of Orbit and CEO of LED Medical Diagnostics.

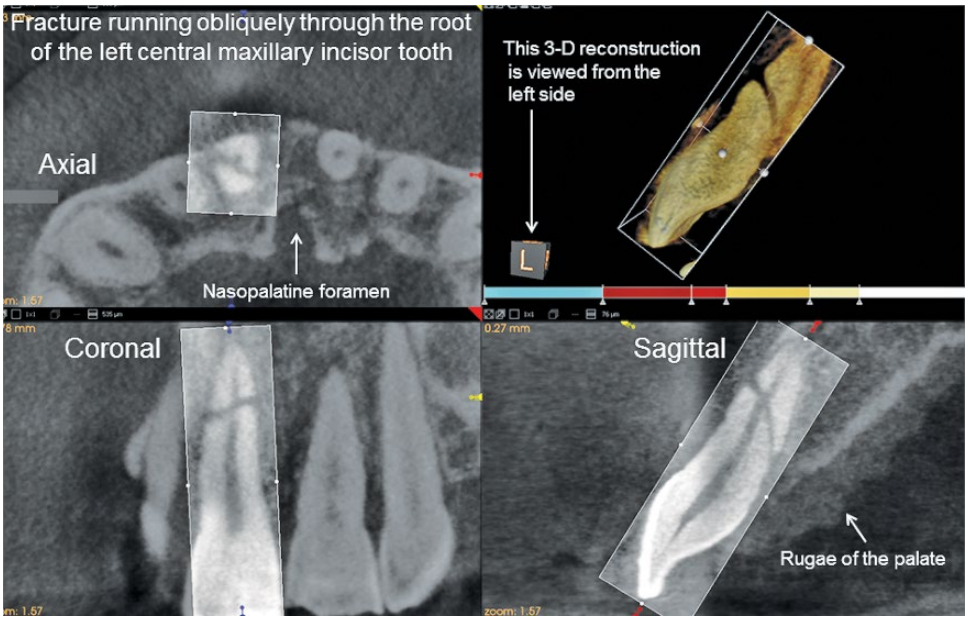


Figure 5.10 Small field-of-view multiplanar reformatted cone-beam computed tomography of the anterior sextant of the maxilla, displaying an oblique fracture through the root of the left central incisor. The three-dimensional reconstruction is orientated facing the left. Source: Courtesy of Dr. David Gane, Founder and Managing Director of Orbit and CEO of LED Medical Diagnostics.

(Figure 5.10), as well as find missing (unfilled) canals in previously (unsuccessfully) treated teeth (Figure 5.11) and thus effect better retreatment. A retained natural tooth may serve to obviate many of the contraindications for implants in the elder patient. Indeed, the loss of implants is higher than the loss of natural teeth [21].

As earlier made obvious by Figures 5.2 and 5.8, CBCT is invaluable for the evaluation of impacted teeth whenever CR, including parallax, is equivocal.

CBCT was also shown recently to be useful in the diagnosis and assessment of some of the most frequent and/or important lesions that affect the face and jaws [2, 3]. Although CBCT can also substantially replace medical hospital-based MDCT when cross-sectional imaging is required for benign lesions [2, 3], CBCT can reveal features that indicate a prompt referral to hospital specialties. This was recently revealed in a case of lymphoma [22].

5.5 Important Points to Consider Prior to Prescribing CBCT

The dataset taken by current units will generally reflect the FOV and the spatial resolution selected by the operator prior to exposure. Therefore, it is necessary that these are chosen in advance of the exposure and that they correspond to the precise clinical purpose (Figure 5.7) clinicians needing the information expect that particular CBCT to provide. If the procedure is to be performed at another site, then clinicians must ensure that the FOV and spatial resolution they select are clearly indicated in the prescription form. Prior to this, clinicians should have ascertained that the unit they are prescribing to is capable of meeting their expectations. All CBCT units are not created equally. Indeed, although the more modern units

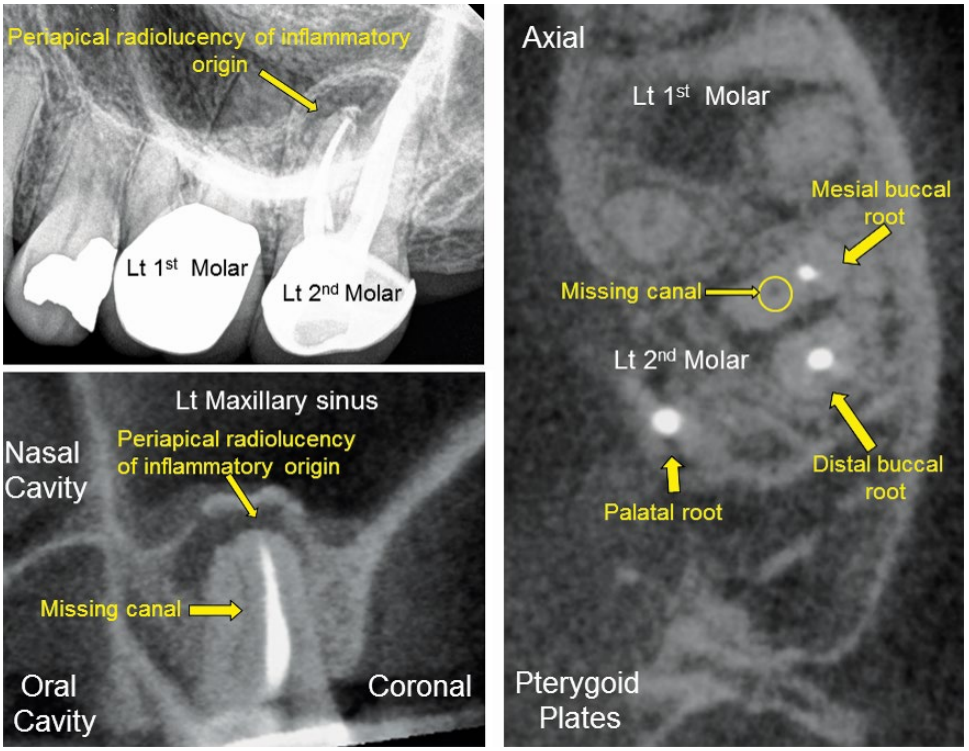


Figure 5.11 Periapical radiograph and axial and coronal reconstructions of small field-of-view multiplanar reformatted cone-beam computed tomography of the posterior sextant of the maxilla (including the floor and the inferior aspect of the maxillary sinus), displaying a missed second canal in the mesial buccal root of the left second molar. The periapical radiograph displays a periapical radiolucency of inflammatory origin around the mesial buccal root of the already root-treated left second maxillary molar. The failure to find and treat this canal resulted in failure of the initial root-canal treatment. The mesial buccal canal and those of the distal buccal and palatal roots had been successfully obdurated by the radiopaque root-filling material (axial). Note: Both roots are associated with black bands (see the yellow arrows) that look like the root fracture observed in Figure 5.10. This is a beam-hardening artifact. The coronal reconstruction calcified canal displays periapical radiolucency. The superjacent sinus mucosa is thickened, suggesting that the inflammatory products have penetrated the bony floor (see break). Source: Courtesy of Dr. David Gane, Founder and Managing Director of Orbit and CEO of LED Medical Diagnostics.

generally produce images with better quality (spatial resolution) for a lower radiation dose and with better software, this should not be taken at face value, but rather evidence should be provided that that is the case. It is most likely that a court would deem that the prospective prescriber of a CBCT, to be performed at another office, is just as duty bound as the prospective owner to ensure that the degree of image quality necessary for the patient's treatment is produced at the lowest radiation dose to that patient.

5.6 Viewing a CBCT Dataset

Once the procedure has been performed, the dataset is ready for viewing, either on the monitor associated with the unit or

that of the referring clinician who generated the prescription. The latter will review the dataset after transfer on a *digital video disc* (DVD), a *compact disc* (CD), a *universal serial bus* (USB) flash drive, or a selection of screenshots on photographic paper.

The dataset will usually open on the standard multiplanar display of axial, coronal, and sagittal reconstructions. The axial is viewed, as are all cross-sectional modalities, from below, from the feet, looking upward to the vertex of the head. The orientation of the images is revealed by R (right) and L (left) side markers and A (anterior) and P (posterior) markers. When the curved reconstruction (analogous to Dentoscan) is used to generate a synthesized panoramic display, it is viewed as one would a conventional panoramic radiograph. Since screenshots of the reconstructed images include much "wasted space," the images are selected, enlarged, and repositioned within the figures of this textbook in order to enhance the quality of the reader's experience. In those situations where a side marker would assist the reader's understanding, a "R" for right side is inserted.

Unless the provider of the CBCT is a credentialed radiologist working in the same jurisdiction as the prescriber, it would be more medicolegally prudent to supply prescribers with the complete dataset and the appropriate software, advising them of their duty to review and report the dataset.

5.7 What Are the Disadvantages of CBCT?

5.7.1 THE RADIATION DOSE IMPARTED BY CBCT IS MUCH HIGHER THAN GENERALLY UNDERSTOOD BY THE DENTAL PROFESSION

As CBCT imparts a higher radiation dose than conventional imaging, it can only supplement CR rather than replace it (Figures 5.2 and 5.11). Figure 5.4 sets out the appropriate place that CBCT plays in the diagnostic process of the dental patient. Although this varies widely between different CBCT units – as is made clear in Table 5.3, which summarizes the effective doses delivered to adult and child patients from large, medium, and small FOVs derived from a meta-analysis of 20 reports [23] – it is on average more like 10 times more than a conventional panoramic radiograph, rather than just equivalent to one

Table 5.3 Summary of effective doses delivered to adult and child patients from large, medium, and small fields of view.

Size of field of view	Adult	Child
Large	Range = 46–1073 μSv Mean = 212 μSv	Range = 13–769 μSv Mean = 175 μSv
Medium	Range = 9–560 μSv Mean = 177 μSv	
Small	Range = 5–652 μSv Mean = 84 μSv	Range = 7–521 μSv Mean = 103 μSv

Source: Data from Ludlow, J.B., Timothy, R., Walker, C. et al. (2015). Effective dose of dental CBCT—a meta analysis of published data and additional data for nine CBCT units. *Dentomaxillofac. Radiol.* 2015; 44: 20140197. Erratum in: *Dentomaxillofac Radiol* 2015;44:20159003.

or two panoramic radiographs as is commonly (mis)understood [24]. Furthermore, the better spatial resolution inflicts a higher radiation dose burden [23]. This burden can be reduced, in many modern units, by selecting as small an FOV as possible (see Table 5.1).

Pauwels et al. reported that "a 180° rotation resulted in an average dose reduction of 45% compared with a 360° rotation" [4]. They also reported that radiation dose to the lens of the eyes was reduced by reducing the height of the FOV. This was preferable to simply displacing the FOV inferiorly, which instead increased the effective dose [4]. This increase would have been due to the greater radiation dose delivered to the thyroid and salivary glands as a result of this inferior displacement of the FOV.

Radiation dose in a clinical situation is best defined by effective dose. Although this is usually calculated by *dose area product* (DAP), Ludlow et al. offered a perhaps more accurate system, which they called *dose height product* (DHP) [23].

5.7.2 CBCT DOES NOT NEED TO BE "PRETTY" IN ORDER TO BE DIAGNOSTIC

It is well understood that the nonradiologist dentist prefers a high signal-to-noise ratio and high spatial resolution, resulting in "pretty pictures." Unfortunately, these two criteria can add significantly to the radiation dose to the patient. Therefore, Ludlow et al. suggest that dentists should be encouraged to focus on "just diagnostic" images. Furthermore, radiation dose reduction should be driven more by *as low as diagnostically acceptable* (ALADA) rather than the better known *as low as reasonably achievable* (ALARA) [23].

5.7.3 THE PRESCRIBING CLINICIAN IS RESPONSIBLE FOR THE REVIEW OF THE ENTIRE DATASET

The size of the FOV is also important in another regard. While the small (5 × 5 cm or smaller; sometimes called "focused") and medium (8 × 8 to 10 × 10 cm) FOVs are adequate for imaging the jaws, the large FOV (more or less anything in excess of 10 × 10 cm) will include extragnathic areas (Figures 1.5, 1.6 and 5.12). These areas, particularly the eyes, brain, and neck, are outside the remit of the dentist. As their anatomy, pathology, and clinical evaluation do not form part of the undergraduate dental curriculum, the dentist is advised to refer large FOV datasets to a radiologist for review and report.

Meanwhile, the American [25] and European [26, 27] Oral/Dental and Maxillofacial Radiology Academies and the American Dental Association [28] have also already published their own guidelines for proper CBCT use.

5.7.4 THE PEDIATRIC PATIENT IS MORE LIKELY TO EXPERIENCE RADIATION-INDUCED NEOPLASIA

The advice from the US Food and Drug Administration (FDA) is that "The level of ionizing radiation from X-ray imaging is generally very low, but can contribute to an increased risk of cancer. Because children have longer expected lifetimes ahead of them for potential effects to appear and the risk for cancer is not fully understood, it's important to use the lowest radiation dose necessary to provide a diagnostic exam" [29]. Therefore, the dentist needs to have clear clinical indications prior to exposing a child to any radiation, and in particular to CBCT investigations.

In 2013, 680 211 Australians aged from infancy to 19 years, when exposed to a CT scan, experienced a 24% greater cancer incidence after a mean follow-up period of nearly 10 years [30]. While this study has been concluded, this cancer excess is likely to continue to increase. The authors recommended that "Future CT scans should be limited to situations where is there is a definite clinical indication, with every scan optimised to provide a diagnostic CT image at the lowest possible radiation dose." Just prior to publication of this Australian report was a British report, reviewing a selection of patients with leukemia and brain tumors, who had been investigated earlier by CT and were no older than 22 years at that time [31]. This report reached broadly similar conclusions. Its authors subsequently reviewed their data to ensure that a genetic disposition to radiation-induced tumors was not present or that subsequent neoplasia was not simply a recurrence of tumors for which the CT had been initially performed [32]. They reported that although some such bias was present, the reanalysis (which included additional clinical data) still revealed "an increased cancer risk after low-dose radiation exposure from CT scans in younger patients" [32]. Furthermore, another study by the same authors put their British studies in a clearer context. The "mAs [milliampere seconds] for head and trunk CTs had been approximately halved starting around 1990 and age-specific mAs was generally used for paediatric scans after that date" [33]. That means that even though the radiation dose delivered by CT to these British children had already been substantially optimized, there was still "an increased cancer risk after low-dose radiation exposure" [33]. Recently guidelines for the appropriate use of CBCT on the child dental patient have been published [34].

5.7.5 HOUNSFIELD UNITS CANNOT YET BE ACCURATELY USED FOR CBCT

Although bone density in Hounsfield units can be determined from the MDCT dataset, this is not yet reliably available for CBCT due to important differences between these technologies. The resultant great variability of *gray values* (GVs) for CBCT is "inherently associated with this technique (i.e. the limited field size, relatively high amount of scattered radiation and limitations of currently applied reconstruction algorithms). Although attempts have been made to correct for GV variability, it can be postulated that the quantitative use of GVs in CBCT should be generally avoided at this time" [35].

5.7.6 METAL ARTIFACTS

Unlike the displays at trade shows and in brochures, many CBCT images will display beam hardening and scatter (spray) artifacts arising from dental restorations [13]. A major problem in any CT scanning of the jaws is image artifacts caused by metallic restorations in the dentition. Such artifacts in fan-beam systems (see Figure 4.7) extend throughout that whole axial section, whereas most of those in CBCT are shorter (Figure 5.12), additional information is available sampled along the direction of the rotation axis [36].

High-density alloys in crowns (the atomic number of gold is 79) and large amalgams (the atomic number of mercury is 80 and of silver is 47) significantly attenuate the primary X-ray beam [36].

Although the majority of implants are made of titanium (Ti), which has an atomic number of 22, Zirconium (Zr) with an atomic number of 40 is now being used. This contains trace amounts of hafnium (Hf) and yttrium (Y), both metals, to

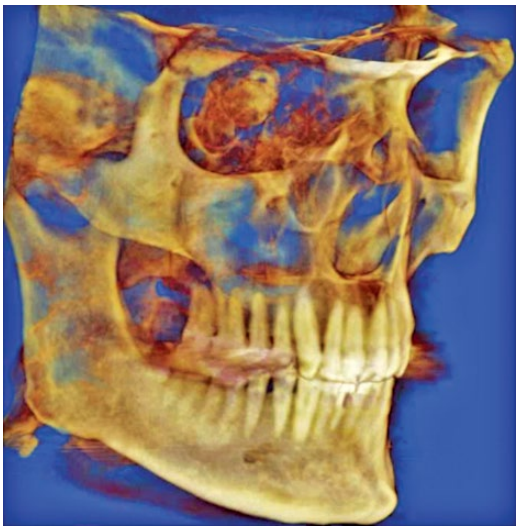


Figure 5.12 Three-dimensional reconstruction or reformation of a large field-of-view dataset captured by cone-beam computed tomography (CBCT). The effects of the beam hardening caused by metal dental restorations is represented by short horizontal flares that do not extend far throughout the horizontal plane, as would be apparent in fan-beam CT (see Figure 4.7); compare with Figure 4.7. Source: Courtesy of Dr. Babak Chehroudi, Faculty of Dentistry, University of British Columbia.

improve its properties. Schulze et al., when comparing the beam hardening in a CBCT at 80 and 110 kV, found that the beam hardening was more pronounced for 80 kV [36].

Schulze et al. also discussed the various *metal-artifact reduction* (MAR) algorithms and reported that they were both crude and produced errors. They pronounced as unreliable the reconstructed regions either close to the surface of a titanium implant or in the line/s connecting two or more implants [36]. Furthermore, they advised that meaningful MAR "had to be based on more sophisticated mathematical modelling of the actual physical image acquisition process." Nevertheless, a more recent report by Korpics et al. determined their interpolation-substitution algorithm "to be efficient and effective for reducing metal artifacts caused by dental fillings and implants on CBCT images" [37]. Although this study was performed on the datasets of head and neck cancer patients and therefore not in vitro like many other such studies, the investigators were radiation oncologists rather than diagnostic radiologists. This study, though encouraging, does not assuage the discomfort many radiologists have on reading what are effectively "Photoshopped" images. More persuasive in vivo evidence for the effectiveness of MAR or other strategies to reduce the effect of metal artifacts on areas of clinical interest is required.

5.7.7 PATIENT MOVEMENT ARTIFACTS

Spin-Neto and Wenzel's systematic review revealed that "Investigations that monitored patients during CBCT reported a movement prevalence of 20%, and studies based on CBCT image artefact recognition, without knowledge of movement, reported prevalence of artefacts in the range of 4.5% to 41.5%. There seems to be a consensus on the fact that young patients (children and adolescents) move more often compared with older patients" [38]. This would call for operator vigilance during the exposure of patients, particularly of child patients, which would allow prompt termination of the exposure. That would reduce the amount of unnecessary radiation that patients would receive for this suboptimum investigation. It is also prudent, particularly in the case of child patients, to rehearse the exposure by a "dry run." This dry run permits the rotation of the tube and sensor around the patient, without activation of the X-ray beam. Many units permit such dry runs.

5.7.8 IMPORTANCE OF PROPER DISPLAY

Pauwels et al. state that the "images should be displayed at their native resolutions (i.e. a 1:1 ratio between the display pixel and the image pixel) or better (i.e. having multiple display pixels for every image pixel) for optimal image sharpness" [5]. They illustrate this by reference to small (6 × 6) FOV with a good spatial resolution of 0.1 mm voxel size. In order to display this entire image with a 1 : 1 ratio, the monitor would need to have at least 1200 × 1200 pixels [5]. This indicates the acquisition of large, high spatial resolution monitors. Finally, as the acquisition of such a monitor may still not be adequate, Pauwels et al. encourage the use of the zooming tool and maximizing of windows whenever necessary. Although Pauwels et al. identified the contrast ratio and luminance only to be of secondary importance [5], the standard radiologist's review of the entire dataset under reduced ambient lighting is to be commended.

5.8 Notes for the Potential Owner or User of a CBCT Unit

5.8.1 CHOOSE THE UNIT WHICH BEST ADDRESSES YOUR CLINICAL NEED/S

Potential owners of a CBCT must be aware that there is a wide range of CBCT units currently on the market. Most units are designed to perform one task optimally. Therefore, potential owners must ensure that the protocols of their chosen unit are appropriate for their patient base and the services they provide. For example, a small FOV, very high spatial resolution unit is optimal for endodontics. (Note: Not all units are wheelchair accessible.)

5.8.2 CBCT UNITS ARE NOT EASY TO USE

The dental team requires considerably more training than a day or half a day provided by the vendor/manufacturer upon installation. Vendor/manufacturer training tends to focus more on the software and is frequently very inadequate with regard to mastery of technique. The dental team will need much practice. While it is almost inevitable, especially at the beginning, that the occasional failure may require reimaging (re-exposure) of the patient, this should be the exception. Ideally, an anatomical head phantom, preferably with a natural skull embedded, should be used for team training or practicing the technique of an unfamiliar program prior to exposing the patient [39]. An example of such an anatomical head phantom is displayed in Figure 5.13.

The patient must be stationary for the entire scan [38]. Although most scans by modern machines can be completed in less than 30 seconds, the extra time required to optimally position the patient must also be taken into account. This positioning time will be reduced by the skill and experience of a well-practiced dental team. Furthermore, the nervous patient's fears may be addressed by the use of dry-run rotations to develop the patient's confidence prior to doing it for real, when X-rays are generated to produce the image. A facility that almost all modern CBCT units have is the generation of a "scout view" at the beginning of the scan. This will allow the operator to determine whether the patient has been optimally positioned prior to proceeding with the full exposure. As the taking of a scout view imparts a fraction of the dose of the overall scan, the exposure can then be terminated, preventing unnecessary further exposure of the patient [39].

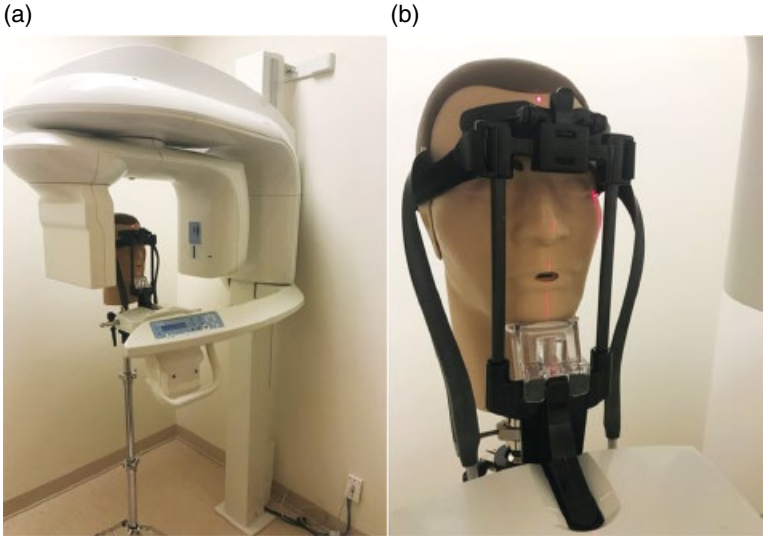


Figure 5.13 (a) Carestream 9300 cone-beam computed tomography (CBCT) unit and (b) head phantom (with natural skull imbedded) on a fully adjustable stand, allowing movement in all directions to facilitate ease of optimal positioning for student, staff, and faculty training and practice of infrequently used programs. Source: Courtesy of Sabina Reitzik, Clinical Instructor (Radiography), Oral and Maxillofacial Radiology, University of British Columbia, Canada.

5.8.3 A ROUTINE QUALITY ASSURANCE PROGRAM IS REQUIRED

Horner et al. reviewed a number of CBCT performance issues [40] that compel the application of *quality assurance* (QA). The purpose of a QA program is to ensure not only that image quality is optimal, but that also the radiation dose is minimal for the desired image quality and for that particular unit. Most dental offices are already performing QA for many clinic-related activities, such as infection control (including instrument sterilization) and CR. These QA programs are mandated either by regulatory and other professional bodies or directly by the government. QA for CBCT is no different in this regard. Because of the complexity of this technology, the office owner may leave this to the manufacturer or installer to address periodically under a service agreement, whereas teaching institutions and hospitals will direct their radiation physicists and engineers to perform this QA task with their own QA programs. The need for the individual owner or institution to perform regular QA is important, because most CBCT manufacturers "remote-in" online to the CBCT software to upgrade it. Generally, while improving the performance of the unit, often with an improvement in image quality, these upgrades may also result in an increase in the radiation dose for a particular protocol. Unless QA is performed routinely, such increases may pass unnoticed. In most jurisdictions owners are ultimately responsible for all activities which may have an impact on their patients and staff. Therefore, ignorance may not be an effective defense. In addition to the anatomical phantom for training (Figure 5.13), there are a number of phantoms for QA purposes. The most commonly used QA phantom is *Safety and Efficiency of a New Emerging Dental X-ray* (SEDENTEXCT) [41].

5.9 Notes for the Medical Radiologist

The advent of CBCT and its increasing ubiquitous availability for the dentist in part relieves hospital-based radiology departments of the added burden of having to provide imaging for all such patients. The main downside of this technology's widespread availability is that the radiological knowledge of many of the dentists who own and operate these units may not yet be adequate for interpretation of a CBCT dataset. Therefore, until dental education catches up, medical radiologists may be approached to interpret some datasets, particularly where the availability of oral and maxillofacial radiologists is sparse or nonexistent [2].

Lesions of the jaws which can be fully encompassed within a small FOV (5 × 5 cm or smaller) should be imaged at a high spatial resolution, which may be as high as 0.076 mm voxel size. Any lesion larger than this would most likely require in-hospital management and should be referred to such a facility for imaging and treatment. Unlike CBCT, MDCT images the patient supine rather than upright and therefore allows the use of *intravenous contrast medium* (IVCM). IVCM has so far not been shown to contribute to management or treatment outcomes, certainly of ameloblastomas and odontogenic myxomas [2].

5.10 Concluding Remarks

CBCT has over the last decade enhanced the diagnosis and subsequent management of certain clinical phenomena, such as preimplant planning, difficult endodontic cases, and difficult impacted teeth and lesions that are not adequately displayed by CR alone. This has been achieved by its better spatial resolution for a lower radiation dose than MDCT. The now widespread use of CBCT has been facilitated by its small footprint and moderate exposure factors, which lend themselves to easy installation in a dental office. Although there is an overwhelming drive to restrict its use for and by dentists to the face and jaws, the primary region of professional knowledge and expertise of the dental clinician, large FOVs are still frequently produced. Not only do these impart a larger radiation dose, particularly worrisome when the patient is a child, but the need for a review of and report on the entire dataset, legally mandated by most jurisdictions, is a challenge to dental prescribers. They will need the assistance of a radiologist, ideally registered in the same jurisdiction.

At the time of writing, it is commonplace in the United States and Canada for reports to be provided by radiologists who are not registered in that jurisdiction, due to the dearth of radiologists, particularly oral and maxillofacial radiologists, in certain states and provinces. Until this practice has been upheld by the courts, it has to be considered unsound. It is better if the prescribers restrict their FOV to that covering the jaws only, employing their already substantial knowledge of the anatomy and pathology of that albeit limited region. This is being addressed by instruction on CBCT use, technique, and radiology in some North American dental schools, both to dental undergraduates and to specialist students, and in an increasing number of continuing professional development courses. This duty is not merely restricted to calcified and osseous tissues, which until recently were the only structures apparent on CBCT. Calcification of the carotid arteries should be actively searched, particularly in datasets with a large FOV (Figure 5.14). This is comprehensively discussed in Chapter 12. The advent of CBCT using a contrast resolution of 16-bit depth can

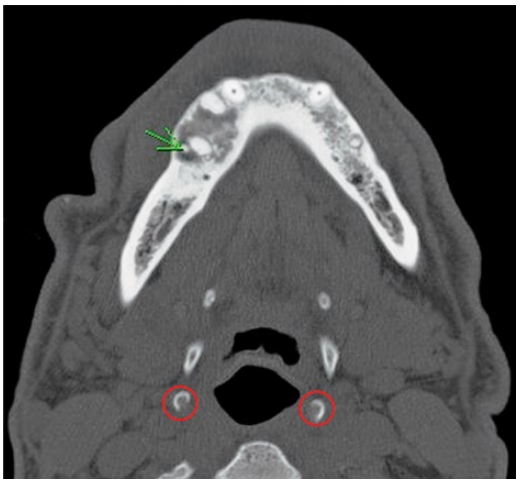


Figure 5.14 Axial reconstruction of large field-of-view cone-beam computed tomography (CBCT), displaying a lesion in the right premolar region of the mandible, marked by a green arrow. It is mainly a radiolucency with some internal opacification. The red rings encircle calcified carotid artery atheromas (CCAA). Since calcification occurs in the oldest and most mature part of the CCAA, it can be surmised that these atheromas have already caused significant stenosis, placing the patient at a severe risk of a stroke. This is discussed comprehensively in Chapter 11. Note: This CBCT, using a contrast resolution of 16-bit depth, can now display various soft-tissue structures such as muscles and the major salivary glands. Source: Courtesy of Dr. Lewei Zhang, Faculty of Dentistry, University of British Columbia.

now display various soft-tissue structures such as muscles, lymph nodes, major salivary glands, eyes, and optic nerves. Figure 5.14 displays the first two of these.

References

1. MacDonald, D. (2017). Cone-beam computed tomography and the dentist. *J. Investig. Clin. Dent.* 8 (1): e12178. https://doi.org/10.1111/jicd.12178.
2. MacDonald, D. (2016). Lesions of the jaws presenting as radiolucencies on cone-beam CT. *Clin. Radiol.* 71: 972–985.
3. MacDonald, D.S. (2015). Maxillofacial fibro-osseous lesions. *Clin. Radiol.* 70: 25–36.
4. Pauwels, R., Zhang, G., Theodorakou, C. et al. (2014). SEDENTEXCT project consortium. Effective radiation dose and eye lens dose in dental cone beam CT: effect of field of view and angle of rotation. *Br. J. Radiol.* 87: 20130654. https://doi.org/10.1259/bjr.20130654.
5. Pauwels, R., Araki, K., Siewerdsen, J.H., and Thongvigitmanee, S.S. (2015). Technical aspects of dental CBCT: state of the art. *Dentomaxillofac. Radiol.* 44: 20140224.
6. MacDonald-Jankowski, D.S. and Orpe, E.C. (2007). Some current legal issues that may affect oral and maxillofacial radiology. Part 2: digital monitors and cone-beam computed tomography. *J. Can. Dent. Assoc.* 73: 507–511.
7. Güldner, C., Diogo, I., Bernd, E. et al. (2017). Visualization of anatomy in normal and pathologic middle ears by cone beam CT. *Eur. Arch. Otorhinolaryngol.* 274: 737–742.
8. Stutzki, M., Jahns, E., Mandapathil, M.M. et al. (2015). Indications of cone beam CT in head and neck imaging. *Acta Otolaryngol.* 135: 1337–1343.
9. Osgood, G.M., Thawait, G.K., Hafezi-Nejad, N. et al. (2017). Image quality of cone beam computed tomography for evaluation of extremity fractures in the presence of metal hardware: visual grading characteristics analysis. *Br. J. Radiol.* 90 (1073): 20160539. https://doi.org/10.1259/bjr.20160539.
10. Brasileiro, C.B., Chalub, L.L., Abreu, M.H. et al. (2017). Use of cone beam computed tomography in identifying postmenopausal women with osteoporosis. *Arch. Osteoporos.* 12: 26. https://doi.org/10.1007/s11657-017-0314-7.
11. Ogo, T., Fukuda, T., Tsuji, A. et al. (2017). Efficacy and safety of balloon pulmonary angioplasty for chronic thromboembolic pulmonary hypertension guided by cone-beam computed tomography and electrocardiogram-gated area detector computed tomography. *Eur. J. Radiol.* 89: 270–276.
12. Brüllmann, D. and Schulze, R.K. (2015). Spatial resolution in CBCT machines for dental/maxillofacial applications—what do we know today? *Dentomaxillofac. Radiol.* 44: 20140204.

13. Abramovitch, K. and Rice, D.D. (2014). Basic principles of cone beam computed tomography. *Dent. Clin. N. Am.* 58: 463–484.
14. Baba, R., Ueda, K., and Okabe, M. (2004). Using a flat-panel detector in high resolution cone beam CT for dental imaging. *Dentomaxillofac. Radiol.* 33: 285–290.
15. Eslami, E., Barkhordar, H., Abramovitch, K. et al. (2017). Cone-beam computed tomography vs conventional radiography in visualization of maxillary impacted-canine localization: a systematic review of comparative studies. *Am. J. Orthod. Dentofac. Orthop.* 151: 248–258.
16. Cassetta, M., Altieri, F., Di Giorgio, R., and Silvestri, A. (2015). Two-dimensional and three-dimensional cephalometry using cone beam computed tomography scans. *J. Craniofac. Surg.* 26: e311–e315.
17. Brånemark, P.I., Hansson, B.O., Adell, R. et al. (1977). Osseointegrated implants in the treatment of the edentulous jaw. Experience from a 10-year period. *Scand. J. Plast. Reconstr. Surg. Suppl.* 16: 1–132.
18. Bryant, S.R., MacDonald-Jankowski, D., and Kim, K. (2007). Does the type of implant prosthesis affect outcomes for the completely edentulous arch? *Int. J. Oral Maxillofac. Implants* 22 (Suppl): 117–139. Erratum in: *Int J Oral Maxillofac Implants* 2008;**23**:56.
19. Hatcher, D.C., Dial, C., and Mayorga, C. (2003). Cone beam CT for pre-surgical assessment of implant sites. *J. Calif. Dent. Assoc.* 31: 825–833.
20. Wanner, L., Manegold-Brauer, G., and Brauer, H.U. (2013). Review of unusual intraoperative and postoperative complications associated with endosseous implant placement. *Quintessence Int.* 44: 773–781.
21. Setzer, F.C. and Kim, S. (2014). Comparison of long-term survival of implants and endodontically treated teeth. *J. Dent. Res.* 93: 19–26.
22. MacDonald, D., Li, T., Leung, S.F. et al. (2017). Extranodal lymphoma arising within the maxillary alveolus: a case report. *Oral Surg. Oral Med. Oral Pathol. Oral Radiol.* 124 (3): e223–e238.
23. Ludlow, J.B., Timothy, R., Walker, C. et al. (2015). Effective dose of dental CBCT—a meta analysis of published data and additional data for nine CBCT units. *Dentomaxillofac. Radiol.* 44: 20140197.
24. Benavides, E., Rios, H.F., Ganz, S.D. et al. (2012). Use of cone beam computed tomography in implant dentistry: the International Congress of Oral Implantologists consensus report. *Implant. Dent.* 21: 78–86.
25. Tyndall, D.A., Price, J.B., Tetradis, S. et al. (2012). Position statement of the American Academy of Oral and Maxillofacial Radiology on selection criteria for the use of radiology in dental implantology with emphasis on cone beam computed tomography. *Oral Surg. Oral Med. Oral Pathol. Oral Radiol.* 113: 817–826.
26. **European** Commission. Radiation Protection No. 172. Cone Beam CT for Dental and Maxillofacial Radiology: Evidence-based Guidelines. 2012 http://www.sedentexct.eu/files/radiation_protection_172.pdf (Accessed December 3, 2018)
27. Brown, J., Jacobs, R., Levring Jäghagen, E. et al. (2013). Basic training requirements for the use of dental CBCT by dentists: a position paper prepared by the European Academy of DentoMaxilloFacial Radiology. *Dentomaxillofac. Radiol.* 43: 20130291.
28. American Dental Association Council on Scientific Affairs (2012). The use of cone-beam computed tomography in dentistry: an advisory statement from the American Dental Association Council on Scientific Affairs. *J. Am. Dent. Assoc.* 143: 899–902.
29. Food and Drug Agency (FDA). Dose matters: FDA's guidance on children's X-rays. 2018. https://www.fda.gov/ForConsumers/ConsumerUpdates/ucm591750.htm (Accessed December 27, 2018.)
30. Mathews, J.D., Forsythe, A.V., Brady, Z. et al. (2013). Cancer risk in 680,000 people exposed to computed tomography scans in childhood or adolescence: data linkage study of 11 million Australians. *BMJ* 346: f2360.
31. Pearce, M.S., Salotti, J.A., Little, M.P. et al. (2012). Radiation exposure from CT scans in childhood and subsequent risk of leukaemia and brain tumours: a retrospective cohort study. *Lancet* 380 (9840): 499–505.
32. Berrington de Gonzalez, A., Salotti, J.A., McHugh, K. et al. (2016). Relationship between paediatric CT scans and subsequent risk of leukaemia and brain tumours: assessment of the impact of underlying conditions. *Br. J. Cancer* 114: 388–394.

33. Lee, C., Pearce, M.S., Salotti, J.A. et al. (2016). Reduction in radiation doses from paediatric CT scans in Great Britain. *Br. J. Radiol.* 89 (1060): 20150305.
34. White, S.C., Scarfe, W.C., Schulze, R.K. et al. (2014). The Image Gently in Dentistry campaign: promotion of responsible use of maxillofacial radiology in dentistry for children. *Oral Surg. Oral Med. Oral Pathol. Oral Radiol.* 118: 257–261.
35. Pauwels, R., Jacobs, R., Singer, S.R., and Mupparapu, M. (2015). CBCT-based bone quality assessment: are Hounsfield units applicable? *Dentomaxillofac. Radiol.* 44: 20140238.
36. Schulze, R.K., Berndt, D., and d'Hoedt, B. (2010). On cone-beam computed tomography artifacts induced by titanium implants. *Clin. Oral Implants Res.* 21: 100–107.
37. Korpics, M., Surucu, M., Mescioglu, I. et al. (2016). Observer evaluation of a metal artifact reduction algorithm applied to head and neck cone beam computed tomographic images. *Int. J. Radiat. Oncol. Biol. Phys.* 96: 897–904.
38. Spin-Neto, R. and Wenzel, A. (2016). Patient movement and motion artefacts in cone beam computed tomography of the dentomaxillofacial region: a systematic literature review. *Oral Surg. Oral Med. Oral Pathol. Oral Radiol.* 121: 425–433.
39. MacDonald, D., Ford, N., and Bunting, N. (2013). CBCT: training and patient selection. *The Bridge*. (magazine of the British Columbia Dental Association) Nov/Dec: 18–20.
40. Horner, K., Jacobs, R., and Schulze, R. (2013). Dental CBCT equipment and performance issues. *Radiat. Prot. Dosim.* 153: 212–218.
41. de Oliveira, M.V., Wenzel, A., Campos, P.S., and Spin-Neto, R. (2017). Quality assurance phantoms for cone beam computed tomography: a systematic literature review. *Dentomaxillofac. Radiol.* 46: 20160329.

Chapter 6

Magnetic resonance imaging

6.1 Introduction

During the four decades since *magnetic resonance imaging* (MRI) was first used to investigate a patient in Aberdeen, Scotland [1], it has become the first-choice investigation for a number of lesions affecting the face and jaws, because of its ability to distinguish clearly soft-tissue lesions from adjacent healthy tissue. However, *computed tomography* (CT) remains the primary cross-sectional modality for the majority of cases, because of its shorter scanning time, among other reasons such as being better for evaluating cortical bone, less susceptible to motion artifacts, and so on [2]. MRI already plays an important role in the evaluation and diagnosis of *temporomandibular joint* (TMJ) disorders and neoplasms of the face and jaws. The first part of this chapter introduces the principles of MRI and the terms most likely to be used in a surgeon–radiologist dialog. The second part will explain the jargon and other features of MRI that are most likely to appear in a radiologist's report. The final part will focus on some of the pathology of the face and jaws displayed by MRI.

The MRI signal intensity depends on many factors, including the sequence used. The most common sequences used to image the jaws and their lesions are T1 weighted and T2 weighted, which will be explained later. New users must address a steep learning curve, which includes an understanding not only of this technology, but also of the images it produces; for example, most oral and maxillofacial clinicians are used to seeing bone as white, not black. Oral and maxillofacial clinicians already familiar with CT images will need to adjust further to the grayscale for soft tissues, because fat shows up as "very bright" in contrast to black in the bone and soft-tissue windows of CT.

6.2 Basic Principles

6.2.1 WHAT IS MAGNETIC RESONANCE IMAGING?

Although the MRI scanner and its images bear a superficial resemblance to CT, the two imaging modalities are completely different. MRI does not use ionizing radiation, but rather a radiowave "dialog" with the patient's tissues and lesion within a magnetic field. Its efficacy as a clinical imaging modality is based primarily upon the soft tissues being proton rich; they are composed of between 70% and 90% water, which is concentrated hydrogen nuclei composed of solitary protons. As McRobbie et al. explain, "MRI images are obtained by measuring how rapidly hydrogen nuclei of different tissues return to their resting energy states after being excited by a strong magnetic field" [3].

Oral and Maxillofacial Radiology: A Diagnostic Approach, Second Edition. Edited by David MacDonald.
© 2020 John Wiley & Sons, Inc. Published 2020 by John Wiley & Sons, Inc.

The properties and amount of water within a tissue can alter drastically with disease or injury, to which MRI is very sensitive [3]. MRI images display better definition between the lesion and the adjacent normal tissue than other imaging modalities [2] generally available to the oral and maxillofacial clinician.

6.2.2 WHY IS MAGNETIC RESONANCE IMAGING SO SENSITIVE?

MRI detects subtle changes in the magnetism of the atomic nucleus and thus probes much deeper than X-rays, which interact only with the electron shells. In addition to merely imaging anatomy and pathology, MRI can, at its most advanced, investigate organ function, probing in vivo chemistry and visualizing brain activity [3].

6.2.3 COMPONENTS OF THE MAGNETIC RESONANCE IMAGING SUITE

The MRI suite has three components: the magnet room, the technical room, and the console room. The magnet room contains the magnet and *radiofrequency* (RF) coils. It is enclosed within a Faraday cage, which limits the influence of electromagnetic radiation (RF waves) arising outside the magnet contaminating or distorting those generated by the MRI scanner, because the latter are very weak and sensitive to electrical interference [3]. This cage is an RF-shielded enclosure made of copper, aluminum, or steel sheets, and includes the door and windows, which are made of special wire-embedded glass. The door should be closed at all times, save for entry or exit. Magnetic shielding limits the extent to which electromagnetic radiation (RF waves) generated by the MRI scanner interfere with medical equipment (including pacemakers) and other sensitive items such as personal phones and electronic cards outside the magnet room. All equipment present or entering the magnet room must be MRI compatible (more on this later). Figure 6.1 is a schematic diagram displaying the principal components of the MRI scanner.

6.2.4 THE MAGNET

The magnet is the main component of the MRI scanner. There are four types of magnets: air-cored resistive magnets, iron-cored electromagnets, permanent magnets, and superconducting magnets. The last produce excellent field uniformity and stability and are the most frequently encountered type. They are liquid nitrogen or helium cooled to 0°K (absolute zero). This allows the niobium-aluminum alloy magnet to lose all its resistance to electrical current, enhancing its field strength. Although most magnets in clinical use in North America are 1.5 Tesla (T; a measure of magnetic field strength), there is an increasing move toward 3 T and above. Although 3 T scanners offer superior *signal-to-noise ratio* (SNR), since SNR is proportional to field strength [4], their installation within an existing facility may require substantial rebuilding.

6.2.5 DISADVANTAGES OF MAGNETIC RESONANCE IMAGING

Even when produced by the same manufacturer, each magnet has its own inhomogeneities, which uniquely affect the images produced. Therefore, if the patient were to be reinvestigated on a different MRI scanner, the exact images are unlikely to be repeated; this is unlike CT.

Air and bone appear to be black on an MRI scan, because they have fewer protons and give virtually no signal. This

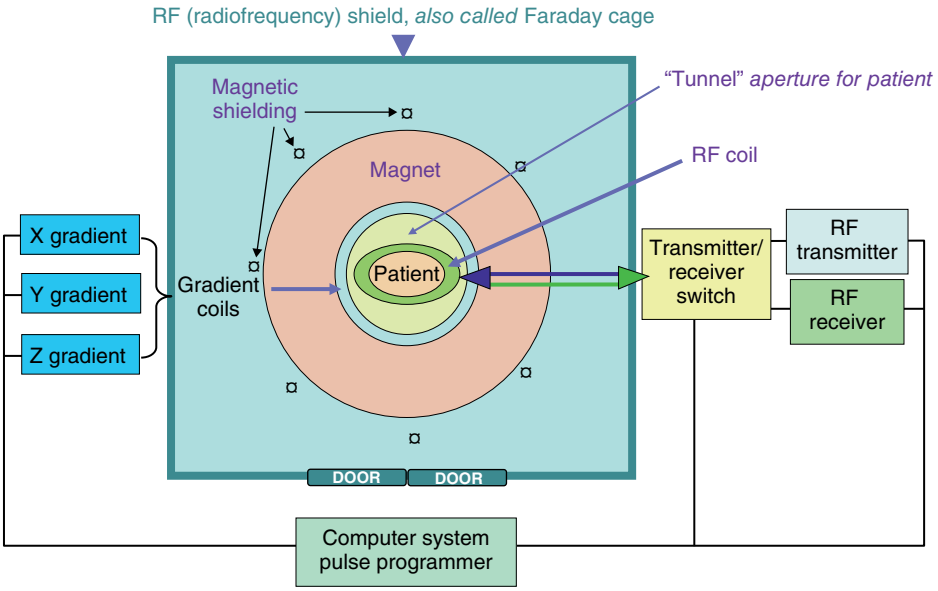


Figure 6.1 Schematic diagram displaying the main components of the magnetic resonance imaging scanner properly juxtaposed. The Faraday cage is formed within the walls of the magnet room and includes the doors. The radiofrequency coils are applied directly to the part of the patient to be investigated, whereas the gradient coils remain part of the scanner. Source: Adapted from Figure 1 in MacDonald-Jankowski, D.S. (2006). Magnetic resonance imaging for oral and maxillofacial surgeons. Part 1: basic principles. *Asian J. Oral Maxillofac. Surg.* 18: 165–171.

is a problem for the maxillary antrum, in which the air-filled antrum is normally separated from the thin bony walls by a thin antral mucosa, which may not always be obvious, depending both on its thinness and on the spatial resolution of the MRI scanner.

Like any other type of medical imaging, movement has a deleterious effect on the resultant images. This is particularly important in view of the relatively long scanning time: a routine MRI scan can take 30–40 minutes, compared with only 10–15 minutes for CT [2]. Unlike CT, in which the entire volume data is available to manipulate, for example to produce bone and soft-tissue windows and their variable widths, MRI has to scan each sequence separately. Therefore, sections reformatted from the T1-weighted (anatomy) and T2-weighted (pathology) scans may not necessarily be from exactly the corresponding anatomical sections, due to some change in patient position between the sequences. Nevertheless, MRI technicians take very great care to ensure that the patient's head is effectively, but comfortably, immobilized throughout the MRI investigation.

6.2.6 PULSE SEQUENCE

All MR images are produced using a pulse sequence. The sequence contains RF pulses and gradient pulses that have carefully controlled durations and timings. There are many different sequences, but they all have timing values that can be modified to obtain the required image contrast [5]. All sequences are dependent on the two *timing values*: *echo time* (TE) and *repetition time* (TR) [3].

6.2.7 PROTON DENSITY

MRI is based on the natural magnetism that is induced in the human body when it is placed in the scanner's magnetic field. The strength of this magnetism depends on the *proton density* (PD) of the tissues. PD is dependent on the number of hydrogen atoms in the tissues. Because fluids and fats both have high PDs, the contrast between them is poor, unless "fat suppressed" (Figure 6.2). Fat suppression is discussed later in this chapter. The PD sequence uses a short TE (less than 40 ms) and a long TR (longer than 1500 ms) [3].

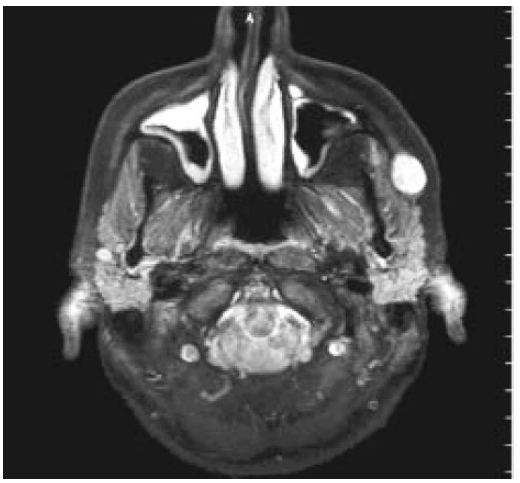


Figure 6.2 Proton density scan through the maxilla. Because fat and soft tissues (containing water) are rich in protons (hydrogen nuclei), they have a similar intensity; both display gray shades. Contrast between fat and soft tissues has been enhanced by fat suppression, which is discussed later in this chapter. Note the bright round "lump" on the left face. This painless, gradually enlarging swelling was a pleomorphic salivary adenoma. Compare its appearance in Figures 6.4 and 6.5. Compare also the hyperintense inflamed and nasal and antral mucosae with their presentations in Figures 6.4 and 6.5. Source: Reproduced with permission from MacDonald-Jankowski, D.S. (2006). Magnetic resonance imaging for oral and maxillofacial surgeons. Part 1: basic principles. *Asian J. Oral Maxillofac. Surg.* 18:165–171.

6.2.8 WHAT HAPPENS DURING A MAGNETIC RESONANCE IMAGING SEQUENCE?

When a scanning sequence begins, the magnetism within the tissues is knocked out of alignment with the main field of the scanner (Z or longitudinal axis) by the RF excitational pulses into the XY or transverse plane. The XY-realigned magnetism has the potential to create its own signal. The characteristics of this signal are determined by the gradient, timing, and RF of the sequence [3]. Once the RF signal is turned off, the protons relax (by "precession" similar to a spinning top) by giving off energy (this energy loss is called *free induction decay*, FID) to get back to the equilibrium position along the Z axis. This energy loss is transferred to surrounding molecules and results in a T1-weighted signal. When the magnetic moments interfere with adjacent protons, this causes dephasing and loss of transverse magnetism, resulting in a T2-weighted signal [5]. Relaxation, T1 weighted, and T2 weighted will be discussed in more detail later in this chapter.

6.2.9 RADIOFREQUENCY COIL

The RF coil is made up of two separate coils: one to transmit the RF pulse to the patient's tissues and lesion, and the other to receive the MRI signal from the patient's tissues and lesion. The RF coil's shape and size are appropriate to the part of the body to be investigated. There is a whole range of coils for the head, parts of the spine, and major joints, and even one for the TMJ [3]. Figure 6.3 displays Gradl et al.'s coil for the jaws [6].



Figure 6.3 Specially designed dental coil which encloses the jaws. The patient is wearing ear defenders, which both protect the patient from the loud noise and allow the patient to listen to relaxing music during the long magnetic resonance imaging acquisition time and any instructions the operator may give. This and the "pillow" contoured to the back of the head help the patient to remain still during the acquisition. The lower part of the magnet ring is immediately behind the patient's head and the aperture of the bore in the center of the magnet is seen just above it. The bed or couch the patient is lying on will be raised and inserted for the exam. Source: Reproduced with permission from Gradl, J., Höreth, M., Pfefferle, T., et al. (2017). Application of a dedicated surface coil in dental MRI provides superior image quality in comparison with a standard coil. *Clin. Neuroradiol.* 27:371–378.

6.2.9.1 How Can the Radiofrequency Coil Affect Image Quality?

Selection of the appropriate coil is of paramount importance to achieve a high SNR and, consequently, high spatial resolution. A coil should be chosen that is able to completely cover the region of interest so as to produce an image with the highest SNR and homogeneity. The coil must be correctly positioned, because the signal decreases as the distance from the coil increases. The decrease in signal also produces a decrease in SNR [3, 5].

The *bandwidth* (BW) of RF frequencies needed to encode the spatial positions of signals is also important for the SNR – the wider the BW, the noisier the image and the lower the SNR [7]. If the SNR is too low (the image appears fuzzy when very low), the contrast will be poor and subtle contrast changes may be obscured. Therefore, according to McRobbie et al., the *contrast-to-noise ratio* (CNR) is the most important aspect of the MRI's image quality [3].

6.2.10 DISPLAYING AND REVIEWING THE IMAGES

As MRI units are almost always sited in a medical facility, the sequences are reviewed and then reported by a medical radiologist. Referring/prescribing clinicians will review the sequences transferred to them on a *digital video disc* (DVD), *compact disc* (CD), or *universal serial bus* (USB) flash drive with the appropriate software. These should be read in conjunction with the radiologist's report.

6.2.11 RELAXATION

Relaxation is the process the magnetization experiences as it fades (like a tuning fork) or processes (like a spinning top) from the XY plane to the Z axis. There are two relaxation processes: "spin–lattice" and "spin–spin." Spin–lattice controls the growth/recovery of the magnetization along the Z axis, and is also known as the longitudinal proton relaxation time or the T1-weighted sequence. Spin–spin controls the decay of the signal in the XY plane, and is also known as the transverse proton relaxation time or the T2-weighted sequence. Spin–lattice and spin–spin will now be referred to as T1 weighted and T2 weighted, respectively [5].

6.2.12 T1 WEIGHTING

T1-weighted scans are often known as "anatomy scans," because their images display excellent contrast and most clearly show the boundaries between different tissues (Figure 6.4). These boundaries are made obvious by the fat-filled fascial planes; the T1-weighted scan is also termed a "fat scan" [3]. The central role of T1-weighted scans to display anatomy has been illustrated by Li et al. in their report on the presurgical evaluation of the parapharyngeal space. The parameters of this space are defined by important structures such as blood vessels, which can be difficult to evaluate by clinical and other radiological modalities [7]. Further discussion of this and other spaces is found in Chapter 17. T1 weighted on its own has been applied to the TMJ to determine the position of the articular disc (see Figure 16.14). For a T1-weighted image, a short TE (less than 40 ms) and a short TR (less than 750 ms) are required [3].

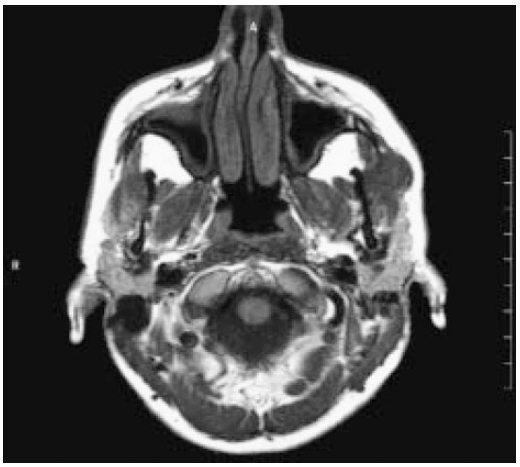


Figure 6.4 T1-weighted scan of the same section as displayed in Figure 6.2. The subcutaneous fat and peripharyngeal fat appear white ("bright" or "hyperintense"), whereas the other soft tissues display a range of grays, from very light ("hypointense") to those represented by skeletal muscle and the pleomorphic salivary adenoma ("isointense"). The black areas represent air-filled spaces, bone, or blood vessels containing fast-flowing blood. Source: Reproduced with permission from MacDonald-Jankowski, D.S. (2006). Magnetic resonance imaging for oral and maxillofacial surgeons. Part 1: basic principles. *Asian J. Oral Maxillofac. Surg.* 18: 165–171.

6.2.13 T2 WEIGHTING

T2-weighted images take longer to acquire than T1-weighted images. T2-weighted images are often termed "pathology scans," because collections of abnormal fluid are bright against the darker normal tissue (Figure 6.5). T2-weighted images are also

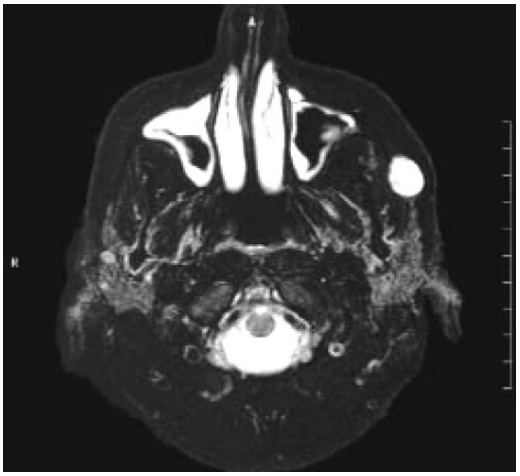


Figure 6.5 T2-weighted scan of the same section as displayed in Figures 6.2 and 6.4. This scan accentuates water-rich tissues, including most lesions such as pleomorphic adenoma, and renders them hyperintense. In some cases it may be difficult to differentiate these areas from fat, which is also hyperintense on T2-weighted scans. Frequently, the fat signal is suppressed on T2-weighted scans to further accentuate the water-containing features. This image displays fat suppression, which is discussed later in the chapter. Source: Reproduced with permission from MacDonald-Jankowski, D.S. (2006). Magnetic resonance imaging for oral and maxillofacial surgeons. Part 1: basic principles. *Asian J. Oral Maxillofac. Surg.* 18: 165–171.

called "water images" [3]. T2-weighted images are useful for detecting infection, hemorrhage, and neoplasms [1]. For a T2-weighted image, a long TE (greater than 75 ms) and a long TR (less than 1500 ms) are required [3]. Further discussion of T2 weighted is deferred to later in the chapter. T1-weighted and T2-weighted processes are independent of each other.

The reader should be aware that not all lesions are hyperintense on the T2-weighted sequence, nor are they always distinguishable. The more important of the strategies developed to address these feature later in this chapter. They are contrast media, fat suppression (particularly fat saturation), and other sequences.

6.2.14 WHAT ARE SPIN ECHO AND GRADIENT ECHO SEQUENCES?

The signal that comes back from the patient is collected as an echo. Echoes are produced in two ways by the pulse sequence. The most common pulse sequence is the *spin echo* (SE), because it makes the best-quality images. Because the SE takes a long time – minutes rather than seconds – *fast (or turbo) spin echo* (FSE), a variation of SE, is often used to speed up the process [3].

The gradient echo is represented by a whole family of different pulse sequences. Examples of these are *fast low angle shot* (FLASH) and *fast imaging with steady state precession* (FISP) (Figures 18.7b and 18.8b). These have been developed to provide rapid acquisition, in seconds rather than minutes. This minimizes movement and physiological artifacts, increases patient throughput, and allows dynamic studies [4].

Other sequences that may be used in the head and neck and their specific applications have been discussed recently by Widmann et al [8]. Some of these sequences that employ fat suppression are discussed later in this chapter.

6.2.15 ARTIFACTS

Gray et al. identified two types of artifacts that may be produced in the MRI of dental structures [1]: those due to patient motion (Figure 6.6) and those due to inhomogeneities in the magnetic field caused by magnet susceptibility effects. Patient motion is seldom the cause of artifacts when the patient has been well instructed and is comfortably positioned. Nevertheless, the trend toward using MRI units with high magnetic fields – as high as 7 T – because of their better spatial resolution (0.4 mm voxel size, equivalent to that of multidetector computed tomography, MDCT) requires a long acquisition time, which in turn is accompanied by worsening

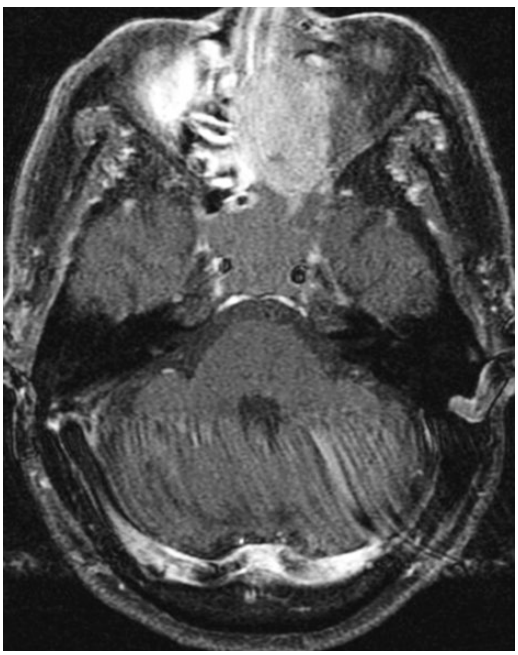


Figure 6.6 Axial magnetic resonance imaging displaying movement artifact. Source: Courtesy of Dr. Montgomery Martin, British Columbia Cancer Agency.

motion artifacts. This offsets the gain in a higher resolution in particular regard to small objects [9].

The susceptibility artifacts presenting as geometric distortions are caused by air/tissue or bone/tissue artifacts and by the effect of ferromagnetic metals. The former is more likely to be a problem in high-field scanners (those operating above 1.5 T), but Gray et al. list strategies to minimize this effect [1]. The latter, occasioned by metal, are usually localized areas of signal distortion adjacent to the metal structure (Figure 6.7), except for orthodontic bands, which may cause severe geometric distortion. Concerns that the MRI image may have been distorted can be checked by using *spatial modulation of magnetization* (SPAMM). This has been done by Bridcut et al. using a 0.95 T scanner "to provide a qualitative estimate of the accuracy of the MRI when planning dental implants" [10].

Jungmann et al. reviewed the problem of the increasing prevalence of orthopedic metal implants in an aging population, precisely the community which requires MRI to investigate the various arthoses and neoplasias which also become prevalent with age [11]. They discussed various metal artifact reduction solutions which are available to the radiologist. Eggers et al. [12] reported that all dental restorative materials, particularly amalgam and titanium implants, are magnetic resonance compatible; Starcuková et al. [13] reported that titanium is less so. Nevertheless, its artifact was limited only to the immediate area. Both studies [12, 13] used 1.5 T MRI units. Lee et al. [14] reported that the orientation of metallic orthopedic implants was minimized if their long axis was parallel to the direction of the main magnetic field. As dental implants are, or are close to being, parallel to the main magnetic field, this criterion should be achievable in most cases. Nevertheless, titanium and titanium-zirconium implants induced extensive signal voids on 3 T MRI, more than they do on MDCT and cone-beam computed tomography [15]. On the other

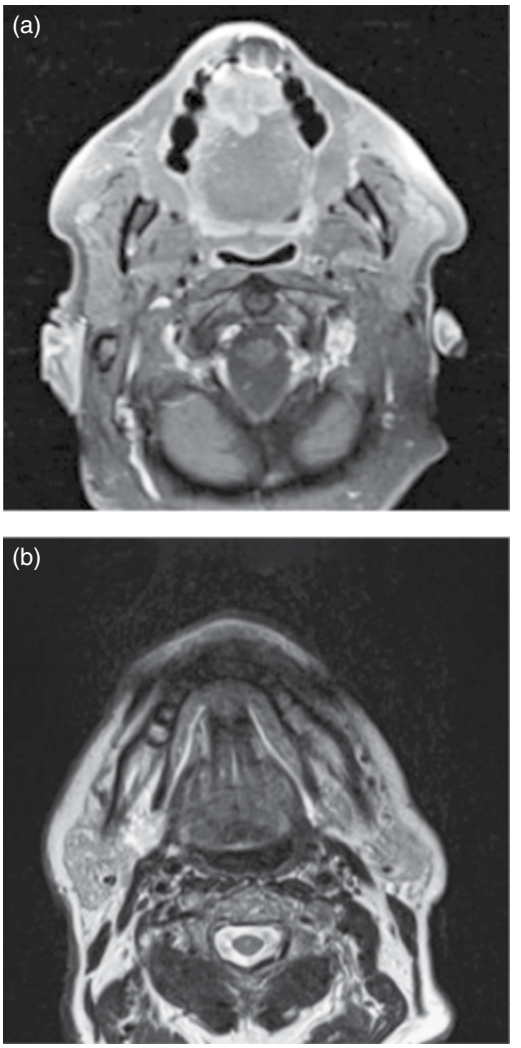


Figure 6.7 Magnetic resonance imaging of a squamous cell carcinoma of the floor of the mouth. Both T1-weighted (a) and T2-weighted (b) images of the lesion have been degraded by an artifact arising from restorations in the dentition immediately adjacent to it. Source: Courtesy of Dr. Montgomery Martin, British Columbia Cancer Agency.

hand zirconium-only implants produce more limited artifacts [15, 16]. Hilgenfeld et al. also noted that it is just not the implant metal that is important, but also the material of which the crown framework is made. A single titanium implant with a nonprecious metal alloy crown framework induced more unfavorable artifacts than titanium implants with precious alloy and zirconium crown frameworks [16]. This knowledge should prompt consideration of the precise composition of the implant to be included in decision making as to the best imaging modality for that particular patient's clinical needs [15].

Although in 3 T MRI there is no risk posed by dental magnetic attachments with regard to RF heating and magnetically induced displacement, the secure attachment of magnetic keepers (which hold a magnet-retained dental prosthesis in place) to their osseointegrated implants must be confirmed prior to the MRI investigation [17]. The magnetic-retained prosthesis is removable and should be removed prior to the MRI investigation [18].

The adoption of high magnetic field MRI units, namely 7 T, has conferred substantial advantages to the user. These have better SNRs. Oriso et al. revealed that dental materials, including implants, displayed "no apparent translational or heating" at 7 T [19]. They reported that "substantial forces on the magnetic attachment keepers suggested potential risks to patients and research participants undergoing MR imaging examinations" [19].

6.2.16 SAFETY FIRST

Up to 2005, there were at least 13 reported deaths due to MRI accidents [20]: 10 people with pacemakers died during a sequence and 3 patients died following entry into the core by ferrous equipment, including an oxygen cylinder, while the patient was present [3]. Since then, there do not appear to have been similar fatalities. To minimize such events, the US Food and Drug Administration (FDA) [21, 22] has produced labels that alert the user to the safety or otherwise of an item of equipment [23]. These are set out in Figure 6.8. Furthermore, as it is estimated that up to 75% of patients with a *cardiac implantable electronic device* (CIED) – also known

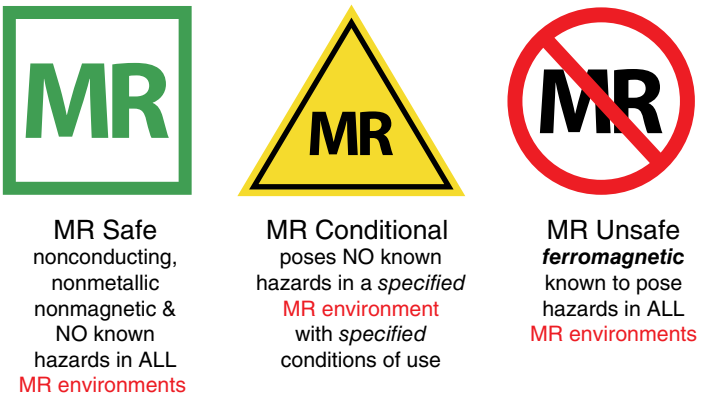


Figure 6.8 Labeling criteria related to magnetic resonance imaging (MRI) safety for portable objects by the US Food and Drug Administration (FDA). These are set out in the 2013 American College of Radiologists' Guidance Document on MR Safe Practices [23]. Note: Conditions that define the MRI environment include static magnetic field strength, radio frequency fields, specific absorption rate, and other factors.

as a pacemaker or *implanted cardiac defibrillator* (ICD) – will need an MRI, CIED technology has been developed to address this, making it either *MRI compatible* or *MRI conditional*. The use of MRI conditional is restricted with regard to the patient's size, body temperature, and the position of the CIED within the MRI. The older CIEDs in use remain *MRI incompatible* [24]. Strom et al. performed MRI on patients with MRI-incompatible CIEDs, which "under strict protocol demonstrated excellent short- and medium-term safety while providing interpretable imaging that frequently influences clinical care" [25]. Only one patient suffered a loss of pacing, and there were no deaths [25].

Another MRI safety risk is the aneurysm clip. Although the clips manufactured after 1995 have been safely used in MRI investigations, with the advent of stronger magnetic fields and other developments this lack of an adverse event should not be relied upon [23]. Furthermore, the American College of Radiologists (ACR) has recommended a four-zone level of access to an MRI suite (Table 6.1) and three levels of MR imaging personnel (Table 6.2) [23]. A detailed ideal layout of an MRI suite addressing these four zones is set out in Figure 1 in Kanal et al. [23].

Table 6.1 American College of Radiologists' four-zone recommendation.

Zone	Access and need for supervision
I	Unrestricted access to general public
II	Patient reception and screening
III	Lock/key-card access to control room – entry of all non-MR imaging personnel supervised by MR imaging personnel
IV	Magnet room – all entries supervised by MR imaging personnel

MR, magnetic resonance. See [23] for more details.

Table 6.2 American College of Radiologists' recommendations for three levels of magnetic resonance imaging personnel.

Level of personnel	Training and duties
Level 1 MR imaging personnel	Basic MR safety training – to work in Zone III only
Level 2 MR imaging personnel	Advanced MR safety training – to work also in Zone IV
Non-MR imaging personnel	No expected MR safety training – therefore presence in Zones III and IV must be supervised by Level 2 MR imaging personnel

MR, magnetic resonance. See [23] for more details.

6.2.17 THE DANGERS OF MAGNETIC RESONANCE IMAGING

The various components of the MRI subject the patient to potential harm. The most important adverse effects caused by MRI units operating up to 3 T are set out in Table 6.3.

6.2.17.1 The Magnet

Semiconducting magnets are on all the time. In addition to attracting ferrous metal equipment into the core and causing malfunction of MR-incompatible pacemakers, the magnet can displace arterial clips and metallic foreign bodies (such as shrapnel) near the eye or major vessels

Table 6.3 The principal adverse effects caused by the various magnetic resonance imaging (MRI) components operating up to 3T.

MRI component	Adverse effect		Remarks
Static magnetic field	Metallic equipment projectile		Restrict access of equipment according to MR compatibility status
	Displacement of implantable medical devices and/or tearing of adjacent tissue	Aneurysm clips	Clips have been MR safe since 1995
		Cardiac and vascular stents leading to hemorrhage	Generally safe 6 weeks post-implantation –caution still needed
		Implanted active devices – pacemakers (PMs), defibrillators (ICDs), neurostimulators, medication pumps and cochlear implants	Some cardiac implantable electronic devices (CIEDs) – PMs and ICDs – can be used in MRI
		Ballistic (shrapnel etc.)	Copper and lead are MR safe
		Eyes of metal workers (especially iron) or history of prior orbital trauma	Metal in eyes of 0.3% of general population and 2.5% of at-risk population Ophthalmic exam and radiographs
Gradient magnetic field	Acoustic noise 3T twice the noise of 1.5T	MR should not exceed 140 dB	If exceeds 99 dB, apply noise protection to patient
	Neurostimulation	Tingling to severe pain	
Radiofrequency field	Burns	Tattoos and dermal drug patches with metal backing	
	Most common MR adverse effect	Thighs and calves touching or hands clasped	Separate legs and arms
		Leads and electrodes on the skin or inside patient	
		Metal implants (including dental)	
Cryogen-liquid helium cooled to absolute zero	If it escapes in an explosive event (quench)	Frostbite – immediate risk	
		Helium fog eliminates visibility	
		Asphyxiant only if the “quench” causes substantial oxygen displacement	

[20]. Although tattoos (which include tattooed eyeliner) can cause skin reactions, they are not a contraindication for MRI [23]. Cold compresses or ice packs should be placed in contact with the tattooed areas throughout the scan, particularly if they are in a region to undergo RF irradiation [23]. The magnet is associated with claustrophobia, which can be experienced by as many as a quarter of all patients [1]. Although most modern units have a two-way intercom to facilitate communication between patients and MRI staff, the patient should be discouraged from talking, because movement would invalidate the images for that sequence. Occasionally, it may be necessary to sedate or even anesthetize a patient. Extremely obese patients cannot fit in the aperture of many machines [3]. Finally, the escape of the liquid helium coolant poses an immediate risk of frostbite. If it substantially displaces oxygen from the room's atmosphere, there is a risk of asphyxiation.

6.2.17.2 Radiofrequency Exposure

The main danger associated with RF is tissue heating due to RF exposure (akin to a microwave). The patient's temperature should not increase by more than 1 °C. This is achieved automatically by monitoring and limiting the specific absorption rate based on the patient's weight; therefore, the patient's weight is ascertained prior to the procedure [3]. Furthermore, to avoid the risk of burns, patients should be directed not to clasp their hands or cross their legs [23]. Nor should any part of the patient's body come into contact with the core.[23]. In order to make this less possible, the arms are separated from the body by foam wedges. These wedges are also inserted between the legs to keep them apart. This separation is particularly important "in or near the regions undergoing radiofrequency energy irradiation" [23].

A recent study on MRI workers reported an association between MRI-related static magnetic field exposure and an increased risk of accidents leading to injury among MRI workers. This association was also found for accidents sustained by these workers while commuting to work [26].

6.2.17.3 Acoustic Noise Caused by Changes in Gradient Magnetic Fields

The MRI scanner is very noisy. It makes a "knocking" sound, which can provoke headaches. This noise is caused by the movement of the gradient coils against their mountings during the scan. The noise can be more than 100 dB for some sequences. Hearing protection is recommended for patients during scanning and for any clinical staff within the Faraday cage with the patient. Noise reduction is an active area of development for manufacturers [3].

6.2.17.4 Pregnancy and MRI

To date, there have been no reported adverse effects following MRI of pregnant women. Their absence reflects an abundance of caution exercised by clinicians with regard to their concerns about teratogenesis, and potential damage to the fetus caused by tissue heating and acoustic energy. These concerns are reflected in the ACR guidelines [23], which suggest that the radiologist and referring clinician should first determine whether an MRI is absolutely necessary for the following reasons:

1. The anticipated results from the MRI cannot be obtained from any alternative nonionizing radiation modality.
2. The MRI study is necessary for the care of the mother or the fetus during pregnancy.

3. It is not considered prudent to delay the MRI until the patient is no longer pregnant.

6.3 MRI Terminology Most Frequent in the Radiologist's Report

In addition to T1 weighted and T2 weighted, the clinician is likely to see reference to intensity, fat suppression (usually fat saturation), and gadolinium.

6.3.1 MAGNETIC RESONANCE IMAGING JARGON

Hyperintensity can be used to describe a bright structure, due to fat in the case of T1-weighted (Figure 6.4) and T2-weighted images, and fluid-filled lesions in the case of T2-weighted images (Figure 6.5). Hypointense structures, in both T1-weighted and T2-weighted images, are dense calcified tissues (including calcified lesions) and fast-flowing blood. *Isointensity* is exhibited by the skeletal muscle in T1-weighted images (Figure 6.9).

6.3.2 FAT SUPPRESSION

Fat normally appears hyperintense on both T1-weighted and T2-weighted scans. Unfortunately, particularly in T2-weighted scans, most lesions (neoplastic, cystic, and inflammatory) are also hyperintense. Therefore, in order to identify them, the hyperintense fat signal has to be suppressed. When contrast media is used in T1-weighted scans, fat suppression is required to detect subtle lesions that normally occur within fat-filled structures such as bone marrow. Figure 6.10 displays T1-weighted and T2-weighted images that have been fat suppressed; the hyperintense signal of the subcutaneous fat has

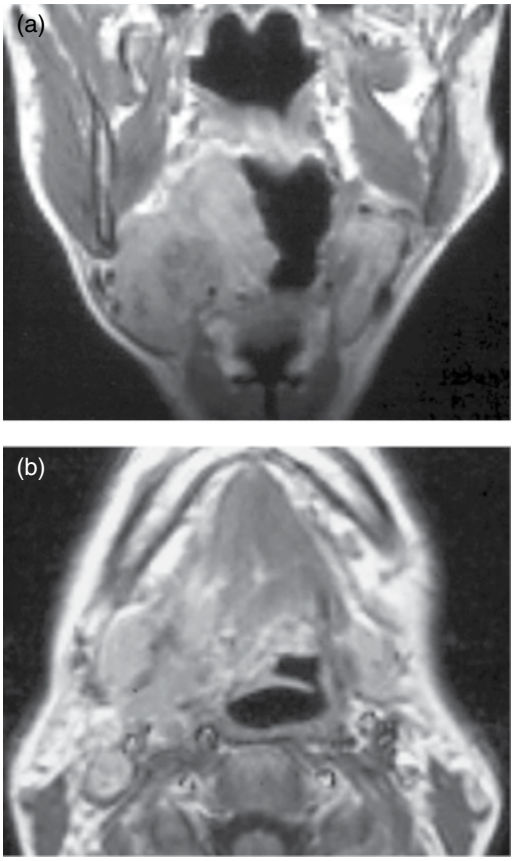


Figure 6.9 T1-weighted gadolinium-enhanced images of an advanced squamous cell carcinoma of the tongue. The hyperintensity of fat in both images has not been fat suppressed. (a) Coronal T1-weighted image showing the bilateral lesion partially obturating the oropharynx and invading the submandibular space. Note: The center of this lesion is not very hyperintense, because it is relatively not enhanced and is as isointense as the skeletal muscle. This area represents central necrosis. (b) Axial T1-weighted image showing the lesion to have extensively invaded the lateral pharyngeal space and obturated the ipsilateral vallecula. Source: Reproduced with permission from MacDonald-Jankowski, D.S., Li, T.K., and Matthew, I. (2006). Magnetic resonance imaging for oral and maxillofacial surgeons. Part 2: clinical applications. *Asian J. Oral Maxillofac. Surg.* 18: 236–247.

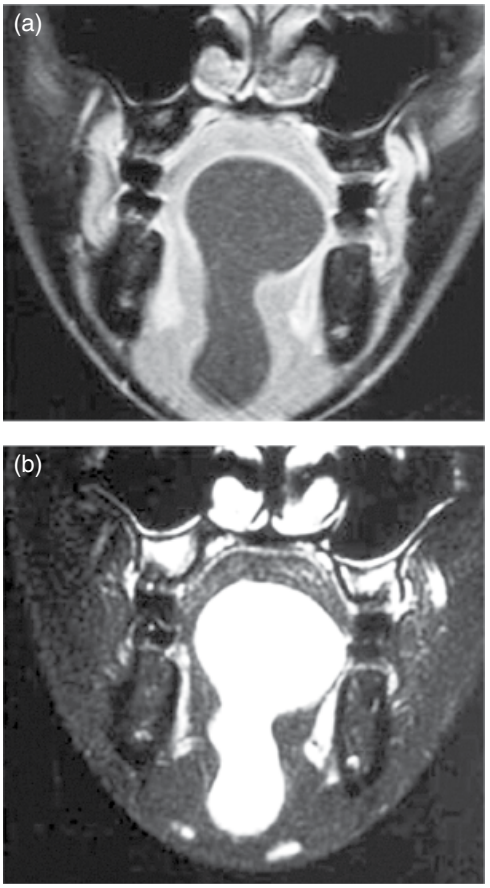


Figure 6.10 Fat-suppressed T1-weighted and T2-weighted images of a seven-year-old child with painless progressive sublingual swelling. A dermoid cyst is situated between the genioglossus. Other differential diagnoses were thyroglossal cysts and cystic hygroma. (a) Gadolinium and fat-suppressed coronal T1-weighted image showing gadolinium-enhanced blood vessels in the capsule around the superior aspect of the cyst. Note: The normally hyperintense signal of the subcutaneous fat has been suppressed (compare with Figure 6.5). (b) Fat-suppressed coronal T2-weighted image showing the hyperintense signal completely occupying the hypointense structure observed on the T1-weighted scan. The bilateral teardrop-shaped structures are the saliva-filled sulci of the floor of the mouth. Source: Reproduced with permission from MacDonald-Jankowski, D.S., Li, T.K., and Matthew, I. (2006). Magnetic resonance imaging for oral and maxillofacial surgeons. Part 2: clinical applications. *Asian J. Oral Maxillofac. Surg.* 18: 236–247.

been suppressed in both scans. Another reason for fat suppression is that a very hyperintense fat signal can create an artifact a few pixels distant to its real position; this is called the *chemical shift* [3, 27]. The clinical implications of this phenomenon will be revealed later in this chapter.

The two main fat suppression methods in head and neck MRI use are *fat saturation* (FatSat or simply FS) and *short T1 inversion recovery* (or STIR). Although FS is frequently used, it operates best in strong fields, which better distinguish between fat and water. STIR, using a completely different mechanism, takes advantage of fat's shorter T1 and completely eliminates the fat signal. The advantage of the latter is that the magnet need not be perfectly shimmed. *Shimming* is the reduction of inhomogeneities within the magnet or ferromagnetic metals outside it. It can be fixed or dynamic. Fixed shimming can be active (using shimming coils) or passive [3].

The increasing use of 3 T MRI has been accompanied by other fat suppression techniques such *chemical shift (spectral) selective* (CHESS), STIR, *spectral attenuated inversion recovery* (SPAIR), *water excitation* (WEX), and "Dixon" [28]. CHESS is used extensively for knee, wrist, and hand joints, but so far there have been no reports on its use in investigations of the TMJ. STIR can be used in the presence of metal, which has only a minimal impact on the fat suppression's homogeneity [28]. STIR hybridized with SPAIR gives a higher SNR than STIR alone. Dixon provides "SNR-efficient fat-suppression even in fields of magnetic susceptibility," such as metallic implants [28].

6.3.3 CONTRAST MEDIA

Contrast media have already been encountered with regard to CT, where they are used to enhance blood vessels and vascularized tissues. To determine whether enhancement has occurred, it is standard

to compare the contrast images (usually T1 weighted with gadolinium) with the previously taken noncontrast images, often referred to as "precontrast" and "postcontrast," respectively. Any areas of increased intensity in the postcontrast images represent enhancement. Figures 6.9 is a postcontrast T1-weighted MRI displaying an area of central necrosis within a squamous cell carcinoma of the tongue. The central necrosis is displayed as an unenhanced area, because of the absence of blood vessels within it.

6.3.3.1 How Do Gadolinium-based Contrast Agents Work?

All tissues have some degree of magnetic susceptibility; that is, the degree to which they can become magnetized when placed in a strong magnetic field. Magnetic susceptibility ranges from diamagnetic (from zero for bone and air to some for most other tissues, including fully oxygenated hemoglobulin), paramagnetic (deoxyhemoglobulin and gadolinium), superparamagnetic (ferritin and hemosiderin), and ferromagnetic (iron, nickel, and cobalt) [3]. While the weak susceptibility of diamagnetic materials and tissues produces an internal magnetic field in the opposite direction to the applied magnetic field, the stronger susceptibility of paramagnetic materials, such as by gadolinium, produces a magnetic field in the same direction as the main magnetic field [3].

After *gadolinium-based contrast agents* (GBCAs) are injected into the body, the gadolinium is rapidly distributed in the blood and is gradually excreted by the kidneys over 24 hours. Gadolinium enhances T1-weighted signals in the tissues as it accumulates in richly vascular lesions (such as most neoplasms) that become hyperintense (Figures 6.9 and 6.11). Because gadolinium and fat are hyperintense, the definition of gadolinium-enhanced tissue within a fat-rich region is further enhanced by fat suppression [2].

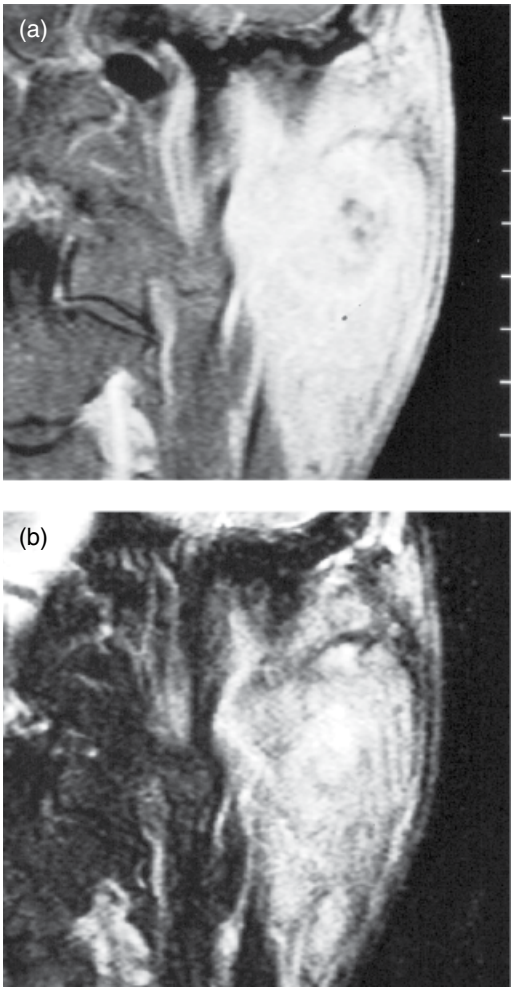


Figure 6.11 Left buccal swelling and acute pain with no pus or discharge. It was considered to be a pleomorphic salivary adenoma with malignant transformation, adenocystic carcinoma, and mucoepidermoid carcinoma. Aspirate showed actinomyces-like organisms. (a) Gadolinium and fat-suppressed coronal T1-weighted image showing that gadolinium enhances the blood supply to the parotid gland, which is very hyperintense. Few hypointense areas are visible at the center. (b) Fat-suppressed coronal T2-weighted image: the hypointensities on the T1-weighted scan now appear hyperintense. Source: Reproduced with permission from MacDonald-Jankowski, D.S,, Li, T.K., Matthew, I. (2006). Magnetic resonance imaging for oral and maxillofacial surgeons. Part 2: clinical applications. *Asian J. Oral Maxillofac. Surg.* 18: 236–247.

6.3.3.2 What Risks Are Posed by Gadolinium-based Contrast Agents?

All clinically approved GBCAs are generally considered safe when delivered in doses as low as 0.1–0.3 mmol/kg patient weight in a patient with normal kidney function [29]. Although it has long been recognized that up to 25% of gadolinium is deposited in the tissues (mainly the bone) even in patients with normal renal function, it has only relatively recently been appreciated that these GBCAs have provoked disease [29], such as *nephrogenic systemic fibrosis* (NSF). NSF, occurring in most cases within days to months after administration, presents as a progressive fibrosis of the tissues, particularly the skin, leading to a woody texture [29]. Although caution is advised when using GBCAs in patients with moderately severe to severe renal insufficiency, NSF has been particularly associated with certain preparations rather than with gadolinium per se [29]. Semelka et al. discuss these individual preparations in detail [29].

Even when GBCAs are delivered in the aforementioned dose, an adverse event may occur in from 0.07% to 2.4% of administrations. Most are mild and physiological, ranging from coldness or warmth at the injection site to nausea (perhaps with vomiting), headache, or dizziness. Such reactions occur from immediately to within 24 hours of administration, most within minutes. The allergy-like response is similar in presentation to that experienced with iodinated contrast media [29]. Out of 51 million administrations performed between 2004 and 2009, 40 deaths due to anaphylaxis were recorded [29].

In addition to NSF and severe acute adverse events, repeated delivery of GBCAs in patients with normal renal function has resulted in gadolinium deposition in the brain. This has led to hyperintense signals in the dentate nucleus and globus pallidus on unenhanced T1-weighted MRIs. Although there is no associated disease, this deposition in both the brain and bone is called gadolinium storage condition [30]. A recent systematic review stated: "There is a strong need for further research to identify [the] type of gadolinium deposited in the brain as well as to gather knowledge about long-term consequences" [30]. Although the most recent FDA update "identified no adverse health effects with gadolinium retention in the brain," the "Committee recommended suspending the marketing authorization of certain *linear* GBCAs because they cause a greater retention of gadolinium in the brain compared to *macrocyclic* GBCAs" [31]. The identity of these is set out in the December 2017 update [31]. However, the FDA's review "did not identify adverse health effects related to this brain retention." Nevertheless, as always, clinicians should report any side effects to the FDA through its "contact FDA" box on its website [31].

6.3.4 TIME OF FLIGHT

Time of flight (TOF) is used in MR angiography particularly in the head and neck area. It obviates the need for the use of intravenous contrast medium, particularly GBCAs. Its purpose is to make flowing blood hyperintense, which distinguishes it from the stationary blood that may be found in aneurysms. It works by virtue of the fact that the blood which is already in the *field of view* (FOV) is already saturated, as it is either stationary or at least flowing very slowly. "Saturated" means that the signal from the protons is suppressed and the saturated tissues appear hypointense (black), as does fat when it has undergone fat saturation. The blood flowing into the FOV exhibits the "unsaturated" spin of the protons in the blood due to their experiencing excitations outside

the FOV. As a result, these protons can still give a signal that appears hyperintense (whiter) than the saturated stationary tissues, which are black. This has been used in the head and neck to determine the prevalence and characteristic features of a persistent trigeminal artery and its variant and other variants of the head and neck vessels [32].

6.4 Pathology of the Face and Jaws That May Be Apparent on Magnetic Resonance Imaging

This part of the chapter focuses on the pathology of the face and jaws displayed by MRI.

6.4.1 FACIAL PAIN

Facial pain arises most frequently from an infection. Infections will be addressed later in this chapter, but it is important to note that pain associated with a swelling that is suggestive of a neoplasm needs prompt investigation. Figure 6.11 illustrates such a case.

Hughes et al. reported that "trigeminal neuralgia (TN) is a debilitating facial pain disorder, frequently caused by vascular compression of the trigeminal nerve" [33]. This vascular compression inflicts atrophy on the trigeminal nerves [34]. The atrophic changes in volume and cross-sectional areas of the affected trigeminal nerves are optimally displayed by high-resolution 3 T MRI [34]. Therefore, surgery is indicated for those trigeminal neuralgia patients who have not responded to a pharmacological solution. *Microvascular decompression* (MVD) was the most frequently applied surgical approach in a retrospective study [35].

Lee et al. reported that "*complex regional pain syndrome* (CRPS) is one of the most challenging chronic pain conditions and is characterized by burning pain, allodynia, hyperalgesia, autonomic changes, trophic changes, edema, and functional loss involving mainly the extremities" [36]. They discussed a case presenting unbearable pain in all teeth and hypersensitivity of the skin of the face. Functional MRI revealed that complex regional pain syndrome correlated with trigeminal neuropathy in the orofacial area [36].

6.4.2 MALIGNANCIES

6.4.2.1 Diagnosis and Preoperative Assessment

Despite many advances in our understanding of head and neck cancer, the survival rates are still poor. This is largely a result of advanced disease upon first presentation. Figure 6.9 presents one such case. Most head and neck malignancies are associated with *squamous cell carcinoma* (SCC), predominantly of the mouth and pharynx. Although imaging is infrequently the primary mode of diagnosis, as most SCCs (except primary intraosseous SCC; see Chapter 9) affecting the mouth occur in the mucosa and are readily visible to a properly executed clinical examination, it is invaluable in assisting the surgeon to stage the lesion and begin to determine the optimum course of treatment; see Chapter 19. Although conventional radiography and CT are routinely performed in such cases to determine whether the underlying bony jaws have been invaded, MRI provides the highest-quality images of soft tissues. These lesions can be displayed in very thin sections, of the order of millimeters [37].

A recent systematic review reported that three types of MRI – namely diffusion-weighted (DWI) MRI, dynamic contrast-enhanced (DCE) MRI, and traditional MRI – exhibited "satisfactory" accuracy for

the diagnosis of oral cancer compared to biopsy [37]. Moreira et al. recommended any type of MRI as part of a pretreatment and assessment protocol. Nevertheless, their meta-regression analysis revealed that there were heterogeneities in the DWI MRI results, which could be due to magnetic field strength: 1.5 T versus 3 T [37].

SCC is displayed on a T1-weighted scan as isointense, which (particularly in case of the tongue) can make it difficult to distinguish from adjacent skeletal muscle. Figure 6.9 compares the central, relatively unenhanced area with skeletal muscle. Hsu et al. (using 1.5 T) maintain that direct laryngoscopy is the most accurate in evaluating the mucosal surface of the aerodigestive tract [38]. Gadolinium-enhanced T1-weighted images can display the lingual lesion (Figures 6.9 and 6.12). On a T2-weighted scan, SCC is hyperintense and can be readily distinguished without fat suppression because the tongue, which is a muscular structure, contains little fat (Figure 6.12).

The introduction of 3 T MRI correlated very well with the histological findings with regard to tongue tumor thickness [39].

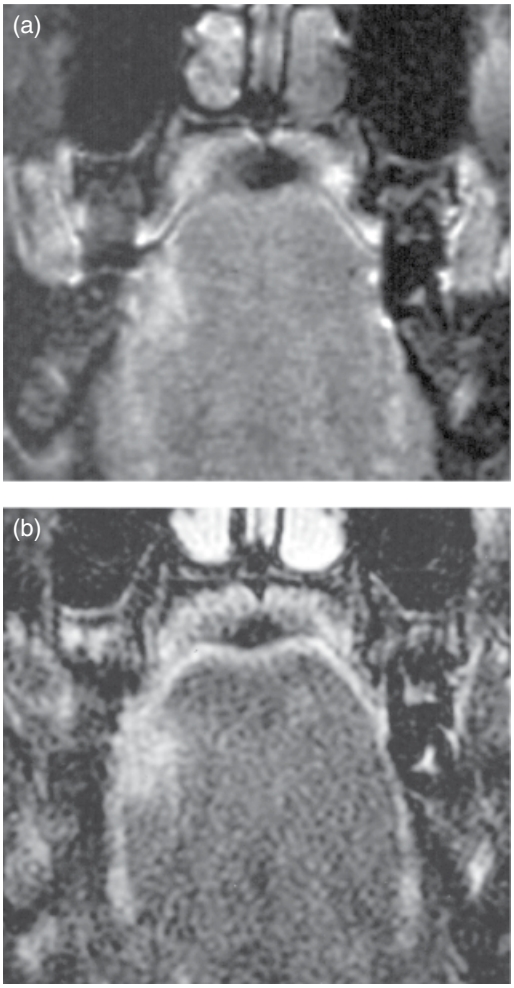


Figure 6.12 Fat-suppressed T2-weighted scan displaying squamous cell carcinoma of the tongue more prominently than that displayed in a T1-weighted scan enhanced by gadolinium and fat suppression. (a) Gadolinium fat-suppressed coronal T1-weighted image showing gadolinium-enhanced blood vessels at the periphery of the lesion; and (b) fat-suppressed coronal T2-weighted image showing fat suppression accentuates the water-rich neoplasm. Note: This enhancement is less within the tongue, because the tongue is a muscular structure that contains very little fat. Source: Reproduced with permission from MacDonald-Jankowski, D.S., Li, T.K., and Matthew, I. (2006). Magnetic resonance imaging for oral and maxillofacial surgeons. Part 2: clinical applications. *Asian J. Oral Maxillofac. Surg.* 18: 236–247.

6.4.2.2 Involvement of Adjacent Bone

Imaizumi et al. (using 1.5 T) reported that the specificity of MRI for cortical invasion was significantly lower than for CT ($p < 0.001$) [27]. They postulated that most of these false positives were due to the chemical shift artifact of the bone marrow fat.

6.4.3 ASSESSMENT OF REGIONAL LYMPH NODES

Central necrosis within a lymph node appears within a prominent "ring" due to the enhancement by gadolinium on a

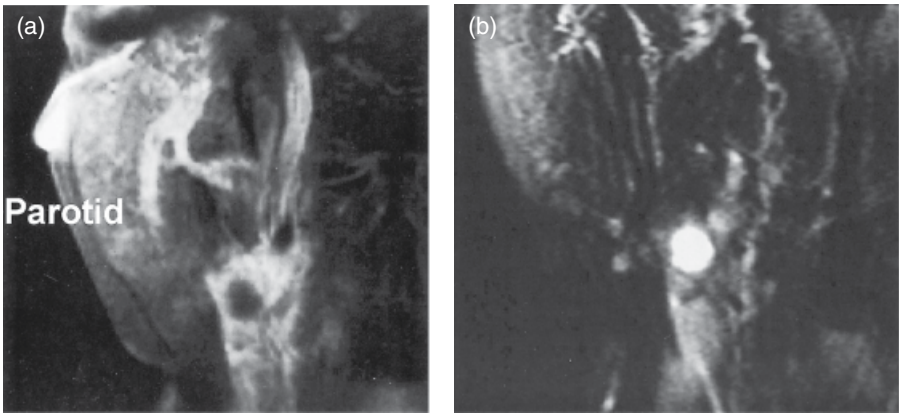


Figure 6.13 New, enlarged jugulodigastric node after partial glossectomy for squamous cell carcinoma. (a) Gadolinium and fat-suppressed coronal T1-weighted image showing the gadolinium (hyperintense) "ring" enhancement of the jugulodigastric node, suggesting central necrosis indicative of metastasis; and (b) fat-suppressed coronal T2-weighted image confirming hyperintense signal from the area of central necrosis, which has been defined by fat suppression. Source: Reproduced with permission from MacDonald-Jankowski, D.S., Li, T.K., and Matthew, I. (2006). Magnetic resonance imaging for oral and maxillofacial surgeons. Part 2: clinical applications. *Asian J. Oral Maxillofac. Surg.* 18: 236–247.

T1-weighted scan. This is a key indicator of metastasis (see Figure 6.13). Furthermore, a neoplastic node is more likely to be round, with its shortest diameter being greater than 1 cm. Reactive or inflammatory nodes are more likely to be ovoid, with the shortest diameter being less than 1 cm. This is discussed more fully in Chapter 19.

For the detection of metastatic lymph nodes with extracapsular spread, 3 T MRI was effective [39]. This is also commonly referred to as extranodal extension and will be discussed further in Chapter 19.

6.4.4 INFECTIONS

Although infections of the face generally arise from a dental cause (periodontitis arising from periodontal disease or from a necrosis of the dental pulp due to dental caries) or from the skin (acne), some now arise as complications of injectable facial filters. As these fillers are injected into the soft tissues, the term *soft-tissue filler* (STF) would appear to be that currently in vogue in the United States [40]. STFs have for decades been inserted or injected into the lips in particular, to address a cosmetic issue, namely to offset the effects of aging, such as facial lines and wrinkles. The US FDA has stipulated its approved reasons for such fillers, ranging from filling out nasolabial folds and acne scars to addressing the lipoatrophy of the cheeks of AIDS patients [41, 42]. Although the FDA expressly disapproves of any free injection of silicon, this and a whole host of other materials have been used globally. These fillers remain within the tissues for variable periods of time, from up to three months to indefinitely [43]. Since fillers are generally radiopaque and in the soft tissues, MRI's excellent soft-tissue contrast is employed to define their extent as a prelude to their surgical removal. Table 6.4 displays the MRI findings on some of the more frequently used injectable facial fillers; these were derived from

Table 6.4 Intensities of some of the injectable facial fillers most likely to be encountered in North America.

Injectable facial fillers	Duration (months)	Magnetic resonance imaging intensities			
		T1W	T2W	T1W + FS	T2W + FS
Collagen	0–3	Hypo	Hyper	Iso-hyper	Hyper
Hyaluronic acid	9–12	Hypo	Hyper	Hypo	Hyper
Plasma	12–18	N/A	N/A	N/A	N/A
Hydroxyapatite	24+	Hypo-iso	Hypo-iso	N/A	N/A
Fat (patient's own)	Semi-permanent	Hyper	Hyper	Hypo	Hypo
Liquid silicon	Indefinitely	Hyper	Hypo	Hypo	Hypo
Polyacrylamidegel	Indefinitely	Hypo-iso	Hyper	Iso-hyper	Hyper
Polytetrafluoroethylene	Indefinitely	Hypo	Hypo	N/A	N/A

hyper, hyper intense; hypo, hypointense; iso, isointense; N/A, information not available; T1W, T1 weighted; T2W, T2 weighted; T1W + FS, T1 weighted and fat saturation; T2W + FS, T2 weighted and fat saturation.

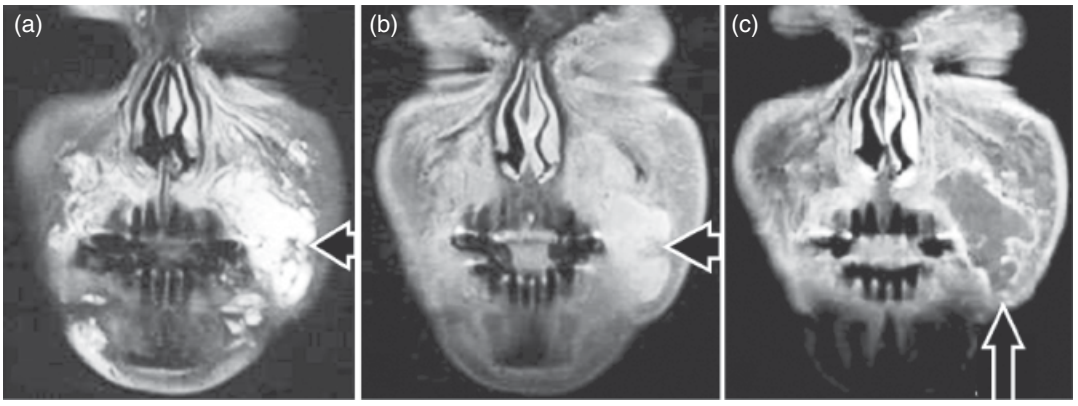


Figure 6.14 Abscess formation in the left nasolabial sulcus region following an injection of polyacrylamide. (a) T2 weighted and fat saturation; (b) T1 weighted and fat saturation; (c) T1 weighted and fat saturation post-gadolinium. The ring-like enhancement in (c) is typical of an abscess. Source: Tal, https://head-face-med.biomedcentral.com/articles/10.1186/s13005-016-0124-y. (See Ref 42.).

reports by Ginat and Schatz [41] and Tal et al. [42]. Short-term complications of fillers are infections, bleeding edema, and filler migration. Over a longer period of time, abscesses and hard lumps form, with perhaps discoloration of the overlying skin [43]. Tal et al. presented a series of cases investigated by MRI [42]. Figure 6.14 concerns an abscess complicating a polyacrylamide filler in the left-hand side of the face.

Terra et al. suggested that DWI MRI assists in differentiating sialadenitis from pleomorphic adenoma [44].

6.4.5 FUNCTIONAL MAGNETIC RESONANCE IMAGING

A recent meta-analysis on MRI in oral cancer reported that DCE MRI had the highest sensitivity, *diagnostic odds ratio* (DOR), and *area under the curve* (AUC), and DWI MRI had the highest specificity [37].

DWI is a noncontrast MRI technique [45]. The information it provides is affected by tissue cell density. DWI is based on the diffusion (movement) of water molecules through the tissues, and this movement is inversely proportion to the tissues' cellularity. The integrity of cell membranes also contributes. The greater the cell density, the less the diffusion, and the greater the signal. This directs the clinician to consider a neoplasm. Soni et al.'s pictorial review of skull base lesions display this advantage of DWI [46].

DWI and DCE are of potential value in distinguishing between benign and malignant neoplasms prior to surgery [47]. This is necessary because the surgical technique varies markedly for parotid neoplasms diagnosed as malignant compared to those diagnosed as benign. The hitherto go-to minimally invasive test, *fine-needle aspiration cytology* (FNAC), cannot always produce a sufficient specimen for a conclusive presurgical diagnosis [47]. Two reports from the same Chinese hospital (Tao et al. [47] and Yuan et al. [48]) separately evaluated the ability of conventional, DWI, and DCE MRI to differentiate between malignant and benign parotid lesions. Tao et al. reported that the lesion's shape, capsule (if present), and intensity were determined by conventional MRI, whereas DWI determined the *apparent diffusion coefficient* (ADC) and DCE the *time-intensity curve* (TIC) [47]. Yuan et al. concluded more simply that the diagnostic value of MRI improved when DWI was used in conjunction with conventional MRI [48].

6.4.6 FUSION WITH OTHER MODALITIES

MRI's fusion with *positron emission tomography* (PET/MRI) is discussed and compared with PET fused with CT in Chapter 7. MRI fused with *ultrasound* (MR/US) has been used in the investigation of prostate cancer. MR/US is indicated when there is a sustained suspicion of prostate cancer in face of a prior negative *transrectal ultrasound* (TRUS)–guided biopsy [49]. MR/US allows the new biopsy to be specifically directed toward "image-based targets" [49].

6.5 Concluding Remarks

Moreira et al. recently summarized the clinical utility of MRI as follows: "MRI… provides the highest-quality images of soft-tissue, without employing ionizing radiation and without known biological risks. MRI also enables multiplanar studies… and provides images with high anatomical definition. The very low section thickness allows visualizing structural lesion on the order of millimeters" [37].

References

1. Gray, C.F., Redpath, T.W., Smith, F., and Staff, R.T. (2003). Advanced imaging: magnetic resonance imaging in implant dentistry. *Clin. Oral Implants Res.* 14: 18–27.
2. Silvers, A. (2006). Imaging of the neck. In: *Otolaryngology: Basic Science and Clinical Review* (ed. T.R. Van de Water and H. Straecker), 667–681. New York: Thieme.
3. McRobbie, D.W., Moore, E.A., Graves, M.J., and Prince, M.R. (2007). *MRI: From Picture to Proton*, 2e. Cambridge: Cambridge University Press.
4. English, P.T. and Moore, C. (1995). *MRI for Radiographers*. Berlin: Springer.

5. Tutton, L.M. and Goddard, P.R. (2002). MRI of the teeth. *Br. J. Radiol.* 75: 552–562.
6. Gradl, J., Höreth, M., Pfefferle, T. et al. (2017). Application of a dedicated surface coil in dental MRI provides superior image quality in comparison with a standard coil. *Clin. Neuroradiol.* 27: 371–378.
7. Li, Q.Y., Zhang, S.X., Liu, Z.J. et al. (2004). The pre-styloid compartment of the parapharyngeal space: a three-dimensional digitized model based on the Chinese visible human. *Surg. Radiol. Anat.* 26: 411–416.
8. Widmann, G., Henninger, B., Kremser, C., and Jaschke, W. (2017). MRI sequences in head & neck radiology – state of the art. *Rofo* 189: 413–422.
9. Havsteen, I., Ohlhues, A., Madsen, K.H. et al. (2017). Are movement artifacts in magnetic resonance imaging a real problem? A narrative review. *Front. Neurol.* 8: 232. https://doi.org/10.3389/fneur.2017.00232.
10. Bridcut, R.R., Redpath, T.W., Gray, C.E., and Staff, T.R. (2001). The use of SPAMM to assess spatial distortion due to static field inhomogeneity in dental MRI. *Phys. Med. Biol.* 46: 1357–1367.
11. Jungmann, P.M., Agten, C.A., Pfirrmann, C.W., and Sutter, R. (2017). Advances in MRI around metal. *J. Magn. Reson. Imaging* 46 (4): 972–991.
12. Eggers, G., Rieker, M., Kress, B. et al. (2005). Artefacts in magnetic resonance imaging caused by dental material. *MAGMA* 18: 103–111.
13. Starcuková, J., Starcuk, Z. Jr., Hubálková, H., and Linetskiy, I. (2008). Magnetic susceptibility and electrical conductivity of metallic dental materials and their impact on MR imaging artifacts. *Dent. Mater.* 24: 715–723.
14. Lee, M.J., Kim, S., Lee, S.A. et al. (2007). Overcoming artifacts from metallic orthopedic implants at high-field-strength MR imaging and multi-detector CT. *Radiographics* 27: 791–803.
15. Smeets, R., Schöllchen, M., Gauer, T. et al. (2017). Artefacts in multimodal imaging of titanium, zirconium and binary titanium-zirconium alloy dental implants: an in vitro study. *Dentomaxillofac. Radiol.* 46: 20160267.
16. Hilgenfeld, T., Prager, M., Schwindling, F.S. et al. (2016). Artefacts of implant-supported single crowns – impact of material composition on artefact volume on dental MRI. *Eur. J. Oral Implantol.* 9: 301–308.
17. Miyata, K., Hasegawa, M., Abe, Y. et al. (2012). Radiofrequency heating and magnetically induced displacement of dental magnetic attachments during 3.0 T MRI. *Dentomaxillofac. Radiol.* 41: 668–674.
18. Hasegawa, M., Miyata, K., Abe, Y. et al. (2015). 3-T MRI safety assessments of magnetic dental attachments and castable magnetic alloys. *Dentomaxillofac. Radiol.* 44: 20150011. https://doi.org/10.1259/dmfr.20150011.
19. Oriso, K., Kobayashi, T., Sasaki, M. et al. (2016). Impact of the static and radiofrequency magnetic fields produced by a 7T MR imager on metallic dental materials. *Magn. Reson. Med. Sci.* 15: 26–33.
20. Shellock, F.G. and Crues, J.V. (2004). MR procedures: biologic effects, safety, and patient care. *Radiology* 232: 635–652.
21. United States Food and Drug Administration. Magnetic resonance imaging (MRI): benefits and risks. 2017. https://www.fda.gov/RadiationEmittingProducts/RadiationEmittingProductsandProcedures/MedicalImaging/MRI/ucm482765.htm. (Accessed April 2, 2018)
22. United States Food and Drug Administration. Understanding MRI safety labeling. https://www.fda.gov/downloads/RadiationEmittingProducts/RadiationEmittingProductsandProcedures/MedicalImaging/MRI/UCM528080.pdf; Magnetic resonance imaging: tips for scanning patients with implants. https://www.fda.gov/downloads/RadiationEmittingProducts/RadiationEmittingProductsandProcedures/MedicalImaging/MRI/UCM528077.pdf n.d. (Accessed April 2, 2018)
23. Expert Panel on MR Safety, Kanal, E., Barkovich, A.J. et al. (2013). ACR guidance document on MR safe practices: 2013. *J. Magn. Reson. Imaging* 37: 501–530.
24. Cadieu, R., Peron, M., Le Ven, F. et al. (2017). Central nervous system MRI and cardiac implantable electronic devices. *J. Neuroradiol.* 44: 1–9.
25. Strom, J.B., Whelan, J.B., Shen, C. et al. (2017). Safety and utility of magnetic resonance imaging in patients with cardiac implantable electronic devices. *Heart Rhythm* 14: 1138–1144.

26. Bongers, S., Slottje, P., Portengen, L., and Kromhout, H. (2016). Exposure to static magnetic fields and risk of accidents among a cohort of workers from a medical imaging device manufacturing facility. *Magn. Reson. Med.* 75: 2165–2174.
27. Imaizumi, A., Yoshino, N., Yamada, I. et al. (2006). A potential pitfall of MR imaging for assessing mandibular invasion of squamous cell carcinoma in the oral cavity. *AJNR Am. J. Neuroradiol.* 27: 114–122.
28. Del Grande, F., Santini, F., Herzka, D.A. et al. (2014). Fat-suppression techniques for 3-T MR imaging of the musculoskeletal system. *Radiographics* 34: 217–233.
29. Semelka, R.C., Ramalho, M., AlObaidy, M., and Ramalho, J. (2016). Gadolinium in humans: a family of disorders. *AJR Am. J. Roentgenol.* 207: 229–233.
30. Olchowy, C., Cebulski, K., Łasecki, M. et al. (2017). The presence of the gadolinium-based contrast agent depositions in the brain and symptoms of gadolinium neurotoxicity – a systematic review. *PLoS One* 12: e0171704. https://doi.org/10.1371/journal.pone.0171704.
31. United States Food and Drug Adminstration. FDA Drug Safety Communication: FDA evaluating the risk of brain deposits with repeated use of gadolinium-based contrast agents for magnetic resonance imaging (MRI). 2015. https://www.fda.gov/Drugs/DrugSafety/ucm455386.htm; FDA Drug Safety Communication: FDA identifies no harmful effects to date with brain retention of gadolinium-based contrast agents for MRIs; review to continue. 2017. https://www.fda.gov/Drugs/DrugSafety/ucm559007.htm (Accessed December 3, 2018)
32. Bai, M., Guo, Q., and Li, S. (2013). Persistent trigeminal artery/persistent trigeminal artery variant and coexisting variants of the head and neck vessels diagnosed using 3 T MRA. *Clin. Radiol.* 68: e578–e585.
33. Hughes, M.A., Frederickson, A.M., Branstetter, B.F. et al. (2016). MRI of the trigeminal nerve in patients with trigeminal neuralgia secondary to vascular compression. *AJR Am. J. Roentgenol.* 206: 595–600.
34. Leal, P.R., Barbier, C., Hermier, M. et al. (2014). Atrophic changes in the trigeminal nerves of patients with trigeminal neuralgia due to neurovascular compression and their association with the severity of compression and clinical outcomes. *J. Neurosurg.* 120: 1484–1495.
35. Hitchon, P.W., Holland, M., Noeller, J. et al. (2016). Options in treating trigeminal neuralgia: experience with 195 patients. *Clin. Neurol. Neurosurg.* 149: 166–170.
36. Lee, Y.H., Lee, K.M., Kim, H.G. et al. (2017). Orofacial complex regional pain syndrome: pathophysiologic mechanisms and functional MRI. *Oral Surg. Oral Med. Oral Pathol. Oral Radiol.* 124: e164–e170.
37. Moreira, M.A., Lessa, L.S., Bortoli, F.R. et al. (2017). Meta-analysis of magnetic resonance imaging accuracy for diagnosis of oral cancer. *PLoS One* 12: e0177462. https://doi.org/10.1371/journal.pone.0177462.
38. Hsu, W.C., Loevner, L.A., Karpati, R. et al. (2005). Accuracy of magnetic resonance imaging in predicting absence of fixation of head and neck cancer to the prevertebral space. *Head Neck* 27: 95–100.
39. Moreno, K.F., Cornelius, R.S., Lucas, F.V. et al. (2017). Using 3 Tesla magnetic resonance imaging in the pre-operative evaluation of tongue carcinoma. *J. Laryngol. Otol.* 131: 793–800.
40. Lohman, M.E., Ghobadi, C.W., and Xu, S. (2017). Device safety implications of the clinical data leading to US Food and Drug Administration approval of soft-tissue fillers: a systematic review. *JAMA Facial Plast. Surg.* 19: 421–429.
41. Ginat, D.T. and Schatz, C.J. (2013). Imaging features of midface injectable fillers and associated complications. *AJNR Am. J. Neuroradiol.* 34: 1488–1495.
42. Tal, S., Maresky, H.S., Bryan, T. et al. (2016). MRI in detecting facial cosmetic injectable fillers. *Head Face Med.* 12: 27. https://doi.org/10.1186/s13005-016-0124-y.
43. United States Food and Drug Administration. Dermal fillers approved by the Center for Devices and Radiological Health. 2018. https://www.fda.gov/MedicalDevices/ProductsandMedicalProcedures/CosmeticDevices/ucm619846.htm (accessed December 3, 2018)
44. Terra, G.T., Oliveira, J.X., Hernandez, A. et al. (2017). Diffusion-weighted MRI for differentiation between sialadenitis and pleomorphic adenoma. *Dentomaxillofac. Radiol.* 46: 20160257.

45. Wang, L.C. (2017). MR imaging: future imaging techniques. *Radiol. Clin. N. Am.* 55: 553–577.
46. Soni, N., Gupta, N., Kumar, Y. et al. (2017). Role of diffusion-weighted imaging in skull base lesions: a pictorial review. *Neuroradiol J.* 30: 370–384.
47. Tao, X., Yang, G., Wang, P. et al. (2017). The value of combining conventional, diffusion-weighted and dynamic contrast-enhanced MR imaging for the diagnosis of parotid gland tumours. *Dentomaxillofac. Radiol.* 20160434. https://doi.org/10.1259/dmfr.20160434.
48. Yuan, Y., Tang, W., and Tao, X. (2016). Parotid gland lesions: separate and combined diagnostic value of conventional MRI, diffusion-weighted imaging and dynamic contrast-enhanced MRI. *Br. J. Radiol.* 89: 20150912. https://doi.org/10.1259/bjr.20150912.
49. Vourganti, S., Starkweather, N., and Wojtowycz, A. (2017). MR/US fusion technology: what makes it tick? *Curr. Urol. Rep.* 18: 20. https://doi.org/10.1007/s11934-017-0671-1.

Chapter 7

Positron emission tomography

7.1 Introduction

The basics of *positron emission tomography* (PET) are introduced in this chapter; the clinical applications are further discussed in Chapter 19, with regard to the diagnosis of cancer and the assessment of its response to treatment, respectively. PET is a nuclear imaging technique based on metabolic mechanisms. These mechanisms can be enzymatic, hormonal, or pharmacological. PET uses the unique decay characteristics of nucleotides that decay by positron emission. The labeled compound is introduced into the body, usually intravenously, and is distributed in the tissues in a manner determined by its biological properties

When the radioactive atom of a particular labeled molecule decays, a positron is emitted from the nucleus. The positron is an antimatter analog of an electron. It has the same mass as an electron, but it carries a positive charge. It is produced when the fluorine-18 isotope decays to the oxygen-18 isotope. When a positron meets an electron they mutually annihilate each other, completely converted into two photons, each of energy 511 KeV (*annihilation radiation*), traveling in opposite directions.

Such an event will be detected when each of the two photons interacts simultaneously with two detectors on opposite sides of the detector ring surrounding that part of the patient (Figure 7.1). These detectors must lie within a column joining the two, which passes through the site of annihilation. This is called *coincidence* [1].

7.2 PET Scanner

At a first glance the PET scanner, as set out schematically in Figure 7.1, looks like a *computed tomography* (CT) unit. Unlike CT, where the source of radiation arising from the unit itself is outside the patient, in PET the source of radiation arises from within the patient. The PET scanner merely detects this radiation. It achieves this by a stationary ring of detectors that surround the patient or part of the patient to be imaged. It converts and reconstructs the signals from the detectors into a three-dimensional image. The signal intensity of any particular image voxel is proportional to the amount of the radionucleotide (and hence the amount of molecule to which it is attached) in that voxel.

Since the majority of PET units have been fused with CT, most of the images displayed in this textbook will be PET/CT, although discussions of the technologies of PET/CT and the emerging PET fused with *magnetic resonance imaging* (MRI), rendered simply as PET/MR, will occur later in this chapter. The clinical importance of PET/CT will be introduced first.

Oral and Maxillofacial Radiology: A Diagnostic Approach, Second Edition. Edited by David MacDonald.
© 2020 John Wiley & Sons, Inc. Published 2020 by John Wiley & Sons, Inc.

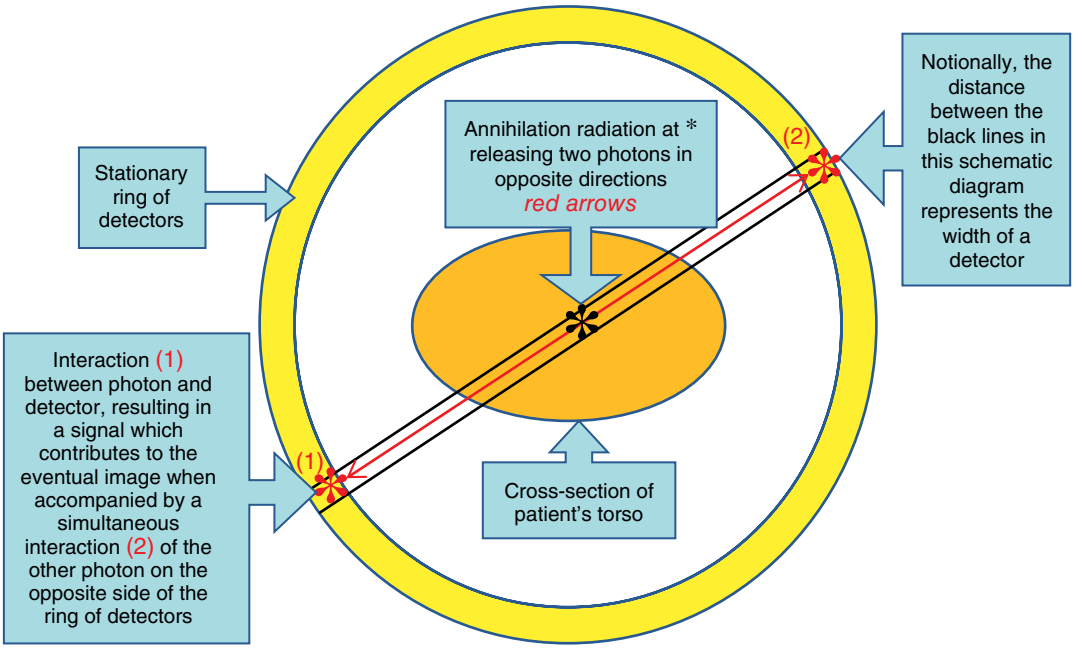


Figure 7.1 Schematic diagram illustrating coincidence. At the site of annihilation, two photons of energy 511 KeV are released and travel in opposite directions to interact with a detector at diametrically opposite sites on the stationary ring of detectors. These interactions result in signals that then contribute to the subsequent image. Note: The asterisk represents the site of close to optimal spatial resolution, because it is near the center of the ring of detectors. The spatial resolution and signal-to-noise ratio at other sites are optimized by introduction of a time-of-flight facility.

Figure 7.2 shows a whole-body PET/CT displaying the normal increased avidity of the kidneys and bladder (both of which contain urine with concentrated filtered radioactive tracer) and of the apex of the heart due to its high muscular activity. Figure 7.3 shows hyperavidity of a large primary *squamous cell carcinoma* (SCC) in the base of the tongue, in comparison to a contemporaneous and similar section in *multidetector computed tomography* (MDCT). Even though the SCC in the latter is contrast enhanced, it is not as obvious as in the PET/CT. Furthermore, the differences of position of the patient during the making of these images in different units at different times make direct comparisons more challenging for radiologists or functional imaging specialists as they present them simultaneously to clinical colleagues in interdisciplinary case conferences. All subsequent PET/CT figures (Figures 7.4–7.8) display PET, CT, and PET/CT separately. Note the exact anatomical concordance of these images in each case.

7.3 FDG Tracer

There are a number of potential tracers, but *18-fluorine fluorodeoxyglucose* (FDG) is preferred, because of its intense accumulation in malignant neoplasms. This reflects the increased glycolytic rate of the malignant neoplasm and was first observed by



Figure 7.2 Image derived from a fused positron emission tomography (PET) and computed tomography (CT) – PET/CT. This almost whole-body PET/CT image can display areas of increased metabolism. Yellow areas represent hyperavidity due to radioisotope tracer uptake. The brain is always hyperavid. The apex of the heart is obvious in the left side of the thorax. This is normal. Other areas are observed in both kidneys and the bladder, suggesting that in addition to radioactive decay, which is necessary to produce the PET image, the radioisotope is being removed from the body in the usual way. This is particularly important after the examination has been completed so as to minimize radiation dose to the patient. Source: Courtesy of Dr. Thomas Li, Oral and maxillofacial radiologist.

Warberg 80 years ago [2]. Many, but not all, cancer cells display an upregulation of the *glucose transporter1* (GLUT 1), which facilitates the transport of glucose through the cell membrane into the cells, where it is metabolized to *adenosine triphosphate* (ATP) by the anaerobic glycolytic pathway [2]. In the cell, FDG is metabolized to FDG-6-phosphate (thus phosphorylated). In that form it cannot be metabolized further by glucose-6-phosphate isomerase, and becomes trapped in the cell until it decays [3]. When the FDG decays, its photons indicate the precise location of the cell. (Note: the FDG's half-life of 110 minutes allows sufficient time to transport it from the cyclotron where it is produced to the hospital where it will be delivered to the patient.)

The area in which the cells have thus been marked will appear brighter (FDG avid) as FDG decays by annihilation radiation, in contrast to those areas with few or no FDG-marked cells. During the examination the kidneys are removing FDG, which has not passed into the cell. This results in areas of increased avidity in the kidneys and bladder (Figure 7.2). FDG is also excreted by the bowels. This emphasizes that the uptake and distribution of FDG in the tissues is a dynamic process, comprising blood flow, GLUTs, and *glucose phosphorylation enzyme type II* (hexokinase-II) and glucose-6-phosphatase activities [2, 3]. During the first hour after injection. the normal and inflamed tissues attain their maximum uptake of FDG, whereas the uptake of FDG in malignant tissue will plateau out two to three hours later [2], during which time the patient will continue to avoid unnecessary activity.

It should be appreciated that FDG uptake is nonspecific: not only do tissues with inflammation also appear FDG avid, so also does skeletal muscle. Skeletal muscle uses glucose physiologically when it is active and will not only be FDG avid, but will overall reduce delivery of FDG to the target tissue. Therefore the patient is advised to avoid physical exertion prior to and during the investigation. This curtailment of

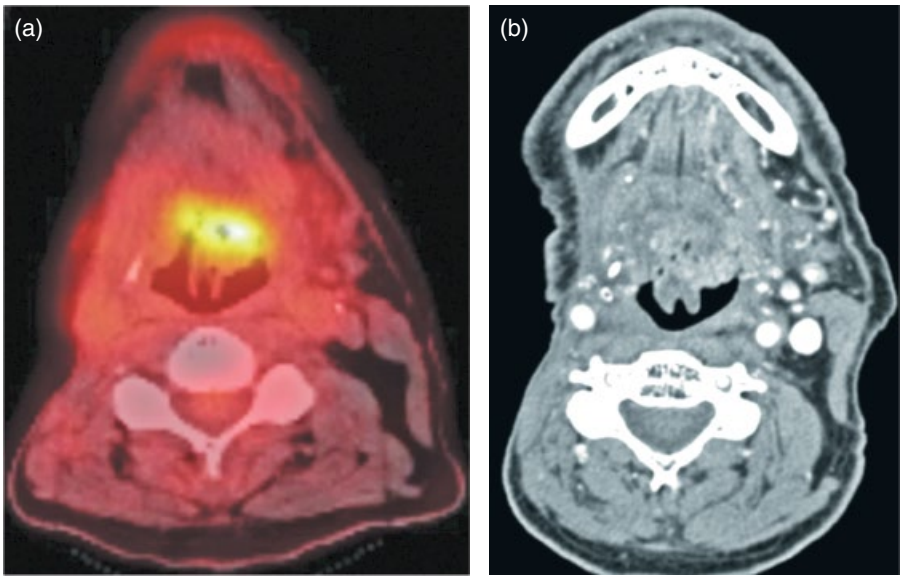


Figure 7.3 Axial fused modalities positron emission tomography (PET) and computed tomography (CT) (a) and a separate multidetector computed tomography (MDCT) examination (b) of a squamous cell carcinoma (SCC) affecting the base or dorsum of the tongue. The avidity of the SCC is clearly seen on the PET/CT image (a), whereas on the MDCT with intravenous contrast (b) it is less obviously enhanced. Note: The sternocleidomastoid and the platysma muscles have been removed on one side. Source: Courtesy of Dr. Montgomery Martin, British Columbia Cancer Agency.

activity is also extended to speech and swallowing, as the increased avidity of the musculature of the face, jaws, and neck will interfere with the examination, particularly for oral cancer. Patients should also be advised that chewing gum prior to the investigation increases the avidity of muscles of mastication and of the tongue (Figure 7.4).

Inflammation, as already mentioned, is FDG avid and is usually clinically apparent. Nevertheless, when considering the possibility that a lesion is malignant or already knowing that it is malignant, it is easy to overlook concurrent dental disease such as periodontal and periapical pathology, as this increases the uptake of FDG [4]. Therefore, care is required in the interpretation of such hypermetabolic areas near suspected cancer. It also goes without saying, following from Chapter 1, that biopsies should be deferred until after the completion of any necessary imaging. Figure 7.5 displays a hyperavid area arising from a dental infection.

It should be noted that nonmalignant lesions such as inverted papillomas and oncocytomas, in addition to aggressive presentations on CT and MRI, also have high avidity. This places the whole weight of the diagnosis of these lesions solely on the pathologist's shoulders. Nevertheless, although this may result in doubt as to whether a representational site was biopsied, such doubt results in cautious follow-up, which is not a disadvantage.

Although FDG is still the workhorse for head and neck PET, principally SCC, other markers are used for parathyroid adenoma and neurogangliomas.

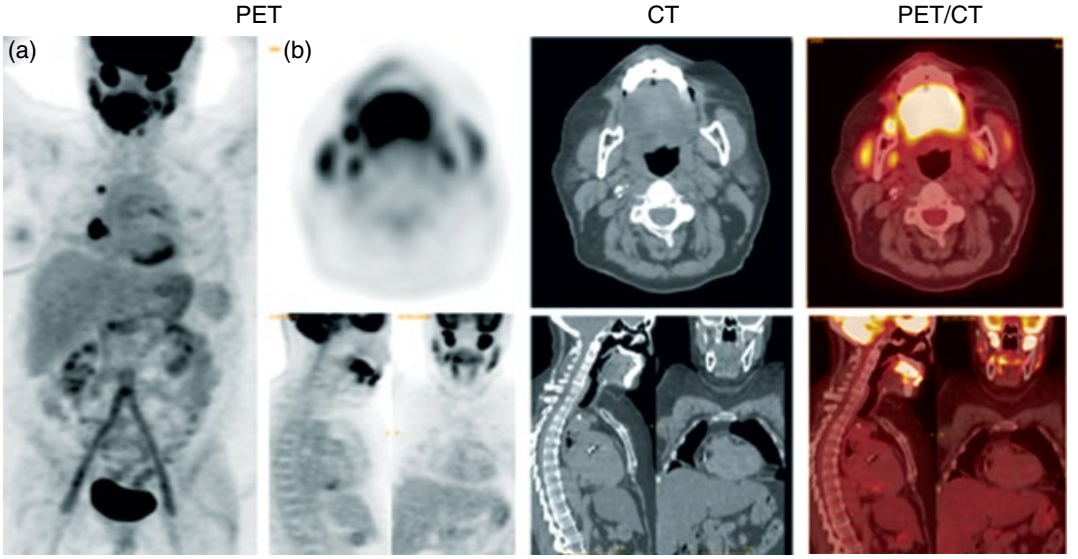


Figure 7.4 Fused positron emission tomography and computed tomography (PET/CT) of a patient displaying hyperavidity of the skeletal muscles of the face and jaws, namely the muscles of mastication and the tongue, due to the chewing of gum immediately prior to the examination. (a) Whole-body PET displaying the normal avid areas of the brain and bladder. The femoral vessels are displayed as an inverted "V" enclosing the hyperavid bladder. (b) PET multiplanar reformation (MPR); axial above sagittal then coronal below. These display the individual muscles more clearly. CT reveals the anatomy of the head and neck. Fused PET/CT revealing the precise muscles which now display avidity due to gum chewing prior to the investigation. The patient should be advised to avoid all physical exertion prior to the investigation. The standard uptake value of the now avid muscles in (b) and PET/CT is 5.1.

7.4 Standard Uptake Value

The *standard uptake value* (SUV) is the ratio between measured uptake in a *region of interest* (ROI) and the expected uptake if the FDG had been evenly distributed throughout the patient [5]. It determines the sites of high activity, particularly of metastatic lesions. Infections and rheumatoid arthritis can cause false positives, whereas slow-growing adenocarcinomas or malignant neoplasms that are smaller than 1 cm can produce false negatives [5]. Although FDG can also be used to distinguish between high-grade and low-grade lymphomas, the avidity of some low-grade lymphomas is so mild that a false negative can ensue [1].

The SUV has been of limited value, but has been transformed by the use of the *maximum standard uptake value* (SUV_{max}). This is a single pixel that reflects the maximum FDG uptake by the tumor, the *metabolic tumor volume* (MTV), and *total lesion glycolysis* (TLG). As Pasha et al. note, "The MTV is defined as the volume of tumor with FDG uptake. It is a volumetric and metabolic biomarker and is an estimate of the tumor volume based on the distribution of metabolic activity" [6]. TLG is defined as tumor volume multiplied by the SUV_{max} of the included voxel. It incorporates both MTV and SUV and represents both the degree of FDG uptake and the size of the tumor [6]. In a recent systematic review, MTV was strongly

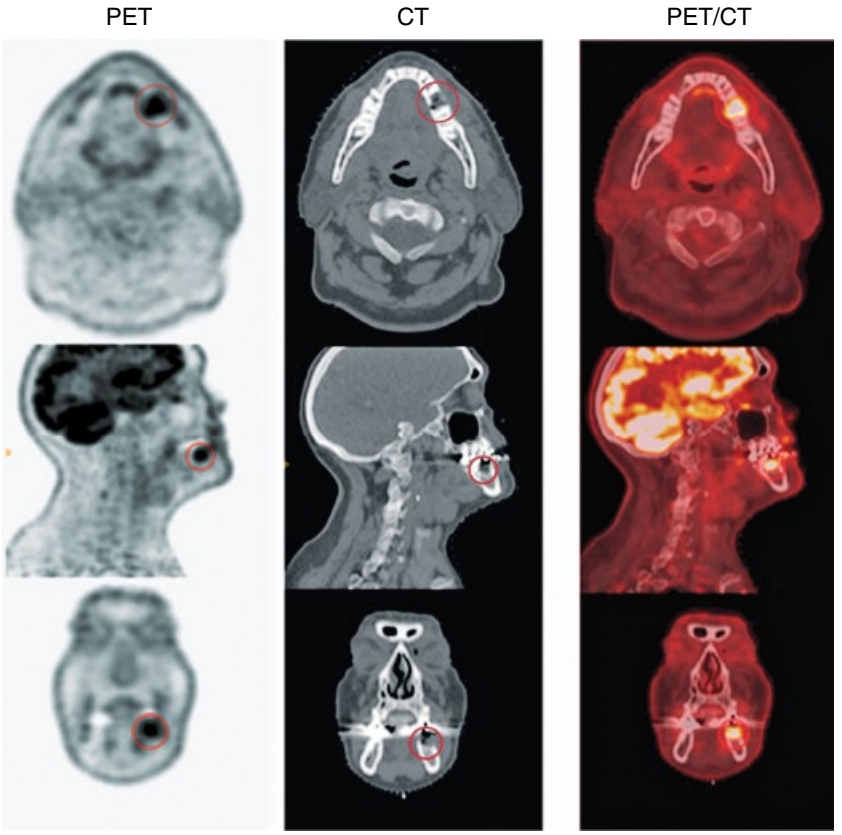


Figure 7.5 Fused positron emission tomography and computed tomography (PET/CT) displaying inflammation arising within the alveolus of the left mandible. The reconstructions are arranged, from the top of each column, as axial, sagittal, and coronal. Note: The brain displayed in the sagittal reconstructions is as always i highly avid. The standard uptake value is 11.1.

associated with worsening overall survival (hazard ratio). Pooled hazard ratios with MTV and TLG confirmed that high MTV and TLG values were associated with increased occurrence of adverse effects or death [7].

SUV is today not as useful an indicator of a particular malignant process. A citation of its numerical value outside the context of a particular patient has little real meaning. Simply put, an increased SUV of a particular tumor indicates that treatment so far has not been effective, whereas a decrease in SUV indicates that so far treatment has been effective.

7.5 Time of Flight

A problem with PET is that in the axial plane the spatial resolution decreases with increased distance from the center of the detector ring [8]. This problem arises from the ability of the PET detector to time-link both opposite traveling annihilation photons so they are coincident. This is a problem for whole-body PET and particularly for large patients. Therefore, the ability of the PET unit to detect the tiny time differences for those photon pairs produced outside the center of the detector ring allows the precise annihilation site to be

determined, increasing the spatial resolution of the image. This is the *time of flight* (TOF). Improved TOF time resolution improves in turn the *signal-to-noise ratio* (SNR). This is particularly advantageous for whole-body imaging, since the theoretical improvement with TOF is predicted to increase with the size of the patient. That is fortuitous, since conventional PET image quality degrades noticeably for large patients due to increased attenuation, which leads to both the loss of true counts and the increase of scattered counts. TOF brings the image quality (SNR, contrast, and spatial resolution) up to par with that of the average-sized patient [9]. The other advantages of TOF shorter scan times and lower radiation dose [9].

7.6 Clinical Applications

The main clinical application of PET in head and neck oncology is the diagnosis of SCC (Table 7.1, Figure 7.3; see also Figures 19.24, 19.25, 19.31, and 19.32). A systematic review by Facey et al. [10] revealed that FDG PET improved the detection of occult head and neck tumors – a task in which all other modalities failed. The authors also observed that it improved the staging of clinically positive regional cervical lymph nodes. A further systematic review by Isles et al. reported that PET was highly accurate in the detection of recurrent or persistent SCC of the head and neck. Nevertheless, it was less sensitive for recurrences within 10 weeks postoperatively [11].

PET's ability to measure accurately the extent of a primary tumor is markedly inferior to that of CT and MRI, simply because of its inferior display of anatomical detail. This accuracy is necessary to determine optimally the surgical approach [6].

Nevertheless, this inferiority is offset when a *carcinoma of unknown primary* (CUP) is encountered, in which neither CT nor MRI's superior anatomical display has hitherto been of much avail. A CUP is "defined as a biopsy-proven metastatic malignancy in which the primary tumor could not be detected despite thorough diagnostic evaluation" [12]. The implication of this for patients and their clinicians is that it may not be possible to optimize treatment planning and therefore treatment outcomes [12]. Because of the ability of FDG PET/CT to identify the primary only by its FDG avidity (if it were clinically detectable it would have already been detected), a staging of the disease can now be achieved and an optimized treatment plan to address it formulated. Indeed, it has been suggested that FDG PET/CT should be the first-line imaging for CUP, rather than being used after other imaging investigations have been exhausted [12]. It should be appreciated that despite FDG PET/CT, the CUP may still remain undetected.

The role of FDG PET/CT in the pretreatment staging of locally advanced SCC of the head and neck is well established [13]. Figure 7.6 displays a primary arising in the supraglottic area with metastasis to local lymph nodes. Although SCC accounts for 95% of all head and neck tumors, most of the remaining 5% are lymphomas, which most frequently first present in the head and neck. Decades ago it became apparent that it was crucial to determine which lymphomas best respond to radiotherapy alone and which require chemotherapy [14]. FDG PET/CT has superior sensitivity and specificity to diffusion-weighted MRI with regard to the detection of bone-marrow infiltration by the lymphoma [15]. FDG PET/CT should be used routinely to stage FDG-avid lymphomas prior to treatment, because it is more sensitive than MDCT alone. This is particularly for detection of extranodal lymphomas, all *Hodgkin lymphomas* (HLs), and most *non-Hodgkin lymphomas* (NHLs) [13].

Table 7.1 Indications for FDG PET in the clinical management of adult oncology patients with a primary cancer arising anywhere in the head and neck, except the brain, spinal cord, and thyroid gland.

1.	Diagnosis of primary site in patients presenting with squamous cell carcinoma metastatic to cervical lymph nodes with no obvious primary on conventional work-up.
2.	Staging in patients with nasopharyngeal carcinoma and N2 or N3 nodal disease.
3.	Staging in patients with level IV cervical lymph node metastases.
4.	Diagnosis of suspected recurrence in the absence of other definitive evidence in patients being considered for salvage therapy.
5.	Evaluation of cervical lymph nodes in patients for whom radical neck dissection is a part of the treatment plan for advanced primary disease.

Source: Derived from British Columbia Cancer Agency. BCCA approved indications for FDG-PET in the clinical management of adult oncology patients. 2017. http://www.bccancer.bc.ca/pet-site/Documents/Clinical%20Indications/CurrentAdultIndicationsMarch2012.pdf. (Accessed December 4, 2018). Courtesy of Dr. Donald Wilson and Dr Jonn Wu, British Columbia Cancer Agency.

Although not recommended for low FDG-avid lymphomas, it can nevertheless determine the extent of the disease and the most suitable sites for biopsy.

PET/CT is invaluable in the assessment of the response to treatment. Figure 7.7 reveals the initial success of the treatment delivered to the lesion displayed in Figure 7.6. Further follow-up has revealed that the now treated primary had already spread to the liver and a thoracic vertebra (Figure 7.8).

Metastasis of carcinomas to the skeleton is important to detect early, since they have a better prognosis than those which metastasize to soft tissues [16]. Although this was recently confirmed in a case series of metastatic lesions in the jaws, nearly 90% of adults died of their disease [17]. Nevertheless, survival is enhanced and morbidly reduced if single metastatic bone lesion is detected early. Bone scintigraphy has long proven invaluable in detecting such lesions nearly two years before they are perceptible on conventional radiography. The lesions may be osteoblastic (prostate cancer), osteolytic (myeloma, thyroid, and lung cancer), or both (breast cancer) [16]. Although a range of imaging modalities has been applied to the detection of metastatic lesions, FDG PET has been most effective for detecting bone metastasis [16].

The diagnosis of osteomyelitis is not always obvious [18]. Osteomyelitis represents a broad spectrum of disease, which is variable in its etiology (hematogenous or by inoculation due to trauma or surgery), clinical presentation (acute, subacute, and chronic), and whether it affects the bone or bone marrow. Bone scintigraphy using *technetium-99m* (^{99m}Tc) diphosphonate is most usual. The degree of uptake depends upon blood flow and rate of bone formation. This scintigraphy uses three phases: dynamic, perfusion, and finally the bone phase a few hours later. The presence of focal hyperperfusion, hyperemia, and increased bone activity confirms a diagnosis of osteomyelitis within a few hours. Furthermore, not only is the spatial resolution of ^{99m}Tc imaging high, so also is that of FDG PET. Nevertheless, pre-existing fractures and plates can affect the specificity of any such test. Uptake usually normalizes within three to four months after trauma or surgery [18].

In addition to diagnosis of cancers, functional imaging is invaluable for their treatment planning and assessment of their response to treatment [19].

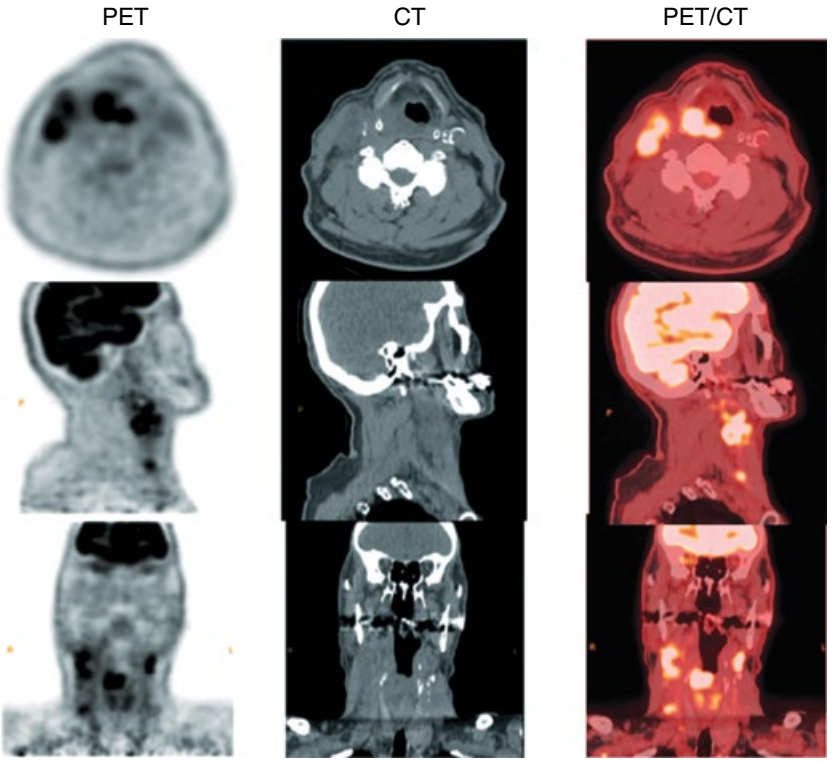


Figure 7.6 Fused positron emission tomography and computed tomography (PET/CT) displaying a large primary in the right suprahyoid triangle, with metastasis to the upper cervical lymph nodes bilaterally (see the coronal PET). The reconstructions are arranged, from the top of each column, as axial, sagittal, and coronal. Note: The axial CT reveals calcification within the left common carotid artery. The coronal CT displays a photon starvation artifact through the base of the neck due to the shoulders. The standard uptake value is 4.2.

7.7 Multimodality PET Imaging

In order to address PET's poor display of anatomy, it was successfully fused with CT and more recently with MRI. Although initially CT was fused with PET to provide anatomical co-registration, today a major advantage of fused imaging is that the patient's whole-body disease can be imaged by two of the three major imaging modalities on a single occasion [3]. Although PET/CT has now been widely installed in hospitals serving major population centers throughout North America, PET/MR is beginning to make an impact. A comparison of the two modalities is set out in Table 7.2 (see also Ehman et al. [20]).

7.7.1 PET/CT

This combines PET and CT technology in a single gantry system, with the CT unit installed in front of the PET scanner. The images acquired from both devices can be taken sequentially, in the same session, and combined into a single superposed (co-registered) image. The advantage of this combined-modality imaging is that the

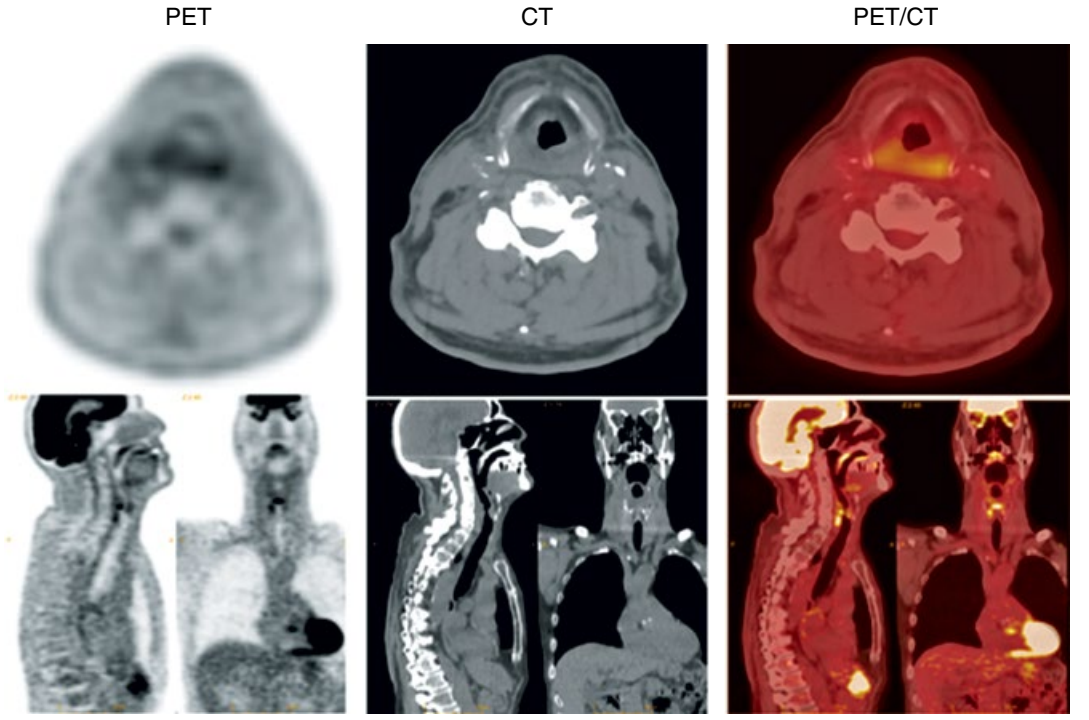


Figure 7.7 Fused positron emission tomography and computed tomography (PET/CT) follow-up of the large primary in the right suprahyoid triangle, with metastasis to the upper cervical lymph nodes bilaterally (see Figure 7.6). The reconstructions are arranged, from the top of each column, as axial, then sagittal and coronal together. The previously avidities are substantially less avid. The standard uptake value is 2.6, suggesting they are responding to treatment. The apex of the heart is avid as expected.

tissue density information provided by the CT can now be used to calculate an attenuation correction for the PET image [21].

Although Pasha et al. report that "a major benefit of PET/CT is that the whole body can be imaged, which is important in detecting distant metastasis" [6], the evidence, while promising, is not yet conclusive [6]. PET/CT is more effective in identifying distant metastasis than CT alone, though this is not substantial. Nevertheless, the low false-negative rate of 3% makes PET/CT a reliable screening test for ruling out distant metastasis [22].

In addition to identifying unknown primaries and distant metastasis, FDG PET/CT in the diagnosis of oral SCC is accurate for identifying metastasis in nodes which are less than 1 cm in diameter and otherwise normal on standard CT. Furthermore, FDG PET/CT also assists with effective treatment planning and assessment of response to treatment [6].

Although interim PET alone has high prognostic value in lymphomas and is the main determinant of response of NHL, PET/CT has little role in routine surveillance imaging [23]. Nevertheless, FDG PET/CT is used instead of a bone marrow biopsy for the routine staging of HL and most *diffuse large B-cell lymphomas* (DLBCL, an NHL subtype) [24]. Although a positive PET of bone or bone marrow is adequate to designate advanced-stage DLBCL, a negative PET of the bone marrow can indicate a bone-marrow biopsy [24].

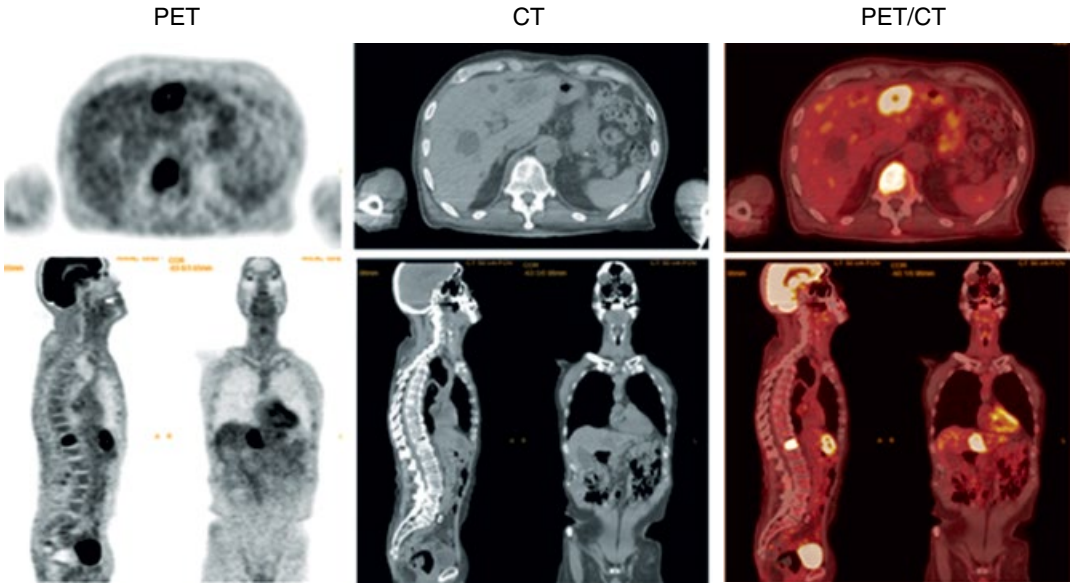


Figure 7.8 Fused positron emission tomography and computed tomography (PET/CT) for further follow-up of the large primary in the right suprahyoid triangle, with metastasis to the upper cervical lymph nodes bilaterally, which appear to have responded to treatment (see Figure 7.7). The reconstructions are arranged, from the top of each column, as axial, then sagittal and coronal together. These reveal that although the primary lesion and its immediate metastasis remain inactive, avidities are observed in a thoracic vertebra and in the liver. The bladder and apex of the heart are avid, as would be expected. The standard uptake value is 5.0.

Because salivary gland tumors (SGT) are rare, large case series are infrequent. Nevertheless, it would appear that PET may not be able to distinguish benign from malignant SGTs because of the considerable overlap in uptake between them [25]. In addition to CUP, FDG PET/CT is increasingly used in patients with *pyrexia of unknown origin* (PUO) [3].

PET/CT is limited by the soft-tissue resolution of CT and its high radiation dose, which is particularly pertinent in those lesions, such as lymphomas, that require repeated PET/CTs in order to monitor their progress. Furthermore, as these lesions are particularly prevalent in young adults, this high and repeated radiation dose is especially relevant. All of these deficiencies have prompted clinicians to consider PET/MR hybrids [26].

7.7.2 WHOLE-BODY PET/MR

Whole-body PET/MR inserts the PET element within the magnet. The advantages that PET/MR has over PET/CT are better soft-tissue contrast, less ionizing radiation (only the PET component now uses ionizing radiation), and the benefits of MR-only imaging, such as diffusion-weighted imaging [2] and TOF. In addition to the patient preparation required for PET, the patient must also be MRI safety compliant (see Chapter 6). PET/MR's long gestation period arose from the need to address a host of very difficult and at times mutually exclusive technical challenges. PET, using

Table 7.2 Comparison of the main attributes of positron emission tomography fused with computed tomography (PET/CT) and positron emission tomography fused with magnetic resonance imaging (PET/MR).

Attribute	PET/CT	PET/MR
Availability (in 2017)	Widely in USA with 1600 units	Limited in USA with 30 units
Improved soft-tissue contrast	No	Yes – a major advantage
Well-established evidence-based protocols	Yes – a major advantage	Still in development
Familiarity among prescribers	Yes – a major advantage	No
Well-established quantitative accuracy	Yes – a major advantage	Still being determined
Examination time	As short as 30 minutes	60 or more minutes, but also better motion correction
Extra time for PET acquisition	No	Yes – a major advantage
Ionizing radiation in addition to that from PET	Yes, from CT component	No – a major advantage
Convenience and time saved with combined examinations	No – if focused MRI is required then a separate examination is needed	Yes
Use of MRI-specific contrast agent	No – if required then a separate examination is needed	Yes
Patient comfort (also considering claustrophobia)	Yes – shorter scan time, wider bore (70 cm)	No – longer scan time, narrower bore (60 cm), and claustrophobic coils
Technologist training	Nuclear medicine certification	Nuclear medicine certification and MRI expertise

Source: Adapted from Table 1 in Ehman, E.C., Johnson, G.B., Villanueva-Meyer, J.E. et al. (2017). PET/MRI: Where might it replace PET/CT? J. Magn. Reson. Imaging. 46:1247–1262. doi: 10.1002/jmri.25711.

photomultiplier tubes (PMTs), by itself or fused to CT, cannot work in a strong magnetic field. The replacement of PMTs with *avalanche photodiodes* (APDs), a semiconductor material, can operate in conjunction with MRI up to 9.4 T [8]. Although APDs' timing resolution is inferior to PMTs', another technology, *silicon photon multipliers* (SiPM), has TOF capabilities. The co-registration between PET and CT is achieved by way of CT's *Hounsfield units* (HUs). HUs are derived from the attenuation coefficients of the X-ray beam by the various tissues, whereas the MRI image is

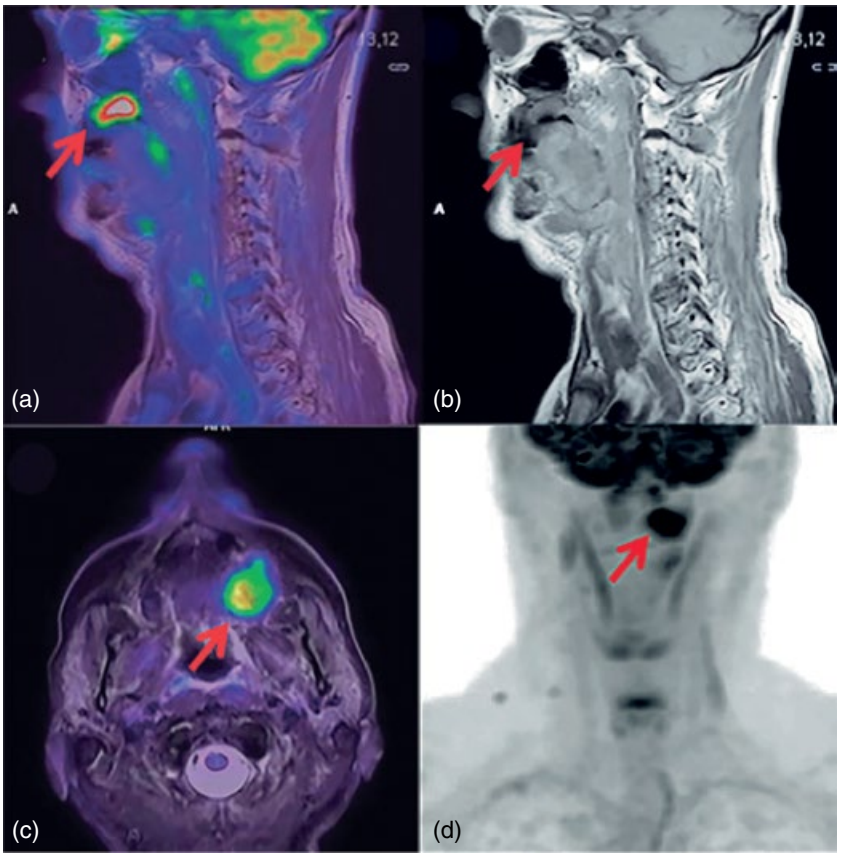


Figure 7.9 Axial fused modalities positron emission tomography (PET) and magnetic resonance imaging (MRI). The red arrows indicate a tumor in the maxillary alveolus. (a) PET/MRI T1-weighted coronal section through the lesions; (b) the equivalent MRI-alone T1-weighted coronal section; (c) PET/MRI T2 weighted with fat saturation axial section; and (d) PET-alone maximum intensity projection image. Source: Vitor, http://www.scielo.br/scielo.php?script=sci_arttext&pid=S1679-45082017000100115&lng=en&nrm=iso&tlng=en. CC BY 4.0.

derived from proton density and relaxation properties. Also, air-filled structures and highly mineralized tissues, such as bone, do not provide a signal on conventional MRI; both appear black. The *attenuation correction* (AC) for CT has been achieved by calculating attenuation maps (μ [Mu] maps), providing appropriate "energy scaling" of CT. HUs are directly converted from the CT's energy level (80–140 keV) by bilinear conversion models to the *linear attenuation coefficients* (LAC) of PET at a 511 keV energy level. For PET/MR this is very different. MR images are segmented into various tissue classes such as fat, water, lungs, and air. A predetermined LAC is then assigned to these in order to derive an attenuation map for subsequent correction of PET emission data during reconstruction. Furthermore, MRI can only be used with smallish head-sized *fields of view* (FOVs), resulting in everything outside the FOV suffering "truncation artifacts." These and other deficiencies have now been addressed by an extensive array of technological developments.

The major advantage of PET/MR, imparting less ionizing radiation, is

particularly valuable for the younger patient with potentially curable malignancies such as lymphomas, since these patients will experience multiple PET studies over the course of their treatment [27]. The other advantages of PET fused with MRI will be enhanced, such as better soft-tissue contrast, MRI-specific contrast media, or even TOF. Figure 7.9 is an example of PET/MR of a tumor arising within the maxillary alveolus [28].

Sekine et al. [29] reviewed PET/CT and PET/MR with regard to their display of those findings which imply obstacles to a cure by local resection. These findings were T4b stage (mediastinal invasion, invasion of the prevertebral space, and vascular encasement), invasion of the laryngeal cartilage, invasion of the pre-epiglottic fat pad, perineural spread, orbital invasion, bone infiltration, skull base invasion, dural infiltration, and invasion of the brachial plexus. After finding no statistical difference in the sensitivity, specificity, and accuracy of these factors for either lesion or patient, Sekina et al. pronounced that "contrast-enhanced PET/MRI and contrast-enhanced PET/CT can serve as reliable examinations for defining local resectability of head and neck cancer" [29].

References

1. Rohren, E.M., Turkington, T.G., and Coleman, R.E. (2004). Clinical applications of PET in oncology. *Radiology* 231: 305–332.
2. Hess, S., Blomberg, B.A., Zhu, H.J. et al. (2014). The pivotal role of FDG-PET/CT in modern medicine. *Acad. Radiol.* 21: 232–249.
3. Beadsmoore, C., Newman, D., MacIver, D., and Pawaroo, D. (2015). Positron emission tomography computed tomography: a guide for the general radiologist. *Can. Assoc. Radiol. J.* 66: 332–347.
4. Shimamoto, H., Tatsumi, M., Kakimoto, N. et al. (2008). (18)F-FDG accumulation in the oral cavity is associated with periodontal disease and apical periodontitis: an initial demonstration on PET/CT. *Ann. Nucl. Med.* 22: 587–593.
5. Kuhlman, J.E., Perlman, S.B., Weigel, T. et al. (2004). PET scan-CT correlation: what the chest radiologist needs to know. *Curr. Probl. Diagn. Radiol.* 33: 171–188.
6. Pasha, M.A., Marcus, C., Fakhry, C. et al. (2015). FDG PET/CT for management and assessing outcomes of squamous cell cancer of the oral cavity. *AJR Am. J. Roentgenol.* 205: W150–W161.
7. Pak, K., Cheon, G.J., Nam, H.Y. et al. (2014). Prognostic value of metabolic tumor volume and total lesion glycolysis in head and neck cancer: a systematic review and meta-analysis. *J. Nucl. Med.* 55: 884–890.
8. de Galiza Barbosa, F., Delso, G., Ter Voert, E.E. et al. (2016). Multi-technique hybrid imaging in PET/CT and PET/MR: what does the future hold? *Clin. Radiol.* 71: 660–672.
9. Conti, M. (2011). Focus on time-of-flight PET: the benefits of improved time resolution. *Eur. J. Nucl. Med. Mol. Imaging* 38: 1147–1157. Erratum in: *Eur. J. Nucl. Med. Mol. Imaging* 2011;38:1171.
10. Facey, K., Bradbury, I., Laking, G., and Payne, E. (2007). Overview of the clinical effectiveness of positron emission tomography imaging in selected cancers. *Health Technol. Assess.* 11: iii–iv. xi–267. https://doi.org/10.3310/hta11440.
11. Isles, M.G., McConkey, C., and Mehanna, H.M. (2008). A systematic review and meta-analysis of the role of positron emission tomography in the follow up of head and neck squamous cell carcinoma following radiotherapy or chemoradiotherapy. *Clin. Otolaryngol.* 33: 210–222.
12. Han, A., Xue, J., Hu, M. et al. (2012). Clinical value of 18F-FDG PET-CT in detecting primary tumor for patients with carcinoma of unknown primary. *Cancer Epidemiol.* 36: 470–475.
13. Scarsbrook, A.F. and Barrington, S.F. (2016). PET-CT in the UK: current status and future directions. *Clin. Radiol.* 71: 673–690.

14. Schwenzer, N.F. and Pfannenberg, A.C. (2015). PET/CT, MR, and PET/MR in lymphoma and melanoma. *Semin. Nucl. Med.* 45: 322–331.
15. Wu, L.M., Chen, F.Y., Jiang, X.X. et al. (2012). 18F-FDG PET, combined FDG-PET/CT and MRI for evaluation of bone marrow infiltration in staging of lymphoma: a systematic review and meta-analysis. *Eur. J. Radiol.* 81: 303–311.
16. Azad, G.K. and Cook, G.J. (2016). Multitechnique imaging of bone metastases: spotlight on PET-CT. *Clin. Radiol.* 71: 620–631.
17. Owosho, A.A., Xu, B., Kadempour, A. et al. (2016). Metastatic solid tumors to the jaw and oral soft tissue: a retrospective clinical analysis of 44 patients from a single institution. *J. Craniomaxillofac. Surg.* 44: 1047–1053.
18. Love, C. and Palestro, C.J. (2016). Nuclear medicine imaging of bone infections. *Clin. Radiol.* 71: 632.
19. Bhatnagar, P., Subesinghe, M., Patel, C. et al. (2013). Functional imaging for radiation treatment planning, response assessment, and adaptive therapy in head and neck cancer. *Radiographics* 33: 1909–1929.
20. Ehman, E.C., Johnson, G.B., Villanueva-Meyer, J.E. et al. (2017). PET/MRI: where might it replace PET/CT? *J. Magn. Reson. Imaging* 46: 1247–1262. https://doi.org/10.1002/jmri.25711.
21. Beyer, T. and Townsend, D.W. (2006). Putting "clear" into nuclear medicine: a decade of PET/CT development. *Eur. J. Nucl. Med. Mol. Imaging* 33: 857–861.
22. Haerle, S.K., Schmid, D.T., Ahmad, N. et al. (2011). The value of (18)F-FDG PET/CT for the detection of distant metastases in high-risk patients with head and neck squamous cell carcinoma. *Oral Oncol.* 47: 653–659.
23. El-Galaly, T.C. and Hutchings, M. (2015). Imaging of non-Hodgkin lymphomas: diagnosis and response-adapted strategies. *Cancer Treat. Res.* 165: 125–146.
24. Cheson, B.D., Fisher, R.I., Barrington, S.F. et al. (2014). Recommendations for initial evaluation, staging, and response assessment of Hodgkin and non-Hodgkin lymphoma: the Lugano classification. *J. Clin. Oncol.* 32: 3059–3068.
25. Bertagna, F., Nicolai, P., Maroldi, R. et al. (2015). Diagnostic role of (18)F-FDG-PET or PET/CT in salivary gland tumors: a systematic review. *Rev. Esp. Med. Nucl. Imaging Mol.* 34: 295–302.
26. Boellaard, R. and Quick, H.H. (2015). Current image acquisition options in PET/MR. *Semin. Nucl. Med.* 45: 192–200.
27. Sotoudeh, H., Sharma, A., Fowler, K.J. et al. (2016). Clinical application of PET/MRI in oncology. *J. Magn. Reson. Imaging* 44: 265–276.
28. Vitor, T., Martins, K.M., Ionescu, T.M. et al. (2017). PET/MRI: a novel hybrid imaging technique. Major clinical indications and preliminary experience in Brazil. *Einstein (Sao Paulo)* 15: 115–118.
29. Sekine, T., Barbosa, F.G., Delso, G. et al. (2017). Local resectability assessment of head and neck cancer: positron emission tomography/MRI versus positron emission tomography/CT. *Head Neck* 39: 1550–1558. https://doi.org/10.1002/hed.24783.

Chapter 8

Basics of ultrasound

8.1 Introduction

Ultrasound or *ultrasonography* (US) has become a common applied modality in *oral and maxillofacial radiology* (OMFR) [1, 2]. The main advantages of US, as a diagnostic tool, are that it is not invasive or painful and imparts no potentially harmful energy to the patient, unlike ionizing radiation [3]. On the other hand, though cheaper and generally more accessible than other cross-sectional technology, the steep and fairly long learning curve means it cannot be competently used by many practitioners until they have acquired sufficient experience in its use [4]. In addition to its primary diagnostic role, US has been also used as a therapeutic instrument. This takes two quite different technical approaches. The first and most frequent approach is to use standard diagnostic US to guide microsurgery, usually mediated by baskets and microforceps to capture and deliver calculi situated within the duct or hilum, or by the use of boogies or balloons to dilate strictures within the duct [5]. The second approach is to use *lithotripsy* to break up larger calculi, which cannot be delivered by the first method. The first approach may subsequently be employed to capture and deliver the now-fragmented calculi [6, 7].

8.2 Overview of Ultrasound Technology and Terminology

US is a medical imaging technique that uses high-frequency sound waves and their echoes. Since sound waves require a medium to propagate, their interactions will depend upon the densities of media encountered and the interfaces between them. Although the range of diagnostic US lies within 1–20 MHz, which is well above the upper acoustic limit of human hearing of 20 kHz, the more usual range for diagnostic head and neck US is 7.5–15 MHz [8].

The technology is complex and relies upon a range of physical properties that include electronic and mechanical physics in addition to the obvious physical properties of sound such as frequency, wavelength, period, and amplitude. Figure 8.1 sets out the main physical properties and some of their important relationships.

A wave cycle is composed of a whole crest and a whole trough. A whole wave cycle constitutes a *period*, which begins at a particular point on a cycle and ends at a corresponding point, denoting the beginning of the next cycle. The *wavelength* (λ) is the entire distance or length of a complete cycle. The *frequency* (f) is the number of complete wavelengths that pass a point within a second.

Oral and Maxillofacial Radiology: A Diagnostic Approach, Second Edition. Edited by David MacDonald.
© 2020 John Wiley & Sons, Inc. Published 2020 by John Wiley & Sons, Inc.

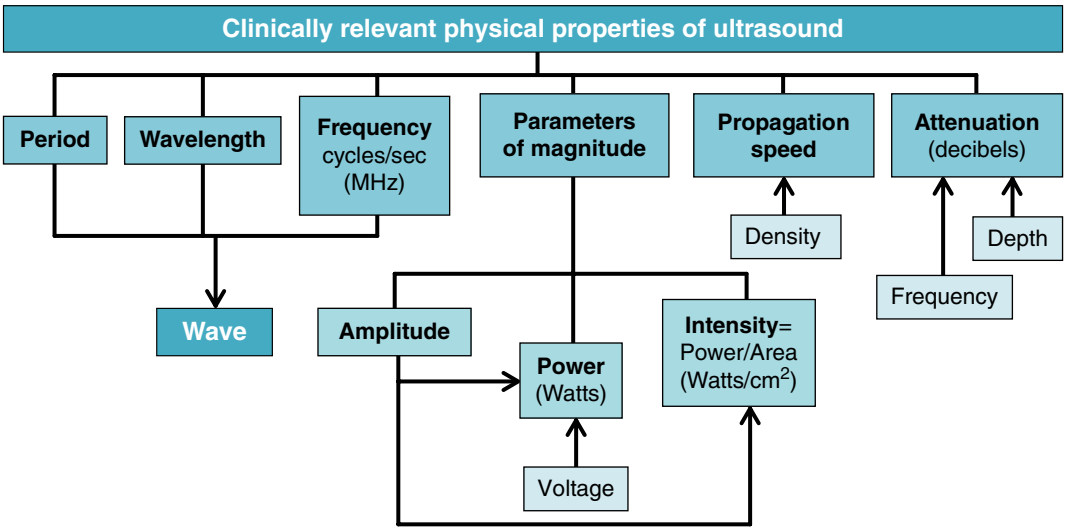


Figure 8.1 Flowchart revealing most of the most relevant physical properties of ultrasound and some of their relationships.

A US scanner transducer converts electrical energy into sonic energy. The *piezoelectric* crystal, the most important component of the transducer, undergoes rapid changes in thickness in response to an electric current. Such changes induce the sound waves, which then enter the patient. Upon receipt of the reflected-back US energy, that very same piezoelectric crystal again changes shape. This time, the change in shape produces an electric current which conveys the clinical information onward for amplification and processing, until it is finally displayed on the monitor as a real-time clinical image.

Each tissue has a different *acoustic impedance* (Z). Z is a measure of the opposition a medium presents to the transmission of sound through it. Z is directly proportional to the medium's density and to the frequency of the US beam. Sound travels faster through solids than through liquids and through air. Therefore, as disease can change the tissue's density, it will also change its Z. When the US wave reaches an interface between two structures with different densities (therefore Zs), more ultrasound energy is reflected back rather than transmitted onward into the second structure. Furthermore, some of the onwardly transmitted sound wave will be attenuated by the second tissue/structure. *Attenuation* in a homogeneous medium is mainly *absorption*, whereas in a heterogeneous medium *scattering* also becomes important. The proportion attenuated will depend upon both the density of this second material and the velocity of the sound wave. The higher the frequency, the greater the attenuation and the less deep will be the investigation. On the other hand, the higher the frequency, the better the spatial resolution. Therefore, more superficially accessible organs such as the eyes can be investigated to a higher spatial resolution by a higher frequency, whereas deeper structures such as lymph nodes of the neck need a lower frequency in order that they may be reached and therefore imaged. The resultant images of the latter will not be at such a high spatial resolution.

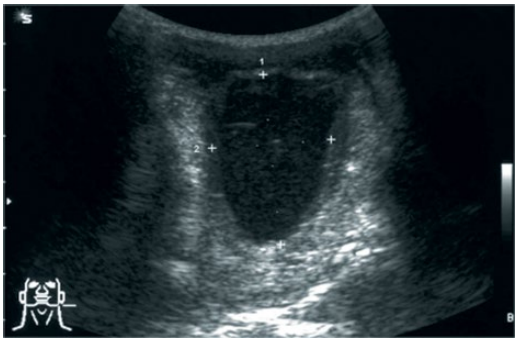


Figure 8.2 Ultrasound of a dermoid cyst. The magnetic resonance images of the case are displayed in Figure 6.10.

Figure 8.2 displays a US of a dermoid cyst in the tongue as an example of the use of US for investigation of an oral cyst.

Thus, in a case of a salivary calculus or a *calcified carotid artery atheroma* (CCAA), the interface between the liquid-like tissue (which includes most soft tissue) and the calculus or CCAA is very bright (*hyperechoic*), representing most of the energy being reflected back to the transducers, whereas the soft tissue immediately behind these structures is dark in comparison to soft tissue of a similar distance to the transducer. This dark (*hypoechoic*) area or signal void is often called the *acoustic shadow* (see Figure 12.17) [9–11].

8.3 Ultrasound Equipment

US equipment is designed to address different functions or modes. The two main ones are B mode, *brightness mode*, which produces grayscale images, and Doppler, which allows blood flow to be determined by a color depending upon whether the blood is flowing toward or away from the transducer. These are often combined in the same unit to produce Duplex ultrasound (see Figures 12.17–12.19) [9–11].

A US unit is made up of transmitter/receiver probe, coaxial cable, acquisition system, and computer. There are four types of probes [12]: curvilinear, linear, intra/endocavitary, and phased array probes. Curvilinear probes produce a fan-shaped beam and a low frequency (2–5 MHz – deepest penetration), used for examinations of the abdomen and pelvis or trauma cases. The linear probe and its higher frequency (6–15 MHz) are used for superficial examinations, including salivary glands. The intra/endocavitary probe uses a wide curvilinear array, but with a high frequency (8–13 MHz), and is used mainly for detailed pelvic examinations. Although generally utilized in transvaginal US for pregnancies, it has been used to detect peritonsillar abscesses. The phased array with its lower frequency (1–5 MHz) is used again for abdominal and pelvic examinations and trauma cases, and also for children [12].

8.4 Applications of Ultrasound

US has been used to diagnose calculi and other pathology affecting the submandibular and parotid glands [1, 2]. Figure 8.2 shows a dermoid cyst within the tongue, and Figures 13.4–13.10 and 13.18 display normal glands, Sjogren's, IgG4 disease, radiation-induced sialadenitis, cysts, mumps, juvenile parotiditis, and Warthin's tumor, respectively.

8.4.1 INTERVENTIONAL SIALOGRAPHY

Calculi, if small enough, can be retrieved by a wire basket under US guidance. This can all be achieved under local anesthesia in the dental chair in an outpatient facility. The only surgery required is of the ostium to facilitate delivery of the basket

containing the stone [3]. Microforceps can also be used instead of baskets.

8.4.2 LITHOTRIPSY

Lithotripsy breaks the larger calculi by therapeutic US. *Extracorporeal shock wave lithotripsy* (ESWL) is a procedure used to shatter simple stones [5]. Pulses of ultrasonic waves are passed through the body until they strike the dense stones, which they pulverize so that they are more easily passed out of the gland and its duct by the salivary flow. It is generally now only used on parotid calculi, except in cases of calculi within the submandibular gland. The lithotripter is placed on the overlying skin, with cotton wool in the buccal sulcus to protect the teeth. Each session lasts one hour, with a week between sessions.

The range of US for lithotripsy operates at several *mega-Pascals* (MPa) [3]. The Pascal is the unit of pressure used to quantify internal pressure, stress, Young's modulus, and ultimate tensile strength. It is defined as *one newton per square meter* (N/m^2). The "damage" in this situation is a desired and predicted outcome; undesired damage will be discussed later in the chapter.

8.4.3 ULTRASOUND-GUIDED FINE NEEDLE ASPIRATION

Ultrasound-guided fine needle aspiration (UG-FNA) biopsy of lesions of the neck is now indicated when the clinical and radiological findings are uncertain. UG-FNA assists with initial tumor staging and treatment planning, and finally helps in post-therapeutic follow-up [13]. UG-FNA is reported to have high sensitivity and specificity for salivary gland neoplasms [14].

A major challenge for UG-FNA of the neck is the presence of major blood vessels such as the carotid arteries and jugular veins. In trained hands not only are these avoided by real-time grayscale US, assisted by Doppler US, but the needle tip can be directed to the most desired site for sampling. This means that cystic areas are avoided, as they are less likely to contain the neoplastic cells required for diagnosis. Although FNA of a salivary gland is unlikely to reveal the precise type, since there are currently 36 World Health Organization–recognized salivary gland neoplasms (with the prospect of more in the near future [14–16]), the purpose of FNA is to assist in treatment planning and initial therapy by determining whether the lesion is neoplastic or non-neoplastic and, if neoplastic, to differentiate benign and low-grade malignant lesions from high-grade malignant lesions [14].

While lymph node and salivary glands are readily assessable to UG-FNA, they can lie up to 3 cm deep under the skin surface. Nevertheless, due to compression of overlying tissue by the transducer [17], this depth may be no more than 2 cm. On the other hand, those which are deeper sited or are obstructed by the mandible, such as the parapharyngeal regions, are not accessible to UG-FNA using a linear probe. Although Lorenzo et al. have suggested these be sampled under sedation and by CT guidance as they are painful, recently a few have been successfully accessed by the use of intra/endocavitary transducers [17]. Fornage et al. were able to localize and sample masses in the retropharyngeal space in patients with a history of head and neck cancer [18].

8.4.4 DOPPLER

Riccabona notes that "Doppler ultrasonography relies on the frequency shift that occurs when the sound is reflected by a moving surface. An analysis of this frequency shift will

allow calculation of flow direction and the velocity" [19]. Doppler US is used in conjunction with grayscale US in duplex US for carotid artery flow, to assess the degree of stenosis caused by atheromatous plaques in the tunica intima of the common and internal carotid arteries (Figures 12.17–12.19) [9–11]. Figures 13.6 and 13.9 are other examples of the use of Doppler US in the oral and maxillofacial region. The direction of blood flow is shown in different colors on the screen. Doppler US occurs when the object reflecting the US waves is moving; it creates a higher frequency if it is moving toward the probe and a lower frequency if it is moving away from the probe. How much the frequency is changed depends upon how fast the object is moving.

Doppler US has recently been used intraorally. Ariji et al. have determined that its application to early-stage oral cancers may identify predictive factors for neck lymph node metastasis [20].

8.4.5 CONTRAST-ENHANCED ULTRASOUND

Contrast-enhanced US using nontargeted contrast microbubbles already has an established role in the clinic for the assessment of myocardial function and perfusion, as well as the detection and characterization of focal liver lesions. Mansour et al. used contrast-enhanced US along with other modalities in their multimodal pathway [21]. They found this method useful in predicting the status of over 200 parotid gland lesions (80% were neoplasms) and to reduce the number of repeat surgeries. They also included sonoelastography (Figure 8.3).

8.4.6 SONOELASTOGRAPHY

US elastography or sonoelastography is a noninvasive imaging technique for evaluating cervical lymph nodes. It operates on the principle that different tissues display varying degrees of strain when subjected to a force delivered by US. Since metastatic lymph nodes display more stiffness than benign lymph nodes, sonoelastography may be able to differentiate benign from malignant cervical lymph nodes [22]. Choi et al. stated that "for US elastography to be accepted into clinical practice, however, its techniques, associated diagnostic criteria, and reliability need to be further refined" [22]. Nakayama et al. reported no difference between genders in the *elasticity index* (EI) of the masseters of young healthy volunteers [23]. The only change occurred when the muscles were clenched [23]. Figure 8.3 illustrates the use of Duplex US (gray scale + Doppler US) and sonoelastography.

8.5 Limitations of Ultrasonography

8.5.1 ARTIFACTS

Because the US image is a result of calculations rather than a photograph, it may produce artifacts that detract from the appreciation of the anatomy and attendant pathology. Generally, US design incorporates six assumptions: that sound waves travel in straight lines; that they go directly to a reflector and back; that they move through soft tissue at exactly 1540 m/s; that the imaging plane is very thin; that the reflection only occurs from structures in the beam's main axis; and that the strength of the reflection is related to the tissue characteristics. If any of these six assumptions are not met, then an artifact could occur [24].

Nevertheless, these artifacts are so well understood that they are utilized to enhance the diagnosis. The presence of the aforementioned "shadowing" confirms

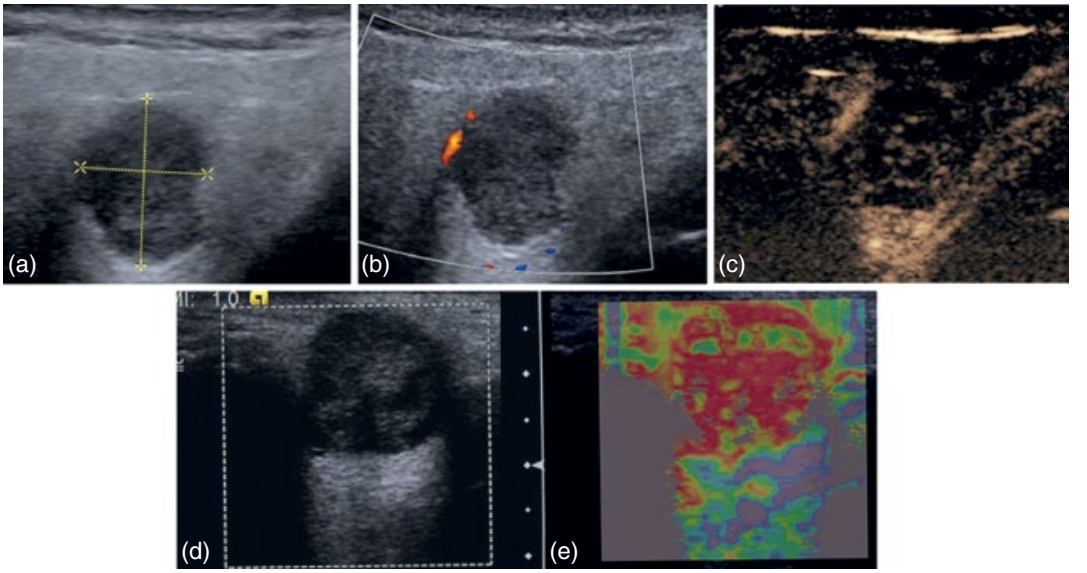


Figure 8.3 (a) Pleomorphic adenoma of the right parotid gland on B-mode (gray scale) ultrasound (US) with sharp borders and hypoechoic echotexture. (b) Color-coded duplex sonography with weak peripheral vessel formation. (c) Contrast-enhanced US with delayed perfusion kinetics compared to the circumjacent parotid tissue. (d) Accompanying B-node US to (e) real-time sonoelastography with a stiff pattern compared to the circumjacent healthy parotid tissue in (d). Mansour, N., Bas, M., Stock, K.F. et al. (2017). Multimodal ultrasonographic pathway of parotid gland lesions. *Ultraschall. Med*. 38: 166–173. [German].

that the hyperechoic structure preceding it is calcified (Figures 12.17 and 13.13a). In the face, jaws, and neck, these are salivary duct calculi and CCAAs. Other artifacts which happen elsewhere outside the face, jaw, and neck are edge, mirror, and reverberation artifacts [24].

8.5.2 INTEROBSERVER VARIATION

Another limitation is interobserver variation. This arises because of differing probe handling and the difficulty in establishing a standardized approach. This is further complicated by the steep learning curve that must be addressed by the neophyte [4, 25, 26]. Competency in a particular technique may be acquired after over 50 cases. Although one authority has suggested that this expertise be restricted to specialist centers serving communities of 1 to 2 million potential patients [4], McGurk's commentary reveals a number of technical developments which may enhance both competency and effectiveness [27].

8.5.3 RISK OF DAMAGE

The risk of damage to the patient from US for diagnostic purposes is negligible, whereas postprocedure discomfort of therapeutic US is well known. Lithotripsy necessarily destroys stones, whether in the kidney, gall bladder, or salivary gland or duct. This discomfort reflects the necessary transmission of energy to the patient's tissues, energy that can cause both mechanical and thermal effects within the tissues. To this end, such equipment prominently displays the *mechanical index* (MI) and the *thermal index* (TI) for each tissue [19]. Although MI and TI around 1 may be considered safe, caution

must be taken, particularly around the eye and brain and any strong US-reflecting media. In such situations, the operator should use lower parameters [19].

Another US-induced phenomenon is cavitation. Although sound waves are likely to be reflected back strongly from an interface of soft tissue with air, a high pulse frequency of 120 shocks per minute may induce gas/air bubbles in the US field to implode – cavitation – producing a secondary pressure wave which damages the tissues immediately adjacent to it [19].

References

1. Poul, J.H., Brown, J.E., and Davies, J. (2008). Retrospective study of the effectiveness of high-resolution ultrasound compared with sialography in the diagnosis of Sjogren's syndrome. *Dentomaxillofac. Radiol.* 37: 392–397.
2. Marotti, J., Heger, S., Tinschert, J. et al. (2013). Recent advances of ultrasound imaging in dentistry – a review of the literature. *Oral Surg. Oral Med. Oral Pathol. Oral Radiol.* 115: 819–832.
3. Miller, D.L., Smith, N.B., Bailey, M.R. et al. (2012). Bioeffects Committee of the American Institute of Ultrasound in Medicine. Overview of therapeutic ultrasound applications and safety considerations. *J. Ultrasound Med.* 31: 623–634.
4. Farneti, P., Macrì, G., Gramellini, G. et al. (2015). Learning curve in diagnostic and interventional sialendoscopy for obstructive salivary diseases. *Acta Otorhinolaryngol. Ital.* 35: 325–331.
5. Iro, H., Zenk, J., Escudier, M.P. et al. (2009). Outcome of minimally invasive management of salivary calculi in 4,691 patients. *Laryngoscope* 119: 263–268.
6. Escudier, M.P., Brown, J.E., Drage, N.A., and McGurk, M. (2003). Extracorporeal shockwave lithotripsy in the management of salivary calculi. *Br. J. Surg.* 90: 482–485.
7. Zenk, J., Koch, M., Mantsopoulos, K. et al. (2013). The significance of extracorporeal shock wave lithotripsy in sialolithiasis therapy. *HNO* 61: 306–311. [German].
8. Coltrera, M.D. (2010). Ultrasound physics in a nutshell. *Otolaryngol. Clin. North Am.* 43: 1149–1159.
9. MacDonald, D., Chan, A., Harris, A. et al. (2012). Diagnosis and management of calcified carotid artery atheroma: dental perspectives. *Oral Surg. Oral Med. Oral Pathol. Oral Radiol.* 114: 533–547.
10. MacDonald, D., Chan, A., Harris, A. et al. (2013). In reply. *Oral Surg. Oral Med. Oral Pathol. Oral Radiol.* 115: 700–701.
11. MacDonald, D. (2013). How should dentists recognise calcified carotid artery atheromas? *Gerodontology* 30: 169–170.
12. Enriquez, J.L. and Wu, T.S. (2014). An introduction to ultrasound equipment and knobology. *Crit. Care Clin.* 30: 25–45.
13. Jakowski, J.D. and DiNardo, L.J. (2015). Advances in head and neck fine-needle aspiration and ultrasound technique for the pathologist. *Semin. Diagn. Pathol.* 32: 284–295.
14. Pusztaszeri, M.P., García, J.J., and Faquin, W.C. (2016). Salivary gland FNA: new markers and new opportunities for improved diagnosis. *Cancer Cytopathol.* 124: 307–316.
15. Pusztaszeri, M.P. and Faquin, W.C. (2015). Cytologic evaluation of cervical lymph node metastases from cancers of unknown primary origin. *Semin. Diagn. Pathol.* 32: 32–41.
16. Pusztaszeri, M.P. and Faquin, W.C. (2015). Update in salivary gland cytopathology: recent molecular advances and diagnostic applications. *Semin. Diagn. Pathol.* 32 (4): 264–274.
17. Lorenzo, G. and Saindane, A.M. (2013). Pitfalls in image guided tissue sampling in the head and neck. *Neuroimaging Clin. N. Am.* 23: 167–178.
18. Fornage, B.D., Edeiken, B.S., and Clayman, G.L. (2014). Use of transoral sonography with an endocavitary transducer in diagnosis, fine-needle aspiration biopsy, and intraoperative localization of retropharyngeal masses. *AJR Am. J. Roentgenol.* 202: W481–W486.
19. Riccabona, M. (2014). Basics, principles, techniques and modern methods in paediatric ultrasonography. *Eur. J. Radiol.* 83: 1487–1494.
20. Ariji, Y., Goto, M., Fukano, H. et al. (2015). Role of intraoral color Doppler sonography

in predicting delayed cervical lymph node metastasis in patients with early-stage tongue cancer: a pilot study. *Oral Surg. Oral Med. Oral Pathol. Oral Radiol.* 119: 246–253.
21. Mansour, N., Bas, M., Stock, K.F. et al. (2017). Multimodal ultrasonographic pathway of parotid gland lesions. *Ultraschall. Med.* 38: 166–173. [German].
22. Choi, Y.J., Lee, J.H., and Baek, J.H. (2015). Ultrasound elastography for evaluation of cervical lymph nodes. *Ultrasonography* 34: 157–164.
23. Nakayama, M., Ariji, Y., Nishiyama, W., and Ariji, E. (2015). Evaluation of the masseter muscle elasticity with the use of acoustic coupling agents as references in strain sonoelastography. *Dentomaxillofac. Radiol.* 44: 20140258.
24. Shriki, J. (2014). Ultrasound physics. *Crit. Care Clin.* 30: 1–24.
25. Steck, J.H., Stabenow, E., Volpi, E.M., and Vasconcelos, E.C. (2016). The learning progression of diagnostic sialendoscopy. *Braz. J. Otorhinolaryngol.* 82: 170–176.
26. Modest, M.C., Galinat, L., Rabinowitz, M.R. et al. (2014). Learning progression in the use of sialendoscopy for sialolithiasis: effect on gland preservation. *Otolaryngol. Head Neck Surg.* 151: 240–245.
27. McGurk, M. (2016). Commentary: clinical evaluation of a two-incision fistula technique for the treatment of oral ranulas. *Br. J. Oral Maxillofac. Surg.* 54: 25.

Part 3

Radiological pathology of the jaws



Chapter 9
Radiolucencies

9.1 Introduction

A radiolucency is the black or darker area within a bone on a conventional radiograph. It suggests an osteolytic process, particularly when it presents in bone. Although the radiology, including the application of *cone-beam computed tomography* (CBCT), of the most important and/or frequent lesions producing radiolucencies in the bones of the face and jaws were overviewed recently [1], this chapter will address these and other lesions in more detail. The chapter will also compare their clinical, radiological, and treatment outcomes as they present in the four global groups as discussed and cartographically displayed in Chapter 1. Most lesions associated with this process remain radiolucent, whereas some, although completely radiolucent in their earliest stage, subsequently acquire a central opacity or opacities, or eventually become completely radiopaque. The latter are more fully addressed in Chapter 10. The radiolucent stage associated with this group of lesions may be understood as analogous to the clearing of a building site and excavating to establish the foundations of the new building to be erected. That building is the subsequent radiopacity.

Conventional panoramic radiography plays a prominent role in the evaluation of a lesion. It may be prescribed for further evaluation of a lesion already apparent on the clinical examination of intraoral conventional radiography, or may display a lesion that had not been suspected; the lesion is an incidental finding. In either case, the "lesion" may be an artifact (Figure 9.1).

The overwhelming proportion of radiolucencies in the jaws, particularly the mandible and maxillary alveolus, reflect lesions arising within the jawbones, but some reflect lesions arising outside the jawbones and secondarily invading them, as in the case of *squamous cell carcinomas* (SCCs) arising in the overlying or adjacent mucosal epithelium (Figure 9.2) or eroding them, as in cases of *systemic sclerosis* (SSc) (Figures 9.3 and 9.4), or by an osteolytic disease such as *Gorham's disease* (Figure 9.5). Before addressing these lesions, an overview of the most frequent and/or important lesions that present as radiolucencies arising within the face and jaws is necessary to orientate the reader.

There are four editions of the *World Health Organization's* (WHO) classification of lesions of the jaws, which will be referred to by the date of their publication: 1972, 1992, 2005, and 2017.

Oral and Maxillofacial Radiology: A Diagnostic Approach, Second Edition. Edited by David MacDonald.
© 2020 John Wiley & Sons, Inc. Published 2020 by John Wiley & Sons, Inc.

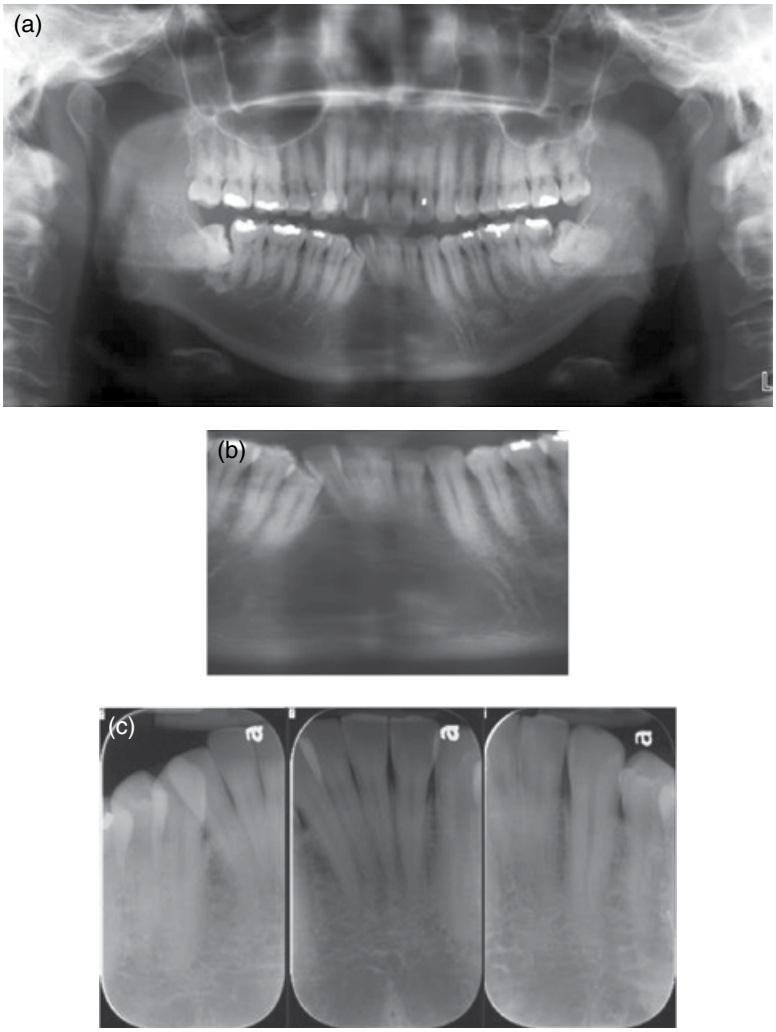


Figure 9.1 Panoramic radiograph (a) revealing a radiolucency in the anterior sextant of the mandible. The cropped-down image (b) shows that this radiolucency has a well-defined superior margin and is associated with displaced lower incisors. Periapical radiographs prescribed afterwards revealed that the "lesion" was an artifact. The "a" in (c) is a manufacturer's mark for its phosphor plate detectors (see Table 2.1).

9.2 Overview of the Most Frequent and/or Important Lesions

This overview will be performed with the assistance of flowcharts. In addition, to give the reader some idea of the relative frequencies of these lesions, the relative period prevalences (RPPs, discussed in Chapter 1) of the majority of lesions appearing in children and adolescents [2] and in adults [3] are set out in Table 9.1, beginning with those with the highest RPP. The reader should be aware that these RPPs reflect specimens obtained

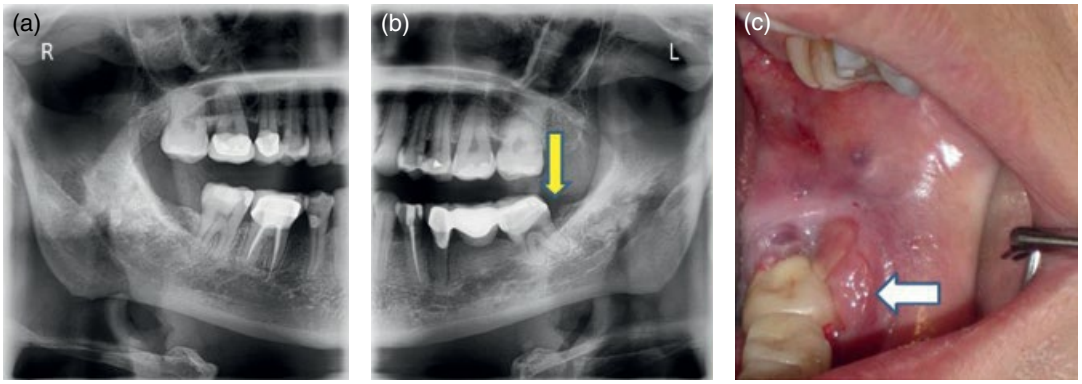


Figure 9.2 "Bitewing mode" panoramic radiograph (a and b) displaying multiple poorly defined radiolucencies in the left alveolus, caused by a metastasis from a breast carcinoma (compare with the relatively normal right side). The yellow arrow indicates an irregularly shaped defect distal to the last molar tooth. Intraoral clinical photograph (c) revealing the metastatic lesion at the gingival margin (white arrow) around that last molar tooth. Source: Dr. David Yang, oral and maxillofacial surgeon, British Columbia, Canada.

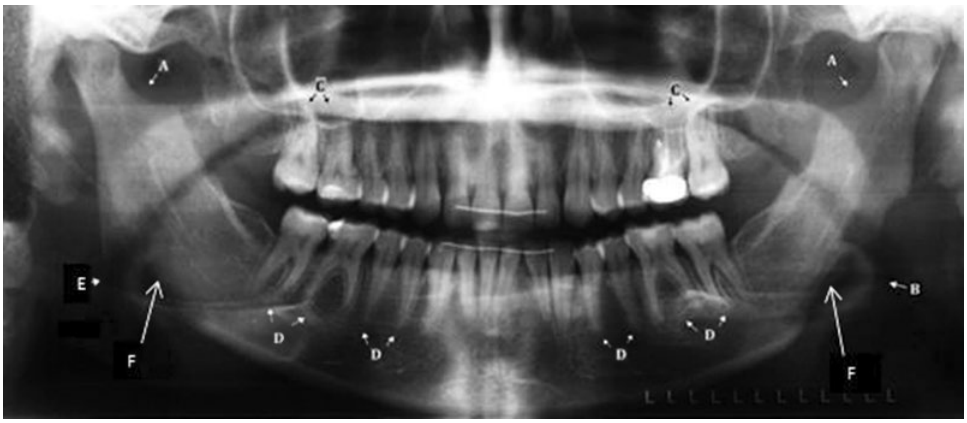


Figure 9.3 Panoramic radiograph of scleroderma (systemic sclerosis) patient with severe erosions at (A) the coronoid processes and (B) the angles of the mandible. Also shown is periodontal ligament space widening in (C) maxillary posterior teeth and (D) mandibular posterior teeth. The distal end of the air-filled space between the dorsum of the tongue and the soft palate, traversing the vertical ramus of the mandible, is indicated at (E). The bilateral erosions of the coronoid processes (including occasionally the anterior margin of the adjacent vertical ramus) are easily distinguished from the superimposed nasopharyngeal airway, whereas the erosions of the vertical ramus need to be distinguished, particularly on the right from the superimposed air-filled space delineating the dorsum of the tongue and the vallecula (F), delineated in turn by the epiglottis. Note 1: Widening of the periodontal ligament spaces is another important indicator of this serious disease. Note 2: Although the technique is very good, the hyoid bones are superimposed upon the body of the mandible. Source: Reproduced with permission from Dagenais, M., MacDonald, D., Barron, M., et al. (2015). The Canadian Systemic Sclerosis Oral Health Study IV: oral radiographic manifestations in systemic sclerosis compared with the general population. *Oral Surg. Oral Med. Oral Pathol. Oral Radiol.* 120: 104–111.

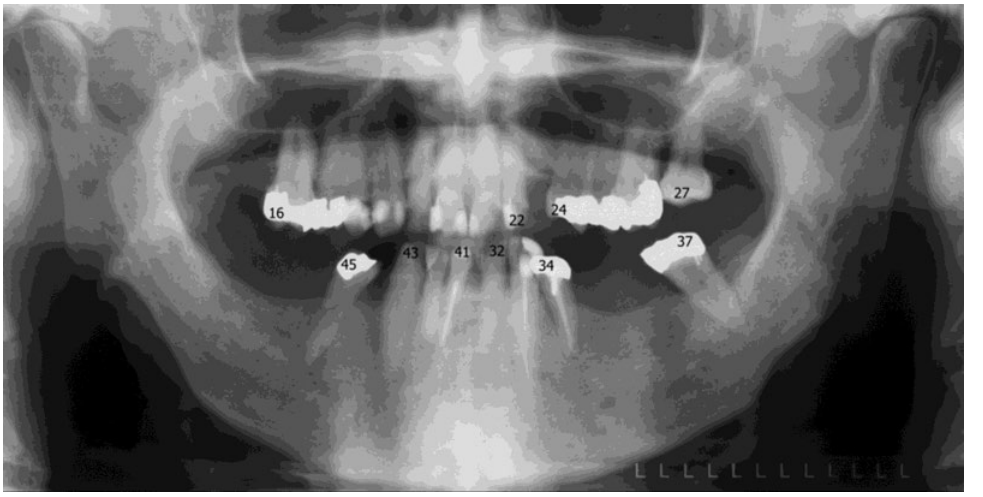


Figure 9.4 Panoramic radiograph of scleroderma (systemic sclerosis) patient with severe bilateral erosions, particularly at the digastric areas. Note: The dental notation is that of the Fédération Dentaire Internationale and has been set out in Figure 1.21. Source: Courtesy of Dr. Mervyn Gornytsky, Jewish General Hospital, Montreal, Quebec.

from hospital or related clinics and referred to a major oral pathology institution. As Franklin and Jones remark, "Few *dentists in general or family practice* regularly submit specimens despite the importance of histopathological confirmation of a clinical diagnosis" (my italics) [4]. The reader should also note that the order of appearance of these lesions in this chapter will reflect the order they appear in the diagnostic flowcharts. Lesions that present as multiple lesions or as poorly defined solitary lesions, suggesting a potentially serious outcome, threatening vision or life, will be addressed first.

The flowcharts are based on the best evidence, either from recent systematic reviews or, where those are lacking, traditional narrative reviews or recently reported large case series. As can be seen, particularly in Figures 9.6–9.10, they generally flow from the most important clinical and radiological findings, addressing systemic lesions and malignancies first and then cysts and benign neoplasms. The flowcharts focus on the most common and important lesions, and are not always exhaustive with regard to the rarer lesions, particularly those which respond well to initial treatment – i.e. they do not recur.

Multiple radiolucencies, particularly if they are distributed throughout the jaws, suggest a systemic cause, whereas a single radiolucency suggests a local cause.

The degree of marginal definition is crucial for determining potentially serious disease. If it is well defined, the radiolucency is likely to be a benign neoplasm or a cyst. A poorly defined radiolucency, on the other hand, could represent a malignancy or infection.

Locularity is essentially a feature of radiolucencies: most are either unilocular or multilocular. It is important to differentiate between multilocular and scalloped radiolucencies, because the latter type is a variant of a unilocular radiolucency. Although unilocular radiolucencies are more likely to be odontogenic or simple bone cysts, multilocular radiolucencies

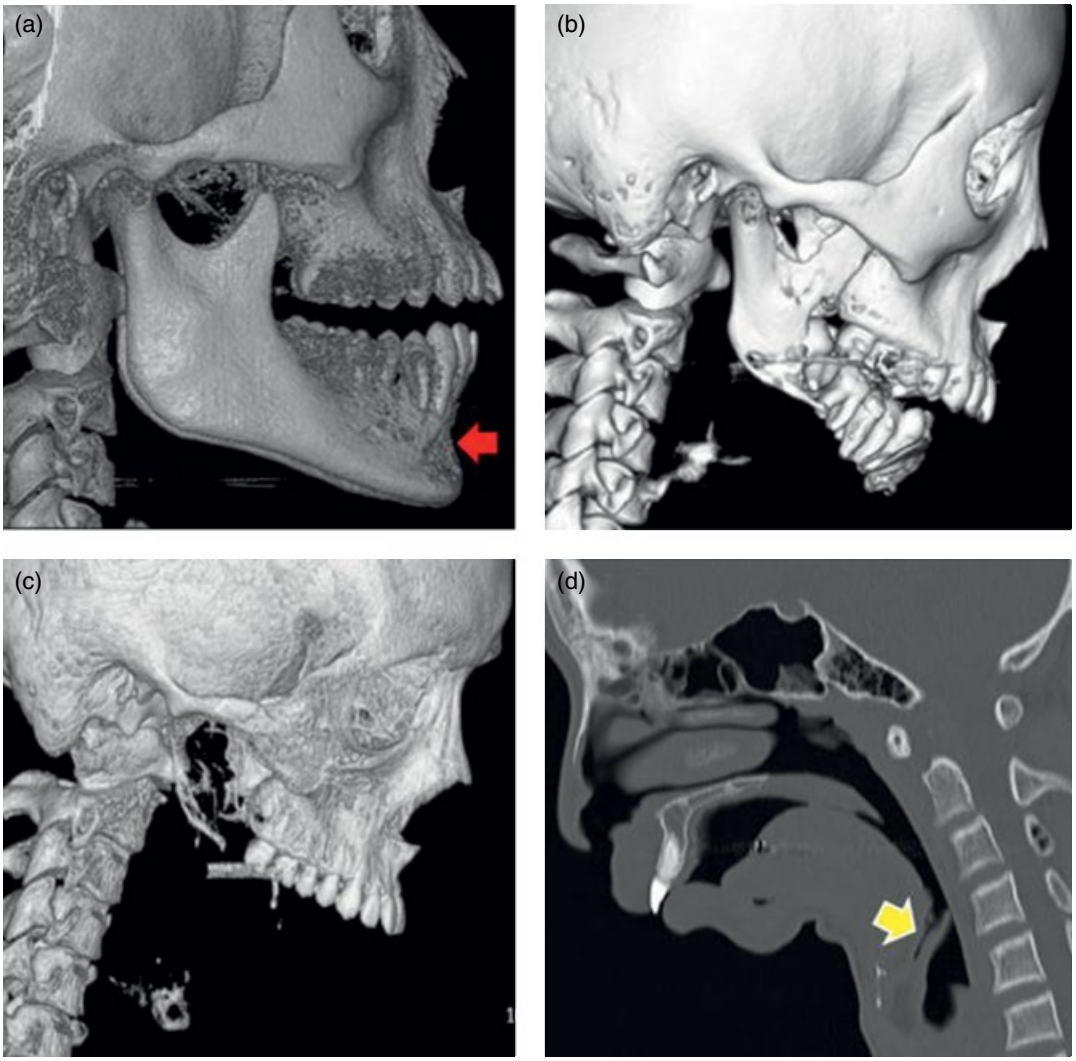


Figure 9.5 Computed tomography of a case of Gorham's disease. (a) The red arrow indicates the osteolysis of the mandible at first in the anterior sextant. (b) A year later that anterior sextant is absent. (c) Another year later the mandible is almost completely absent, as is also the hyoid bone. (d) The yellow arrow indicates the narrowing of the airway. Source: Reproduced with permission from Kim, M.K., Hong, J.R., Kim, S.G., and Lee, S.K. (2015) Fatal progression of Gorham disease: a case report and review of the literature. *J. Oral Maxillofac. Surg.* 73: 2352–2360.

almost always are odontogenic neoplasms. Nevertheless, the early, and therefore dimensionally small, stage of some odontogenic neoplasms may present as a unilocular radiolucency. Multilocular radiolucencies can be characterized according to three patterns: although the soap-bubble and honeycomb would appear to be nonspecific, the tennis racket is virtually pathognomonic of odontogenic myxoma.

The radiolucency's relationship to the mandibular canal or the image of the

Table 9.1 Relative period prevalences of surgical specimens of lesions affecting the face and jaws registered in the pathology files of a major center in the United Kingdom.

Lesions	Child patient/year	Adult patient/year
Malignant tumors	1.0	78.7
Squamous cell carcinoma	0.1	52.0
Periapical granuloma	11.1	56.0
Radicular cyst	7.9	107.6
Dentigerous cyst	5.2	36.4
Odontogenic keratocyst[a]	2.4	19.7
Nasopalatine duct cyst	0.6	7.9
Ameloblastoma	0.3	3.4
Odontogenic myxoma	0.2	0.7
Simple bone cyst	0.6	0.6
Glandular odontogenic cyst	0.0	0.3
Cherubism	0.2	0.0
Nevoid basal cell carcinoma syndrome	0.1	0.0

[a] The majority over 80% in a recent systematic review are keratocystic odontogenic tumors, whereas about 10% are orthokeratinized odontogenic cysts and the remainder exhibit a mixture of parakeratotic and orthokeratotic epithelium.
Source: Data derived from Jones, A.V., Franklin, C.D. An analysis of oral and maxillofacial pathology found in children over a 30-year period. *Int. J. Paediatr. Dent.* 2006;16:19–30 and Jones, A.V., Franklin, C.D. An analysis of oral and maxillofacial pathology found in adults over a 30-year period. *J. Oral Pathol. Med.* 2006;35:392–401.

hard palate (on panoramic or cephalometric radiographs) indicates whether it is likely to be of odontogenic origin. If the radiolucency is above the mandibular canal or below the image of the hard palate, it is within the dental alveolus and therefore likely to be of odontogenic origin. If the radiolucency is sited within the alveolus, its relationship to teeth is important to further refine the differential diagnosis. An association with the root of an erupted tooth, particularly if it has a large carious lesion or a large restoration, suggests the possibility of a necrotic pulp, and then the radiolucency is likely to have an inflammatory cause. This finding/s should be confirmed clinically by dental-pulp vitality testing. If the radiolucency is associated with the crown of an unerupted tooth, a *dentigerous cyst* (DC) or an odontogenic neoplasm (assuming a secondary relationship to it) should be considered.

Almost all true cysts and those neoplasms with a substantial cystic element expand by hydrostatic pressure and are therefore frequently spherical or nearly spherical in shape. Since solid benign neoplasms arise from a single neoplastic cell, they may also initially present with a spherical or nearly spherical shape. This spherical or near spherical shape is achieved by displacing the buccal and lingual cortices and thus causing buccolingual expansion. Odontogenic lesions

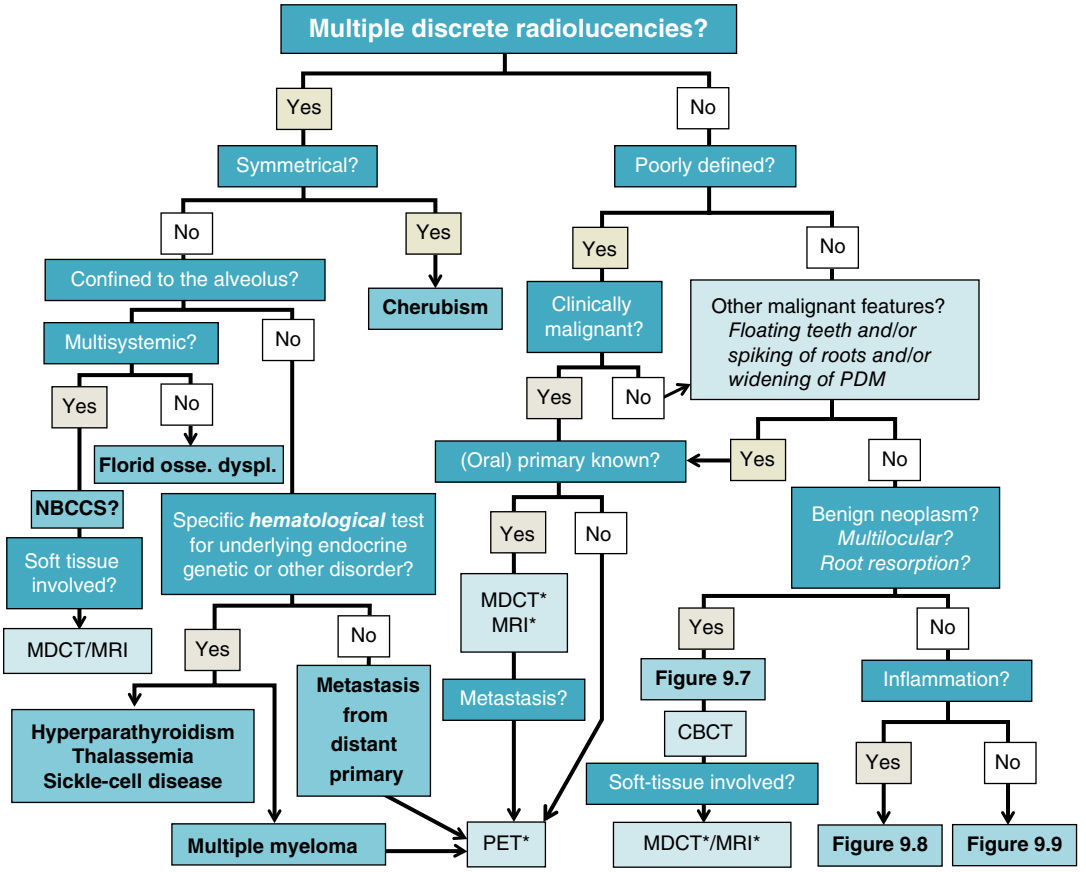


Figure 9.6 Flowchart displaying imaging strategies for radiolucencies initially observed on conventional radiography of the bones of the face and jaws. Multiple radiolucencies indicate that a systemic disease process should be considered and excluded first. Generally, a clinical presentation suggesting malignancy and a poorly defined radiolucency within the affected jawbone should be referred for further advanced imaging. Key: CBCT, cone-beam computed tomography; Florid osse. dyspl., florid osseous dysplasia; MDCT, multidetector computed tomography; MRI, magnetic resonance imaging; NBCCS, nevoid basal cell carcinoma syndrome; PDM, periodontal membrane; PET, positron emission tomography. Modalities marked with an asterisk are mainly sited within medical hospitals and operated under the supervision of medical radiologists, who also supply the reports. MDCT and MRI investigations may be undertaken with the use of intravenous contrast media: iodine based for MDCT and gadolinium based for MRI.

arising within the alveolus, if sufficiently large, will displace the mandibular canal downward. Additionally, all lesions can reduce the diameter of the canal or completely erode its cortex (so that it is no longer visible) if they are enveloping it.

The effect of the radiolucency on the adjacent teeth or anatomical structures is important. This effect is manifested by either displacement or erosion. When applied to teeth, particularly their roots, the latter is termed *root resorption*. Although all

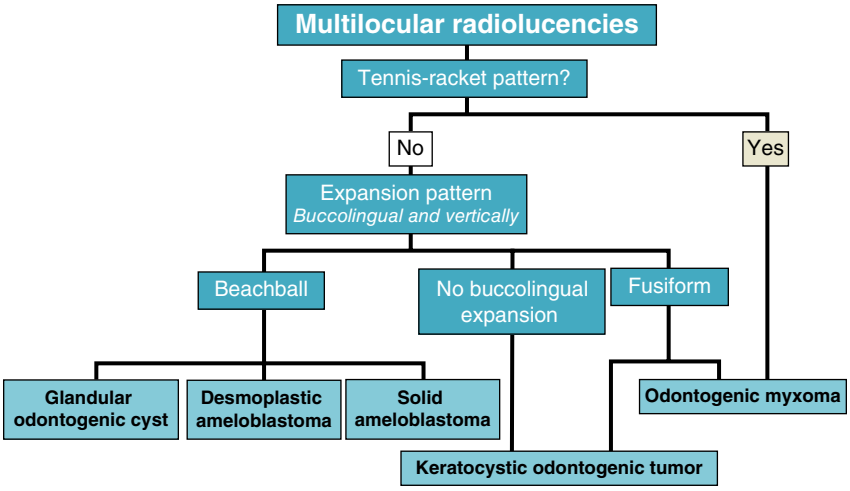


Figure 9.7 Solitary multilocular radiolucency occurring within the bony jaws. A multilocular radiolucent presentation is strongly suggestive of benign neoplastic lesions. Although not all glandular odontogenic cysts are neoplastic, some behave like neoplasms, recurring following surgical treatment, usually enucleation. The tennis-racket pattern, though pathognomic of an odontogenic myxoma, only presents in a small proportion of such cases.

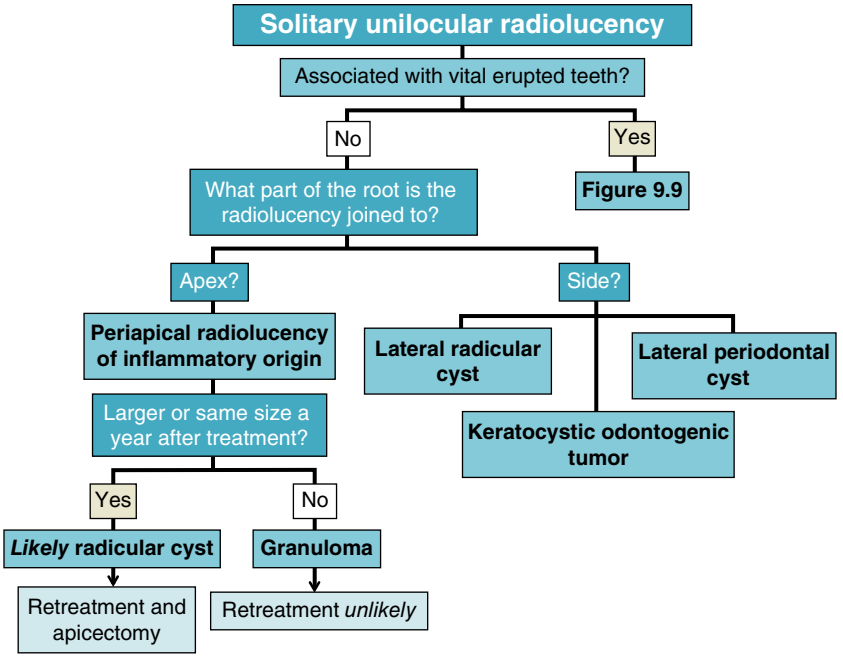


Figure 9.8 Solitary unilocular radiolucency occurring within the bony jaws and its relationship to a nonvital erupted tooth.

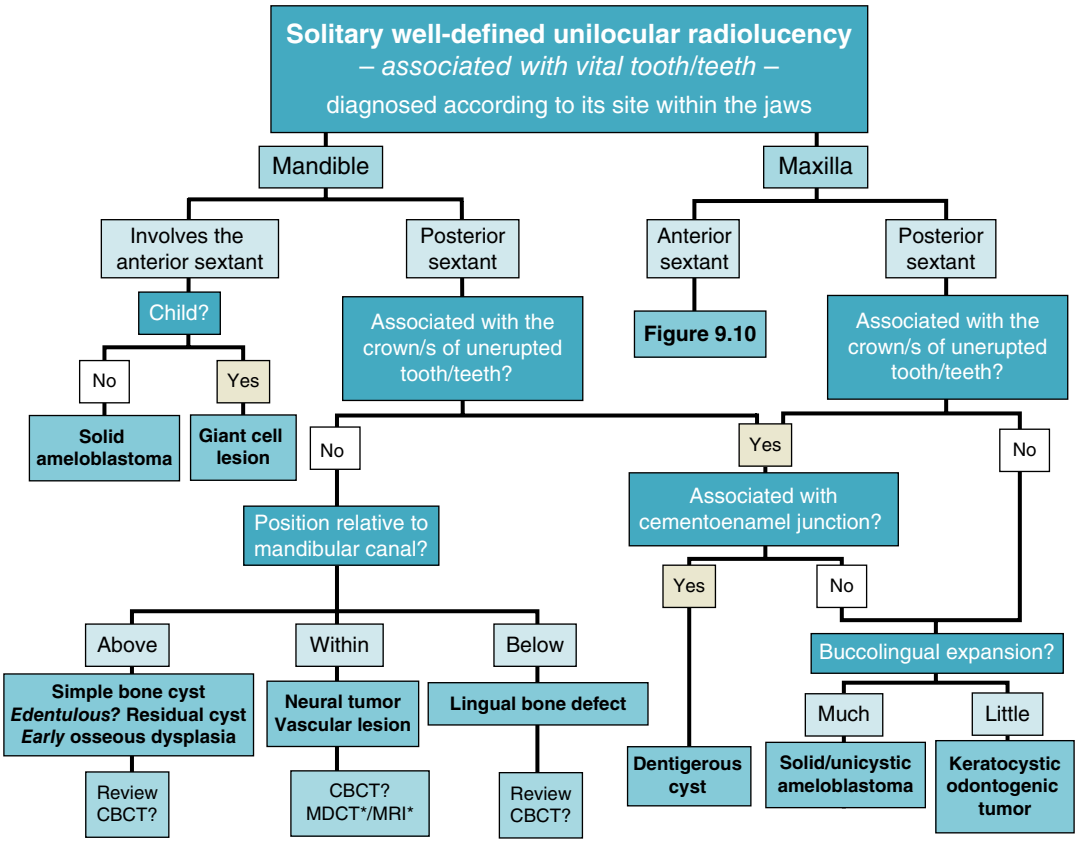


Figure 9.9 Flowchart displaying differential diagnoses of solitary well-defined unilocular radiolucencies initially observed on conventional radiography of the bones of the face and jaws. Key: CBCT, cone-beam computed tomography; MDCT, multidetector computed tomography; MRI, magnetic resonance imaging.

lesions presenting as radiolucencies may in due course cause root resorption, this would appear to be a particular feature of certain odontogenic neoplasms. Displacement of teeth and buccolingual cortices are universal to all expansile lesions.

In addition to conventional radiography, advanced imaging modalities such as fan-beam *computed tomography* (CT) and *magnetic resonance imaging* (MRI) are frequently used to investigate jaw lesions. Fan-beam CT is the basic vehicle for all hospital-based or medical facility–installed CT. Today it is most frequently *multidetector computed tomography* (MDCT; Chapter 4). Although osteolytic lesions and structures are still black on bone-window images made by either fan-beam CT; see Chapter 4) or CBCT (Chapter 5), they appear white on soft-tissue-window CT (Chapter 4) and MRI (see Chapter 6). Furthermore, they may enhance with iodine-based or gadolinium intravenous contrast for CT and MRI, respectively.

The term *significant* will be used only when the feature it is qualifying is $P < 0.05$.

Artifacts causing radiolucencies arise from three main sources: image

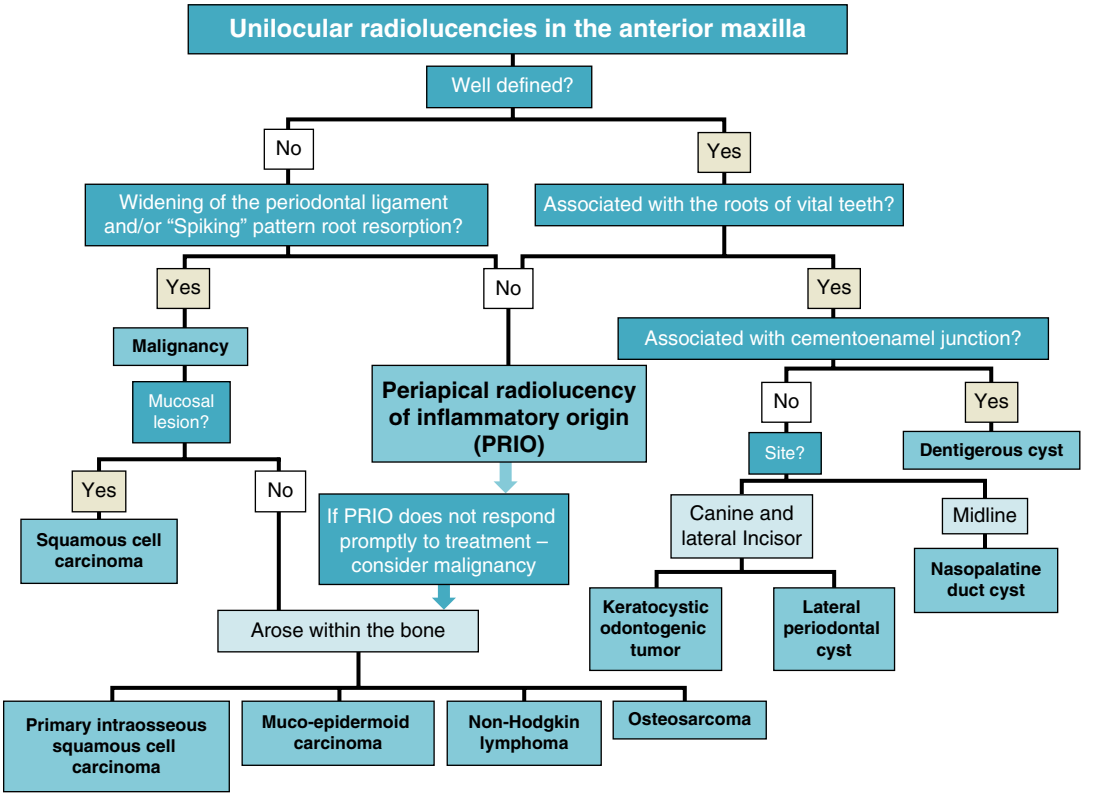


Figure 9.10 Flowchart displaying imaging strategies for unilocular radiolucencies presenting in the alveolus of the anterior sextant of the maxilla.

development, normal anatomy and variants, and earlier treatment. Because these have already been addressed in other texts, they will not be considered further.

9.3 Erosion of the Bones of the Face and Jaws from Disease Processes Arising in the Adjacent Soft Tissues

Although the most important disease which exhibits such erosion is SCC arising from the oral mucosa, including the gingiva, this will be discussed in more detail later in this chapter and again in Chapter 19. Figure 9.2 prompts the reader to consider this lesion whenever there is a suggestion of a malignant lesion. SSc and Gorhan's disease will be addressed at this point.

9.3.1 SYSTEMIC SCLEROSIS

As Dagenais et al. note, SSc, also known as *scleroderma* and *progressive systemic sclerosis* (Figure 9.3), "is a multisystem disorder of the connective tissue characterized clinically by thickening and fibrosis of the skin and involvement of internal organs" [5]. It predominantly (91%) arises in young adult females [6]. The mandibular erosions of SSc occur in 14% of those covered by the most recent and largest multisite cross-sectional study of

SSc [5, 6]. It presents at the attachment of muscles to the condyle, to the coronoid, and to the posterior ramus (Figure 9.3) in 6%, 5%, and 5% of patients, respectively [5]. Figure 9.4 displays bilateral erosions of the digastric areas involving the angles and the posterior margins of the vertical rami. These erosions are symptom free and are therefore likely to be discovered incidentally. Their presentation indicates more advanced disease and should be referred to an appropriate specialist (rheumatologist or dermatologist). Nevertheless, some of these sites need to be distinguished from artifacts on panoramic radiographs arising from the superimposition of air-filled spaces. Another feature of SSc that can be observed in the jaws is widening of the periodontal space. The above study revealed that this occurred in 38% of SSc patients and is significantly associated with severe disease [5, 6]. This widening may reflect generalized overproduction of collagen [6].

9.3.2 GORHAM'S DISEASE

Gorham's disease (also known as Gorham-Stout syndrome) is another important, albeit rare, cause of erosion of the jaws. It is sometimes called *vanishing bone disease*, among many other terms [7]. Its pathogenesis so far is not known. Although Gorham's disease affecting the jaws is of most interest to the oral clinician, it is more common elsewhere in the body, particularly in the skull, shoulder, and pelvis. This disease presents as a painless and progressive osteolysis of the affected bone/s. Figure 9.3 reveals such a case affecting the mandible. In the jaw, most frequently the mandible appears to vanish. A case of Gorham's disease affecting the maxilla has been reported [7]. CT, MRI, and bone scintigraphy been applied to the diagnosis and assessment of this lesion [8]. A recent review of the literature revealed 64 cases affecting the jaws, of which 11% resulted in death from chylothorax (leakage of lymph from the thoracic duct into the pleural cavity) or fractures of the ribs or spine [9].

9.4 Systemic Disease That Produces Radiolucencies in the Face and Jaws

An early consideration in the review of clinical and radiological findings is whether the patient is suffering from a generalized or systemic condition, or whether it is of a local nature. Generalized disease can manifest in the context of radiolucencies by a generalized osteopenia – a reduction in trabeculae, both in number and thickness, and thin cortices, throughout the skeleton, including the jaws, or as a syndrome. The former is represented by metastases from a distant primary, blood dyscrasias, such as lymphomas, Langerhans cell histiocytosis, thalassemia, and sickle cell disease, or endocrine diseases, such as hyperparathyroidism. Nevertheless, the most striking multiple lesions are well-defined radiolucencies associated with two syndromes: *cherubism* and the multiple keratocystic odontogenic tumors of *nevoid basal cell carcinoma syndrome* (NBCCS). We shall consider these first.

9.4.1 CHERUBISM

Jundt defined cherubism as "an autosomal dominant inherited disease that is characterized by a symmetrical distension of the jaws, often leading to a typical facial expression. The histology is indistinguishable from a central giant cell lesion" [10]. He continued, "Although the histology is not specific, the combination of clinical

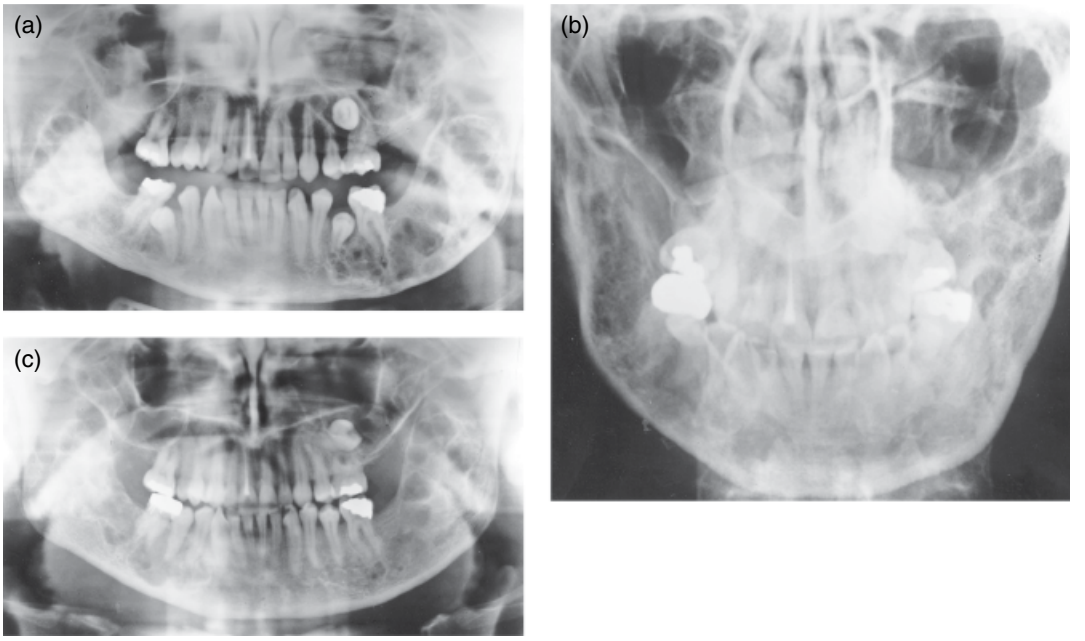


Figure 9.11 Conventional images of a case of cherubism observed at earlier (a and b) and later (c) stages. (a) Panoramic radiograph displays bilateral and bimaxillary radiolucencies confined to the posterior sextants. This is cherubism. It also displays absence (agenesis) of some molars and tooth displacement. (b) Posterioanterior projection reveals substantial buccolingual expansion of the vertical rami. The pattern of the radiolucencies is multilocular. (c) Later panoramic radiograph reveals regression of the lesions. They are now more radiodense and normal bone has infilled the earlier radiolucencies. The sketched outlines of these earlier radiolucencies can still be discerned.

appearance, radiology and central giant-cell lesionlike histology is diagnostic" [10]. This definition was substantially upheld by the WHO's 2017 edition [11].

Cherubism is autosomal dominant and is due to a defect in the *SRC homology 3 domain-binding protein 2* (SH3BP) gene [12]. During its active stage, cherubism classically presents on conventional radiography as bilateral, almost symmetrical, multilocular radiolucencies affecting the posterior sextants (the mandible always and the maxilla frequently; see Figure 9.11) of children, adolescents, or young adults (see its RPP in Table 9.1). Clinically it manifests as the bilateral swollen cheeks and "heavenward gaze" of "cherubs" as displayed in European art. At the earliest and active stage, biopsy reveals giant cells. When cherubism becomes inactive, it involutes to woven bone (Figure 9.11) and finally to lamella bone. The woven bone stage is within a "sketch line" (denoting the original margin of the radiolucency). The initial osseous infilling by woven bone initially assumes a ground-glass appearance arising from the small, tightly compressed trabecular pattern [13]. This led to cherubism's earlier diagnosis as the now defunct synonym "familial fibrous dysplasia."

Two reports of multiple kindred published in the last decade are Von Wowern's 18 cases from 6 Danish kindred [13] and Meng et al.'s 14 cases from 6 Chinese kindred [14]. The latter also included 10

nonfamilial cases [14]. Von Wowern followed up 18 individuals for 36 years [13]. Both studies [13, 14] used variations of the Seward and Hankey grading system:

Grade 1. Involvement of the bilateral mandible vertical ramus and posterior body.
Grade 2. In addition to grade 1, the maxillary tuberosities are involved.
Grade 3. Massive involvement of the entire maxilla and mandible except the condyles.

Grade 1 accounted for 79% in Von Wowern's [13] and 33% in Meng et al.'s [14] reports.

Although both reports revealed that, proportionally, males rather than females within a kindred are more likely to be affected, this was not so in one of Von Wowern's kindred [13]. Nevertheless, males were more likely to be affected by the more severe grades.

Although Von Wowern reported, on the basis of conventional radiography, that the lingual cortex was not expanded [13], lingual expansion may be apparent on CT.

Meng et al. did report one case that affected the condyles [14], but all of the condyles of Von Wowern's cases were unaffected [13]. Meng et al. reported that all cases displayed tooth displacement, one-half aplasia, one-third non-eruption, and one-quarter root resorption [14]. Furthermore, three of Meng et al.'s cases exceptionally displayed an increase in serum phosphorous and alkaline phosphatase [14]. Screening of the entire skeleton did not reveal the involvement of any other bone outside the jaws.

In those few cases of asymmetrical cherubism, Roginsky et al., reporting a Russian series, advised that minor features such as tooth malposition, premature tooth loss, or rare or previously unreported features such as gingival hyperplasia and enamel hypoplasia should suggest cherubism [15].

It would appear that not all cases of cherubism may be sufficiently clinically obvious. Of the 15 adults related to 3 child probands with cherubism, 11 (29–77 years old) had bony anomalies of the jaws [12, 16]. Of these 15 adults, 5 had radiolucencies greater than 1 cm, of which 3 were multilocular [16]. Although multilocular radiolucencies should have prompted consideration of a neoplasm, it was determined that MDCT (CBCT was not used in this study) was superior to panoramic radiography [16]. A simple reason for this was that "a specific feature in the adults was the high frequency of abnormalities in the anterior part of the mandible" [16], precisely where the panoramic radiograph is compromised by its narrow focal trough and superimposition of the vertebral column. Usually panoramic radiography of lesions in this area is supplemented by intraoral radiographs (periapical and occlusal radiographs; see Figure 9.1). A similar comparison revealed that septae were better displayed on CT than on conventional radiography, which included periapical and occlusal radiographs in addition to panoramic radiography [17]. MDCT of one of the cases displayed bilateral multilocular lesions (Redfors et al.'s Figure 4 [16]). These lesions occupied the superior half of the maxillary sinuses, another region that is not effectively imaged on a panoramic radiograph. Although it would also have been displayed by CT or more likely today by CBCT because of its widespread availability (Figure 9.12) [1], the dentist would have to have clear clinical and/or conventional radiographic indications for its prescription.

Von Wowern's long-term follow-up revealed that although the lesions of most

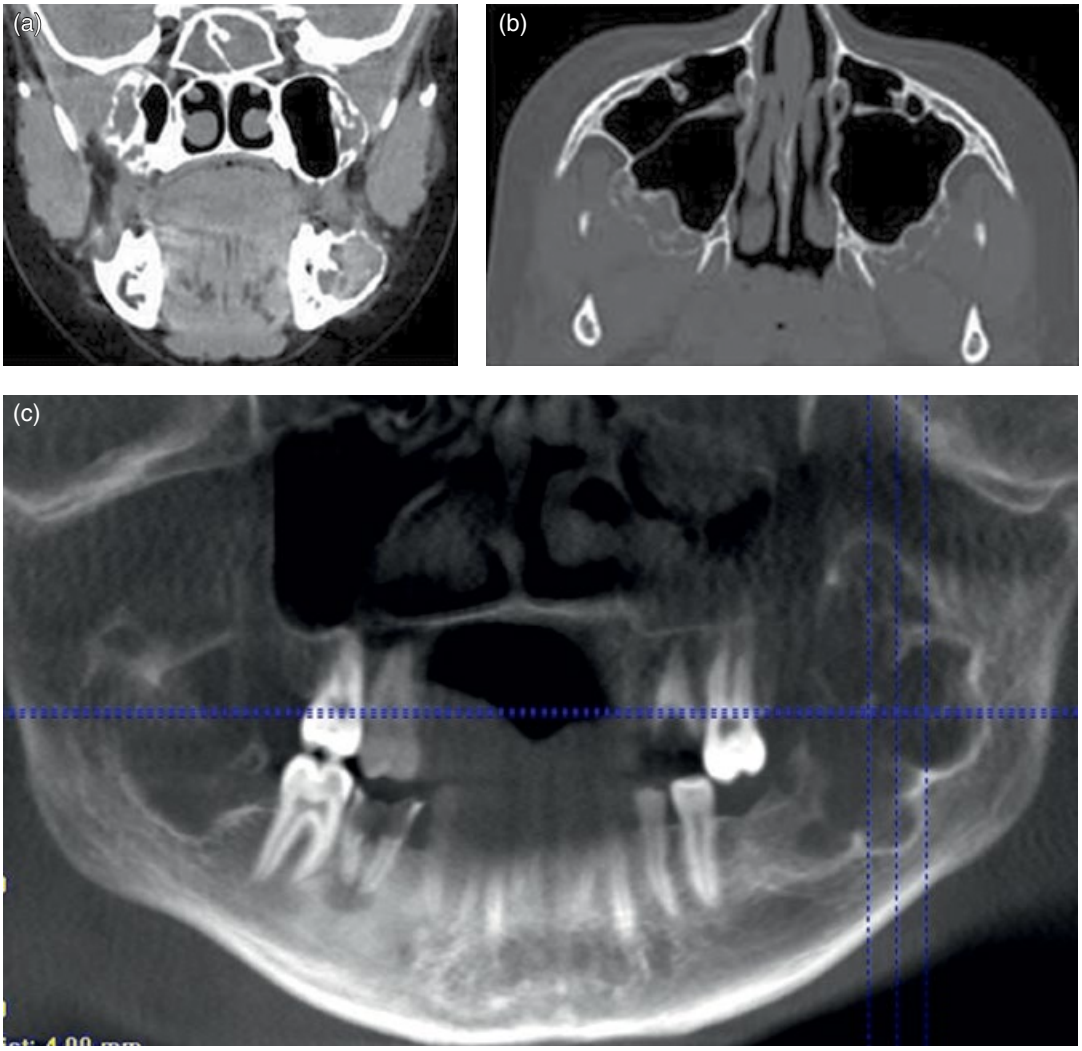


Figure 9.12 Cross-sectional imaging of two cases of cherubism. (a and b) Computed tomography of one case and (c) cone-beam computed tomography (CBCT) of another. (a) Coronal computed tomography just anterior to the hard palate–soft palate junction, exhibiting bilateral partial obliteration of the maxillary sinuses. The lesions are also expanding laterally into the infratemporal fossa. This also apparent in (b) an axial section just above the sigmoid notch of the mandible. (c) Panoramic reconstruction of CBCT of cherubism in a teenager. It displays lesions affecting the mandible and the left posterior maxilla. The most obvious lesions are the bilateral radiolucencies with corticated margins in the posterior sextants of the mandible. The lesion on the left is multilocular. The grossly carious right mandibular first molar also displays a periapical radiolucent lesion of inflammatory origin. Source: (a) and (b) Sidorowicz W, Kubasiewicz-Ross P, Dominiak M. Familial cherubism: clinical and radiological features. Case report and review of the literature. Eur J Paediatr Dent 2018 Sep;19(3):213-217. doi: 10.23804/ejpd.2018.19.03.08. Reproduced with permission of Ariesdue srl. (c) Courtesy of Professor Alexandre Khaireallah, Dean Emeritus and oral maxillofacial radiologist, University of Lebanon. Reproduced with permission from MacDonald, D.S. (2016). Lesions of the jaws presenting as radiolucencies on cone-beam computed tomography. *Clin. Radiol.* 71: 972–985.

of her cases became apparent by 7 years of age [13] (only 62% of Meng et al.'s cases became apparent by 10 years of age [14]), they achieved maximum buccal expansion by 12 years of age. The 15 patients with grade 1 returned to normality by their late teens, and grade 2 by their mid to late twenties [13]. The grade 3 patients still showed a modest expansion by 23 years of age and a mild expansion at the end of the reported period of follow-up [13].

Not only is the degree of buccal expansion proportional to the grade, so also is the degree of aplasia (Figure 9.11) [14]. Furthermore, two patients with the most severe grade displayed root resorption of the remaining mandibular teeth, resulting in total mandibular tooth loss before 24 years of age in one patient [14]. Root malformations of the lower first molar were observed in two-thirds of patients [14].

Although conventional radiography was clearly adequate for both Von Wowern's [13] and Meng et al.'s [14] reports, the latter advised that CT (including CBCT) may be indicated for the rare severe cases of grade 3 [14]. Other than better delineation of the extent of the lesions, their expansion, and the lack of a periosteal reaction, advanced imaging contributed little to our understanding of grade 1 and 2 cherubism [18]. Occasionally advanced imaging, particularly by CT, of very extensive cases complemented conventional radiography [19]. This was especially so in those exceptionally rare cases involving the orbit [20–22]. The RPP of cherubism affecting the orbit and disturbing vision in a major American craniofacial unit was 0.1 case per year [23]. This is half the RPP of cherubism affecting a major British center (see Table 9.1). The ophthalmic lesions caused by the cherubism pushing on the eyes were optic neuropathy and macular chorioretinal folds [24].

Although, Beaman et al.'s report functions as a reasonable pictorial essay of CT and MRI in cherubism [18], MRI has been performed for only a few cases. Nevertheless, the little evidence available to us so far does not indicate a clear role for MRI in the management of cherubism. Scintigraphy also has little role in the diagnosis of cherubism because it is most frequently negative [25].

Raubenheimer and Jordan detected that cherubism exhibits no histological difference from other giant cell lesions [11]. One of these is *Noonan syndrome* (NS), which Reichenberger et al. explain is "an autosomal dominant multisystem disorder, is caused by the dysregulation of the RAS-MAPK (*mitogen-activated protein kinase*) pathway and is characterized by short stature, heart defects, pectus excavatum, webbed neck, learning problems, cryptorchidism and facial dysmorphism" [26]. Carapito et al. present a family with NS with multiple giant cell lesions in the hemimandible of the proband [27]. Reichenberger et al. suggested that those patients diagnosed with cherubism but who were *SH3BP2* negative should be tested for mutations in other genes within the RAS-MAPK axis [26]. They added that "bilateral mandibular cherubism-like lesions and giant cell lesions in the mandible and in long bones have been described in neurofibromatosis patients and are associated with mutations in the neurofibromin gene (NF1)" [26]. Additionally, "NF1 is known as a regulator of the RAS pathway and mutations in NF1 are associated with neurofibromatosis and Noonan syndrome" [27].

In view of the self-regressive nature of most definitively diagnosed cases of cherubism after the onset of puberty and the likelihood of postsurgical complications, Von Wowern advises that "conservative management is appropriate until functional or emotional disturbances demand surgical intervention" [13].

9.4.2 NEVOID BASAL CELL CARCINOMA SYNDROME

It is clearly apparent from Table 9.2 [28] that NBCCS is a multisystem disease which requires a multidisciplinary approach, involving head and neck (including maxillofacial) specialties in addition to dermatologists, ophthalmologists, and others [29]. In addition to basal cell carcinomas (BCCs), NBCCS has six other major criteria, of which multiple keratocystic odontogenic tumors (KCOTs; Figure 9.13) [1] is one. A recent systematic review revealed that although BCCs are significantly most frequent in North Europeans, multiple KCOTs are significantly most frequent in East Asians [28]. The significantly lower incidence of BCCs in East Asians and South Asians was attributed to their darker skin [30, 31]. Syndromic KCOTs first present in the second and third decades [30], at least a full decade earlier than solitary (nonsyndromic) KCOTs in the same hospital community [32, 33]. Although a positive test of mutations of the protein patched homolog 1 (PTCH1) gene, a major criterion for NBCCS, is very sensitive for NBCCS (Table 3.1), due to its low specificity it cannot distinguish between syndromic and nonsyndromic KCOTs, for instance in an East Asian community in which nonsyndromic multiple KCOTs are significantly more frequent [30]. The PTCH1 gene is the negative regulator of hedgehog Hh signaling, PTCH1 [34]. The discussion of the PTCH1 test began in Chapter 3 and will be concluded later in this chapter in relation to solitary or sporadic KCOTs.

The global distribution of reports included in the systematic review [28], from which much of the following is derived, is set out in Figure 1.56 and the details of North Europeans and East Asians are in Table 9.2.

Although the Basal Cell Nevus Syndrome (BCNS) Colloquium Group [29] advised against the use of ionizing radiation for the detection of skeletal criteria of NBCCS so as to reduce the number of radiation-induced BCCs, it recommended that panoramic radiographs be made to detect KCOTs because they require treatment [29]. Furthermore, syndromic KCOTs [28, 30] are significantly more likely to recur after surgery than nonsyndromic KCOTs [32, 33].

The clinician should be aware that multiple radiolucencies confined to the alveolar process could also be multiple osseous dysplastic lesions (Figures 10.23–10.29), which generally require no treatment. They present in most sextants of middle-aged to older females of East Asian or sub-Saharan African origin as florid osseous dysplasia (Figures 10.23–10.29), or solely confined to the anterior sextant of the mandible, mainly in young females of European origin, as periapical osseous (formerly "cemental") dysplasia (Figure 10.32). These are more fully discussed in Chapter 10.

9.5 Hemoglobinopathies

Javid and Said-Al-Naief report that "Hemoglobinopathies are by far the most common genetic disease, affecting millions worldwide" [35]. These include the thalassemias, sickle-cell disease/trait, and *hereditary persistence of fetal hemoglobin* (HPFH). The two most important are thalassemia beta and *sickle-cell disease* (SCD). Although they both largely share the same geographic distribution of the Mediterranean, the Middle East, the Indian subcontinent, and West Africa, thalassemia extends to subtropical East Asia and SCD into the rest of sub-Saharan Africa. SCD overlaps with the distribution of malaria. Although

Table 9.2 Summary comparison of statistically significant differences in the features of nevoid basal cell carcinoma syndrome presenting in North Europeans and East Asians.

CRITERIA	Predilection for
Probands only	*Neither ethnicity*
Male (M): Female (F)	*Neither ethnicity*
Source: dental or medical literature	*Neither ethnicity*
MAJOR CRITERIA	
Basal cell carcinoma	North European
Basal cell nevus	*Neither ethnicity*
Keratocystic odontogenic tumor	East Asian
Palmar and/or plantar pits	North European
Calcified falx cerebri	North European
Medulloblastoma	*Neither ethnicity*
Family history	North European
MINOR CRITERIA	
Rib anomalies	*Neither ethnicity*
Sella bridge	North European
Hypertelorism	North European
Broad nasal ridge	*Neither ethnicity*
Strabismus	North European
Other eye anomalies	North European
Blindness or visual disturbance	*Neither ethnicity*
Highly arched eyebrows	*Neither ethnicity*
Bossing of the skull	*Neither ethnicity*
Coarse facies	North European
Cleft lip and palate	East Asian
High arched palate	North European[a]
Mandibular prognathism	*Neither ethnicity*
Ovarian fibroma	*Neither ethnicity*
Cardiac fibroma	*Neither ethnicity*
Syndactyly and/or polydactyly	North European
Short fourth metacarpal	*Neither ethnicity*
Flame-shaped radiolucencies	North European
Macrocephaly	North European
Hydrocephalus	*Neither ethnicity*
Corpus callosum agenesis	*Neither ethnicity*
Mental retardation	*Neither ethnicity*
Epilepsy	*Neither ethnicity*
Sprengel deformity	*Neither ethnicity*
Pectus deformity	North European
Scoliosis or vertebral anomalies	North European
Ameloblastoma	*Neither ethnicity*
Presence of the PTCH1 gene	*Neither ethnicity*

[a] Although East Asians did not exhibit this feature, it was assumed that it would be nil out of 187 cases in which the palate had been inspected for clefts. The PTCH1 gene encodes for the patched homolog 1 protein.

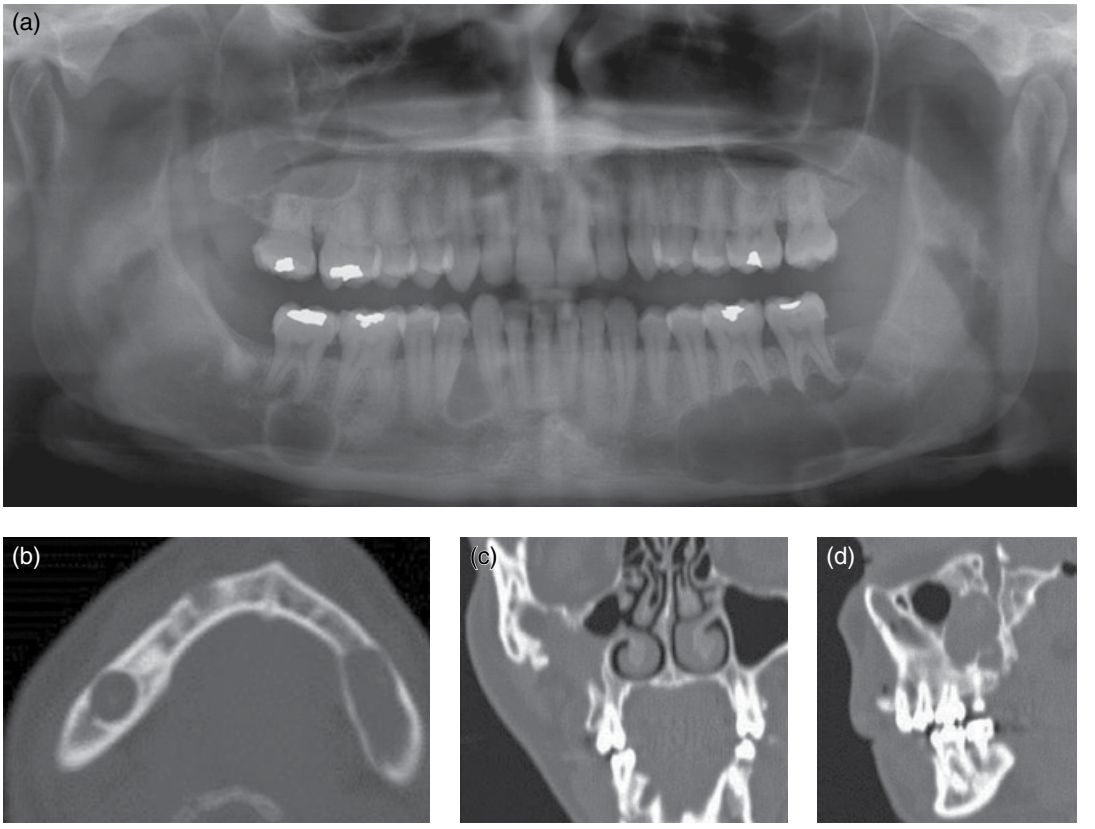


Figure 9.13 Conventional panoramic radiograph (a) and axial (b), coronal (c), and sagittal (d) reconstructions of cone-beam computed tomography displaying multiple keratocystic odontogenic tumors in a case of nevoid basal cell carcinoma syndrome. The axial reconstruction displays substantial erosion of the lingual cortex with regard to the left mandibular lesion, but with minimal buccolingual expansion. The maxillary lesion has substantially obturated the lumen of the right maxillary sinus. The defect in the buccal wall of the right maxillary sinus on the coronal reconstruction was due to a biopsy. (a) Reproduced with permission from MacDonald, D.S. (2016). Lesions of the jaws presenting as radiolucencies on cone-beam computed tomography. *Clin. Radiol.* 71: 972–985

Sayani and Kwiatkowski stated that hitherto thalassemia was rare in the USA, this is no longer the case due to immigration from the "thalassemia belt" [36].

Hematopoieis normally occurs in children in the axial skeleton, namely the vertebral bodies, ribs and sternum, hip, and long bones of the legs. In the adult this is restricted only to the vertebral bodies and sternum [37]. Due the inadequate production of blood cells, the thalassemias, SCD, and other causes (leukemia, myelofibrosis, diffuse osseous metabolic disease) affect not only the rest of the skeleton, including the face, jaws, and skull, but also lead to *extramedullary hematopoiesis* (EMH) in tissues outside the bone marrow, namely in the liver and spleen and elsewhere in the

abdominal cavity [37]. The present text will be confined to the presentation of these hemoglobinopathies in the head.

9.5.1 THALASSEMIAS

The thalassemias constitute a group of lesions according to the globin affected (alpha, beta, or intermedia, a combination of both) [35]. Alpha and beta are further divided in homozygous (major) and heterozygous (minor) forms. Although the heterogenous forms generally display minimal clinical manifestations of thalassemia, they are a concern as offspring are at risk of the homozygous form if inadequately genetically counseled [35]. The changing epidemiology of thalassemias, including *non-transfusion-dependent thalassemia* (NTDT) and the problems it brings, is prompting a growing health problem and increased clinical awareness [38]. The classical features of thalassemias are a hair-on-end appearance of the vault of the skull, obliteration of the air sinuses, and replacement of the normal trabecular pattern by fewer coarse straight trabeculae (Figure 9.14; see also Figures 11.10 and 18.19 for other images of the same patient).

The conventional radiological features of thalassemia affecting the jaws were reported in a Middle Eastern community by Hazza'a and Al Jamal [39, 40]. The maxillary antrum was obliterated in every case (see Figure 11.10). The teeth displayed "spiky" roots, an increased crown/root ratio, a reduction in the lamina dura, and taurodontism. In addition, the teeth showed some delay in their development.

Thalassemias have a specific presentation not only upon diagnosis, but also subsequently according to the mode of treatment. Hypertransfusions and chelating agents also affect changes in both the skeleton and the extraskeletal organs [41], which may be observed by radiology.

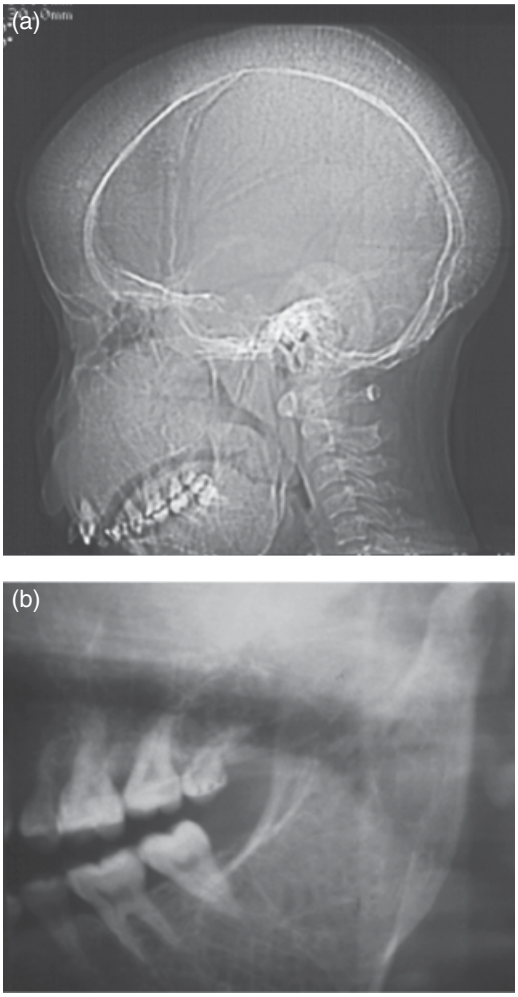


Figure 9.14 Lateral projection of the skull and panoramic radiograph of thalassemia. (a) Lateral projection of the skull displaying typical radiological features of thalassemia: hair-on-end appearance of vault of skull, completely obturated air sinuses (frontal, ethmoidal, sphenoidal, and maxillary). The mandible is also affected. (b) Panoramic radiograph exhibiting few, but coarse and linear, trabeculae within the enlarged mandible.

Although NTDT is sometimes regarded as less severe than those forms that need transfusions, it should be monitored for iron overload [38].

The significant improvement in thalassemia patient survival has been accompanied by an increase in cancers, mainly hepatocellular carcinomas, thyroid cancers, lymphomas, and leukemias [42].

9.5.2 SICKLE-CELL DISEASE

SCD is one of the most common diseases globally and constitutes a public health problem [43]. Although it is most frequently found among West Africans and their Afro-Caribbean and African-American descendants, it is also found among Mediterranean, Middle Eastern, and East Indian communities [44]. SCD is an autosomal recessive hemoglobinopathy due to a single nucleotide mutation of the β-globin gene. Hemorrhagic and ischemic stroke is the leading cause of death and a major cause of morbidity in SCD patients [45]. Other important complications of SCD are anemia, leg ulcers, and pulmonary hypertensions [46]. It is properly termed *sickle-cell anemia* (SCA) when the patient is homozygous for the abnormal hemoglobin *hemoglobin S* (HbS), but if the patient is heterozygous then it should be termed *sickle-cell trait* (SCT) [43]. Patients with SCA and SCT exhibited characteristics of class II skeletal (maxilla/mandible skeletal base relationship) pattern because of mandibular retrusion. Although Pithon et al. reported that the maxilla was otherwise of normal dimensions [43], Javed et al. reported that maxillary overgrowth and subsequent malocclusion occur in young SCD patients [46]. Furthermore, midface overgrowth has been occasionally reported as a result of bone-marrow hyperplasia [46]. Bone-marrow hyperplasia can affect the calvarium, causing frontal bossing [46]. Vaso-occlusive crisis in the mandible may cause persistent or even permanent mental nerve paresthesia, resulting in a numb chin. This phenomenon is significantly higher in SCD patients than in normal controls [46]. Although SCD patients have significantly more dental decay than normal controls, noncarious teeth may experience toothache due to infarction/thrombosis of the dental pulp vessels two to three days after a "crisis" [46]. Other manifestations of SCD are adenoidal hypertrophy (with associated nasal obstruction due to the narrowing of the nasal pharynx), prominent upper cervical lymph nodes, and delayed pneumatization of the paranasal sinuses [45]. Occasional avascular necrosis of the condyle has been recently displayed [45]. Souza et al. reported that pulp calcification and external root resorption were most frequent in SCA cases, and that changes in shape and size of the dental roots were most frequent in SCT cases [47]. SCA cases also displayed step-ladder and spider-web trabecular patterns [48]. Neves et al. reported significant associations between clinical jaundice and increased spacing between trabeculae, and also between strokes and the presence of horizontal trabeculae in the jaws. The lamina dura was most frequently absent and hypotaurodontism occurred twice as frequently in SCA cases as in the controls [49].

Neves et al.'s case series of over 70 SCD patients demonstrated "statistically significant associations" between a history of clinical jaundice and the presence of increased spacing of bony trabeculae on panoramic radiographs, and between a history of stroke and the presence of horizontal arrangement of these trabeculae [49].

9.6 Lymphoid Cancers

Lymphoid cancers, which in addition to non-Hodgkin lymphoma (NHL) and Hodgkin lymphoma (HL) includes myeloma and lymphocytic leukemia, vary between global communities. NHL and HL are lowest in East Asians, Hong Kong Chinese in particular, and highest in Western Europe, the United States, and Australia [50].

9.6.1 MULTIPLE MYELOMA

Multiple myeloma is a plasma cell malignancy. Its most frequent manifestation is widespread disseminated disease. The multiple radiolucencies affecting the vault of the skull classically confer a pepper-pot appearance (see Figure 19.2). Bone lesions develop in 90% of patients, making it the most common cancer to affect bone [51].

Multiple myeloma accounted for 43% of all bone malignancies in one patient database [52]. Although the jaws are affected in 30% of cases, 16% of multiple myeloma cases first manifest in the jaws [52]. Generally, whole-body scanning is achieved by positron emission tomography fused with computed tomography (PET/CT; see Chapter 7) using 18-fluorine fluorodeoxyglucose (FDG) rather than technetium-99m [51]. Pathological fractures develop in 60% of patients [51].

Conventional radiographic screening, by skeletal survey, in order to display the osteolytic lesions of multiple myeloma is still the standard staging modality, mainly because of its availability and low cost. Furthermore, in spite of its lower sensitivity in comparison to advanced imaging modalities, it remains the gold standard for the detection of fractures, a frequent complication of multiple myeloma [53]. Nevertheless, MDCT is prescribed in almost all cases because of its superior sensitivity, diagnostic accuracy (90% to conventional radiography's 69%), fracture detection, and identification of osteopenia and other extraskeletal lesions [53]. Nevertheless, MRI remains the most sensitive modality for the detection of marrow infiltration before bone has been lost [53]. Figure 19.1 displays the loss of trabeculation of the base of the skull due to infiltration.

Observation of *solitary osseous plasmacytoma* (SOP) in a radiograph of the jaws may enhance the patient's prognosis by earlier local treatment prior to its becoming widespread disease. If untreated, 70% of cases progress to multiple myeloma, while 30% progress to multiple osteolytic (radiolucent) lesions without marginal sclerosis; in other words, they have the classical "punched-out" radiolucent presentation of multiple myeloma going on to diffuse osteoporosis and finally diffuse osteosclerosis [54]. Witt et al. declared that neither diffuse osteoporosis nor diffuse osteosclerosis was observed in their case series [54]. Half of the SOPs affecting the jaws were observed on radiographs, and they were radiolucent [54]. Pisano et al. reported that plasmacytoma of the oral cavity frequently appeared superimposed upon the roots of adjacent teeth, and were accompanied by pain and a raised red mucosal lesion on the alveolar ridge. They need to be distinguished from a *periapical radiolucency of inflammatory origin* (PRIO) [55]. In addition to the skeleton, multiple myeloma can infiltrate soft tissues, which becomes obvious on MRI (Figure 9.15).

Dutoit and Verstraete reported that the International Myeloma Working Group (IMWG) recently included MRI in its diagnostic criteria, because MRI is the most sensitive imaging modality for the detection of bone-marrow infiltration [53]. IMWG recommends that a patient who presents with a *monoclonal gammopathy of undetermined significance* (MGUS) and with a focal lesion of greater than 0.5 mm should be treated for myeloma. The quality of the conventional MRI evaluation can be enhanced by *diffusion-weighted MRI* (DWI) and *dynamic contrast-enhanced MRI* (DCE-MRI). The former informs on the bone marrow's cellularity and the latter on its vascularization [53].

Follow-up MRI will indicate whether the multiple myeloma is responding to treatment by regressing or whether it is still progressing. The normal yellow (fatty) marrow presents as hyperintense on T1-weighted MRI and hypointense on T2-weighted MRI with fat saturation, whereas the normal red marrow (due to hematopoiesis) is less intense on T1-weighted MRI, but higher in intensity compared to muscle [53]. The development of hypointense foci, diffuse involvement, or an increase in number on T1-weighted MRI indicates continued progression, whereas a reduction in the number of foci or an increase in the intensity of one or more foci indicates a positive response to treatment [53].

The literature emphasizes multiple myeloma's widespread manifestation in the skeleton. Nevertheless, it should be appreciated that this multisystemic disease also affects soft tissues, as is made obvious by the MRI images in Figure 9.15.

9.6.2 NON-HODGKIN LYMPHOMA

Lymphomas account for about 5% of head and neck malignancies [56]. Over the last 50 years, a new classification of lymphomas has appeared almost every decade, the WHO's 2016 classification [57] being the most recent. Lymphomas are divided into HL and NHL on the basis of their histopathological and clinical features. NHL is further divided into B- and T-cell lymphomas.

The global distribution of reports of extranodal NHLs which arise in the maxillary alveolus included in the systematic review [50], from which much of the following is derived, is set out in Figure 1.57.

Extranodal lymphomas are the 30% of lymphomas that arise in tissues outside the lymph nodes [56, 58]. They can be either HL or NHL [58]. Extranodal lymphomas arising within the jawbones are so rare that not one presented in a case series of 361 "oral or paraoral lymphomas" [59]. Over the last few decades, since the case series reported by Eisenbud et al. [60], there has been a steady drum beat of extranodal lymphomas arising within the jaw bones. A possible reason for the initial accumulation of lymphoid tissue (from which the lymphoma arose) within the jawbones is chronic dental disease, which may have developed from an untreated or inadequately treated nonvital tooth or periodontal disease. So far there have been six cases of extranodal lymphoma arising within the maxillary alveolus associated with completed endodontic treatment [61]. The most recent of these emphasized the importance not only of cross-sectional radiology in this lesion's early evaluation, but also careful review

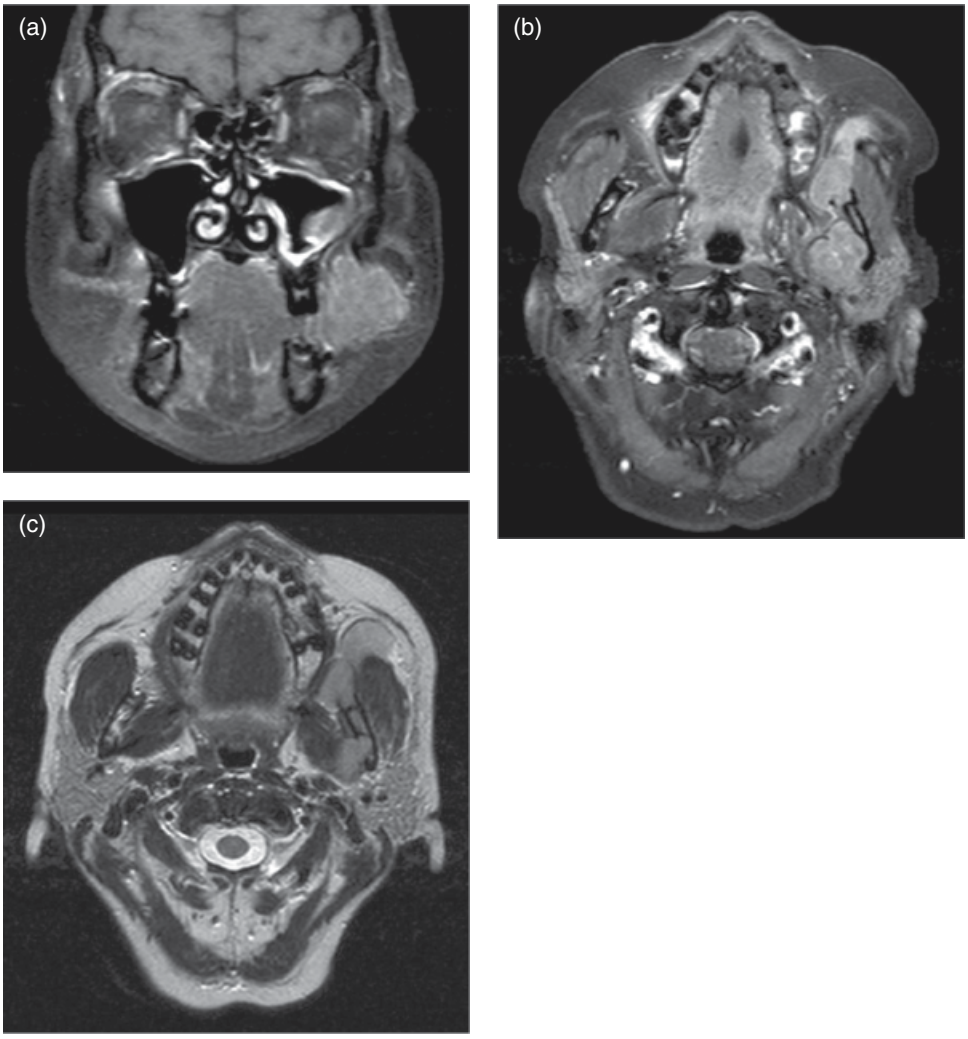
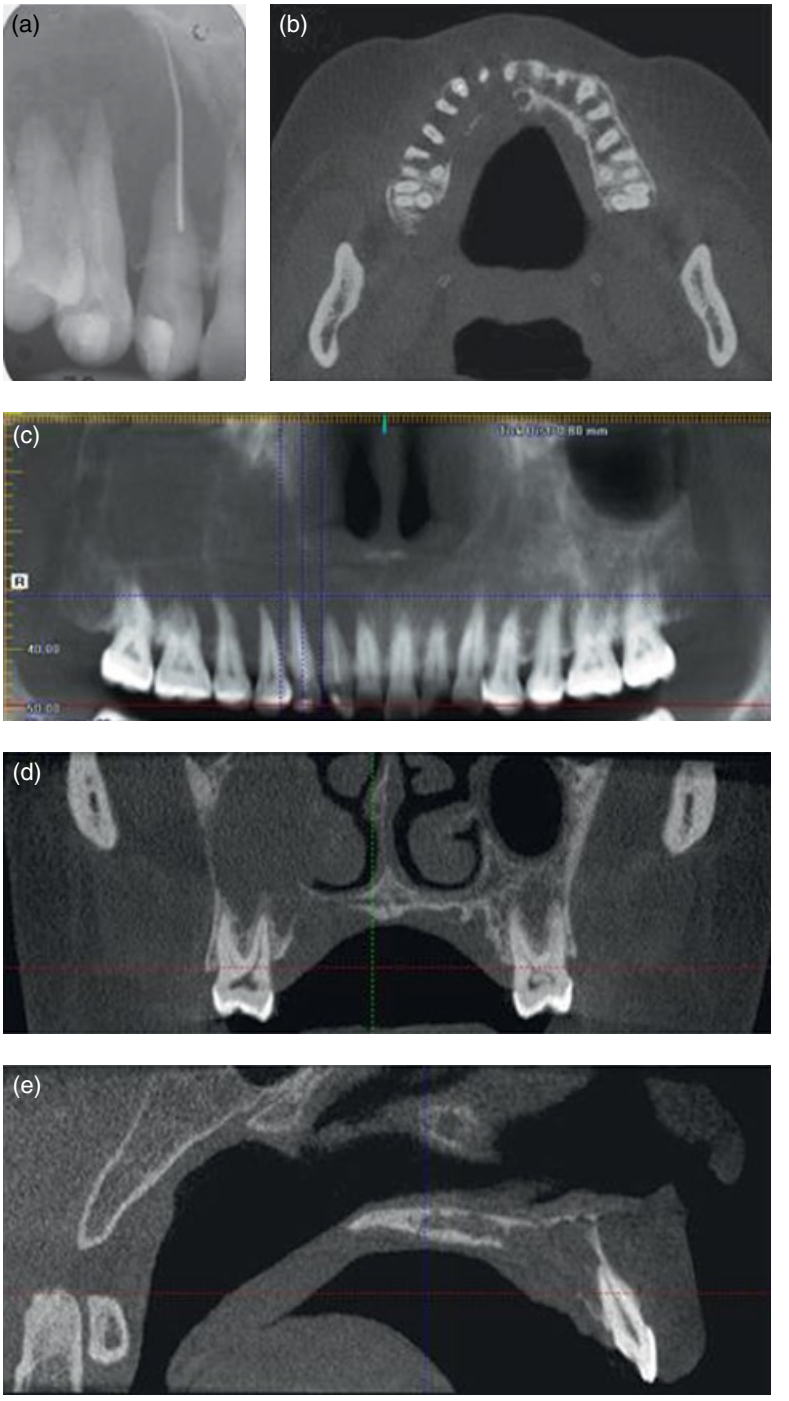


Figure 9.15 Magnetic resonance imaging (MRI) of a case of multiple myeloma. See Figure 19.2 for a lateral conventional radiograph of the skull displaying the salt-and-pepper pattern or pepper-pot pattern skull. (a) Coronal T2-weighted MRI displays the neoplasm as a mass within the buccal tissues. It has a heterogeneous hyperintensity within it. The mucosa of the ipsilateral maxillary antrum is very hyperintense, suggestive of sinusitis. The lateral exophytic mass is suggestive of the neoplastic invasion. There is also a hyperintense area within the bone marrow superolateral to the contralateral orbit, the cortex is absent, and the lesion is in continuity with a hyperintense lesion within the orbit. This is suggestive of multiple lesions. (b) Axial T2-weighted MRI displays the neoplasm as a mass within the buccal tissues. It is more hyperintense than the adjacent isointense masseter around whose anterior margin it expands into the deep tissues of the cheek, displacing the parotid duct and the subcutaneous tissues outward. The posterior aspect of the lesion abuts the deep pole of the left parotid gland. The neck of the condyle appears substantially eroded. The ipsilateral lateral pterygoid muscle has been substantially infiltrated. (c) Axial (non-fat-saturated) T1-weighted MRI displays the neoplasm as a mass within the buccal tissues. It appears more isointense in contrast to the more hyperintense fat tissues. Although it is clearly distinguished from the parotid gland, the lingual cortex of the base of the neck of the condyle is absent, suggesting its infiltration of the marrow space. The attachment of the ipsilateral lateral pterygoid to the neck of the condyle has been completely infiltrated. Source: Courtesy of Dr. Montgomery Martin, British Columbia Cancer Agency.


(a)
(b)
(c)
(d)
(e)

of the conventional radiographs for those features suggestive of malignancy (Figure 9.16) [50, 61]. Although cross-sectional imaging has been applied to these lesions, recently MDCT (Figure 11.14), CBCT (Figures 9.16 and 11.14), and MRI (Figure 11.14) were applied and compared in one case [61].

Generally, extranodal lymphomas affecting the head and neck arise within soft tissues, but infrequently they may arise within the bones of the jaws. Although a clinical examination and conventional radiography may suffice for such lesions arising within the mandible, those arising within the maxillary alveolus generally require cross-sectional imaging due to its complex anatomy. Most case series included in the systematic reviews were derived from just four nations (the Netherlands, Greece, Iran, and the USA), whereas the case reports included were derived from a wider range of ethnicities. The more detailed case reports significantly reported at least one imaging modality. Most patients were aware of their lesions for nearly two months prior to presentation, many presenting as inflammatory lesions [50].

Swelling was the predominant symptom at first presentation, whereas pain and numbness were less frequent [50]. Numbness, an important indicator of a malignancy within the mandible, is a frequently reported symptom of lymphoma arising within the mandible [62]. Nevertheless, it has been less frequently reported for those lymphomas arising within the alveolus of the maxilla [50]. This may reflect the fact that the inferior orbital nerve, the supplier of innervation to the upper lip, is separated from an extranodal lymphoma arising with the alveolus by the frequently voluminous lumen of the maxillary sinus [50]. Conversely, the inferior alveolar nerve, the supplier of innervation to the lower lip, courses through the mandibular canal and is therefore in closer proximity to an extranodal lymphoma

Figure 9.16 (a) Periapical radiograph and (b–e) large field of view of cone-beam computed tomography (CBCT) of a non-Hodgkin lymphoma (NHL) arising within the alveolus. This NHL was discovered incidental to an examination of the previously endodontically treated upper right canine and lateral incisor. (a) Periapical radiograph of a previously root-filled right maxillary lateral incisor and canine. A gutta-percha point was inserted into a fistula buccal to the lateral incisor. This point had entered the lesion, to come to rest on the bony margin within the lesion. The lesion presents as a fairly well-defined radiolucency that has substantially resorbed the bone up to the alveolar crest. The roots of the lateral incisor, the canine, and the first premolar are "floating" in the radiolucency. (b) Axial reconstruction of the CBCT dataset, through the maxillary alveolus, reveals a loss of bone structure extending from the right central incisor and nasopalatine canal back to the second molar. The buccal cortex has been substantially destroyed. The palatal cortex displays several perforations. (c) Panoramic reconstruction of the CBCT dataset reveals the complete obturation of the lumen right maxillary sinus. (d) Coronal reconstruction of the CBCT dataset displays the lesion within the right maxillary sinus also destroying the medial wall. (e) Sagittal reconstruction of the CBCT dataset through the dens and anterior arch of the atlas reveals the extension of the lesion throughout the palate, removing trabecular bone. The palatal cortex is eroded. Note: The extension of this NHL into the maxillary sinus is displayed on CT and MRI in Figure 11.14. Source: Reproduced with permission from MacDonald, D., Li, T., Leung, S.F., et al. (2017). Extranodal lymphoma arising within the maxillary alveolus: a case report. *Oral Surg. Oral Med. Oral Pathol. Oral Radiol*. 124:e233–e238.

arising within the mandibular alveolus. Although it is reasonably expected that NHLs arising within the maxillary sinus would be in closer proximity to the inferior orbital nerve and therefore would be more likely to be associated with a numb upper lip [50], Kato et al. made no mention of this [63]. Instead, they reported that the most frequent symptoms of NHL arising within the maxillary sinus are facial swelling, epitaxis, nasal obstruction, and headaches [63].

While conventional imaging of lesions in the maxilla displayed floating teeth and spiking-pattern root resorption indicative of malignancy, cross-sectional modalities did not distinguish carcinomas from lymphomas [50, 61]. Furthermore, CBCT's better spatial resolution may assist the primary care dentist to determine more promptly that a lesion is neoplastic rather than inflammatory.

Environmental and health-care factors (vaccinations) can influence *Epstein–Barr virus* (EBV) positivity [64]. The EBV positivity in T-cell and B-cell lymphomas was 36% and 7%, respectively [65]. The sole T-cell lymphoma in MacDonald and Lim's systematic review was Japanese from Kyushu [50], where T-cell lymphomas account for 74% of NHLs, in contrast to 25% for most of East Asia and about 5% for communities largely of European origin [65].

9.7 Langerhans Cell Histiocytosis

Langerhans cell histiocytosis (LCH), formerly called histiocytosis X, is a rare disease. Although most patients with this condition present with localized disease which only requires local or even no therapy, a minority of cases with disseminated "multisystem" disease are at risk for serious outcomes, even death [66]. These cases require treatment. Although LCH can present at any age, two cases recently presented in patients in the eighth decade [67]; 90% of LCH cases present in individuals younger than 40 years of age and the mean age is 19 years [68].

Dagenais et al. [69] were the first to identify and qualify the radiological features of LCH affecting the jaws. They reported that almost all cases affected the posterior sextant of the mandible and, in a third of those cases, the posterior sextant of the maxilla. They found that almost all cases presented as circular or elliptical radiolucencies (Figure 9.17). Although most were well defined, particularly those affecting the alveolus, a cortex or sclerosis was generally observed only in that part



Figure 9.17 Panoramic radiograph of Langerhans histiocytosis. There are two well-defined radiolucencies in the posterior mandible superimposed upon the mandibular canal. The more distal radiolucency is more translucent and the mandibular canal not only appears widened, but does not exhibit the canal's superior or inferior cortex. Its margin is delimited by some sclerosis. The mesial radiolucency's mesial border has the contralateral lower border of the mandible superimposed upon it.

of the lesion close to the alveolar crest. Those in the alveolus were multiple, whereas those in the basal process were solitary. The majority of the alveolar lesions were sited about the apices. The lamina dura was absent. Root resorption, though common, was slight. Although periosteal new bone was observed on occlusal radiographs of lesions affecting the basal process, buccolingual expansion was not observed, except for involvement of the condyle and coronoid processes. This report, largely consistent with most earlier literature, did not mention "floating teeth," perhaps because almost all the lesions were small, and not one case presented with such a feature. Tooth displacement was observed in half of cases [68]. Figure 9.18 reveals that LCH in the jaws can progress quickly within a few months.

9.8 Osteoporosis

Osteoporosis is a serious disease, but can be treated if detected early, thus avoiding a hip fracture, which, in the elderly, can be fatal [70]. In addition to being a cause of death, these fractures result in reduced mobility and an increase in pain, and in an increase in cost to public funds [71]. The WHO defines osteoporosis as "a disease characterized by low bone mass and deterioration of bone microarchitecture, leading to increased bone fragility and a consequent increase in fracture risk" [72]. Osteoporosis presents in primary or secondary forms; the former is due to aging and the reduction of estrogen in postmenopausal women, whereas the latter is due to various medicines [73]. It is the primary form with which we are most concerned. Osteoporosis affected more than 75 million people in the developed world, but globally causes 9 million fractures each year. Calciolari et al. noted that "The lifetime risk for a wrist, hip, or vertebral fracture has been estimated to be in the order of 30–40% in developed countries – in other words, very close to that for coronary heart disease." In Europe, 80% of the 29 million sufferers are female [74]. Images of osteoporosis as it presents on a panoramic radiograph and by *dual-energy X-ray absorptiometry* (DXA) are displayed in Figure 9.19. There are three DXA manufacturers, and the results of two of them, Lunar and Hologic, are shown in Figure 9.19 for the same patient.

Unlike osteoporosis, which is a disease, osteopenia, a reduction in bone density, is *not* a disease and is simply a risk factor for the former. Previously radiologists applied the term osteopenia to bones that *subjectively* appeared more translucent than normal on conventional radiographs, and termed it osteoporosis when fractures were apparent in the vertebra [75]. Although this activity has largely been supplemented if not replaced by the more objective bone density scans via DXA, dental and oral and maxillofacial practitioners generally "screen" radiographs, particularly panoramic radiographs, for incidental findings such as calcified carotid artery atheromas (see Chapter 12). These clinicians are well placed to perform this function, since they investigate the jaws for diseases ranging from caries to neoplasms of a much larger proportion of the populations in the developed world than any other medical discipline. An additional reason for this activity is that although the gold standard for measuring *bone mineral density* (BMD) is DXA of the proximal femur [76], it is usually applied to patients who have developed a fracture indicative of osteoporosis of the femur, the vertebra, and the wrist. While not subject to fracture, the jaws are affected by an association of increased alveolar porosity but decreased height and tooth loss with osteoporosis. A decade ago

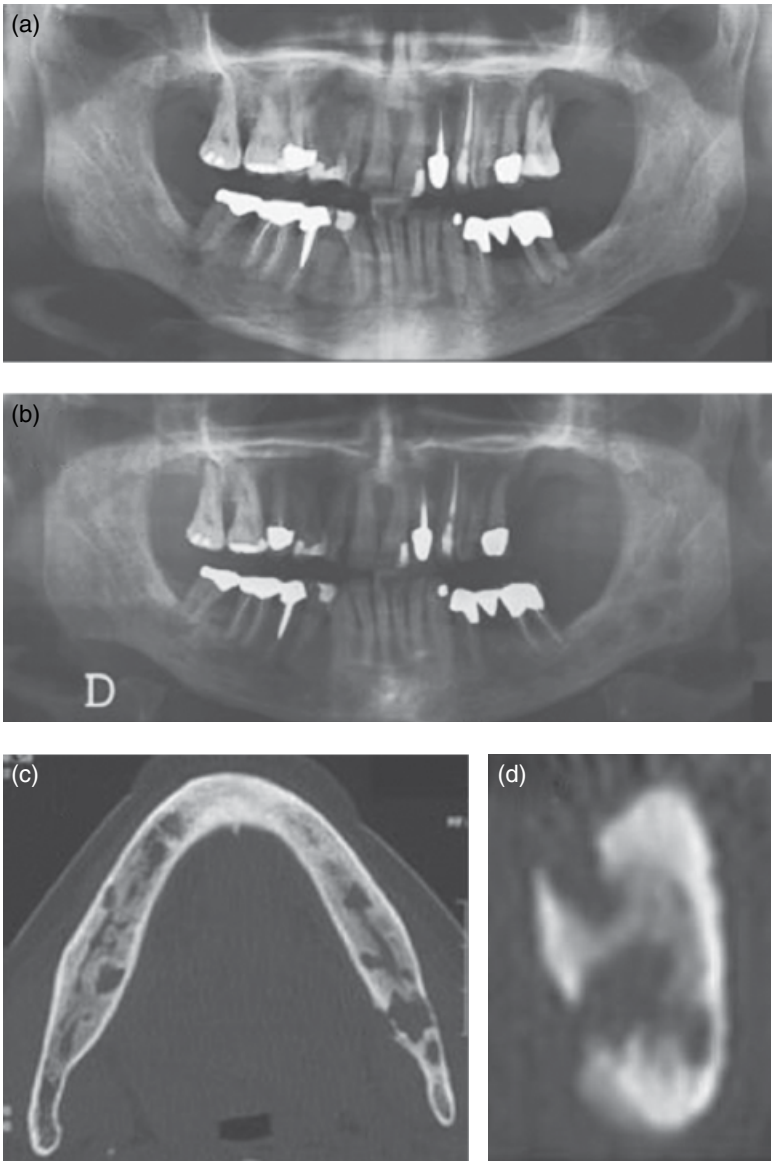


Figure 9.18 Langerhans cell histiocytosis presenting in a patient in the eighth decade. (a) Panoramic radiograph displaying a periapical radiolucency of the lower left first molar and lower right second molar and diffuse periodontal disease (mostly related to maxilla). (b) Second panoramic radiograph performed a few months later, showing some new radiolucent areas, mainly located in the left mandible. The lesions were multiple and unilocular. Although with well-defined margins, they did not display sclerotic reactive halos. (c) Axial CT reconstruction of the mandible (bone window) showing many diffuse osteolytic lesions within the cancellous bone of the mandibular body. The last lesion on the lower left markedly eroded the buccal cortex and perforated the lingual cortex. D, Dexter. (d) Coronal reconstruction through that last lesion also displaying that perforation of the lingual cortex. Source: Reproduced with permission from Lajolo, C., Campisi, G., Deli, G., et al. (2012). Langerhans's cell histiocytosis in old subjects: two rare case reports and review of the literature. *Gerodontology* 29:e1207–e1204.

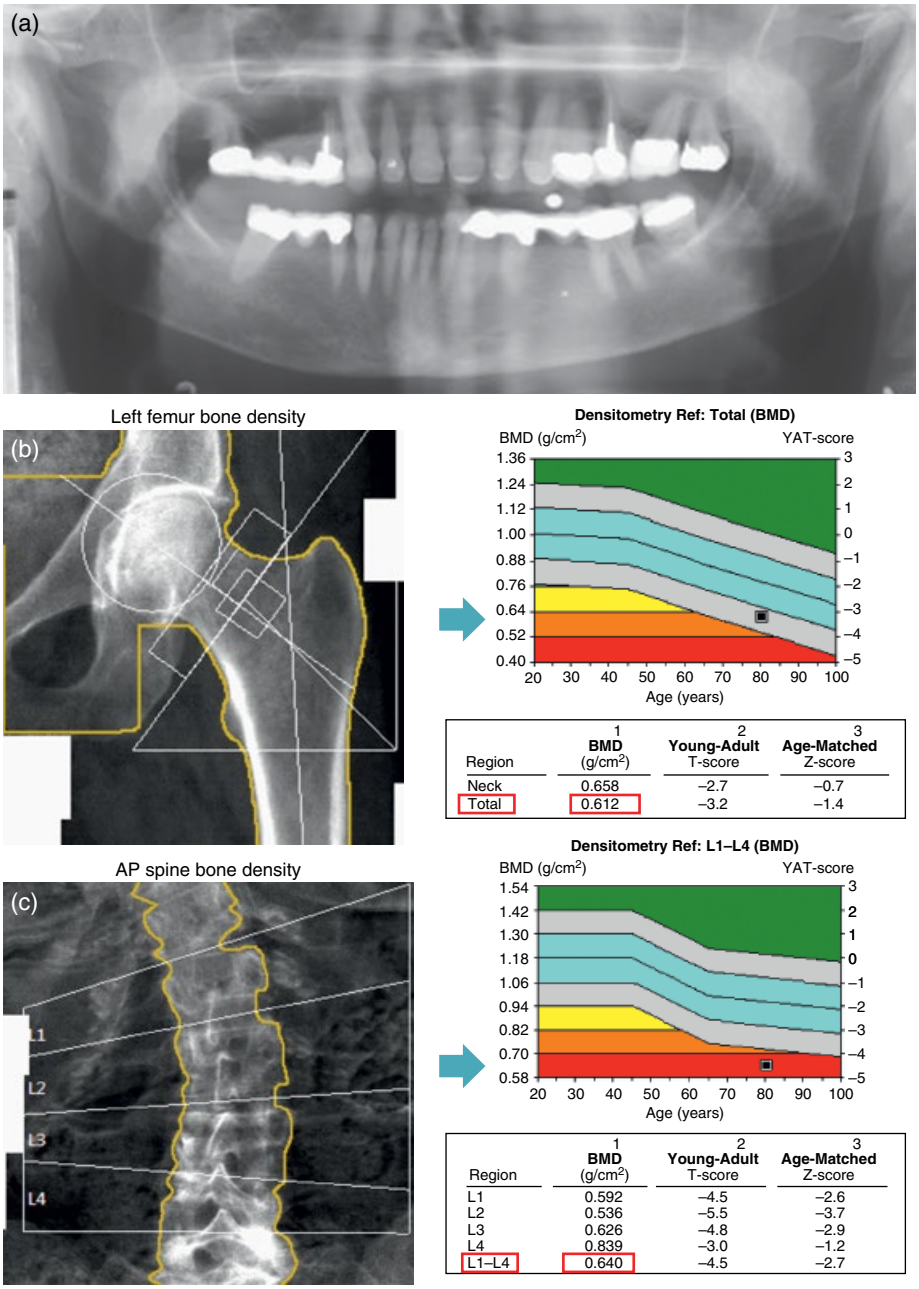


Figure 9.19 Osteoporosis. (a) Panoramic radiograph displaying osteoporosis in the mandible. The most striking features are the very thin lower border of the mandible and the very fine trabecular pattern, particularly in the alveolus of this almost fully dentate patient. (b and c) Dual-energy X-ray absorptiometry (DXA) of the left hip and first four lumbar vertebrae of an 80 year-old woman, not the same case as (a). The colored Lunar graphs reflected bone mineral density (BMD) plotted against age. The pale blue band represents the mean BMD and one standard deviation about the mean as it varies with increasing age. The Hologic tables (gray) display, in the red boxes, the values for total hip (b) and the first four lumbar vertebrae (L1–L4; (c)). The blue arrows indicate these on the BMD scales on the accompanying graphs; the blue square with an asterisk at its center (b) indicates where that particular patient is with regard to the mean and one standard deviation for her age. She is just outside it for the hip, but is severely osteoporotic for the vertebrae, which in part explains the compression of the vertebral bodies of the first four lumbar vertebrae (L1–L4) in (c). Note: Lunar and Hologic are two different DXA manufacturers, but have produced broadly similar results for the patient in (b) and (c). Source: Courtesy of Professor Keith Horner, oral and maxillofacial radiologist, Faculty of Dentistry, University of Manchester.

the Osteodent research project indicated the role dentists could play in the detection of patients with osteoporosis, namely a visual evaluation of the thickness of the lower border of the mandible and the trabecular pattern on intraoral radiographs [77]. This can be achieved visually [78].

Osteoporosis is objectively defined when the DXA T score is 2.5 standard deviations (SDs) or more from the mean BMD of a 20–29-year-old of the appropriate sex, whereas a T score less than 1 SD below the appropriate mean BMD is "normal." Between the less than 2.5 SDs of osteoporosis and the 1 SD of normal is osteopenia, a reduction in bone density.

Furthermore, although DXA is classically applied to the proximal femur, it has also been applied to the mandible; unfortunately, the results in the latter are inconclusive [79]. Jonasson and Billhult reported that the *fracture risk assessment tool* (FRAX) was one of the superior tools for determining osteoporosis [76]. It is a diagnostic tool, developed by the WHO, to evaluate the 10-year probability of bone fracture risk. It integrates both clinical risk factors – mainly *body mass index* (BMI), parental hip and patient's own fracture history, steroids, and rheumatoid arthritis – and classical DXA data to calculate the 10-year probability of hip fracture and the 10-year probability of one of the already-mentioned major fractures. This probability guides the attending clinician toward the most appropriate treatment regimen. FRAX is available in a variety of media in nearly all major languages and is also freely accessible online [80, 81]. This is invaluable, as it not only ensures that treatment is directed to those who would benefit from it, but also minimizes the prevalence of side effects. The most all-consuming side effect of antiresorptive drug therapy for osteoporosis is *medicinal-related osteonecrosis of the jaws* (MRONJ), which will be fully addressed in Chapter 10. Of over 100 MRONJ cases, 3% exhibited a pathological fracture of the mandible [82]. Ironically, although fractures of the mandible due to osteoporosis are very uncommon, fractures resulting from its treatment could be more common [82].

9.9 Metastasis to the Jaws

Although metastasis to the jaws is rare, it is indicative of already widespread disease and an average survival of seven months [83]. In almost a quarter of cases the manifestation of the oral lesion was the first indicator of widespread occult disease [84]. Hirshberg et al. revealed that the metastasis may arise in any organ, but most frequently in the lungs (predominantly in males) and the female breast. The metastasis can manifest in either the jaw bones or the oral mucosa [83], most frequently in the posterior mandible and in the gingiva, respectively [85]. Although the majority arise in the breast, a minority do metastasize to the oral mucosa, as Figure 9.2 displays. The most frequent clinical presentations are jaw pain, paresthesia (including numbness), and exophytic swelling. In other cases it may manifest as toothache, loosening of a tooth, and a dentoalveolar swelling, all suggestive of dental disease [85].

9.10 Hyperparathyroidism

The radiology of hyperparathyroidism affecting the jaws, in addition to generalized bone resorption, osteopenia, and osteosclerosis, may reveal localized lesions. These are "brown tumors" and are rarely reported [86]. They may appear either as radiolucencies or leontiasis ossea (discussed further in Chapter 10). A brown tumor presenting as a radiolucency is displayed in Figure 9.20.

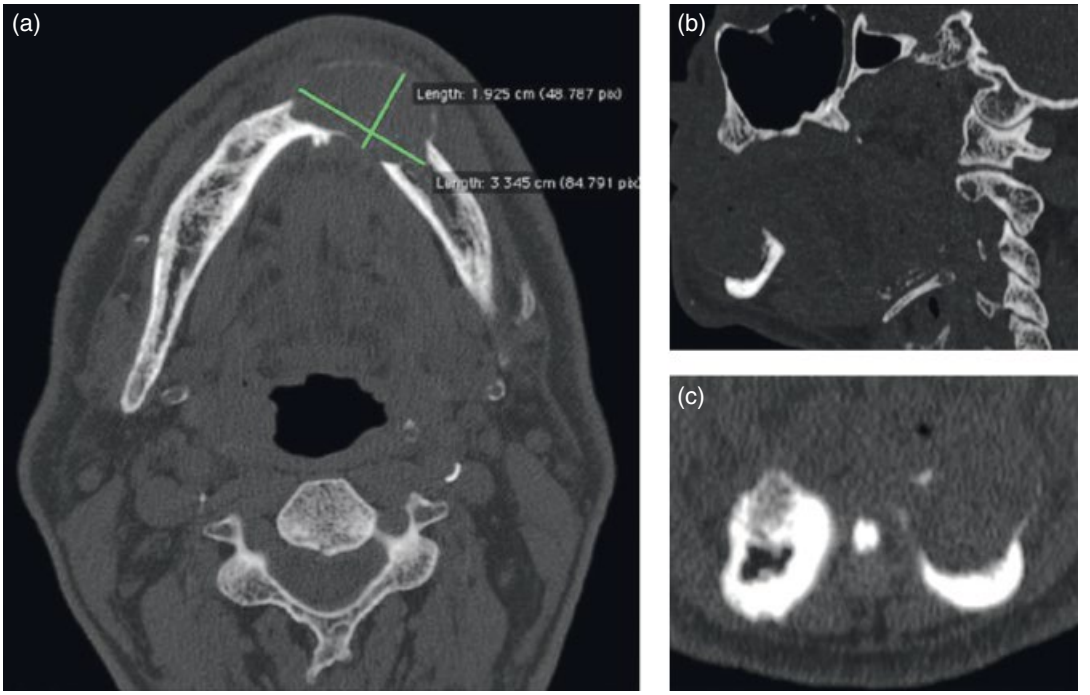


Figure 9.20 Brown tumor in the anterior sextant of the mandible, noticed when the patient's denture no longer fitted. Provisionally diagnosed clinically as an ameloblastoma, computed tomography (a, axial; b, sagittal; c, coronal) revealed a lesion with extensive buccal expansion (nearly 2 cm) and over 3 cm mesiodistally. As incidental findings, calcifications of the internal carotid artery consistent with carotid artery atheroma and calcifications of the branches of the external carotid (a and c, around the hyoid bone) were observed subsequent to the histopathological finding of giant cells. The three-dimensional reconstruction of this case is displayed in Figure 12.13b. Source: (a) MacDonald, D.S., Zhang, L., and Gu, Y. (2012). Calcification of the external carotid arteries and their branches. 41: 615–618.

There are three types of hyperparathyroidism, and they all have their effects by disrupting normal calcium homeostasis [87, 88]. The most common type is primary hyperparathyroidism, which presents as a disease in middle-aged to older patients, principally women. Its most common cause is a secreting adenoma arising in one of the four parathyroid glands. Occasionally, a secreting carcinoma can cause it [89].

A further type frequently is secondary to *chronic renal insufficiency* (CRI) [87] and familial disease [88]. The third type may arise from neoplasia within the parathyroid glands. These glands' hyperactivity is induced by the above and other diseases and generally persists even after the disease that induced them has been treated. Although hemodialysis has greatly improved the longevity of patients suffering from CRI, its side effect of *renal osteodystrophy* (ROD) remains a real risk, particularly in those patients whose adherence to the recommended diet is poor. ROD manifests itself as calcified deposits. Although Asaumi et al. [90] indicated that these calcified deposits around the jaws can be adequately displayed by conventional radiography and that advanced imaging such as CT and MRI adds little, Chang et al. illustrated that the extent and

structure of ROD within the hard palate were best displayed by CT [87]. Calcification within the arteries is discussed further in Chapter 12.

9.11 Localized Poorly Defined Radiolucencies

Localized poorly defined radiolucencies suggest lesions both of local origin and of an aggressive nature. Such disease could be either infections or malignant neoplasms. The primary differentiation between them, in the majority of cases, is dependent upon the clinical findings.

The majority of malignant neoplasms, particularly SCC, are poorly defined (Figure 1.38) or have irregular margins (Figures 9.21 and 9.22) and destroy rather than displace bony structures. On occasion, malignancies may present with well-defined margins (Figures 9.21 and 9.22). In such cases, other features such as widening of the periodontal ligament space (Figure 9.21) and "floating teeth" (Figures 9.21 and 9.22) and the "spiking" pattern of root resorption (Figure 9.22) may direct the clinician toward consideration of a malignancy.



Figure 9.21 Panoramic radiograph of a well-differentiated carcinoma. Although its margin is largely well defined, the widening of the periodontal ligament space on the mesial root of the first molar and the "floating" premolars directs the clinician to consider a malignancy; there is also some resorption of the apices of the premolars. Note: This case should be assessed for paresthesia of the lip. The lesion is sited at the mental foramen.

SCC is the most frequent malignancy of the oral cavity and oropharynx. The WHO Oral Health Program reveals that annually there are about 529 000 new cases and more than 300 000 deaths [91]. Although it primarily presents as a lesion on the oral mucosa, which will be addressed in Chapter 19, some cases arise within the odontogenic epithelial remnants or "rests," within the jaw bones. Although relatively rare, these have been separated out into a number of lesion types by histology: ameloblastic carcinoma, primary intraosseous SCC, clear cell odontogenic carcinoma, sclerosing odontogenic carcinoma, and ghost cell odontogenic carcinoma. Each of the first three has had 100 cases reported and the last two even fewer [92].

9.11.1 PRIMARY INTRAOSSEOUS CARCINOMAS (ICD-O 9270/3)

Odell et al. defined *primary intraosseous carcinoma* (PIOC) as "a central jaw carcinoma that cannot be categorized as any type of carcinoma. It is assumed to arise from odontogenic epithelium. Some cases arise in odontogenic cysts or other benign precursors" [92]. Although Odell et al.'s PIOC replaces *primary intraosseous squamous cell carcinoma* (PIOSCC), the latter term will be retained, as almost all are identified histologically as SCC. Odell et al. also defined ameloblastic carcinoma as "a rare primary epithelial odontogenic malignant neoplasm. It is the malignant counterpart of ameloblastoma" [92].

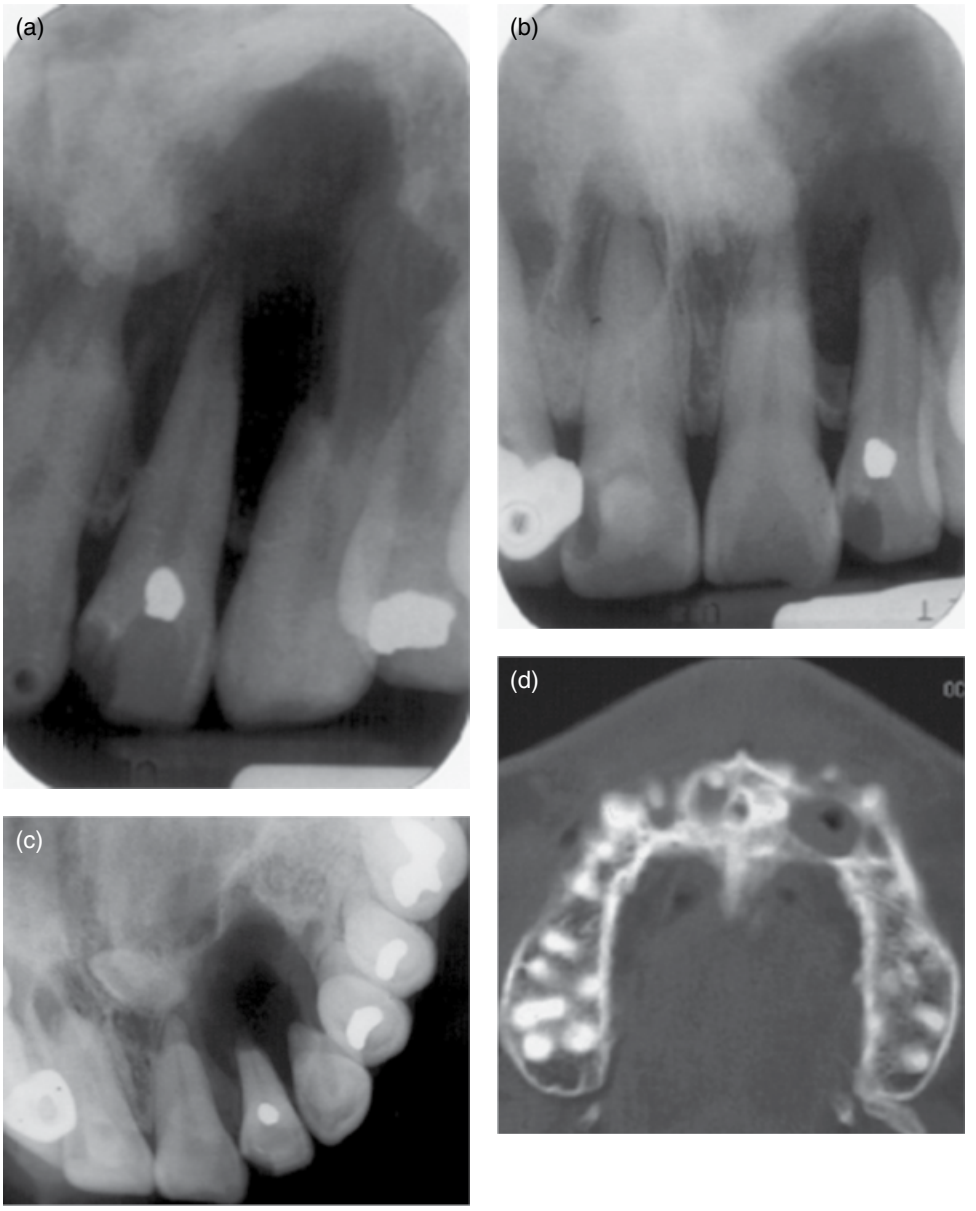


Figure 9.22 Conventional radiographs and computed tomography (CT) of a case of poorly differentiated mucoepidermoid carcinoma. (a) Periapical radiograph exhibiting irregular bone loss (radiolucency) around the left lateral incisor. It is "floating" and its root apex displays spiking pattern resorption. The canine's root has also been resorbed, but largely upon its mesial surface. There is some spiking pattern root resorption on the ipsilateral central incisor. A mesiodens is also included within the radiolucency. (b) Periapical radiolucency in addition shows periapical radiolucencies on the contralateral restored incisors. (c) Anterior occlusal displays involvement of the floor of the nose. (d) Axial CT (bone window) reveals radiolucency displacing the left lateral incisor buccally. It has a soft-tissue radiodensity at the periphery and an air- or gas-filled center.

Eversole et al. state that "When the tumor destroys the cortex and merges with the surface mucosa, it may be difficult to distinguish between a PIOSCC and a true carcinoma arising from the oral mucosa. Invasion from an antral primary must also be excluded" [93]. These authors also report that PIOSCCs are found twice more frequently in males [93]. Although they generally first present with a mean age of 55 years, cases affecting infants have been reported. PIOSCCs are usually found in the posterior sextant of the mandible (Figure 9.23). If they affect the maxilla, they are most frequently observed in the anterior sextant. Although some produce swelling and/or mental paresthesia, the majority are symptom free and found incidentally on radiographs. Radiographically, early lesions are often indistinguishable from odontogenic cysts. Cortical destruction and invasion of the adjacent soft tissue are features of late lesions (see Figure 9.23).

A PIOSCC associated with an impacted mandibular third molar (see Figure 9.23) is associated with a more favorable prognosis. These are, nevertheless, infrequently reported [93].

Huang et al.'s report on Chinese solid-type PIOSCCs reported them as high-grade malignancies which frequently metastasize to regional lymph nodes [94]. They also have a high recurrence rate (76% at five years post-treatment) and thus a high mortality [94].

9.12 Periapical Radiolucencies of Inflammatory Origin

A periapical radiolucency associated with a nonvital tooth, PRIO is the most appropriate radiological diagnostic term [1]. PRIOs represent the three histological diagnoses of granuloma, radicular cyst, and abscess, which differ also in both clinical presentation and outcomes of treatment. The RPPs for granulomas and radicular cysts are set out in Table 9.1. They are all unilocular and arise secondary to necrosis of the dental pulp due to caries or trauma. Nevertheless, such a finding should prompt pulp-vitality testing of the affected tooth/teeth, because any lesion can present first as a periapical radiolucency, such as osseous dysplasia (Figure 9.24), the already-mentioned SCC and PIOSCC (Figures 9.21 and 9.23). Other clinically significant lesions that have been reported recently to present as a periapical radiolucency have been the ameloblastomas (Figure 9.25) [95, 96] and the giant cell lesion [97].

PRIOs begin as a thickening of the periodontal ligament, frequently accompanied by toothache and a tenderness of biting and/or percussion. If left untreated, this becomes larger and develops a "shoulder" with the intact unaffected periodontal ligament (the normal radiolucent space separating the tooth root from the alveolar bone; Figure 9.26). After successful treatment, either by root treatment (endodontics) or extraction, PRIOs generally regress, unless they are already cystic. After root treatment most PRIOs resolve within a year, but some may persist for decades before resolving [98]. Those PRIOs which persisted were probably already radicular cysts (Figures 9.27) at the time of endodontic treatment and were therefore "self-sustaining" and "no longer dependent on the presence or absence of root canal infection," whereas the quicker-resolving former were more likely granulomas [99]. Some PRIOs associated with teeth which were subsequently extracted may have been left behind as "residual cysts," unilocular radiolucencies occupying the now edentulous region of the alveolus.

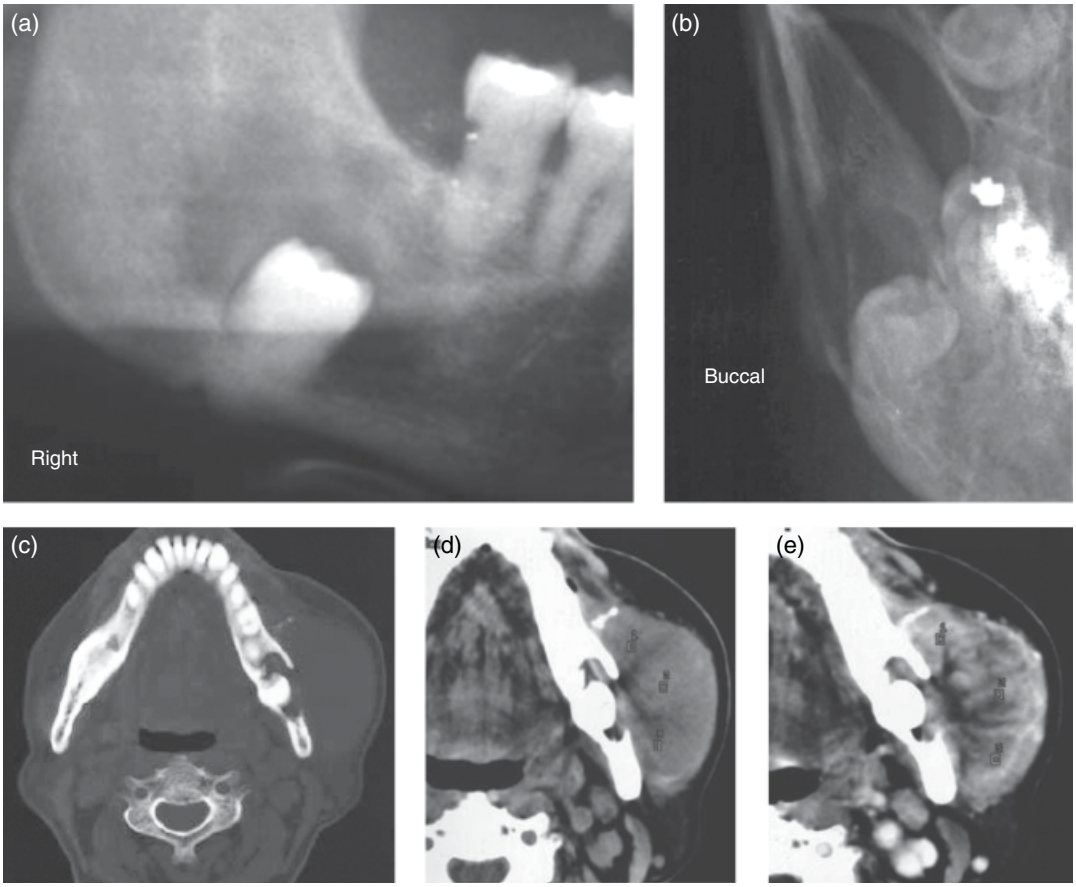


Figure 9.23 Conventional radiographs, computed tomography (CT), of a carcinoma arising from an odontogenic origin. (a) The panoramic radiograph displays an unerupted third molar with the apex of its completely formed root displaced through the lower border of the mandible. Although a normal follicle space is apparent on the mesial and distal aspects of the crown of this tooth, the occlusal part has been irregularly expanded and largely delineated by a band of sclerosis. Outside this band there is a large area of radiolucency that has a poorly defined periphery. (b) The posterioanterior projection of the mandible does not delineate the buccal cortex, which must now be presumed to have been perforated. The axial (c) bone-window CT confirms the substantial loss of the buccal cortex. The neoplasm has now substantially expanded into the adjacent soft tissue. Fragments of bone are observed at the anterior periphery of the lesion (c–e). The precontrast axial soft-tissue window (d) shows that the neoplasm is subjacent to the subcutaneous tissue of the facial skin. (e) The postcontrast CT of similar sections as in (c) and (d) reveals enhancement at the periphery, but also as chords extending toward the neoplasm's center, indicating an extensive intralesional vasculature. The nonenhanced areas (appearing black in the center of the lesion) represent central necrosis. Note: The small boxes in the precontrast (d) and postcontrast (e) images are the sampling sites for determination of Hounsfield units (HU). The increase in HU after administration of the intravenous contrast medium indicates the "enhancement" in (c).

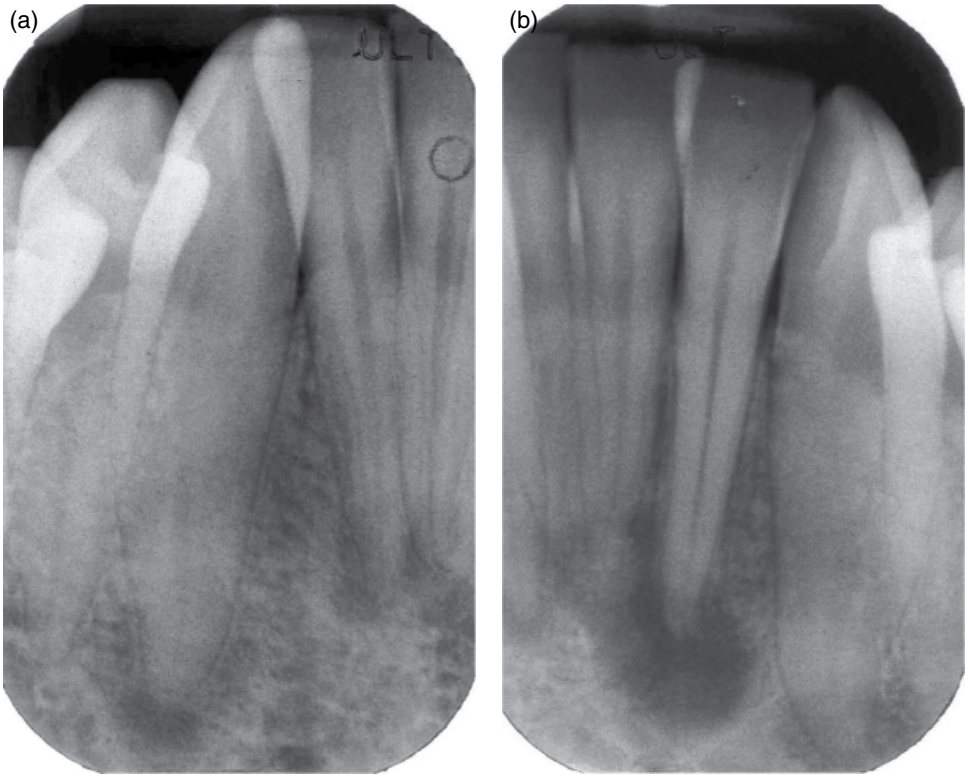


Figure 9.24 Periapical radiographs (a and b) display periapical radiolucencies associated with non-carious and pristine lower incisors. These are most likely to represent early-stage osseous dysplastic lesions. A positive response to pulp-vitality testing is sufficient to confirm their diagnosis.

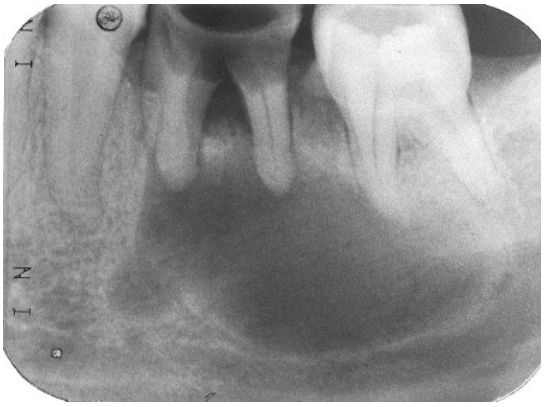


Figure 9.25 Periapical radiolucency of a multilocular ameloblastoma. It presents as a radiolucency, which has a well-defined inferior margin, but a poorly defined superior margin subjacent to a grossly carious first molar with a large furcation radiolucency. The two clues that this lesion is not primarily of inflammatory origin are its multilocular appearance and the fact that its epicenter is not at or close to the origin of inflammation.

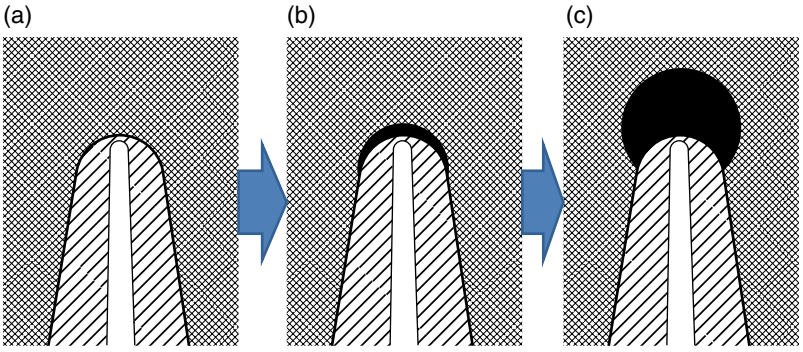


Figure 9.26 Schematic diagrams displaying radiologically the progression of a periapical radiolucency of inflammatory origin (PRIO), from a periodontal ligament space (black line around the root) of normal and uniform thickness in (a), to widening at the apex of the root (b), to a PRIO (c). Source: Adapted from Molven O, Halse A, Fristad I, MacDonald-Jankowski D. Periapical changes following root-canal treatment observed 20–27 years postoperatively. *Int. Endod. J.* 2002;35:784–90.

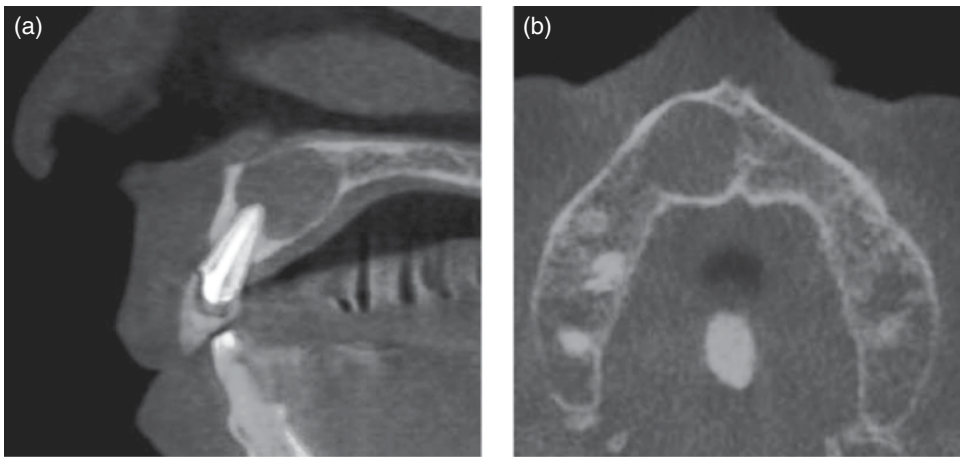


Figure 9.27 Cone-beam computed tomography (CBCT) of a radicular cyst associated with an already endodontically treated central incisor. Displayed are (a) sagittal and (b) axial reconstructions of CBCT. The cyst on sagittal reconstruction presents as a spherical unilocular radiolucency extending up to the floor of the nose and to the midline of the maxilla. In the latter the cyst also directly abuts onto the nasopalatine duct. The radiopacity in the center of the palate on the axial reconstruction is a torus palatinus, a normal anatomical variant. Source: Reproduced with permission from MacDonald, D. (2016). Lesions of the jaws presenting as radiolucencies on cone-beam CT. *Clin. Radiol*. 71: 972–985.

Although CBCT findings cannot reliably distinguish a granuloma from a cyst [100], very large PRIOs are radicular cysts. PRIOs which are 1.5 cm or more in diameter are generally considered to be radical cysts (see later Figure 9.30). Figure 9.27 displays such a lesion associated with an endodontically treated maxillary central incisor, and Figure 9.28 shows another associated with a grossly carious first molar. Whenever the PRIO is excessively large, such as the case Figure 11.19, then

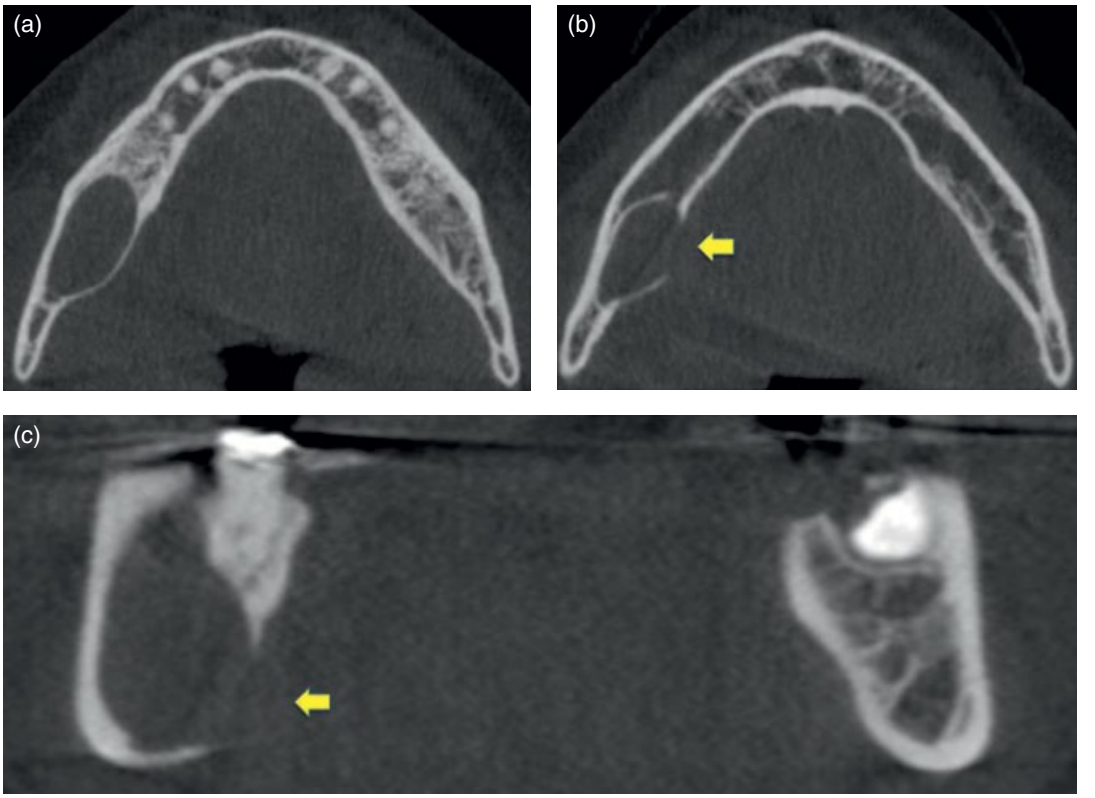


Figure 9.28 Cone-beam computed tomography of a radicular cyst from a carious left mandibular molar. It presents as a unilocular radiolucency extending down to the lower border of the mandible and displacing and eroding the lingual cortex (arrows). The axial reconstruction in (a) is superior to (b). The coronal reconstruction (c) shows a fistula communicating with the oral cavity buccal to the molar. Source: Reproduced with permission from MacDonald, D. (2016). Lesions of the jaws presenting as radiolucencies on cone-beam CT. *Clin. Radiol.* 71: 972–985.

CT rather than CBCT would be indicated, as the PRIO would need to be treated as an inpatient because its extent may lead to the requirement for advice from a radiologist.

The WHO's 1992 edition describes radicular cysts as "a cyst arising from the epithelial residues (rests of Malassez) on the periodontal ligament as a consequence of inflammation, usually following the death of the dental pulp" [101]. Radicular cysts are the most common cyst found in the jaws. Although they may occur in relation to any nonvital tooth, they are infrequently associated with deciduous teeth. They are most frequently associated with teeth of the maxillary anterior sextant. Their peak age at first presentation is the third and fourth decades. Males are more frequently affected [101].

Gundappa et al. compared the images of periapical lesions of ultrasound (US) with analog (film) and digital (charge-couple device) dental radiography [102]. The two dental radiographic technologies did not allow differentiation between cysts and granulomas, whereas US did in each of 15 cases. The authors

concluded that while dental radiography determines the existence of the periapical disease and its extent, US can determine whether the lesion is or is not cystic if sufficient buccal cortex has been resorbed. The underestimate of the lesion's size by US was attributed to the acoustic shadow cast by the bony edges of the lesion on its lateral walls [102].

Not all unilocular radiolucencies associated with the roots of adjacent teeth are PRIOs. Although they are most common in the anterior maxilla (Figure 9.27), PRIOs should be distinguished from nasopalatine duct cysts (NDCs; see later Figures 9.63–9.66). Figure 9.16 displays a periapical radiolucency which was subsequently discovered to be an NHL.

Although root resorption is generally associated with neoplasms, a longstanding PRIO can also cause root resorption (Figure 1.40).

The small field of view (FOV) and high spatial resolution of CBCT were established nearly a decade ago as an important diagnostic tool in endodontics. It has been applied to calcified root canals (Figure 5.9), fractured roots (Figure 5.10), and missed canals (Figure 5.11).

9.12.1 PARADENTAL CYST

The paradental cyst, also called *buccal bifurcation cyst* (BBC), was defined by the WHO's 1992 edition as "a cyst occurring near to the cervical margin of the lateral aspect of a root as a consequence of an inflammatory process in a periodontal pocket… the histological features are… the same as those of the radicular cyst" [103]. It arises from the odontogenic epithelium of the periodontal ligament of a vital tooth. Its distinctive feature is its association with the buccal or distal aspects of an erupted mandibular molar tooth. This tooth is most frequently the third molar (Figure 9.29). Similar cysts can arise from the buccal aspect of the first molar tooth in 6–8-year-old children [103].



Figure 9.29 Panoramic radiograph of buccal bifurcation cyst. A well-defined, partially corticated radiolucency is superimposed upon the root of an unerupted third molar. It has displaced the mandibular canal downward in addition to reducing its diameter.

Pompura et al. reported the largest case series of 44 cases in 31 patients attending a children's hospital over three years [104]. They all presented with tenderness and discomfort about the time of eruption of the first molar. The eruption of the lingual cusps occurs first and some buccal swelling may be present. The true occlusal radiograph best displays most of the radiological characteristics of the BBC and is a recommended projection to complete investigation of the BBC. Figure 3 in Pompura et al. is a panoramic radiograph that displays a BBC that looks identical to a DC [104].

The rarity of reports other that the preceding indicates the infrequency of this lesion. Iatrou et al. found it in only 9% of all intraosseous lesions of the jaws of children [105].

9.12.2 LATERAL PERIODONTAL CYST AND BOTRYOID ODONTOGENIC CYST

The *lateral periodontal cyst* (LPC) was defined by the WHO's 2017 edition as "a developmental odontogenic cyst lined by non-keratinized epithelium, occurring on the lateral aspect or between the roots of erupted teeth" (Figure 9.30) [106]. The WHO's 1992 edition noted that these teeth should be vital and should not arise as a result of inflammatory stimuli [107]. The 2017 edition also defined the *botryoid odontogenic cyst* (BOC) as a multicystic variant of the LPC [106]. It further asserts that the source of the epithelium from which the LPC/BOC arises remains controversial; the dental lamina, reduced enamel epilelium, and rests of Malassez have all been proposed [106]. Though usually symptom free, LPC/BOCs may present as an expansion of the buccal cortex. Radiologically they present as well-defined unilocular, often corticated radiolucencies; BOCs are often multilocular. They are usually 1 cm or less in size [106]. Although LPCs themselves rarely recur after enucleation, BOCs do, due to their multicystic nature [106].

MacDonald et al. reported that some of the many KCOTs presenting as small unilocular radiolucencies in the mandibular premolar and maxillary lateral incisor–canine regions were misdiagnosed prior to surgery as LPCs [108]. Due to their very conservative treatment, they recurred in under a year [108]. This is discussed later in this chapter.

9.12.3 PERICORONAL RADIOLUCENCIES

Pericoronal radiolucencies, particularly of mandibular third molars, occur frequently. They are particularly important because they not only suggest cystic change within the follicle of the unerupted tooth, but may perhaps represent a neoplastic change within that follicle or a secondary envelopment of it by a neoplasm. This neoplastic change is most frequently benign, but it can be malignant (see Figure 9.23). The mandibular third molar site is also the most frequent for occurrence of many odontogenic neoplasms;

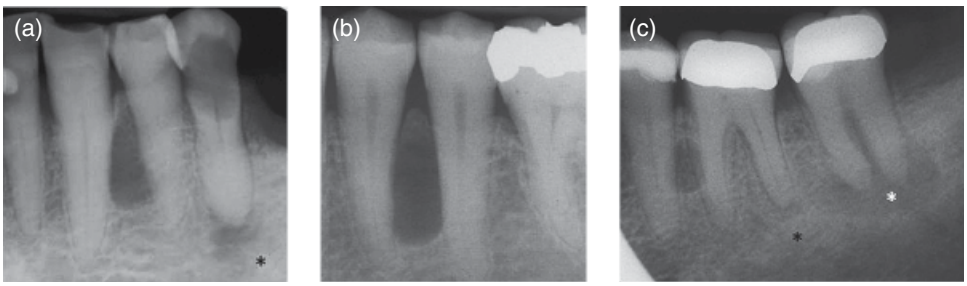


Figure 9.30 Three periapical radiographs displaying lateral periodontal cysts between the mandibular incisors (a), premolars (b), and the second premolar and first molar (c). They are all well-defined unilocular radiolucencies with thin but discernable cortices. Note: The periapical radiolucencies of inflammatory origin (PRIOs) are marked by asterisks, associated with a very large carious lesion (a) and crowned teeth (c). The smaller PRIOs with the adjacent black asterisk could be either granulomas or early radicular cysts. The larger PRIO, marked with a white asterisk, has a well-defined corticated periphery and a diameter of over 1.5 cm. This is more likely to be a radicular cyst. Source: Courtesy of Dr. Lewei Zhang, University of British Columbia.



Figure 9.31 Panoramic radiograph displaying a classical "central" pattern dentigerous cyst (DC) on the left. The coronal radiolucency is attached at the cementoenamel junction at the mesial and distal aspects. The symmetrical enclosure of the crown within the radiolucency is typical of the "central" pattern of radiological presentation of a DC. Note: The DC has essentially two parts: the cystic cavity itself and the tooth it is attached to. Therefore the DC can affect adjacent structures directly (due to direct contact between the cyst and them) or indirectly (by the tooth it is attached to and them). This DC is affecting the mandibular canal both directly (reducing the mandibular canal's diameter mesially to the unerupted third molar) and indirectly (reduction in the mandibular canal's diameter and its downward displacement by the tooth).

some recur if misdiagnosed and inappropriately treated.

Radiolucencies associated with the crown of an unerupted tooth are usually suggestive of DCs, but not always. The review by Curran et al. of over 2600 pericoronal surgical specimens that had been referred to their pathological service over six years revealed that only 67% were not pathological, but were simply normal dental follicles [109]. A further 28% were DCs, of which 35 included mucous cells. Of the remaining 5%, 71 were "keratocysts" (see KCOTs later), 13 each were ameloblastomas and carcinomas, 6 were calcifying cystic odontogenic tumors, 4 were calcifying epithelial odontogenic tumors, and 1 was an odontogenic myxoma. The reader should note that the Curran et al., considered that only a fraction of all specimens arising from unerupted teeth within their community had actually been referred to them. Furthermore, the specimens sent were considered by the referring surgeon to be potentially pathological. Not only did most come from older patients, but also, on subsequent histopathology, those were found most likely to be pathological.

An important feature which distinguishes DCs and follicle spaces from more serious lesions is the relationship of the cyst to the *cementoenamel junction* (CEJ; Figure 9.31). Ikeshima and Tamura noted that the DC attachment was closer to the CEJ than that of the ameloblastoma [110]. Other important features that tend toward the likelihood of a DC are unilocular radiolucency and an absence of root resorption.

9.12.4 DENTIGEROUS CYST

The DC is the most common developmental cyst. Its RPP is set out in Table 9.1. The WHO's 2017 edition reiterated its longstanding definition as "an odontogenic cyst which is attached to the cervical

region of an unerupted tooth and envelops the crown." Although the DC's parthenogenesis is uncertain, it "arises due to an accumulation of fluid between the reduced enamel epithelium of the dental follicle and the crown of the unerupted tooth" [111].

The relationship of the radiographic periphery of the radiolucency surrounding the crown to the "neck" or CEJ is crucial to a diagnosis of a DC radiologically. Based upon the study by Ikeshima and Tamura [110], I conclude that an attachment that is less that 1 mm apical to the CEJ is strongly suggestive that the lesion could be a DC.

The global distribution of reports included in the systematic review [112] from which much of the following is derived is set out in Figure 1.48 and the details are in Table 9.1.

The prevalence of DC could be high, and is so at least in one Turkish community. Yildirim et al. reported that pathological changes among symptom-free third molars represented 23%, of which two-thirds were DCs; the rest were calcifying cystic odontogenic tumors and "odontogenic keratocysts" [113].

DCs are most commonly associated with a mandibular third molar (48%; see Figure 9.31), a maxillary canine (17%) (Figure 9.32), a mandibular premolar (10%), and a maxillary third molar (4%) [114]. They are also associated with supernumeraries; 90% of such cysts are

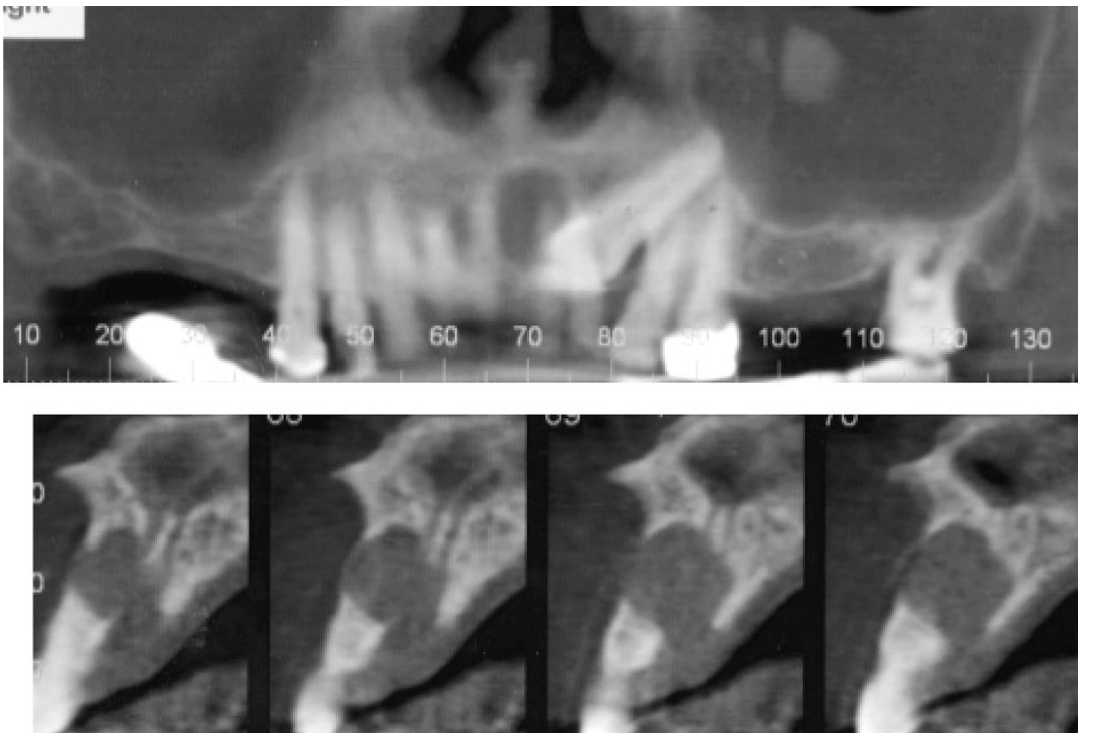


Figure 9.32 Cone-beam computed tomography of a "lateral" pattern dentigerous cyst affecting a maxillary canine. The tangential sections display not only buccolingual expansion, but also perforation of the labial (buccal) and palatal cortical plates. Note: The radiopacity within the left maxillary antrum is most likely to be an anterolith or an exotosis.



Figure 9.33 Standard anterior occlusal radiograph displaying a well-defined radiolucency associated with the crown of an inverted mesiodens as it arises from the cementoenamel junction. This is a "central" pattern dentigerous cyst (DC). This DC is also associated with root resorption.

associated with mesiodens (Figures 9.33 and 11.20). Kaugars et al. reported that 28% of odontomas had DCs [115].

DCs affect males in 61% of cases from all ethnic groups (Table 9.3) [112]. Shear and Speight reported it more frequently in South African Whites than in South African Blacks [114]. The mandible is affected in over two-thirds of cases (64%), while 92% of mandibular cases are found in the posterior sextant. This feature was significantly more likely in the East Asian global group than in the Caucasian. In the maxilla, it is found in the anterior sextant in 69% of cases. It is an incidental finding in 21% of cases and with a swelling or pain in 58% and 32%, respectively.

Although the DC is the second most common cyst after the radicular cyst (Table 9.1) [2, 3] and has been reasonably frequently reported (see Figure 1.41), its radiology, as revealed in the systematic review, has not yet been subject to a single detailed reported series of consecutive (nonselected) cases affecting a community [112]. The only systematic review–included reports that feature such details are Ioannidou et al. [116], who reported all DCs as well defined, and Ledesma-Montes et al. [117], who reported them as radiolucent. Clearly, these observations do not take us beyond what we already know. Nevertheless, it is generally recognized that, in addition to their intimate relationship to the CEJ, all DCs present on radiographs as unilocular radiolucencies. A multilocular appearance should direct the clinician straightaway to consider other lesions; these lesions (see Figure 9.4) are locally invasive and have a tendency to recur after primary surgery. The DC is simply enucleated with the attached tooth, with no recurrence.

The DC presents as one of three radiological patterns [114]. In the central or "classical" pattern, the cyst is attached to both the mesial and distal CEJ and symmetrically envelops the crown of the unerupted tooth (see Figure 9.31). As it expands, it can displace the tooth in an apical direction toward the lower border of the mandible or as far as the floor of the orbit in the maxilla. The second, the "lateral" pattern, arises from the side of the crown (Figure 9.32). This is frequently associated with teeth which are mesially or vertically impacted. The third pattern, the "circumferential," is an exaggerated version of the central pattern; the cyst cavity expands down past the level of the CEJ. Its attachment to the root is still at the CEJ. The cyst is separated from the rest of the root by a bony sleeve containing the lamina dura. Frequently this pattern is seen when the tooth cannot be further displaced apically (see Figure 11.26). This pattern of DC needs to be distinguished from a KCOT or ameloblastoma. The last two generally do not appear to be attached at the CEJ.

Table 9.3 Dentigerous cyst: systematic review.

Feature	Total	Caucasian	East Asian	Sub-Saharan African	Latin American
Male: Female	60% : 40%	60% : 40%	61% : 39%	50% : 50%[a]	53% : 47%
Mean number per year per report	5.8	6.5	6.3	0.0[a]	3.7
Mean age	38 years	40 years	35 years	43 years[a]	34 years
Mean prior awareness	0.7 years	N/A	0.6 years	2.1 years[a]	N/A
Mandible: Maxilla	72% : 28%	65% : 35%	77% : 23%	100% : 0%[a]	73% : 27%
Mandible: *Anterior: Posterior*	8% : 92%	11% : 89%	12% : 88%	0% : 100%[a]	0% : 100%[a]
Maxilla: *Anterior: Posterior*	31% : 69%	37% : 63%[a]	31% : 69%	N/A	N/A
Swelling: *Yes: No*	58% : 42%	68% : 32%	60% : 40%	100% : 0%[a]	37% : 63%
Pain: *Yes: No*	32% : 68%	17% : 83%	41% : 39%	100% : 0%[a]	0% : 100%[a]
Incidental finding: *Yes: No*	21% : 79%	26% : 74%	11% : 89%	0% : 100%[a]	58% : 42%
Numbness: *Yes: No*	2% : 98%	N/A	1% : 99%	N/A	21% : 79%[a]
Discharge: *Yes: No*	12% : 88%	22% : 78%	9% : 91%	67% : 33%[a]	28% : 72%[a]
Radiolucent: *Yes: No*	100% : 0%	100% : 0%	100% : 0%	100% : 0%[a]	100% : 0%
Unilocular: Multilocular	72% : 28%	80% : 20%	63% : 37%	0% : 100%[a]	76% : 24%
Well defined: *Yes: No*	64% : 36%	45% : 55%	100% : 0%[a]	N/A	N/A
Cortex: *Yes: No*	60% : 40%	26% : 74%[a]	88% : 12%[a]	N/A	N/A
Expansion: *Yes: No*	62% : 38%[a]	14% : 86%[a]	82% : 18%[a]	N/A	N/A
Downward expansion of lower border of mandible: *Yes: No*	71% : 29%[a]	N/A	71% : 29%[a]	N/A	N/A
Affects maxillary sinus: *Yes: No*	100% : 0%[a]	N/A	100% : 0%[a]	N/A	N/A
Tooth displacement: *Yes: No*	69% : 31%[a]	N/A	69% : 31%[a]	N/A	N/A
Root resorption: *Yes: No*	23% : 77%	8% : 92%[a]	41% : 59%[a]	N/A	N/A
Associated with unerupted teeth: *Yes: No*	35% : 65%	44% : 56%	31% : 69%	N/A	20% : 80%
Syndromic: *Yes: No*	6% : 94%	6% : 94%	5% : 95%	25% : 75%[a]	14% : 86%
Mixed (Ex): *Yes: No*	7% : 93%	8% : 92%	9% : 91%	11% : 89%	2% : 98%
Orthokeratinized (Ex): *Yes: No*	10% : 90%	11% : 89%	8% : 92%	8% : 92%	8% : 92%
Recurrence: *Yes: No*	28% : 72%	33% : 67%	24% : 76%	50% : 50%[a]	17% : 83%[a]

[a] Percentages derived either from one report or from a synthesis of no more than 50 cases.
Key: (Ex), cases exhibiting orthokeratotic epithelium alone or mixed with parakeratotic epithelium excluded from systematic review; Mixed, cases with mixed orthokeratotic and parakeratotic epithelium; N/A, information not available.

Trying to distinguish between a DC and a follicle space can be difficult, particularly when the suspected DC is small, about 3–4 mm wide. Daley and Wysocki, following their study of this problem, concluded that certainty can be achieved only at the time of surgery [118].

Struthers and Shear reported that a high percentage of DCs in their study were associated with root resorption [119]. Although this phenomenon does not appear to have been reported elsewhere in the literature, root resorption of multiple adjacent teeth was observed in an exceptionally large DC (see Figure 11.27).

The DC is unlike most other odontogenic lesions. It has both direct and indirect effects on adjacent structures by virtue of the associated unerupted tooth being an integral part of it. In addition to its direct effect on adjacent teeth, cortices, and the mandibular canal, it can exert the same impact indirectly by its displacement of the attached tooth. Thus, in addition to a complete evaluation of the cyst itself, attention should be paid to the associated tooth and its effects on related structures, to ensure minimal injury to them upon its extraction along with the enucleated cyst.

Although conventional radiography, usually only a panoramic radiograph, is adequate presurgical imaging for the majority of DCs, CBCT may be necessary for those DCs which present as a surgical challenge because of their size and/or their intimate relationship to adjacent structures such as other teeth (Figure 9.31) and the mandibular canal (Figures 9.31 and 9.34).

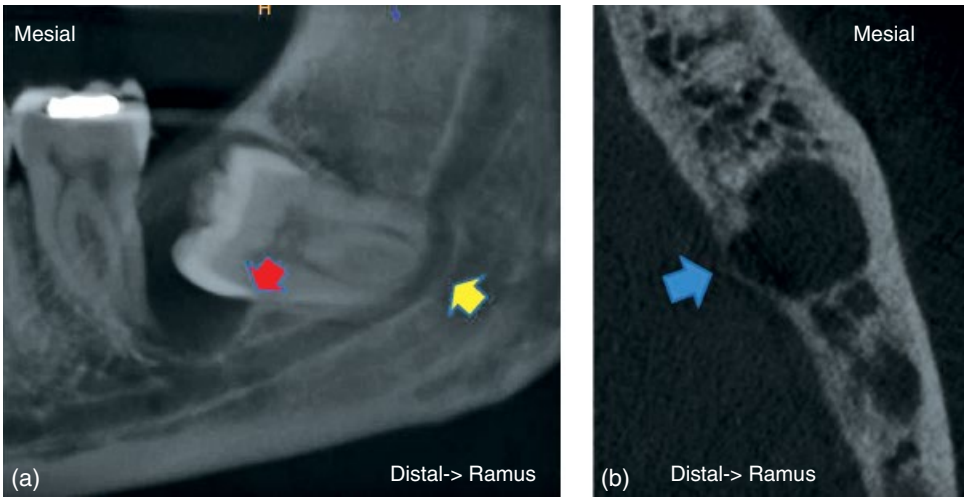


Figure 9.34 (a) Panoramic and (b) axial reconstructions of cone-beam computed tomography (CBCT) of a dentigerous cyst (DC) arising from the crown of an unerupted third mandibular molar. The unilocular radiolucency arises from the cementoenamel junctions of the unerupted molar. Although this and the unilocular shape of the lesion on the conventional radiograph are sufficient for diagnosis of a DC, the CBCT was prescribed to ascertain the closeness of its relationship with the mandibular canal, which has been displaced down and back and the diameter of which has been reduced. These suggest an intimate relationship with the canal, which may result in postoperative paresthesia, of which the patient should be warned preoperatively. The axial reconstruction through the apex of the second molar root displays a round shape and expansion and erosion of the lingual cortex. Source: Reproduced with permission from MacDonald, D. (2016). Lesions of the jaws presenting as radiolucencies on cone-beam CT. *Clin. Radiol.* 71: 972–985.

The treatment of choice for the DC is enucleation. Although a DC does not recur, 15 out of 19 unicystic ameloblastomas were clinically diagnosed as DCs [120]. Therefore, the surgical specimen derived from enucleation of such a DC should be submitted for histopathology. Wang also reported that three partial surgical specimens, one derived from a marsupialization and two biopsies, displayed no histopathology suggestive of the ameloblastoma that was subsequently definitively diagnosed after histopathological examination of the entire surgical specimen [120].

Shear and Speight address a common misapprehension that DCs can readily undergo transformation to ameloblastomas, which was the definitive diagnosis once the whole lesion had been removed and histopathologically reviewed [114]. Their argument challenging this view is that DCs in Shear and Singh's South African study were far more common in Caucasian patients than in Black patients, in which they were uncommon, whereas the ameloblastoma was far more common in the latter, but infrequent in the former [121].

9.13 Odontogenic Neoplasms

Odontogenic neoplasms arise from odontogenic epithelium from which the teeth develop or are left over from tooth formation. Therefore, they are most frequently found in the alveolus. Although odontogenic neoplasms are mainly "benign," the majority of these display a tendency to recur if not appropriately treated. While many cases of all odontogenic neoplasms have similar radiological presentations to those of non-neoplastic lesions (unilocular with little or no root resorption), the presence of well-defined multilocular radiolucencies and/or root resorption should prompt consideration of a neoplasm regardless of any other feature that may suggest a particular PRIO (association with apex of a nonvital tooth) or a DC (attached to the CEJ of an unerupted tooth). Ameloblastomas and KCOTs are the most frequent odontogenic neoplasms, followed at some distance by odontogenic myxomas (Table 9.1).

Although neoplasms associated with the term "odontogenic" have more severe outcomes than other jaw lesions (see Table 1.3), they are unlikely to result in the patient's death. Nevertheless, there have been sporadic reports of ameloblastomas invading the brain [122] (see Figure 11.24) or metastasizing to the lungs. It should be noted that the "metastasizing ameloblastoma" (formerly called malignant ameloblastoma) and ameloblastic carcinoma are completely different lesions; the former is histologically benign, whereas the latter is malignant [123].

There have been no reported deaths with KCOTs, but there have been for odontogenic myxoma. Relatively recently an odontogenic myxoma invaded the brain, after several recurrences [124].

In addition to these three lesions, there is another lesion, the glandular odontogenic cyst (GOC), that should be considered, since many display neoplastic behavior.

9.13.1 AMELOBLASTOMA (ICD-O 9310/0)

The development of the classification of the ameloblastoma over the course of the WHO's four editions is displayed in Figure 9.35. Figure 9.36 exhibits the three intraosseous types revealed by the WHO's 2005 edition. Although many if not most are multilocular and therefore clearly neoplastic, the unicystic ameloblastoma is almost wholly unilocular. Nevertheless, regardless of type, the two main

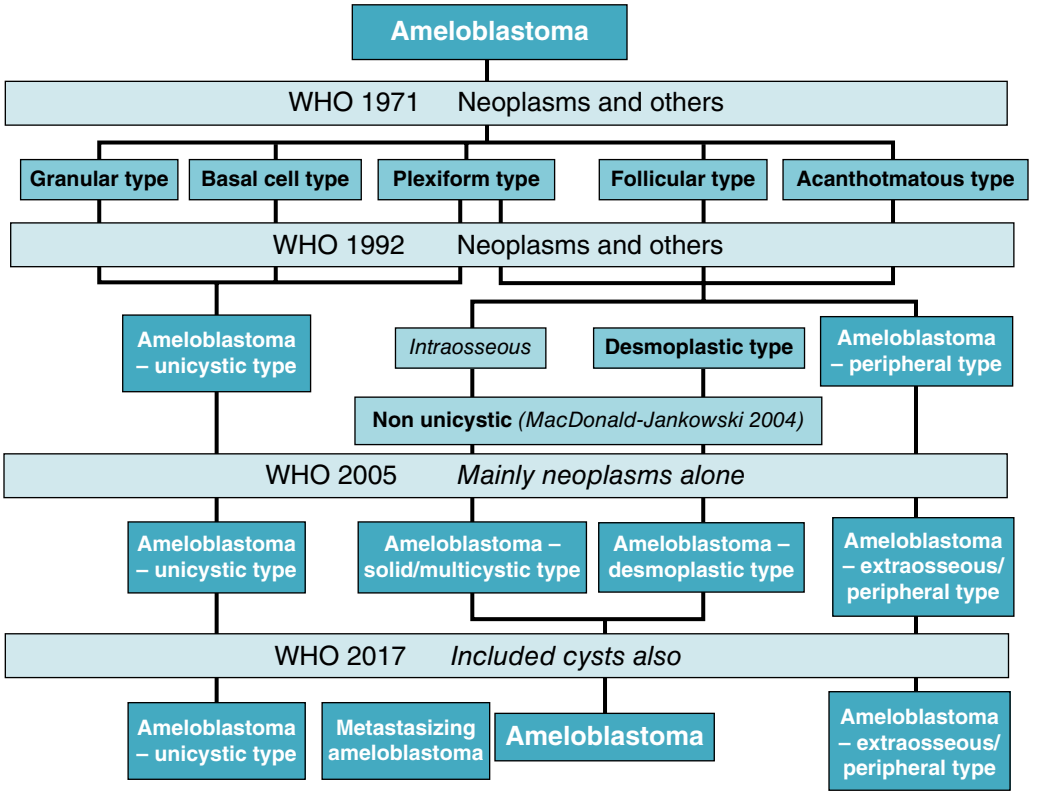


Figure 9.35 Evolution of the classification of the ameloblastoma through four editions of the World Health Organization's (WHO) classifications of head and neck tumors. The above four banner headings, one for each edition, includes a remark about how extensive the coverage of jaw lesions each edition was.

radiological features that direct the clinician to consider an ameloblastoma are substantial buccolingual expansion and root resorption.

The WHO's 2017 edition defined the ameloblastoma as "a benign intraosseous progressively growing epithelial odontogenic neoplasm characterized by expansion and a tendency for local recurrence if not adequately removed." This edition, retaining the unicystic and extraosseous/peripheral types, replaced both the solid/multilocular and desmoplastic types simply with "ameloblastoma." This type ranges histologically "from entirely solid to variably cystic" [125]. This reduction of intraosseous ameloblastoma types to unicystic ameloblastoma and ameloblastoma replicates MacDonald-Jankowski et al.'s earlier division of intraosseous ameloblastomas into unicystic and nonunicystic ameloblastomas [126, 127]. The reasoning for this was that unicystic ameloblastomas respond to more conservative enucleation and adjuvant treatment, mainly by Carnoy's solution, whereas the other intraosseous ameloblastomas require more radical treatment, namely resection. The unicystic ameloblastoma is defined as "a variant of intra-osseous ameloblastoma that occurs as a single cystic cavity with or without luminal proliferation" [128]. Of the ameloblastomas, 90% exhibit mutations in genes that belong

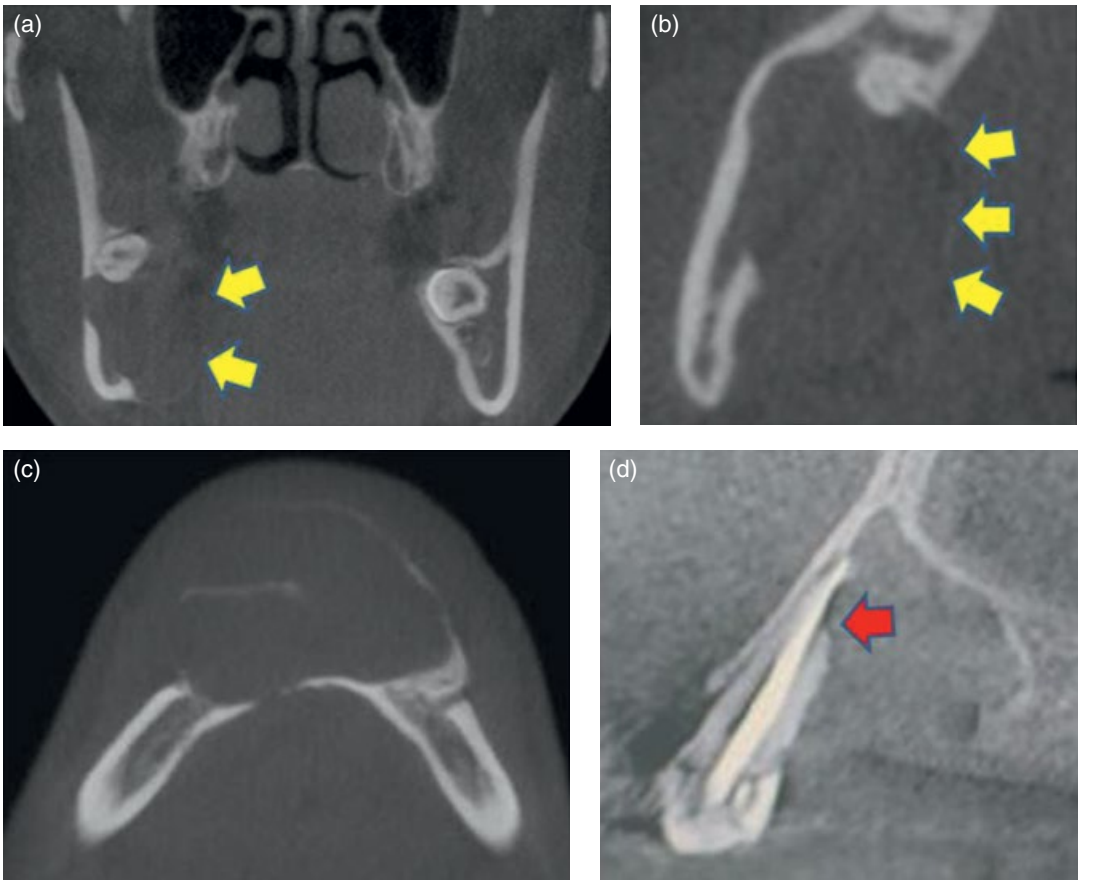


Figure 9.36 Reconstructions of cone-beam computed tomography of the three intraosseous subtypes of ameloblastomas. (a) Coronal and (b) axial reconstructions of a unicystic ameloblastoma, the most frequent subtype in the Chinese population. The yellow arrows indicate the extent of the eroded and displaced lingual cortex. Note its lingual extension down past the uneroded and undisplaced lower border of the mandible on the coronal reconstruction. This is a feature of the ameloblastoma so far not displayed by other odontogenic neoplasms. (c) Axial reconstruction of a solid subtype of ameloblastoma, the most frequent type. A septum has been cut transversely. (d) Sagittal reconstruction of a desmoplastic subtype of ameloblastoma eroding the root of the root-filled incisor (red arrow). The radiopaque structures immediately adjacent to the well-defined cortex are reminiscent of those seen in Figures 9.38 and 9.41 and suggestive of a honeycomb multiloculation. The desmoplastic subtype is the least frequent subtype of ameloblastoma. Source: Reproduced with permission from MacDonald, D. (2016). Lesions of the jaws presenting as radiolucencies on cone-beam CT. *Clin. Radiol.* 71:972–985.

to the MAPK pathways, *BRAF* V600E being the most common for both the ameloblastoma and the unicystic ameloblastoma [125, 128]. Wright and Vered reported that patients with *BRAF* V600E ameloblastomas have a mean age at diagnosis of 35 years, in comparison to those with the *BRAF* wild type presenting at a mean age of 54 years [129]. They added that *BRAF* in addition to hedgehog-related *SMO* mutations also were present in a series of odontogenic carcinomas [129].

In contradiction to the WHO's 2005 edition, which stated that the ameloblastoma had "virtually no tendency to metastasize" [130], the WHO's 2017 edition recognized the "metastasizing ameloblastoma" as a fourth type, but with the ICD-D code 9310/3 [123]. "It metastasizes despite its benign histological appearance" and "with no specific features predicting metastasis." It is still known by many authorities by its synonym "malignant ameloblastoma" and should never be confused with the entity "ameloblastic carcinoma," which displays malignant histological features and not those of an ameloblastoma. Therefore, the metastasizing ameloblastoma is defined by its behavior rather than its appearance. Because of "the long latent period before metastasis" and because "some cases occur after repeated surgical intervention," the attending clinician must firmly resolve to effect complete treatment at the first intervention and advise the patient to expect life-long follow-up. The seemingly favorable five-year survival of 70% is very dependent on site and ease of access to the surgeon. So far, neither chemotherapy nor radiotherapy has been effective [123]. Although the metastasizing ameloblastoma is exceedingly rare, the clinician should never lose sight of the fact that the ameloblastoma is very locally invasive, and that failure to ablate it completely at primary surgery may have truly unfortunate consequences for the patient. Figure 11.21 displays recurrence in a reconstruction after resection of an ameloblastoma arising in the maxilla, invading the brain.

Gathering the previously separate types of ameloblastoma into a single group is commendable when there is no longer any pressing need to maintain their separate identities simply because they behave in the same way; that is, they are locally invasive and require resection. Unfortunately, simply using the bare term "ameloblastoma" for this group of lesions leads to confusion as to whether it means this is a new group of ameloblastomas in general. This is important, because although the solid subtype constitutes the majority of ameloblastomas in Caucasian communities, over half of the ameloblastomas in the Chinese population are unicystic, which responds to more conservative treatment as already outlined [126, 127, 131]. Having not been able to determine differences between all the nonunicystic types as identified by the WHO's 1972 and 1992 editions (thereby anticipating the similar conclusions found in both the WHO's 2005 and 2017 editions), MacDonald-Jankowski grouped his case series of ameloblastomas into two groups, unicystic and the nonunicystic, in order to reveal clinical and radiological differences between them [126, 127]. The point is that terms such as "solid" and "multilocular" in relation to a particular group no longer make sense and, as MacDonald-Jankowski showed, 20% of the nonunicystic ameloblastomas were unilocular [126, 127].

In an East Asian community, the unicystic subtype was typically unilocular, affecting the posterior sextant of the mandible (Figure 9.45a and b) and first presenting before 25 years of age, whereas the solid subtype generally presented after that age and was more likely to be multilocular and to affect the anterior sextant of either jaw [126, 127]. Although a prominent feature of an ameloblastoma is root resorption, other odontogenic neoplasms, such as KCOTs [1], also cause root resorption, but less so in degree (see later Figure 9.45) and frequency [1]. Another feature of ameloblastomas is substantial buccolingual expansion (Figures 1.11, 1.43, and 9.38), which is more ball-like [126, 127] than that of the other equally frequent odontogenic neoplasm, KCOTs,

which are minimally expansile, particularly when they affect the body of the mandible (see later Figure 9.44) [1]. The expansion of the lingual cortex by an ameloblastoma sited in the body of the mandible was, in addition to being directed lingually, also frequently directed inferiorly, down past the lower border of the mandible rather than displacing it downward (Figure 9.45a) [126, 127].

Although the WHO's 2017 edition regrouped the once independent desmoplastic type into the ameloblastoma group, there is still merit in continuing to recognize its independence [125]. A recent case series on desmoplastic ameloblastomas reported that although most appeared as poorly defined unilocular radiolucencies on conventional radiography, all presented with a honeycomb pattern on CBCT [132]. Other attributes of the desmoplastic type that set it apart from the WHO's 2017 edition promulgations will be discussed later in this section. Furthermore, in view of this and in order to make it easier for the reader to follow, the terms "solid type" and "desmoplastic type" will be preserved in addition to "unicystic." The peripheral type, which is histologically similar to the solid type but in the majority of cases is confined to the soft tissues, principally of the gingivae, thereby producing little in way of a radiologically observable signature, will not be considered further.

The global distribution of reports included in the systematic review [126, 127], from which much of the following is derived, is set out in Figure 1.45 and the details are in Table 9.4.

The mean number of ameloblastomas per year globally is 4.8 (Table 9.4). It is significantly greater for both the East Asian and sub-Saharan African global groups, 8.5 ameloblastomas per year for each, than it is for either the Caucasian (2.3) and Latin American (0.8) global groups.

This significantly higher incidence is also accompanied by a significantly younger age on first presentation for the East Asian and sub-Saharan African global groups, both about 33 years. These differences may in part reflect the proportions of the solid, desmoplastic, and unicystic variants. The desmoplastic variant generally has an older mean age. After a synthesis of the literature, Philipsen et al. reported the mean age of the desmoplastic variant at 42 years, in contrast to the solid variant's 36 years [132], whereas in another study the mean age of first presentation of the unicystic variant is significantly younger [126, 127]. Following on from the genetic discussion at the beginning of this section, *BRAF* V600E was followed in those unicystic found ameloblastomas. Furthermore, ameloblastomas with *BRAF* V600E were predominantly found in the mandible, where almost all unicystic ameloblastomas in a large case series were found, whereas those with *SMO* mutations were predominantly found in the maxilla [129]. This emerging genetic dichotomy between the jaws has not yet been elucidated [129].

The age at first presentation was earliest for Bangladeshis and Koreans and oldest for Chinese, among whom the earliest, a mean of only 30 years, was for Hong Kong Chinese [126]. This early age of first presentation may have been affected by the very short period of prior awareness of the lesion before presentation in this community. This 0.7 years compared to 2.5 years overall for Table 9.4. This period was even shorter for the younger patients in this Chinese community [126].

Although overall ameloblastomas are almost equally distributed between sexes, Western, East Asian, and sub-Saharan African reports displayed a predilection for males, whereas Latin America showed a predilection for females, which was significant when compared to the

Table 9.4 Ameloblastoma: systematic review.

Feature	Total	Caucasian	East Asian	Sub-Saharan African	Latin American
Male: Female	56% : 44%	56% : 44%	56% : 44%	60% : 40%	46% : 54%
Mean number per year per report	4.8	2.3	8.5	8.5	0.8
Mean age[a]	35.4 years	40.9 years	33.1 years	32.3 years	38.5 years
Mean prior awareness[a]	2.5 years	1.6 years[b]	2.7 years	1.8 years[b]	N/A
Mandible: Maxilla	91% : 9%	85% : 15%	92% : 8%	93% : 7%	93% : 7%
Mandible: *Anterior: Posterior*	16% : 84%	13% : 87%	12% : 88%	17% : 83%	48% : 52%
Maxilla: *Anterior: Posterior*	18% : 82%	8% : 92%	24% : 76%[b]	0% : 100%[b]	10% : 90%[b]
Swelling: *Yes: No*	68% : 32%	52% : 48%[b]	76% : 24%	58% : 42%[b]	N/A
Pain: *Yes: No*	18% : 82%	44% : 56%[b]	15% : 85%[b]	25% : 75%[a]	18% : 82%[b]
Numbness: *Yes: No*	12% : 88%	N/A	7% : 93%[b]	8% : 92%[b]	N/A
Radiolucent: *Yes: No*	96% : 4%	86% : 14%	99% : 1%	98% : 2%	100% : 0%[b]
Unilocular: Multilocular	29% : 71%	18% : 82%	38% : 62%	11% : 89%	44% : 56%[b]
Well defined: *Yes: No*	96% : 4%	N/A	100% : 0%	N/A	79% : 21%[b]
Cortex: *Yes: No*	78% : 22%	100% : 0%[b]	77% : 23%[b]	N/A	N/A
Expansion: *Yes: No*	91% : 9%	66% : 34%	95% : 5%	100% : 0%[b]	N/A
Affects maxillary sinus: *Yes: No*	75% : 25%[ab]	N/A	75% : 25%[b]	N/A	N/A
Tooth displacement: *Yes: No*	73% : 27%[b]	N/A	73% : 27%[b]	N/A	N/A
Root resorption: *Yes: No*	59% : 41%	56% : 44%[b]	64% : 36%	N/A	N/A
Recurrence: *Yes: No*	14% : 86%	16% : 84%	15% : 85%	9% : 91%	4% : 96%

[a] Not the cumulative mean calculated for the published report.
[b] Percentages derived either from one report or from a synthesis of no more than 50 cases.
Key: N/A, information not available.

0004257464.INDD 211 9/5/2019 10:36:13 PM

sub-Saharan African global group's greater predilection for males [126, 127].

Overall, in the systematic review [126, 127], 68% presented with swelling, 18% with pain, 12% with paresthesia or numbness, 6% with discharge and/or fistulae, and 6% with ulceration. Swelling was significantly more frequent on first presentation in the East Asian global group than in the Caucasian, and pain was more frequent in the Caucasian global group than in the East Asian global group.

The mandible is affected in 91% and the maxilla in 9% of cases. The ameloblastomas display a predilection for the posterior sextants rather than the anterior sextants for both jaws. Although overall these were 84% and 82% for the mandible and maxilla, respectively, the Latin American global group displayed a significant equal distribution between mandibular sextants. The Caucasian global group exhibited a much greater predilection for the posterior maxillary sextant than the East Asian global group. Those cases affecting the posterior sextants, particularly of the mandible in one East Asian report, presented below the age of 25 years and were not only unilocular but unicystic ameloblastomas [126, 127]. Luo et al.'s report confirms this phenomenon [133].

Generally, the ameloblastoma appears as a well-defined radiolucency (96%) on conventional radiographs [127]; the only exception is cases of the desmoplastic type, which appear as poorly defined [132]. In addition, many cases of the desmoplastic type exhibit a mixed radiolucent-radiopaque appearance [132]. This feature, in conjunction with a poorly defined border, "suggested fibro-osseous lesions" [133]. Unlike most other ameloblastomas, the desmoplastic type displayed a greater proclivity for the maxilla than the solid type; the former affects both jaws equally, whereas the latter has an overwhelming predilection for the mandible [132].

Although the vast majority of ameloblastomas are radiolucent, the Caucasian global group has a significantly higher proportion presenting as radiopacities than those of the East Asian and sub-Saharan African global groups. This may in part reflect the higher proportion of the desmoplastic type that is purported to be more prevalent in the Caucasian global group [132].

The East Asian global group displays a significantly higher proportion of unilocular, rather than multilocular, radiolucencies than either the Caucasian or sub-Saharan African global groups. This may represent the higher prevalence of the unicystic type, which presents almost exclusively as a unilocular radiolucency, reported in communities in the East Asian global group [127, 131].

The systematic review reveals that 91% of ameloblastomas are associated with buccolingual expansion (Figure 1.36), which is significantly less in the Caucasian global group than in the East Asian and sub-Saharan African global groups.

Root resorption occurred in 59% (Figures 1.30, 1.31, 1.37, 1.41, and 9.37) and tooth displacement occurred in 64% (Figures 1.11 and 9.38) of the East Asian global group [127]. Almost all ameloblastomas presenting in this group are radiolucent [127]. Of these, 96% are well defined; 29% of the radiolucencies are unilocular (see Figures 1.11, 1.30, 1.41, 1.42, and 9.36) and 71% are multilocular (Figures 1.31, 1.37, 9.38, 9.39, later 9.41, and 11.23). A downward displacement of the lower border of the mandible (see Figure 1.11) and an involvement of the maxillary antrum (11.23) occurred in 42% and 75%, respectively, in this East Asian report [127].

A hitherto previously unobserved feature of the ameloblastoma is the displacement of a lateral cortex down past the undisplaced lower border of the mandible (see Figure 1.37). The only other lesion in

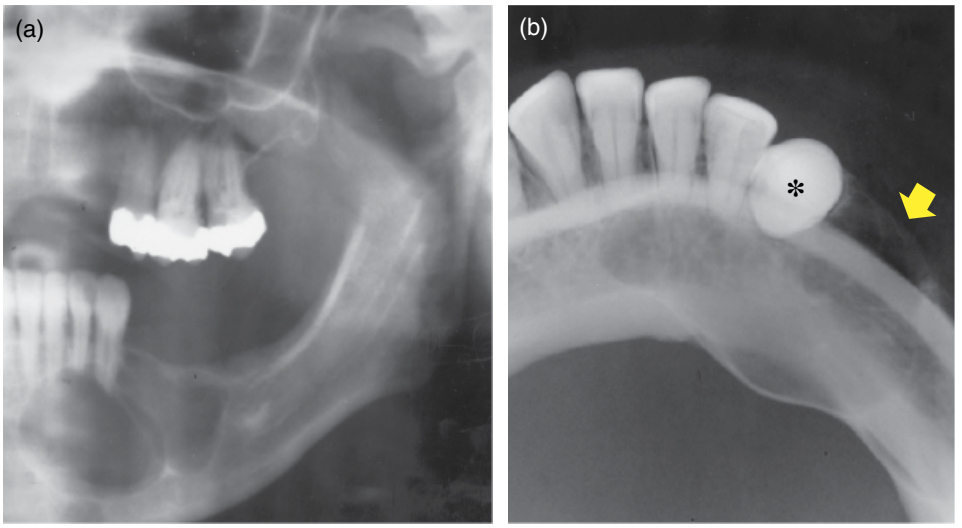


Figure 9.37 Panoramic radiograph (a) exhibiting a solid ameloblastoma affecting the anterior teeth and left premolar–first molar region. It is multilocular and displays root resorption. The periapical of this case is displayed in Figure 1.37 and exhibits marked root resorption. Occlusal radiograph (b) displaying a very thin cortex. It exhibits substantial buccolingual expansion – the arrow defines the most buccal limit of the extension, which in conjunction with (a) imparts a beachball-shaped appreciation of the solid ameloblastoma in three dimensions. The asterisk denotes the crown of the canine. Its apex does not appear because it has been displaced buccally, by the ameloblastoma.

which this feature has also been observed is the orthokeratinized odontogenic cyst (OOC; see later Figures 9.53 and 9.54).

Root resorption, tooth displacement, and unerupted teeth were significantly more associated with the unicystic variant than the other variants in this East Asian (Hong Kong Chinese) report [127]. This means that root resorption affecting ameloblastomas in this community is more likely to be observed in those lesions that first present on or before 25 years old.

Another report did not observe statistical differences between multilocular and unilocular radiolucencies with regard to root resorption and unerupted teeth [134]. The differences between these reports may reflect the different ethnic origin, East Asian [127] and sub-Saharan African [134], and the fact that the latter was derived from selected cases first presenting within a narrow age range (first two decades of life).

Accurate diagnosis is necessary for appropriate treatment that minimizes both recurrence and morbidity. This accuracy is not merely confined to determining whether the lesion is an ameloblastoma or not, but also to the correct identification of the particular type of ameloblastoma. The majority of cases are generally of the solid variant, which needs to be resected with a margin. The unicystic type is generally conservatively treated by enucleation and a cytotoxic agent such as Carnoy's solution [135]. Although this treatment is associated with a 11–16% recurrence rate, which is higher than the 3–4.5% associated with resection, it is much less than the 30% associated with enucleation alone [136, 137]. Nevertheless, long-term follow-up of this type, as with the others, is recommended regardless of the mode of treatment [138].

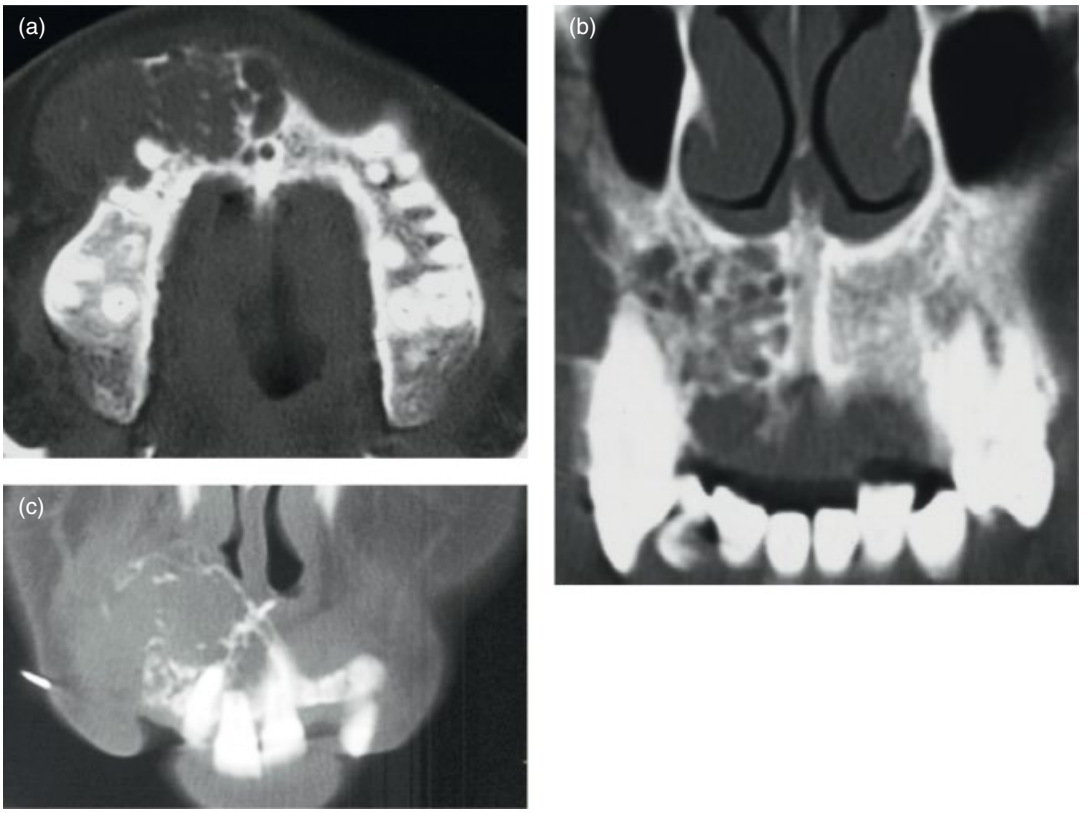


Figure 9.38 Computed tomography (CT) of a solid (multilocular) ameloblastoma affecting the anterior sextant of the maxilla. (a) Axial CT (bone window) displaying a multilocular radiolucency affecting the anterior maxilla. It exhibits substantial labial expansion. (b) Coronal CT (bone window) displaying a honeycomb appearance extending from the nasopalatine canal to the canine. It has eroded the mesial aspect of the cortex of the floor of the nasal cavity. (c) Coronal CT (bone window) anterior to (b) displaying a substantial expansion into the soft tissue of the nose and has expanded into the anterior nares. A multilocular pattern is evident throughout. The pattern is honeycomb distal to the lateral incisor.

Conventional radiography reveals that the majority of ameloblastomas are multilocular [127]. This generally ensures that the solid ameloblastoma appears high on the differential diagnosis, particularly if it also displays expansion. The same is not true for the unicystic ameloblastoma, because most present as unilocular radiolucencies, and it may be difficult for many clinicians to distinguish them from DCs, which respond to enucleation without recurrence. Much of the lining of a unicystic ameloblastoma may be non-neoplastic and similar to that of a DC, thereby making preoperative biopsy a hit-or-miss affair [120]. Furthermore, Zhang et al.'s histopathological observation of a unicystic ameloblastoma concurrent with a DC supports the notion that occasionally a DC may evolve into more serious disease, certainly in this Canadian community [139]. This is contrary to Shear and Singh's findings within a South African community [121].

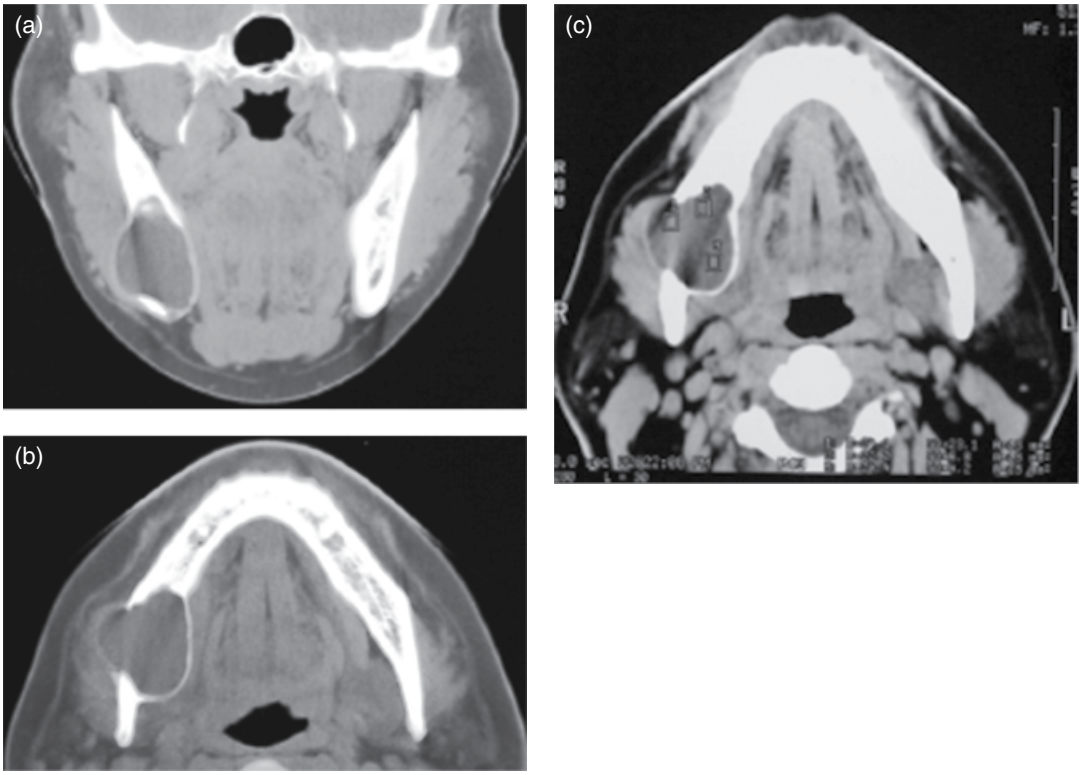


Figure 9.39 Computed tomography (CT) of a unicystic ameloblastoma affecting the posterior sextant of the mandible. (a) Coronal CT (bone window) displaying buccal and lingual expansion. (b) Axial CT (bone window) displaying buccal and lingual expansion. (c) Axial CT (soft-tissue window) also displaying buccal and lingual expansion. The CT number, as measured in the 'boxes,' is 22–24 Hounsfield units.

There are several subtypes of the unicystic ameloblastoma that are not readily distinguishable radiologically [127]. Gardner et al. identified three variants of the unicystic ameloblastoma that are obvious to the histopathologist [130]: luminal, intraluminal, and mural (see their Figure 6.22). The cyst lining of the *luminal* variant is composed of ameloblastic cyst epithelium. The *intraluminal* variant displays an ameloblastic mass protruding into the lumen. The *mural* variant exhibits an ameloblastic mass invading the adjacent fibrous tissue wall. Although Li et al. reported that the simple cystic forms of the unicystic ameloblastoma (presumably the luminal variant) are less likely to recur than the other forms [140], Lee et al. reported that 93% of unicystic ameloblastomas displayed mural invasion of the fibrous tissue wall (the mural variant) [135]. This preponderance of the mural variant may explain the still relatively high recurrence rate even after the use of an adjuvant (such as Carnoy's solution) with the enucleation.

Although advanced imaging can assist further as a preoperative (including biopsy) investigation, there is a general dearth of such literature for odontogenic neoplasms, particularly with regard to CT. This may very well indicate that surgeons have hitherto considered conventional radiography to be adequate for diagnosis

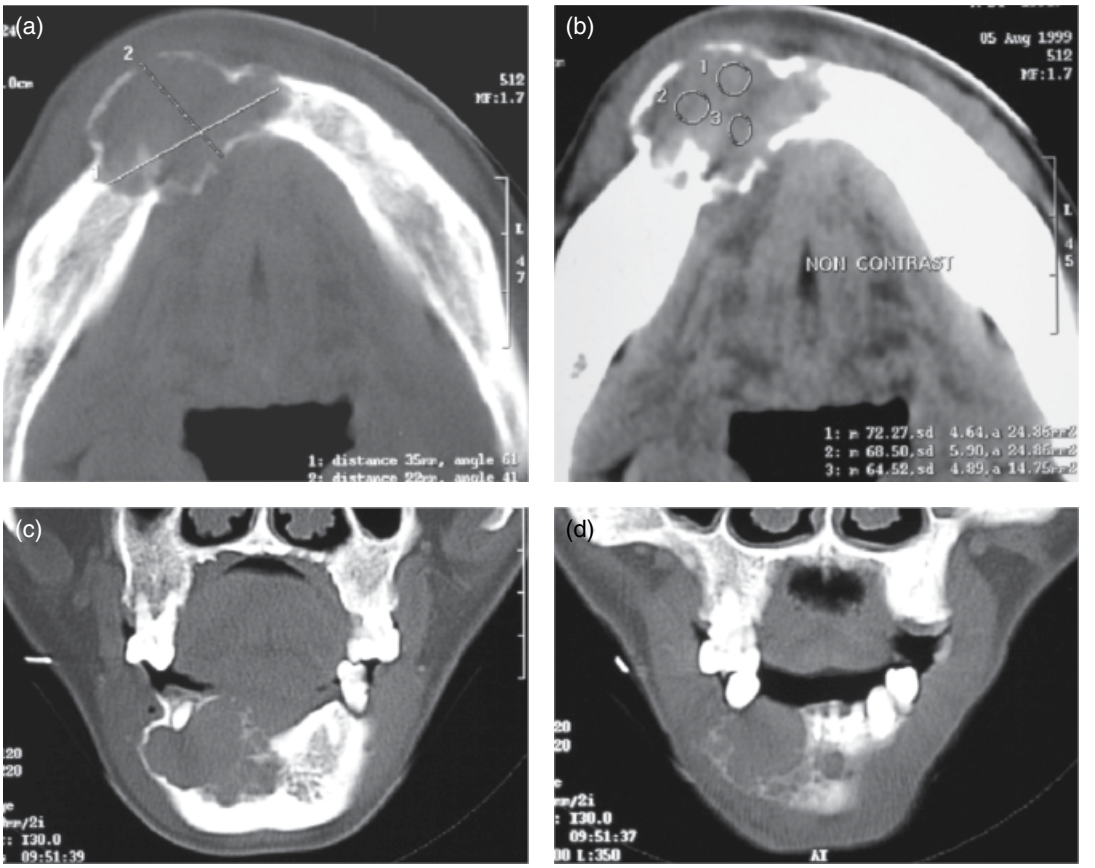


Figure 9.40 Computed tomography (CT) of a solid (multilocular) ameloblastoma affecting the anterior sextant of the mandible. (a) Axial CT (bone window) displaying buccal expansion with some perforation of the cortex. (b) Axial CT (soft-tissue window) displaying a higher CT number than Figure 9.39, 64–72 Hounsfield units. (c and d) Coronal CT (bone window) displaying a multilocular pattern, which ranges from large soap-bubble to honeycomb.

and treatment planning for the majority of ameloblastomas.

Of the 61 consecutive cases of ameloblastoma, only 32 patients were referred for CT [141]. The unicystic variant (Figure 9.36) was significantly less likely to be referred in comparison to those of the nonunicystic variant (solid variant, Figures 9.39, 9.40; and desmoplastic variant, Figure 9.41). This lack of referral for CT may be due to the fact that cases of the unicystic variant are relatively easy to diagnose on the basis of conventional radiography, they can be conservatively treated (enucleated and Carnoy's solution) with a subsequently good prognosis, and finally that they affect young patients, who are at a higher risk of radiation-induced disease. The other most significant feature of those patients referred was that they were older males. It is possible that the desire to avoid increasing the radiation dose in general to young patients and more particularly to females of reproductive age inhibited the referral of younger patients for CT [141]. Nevertheless, CT of certain cases can reveal and allow better assessment of

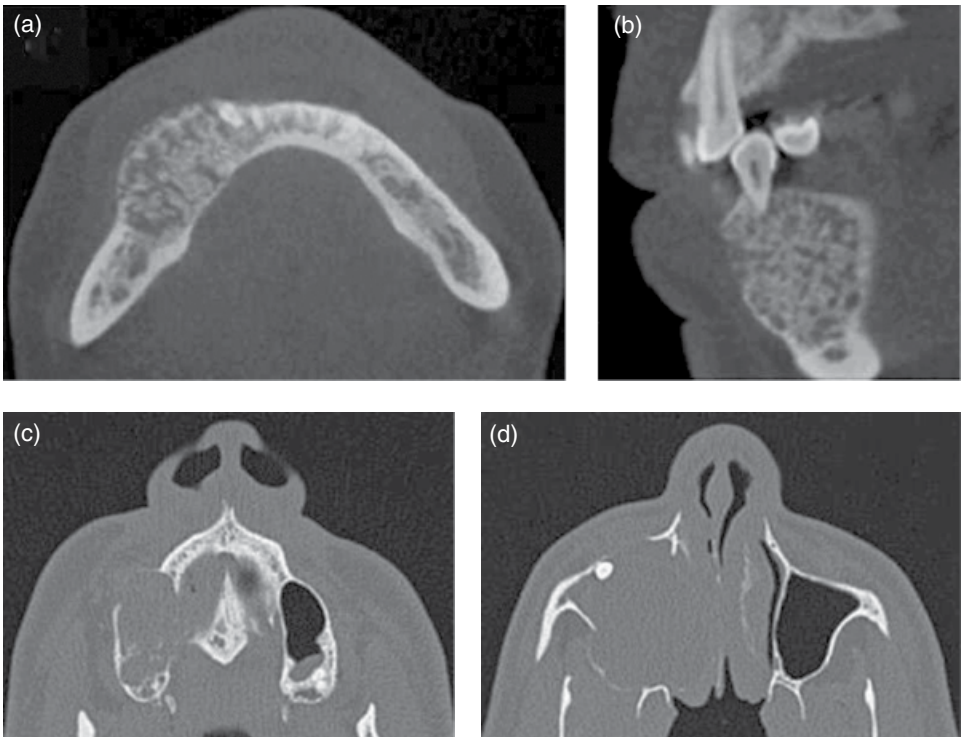


Figure 9.41 Cone-beam computed tomography of a case of desmoplastic ameloblastoma.(a and b) in the Right premolar area of the mandible. The axial (a) and sagittal (b) reconstructions display a 'snow-storm' pattern of opacities that suggests a differential diagnosis that would not include an ameloblastoma. The buccal cortex is expanded and so eroded in places to suggest perforation. The lingual cortex has been minimally expanded, but has been substantially eroded. Computed tomography (c and d) of a case of desmoplastic ameloblastoma in the right maxilla which has undergone malignant transformation to a squamous cell carcinoma. (c) is an axial section throught the alveolus at the level of the mandibular foramen and Hamulus. It exhibits a radiolucency containing 'snowstorm' pattern of opacities in its posterior half. It displays substantial buccal expansion anteriorly with marked erosion and lesser expansion palatally but with more marked erosion and perforations in places. (d) is an axial section at the level of the zygomatic arch. (d) reveals complete obturation of the maxillary sinus and expansion of the posteriolateral, medial and anterior walls of the sinus. These walls are also eroded; the medial wall is substantially perforated and has obturated the right nasal cavity and has almost completely eroded the bone of the inferior concha (turbinate). The right body of the pterygoid is eroded and the pterygoid plates slightly displaced posteriorly. (d) also displays a displaced tooth at the anterior sinus wall. (a) and (b) are reprinted with permission: Luo J, You M, Zheng G, Xu L. Cone beam computed tomography signs of desmoplastic ameloblastoma: review of 7 cases. Oral Surg Oral Med Oral Pathol Oral Radiol 2014;118:e126-33. (c) and (d) are reprinted with permission: Rais R, El-Mofty SK. Malignant transformation of a desmoplastic ameloblastoma to squamous cell carcinoma: a case report. Head Neck Pathol. 2018 Jul 4. doi: 10.1007/s12105-018-0946-y.

soft-tissue involvement following perforation (Figure 9.42). Furthermore, it allows a fuller evaluation of the extent of ameloblastoma affecting the anterior maxilla (see Figures 9.39 and 11.23). Although the multilocular pattern does not vary greatly between solid ameloblastomas, in the few cases reported it appears that those affecting the anterior maxilla present with the honeycomb pattern.

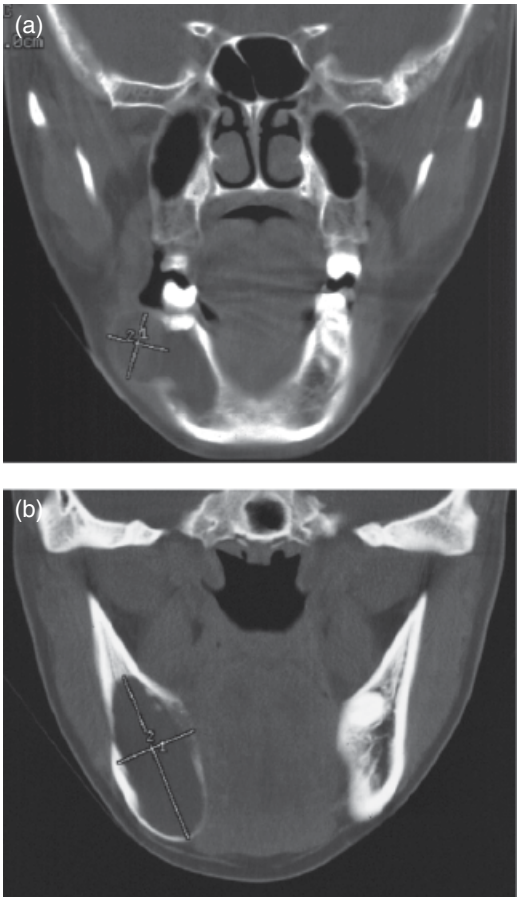


Figure 9.42 Coronal computed tomography (bone window) displaying an ameloblastoma affecting the mandible (a), which has resorbed the tooth root and expanded the adjacent buccal cortex and obturated the buccal sulcus (measurements are 17×18 mm). (b) It has expanded the body of the mandible buccolingually and vertically (measurements are 48×23 mm). The lower border has been displaced downward.

9.13.1.1 Magnetic Resonance to Discern between Ameloblastomas and Other Jaw Lesions

Asaumi et al. reported that MRI can distinguish between the ameloblastoma and the odontogenic myxoma on the basis of their dynamic behaviors [142]. The ameloblastoma enhances rapidly, within 45–60 seconds, whereas the odontogenic myxoma enhances after 500–600 seconds. The authors suggested that MRI may assist more because of its better spatial resolution and multiplanar features [143]. The mural nodule is easier to identify with MRI. Furthermore, dynamic contrast can reflect the intratumor angiogenesis. The essential cystic nature of the unicystic ameloblastoma can be distinguished from the solid variant by a homogeneous hyperintense signal on T2 weighting. The follicular histopathology of the solid ameloblastoma can be predicted by the multiple cystic spaces on T2 weighting.

The "contrast index" is computed by subtracting the precontrast plotting from the postcontrast plotting [142]. Although the MRI allows the potential to determine differences in the contrast index for different lesions, unfortunately no differences have been observed between primary and recurrent ameloblastoma or between the ameloblastoma [142] and the GOC.

Konouchi et al. set out a four-step process using MRI to distinguish between lesions that commonly present as unilocular radiolucencies [144]. The first step separates out the solid tumors, such as solid ameloblastomas and adenoid odontogenic tumors, the second the cyst lesions, the third KCOTs, and the fourth simple bone cysts [144].

9.13.1.2 Cone-beam Computed Tomography

There are two reports of case series of ameloblastomas investigated by CBCT [145, 146]. Most of the lesions displayed in one report [146] were at least four dental units in their mesiodistal dimensions [146] (see Figure 1.35) and, as they would have been treated as inpatients, MDCT rather than CBCT would be optimal. Since 34 of the 37 cases displayed buccolingual

expansion and erosion of the cortex [145], a preoperative evaluation for involvement of the adjacent soft tissues should prompt an MDCT with intravenous contrast [1, 147]. This would be particularly necessary for the 6 recurrent cases, whose anatomy would have been compromised by the primary surgery. The intravenous contrast is only possible when the patient is supine as for MDCT (and not vertical as for the CBCT units used) and in a medical facility so that adverse contrast media reactions could be promptly and properly attended to. The authors' second report of desmoplastic ameloblastomas [146] reinforces the case for retention of the desmoplastic ameloblastoma as proclaimed by the WHO's 2005 edition [130]. Unlike the radiolucencies associated with the other ameloblastomas, desmoplastic ameloblastomas present in conventional imaging as poorly defined, or in CBCT as with a snowstorm pattern (Figure 11.23), honeycomb, or irregular radiolucencies such as in Figure 9.41. This report makes a clear case that suspected ameloblastomas, particularly if small (no more than 4 dental units; see Figure 1.35 for the definition of dental units), should be investigated by CBCT, as many small ones can be treated as outpatients. Larger such lesions, which are most likely to be treated as inpatients, would be better investigated by MDCT.

9.13.1.3 The Desmoplastic Variant or Type

The desmoplastic variant's purported reduced tendency to recur flies in the face of its frequently poorly defined margins, which underscores both its lack of a capsule and its infiltrative microscopic character and frequent perforation of cortices. These features make it very difficult to reassure the pathologist and clinician that these lesions should benefit from more conservative treatment. Furthermore, as remarked earlier, the fact that the desmoplastic type displayed a greater proclivity for the maxilla than the solid type [132] aggravates this discomfort, as the maxilla is precisely where a recurrence is least welcomed due to the maxillary ameloblastoma's reputation for invading the brain, as displayed in Figure 11.24. Therefore, Philipsen et al.'s advice that treatment of this variant, despite its hitherto acknowledged reduced tendency to recur, should "follow the same radical treatment modality… as that of the 'classical' ameloblastoma" [132] is prudent. Rais and El-Mofty's recent review of the literature on this subject reaffirmed Philipsen et al.'s advice [132]. Although the desmoplastic variant has a much reduced tendency to recur after conservative treatment in comparison to that for the conventional variants (21% to 60–80%), its recurrence after resection is 3%. They reported a case of malignant transformation of a desmoplastic ameloblastoma to squamous cell carcinoma (Figure 9.41 c and d). This would appear to be the first such report [148]. Nevertheless, the desmoplastic ameloblastoma differs from other ameloblastomas radiologically in significant ways. This makes its diagnosis as an ameloblastoma more challenging to the clinician.

The aforementioned snowstorm and honeycomb presentations are not typical of most ameloblastomas. Nevertheless, Philipsen et al. determined that about 10% of desmoplastic ameloblastomas are "hybrids" [132]. Therefore, it is possible that the desmoplastic ameloblastomas in Figure 9.41 and the solid ameloblastoma in Figure 11.23 displaying a snowstorm appearance in part of the lesion could be such hybrids. This supports in part the WHO's 2017 edition's subsuming of the desmoplastic ameloblastoma into its nonunicystic ameloblastoma class.

9.13.1.4 Recurrence

The systematic review's overall recurrence rate of ameloblastomas was 14% [126, 127]. This recurrence rate will be affected by the period and quality of follow-up and the proportion of the unicystic variant, which is less likely to be resected. The Hong Kong case series exhibits these. After five years' follow-up, 12% recurred. Although 86% of these had been conservatively treated unicystic ameloblastomas, Parmar et al. recently reported that resection of recurrent unicystic ameloblastomas may be preferred in the now mature adult, while still performing conservative intervention in growing adolescent and young adults [149]. They reaffirmed that all solid ameloblastomas and those affecting the maxilla should be resected [149].

Although Hong et al. suggested that preoperative biopsy had no significant effect on recurrence, the particular histopathological pattern could be important; the follicular pattern had the most recurrences [136]. Half recurred after conservative treatment.

In addition to recurrence, the clinician is reminded of the remote risk of concern with pulmonary metastasis of otherwise benign-appearing ameloblastoma cells, because, if untreated, it can lead to death.

9.13.2 KERATOCYSTIC ODONTOGENIC TUMOR (ICD-O 9270/0)

The development of the classification and nomenclature of the KCOT is displayed in Figure 9.43. Prior to the WHO's 2005 edition of the classification of neoplasms affecting the jaws, the KCOT was known as the *odontogenic keratocyst* (OKC) [150] and was generally considered and classified as a cyst. The RPP of OKC is set out in Table 9.1. The majority (over 80%) of the former OKC which are parakeratotic are now called KCOTs, whereas the minority, orthokeratotic OKCs (10%), are true cysts, OOCs [151]. It has been shown that KCOTs and OOCs differ radiologically [32, 152]. The small proportion of OKC cases (7%) [33] that are mixed parakeratotic-orthokeratotic, due to their moderate recurrence rate relative to KCOTs, should be treated as if they were KCOTs, which includes enucleation with Carnoy's solution and long-term follow-up. The KCOT presents either as a single/solitary/sporadic or multiple lesion. The latter is frequently, but not always, part of the NBCCS, discussed earlier in this chapter. Before launching into a necessarily lengthy discourse concerning the recent WHO's 2017 edition's position with regard to this lesion, a brief overview of the main radiological features of KCOTs follows.

9.13.2.1 Brief Overview of the Main Radiological Features of KCOTs

Figures 9.44 and 11.28 are representative of KCOTs as they may first present. Both are imaged by CBCT, which is the appropriate modality after completion of clinical and conventional radiographic examinations. Both demonstrate the essential radiographic characteristics in either jaw. The KCOTs' propensity for mesiodistally directed extension throughout the bone marrow of the body of the mandible and anterior maxilla for little, or no, buccolingual expansion is demonstrated. This buccolingual expansion is least for the body of the mandible due to its thicker cortices.

9.13.2.2 Discourse on the Recent WHO Position on KCOTs

The principal author of the WHO's 2005 edition was Philipsen, who in 1956 classified the OKC [153]. Although having as a principal author a clinician who has been

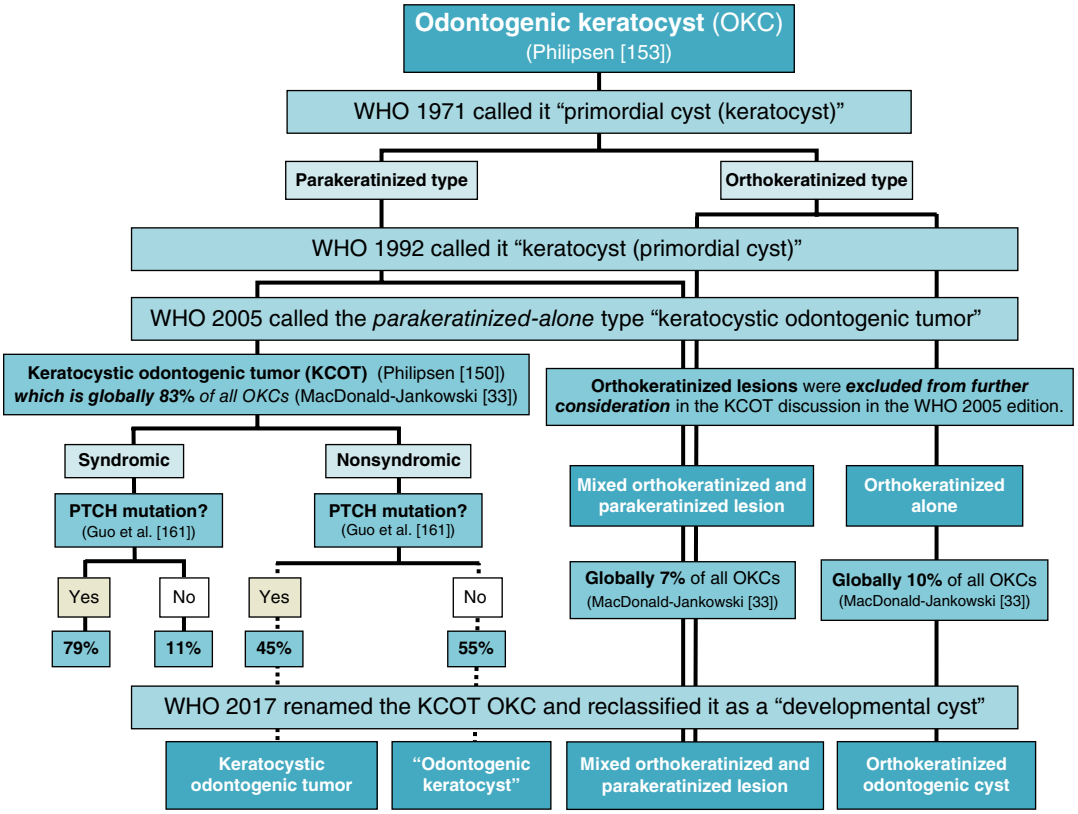


Figure 9.43 Evolution of the terminology and classification of the keratocystic odontogenic tumor from the original odontogenic keratocyst (OKC) over the four World Health Organization (WHO) editions. The dotted lines suggest a possible relationship between the presence or absence of protein patched homolog 1 (PTCH1) gene mutations, for which evidence has not yet been firmly adduced in the literature. This is discussed later in the chapter. The dotted lines, based on Guo et al.'s report [161], indicate a possible dichotomy in what was hitherto considered to be a single lesion. The sensitivity and specificity of Guo et al.'s study are displayed in Table 3.1.

continually engaged with the OKC/KCOT since its inception as a defined lesion is a strong if not compelling reason to take special note of his promulgations, it is not the only one. Recently the WHO's 2017 edition has advocated the reinstatement of the term OKC and reclassified it as a cyst [154]. The rationale for these recommendations was not compelling. Some of the authorities on which the WHO based its 2012 paper were decades old and therefore could not take account of the current clinical reality [155]. Furthermore. it would appear from a 2014 paper [156] that the authors' position was already established in response to the WHO's 2005 edition. In addition to acknowledging that the WHO's KCOT/OKC debate was "contentious" in comparison to the WHO's 2017 edition's reversal of many cases reclassified as calcified cystic odontogenic tumors (CCOT) by the WHO's 2005 edition back to calcified odontogenic cysts (COC; see Chapter 10 for a full discussion), Wright and Vered more clearly set out the grounds upon which these decisions were made [129]. A crucial point was that "OKCs are well documented to completely

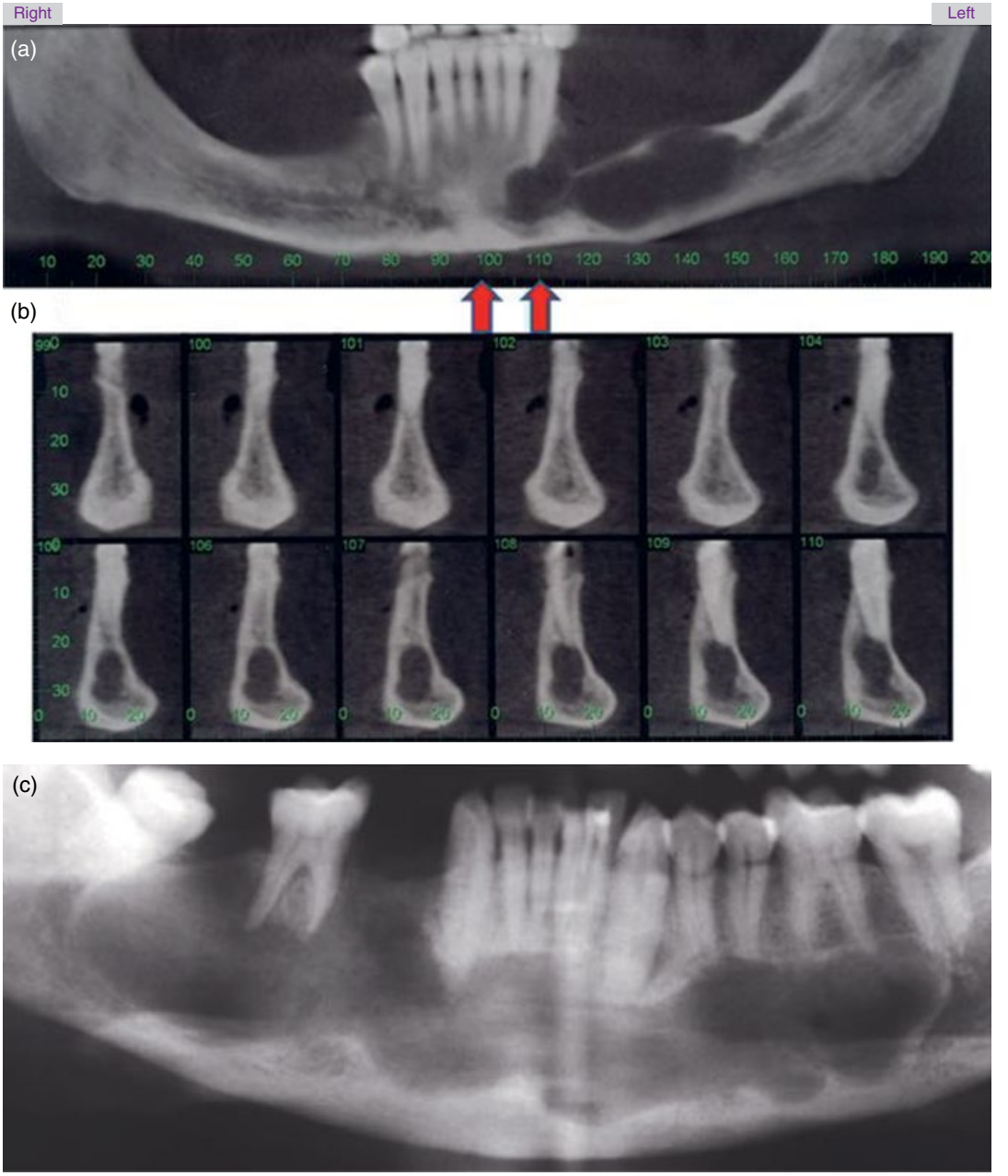


Figure 9.44 Panoramic (a) and transaxial (b) reconstructions cone-beam computed tomography of a recurrent case of a keratocystic odontogenic tumor (KCOT) arising in the mandible. The neoplasm presents as a unilocular radiolucency on the panoramic reconstruction, extending from close to the midline to the left third molar area. The anterior transaxial sections (from between the red arrows) display a little displacement and erosion of the lingual cortex. The lamina dura on the apex of the left canine is not apparent and there is some root resorption. (c) Part of a panoramic radiograph of a mandibular case of KCOT presenting as a well-defined multiloculated radiolucency that has extended throughout the body of the mandible. It has reached the lower border of the mandible. Source: (a) and (b) reproduced with permission from MacDonald, D. (2016). Lesions of the jaws presenting as radiolucencies on cone-beam CT. *Clin. Radiol.* 71 :972–985. (c) Reproduced with permission from Macdonald-Jankowski, D.S., and Li, T.K. (2010). Keratocystic odontogenic tumour in a Hong Kong community: the clinical and radiological features. *Dentomaxillofac. Radiol.* 39: 167–175.

regress following decompression (citing reference [157]) and the lining of many decompressed cysts appears more like oral mucosa than OKC histologically" [129]. This position did not take account that the success of the decompression [157, 158] upon which their position substantially relied was short-lived, leading to the partial withdrawal of both those papers (see errata to [157, 158] published in 2007). Furthermore, they did not note that the principal author of these papers more recently co-authored a paper declaring decompression's inferiority to the standard alternative of enucleation and curettage [159], thereby removing a plank upon which their thesis was based. Even more recently it was suggested that "the statistically significant increase of p53 expression with increased duration of treatment and increase of inflammation may also indicate the possibility of high rates of recurrence" [160].

Although the WHO's 2017 edition [154] correctly questioned the validity of mutation of the PTCH1 gene which had been proposed in the WHO's 2005 edition [150] as a marker for KCOT, the present author's revisiting [28] of the excellent work by the Beijing team led by T.J. Li [161] revealed that the significant difference between solitary (also called sporadic) and syndromic cases suggests that a PTCH1 test could be used to distinguish between them, particularly in those cases of multiple KCOTs which are not accompanied by any other criteria suggestive of NBCCS. A positive PTCH1 test is currently a major criterion for NBCCS [29]. The Beijing team's report revealed that nearly every syndromic case was PTCH1 test positive, whereas less than a half of the sporadic cases were test positive [161]. (It should be noted that this test may be complicated by the complete absence of the PTCH1 gene in some Japanese NBCSS kindreds [162].)

Guo et al. reported that all of their NBCCS cases (11 out of 14) which presented younger than 20 years of age, were PTCH1 mutation positive, whereas the 3 that presented older were not. They suggested that the genetic mutations in these cases are unknown [161].

There is a possibility that has not yet been considered that sporadic KCOT/OKC may actually not be a single entity, but rather at least two separate entities, one a neoplasm and the other a cyst. The Beijing study revealed that nearly a half of its sporadic KCOTs were PTCH1 mutation negative. It could be possible that the PTCH1 mutation–positive cases could be neoplastic and the PTCH1-negative lesions cystic. This can only be determined by a carefully designed prospective study. Finally, the WHO's 2017 edition's recommendation that the mixed parakeratotic and orthokeratotic lesions be bundled together with the pure orthokeratotic lesions, now called the OOCs, is addressed later in this chapter.

Reflecting this discussion and the persistent clinical evidence that KCOTs recur [162–165], this textbook will continue to follow the WHO's 2005 edition's recommendations that these be considered neoplasms and that KCOT is an appropriate term. The present author has already set out his case in brief and maintained the status quo (as defined in the WHO's 2005 edition [149]) elsewhere [166].

9.13.2.3 Clinical and Radiological Presentations of KCOTs

Although the KCOT is now the third most common odontogenic neoplasm after the odontoma and ameloblastoma, it is the second most common neoplasm that produces a radiolucency. The global distribution of reports included in the systematic review [33], from which much of the following is derived, is set out in Figure 1.47 and the details are in Table 9.5.

Table 9.5 Keratocystic odontogenic tumor; non-syndromic: systematic review.

Feature	Total	Caucasian	East Asian	Sub-Saharan African	Latin American
Male: Female	60% : 40%	60% : 40%	61% : 39%	50% : 50%[a]	53% : 47%
Mean number per year per report	5.8	6.5	6.3	0.0[a]	3.7
Mean age	38 years	40 years	35 years	43 years[a]	34 years
Mean prior awareness	0.7 years	N/A	0.6 years	2.1 years[a]	N/A
Mandible: Maxilla	72% : 28%	65% : 35%	77% : 23%	100% : 0%[a]	73% : 27%
Mandible: *Anterior: Posterior*	12% : 88%	11% : 89%	12% : 88%	0% : 100%[a]	0% : 100%[a]
Maxilla: *Anterior: Posterior*	31% : 69%	37% : 63%[a]	31% : 69%	N/A	N/A
Swelling: *Yes: No*	58% : 42%	68% : 32%	60% : 40%	100% : 0%[a]	37% : 63%
Pain: *Yes: No*	32% : 68%	17% : 83%	41% : 39%	100% : 0%[a]	0% : 100%[a]
Incidental finding: *Yes: No*	21% : 79%	26% : 74%	11% : 89%	0% : 100%[a]	58% : 42%
Numbness: *Yes: No*	2% : 98%	N/A	1% : 99%	N/A	21% : 79%[a]
Discharge: *Yes: No*	12% : 88%	22% : 78%	9% : 91%	67% : 33%[a]	28% : 72%[a]
Radiolucent: *Yes: No*	100% : 0%	100% : 0%	100% : 0%	100% : 0%[a]	100% : 0%
Unilocular: Multilocular	72% : 28%	80% : 20%	63% : 37%	0% : 100%[a]	76% : 24%
Well defined: *Yes: No*	64% : 36%	45% : 55%	100% : 0%[a]	N/A	N/A
Cortex: *Yes: No*	60% : 40%	26% : 74%[a]	88% : 12%[a]	N/A	N/A
Expansion: *Yes: No*	62% : 38%[a]	14% : 86%[a]	82% : 18%[a]	N/A	N/A
Downward expansion of lower border of mandible: *Yes: No*	71% : 29%[a]	N/A	71% : 29%[a]	N/A	N/A
Affects maxillary sinus: *Yes: No*	100% : 0%[a]	N/A	100% : 0%[a]	N/A	N/A
Tooth displacement: *Yes: No*	69% : 31%[a]	N/A	69% : 31%[a]	N/A	N/A
Root resorption: *Yes: No*	23% : 77%	8% : 92%[a]	41% : 59%[a]	N/A	N/A
Associated with unerupted teeth: *Yes: No*	35% : 65%	44% : 56%	31% : 69%	N/A	20% : 80%
Syndromic: *Yes: No*	6% : 94%	6% : 94%	5% : 95%	25% : 75%[a]	14% : 86%
Mixed (Ex): *Yes: No*	7% : 93%	8% : 92%	9% : 91%	11% : 89%	2% : 98%
Orthokeratinized (Ex): *Yes: No*	10% : 90%	11% : 89%	8% : 92%	8% : 92%	8% : 92%
Recurrence: *Yes: No*	28% : 72%	33% : 67%	24% : 76%	50% : 50%[a]	17% : 83%[a]

[a] Percentages derived either from one report or from a synthesis of no more than 50 cases.
Key: (Ex), cases exhibiting orthokeratotic epithelium alone or mixed with parakeratotic epithelium excluded from systematic review; of keratocyst odontogenic tumors; Mixed, cases with mixed orthokeratotic and parakeratotic epithelium; N/A, information not available;

The mean number of KCOTs per year is almost 6 globally. Although globally 6% of cases are syndromic, the proportion rises to 14% among Latin Americans, which is significantly greater than those of the East Asian (5%) and Western (6%) global groups [33].

The clinical and radiological features described in this section particularly pertain to nonsyndromic KCOT. Syndromic cases, which are more prone to recur, first present at a significantly younger age in an East Asian report [32].

The mean age at first presentation is 38 years. Although the mean ages for the global groups range between 34 years for Latin Americans and 43 years for sub-Saharan Africans, the differences are not significant. The most frequent decade is the third (29%) [33]. Females predominate in the first decade (91%), whereas males generally predominate in subsequent decades.

The majority (60%) of nonsyndromic patients are males. The predilection for males in East Asian and Caucasian global groups is significantly greater than that for the Latin American group [33].

Swelling is the most common presenting symptom; it occurs in 58% of cases. It is significantly less frequent in the Latin American global group than in the East Asian and Caucasian global groups. Pain presents in 32% and significantly more frequently in the East Asian global group than in the Caucasian global group. Those patients first presenting with pain were significantly older than those who did not [33]. The East Asian, Latin American, and Caucasian groups differ significantly in the 21% of nonsyndromic KCOTs found as incidental findings. Although numbness is infrequent (2%), it may be more prevalent among Latin Americans (21%), but their sample is small. A purulent discharge presented in 12%; it occurred significantly more in the Caucasian (22%) than in the East Asian global group (9%) [33].

The mandible overall is affected in 72% of cases, moreso among East Asian and Latin American global groups. It was significantly less frequent for the Caucasian global group [33]. KCOTs in the Hong Kong Chinese, affecting the maxilla, first presented significantly earlier (22 years old) than those of the mandible (36 years old) [32]; this was contrary to that in the ameloblastoma affecting the same community [126, 127]. The posterior sextants are more frequently affected for both jaws: 88% for the mandible and 69% for the maxilla. Almost all cases confined to the posterior sextant, like that already reported for the ameloblastoma [126, 127] with regard to the posterior sextant of the mandible in the same community, were 25 years old or younger [32]. The association between involvement of the posterior sextant and younger presentation was also a feature of the maxillary cases in the Hong Kong Chinese report [32]. Conversely, the maxillary ameloblastomas affecting the Hong Kong Chinese exhibit a predilection for the anterior sextant, which may extend to the anterior aspect of the posterior sextant. Maxillary ameloblastomas also first present significantly later in life [126, 127].

All KCOTs are radiolucent and nearly three-quarters (72%) are unilocular (Figures 9.44 and 9.45) [33]. The unilocular KCOTs (24 years old) presented significantly earlier than the multilocular KCOTs (36 years old) [32]. The mesiodistal length of the unilocular KCOTs in dental units is 4.22, in comparison to the multilocular KCOT's 5.70; this was not significant [32]. Nevertheless, in the mandible, the unilocular KCOTs (3.20) were much smaller than the multilocular KCOTs (6.17); this tended to significance [32].

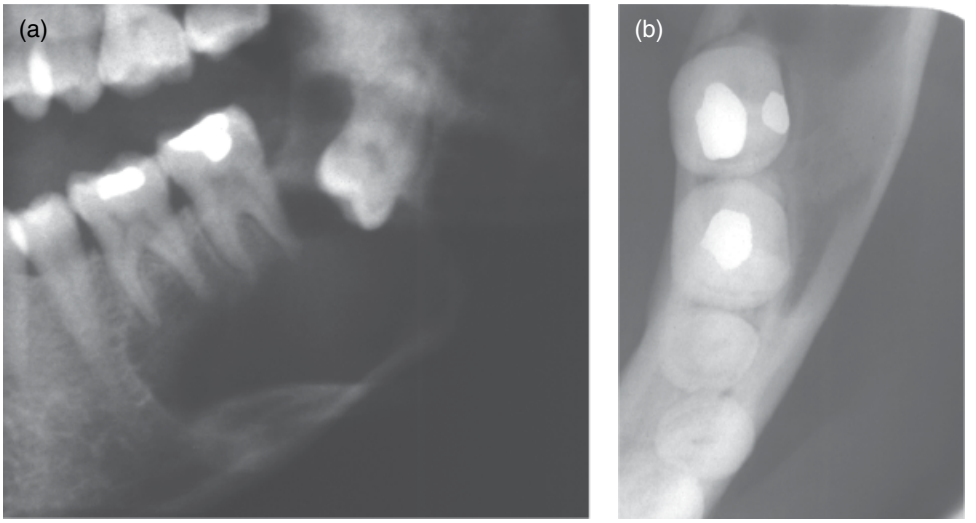


Figure 9.45 Panoramic radiograph (a) and true occlusal radiograph (b) of a keratocystic odontogenic tumor. It presents as a radiolucency associated with the crown of an unerupted third molar. Although it is "attached" to the tooth's mesial (or inferior) cementoenamel junction (CEJ), its distal (superior) "attachment" is to the root distant from the CEJ. It almost extends through the entire vertical height of the body of the mandible without expanding it. It also minimally expands the mandible buccolingually. There is some root resorption. Note: The body of the hyoid is superimposed upon the inferior anterior aspect of the lesion in (a). Source: MacDonald-Jankowski, D.S., and Li, T.K. (2010). Keratocystic odontogenic tumor in a Hong Kong community; the clinical and radiological presentations and the outcomes of treatment and follow-up. *Dentomaxillofac. Radiol.* 39: 167–175.

Well-defined cases represented 64%, of which 60% were corticated [33]. The East Asian global group's 100% well-defined cases were significant compared to 45% in the Caucasian global group. Also, the East Asian global group's 88% cortication was significantly greater than the Caucasian global group's 26% [33]. Although buccolingual expansion was observed in 62% of KCOTs, this assumed a pattern similar to the fusiform expansion of fibrous dysplasia (Figure 9.45). It was significantly more prevalent in the East Asian global group (82%) than in the Caucasian global group (14%) [33]. This pattern of expansion is most frequently observed in those KCOTs involving the body of the mandible [33]. Therefore, a low buccolingual: mesiodistal ratio of a radiolucency in the body of the mandible should suggest a KCOT (and also an odontogenic myxoma and simple bone cyst), whereas a high buccolingual: mesiodistal ratio would suggest an ameloblastoma or an OOC.

Tooth displacement was recorded in one East Asian report; it occurred in 69% of cases [32]. Contrary to a statement in the WHO's 2005 edition that root resorption is very rare [150], it occurred in 41% and 9% of cases, in East Asian [32] and Caucasian [167] reports, respectively. By virtue of these two reports, root resorption occurred in 23% of cases in the systematic review [33]. Although its occurrence of 41% in KCOTs of the Hong Kong Chinese [32] was less than ameloblastoma's 59% in the same community [126, 127], this was not significant [32]. Furthermore, the presentation of Hong Kong Chinese KCOTs

with root resorption in older patients [32] differs from the first presentation of ameloblastomas in Hong Kong Chinese among younger patients; this phenomenon is significantly more frequent in earlier-presenting unicystic lesions than in the nonunicystic (predominantly solid variant) and predominantly radiologically multilocular lesions, which first present later in life [126, 127].

An association with unerupted teeth occurred in a third of cases overall [33]. It differed significantly between the East Asian, Latin American, and Caucasian global groups. The surprise that defies easy explanation was that one of the Caucasian reports was American, in which prophylactic removal of unerupted teeth has been practiced for decades. Those KCOTs in the Hong Kong Chinese presenting with associated unerupted teeth were significantly younger than those that did not [32].

All nonsyndromic KCOTs affecting the posterior maxilla affected the maxillary antrum, expanding up into it in a balloon-like fashion. Figure 11.26 displays such an example [32]. The KCOT in Figure 11.28 originated in the anterior maxilla and has extended distally and displaced the anterior floor of the maxillary sinus upward into the lumen in a balloon-like manner.

KCOTs affecting the anterior maxilla appear to have some predilection for the canine-lateral incisor site (Figures 9.46, 9.47, and 11.28).

While the KCOT affecting the mandible is minimally expansive, the OOC exhibits extensive expansion buccolingually (Figure 9.43) [152]. Like the ameloblastoma, its lingual cortex expands down

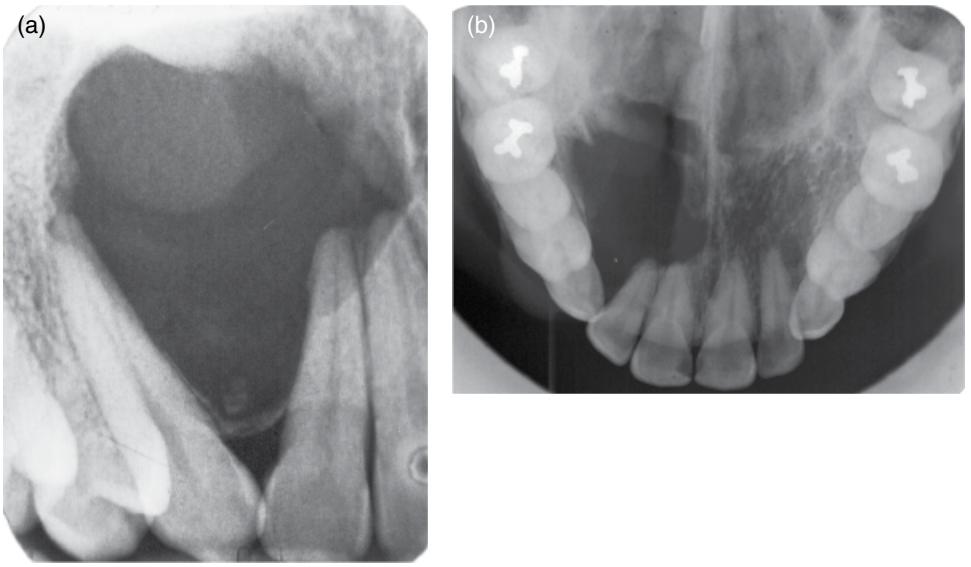


Figure 9.46 Conventional images of a keratocystic odontogenic tumor affecting the anterior maxilla. In contrast to the periapical radiograph (a), the standard anterior occlusal (b) reveals the full vertical extent of the lesion that caused this well-defined radiolucency, displacing the lateral incisor and the canine. The image in (a) reveals the absence of the root resorption, which is suspected on (b). Note: The tip of the nose is obvious in the upper half of the radiolucency in (a).

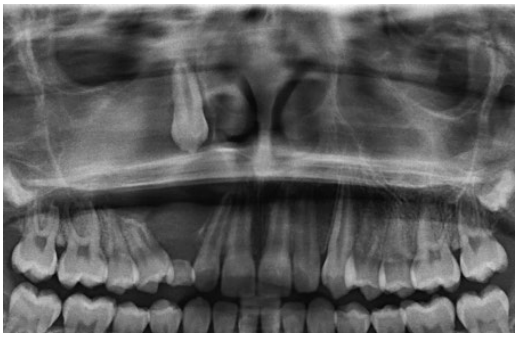


Figure 9.47 Panoramic radiograph depicting a radiolucent lesion in the canine site splaying the lateral incisor and first premolar. The canine is unerupted and its root completely formed. This phenomenon earlier would have invoked consideration of the now-defunct globulomaxillary cyst. Currently this presentation invokes a lateral radicular cyst, lateral periodontal cyst, and keratocystic odontogenic tumor. This is a keratocystic odontogenic tumor.

past the otherwise unaffected lower border of the mandible [39]. Unlike the KCOT, the OOC has so far not exhibited root resorption [152]. Although the WHO's 2005 edition expressly stated that KCOTs did not resorb roots [150], this was subsequently refuted [32]. The frequency of root resorption varied between two world communities; it was 41% in Hong Kong [32] and 7% in British Columbia, Canada [108].

In addition to the thicker cortices of the body of the mandible, the buccolingual expansion of KCOT may reflect the low osmolarity of the KCOT's cystic fluid [168]. It has been noted that the older KCOTs were more likely to be more extensive mesiodistally and multilocular [169]; this may reflect "a multicentric pattern of cyst growth brought about by the proliferation of local groups of epithelial cells" [168].

Treatment of nonsyndromic KCOT is usually conservative; in one report, 79% of cases were treated by enucleation and Carnoy's solution [32].

The global recurrence rate for nonsyndromic KCOTs is 28% [33]. It is significantly greater in the Caucasian global group (33%) than in East Asians (24%). This recurrence rate is far higher than that of the ameloblastoma (14%) and the odontogenic myxoma (18%), emphasizing the need for long-term follow-up [32]. Although a reason for this high recurrence with regard to KCOT is the general conservative approach to its treatment, both the degree of follow-up and the recurrence rates for both KCOT [32] and ameloblastoma [126, 127] in a Hong Kong Chinese community were equally high and low, respectively. Follow-up for a mean of five years each for KCOTs and ameloblastomas were 73% [152] and 89% [126, 127], respectively. The recurrence rates for KCOTs and ameloblastomas were 9% [152] and 11% [126, 127], respectively. The reasons for this degree of follow-up for both lesions are both the surgeons' vigorous follow-up protocol and the relative stability of the Hong Kong community as a whole [126, 127].

9.13.2.4 Surgical Treatment of KCOTs

The conservative approach applied in Hong Kong was not followed in North America due to the US Food and Drug Administration (FDA) banning pharmacies from compounding chloroform, a central ingredient of Carnoy's solution, because it is a carcinogen. Carnoy's solution, originally developed as a histological fixing agent, had been used as a chemical cauterization agent in the USA and elsewhere to treat KCOT. It is composed of "100% ethanol, chloroform, and glacial acetic acid in a 6 : 3 : 1 ratio with added ferric chloride" [169]. A five-minute application of it to the bone cavity wall, following enucleation of the KCOT, treated the satellite cysts and other epithelial remnants within that wall, enhancing the treatment's success. Following the ban many surgeons turned to

other methods of treatment, such as enucleation and curettage, or in the case of Pogrel et al. to marsupialization and decompression [157, 158]. Marsupialization and decompression, as mentioned earlier, were initially successful, but were subsequently abandoned [158]. Oral and maxillofacial surgeons in British Columbia used enucleation and curettage. Their cases were followed up by MacDonald et al. [108], who reported that large KCOTs in the posterior sextant of the mandible provisionally diagnosed simply on clinical examination and a panoramic radiograph were successfully enucleated alone without recurrence after at least five years' follow-up, whereas almost all of the much smaller lesions in the premolar and anterior sextant in the same series recurred within a year of the enucleation [108]. A reason for the success for enucleation alone on such large KCOTs was that the surgeons may have more radically excavated the adjacent bone in addition to removing the affected teeth in the larger posterior lesions, which the surgeon had prior to surgery determined were KCOTs. Conversely, they had been considerably more conservative in their enucleation of the smaller, more anterior KCOTs, which the clinician had determined presurgically were cysts [108]. Another point was that teeth associated with those determined to be KCOTs prior to surgery were removed along with the lesions, whereas the teeth associated with those lesions determined to be cysts were retained. A recent study has reinforced the necessity of this practice [108].

9.13.2.5 Radiological Variation in KCOTs in Different Parts of the Jaws

KCOTs affecting the body of the mandible, though mesiodistally extensive, are minimally buccolingually expansive, whereas KCOTs affecting the maxilla are more buccolingually expansive (see Min et al.'s Table 7 [170]). An explanation is the thickness of the cortices of the body of the mandible in comparison to the maxilla. When it affects the ramus of the mandible it is more expansile, but not the ball-like expansion observed for the ameloblastoma, as we shall see also for the OOC (see later Figure 9.53). KCOTs affecting the anterior maxilla are frequently found between the lateral incisor and canine and may also be mistaken for an LPC. Due to the thinner maxillary cortex, it is a little more expansile (see Figure 11.28). When the KCOT arises subjacent to the maxillary sinus or secondarily involves it, as in Figure 11.28, it will expand into it and, if undiscovered earlier, may obturate the lumen. It will minimally expand the sinus walls (see Figure 11.26).

In Figure 11.26, an unerupted third molar displaced high into the lumen; this happens frequently. In such cases, first consideration should be given to a KCOT rather than a DC. Root resorption occurs in a quarter of all cases [33], particularly in the older patient, whereas an association with an unerupted tooth occurs particularly in the younger patient. In the Hong Kong Chinese case series, unilocular lesions were smaller and presented in younger patients than multilocular lesions, which were larger [32].

9.13.2.6 Importance of Discerning Lesions with Mixed Parakeratotic and Orthokeratotic Histopathology

Although these account for a minority of cases (7%), there have been very few reports on their clinical and radiological features and treatment outcomes. Nevertheless, because of their parakeratinized component, they should be treated and followed up as if they were KCOTs [91]. Neither the WHO's 2005 or 2017 edition has addressed the mixed parakeratotic and

orthokeratotic lesions as a separate entity. The WHO's 2005 edition completely excluded any orthokeratosis-containing lesion from its definition of a KCOT, whereas the WHO's 2017 edition included mixed lesions in the OOC group. Radiologically not only are KCOTs and OOCs different (compare Figure 9.45 with the later Figure 9.53), but so are mixed ones (certainly at least with regard to the later Figure 9.55, the mixed lesion in which is minimally buccolingually expansile) compared to OOCs (Figure 9.53).

Guo et al. [161] identified mutations in the PTCH1 gene in most of the cases with syndromic KCOTs, but in less than half of the nonsyndromic KCOT cases (see Table 3.1).

9.13.2.7 Where Does the KCOT versus OKC Debate Go from Here?

Wright, a WHO's 2017 edition 'Consensus and Editorial Panel' member, remarked upon the contentiousness of the KCOT versus the OKC debate in comparison to none concerning the CCOT versus the COC; Chapter 10 at 10.23.3 [129]. In Chapter 3, I raised the possibility of solitary (sporadic or nonsyndromic) KCOT/OKC being not just a single lesion, but perhaps at least two: one a cyst which responds to a simple enucleation with or without marsupialization/compression, and another a locally invasive neoplasm, which requires at least curettage accompanying the enucleation, if not adjuvant treatment such as Carnoy's. Table 3.1 gives us an insight into at least one basis for this dichotomy, whether the lesion is positive for mutations of the PTCH1 gene. Regrettably, Guo et al. [161] did not correlate this feature with recurrence or any demographic or radiological feature.

Although it has been well settled that a similar histopathology may be shared by entirely different lesions which behave very differently, as exemplified by the fibro-osseous lesions discussed in Chapter 10, in view of the present uncertainty about the nature of each sporadic lesion, it would be prudent to treat them all as if they were neoplasms. Thus they should be subject to long-term follow-up, namely over five years, particularly if they have been primarily treated by enucleation. MacDonald et al. in their small Canadian case series discovered that two cases recurred after five years of follow-up of such cases [108].

9.14 Odontogenic Myxoma (ICD-O 9320/0)

The odontogenic myxoma is defined by the WHO's 2005 edition as "an intraosseous neoplasm characterized by stellate and spindle-shaped cells embedded in an abundant myxoid or mucoid extracellular matrix. When a relatively greater amount of collagen is evident, the term myxofibroma may be used" [171]. This definition was upheld in the WHO's 2017 edition [172]. The odontogenic myxoma is the fourth most common odontogenic neoplasm [171], after odontomas, ameloblastomas, and KCOTs.

The global distribution of reports included in a recent update of the sole systematic review on odontogenic myxomas, published in 2002 [173], is set out in Figure 1.46 and the details are in Table 9.6. This update not only addressed the many hiatuses, particularly with regard to sub-Saharan African and Latin American global groups, revealed by the original systematic review [80], it also revealed significant differences between the global groups, which were not apparent in the original systematic review [173].

The mean number of odontogenic myxomas per year is globally 0.9 (Table 9.6). Although not significant, it is

Table 9.6 Odontogenic myxoma: systematic review.

Feature	Total	Caucasian	East Asian	Sub-Saharan African	Latin American
Male: Female	40% : 60%	40% : 60%	49% : 51%	36% : 64%	36% : 64%
Mean number per year per report	0.9	0.8	1.0	1.3	0.9
Mean age[a]	30.5 years	31.0 years	29.0 years	27.8 years	28.3 years
Mean prior awareness[a]	1.9 years	1.8 years	2.2 years	N/A	1.8 years[b]
Mandible: Maxilla	56% : 44%	55% : 45%	54% : 46%	63% : 37%	53% : 47%
Mandible: *Anterior: Posterior*	19% : 81%	23% : 77%	5% : 95%	28% : 72%[b]	27% : 73%
Maxilla: *Anterior: Posterior*	25% : 75%	45% : 55%	4% : 96%	32% : 68%[b]	14% : 86%[b]
Swelling: *Yes: No*	56% : 44%	68% : 32%	49% : 51%[b]	80% : 20%[b]	58% : 42%
Pain: *Yes: No*	28% : 72%	14% : 86%	72% : 28%[b]	14% : 86%[b]	30% : 70%
Incidental: *Yes: No*	14% : 86%	12% : 88%[b]	6% : 94%[b]	N/A	19% : 81%
Loose teeth: *Yes: No*	19% : 80%	20% : 80%[b]	20% : 80%[b]	N/A	15% : 85%
Displaced teeth (patient complaint): *Yes: No*	28% : 72%	34% : 66%	50% : 50%[b]	19% : 81%[b]	N/A
Numbness: *Yes: No*	8% : 92%	7% : 93%[b]	10% : 90%[b]	8% : 92%	N/A
Radiolucent: *Yes: No*	83% : 17%	98% : 2%	100% : 0%[b]	71% : 29%	97% : 3%
Unilocular: Multilocular	32% : 68%	43% : 55%[b]	27% : 73%	23% : 77%	40% : 60%[b]
Well defined: *Yes: No*	51% : 49%	53% : 47%	50% : 50%	39% : 61%[b]	85% : 15%[b]
Cortex: *Yes: No*	45% : 55%[b]	38% : 62%[b]	100% : 0%[b]	64% : 36%[b]	N/A
Expansion: *Yes: No*	84% : 16%	97% : 3%[b]	80% : 20%[b]	95% : 5%[b]	70% : 30%[b]
Downward expansion of lower border of mandible: *Yes: No*	30% : 70%[b]	0% : 100%[b]	50% : 50%[b]	N/A	N/A
Affects maxillary sinus: *Yes: No*	91% : 9%[b]	90% : 10%[b]	86% : 14%[b]	100% : 0%[b]	N/A
Tooth displacement (clinical finding): *Yes: No*	47% : 53%	39% : 61%[b]	80% : 20%[b]	N/A	57% : 43%[b]
Root resorption: *Yes: No*	27% : 73%	18% : 82%	35% : 65%[b]	52% : 48%[a]	0% : 100%[b]
Recurrence: *Yes: No*	18% : 82%	20% : 80%	0% : 100%[b]	13% : 87%[b]	29% : 71%[b]

[a] Not the cumulative means calculated for the published report.
[b] Percentages derived either from one report or from a synthesis of no more than 50 cases.
Key: N/A, information not available.

greater for the sub-Saharan African global group than for the Caucasian and Latin American global groups.

The mean age for first presentation is about 30 years for all global groups. Patients may first become aware of their disease a mean of 1.9 years before presenting [173].

Although odontogenic myxoma globally displays a predilection for females (60%), the East Asian global group significantly approximates to equality.

Overall swellings present in 56% of cases. Swellings present significantly less in the East Asian global group. Those cases first presenting with pain present only in 28% overall, whereas 72% of East Asian cases significantly report pain. About 8% of cases in all global groups present with numbness, while 28% present with displaced teeth and 19% with loose teeth. Only 14% of cases are discovered as incidental findings.

The mandible is most frequently affected (56%) in all global groups. Although 81% of mandibular cases and 75% of maxillary cases overall affect the posterior sextants, this predilection was significantly greatest in the East Asian global group for both jaws.

In the original systematic review, odontogenic myxomas generally appeared on conventional radiography as radiolucencies (98%) [173]. Although reports published since 2002 reported that a higher proportion of odontogenic myxomas were described as "radiopacities" [174, 175], the most recent case series reported them all as radiolucencies [176]. The Caucasian, East Asian, and Latin American global groups display a significantly higher proportion of radiolucencies than sub-Saharan African global groups. Two reports [174, 175] reveal that the radiopaque pattern ranges from ground glass to a mixed appearance. These, together with a poorly defined margin, appear like fibrous dysplasia [81]. Furthermore, three of Zhang et al.'s cases had a "motheaten appearance," which could not be distinguished from a malignant lesion [174].

The poorly defined margins (51%) and the general lack of a cortex or sclerosis when well defined (these present in only 51% of all cases with well-defined margins; Table 9.3) are consistent with the gelatinous nonencapsulated histopathology and the high recidivist nature of this lesion [173].

Odontogenic myxomas display buccolingual expansion in 84% of cases (Table 9.6). Buccolingual expansion is significantly more frequently observed in Caucasian and sub-Saharan African global groups than in East Asian and Latin American global groups.

Odontogenic myxomas, if large enough, do expand the lesion in all directions. This expansion outwith the maxillary antrum (Figure 11.29) is not the balloon-like expansion frequently observed in ameloblastomas or most odontogenic cysts. Instead, the pattern of expansion of the odontogenic myxoma is very similar to that observed for fibrous dysplasia; it is almost fusiform (Figure 9.48; see also Figures 1.32, 11.29, and 11.30) [17, 173]. This shape reflects the infiltrative nature of this lesion, which incidentally, like fibrous dysplasia, "shows little encapsulation" [177]. This lack of a capsule reflects the degree of definition of the lesion–normal adjacent bone interface. As already mentioned, not only is this margin poorly defined in half of all cases, but also half of the well-defined margins neither have a cortex nor are sclerotic. The radiologically apparent "normal" trabeculae immediately adjacent to the lesion are encased in tumor (see Buchner and Odell's Figure 6.64 [171]), because "some odontogenic myxomas permeate into the marrow

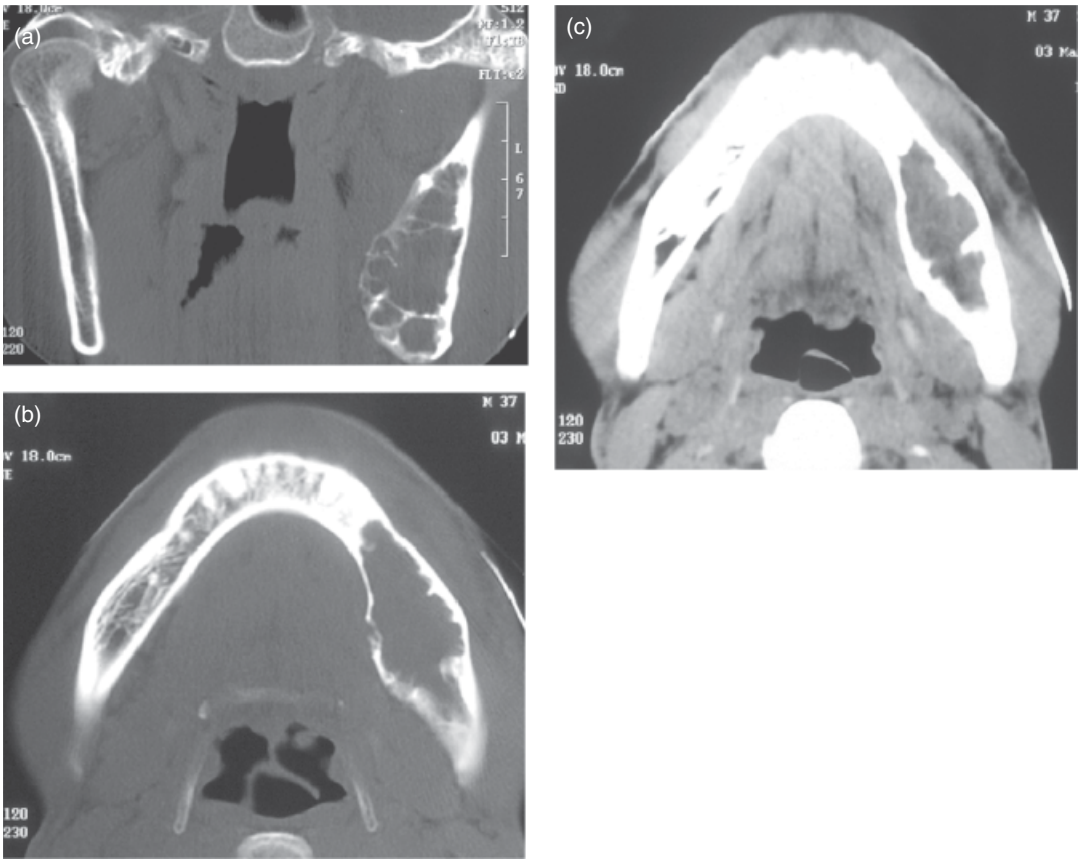


Figure 9.48 Computed tomography (CT) of an odontogenic myxoma affecting the posterior sextant of the mandible. Coronal (a) and axial (b) computed tomography (bone window) display the peripheral arrangement of the septa and cells around a center devoid of septa. (c) Axial CT (soft-tissue window) is the precontrast image that corresponds to Figure 1.2c of the same patient, which displays enhancement of a biopsy site taken prior to the CT. Source: (a) Reproduced with permission from MacDonald-Jankowski, D.S., Yeung, R., Li, T.K., and Lee, K.M. (2004). Computed tomography of odontogenic myxoma. *Clin. Radiol.* 59: 281–287.

spaces in a pseudomalignant pattern" [171]. Therefore, in order to ensure that all the neoplastic cells have been removed, the adjacent "normal-appearing" bone should also be removed with the lesion. In other words, the odontogenic myxoma should be routinely resected.

In addition to buccolingual expansion, odontogenic myxomas displace the lower border of the mandible downward in nearly a quarter of the few reported cases that reach the lower border. Table 9.6 reveals that nearly every lesion subjacent to the maxillary antrum involves displacement. Zhang et al. reported that such antral lesions displayed a "reticular appearance (see [their] Figure 4) at the anterior part and a unilocular lesion in the posterior part on a panoramic radiograph" [174]. This reticular (net-like) pattern can be observed in Figures 9.49 and 9.50, whereas Figure 9.51 displays in part a honeycomb pattern.



Figure 9.49 Upper occlusal radiograph displaying a well-defined radiolucency between the canine and first premolar. The multilocular presentation excluded consideration of the lateral periodontal cyst. This was an odontogenic myxoma. Source: MacDonald-Jankowski, D.S., Yeung, R., Lee, K.M., and Li, T.K. (2002). Odontogenic myxomas in the Hong Kong Chinese: clinicoradiological presentation and systematic review. *Dentomaxillofac. Radiol.* 31:71–83.

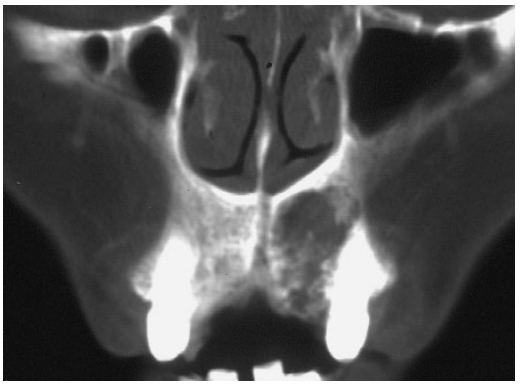


Figure 9.50 Coronal tomography displaying a multilocular radiolucency within the anterior maxilla. This is an odontogenic myxoma. The multilocular pattern is honeycomb and made up of small cells. The closeness of the radiodense septa may occasionally lead to a radiopaque appearance. Source: MacDonald-Jankowski, D.S., Yeung, R., Li, T.K., and Lee, K.M. (2004). Computed tomography of odontogenic myxoma. *Clin. Radiol.* 59:281–287.

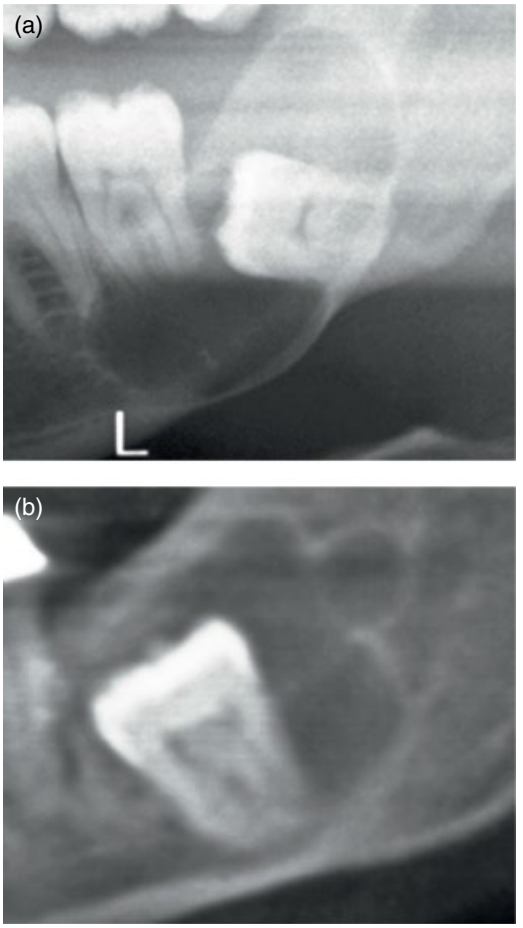


Figure 9.51 Panoramic radiographs of two separate glandular odontogenic cysts (GOC). (a) A unilocular GOC has enveloped the crown and root of an unerupted third molar. The GOC has no attachment with the cementoenamel junction. The tooth has been displaced to the lower border of the mandible. The latter and the mandibular canal have been displaced downward. (b) A multilocular GOC associated with the distal side of the crown and root of an unerupted third molar. The mandibular canal has been displaced downward.

In the original systematic review [173], odontogenic myxomas were almost evenly divided between unilocular and multilocular radiolucencies on their presentation on conventional radiography.

In contrast, the update of this systematic review includes a larger proportion of multilocular lesions; this is now 68% in comparison to the former's 53% [173]. This dramatic shift in presentation within such a short space of time may be in part explained by the increased use of advanced imaging [17] that would have made more obvious the presence of septae [178]. The multilocular cases are evenly distributed between coarse (see Figures 1.32 and 9.48) and fine (Figure 9.49) septae [173].

A quarter of odontogenic myxomas in a Black South African report [175] and a third in a Japanese report [179] presented with the tennis-racket pattern (Figure 1.32), which, although it is pathognomonic for odontogenic myxoma, was generally otherwise infrequently seen in the original systematic review [173]. The sunburst or sunray appearance typical of the osteogenic sarcoma (Figure 11.29) [174, 175] was also displayed on CT images of large odontogenic myxomas affecting a Chinese community [17]. A suggestion for this pattern is that it may represent the honeycomb pattern in profile [17].

The multilocular lesions reported by Noffke et al. [175] and Martinez-Mata et al. [180] were significantly larger than the unilocular lesions, suggesting that multilocularity is a feature of the larger lesion. Noffke et al. found that the relationship between the multilocular lesion and the age of the female (but not male) patient was also significant [175]. Hisatomi et al. revealed that the smaller lesion, displacing adjacent roots, presented as a nonspecific radiolucency [181]. They presented almost identical images of ameloblastomas, keratocyst odontogenic tumors, simple bone cysts, and odontogenic myxomas (see Figure 1.28). To this list can be added the LPC.

The few cases reporting the radiology of odontogenic myxoma affecting the anterior maxilla suggest that the honeycomb pattern is frequent (see Figure 9.50). Figure 9.10 is a flowchart for lesions that most frequently present as radiolucencies in the anterior maxilla.

The multilocular pattern observed on the conventional radiograph appears entirely different on CT (see Figures 1.32 and 11.29). Instead of dividing the entire lesion into locules, the locules are confined to the periphery of the lesion, leaving, the center, of the lesion, which I term the 'atrium,' almost completely devoid of septae [17].

Displacement of teeth in the systematic review is 47%, but it is significantly more marked in the sole East Asian global report than in the Caucasian global group. Root resorption occurs in 27% of lesions, but it is significantly more frequent in a single report [182] representing the entire sub-Saharan African global group than in the Caucasian global group.

Li et al. reported a few cases with an association with unerupted teeth [183].

9.14.1 CROSS-SECTIONAL IMAGING OF ODONTOGENIC MYXOMA

As already indicated, the increased use of cross-sectional imaging of odontogenic myxoma has already transformed a recent systematic review. It displayed a higher proportion of odontogenic myxomas presenting as multilocular radiolucencies. Although CBCT produces images of the better spatial resolution necessary for highly detailed images of the bone [178], it is not recommended for infiltrative benign odontogenic neoplasms (including ameloblastoma and KCOT), because it cannot show the soft tissue. If advanced imaging is indicated, it would be better to refer for a CT so that its soft-tissue

window could permit determination of infiltration of the adjacent soft tissue, particularly if the cortex has been perforated or extensively eroded.

Koseki et al. reported that two-thirds of their CT cases displayed interruption of the cortices [179]. The margins of the now extraosseous lesions to surrounding soft tissue were clearly recognized and smooth on the CT images, even without cortical continuity [179]. Nevertheless, in order to determine whether the adjacent soft tissue has been infiltrated, intravenous contrast medium (see Chapter 4) should be routinely used, as it also should be for the ameloblastoma. Infiltration may be indicated by "enhancement."

Although the contrast medium enhances the peripheral vascular system supplying the odontogenic myxoma [17], it is infrequent to find enhancement in the center of the lesion, unless the lesion has been recently biopsied prior to the CT (see Figure 1.2) [17].

When MRI is used, the bulk of the lesion T1-weighted MRI presents as a hypointense homogeneous signal [171], but on T2-weighted MRI it presents as a hyperintense homogeneous signal [181]. Asaumi et al. reported that odontogenic myxoma and ameloblastoma can be distinguished, as the myxoma enhances after 500–600 seconds in contrast to the ameloblastoma's 45–60 seconds [142].

9.14.2 TREATMENT AND RECURRENCE

Resection is necessary, because the systematic review on odontogenic myxoma revealed an overall recurrence rate of 18% even after resection. This is higher than the 14% of ameloblastoma. The Caucasian and Latin American global groups exhibited significantly greater recurrence rates than that observed for the East Asian global group (Table 9.3). Li et al. reiterated the need for radical treatment of this lesion; after follow-up, the only odontogenic myxoma that recurred had only been enucleated [183].

9.15 Glandular Odontogenic Cyst

The term "cyst" has been applied to the GOCs since it was first characterized in 1988 as the "sialo-odontogenic cyst" by Gardner et al. [184]. The WHO's 1992 edition's histological classification of odontogenic tumors recognized it as "a cyst arising in the tooth-bearing areas of the jaws and characterized by an epithelial lining with cuboidal or columnar cells both at the surface and lining crypts or cyst-like spaces within the thickness of the epithelium" [185]. Slootweg added that this complex epithelium is also partly nonkeratinized and that mucus-producing cells may be present [186]. Its complex histopathology ranges in appearance from well-defined mucoepidermoid carcinoma to the more innocent mucous metaplasia in a DC [186]. This was discussed most recently by Fowler et al. [187]. GOCs can display neoplastic behavior, mainly recurrence after primary surgery (18%) [188].

The WHO's 2017 edition, of which Fowler was a co-author, redefined the GOC as "a developmental cyst with epithelial features that simulate salivary gland or glandular differentiation" [189]. It added that the GOC is thought to arise from remnants of the dental lamina. It further added that though it is most commonly treated by enucleation, it has a very high recurrence rate: "For this reason resection has been advocated, particularly of large or multilocular lesions" [189]. Although Wright and Vered acknowledged the histological overlap between GOC and cystic mucoepidermoid carcinoma, they cautioned against making

a definitive diagnosis based on a small incisional biopsy [129]. Furthermore, "initial studies have not shown *Mastermind-like protein 2* (MAML2) gene rearrangements in GOCs that are seen in many mucoepidermoid carcinomas" [129]. Nagasaki et al. subsequently reported an intraosseous mucoepidermoid carcinoma arising from a GOC confirmed by analysis of MAML2 rearrangement [190]. This was observed in a recurrent GOC, but not in the primary GOC treated nine years earlier [190].

The global distribution of reports included in the systematic review [188] from which much of the following is derived is set out in Figure 1.50 and the details are in Table 9.7.

The mean number of GOCs per year globally is 0.4. The sub-Saharan African global group had the highest mean number, which was significantly greater than that for the Latin American global group, with the least [188].

The GOC has a predilection for males (64%) [188]. Its mean age on first presentation is 45 years, ranging significantly between the global groups from 35 (sub-Saharan African) and 37 (East Asian), through 46 (Caucasian), to 52 (Latin-American). The decade with the most frequent first presentations is the fifth (26%). The period of prior awareness was 10 years for two small European reports [188].

Of the vast majority presenting with symptoms, only 10% of cases are found incidentally. The most frequent symptom was swelling (88%), followed by pain (37%) and numbness (15%) [188].

The mandible is affected in 80% of cases. The anterior sextants are more frequently affected: 78% and 100% for the mandible and maxilla, respectively [188].

Radiographically 98% are radiolucent [188]; 58% are unilocular (Figure 9.51a), and the rest are multilocular (Figure 9.51b). Furthermore, 96% are well defined, of which 30% are corticated. Additionally, 82% display buccolingual expansion; in a small report, when subjacent to the maxillary antrum, 3 out of 4 cases involve it. Tooth displacement occurs in 50% of cases, 32% resorb roots, and 11% are associated with a unerupted tooth. The prevalence of tooth displacement varies significantly between the global groups: it is most frequent for the sub-Saharan African and least frequent for the East Asian global group. Also, root resorption occurs significantly least in the sub-Saharan African and most in the Caucasian global group. With regard to unerupted teeth, although the unilocular lesions appear like DCs, most infrequently affect third molars because of their anterior location [188]. Although a third of cases present globally with root resorption, this is significantly most frequent in those of European or Middle Eastern origin [188]. Recurrence after treatment is seen in 18% of cases [188].

In the absence of better information, a multilocular radiolucency accompanied by root resorption and histopathologically determined to be a GOC should be considered definitely neoplastic (such as the ameloblastoma), whereas a unilocular radiolucency arising from the amelocemental junction of an unerupted tooth directs the clinician to consider a DC with mucous metaplasia. Nevertheless, until more is known about the GOC, it would be prudent that all such lesions be followed up over an extended period [1]. Figure 9.52 displays a minimally buccolingually expansive GOC, which had been provisionally diagnosed as a KCOT prior to surgery. This reinforces the opinion that the wide range of radiological and histological presentations of the GOC and its outcomes suggest that this entity may be a collection of lesions which have not yet been identified and characterized [1].

Table 9.7 Glandular odontogenic cyst: systematic review.

Feature	Total	Caucasian	East Asian	Sub-Saharan African	Latin American
Male: Female	64% : 36%	70% : 30%[a]	67% : 33%[a]	44% : 56%[a]	57% : 43%[a]
Mean number per year per report	0.4	0.5	0.4	0.7	0.2
Mean age	45 years	46 years	38 years[a]	35 years[a]	52 years[a]
Mean prior awareness	10 years[a]	10 years[a]	N/A	N/A	N/A
Mandible: Maxilla	80% : 20%	82% : 18%[a]	58% : 42%[a]	67% : 33%[a]	91% : 9%[a]
Mandible: *Anterior: Posterior*	78% : 22%[a]	84% : 16%[a]	100% : 0%[a]	0% : 100%[a]	50% : 50%[a]
Maxilla: *Anterior: Posterior*	100% : 0%[a]	100% : 0%[a]	N/A	100% : 0%[a]	100% : 0%[a]
Swelling: *Yes: No*	88% : 12%[a]	81% : 19%[a]	92% : 8%[a]	N/A	100% : 0%[a]
Pain: *Yes: No*	37% : 63%[a]	23% : 77%[a]	25% : 75%[a]	N/A	40% : 60%[a]
Incidental: *Yes: No*	10% : 90%[a]	14% : 86%[a]	8% : 92%[a]	N/A	0% : 100%[a]
Numbness: *Yes: No*	15% : 85%[a]	14% : 86%[a]	0% : 100%[a]	N/A	N/A
Radiolucent: *Yes: No*	98% : 2%	95% : 5%[a]	100% :0%[a]	100% : 0%[a]	100% : 0%[a]
Unilocular: Multilocular	58% : 42%	65% : 35%[a]	58% : 42%[a]	67% : 33%[a]	20% : 80%[a]
Well-defined: *Yes: No*	96% : 4%[a]	100% : 0%[a]	100% : 0%[a]	87% : 13%[a]	N/A
Cortex: *Yes: No*	30% : 70%[a]	36% : 64%[a]	N/A	22% : 78%[a]	NA
Perforation: *Yes: No*	52% : 48%[a]	57% : 43%[a]	N/A	44% : 56%[a]	N/A
Expansion: *Yes: No*	82% : 18%[a]	57% : 43%[a]	N/A	100% : 0%[a]	100% : 0%[a]
Downward expansion of lower border of mandible: *Yes: No*	N/A	N/A	N/A	N/A	N/A
Affects maxillary sinus: *Yes: No*	75% : 25%	75% : 25%	N/A	N/A	N/A
Tooth displacement: *Yes: No*	50% : 50%[a]	50% : 50%[a]	17% : 83%[a]	100% : 0%[a]	N/A
Root resorption: *Yes: No*	32% : 68%[a]	54% : 46%[a]	33% : 67%[a]	0% : 100%[a]	N/A
Associated with unerupted teeth: *Yes: No*	11% : 89%[a]	14% : 86%[a]	17% : 83%[a]	0% : 100%[a]	N/A
Recurrence: *Yes: No*	18% : 82%	25% : 75%[a]	10% : 90%[a]	0% : 100%[a]	20% : 80%[a]

[a] Percentages derived either from one report or from a synthesis of no more than 50 cases.
Key: N/A, information not available.

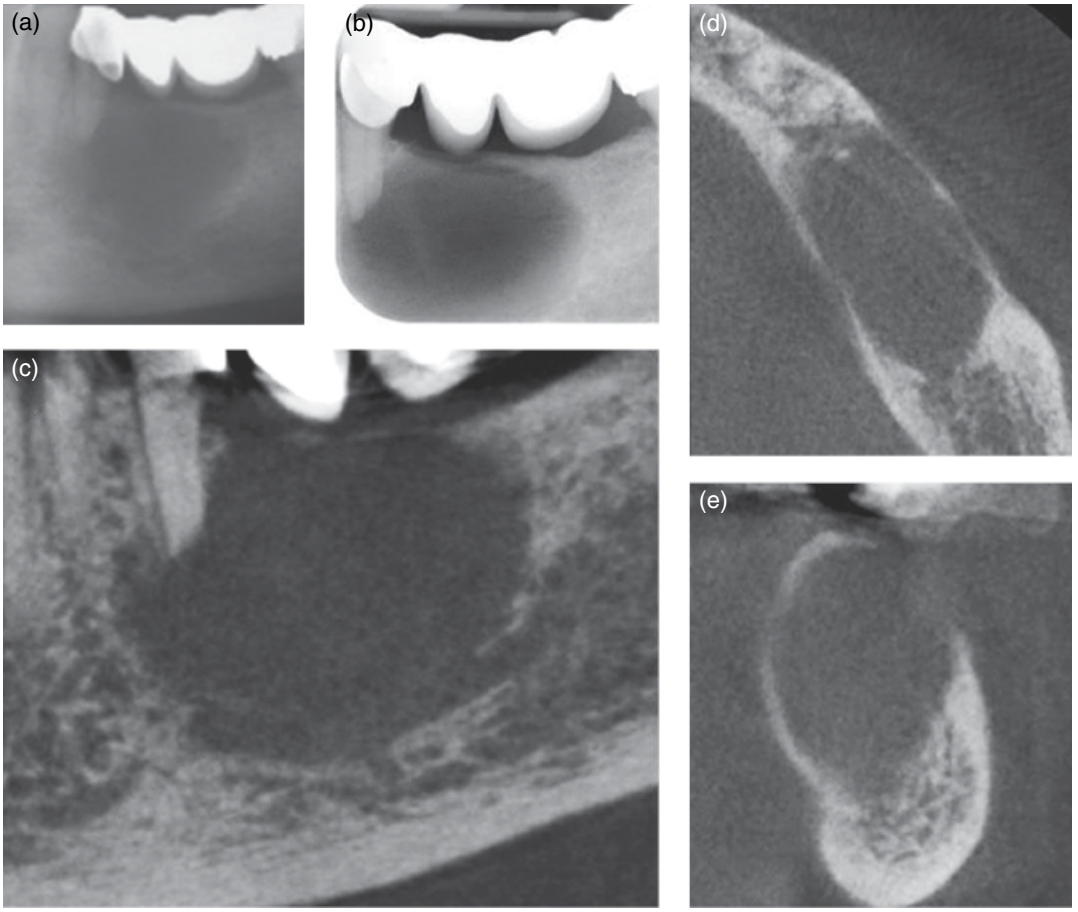


Figure 9.52 Conventional panoramic radiograph (a), periapical radiograph taken six months later (b), and panoramic (c), axial (d), and transaxial (e) reconstructions of cone-beam computed tomography of a glandular odontogenic cyst arising in the premolar–first molar area of the mandible. The margin of the lesion was not particularly well defined (a–c and e). The unilocular radiolucency is associated with root resorption of the second premolar (a–c). There is some buccolingual expansion and some extension from the alveolus into the basal process (e). The lingual and particularly the buccal cortices have been eroded (d and e). The mandibular canal appears slightly displaced downward (c). The superior cortex of the mandibular canal has been eroded with regard to the posterior aspect of the lesion (c and e).

9.16 Orthokeratinized Odontogenic Cyst

The OOC was first clearly identified as the orthokeratotic variant of the OKC by Wright in 1981 [191], due to its different histopathology and reduced likelihood of recurrence. The latter was confirmed in a systematic review [151]. Although the WHO's 1972 and 1992 editions recognized that "cases with orthokeratosis are seen" [192], the WHO's 2005 edition expressly excluded it from its definition of a KCOT [150].

The WHO's 2017 edition defined the OOC as "an odontogenic cyst that is entirely or predominantly lined by orthokeratinized stratified squamous epithelium" [193].

Nevertheless, those mixed lesions that contain a substantial component of parakeratotic epithelium should be regarded with caution. As already mentioned, such mixed cases (Figure 9.33), which account for 7% of all cases formerly considered to be odontogenic keratocysts, should be managed as if they were KCOTs [151].

The global distribution of reports included in the systematic review [151] from which much of the following is derived is set out in Figure 1.49 and the details are in Table 9.8.

The mean number of OOCs per year globally is 0.8. The OOC accounts for 10% of all nonsyndromic former odontogenic keratocysts [151]. The mean age at first presentation is 35 years. Patients have a very short period of first awareness of their lesions. Although this is 0.9 years for the East Asian global group alone, that of the Hong Kong study was significantly shorter than that of the Malaysian report [151]. Most (32%) first present in the third decade.

While 48% of cases are found incidentally, the rest present with symptoms. Swelling occurs in 41%, significantly most frequently in the East Asian global group (58%). Pain and discharge occur in 24% and 16%, respectively. The mandible is affected in 71% of cases. The posterior mandibular sextant is affected (92%) more frequently than the anterior sextant. The anterior and posterior maxillary sextants are affected equally [151].

All OOCs present as radiolucencies (Figure 9.53). Although 93% are unilocular (Figure 9.53), some are multilocular (Figure 9.54). Marginal definition is recorded for only two reports included in the systematic review; OOCs are well defined with corticated margins. There is an association with unerupted teeth in 69%, the majority of which are third molars [151]. One report indicates that OOCs may affect the maxillary antrum and displace teeth [152].

Two out of three consecutive mandibular OOCs displayed the downward displacement of a lateral cortex past the otherwise undisplaced lower border of the mandible (Figures 9.53 and 9.54) [152], hitherto a feature observed only in ameloblastomas [126, 127].

Although the overall recurrence rate is 4% [151], this may be an overestimate because it is very likely that a few "mixed" cases displaying both parakeratotic and orthokeratotic epithelium may have been simply assigned the diagnosis of an orthokeratotic variant of OKC or OOC because no alternative was available. Figure 9.55 displays an occlusal radiograph of a mixed parakeratotic and orthokeratotic case. The complete absence of buccolingual expansion makes it appear more like a KCOT than the OOCs already shown in Figures 9.53 and 9.54. Dong et al. reported that 42 out of their 61 cases of OOC, of which nearly 90% were treated conservatively, did not display any recurrence after a mean of six years of follow-up [194].

The OOC differs significantly from the KCOT by being observed as an incidental finding with a well-defined margin and an association with an unerupted tooth [151].

9.17 Squamous Odontogenic Tumor (ICD-O 9312/0)

The WHO's 2017 edition defined the *squamous odontogenic tumor* (SOT) as "a benign epithelial tumor in which the tumor cells show terminal squamous differentiation," and noted that "NOTCH receptors and their ligands may play a role in the cytodifferentiation of SOT" [195]. Less than 50 cases have been reported, arising in a very wide age range of patients; the mean age is

Table 9.8 Orthokeratinized odontogenic cyst: systematic review.

Feature	Total	Caucasian	East Asian	Sub-Saharan African	Latin American
Male: Female	66% : 34%	67% : 33%	65% : 35%	N/A	67% : 35%[a]
Mean number per year per report	0.8	1.1	0.8	N/A	0.4
Mean age	35 years	35 years	35 years	N/A	37 years[a]
Mean prior awareness	0.9 years[a]	N/A	0.9 years[a]	N/A	N/A
Mandible: Maxilla	71% : 29%	69% : 31%	79% : 21%	N/A	50% : 50%[a]
Mandible: *Anterior: Posterior*	8% : 92%	10% : 90%[a]	4% : 96%[a]	N/A	N/A
Maxilla: *Anterior: Posterior*	50% : 50%[a]	50% : 50%[a]	50% : 50%[a]	N/A	N/A
Swelling: *Yes: No*	41% : 59%	23% : 77%[a]	58% : 42%[a]	N/A	67% : 33%[a]
Pain: *Yes: No*	24% : 76%	23% : 77%[a]	22% : 78%	N/A	0% : 100%[a]
Incidental: *Yes: No*	48% : 52%	53% : 47%[a]	31% : 69%[a]	N/A	N/A
Discharge: *Yes: No*	16% : 84%[a]	11% : 89%[a]	31% : 69%[a]	N/A	33% : 67%[a]
Radiolucent: *Yes: No*	100% : 0%	100% : 0%	100% : 0%	N/A	100% : 0%[a]
Unilocular: Multilocular	93% : 7%	95% : 5%	89% : 11%	N/A	100% : 0%[a]
Well defined: *Yes: No*	100% : 0%[a]	N/A	100% : 0%[a]	N/A	N/A
Cortex: *Yes: No*	100% : 0%[a]	N/A	100% : 0%[a]	N/A	N/A
Expansion: *Yes: No*	100% : 0%[a]	N/A	100% : 0%[a]	N/A	N/A
Downward expansion of lower border of mandible: *Yes: No*	25% : 75%[a]	N/A	25% : 75%[a]	N/A	N/A
Affects maxillary sinus: *Yes: No*	100% : 0%[a]	N/A	100% : 0%[a]	N/A	N/A
Tooth displacement: *Yes: No*	80% : 20%[a]	N/A	80% : 20%[a]	N/A	50% : 50%[a]
Root resorption: *Yes: No*	0% : 100%[a]	N/A	0% : 100%[a]	N/A	N/A
Associated with unerupted teeth: *Yes: No*	69% : 31%	76% : 24%[a]	63% : 37%[a]	N/A	62% : 38%[a]
Recurrence: *Yes: No*	4% : 96%	5% : 95%	0% : 100%[a]	N/A	0% : 100%[a]

[a] Percentages derived either from one report or from a synthesis of no more than 50 cases.
Key: N/A, information not available.

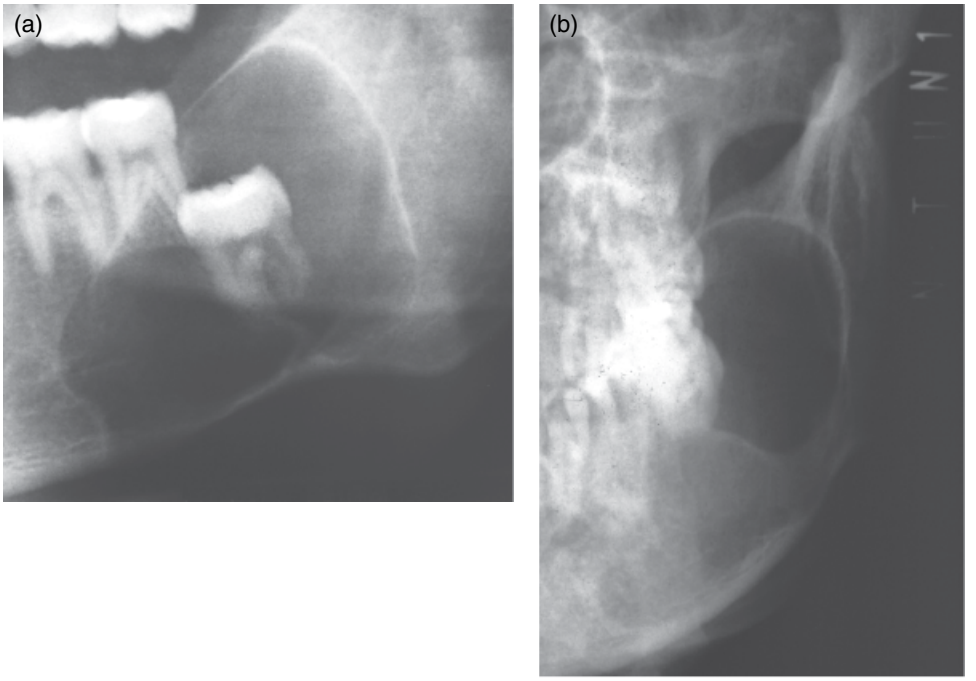


Figure 9.53 Panoramic radiograph (a) and posterioanterior projection (b) of the mandible displaying an orthokeratinized odontogenic cyst (OOC). This presents as a well-defined corticated unilocular radiolucency, which not only exhibits buccolingual expansion but also downward expansion of either lateral cortex past the undisplaced lower border of the mandible anteriorly. The associated unerupted tooth, with which the OOC has no obvious relationship to the cementoenamel junction, in (a) has been displaced lingually in (b). The mandibular canal has been displaced to the lower border of the mandible. Source: MacDonald-Jankowski, D.S., and Li, T.K. (2010). Orthokeratinising odontogenic cyst in a Hong Kong community; the clinical and radiological presentations and the outcomes of treatment and follow-up. *Dentomaxillofac. Radiol.* 39:238–243.

38 years. They affect either jaw equally. Most are symptom free and most are observed as unilocular radiolucencies, often between the roots of teeth, displacing them (creating a triangular shape) but rarely resorbing them. Most respond to conservative surgery and rarely occur [195].

9.18 Primordial Odontogenic Tumor

The *primordial odontogenic tumor* (POT) was only recently characterized from a handful of cases discovered in children and adolescents [196, 197]. Although it is called a tumor, it has not yet acquired an ICD-O code. The WHO's 2017 edition defined it as "a tumor composed of variably cellular loose fibrous tissue with areas similar to the dental papilla, entirely surrounded by cuboidal to columnar epithelium resembling the internal epithelium of the enamel organ" [198]. The few cases reported so far first presented in children and adolescents with a mean age of 12 years. In the case series of POTs, in all cases there were well-defined radiolucencies associated with unerupted teeth (most commonly mandibular third



Figure 9.54 Panoramic radiograph of an orthokeratinized odontogenic cyst affecting the posterior sextant of the mandible. It exhibits a well-defined multilocular radiolucency with a corticated margin. Extending from the distal aspect of the second premolar back to the base of the sigmoid notch, it expands the anterior margin of the vertical ramus and displaces a lateral cortex down past the lower border of the mandible. Source: MacDonald-Jankowski, D.S., and Li, T.K. (2010). Orthokeratinising odontogenic cyst in a Hong Kong community; the clinical and radiological presentations and the outcomes of treatment and follow-up. *Dentomaxillofac. Radiol.* 39: 238–243.



Figure 9.55 True occlusal projection of a case exhibiting a mixture of parakeratin and orthokeratin. Although extensive in its mesiodistal extent, it displays no buccolingual expansion.

molars) apparently showing a pericoronal relationship (Figure 9.56). Although symptom free, they may cause cortical expansion and also tooth displacement and root resorption. On the basis of the panoramic radiographs of four cases displayed in this case series, two are multilocular and two are unilocular [196]. At least one case has displaced, presumably, the lingual cortex down past the undisplaced lower border of the mandible. This feature had already been reported for ameloblastomas and OOCs. Although no case has recurred after up to 20 years in one instance, only a few cases have been reported [196–198].

9.19 Giant Cell Granuloma

This is divided into two lesions, *central giant cell granuloma* (CGCG) [199] and the peripheral giant cell granuloma [200]. The latter occurs in the gingivae and alveolar mucosa as a purplish-blue lump, also called a giant cell epulis, and may create nothing more than a shallow indentation of the adjacent alveolar bone [200]. The CGCG, is more important [199]. The WHO's 2017 edition defined the CGCG as "a localized benign but sometimes aggressive osteolytic lesion of the jaws characterised by osteoclast-type giant cell in a vascular stroma"

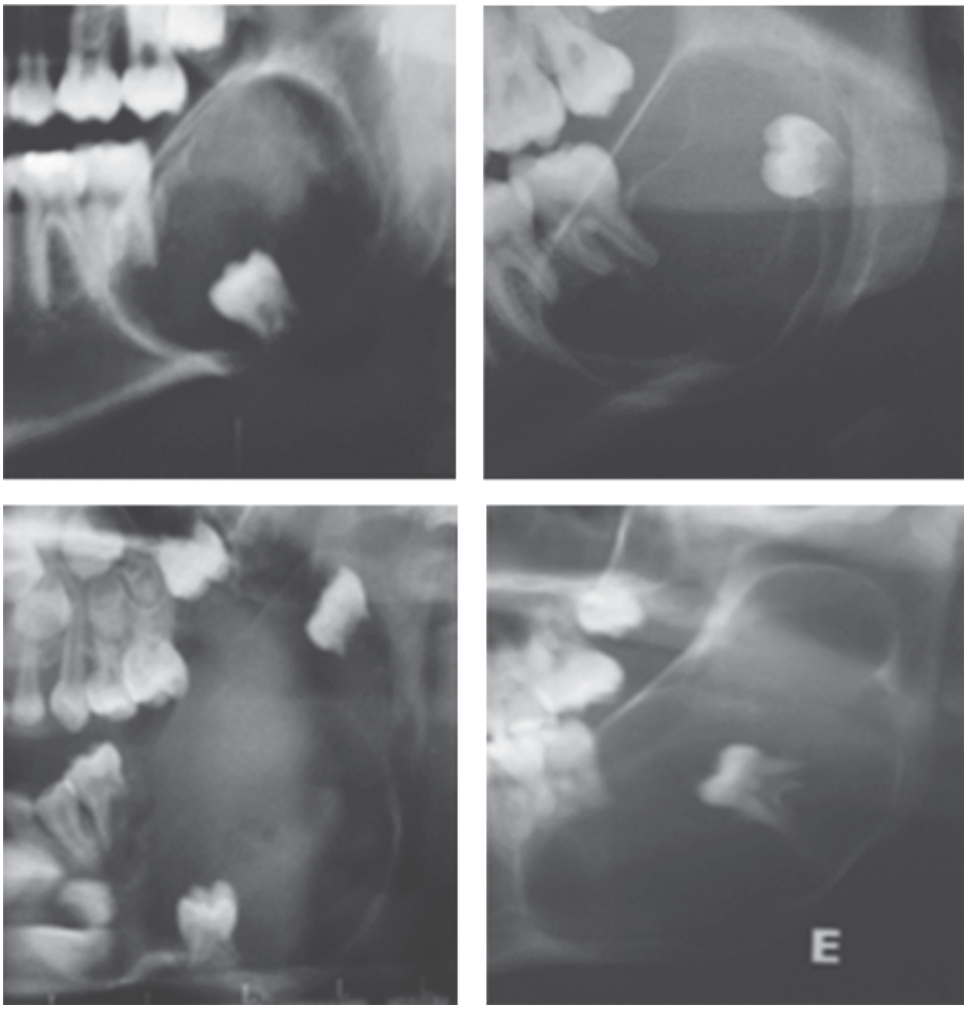


Figure 9.56 Primordial odontogenic tumor (POT). Panoramic radiographs display the POTs in the posterior sextant of the mandible. All four lesions have displaced teeth. Source: Reproduced with permission from Mosqueda-Taylor A, Pires FR, Aguirre-Urízar JM, et al. (2014). Primordial odontogenic tumor: clinicopathological analysis of six cases of a previously undescribed entity. *Histopathology* 65:606–612.

[199]. It has no capsule. It needs to be distinguished from other giant cell lesions such as cherubism, hyperparathyroidism, and the aneurysmal bone cyst (ABC). It accounts for 10% of all jaw tumors and occurs most frequently in the anterior sextant of the mandible, mainly presenting in females and in the first two decades of life. If presenting in these and as a multilocular radiolucency, then one should consider *Noonan syndrome* (NS) or Leopard syndrome and also neurofibromatosis type 1. NS and Leopard syndrome (NS with multiple lentigines) are respectively the first and second most common *neuro-cardio-facial-cutaneous* (NCFC) syndromes. NS is autosomal dominant. It is also often called the male version of Turner's syndrome. It

is one of the genetic defects with high congenital heart defect prevalence. Both syndromes arise in patients with gene mutations in the RAS/MAPK pathway. Other than these syndromes, CGCG has no genetic profile. It lacks the point mutation in the *H3F3A* gene that characterizes "giant cell tumor of the bone" [199].

Stavropoulos and Katz, in reporting their own case series, observed that 81% of cases were anterior to the molars. There was no association between size (some were over 6 cm, although the mean was 3.6) and age [201].

Radiologically, Stavropoulos and Katz's Table 2 revealed that 45% of cases presented as radiolucencies and 55% were "mixed radiolucent-radiopaque." Their systematic review revealed that the lesions were wholly well defined in 34% of cases, whereas their own report found that all were wholly or partly well defined. In their systematic review 46% were uniocular, whereas in their study 45% were multilocular. "Trabeculae" within the lesions were displayed in 50%. Scalloping between teeth was observed in 53% of cases in their study [201].

Stavropoulos and Katz's study reported that 45% of cases displayed buccolingual expansion and 50% displayed perforation of the cortex, whereas their systematic review revealed 51% and 38% for these features, respectively [201].

The study reported that tooth and follicle displacement occurred in 45% of cases (Figure 9.57). The mandibular canal was inferiorly displaced in 5% and the lamina dura was absent in 94% of cases (Figure 9.57) [201].

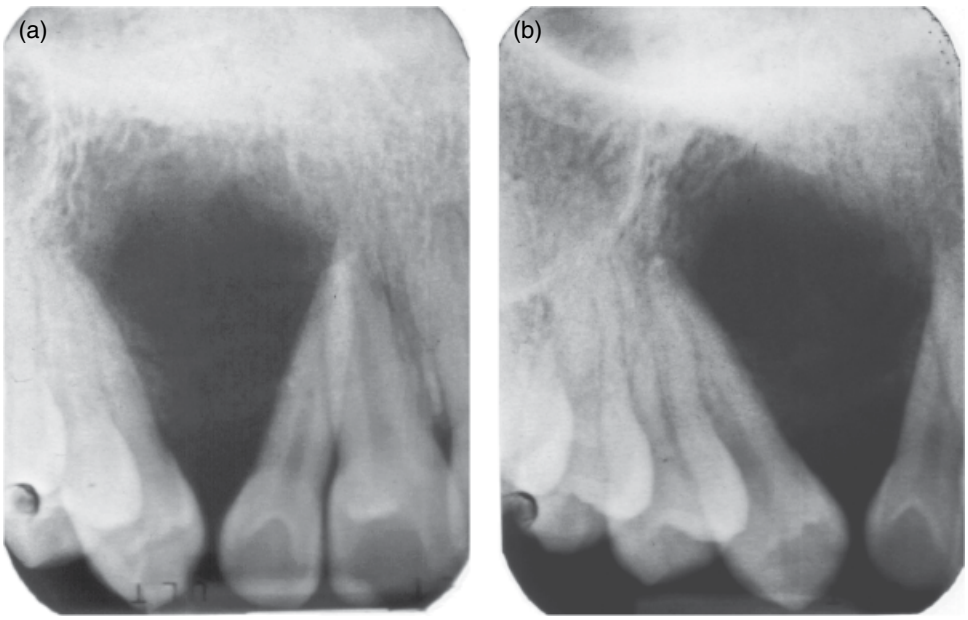


Figure 9.57 (a and b) Periapical radiographs of a giant cell granuloma affecting the anterior sextant of the maxilla. This case appears similar to Figure 9.46 in the way it displays the roots of the maxillary canine and lateral incisor.

Root resorption was 37% of cases in Stavropoulos and Katz's study and 33% in their systematic review [201].

In addition to the syndromes mentioned earlier, the clinician needs to be aware that the multilocular manifestation may represent advanced disease. There is an aggressive presentation in 30% of all CGCGs, occasioning pain, tooth displacement, root resorption, and cortical perforation, and even the invasion of adjacent structure. MRI and PET/CT many be required to delineate the latter [199].

Although the majority of CGCGs regress after puberty, some continue to grow. Bredell et al. reported that denosumab therapy should be considered a therapeutic option for large central CGCGs of the jaws [204]. The results of their application to five patients with large CGCGs, followed up for at least two years, suggest that denosumab is a successful treatment option. They recommended that the length of this treatment be no shorter than 12 months. They also advised that the response to treatment should be investigated by PET/CT or MRI [202].

9.20 Ameloblastic Fibroma (ICD-O 9330/0)

The WHO's 2017 edition defined *ameloblastic fibroma* (AF) as "a rare, benign, true mixed tumor composed of odontogenic mesenchyme resembling dental papilla and epithelial resembling odontogenic epithelium" [203]. The WHO's 2005 edition identified *ameloblastic fibrodentinoma* (ICD-O 9271/0) and *ameloblastic fibroodontoma* (ICD-O 9290/0), respectively [204]. These are now considered to be early manifestations of odontomas [129].

Buchner and Vered recently synthesized the literature on ameloblastic fibroma [205], analyzing 172 cases. Although the mean age was 14.9 years, 80% were diagnosed upon completion of odontogenesis at just over 20 years of age. Nearly 80% of cases affected the mandible, with 82% overall in the posterior sextants of the mandible. The ameloblastic fibroma presented as a painless swelling in about half of cases. The degree of expansion in 18% was so severe it caused facial asymmetry. Although the histology would lead one to expect a radiolucency, the presence of a sclerotic cortex in 94% of cases (Figure 9.58) on conventional radiography (Figure 9.59) gave rise on occasion to an impression that it was a radiopacity. Most small lesions were unilocular and most large ones were multilocular [205].

Nearly 90% were conservatively treated [205]. While 16% recurred, 6%

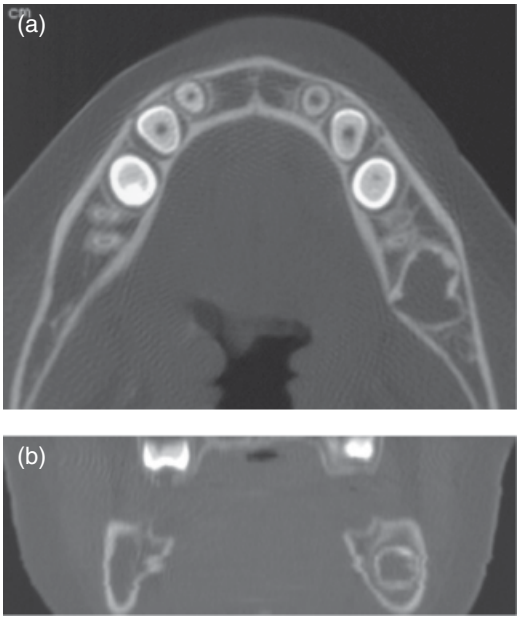


Figure 9.58 Computed tomography (CT) of an ameloblastic fibroma. (a) Axial CT (bone window) displaying a well-defined radiolucency with a sclerotic margin. (b) Coronal CT (bone window) displaying a well-defined radiolucency with a sclerotic margin. It exhibits lingual expansion obliterating the submandibular fossa.

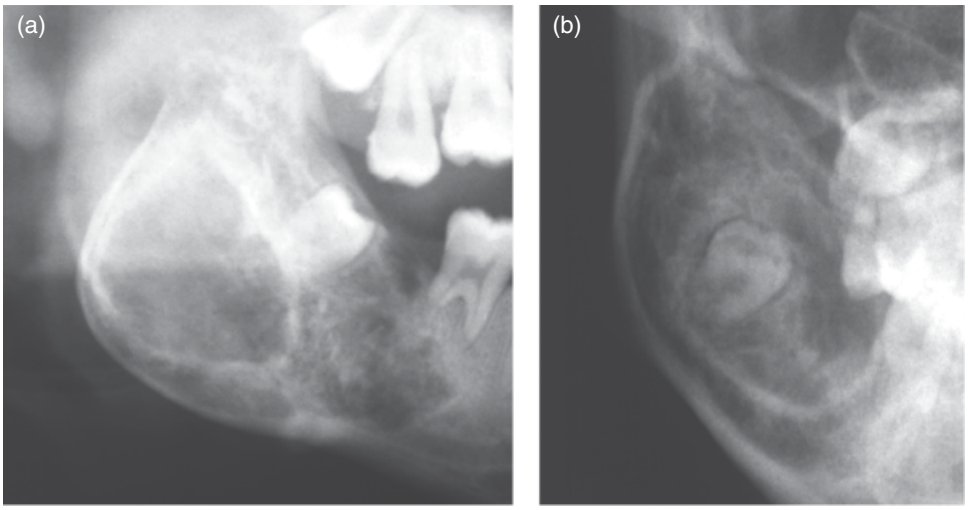


Figure 9.59 Conventional radiography of an ameloblastic fibroma. Panoramic radiograph (a) and anterioposterior projection of the mandible (b) displaying an ameloblastic fibroma sited within the angle of the mandible and posterior body of the mandible. This lesion presents with buccolingual expansion. Its margin is well defined and sclerotic. Its internal structure is complex. Although largely translucent, it contains a separate radiolucency well defined by a sclerotic margin. The lesion also encompasses an unerupted third molar, whose normal-sized follicle space is still patent. The distal root of the second molar has been resorbed.

underwent malignant transformation. This transformation occurred after the first or second recurrence [205], suggesting that ameloblastic fibroma should be subject to long-term follow-up.

9.21 Simple Bone Cyst

The WHO's 2017 edition [206] upheld the WHO's 2005 edition's definition of the *simple bone cyst* (SBC) as "an intraosseous pseudocyst devoid of an epithelial lining, either empty or filled with serous or sanguineous fluid" [207].

The SBC has a number of synonyms, which have been set out by Suei et al. [208]. The possible etiologies have been reviewed by Harnet et al. [209]. It is not a common lesion [210]. Although there is a view that SBCs are rarely detected after 25 years of age [211], another report indicates that this is not true for every community; in one report some SBCs presented later in the Hong Kong Chinese [212].

SBC of the jaws affects both sexes equally [212]. Suei et al. [208] suggested that a proportion of female patients with SBC are afflicted by osseous dysplasia (Figure 1.20), which can itself be accompanied by SBC [213]. Therefore, it may be difficult to determine in some cases whether a particular lesion is primarily an SBC or an osseous dysplasia (discussed in full in Chapter 10).

Because SBC affecting the jaw is rarely symptomatic, it is frequently discovered incidentally on a radiograph prescribed for another purpose [213]. Although SBCs may be associated intimately with teeth, these teeth are almost

always vital. SBCs predominantly affect the mandible (94%) [214].

On the conventional radiograph a frequent presentation is as a unilocular radiolucency with no or minimal buccolingual expansion. To distinguish it from the KCOT, which has a similar presentation, Ferreira et al. reported that the SBC is significantly more likely to display scalloping between the roots of teeth (Figure 1.23) [215].

The degree of marginal definition can vary from corticated to poorly defined [212]. Ferreira et al. reported that the SBC may also be distinguished from the KCOT because the latter's border was frequently more corticated [215].

Expansion was present in 40% of Suei et al.'s case series [216] and in 21% of MacDonald-Jankowski's case series [212]. Although the inferior dental canal was displaced in 54% of Matsumura et al.'s cases [214], this was only observed in one case in MacDonald-Jankowski's report [212]. Furthermore, although that report observed the constriction of the canal in one case and absence of its outline in two cases, the canal was unaffected, although superimposed upon the SBC, in another eight cases [212]. Root resorption or tooth displacement was not observed [212, 214].

Although the majority present as radiolucencies, at least one report included a high proportion of cases that include central radiopacities (Figure 1.26) [214]. Matsumura et al. divided their 53 simple bone cysts into two groups [214]. Type A has a connective tissue lining, whereas Type B has a partially thickened wall with dysplastic bone formation. Recurrence was more associated with Type B [214].

Suei et al. [217] and Eriksson et al. [218] could not substantiate, by CT and MRI, respectively, the frequent observation that, at the time of surgery, SBCs were air-filled.

Suei et al., in their recent report of their case series and synthesis of the literature, reported that 26% of 132 cases recurred [217]. This is much higher than hitherto reported. Yanagi et al. showed that contrast-enhanced T1-weighted MRI showed not only marked enhancement of the margin, but also slight enhancement of the inner part of the cyst cavity. The latter distinguishes SBCs from true cysts; that is, those with an epithelial lining, which exhibit no enhancement within a cavity (Figure 9.60) [219].

A case series of SBCs discovered as incidental findings in children, which were surgically explored and curetted, revealed that only 43% subsequently displayed bone infilling, whereas the rest did not. Nevertheless, this latter group exhibited no subsequent symptoms, enlargement in size, or pathological fracture [220].

Although the SBC in the jaws is more innocuous than SBCs elsewhere in the skeleton, it may achieve considerable mesiodistal dimensions, but with little buccolingual expansion. Therefore, it needs to be distinguished from other lesions, such as KCOTs, that require treatment. Having said that, some ABCs can be very expansive. Mathew et al. display a CBCT of a very extensive and expansile SBC affecting the posterior mandible [221]. Frequently, definitive diagnosis of an SBC is only established at surgery when a cavity devoid of an epithelium is found. Although most heal uneventfully after that, 28% recurred in a recent Japanese report [222]. This recurrence rate was even higher for cases with multiple cysts and osseous dysplasia, 71% and 75%, respectively [217]. Healing occurred within 1–1.5 years and recurrence up to 2.5 years. Suei et al. recommended that follow-up is continued until healing has been radiographically confirmed, particularly with regard to those cases with multiple cysts

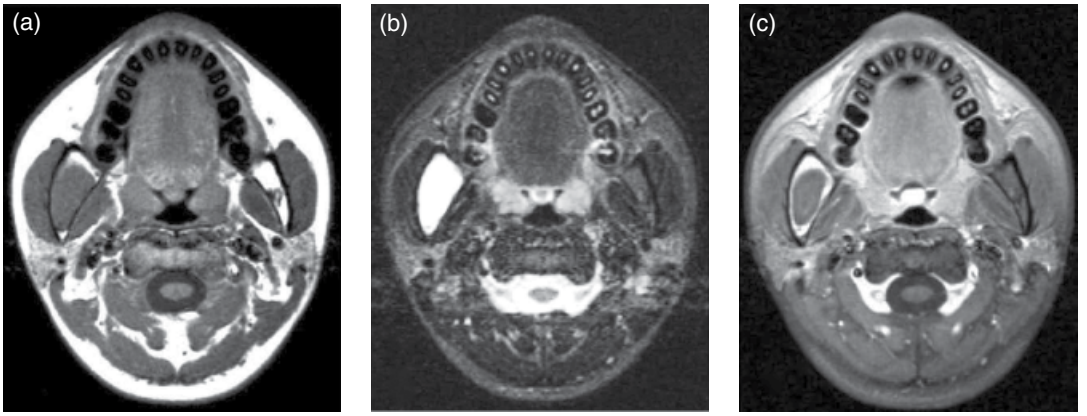


Figure 9.60 Magnetic resonance imaging of simple bone cyst showing a homogeneous intermediate signal intensity (SI) on T1-weighted imaging (a) and a homogeneous high SI on T2-weighted imaging with clear borders (b). The contrast-enhanced T1-weighted image acquired approximately six minutes after the administration of gadolinium–diethylenetriamine penta-acetic acid showed marked enhancement of the margin and slight enhancement of the inner part of the cyst cavity in all cases (c). Source: Reproduced with permission from Yanagi, Y., Asaumi, J., Unetsubo, T., et al. (2010). Usefulness of MRI and dynamic contrast-enhanced MRI for differential diagnosis of simple bone cysts from true cysts in the jaw. *Oral Surg. Oral Med. Oral Pathol. Oral Radiol. Endod.* 110:364–369.

or osseous dysplasia [217]. MacDonald-Jankowski reported a case that recurred at least six times in nine years [212]. The initially four separate lesions coalesced into a lesion that occupied the entire body of the mandible (Figure 1.23) [212]. The need for follow-up until complete healing occurred was emphasized, because frequently some bone regeneration was apparent before it regressed [212].

The features which may suggest a potential to recur are loss of lamina dura, root resorption, nodular bone expansion, multilocularity, and the presence of osseous dysplasia [222]. Suei et al. based this conclusion on their observation of 31 cases of SBCs, of which "most of the lesions with a radiographic finding of an intact lamina dura or smooth margin healed after surgery, whereas more than 60% recurred in cases with the finding of an absent lamina dura, root resorption, scalloped margin, radiopaque mass or multiple cavities" [222].

Figure 9.61 exhibits an SBC as it first presented on a conventional panoramic radiograph. The poorly defined radiolucency on the conventional panoramic radiograph was shown on the subsequent CBCT to be well defined with a thin cortex.

9.22 Aneurysmal Bone Cyst (ICD-O Code 9260/0)

The WHO's 2017 edition defines the ABC as a cystic or multicystic expansile osteolytic neoplasm composed of blood-filled spaces separated by fibrous septa containing an osteoclast-type giant cell. It is overall a very rare lesion, of which 15% arise in the jaws [223]. Although any age can be affected, over 80% arise in the young, particularly in the first two decades of life. Most occur in the mandible and particularly in the posterior sextants (Figure 9.62). Swelling and pain are frequent. Although the teeth remain vital, they are subject to

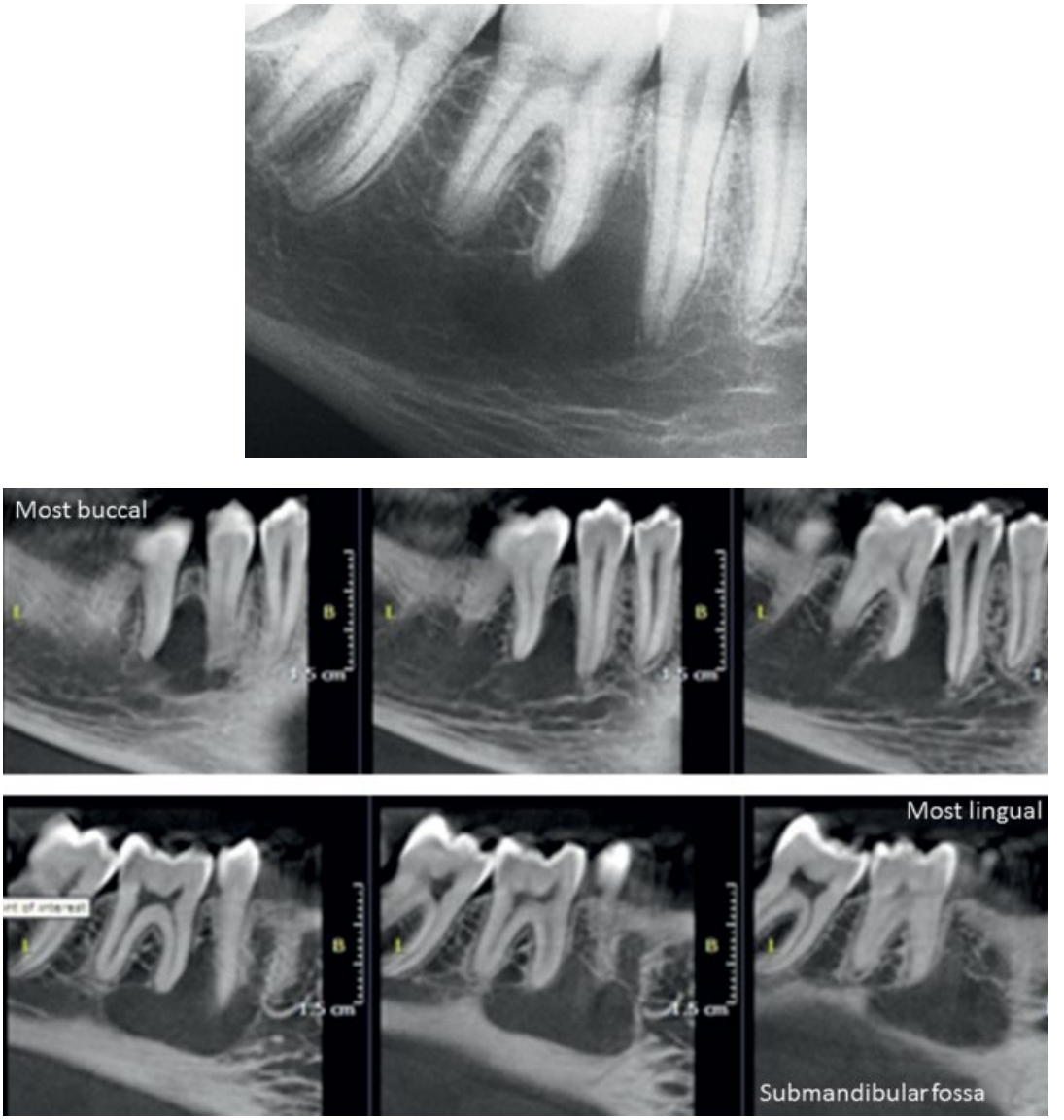


Figure 9.61 Conventional panoramic radiography (top) displaying a simple bone cyst scalloping up between the roots of the second premolar and the first molar of the right mandible. Panoramic reconstructions of the subsequent cone-beam computed tomography (CBCT) of a simple bone cyst, both rows have three images each. Note that the top three CBCT reconstructions are more buccal and the bottom three are more lingual, with the submandibular fossa present in the last. The lamina dura is absent from the root of the first molar where the simple bone cyst engages it, but only partly absent from the distal surface of the root of the second premolar. The CBCT displays a thin cortex, which is not obvious in the conventional panoramic radiograph.

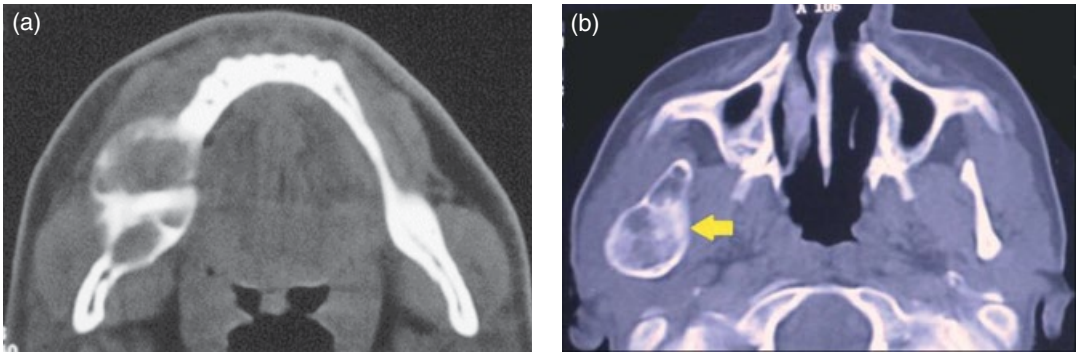


Figure 9.62 Axial reconstructions of computed tomography of cases of aneurysmal bone cysts (ABCs). (a) ABC of the body of the mandible displaying septa. (b) ABC in the vertical ramus of the mandible. The yellow arrow indicates perforation of the cortex. Source: (a) Reproduced with permission from Triantafillidou, K., Venetis, G., Karakinaris, G., et al. (2012). Variable histopathological features of 6 cases of aneurysmal bone cysts developed in the jaws: review of the literature. *J. Craniomaxillofac. Surg.* 40: e33–e38. (b) Reproduced with permission from Urs, A.B., Augustine, J., and Chawla, H. Aneurysmal bone cyst of the jaws: clinicopathological study. *J. Maxillofac. Oral Surg.* 2014;13:458–463.

displacement and root resorption, and frequently become mobile. There may be perforation of cortices and extension into adjacent soft tissue. In the maxilla they extend into the nose, sinuses, and orbits, in the latter effecting exophthalmos. CT reveals septae and CT and MRI can demonstrate fluid–fluid levels [223].

Although ABCs can be treated with curettage, resection may be required for very large destructive lesions. They recur in 10% of cases with involvement of the adjacent soft tissues [223].

Sun et al. synthesized the literature, capturing 92 cases out of 75 reports [224]. Nearly three-quarters first present in the first two decades. Two-thirds affect the mandible, of which 85% affect the posterior body and vertical ramus. A bony swelling with or without pain is the most common clinical presentation. Kaffe et al. additionally reported that paresthesia occurred in 9% of cases [225].

Of Sun et al.'s 49 cases for which radiology could be determined, 94 presented as radiolucencies, of which two-thirds are multilocular; 2 maxillary cases were radiopaque and 1 mandibular case was mixed [224]. Kaffe et al.'s synthesis of 64 cases reported 87% as radiolucent (53% multilocular); 1 maxillary case was radiopaque and 6 (4 mandible and 2 maxilla) were "mixed" [225]. The mixed and radiopaque cases may reflect reactive bone formation within the ABC [225].

Both Sun et al. [224] and Kaffe et al.'s [225] findings differ from those in Motamedi et al.'s Iranian case series [226], the largest and most recently reported case series of ABCs affecting the jaws. The latter cases displayed a similar age and anatomical distribution to that reported by Sun et al. [224], except that there was a more equal distribution between the mandibular sextants. All were radiolucent [226].

Of Kaffe et al.'s multilocular ABCs, 65% were greater than 4 cm, whereas 60% of the unilocular ABCs were smaller than 4 cm [225]. This may suggest that multilocularity may depend on the lesion's size.

There was a cortex in 39% of Kaffe et al.'s 64 cases, while 33% of the rest were well defined, and 28% poorly defined [225].

Expansion was displayed in 55% of Kaffe et al.'s cases, 26% of ABCs in dentate areas exhibited tooth displacement, and 14% showed root resorption [225].

Five of Kaffe et al.'s cases were also associated with unerupted teeth [225], which may reflect the ABC's predilection for the posterior sextants and the child and adolescent.

Of Sun et al.'s ABCs, 15% were considered to arise secondarily to other lesions; the majority were fibrous dysplasia [224]. It is an indication of the ABC's rarity that no clear mention of ABCs being secondary to fibrous dysplasia appeared in any reported case series on fibrous dysplasia. Nevertheless, Saad et al. reported a case of an adult patient presenting with an asymptomatic lesion with a dual component of ossifying fibroma and ABC affecting the maxillary sinus [227].

The overall recurrence rate of ABCs is 13% and is not influenced by resection or curettage. Motamedi et al. reported a similar recurrence rate of 16% after follow-up ranging from 2 to 30 years [226]. ABCs affecting the mandible can achieve substantial dimensions on occasion [228].

9.23 Nasopalatine (Duct) Cyst

The WHO's 2017 edition defines the NDC as "a non-odontogenic cyst of developmental origin that arises in the midline of the anterior maxilla" [229]. Wright and Vered emphasized that the NDC is the only nonodontogenic cyst to be included in the 2017 edition [129]. The WHO's 1992 edition had specified the originating tissue for the NDC as "the epithelial residues in the nasopalatine (incisive) canal" [230]. This epithelium is most frequently stratified squamous, with half of cases containing areas of respiratory epithelium. The NDC accounts for 5% of all jaw cysts and 80% of all nonodontogenic cysts [229]. It presents most frequently in the 30–60-year age range and three times more frequently in males. The radiological presentation is almost always diagnostic [229]. The NDC is a well-defined, "often corticated radiolucency in the midline of the hard palate between the roots of the incisors, which may be displaced but are vital. The lamina dura of the teeth is intact" [229]. Figure 9.63 displays an NDC as seen on conventional radiography. Generally, symptom-free radiolucencies less than 6 mm should be considered as normal nasopalatine ducts [229].

NDCs were found twice as frequently in males; there was no difference between White and Black South Africans in this regard [231].

The most common symptom is swelling [231], which may be both palatal and buccal. Symptoms are generally not severe and are often ignored by the patient for several years prior to presentation [231]. Nevertheless, Nortjé and Farman reported that the symptoms may be severe in Black South Africans [232]. Hertzamu et al. reported that all cysts over 3 cm were in Black South Africans [233]. Tooth displacement was observed often [231].

Radiographically, a diagnosis of NDC may be considered if the width of the canal exceeds 4.79 mm (standard deviation 1.33 mm) and if the anterior–posterior length exceeds 10.19 mm (standard deviation 3.34 mm) [231].

Figure 20.15 is normal, whereas Figures 9.64 and 20.17a are likely to represent NDCs at the earliest stages. Figures 9.65 and 9.66 exhibit NDCs.

The NPC, if unnoticed, can achieve substantial dimensions, expanding into the nasal cavity to lie directly under the nasal mucosa (Figure 9.66), thus making their enucleation difficult. Although the adjacent teeth are usually vital, these so-called fissural cysts may become secondarily infected.

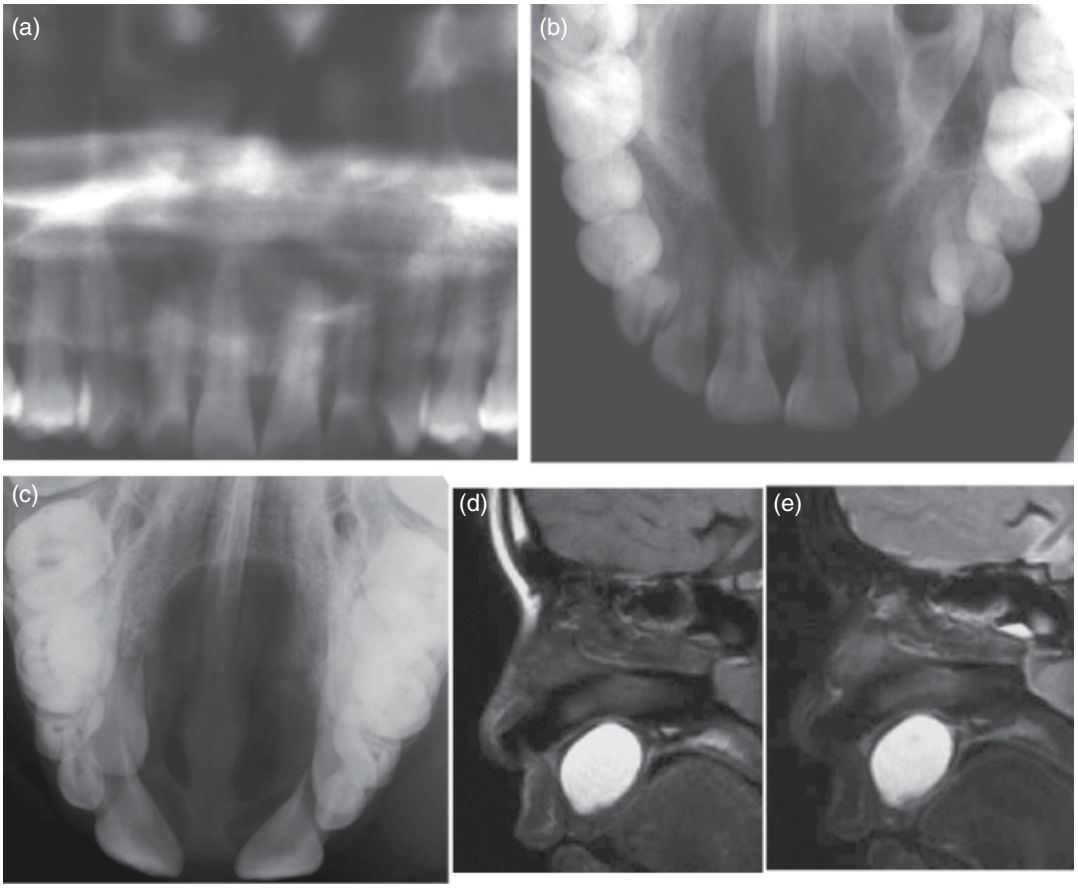


Figure 9.63 (a–c) Conventional radiographs of a nasopalatine duct cyst (NDC). (a) Panoramic radiograph reveals a well-defined radiolucency in the anterior maxilla. (b and c) Anterior standard occlusal projections revealed that there was a well-defined radiolucency occupying the midline of the hard palate. If adjacent teeth were carious or restored, pulp-vitality testing may be required to distinguish between an NDC and a periapical radiolucency of inflammatory origin. Sagittal magnetic resonance imaging (MRI) exhibits the NDC with a homogeneous high signal intensity on both T1-weighted (d) and T2-weighted (e) MRI. Source: (c–e) Reproduced with permission from Hisatomi, M., Asaumi, J., Konouchi, H., et al. (2003). MR imaging of epithelial cysts of the oral and maxillofacial region. *Eur. J. Radiol.* 48: 178–182.

9.24 Lingual Bone Defect

The *lingual bone defect* (LBD) was formerly known as "Stafne's bone cyst." The vast majority of LBD present, on a panoramic radiograph, as well-defined ovoid radiolucencies in the basal process of the posterior mandible, in relation to the submandibular fossa, below or substantially below the mandibular canal (Figure 9.67). The LBD develops in middle age. Figure 9.68 displays two panoramic radiographs of the same patient separated by a few years. What is seen is not a true cyst, but a concavity within the mandible arising from the lingual

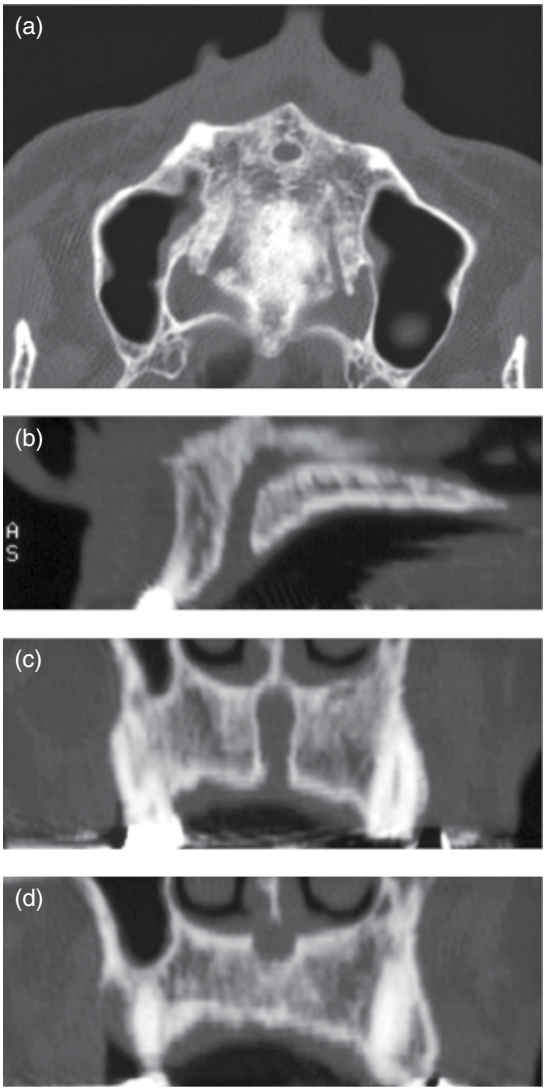


Figure 9.64 Computed tomography (CT) of a widened nasopalatine canal. (a) Axial CT (bone window) displaying the widened canal. (b) Sagittal CT (bone window). (c and d) Coronal CT (bone window); (d) is more posterior to (c).

surface. The LBD not only excavates out the body of the mandible, but may also erode and even displace the buccal cortex (Figures 9.69–9.71). Although such excavation must weaken the mandible, so far not a case of an LBD directly causing a fracture has been reported. A reason for this absence could be that, although overwhelmingly reported in males, LBDs rarely occur earlier than the fifth decade of life, when participation in contact sports and other risk-taking behavior is

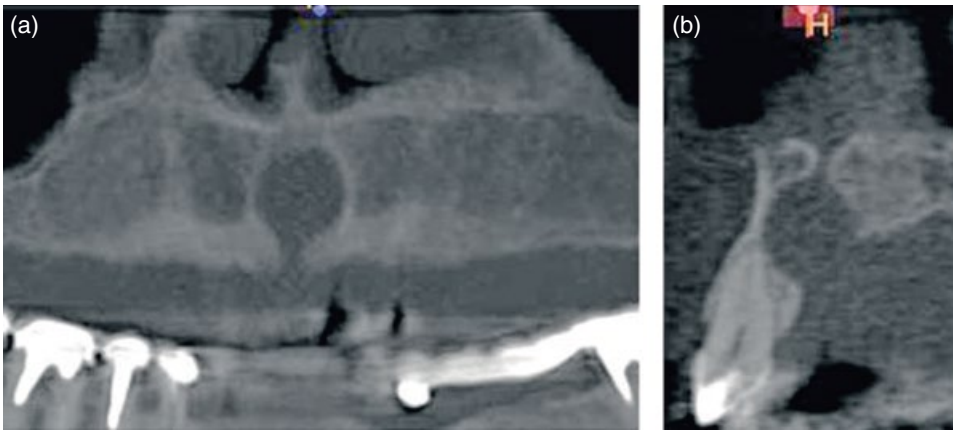


Figure 9.65 (a) Panoramic and (b) sagittal reconstructions of cone-beam computed tomography of a nasopalatine duct cyst. It presents as a spherical unilocular radiolucency. The panoramic reconstruction displays the cyst's continuity with the oral surface of the palate, whereas the sagittal reconstructions displays its continuity with the nasal surface.

less likely. Nevertheless, the diagnostic work-up of such lesions should now include CBCT (Figure 9.72). Kao et al. reported a fracture following an extraction of a mandibular third molar six weeks earlier in a 54-year-old male [234]. The panoramic radiograph taken to investigate the fracture revealed a radiolucency. After the fracture healed, a CT and surgical exploration revealed that this was an LBD [234].

Philipsen et al. have defined four subtypes of LBD [235]. The "lingual posterior" subtype constitutes the majority, and occurs in 0.10–0.48% of panoramic radiographs. Its radiographic visibility requires a reduction in the mineralized tissue by 12% [235].

The second most frequent subtype, the "lingual anterior," lies lingual to the incisors, canines, and premolars. As it also lies above the mylohyoid muscle, it may appear superimposed upon the apices of these teeth. In this position its differential diagnosis includes a simple bone cyst and periapical radiolucency. As the border of this radiolucency may be less distinct than those of the lingual posterior subtype [235], it may be less obvious.

The remaining two subtypes are the buccal ramus and the lingual ramus, sited just below the neck of the condyle.

The occurrence of LBDs later in life suggests that the process that creates them is not merely the passive development of the mandible around a submandibular gland, as was once thought, but is instead more active (Figure 9.68) [235]. Philipsen et al. discuss the possible etiologies, clearly favoring the "glandular" hypothesis [235]. This suggests the presence of a hyperplastic or hypertrophic lobe of the submandibular (lingual posterior), sublingual (lingual anterior), and parotid (lingual or buccal ramus) glands, putting pressure on the adjacent bone and causing focal bone atrophy or resorption [235].

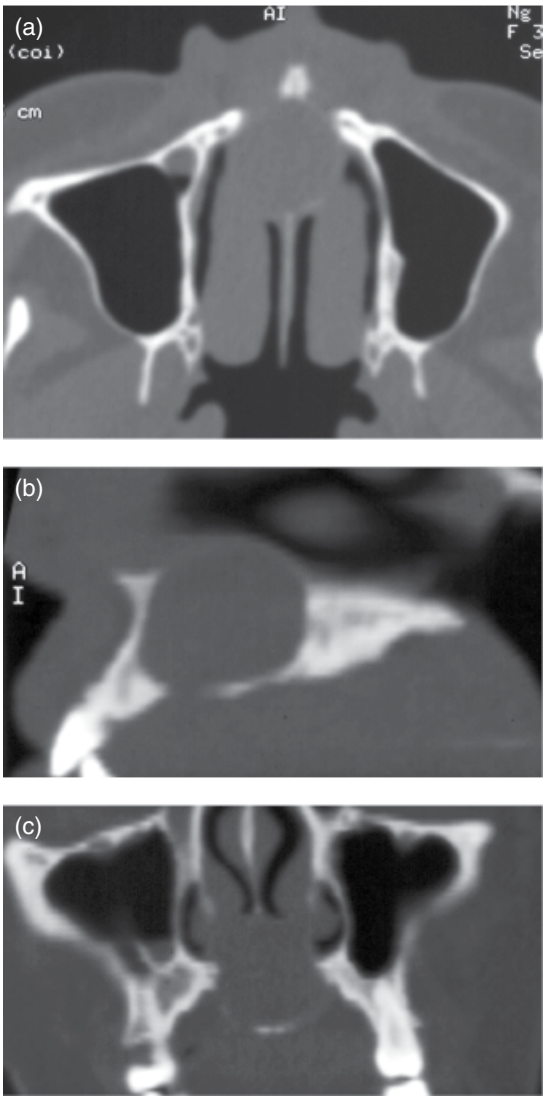


Figure 9.66 Computed tomography (CT) of a large nasopalatinal duct cyst. (a) Axial CT (bone window), above the floor of the nasal cavity, displaying round shape and thin cortex in places. (b) Sagittal CT (bone window) showing upward displacement of the nasal floor. (c) Coronal CT (bone window), at the level of the premolars, exhibiting substantial expansion up into the nasal cavity and downward into the oral cavity.

Among their 32 cases, Shimizu et al. reported two patterns on panoramic radiographs of what appears to be, from their images, the lingual posterior subtype [236]. These are "Stafne type" (Figure 9.69) or "cyst type" (Figure 9.70); the former shows a connection to the lower border of the mandible, whereas the latter does not [236]. Shimizu et al.'s CT study revealed that the cyst type included only fat and the Stafne type

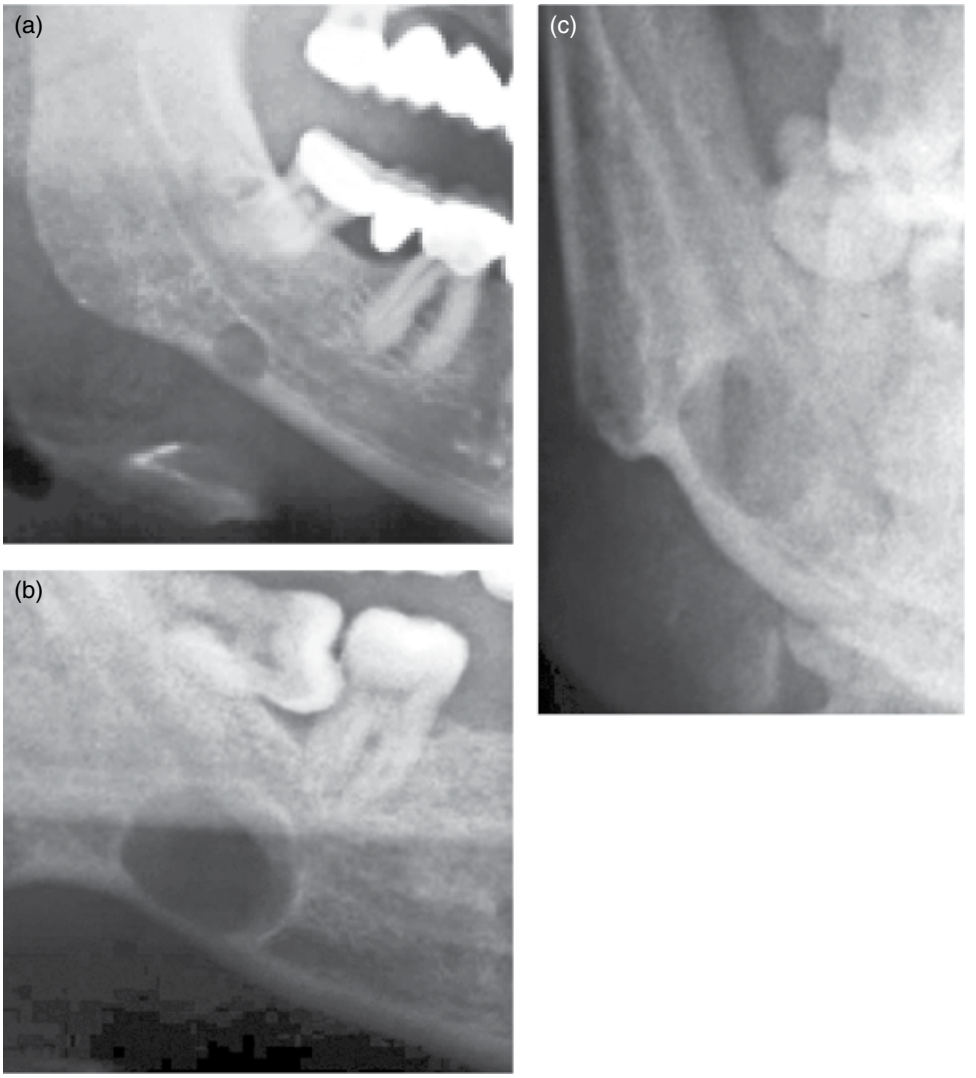


Figure 9.67 Conventional radiography of lingual bone defects (LBD), formerly called Stafne bone cysts. (a) Panoramic radiograph exhibiting a classic LBD. This is a round or oval-shaped, well-defined radiolucency, lying anterior to the gonial notch, between the lower border of the mandible and mandibular canal. (b) Panoramic radiograph of another case showing extension above the mandibular canal. (c) Posterioanterior projection of the mandible of the case in (b).

contained other soft tissues. The submandibular glands were more anteriorly positioned in contrast to their contralateral controls. In addition, the glands associated with the Stafne type were more laterally placed [236].

Smith et al. reported a case of the bilateral lingual anterior subtype [237]. The use of MRI confirmed the presence of sublingual glands within the defects, obviating the need for a biopsy [237].

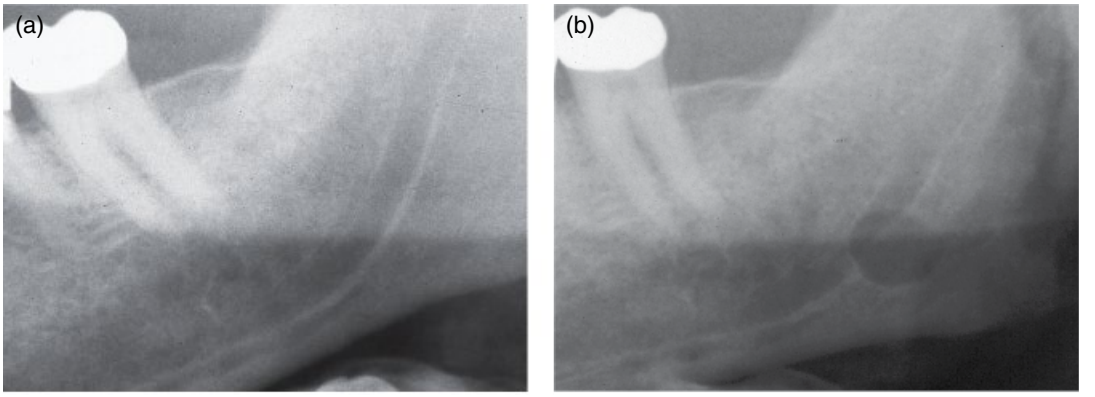


Figure 9.68 Panoramic radiographs taken of the same area of a lingual bone defect (LBD) separated by a few years. (a) A well-defined radiolucency partly superimposed upon the inferior aspect of the inferior dental canal and the lower border of the mandible. A panoramic radiograph taken earlier (b) does not display it at all. LBDs generally appear in later life. Although related to the contact between the submandibular gland and the mandible, the mechanism is not yet fully understood.

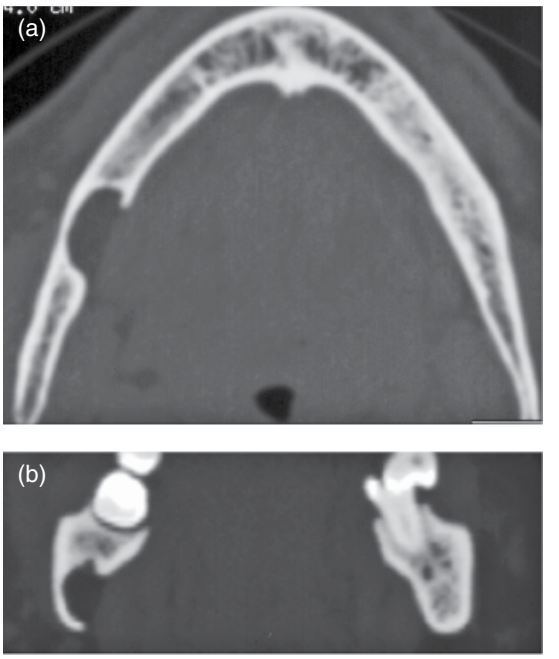


Figure 9.69 Computed tomography (CT) of a lingual bone defect (LBD) in the posterior sextant of an edentulous mandible. (a) Axial CT displays the LBD reaching the inside of the buccal cortex and extending mesially into the bone marrow, past the most anterior aspect of the lingual cortical defect. (b) Coronal CT reveals that it extends fully to the lower border of the mandible and extends upward past its most superior aspect of the lingual cortical defect.

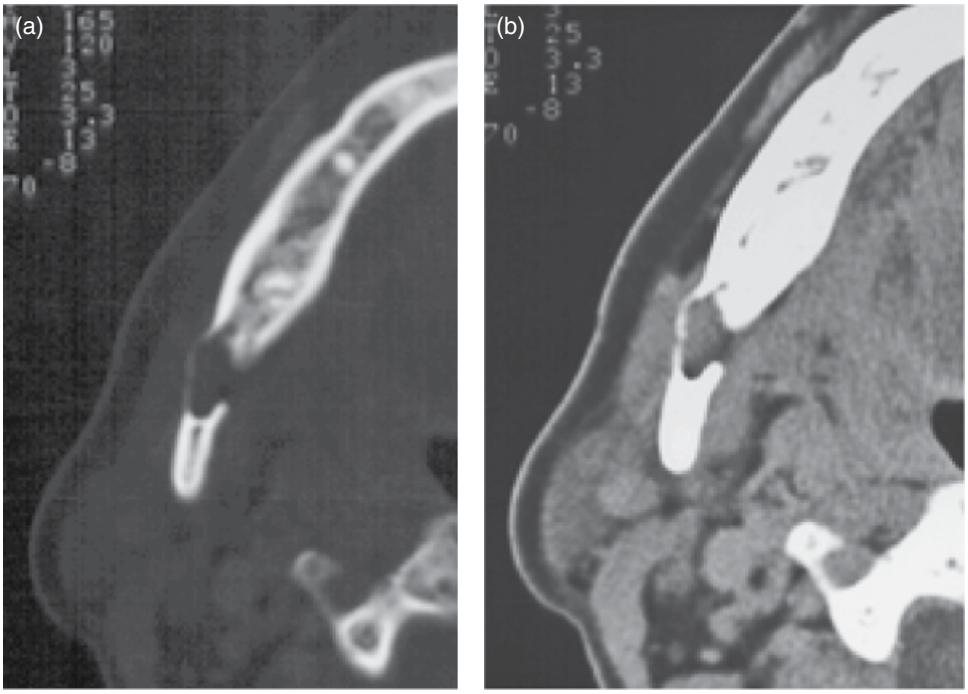


Figure 9.70 Axial computed tomography displaying a lingual bone defect. The bone window (a) depicts the lingual osteum of the defect as being narrower than the mesiodistal extent of the defect within the mandible. The intraosseous defect is substantially lined by a cortex. The buccal cortex is eroded and slightly expanded. The soft-tissue window (b) reveals soft-tissue density. Note: The radiolucent band separating the soft tissue with the defect from that lingual to it is due to beam hardening caused by the adjacent lingual cortex bordering the defect.

9.25 Concluding Remarks with Particular Regard to the Imaging of Radiolucencies

Although the diagnosis and definitive treatment of the majority of lesions, especially periapical lesions (including PRIOs and idiopathic osteosclerosis; see Chapter 10) and DCs arising in the bones of the jaws, are achieved by a thorough clinical examination and appropriate conventional radiography alone, further imaging is required for those lesions which are likely to be neoplastic.

While large KCOTs affecting the posterior mandible recently were accurately diagnosed solely by a clinical examination and their presentation on a panoramic radiograph [108], this should not be extended to other suspected neoplasms. At least a CBCT should be performed prior to biopsy of an intraosseous lesion, since, as displayed in the CT in Figure 1.3, such biopsies distort subsequent imaging. This biopsy can either confirm the working or provisional diagnosis or indicate an



Figure 9.71 Panoramic radiography of a lingual bone defect (LBD) separated by a few years. Other than the extraction of the third molar tooth, there has been little change. The axial, panoramic, and transaxial reconstructions of the cone-beam computed tomography display a lingual bone defect. The axial reconstruction displays the lingual osteum of the LBD. The LBD has reached the buccal bone. The panoramic reconstruction exhibits erosion of the inferior cortex of the mandibular canal by the LBD. The transaxial reconstruction through the healing third molar socket reveals also that the cortex on the mandibular canal is eroded. Source: Reproduced with permission from MacDonald, D.S. (2016). Lesions of the jaws presenting as radiolucencies on cone-beam computed tomography. *Clin. Radiol.* 71: 972–985.

entirely different lesion. Recently, a suspected solid ameloblastoma, which if confirmed would have been resected, was biopsied and found to be a "brown tumor," which, after appropriate treatment of the underlying tertiary hyperparathyroidism and chronic renal failure, resulted in the lesion's spontaneous and complete regression without surgery [86]. This case also highlighted the importance of detection of those at risk of carotid artery atheroma and the role the dentist can play in identifying such at-risk patients. This topic is fully discussed in Chapter 13.

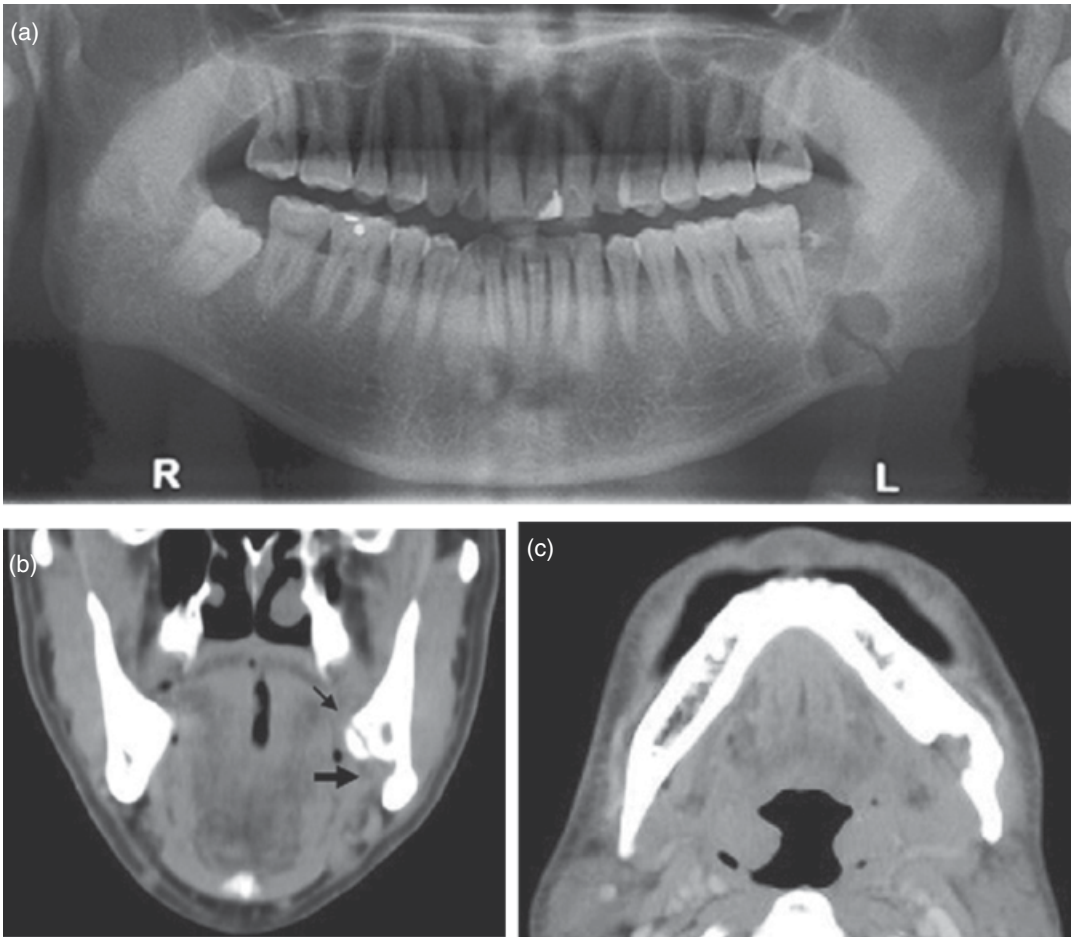


Figure 9.72 A case of a pathological fracture through a lingual bone defect (LBD) occurring 6 weeks after the extraction of the adjacent third molar. (a) is the panoramic radiograph taken after the fracture. The fracture line runs from the base of the socket to the lower border. (b) and (c) are the coronal and axial computed tomographic sections, respectively. They display the LBD reaching laterally to the mandibular canal. Upon subsequent surgical exploration the neurovascular bundle was visible within the mandibular canal. Source: Reproduced with permission from Kao YH, Huang IY, Chen CM, Wu CW, Hsu KJ, Chen CM. (2010). Late mandibular fracture after lower third molar extraction in a patient with Stafne bone cavity: a case report. *J Oral Maxillofac Surg*. 68:1698–700.

References

1. MacDonald, D.S. (2016). Lesions of the jaws presenting as radiolucencies on cone-beam computed tomography. *Clin. Radiol.* 71: 972–985.
2. Jones, A.V. and Franklin, C.D. (2006). An analysis of oral and maxillofacial pathology found in children over a 30-year period. *Int. J. Paediatr. Dent.* 16: 19–30.
3. Jones, A.V. and Franklin, C.D. (2006). An analysis of oral and maxillofacial pathology

found in adults over a 30-year period. *J. Oral Pathol. Med.* 35: 392–401.
4. Franklin, C.D. and Jones, A.V. (2006). A survey of oral and maxillofacial pathology specimens submitted by general dental practitioners over a 30-year period. *Br. Dent. J.* 200: 447–450; discussion p. 443.
5. Dagenais, M., MacDonald, D., Baron, M. et al. (2015). The Canadian Systemic Sclerosis Oral Health Study IV: oral radiographic manifestations in systemic sclerosis compared with the general population. *Oral Surg. Oral Med. Oral Pathol. Oral Radiol.* 120: 104–111.
6. Baron, M., Hudson, M., Dagenais, M. et al. (2016). Relationship between disease characteristics and oral radiologic findings in systemic sclerosis: results from a Canadian oral health study. *Arthritis Care Res. (Hoboken)* 68: 673–680.
7. Perschbacher, S.E., Perschbacher, K.A., Pharoah, M.J. et al. (2010). Gorham's disease of the maxilla: a case report. *Dentomaxillofac. Radiol.* 39: 119–123.
8. Gondivkar, S.M. and Gadbail, A.R. (2010). Gorham-Stout syndrome: a rare clinical entity and review of literature. *Oral Surg. Oral Med. Oral Pathol. Oral Radiol. Endod.* 109: e41–e48.
9. Kim, M.K., Hong, J.R., Kim, S.G., and Lee, S.K. (2015). Fatal progression of Gorham disease: a case report and review of the literature. *J. Oral Maxillofac. Surg.* 73: 2352–2360.
10. Jundt, G. (2005). Cherubism. In: *WHO Classification of Tumours, Pathology and Genetics of Tumours of the Head and Neck* (ed. L. Barnes, J. Eveson, P. Reichert and D. Sidransky), 325. Lyon: International Agency for Research on Cancer (IARC).
11. Raubenheimer, E. and Jordan, R.C. (2017). Cherubism. In: *WHO Classification of Head and Neck Tumours* (ed. A.K. El-Naggar, J.K.C. Chan, J.R. Grandis, et al.), 256–257. Lyon: International Agency for Research on Cancer (IARC).
12. Prescott, T., Redfors, M., Rustad, C.F. et al. (2013). Characterization of a Norwegian cherubism cohort; molecular genetic findings, oral manifestations and quality of life. *Eur. J. Med. Genet.* 56: 131–137.
13. Von Wowern, N. (2000). Cherubism: a 36-year long-term follow-up of 2 generations in different families and review of the literature. *Oral Surg. Oral Med. Oral Pathol. Oral Radiol. Endod.* 90: 765–772.
14. Meng, X.M., Yu, S.F., and Yu, G.Y. (2005). Clinic pathologic study of 24 cases of cherubism. *Int. J. Oral Maxillofac. Surg.* 34: 350–356.
15. Roginsky, V.V., Ivanov, A.L., Ovtchinnikov, I.A., and Khonsari, R.H. (2009). Familial cherubism: the experience of the Moscow Central Institute for Stomatology and Maxillo-Facial Surgery. *Int. J. Oral Maxillofac. Surg.* 38: 218–223.
16. Redfors, M., Jensen, J.L., Storhaug, K. et al. (2013). Cherubism: panoramic and CT features in adults. *Dentomaxillofac. Radiol.* 42: 20130034.
17. MacDonald-Jankowski, D.S., Yeung, R.W., Li, T., and Lee, K.M. (2004). Computed tomography of odontogenic myxoma. *Clin. Radiol.* 59: 281–287.
18. Beaman, F.D., Bancroft, L.W., Peterson, J.J. et al. (2004). Imaging characteristics of cherubism. *AJR Am. J. Roentgenol.* 182: 1051–1054.
19. Pontes, F.S., Ferreira, A.C., Kato, A.M. et al. (2007). Aggressive case of cherubism: 17-year follow-up. *Int. J. Pediatr. Otorhinolaryngol.* 71: 831–835.
20. Carroll, A.L. and Sullivan, T.J. (2001). Orbital involvement in cherubism. *Clin. Exp. Ophthalmol.* 29: 38–40.
21. Ozkan, Y., Varol, A., Turker, N. et al. (2003). Clinical and radiological evaluation of cherubism: a sporadic case report and review of the literature. *Int. J. Pediatr. Otorhinolaryngol.* 67: 1005–1012.
22. Elfahsi, A., Oujilal, A., Lahlou, M. et al. (2007). An ophthalmological complication of cherubism. *Rev. Stomatol. Chir. Maxillofac.* 108: 58–60. (French).
23. Yoo, S.H., Pineles, S.L., Jarrahy, R., and Velez, F.G. (2015). Ophthalmic manifestations of cherubism. *J. AAPOS* 19 (1): 70–72.
24. Ahmadi, A.J., Pirinjian, G.E., and Sires, B.S. (2003). Optic neuropathy and macular chorioretinal folds caused by orbital cherubism. *Arch. Ophthalmol.* 121: 570–573.
25. Von Wowern, N., Hjørting-Hansen, E., and Edeling, C.J. (1978). Bone scintigraphy of benign jaw lesions. *Int. J. Oral Surg.* 7: 528–533.
26. Reichenberger, E.J., Levine, M.A., Olsen, B.R. et al. (2012). The role of SH3BP2 in the

pathophysiology of cherubism. *Orphanet J. Rare Dis.* 7 (Suppl 1): S5. https://doi.org/10.1186/1750-1172-7-S1-S5.
27. Carapito, R., Paul, N., Untrau, M. et al. (2014). A new mutation in the C-SH2 domain of PTPN11 causes Noonan syndrome with multiple giant cell lesions. *J. Hum. Genet.* 59: 57–59.
28. MacDonald, D.S. (2015). A systematic review of the literature of nevoid basal cell carcinoma syndrome affecting east Asians and north Europeans. *Oral Surg. Oral Med. Oral Pathol. Oral Radiol.* 120: 396–407.
29. Bree, A.F., Shah, M.R., and BCNS Colloquium Group (2011). Consensus statement from the first international colloquium on basal cell nevus syndrome (BCNS). *Am. J. Med. Genet. A* 155A: 2091–2097.
30. MacDonald, D.S., Li, T.K., and Goto, T.K. (2015). A consecutive case series of nevoid basal cell carcinoma syndrome affecting the Hong Kong Chinese. *Oral Surg. Oral Med. Oral Pathol. Oral Radiol.* 120: 408–415.
31. Gupta, S.R., Jaetli, V., Mohanty, S. et al. (2012). Nevoid basal cell carcinoma syndrome in Indian patients: a clinical and radiological study of 6 cases and review of literature. *Oral Surg. Oral Med. Oral Pathol. Oral Radiol.* 113: 99–110.
32. MacDonald-Jankowski, D.S. and Li, T.K. (2010). Keratocystic odontogenic tumour in a Hong Kong community: the clinical and radiological features. *Dentomaxillofac. Radiol.* 39: 167–175.
33. MacDonald-Jankowski, D.S. (2011). Keratocystic odontogenic tumour: systematic review. *Dentomaxillofac. Radiol.* 40: 1–23.
34. Mamtani, R., Yang, Y.X., Scott, F.I. et al. (2016). Association between itraconazole, a hedgehog-inhibitor, and bladder cancer. *J. Urol.* 196: 343–348.
35. Javid, B. and Said-Al-Naief, N. (2015). Craniofacial manifestations of β-thalassemia major. *Oral Surg. Oral Med. Oral Pathol. Oral Radiol.* 119: e33–e40.
36. Sayani, F.A. and Kwiatkowski, J.L. (2015). Increasing prevalence of thalassemia in America: implications for primary care. *Ann. Med.* 47: 592–604.
37. Roberts, A.S., Shetty, A.S., Mellnick, V.M. et al. (2016). Extramedullary haematopoiesis: radiological imaging features. *Clin. Radiol.* 71: 807–814.
38. Vichinsky, E. (2016). Non-transfusion-dependent thalassemia and thalassemia intermedia: epidemiology, complications, and management. *Curr. Med. Res. Opin.* 32: 191–204.
39. Hazza'a, A.M. and Al-Jamal, G. (2006). Dental development in subjects with thalassemia major. *J. Contemp. Dent. Pract.* 7: 63–70.
40. Hazza'a, A.M. and Al-Jamal, G. (2006). Radiographic features of the jaws and teeth in thalassaemia major. *Dentomaxillofac. Radiol.* 35: 283–388.
41. Tyler, P.A., Madani, G., Chaudhuri, R. et al. (2006). The radiological appearances of thalassaemia. *Clin. Radiol.* 61: 40–52.70.
42. Zanella, S., Garani, M.C., and Borgna-Pignatti, C. (2016). Malignancies and thalassemia: a review of the literature. *Ann. N. Y. Acad. Sci.* 1368: 140–148.
43. Pithon, M.M., Palmeira, L.M., Barbosa, A.A. et al. (2014). Craniofacial features of patients with sickle cell anemia and sickle cell trait. *Angle Orthod.* 84: 825–829.
44. Demirbaş, A.K., Ergün, S., Güneri, P. et al. (2008). Mandibular bone changes in sickle cell anemia: fractal analysis. *Oral Surg. Oral Med. Oral Pathol. Oral Radiol. Endod.* 106: e41–e48.
45. Steven, A., Raghavan, P., Rath, T.J., and Gandhi, D. (2016). Neurologic and head and neck manifestations of sickle cell disease. *Hematol. Oncol. Clin. N. Am.* 30: 779–798.
46. Javed, F., Correa, F.O., Nooh, N. et al. (2013). Orofacial manifestations in patients with sickle cell disease. *Am. J. Med. Sci.* 345: 234–237.
47. Souza, S., de Carvalho, H., Costa, C., and Thomaz, E. (2018). Association of sickle cell haemoglobinopathies with dental and jaw bone abnormalities. *Oral Dis.* 24: 393–403.
48. de Carvalho, H.L.C.C., Rolim, J.Y.S., Thomaz, É.B.A.F., and Souza, S.F.C. (2017). Are dental and jaw changes more prevalent in a Brazilian population with sickle cell anemia? *Oral Surg. Oral Med. Oral Pathol. Oral Radiol.* 124: 76–84.
49. Neves, F.S., Passos, C.P., Oliveira-Santos, C. et al. (2012). Correlation between maxillofacial radiographic features and systemic severity as sickle cell disease severity predictor. *Clin. Oral Investig.* 16: 827–833.
50. MacDonald, D. and Lim, S. (2018). Extranodal lymphoma arising within the maxillary alveolus;

a systematic review. *Oral Radiol.* 34: 113–126. https://doi.org/10.1007/s11282-017-0309-5.
51. Roodman, G.D. (2008). Skeletal imaging and management of bone disease. *Hematol. Am. Soc. Hematol. Educ. Program* 2008: 313–319. https://doi.org/10.1182/asheducation-2008.1.313.
52. Lae, M.E., Vencio, E.F., Inwards, C.Y. et al. (2003). Myeloma of the jaw bones: a clinicopathologic study of 33 cases. *Head Neck* 25: 373–381.
53. Dutoit, J.C. and Verstraete, K.L. (2017). Whole-body MRI, dynamic contrast-enhanced MRI, and diffusion-weighted imaging for the staging of multiple myeloma. *Skeletal Radiol.* 46: 733–750.
54. Witt, C., Borges, A.C., Klein, K., and Neumann, H.J. (1997). Radiographic manifestations of multiple myeloma in the mandible: a retrospective study of 77 patients. *J. Oral Maxillofac. Surg.* 55: 450–453; discussion 454–455.
55. Pisano, J.J., Coupland, R., Chen, S.Y., and Miller, A.S. (1997). Plasmacytoma of the oral cavity and jaws: a clinicopathologic study of 13 cases. *Oral Surg. Oral Med. Oral Pathol. Oral Radiol. Endod.* 83: 265–271.
56. Lubek, J.E., Shihabi, A., Murphy, L.A., and Berman, J.N. (2015). Hematopoietic neck lesions. *Atlas Oral Maxillofac. Surg. Clin. N. Am.* 23: 31–37.
57. Swerdlow, S.H., Campo, E., Pileri, S.A. et al. (2016). The 2016 revision of the World Health Organization classification of lymphoid neoplasms. *Blood* 127: 2375–2390.
58. Paes, F.M., Kalkanis, D.G., Sideras, P.A., and Serafini, A.N. (2010). FDG PET/CT of extranodal involvement in non-Hodgkin lymphoma and Hodgkin disease. *Radiographics* 30: 269–291.
59. Epstein, J.B., Epstein, J.D., Le, N.D., and Gorsky, M. (2001). Characteristics of oral and paraoral malignant lymphoma: a population-based review of 361 cases. *Oral Surg. Oral Med. Oral Pathol. Oral Radiol. Endod.* 92: 519–525.
60. Eisenbud, L., Sciubba, J., Mir, R., and Sachs, S.A. (1984). Oral presentations in non-Hodgkin's lymphoma: a review of thirty-one cases. Part II. Fourteen cases arising in bone. *Oral Surg. Oral Med. Oral Pathol.* 57: 272–280.
61. MacDonald, D.S., Li, T., Leung, S.F., and Curtin, J. (2017). Extranodal lymphoma arising within the maxillary alveolus: a case report. *Oral Surg. Oral Med. Oral Pathol. Oral Radiol. Endod.* 124: e233–e238. https://doi.org/10.1016/j.oooo.2017.04.015.
62. Tejani, N., Cooper, A., Rezo, A. et al. (2014). Numb chin syndrome: a case series of a clinical syndrome associated with malignancy. *J. Med. Imaging Radiat. Oncol.* 58: 700–705.
63. Kato, H., Kanematsu, M., Watanabe, H. et al. (2015). Differentiation of extranodal non-Hodgkins lymphoma from squamous cell carcinoma of the maxillary sinus: a multimodality imaging approach. *Springerplus* 4: 228. https://doi.org/10.1186/s40064-015-0974.
64. Condon, L.M., Cederberg, L.E., Rabinovitch, M.D. et al. (2014). Age-specific prevalence of Epstein-Barr virus infection among Minnesota children: effects of race/ethnicity and family environment. *Clin. Infect. Dis.* 59: 501–508.
65. Peh, S.C. (2001). Host ethnicity influences non-Hodgkin's lymphoma subtype frequency and Epstein-Barr virus association rate: the experience of a multi-ethnic patient population in Malaysia. *Histopathology* 38: 458–465.
66. Aricò, M. (2016). Langerhans cell histiocytosis in children: from the bench to bedside for an updated therapy. *Br. J. Haematol.* 173: 663–670.
67. Lajolo, C., Campisi, G., Deli, G. et al. (2012). Langerhans's cell histiocytosis in old subjects: two rare case reports and review of the literature. *Gerodontology* 29: e1207–e1214.
68. Hicks, J. and Flaitz, C.M. (2005). Langerhans cell histiocytosis: current insights in a molecular age with emphasis on clinical oral and maxillofacial pathology practice. *Oral Surg. Oral Med. Oral Pathol. Oral Radiol. Endod.* 100: S42–S66.
69. Dagenais, M., Pharoah, M.J., and Sikorski, P.A. (1992). The radiographic characteristics of histiocytosis X. a study of 29 cases that involve the jaws. *Oral Surg. Oral Med. Oral Pathol.* 74: 230–236.
70. Devlin, H., Allen, P., Graham, J. et al. (2008). The role of the dental surgeon in detecting osteoporosis: the OSTEODENT study. *Br. Dent. J.* 204: E16; discussion 560–561.
71. Damilakis, J. and Vlasiadis, K. (2011). Have panoramic indices the power to identify

women with low BMD at the axial skeleton? *Phys. Med.* 27: 39–43.
72. WHO Scientific Group on the Assessment of Osteoporosis at Primary Care Level. Summary meeting report. Brussels, Belgium, 5–7 May 2004 http://www.who.int/chp/topics/Osteoporosis.pdf (Accessed April 6, 2018)
73. Anil, S., Preethanath, R.S., AlMoharib, H.S. et al. (2013). Impact of osteoporosis and its treatment on oral health. *Am. J. Med. Sci.* 346: 396–401.
74. Calciolari, E., Donos, N., Park, J.C. et al. (2015). Panoramic measures for oral bone mass in detecting osteoporosis: a systematic review and meta-analysis. *J. Dent. Res.* 94 (Suppl): 17S–27S.
75. Anil, G., Guglielmi, G., and Peh, W.C. (2010). Radiology of osteoporosis. *Radiol. Clin. N. Am.* 48: 497–518.
76. Jonasson, G. and Billhult, A. (2013). Mandibular bone structure, bone mineral density, and clinical variables as fracture predictors: a 15-year follow-up of female patients in a dental clinic. *Oral Surg. Oral Med. Oral Pathol. Oral Radiol.* 116: 362–368.
77. Geraets, W.G., Verheij, J.G., van der Stelt, P.F. et al. (2008). Selecting regions of interest on intraoral radiographs for the prediction of bone mineral density. *Dentomaxillofac. Radiol.* 37: 375–379.
78. Lindh, C., Horner, K., Jonasson, G. et al. (2008). The use of visual assessment of dental radiographs for identifying women at risk of having osteoporosis: the OSTEODENT project. *Oral Surg. Oral Med. Oral Pathol. Oral Radiol. Endod.* 106: 285–293.
79. López-López, J., Estrugo-Devesa, A., Jane-Salas, E. et al. (2011). Early diagnosis of osteoporosis by means of orthopantomograms and oral X-rays: a systematic review. *Med. Oral Patol. Oral Cir. Bucal* 16: e905–e913.
80. Centre for Metabolic Bone Diseases. FRAX® Fracture Risk Assessment Tool. University of Sheffield. 2018. https://www.shef.ac.uk/FRAX/tool.jsp (Accessed April 8, 2018)
81. McCloskey E. FRAX® Identifying people at high risk of fracture. WHO Fracture Risk Assessment Tool, a new clinical tool for informed treatment decisions. International Osteoporosis Foundation. 2009. https://www.iofbonehealth.org/sites/default/files/PDFs/WOD%20Reports/FRAX_report_09.pdf (Accessed April 8, 2018)
82. Otto, S., Pautke, C., Hafner, S. et al. (2013). Pathologic fractures in bisphosphonate-related osteonecrosis of the jaw – review of the literature and review of our own cases. *Craniomaxillofac. Trauma Reconstr.* 6: 147–154.
83. Hirshberg, A., Berger, R., Allon, I., and Kaplan, I. (2014). Metastatic tumors to the jaws and mouth. *Head Neck Pathol.* 8: 463–474.
84. Hirshberg, A., Shnaiderman-Shapiro, A., Kaplan, I., and Berger, R. (2008). Metastatic tumours to the oral cavity – pathogenesis and analysis of 673 cases. *Oral Oncol.* 44: 743–752.
85. Owosho, A.A., Xu, B., Kadempour, A. et al. (2016). Metastatic solid tumors to the jaw and oral soft tissue: a retrospective clinical analysis of 44 patients from a single institution. *J. Craniomaxillofac. Surg.* 44: 1047–1053.
86. MacDonald, D.S., Zhang, L., and Gu, Y. (2012). Calcification of the external carotid arteries and their branches. *Dentomaxillofac. Radiol.* 41: 356–361.
87. Chang, J.I., Som, P.M., and Lawson, W. (2007). Unique imaging findings in the facial bones of renal osteodystrophy. *AJNR Am. J. Neuroradiol.* 28: 608–609.
88. Stålberg, P. and Carling, T. (2009). Familial parathyroid tumors: diagnosis and management. *World J. Surg.* 33: 2234–2243.
89. DeLellis, R.A., Mazzaglia, P., and Mangray, S. (2008). Primary hyperparathyroidism: a current perspective. *Arch. Pathol. Lab. Med.* 132: 1251–1262.
90. Asaumi, J., Aiga, H., Hisatomi, M. et al. (2001). Advanced imaging in renal osteodystrophy of the oral and maxillofacial region. *Dentomaxillofac. Radiol.* 30: 59–62.
91. World Health Organization. Oral cancer. 2018. http://www.who.int/cancer/prevention/diagnosis-screening/oral-cancer/en. (Accessed April 8, 2018)
92. Odell, E.W., and others. (2017). Odontogenic carcinomas. In: *WHO Classification of Head and Neck Tumours* (ed. A.K. El-Naggar, J.K.C. Chan, J.R. Grandis, et al.), 206–211. Lyon: International Agency for Research on Cancer (IARC).
93. Eversole, L.R., Siar, C.H., and van der Waal, I. (1992). Primary intraosseous squamous cell carcinomas. In: *Clinical Outline of Oral Pathology: Diagnosis and Treatment* (ed. L.R. Eversole), 290–291. Philadelphia: Lea & Febiger.

94. Huang, J.W., Luo, H.Y., Li, O., and Li, T.J. (2009). Primary intraosseous squamous cell carcinoma of the jaws. Clinicopathological presentation and prognostic factors. *Arch. Pathol. Lab. Med.* 133: 1834–1840.
95. Faitaroni, L.A., Bueno, M.R., De Carvalhosa, A.A. et al. (2008). Ameloblastoma suggesting large apical periodontitis. *J. Endod.* 34: 216–219.
96. Cunha, E.M., Fernandes, A.V., Versiani, M.A., and Loyola, A.M. (2005). Unicystic ameloblastoma: a possible pitfall in periapical diagnosis. *Int. Endod. J.* 38: 334–340.
97. Lombardi, T., Bischof, M., Nedir, R. et al. (2006). Periapical central giant cell granuloma misdiagnosed as odontogenic cyst. *Int. Endod. J.* 39: 510–515.
98. Molven, O., Halse, A., Fristad, I., and MacDonald-Jankowski, D. (2002). Periapical changes following root-canal treatment observed 20–27 years postoperatively. *Int. Endod. J.* 35: 784–790.
99. Nair, P.N. (2006). On the causes of persistent apical periodontitis: a review. *Int. Endod. J.* 39: 249–281.
100. Rosenberg, P.A., Frisbie, J., Lee, J. et al. (2010). Evaluation of pathologists (histopathology) and radiologists (cone beam computed tomography) differentiating radicular cysts from granulomas. *J. Endod.* 36: 423–428.
101. Kramer, I.R.H., Pindborg, J.J., and Shear, M. (1992). *Histological Typing of Odontogenic Tumours*, 2e, 40–41. London: Springer-Verlag.
102. Gundappa, M., Ng, S.Y., and Whaites, E.J. (2006). Comparison of ultrasound, digital and conventional radiography in differentiating periapical lesions. *Dentomaxillofac. Radiol.* 35: 326–333.
103. Kramer, I.R.H., Pindborg, J.J., and Shear, M. (1992). *Histological Typing of Odontogenic Tumours*, 2e, 42. London: Springer-Verlag.
104. Pompura, J.R., Sándor, G.K., and Stoneman, D.W. (1997). The buccal bifurcation cyst: a prospective study of treatment outcomes in 44 sites. *Oral Surg. Oral Med. Oral Pathol. Oral Radiol. Endod.* 83: 215–221.
105. Iatrou, I., Theologie-Lygidakis, N., and Leventis, M. (2009). Intraosseous cystic lesions of the jaws in children: a retrospective analysis of 47 consecutive cases. *Oral Surg. Oral Med. Oral Pathol. Oral Radiol. Endod.* 107: 485–492.
106. Speight, P., Fantasia, J.E., and Neville, B.W. (2017). Lateral periodontal cyst and botryoid odontogenic cyst. In: *WHO Classification of Head and Neck Tumours* (ed. A.K. El-Naggar, J.K.C. Chan, J.R. Grandis, et al.), 236–237. Lyon: International Agency for Research on Cancer (IARC).
107. Kramer, I.R.H., Pindborg, J.J., and Shear, M. (1992). *Histological Typing of Odontogenic Tumours*, 2e, 37. London: Springer-Verlag.
108. MacDonald, D.S., Gu, Y., Poh, C., and Zhang, L. (2013). Can clinical and radiographic features predict recurrence in solitary keratocystic odontogenic tumours? *Oral Surg. Oral Med. Oral Pathol. Oral Radiol.* 115: 263–271.
109. Curran, A.E., Damm, D.D., and Drummond, J.F. (2002). Pathologically significant pericoronal lesions in adults: histopathologic evaluation. *J. Oral Maxillofac. Surg.* 60: 613–617; discussion 618. Comments by Slater and Flick in J Oral Maxillofac Surg 2003;61:149–150; author reply 150.
110. Ikeshima, A. and Tamura, Y. (2002). Differential diagnosis between dentigerous cyst and benign tumor with an embedded tooth. *J. Oral Sci.* 44: 13–17.
111. Speight, P., Fantasia, J.E., and Neville, B.W. (2017). Dentigerous cyst. In: *WHO Classification of Head and Neck Tumours* (ed. A.K. El-Naggar, J.K.C. Chan, J.R. Grandis, et al.), 234–235. Lyon: International Agency for Research on Cancer (IARC).
112. MacDonald-Jankowski, D.S. and Chan, K.C. (2005). Clinical presentation of dentigerous cysts: systematic review. *Asian J. Oral Maxillofac. Surg.* 15: 109–120.
113. Yildirim, G., Ataoğlu, H., Mihmanli, A. et al. (2008). Pathologic changes in soft tissues associated with asymptomatic impacted third molars. *Oral Surg. Oral Med. Oral Pathol. Oral Radiol. Endod.* 106: 14–18.
114. Shear, M. and Speight, P. (2006). *Cysts of the Oral and Maxillofacial Regions*, 4e, 59–79. Munksgaard: Blackwell.
115. Kaugars, G.E., Miller, M.E., and Abbey, L.M. (1989). Odontomas. *Oral Surg. Oral Med. Oral Pathol.* 67: 172–176.

116. Ioannidou, F., Mustafa, B., and Seferiadou-Mavropoulou, T. (1989). Odontogenic cysts of the jaws. A clinicostatistical study. *Stomatologia (Athenai)* 46: 81–90. (Greek).
117. Ledesma-Montes, C., Hernández-Guerrero, J.C., and Garcés-Ortíz, M. (2000). Clinicopathologic study of odontogenic cysts in a Mexican sample population. *Arch. Med. Res.* 31: 373–376.
118. Daley, T.D. and Wysocki, G.P. (1995). The small dentigerous cyst. A diagnostic dilemma. *Oral Surg. Oral Med. Oral Pathol. Oral Radiol. Endod.* 79: 77–81.
119. Struthers, P. and Shear, M. (1976). Root resorption by ameloblastomas and cysts of the jaws. *Int. J. Oral Surg.* 5: 128–132.
120. Wang, J.T. (1985). Unicystic ameloblastoma: a clinicopathological appraisal. *Taiwan Yi Xue Hui Za Zhi* 84: 1363–1370.
121. Shear, M. and Singh, S. (1978). Age-standardized incidence rates of ameloblastoma and dentigerous cyst on the Witwatersrand, South Africa. *Community Dent. Oral Epidemiol.* 6: 195–199.
122. Woodroffe, R.W., Abel, T.J., Fletcher, A. et al. (2014). Endoscopic transnasal resection of ameloblastoma with intracranial extension. *J. Clin. Neurosci.* 21: 855–859.
123. Odell, E.W. and Tilakaratne, W.M. (2017). Metastasizing ameloblastoma. In: *WHO Classification of Head and Neck Tumours* (ed. A.K. El-Naggar, J.K.C. Chan, J.R. Grandis, et al.), 218–219. Lyon: International Agency for Research on Cancer (IARC).
124. Pahl, S., Henn, W., Binger, T. et al. (2000). Malignant odontogenic myxoma of the maxilla: case with cytogenetic confirmation. *J. Laryngol. Otol.* 114: 533–535.
125. Vered, M., Muller, S., and Heikinheimo, K. (2017). Ameloblastoma. In: *WHO Classification of Head and Neck Tumours* (ed. A.K. El-Naggar, J.K.C. Chan, J.R. Grandis, et al.), 215–217. Lyon: International Agency for Research on Cancer (IARC).
126. MacDonald-Jankowski, D.S., Yeung, R., Lee, K.M., and Li, T.K. (2004). Ameloblastoma in the Hong Kong Chinese. Part 1: systematic review and clinical presentation. *Dentomaxillofac. Radiol.* 33: 71–82.
127. MacDonald-Jankowski, D.S., Yeung, R., Lee, K.M., and Li, T.K. (2004). Ameloblastoma in the Hong Kong Chinese. Part 2: systematic review and radiological presentation. *Dentomaxillofac. Radiol.* 33: 141–151.
128. Vered, M., Muller, S., and Heikinheimo, K. (2017). Ameloblastoma, unicystic type. In: *WHO Classification of Head and Neck Tumours* (ed. A.K. El-Naggar, J.K.C. Chan, J.R. Grandis, et al.), 217–218. Lyon: International Agency for Research on Cancer (IARC).
129. Wright, J.M. and Vered, M. (2017). Update from the 4th edition of the World Health Organization Classification of Head and Neck Tumours: odontogenic and maxillofacial bone tumors. *Head Neck Pathol.* 11: 68–77.
130. Gardner, D.G., Heikinheimo, K., Shear, M. et al. (2005). Ameloblastomas. In: *WHO Classification of Tumours, Pathology and Genetics of Tumours of the Head and Neck* (ed. L. Barnes, J. Eveson, P. Reichert and D. Sidransky), 296–300. Lyon: International Agency for Research on Cancer (IARC).
131. Liu, L., Zhang, X.Y., Hu, Y.J. et al. (2015). Clinical and pathological analysis of jaw ameloblastomas in 890 patients. *Shanghai Kou Qiang Yi Xue* 24: 338–340. [Chinese].
132. Philipsen, H.P., Reichart, P.A., and Takata, T. (2001). Desmoplastic ameloblastoma (including "hybrid" lesion of ameloblastoma). Biological profile based on 100 cases from the literature and own files. *Oral Oncol.* 37: 455–460.
133. Luo, H.Y. and Li, T.J. (2009). Odontogenic tumors: a study of 1309 cases in a Chinese population. *Oral Oncol.* 45: 706–711.
134. Arotiba, G.T., Ladeinde, A.L., Arotiba, J.T. et al. (2005). Ameloblastoma in Nigerian children and adolescents: a review of 79 cases. *J. Oral Maxillofac. Surg.* 63: 747–751.
135. Lee, P.K., Samman, N., and Ng, I.O. (2004). Unicystic ameloblastoma—use of Carnoy's solution after enucleation. *Int. J. Oral Maxillofac. Surg.* 33: 263–267.
136. Hong, J., Yun, P.Y., Chung, I.H. et al. (2007). Long-term follow up on recurrence of 305 ameloblastoma cases. *Int. J. Oral Maxillofac. Surg.* 36: 283–288.
137. Lau, S.L. and Samman, N. (2006). Recurrence related to treatment modalities of unicystic ameloblastoma: a systematic

review. *Int. J. Oral Maxillofac. Surg.* 35: 681–690.
138. Philipsen, H.P. and Reichart, P.A. (1998). Unicystic ameloblastoma. A review of 193 cases from the literature. *Oral Oncol.* 34: 317–325.
139. Zhang, L.L., Yang, R., Zhang, L. et al. (2010). Dentigerous cyst: a retrospective clinicopathological analysis of 2082 dentigerous cysts in British Columbia, Canada. *Int. J. Oral Maxillofac. Surg.* 39: 878–882.
140. Li, T.J., Wu, Y.T., Yu, S.F., and Yu, G.Y. (2000). Unicystic ameloblastoma: a clinicopathologic study of 33 Chinese patients. *Am. J. Surg. Pathol.* 24: 1385–1392.
141. MacDonald-Jankowski DS, Li TK. Computed tomography of ameloblastomas affecting a Hong Kong Chinese community. Part presented at the 17th International Congress of Dental and Maxillofacial Radiology in Amsterdam. June 28–July 2, 2009.
142. Asaumi, J., Matsuzaki, H., Hisatomi, M. et al. (2002). Application of dynamic MRI to differentiating odontogenic myxomas from ameloblastomas. *Eur. J. Radiol.* 43: 37–41.
143. Asaumi, J., Hisatomi, M., Yanagi, Y. et al. (2005). Assessment of ameloblastomas using MRI and dynamic contrast-enhanced MRI. *Eur. J. Radiol.* 56: 25–30.
144. Konouchi, H., Yanagi, Y., Hisatomi, M. et al. (2012). MR imaging diagnostic protocol for unilocular lesions of the jaw. *Jap. Dent. Sci. Rev.* 48: 81–91.
145. Luo, J., You, M., Wen, C. et al. (2014). Cone-beam CT features of ameloblastomas. *Hua Xi Kou Qiang Yi Xue Za Zhi* 32: 373–377. (Chinese).
146. Luo, J., You, M., Zheng, G., and Xu, L. (2014). Cone beam computed tomography signs of desmoplastic ameloblastoma: review of 7 cases. *Oral Surg. Oral Med. Oral Pathol. Oral Radiol.* 118: e126–e133.
147. MacDonald D, Li T, Lee J, Yeung A, Goto T. A profile of intravenous contrast use in computer tomographic investigations of ameloblastomas. International Congress of Dento-Maxillofacial Radiology, Bergen, June 2013. #P-049.
148. Rais, R. and El Mofty, S.K. (2018). Malignant transformation of a desmoplastic ameloblastoma to squamous cell carcinoma: a case report. *Head Neck Pathol.* https://doi.org/10.1007/s12105-018-0946-y.
149. Parmar, S., Al-Qamachi, L., and Aga, H. (2016). Ameloblastomas of the mandible and maxilla. *Curr. Opin. Otolaryngol. Head Neck Surg.* 24: 148–154.
150. Philipsen, H.P. (2005). Keratocystic odontogenic tumour. In: *WHO Classification of Tumours, Pathology and Genetics of Tumours of the Head and Neck* (ed. L. Barnes, J. Eveson, P. Reichert and D. Sidransky), 306–307. Lyon: International Agency for Research on Cancer (IARC).
151. MacDonald-Jankowski, D.S. (2010). Orthokeratinized odontogenic cyst; systematic review. *Dentomaxillofac. Radiol.* 39: 455–467.
152. MacDonald-Jankowski, D.S. and Li, T.K.L. (2010). Orthokeratinized odontogenic cyst in a Hong Kong community; the clinical and radiological presentations and the outcomes of treatment and follow-up. *Dentomaxillofac. Radiol.* 39: 240–245.
153. Philipsen, H.P. (1956). Om keratocyster (kolesteatom) i kaeberne. *Tandlaege Bladet* 60: 963–981.
154. Speight, P., Devilliers, P., Li, T.J. et al. (2017). Odontogenic keratocyst. In: *WHO Classification of Head and Neck Tumours* (ed. A.K. El-Naggar, J.K.C. Chan, J.R. Grandis, et al.), 229–230. Lyon: International Agency for Research on Cancer (IARC).
155. Cottom, H.E., Bshena, F.I., Speight, P.M. et al. (2012). Histopathological features that predict the recurrence of odontogenic keratocysts. *J. Oral Pathol. Med.* 41: 408–414.
156. Wright, J.M., Odell, E.W., Speight, P.M., and Takata, T. (2014). Odontogenic tumors, WHO 2005: where do we go from here? *Head Neck Pathol.* 8: 373–382.
157. Pogrel, M.A. and Jordan, R.C. (2004). Marsupialization as a definitive treatment for the odontogenic keratocyst. *J. Oral Maxillofac. Surg.* 62: 651–655; discussion and erratum in *J. Oral Maxillofac. Surg.* 2007;65:362–363.
158. Pogrel, M.A. (2005). Treatment of keratocysts: the case for decompression and marsupialization. *J. Oral Maxillofac. Surg.* 63: 1667–1673; Erratum in *J. Oral Maxillofac. Surg.* 2007;65:362–363.

159. Al-Moraissi, E.A., Pogrel, M.A., and Ellis, E. 3rd (2016). Enucleation with or without adjuvant therapy versus marsupialization with or without secondary enucleation in the treatment of keratocystic odontogenic tumors: a systematic review and meta-analysis. *J. Craniomaxillofac. Surg.* 44: 1395–1403.
160. Awni, S. and Conn, B. (2017). Decompression of keratocystic odontogenic tumors leading to increased fibrosis, but without any change in epithelial proliferation. *Oral Surg. Oral Med. Oral Pathol. Oral Radiol.* 123: 634–644.
161. Guo, Y.Y., Zhang, J.Y., Li, X.F. et al. (2013). PTCH1 gene mutations in keratocystic odontogenic tumors: a study of 43 Chinese patients and a systematic review. *PLoS One* 8: e77305. https://doi.org/10.1371/journal.pone.0077305.
162. Nagao, K., Fujii, K., Saito, K. et al. (2011). Entire PTCH1 deletion is a common event in point mutation-negative cases with nevoid basal cell carcinoma syndrome in Japan. *Clin. Genet.* 79: 196–198.
163. Naruse, T., Yamashita, K., Yanamoto, S. et al. (2017). Histopathological and immunohistochemical study in keratocystic odontogenic tumors: predictive factors of recurrence. *Oncol. Lett.* 13: 3487–3493.
164. Noy, D., Rachmiel, A., Zar, K. et al. (2017). Sporadic versus syndromic keratocysts – can we predict treatment outcome? A review of 102 cysts. *Oral Dis.* 23: 1058–1065.
165. Chrcanovic, B.R. and Gomez, R.S. (2017). Recurrence probability for keratocystic odontogenic tumors: an analysis of 6427 cases. *J. Craniomaxillofac. Surg.* 45: 244–251.
166. MacDonald, D., Angelopoulos, C., and Scarfe, W.C. (2018). Cone beam computed tomography and maxillofacial diagnosis. In: *Maxillofacial Cone Beam Computed Tomography* (ed. W. Scarfe and C. Angelopoulos), 469–551. Springer Nature.
167. Haring, J.I. and Van Dis, M.L. (1988). Odontogenic keratocysts: a clinical, radiographic, and histopathologic study. *Oral Surg. Oral Med. Oral Pathol.* 66: 145–153.
168. Shear, M. and Speight, P. (2006). *Cysts of the Oral and Maxillofacial Regions*, 4e, 6–58. Munksgaard: Blackwell.
169. Ecker, J., Horst, R.T., and Koslovsky, D. (2016). Current role of Carnoy's solution in treating keratocystic odontogenic tumors. *J. Oral Maxillofac. Surg.* 74: 278–282.
170. Min, J.H., Huh, K.H., Heo, M.S. et al. (2013). The relationship between radiological features and clinical manifestation and dental expenses of keratocystic odontogenic tumor. *Imaging Sci. Dent.* 43: 91–98.
171. Buchner, A. and Odell, E.W. (2005). Odontogenic myxoma/myxofibroma. In: *WHO Classification of Tumours, Pathology and Genetics of Tumours of the Head and Neck* (ed. L. Barnes, J. Eveson, P. Reichert and D. Sidransky), 316–317. Lyon: International Agency for Research on Cancer (IARC).
172. Odell, E.W. and Abibiyi, K. (2017). Odontogenic myxoma/myxofibroma. In: *WHO Classification of Head and Neck Tumours* (ed. A.K. El-Naggar, J.K.C. Chan, J.R. Grandis, et al.), 229–230. Lyon: International Agency for Research on Cancer (IARC).
173. MacDonald-Jankowski, D.S., Yeung, R., Lee, K.M., and Li, T.K. (2002). Odontogenic myxomas in the Hong Kong Chinese: clinico-radiological presentation and systematic review. *Dentomaxillofac. Radiol.* 31: 71–83.
174. Zhang, J., Wang, H., He, X. et al. (2007). Radiographic examination of 41 cases of odontogenic myxomas on the basis of conventional radiographs. *Dentomaxillofac. Radiol.* 36: 160–167.
175. Noffke, C.E., Raubenheimer, E.J., Chabikuli, N.J., and Bouckaert, M.M. (2007). Odontogenic myxoma: review of the literature and report of 30 cases from South Africa. *Oral Surg. Oral Med. Oral Pathol. Oral Radiol. Endod.* 104: 101–119.
176. Titinchi, F., Hassan, B.A., Morkel, J.A., and Nortje, C. (2016). Odontogenic myxoma: a clinicopathological study in a South African population. *J. Oral Pathol. Med.* 45: 599–604.
177. Kramer, I.R.H., Pindborg, J.J., and Shear, M. (1992). *Histological Typing of Odontogenic Tumours*, 2e, 23. London: Springer-Verlag.
178. Araki, M., Kameoka, S., Mastumoto, N., and Komiyama, K. (2007). Usefulness of cone beam computed tomography for odontogenic

myxoma. *Dentomaxillofac. Radiol.* 36: 423–427.
179. Koseki, T., Kobayashi, K., Hashimoto, K. et al. (2003). Computed tomography of odontogenic myxoma. *Dentomaxillofac. Radiol.* 32: 160–165.
180. Martínez-Mata, G., Mosqueda-Taylor, A., Carlos-Bregni, R. et al. (2008). Odontogenic myxoma: clinico-pathological, immunohistochemical and ultrastructural findings of a multicentric series. *Oral Oncol.* 44: 601–607.
181. Hisatomi, M., Asaumi, J., Konouchi, H. et al. (2003). Comparison of radiographic and MRI features of a root-diverging odontogenic myxoma, with discussion of the differential diagnosis of lesions likely to move roots. *Oral Dis.* 9: 152–157.
182. Simon, E.N., Merkx, M.A., Vuhahula, E. et al. (2004). Odontogenic myxoma: a clinicopathological study of 33 cases. *Int. J. Oral Maxillofac. Surg.* 33: 333–337.
183. Li, T.J., Sun, L.S., and Luo, H.Y. (2006). Odontogenic myxoma: a clinicopathologic study of 25 cases. *Arch. Pathol. Lab. Med.* 130: 1799–1806.
184. Gardner, D.G., Kessler, H.P., Morency, R., and Schaffner, D.L. (1988). The glandular odontogenic cyst: an apparent entity. *J. Oral Pathol.* 17: 359–366.
185. Kramer, I.R.H., Pindborg, J.J., and Shear, M. (1992). *Histological Typing of Odontogenic Tumours*, 2e, 38. London: Springer-Verlag.
186. Slootweg, P.J. (2009). Lesions of the jaws. *Histopathology* 54: 401–418.
187. Fowler, C.B., Brannon, R.B., Kessler, H.P. et al. (2011). Glandular odontogenic cyst: analysis of 46 cases with special emphasis on microscopic criteria for diagnosis. *Head Neck Pathol.* 5: 364–375.
188. MacDonald-Jankowski, D.S. (2010). Glandular odontogenic cyst: a systematic review. *Dentomaxillofac. Radiol.* 39: 127–139.
189. Speight, P., Fowler, C.B., and Kessler, H. (2017). Glandular odontogenic cyst. In: *WHO Classification of Head and Neck Tumours* (ed. A.K. El-Naggar, J.K.C. Chan, J.R. Grandis, et al.), 238–239. Lyon: International Agency for Research on Cancer (IARC).
190. Nagasaki, A., Ogawa, I., Sato, Y. et al. (2018). Central mucoepidermoid carcinoma arising from glandular odontogenic cyst confirmed by analysis of MAML2 rearrangement: a case report. *Pathol. Int.* 68: 31–35.
191. Wright, J.M. (1981). The odontogenic keratocyst: orthokeratinized variant. *Oral Surg. Oral Med. Oral Pathol.* 51: 609–618.
192. Kramer, I.R.H., Pindborg, J.J., and Shear, M. (1992). *Histological Typing of Odontogenic Tumours*, 2e, 35. London: Springer-Verlag.
193. Speight, P., Fantasia, J.E., and Neville, B.W. (2017). Orthokeratinized odontogenic cyst. In: *WHO Classification of Head and Neck Tumours* (ed. A.K. El-Naggar, J.K.C. Chan, J.R. Grandis, et al.), 241. Lyon: International Agency for Research on Cancer (IARC).
194. Dong, Q., Pan, S., Sun, L.S., and Li, T.J. (2010). Orthokeratinized odontogenic cyst: a clinicopathologic study of 61 cases. *Arch. Pathol. Lab. Med.* 134: 271–275.
195. Wright, J.M., Deviliers, P., and Hille, J. (2017). Squamous odontogenic tumor. In: *WHO Classification of Head and Neck Tumours* (ed. A.K. El-Naggar, J.K.C. Chan, J.R. Grandis, et al.), 219–229. Lyon: International Agency for Research on Cancer (IARC).
196. Mosqueda-Taylor, A., Pires, F.R., Aguirre-Urízar, J.M. et al. (2014). Primordial odontogenic tumour: clinicopathological analysis of six cases of a previously undescribed entity. *Histopathology* 65: 606–612.
197. Mosqueda-Taylor, A., Carlos-Bregni, R., Ramoa-Pires, F. et al. (2015). Reply: primordial odontogenic tumour: it is truly novel. *Histopathology* 66: 604–605.
198. Mosqueda-Taylor, A. and Neville, B.W. (2017). Primordial odontogenic tumor. In: *WHO Classification of Head and Neck Tumours* (ed. A.K. El-Naggar, J.K.C. Chan, J.R. Grandis, et al.), 223–224. Lyon: International Agency for Research on Cancer (IARC).
199. Raubenheimer, E. and Jordan, R.C. (2017). Central giant cell granuloma. In: *WHO Classification of Head and Neck Tumours* (ed. A.K. El-Naggar, J.K.C. Chan, J.R. Grandis, et al.), 256–257. Lyon: International Agency for Research on Cancer (IARC).
200. Raubenheimer, E. and Jordan, R.C. (2017). Peripheral giant cell granuloma. In: *WHO*

Classification of Head and Neck Tumours (ed. A.K. El-Naggar, J.K.C. Chan, J.R. Grandis, et al.), 257–258. Lyon: International Agency for Research on Cancer (IARC).

201. Stavropoulos, F. and Katz, J. (2002). Central giant cell granulomas: a systematic review of the radiographic characteristics with the addition of 20 new cases. *Dentomaxillofac. Radiol.* 31: 213–217. Review. Erratum in Dentomaxillofac Radiol 2002;31:394.
202. Muller, S. and Vered, M. (2017). Ameloblastic fibroma. In: *WHO Classification of Head and Neck Tumours* (ed. A.K. El-Naggar, C. JKC, J.R. Grandis, et al.), 222–223. Lyon: International Agency for Research on Cancer (IARC).
203. Slootweg, P.J. (2005). Ameloblastic fibroma. In: *WHO Classification of Tumours, Pathology and Genetics of Tumours of the Head and Neck* (ed. L. Barnes, J. Eveson, P. Reichert and D. Sidransky), 308. Lyon: International Agency for Research on Cancer (IARC).
204. Bredell, M., Rordorf, T., Kroiss, S. et al. (2018). Denosumab as a treatment alternative for central giant cell granuloma: a long-term retrospective cohort study. *J. Oral Maxillofac. Surg.* 76: 775–784.
205. Buchner, A. and Vered, M. (2013). Ameloblastic fibroma: a stage in the development of a hamartomatous odontoma or a true neoplasm? Critical analysis of 162 previously reported cases plus 10 new cases. *Oral Surg. Oral Med. Oral Pathol. Oral Radiol.* 116: 598–606.
206. Raubenheimer, E., van Heerden, W.F.P., and Wright, J.M. (2017). Simple bone cyst. In: *WHO Classification of Head and Neck Tumours* (ed. A.K. El-Naggar, J.K.C. Chan, J.R. Grandis, et al.), 259–260. Lyon: International Agency for Research on Cancer (IARC).
207. Jundt, G. (2005). Simple bone cyst. In: *WHO Classification of Tumours, Pathology and Genetics of Tumours of the Head and Neck* (ed. L. Barnes, J. Eveson, P. Reichert and D. Sidransky), 327. Lyon: International Agency for Research on Cancer (IARC).
208. Suei, Y., Taguchi, A., and Tanimoto, K. (2007). A comparative study of simple bone cysts of the jaw and extracranial bones. *Dentomaxillofac. Radiol.* 36: 125–129.
209. Harnet, J.C., Lombardi, T., Klewansky, P. et al. (2008). Solitary bone cyst of the jaws: a review of the etiopathogenic hypotheses. *J. Oral Maxillofac. Surg.* 66: 2345–2348.
210. Shear, M. and Speight, P. (2006). *Cysts of the Oral and Maxillofacial Regions*, 4e, 156–161. Munksgaard: Blackwell.
211. Beasley, J.D. 3rd. (1976). Traumatic cyst of the jaws: report of 30 cases. *J. Am. Dent. Assoc.* 92: 145–152.
212. MacDonald-Jankowski, D.S. (1995). Traumatic bone cysts in the jaws of a Hong Kong Chinese population. *Clin. Radiol.* 50: 787–791.
213. Melrose, R.J., Abrams, A.M., and Mills, B.G. (1976). Florid osseous dysplasia. A clinical-pathologic study of thirty-four cases. *Oral Surg. Oral Med. Oral Pathol.* 41: 62–82.
214. Matsumura, S., Murakami, S., Kakimoto, N. et al. (1998). Histopathologic and radiographic findings of the simple bone cyst. *Oral Surg. Oral Med. Oral Pathol. Oral Radiol. Endod.* 85: 619–625.
215. Ferreira, O. Jr., Damante, J.H., and Lauris, J.R. (2004). Simple bone cyst versus odontogenic keratocyst: differential diagnosis by digitized panoramic radiography. *Dentomaxillofac. Radiol.* 33: 373–378.
216. Suei, Y., Taguchi, A., Kurabayashi, T. et al. (1998). Simple bone cyst: investigation on the presence of gas in the cavity using computed tomography—review of 52 cases. *Oral Surg. Oral Med. Oral Pathol. Oral Radiol. Endod.* 86: 592–594.
217. Suei, Y., Taguchi, A., and Tanimoto, K. (2007). Simple bone cyst of the jaws: evaluation of treatment outcome by review of 132 cases. *J. Oral Maxillofac. Surg.* 65: 918–923.
218. Eriksson, L., Hansson, L.G., Akesson, L., and Ståhlberg, F. (2001). Simple bone cyst: a discrepancy between magnetic resonance imaging and surgical observations. *Oral Surg. Oral Med. Oral Pathol. Oral Radiol. Endod.* 92: 694–698.
219. Yanagi, Y., Asaumi, J., Unetsubo, T. et al. (2010). Usefulness of MRI and dynamic contrast-enhanced MRI for differential diagnosis of simple bone cysts from true cysts in the jaw. *Oral Surg. Oral Med. Oral Pathol. Oral Radiol. Endod.* 110: 364–369.
220. Resnick, C.M., Dentino, K.M., Garza, R., and Padwa, B.L. (2016). A management strategy for idiopathic bone cavities of the jaws. *J. Oral Maxillofac. Surg.* 74: 1153–1158.

221. Mathew, R., Omami, G., Gianoli, D., and Lurie, A. (2012). Unusual cone-beam computerized tomography presentation of traumatic (simple) bone cyst: case report and radiographic analysis. *Oral Surg. Oral Med. Oral Pathol. Oral Radiol.* 113: 410–413.
222. Suei, Y., Taguchi, A., Nagasaki, T., and Tanimoto, K. (2010). Radiographic findings and prognosis of simple bone cysts of the jaws. *Dentomaxillofac. Radiol.* 39: 65–71.
223. Jordan, R.C., Koultas, I., and Raubenheimer, E. (2017). Aneurysmal bone cyst. In: *WHO Classification of Head and Neck Tumours* (ed. A.K. El-Naggar, J.K.C. Chan, J.R. Grandis, et al.), 258–259. Lyon: International Agency for Research on Cancer (IARC).
224. Sun, Z.J., Sun, H.L., Yang, R.L. et al. (2009). Aneurysmal bone cysts of the jaws. *Int. J. Surg. Pathol.* 17: 311–322.
225. Kaffe, I., Naor, H., Calderon, S., and Buchner, A. (1999). Radiological and clinical features of aneurysmal bone cyst of the jaws. *Dentomaxillofac. Radiol.* 28: 167–172.
226. Motamedi, M.H., Navi, F., Eshkevari, P.S. et al. (2008). Variable presentations of aneurysmal bone cysts of the jaws: 51 cases treated during a 30-year period. *J. Oral Maxillofac. Surg.* 66: 2098–2103.
227. Saad, R., Lutz, J.C., Riehm, S. et al. (2018). Conservative management of an atypical intra-sinusal ossifying fibroma associated to an aneurysmal bone cyst. *J. Stomatol. Oral Maxillofac. Surg.* 119: 140–144.
228. Omami, G., Mathew, R., Gianoli, D., and Lurie, A. (2012). Enormous aneurysmal bone cyst of the mandible: case report and radiologic-pathologic correlation. *Oral Surg. Oral Med. Oral Pathol. Oral Radiol.* 114: e75–e79.
229. Speight, P. and Wright, J.M. (2017). Nasopalatine duct cyst. In: *WHO Classification of Head and Neck Tumours* (ed. A.K. El-Naggar, J.K.C. Chan, J.R. Grandis, et al.), 241–242. Lyon: International Agency for Research on Cancer (IARC).
230. Kramer, I.R.H., Pindborg, J.J., and Shear, M. (1992). *Histological Typing of Odontogenic Tumours*, 2e, 39. London: Springer-Verlag.
231. Shear, M. and Speight, P. (2006). *Cysts of the Oral and Maxillofacial Regions*, 4e, 108–118. Munksgaard: Blackwell.
232. Nortjé, C.J. and Farman, A.G. (1978). Nasopalatine duct cyst. An aggressive condition in adolescent Negroes from South Africa? *Int. J. Oral Surg.* 7: 65–72.
233. Hertzamu, Y., Cohen, M., and Mendelsohn, D.B. (1985). Nasopalatine duct cyst. *Clin. Radiol.* 36: 153–158.
234. Kao, Y.H., Huang, I.Y., Chen, C.M. et al. (2010). Late mandibular fracture after lower third molar extraction in a patient with Stafne bone cavity: a case report. *J. Oral Maxillofac. Surg.* 68: 1698–1700.
235. Philipsen, H.P., Takata, T., Reichart, P.A. et al. (2002). Lingual and buccal mandibular bone depressions: a review based on 583 cases from a world-wide literature survey, including 69 new cases from Japan. *Dentomaxillofac. Radiol.* 31: 281–290.
236. Shimizu, M., Osa, N., Okamura, K., and Yoshiura, K. (2006). CT analysis of the Stafne's bone defects of the mandible. *Dentomaxillofac. Radiol.* 35: 95–102.
237. Smith, M.H., Brooks, S.L., Eldevik, O.P., and Helman, J.I. (2007). Anterior mandibular lingual salivary gland defect: a report of a case diagnosed with cone-beam computed tomography and magnetic resonance imaging. *Oral Surg. Oral Med. Oral Pathol. Oral Radiol. Endod.* 103: e71–e78.

Chapter 10
Radiopacities

10.1 Introduction

A radiopacity is the white area on a conventional radiograph. It represents a tissue or a structure within the patient, which attenuates the primary beam of X-rays more than adjacent tissue or structures. The radiopacities observable on conventional radiographs of the neck, face, and jaws are set out in Table 10.1. In the normal patient presenting to the oral and maxillofacial practitioner, the normal radiopaque structures are anatomical: the teeth, the bones of the jaws (including the middle third of the face and nasal bones), the stylohyoid complex (including the hyoid bone), the skull base, and the cervical vertebrae. Although the term radiopacity can be used for any such tissue or structure, it is frequently applied only to those which suggest a lesion or disease process. These radiopacities are due to deposition of mineralized tissue. This deposition reflects two different processes: deposition either by bone cells in dysplastic and neoplastic lesions or by nonbone cells in dystrophic processes. The last arise usually in chronic inflammatory lesions or those with multiple episodes of inflammation. Dystrophic calcification is commonly observed in the soft tissues of the jaws as calcification of the tonsils (now usually secondary to tonsillitis) or cervical lymph nodes. It also occasionally presents in atherosclerotic plaques in blood vessel walls.

In addition to conventional radiography, advanced imaging modalities such as *computed tomography* (CT) and *magnetic resonance imaging* (MRI) are frequently used to investigate jaw lesions. Although calcified lesions and structures are still white on images made by either medical computed tomography (CT, see Chapter 4) or *cone-beam computed tomography* (CBCT, see Chapter 5), they appear black on MRI, as do the air-filled spaces and blood vessels (see Chapter 6).

The term *significant* will be used only when the feature it is qualifying is $P < 0.05$. Table 10.1 overviews the causes of radiopacities of the jaws. Because almost all of these have been addressed in other texts, they will not be pursued further here. For radiopacities within the bony jaws, refer to Figures 10.1 and 10.2.

There are four editions of the *World Health Organization's* (WHO) classification of lesions of the jaws, which will be referred by the date of their publication: 1971, 1992, 2005, and 2017.

Oral and Maxillofacial Radiology: A Diagnostic Approach, Second Edition. Edited by David MacDonald.
© 2020 John Wiley & Sons, Inc. Published 2020 by John Wiley & Sons, Inc.

Table 10.1 Radiopacities occurring in conventional radiographic images of the neck, face, and jaws.

Observed radiopacity	Cause of radiopacity
Artifacts on receptor *See standard dental textbook*	Film/analog development error – mainly fixer splashes
	Damaged sensor – PSP
Inadequate patient preparation *See standard dental textbook*	Jewelry on face, ears, or hair, and around neck
	Removable dental appliances and hearing aids
Variants of normal anatomy *See Chapter 12*	Over mandibular premolar roots – torus mandibularis
	In soft tissues of neck – stylohyoid complex and calcified thyroid and laryngeal cartilages
Lesions in soft tissues at specific anatomical sites *See Chapter 12*	Submandibular and parotid glands – calculus
	Lymph nodes (TB) and tonsilloliths
	Calcified carotid arteries
Lesions anywhere in soft tissues	Gardner's syndrome – multiple osteomas
Lesions arising within the bones of the face and jaws *This chapter*	Infections, dysplasias, cysts, and neoplasms. These arise either from a general osseous (same as the rest of the skeleton) or from an odontogenic (tooth-forming) origin
Metal in face and jaws	Resulting from accidents (e.g. auto glass) or violence (shrapnel) and their treatment (wires and plates)
	Iatrogenic – dental treatment (restorations and implants)

PSP, photo-stimulable phosphor; TB, tuberculosis.

10.2 Radiopacities Occurring within the Bony Jaws

The flowcharts in Figures 10.1 and 10.2 generally flow from the most important clinical and radiological findings, addressing systemic lesions and malignancies first. Multiple radiopacities, particularly if they are distributed throughout the jaws, suggest a systemic cause, whereas a single radiopacity suggests a local cause.

The degree of marginal definition is crucial to determining potentially serious disease. If it is well defined, the radiopacity is more likely to be benign, whereas a poorly defined radiopacity, in addition to inflammation or *fibrous dysplasia* (FD), could represent a malignancy. The radiopacity's relationship to the mandibular canal or the image of the hard palate (on panoramic or cephalometric radiographs) indicates whether it is likely to be of odontogenic origin. A radiopacity occurring above the mandibular canal or below the image of the hard palate is within the dental alveolus and therefore could be of odontogenic origin.

If the radiopacity is sited within the alveolus, its relationship to teeth is important, in order to refine further the differential diagnosis. If it is associated with the root of an erupted tooth, which has a large carious lesion or a large restoration, suggesting the possibility of a necrotic pulp, inflammation is a likely cause. If the radiopacity is associated with the crown of an unerupted tooth, an odontogenic lesion, most likely a neoplasm, should be considered.

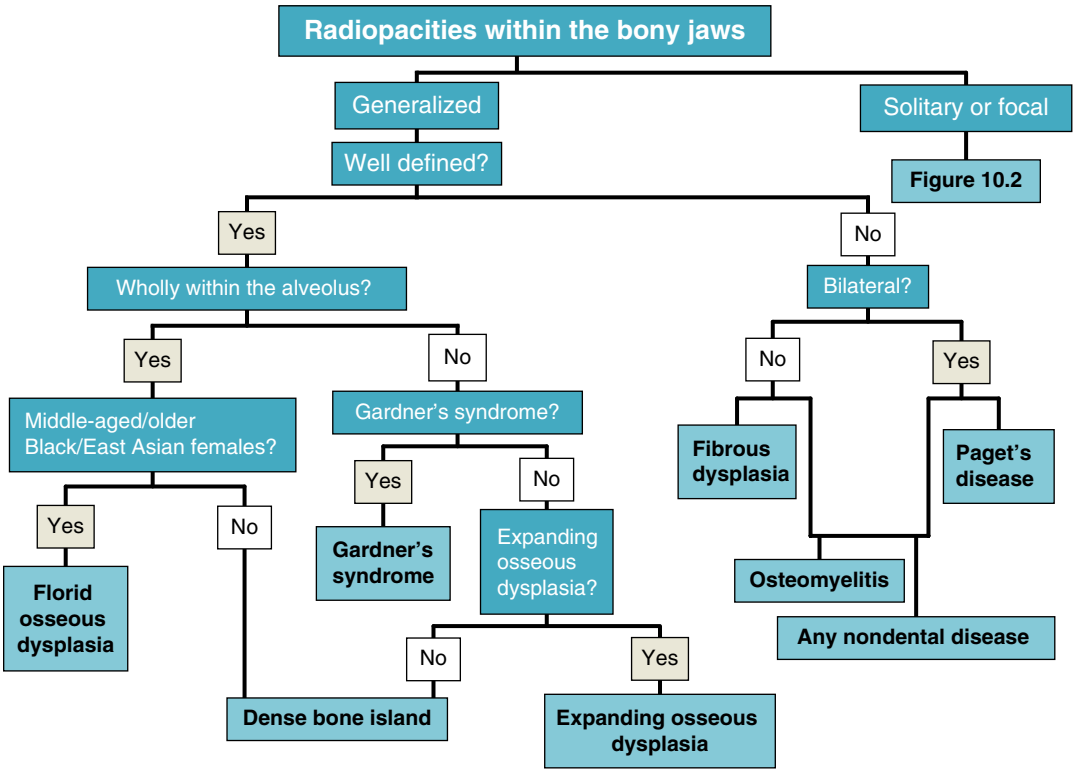


Figure 10.1 Radiopacities occurring within the bony jaws.

The effect of the radiopacity on the tooth or adjacent structures is manifested by either displacement or erosion. The latter when applied to teeth, particularly their roots, is termed root resorption. Although all lesions presenting as radiopacities may in due course cause root resorption, this would appear to be a particular feature of certain odontogenic neoplasms. Displacement of teeth and buccolingual cortices is universal to all expansile lesions.

The flowcharts focus on the most common and important lesions and are not exhaustive with regard to the rarer lesions, particularly if they respond well to the initial treatment – i.e. they are very unlikely to recur.

10.3 Multiple Radiopacities

Multiple or widely distributed lesions suggest a systemic rather than a local cause. Therefore, it is necessary to identify such lesions early. Although these lesions are not common, failure to identify them early may have significant implications for the patient's continued well-being. Polyostotic FD, particularly *McCune-Albright syndrome* (MAS), will have already been diagnosed early in life. Paget's disease and *Gardner's syndrome* (GS) are very important lesions that present later in life. Before proceeding to these lesions, a unique radiological phenomenon should be introduced: leontiasis ossea.

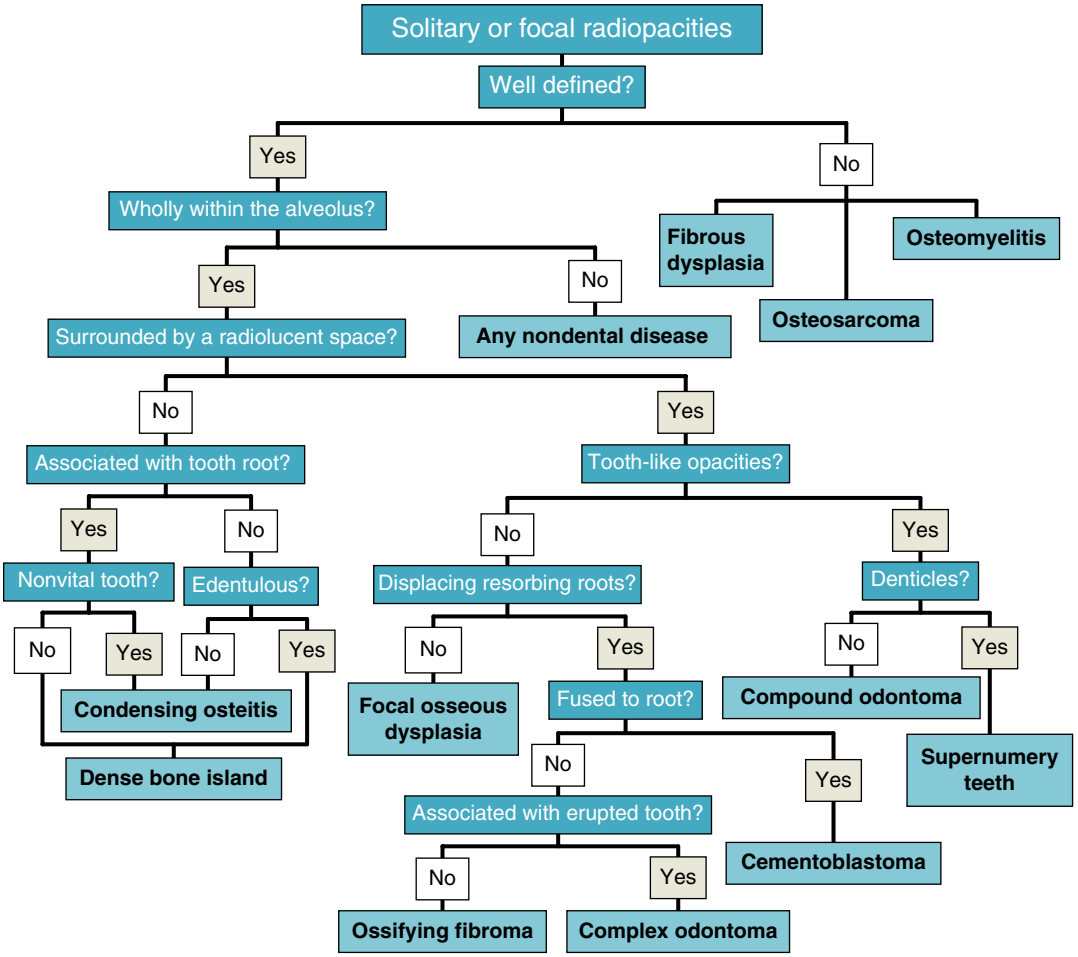


Figure 10.2 Radiopacities occurring within the bony jaws: solitary or focal.

10.3.1 LEONTIASIS OSSEA

Leontiasis ossea, although infrequently observed, represents important lesions such as Paget's disease of bone (PDB) and hyperparathyroidism [1]. Its name precisely reflects the appearance of a lion's maxilla. Classically, both cheeks are very full and the external nose is small. The latter effect is achieved by the following: the external nose, which itself remains essentially unchanged, becomes submerged within the outwardly expanded anterior wall of the maxilla. As a result, the external nose is now both relatively smaller and flatter due to a more obtuse angle formed between the alae.

The presentation on CT of the internal structure is usually ground glass or an extensive network of serpentine channels within the radiopacity. Its frequently bilateral presentation usually distinguishes it from FD.

10.3.2 PAGET'S DISEASE OF BONE

PDB was originally called "osteitis deformans" by Paget himself [2], and that vividly describes this disease. Although PDB is still reputed to be the "second most common metabolic bone disease after osteoporosis" [3], it has generally become less frequently

apparent in its traditional community of persons of middle age or over and of British, more particularly of Scottish, descent. It classically presents with the "Tam O'Shanter" skull, named after the usual depiction of one of Robert Burns' (Scotland's national eighteenth-century poet) most famous characters. Although examples of this and other advanced cases are displayed in many textbooks, they are most frequently of cases which are decades old and are also most likely to represent the most severe manifestations of this disease. Furthermore, the WHO's 2017 edition, the most comprehensive and inclusive edition for over two decades, does not mention PDB at all. Nevertheless, later in this section the reader will learn of the emergence of what is perhaps PDB in communities which are outside the traditional community for the disease.

Unlike osteoporosis and other metabolic diseases, PDB "has a focal nature affecting one or several bones in a seemingly random fashion" [3]. It classically affects the axial skeleton and weight-bearing bones (pelvis 70%, femur 55%, lumbar spine 53%, skull 42%, and tibia 32% [4]); other bones such as those of the jaws are infrequently affected. It is characterized by rapid bone remodeling leading to "bone deformity, pathological fractures, deafness, and nerve compression syndromes" [2, 3]. Although it classically affects individuals usually in the eighth decade, it is rare before 55 years of age [4]; a subset of patients are juveniles. The last is called *juvenile Paget's disease* (JPD) and is primarily genetic [5, 6] and autosomal recessive [6], whereas the classical adult-onset PDB is autosomal dominant [2].

Although the substantial minority (22%) of PDB cases in one case series were symptom free [7], another authority reported that the majority of cases of PDB are discovered incidentally to radiography or to biochemistry prescribed for other purposes [4]. The case series pronounced that the majority (74%) presented with bone pain. A large proportion of patients already had irreversible skeletal damage at first presentation: 18% had bone deformity, 6% had a pathological fracture, and 7% had deafness [7]. Nevertheless, taking all these together, it is clear that the majority did not exhibit any clinically discernible signs, which would include warmth of the skin overlying the painful area [4]. Therefore, diagnosis of a symptomatic case of PDB will be dependent on a family history, ethnicity, biochemistry, bone scintigraphy.

There was a family history in 10% in one case series [6]. First-degree relatives have a 7–10-fold risk for PDB: 5% in Belgium, 15% in the United Kingdom, and 40% in Quebec and parts of Spain [2]. In addition to the aforementioned features [2, 4], JPD includes rapid bone remodeling, tooth loss, carotid aneurysms in childhood, and retinopathy leading to blindness later [6]. The decline in the severity of PDB may in part be due to the adoption of a healthier diet (low calcium intake and Vitamin D deficiency are implicated in PDB [2]), reduced exposure to infections, and a more sedentary lifestyle, the last perhaps by imposing less wear and tear on the skeleton [3]. Most cases of PDB occur in communities originating from the United Kingdom. Its decline in some areas of the United Kingdom can be perhaps in part attributed to the influx of immigrants from parts of the world with a lower prevalence [2]. Nevertheless, a rising incidence has been reported recently in East Asians [8–11].

Although the radiological presentation is broadly similar to FD, PDB is generally bilateral and first presents over the age of 50 years, whereas FD first presents on average three decades earlier and is unilateral. When the jaws are affected the lumen of the maxillary sinus is frequently spared, whereas it is obturated in FD.

The radiological presentation of lesions in the alveolus is similar to *florid osseous dysplasia* (FOD), but extends into basal bone. Note that, although classically polyostotic, nearly half of cases in a recent report were monostotic [7]. At least seven cases of monostotic PDB affecting the mandible alone have been reported in the literature [12]. Although bone scintigraphy and serum alkaline phosphatase are sensitive screening modalities for PDB, the latter, which is raised in 86% of cases, may not be raised during the more inactive periods of the disease. Alkaline phosphatase is also higher for polyostotic disease than for monostotic disease [13]. The investigation of choice is a bone scan/scintigraphy in order to show the extent of the disease [4]. The hyperavid areas displayed by scintigraphy can be further reviewed by CT. Furthermore, CT may be indicated in those patients for whom spinal stenosis or osteosarcoma is suspected. Although rare (about of 0.5% of all PDB), osteosarcoma should be strongly suspected when there is a sudden onset of bone pain and swelling [4]. Cheng et al., in their synthesis of the English-language literature, reported significantly more cases of osteosarcoma secondary to PDB of the jaws in contrast to osteosarcoma arising from PDB elsewhere in the skeleton and osteosarcoma arising within the jaws [14]. Osteosarcoma arising from PDB of the jaws has a predilection for females and those of sub-Saharan African origin. Although the five-year survival is poor (21%), it is better than that for osteosarcoma arising from PDB elsewhere in the skeleton, which is 5%. The survival of the former is lower than that for primary osteosarcoma arising within the jaws [14].

Cases of PDB that are symptom free require no treatment [4]. Bisphosphonates are used to treat PDB, particularly when there is localized pain, for which it is particularly effective [4]. Bisphosphonates normalize the alkaline phosphatase in 60% of cases of PDBs [15]. If the pain is not responding to the bisphosphonates, then consideration should be given to the possibility that the pain may actually come from arthritis [4], which responds to an entirely different set of drugs: analgesics [4].

10.3.3 GARDNER'S SYNDROME

The main clinical feature of GS, an autosomal disease, is *familial adenomatous polyposis* (FAP). GS affects only 10% of FAP cases [16]. Any one or more of these polyps at any time can undergo malignant change to adenocarcinoma, which killed the father and sister of the proband in the fifth decade in a report of GS affecting three generations [17]. Polyps arise after 20 years of life [18]. Therefore, it is important to diagnose the syndrome as early as possible. Although the taking of a good family history may assist in identification of polyps, the vigilance of oral and maxillofacial practitioners is crucial, because they are more likely to observe the hard-tissue lesions earlier than the onset of symptoms and signs of FAP. Those hard-tissue lesions affecting the jaws are osteomas (Figure 10.3), odontomas, and supernumerary and impacted teeth [19]. They will be most likely to be observed as an incidental finding on a panoramic radiograph. Takeuchi et al. reported the largest series of GS cases [20]. They found 23 cases of GS out of 48 cases of FAP. The average age when diagnosed was 26 years of age. They followed these patients for an average of seven years and noted that in half of the cases the number and size of the osteomas continued to increase. Although one-third developed colonic cancer, there was no significance between malignant transformation and the extent of the jaw lesions; indeed, the four cases displaying widespread lesions were not associated with malignant change.

The multiple osteomas affecting the mandible of a middle-aged East Asian woman in Lee et al.'s case have a radiological



Figure 10.3 Panoramic radiograph displaying multiple osteomas in both the alveolar and basal processes of both jaws of a patient with Gardner's syndrome (polyposis coli). The osteomas have almost completely obliterated the maxillary antrum. See Figure 18.18 for other views of this case. Source: Reproduced with permission from Lee, B.D., Lee, W., Oh, S.H. et al. (2009). A case report of Gardner syndrome with hereditary widespread osteomatous jaw lesions. *Oral Surg. Oral Med. Oral Pathol. Oral Radiol. Endod.* 107: e68–e72.

presentation similar to familial gigantiform cementoma (FGC; Figure 10.3) [21]. The CT of this case additionally revealed an osteoma expanding into the orbit, displacing the optic nerve and the globe (eyeball; see Figure 18.18). In addition to similar FGC-like lesions in two of her adult children, there was a definite family history of abdominal tumors. On endoscopy the patient was found to have multiple intestinal polyps. The sole dental anomaly was an impacted premolar.

Fonseca et al. [22], Madani and Madani [23], and Ramaglia et al. [16] reported peripheral (periosteal) osteomas; such osteomas are rarely seen in nonsyndromic cases.

10.4 Poorly Defined Radiopacities

Poorly defined lesions are generally suggestive of aggressive disease such as malignancies or infections. This criterion by itself is not entirely decisive with regard to those jaw lesions, which frequently present as radiopacities. FD, a fibro-osseous lesion affecting the jaws, also presents with a poorly defined margin, which is central in differentiating it from another fibro-osseous lesion. Nevertheless, there is one other criterion that can assist in the identification of these aggressive lesions: the periosteal reaction. This is a prominent feature of general radiology, but other than expansion of the cortices it is infrequently observed in the jaws, except in regard to chronic infection and some malignant neoplasms, such as osteosarcoma [24].

10.5 Sarcomas

Sarcomas are primary malignant tumors of the skeleton. Osteosarcoma is the most common of the sarcomas affecting the jaws; in an American National Cancer Database Report, osteosarcoma accounted for 78% of sarcomas affecting the mandible, in contrast to chondrosarcoma's 14% and *Ewing's sarcoma's* (ES) 8% [25].

10.5.1 OSTEOSARCOMA

A major problem with osteosarcoma is that until recently there have been very few large case series on osteosarcoma of the

jaws, which is extremely rare, accounting for 7% of all osteosarcomas and 1% of all head and neck malignancies [26]. Hitherto, the result of this is a difficulty in optimizing management of this important lesion. The American Surveillance, Epidemiology and End Results (SEER) cancer registry, specifically the "18" registry which covers 28% of the American population, revealed over 500 sarcomas of the jaws which presented between 1973 and 2011 (nearly four decades) [26]. The entire Dutch registry (PALGA) from 1991 to 2011 (two decades) revealed almost 500 cases affecting the face and jaws [27]. Simple comparison of these reports reveals that osteosarcoma may be as much as 10 times more prevalent in the Dutch. Both SEER [26] and PALGA [27] gave virtually identical mean ages at presentation, 41 [26] and 42 [27], respectively, and were equal for gender. Caucasians represented 75% of cases and Afro-Americans 17% (SEER) [26]. The mandible was affected in 44% and the face and maxilla in 56% of cases in SEER; the mandible 51% and the maxilla alone in 35% of cases in PALGA [27]. Presentation was with higher-grade tumors (Grades III and IV) in 61% of PALGA cases [27], which was comparable with SEER for those tumors whose grade was known [26]. PALGA revealed that the grading of osteosarcomas affecting the maxilla was significantly lower than for the mandible [27]. Although in SEER cases surgery alone was performed in 59% and in combination with radiotherapy in 23%, the former would have been more frequent recently due to the developments in surgery, which enhance complete removal of the primary lesion [26]. Disease-specific survival was 62% for 5 years and 54% for 10 years [26]. The strikingly low five-year survival rate of osteosarcoma in PDB, which accounted for 2% of all sarcomas, was consistent with earlier studies which set it at 5% [26]. On the other hand, only one osteosarcoma with PDB was observed in the PALGA study [27]. Osteosarcomas have a long-established reputation for occurring in FD; this will be addressed later in this chapter.

The first presentation of osteosarcomas affecting the jaws of Americans [26] and the Dutch [27] occurred early in the fifth decade, considerably later than those osteosarcomas arising elsewhere in the skeleton, the majority of which occurred under 15 years of age [28]. Those arising in other global communities outside America and Europe exhibited markedly different ages at first presentation: Israelis [29], Nigerians [30], Japanese [31], Malaysians [32], and Peruvians [33] first presented at 33, 27, 51, 34, and 32 years, respectively.

Most osteosarcomas of the jaws presented as swellings, whereas those in the long bone presented with bone pain [26]. The sudden onset of numbness of the lower lip without a recent history of trauma or any evidence of an infection should prompt consideration of an osteosarcoma.

The variety in radiological presentation may merely reflect the ethnic origin of the community reported. Ogunlewe et al. reported that most cases showed a nonspecific radiolucent lesion [30]. Givol et al. reported that overall 78% had poorly defined margins and 29% displayed a locular pattern [34]; 41% were "mixed," 29% were radiolucent, and 29% were radiopaque [34]. Fernandes et al. reported a "sunray appearance" (Figure 10.4) in 54% [35].

10.5.2 CHONDROSARCOMA

Chondrosarcoma is even rarer, accounting for 11% of all primary malignant tumors, mainly in the limbs. It is even rarer to find within the head and neck, ranging from 1 to 12% [36]. It generally arises within cartilage, such as the chondrocranium (Figure 19.4) and the laryngeal cartilage (Figure 19.5). With the exception of islands of hyaline cartilage in the nasopalatine duct, which can

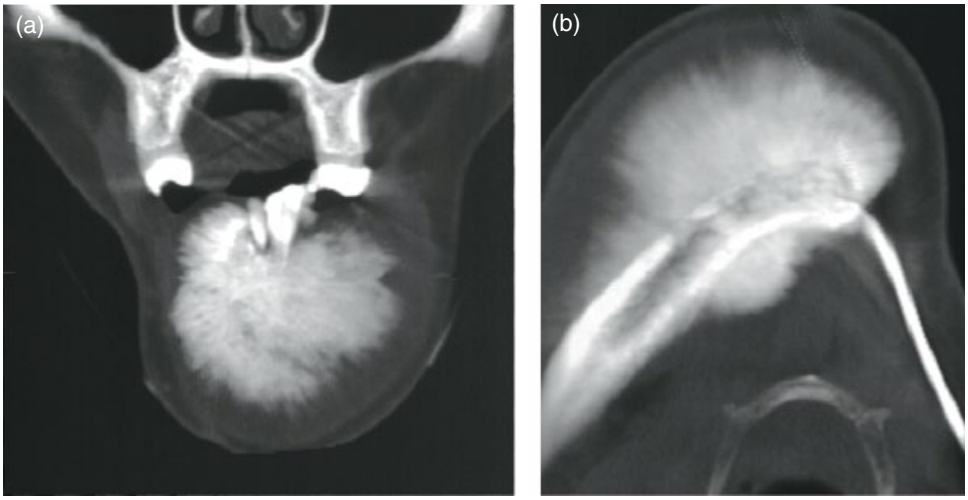


Figure 10.4 Computed tomography (CT) of a case of recurring osteosarcoma. (a) Coronal CT (bone window) exhibiting the sunburst pattern. (b) Axial CT displaying the osteosarcoma affecting almost the whole of the remaining body of the mandible.

account for chondrosarcoma in the anterior palate, it is very difficult to identify similar cartilaginous islands elsewhere in the jaws; any remnants of Meckel's cartilage do not persist after birth. A reason for those occurring in the jaws is that they develop within enchondromas, which characterize diseases such as Ollier disease and Maffucci syndrome [36]. Nearly 30 cases of chondrosarcoma have been reported arising within the temporomandibular joint [37].

Although chondrosarcomas display an aggressive growth pattern, they seldom metastasize. Therefore, resection with adequate margins is usually curative. Nevertheless, long term follow-up is recommended, as these may exhibit a late recurrence [36]; one chondrosarcoma recurred for the second time 10 years after the first recurrence a year after primary surgery [37].

10.5.3 EWING'S SARCOMA

ES is an aggressive tumor, which predominantly affects children and adolescents [38]. Although there was a discovery, two decades ago, of the EWS-FL11 fusion gene, which is pathognomonic for ES, the mechanisms behind the tumor's relapse and metastasis are still not understood [39]. Individuals of European origin are more frequently affected than those of sub-Saharan African origin [40].

A major problem with ES is that its earliest clinical presentation may be misinterpreted as a dental or periodontal infection, which delays its diagnosis and timely treatment, resulting in a poorer prognosis, which on average is circa 70% five-year survival for localized disease, plummeting to 30% if already metastasized [38]. A radiolucency and a failure to respond to appropriate treatment should prompt consideration of ES [41].

10.6 Osteomyelitis

Osteomyelitis of the jaws frequently arises from a dental infection (Figure 10.5). Petrikowski et al. reviewed 10 cases each of osteomyelitis, FD, and osteosarcoma – three lesions with radiological similarities [42]. They reported that the only two features that most usefully distinguish osteomyelitis are "sequestra and laminations of periosteal

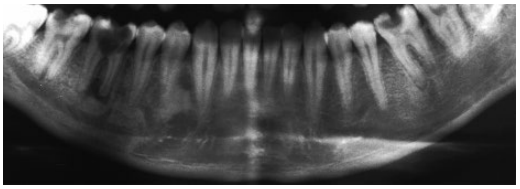


Figure 10.5 Panoramic radiograph displaying a diffuse sclerosing osteomyelitis arising from a carious first molar. This osteomyelitis has affected both the alveolar and basal processes, resulting in the accentuation of the mandibular canal (compare with the normal contralateral side).

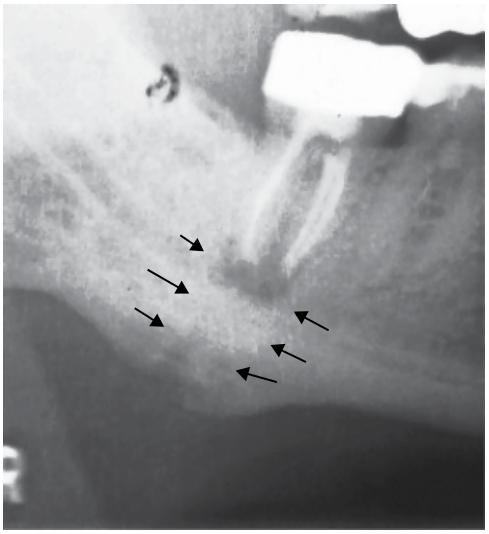


Figure 10.6 Panoramic radiograph of a periosteal reaction at the lower border of the mandible apical to the root-filled first molar, resulting in an involucrum. This is represented by a suggestion of laminations running approximately parallel to the lower border of the mandible, giving rise to an onion-skin appearance. A wide draining tract is obvious (arrows), running, through this onion-skin structure, from the periapical radiolucency to the most dependent part of the periosteal reaction. Sclerosing osteomyelitis is observed in the bone adjacent to this tooth, particularly inferiorly and distally.

new bone" (Figure 10.6) [42]. This new bone is called an involucrum. As revealed by Figure 10.7, teeth within the affected bone can be lost.

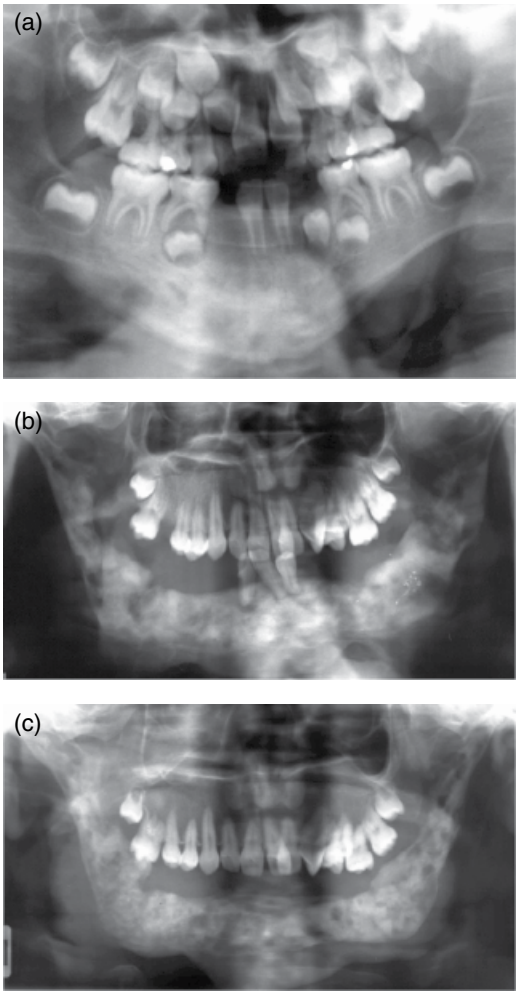


Figure 10.7 Consecutive series of panoramic radiographs displaying the progression of osteomyelitis from the midline (a) through (b) to affect the entire mandible except for the condyles in (c).

Figure 10.7 displays a case of osteomyelitis, which began in the anterior mandible and over the years gradually involved almost the entire mandible. In addition to those features observable on conventional radiography, CT additionally reveals cortical bone defects and soft-tissue involvement of osteomyelitis [43]. The maxillary cortical defect is more common buccally and the mandibular cortical defect most common lingually. The buccinator is more

frequently affected by osteomyelitis of the maxilla and the masseter by osteomyelitis of the mandible [43].

10.7 SAPHO

Although *synovitis, acne, pustulosis, hyperostosis, and osteitis* (SAPHO) syndrome is a rare disease presenting with those symptoms [44], awareness of it among oral and maxillofacial clinicians is necessary to ensure its early diagnosis and effective treatment. To date at least 14 case reports, all affecting the mandible, have been reported [44]. Although the bone lesions are indistinguishable from infective osteomyelitis, they are generally sterile. Failure to appreciate that may result in a mean four-year duration of symptoms until diagnosis [45]. Suspicion of SAPHO should be considered if "an osteomyelitis" does not respond as expected to a normally appropriate antibiotic. An interdisciplinary approach is advised, involving dermatologists and rheumatologists [45]: the former to look for and evaluate skin lesions, such as acne, pustulosis [45], and psoriasis vulgaris [46], and the latter osteoarticular anomalies [45]. These last may require whole-body bone scintigraphy using *technetium 99-methylene diphosphonate* (^{99m}Tc-MDP) [47]. Earlier, much was made of the "bullhead" sign of involvement of the frequently affected sterno-clavicular region [44] as a common and reliable diagnostic feature of SAPHO, but recently this has been dismissed, certainly in Chinese SAPHO cases [47]. Interestingly, the same reported that the mandible was affected in only 1 out of nearly 50 consecutive cases [47]. Although frequently found in young adults, SAPHO has also been reported in the elderly [46]. Effective treatment of the skeletal aspects of SAPHO is by corticosteroids to reduce accelerated bone remodeling and bisphosphonates for advanced sclerosis or severe bone pain [45].

10.8 Medication-related Osteonecrosis of the Jaw

Medication-related osteonecrosis of the jaw (MRONJ) [48, 49] was first reported in 2003 [50]. Up until very recently, it was known as *bisphosphonate-related osteonecrosis of the jaw* (BRONJ) [51], among other names [48]. Ruggiero stated that the term MRONJ was proposed by the American Academy of Oral and Maxillofacial Surgeons' (AAOMS) position paper [48]. MRONJ occurs in 1% of all patients taking antiresorptive (bisphosphonates and denosumab) or antiangiogenic (bevacizumab) medications [49]. Although it is a serious condition, it is relatively infrequent and arises from treatment necessary for other diseases. In addition to treating osteosarcoma, PDB, osteogenesis imperfecta, and SAPHO syndrome, the drugs which cause MRONJ, particularly *antiresorptive medications* (ARM), are also central in the treatment of osteoporosis, multiple myeloma, and metastatic disease. Bisphosphonates reduce the risk of fracture, reduce mortality, and increase survival of patients with osteoporosis [15]. As with many treatment regimens, there is a downside. In addition to MRONJ, bisphosphonates have been associated with increased risk of atypical femur fractures, gastrointestinal side effects, and atrial fibrillation [52].

The International Task Force on Osteonecrosis of the Jaws [50, 53, 54] slightly amended the AAOMS criteria so that a diagnosis of MRONJ is reached when there is the following:

1. Presence of exposed bone in the maxillofacial region which does not heal within 8 weeks after identification by a health care provider.

2. Exposure to an antiresorptive agent (bisphosphonate or denosumab).
3. No history of radiation therapy to the craniofacial region.

Ruggiero set out the grading of MRONJ, which has been gently adapted in Table 10.2 [48]. It should be noted that the International Task Force could not agree on what features constituted Grade 0 [54].

In a case series of 91 patients affected by MRONJ, 73 occurred in those treated for osteoporosis and 18 in those treated for cancer [51]. Overall, 94% were female and the median age was 71 years. Nearly two-thirds reported pain. The mandible was affected more frequently than the maxilla. The MRONJ in 80% improved with treatment [51].

Although conventional dental radiography (intraoral and panoramic) amply displays an advanced case of MRONJ (Figures 10.8 and 10.9), it is either nonspecific or insufficiently sensitive to display the condition in its earliest stages [48]. Nevertheless, features such as osteosclerosis, a

Table 10.2 Medication-related osteonecrosis of the jaw (MRONJ): Grading.

Grade 0	Symptoms	Dental pain without an obvious dental cause
		Dull, aching jaw-bone pain: may radiate to temporomandibular joint region
		Sinus pain, perhaps with thickening of sinus wall
		Altered neurosensory function
	Clinical	Loosening of teeth not explained by chronic periodontal disease
		Periapical fistula not associated with pulpal necrosis
	Radiology	Alveolar bone loss or resorption not associated with chronic periodontal disease
		Changes in trabecular pattern: (a) dense bone; (b) no new bone in socket
		Regions of osteosclerosis involving the alveolar bone +/– basal process
		Thickening of the periodontal ligament space
		Thickening of the lamina dura
		Thickening/obscuring/decreasing of the periodontal ligament space
Grade 1	Symptoms	None
	Clinical	Exposed, necrotic bone or fistula that probes to bone
Grade 2	Symptoms	Pain
	Clinical	Exposed, necrotic bone or fistula that probes to bone *PLUS*
		Erythema in the regions of exposed bone *PLUS perhaps also*
		Purulent drainage
Grade 3	Symptoms	Pain
	Clinical	Exposed, necrotic bone or fistula that probes to bone *PLUS 1 or more of:*
		Pathological fracture
		Extraoral fistula
		Oral antral or oral nasal communication
		Osteolysis extending to the lower border of the mandible/sinus floor

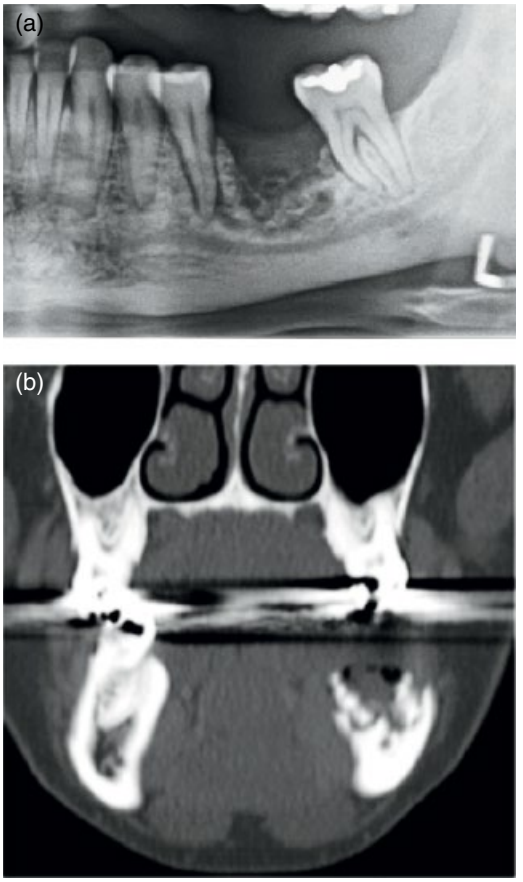


Figure 10.8 Panoramic radiograph and computed tomography (CT) of a case of medication-related osteonecrosis of the jaw. (a) Panoramic radiograph displaying affected edentulous site. The affected bone is delimited by a broad radiolucent band running parallel and above the mandibular canal. The bone above it is being sequestrated (b). The coronal CT exhibits the sequestrum. Note: Horizontal lines; beam hardening (black) and spray artfacts (white) Source: Courtesy of the late Dr. Michele Williams, British Columbia Cancer Agency.

thickening of the lamina dura, or a failure of a previous extraction site to ossify may serve as early radiological signs [48]. CT (Figure 10.8), in addition to thickened lamina dura, will display sclerosis, early sequestra, and a periosteal reaction, and will finally better delineate the area of MRONJ [48]. This last feature will be better

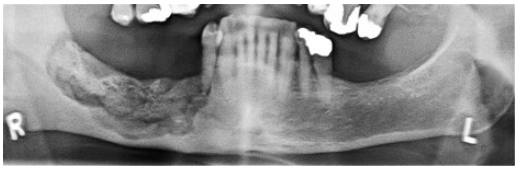


Figure 10.9 Panoramic radiograph displaying medication-related osteonecrosis of the jaw affecting the entire posterior alveolus of the right mandible. Posteriorly this reaches down to the mandibular canal and reaches the lower border of the mandible anteriorly. Source: Courtesy of the late Dr. Michele Williams, British Columbia Cancer Agency.

displayed by virtue of CT's poorer spatial resolution than conventional dental radiography, a phenomenon that will be discussed later in this chapter in relation to FD. The recurrent widespread availability of CBCT with its lower radiation dose means that it can be used instead of CT (Figure 10.10). See also Ruggiero's Figures 3 and 4 for further examples of CBCT and MRONJ [48].

Bone scintigraphy is valuable in early-stage MRONJ in revealing affected areas [48]. *Fluorodeoxyglucose* (FDG) *positron emission tomography* (PET) fused with CT was used postoperatively to predict healing [55].

MRONJ after an extraction was significantly more frequent for antiresorptive drug treatment for oncological reasons (3.20%) than for osteoporosis (0.15%) [56]. A reason for this difference is that in Mercer et al.'s report, the bisphosphonate dose to cancer patients was much higher than that to osteoporosis patients [50]. Increased dental awareness and enhanced dental intervention were associated with a decline in the incidence of MRONJ in cancer patients [57].

Currently, there is no universally accepted treatment protocol for MRONJ. The extent of surgery depends on the

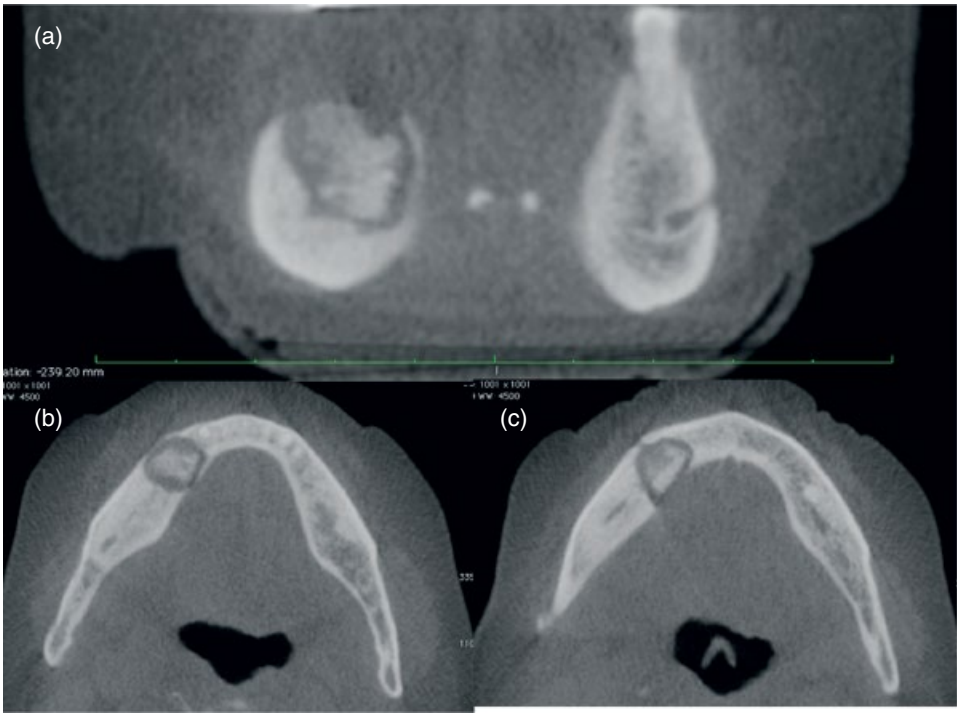


Figure 10.10 Cone-beam computed tomography (CBCT) displaying medication-related osteonecrosis of the jaw affecting the premolar alveolus of the right mandible. This reaches down to the mandibular canal. The coronal (a) and axial (b and c) reconstructions exhibit a sequestrum, buccolingual expansion suggestive of an involucrum and increase the density of the affected side. Note: The two radiopaque "dots" in the midline in (a) are the genio tubercles; (c) also displays a partial thickness of these tubercles at the level of the superior aspect of the epiglottis. Source: Courtesy of the late Dr. Michele Williams, British Columbia Cancer Agency.

stage of the disease [53]. Nevertheless, a conservative surgical approach to MRONJ has been outlined recently [55].

10.9 Fibro-osseous Lesions

Fibro-osseous lesions (FOL), an important group of lesions of the face and jaws, have experienced many significant changes in their nomenclature and classification over the last half-century. These changes are set out in Figure 10.11, which has been adapted from MacDonald-Jankowski's Figure 1 [58] and MacDonald's Figure 1 [41]. Although they display similar histopathology, a spectrum between cementoid and osteoid, their clinical and radiological presentations and treatment outcomes differ [59–62]. As observed in Figures 10.1 and 10.2, FOLs are central in the differential diagnosis of a radiopacity affecting the jaws. The WHO's 2005 edition [63, 64] adopted Brannon and Fowler's histopathological redefinition of the "cementoid" elements found in cemento-osseous dysplasia (COD) and cement-ossifying fibromas [65]. They reported that these cementoid elements are truly manifestations of abnormal bone and not a form of cementum. As a result, cement-ossifying fibroma and cemento-osseous dysplasia were renamed *ossifying fibroma* (OF) and *osseous dysplasia* (OD). OF is the jaw's equivalent of extragnathic

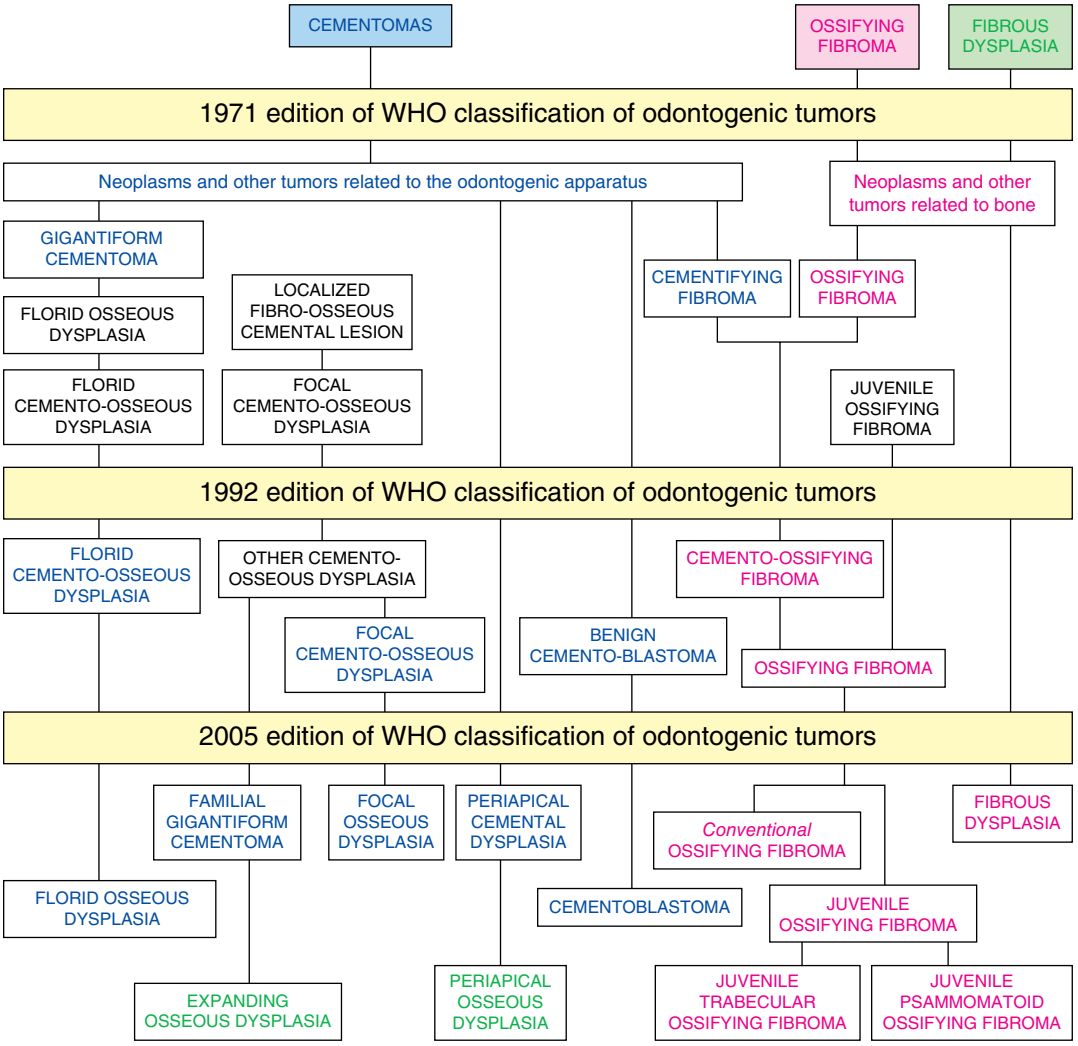


Figure 10.11 Development of the nomenclature and classification of fibro-osseous lesions (FOLs) of the jaws from the original three lesions cementomas, ossifying fibroma, and fibrous dysplasia of 50 years earlier. Although this flowchart is a simplified rendering of MacDonald-Jankowski's Figure 1, it still reveals some of the "lumping and splitting" which had taken place in the intervening 50 years. Terms in magenta are lesions arising in the bone and terms in blue are lesions arising from odontogenic tissues; these are still in current regular use. Terms in black indicate broadly when they were first used; many are still in regular use. Those terms in green have emerged in the last decade to describe some of the lesions better. NOTE: Although the above WHO editions do not specifically address the FOLs as a category of lesions, they serve as milestones for the development of the classification and nomenclature of the individual FOL lesions. Source: Adapted from Figure 1 in MacDonald-Jankowski DS. Fibro-osseous lesions of the face and jaws. *Clin. Radiol.* 2004;59:11–25 and Figure 1 in MacDonald DS. Maxillofacial fibro-osseous lesions. *Clin. Radiol.* 2015;70:25–36.

osteofibroma, which also was called "ossifying fibroma" until it was renamed in the WHO's second edition of classifications of neoplasms of the bone [66]. Although the name of the third FOL, "fibrous dysplasia of the jaws," remained unchanged (Figure 10.11), we now understand its etiology, presentation, and behavior better.

Although Figure 10.11 includes only those alternative terms that may still be in use, this simplified figure is still able to display the "lumping" and "splitting" which appear to attend frequently the development of most classifications and systems of nomenclature for any group of lesions [58].

The most important technology to have an impact on the imaging of FOLs of the jaws in the last decade was CBCT [41]. Other than the report by MacDonald which covers the FOL spectrum [41], the use of CBCT, which has been widely available for 10 years, has been absent from the literature. A reason for this dearth up to now is that if large in size FOLs, whether incidental or symptomatic, were most likely to be investigated by conventional CT in a medical hospital [41]. CBCT has three main advantages over CT: CBCT imparts a much lower radiation dose; is more readily available; and can be sited in almost any clinical space, due to its lower weight, smaller footprint, and no need for a high-tension electricity supply. The main disadvantage of CBCT is its poorer contrast resolution (15-bit depth or less, therefore it essentially displays only a "bone window") [41]. (For more see Table 5.1)

The late Charles Waldron wrote: "In absence of good clinical and radiologic information a pathologist can only state that a given biopsy is consistent with a FOL. With adequate clinical and radiologic information most lesions can be assigned with reasonable certainty into one of several categories" [67]. Conversely, in the absence of such information Eisenberg and Eisenbud stated that "pathologists today will often rightly decline to render a definitive diagnosis… Instead, the pathologist will resort to the noncommittal designation of *benign fibro-osseous lesions* [their italics]. This is the only acceptable approach considering the potential for inappropriate treatment otherwise" [68]. Therefore, the identification or clarification of the majority of histopathologically proven FOLs affecting the jaws is made upon clinical and radiological features.

Conventional radiography is still sufficient for the diagnosis of almost all cases of FOLs. FD can be distinguished from OF on the basis of the margins, which are poorly defined for FD and well defined for OF. Although this radiological feature remains the gold standard for distinguishing between FD and OF, over the last decade a genetic test has been able to distinguish between them with increasing confidence. This test is based on *guanine nucleotide-binding protein* (GNAS) mutations. Jundt stated that in FD, "Mutations in the gene (GNAS I) encoding for the *G-protein* (Gs-α) lead to increased c-AMP production affecting proliferation and differentiation of preosteoblasts" [69]. Shi et al. reported that while GNAS mutations were found in most cases of FD, they were not found in any case of OF [70]. Patel and co-workers reported GNAS to be absent not only in cases of OF, but also OD [71]. Therefore, a positive GNAS response is a strong indicator of FD and may be useful in the few cases in which clinical and radiological presentations are unclear to allow for distinction between FD and OF.

Recently the WHO formally acknowledged, for the first time, the FOLs "as a group because of their similar and overlapping fibro-osseous appearance histologically" [72]. Although the WHO's 2017 edition suggested that the older names of some FOLs be restored, these amendments were not as disrupting to clinical practice as some of those already discussed in Chapter 9. Furthermore, as the rationale for the nomenclature change of some FOLs was not compelling, this textbook will retain the WHO's 2005 edition's nomenclature, with the exception of FGC, which is replaced for reasons explained

later with "expanding osseous dysplasia." Reading of the WHO's 2017 edition, generously illustrated with micrographs, with particular regard to FOLs may induce the reader to understand that diagnosis of the various FOLs can be reliably achieved by histopathology alone. This is not true and has not been stated anywhere in the WHO's 2017 edition, nor in contemporaneous texts or statements such as that by Wright and Vered [72]. Therefore, the statements by Waldron [67] and Eisenberg and Eisenbud [68] are still valid. Nevertheless, we may yet in due course acquire further genetic markers such as GNAS-1 that will assist us further in our understanding and diagnosis of these lesions.

10.10 Fibrous Dysplasia

FD is an important lesion affecting the maxillofacial region because, in addition to severe deformity and a likelihood that it may become reactivated after a period of quiescence, most devastatingly of all it can cause blindness. As discussed in the previous section, Jundt [69] defined FD as "a genetically based sporadic disease of bone that may affect single or multiple bones."

FD affecting the jaws differs radiologically and histologically from that of the rest of the skeleton on conventional radiography. FD affecting the jaws is poorly defined, according to Slootweg and Müller's 1 mm "zone-of-transition" criterion (Figure 10.12) [73], whereas that of the extragnathic FD is well defined [66, 74]. A possible reason for this difference is that the jaws are derived from membrane and long bones are from cartilage [74]. Support for this contention comes from the WHO's second edition of the classification of neoplasms affecting the extragnathic skeleton, which included cartilage as an expected

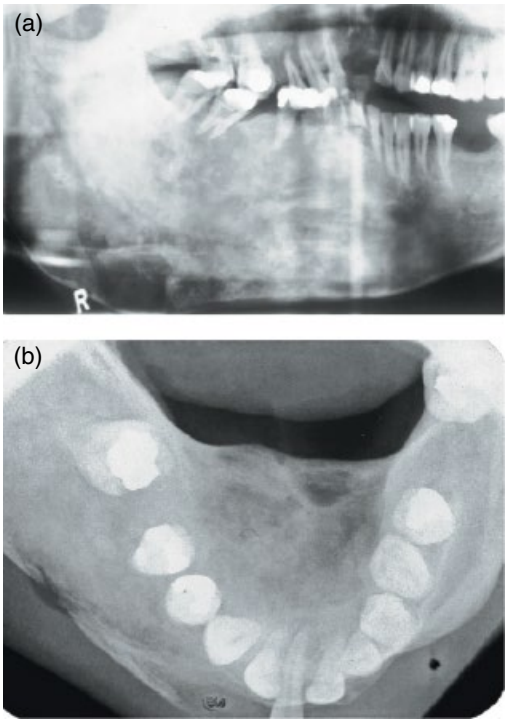


Figure 10.12 Conventional radiography of bimaxillary fibrous dysplasia (FD). (a) Panoramic radiograph of a case of FD affecting the right hemimandible and the right hemimaxilla. The right dysplastic lesion of the mandible has crossed the midline of the mandible. The midline has been denoted by the image of the post of the bite block. The dysplastic areas are readily distinguishable from those that remain normal; the wide zone of transition between the dysplastic and normal adjacent bone means that there is a poorly defined margin between them. The fusiform expansion of the mandible is obvious in the vertical dimension. The dysplastic lesions of both jaws have displaced the teeth toward each other, resulting in an open bite of the largely unaffected left side. (b) True occlusal radiograph. The teeth still generally follow a catenary curve, although a central incisor has been displaced buccally. The patterns of the dysplastic bone vary throughout from ground glass, to peau d'orange, to radiolucency, progressing from the right to left paramedial regions. The buccal dysplastic cortex is very thin in comparison to the normal contralateral side.

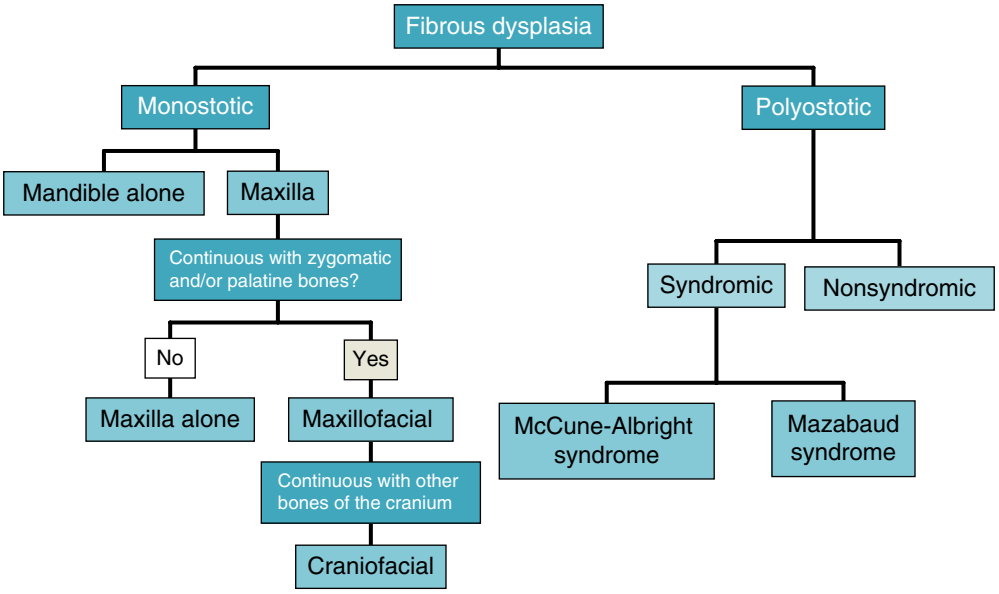


Figure 10.13 Flowchart revealing the classification and nomenclature of fibrous dysplasia affecting the face and jaws.

histopathological element of FD affecting the skeleton outside the jaws [66]. Conversely, the WHO's 2005 edition [69] did not include cartilage as an expected feature of FD affecting the jaws.

FD is a benign noninheritable disease and affects about 1:30 000 individuals [75]. Figure 10.13 reveals the classification and nomenclature of FD affecting the face and jaws. It presents either as a local lesion, the monostotic form, or as a systemic lesion, the polyostotic form. When this last form is combined with hormonal changes, it is *McCune-Albright syndrome* (MAS). Although precocious puberty is one of the most striking features of MAS, there are other causes, which have been extensively discussed by Fahmy et al. [76] A diagnosis of precocious puberty requires radiography of the bones of the wrist to determine the developmental age. Precocious puberty in addition to café-au-lait spots, another striking feature of MAS, indicates a bone scan or other radiology to determine the presence of polyostotic FD [76]. MAS is also now associated with other endocrinopathies [77] and other lesions such as ovarian-follicular cysts [78]. Although Mazabraud syndrome is associated with FD with or without MAS, so far no intramuscular myxomas typical of this syndrome have been reported in the head, face, or jaws [79].

The systematic review on FD affecting the jaws demonstrated that although polyostotic cases occurred in 39% of systematic review–included reports, they constituted only 12% of all cases contained within these reports [80]. It was most likely that these polyostotic cases were already known to the patient due to earlier diagnosis of the perhaps more obvious extragnathic lesions, such as those affecting the limbs. Furthermore, menstruation in an infant girl with MAS would be obvious to her parents. Therefore, for these reasons the polyostotic form is easier to

observe and diagnose. Furthermore, Völkl and Dörr recently suggested that nonendocrine afflictions may accompany polyostotic FD. These include hepatobiliary dysfunction and cardiac disease [81], which may be important risk factors for early death [81], enhancing the importance of the early diagnosis of the polyostotic form. Monostotic FD of the face and jaws, on the other hand, may not be obvious either to the patient or to the clinician, particularly if it has not caused symptoms.

A systematic review of consecutive case series of FD affecting the jaws reveals that over 96% were monostotic (88% for those reports which expressly included polyostotic FD) [80], which is higher than the 60% monostotic overall [75]. A third of cases of monostotic FD affect craniofacial bones [82]. Monostotic means "one bone," which is the correct term when applied to FD affecting the mandible, but is not strictly true when applied to FD affecting the maxilla. The latter may involve one or more contiguous bones such as the zygomatic (malar) and palatine bones. Therefore, "craniofacial fibrous dysplasia" has been coined for such cases and was used by Jundt in the WHO's 2005 edition [69]. The maxillofacial subset of craniofacial FD accounted for 13% in the systematic review [80].

The global distribution of systematic review–included reports is displayed in Figure 1.44 and the details are in Table 10.3. The mean number of cases of monostotic FD per year globally was 1.6. Although this was highest for the sub-Saharan African global group and least for the Western, the difference was not significant [80].

Although it is generally accepted that FD is a disease affecting children and adolescents and burns out at the end of puberty in most cases, this systematic review refutes this contention. Indeed, the majority of cases of monostotic FD first present at over 20 years old (some even as late as the eighth decade), with an overall mean of 24 years (Table 10.3), in contrast to a mean age of 15 years at first presentation overall for all cases of FD [75]. In addition, the period of the patient's prior awareness before first presentation is five years [80]. Taken together, the average patient first becomes aware of the disease at 19 years old, precisely when it is traditionally expected to "burn out" [80]. Burnout will be discussed in more detail later in this chapter. Nevertheless, almost all polyostotic cases first present early in infancy.

Therefore, if it is supposed that all FDs arise during childhood or puberty, most monostotic cases remain undetected, only to become active or be reactivated later and thus be detected for the first time later in life. This conclusion is feasible if the classical division of FD into monostotic, polyostotic, and MAS forms is considered to reflect the timing of the mutation and, thereby, the initial size of the mass of FD precursor cells [75, 83]. The polyostotic form may arise in fetal life, whereas the monostotic form may arise postnatally [83]. Therefore, the earlier the mutation, the more widespread and more severe will be the manifestations [75]. In addition to discussing how the different forms of FD arose, the two cited authorities [75, 83] together comprehensively discuss the genetic basis of this lesion. Some of the discussion on both topics was detailed in their earlier publications, which they cite clearly.

10.11 Demographic and Clinical Presentations

These presentations are detailed in Table 10.3. Although the distribution between the sexes is almost equal, with females prevailing slightly, males

Table 10.3 Fibrous dysplasia: systematic review.

Feature	Total	Caucasian	East Asian	Sub-Saharan African	Latin American
Male: Female	48% : 52%	46% : 54%	50% : 50%	42% : 58%	88% : 12%[a]
Mean number per year per report	1.6	0.9	1.9	3.2	0.1
Mean prior awareness	5.2 years	5.7 years	3.6 years	6.3 years	4.5 years
Mean age	24 years	25 years	24 years	23 years	16 years
Mandible: Maxilla	42% : 58%	48% : 52%	41% : 59%	39% : 61%	0% : 100%[a]
Mandible: *Anterior: Posterior*	14% : 86%[a]	7% : 93%[a]	30% : 70%[a]	0% : 100%[a]	N/A
Maxilla: *Anterior: Posterior*	19% : 81%	25% : 75%[a]	12% : 88%[a]	57% : 43%[a]	0% : 100%[a]
Swelling: *Yes: No*	93% : 7%	98% : 2%	90% : 10%	95% : 5%[a]	100% : 0%[a]
Pain: *Yes: No*	19% : 81%	12% : 88%	26% : 74%	5% : 95%[a]	50% : 50%[a]
Incidental finding: *Yes: No*	2% : 98%	2% : 98%	3% : 97%	100% : 0%[a]	100% : 0%[a]
Radiolucent: *Yes: No*	5% : 95%	7% : 93%	4% : 96%	8% : 92%[a]	N/A
Ground glass: *Yes: No*	38% : 62%	54% : 46%	38% : 62%	28% : 72%	N/A
Expansion: *Yes: No*	100% : 0%	100% : 0%[a]	100% : 0%	100% : 0%[a]	N/A
Downward expansion of lower border of mandible: *Yes: No*	100% : 0%[a]	100% : 0%[a]	100% : 0%[a]	100% : 0%[a]	N/A
Affects maxillary sinus: *Yes: No*	98% : 2%[a]	100% : 0%[a]	100% : 0%[a]	88% : 12%[a]	N/A
Tooth displacement: *Yes: No*	35% : 65%	41% : 59%[a]	28% : 73%[a]	75% : 25%[a]	N/A
Root resorption: *Yes: No*	2% : 98%	100% : 0%[a]	2% : 98%	N/A	N/A
Reactivation: *Yes: No*	18% : 82%	4% : 96%	16% : 84%[a]	72% : 28%[a]	18% : 82%[a]

[a] Percentages derived either from one report or from a synthesis of no more than 50 cases.
N/A, information not available.

predominated 2 : 1 in the second decade, in which 36% of all FDs of the jaws first presented. Males also slightly predominated in the third decade, but are in the minority in all other decades [80].

Most cases of FD affecting the jaws do not become "quiescent during puberty" as is typical of extragnathic cases of FD [74]. Instead, almost all cases first present to the clinician with symptoms. In spite of the fact that, at first presentation, the FD lesions in one recent report were so large that many affected all or most of the hemimandible or hemimaxilla, very few

were discovered as incidental findings. Furthermore, the clinicians offered solely fibrous dysplasia as their provisional diagnosis only on the basis of their clinical and radiological findings [59].

Only 2% of FDs are discovered as incidental findings in the systematic review; the rest presented with symptoms [80], swelling in 93% of cases. Swelling was significantly more frequent in the Caucasian global group than in the East Asian global group. Overall, 19% presented with pain [80]. A higher proportion of East Asian cases presented with pain in comparison to other global communities. In the jaws, the maxilla is affected in 58% of cases; the Caucasian global group approached equal distribution between the jaws. FD displays an overwhelming predilection for the posterior sextants of both jaws [80].

The fact that only 2% of monostotic FDs were discovered incidentally may be due to the fact that FDs on conventional radiographs have poorly defined margins and therefore do not readily draw the dentist's attention to their presence, unless they are so large that they affect all or most of the hemimandible or hemimaxilla, as in the aforementioned case series [59]. Although FDs may not be readily obvious as incidental findings, nevertheless, as already discussed, many patients may be well aware of their lesions on average five years prior to first presenting with them [80].

10.12 Radiology

These presentations are detailed in Table 10.3. Radiologically, overall FD presents with the classical fusiform (spindle) shape (Figures 10.12, 10.14–10.16), which is even observed if the lateral wall of the antrum is affected (see Figure 11.39) [84].

The fusiform shape is not only obvious on lateral projections, such as panoramic radiographs (Figure 10.14), but on true occlusals (Figure 10.12) and axial reconstructions of CT (Figures 10.14 and 10.15) and CBCT (Figure 10.16) datasets. All cases displayed expansion, which was fusiform in the mandible (see Figures 10.12, 10.14–10.16), and an enlargement of the normal contour in the maxilla (see Figure 11.37).

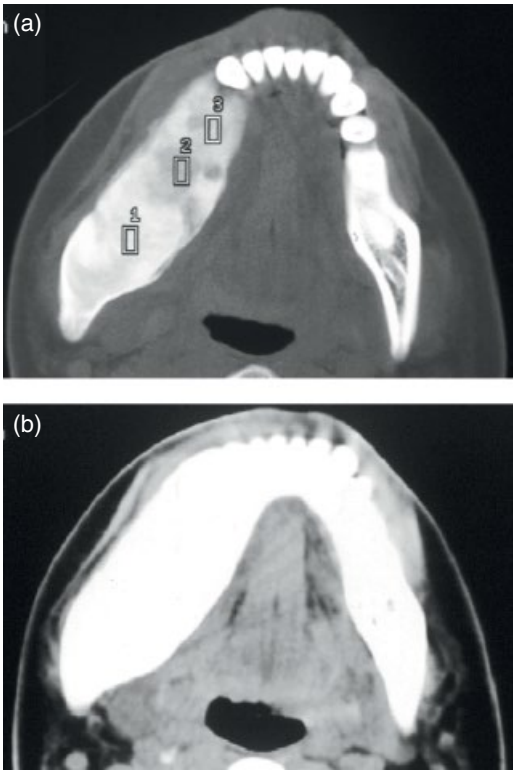


Figure 10.14 Axial bone window (a) and soft-tissue window (b) computed tomography of the same case displaying a fusiform shape. Note: The area covered by the image of the bone in a soft-tissue window is larger than that covered by the image of the same bone in the bone window.

The fusiform shape of FD is not the only feature that distinguishes it from the frequently ball-like expansion of OF, the other important FOL, which is treated entirely differently to FD. Unlike OF, which is well defined, FD has a poorly defined margin with regard to adjacent

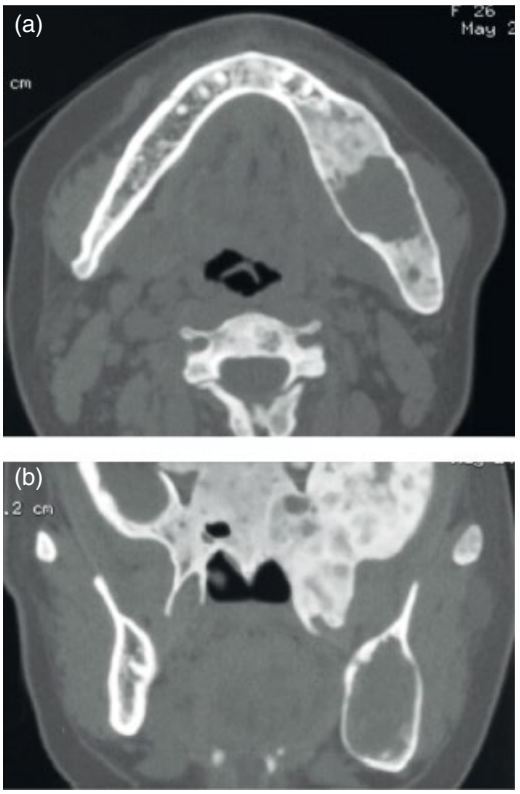


Figure 10.15 Computed tomography (CT) of a polyostotic case. (a) Axial CT (bone window) displays fusiform expansion and a radiolucent area in the center of the lesion. This is generally unusual in monostotic cases. (b) Coronal CT (bone window) through the same radiolucency displaying expansion in all directions in comparison with the normal contralateral side. The ipsilateral maxilla also is affected in this polyostotic case. See Figure 18.22, which displays a sagittal section exhibiting involvement of the basioccipital bone.

normal bone; this is particularly obvious in the mandible on panoramic radiographs (Figure 10.12). As already stated, in addition to an FOL histopathology, a radiologically poorly defined margin is an essential criterion for a firm diagnosis of FD. This feature is best displayed by conventional radiography by virtue of its superior spatial resolution [84], and is not so obvious on CT due to its poorer spatial resolution. The recent advent of CBCT (Figures 10.16 and 11.40) now means that this feature in the jaws can be displayed with a better spatial resolution and a reduced radiation dose, but really only with a small field of view (FOV), as many current CBCT units rightly restrict the highest spatial resolution only to the smallest FOV in order to limit the radiation dose to the patient. Nevertheless, once a diagnosis has been made on conventional radiography, CT (including CBCT) can more readily display the full extent of the lesion, particularly within the more anatomically complex maxilla (see Figures 11.37–11.44) [84].

The pattern of the dysplastic bone in 38% of cases is predominantly ground glass (Figure 10.12). This pattern is significantly more frequently observed in Caucasian than in sub-Saharan African communities. Presentation was predominantly sclerotic in 7% of cases and radiolucent in 5% (Figure 10.15), while 7% presented as peau d'orange (Figures 10.17 and 10.18) [80]. Only one report in a recent systematic review on FD reported three of its cases as multilocular radiolucencies [80]. These cases appeared in a report four decades ago and can be discounted because they may represent cherubism (see Chapter 9), which had at that time been considered a manifestation of FD. The radiolucency in Figure 10.15 occurred within the dysplastic bone and did not abut normal adjacent bone.

The lower proportion of the ground-glass pattern in this systematic review [80] conflicts with Jundt's definition of FD [69]. His specification of ground glass as the sole pattern in his definition may be understood as perhaps being derived from the presentation of FD on CT [83], the modality he clearly favored. Nevertheless, by reference to Figures 10.12, 10.14–10.18 and 11.37–11.44, it can be seen that FD

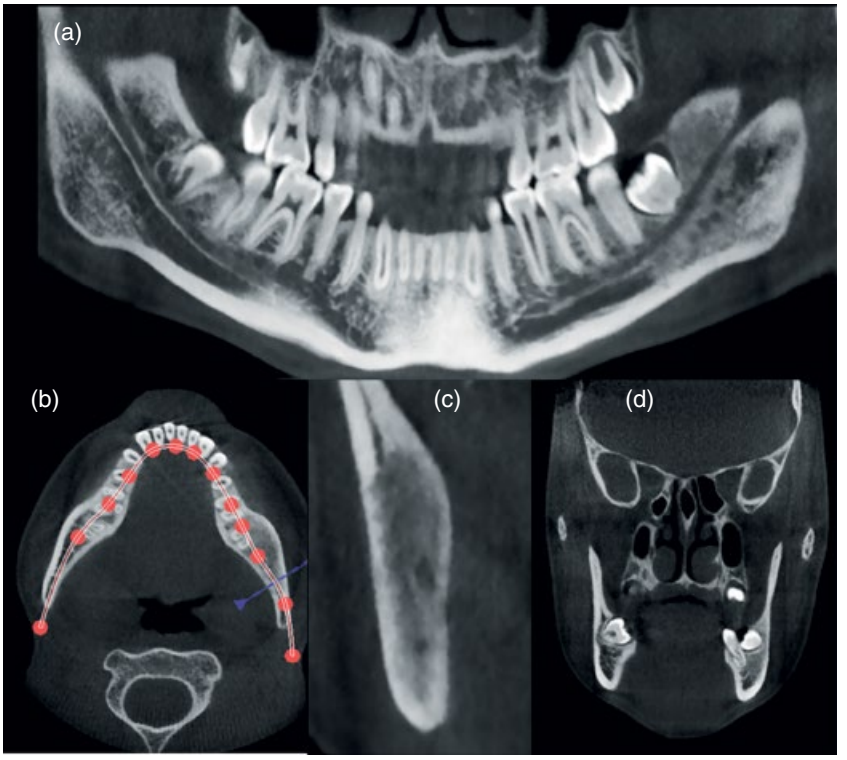


Figure 10.16 Cone-beam computed tomography (CBCT) of a case of fibrous dysplasia (FD) affecting the ramus and posterior body of the left side of the mandible. (a) Panoramic reconstruction; (b) Axial reconstruction from which the panoramic (a) and transaxial (c) reconstructions were derived. (d) Coronal reconstruction of this large field-of view CBCT through the anterior-most part of the middle cranial fossa and the third molar teeth. The most striking feature is the mandibular canal on the left side, in contrast to its less obvious equivalent on the right side. The lesion's margin is poorly defined in (a). The little buccolingual expansion in (b) is suggestive of fusiform expansion. The dysplastic bone generally has a ground-glass appearance, certainly in (b–d). The only dysplastic area displayed in (d) is in the already identified left mandible. This observation, in the absence of similar lesions elsewhere in the skeleton, is suggestive of the monostotic form of FD. Source: MacDonald, D.S. (2015). Maxillofacial fibro-osseous lesions. *Clin. Radiol.* 70: 25–36 and courtesy of Dr. David Gane, CEO and President, LED Medical Diagnostics.

has a wide range of presentations on conventional radiography as well as CBCT and CT. The better spatial resolution of conventional dental radiography in comparison to CT permits more patterns of dysplastic bone to be seen, not only the ground-glass pattern [59]; the latter was only apparent in 38% of FD cases on conventional radiography, in contrast to 100% on CT [80]. This was confirmed in another consecutive case series of FD investigated by CT [85]. Nevertheless, CT can more readily display the full extent of the lesion, particularly within the more anatomically complex maxilla (Figures 11.37–11.44) [84]. The maxillary sinus is completely or partially obturated in nearly every case of FD (Figures 11.37–11.43).

The displacement of the mandibular canal differed between reports. It was

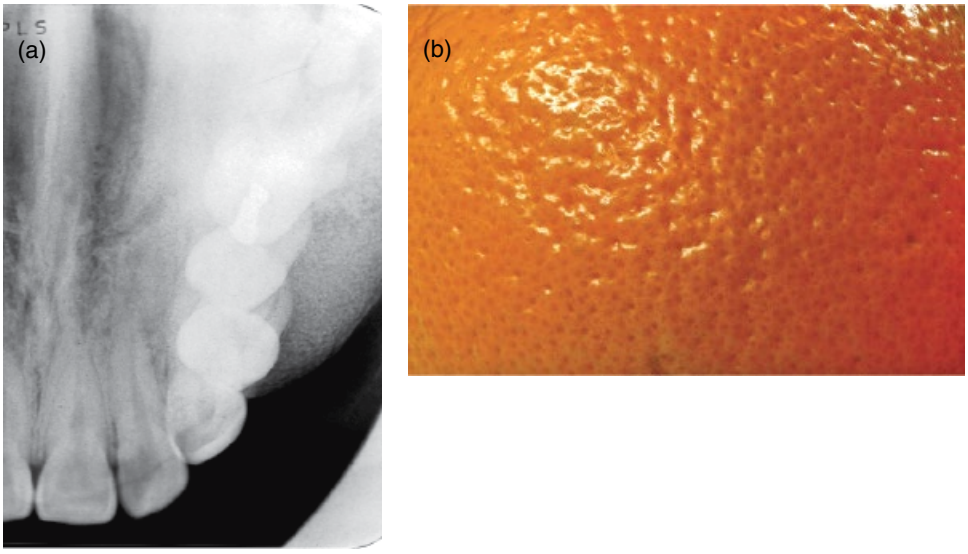


Figure 10.17 (a) Standard occlusal image of the maxilla displaying fibrous dysplasia. There is no displacement of teeth. The buccal cortex has been expanded and exhibits a peau d'orange (orange peel) appearance, whereas the palatal portion displays a ground-glass appearance. (b) Photograph of orange skin (peau d'orange) displaying its characteristic stippled surface. Source: (a) MacDonald-Jankowski, D.S. and Li, T.K. (2009). Fibrous dysplasia in a Hong Kong community: the clinical and radiological features and outcomes of treatment. *Dentomaxillofac. Radiol.* 38: 63–72.

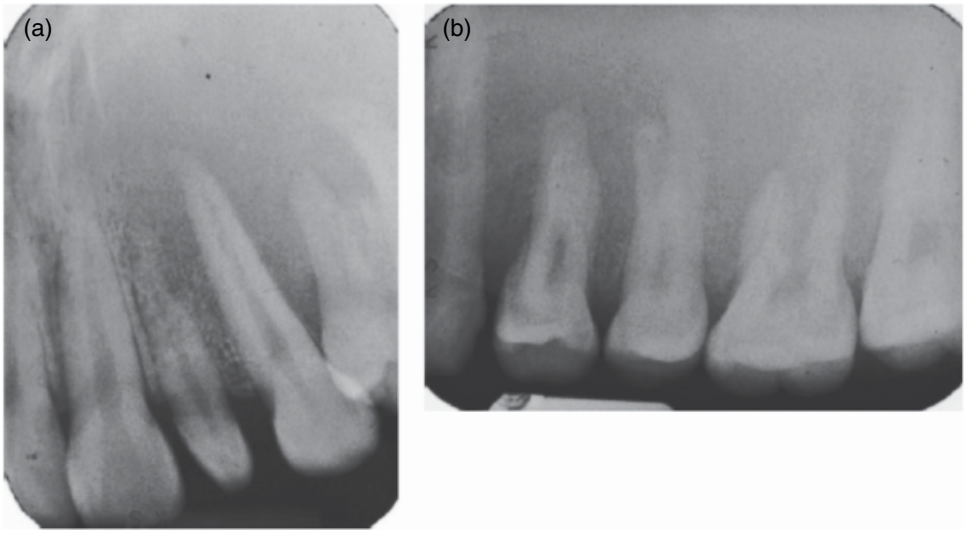


Figure 10.18 Periapical radiographs of fibrous dysplastic lesions affecting the maxilla. The teeth embedded within the dysplastic bone have no lamina dura, although a periodontal space is apparent. (a) A peau d'orange pattern; (b) a ground-glass pattern. In (b) the roots within the dysplastic bone display an abnormal shape and root resorption.

displaced downward (see Figures 1.12 and 10.12) in a Canadian report [42], and either upward or downward in a Hong Kong Chinese report [59]. This may reflect differences between global communities. Petrikowski et al. [42] suggested that the loss of the lamina dura within the dysplastic lesion can be used to confirm a radiological diagnosis of FD (see Figure 10.18).

Teeth were displaced in 35% of cases, significantly more in Caucasian than in East Asian reports. Root resorption (see Figure 10.18) was observed in only two cases in an East Asian report [80].

Teeth were displaced in 35% of cases (see Figures 1.12 and 10.12) [80]. This tooth displacement was observed significantly more in Caucasian than in East Asian reports [80]. It contributes to a malocclusion, which may require orthodontics. Although osseointegrated implants into the dysplastic bone have so far survived for up to five years, their longer-term survival is uncertain [86]. In addition, one of these cases displayed abnormally shaped roots (see Figure 10.18). This may have been induced by the adjacent dysplastic process during the development of the root [59]. Although root resorption is rarely observed [80], the loss of the lamina dura within the dysplastic lesion can be used to confirm a radiological diagnosis of FD [42].

When displayed on CT the cortex is generally intact, except when adjacent to the teeth in the maxilla. The margins were usually poorly defined, but were well defined on at least some sections of each maxillary case [84].

The bone windows generally displayed a ground-glass pattern; one also displayed cyst-like radiolucencies (see Figures 10.15 and 11.37). The soft-tissue window, which depicts mineralized tissue as white, showed that five cases were completely mineralized. Compare the bone windows of Figures 4.5a and 10.14a with their corresponding soft-tissue windows, Figures 4.5b and 10.14b [84].

10.13 Clinical Implications and Considerations

10.13.1 BURNOUT AND REACTIVATION

Although surgery of FD during its active growth period may cause increased growth, in the past it was generally the view that it would best to await "burnout" of the lesion's growth, which should coincide with the cessation of the individual's growth, namely early adulthood. As already noted, the view that burnout occurs in late adolescence has been refuted by the systematic review [80]; the majority of cases in the systematic review first presented older than the second decade. Although "burnt out," the now quiescent FD does not involute back to normal lamellar bone, certainly in the case of a woman whose first diagnosis of FD had been made 60 years earlier. Her autopsy revealed that the dysplastic bone was similar to that seen in active cases, with no evidence of involution to normal lamellar bone [87].

There have been very few case series that have been followed up for a long period. The longest and largest case series of FD of the jaws is that of the Hong Kong Chinese, in which 17 patients were followed up for a mean of nine years [59]. Follow-up is important, because not only does FD generally not involute to lamellar bone, except perhaps in one case [88], it may undergo reactivation in adult life by a precipitating event such as pregnancy. A woman was blinded in one eye by the reactivation of FD during her pregnancy [89]. This reactivation in the pregnant female may be due to the elevation in sex hormone receptors in the mutated cells [75]. Furthermore, Jacobsson et al. reported recurrent episodes of pain

and swelling in 15 females followed over 15 years [90]. Reactivation is not just confirmed to females with FD; males have also occasionally exhibited reactivation [59].

Despite the paucity in follow-up, 18% of cases in a systematic review exhibited reactivation [80]. This happens significantly more in the sub-Saharan African global group than in the Caucasian and East Asian global groups [80]. I have used the term "reactivation" rather than "recurrence," because the former more accurately describes FD's response to life events, such as pregnancy, rather than to a failure to ablate the lesion completely in the manner of a neoplasm, which is generally implied by the term recurrence. Although it is clear from the preceding paragraph that the majority of FDs do not comfortably rest within the definition of a harmatoma, neither are they neoplasms. Therefore, it is for this reason that FDs are placed at point 2 in the scale of severity of outcomes (see Table 1.3).

10.14 Surgery: What Kind? When and When Not

Readers should be aware that there is a misunderstanding among some head and neck surgeons that FD and OF are part of the same disease spectrum [91] and that FD is a true neoplasm. As a result, FD of the face and jaws in these communities has been routinely and unnecessarily resected [92]. Furthermore, due to previous subjective reports of reactivation of FD by jaw surgery, some dentists are uncomfortable about treating FD patients [93]. Fortunately, if the lesion is monostotic and confined to either jaw, then no treatment is required except to address a disfiguring deformity. Awaiting the onset of burnout in late adolescence may not be a real option for a severe deformity in early adolescence, because of the psychological injury it may provoke. In such cases surgical reduction is usually achieved conservatively by "shaving."

Surgery is generally indicated if there is a threat to vision, which occurs particularly when the FD reduces the diameter of the optic canal [86]. Although blindness is a real risk for FD primarily involving the skull base (optic canal), there appears to be no report of blindness caused directly by FD arising from the jaws. While CT is invaluable for measurement of the optic canal's diameter in cases of craniofacial FD encasing the optic canal, MRI may be more appropriate for children [75]. Ricalde et al. stated that although detailed visual field assessments performed by an ophthalmologist are more sensitive than CT, it remains critical to survey patients with CT at established intervals [86]. They cautioned that, regardless of the diameter of the optic canal, "immediate surgical decompression can be considered for patients with acute visual loss in the presence of objective signs of neuropathy and deteriorating vision" [86]. The fact that not one case of proptosis was reported in a total of over 336 maxillary cases of FD in a systematic review [80] indicates that this is not a frequent finding of cases of FD arising primarily in the jaws. This is particularly surprising considering the substantial increase in the vertical dimension of the maxilla observed in one CT series [84]. Nevertheless, at least one case of proptosis has occurred in a case of monostotic FD (Figure 11.37) affecting the maxilla alone [84].

Similarly, some oral and maxillofacial clinicians may express concern that bisphosphonate treatment, albeit low dose, for FD may provoke bisphosphonate-osteonecrosis of the jaws [93]; see the discussion of MRONJ earlier in the chapter.

10.15 Risk of Pathological Fracture of Fibrous Dysplasia of the Jaws

Although the risk of pathological fracture is highest in polyostotic cases, especially in MAS, de Mattos et al. report that around 50% of monostotic cases fracture [94]. Nevertheless, this risk does not appear to extend to FD affecting the jaws, as only one case of apparent pathological fracture and nonunion has been reported for FD affecting the mandible [95]. Therefore, although biopsy may result in a fracture risk in FD affecting the extragnathic skeleton [75], this may not be so for FD in the jaws. However, it is a generally accepted principle that the biopsy should be deferred until all necessary imaging has been completed; otherwise, the radiological presentation may be compromised (see Figure 1.3). Biopsies are still necessary for the histopathological diagnosis of FOL, which in conjunction with a poorly defined margin of a radiopaque lesion on conventional radiography is necessary for the diagnosis of FD. Biopsy is also required to refine our understanding of the genetics of FD. It is needed too for the identification of markers for future adverse conduct such as reactivation.

10.16 Aneurysmal Bone Cysts and Osteosarcomas

In addition to reactivation, follow-up is recommended for other lesions arising secondarily within the FD lesion. The two most important are *aneurysmal bone cysts* (ABCs) and osteosarcomas.

The association of ABCs with FD of the long bones and spine is well known. Although ABCs have occasionally been found in FD of the base of the skull [96], no detailed report of ABC arising in FD of the jaws has so far been recorded.

FD's reputation for undergoing sarcomatous change was not reflected in any case series of monostotic FD of the jaws recently [80]. Cheng et al. reported three cases of sarcomatous transformation in the 324 cases of craniofacial FD that presented to them over 17 years [97]. All three cases were polyostotic. Cheng et al. [97] suggested that sarcomatous transformation occurs spontaneously with MAS more frequently than for the monostotic form, reinforcing the results of the systematic review [80]. A periosteal reaction was only apparent in one of eight cases of sarcomatous transformation in FD investigated by CT, but mineralization of the tumor matrix was observed in six [98]. Furthermore, though soft-tissue extension was observed in six cases, postcontrast enhancement was observed only in one [98]. Although the lamina dura of the periodontal ligament is replaced by dysplastic bone, the space is not only still patent, but subjectively it appears to be narrower than normal [42], therefore any widening should be viewed as suspicious. Nevertheless, "the majority of high-grade central osteosarcomas do not pose diagnostic difficulties, especially when histological features are correlated with radiological and clinical findings" [99]. This is not true for many low-grade osteosarcomas [100]. In such cases the markers for osteosarcoma, *cyclindependent kinase 4* (CDK4) and *murine double-minute type 2* (MDM2), may assist [99, 100].

10.17 Ossifying Fibroma (ICD-O 9262/0)

The term OF has been adopted by the WHO's 2005 edition [63] in preference to its 1992 edition's cemento-ossifying fibroma [101], a histopathological descriptive

term denoting the varying mixture of osseous and cementoid elements. As both elements are now recognized as variants of abnormal bone, the term "cemento-ossifying" is redundant.

Slootweg and El Mofty defined OF as "a well-demarcated lesion composed of fibrocellular tissue and mineralised material of varying appearances" [63]. The majority present in adulthood in the teeth-bearing jaws (Figure 10.19), whereas a few present in younger individuals as *juvenile trabecular ossifying fibroma* (JTOF) and *juvenile psammamatoid ossifying fibroma* (JPOF) [63]. JTOF arises in the maxilla of children at 8–12 years old (Figure 11.45), whereas JPOF arises in the bony walls of paranasal sinuses (Slootweg's Figure 6.72) of older teenagers or young adults [63]. In addition to these features, conventional OF can be further distinguished from JTOF and JPOF. Conventional OF has an observable capsule radiologically and histologically (Figures 10.19 and 10.20), whereas JTOF and JPOF do not (Figure 11.45) [102, 103]. The appearance of this capsule radiologically clearly depends upon the spatial resolution of the imaging technology used. Figure 10.20a displays a definite but thin capsule (appearing as a radiolucent line) on a conventional intraoral sensor, which is not as easily visible on the CBCT images (Figure 10.20b, c).

The global distribution of reports included in the systematic review [104] from which much of the following is derived is set out in Figure 1.45 and the details are in Table 10.4.

A hitherto underconsidered aspect of OF is a possible association with familial hyperparathyroidism, *hyperparathyroidism–jaw tumor syndrome* (HPT-JT). This is autosomal dominant [105]. A secreting carcinoma is the cause in 10–15% of

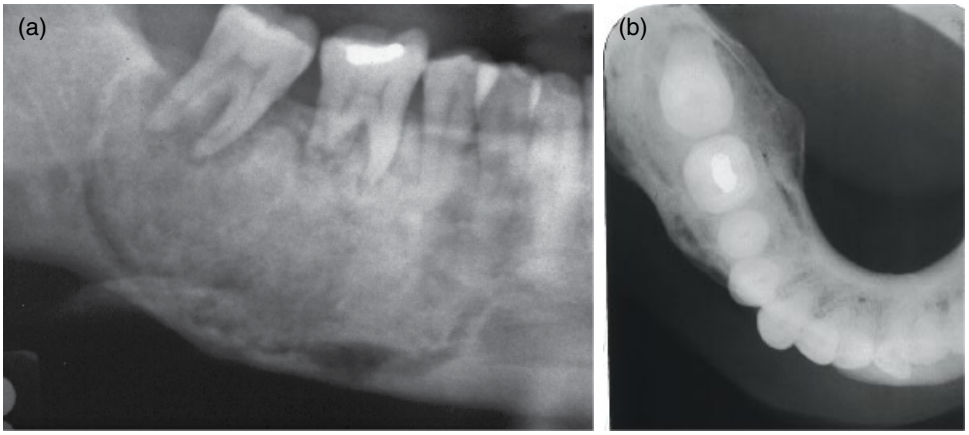


Figure 10.19 Conventional radiography of ossifying fibroma (OF) affecting the posterior mandible. (a) Panoramic radiograph displaying an OF with a well-defined periphery. The central radiopacity is separated from the normal adjacent bone by a radiolucent space representing the capsule. The central radiopacity displays both peau d'orange and cotton-wool sclerosis. The mandibular canal has been displaced. The lower border of the mandible has not only been displaced, but is also eroded. The roots of the first molar tooth have been resorbed and the roots of the second molar appear to be displaced distally. (b) True occlusal radiograph displaying buccolingual expansion. Source: MacDonald-Jankowski, D.S. and Li, T.K. (2009). Ossifying fibroma in a Hong Kong community: the clinical and radiological features and outcomes of treatment. *Dentomaxillofac. Radiol.* 38: 514–523.

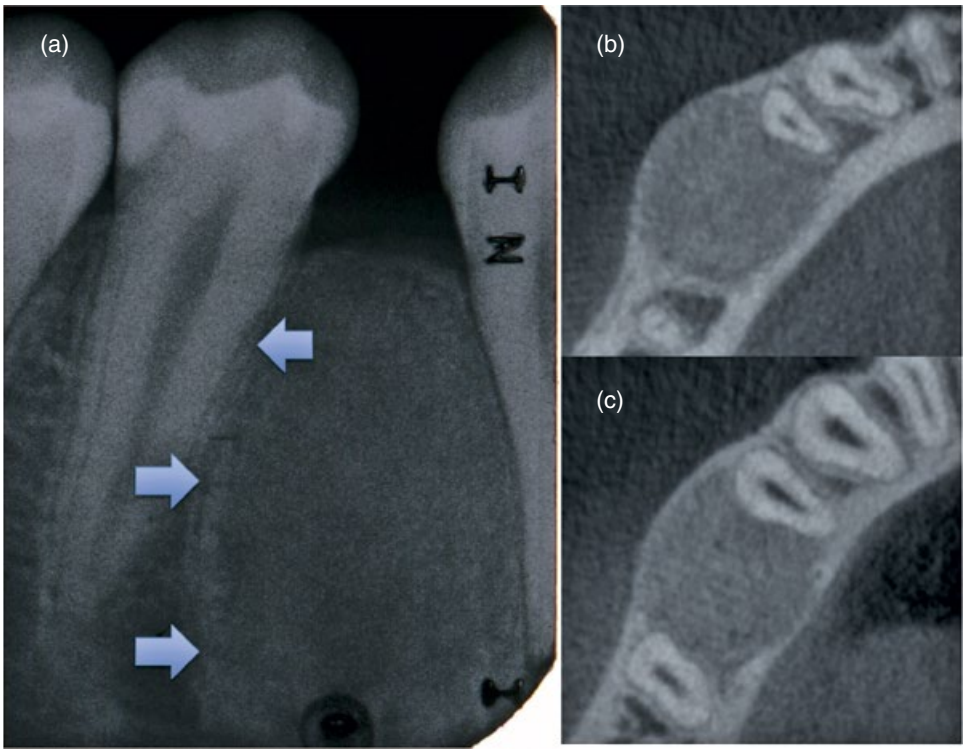


Figure 10.20 Periapical radiograph (a) displaying a well-defined "ground-glass" radiopacity displacing the adjacent teeth. It is separated from the normal adjacent bone by a thin radiolucent space (blue arrows). This space represents the capsule. The cone-beam computed tomography axial reconstructions of the dataset (b and c) exhibit a rounded buccolingual expansion, particularly in (b). Both the buccal and lingual cortices are also eroded (thinned). The radiolucent space on the distal aspect of the lesion represents the capsule space seen on its mesial aspect in (a). This lesion is an ossifying fibroma. Source: MacDonald, D.S. (2015). Maxillofacial fibro-osseous lesions. *Clin. Radiol.* 70: 25–36.

cases [105]. The loss of staining for parafibromin, caused by its inactivation by the HRPT2 gene [106], can be used to predict an increased risk of death or recurrence [107]. Furthermore, its course is more aggressive, causing more severe hypercalcemia, which may actually precipitate a hypercalcemic crisis [105].

The mean number of cases of OF per year globally was 1.7 [104], similar to FD [80]. Again, as for FD, although this was highest for the sub-Saharan African global group and lowest for the Caucasian, the difference was not significant [104].

OF has a predilection for females (71%) and is similar for all global groups. Mean age at first presentation is 31 years. The East Asian global group with the oldest mean age (35 years) is significantly older than the sub-Saharan African group with the youngest mean age (19 years) [104]. The peak decade for first presentation is the third and fourth decades equally; they account for nearly half of all cases. Sub-Saharan Africans present in the second decade, whereas the other three global groups present in the fourth decade [104]. Males account for nearly half of cases in the second decade, but for only 15–20%

Table 10.4 Ossifying fibroma: systematic review.

Feature	Total	Caucasian	East Asian	Sub-Saharan African	Latin American
Male: Female	29% : 71%	31% : 69%	26% : 74%	33% : 67%[a]	25% : 75%[a]
Mean number per year per report	1.7	1.1	1.6	3.0	0.5
Mean prior awareness	1.7 years	0.9 year	2.8 years	1.4 years	N/A
Mean age	31 years	32 years	35 years	19 years	33 years[a]
Mandible: Maxilla	75% : 25%	78% : 22%	83% : 17%	48% : 52%	65% : 35%[a]
Mandible: *Anterior: Posterior*	37% : 63%	50% : 50%	17% : 83%	33% : 67%[a]	18% : 82%[a]
Maxilla: *Anterior: Posterior*	32% : 68%	35% : 65%[a]	25% : 75%[a]	50% : 50%[a]	17% : 83%[a]
Swelling: *Yes: No*	66% : 34%	42% : 58%	79% : 21%	100% : 0%[a]	N/A
Pain: *Yes: No*	16% : 84%	13% : 87%	20% : 80%	0% : 100%[a]	N/A
Incidental finding: *Yes: No*	31% : 69%	43% : 57%	23% : 77%	0% : 100%[a]	N/A
Radiolucent: *Yes: No*	26% : 74%	36% : 64%	21% : 79%	10% : 90%[a]	N/A
Unilocular: Multilocular	80% : 20%	76% : 24%	90% : 10%[a]	N/A	N/A
Cortex: *Yes: No*	53% : 47%	53% : 47%[a]	52% : 48%	N/A	N/A
Expansion: *Yes: No*	84% : 16%	72% : 28%[a]	86% : 14%	100% : 0%[a]	N/A
Downward expansion of lower border of mandible: *Yes: No*	50% : 50%[a]	25% : 75%[a]	45% : 55%[a]	100% : 0%[a]	N/A
Affects maxillary sinus: *Yes: No*	90% : 10%[a]	100% : 0%[a]	100% : 0%[a]	67% : 33%[a]	N/A
Tooth displacement: *Yes: No*	27% : 73%	28% : 72%	25% : 75%[a]	N/A	N/A
Root resorption: *Yes: No*	20% : 80%	25% : 75%	4% : 96%[a]	N/A	N/A
Recurrent: *Yes: No*	12% : 88%	16% : 84%	7% : 93%[a]	10% : 90%[a]	N/A

[a] Percentages derived either from one report or from a synthesis of no more than 50 cases.
N/A, information not available.

in the subsequent three decades. The mean period of prior awareness for OF is 1.7 years [104].

Detection as incidental findings occurs in 31% of cases, whereas 66% first present with swelling and 16% with pain. Swelling presents significantly more frequently in the East Asian than in the Caucasian global group and vice versa for cases discovered as incidental findings. The mandible is affected in 75% of cases, except for sub-Saharan Africans, among whom both jaws are affected equally. This was particularly significant in comparison to the 83% : 17% (5:1) mandible : maxilla ratio in East Asians. Mandibular cases of OF are equally distributed between the anterior and posterior sextants only in the Caucasian global group. The other global groups display a predilection for the posterior sextant, particularly in East Asians with an anterior : posterior sextant ratio of 17% : 83%. Overall, the anterior sextant of the maxilla is affected in only 32% of cases [104].

Although the internal structure of OF on conventional radiography is similar to FD, reflecting their similar histopathology, OF has a capsule. This capsule is represented by a well-defined radiolucent line sharply separating the lesion from the adjacent normal bone [108]. This feature can be easily and cheaply appreciated on a single conventional image, such as a panoramic radiograph (see Figure 10.19a). This image can be, if necessary, supplemented by intraoral images, such as a true occlusal (Figure 10.19b) or a periapical (Figure 10.20b).

The predominant radiological pattern (radiolucency, radiopacity within a radiolucency, or completely radiopaque) varied significantly between global groups. It also varied between reports within these groups, indicating that the pattern will vary with the community reported, which may be in turn be influenced by age at first presentation [104]. The classical presentation of a radiopacity within a radiolucency (see Figure 10.19a) is the case for 58%, while 26% are radiolucent (Figure 10.21) and 16% are completely opaque. The OFs in an East Asian report are equally divided between those that have a round or oval shape [60]. The oval-shaped OFs are significantly larger. Half of them present in females of 45 years or older [60].

The juvenile OF variants (JTOF and JPOF), with no capsule, displayed no radiolucent line separating the neoplastic tissue from the adjacent normal bone. This lack of a clear margin may contribute to their

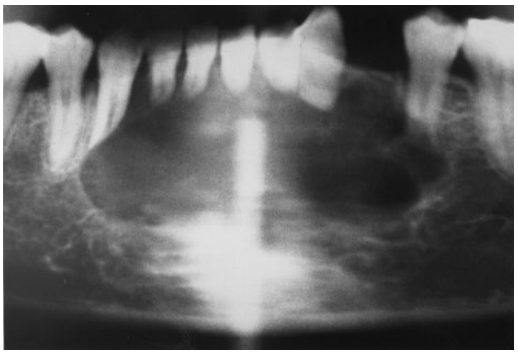


Figure 10.21 Panoramic radiograph of an ossifying fibroma presenting in its initial or early radiolucent stage. The presentation in this stage can be as multilocular radiolucencies. In addition to tooth displacement, this case also displays root resorption, which is strongly suggestive of a solid ameloblastoma. Note: Generally, lesions are infrequently as well and accurately displayed in the midline of a panoramic radiograph as in this case. This investigation should normally be supplemented by pulp testing and intraoral radiographs. Source: Reproduced with permission from MacDonald-Jankowski, D.S. (2004). Fibro-osseous lesions of the face and jaws. *Clin. Radiol.* 59:11–25.

higher recurrence rates, since surgeons are deprived of a clear margin during surgery. This is a problem if a conservative approach is adopted. In a recent study, all 3 cases of JOF that were curetted out alone recurred, whereas the 12 which were more radically treated did not [109].

Fifty three percent present with a cortex and buccolingual expansion in 84% of cases (Figure 11.45). Although OF can display substantial buccolingual expansion, this is not always so, because the buccolingual expansion may not always reflect the mesiodistal extension of the neoplasm (see Figures 10.19 and 10.22) [104]. The buccolingual expansion displayed in Figure 10.22 varies with the extent of erosion of the buccal and lingual cortices. Those of the body of the mandible as in Figure 10.22 are thicker than elsewhere in the jaws (see Figure 11.45). This difference was also reported in Chapters 9 and 11 for the keratocystic odontogenic tumor (KCOT). The degrees of cortical erosion and of buccolingual expansion are not consistent for every lesion. An extensive cortical erosion, but minimal buccolingual expansion, is obvious in the later Figures 10.24, 10.28 and 10.29, examples of ODs, another FOL, affecting the body of the mandible.

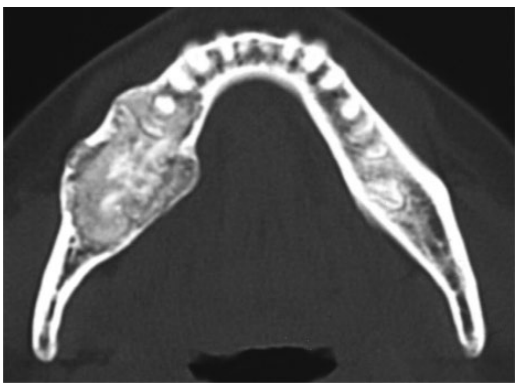


Figure 10.22 Axial computed tomography (bone window) of an ossifying fibroma displaying buccolingual expansion. The periphery of the lesion is well defined. The cortex is eroded at several points.

The lower border of the mandible presents with erosion and/or displacement (see Figures 1.8, 10.19, and 10.20) in half of mandibular cases [104]. The maxillary antrum is involved in 90% of cases of OF subjacent to it [104].

Teeth are displaced in 27% of cases (Figures 10.20) and roots are resorbed in 20% of cases (see Figure 10.19 and 10.21) [104]. The sole East Asian report in the systematic review displayed significantly fewer cases of root resorption in comparison to one of two Caucasian reports [104]. There was no overall significant difference between the East Asian and Caucasian global groups [104].

Brannon and Fowler determined that all OFs need to be enucleated completely to prevent recurrence [65]. Nevertheless, OFs do recur after careful surgery; 12% recurred overall, with no difference between global groups [104].

10.17.1 ADVANCED IMAGING OF FIBRO-OSSEOUS LESIONS

Although FD extensively involving the skull and especially the skull base should be examined by CT and perhaps also MRI, FD confined to the jaws may require this, particularly when encasing of the optic foramen is suspected. As already revealed, the distinguishing of FD of the jaw from OF is primarily achieved by conventional radiography. Other than delineating the full extent of the FOL, particularly of the maxilla, on the basis of the literature to date CT contributes little extra clinically important information. Nevertheless, it is important to report what the other literature has revealed about the application of CT and/or MRI to FD and/or OF so far.

Because the signal intensity on T1-weighted and T2-weighted MRI images is dependent upon a number of factors, such as the amount of bone trabeculae and degree of cellularity [110], FD and OF both show an intermediate signal on T1-weighted and a hypointense signal on T2-weighted images [111]. The hypointense signal intensity on T2-weighted images is caused by numerous bony trabeculae [24]. In the early stage of FD, there may be areas of T2-weighted hyperintensity [111]. This may correlate with the bone resorption phase of early FD. Although intravenous contrast (gadolinium) produces a moderately enhanced signal for OF, it is often marked for FD. In the two decades since the publication of these papers, there have been no others on this topic. This may reflect not only the adequacy of these sources that needed no improvement, but also that conventional radiography is adequate in distinguishing FD of the jaws from OF in almost every case [41].

10.17.2 A NEW POINT RAISED BY THE WHO'S 2017 EDITION

The WHO's 2017 edition included a species of lesion termed the cemento-ossifying fibroma (COF), which was also awarded a separate ICD-O code (ICD-O 9274/0) in the chapter on benign mesenchymal odontogenic tumors [112], whereas the ossifying fibroma was cited in the chapter on fibro-osseous and osteochondromatous lesions with ICD-O 9262/0 [113]. The case for this dichotomy has not been made upon strong evidence. MacDonald's doctoral dissertation considered the differences between the three histological subtypes of OF – OF, COF, and *cementifying fibroma* (CF) – and found no clinically significant difference, save that the "OF form predominates in the first 3 decades, and the CF in the next 3 decades and disappears from the last 2" [114]. COFs were found in all but the youngest and oldest decades (70 years of age and above) [114]. According to Wright and Vered, this was done "to distinguish it from the juvenile categories of ossifying fibroma, but for practical reasons, it will be discussed with the other ossifying fibromas under fibro-osseous lesions" [72]. In summary, confusingly, "ossifying fibroma" remains the overarching term for all three subtypes of OFs, even though one, COF, now has its own separate ICD-O code.

10.17.3 CLINICAL IMPLICATIONS OF OSSIFYING FIBROMA

After treatment, which is generally enucleation, 12% of OFs recur [104]. There was no difference in recurrence between global groups. There is some circumstantial evidence that the onset of menopause may initiate, reactivate, or accelerate growth. Those cases first presenting during menopause were significantly larger than those first presenting between attainment of the peak bone mass and menopause [60].

10.18 Osseous Dysplasia

For the same reasons given earlier for OF, the WHO's 2005 edition [91] preferred to use osseous dysplasia (OD) rather than the cemento-osseous dysplasia (COD) used in the WHO's 1992 edition [101]. As the reasoning for the WHO's 2017 edition's reversion to COD was not compelling, this textbook will continue to use OD.

This FOL has now been divided into two broad categories, FOD and *focal osseous dysplasia* (FocOD). The former generally present almost symmetrically in all if not most sextants in both jaws, whereas the latter affects one or more adjacent teeth in a single sextant. Although

they are not neoplasms, they have exceptionally been included in the WHO's 2005 edition [64], which excluded almost all the other non-neoplasms, with the exception of FD and a few others. Although they are generally not considered to be odontogenic lesions, almost all appear above the mandibular canal or below the junction of the hard palate and thus are confined to the alveolar process [58]. This suggests, at least, some odontogenic influence upon their genesis.

ODs are the most frequent of the FOLs affecting the jaws. Although they are least likely to require treatment unless secondarily infected, a few variants do. These are expanding osseous dysplasia (EOD), formerly called FGC, and those associated with *neurofibromatosis type 1* (NF1). The former will be addressed later and the latter now.

In a case series of Caucasian Finns, OD has been reported in association with NF1, an autosomal dominant disease, with some malignant transformation potential [115]. Missing and unerupted teeth, overgrowth of the alveolus, and dilated mandibular canals and mandibular foramina are well-recognized dental manifestations of NF1. The radiolucent-staged lesions appeared as periapical radiolucencies and, though suggestive of inflammatory disease, responded positively to pulp-vitality testing. Although a few presented with a "central radiopacity within a radiolucency," the reader should be cautious, as not one case in Visnapuu et al.'s report [115] had been confirmed by histopathological examination. While these features presented in 35% of women in that report [115], five years later reporting another group of NF1 patients, the authors did not reveal a single case with an OD [116]. Although a separate report [117] summarizing the clinical and genetic features of NF1 did not mention ODs, it did state: "Some individuals with NF1 have distinctive phenotypes composed of unusual combinations of clinical features that cluster together. Recognition of these distinctive phenotypes may aid in diagnosis and prognosis." When these reports are taken together, it can be surmised that the association between OD and NF1 in the earlier Finnish report was unusual.

10.18.1 FLORID OSSEOUS DYSPLASIA

The global distribution of reports of FOD included in the systematic review [61] from which much of the following is derived is set out in Figure 1.46 and the details are in Table 10.5. This lesion was initially associated with middle-aged to older females of sub-Saharan African origin, but also more recently with those of East Asian origin. The mean number of cases of FOD per year globally is 1.2.

FOD overwhelmingly affects females (97%) [61]. The mean number of cases is highest for the Western global group, but surprisingly lowest for the sub-Saharan African global group. This may reflect the greater ethnic diversity within the former, particularly the United States of America where those of non-European origin account for nearly a third of the population, and the lower life expectancy in the latter. In the sub-Saharan African global group, potential OD (FOD and FocOD) victims are more likely to die earlier in life of other causes before they could acquire the OD lesions [62].

The mean age at first presentation is 49 years old (Table 10.5). The age range is 21–83 years [61]. Almost a half of cases are discovered as incidental findings; 48% first present with pain, 31% with swelling, and 30% with a discharge or fistula. Comparison of two case series

Table 10.5 Florid osseous dysplasia: systematic review.

Feature	Total	Western	East Asian	Sub-Saharan African	Latin American
Male: Female	3% : 97%	2% : 98%	4% : 96%[a]	0% : 100%[a]	N/A
Mean number per year per report	1.2	2.2	0.6	0.2	N/A
Mean age	49 years	48 years	51 years	52 years	N/A
Mandible: *Yes: No*	100% : 0%	100% : 0%	100% : 0%	100% : 0%	N/A
Mandible: Anterior: *Yes: No*	64% : 38%	78% : 22%[a]	54% : 45%[a]	20% : 80%[a]	N/A
Mandible: Posterior: *Yes: No*	99% : 1%	100% : 0%	96% : 4%[a]	100% : 0%[a]	N/A
Maxilla: *Yes: No*	68% : 32%	68% : 32%	71% : 29%[a]	60% : 40%[a]	N/A
Maxilla: Anterior: *Yes: No*	53% : 47%	70% : 30%[a]	40% : 60%[a]	0% : 100%[a]	N/A
Maxilla: Posterior: *Yes: No*	100% : 0%	100% : 0%[a]	100% : 0%[a]	100% : 0%[a]	N/A
Swelling: *Yes: No*	31% : 69%	35% : 65%	24% : 76%[a]	N/A	N/A
Pain: *Yes: No*	48% : 52%	35% : 65%	69% : 31%[a]	N/A	N/A
Incidental finding: *Yes: No*	49% : 51%	54% : 46%	40% : 60%[a]	N/A	N/A

[a] Percentages derived either from one report or from a synthesis of no more than 50 cases.
N/A, information not available.
Note: 'Western,' rather than 'Caucasian' is used as the majority cases occurring in an otherwise Caucasian community are of Sub-Saharan African origin.

derived from the same community showed that the series of cases observed as incidental findings on radiographs were significantly older patients than the series of cases that presented with symptoms [61]. More than one sextant needs to be affected to fulfill a diagnosis of FOD. The presentation on a panoramic radiograph or on a full-mouth survey (using intraoral film or digital detectors) is usually bilateral. The mandible is affected in 100% of cases and the maxilla in 67% [61].

Radiologically FOD lesions are generally confined to the alveolus of either or both jaws (Figures 10.23–10.29). Although the classical radiological presentation of the FOD is displayed in the later Figure 10.23, it ranges from radiolucencies (Figure 10.24), to one or more small central radiopacities (Figures 10.25 and 10.29), on to substantial radiopacities with a radiolucent periphery (Figures 10.26–10.28), to complete radiopacities that abut directly onto adjacent normal bone (Figures 1.14 and 10.23).

Diagnosis is readily achieved by conventional radiography; there is little need for CT in the uncomplicated case. Nevertheless, CT, particularly CBCT as it is now ubiquitously available, has revealed some more detail not appreciated by conventional radiography, such as the

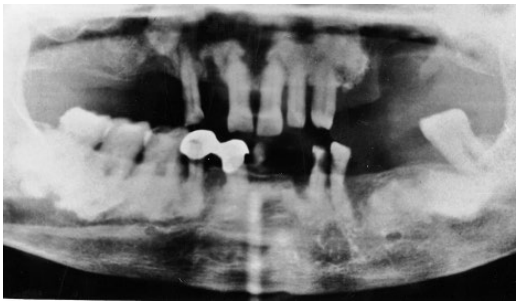


Figure 10.23 Panoramic radiograph displaying multiple well-defined radiopacities affecting most sextants. They are largely confined to the alveolus. This is florid osseous dysplasia and is most frequently found in middle-aged to older females of sub-Saharan African or East Asian origin.

central positioning of the osseous dysplastic tissue within the lesion (Figures 10.27 and 10.28). Radiolucent FOD lesions were more likely to display buccolingual expansion (Figure 10.29) than those that contained high-density masses (osseous dysplastic tissue; Figure 10.27) [118]. These high-density masses had CT numbers of 772–1587 Hounsfield units, which is equivalent to cementum or cortical bone [118]. CT invaluably assisted in the investigation of a recurrent OF, which was subsequently diagnosed as an OD [119]. This lesion eroded the buccal cortex, but caused no expansion. CT imaging

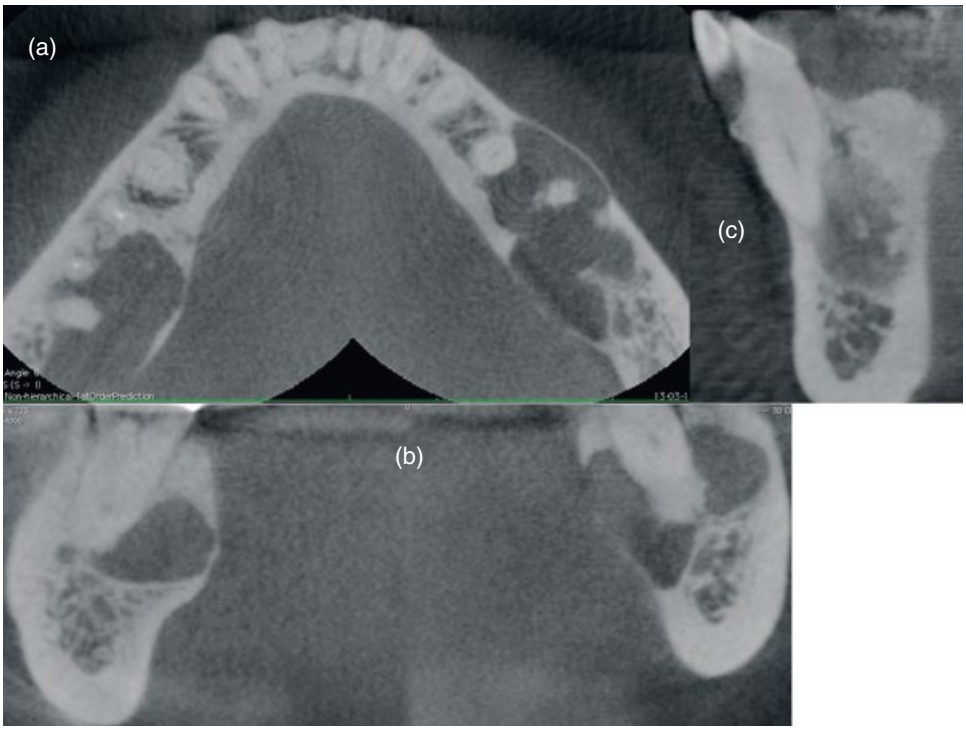


Figure 10.24 Cone-beam computed tomography (CBCT) of florid osseous dysplasia presenting with bilateral lesions in the posterior sextants and one in the anterior sextant of the mandible. Axial reconstruction (a) displays a radiolucency bilaterally in the premolar–molar areas. Although extensive in their mesiodistal extent, there is minimal buccolingual expansion. Nevertheless, the cortices are substantially eroded but remain intact. Coronal reconstruction (b) reveals radiopacities at the apices of the premolar teeth. Sagittal reconstruction (c) reveals a well-defined round radiopacity at the apex of a central incisor. It is mainly ground glass. Note: This CBCT was composed by "stitching" three small field-of-view CBCTs together. Source: (a) MacDonald, D.S (2015). Maxillofacial fibro-osseous lesions. *Clin. Radiol.* 70:25–36.

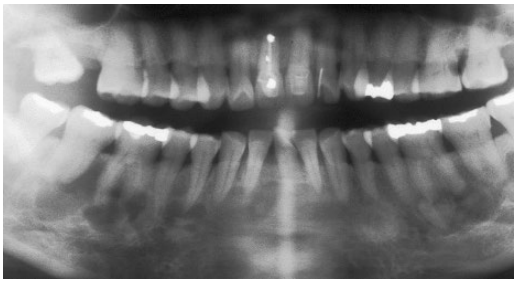


Figure 10.25 Panoramic radiograph displaying multiple well-defined radiolucencies, many containing central opacities. All lesions are confined to the alveolus. This is florid osseous dysplasia and is most frequently found in middle-aged to older females of sub-Saharan African or East Asian origin. Source: Reproduced with permission from MacDonald-Jankowski, D.S (2004). Fibro-osseous lesions of the face and jaws. *Clin. Radiol.* 59: 11–25.

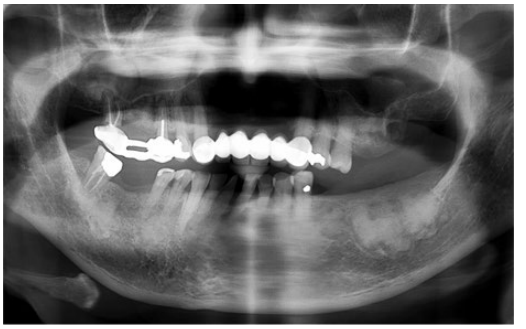


Figure 10.26 Conventional panoramic radiograph of a 60-year-old East Asian female patient. Source: Courtesy of Dr. Raman Sumanth, Melaka Manipal Medical College, Malaysia.

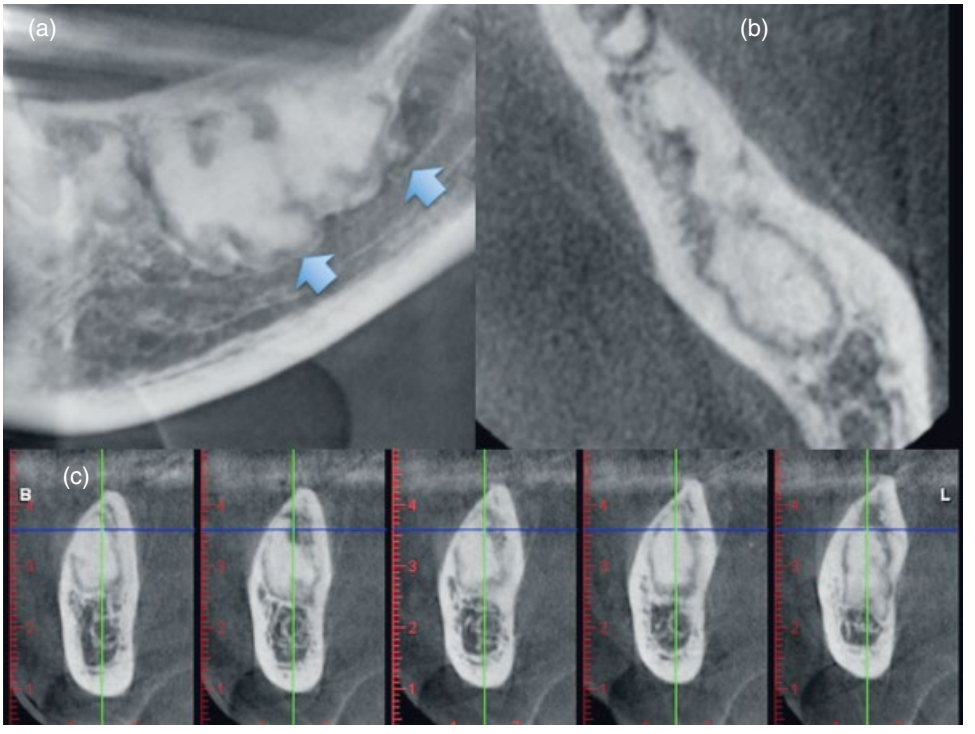


Figure 10.27 Cone-beam computed tomography (CBCT) of florid osseous dysplasia of the left side of the 60-year-old Chinese woman displayed on the conventional panoramic radiograph in Figure 10.26. (a) Panoramic, (b) axial, and (c) transaxial reconstructions. The CBCT panoramic reconstruction of the left side displays multiple well-defined radiopacities within the alveolus of the mandible. Note that they are all positioned above the mandibular canal (blue arrows). The axial and transaxial reconstructions exhibit these lesions within the alveolus without buccolingual expansion. The lesions are separated from their adjacent normal bone by a radiolucent space and a cortex (in places). B, buccal; L, lingual. Source: MacDonald, D.S (2015). Maxillofacial fibro-osseous lesions. *Clin. Radiol.* 70: 25–36.

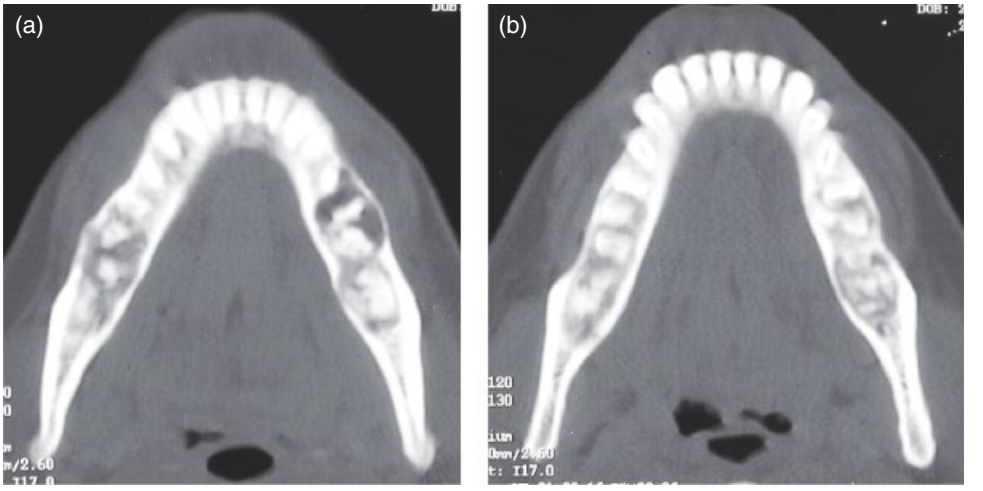


Figure 10.28 (a and b) Axial bone-window sections of computed tomography. The radiolucencies contain central radiopacities. Although extensive mesiodistally, they cause very little buccolingual expansion. The cortex displays erosion in places, particularly the right buccal cortex in (b), which also displays some buccal expansion.

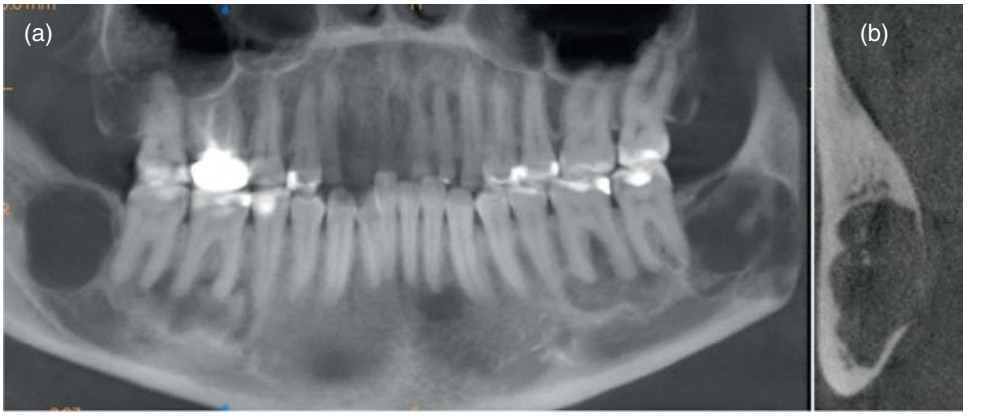


Figure 10.29 Panoramic reconstruction (a) and left coronal section (b) of a cone-beam computed tomography examination of a female patient late in the fourth decade and of South Asian origin. As obvious in (a), she has lesions in all mandibular sextants. Those associated with the mandibular molars bilaterally present with central radiopacities and are suggestive of osseous dysplasia. The bilateral large and expansile radiolucencies in (b) were biopsied and histologically found to be fibro-osseous lesions. This with the accompanying radiology allowed a diagnosis of florid osseous dysplasia to be made. Source: Dr. David Yang, oral and maxillofacial surgeon, British Columbia Cancer Agency.

displayed another FOD lesion that both expanded and breached the cortex [120]. The CT also permitted precise localization of the mandibular canal to the lesions (Figure 10.27) [120].

10.18.2 FOCAL OSSEOUS DYSPLASIA

The global distribution of reports on FocOD included in the systematic review [62] from which much of the following is

Table 10.6 Focal osseous dysplasia: systematic review.

Feature	Total	Western	East Asian	Sub-Saharan African	Latin American
Male: Female	12% : 88%	12% : 88%	14% : 86%	6% : 94%	N/A
Mean number per year per report	4.9	20	1.1	N/A	N/A
Mean age	44 years	39 years	47 years	N/A	N/A
Mandible: Maxilla	85% : 15%	91% : 9%	85% : 15%	N/A	N/A
Mandible: *Anterior: Posterior*	20% : 80%	27% : 73%[a]	1% : 99%	N/A	N/A
Maxilla: *Anterior: Posterior*	26% : 74%	32% : 68%	20% : 80%[a]	N/A	N/A
Swelling: *Yes: No*	25% : 75%	24% : 76%	30% : 70%	N/A	N/A
Pain: *Yes: No*	28% : 72%	24% : 76%	44% : 56%	N/A	N/A
Incidental finding: *Yes: No*	64% : 36%	74% : 26%	14% : 86%	N/A	N/A
Numbness: *Yes: No*	17% : 83%[a]	N/A	17% : 83%[a]	N/A	N/A

[a] Percentages derived either from one report or from a synthesis of no more than 50 cases.
N/A, information not available.
Note: 'Western,' rather than 'Caucasian' is used as the majority cases occurring in an otherwise Caucasian community are of Sub-Saharan African origin.

derived is set out in Figure 1.47 and the details are in Table 10.6.

The mean number of cases of FocOD per year globally was 4.9 [62], which contrasts with 1.2 for FODs [61] and 1.7 each for FD [80] and OF [104]. Therefore, FocOD is the most frequent of all FOLs. As already observed for FOD, the frequency was highest for the Western global group and lowest for the sub-Saharan African global group. The explanation for this difference is the same as that for FOD [61].

FocOD is confined to a single sextant (Figures 10.30 and 10.31) [62]. It may present as a single lesion or as a group of juxtapositioned lesions [62]. If it affects more than one sextant, certainly if it is bilateral or affects both jaws, it should be considered to be a case of FOD. Prior to its recognition as a discrete entity, its frequent solitary clinical presentation led to its inclusion among OFs. This was the experience both of Summerlin and Tomich [121] and of Su et al. [122, 123]. Unfortunately, neither disclosed how many had been misdiagnosed. The first clear differentiation of FocOD as a separate broad entity was established by both the WHO's 1972 edition [124] and the Waldron et al's. report [125]. Unlike OFs, OD (including both FOD and FocOD) would not "shell out," and therefore the specimen was delivered for its histopathological examination in fragments. These centrally important criteria were reiterated by Melrose [126]. Therefore, the definitive feature that distinguishes between OF and OD is the presentation of the gross surgical specimen, which is histopathologically an FOL. The radiological challenge in the diagnosis of FOLs is greatest when attempting to distinguish between an OF and a single FocOD lesion, particularly when the lesion is small (Figure 10.30). Although OFs are associated with root resorption, this is not a feature of most OFs, especially the small ones.



Figure 10.30 Cone-beam computed tomography of an osseous dysplasia arising apically to the second premolar and the mesial root of the first molar. The lesion is a central radiopacity separated from normal adjacent bone by a radiolucent periphery. There is no buccolingual expansion (a). Although there is no evidence of root resorption, the mesial root of the first molar tooth displays hypercementosis (b); compare this with the cementoblastoma of Figure 10.38a. Note the wide and deep periodontal pocket in the mesial aspect of the affected molar in (b) and also the intimate relationship of the lesion to the mandibular canal in (b) and (c). This is focal osseous dysplasia, since it is the sole such lesion in this patient's jaws. Source: MacDonald, D.S. (2015). Maxillofacial fibro-osseous lesions. *Clin. Radiol.* 70: 25–36.

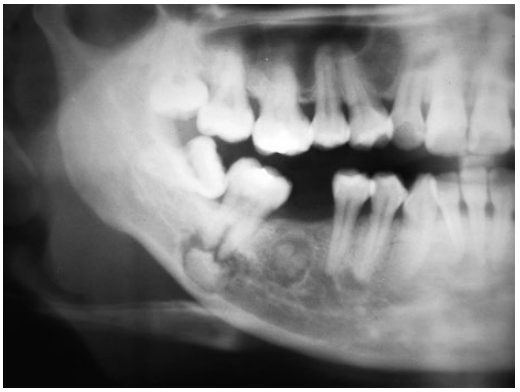


Figure 10.31 Panoramic radiograph displaying two osseous dysplastic lesions within only one sextant. In the absence of symptoms, they can be safely left to occasional radiographic review, as they are most likely to represent focal osseous dysplasia. One is wholly confined to the alveolus, whereas the more distal lesion, while classically sited at the apex of an erupted tooth, is wholly within the basal bone of the mandible. Although this is an exception to the rule that osseous dysplasia affects the alveolus only, the hypoplastic mandible at that site was insufficiently deep vertically to allow accommodation of the distal osseous dysplastic lesion within the alveolus. Source: Courtesy of Dr. Ian Matthew, Faculty of Dentistry, University of British Columbia.

This creates a dilemma for dentists: Should they remove a lesion which may be an OD and therefore better left alone, or risk leaving a lesion that may subsequently prove to be an OF requiring even more extensive surgery? The latter needs to be considered, particularly if complex restorative treatment is being contemplated. Later surgery to remove the now-enlarged OF may compromise the success of that treatment [62].

Although it is generally accepted that symptomless FocODs need no treatment, their clinical importance has been emphasized by their presence in edentulous sites required for osseointegrated implants [62]. As an essential prelude to its management in this regard, a better understanding of the frequency and presentation of the FocOD in the global literature is required.

FocOD overwhelmingly affects females (88%) [62] (Table 10.6). The mean age is 44 years. Presentation of cases is 64% as incidental findings, 25% with swelling, 28% with pain, and 17% with numbness.

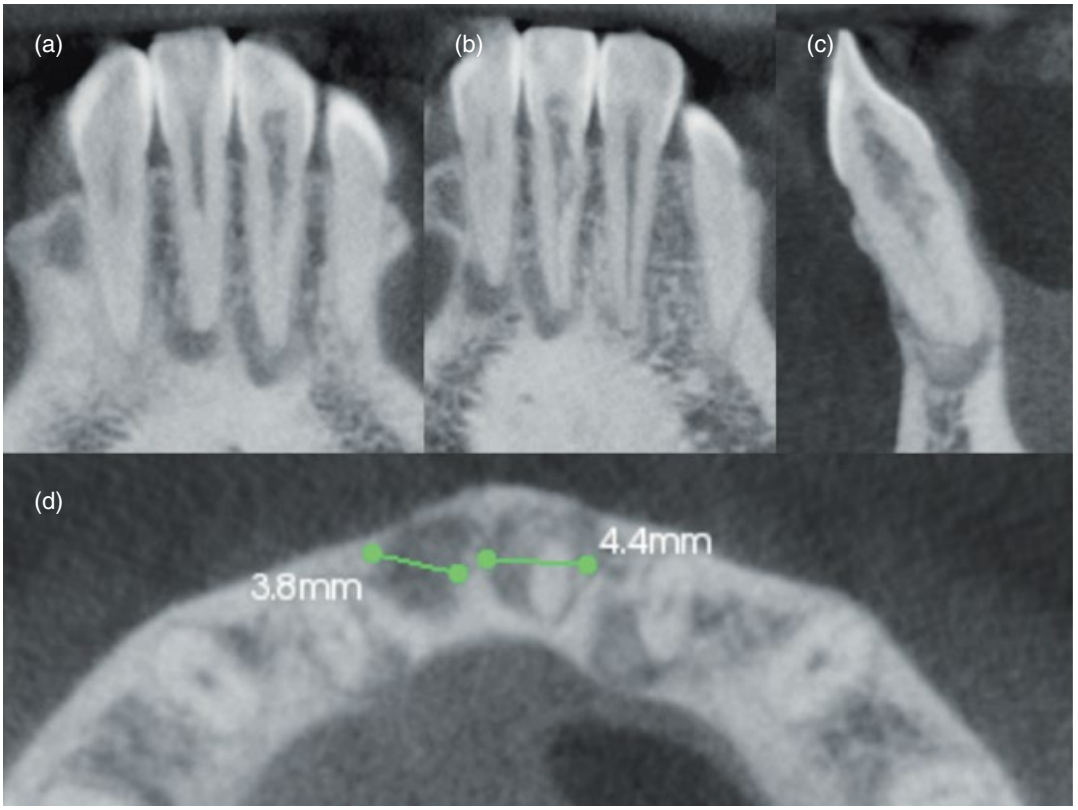


Figure 10.32 Cone-beam computed tomography of multiple periapical lesions affecting the lower anterior sextant of a female of European origin in her third decade. (a and b) Coronal, (c) sagittal and (d) axial reconstructions. The lesions are generally central radiopacities within radiolucencies. They have a small diameter, which is not much larger than the width of the teeth they affect. There is little buccolingual expansion. These are osseous dysplastic lesions, which have been traditionally called periapical cemental dysplasia, although they arise within the alveolar bone and not the cementum. Therefore the term periapical osseous dysplasia (POD) is more appropriate. Note: Although this is a classic case of POD, the associated internal root resorption in the central incisors has hitherto not been reported. Source: MacDonald, D.S. (2015). Maxillofacial fibro-osseous lesions. *Clin. Radiol.* 70:25–36.

The last was reported only in East Asians. The mandible is affected in 85%; the posterior sextants of the mandible and the maxilla are affected in 80% and 68%, respectively [62].

Just over half (53%) of cases were well defined. Of these, 40% displayed a sclerotic periphery; the other 60% of cases were nonsclerotic. The appearance was in dentate areas of the jaws (teeth were still present) in 49% of cases and edentulous areas (teeth had been extracted) in the other 51%. In the dentate areas, no tooth displacement or root resorption was observed [62].

The predominant radiological patterns are radiolucency (31%), "central radiopacity within a radiolucency" (37%), and "complete radiopaque" (32%). East Asian reports display significantly more complete radiopacities and fewer radiolucencies than those of Western communities [62]. This may reflect the older mean age of the East Asian global group at first presentation (47 years) in comparison to that of the Western global group (39 years) [62].

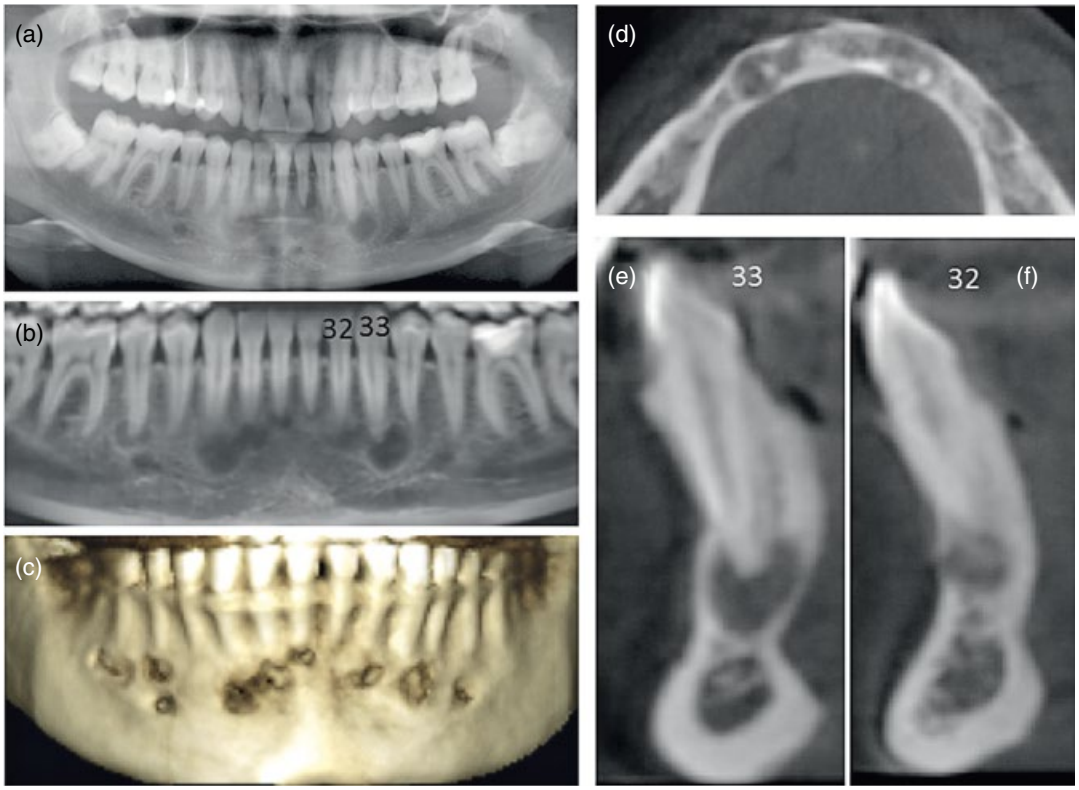


Figure 10.33 A panoramic radiograph (a) and subsequent cone-beam computed tomography (b to f) of multiple periapical lesions substantially affecting the lower anterior sextant of a female of European origin in her fourth decade. (b) Panoramic reconstruction, (c) three-dimensional, (d) axial and (e and f) coronal reconstructions of the lesions on the left canine (33 in Fédération Dentaire Internationale notation) and left lateral incisor (32), respectively. The lesions are generally central radiopacities within radiolucencies. They have a small diameter, which is not much larger than the width of the teeth they affect. There is little buccolingual expansion. Although they are very similar in demographic and radiological presentations to the periapical cemental dysplasia case in Figure 10.32 ,the unusual feature is the lesions on apices of the second premolar and first molar. Nevertheless, no other lesions are observed elsewhere, otherwise a diagnosis of florid osseous dysplasia would be more appropriate, although exceptionally rare in those of European origin. Source: Courtesy of Dr. Mark Parhar, Tri-City Endodontics, Vancouver, British Columbia.

10.18.3 PERIAPICAL CEMENTAL (NOW OSSEOUS) DYSPLASIA

Periapical cemental dysplasia first appeared as an independent entity in the WHO's 1972 edition [124] and became indistinguishable from FOD in the WHO's 1992 edition [101], only to return to the WHO's 1972 edition definition that confined it to the anterior sextant of the mandible in the WHO's 2005 edition [64]. This lesion appears initially as periapical radiolucencies associated with noncarious lower incisors (Figures 10.32, 10.33, and 9.24). With the exception of its histopathologically outdated name and its anterior location, there appears to be nothing else to distinguish it from FocOD.

It is not an infrequent experience for the dental specialist to observe root-treated lower incisors (Figure 1.27) whose apices are now associated with mature OD lesions. Avoidance of unnecessary treatment can be achieved by pulp-vitality testing of all periapical lesions, especially radiolucencies.

10.18.4 EXPANDING OSSEOUS DYSPLASIA/FAMILIAL GIGANTIFORM CEMENTOMA

The term FGC was coined by Young et al. to differentiate this condition from FOD [127]. In addition to FGC cases usually also presenting with multiple lesions, just like FODs, their expansion is so extensive that, unlike FODs, they also occupy the basal as well as the alveolar processes, which the FODs do not. Although the term FGC was affirmed by Waldron [128], its overall appropriateness was recently challenged and the more descriptive EOD offered as an alternative [129]. While no oncogenes have been reported so far, many of these lesions generally exhibit neoplastic behavior. They appear to be autosomal dominant [127, 130, 131], have a family history, and affect the young of both sexes equally [122, 127]. Initially EOD/FGCs were reported in Caucasian kindreds (US [127] and Iranian [130]), then in a kindred of sub-Saharan African origin [132], but have since been reported in other global communities, and most recently East Asians [131, 132]. There have also been cases that present as EOD/FGC, but have no family history. Such cases so far have been reported in adolescent males (of East Asian [133, 134] and Indian origin [135]) and American females [136]. All displayed very aggressive behavior and achieved substantial dimensions. The question of whether these lesions constitute a separate clinical entity to what was formerly the FGC, or are a manifestation of the rarely occurring multiple OFs or even HPT-JT syndrome [105], warrants further and more fully reported cases. Another case was associated with brittle bone disease [137]. An East Asian child first diagnosed at 15 months experienced repeated recurrences over the six years of follow-up (Figure 10.34) [131].

When patients present with extensive bilateral, almost symmetrical, involvement by multiple radiopacities of both the alveolar and basal processes of both jaws, GS should also be considered (see Figure 10.11). Lee et al. reported such a case in a middle-aged woman [21].

Three out of four males with EOD/FGC of an Iranian kindred [130] and eight out of thirteen (three to four per person) affected members of a Chinese kindred [132] presenting with familial EOD/FGC also had multiple long bone fractures in response to minor trauma [62]. In the Iranian kindred these long fractures occurred in middle age, two decades after the onset of the jaw lesions in the early third decade [130]. In the Chinese kindred these occurred in their early teens and affected the femur predominantly [132]. This detailed study reported that symptoms began at 11–13 years of age, followed by a rapid and expansive growth phase during the mid-teens, to abate in the late teens. Although the growth was greater and began earlier in the anterior sextant of the mandible than the maxilla, it abated earlier [132]. No more long-bone fractures occurred after the growth of the jaw lesions abated. Furthermore, all members of the Chinese kindred exhibited elevated alkaline phosphatase and decreased bone mineral content, which in all cases returned to normal after the resection of the jaw lesions [132].

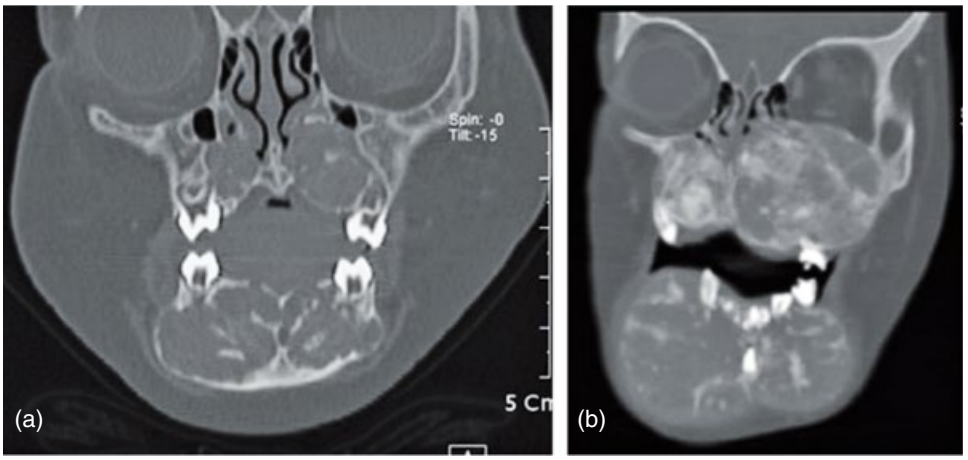


Figure 10.34 Coronal computed tomography (bone window) of multiple expanding osseous dysplastic lesions in an infant female (a) at first presentation when she was 15 months old and (b) one year later through a similar coronal plane to (a). The entire jaws are affected. In (b) the lesions are not merely larger, but also display more calcification. The lesion on the left side has displaced the floor of the orbit upward and displaced the eyeball forward (proptosis). Source: Shah S, Huh, K.H. and Yi, W.J. et al. (2012). Follow-up CT findings of recurrent familial gigantiform cementoma of a female child. *Skelet. Radiol.* 41:341–346.

10.18.5 CONCLUDING REMARKS ON FIBRO-OSSEOUS LESIONS

1. The role of the radiologist is central to the definitive diagnosis of a particular FOL, because the histopathologies of the various types are similar.
2. FOLs affecting the face and jaws differ from their clinical, radiological, and histopathological (no cartilage in maxillofacial cases) presentations elsewhere in the body.
3. Although some, such as ODs, are very prevalent, particularly in middle-aged to older females of East Asian or sub-Saharan African origin, others, such as FD and OF, though less frequent, have more significant management implications for the patient.
4. Their clinical presentations differ. OD is most frequently observed as incidental findings on panoramic radiographs, whereas FD and OF are most frequently discovered when the patient presents with swelling.
5. FOD and FocOD (including periapical cemental dysplasia) are best kept under review. While surgery should be avoided unless the lesions produce symptoms, this option may no longer be tenable if the edentulous site is required for an osseointegrated implant [62]. In such a case, in the current absence of published evidence, it is advised to surgically ablate the lesion by lateral trepanation and curettage, then allow it to heal first. This should minimize a real risk of failure of the implant by insertion into abnormal tissue. Only EOD and FGC require surgical ablation because of their frequently aggressive behavior (see Figure 10.34).
6. Although the primary diagnosis is performed in almost all cases from the clinical findings and conventional radiographs, cross-sectional imaging is frequently required of lesions affecting the anatomically complex maxillary sinus. Since most monostotic

FDs first present in adolescents and young adults, use of CBCT, rather than CT, may be better indicated if such cross-sectional imaging is necessary, since it imparts a reduced radiation dose. For the same reason, CBCT would better assist in the investigation of a reactivated FD of the face and/or jaws.

7. Polyostotic FD would better benefit from MRI, especially in the young patient, particularly if vision is threatened by FD of the base of the skull.
8. Recently malignant transformation in FD of the face and jaws has been reported in polyostotic cases.
9. The clinician should be aware of the association between OF and HPT-JT that may be caused by a secreting carcinoma. It may also provoke a hypercalcemic crisis. Blood chemistry and nuclear medicine may be indicated.

10.19 Osteoma (ICD-O 9180/0)

The WHO's 2017 edition defines osteoma as "a benign neoplasm composed of mature bone, limited almost exclusively to the craniofacial bones" [138]. It features compact and/or cancellous bone or a combination [138]. It can arise from either the periosteal or endosteal bone surfaces to be a peripheral or central osteoma, respectively. Almost are symptom free except the sino-orbitally sited ones, which are associated with pain, headache, or visual changes [138]. Although multiple osteomas of the jaws are a hallmark of GS [138] (FAP; see Figure 10.3), nonsyndromic cases are typically solitary (Figure 10.35). Kaplan et al. synthesized the literature and found 91 solitary cases, of which all but 6 were peripheral [139]. They stated that while peripheral osteomas pose few diagnostic challenges, the central

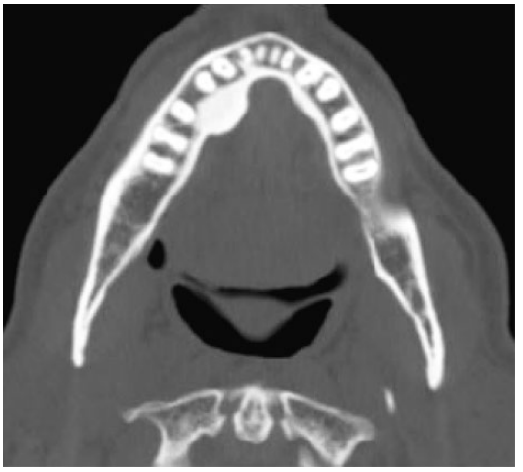


Figure 10.35 Axial computed tomography (bone window) revealing a dense radiopacity on the lingual cortex of the mandible. This is an osteoma. Source: Courtesy of Dr. Montgomery Martin, British Columbia Cancer Agency.

osteoma has to be distinguished from OF, condensing osteitis, idiopathic osteosclerosis, osteoblastoma, cementoblastoma, and complex odontoma [139]. Recurrence is rare [138]. The largest case series of osteomas affecting the face and jaws was reported in a Spanish community [140]. The 132 osteomas arising in 106 patients affected the mandible, the maxilla, and the paranasal sinuses, at 54%, 16%, and 21%, respectively [140]. In contradiction of Kaplan et al.'s synthesis [140], Larrea-Oyarbide et al.'s peripheral osteomas accounted for 59% of those affecting the jaws [140]. Another report of 14 consecutive peripheral osteomas affecting an Israeli community found that 12 arose from the jaws [141].

10.20 Osteoblastoma (ICD-O 9200/0)

The osteoblastoma is a slow-growing benign neoplasm of bone, accounting for 1% of all primary bone neoplasms. Jones

et al. compared 24 of their own cases to their synthesis of 77 cases of osteoblastomas and osteoid osteomas of the jaws reported elsewhere in the literature [142]. Although the osteoblastoma and the histopathologically similar osteoid osteoma are held to be different lesions extragnathically, Jones et al. discussed the latter as an earlier manifestation of the former in the jaws [142]. It is important that the reader understands that these two lesions present differently clinically. They have different ICD-O codes: osteoblastoma is ICD-O 9200/0 [143] and osteoid osteoma is ICD-O 9191/0 [143]. The WHO's 2017 edition described them both as rare [143]. The osteoblastoma can be distinguished from the osteoid osteoma by its size: it is larger than 2 cm in diameter [143]. Although it can be symptom free, it may, like the osteoid osteoma, present with pain. The pain in the latter may be accompanied by swelling and mimics toothache [143]. This pain, unlike that of the osteoid osteoma, does not respond to aspirin [143]. The main radiological distinguishing feature in addition to size is that the osteoid osteoma frequently is surround by sclerosis [143], which is lacking for the osteoblastoma [143].

Pontual et al. displayed on CBCT a large osteoblastoma affecting the mandible (Figure 10.36) [144].

Osteoblastomas are found at a rate of 10% in the craniofacial bones [143] and presented five times more frequently in the mandible [142]. Jones et al. found overall that the osteoblastoma predominantly affects the left posterior mandible [142]. Although 60% of their own 24 cases at the time of discovery were symptom free, the rest were associated with pain and tenderness; this was contrary to the results of their synthesis. Radiologically osteoblastomas are generally well defined and equally distributed between radiolucent, radiopaque, and mixed lesions. The nine cases Jones et al. followed up did not recur [142]. Although already rare, one osteoblastoma of the mandible not only recurred several times, but underwent transformation to an osteosarcoma [145]. Another mandibular case initially mimicked an osteosarcoma on FDG-PET/CT [146].

10.21 Cementoblastoma (ICD-O 9273/0)

El Mofty [147] recently reaffirmed van der Waal's definition of the cementoblastoma [148], which van der Waal defined as "characterized by the formation of cementum-like tissue in connection with the root of a tooth" [148]. Furthermore, according to him, "Radiologically, the tumour is well-defined and is mainly of a radiopaque or mixed-density, surrounded by a thin radiolucent zone. Root resorption, loss of root outline and obliteration of the periodontal ligament space are common findings" [148] (Figure 10.37).

The cementoblastoma is a relatively rare lesion. The largest synthesis of 70 cases is derived from single case reports or small case series [149]. Brannon et al. reported a further 44 cases from the US Army pathology files [150] and Dominguez et al. reported 25 Latin American cases [151].

Although the cementoblastoma is a benign odontogenic neoplasm, Figure 10.38 demonstrates that it can grow quickly. It presents in about half of cases in children and adolescents as pain on biting. The largest case series is that of Brannon et al. [150]. The cementoblastoma affects males and females equally and affects the mandible three times as frequently as the maxilla [149–151]. The mandibular first molar is most frequently affected [149–151]. The mean ages for two syntheses and two case series are 23 [149],



Figure 10.36 Cone-beam computed tomography of an osteoblastoma affecting the left mandible. (a) Panoramic radiographic, (b) transaxial (through the third molar [38]), and (c and d) axial reconstructions. In three dimensions the osteoblastoma is a football-shaped lesions occupying the left body of the mandible, between the mandibular foramen and the canine. Many of the internal radiopacities arise septum-like from the periphery, giving rise to a multilocular presentation. Source: Pontual, http://www.scielo.br/scielo.php?script=sci_arttext&pid=S0103-64402014000500451&lng=en&nrm=iso&tlng=en. CC BY-NC 3.0.

22 [150], 21 [150], and 26 years [151], respectively. Brannon et al. reported that the deciduous dentition is rarely affected [150]. Swelling in both syntheses was nearly 60% [148, 149], whereas it was 86% in the military series [150]. Awareness of lesions prior to presentation was one year [150].

The mean size of the lesion at presentation is 2.1 cm [150]. In a synthesis [149] and the Spanish-language report [151], larger cementoblastomas were found

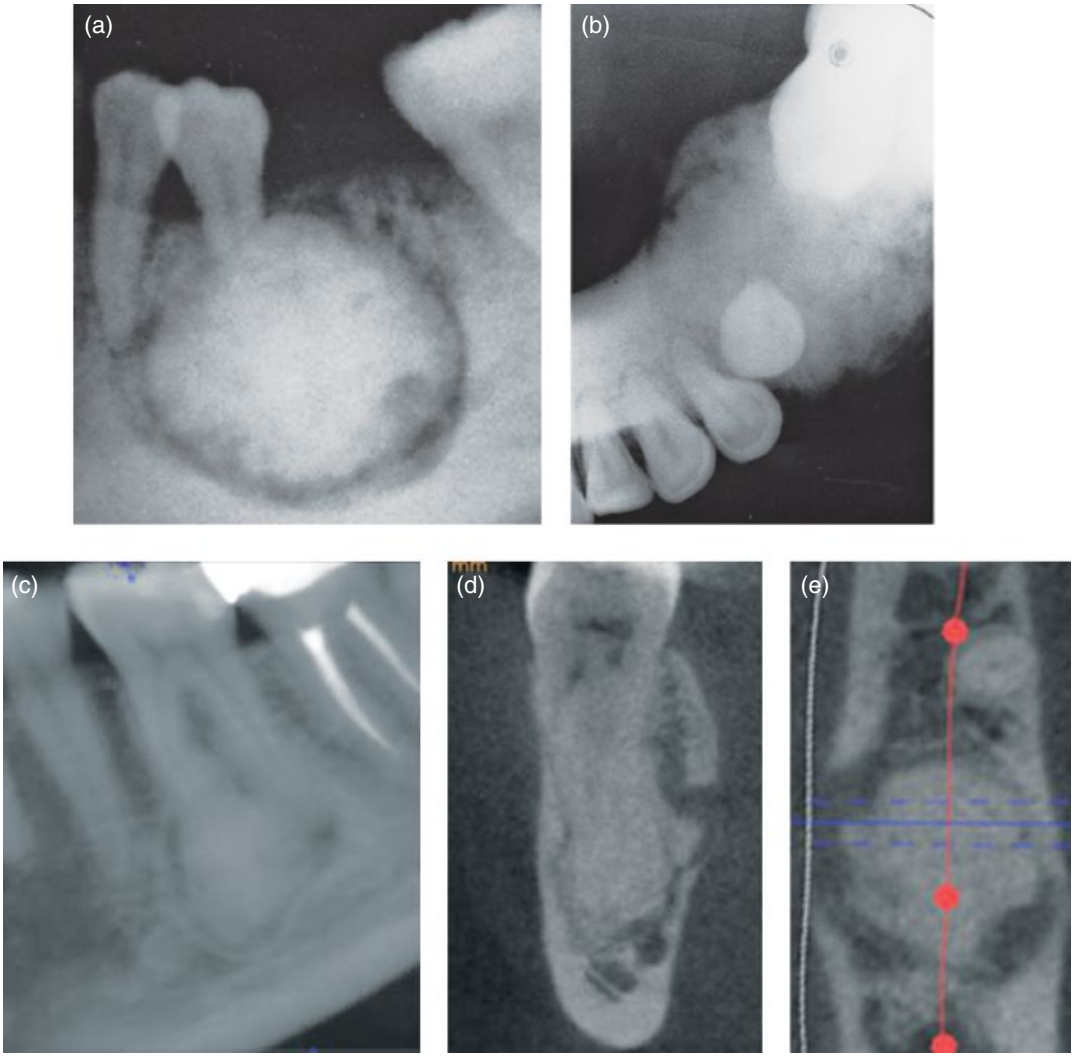


Figure 10.37 Panoramic radiograph (a) and true occlusal radiograph (b) of a cementoblastoma. This presents on the panoramic radiograph as a well-defined radiopacity separated from the adjacent bone by a radiolucent margin, which is continuous with the periodontal ligament space of the affected tooth. The lesion was fused directly to the root, which it has partially resorbed. The lesion is substantial in size and is close to the alveolar crest. The lesion has also expanded to encompass a retained root, which displays resorption by the capsule. The mandibular canal is displaced inferiorly but around the inferior aspect of the lesion. (c–e) are cone-beam computed tomographic panoramic, transaxial and axial reconstructions respectively of a cementoblastoma affecting a mandibular first molar. (c and d) display its fusion to the mesial root. (d and e) exhibit erosion of the buccal cortex. c to e are Reprinted with permission from Dr. Jason Choi, oral and maxillofacial surgeon, Vancouver, Canada. Source: a and b Reproduced with permission from MacDonald-Jankowski, D.S. and Wu, P.C. (1992). Cementoblastoma in Hong Kong Chinese. A report of four cases. *Oral Surg. Oral Med. Oral Pathol*. 73: 760–764.

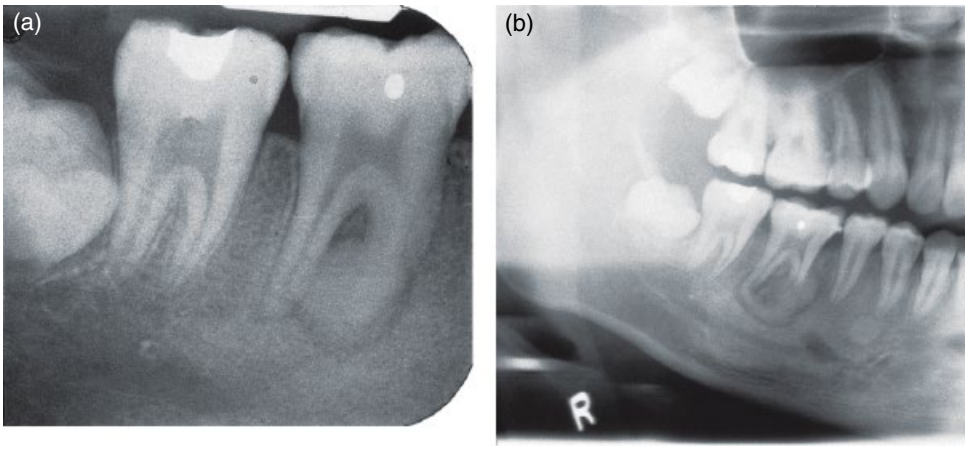


Figure 10.38 Periapical image (a) displaying a cementoblastoma as a small round radiopacity fused to the mesial root of the first molar mandibular tooth. It also displays root resorption. Panoramic image (b) of the same lesion a year later. Meanwhile the lesion has now grown both mesially and distally. This growth in the latter direction has reached the distal root of the same tooth. Its periodontal ligament space on its mesial aspect appears wider. The panoramic radiograph also displays a well-defined round radiopacity at the apex of a carious first premolar. This lesion has no radiolucent space. The reviewer may observe the hint of such a space, which is the Mach band effect. This "space" is traversed by trabeculae. Such radiopacity is termed condensing (or sclerosing) osteitis and represents a sclerotic reaction to infection. The whole area of bone containing both lesions is more sclerotic than the rest. The mandibular canal, which is normally rendered visible as a radiolucent line defined by its cortex, is now obvious because it is contrasted against the sclerotic bone. This zone is diffuse osteosclerosis, suggestive of sclerosing osteomyelitis, and classically affects both the alveolar and basal processes of the mandible. In this case it may have arisen from the periapical infection of the first premolar.

outside the posterior mandibular sextant. In the synthesis, three were located in the maxilla, almost affecting the entire hemimaxilla [149]. In the Spanish-language report, two extensively crossed the midline, one in each jaw, occupying the entire anterior sextant [151].

According to van der Waal, the diagnosis of cementoblastoma cannot be made on the histopathology alone [148]. Although its histopathology can be indistinguishable from osteoblastoma or osteoid osteoma or well-defined osteogenic sarcoma, this neoplasm is easy to distinguish by its radiological presentation, which is almost pathognomonic [148].

Radiological imaging displays a well-defined (94%) circumscribed radiopacity (67%) or mixed density (radiopacity within a radiolucency; 28%) [150]. The attached tooth root not only displays root resorption, but is also fused to the cementoblastoma. This is represented by loss of root outline (see Figures 10.37 and 10.38). Despite this radicular disruption, Brannon et al. reported that the affected tooth was vital in 19 out of 21 cases [150]. Complete enucleation, including extraction of the affected tooth, is required to avoid recurrence. Brannon et al.'s synthesis of the literature revealed that 37% of cases followed up recurred within a mean of 5.5 years [150]. They noted that the cases that recurred displayed more expansion and cortical perforation [150].

Dominquez et al.'s report additionally correlated the radiology and histopathology.



Figure 10.39 Periapical radiograph displaying a unique cementoblastoma arising from closer to the furcation rather than classically from the apex. The mandibular canal is rendered obvious by increased density. Source: Reproduced with permission from MacDonald-Jankowski, D.S. and Wu, P.C. (1992). Cementoblastoma in Hong Kong Chinese. A report of four cases. *Oral Surg. Oral Med. Oral Pathol.* 73: 760–764.

The two radiolucent cases (these appear to be the first such lesions to be reported) were represented by cementoid trabeculae and nodules; the nine mixed cases displayed remodeled trabeculae, which appeared pagetoid. The six dense cases were represented by radial trabeculae [151].

In almost every case, the apices of permanent teeth are affected. In one case the cementoblastoma primarily affected the coronal half of the root (Figure 10.39) [149]. Growth can be rapid (compare Figure 10.38a and b). Furthermore, the prior extraction of the tooth leaving the neoplasm behind deprives the subsequent clinician of an easy diagnosis. This happened in one case in a case series [149]. Exceptionally, the definitive diagnosis was entirely furnished by the histopathologist, who observed the retained root encased by the neoplasm. It displayed the typical root resorption and fusion with the neoplasm [149].

10.22 Odontoma (ICD-O 9280/0)

The WHO 2017 edition defined the odontoma as "mixed epithelial and mesenchymal tumour-like malformations (harmatomas) composed of dental hard and soft tissues" [152]. The odontoma is perhaps the most common odontogenic neoplasm, certainly in reports arising from North America and Europe, where it is most likely to be diagnosed mainly on panoramic radiographs by dentists practicing in the community or in dental schools, where the lesion is removed and the surgical specimen not always referred for subsequent histopathological evaluation [153]. The two basic types of odontoma, the compound and complex types, first formally appeared in the WHO's 1992 edition each with its own ICD-O code, 9281/0 and 9282/0, respectively [154]. This was upheld in both the WHO's subsequent 2005 [155, 156] and 2017 [152] editions.

The compound type first presents frequently in children as noneruption of permanent teeth. It classically presents on a radiograph as a "bag of teeth" (Figure 10.40) about the size of a normal tooth in that site, whereas the complex type frequently presents as a well-defined radiopacity (see Figure 1.20a, b), which can become very large (see Figures 11.47 and 11.48). This radiopacity is frequently demarcated from the adjacent normal bone by a radiolucent space.

The details of the global distribution of reports of complex and compound odontomas are set out in Tables 10.7 and 10.8, respectively.

The mean number of cases of odontomas per year globally was 1.7 and 2.5 for complex and compound odontomas, respectively. The mean number of cases

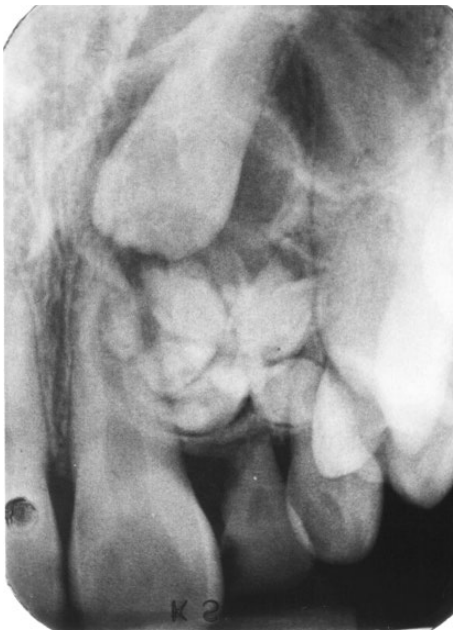


Figure 10.40 Periapical radiograph displaying a compound odontoma preventing the eruption of a permanent incisor tooth. The presence of denticles on the radiograph is pathognomonic for a compound odontoma. Source: MacDonald-Jankowski, D.S. (1996). Odontomas in a Chinese population. *Dentomaxillofac. Radiol.* 25: 186–192.

of odontomas per year was lowest for the sub-Saharan African global group. This may reflect a tendency not to refer these lesions for histopathology rather than a true lower prevalence in this global group, as suggested earlier by Fregnani et al. [153].

The mean age of first presentation of both forms is similar: the complex odontoma first presents consistently a few years later in life. The male : female ratio is almost equal in all respects. The complex form has a greater predilection for the mandible, whereas the compound form shows a predilection for the maxilla. The complex form also displays a clear predisposition (77%) for the posterior sextant of the mandible. Although both forms affect the anterior sextant of the maxilla, the compound form occurs there most frequently (78%).

While almost all reports pool the findings of each type together, this is hard to understand, because they differ in their radiology, disposition between jaws and sextants for each jaw, clinical presentation, and propensity to recur. Therefore,

Table 10.7 Complex odontoma: systematic review.

Feature	Total	Caucasian	East Asian	Sub-Saharan African	Latin American
Male: Female	52% : 48%	54% : 46%	51% : 49%	54% : 6%[a]	42% : 58%
Mean number per year per report	1.7	1.9	1.6	0.5	1.4
Mean age	23 years	22 years	24 years	N/A	21 years
Mandible: Maxilla	53% : 47%	54% : 46%	55% : 45%	80% : 20%[a]	45% : 55%
Mandible: *Anterior: Posterior*	23% : 77%	22% : 78%	21% : 79%	25% : 75%[a]	29% : 71%
Maxilla: *Anterior: Posterior*	60% : 40%	64% : 36%	48% : 53%	0% : 100%[a]	71% : 29%

[a] Percentages derived either from one report or from a synthesis of no more than 50 cases.
N/A, information not available.

Table 10.8 Compound odontoma: systematic review.

Feature	Total	Caucasian	East Asian	Sub-Saharan African	Latin American
Male: Female	49% : 51%	48% : 52%	53% : 47%	43% : 57%[a]	52% : 48%
Mean number per year per report	2.5	3.2	2.2	0.3	1.7
Mean age	20 years	19 years	20 years	N/A	N/A
Mandible: Maxilla	42% : 58%	35% : 65%	47% : 53%	83% : 17%[a]	33% : 67%
Mandible: *Anterior: Posterior*	56% : 44%	60% : 40%	58% : 42%	0% : 100%[a]	36% : 64%
Maxilla: *Anterior: Posterior*	78% : 22%	76% : 24%	80% : 20%	0% : 100%[a]	85% : 15%

[a] Percentages derived either from one report or from a synthesis of no more than 50 cases.
N/A, information not available.

specific information for each with regard to presenting clinical and radiological features is almost wholly absent. Chen et al. [157] synthesized 43 cases, which clearly illustrated the differences in clinical presentation. They found that just over half of their complex odontomas first presented as swellings, but few with noneruption of teeth, whereas just under half of the compound odontomas presented with noneruption of teeth and few with swellings.

Praetorius and Piatelli state that the complex type can recur [155], whereas the compound type never recurs following treatment [156]. This suggests that the complex type has at least one neoplastic feature. There is further circumstantial evidence that the complex type is a neoplasm. In one report, measurements of the complex forms from periapical radiographs displayed an increase in size with advancing age [158]. Furthermore, a synthesis of case reports of large odontomas, in the same report, found that 80% are of the complex type [158]. The likelihood of recurrence of either type of odontoma was considered by the WHO's 2017 edition to be rare [152]. Although the erstwhile independent entity of *ameloblastic fibro-odontoma* (AFO, awarded ICD-O code 9290/0 in the WHO's 1992 edition [159]; the last WHO entry was 2005 [160]) is likely to represent immature stages of the complex odontoma, it was recently reported to recur if inadequately removed [161]. One of the authors of that report contributed to the WHO's 2017 edition's definition. An example of a large AFO is displayed in Figure 11.49. Wright and Vered state that while a "small number of AFOs could conceptually be neoplastic because of their exceptionally large size, the consensus was that once dental hard tissues are produced, these tumors are likely maturing into odontomas." In addition to AFO, they included ameloblastic fibrodentinoma under odontomas [72].

10.23 Rarer Causes of Radiopacities in the Jaws

Before concluding this chapter with the two most frequent causes of radiopacities in the jaws, namely dense bone islands (DBI; also known as idiopathic osteosclerosis) and sclerosing osteitis, we will consider

four lesions. These are the adenomatoid odontogenic tumor (AOT), calcifying epithelial odontogenic tumor (CEOT), calcifying odontogenic cyst (COC), and dentinogenic ghost cell tumor (DGCT). All four present radiologically as containing radiopacities. The first two frequently enclose an unerupted tooth. Although all are very rare, particularly the last three, nevertheless each has provoked the development of considerable bodies of literature, to which the following discussion testifies.

10.23.1 ADENOMATOID ODONTOGENIC TUMOR (ICD-O 9300/0)

The WHO's 2017 edition [162] updated Philipsen and Nikai's definition of the AOT as "composed of odontogenic epithelium in a variety of histoarchitectural patterns, embedded in a mature connective tissue stroma and characterized by slow but progressive growth" [163] by asserting that the "AOT is a benign lesion that shows duct-like structure" [162]. The immunoprofile of the AOT indicates that its nature may be more hamartomatous than neoplastic [164]. This is consistent with the AOT's limited growth potential [72].

Over 95% of AOTs are intraosseous. The AOT is twice as frequently found in the maxilla and particularly in the anterior sextant. In 75% there is a pericoronal association with unerupted teeth, of which canines account for 60% [162]. All of the cases of Swasdison et al. [165] and Leon et al. [166] presented as well-defined unilocular radiolucencies. Both studies reported well-defined margins, which Leon et al. described as "sclerotic" [166]. One-third presented with flecks of calcification (Figure 10.41) [166]. These are best appreciated on intraoral radiographs rather than on panoramic radiographs [167]. The identification of these flecks of calcification facilitates differentiation from those lesions which typically present as radiolucencies [167].

Leon et al. also remarked that most of their cases associated with an unerupted tooth mimicked the dentigerous cyst [166]. Swasdison et al. reported that the initial clinical diagnosis of 26% was as dentigerous cysts, 16% as calcifying cystic odontogenic tumors (CCOT), 4% as ameloblastomas, but only 16% as AOTs [165]. This range of clinical diagnoses reflects the AOT's variable radiology.

Becker et al. reported that a major feature of AOT in patients over 30 years of age was root resorption (Figure 10.41) [168].

Jiang et al. reported that the main contribution of CBCT to the diagnosis of AOTs was the ability to display intralesional radiopacities [169].

As AOTs are encapsulated and are enucleated, their recurrence is very low [162].

10.23.2 CALCIFYING EPITHELIAL ODONTOGENIC TUMOR (ICD-O 9340/0)

The WHO's 2017 edition [170] upheld Takata and Slootweg's definition of the CEOT as "a locally invasive epithelial odontogenic neoplasm, characterised by the presence of amyloid material that may become calcified" [171].

Philipsen and Reichart reported on 181 cases synthesized from the literature in 2000 [172]. The relative period prevalence of the CEOT is 1% [172]. It is equally distributed between the sexes. While 67% of cases are found in the mandible (Figure 10.42), for those that occur in either a posterior or anterior sextant, the posterior prevails: 84% and 76% in the mandible and maxilla, respectively. The mean age for the Western global group is 39 (females) and 40 years (males), whereas that for the East Asian global group is 37 (females) and 37 years (males) [172].

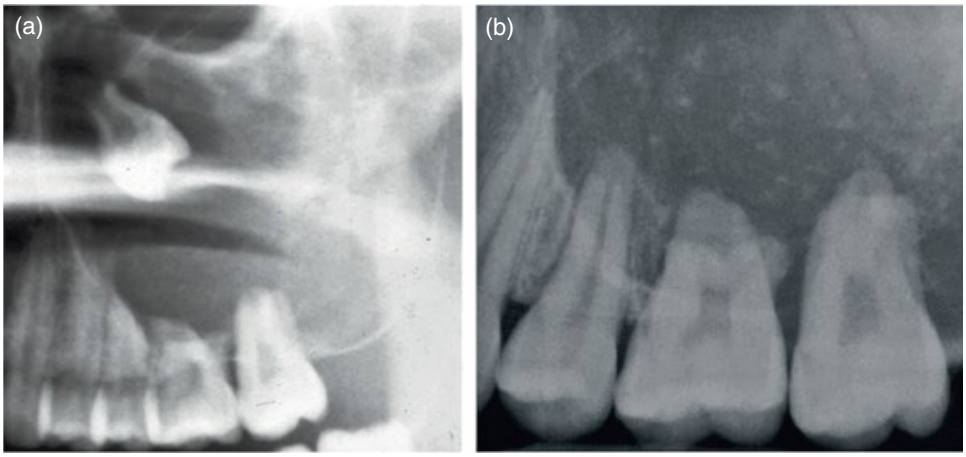


Figure 10.41 Adenomatoid odontogenic tumor (AOT) as displayed on a panoramic radiograph (a) and a periapical radiograph (b). Although the panoramic radiograph displays the AOT almost filling the maxillary sinus and its displacement of the unerupted third molar to the roof of the sinus (floor of the orbit), the periapical radiograph displays better the flecks of calcification within the lesion. Note also the marked root resorption of the erupted premolars and molars. Source: Courtesy of Dr. Frederico Prates, oral maxillofacial radiologist, Porto Alegre, Brazil.

Kaplan et al. synthesized the literature, with particular emphasis on the CEOT's manifestations on conventional radiology [173]. They observed that swelling or expansion was "the most prevalent clinical manifestation" (72%), although 22% were symptom free. The lesions had a mean size of 3.5 (0.5–10) cm [173].

Moreover, 78% of lesions are well defined, of which 28% are corticated (Figure 10.42) [173]. All smaller lesions are well defined, whereas two-thirds of larger lesions are well defined but not corticated; 28% of these larger lesions are poorly defined. The most frequent radiographic presentation is a mixed radiolucent-radiopaque pattern (65%) (Figure 10.42). The radiolucent pattern accounts for 32% of cases. Most of the small lesions are radiolucent (86%), whereas most of the large ones are mixed (74%) [173]. "The coronal clustering (radiopacities close to the crown of the impacted teeth)" is found only in 12% of cases, whereas the "driven snow" pattern is observed only in one case [173]. Although 58% are unilocular and 27% multilocular, those over 3 cm are more likely to be multilocular (Figure 10.42). Nevertheless, those associations with the maxilla are mainly unilocular. There is an association with unerupted teeth in 60% of cases, of which 62% were molars [173].

Philipsen and Reichart report that more than half of cases are associated with a mandibular molar. In order to distinguish pericoronal radiolucent CEOTs from dentigerous cysts, they suggest that whereas the latter is more frequently associated with the third molar, the former is more frequently associated with the first and second molars [172].

Tooth displacement is observed frequently (41%), whereas root resorption is infrequent (4%) [173]. Kaplan et al. suggested that this infrequency for root resorption may distinguish it from the solid ameloblastoma [173], which was reported by Struthers and Shear to exhibit root resorption in 81% of cases [174]. Displacement of anatomical structures, such as the mandibular canal, was also

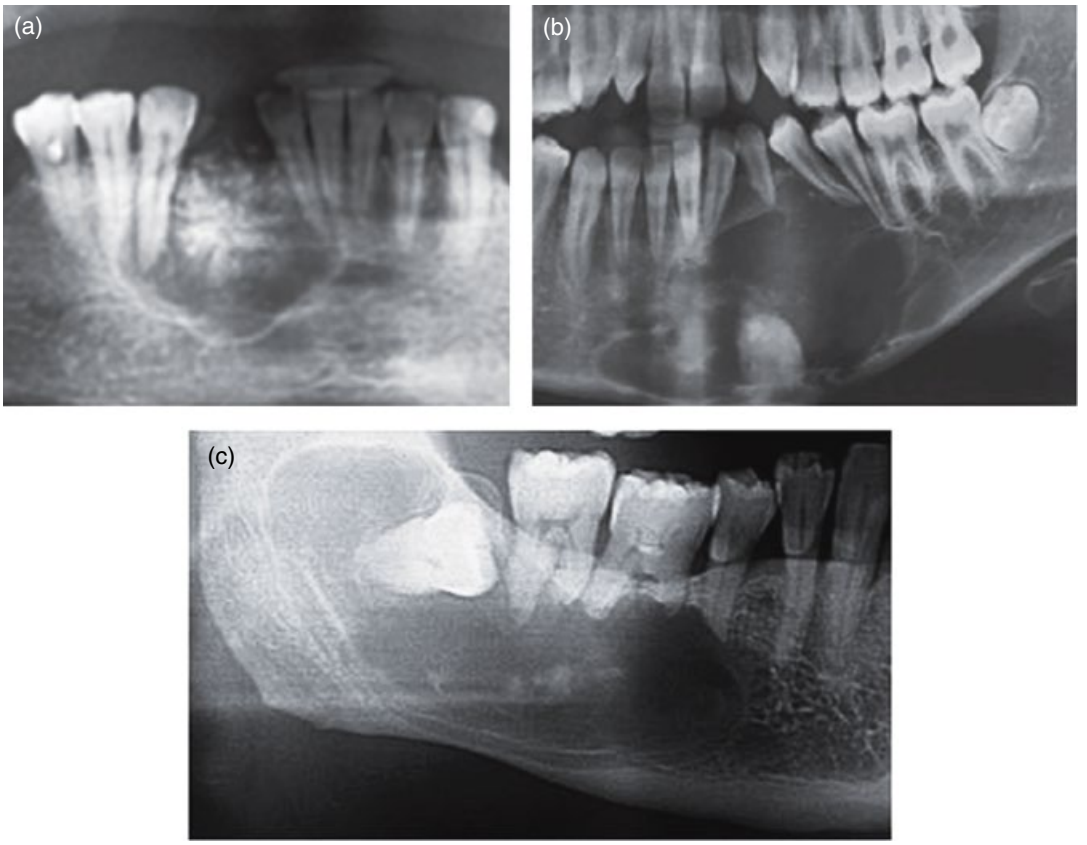


Figure 10.42 Radiographic features of 3 calcifying epithelial odontogenic tumours (CEOT) of the mandible. (a) Panoramic radiograph exhibits a multilocular radiolucency with corticated margin and with central radiopacities extending from the apex of the first right premolar to the midline between the central incisors. It has widely displaced the right canine and lateral incisor (b) Panoramic radiograph of a clear-cell variant CEOT displaying a substantially corticated multilocular radiolucency occupying entire height of the anterior sextant. With downward displacement of the lower border, where an ovoid radiopaque is sited. The left lateral incisor, canine and both premolars have been displaced. The incisive branch of the mandibular canal has also been displaced to the lower border of the mandible. The panoramic radiograph in (c) displays in addition root resorption. (a) and (b) reproduced with permission de Arruda JAA, Abreu LG, Silva LVO, Schuch LF, Monteiro JLGC, Arantes DAC, da Costa AAS, Nóbrega KHS, Vasconcelos ACU, de Andrade BAB, Romañach MJ, Sobral APV, Rivero ERC, da Silva TA, Batista AC, Mesquita RA. Calcifying epithelial odontogenic tumours: Collaborative study of 32 cases and review of literature. *Oral Dis*. 2018 Aug 16. doi: 10.1111/odi.12958. (c) reproduced with permission of Dr. Lewei Zhang, Faculty of Dentistry, University of British Columbia.

infrequent [173]. Although Kaplan et al. observed penetration of the apex of the inferiorly displaced molar through the inferior cortex of the mandible in only 7% of cases in their synthesis, they did suggest that its presence should prompt consideration of a CEOT [173].

Philipsen and Reichart advise that due to the relatively indolent behavior of mandibular cases, they can be effectively treated by enucleation [172]. Maxillary cases, on the other hand, tend to grow more rapidly and do not remain well confined. These should be treated more

radically. Although recurrences are rare, a five-year follow-up period must be considered the absolute minimum. The overall recurrence rate is 14%, but that of the relatively identified clear cell variant is higher; it has a 22% recurrence rate [172].

Anavi et al. synthesized the literature on the clear cell variant of CEOT (Figure 10.42) [175]. They identified 19, of which 12 were central; the other 7 were peripheral. The central cases were evenly distributed between males and females; their mean age at first presentation was 34 years. Three-quarters of the central cases were located in the mandible. Most affected the posterior sextant. All but one were well defined; two-thirds were corticated. Half were radiolucent and half mixed. All but one were unilocular. All affected the alveolus, and one-quarter occurred in edentulous areas. Two more were associated with root resorption, two were associated with tooth displacement without root resorption, and two were associated with the crowns of unerupted teeth. Two-thirds of cases perforated the cortex.

10.23.3 CALCIFYING ODONTOGENIC CYST (ICD-O 9301/0)

In the WHO's 2005 edition, Praetorius and Ledesma-Montes defined the CCOT as a "benign cystic neoplasm of odontogenic origin, characterised by an ameloblastomalike epithelium with ghost cells that may calcify" [176]. In the WHO's 2017 edition [177], CCOT was changed back to the original COC, which was defined as "a simple cyst lined by ameloblastoma-like epithelium, which contained local accumulations of ghost cells." Half contain calcifications of an associated odontoma [177].

According to Wright and Vered, unlike the KCOT/OKC debate, the move of CCOT back to COC was not contentious and was achieved unanimously [72]. Furthermore, "the solid tumor containing ghost cells was updated and continued as the dentinogenic ghost cell tumor" [72].

10.23.4 DENTINOGENIC GHOST CELL TUMOR (ICD-O CODE 9302/0)

The WHO's 2017 edition defined the DGCT, also known as the calcifying ghost cell odontogenic tumor, as "a benign but locally infiltrating neoplasm of odontogenic epithelium. It has biphasic morphology, consisting of a predominant ameloblastomaous proliferation and a less prominent component of basaloid to stellate reticulum cells, The tumour characteristically contains aberrant keratinization, with a variable number of ghost cell and material morphologically resembling dentinoid or osteodentin" [178]. Wright and Vered confirmed that any solid tumor containing ghost cells was a DGCT [72]. The DGCT, of which only 45 cases have been reported, is the rarest of ghost cell tumors. More than half of DGCTs occurred in East Asians. It occurred twice as frequently in males and the mean age of presentation was 40 years, for a range in age at first presentation from the second to the eighth decades. DGCT predominantly presents in the posterior sextants of both jaws, with 80% presenting as unilocular radiolucencies and the rest multilocular [178]. Nearly 80% contain radiopacities [178].

Recurrence after radical treatment is 33%, whereas that after more conservative treatment is 73%. As the DGCT has recurred up to 20 years after primary treatment, long-term follow-up is necessary [178].

10.24 Sclerosing or Condensing Osteitis and Dense Bone Islands or Idiopathic Osteosclerosis

Sclerosing osteitis (SO, also known as "condensing osteitis" [Figure 10.37] and "inflammatory sclerosis") and DBI (also commonly known as "idiopathic osteosclerosis"; see Figures 1.15, 1.16, 2.7, and 10.43) are radiopacities within the bone, representing thickening of the trabeculae [179]. DBI, as its synonym idiopathic osteosclerosis suggests, has no known cause. Therefore, while SO is likely to be accompanied by symptoms associated with a necrotic pulp or its sequelae, DBI would be completely symptom free and observed as an incidental finding in the examination for another clinical reason.

Although well defined, SO and DBI do not have a radiolucent margin. Nevertheless, this may not be so easy to determine, because the Mach band effect may create the illusion of one, and compel consideration of OF and FocOD in the differential diagnosis. To offset this phenomenon, trabeculae are seen crossing the Mach band effect–created radiolucent space (see Figure 2.7).

Both SO and DBI should be distinguished from retained deciduous molar roots and from torus mandibularis. Although the former infrequently have a visible periodontal ligament space, they are typically root shaped and are found mesial and/or distal to the second mandibular premolar. The image of the torus mandibularis on panoramic radiographs is usually displaced more coronally than it appears on clinical examination, due to the upward angulation of the central ray.

The global distribution of reports included in the systematic review [180] from which much of the following is derived is set out in Figure 1.55 and the details are in Table 10.9.

The DBI is a frequently encountered clinical phenomenon, particularly on panoramic radiographs. It was observed more frequently in an East Asian community (Hong Kong) in comparison to two Western communities within the United Kingdom [180]. It displayed a slight predilection for females (58%). The mean age at first presentation is 31 years (Table 10.9). DBI predominantly affected the mandible (94%); this percentage was lower among sub-Saharan Africans [180].

It is important to distinguish between SO and DBI, because they represent different disease processes. For most cases this is not difficult. In a dentate sextant, if the lesion is not in direct association with a tooth, DBI is more likely. If associated with a tooth and the tooth is carious and/or heavily restored, SO is more likely, whereas a noncarious and/or unrestored tooth is virtually pathognomonic of the DBI. It is assumed that pulp-vitality testing has been already performed. A nonvital tooth is indicative of a possible SO, whereas a vital tooth is more certainly a DBI. Difficulty occurs when these lesions arise in the edentulous alveolus (see Figure 20.7). In such a situation, distinguishing between them requires review not just of the radiograph at the time of extraction, but also of those prior to that. Generally, it is expected that the SO would regress once the inflammatory cause has been removed by either tooth extraction or endodontic treatment.

Although DBIs have been shown to be labile [181], environmental factors may influence their prevalence and size. The higher prevalence of DBIs in the Japanese than in the Hong Kong Chinese may be linked to higher fluoridation of the water supply at the relevant time in the patients' lives. Both communities already have a

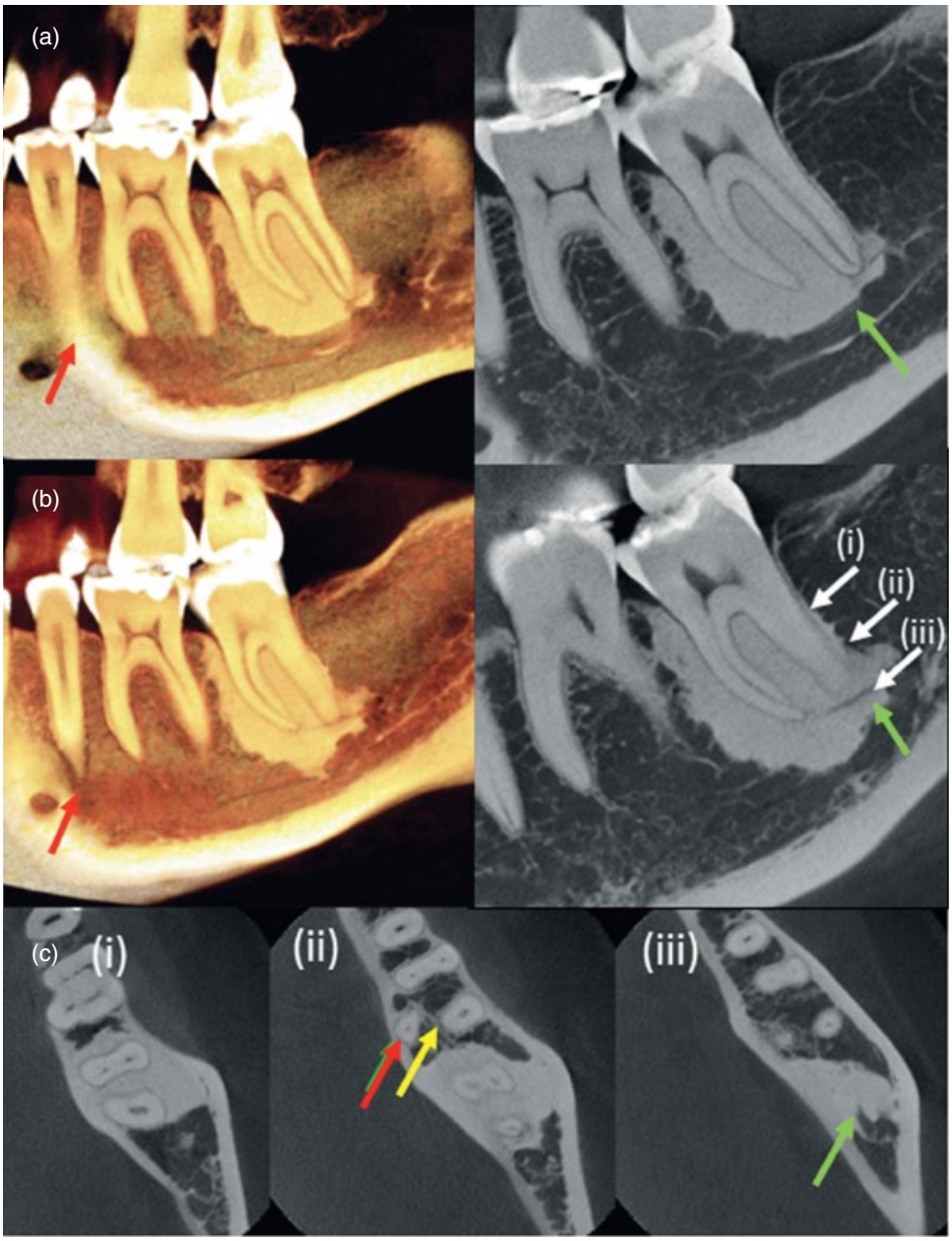


Figure 10.43 Cone-beam computed tomography of a dense bone island (DBI) affecting the roots of the mandibular second molar. The three-dimensional reconstructions (a and b, in color) reveal that the DBI is wholly within the alveolus, enclosing the roots of the molar. The panoramic reconstructions reveal that the well-defined DBI is linked to the trabeculae of the normal adjacent cancellous bone. The axial reconstructions (c) reveal that the DBI abuts directly onto the buccal and lingual cortices, but does not erode or displace them. The notations i, ii, and iii in (b) indicate planes from which the axial reconstructions in (c) are derived. Although the (b) pairing of images reveals that the DBI has extended from the alveolar process into the basal process, the (a) pairing reveals the mandibular canal (green arrow) coursing through the DBI relatively undisturbed. The yellow arrow reveals the mandibular canal coursing between the roots of the second premolar onward to the mental foramen. Note: A small 5 cm by 5 cm field of view was used; see (c ii). The red arrows display the buccal apex of the second premolar lodged in the buccal cortex just distal to the mental foramen. Source: Courtesy of Dr. Frederico Prates, oral maxillofacial radiologist, Porto Alegre, Brazil.

Table 10.9 Dense bone island or idiopathic osteosclerosis: systematic review.

Feature	Total	Caucasian	East Asian	Sub-Saharan African	Latin American
Male: Female	42% : 58%	48% : 52%	40% : 60%	36% : 64%	N/A
Mean age	31 years	29 years	32 years	N/A	N/A
Mandible: Maxilla	94% : 6%	92% : 8%	98% : 2%	74% : 26%[a]	N/A
Mandible: *Anterior: Posterior*	6% : 94%	14% : 86%	10% : 90%	59% : 41%[a]	N/A
Maxilla: *Anterior: Posterior*	0% : 100%[a]	0% : 100%[a]	0% : 100%[a]	33% : 67%[a]	N/A

[a] Percentages derived either from one report or from a synthesis of no more than 50 cases.
N/A, information not available.

high dietary fluoride intake [180]. The Hong Kong Chinese displayed not only a significant reduction in prevalence between two separate but similar consecutive series of nearly 1000 patients 10 years apart, but also a significant reduction in size. After the reduction of concentration of fluoride in the water supply, only those in the fifth decade and above showed very little or no reduction in size. The most likely reason for this phenomenon is that the individuals were already past the age of their peak bone mass (about 30 years of age) [180].

The mean age of first presentation in the systematic review was 31 years [180], which was almost identical to the 32 years for the recently reported Iranians [182]. DBIs were more prevalent in females in the systematic review and among Iranians. While 94% of cases affect the mandible, the mandible and maxilla affect the posterior sextants in 94% and 100% of cases, respectively. DBI are generally not associated with either root resorption or tooth displacement [180].

Furthermore, in following up the findings in the Hong Kong Chinese [180], an increased number of DBI would be expected in those patients who grew up in regions of the world where natural water fluoridation concentration is very high; such regions are found in India, Thailand, China, and Ethiopia, among others [183]. Recently it has been found that fluoride added to drinking water does not cause osteosarcoma or ES [184], certainly in the United Kingdom, but a WHO institution has cautioned that, in addition to the clear dental and skeletal benefits of fluoridation [184], there are possible downsides that require further evaluation [185]. CBCT of large DBIs are displayed in Figures 1.16, 2.7, and 10.43.

References

1. James, B.C., Hwang, J.L., Grogan, R.H. et al. (2014). Leontiasis ossea caused by long-standing hyperparathyroidism secondary to chronic renal failure. *Surgery* 156: 1644–1646.
2. Vallet, M. and Ralston, S.H. (2016). Biology and treatment of Paget's disease of bone. *J. Cell. Biochem.* 117: 289–299.
3. Corral-Gudino, L., Borao-Cengotita-Bengoa, M., Del Pino-Montes, J., and Ralston, S. (2013). Epidemiology of Paget's disease of bone: a systematic review and meta-analysis of secular changes. *Bone* 55: 347–352.
4. Ralston, S.H. (2013). Clinical practice. Paget's disease of bone. *N. Engl. J. Med.* 368: 644–650.
5. Ralston, S.H. (2008). Juvenile Paget's disease, familial expansile osteolysis and other genetic osteolytic disorders. *Best Pract. Res. Clin. Rheumatol.* 22: 101–111.

6. Whyte, M.P., Tau, C., McAlister, W.H. et al. (2014). Juvenile Paget's disease with heterozygous duplication within TNFRSF11A encoding RANK. *Bone* 68: 153–161.
7. Tan, A. and Ralston, S.H. (2014). Clinical presentation of Paget's disease: evaluation of a contemporary cohort and systematic review. *Calcif. Tissue Int.* 95: 385–392.
8. Hashimoto, J., Ohno, I., Nakatsuka, K. et al. (2006). Prevalence and clinical features of Paget's disease of bone in Japan. *J. Bone Miner. Metab.* 24: 186–190.
9. Sirikulchayanonta, V., Jaovisidha, S., Subhadrabandhu, T., and Rajatanavin, R. (2012). Asymptomatic Paget's bone disease in ethnic Thais: a series of four case reports and a review of the literature. *J. Bone Miner. Metab.* 30: 485–492.
10. Nagano, S., Yokouchi, M., Nagayoshi, R. et al. (2013). Paget disease of bone in Japanese patients: a report of three cases. *J. Orthop. Surg. (Hong Kong)* 21: 375–379.
11. Wat, W.Z., Cheung, W.S., and Lau, T.W. (2013). A case series of Paget's disease of bone in Chinese. *Hong Kong Med. J.* 19: 242–248.
12. MacDonald-Jankowski, D.S. (1992). Gigantiform cementoma occurring in two populations, London and Hong Kong. *Clin. Radiol.* 45: 316–318.
13. Takata, S., Hashimoto, J., Nakatsuka, K. et al. (2006). Guidelines for diagnosis and management of Paget's disease of bone in Japan. *J. Bone Miner. Metab.* 24: 359–367.
14. Cheng, Y.S., Wright, J.M., Walstad, W.R., and Finn, M.D. (2002). Osteosarcoma arising in Paget's disease of the mandible. *Oral Oncol.* 38: 785–792.
15. Lozano-Calderon, S.A., Colman, M.W., Raskin, K.A. et al. (2014). Use of bisphosphonates in orthopedic surgery: pearls and pitfalls. *Orthop. Clin. North Am.* 45 (3): 403–416.
16. Ramaglia, L., Morgese, F., Filippella, M., and Colao, A. (2007). Oral and maxillofacial manifestations of Gardner's syndrome associated with growth hormone deficiency: case report and literature review. *Oral Surg. Oral Med. Oral Pathol. Oral Radiol. Endod.* 103: e30–e34.
17. Cristofaro, M.G., Giudice, A., Amantea, M. et al. (2013). Gardner's syndrome: a clinical and genetic study of a family. *Oral Surg. Oral Med. Oral Pathol. Oral Radiol.* 115: e1–e6.
18. Jaiswal, A.S., Balusu, R., and Narayan, S. (2005). Involvement of adenomatous polyposis coli in colorectal tumorigenesis. *Front. Biosci.* 10: 1118–1134.
19. Wijn, M.A., Keller, J.J., Giardiello, F.M., and Brand, H.S. (2007). Oral and maxillofacial manifestations of familial adenomatous polyposis. *Oral Dis.* 13: 360–365.
20. Takeuchi, T., Takenoshita, Y., Kubo, K., and Iida, M. (1993). Natural course of jaw lesions in patients with familial adenomatosis coli (Gardner's syndrome). *Int. J. Oral Maxillofac. Surg.* 22: 226–230.
21. Lee, B.D., Lee, W., Oh, S.H. et al. (2009). A case report of Gardner syndrome with hereditary widespread osteomatous jaw lesions. *Oral Surg. Oral Med. Oral Pathol. Oral Radiol. Endod.* 107: e68–e72.
22. Fonseca, L.C., Kodama, N.K., Nunes, F.C. et al. (2007). Radiographic assessment of Gardner's syndrome. *Dentomaxillofac. Radiol.* 36: 121–124.
23. Madani, M. and Madani, F. (2007). Gardner's syndrome presenting with dental complaints. *Arch. Iran Med.* 10: 535–539.
24. Wenig, B.M., Mafee, M.F., and Ghosh, L. (1998). Fibro-osseous, osseous, and cartilaginous lesions of the orbit and paraorbital region. Correlative clinicopathologic and radiographic features, including the diagnostic role of CT and MR imaging. *Radiol. Clin. N. Am.* 36: 1241–1259.
25. Damron, T.A., Ward, W.G., and Stewart, A. (2007). Osteosarcoma, chondrosarcoma, and Ewing's sarcoma: National Cancer Data Base Report. *Clin. Orthop. Relat. Res.* 459: 40–47.
26. Lee, R.J., Arshi, A., Schwartz, H.C., and Christensen, R.E. (2015). Characteristics and prognostic factors of osteosarcoma of the jaws: a retrospective cohort study. *JAMA Otolaryngol. Head Neck Surg.* 141: 470–477.
27. van den Berg, H. and Merks, J.H. (2014). Incidence and grading of cranio-facial osteosarcomas. *Int. J. Oral Maxillofac. Surg.* 43: 7–12.
28. Friebele, J.C., Peck, J., Pan, X. et al. (2015). Osteosarcoma: a meta-analysis and review of the literature. *Am. J. Orthop (Belle Mead NJ)* 44: 547–553.

29. Mardinger, O., Givol, N., Talmi, Y.P., and Taicher, S. (2001). Osteosarcoma of the jaw. The Chaim Sheba Medical Center experience. *Oral Surg. Oral Med. Oral Pathol. Oral Radiol. Endod.* 91: 445–451.
30. Ogunlewe, M.O., Ajayi, O.F., Adeyemo, W.L. et al. (2006). Osteogenic sarcoma of the jaw bones: a single institution experience over a 21-year period. *Oral Surg. Oral Med. Oral Pathol. Oral Radiol. Endod.* 101: 76–81.
31. Yamaguchi, S., Nagasawa, H., Suzuki, T. et al. (2004). Sarcomas of the oral and maxillofacial region: a review of 32 cases in 25 years. *Clin. Oral Investig.* 8: 52–55.
32. Ajura, A.J. and Lau, S.H. (2010). A retrospective clinicopathological study of 59 osteogenic sarcoma of jaw bone archived in a stomatology unit. *Malays. J. Pathol.* 32: 27–34.
33. Guevara-Canales, J.O., Sacsaquispe-Contreras, S.J., Morales-Vadillo, R., and Sánchez-Lihón, J. (2012). Epidemiology of the sarcomas of the jaws in a Peruvian population. *Med. Oral Patol. Oral Cir. Bucal.* 17: e201–e205.
34. Givol, N., Buchner, A., Taicher, S., and Kaffe, I. (1998). Radiological features of osteogenic sarcoma of the jaws. A comparative study of different radiographic modalities. *Dentomaxillofac. Radiol.* 27: 313–320.
35. Fernandes, R., Nikitakis, N.G., Pazoki, A., and Ord, R.A. (2007). Osteogenic sarcoma of the jaw: a 10-year experience. *J. Oral Maxillofac. Surg.* 65: 1286–1291.
36. Coca-Pelaz, A., Rodrigo, J.P., Triantafyllou, A. et al. (2014). Chondrosarcomas of the head and neck. *Eur. Arch. Otorhinolaryngol.* 271: 2601–2609.
37. MacIntosh, R.B., Khan, F., and Waligora, B.M. (2015). Chondrosarcoma of the temporomandibular disc: behavior over a 28-year observation period. *J. Oral Maxillofac. Surg.* 73: 465–474.
38. Gaspar, N., Hawkins, D.S., Dirksen, U. et al. (2015). Ewing sarcoma: current management and future approaches through collaboration. *J. Clin. Oncol.* 33: 3036–3046.
39. Stewart, B.D., Reith, J.D., Knapik, J.A., and Chi, A.C. (2014). Bone- and cartilage-forming tumors and Ewing sarcoma: an update with a gnathic emphasis. *Head Neck Pathol.* 8: 454–462.
40. Lawlor, E.R. and Sorensen, P.H. (2015). Twenty years on: what do we really know about Ewing sarcoma and what is the path forward? *Crit. Rev. Oncog.* 20: 155–171.
41. MacDonald, D.S. (2015). Maxillofacial fibro-osseous lesions. *Clin. Radiol.* 70: 25–36.
42. Petrikowski, C.G., Pharoah, M.J., Lee, L., and Grace, M.G. (1995). Radiographic differentiation of osteogenic sarcoma, osteomyelitis, and fibrous dysplasia of the jaws. *Oral Surg. Oral Med. Oral Pathol. Oral Radiol. Endod.* 80: 744–750.
43. An, C.H., An, S.Y., Choi, B.R. et al. (2012). Hard and soft tissue changes of osteomyelitis of the jaws on CT images. *Oral Surg. Oral Med. Oral Pathol. Oral Radiol.* 114: 118–126.
44. Chou, A., Schulman, J.M., Gross, A.J. et al. (2016). Gingival pustules and sterile diffuse sclerosing osteomyelitis as a feature of synovitis, acne, pustulosis, hyperostosis, osteitis (SAPHO) syndrome. *Oral Surg. Oral Med. Oral Pathol. Oral Radiol.* 121: e116–e122.
45. Wannfors, K. (2013). SAPHO (synovitis-acne-pustulosis-hyperostosis-osteitis): a multidisciplinary approach. *Oral Surg. Oral Med. Oral Pathol. Oral Radiol.* 116: 692–697.
46. Aljuhani, F., Tournadre, A., Tatar, Z. et al. (2015). The SAPHO syndrome: a single-center study of 41 adult patients. *J. Rheumatol.* 42: 329–334.
47. Fu, Z., Liu, M., Li, Z. et al. (2016). Is the bull-head sign on bone scintigraphy really common in the patient with SAPHO syndrome? A single-center study of a 16-year experience. *Nucl. Med. Commun.* 37: 387–392.
48. Ruggiero, S.L. (2015). Diagnosis and staging of medication-related osteonecrosis of the jaw. *Oral Maxillofac Surg. Clin. North Am.* 27: 479–487.
49. Dodson, T.B. (2015). The frequency of medication-related osteonecrosis of the jaw and its associated risk factors. *Oral Maxillofac Surg. Clin. North Am.* 27: 509–516.
50. Mercer, E., Norton, T., Woo, S. et al. (2013). Ninety-one osteoporosis patients affected with bisphosphonate-related osteonecrosis of the jaw: a case series. *Calcif. Tissue Int.* 93: 241–248.
51. Khan, A., Morrison, A., Cheung, A. et al. (2016). Osteonecrosis of the jaw (ONJ): diagnosis and management in 2015. *Osteoporos. Int.* 27: 853–859.
52. Reyes, C., Hitz, M., Prieto-Alhambra, D., and Abrahamsen, B. (2016). Risks and benefits of

bisphosphonate therapies. *J. Cell. Biochem.* 117: 20–28.
53. Khan, A.A., Morrison, A., Hanley, D.A. et al. (2015). Diagnosis and management of osteonecrosis of the jaw: a systematic review and international consensus. *J. Bone Miner. Res.* 30: 3–23.
54. Khan, A., Morrison, A., Ruggiero, S. et al. (2015). Response to comments on "diagnosis and management of osteoporosis of the jaw: a systematic review and international consensus". *J. Bone Miner. Res.* 30: 1116–1117. l Erratum: *J. Bone Miner. Res*. 2015;30:1941.
55. Fleisher, K.E., Pham, S., Raad, R.A. et al. (2016). Does fluorodeoxyglucose positron emission tomography with computed tomography facilitate treatment of medication-related osteonecrosis of the jaw? *J. Oral Maxillofac. Surg.* 74: 945–958.
56. Gaudin, E., Seidel, L., Bacevic, M. et al. (2015). Occurrence and risk indicators of medication-related osteonecrosis of the jaw after dental extraction: a systematic review and meta-analysis. *J. Clin. Periodontol.* 42: 922–932.
57. Sim, I.W., Sanders, K.M., Borromeo, G.L. et al. (2015). Declining incidence of medication-related osteonecrosis of the jaw in patients with cancer. *J. Clin. Endocrinol. Metab.* 100: 3887–3893.
58. MacDonald-Jankowski, D.S. (2004). Fibro-osseous lesions of the face and jaws. *Clin. Radiol.* 59: 11–25.
59. MacDonald-Jankowski, D.S. and Li, T.K. (2009). Fibrous dysplasia in a Hong Kong community: the clinical and radiological features and outcomes of treatment. *Dentomaxillofac. Radiol.* 38: 63–72.
60. MacDonald-Jankowski, D.S. and Li, T.K. (2009). Ossifying fibroma in a Hong Kong community: the clinical and radiological features and outcomes of treatment. *Dentomaxillofac. Radiol.* 38: 514–523.
61. MacDonald-Jankowski, D.S. (2003). Florid cemento-osseous dysplasia: a systematic review. *Dentomaxillofac. Radiol.* 32: 141–149.
62. MacDonald-Jankowski, D.S. (2008). Focal cemento-osseous dysplasia: a systematic review. *Dentomaxillofac. Radiol.* 37: 350–360.
63. Slootweg, P.J. and El Mofty, S.K. (2005). Ossifying fibroma. In: *WHO Classification of Tumours, Pathology and Genetics of Tumours of the Head and Neck* (ed. L. Barnes, J. Eveson, P. Reichert and D. Sidransky), 319–320. Lyon: International Agency for Research on Cancer (IARC).
64. Slootweg, P.J. (2005). Osseous dysplasia. In: *WHO Classification of Tumours, Pathology and Genetics of Tumours of the Head and Neck* (ed. L. Barnes, J. Eveson, P. Reichert and D. Sidransky), 323. Lyon: International Agency for Research on Cancer (IARC).
65. Brannon, R.B. and Fowler, C.B. (2001). Benign fibro-osseous lesions: a review of current concepts. *Adv. Anat. Pathol.* 8: 126–143.
66. Schajowicz, F.M. (1993). *Histological Typing of Bone Tumours, WHO International Histological Classification of Tumours*, 2e, 39–40. London: Springer-Verlag.
67. Waldron, C.A. (1993). Fibro-osseous lesions of the jaws. *J. Oral Maxillofac. Surg.* 51: 828–835.
68. Eisenberg, E. and Eisenbud, L. (1997). Benign fibro-osseous diseases: current concepts in historical perspective. *Dent. Clin. N. Am.* 9: 551–562.
69. Jundt, G. (2005). Fibrous dysplasia. In: *WHO Classification of Tumours, Pathology and Genetics of Tumours of the Head and Neck* (ed. L. Barnes, J. Eveson, P. Reichert and D. Sidransky), 321–322. Lyon: International Agency for Research on Cancer (IARC).
70. Shi, R.R., Li, X.F., Zhang, R. et al. (2013). GNAS mutational analysis in differentiating fibrous dysplasia and ossifying fibroma of the jaw. *Mod. Pathol.* 26: 1023–1031.
71. Patel, M.M., Wilkey, J.F., Abdelsayed, R. et al. (2010). Analysis of GNAS mutations in cemento-ossifying fibromas and cemento-osseous dysplasias of the jaws. *Oral Surg. Oral Med. Oral Pathol. Oral Radiol. Endod.* 109: 739–743.
72. Wright, J.M. and Vered, M. (2017). Update from the 4th edition of the World Health Organization Classification of Head and Neck Tumours: odontogenic and maxillofacial bone tumors. *Head Neck Pathol.* 11: 68–77.
73. Slootweg, P.J. and Müller, H. (1990). Differential diagnosis of fibroosseous jaw lesions. A histological investigation on 30 cases. *J. Craniomaxillofac. Surg.* 18: 210–214.

74. Wootton-Gorges, S.L. (2009). MR imaging of primary bone tumors and tumor-like conditions in children. *Magn. Reson. Imaging Clin. N. Am.* 17: 469–487.
75. Chapurlat, R.D. and Orcel, P. (2008). Fibrous dysplasia of bone and McCune-Albright syndrome. *Best Pract. Res. Clin. Rheumatol.* 22: 55–69.
76. Fahmy, J.L., Kaminsky, C.K., Kaufman, F. et al. (2000). The radiological approach to precocious puberty. *Br. J. Radiol.* 73: 560–567.
77. Collins, M.T., Singer, F.R., and Eugster, E. (2012). McCune-Albright syndrome and the extraskeletal manifestations of fibrous dysplasia. *Orphanet J. Rare. Dis.* 7 (Suppl 1): S4. https://doi.org/10.1186/1750-1172-7-S1-S4.
78. Ferreira, E.C., Brito, C.C., Domingues, R.C. et al. (2010). Whole-body MR imaging for the evaluation of McCune-albright syndrome. *J. Magn. Reson. Imaging* 31: 706–710.
79. Gaumétou, E., Tomeno, B., and Anract, P. (2012). Mazabraud's syndrome. A case with multiple myxomas. *Orthop Traumatol. Surg. Res.* 98: 455–460.
80. MacDonald-Jankowski, D. (2009). Fibrous dysplasia: a systematic review. *Dentomaxillofac. Radiol.* 38: 196–215.
81. Völkl, T.M. and Dörr, H.G. (2006). McCune-Albright syndrome: clinical picture and natural history in children and adolescents. *J. Pediatr. Endocrinol. Metab.* 19 (Suppl 2): 551–519.
82. Huening, M.A., Reddy, S., and Dodd, L.G. (2008). Fine-needle aspiration of fibrous dysplasia of bone: a worthwhile endeavor or not? *Diagn. Cytopathol.* 36: 325–330.
83. Cohen, M.M. Jr. (2006). The new bone biology: pathologic, molecular, and clinical correlates. *Am. J. Med. Genet. A* 140: 2646–2706.
84. MacDonald-Jankowski, D.S., Yeung, R., Li, T.K., and Lee, K.M. (2004). Computed tomography of fibrous dysplasia. *Dentomaxillofac. Radiol.* 33: 114–118.
85. Sontakke, S.A., Karjodkar, F.R., and Umarji, H.R. (2011). Computed tomographic features of fibrous dysplasia of maxillofacial region. *Imaging Sci. Dent.* 41: 23–38.
86. Ricalde, P., Magliocca, K.R., and Lee, J.S. (2012). Craniofacial fibrous dysplasia. *Oral Maxillofac Surg. Clin. North Am.* 24: 427–441.
87. Sissons, H.A. and Malcolm, A.J. (1997). Fibrous dysplasia of bone: case report with autopsy study 80 years after the original clinical recognition of the bone lesions. *Skelet. Radiol.* 26: 177–183.
88. Alvares, L.C., Capelozza, A.L., Cardoso, C.L. et al. (2009). Monostotic fibrous dysplasia: a 23-year follow-up of a patient with spontaneous bone remodeling. *Oral Surg. Oral Med. Oral Pathol. Oral Radiol. Endod.* 107: 229–234.
89. Daly, B.D., Chow, C.C., and Cockram, C.S. (1994). Unusual manifestations of craniofacial fibrous dysplasia: clinical, endocrinological and computed tomographic features. *Postgrad. Med. J.* 70: 10–16.
90. Jacobsson, S., Hallén, O., Hollender, L. et al. (1975). Fibro-osseous lesion of the mandible mimicking chronic osteomyelitis. *Oral Surg. Oral Med. Oral Pathol.* 40: 433–444.
91. Voytek, T.M., Ro, J.Y., Edeiken, J., and Ayala, A.G. (1995). Fibrous dysplasia and cemento-ossifying fibroma. A histologic spectrum. *Am. J. Surg. Pathol.* 19: 775–781.
92. Yeow, V.K. and Chen, Y.R. (1999). Orthognathic surgery in craniomaxillofacial fibrous dysplasia. *J. Craniofac. Surg.* 10: 155–159.
93. Akintoye, S.O., Boyce, A.M., and Collins, M.T. (2013). Dental perspectives in fibrous dysplasia and McCune–Albright syndrome. *Oral Surg. Oral Med. Oral Pathol. Oral Radiol.* 116: e149–e155.
94. De Mattos, C.B., Binitie, O., and Dormans, J.P. (2012). Pathological fractures in children. *Bone Joint Res.* 1: 272–280.
95. MacDonald-Jankowski, D. (1999). Fibrous dysplasia in the jaws of a Hong-Kong population: radiographic presentation and systematic review. *Dentomaxillofac. Radiol.* 28: 195–202.
96. Salmasi, V., Blitz, A.M., Ishii, M., and Gallia, G.L. (2011). Expanded endonasal endoscopic approach for resection of a large skull base aneurysmal bone cyst in a pediatric patient with extensive cranial fibrous dysplasia. *Child Nerv. Syst.* 27: 649–656.
97. Cheng, J., Yu, H., Wang, D. et al. (2013). Spontaneous malignant transformation in craniomaxillofacial fibrous dysplasia. *J. Craniofac. Surg.* 24: 141–145.
98. Sun, T.T., Tao, X.F., and Shi, H.M. (2014). Spontaneous osteosarcoma in craniomaxillofacial fibrous dysplasia: clinical and CT

imaging features in 8 cases. *Oral Surg. Oral Med. Oral Pathol. Oral Radiol. Endod.* 118: e24–e31.
99. Puls, F., Niblett, A.J., and Mangham, D.C. (2014). Molecular pathology of bone tumours: diagnostic implications. *Histopathology* 64: 461–476.
100. Dujardin, F., Binh, M.B., Bouvier, C. et al. (2011). MDM2 and CDK4 immunohistochemistry is a valuable tool in the differential diagnosis of low-grade osteosarcomas and other primary fibro-osseous lesions of the bone. *Mod. Pathol.* 24: 624–637.
101. Kramer, I.R.M., Pindborg, J.J., and Shear, M. (1992). *Histological Typing of Odontogenic Tumours*, 2e, 27–28. London: Springer-Verlag.
102. Hall, G. (2012). Fibro-osseous lesions of the head and neck. *Diag. Histopathol.* 18: 149–158.
103. Urs, A.B., Kumar, P., Arora, S., and Augustine, J. (2013). Clinicopathologic and radiologic correlation of ossifying fibroma and juvenile ossifying fibroma – an institutional study of 22 cases. *Ann. Diagn. Pathol.* 17: 198–203.
104. MacDonald-Jankowski, D.S. (2009). Ossifying fibroma: a systematic review. *Dentomaxillofac. Radiol.* 38: 495–513.
105. Chen, J.D., Morrison, C., Zhang, C. et al. (2003). Hyperparathyroidism-jaw tumour syndrome. *J. Intern. Med.* 253: 634–642.
106. Aldred, M.J., Talacko, A.A., Savarirayan, R. et al. (2006). Dental findings in a family with hyperparathyroidism-jaw tumor syndrome and a novel HRPT2 gene mutation. *Oral Surg. Oral Med. Oral Pathol. Oral Radiol. Endod.* 101: 212–218.
107. Gill, A.J. (2014). Understanding the genetic basis of parathyroid carcinoma. *Endocr. Pathol.* 25: 30–34.
108. Sherman, R.S. and Sternbergh, W.C. (1948). The roentgen appearance of ossifying fibroma of bone. *Radiology* 50: 595–609.
109. Han, J., Hu, L., Zhang, C. et al. (2016). Juvenile ossifying fibroma of the jaw: a retrospective study of 15 cases. *Int. J. Oral Maxillofac. Surg.* 45: 368–376.
110. Jee, W.H., Choi, K.H., Choe, B.Y. et al. (1996). Fibrous dysplasia: MR imaging characteristics with radiopathologic correlation. *AJR Am. J. Roentgenol.* 167: 1523–1527.
111. Khanna, J.N. and Andrade, N.N. (1992). Giant ossifying fibroma. Case report on a bimaxillary presentation. *Int. J. Oral Maxillofac. Surg.* 21: 233–235.
112. Odell, E.W. (2017). Cemento-ossifying fibroma. In: *WHO Classification of Head and Neck Tumours* (ed. A.K. El-Naggar, J.K.C. Chan, J.R. Grandis, et al.), 231. Lyon: International Agency for Research on Cancer (IARC).
113. El Mofty, S.K., Nelson, B., and Toysawa, S. (2017). Ossifying fibroma. In: *WHO Classification of Head and Neck Tumours* (ed. A.K. El-Naggar, J.K.C. Chan, J.R. Grandis, et al.), 251–252. Lyon: International Agency for Research on Cancer (IARC).
114. MacDonald DS. Fibro-osseous lesions affecting the jaws. Doctoral dissertation (Doctor of Dental Surgery). The University of Edinburgh. 2007. pp 138–139 and 146-147.
115. Visnapuu, V., Peltonen, S., Ellilá, T. et al. (2007). Periapical cemental dysplasia is common in women with NF1. *Eur. J. Med. Genet.* 50: 274–280.
116. Visnapuu, V., Peltonen, S., Tammisalo, T. et al. (2012). Radiographic findings in the jaws of patients with neurofibromatosis 1. *J. Oral Maxillofac. Surg.* 70: 1351–1357.
117. Jett, K. and Friedman, J.M. (2010). Clinical and genetic aspects of neurofibromatosis 1. *Genet. Med.* 12: 1–11.
118. Ariji, Y., Ariji, E., Higuchi, Y. et al. (1994). Florid cemento-osseous dysplasia. Radiographic study with special emphasis on computed tomography. *Oral Surg. Oral Med. Oral Pathol.* 78: 391–396.
119. Knutsen, B.M., Larheim, T.A., Johannessen, S. et al. (2002). Recurrent conventional cemento-ossifying fibroma of the mandible. *Dentomaxillofac. Radiol.* 31: 65–68.
120. Beylouni, I., Farge, P., Mazoyer, J.F., and Coudert, J.L. (1998). Florid cemento-osseous dysplasia: report of a case documented with computed tomography and 3D imaging. *Oral Surg. Oral Med. Oral Pathol. Oral Radiol. Endod.* 85: 707–711.
121. Summerlin, D.J. and Tomich, C.E. (1994). Focal cemento-osseous dysplasia: a clinicopathologic study of 221 cases. *Oral Surg. Oral Med. Oral Pathol.* 78: 611–620.

122. Su, L., Weathers, D.R., and Waldron, C.A. (1997). Distinguishing features of focal cemento-osseous dysplasias and cemento-ossifying fibromas: I. A pathologic spectrum of 316 cases. *Oral Surg. Oral Med. Oral Pathol. Oral Radiol. Endod.* 84: 301–309.
123. Su, L., Weathers, D.R., and Waldron, C.A. (1997). Distinguishing features of focal cemento-osseous dysplasia and cementoossifying fibromas. II. A clinical and radiologic spectrum of 316 cases. *Oral Surg. Oral Med. Oral Pathol. Oral Radiol. Endod.* 84: 540–549.
124. Pindborg, J.J., Kramer, I.R.H., and Torloni, H. (1971). *Histological Typing of Odontogenic Tumours, Jaw Cysts and Allied Lesions*, *WHO International Histological Classifications of Tumours*, No. 5, 31–34. Geneva: World Health Organization.
125. Waldron, C.A., Giansanti, J.S., and Browand, B.C. (1975). Sclerotic cemental masses of the jaws so-called chronic sclerosing osteomyelitis, sclerosing osteitis, multiple enostosis, and gigantiform cementoma. *Oral Surg. Oral Med. Oral Pathol.* 39: 590–604.
126. Melrose, R.J. (1997). The clinic-pathological spectrum of cemento-osseous dysplasia. *Oral Maxillofac. Clin. North Am.* 9: 643–653.
127. Young, S.K., Markowitz, N.R., Sullivan, S. et al. (1989). Familial gigantiform cementoma: classification and presentation of a large pedigree. *Oral Surg. Oral Med. Oral Pathol.* 68: 740–747.
128. Waldron, C.A. (1993). Fibro-osseous lesions of the jaws. *J. Oral Maxillofac. Surg.* 51: 828–835.
129. Noffke, C.E., Raubenheimer, E.J., and MacDonald, D. (2012). Fibro-osseous disease: harmonizing terminology with biology. *Oral Surg. Oral Med. Oral Pathol. Oral Radiol.* 114: 388–392.
130. Moshref, M., Khojasteh, A., Kazemi, B. et al. (2008). Autosomal dominant gigantiform cementoma associated with bone fractures. *Am. J. Med. Genet. A* 146A: 644–648.
131. Shah, S., Huh, K.H., Yi, W.J. et al. (2012). Follow-up CT findings of recurrent familial gigantiform cementoma of a female child. *Skelet. Radiol.* 41: 341–346.
132. Wang, H.W., Yu, M., Qin, X.J., and Zhang, C.P. (2015). Familial gigantiform cementoma: distinctive clinical features of a large Chinese pedigree. *Br. J. Oral Maxillofac. Surg.* 53: 83–35.
133. Miyake, M. and Nagahata, S. (1999). Florid cemento-osseous dysplasia. Report of a case. *Int. J. Oral Maxillofac. Surg.* 28: 56–57.
134. Ong, S.T. and Siar, C.H. (1997). Florid cemento-osseous dysplasia in a young Chinese man. Case report. *Aust. Dent. J.* 42: 404–408.
135. Kumar, V.V., Ebenezer, S., Narayan, T.V., and Wagner, W. (2012). Clinicopathologic conference: multiquadrant expansile fibro-osseous lesion in a juvenile. *Oral Surg. Oral Med. Oral Pathol. Oral Radiol.* 113: 286–292.
136. Abdelsayed, R.A., Eversole, L.R., Singh, B.S., and Scarbrough, F.E. (2001). Gigantiform cementoma: clinicopathologic presentation of 3 cases. *Oral Surg. Oral Med. Oral Pathol. Oral Radiol. Endod.* 91: 438–444.
137. Rossbach, H.C., Letson, D., Lacson, A. et al. (2005). Familial gigantiform cementoma with brittle bone disease, pathologic fractures, and osteosarcoma: a possible explanation of an ancient mystery. *Pediatr. Blood Cancer* 44: 390–396.
138. Toner, M., Allen, C.M., and Castle, J. (2017). Osteoma. In: *WHO Classification of Head and Neck Tumours* (ed. A.K. El-Naggar, J.K.C. Chan, J.R. Grandis, et al.), 246. Lyon: International Agency for Research on Cancer (IARC).
139. Kaplan, I., Nicolaou, Z., Hatuel, D., and Calderon, S. (2008). Solitary central osteoma of the jaws: a diagnostic dilemma. *Oral Surg. Oral Med. Oral Pathol. Oral Radiol. Endod.* 106: e22–e29.
140. Larrea-Oyarbide, N., Valmaseda-Castellón, E., Berini-Aytés, L., and Gay-Escoda, C. (2008). Osteomas of the craniofacial region. Review of 106 cases. *J. Oral Pathol. Med.* 37: 38–42.
141. Woldenberg, Y., Nash, M., and Bodner, L. (2005). Peripheral osteoma of the maxillofacial region. Diagnosis and management: a study of 14 cases. *Med. Oral Patol. Oral Cir. Bucal.* 10: E139–E142.
142. Jones, A.C., Prihoda, T.J., Kacher, J.E. et al. (2006). Osteoblastoma of the maxilla and mandible: a report of 24 cases, review of the literature, and discussion of its relationship to osteoid osteoma of the jaws. *Oral Surg.*

Oral Med. Oral Pathol. Oral Radiol. Endod. 102: 639–650.
143. Toner, M., Allen, C.M., and Castle, J. (2017). Osteoblastoma. In: *WHO Classification of Head and Neck Tumours* (ed. A.K. El-Naggar, J.K.C. Chan, J.R. Grandis, et al.), 249. Lyon: International Agency for Research on Cancer (IARC).
144. Pontual, M.L., Pontual, A.A., Grempel, R.G. et al. (2014). Aggressive multilocular osteoblastoma in the mandible: a rare and difficult case to diagnose. *Braz. Dent. J.* 25: 451–456.
145. Woźniak, A.W., Nowaczyk, M.T., Osmola, K., and Golusinski, W. (2010). Malignant transformation of an osteoblastoma of the mandible: case report and review of the literature. *Eur. Arch. Otorhinolaryngol.* 267: 845–849.
146. Strobel, K., Merwald, M., Huellner, M. et al. (2013). Osteoblastoma of the mandible mimicking osteosarcoma in FDG PET/CT imaging. *Clin. Nucl. Med.* 38: 143–144.
147. El Mofty, S.K. (2017). Cementoblastoma. In: *WHO Classification of Head and Neck Tumours* (ed. A.K. El-Naggar, J.K.C. Chan, J.R. Grandis, et al.), 230–231. Lyon: International Agency for Research on Cancer (IARC).
148. van der Waal, I. (2005). Cementoblastoma. In: *WHO Classification of Tumours, Pathology and Genetics of Tumours of the Head and Neck* (ed. L. Barnes, J. Eveson, P. Reichert and D. Sidransky), 318. Lyon: International Agency for Research on Cancer (IARC).
149. MacDonald-Jankowski, D.S. and Wu, P.C. (1992). Cementoblastoma in Hong Kong Chinese. A report of four cases. *Oral Surg. Oral Med. Oral Pathol.* 73: 760–764.
150. Brannon, R.B., Fowler, C.B., Carpenter, W.M., and Corio, R.L. (2002). Cementoblastoma: an innocuous neoplasm? A clinicopathologic study of 44 cases and review of the literature with special emphasis on recurrence. *Oral Surg. Oral Med. Oral Pathol. Oral Radiol. Endod.* 93: 311–320.
151. Dominguez, F.V., Frenandez, L.R., and Luberti, R.F. (2000). Benign cementoblastoma: analysis of 25 cases. *Rev. Asoc. Odontol. Argent.* 88: 237–244. Spanish.
152. Vered, M., Fowler, C.B., Neville, B.W., and Soluk Tekkesin, M. (2017). Odontoma. In: *WHO Classification of Head and Neck Tumours* (ed. A.K. El-Naggar, J.K.C. Chan, J.R. Grandis, et al.), 220–221. Lyon: International Agency for Research on Cancer (IARC).
153. Fregnani, E.R., Fillipi, R.Z., Oliveira, C.R. et al. (2002). Odontomas and ameloblastomas: variable prevalences around the world? *Oral Oncol.* 38: 807–808.
154. Kramer, I.R.H., Pindborg, J.J., and Shear, M. (1992). *Histological Typing of Odontogenic Tumours*, 2e, 21. London: Springer-Verlag.
155. Praetorius, P. and Piatelli, A. (2005). Odontoma, complex type. In: *WHO Classification of Tumours, Pathology and Genetics of Tumours of the Head and Neck* (ed. L. Barnes, J. Eveson, P. Reichert and D. Sidransky), p310. Lyon: International Agency for Research on Cancer (IARC).
156. Praetorius, P. and Piatelli, A. (2005). Odontoma, compound type. In: *WHO Classification of Tumours, Pathology and Genetics of Tumours of the Head and Neck* (ed. L. Barnes, J. Eveson, P. Reichert and D. Sidransky), p311. Lyon: International Agency for Research on Cancer (IARC).
157. Chen, Y., Li, T.J., Gao, Y., and Yu, S.F. (2005). Ameloblastic fibroma and related lesions: a clinicopathologic study with reference to their nature and interrelationship. *J. Oral Pathol. Med.* 34: 588–595.
158. MacDonald-Jankowski, D.S. (1996). Odontomas in a Chinese population. *Dentomaxillofac. Radiol.* 25: 186–192.
159. Kramer, I.R.H., Pindborg, J.J., and Shear, M. (1992). *Histological Typing of Odontogenic Tumours*, 2e, 18. London: Springer-Verlag.
160. Takeda, Y. and Tomich, C.E. (2005). Ameloblastic fibro-odontoma. In: *WHO Classification of Tumours, Pathology and Genetics of Tumours of the Head and Neck* (ed. L. Barnes, J. Eveson, P. Reichert and D. Sidransky), 309. Lyon: International Agency for Research on Cancer (IARC).
161. Boxberger, N.R., Brannon, R.B., and Fowler, C.B. (2011). Ameloblastic fibro-odontoma: a clinicopathologic study of 12 cases. *J. Clin. Pediatr. Dent.* 35: 397–403.
162. Wright, J.M. and Kusama, K. (2017). Adenomatoid odontogenic tumour. In: *WHO Classification of Head and Neck Tumours* (ed. A.K. El-Naggar, J.K.C. Chan, J.R. Grandis, et al.), 221–222. Lyon: International Agency for Research on Cancer (IARC).

163. Philipsen, H.P. and Nikai, H. (2005). Adenomatoid odontogenic tumour. In: *WHO Classification of Tumours, Pathology and Genetics of Tumours of the Head and Neck* (ed. L. Barnes, J. Eveson, P. Reichert and D. Sidransky), 304. Lyon: International Agency for Research on Cancer (IARC).
164. Reichart, P.A., Philipsen, H.P., Khongkhunthian, P., and Sciubba, J.J. (2017). Immunoprofile of the adenomatoid odontogenic tumor. *Oral Dis.* 23: 731–736.
165. Swasdison, S., Dhanuthai, K., Jainkittivong, A., and Philipsen, H.P. (2008). Adenomatoid odontogenic tumors: an analysis of 67 cases in a Thai population. *Oral Surg. Oral Med. Oral Pathol. Oral Radiol. Endod.* 105: 210–215.
166. Leon, J.E., Mata, G.M., Fregnani, E.R. et al. (2005). Clinicopathological and immunohistochemical study of 39 cases of adenomatoid odontogenic tumour: a multicentric study. *Oral Oncol.* 41: 835–842.
167. Dare, A., Yamaguchi, A., Yoshiki, S., and Okano, T. (1994). Limitation of panoramic radiography in diagnosing adenomatoid odontogenic tumors. *Oral Surg. Oral Med. Oral Pathol.* 77: 662–668.
168. Becker, T., Buchner, A., and Kaffe, I. (2012). Critical evaluation of the radiological and clinical features of adenomatoid odontogenic tumour. *Dentomaxillofac. Radiol.* 41: 533–540.
169. Jiang, M., You, M., Wang, H., and Xu, L. (2014). Characteristic features of the adenomatoid odontogenic tumour on cone beam CT. *Dentomaxillofac. Radiol.* 43: 20140016.
170. Wright, J.M. and Devilliers, P. (2017). Calcifying epithelial odontogenic tumour. In: *WHO Classification of Head and Neck Tumours* (ed. A.K. El-Naggar, J.K.C. Chan, J.R. Grandis, et al.), 220–221. Lyon: International Agency for Research on Cancer (IARC).
171. Takata, T. and Slootweg, P.J. (2005). Calcifying epithelial odontogenic tumour. In: *WHO Classification of Tumours, Pathology and Genetics of Tumours of the Head and Neck* (ed. L. Barnes, J. Eveson, P. Reichert and D. Sidransky), 302. Lyon: International Agency for Research on Cancer (IARC).
172. Philipsen, H.P. and Reichart, P.A. (2000). Calcifying epithelial odontogenic tumour: biological profile based on 181 cases from the literature. *Oral Oncol.* 36: 17–26.
173. Kaplan, I., Buchner, A., Calderon, S., and Kaffe, I. (2001). Radiological and clinical features of calcifying epithelial odontogenic tumour. *Dentomaxillofac. Radiol.* 30: 22–28.
174. Struthers, P. and Shear, M. (1976). Root resorption by ameloblastomas and cysts of the jaws. *Int. J. Oral Surg.* 5: 128–132.
175. Anavi, Y., Kaplan, I., Citir, M., and Calderon, S. (2003). Clear-cell variant of calcifying epithelial odontogenic tumor: clinical and radiographic characteristics. *Oral Surg. Oral Med. Oral Pathol. Oral Radiol. Endod.* 95: 332–329.
176. Praetorius, P. and Ledesma-Montes, C. (2005). Calcifying cystic odontogenic tumour. In: *WHO Classification of Tumours, Pathology and Genetics of Tumours of the Head and Neck* (ed. L. Barnes, J. Eveson, P. Reichert and D. Sidransky), 313. Lyon: International Agency for Research on Cancer (IARC).
177. Speight, P., Ledesma-Montes, C., and Wright, J.M. (2017). Calcified odontogenic cyst. In: *WHO Classification of Head and Neck Tumours* (ed. A.K. El-Naggar, J.K.C. Chan, J.R. Grandis, et al.), 224–226. Lyon: International Agency for Research on Cancer (IARC).
178. Carlos, R. and Ledesmamontes, C. (2017). Dentinogenic ghost cell tumour. In: *WHO Classification of Head and Neck Tumours* (ed. A.K. El-Naggar, J.K.C. Chan, J.R. Grandis, et al.), 226–227. Lyon: International Agency for Research on Cancer (IARC).
179. McDonnell, D. (1993). Dense bone island. A review of 107 patients. *Oral Surg. Oral Med. Oral Pathol.* 76: 124–128.
180. MacDonald-Jankowski, D.S. (1999). Idiopathic osteosclerosis in the jaws of Britons and of the Hong Kong Chinese: radiology and systematic review. *Dentomaxillofac. Radiol.* 28: 357–363.
181. Petrikowski, C.G. and Peters, E. (1997). Longitudinal radiographic assessment of dense bone islands of the jaws. *Oral Surg. Oral Med. Oral Pathol. Oral Radiol. Endod.* 83: 627–634.
182. Moshfeghi, M., Azimi, F., and Anvari, M. (2014). Radiologic assessment and frequency of idiopathic osteosclerosis of jawbones: an

interpopulation comparison. *Acta Radiol.* 55: 1239–1244.
183. Roberts, L.C. and Johnson, A.C. (2017). Nutritional intake and health risks of arsenic and fluouride. In: *Water Resource Quality (WRQ) Geogenic Contamination Handbook. Addressing Arsentic and Fluoride in Drinking Water* (ed. C.A. Johnson and A. Bretzler), 29–32. http://www.eawag.ch/fileadmin/Domain1/Forschung/Menschen/Trinkwasser/Wrq/Handbook/geogenic-contamination-handbook.pdf. Dubendorf: Swiss Federal Institute of Aquatic Science and Technology (EAWAG) http://www.eawag.ch/en/research/humanwelfare/drinkingwater/wrq/risk-maps Accessed December 29, 2018.
184. Blakey, K., Feltbower, R.G., Parslow, R.C. et al. (2014). Is fluoride a risk factor for bone cancer? Small area analysis of osteosarcoma and Ewing sarcoma diagnosed among 0–49-year-olds in Great Britain, 1980–2005. *Int. J. Epidemiol.* 43: 224–234.
185. Zhang, L.E., Huang, D., Yang, J. et al. (2017). Probabilistic risk assessment of Chinese residents' exposure to fluoride in improved drinking water in endemic fluorosis areas. *Environ. Pollut.* 222: 118–125.

Chapter 11

Maxillary sinus

11.1 Introduction

The maxillary sinus (also known as the "maxillary antrum") occupies a considerable part of the midface and is surrounded by important structures and organs. These are the orbits, the nasal and oral cavities, the ethmoid sinuses, and the pterygopalatine and infratemporal fossae. Therefore, disease arising within it can involve these structures in addition to disease arising within them involving it in turn. The shape of the maxillary sinus forms an inverted pyramid with its apex set laterally at the root of the temporal process of the zygoma (Figure 11.1). This shape means that the maxillary sinus is better displayed on cross-sectional imaging modalities rather than on conventional plane radiographs. The modalities displayed in this chapter are *computed tomography* (CT), *cone-beam computed tomography* (CBCT), and *magnetic resonance imaging* (MRI). The role of the recently introduced technology of CBCT in imaging of lesions affecting the maxillary sinus has been illustrated for a number of lesions [1–3].

The central position of the maxillary sinus within the hemi-midface means that it is involved in most fractures of the midface, as the three struts which join the jaws to the skull base frame it. These struts are the frontozygomatic, the zygomaticotemporal, and the frontomaxillary. They transmit the occlusal forces from the dentoalveolar process to the skull base, as shown in Figure 15.2.

The maxillary sinus has a communication with the nasal cavity via an ostium over halfway up the medial wall above the attachment of the inferior turbinate (concha; Figure 11.2). This is the sole or at least the main point of egress for the sinus fluids. An accessory osteum may be present. Normal evacuation is dependent upon the integrity of the pseudostriated squamous epithelium that lines the lumen of the sinus. Although mucosal thickening of the maxillary sinus is common in symptom-free patients, it is considered normal if it is less than 4 mm (Figure 11.2a) [4]. A mucosal thicker than this is suggestive of sinusitis (Figures 11.2b and 11.3). Sinusitis may also result in a fluid-filled sinus (Figures 11.4–11.6).

The hard palate establishes the junction between the alveolar and basal processes of the upper jaw, as does the mandibular canal for the mandible [5]. The profile of the hard palate is readily observed on lateral projections of the jaws, including panoramic radiographs (see Figure 1.24). The maxillary sinus frequently pneumatizes this dentoalveolar process, particularly in the premolar region. Therefore, diseases arising within this process or treatment for these diseases may involve the maxillary sinus. Extensive pneumatization of

Oral and Maxillofacial Radiology: A Diagnostic Approach, Second Edition. Edited by David MacDonald.
© 2020 John Wiley & Sons, Inc. Published 2020 by John Wiley & Sons, Inc.

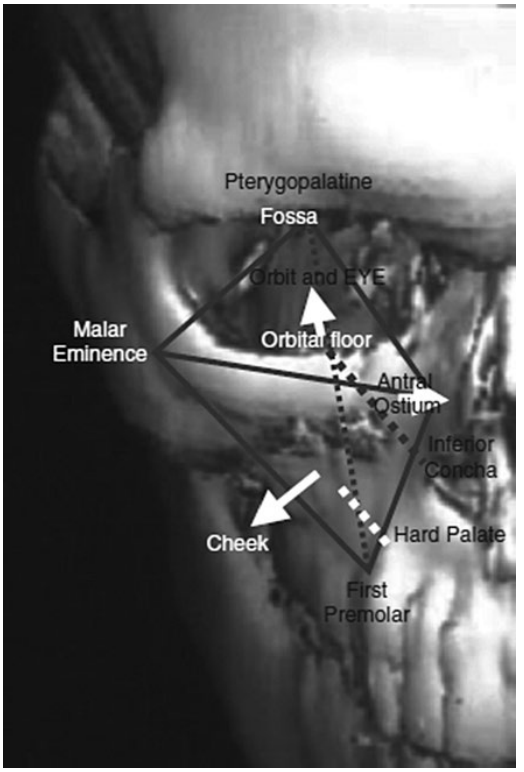


Figure 11.1 Anatomical parameters of the maxillary sinus.

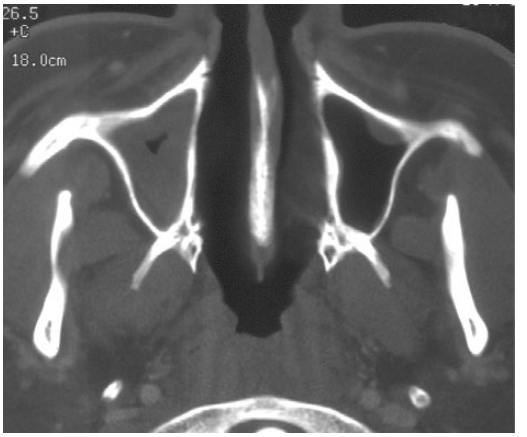


Figure 11.3 Axial computed tomography (bone window) displaying the normal triangular shape of the maxillary sinus (MS). Its degree of pneumatization, size, and shape are generally symmetrical. Note that the normal posteriolateral wall is sigmoid shaped. Lesions arising within the MS lumen generally expand the posterior half of this wall. Lumen of the MS on one side is nearly obturated by substantial expansion of the antral mucosa, leaving only a residual air space in the center. The other side reveals the presence of a shallow dome-shaped opacity of soft-tissue radiodensity arising from the anterior wall of the MS.

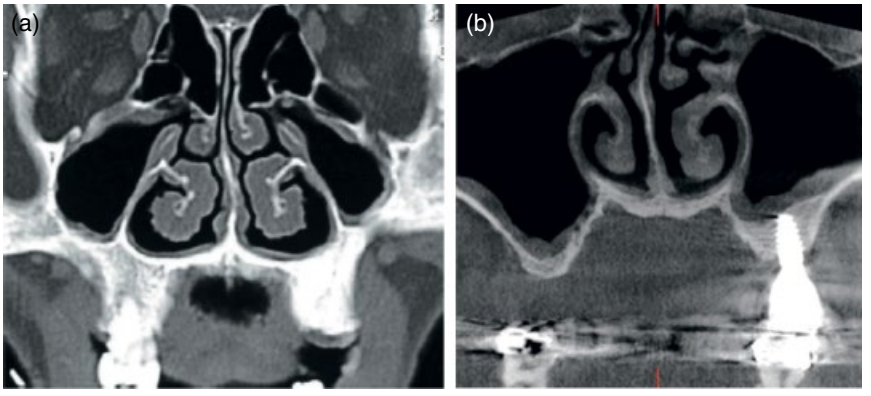


Figure 11.2 (a) Maxillary sinus (MS) displayed on coronal computed tomography and (b) on medium field-of-view cone-beam computed tomography (CBCT), both showing the midface at the level of the ostium of the MS. The ostium's position, above the inferior concha, is toward the roof of the MS. The inferior orbital canal is laterally positioned anteriorly to the lumen of the hypoplastic MS. Note 1: The white rim in (a) represents the mucosal surface, enhancing postcontrast. The darker part is the soft tissue of the turbinates. Note 2: (b) Displays thickening of the sinus mucosa, particularly on the left sinus, associated with an osseointegrated implant. Source: (b) Courtesy of Dr. Frederick Li, Vancouver.

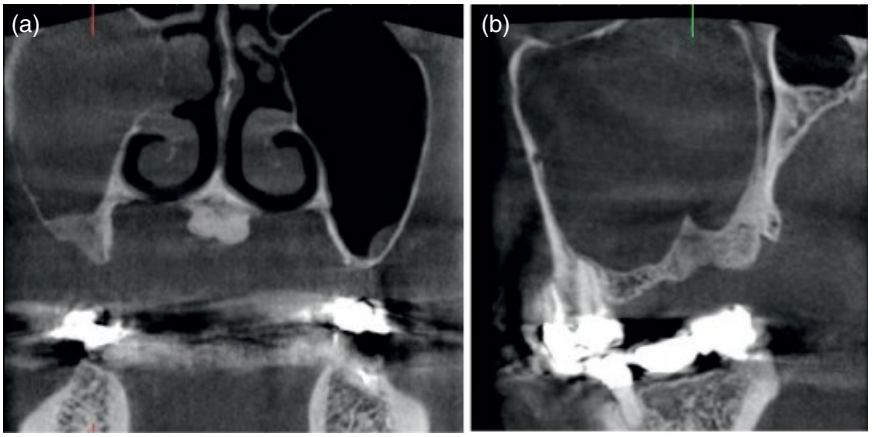


Figure 11.4 Coronal (a) and sagittal (b) reconstructions of medium field-of-view (FOV) cone-beam computed tomography displaying a mucocele in the right maxillary sinus. The coronal reconstruction (a) reveals expansion of the lateral, medial, and superior (roof) walls. The roof is only partially displayed because it has not been wholly encompassed by the median FOV. Note 1: The unaffected left sinus has wholly pneumatized the alveolus in comparison to the right. This suggests that the left alveolus has been edentulous for a longer period in comparison to the right. Note 2: The torus palatinus in (a) is a normal variant and generally requires no treatment. Note 3: Notice the artifacts caused by the metal dental restorations. Source: Courtesy of Dr. Frederick Li, Vancouver.

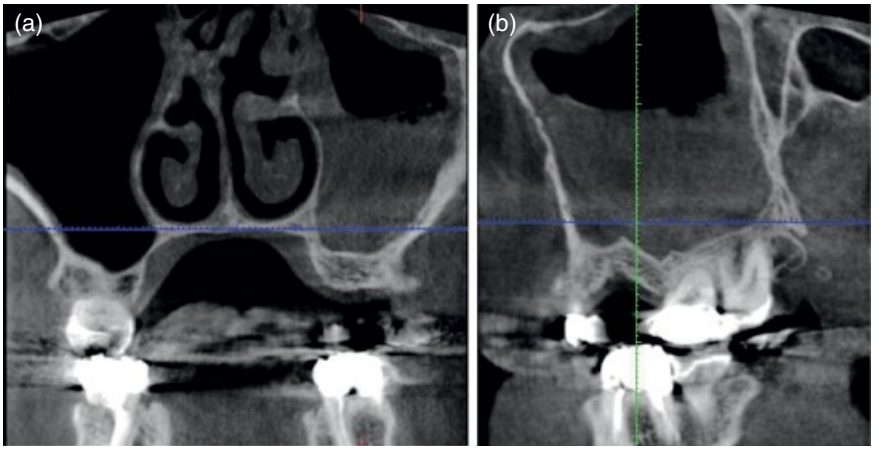


Figure 11.5 Coronal (a) and sagittal (b) reconstructions of medium field-of-view cone-beam computed tomography. (a) Displays sinusitis with a fluid level in the left maxillary sinus (MS); the right side is normal. The fluid level occupies over half of the height of the lumen on the left MS (a and b). Although the remaining lumen is air filled, thickening of the mucosa is obvious. Air bubbles can be seen lying on the surface of the fluid. Note the artifacts caused by the metal dental restorations. The resultant beam hardening has obliterated part of the image of the tongue in (a). Source: Courtesy of Dr. Frederick Li, Vancouver.

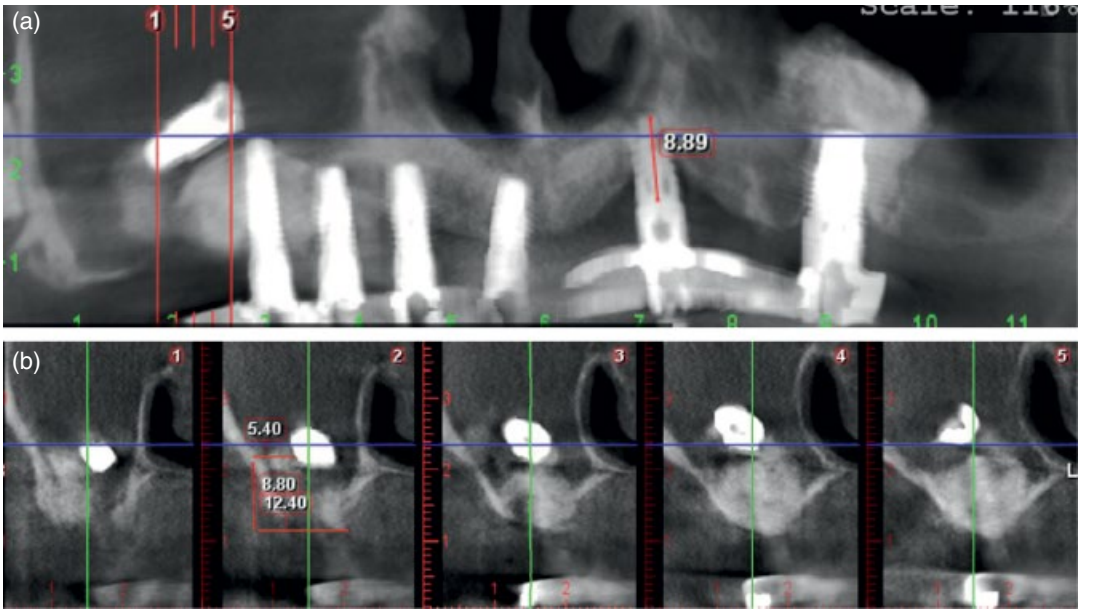


Figure 11.6 Panoramic (a) and transaxial (b) reconstructions of medium field-of-view cone-beam computed tomography. An implant has been displaced through a sinus floor elevation into the right sinus. The positioning of the five transaxial reconstructions is denoted by the vertical red lines on the panoramic reconstruction. Note 1: There is a large oroantral fistula on the right sinus. The lumen of the right sinus is completely opacified. Note 2: The sinus floor elevation has been successful. Note 3: The titanium metal of the implants does not cause the same degree of artifacts as other dental metal reconstructions. Source: Courtesy of Dr. Frederick Li, Vancouver.

the alveolar process, as seen in a panoramic radiograph (Figure 11.7), may indicate the presence of a lesion.

The maxillary sinus reaches adult size at about 12 years of age. Chronic sinusitis during childhood has been suggested to be the cause of its failure to develop (aplasia) or its small size (hypoplasia; Figures 11.8 and 11.9) [4, 6]. Figure 11.9 displays sinus hypoplasia subsequent to osteomyelitis. Osteomyelitis affecting the maxilla is rare due to the excellence of the maxilla's blood supply [7]. When osteomyelitis occurs, it does so in the first decade of life [7], prior to the majority of sinus growth. Pneumatization is reduced by red-marrow conversion during anemia [4]. Figure 11.10 exhibits a case of thalassemia affecting the maxillary sinus.

The maxillary sinuses have septa. Bornstein et al. reported that two-thirds of all their Swiss patients displayed septa on CBCT [8], whereas Sakhdari et al. reported that only 44% of their Iranians had septa [9]. These predominantly arise from the sinus floor (59%), mainly in the first and second molar regions (61%), and are orientated in the coronal plane (62%), as is evident in Figure 11.11 [8]. Sakhdarie et al. reported that 37% arose in the right sinus only, 27% in the left only, and 36% in both [9]. The height of the septa in the right sinus was 6.3 mm and 7.3 mm in the left [9].

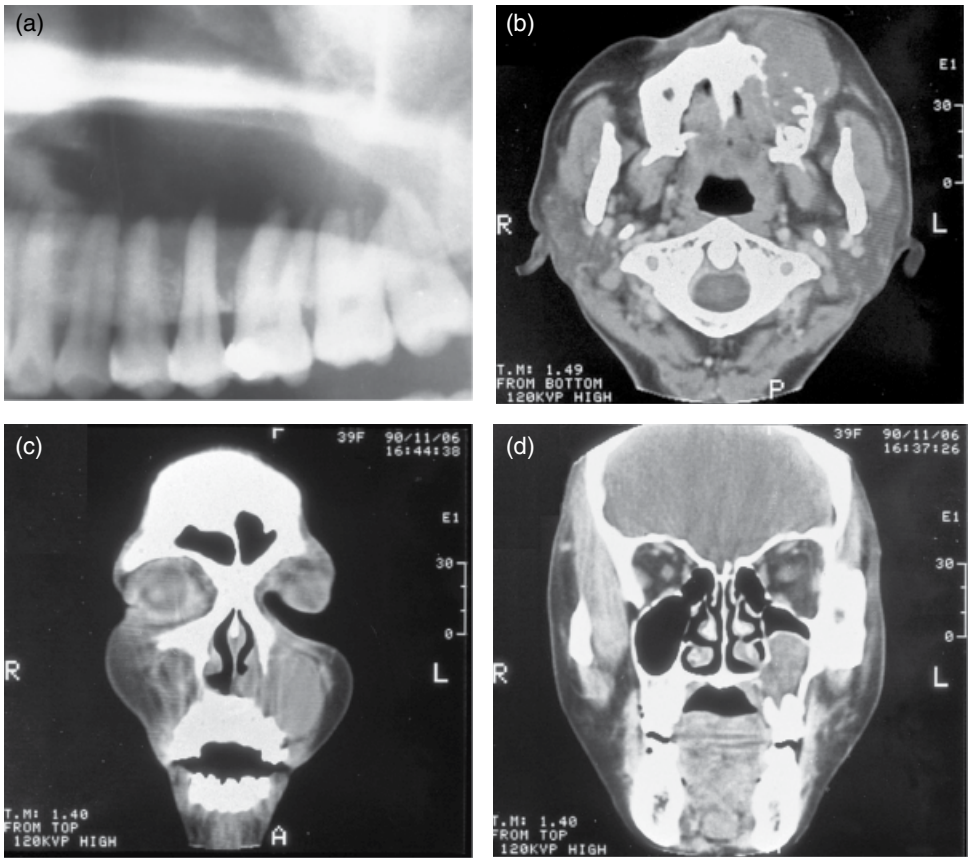


Figure 11.7 Panoramic radiograph and soft-tissue-window computed tomography (CT) of a case of non-Hodgkin lymphoma (NHL) that arose from lymphoid tissue within the alveolus. Although the majority of NHLs occur within Waldeyer's ring, a number can arise outside it. They are generally bone sparing, unless they happen in bone itself. The breaching of the buccal and palatal cortices and substantial soft-tissue mass are reminiscent of a squamous cell carcinoma, but both the substantial palatal expansion and concave upward expansion of the floor of the maxillary sinus are more typical of a benign neoplasm or cyst. (a) Panoramic radiograph displaying extensive loss of bone around the roots of maxillary molars in addition to premolars. This degree of bone loss far exceeds the normal pneumatization of the alveolus. (b) Axial CT, at the level of the first cervical vertebra. The alveolar bone around the roots on the left side appears to have been resorbed. The buccal cortex is absent, whereas the palatal cortex is expanded, but it eroded with some perforations. The buccal soft-tissue mass has extended medially between the surface of the anterior alveolus and the skin of the upper lip. (c) Coronal CT, at the level of the first premolars, almost occludes the left antral and nasal cavities, leaving a residual air space just below the medial portion of the orbital floor. The medial and lateral bony walls, in addition to a considerable portion of the alveolar process, are absent. The soft-tissue mass of the lesions has expanded medially into the nasal cavity. (d) Coronal CT, at the level of the first molars, has perforated the palatal cortex and expanded into the palatal submucosa, whereas the lateral wall appears intact. The lesion is separated from the floor of the orbit by a residual air space. The dome-shaped surface of the lesion is delineated by a well-defined, uniformly thick cortex. This denotes the upwardly displaced sinus floor. Source: Li, T.K., MacDonald-Jankowski, D.S. (1991). An unusual presentation of a high-grade non Hodgkin's lymphoma in the maxilla. *Dentomaxillofac. Radiol.* 20:224–226.



Figure 11.8 (a and b) Axial reconstructions, each of separate large field-of-view cone-beam computed tomography performed on different patients. Hypopneumatization displayed on the right side in (a) and on the left in (b). Three coronal reconstructions from the yellow lines marked on (b) are displayed from the top-most anterior (c), to the middle (d), to the most posterior (e). The ethmoid air cells, nasal cavity, and concha (turbinates), obvious in each of the coronal reconstructions, are minimally affected by the hypopneumatization of the left maxillary sinus. Source: Courtesy of British Columbia Children's Hospital, Vancouver.

11.2 Overview of Lesions Arising in or Adjacent to the Maxillary Sinus

In addition to hypoplasia, Figure 11.12 displays the more frequent and/or important lesions arising within or immediately adjacent to the maxillary sinus. These are generally discovered when radiologically investigating a case of sinusitis which has not responded to the appropriate treatment (Figures 11.2–11.6). This is usually by antibiotics and decongestants. Lesions may also be discovered incidentally to radiology for another clinically indicated reason. The most serious of these are malignancies, which present with destruction of the bone. The most frequent malignancy of the sinus is *squamous cell carcinoma* (SCC; Figure 11.13), then *non-Hodgkin lymphoma* (NHL; Figures 11.7, 11.14, and 11.15), and

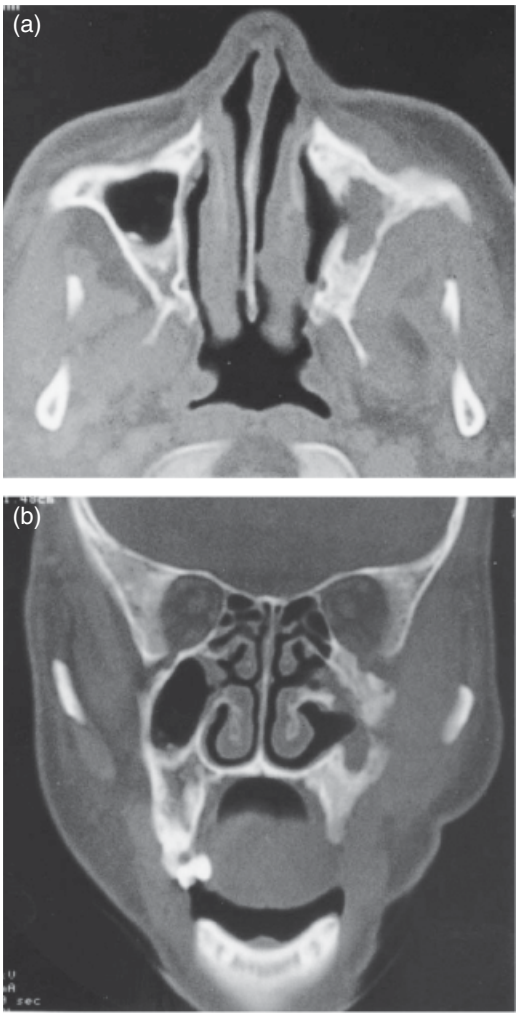


Figure 11.9 Bone-window computed tomography (CT) displaying a hemimaxilla which has been affected by osteomyelitis. This has resulted in loss of teeth and marked hypoplasia of the maxilla and also of the maxillary sinus. (a) Axial CT displaying the hypoplasia of the residual maxilla and of the maxillary sinus. The latter cavity has been obturated with soft tissue. (b) Coronal CT showing the same. The floor of the orbit on the affected side is thicker. The inferior concha is not attached to the affected maxilla in this section. Note: Osteomyelitis affecting the maxilla usually occurs in children and is spread to the maxilla by the blood (hematogenous).

rarely osteosarcoma (Figure 11.16). Although the majority of SCCs and NHLs generally arise within the sinus mucosa (Figure 11.15) [10], occasionally they arise within the maxillary alveolus, such as a *primary intraosseous squamous cell carcinoma* (PIOSCC) [11] (see Chapter 9 for full discussion) or an intra-alveolar NHL (Figures 11.7 and 11.14) [3, 12]. These lesions, like other lesions arising within the alveolus such as odontogenic cysts and neoplasms, secondarily involve the sinus as they grow. Other lesions which are also associated with bone destruction are the inverted papilloma (Figure 11.17), Wegener's granulomatosis (Figure 11.18), and the aforementioned thalassemia (Figure 11.10).

The more benign lesions present as dome-shaped expansions of the sinus floor. Those essentially composed of soft tissue are separated on whether a cortex/bony capsule just under the sinus mucosa is present or not. This cortex represents the floor of the maxillary sinus, which is elevated by the underlying lesion that arises from within the subjacent alveolus. Such lesions are most likely of odontogenic origin, such as cysts (radicular cysts, Figure 11.19; dentigerous cysts, Figures 11.20 and 11.21; and orthokeratinized odontogenic cysts, OOC, Figure 11.22) and neoplasms (ameloblastomas, Figures 11.23 and 11.24; keratocystic odontogenic tumors, KCOTs, Figures 11.25–11.28; and odontogenic myxomas, Figures 11.29 and 11.30). Those lesions without a cortex arise within the sinus mucosa. These are the most frequently found lesions in the maxillary sinus and are *mucosal antral pseudocysts* (MACs; Figures 11.31 and 11.32) and polyps (Figures 11.33–11.35), which arise within the sinus mucosa secondary to sinusitis. Polyps may develop into antrochoanal polyps (Figure 11.36). Radiopacities extending into the sinus lumen may represent any fibro-osseous lesion

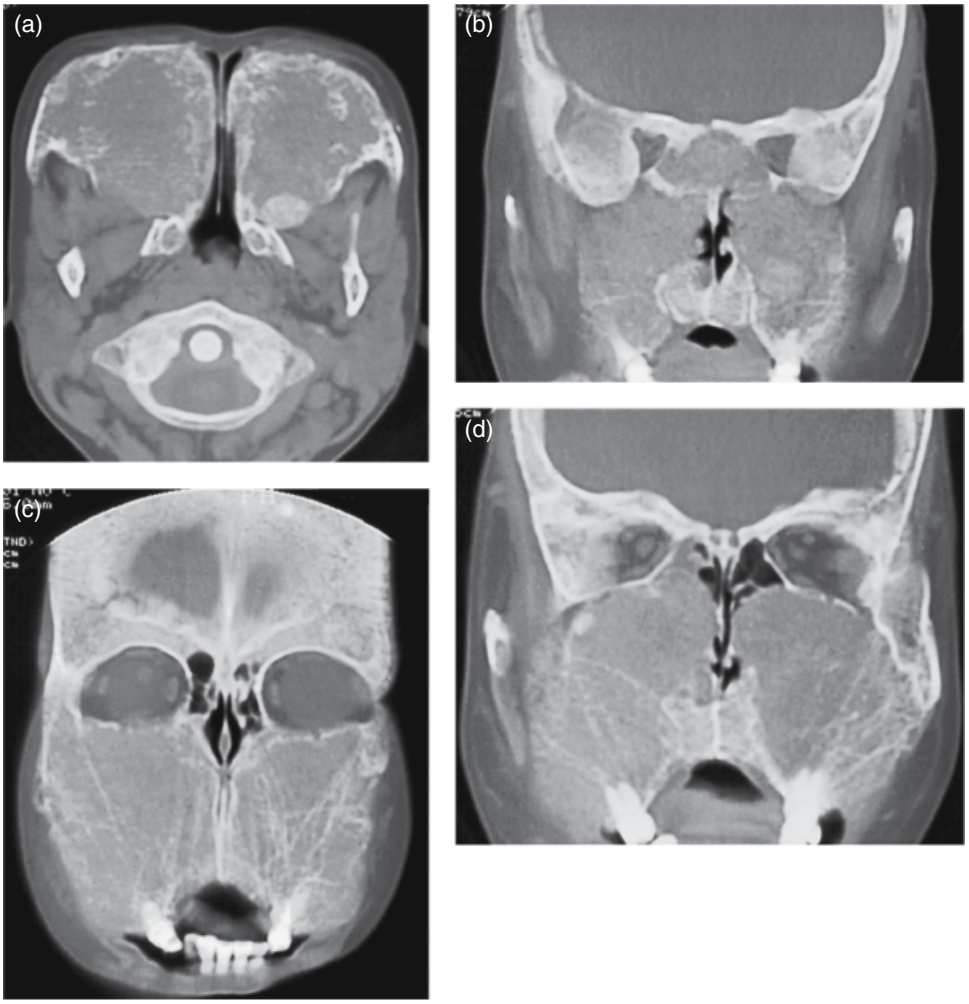


Figure 11.10 Bone-window computed tomography of thalassemia. See also Figures 9.14 and 18.19 for other images from the same patient. (a) Axial section, through the first cervical vertebra revealing the complete absence of a maxillary sinus (MS) and a substantial obstruction of the nasal cavities. The entire normal bone has been replaced by thickened and coarse trabeculae. There is a well-defined ovoid sclerosis on the posterior wall of the right maxilla. The cortex is either diffusely thickened or absent. Both maxillae are expanded. (b–d) Coronal sections confirming the complete absence of the MS observed in. The pattern of the background (a) radiodensity is peau d'orange. (c) Coronal section through the middle of the globe (eyeball) displaying the above. There are fewer trabeculae save for a few vertical trabeculae. The floor of the orbit is diffusely thickened or absent, whereas the roof is distinct and intact. (d) Coronal section, just behind the globe (note the rectus muscles and optic nerve), showing the same pattern as in (c). There is a small, well-defined ovoid sclerosis just below the orbit on the right maxilla.

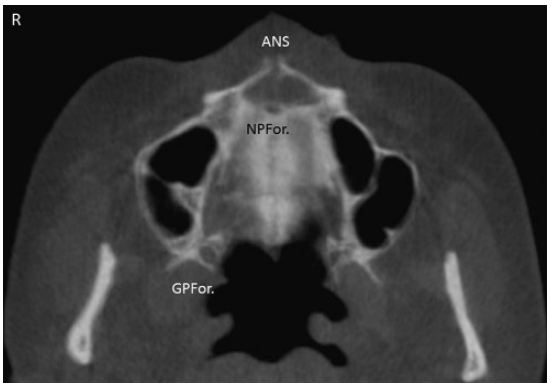


Figure 11.11 Axial reformation of cone-beam computed tomography at the level of the hard palate, displaying septae arising from the floor and posterior wall of the maxillary sinus. Note 1: The nasopalatine foramen (NPFor) and the greater palatine foramina (GPFor) are obvious, as is the suture of the hard palate. Note 2: The oval radiolucency between the nasopalatine foramen anterior nasal spine (ANS) is a radicular cyst. R, right side. Source: Courtesy of Dr. Thomas Li. Oral & maxillofacial radiologist; Hong Kong.

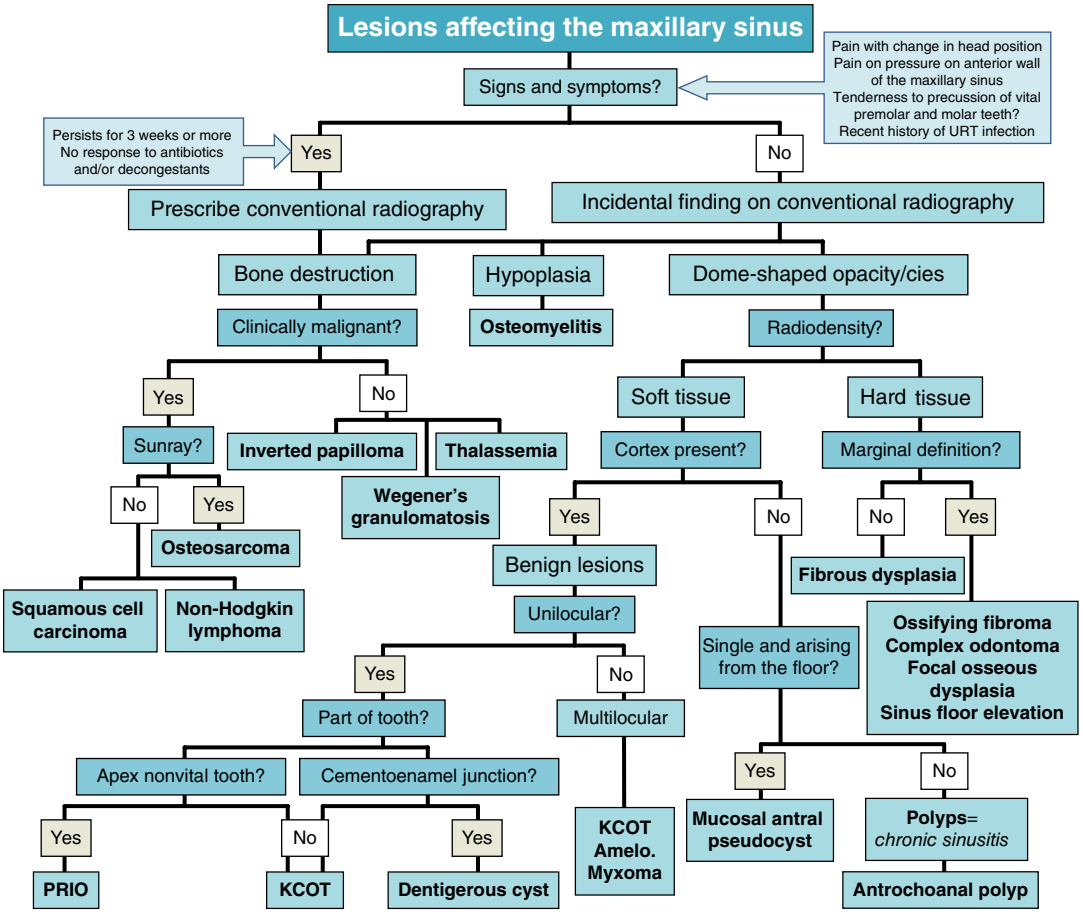


Figure 11.12 Flowchart displaying the most frequent and or important lesions affecting the maxillary sinus. Although the sinus floor elevation is not a lesion, it may be mistaken for one, causing unnecessary alarm to the patient. Amelo, ameloblastoma; KCOT, keratocystic odontogenic tumor; PRIO, periapical radiolucency of inflammatory origin (it can be a periapical granuloma, radicular cyst, or an abscess); URT, upper respiratory tract.

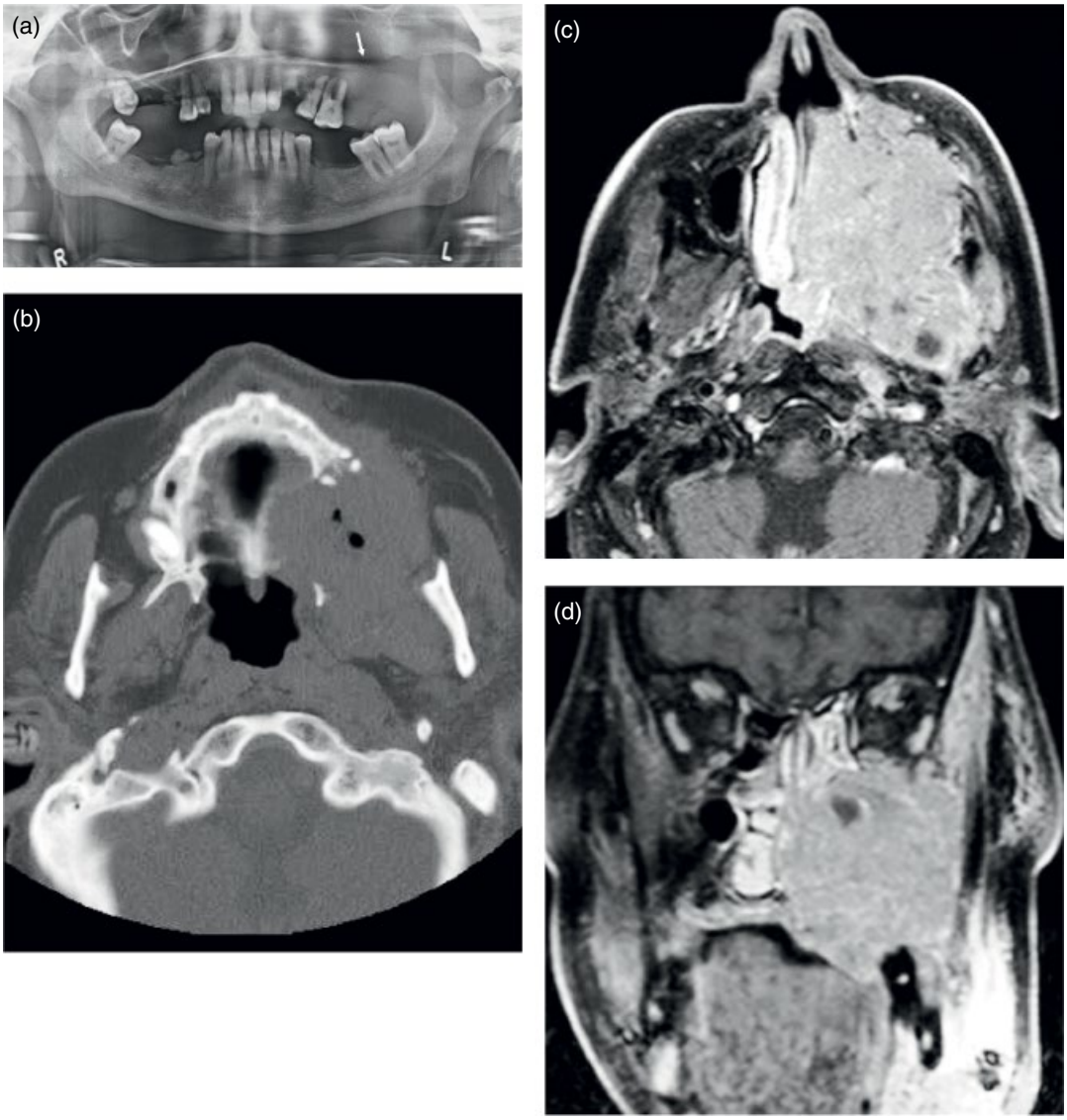


Figure 11.13 Panoramic radiograph, computed tomography (CT) and magnetic resonance imaging (MRI) of a squamous cell carcinoma (SCC) arising in the left maxillary sinus, destroying the adjacent maxilla. (a) Panoramic radiograph showing a soft-tissue mass destroying the left maxillary alveolar ridge (arrow). (b) Axial bone-window CT of the same patient as in (a) showing destruction of the left superior maxillary alveolar ridge by the SCC. (c) Axial postgadolinium fat-saturated T1-weighted MRI of the same patient showing a huge enhancing mass centered in the left maxillary sinus, destroying the medial wall to enter the nasal cavity and extending laterally to partially encase the coronoid process of the left mandible and the left mandibular ramus. The left muscles of mastication are encased by the tumor. (d) Coronal postgadolinium fat-saturated T1-weighted MRI of the same patient showing extensive right maxillary SCC destroying the adjacent maxilla to enter the oral cavity. It is also destroying the orbital floor and partially encasing the inferior rectus muscle. L, left; R, right. Source: Courtesy of Dr. Montgomery Martin, British Columbia Cancer Agency, Vancouver.

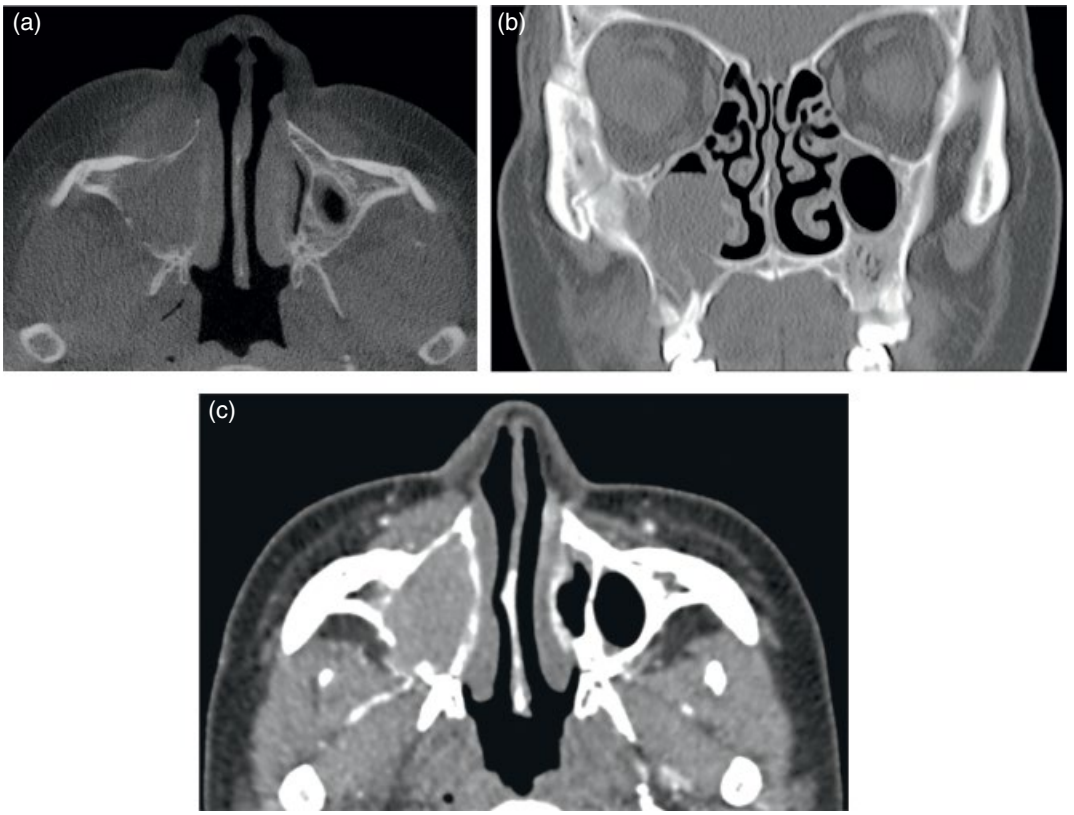


Figure 11.14 Non-Hodgkin lymphoma (NHL) arising from within the maxillary alveolus secondarily affecting the maxillary sinus (MS). The alveolar aspect of this lesion has been exhibited in Figure 9.16. (a) Cone-beam computed tomographic axial reconstruction, through the superior maxillary sinus, exhibiting obturation of the lumen of the maxillary sinus by a soft-tissue mass. The medial cortex has been substantially destroyed, whereas the posterolateral cortex, though undisplaced, has been perforated. (b) Bone window of a coronal reconstruction of the multidetector computed tomography (MDCT) dataset, through the first molar teeth, reveals the almost complete replacement of the right normal air-filled lumen of the maxillary sinus and also of the maxillary bone by a soft-tissue mass. Although substantially eroded, the floor of the MS has been displaced superiorly to delineate the remnant of the air-filled sinus lumen. The floor of the orbit appears to be intact. The medial wall has been completed eroded, leaving only the bone of the inferior turbinate intact. (c) This is a postcontrast soft-tissue window of an axial reconstruction of the MDCT dataset, through the condylar necks, at a lower level than that displayed in (a). The enhanced soft-tissue mass has already extended into the deep tissues of the face close the right ala of the nose. The anterior wall of the MS has an enhanced lesion on both surfaces, indicating that the bony wall has been breached at some point. The lymphoma has perforated the posteriolateral wall at the point already obvious in (a), to invade the fat space of the infratemporal fossa. There is no central necrosis. Note: Although unaffected by the NHL, the left maxillary sinus lumen as displayed on (a–c) is hypoplastic. (d) T1-weighted sagittal magnetic resonance reconstruction with contrast, through the premolar and first molar region of the right dental arch, revealing the complete obturation of the maxillary sinus up to the floor of the orbit. (e) T1-weighted coronal magnetic resonance reconstruction with contrast, through a similar plane to (a), revealing that the lesion is larger; the air-filled space between the inferior turbinate and the nasal septum has been substantially obturated. (f) T2-weighted coronal magnetic resonance reconstruction, through a plane more posterior to that in (d), revealing perforation of the posteriolateral sinus wall. The lesion has infiltrated and displaced the medial wall of the sinus and the inferior turbinate. (g) T2-weighted axial magnetic resonance reconstruction, through the inferior turbinate, revealing the perforation of the anterior sinus wall by the lymphoma and its infiltration of the muscles of facial expression. Another perforation of the posteriolateral sinus wall is also apparent. The lesion has infiltrated and displaced the medial wall of the sinus and the inferior turbinate. Source: Reproduced with permission from MacDonald, D., Li, T., Leung, S.F., et al. (2017). Non-Hodgkin lymphoma arising within the alveolus of the maxilla. *Oral Surg. Oral Med. Oral Pathol. Oral Radiol.* 124: e233–e238.

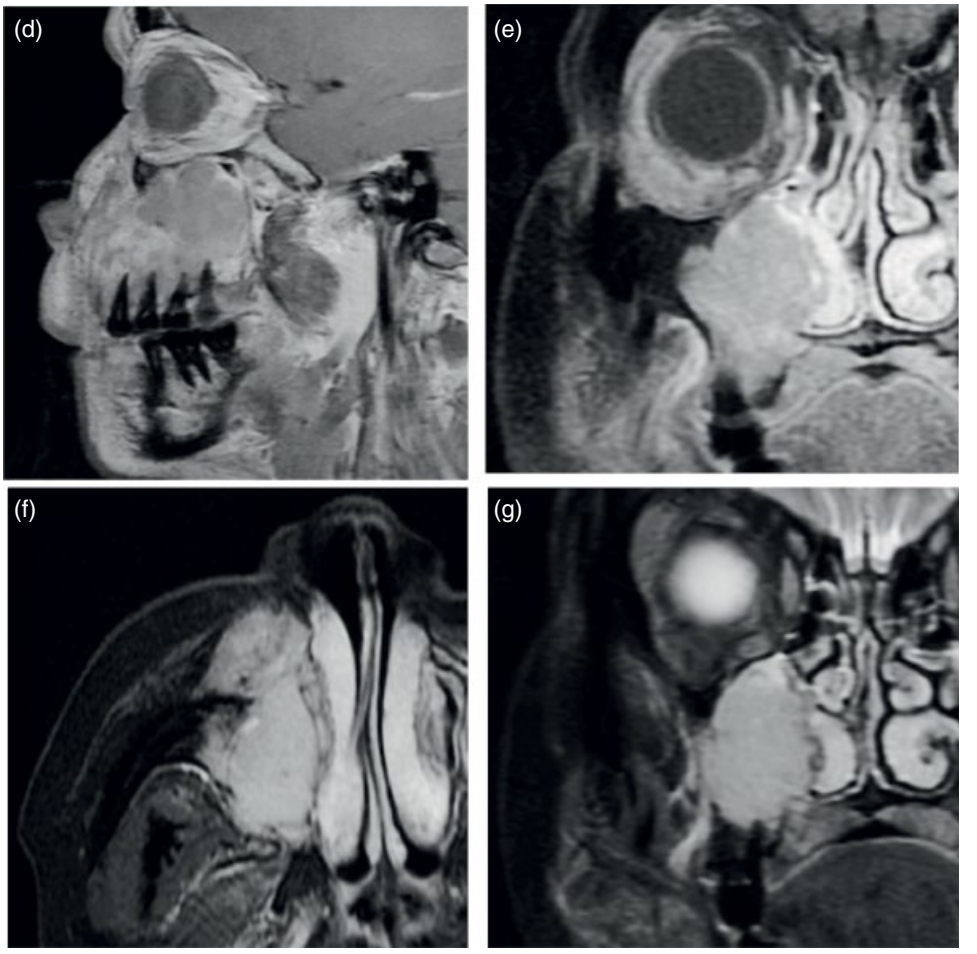


Figure 11.14 (Continued)

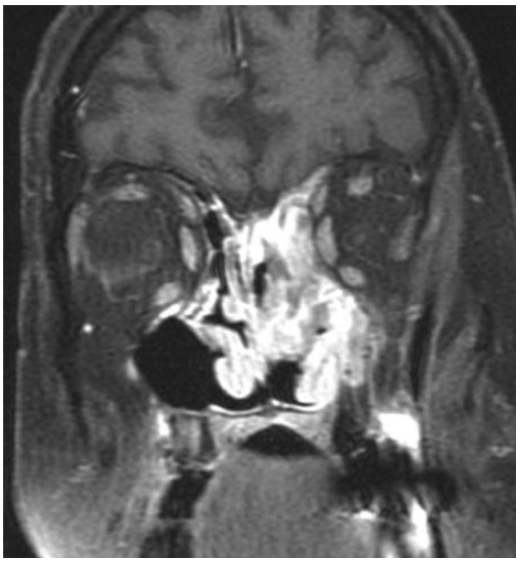


Figure 11.15 Coronal postgadolinium fat-saturated T1-weighted magnetic resonance imaging of a large B-cell lymphoma affecting the left nasal cavity, ethmoid, and maxillary sinuses. Source: Courtesy of Dr. Montgomery Martin, British Columbia Cancer Agency, Vancouver.



Figure 11.16 Computed tomography (CT) of an osteosarcoma affecting the anterior sextant of the maxilla and extending into the maxillary sinus (MS). (a) Sagittal CT (bone window) exhibiting a poorly defined radiopacity displacing the roots of the canine and lateral incisor. Striae are present at the periphery of the lesion. The intraluminal mass is largely soft tissue, with deeper sunburst striae. (b) Axial CT (bone window) displaying a loss of the trabeculae and cortex at the anteriomedial angle of the MS and an invasion by a soft-tissue mass and striae deeper within it. The lateral surface of the medial wall of the MS presents with striae arising from the anterior two-thirds of its length. Just anterior to the anterior (facial) wall of the MS is a small area of periosteal reaction with faint striae. The affected side exhibits substantial swelling of the face.

(fibrous dysplasia, Figures 11.37–11.44; ossifying fibroma, Figure 11.45; and osseous dysplasia, Figure 11.46), odontoma (Figures 11.47–11.49), or a sinus floor elevation (Figure 11.50). Other radiopacities that may be observed are periapical sclerosis (Figure 11.51), endostosis (Figure 11.52), and perhaps the occasional antrolith. Although the last has been mentioned frequently, a recent consecutive case series of over three-quarters of a thousand CTs of the maxillary sinus failed to find a single one [13]. This chapter will close with a very rare, but important phenomenon, *silent sinus syndrome* (SSS, Figure 11.53).

11.3 Sinusitis

Sinusitis is an inflammation of the sinus mucosa, which may arise from an *upper respiratory tract infection* (URTI) or via an infection from the subjacent teeth. Bomeli et al. reviewed the CTs taken for persistent sinus infection and reported that 17% of them were related to a dental cause [14]. These were carious exposure of the dental pulp resulting in a periapical infection and oroantral fistulas. This resulted in both thickening of the sinus mucosa and substantial opacification of the sinus with fluid. Bomeli et al. reported that nearly 80% of sinuses with greater than two-thirds fluid opacification had dental infections [14]. The complete opacification of the sinus with expansion of its walls is called a mucocele (Figure 11.4); while more frequently found in the frontal sinus, provoking neurosurgical intervention, it is uncommon in the maxillary sinus. Nevertheless, it does occur. Costan et al. reported such a case that expanded upward into the orbit, causing exophthalamos [15].

Sinusitis can be acute or chronic. A *de novo* acute sinusitis or an acute exacerbation of existing chronic sinusitis is generally painful. There may be a history of a recent URTI. The intensity of the pain may vary with changes in position of the patient's head. If the maxillary sinus is

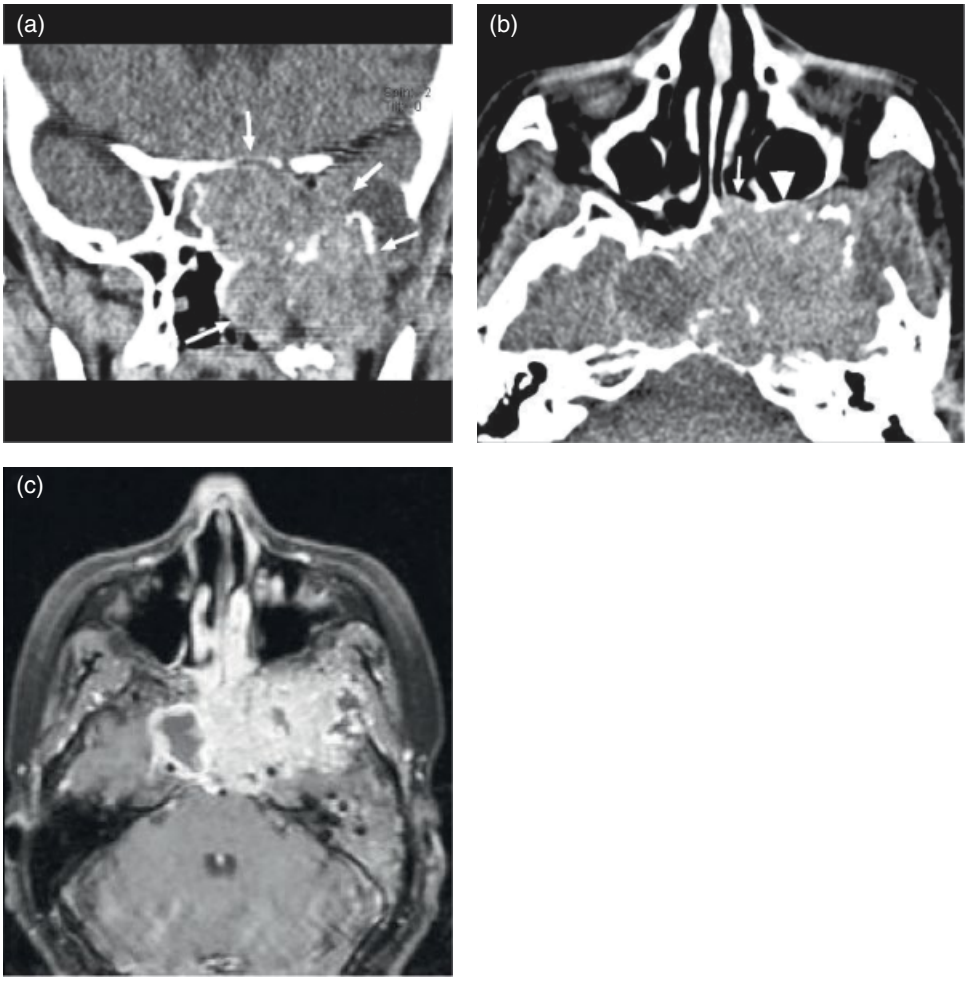


Figure 11.17 Computed tomography (CT) and magnetic resonance imaging (MRI) of an inverted papilloma arising in the left maxillary sinus. (a) Coronal postcontrast CT showing extensive bone destruction (arrows) from a left maxillary sinus inverted papilloma. Although considered benign, this tumor has many of the characteristics seen in malignant tumors (see Chapter 19). (b) Axial postcontrast CT of the same patient. Note how the tumor has invaded anteriorly into the pterygopalatine fossa (arrowhead) and nasal cavity (small arrow). The intervening left sphenopalatine foramen is completely obliterated. (c) Axial postgadolinium fat-saturated T1-weighted MRI. Note how the bones are not seen as well, but the soft-tissue component of the tumor is better visualized. The tumor has crossed midline into the medial right middle cranial fossa. Source: Courtesy of Dr. Montgomery Martin, British Columbia Cancer Agency, Vancouver.

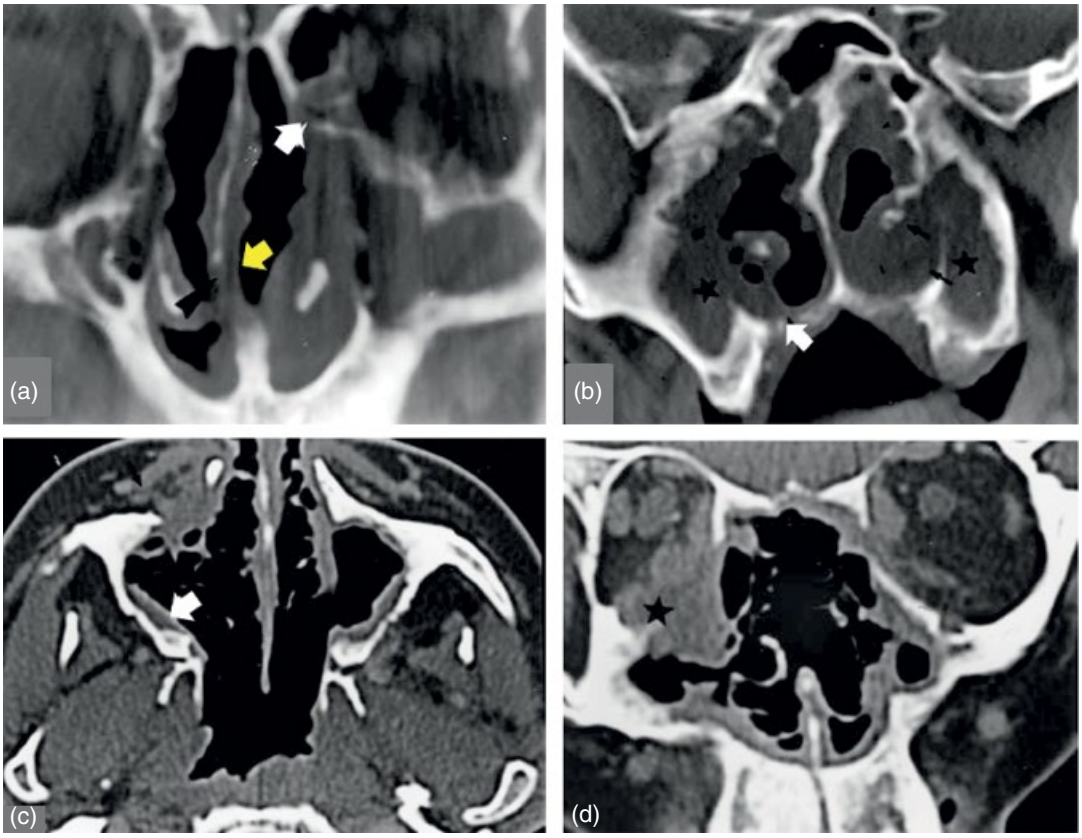


Figure 11.18 Two cases displaying sinonasal manifestation of Wegener's granulomatosis (recently renamed granulomatosis and polyangiitis). In the first case, (a and b) are two coronal computed tomography (CT) bone windows display a filling of the bilateral maxillary sinuses (black asterisks) with osteosclerosis of the maxillary sinus wall (white arrow), nasal septum perforation (yellow arrow), and demineralization of the lamina papyracea (white arrow in a), the turbinates (black arrows in b), and the palate (white arrow in b). In the second case there are soft-tissue windows of axial (c) and coronal (d) CT. These display a destructive lesion in the midline of the maxilla, which has converted the separate cavities of both sinuses and the nasal cavity into a single cavity. They also show bilateral intraorbital spread, particularly in the right orbit (black asterisk), extension into subcutaneous tissue of the face (c), and irregular nodular mucosal thickening (white arrow). Source: Reproduced with permission from Benoudiba, F., Marsot-Dupuch, K., Rabia, M.H., et al. (2003). Sinonasal Wegener's granulomatosis: CT characteristics. *Neuroradiology* 45 : 95–99 and Pakalniskis MG, Berg AD, Policeni BA, Gentry LR, Sato Y, Moritani T, Smoker WR. The many faces of granulomatosis with polyangiitis: a review of the head and neck imaging manifestations. *AJR Am. J. Roentgenol.* 2015;205:W619–W629.

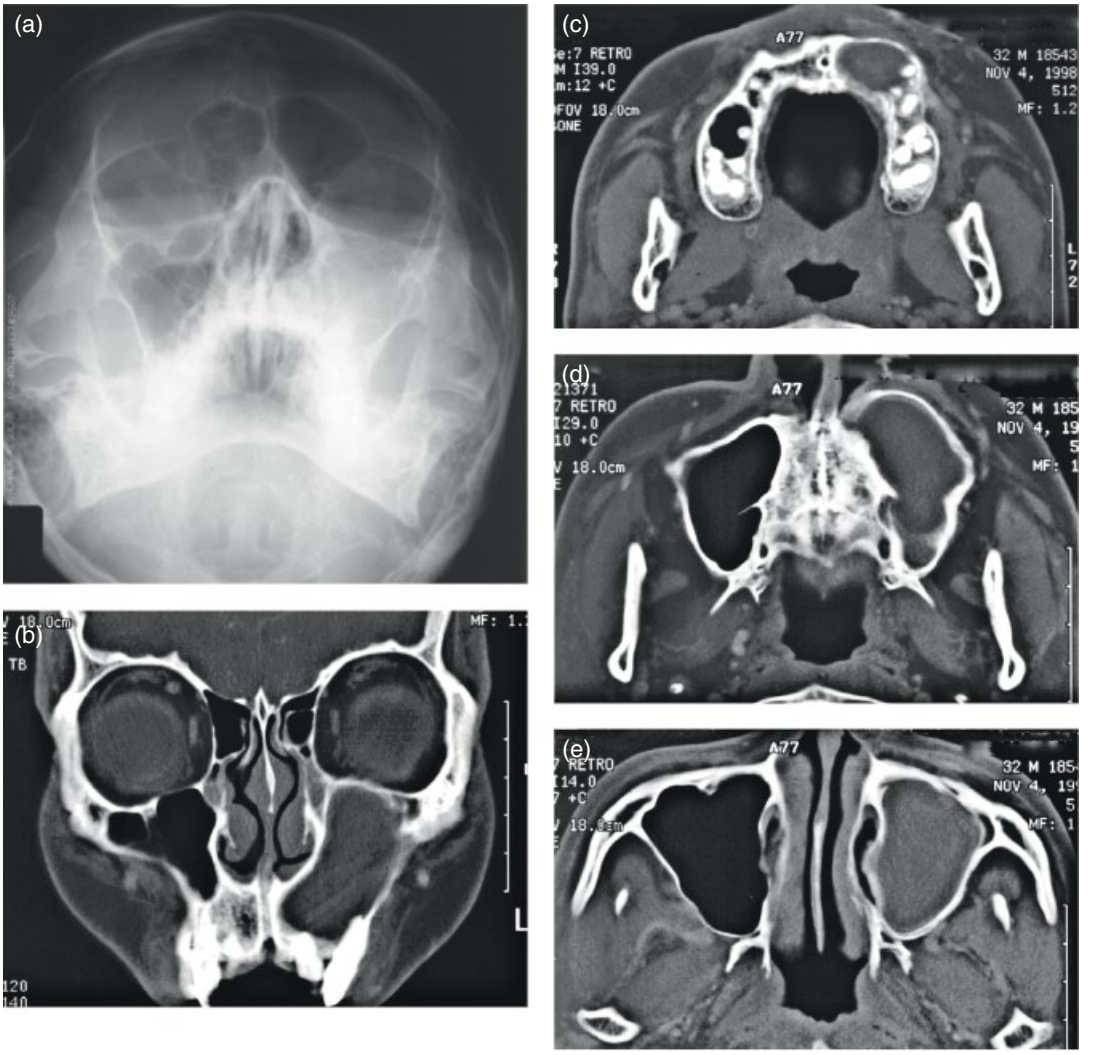


Figure 11.19 Conventional radiography and computed tomography (CT) of a radicular cyst arising in the maxilla's anterior sextant affecting the maxillary sinus (MS). (a) 30° occipitomental projection displaying complete radiopacity of the left MS. Note that the petrous temporal bone is correctly below the floor of the sinus. There is no obvious buccal expansion, but the medial wall appears to have been displaced into the left nasal cavity. (b) Coronal CT (bone window), at the level of the maxillary canines, exhibiting displacement of the lateral and medial walls and the roof of the MS. (c) Axial CT (bone window), through the alveolus, displaying a radiolucency occupying the left anterior region. It is associated with buccal expansion. (d) Axial CT (bone window), through the hard palate, showing an opacification of the entire MS. The anterior wall has been substantially expanded. (e) Axial CT (bone window), at the level of the neck of the condyle, displaying substantial obturation of the sinus by a corticated lesion containing a homogeneous light radiopaque content. The medial wall has been expanded. There is a residual air space at the anteriolateral angle of the MS.



Figure 11.20 Panoramic radiograph and bone-window computed tomography (CT) of a dentigerous cyst arising from a maxillary canine obturating most of the maxillary sinus (MS). (a) Panoramic radiograph displaying the unerupted canine with incompletely formed roots sited high within the MS. The second premolar, second molar, and third molar are unerupted. (b) Axial CT, above the hard palate, showing the canine lodged at the MS's medioanterior angle. It has expanded into the anterior nasal cavity. The cystic cavity has obturated the anterior three-fourths of the MS's lumen and has a well-defined cortex. The posterior fourth is air filled. The most posterior aspect of each MS contains the developing third molar (this is obvious in (a). (c) Coronal CT, at the level of the nasopalatine duct, exhibiting the unerupted canine impacted into the medial wall of the MS apex first. The cyst appears to be attached to the canine at the cementoenamel junction. The cyst has expanded the buccal wall of the maxillary sinus and adjacent alveolus. (d) Coronal CT, at the level of the unerupted second premolar, displaying the cyst filling the inferior four-fifths of the MS. The upwardly displaced former floor of the sinus is clearly present as a well-defined cortex. The residual air-filled space occupies the superior fifth of the MS's lumen. The medial wall of the MS has been displaced medially. (e) Coronal CT, at the level of the lachrymal ducts. The buccal cortex, though largely eroded and indistinct, is clearly expanded.

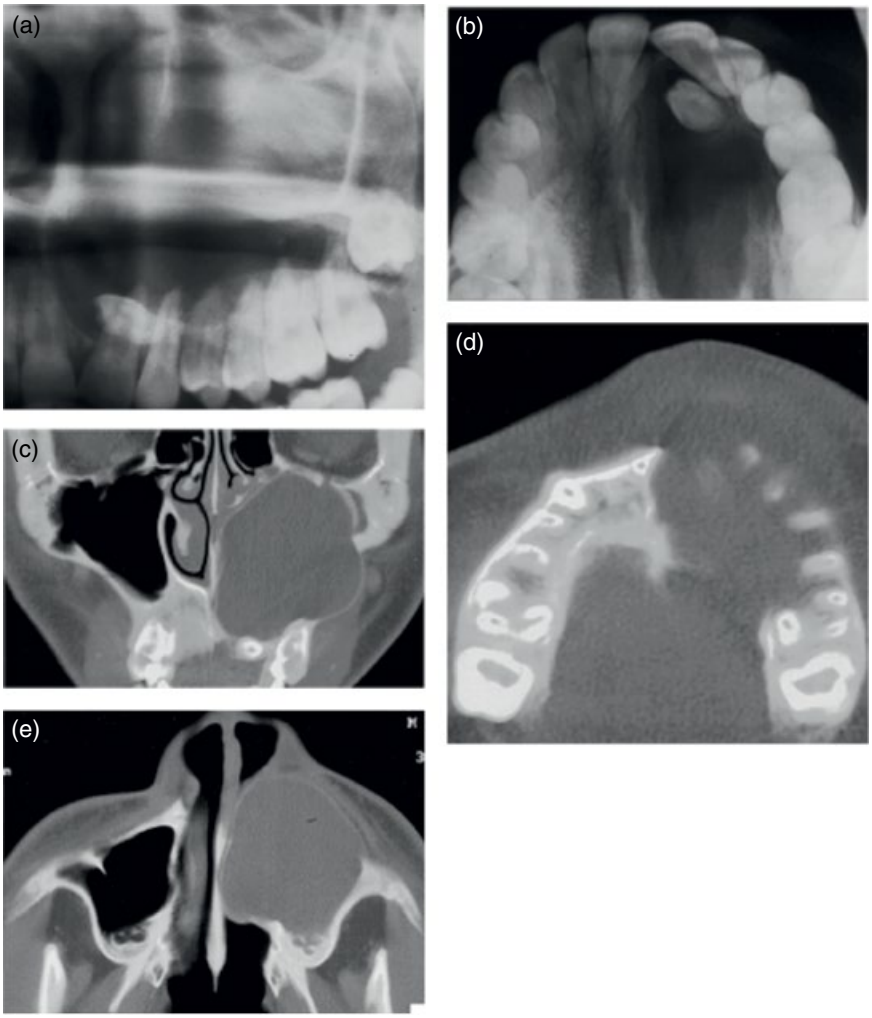


Figure 11.21 Conventional radiographs of a dentigerous cyst (DC) arising from a supernumerary (mesiodens) affecting the maxillary sinus (MS). (a) Panoramic radiograph displaying the DC on the mesiodens obturating the MS. There is marked hyperpneumatization of the alveolus. The DC has also caused substantial root resorption. (b) Anterior occlusal radiography showing the mesiodens between the roots of the central incisors. (c) Coronal computed tomography (CT) taken at the level of the inferior orbital nerve which begins its course from the inferior orbital canal/groove to the infraorbital foramen. It shows the DC obturating the entire MS and expanding its buccal and lingual cortices widely. (d) Axial CT (bone window), through the alveolus, exhibiting substantial root resorption. (e) Axial CT, at the level of the infraorbital foramen, showing substantial expansion anteriorly and medially.

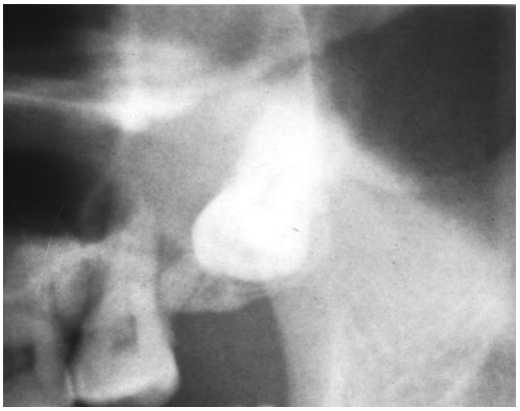


Figure 11.22 Panoramic radiograph displaying an orthokeratinized odontogenic cyst (OOC) affecting the maxillary sinus (MS). The posterior MS is radiopaque, whereas the anterior MS is still translucent. The radiopacity is bounded by a cortex anteriorly. The root of the associated unerupted third molar appears to be in intimate contact with the OOC. The tooth's follicular space is discernible over the entire crown and is unlikely to be continuous with the OOC.



Figure 11.23 Computed tomography (CT) of a solid (multilocular) ameloblastoma affecting the anterior maxilla. (a) Axial CT (bone window), at the level of the hard palate, revealing an ovoid lesion largely expanding out into the soft tissue of the face. The cortex on this surface has been substantially eroded and perforated in places. The lesion that has extended into the alveolus displays a honeycomb pattern. There are some radiopaque features extending partly into the lesion. The lesion has eroded and displaced the medial aspect of the anterior wall of the maxillary sinus (MS) backward into the lumen. Multiple radiopacities are observed in the anterior aspect of the lesion. (b) Coronal CT (bone window) reveals most of the features observed in (a). The multiple radiopacities are localized to the superior aspect of the lesion. (c) Axial CT (bone window), through the inferior concha, displaying the most superior extent of this lesion. It lies upon the surface of the anterior wall of the MS. The lesion has extended onto the facial surface with a honeycomb pattern and has filled out the alar-facial angle on that side. (d) Axial CT (bone window), through the level of the hamulus, displaying the deepest reach of the lesion into the alveolus. The cortex at its anterior periphery appears substantially absent. (e) Coronal CT (bone window) showing both the marked buccal expansion and its extent palatally into the alveolus. It also displays the septa within the lesion and the marked erosion and absence of its buccal cortex toward the gingival margin. The combination of features such as the "snowstorm" and honeycomb pattern are suggestive of a desmoplastic ameloblastoma. There are a small number of desmoplastic-solid hybrid ameloblastomas, discussed in Chapter 9.

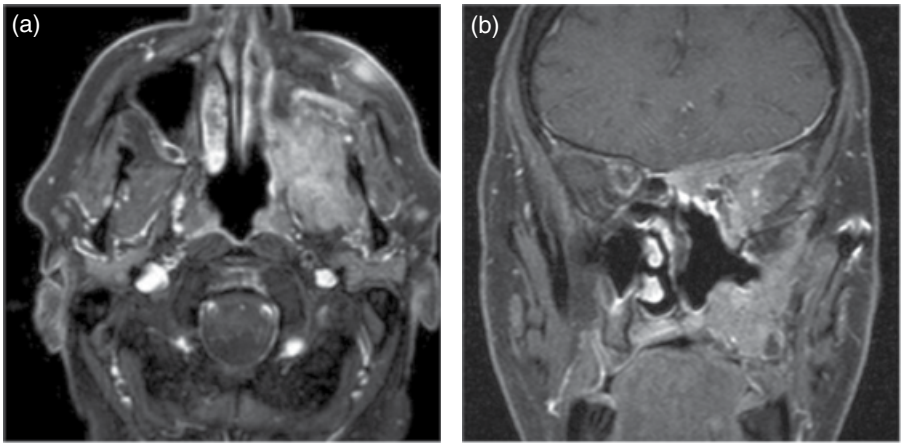


Figure 11.24 Magnetic resonance imaging (MRI) of a recurrent maxillary ameloblastoma invading the brain. This patient has had numerous surgeries, including a left maxillectomy; the surgical defect was filled with a radial forearm reconstruction flap. (a) Axial postgadolinium T1-weighted MRI, at the level of the base of the sigmoid notch, displaying an enhanced lesion occupying the site of the maxillary sinus (MS) and the infratemporal space. (b) Coronal postgadolinium T1-weighted MRI, at the level of the condyle, displays enhancement of a lesion invading a reconstruction flap used to rebuild the inferior and lateral walls of the MS. Above the MS, the ameloblastoma has invaded the ethmoid air cells, the orbital apex, the dura mater of the anterior cranial fossa, and the anterior part of the temporal lobe. Source: Courtesy of Dr. Montgomery Martin, British Columbia Cancer Agency, Vancouver.

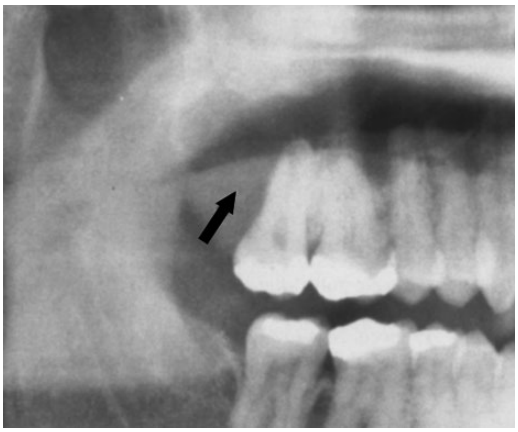


Figure 11.25 Panoramic radiograph displaying a keratocystic odontogenic tumor affecting the maxillary sinus (MS). The MS shows a soft-tissue radiopacity. There is no cortex at the maxillary tuberosity and adjacent posterior antral wall (arrow). This case provoked consideration of a squamous cell carcinoma as the provisional diagnosis. Source: MacDonald-Jankowski, D.S. (1992). The involvement of the maxillary antrum by odontogenic keratocysts. *Clin. Radiol.* 45: 31–33.

Figure 11.27 Computed tomography (CT) of keratocystic odontogenic tumor (KCOT) affecting both maxillary sinuses (MSs) in a case of nevoid basal cell carcinoma syndrome. (a) Axial CT (bone window) displaying KCOTs obturating both MSs. The right MS has been completely obturated, whereas the left has been only partially obturated. The presence of the residual air space (anteriorly) suggests that the MS is draining normally. Each MS shows an expansion of the posterior aspect of the posteriolateral wall. The right KCOT contains an unerupted tooth, the apex of which has been displaced through the posteriolateral wall close to the MS's zygomatic angle. (b) Coronal CT (soft-tissue window) with intravenous contrast (note enhancement of the ophthalmic, facial, and right greater palatine arteries) displaying complete obturation and buccolingual expansion of the right MS (the medial wall has also been displaced medially). The left MS exhibits a residual air space.

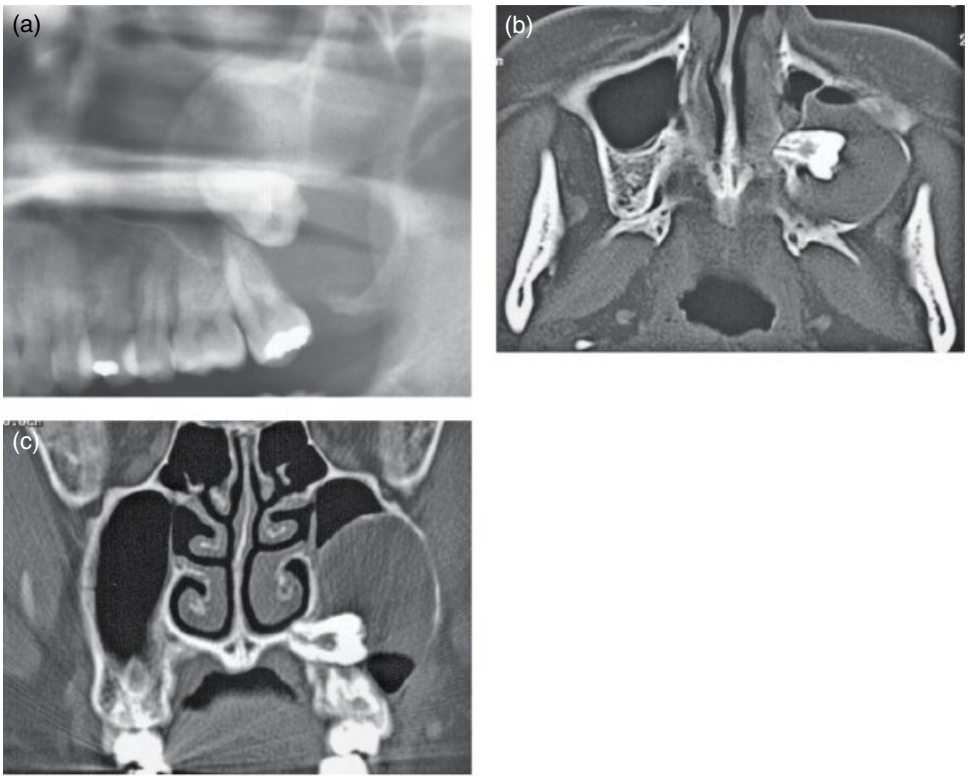
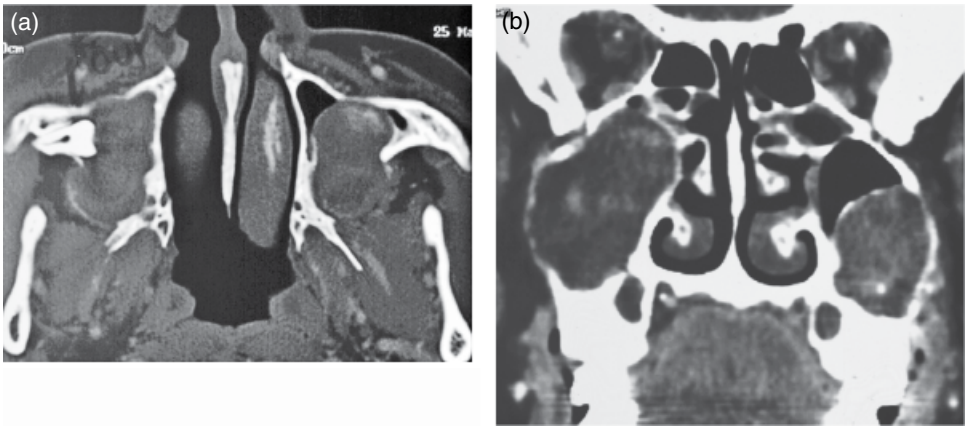


Figure 11.26 Panoramic radiograph (a), coronal (b), and axial (c) computed tomography (bone windows) exhibiting a keratocystic odontogenic tumor (KCOT) within the lumen of the maxillary sinus (MS). The KCOT presents on the panoramic radiograph as a radiopacity above the hard palate and as a radiolucency below it, lying within the alveolus. The radiopacity arises because its soft tissue attenuated the X-ray beam more than the air-filled sinus. The KCOT has obturated most of the MS lumen. The radiolucency in the third permanent molar site of the alveolar bone arises from the KCOT, removing the normal bone for this site as it grows. The most obvious feature displayed is that of the unerupted third molar. This is transversely impacted, with its roots embedded into the attachment of the hard palate with the alveolus. Root formation is still incomplete. The overall presentation is that of a dentigerous cyst. The only clue that this may not be so is the attachment of the lesion to the root surface. It is apical to the cementoenamel junction.



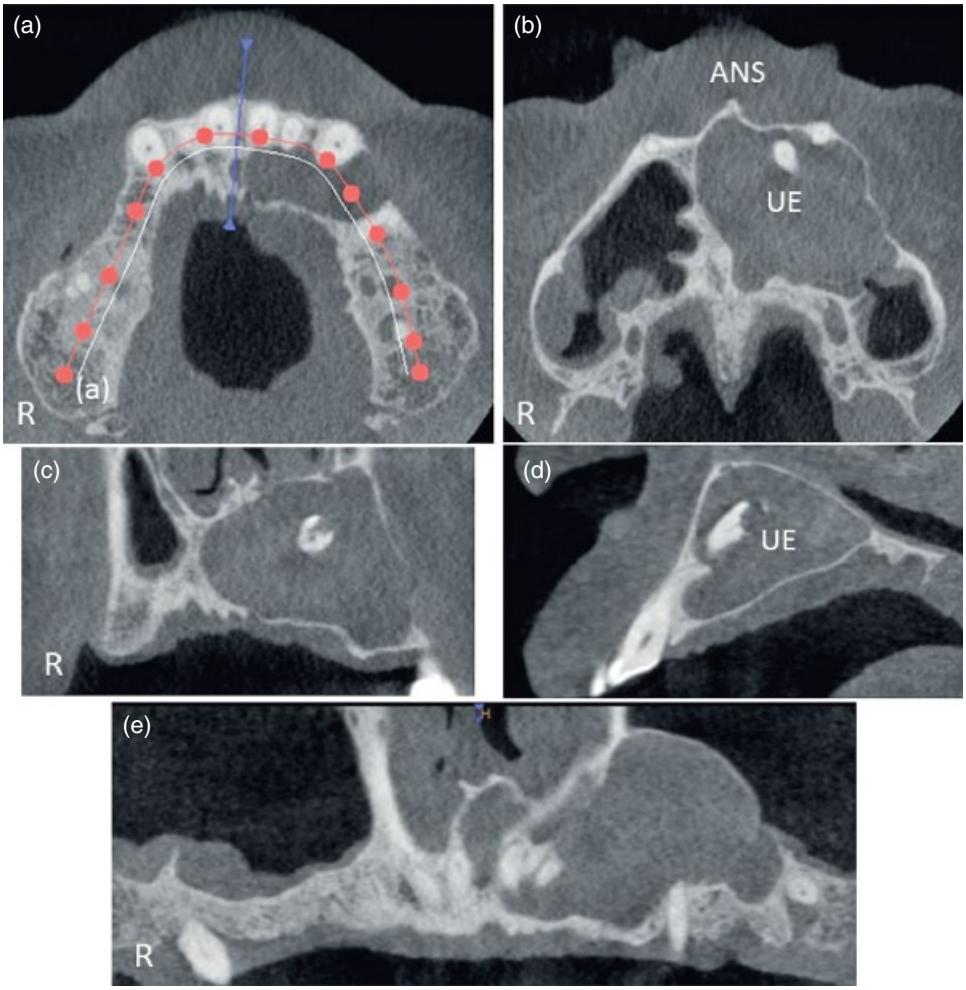


Figure 11.28 These are axial (a and b), coronal (c), sagittal (d), and panoramic reconstructions (e) of cone-beam computed tomography of a keratocystic odontogenic tumor arising in the anterior sextant of the maxilla. It extends from the midline to the junction between the second premolar and first molar area and also backward into the hard palate in (d). It has displaced and eroded the anterior wall (b), displaced upward by the nasal floor (c) and immediately adjacent floor into the lumen of the left maxillary sinus (e). The neoplasm's buccolingual dimension is about half of that of its mesiodistal extent (b). Furthermore, although essentially unilocular, the expansion is variable. An unerupted tooth (UE) is observed within the neoplasm. ANS, anterior nasal spine; R, right. Source: MacDonald, D.S. (2016). Lesions of the jaws presenting as radiolucencies on cone-beam computed tomography. *Clin. Radiol.* 71: 972–985.

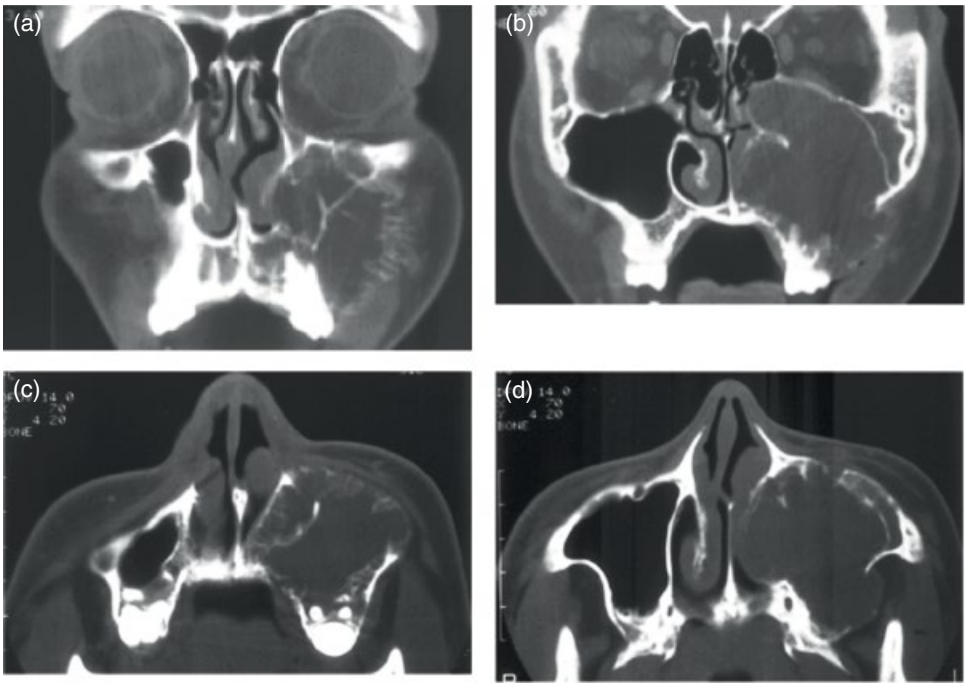


Figure 11.29 Bone-window computed tomography (CT) of odontogenic myxoma affecting the maxilla. It has extensively involved the maxillary sinus (MS). (a) Coronal CT displaying the substantial expansion, medially and laterally, at the level of the maxillary premolars and infraorbital foramen/canal. The medial wall of the MS has been displaced and eroded, whereas the lateral wall has been replaced by striae lined up in the direction of the expansion, presenting as a sunray spicule pattern. A number of large "soap bubbles" are visible medially. The pattern between the anterior teeth appears like the honeycomb. (b) Coronal CT at the level of the first maxillary molar displaying almost complete obliteration of the MS, with the exception of the superiolateral remnant of the lumen, which is no longer air filled. The inferior aspect of the MS has been expanded and eroded. The floor of the orbit has been displaced upward and the medial wall medially. Part of the bone of the inferior concha has been preserved within the lesion. The roots of the first molar have been resorbed. (c) Axial CT, at the level of the molar apices, displaying complete obliteration of the MS. The odontogenic myxoma has expanded anteriorly medially and laterally. The periphery of the lesion has parallel striae and loculi, whereas the center of the odontogenic myxoma is devoid of structure. (d) Axial CT, at the level of the infraorbital foramen, showing almost complete obliteration of the left MS with the exception of a space (no longer air filled) on the anteriolateral aspect of the lesion, extending from the widened infraorbital foramen to the anteriolateral angle. Much of the posteriolateral wall is absent. There is a soft-tissue expansion of the lesion through this perforation. The posterior aspect of this penetration is covered by displaced cortex, which is juxtapositioned to the lateral aspect of the lateral pterygoid plate. It has a smooth contour and its edges overlap the lateral aspect of the perforated bone. The medial wall has been displaced toward the nasal septum. The medial bony wall is largely intact, although substantially eroded. There are two bone density opacities within the lesion at the anteriomedial angle of the MS. Source: (a), (b), and (d) reproduced with permission from MacDonald-Jankowski, D.S. (2004. Fibro-osseous lesions of the face and jaws. *Clin. Radiol.* 59:11–25.

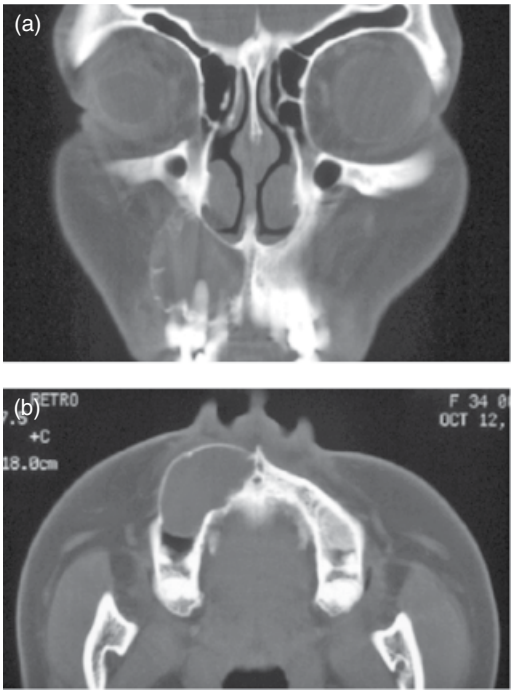


Figure 11.30 Bone-window computed tomography (CT) of an odontogenic myxoma arising from the anterior sextant and involving the maxillary sinus (MS). (a) Coronal CT, at the level of the maxillary canines, displaying a well-defined multilocular radiolucency expanding the buccal cortex. (b) Axial CT, at the level of the anterior nasal spine, showing a radiolucency, which has a largely smooth expanded buccal cortex, but a multiloculated medial border. The buccal surface has a small septum on its internal aspect. The odontogenic myxoma's posterior corticated margin is extending back into the lumen of the MS.

infected, there may be tenderness of the anterior maxilla, and the vital premolar and molar teeth may be tender to percussion or biting. The initial diagnosis can be concluded on clinical evidence alone. Although conventional radiography is often unhelpful, radiographs should be

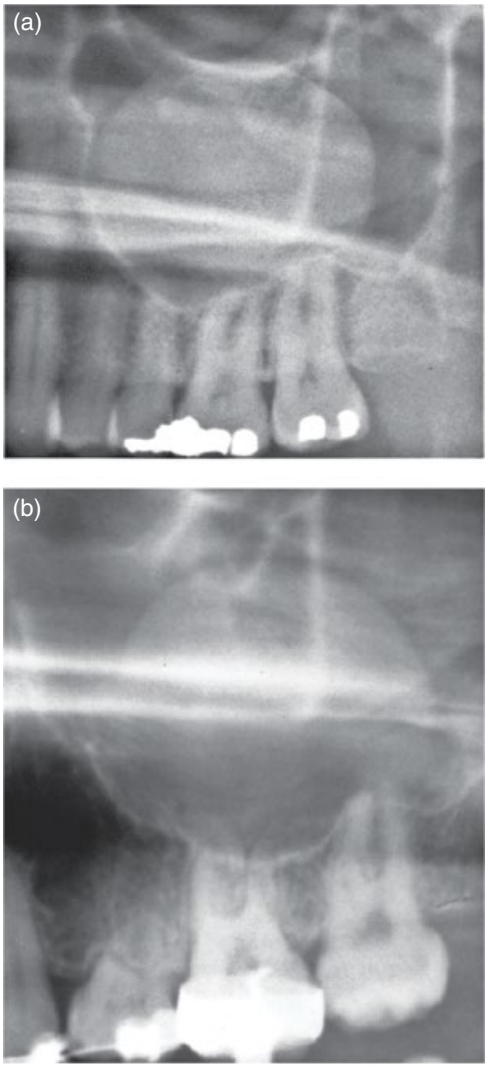


Figure 11.31 Panoramic radiographs of two different mucosal antral cysts (MACs, also called pseudocysts). (a) MAC centered upon the maxillary first molar tooth. Although this tooth has a moderate restoration, the likelihood of pulpal necrosis is low. (b) This MAC's subjacent teeth are undergoing orthodontic treatment and are therefore presumably noncarious. There is agenesis of the second premolar. Source: Reproduced with permission from MacDonald-Jankowski, D.S. (2004). Fibro-osseous lesions of the face and jaws. *Clin. Radiol.* 59: 11–25.

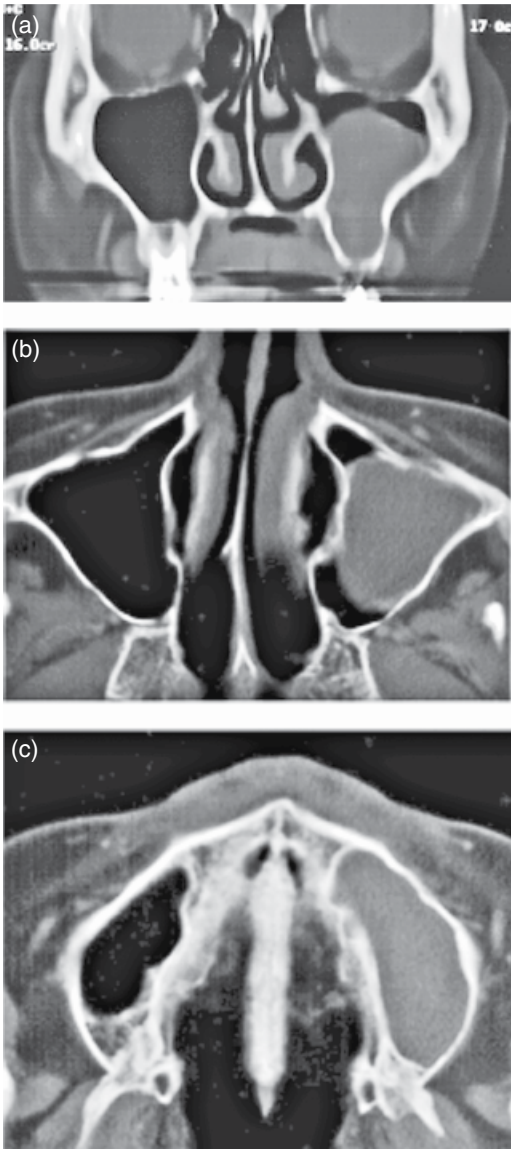


Figure 11.32 Postcontrast computed tomography (a, b, c) of a mucosal antral cyst (or pseudocyst). The cyst presents as a soft-tissue density structure partially filling the maxillary sinus (a,b). The white "rim" denotes contrast "enhancement" of the surface mucosa rather than a bony cortex as observed in Figure 11.20d. The surface mucosa of the turbinates (a) is also enhanced (compare with Figure 11.2). Therefore, this is a large mucosal antral cyst rather than a lesion arising within the alveolus (compare with Figure 11.16).

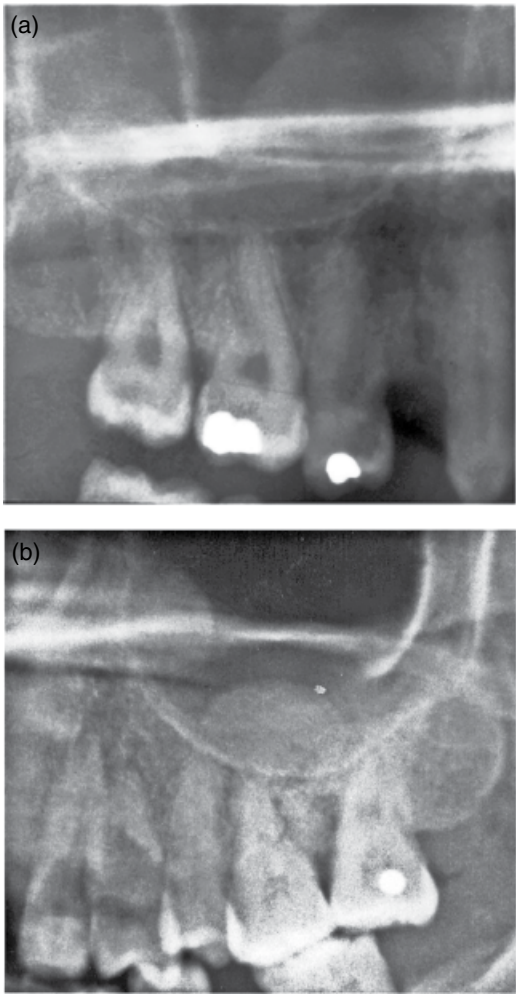


Figure 11.33 (a and b) Panoramic radiographs from cases displaying multiple polyps arising from the floor of the maxillary sinus.

taken in cases of a longstanding history of sinusitis. Unlike the *de novo* acute sinusitis, longstanding chronic sinusitis may present with thickening of the sinus's bony walls [4].

The classical presentation of sinusitis in conventional radiography is thickening of the antral mucosa and the presence of fluid levels (Figure 11.5). The thickened mucosa in infective sinusitis presents as a radiopaque (of soft-tissue density) band

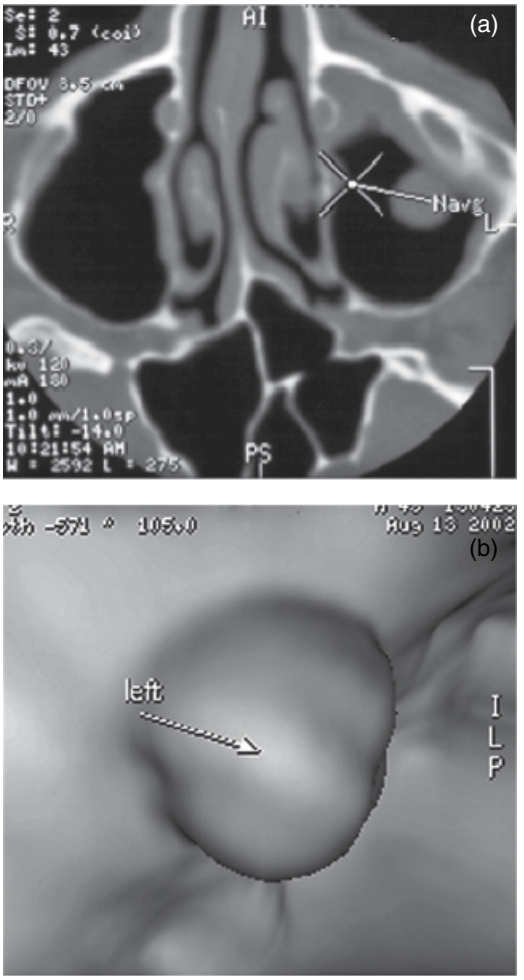


Figure 11.34 (a) Axial reconstruction of computed tomography of the maxillary sinus revealing a polyp and thickening of the sinus mucosa on the anterior sinus wall. (b) Virtual antroscopy displaying another polyp in the same case suspended from the roof of the antral cavity. ILP, inferior lateral posterior. Source: (b) Reproduced with permission from MacDonald-Jankowski, D.S., Li, T.K. (2006). Computed tomography for oral and maxillofacial Surgeons. Part 1: spiral computed tomography. *Asian J. Oral Maxillofac. Surg.* 18: 68–77.

parallel to the bony walls (see Figure 11.3). This may be accompanied by polyps (Figures 11.32–11.35), particularly in allergic sinusitis.

If sinusitis remains unresponsive to antibiotics and decongestants, it is necessary to exclude the possibility of other underlying pathology. An important first step in this regard is taking conventional sinus views. The most usual is the *30° occipitomental* (30° OM) projection (Figure 11.19). The primary concern is the presence of a malignancy.

Trauma to the midface can cause sinusitis, particularly when it disrupts the integrity of the sinus wall. Such events occur as a result of sport, altercations, and vehicular accidents causing facial fractures (see Chapter 15). They can also occur iatrogenically, such as the creation of oroantral fistulas, in the course of extractions, or, as in the case displayed in Figure 11.6, attempts at placing implants into the posterior maxilla.

11.4 Malignancies

Although the most important malignant lesion affecting the sinus is an SCC, NHLs also occur. Successful treatment of SCCs requires complete surgical ablation of the neoplasm, whereas NHLs are generally treated by chemotherapy [3]. Kato et al. were able to distinguish some differences between them [10]. Those observed on CT are set out in Table 11.1. NHLs frequently exhibited permeation of the sinus wall and retention of the sinus wall within the tumor, whereas SCCs exhibited much more frequently destruction of the sinus wall and intratumoral necrosis. Only a

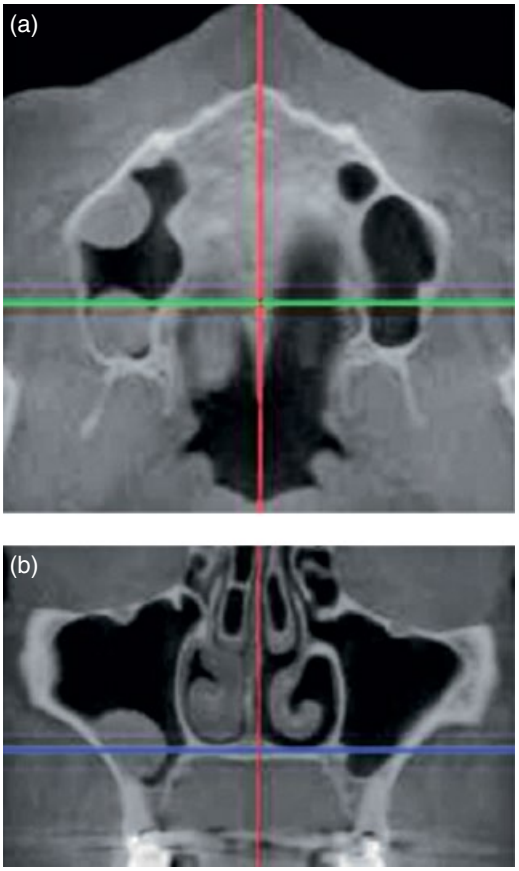


Figure 11.35 Cone-beam computed tomography (CBCT) of the maxillary sinus (MS). (a) Axial CBCT, at the level of the hard palate, displaying the nasopharynx, the mucosal surface silhouetted against the air-filled space. One sinus shows two dome-shaped opacities of a similar radiodensity to that of the nasopharyngeal tissues. These dome-shaped radiopacities are likely to be mucosal antral cysts or polyps. (b) Coronal CBCT section through the more anterior radiopacity. The mucosa of the ipsilateral inferior concha is swollen in comparison to the contralateral. The middle conchae and ethmoid air cells appear normal. Note the inferior orbital canal in the floor of the orbit and the osteum of the left MS. Source: Courtesy of Dr. Babak Chehroudi, Faculty of Dentistry, University of British Columbia.

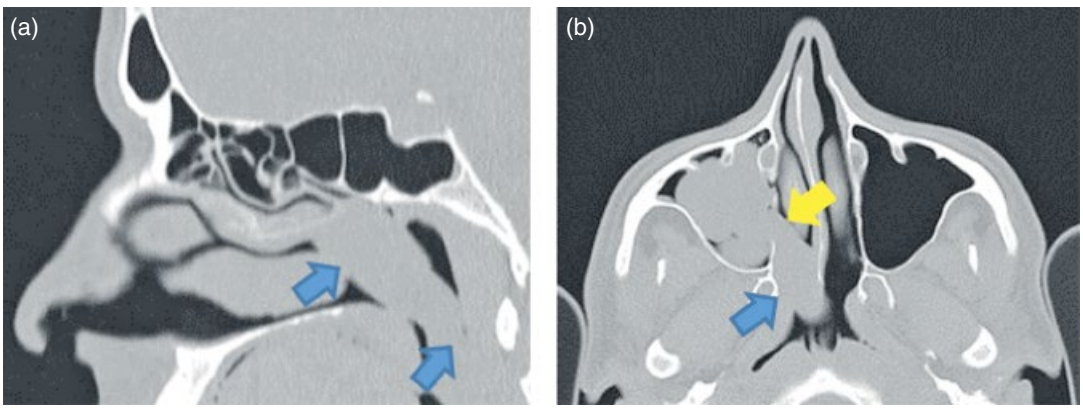


Figure 11.36 Computed tomography images of paranasal sinuses, showing an antrochoanal polyp (ACP, blue arrows). (a) Sagittal view showing extension of soft-tissue lesion from the nasal cavity into the choana. (b) Axial view exhibiting soft-tissue opacification within the right maxillary sinus (MS), with extension into the nasal cavity and choana (blue arrow). The yellow arrow indicates the ostium of the MS through which the ACP has emerged. Source: Choudhury, N., Hariri, A., Saleh, H. (2015). Endoscopic management of antrochoanal polyps: a single UK centre's experience. *Eur. Arch. Otorhinolaryngol.* 272: 2305–2311.

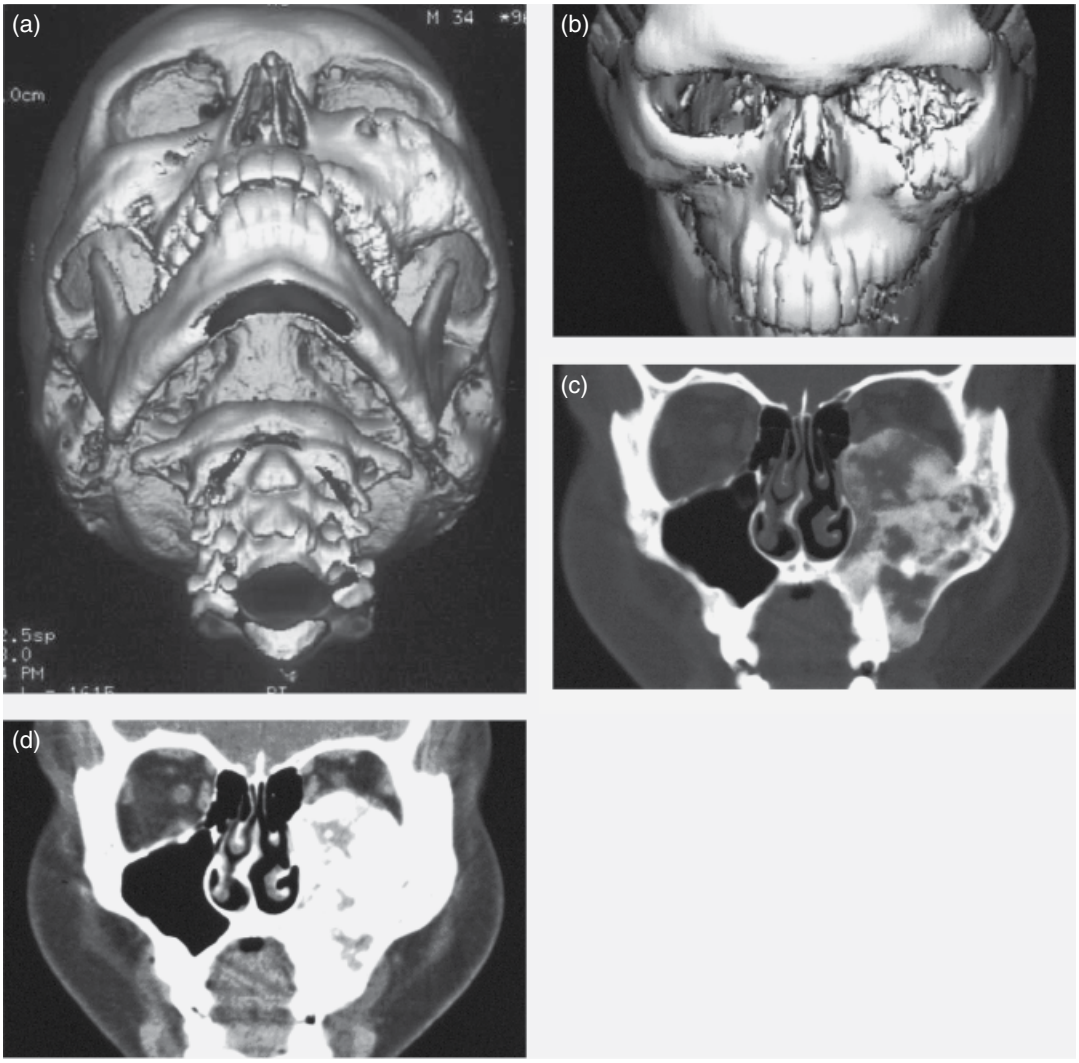


Figure 11.37 Computed tomography (CT) of fibrous dysplasia (FD) affecting the maxilla that presented with proptosis. (a) Three-dimensional reconstruction of a case of FD affecting the maxilla displaying the affected side as a coarse overgrowth of the normal bony profile. (b) Three-dimensional reconstruction of a case of FD affecting the maxilla displaying an upward displacement of the orbital floor. (c) Coronal CT section behind the globe (eyeball). This bone window exhibits a substantial soft-tissue element. The upward expansion is substantial and appreciably constricts the orbital cavity in comparison to the contralateral orbit. (d) Coronal CT section behind the globe (eyeball). This soft-tissue window more clearly displays the optic nerve and four rectus muscles of the eye.



Figure 11.38 Computed tomography (bone window) of fibrous dysplasia (FD) affecting the maxilla. It has obliterated the maxillary sinus. The FD has expanded the buccal aspect of the maxilla and slightly upwardly displaced the floor of the orbit. The vertically directed canal carries the inferior orbital nerve toward the infraorbital foramen.

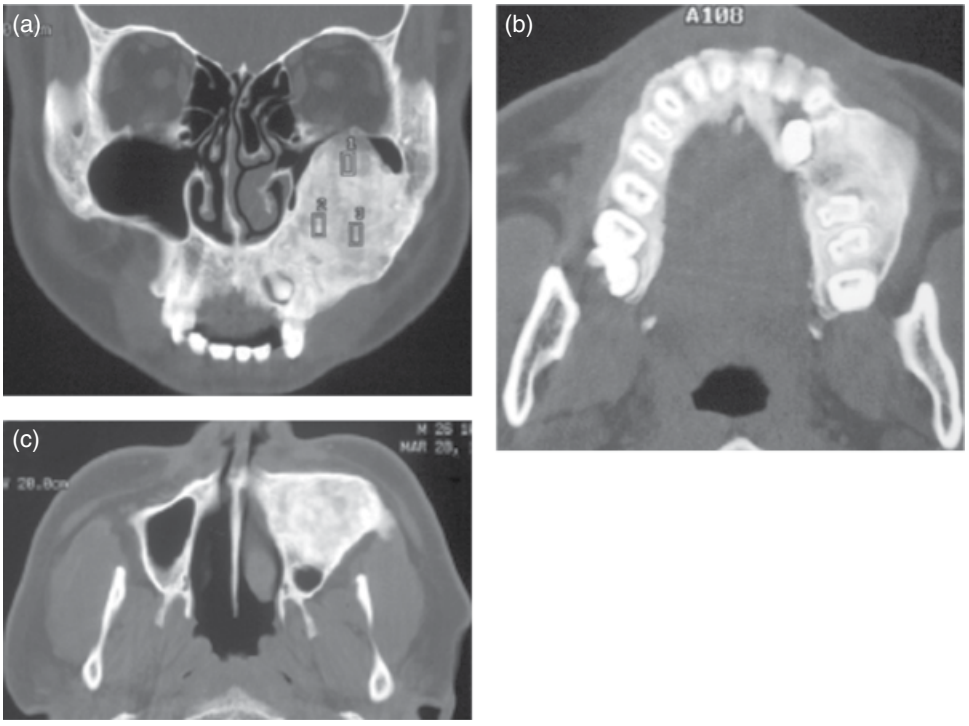


Figure 11.39 Bone-window computed tomography (CT) of fibrous dysplasia (FD) affecting the left maxilla and the maxillary sinus (MS). (a) Coronal CT, at the level of the maxillary canines. The FD extends from the left malar to the midline. Although the FD has also almost completely obliterated the MS in the coronal plane, there are two air-filled spaces superiolaterally (zygomatic recess) and medially. The rounded outline of the antral part of the lesion is unusual for FD and is more indicative of a benign neoplasm, whereas the poorly defined medial margin is indicative of FD. The floor of the orbit is slightly displaced. The general radiopacity is a ground-glass pattern. The cortex of the inferior aspect of the lateral wall is not apparent. There is an unerupted tooth within the FD and the follicular space is clearly visible. The follicle has no lamina dura. The "boxes" represent the density measurement sites (in Hounsfield units). (b) Axial CT, of the maxillary alveolus, displaying the follicle of the unerupted tooth. The buccal aspect of the alveolus has been substantially expanded. (c) Axial CT, at the level of the base of the sigmoid notch, exhibiting this substantial expansion. The bone of the posterior MS appears normal, and the associated antral lumen is still patent and air filled.

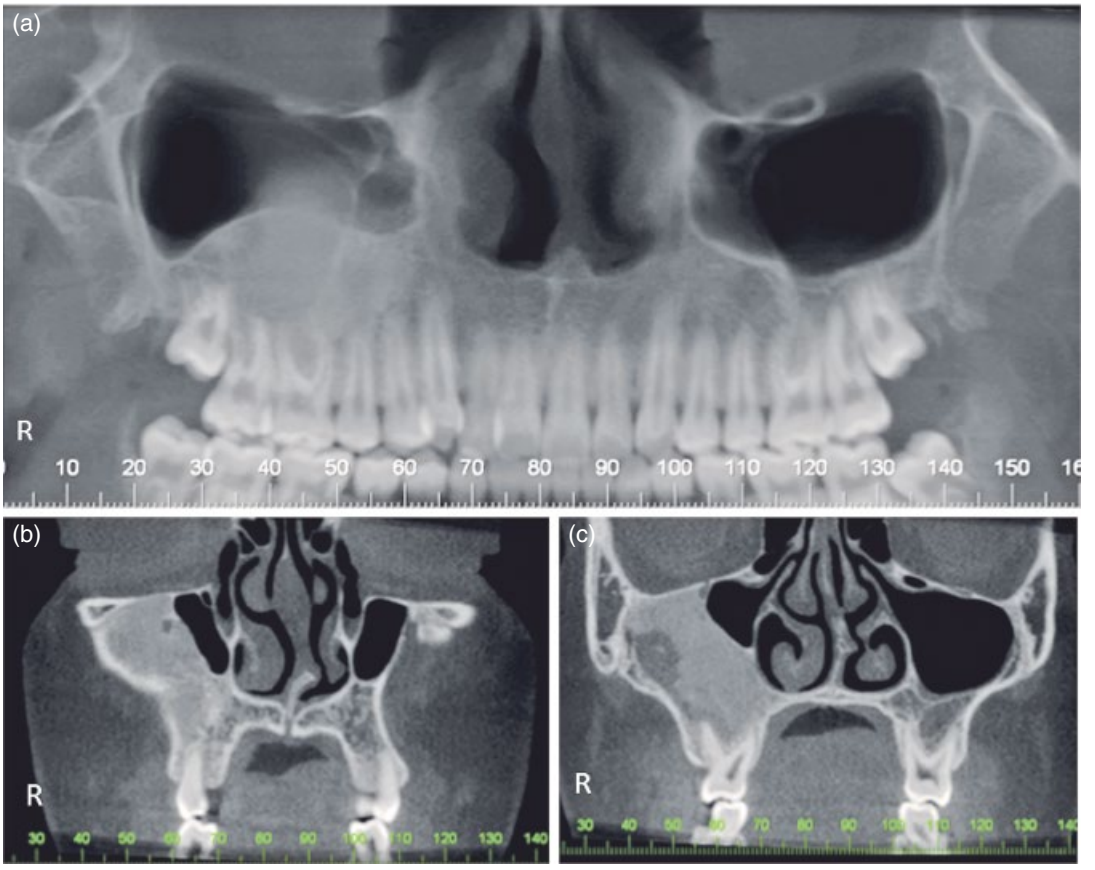


Figure 11.40 Cone-beam computed tomography (CBCT) of fibrous dysplasia affecting the right maxilla in a 60-year-old female. There were no presenting complaints. (a) Panoramic reconstruction displaying an ill-defined ground-glass lesion in the posterior sextant enveloping the apices of subjacent teeth. It has displaced the floor of the maxillary sinus upward. (b) Coronal section from the same case through the nasopalatine duct. Although the spatial resolution is poorer in CBCT in contrast to conventional radiography, the margin between the dysplastic bone and the normal adjacent bone is still not easy to define. (c) Second coronal section, posterior to (b), at the level of the molars. This displays the intact zygomatico-maxillary suture separating the dysplastic maxillary bone and the normal adjacent zygomatic bone. The residual sinus lumen taken together with that in (b) reveals that the almost normal-sized sinus in (a) is deceiving and is created by virtue of the thin plane of panoramic reconstruction passing substantially through the residual sinus. R, right. Source: Reproduced with permission from MacDonald, D.S. (2015). Maxillofacial fibro-osseous lesions. *Clin. Radiol.* 70: 25–36.

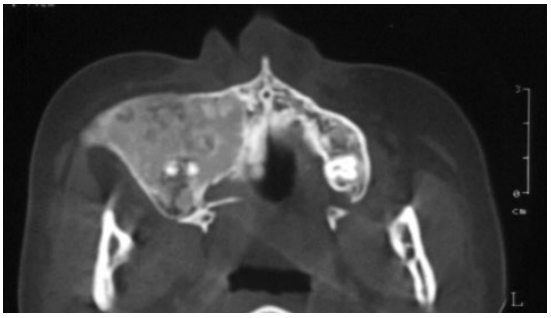


Figure 11.41 Axial computed tomography of fibrous dysplasia completely obturating the maxillary sinus and in apposition with the pterygoid body, which has not been displaced.

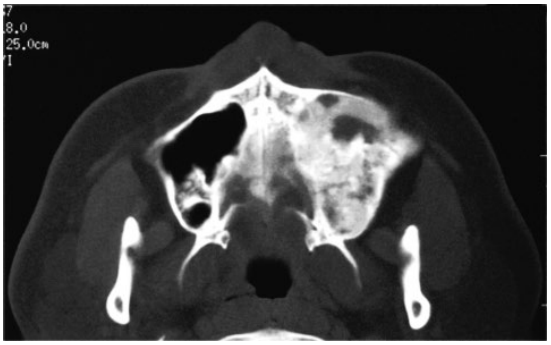


Figure 11.42 Computed tomography of fibrous dysplasia (FD) obturating the maxillary sinus. There is a translucent zone anteriorly. The FD is firmly juxtaposed with regard to the pterygoid plates and is also partly apposed to the lateral aspect of the lateral plate. Source: MacDonald-Jankowski, D.S., Yeung, R., Li, T.K., and Lee, K.M. (2004). Computed tomography of fibrous dysplasia. *Dentomaxillofac. Radiol.* 33: 114–118.

minority of NHLs and SCCs expanded the intact sinus wall.

Although Kato et al. observed no significant difference for MRI sequence (T1, T2, or diffusion weighted), their 17 SCCs exhibited a significantly greater *apparent diffusion coefficient* (ADC) mean of $0.95 \times 10^{-3}\,mm^2/s$ to their 4 NHLs' $0.61 \times 10^{-3}\,mm^2/s$ [10]. There was no difference between them with regard to their *standardized uptake value* (SUV), which was 21 for the 7 NHLs and 17 for the 15 SCCs [10].

Figures 11.7 [16] and 11.14 [3] shows examples of NHL arising from within the alveolus, rather from the sinus mucosa. The intact floor of the maxillary sinus has been displaced upward into the sinus. It is behaving like an odontogenic cyst or a benign odontogenic neoplasm. These will be discussed in detail later in this chapter.

Osteosarcoma affecting the maxillary sinus displays similar features to those reported earlier. This was discussed in

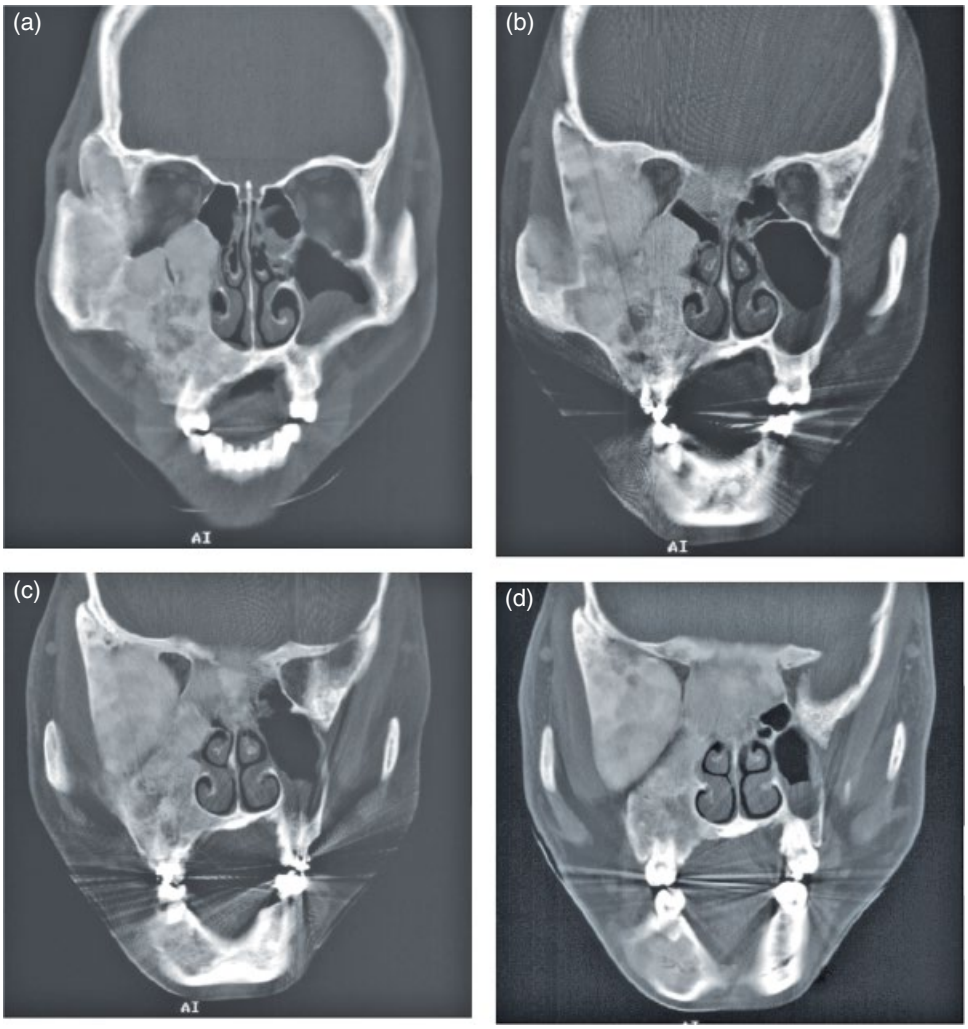


Figure 11.43 Coronal bone-window computed tomography (CT) displaying fibrous dysplasia (FD) affecting the mandible, the maxilla, the zygoma, and the sphenoid. (a) FD affecting the hemimaxilla and contiguous zygoma. The maxillary sinus has been completely obturated. Although the predominant pattern of radiodensity is ground glass, areas of sclerosis and rarefaction are also apparent. The infraorbital canal running toward the infraorbital foramen is still patent as a vertical slit. Although the affected hemimaxilla (and also the zygoma) displays substantial buccal expansion and appreciable medially directed expansion of the lateral wall of the nasal cavity, upward expansion of the floor of the orbit is minimal. The affected alveolus shows buccolingual expansion. The lack of a cortex on the buccal aspect of the alveolus should provoke consideration that this may have been biopsied. (b) Medially directed expansion of the lateral wall of the orbital cavity. The ethmoid air cells are being obturated by the FD affecting the sphenoid. The buccal cortex is intact. (c) FD affecting the ipsilateral hemimandible and the greater wing and body of the sphenoid. The ethmoid air cells have been completely obturated. (d) The superior and inferior orbital fissures, although narrower than the contralateral unaffected side, are nevertheless still patent. The affected hemimandible exhibits substantial buccolingual expansion.

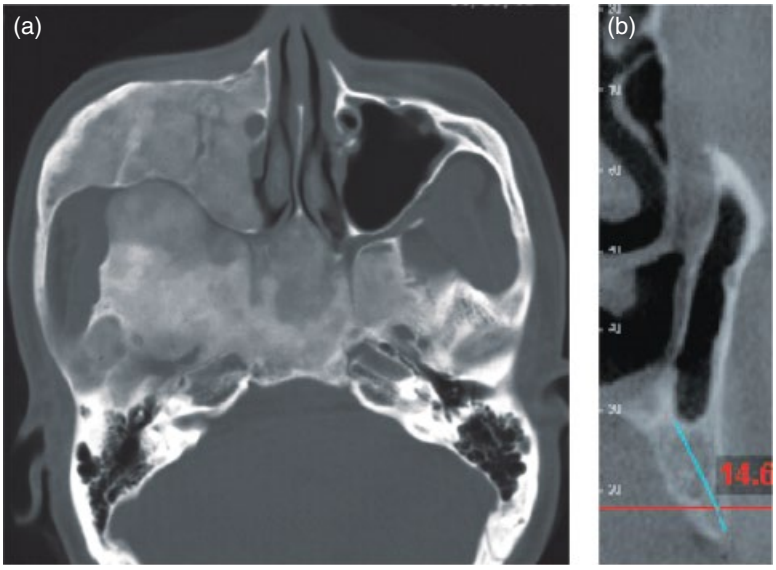


Figure 11.44 (a) Axial (bone-window) computed tomography of polyostotic fibrous dysplasia (FD) affecting a maxillary sinus (MS) on one side and the adjacent base of the skull of the case in Figure 11.40. The MS of the affected side has been completely obliterated by the FD expanding outward into both the anterior wall of the maxilla and the malar bone. Nevertheless, the inferior orbital canal has been preserved, as has the diameter of the nasolacrimal duct. The latter has lost most of its cortex. The anterior portion of the lateral wall of the nasal cavity, although retaining its cortex, has been displaced medially. Although the base of the skull has also been extensively affected, the ipsilateral zygomatic arch has not. Unlike the inferior orbital canal and nasolacrimal duct, the FD has completely obliterated the foramen ovale and spinosum. Also it has crossed the midline. The downwardly expanded base of the skull and the maxilla are still separated by the pterygomaxillary fossa, now both narrowed and lengthened. (b) Coronal cone-beam computed tomography displaying the nasolacrimal canal in a normal patient.

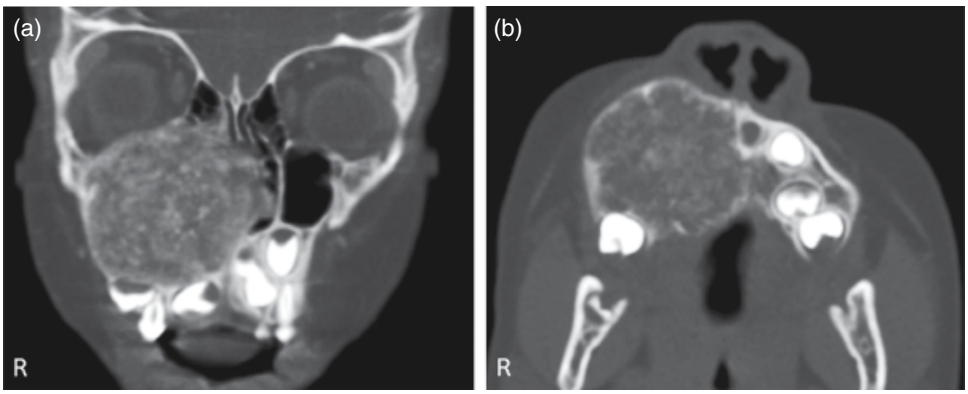


Figure 11.45 Medical computed tomography of a juvenile ossifying fibroma (JOF) affecting the maxilla of a child. Its margins are well defined. The coronal (a) and axial (b) reconstructions exhibit a complete obturation of the maxillary sinus and a ball-shaped expansion of its bony walls, including a substantial buccal expansion. The subjacent teeth are displaced downward and the floor of the orbit is displaced upward. It has obturated the ipsilateral nasal cavity and expanded into the contralateral nasal cavity. Although well defined, there is no discernible capsule space, which is typical for JOF. R, right. Source: Reproduced with permission from MacDonald, D.S. (2015). Maxillofacial fibro-osseous lesions. *Clin. Radiol.* 70:25–36.

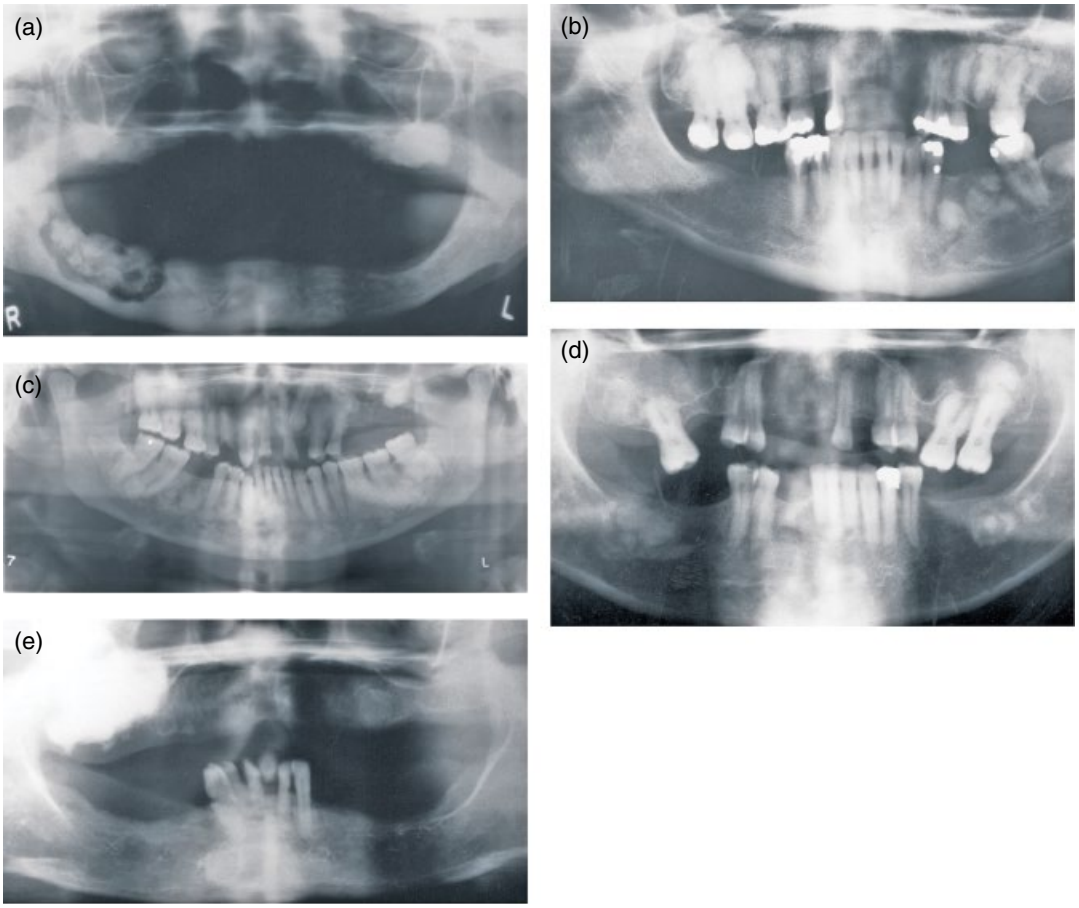


Figure 11.46 Panoramic radiographs of different cases of florid osseous dysplasia (FOD). Each case displays a different presentation of FODs sited in the posterior maxillary sextants and the maxillary sinus (MS). A radiolucent line separating the FOD from the floor of the MS can be discerned wholly in (b–d) and partially in (a) and (e). L, left; R, right. Source: (a) Reproduced with permission from MacDonald-Jankowski, D.S. (1996). Florid osseous dysplasia in the Hong Kong Chinese. *Dentomaxillofac. Radiol.* 25:39–41. (c) Reproduced with permission from MacDonald-Jankowski, D.S. (2004). Fibro-osseous lesions of the face and jaws. *Clin. Radiol.* 59: 11–25.

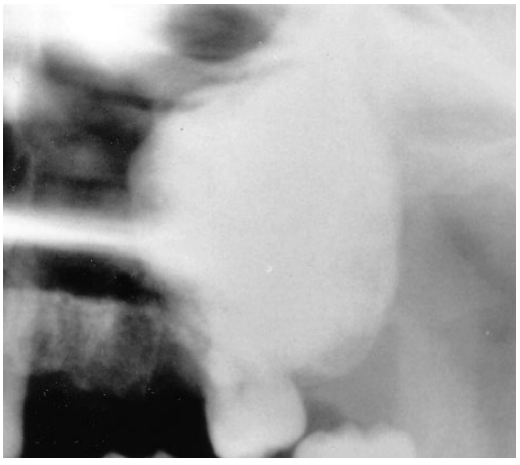


Figure 11.47 Panoramic radiograph displaying a complex odontoma presenting as a well-defined radiopacity completely obturating the posterior part of the lumen of the maxillary sinus. A capsule is apparent as radiolucent spaces on the superior and anterioinferior aspects of the lesion. A cortex is clearly observed on the lesion's anteriosuperior aspect. The radiodensity of a substantial portion of the lesion is similar to that of teeth. It has displaced the root of the erupted maxillary third molar mesially. Source: Reproduced with permission from MacDonald-Jankowski, D.S. (2004). Fibro-osseous lesions of the face and jaws. *Clin. Radiol.* 59:11–25.

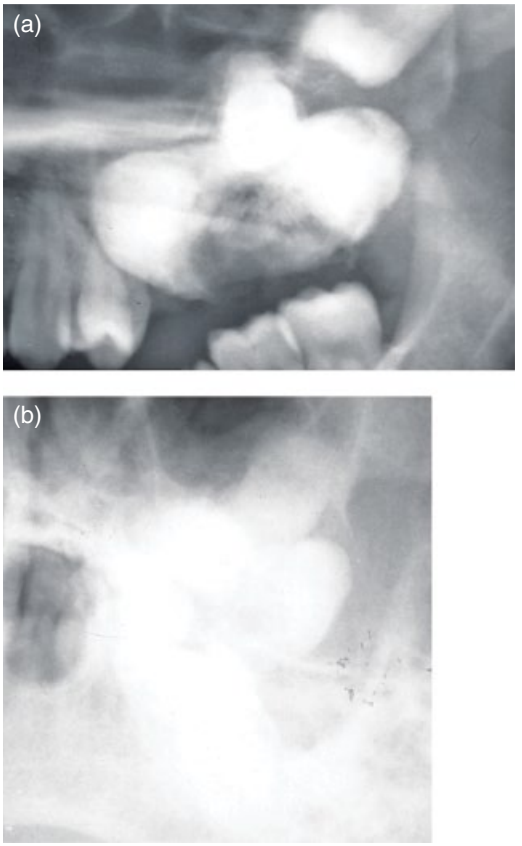


Figure 11.48 Panoramic radiograph (a) and posterioanterior projection (b) displaying a well-defined radiopacity within the maxillary sinus. Upon removal, it was found histopathologically to be a complex odontoma. It has prevented the eruption of a molar tooth.

Chapter 10. Figure 11.16 displays substantial soft-tissue involvement and swelling, which are not reflected by the extent of the radiologically apparent osseous (radiopaque) element of the disease.

In addition to SCC and NHL, there are two other important lesions which cause destruction of the maxillary sinus and other adjacent structures: inverted papilloma (Figure 11.17) and Wegener's granulomatosis (Figure 11.18). Thalassemia (Figure 11.10), which replaces the

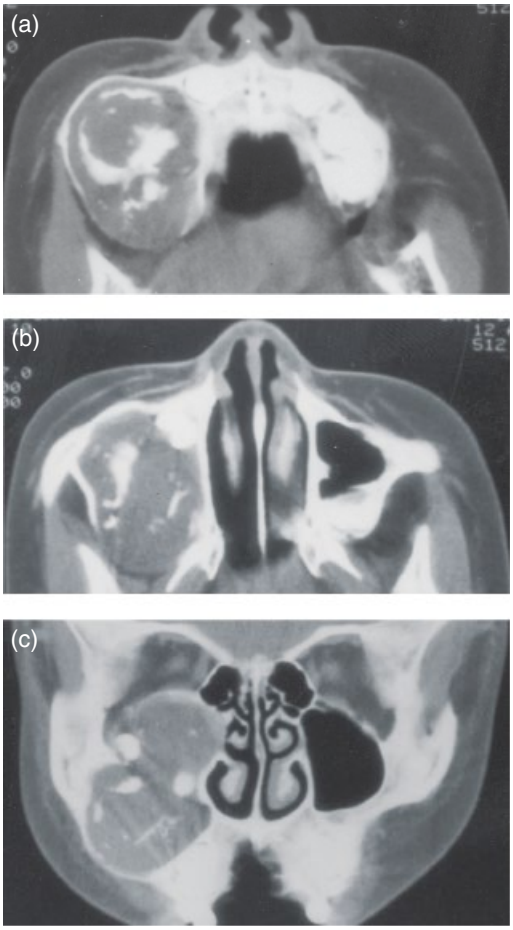


Figure 11.49 Computed tomography (CT) of ameloblastic fibro-odontoma affecting the maxillary sinus (MS). (a) Axial bone-window CT through the maxillary alveolus, displaying a well-defined egg-shaped corticated radiolucent area containing central opacities. There is substantial buccal expansion. (b) Axial bone-window CT through the middle of the nasal cavity, showing a well-defined corticated radiolucent area containing central opacities. The posterior aspect of the posteriolateral wall of the MS has been outwardly displaced. There is a tooth crown impacted into the anteriomedial angle of the MS. (c) Coronal bone-window CT through the maxillary canine, displaying a well-defined corticated radiolucent area containing central opacities. The floor of the orbit has been upwardly displaced.

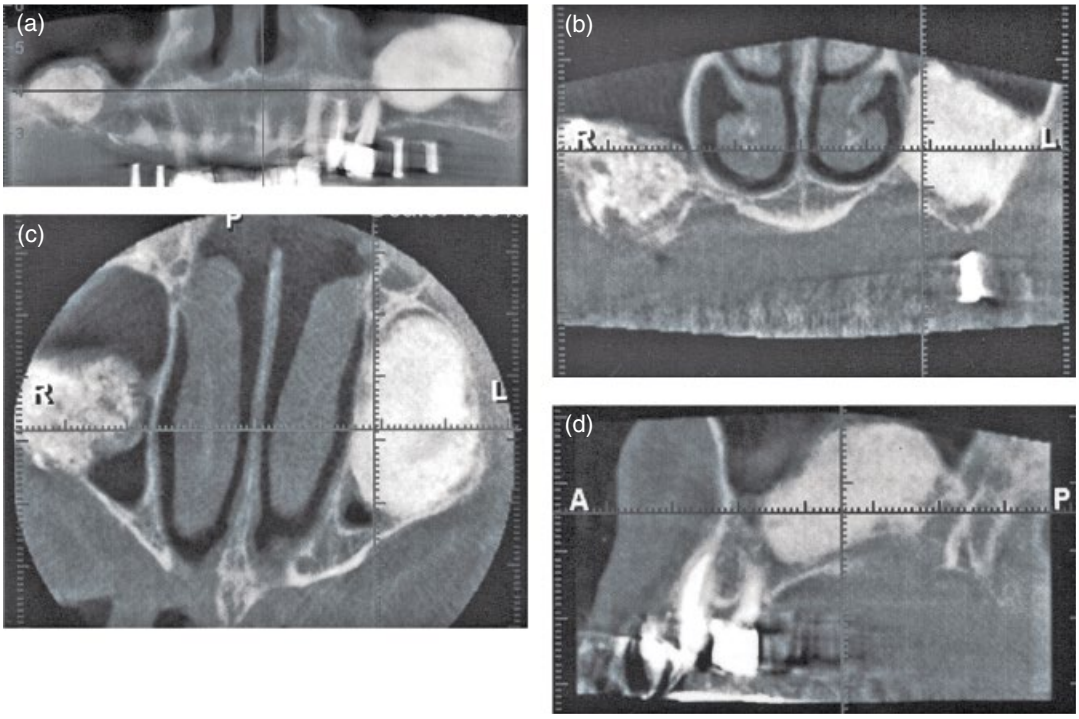


Figure 11.50 Cone-beam computed tomography (CBCT) of bilateral sinus-floor-lift grafts. (a) Panoramic reconstruction displaying the sinus-floor-lift grafts as a bilateral pair of well-defined radiopacities within the posterior maxillary sextants. (b) CBCT coronal reconstruction displaying both radiopacities. The left sinus-lift graft is larger and denser. (c) CBCT axial reconstruction of both sinus-lift grafts. (d) Sagittal reconstruction of the left sinus-lift graft showing the formation of a new bony antral floor over it. A, anterior; L, left; P, posterior; R, right.

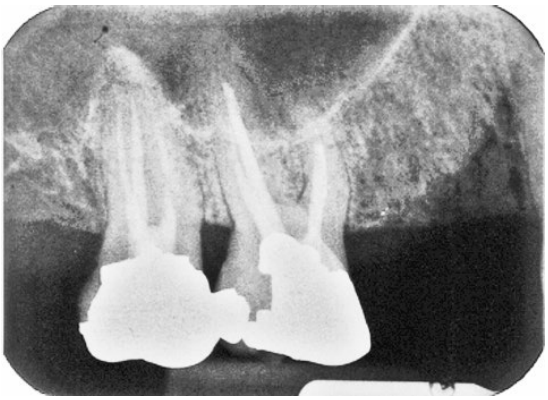


Figure 11.51 Periapical radiograph displaying a root-filled tooth, which exhibits new bone formation at the apex, analogous to the involucrum observed in Figure 10.6.

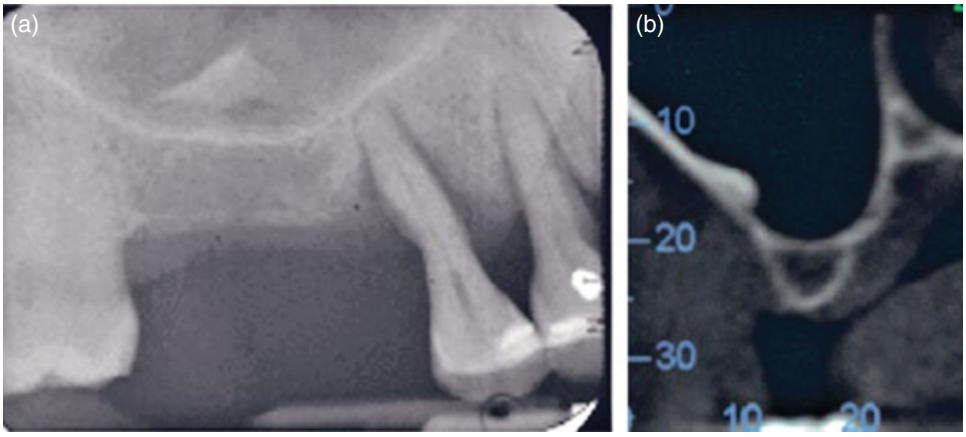


Figure 11.52 Periapical radiography (a) and cone-beam computed tomography (b) of an endostosis within the lateral wall of the maxillary sinus (MS). (a) The superior surfaces are well defined, but the inferior margin is not. (b) The exostosis is on the lateral wall of the MS. The lumen of the MS is otherwise completely normal; that is, the mucosa is not thick enough to be visible and there is no fluid.

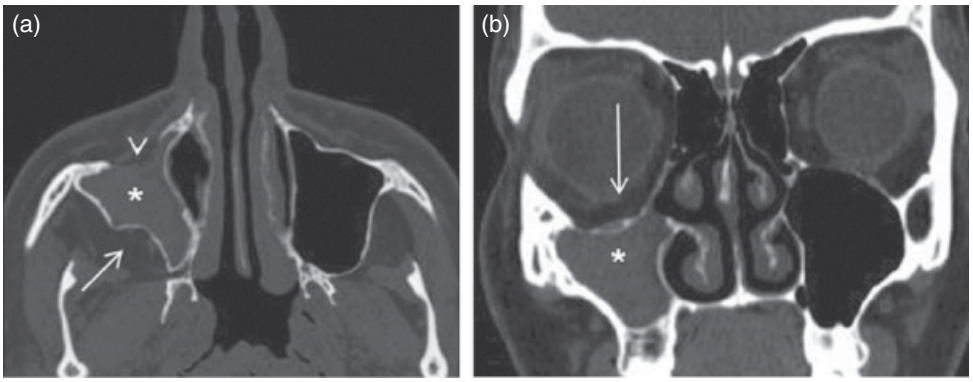


Figure 11.53 Computed tomography (bone windows) of silent sinus syndrome of the right maxillary sinus (MS), marked with an asterisk. (a) Axial reconstruction displaying the inward collapse of the anterior, posteriolateral, and medial walls of the right MS in comparison to the normal left MS. (b) Coronal reconstruction showing the downward displacement of the floor of the orbit and accompanying hypoglobus (downward displacement of the globe or eyeball). Although this is a coronal reconstruction, comparison of the images of the eyeballs would indicate enophthalmos of the right eye. Source: Gaudino, S., Di Lella, G.M., Piludu, F., et al. (2013). CT and MRI diagnosis of silent sinus syndrome. *Radiol. Med.* 118: 265–275.

Table 11.1 Features observed in computed tomography between 12 cases of extranodal non-Hodgkin lymphoma and 29 cases of squamous cell carcinoma of the maxillary sinus.

Features observed on computed tomography	Non-Hodgkin lymphoma	Squamous cell carcinoma	Fisher exact test
Permeation of sinus wall	6/12 (50%)*	3/29 (10%)	P = 0.0106
Destruction of sinus wall	4/12 (33%)	24/29 (83%)*	P = 0.0037
Expansion of intact sinus wall	2/12 (17%)	2/29 (7%)	P = 0.567
Sinus wall remaining in tumor	11/12 (92%)*	10/29 (34%)	P = 0.0014
Intratumoral necrosis	2/12 (17%)	25/29 (86%)*	P = 0.00004

Note: Although the study was performed by Kato et al. [10]. Differentiation of extranodal non-Hodgkins lymphoma from squamous cell carcinoma of the maxillary sinus: a multimodality imaging approach. *SpringerPlus* 4: 228. doi: 10.1186/s40064-015-0974-y, the present author chose the Fisher exact test.
The * represent the most important features for that lesion.

bone and lumen of the maxillary sinus with hemopoietic tissue, was addressed in Chapter 9.

The inverted papilloma (Figure 11.17), though a benign neoplasm, is invasive and has a propensity to recur [17]. It arises from the nose and paranasal sinuses. It accounts for up to 4% of all primary sinonasal tumors and its incidence is about one in a quarter of a million people. The Krouse staging begins with Stage 1, confined to the nose; Stage 2 involves the medial wall of the maxillary sinus, ethmoids, and/or ostiomeatal complex; Stage 3 involves all walls of the maxillary sinus, sphenoid, and frontal sinuses; and Stage 4 extrasinonasal extension. This last suggests that the inverted papilloma has undergone malignant transformation [17]. Malignancy, usually SCC, will arise in 5% of these lesions [18]. Ghosh et al. add that a contrast-enhanced CT and a biopsy are necessary for diagnosis [17]. Figure 11.17 reveals that even benign tumors can be so locally destructive that they can resemble malignant lesions radiologically; compare with the examples of SCC in Figure 11.13.

Wegener's granulomatosis (Figure 11.18), a rare noncaseating [19], polysystemic lesion, has been recently renamed *granulomatosis and polyangiitis* (GPA) [20]. The majority of GPA cases in the United States affect the head and neck [20]. Three-quarters of cases are positive for *antineutrophil cytoplasmic antibodies* (ANCA). Prior to the advent of corticosteroids, 90% of GPA patients died within two years [21]. Although 85% present with sinonasal involvement, a third of GPA cases are solely sinonasal [19]. A third of all cases have ocular involvement, with which they may initially present [19]. The *central nervous system* (CNS) is also affected in a small proportion of cases. Although the International Chapel Hill Consensus Conference on Nomenclature of Systemic Vaculitides developed guidelines for GPA, a recent systematic review revealed that the imaging of GPA was nonspecific. Nevertheless, D'Anza et al. recommend that septal erosion, mucosal thickening, and bone changes are suggestive of GPA [19]. Pakalniskis et al. reported that the bony changes were neoosteogenetic rather than periostitic [20].

11.5 Dome-shaped Radiopacities Arising from the Sinus Floor

11.5.1 WITH A CORTEX

11.5.1.1 Lesions Arising from within the Alveolus Subjacent to the Maxillary Sinus

The portion of those lesions below the image of the hard palate on panoramic radiographs which arise from within the maxillary alveolus and expand into the maxillary sinus appears radiolucent, whereas that portion appearing above it and thus completely enveloped by the air-filled space of the maxillary sinus is radiopaque (see Figure 11.20a).

Furthermore, if the lesion arising from the alveolus becomes infected, the cortex representing the upwardly expanded floor of the maxillary sinus can be lost. The lesion may become indistinguishable from the MAC or other pathology intrinsic to the maxillary sinus, except for the radiolucency within the alveolus (Figure 11.20) or "hyperpneumatization" (see Figure 11.7). This loss of the upwardly displaced floor of the maxillary sinus can be readily appreciated in infected KCOTs (Figure 11.25) [22]. In addition to the loss of the antral floor, much of the maxillary tuberosity and posterior antral wall was absent, strongly suggesting the presence of malignancy, more specifically an SCC.

The most frequent lesions that occur in the alveolus are *periapical radiolucencies of inflammatory origin* (PRIOs) and dentigerous cysts. As mentioned earlier, Bomeli et al. identified that 17% of the sinus lesions for which a CT was prescribed were for a dental infection [14]. Some PRIOs become radicular cysts and can expand extensively up into the sinus cavity (Figure 11.19). Dentigerous cysts arise not only from the unerupted third molar (wisdom) teeth, but also canine (Figure 11.20) and supernumerary (Figure 11.21) teeth, and substantially obturate the sinus. Another cyst is the OOC [23] (Figure 11.22). An important lesion that so far has not affected the posterior sextant of the maxillary alveolus is the *glandular odontogenic cyst* (GOC) [24].

11.5.1.2 Odontogenic Neoplasms

Odontogenic neoplasms arising in the subjacent alveolus can involve the maxillary sinus secondarily. The most frequent of these are three of the most important – the ameloblastoma, KCOT, and odontogenic myxoma – because of their propensity to recur.

Although a systemic review revealed that only 9% of ameloblastomas affect the maxilla and 82% of those affected the posterior sextant, in the detailed Hong Kong series within the same report the majority were solid ameloblastomas. These maxillary cases first presented later in life than the average mandibular ameloblastoma within the same report and are more likely to affect the anterior sextant wholly or in part [25, 26]. This pattern has now been substantially confirmed in another Chinese report [27]. If these ameloblastomas become sufficiently large, they can affect the maxillary sinus (Figure 11.23). Solid ameloblastomas require resection with a margin to minimize recurrence. If untreated or inadequately treated, they can spread to the orbit or even the skull base (Figure 11.24) and may cause death [28].

The KCOT affects the maxilla as frequently as the mandible. Although most mandibular KCOTs in the Hong Kong Chinese are multilocular, most of those that affect the posterior maxilla are not

only unilocular (Figures 11.25–11.27), but the majority present earlier in life [29]. Although most cases that recurred in a case series on Canadian KCOTs followed up after primary surgery occurred in those patients who were first treated by enucleation alone in the fifth decade, the majority of patients with KCOTs in the posterior maxilla first presented in the second decade [30]. While the earlier age of presentation in the Hong Kong Chinese is similar to that observed for syndromic KCOTs (nevoid basal cell carcinoma syndrome, NBCCS) in the same community, the latter can be distinguished by its other "criteria" [31], which may include multiple KCOTs (Figure 11.27), already discussed in Chapter 9. A reason for the unilocular presentation and buccolingual expansion of the KCOT arising subjacent to the maxillary sinus could be that the buccal and lingual cortices of the maxillary alveolus and the cortex of the floor of the maxillary sinus are considerably thinner than those of the body of the mandible, where expansion, if it occurs, is minimal [32]. Figure 11.28 displays a KCOT that arose in the anterior sextant; its expansion into the anterior portion of the maxillary sinus has a unilocular profile.

KCOTs affecting the maxillary sinus generally present with substantial expansion during adolescence or early adulthood. If presenting with unerupted teeth, particularly third molars, they should be distinguished from dentigerous cysts.

In a systematic review, 75% of the maxillary cases of odontogenic myxoma affected the posterior sextant (see Table 9.6) [33]. The odontogenic myxoma can achieve substantial dimensions, obturating the sinus and expanding and eroding its walls (Figure 11.29) [34]. The computed tomography in Figure 11.29 displays striae that resemble a sunray pattern. Although the odontogenic myxoma arising primarily within the anterior sextant (Figure 11.30) is not yet of substantial dimensions, it can still involve the maxillary sinus without the expansion observed in Figure 11.29. The odontogenic myxoma requires resection to minimize recurrence.

11.5.2 WITHOUT A CORTEX

11.5.2.1 Mucosal Antral (Pseudo) Cyst and Polyps

The MAC is the most commonly discovered lesion affecting the maxillary sinus. It is most frequently uncovered as an incidental finding. As the MAC represents an accumulation of fluid within the antral mucosa, but without an epithelial lining, it may be referred to as a "pseudocyst." It varies in frequency in different communities, depending upon local climate and culture. It is more frequent in Hong Kong [35] than in inner-city London [36], at least during late summer to early autumn when the radiographs were taken. It may also vary within the community according to the seasons. MACs are dome shaped and on panoramic radiography appear to rise most frequently from the antral floor. On CT they are observed arising from other walls, particularly the lateral wall, which is outside the panoramic radiograph's focal trough. Features of periapical pathosis are classically absent in the alveolar bone subjacent to the MACs (Figures 11.31 and 11.32).

Unlike the MAC, the polyp is a sac of inflammatory exudate under the sinus mucosa. It may be dome shaped when arising from the sinus floor, or more pendulous when arising from the roof. It is frequently multiple (Figures 11.33–11.35), whereas the MAC is more likely to be single.

The *antrochoanal polyp* (ACP) arises from the maxillary sinus mucosa and extends through the osteum to reach the choana, and even the nasopharynx

(Figure 11.36) [37]. Although it is most frequent in childhood (15 years mean age), it does occasionally occur in adults (49 years mean age) [38]. The main complaint for both ages was nasal obstruction. A purely endoscopic approach is preferred to the original Caldwell-luc approach, since it is attended by risks of infraorbital paresthesia and damage to the child's developing dentition [37].

The MAC and the polyp, although soft-tissue structures, become apparent on conventional radiography by virtue of the silhouette effect (see Figures 11.31 and 11.33). This allows the surface contour of soft-tissue structures to become visible by contrasting them against air-filled spaces. For this reason, the outlines of the heart, the aorta, and the pulmonary veins are made visible, because they are silhouetted against the translucent air-filled lung fields on the chest radiograph. On occasion these soft-tissue structures may also appear to have a slight radiopaque periphery, which is clearly not a cortex (Figure 1.22), or contrast-enhanced mucosa, as displayed in Figure 11.2. The phenomenon in Figure 2.7 is a result of the Mach band effect and is accompanied by a black line immediately surrounding the entire MAC. The Mach band effect has already been fully discussed in Chapter 2.

11.5.2.2 Mineralized Radiopacities

Fibrous dysplasia (FD) affects the maxillary sinus, either from its origin within the alveolus or within the base of the skull. The latter is obviously more likely to affect vision. A recent systemic review has revealed that cases of monostatic FD arising within the alveolus are very unlikely to cause ocular problems [39]. Therefore, with the exception of the occasionally sporadic case, the patient's vision is unlikely to be threatened by FD arising within the alveolus. Of those FDs included in the systematic review, 58% affect the maxilla [39]. FD affecting the maxilla enlarges it, sometimes grotesquely, although it retains a broad resemblance to its original (normal) shape (Figure 11.37). The predominant pattern of radiodensity on conventional radiography is generally ground glass [40]. CT may display a wider range of radiodensities (Figures 11.37–11.44). All maxillary cases in a recent case series affected the maxillary sinus [40]. In a series of cases investigated by CT [41], in one case the lateral wall displayed the fusiform expansion classically observed in the mandible (Figure 11.39). As the lesion grows, the lumen of the maxillary sinus is gradually obliterated (progressing from Figure 11.39 to Figure 11.38) [41]. The vertical dimension of the maxilla is increased both vertically and horizontally [41], which gives rise to the clinically apparent grossly expanded maxilla already observed in Figure 11.37. In most cases of monostotic fibrous dysplasia affecting the jaws, arising within the alveolus or at least close to it, the pterygoid body and plates are not generally affected. The anteriorly apparent expansion of the maxillary FD appears to use the pterygoid bone as a base to push off against (Figures 11.39, 11.41, and 11.42). Although occasionally the pterygoid bone may be displaced backward, in other cases it remains undisplaced, but with some posteriolaterally expanded dysplastic maxilla lying against, but separate from, the lateral surface of the lateral pterygoid plate (Figures 11.41 and 11.42). The vertical expansion raises the floor of the orbit, but infrequently to such an extent as to occasion ocular signs, such as proptosis as observed in Figure 11.37. The more usual upward expansion of FD arising within the jaws is exhibited in Figures 11.38 and 11.39. The upward

expansion in monostotic FDs, arising within the maxilla, very rarely causes proptosis. The monostotic FD case displayed in Figure 11.37 is exceptionally rare. In a systematic review of FD, not one case of monostotic FD caused proptosis [39].

Polyostotic fibrous dysplasia can, in addition to the jaws, affect other facial and skull bones, including the base of the skull (see Figures 11.43 and 11.44). Involvement of the last can threaten vision by compressing the optic nerve and causing proptosis (see Figure 18.20). Other cases of polyostotic fibrous dysplasia affecting the base of the skull are displayed in Figures 18.21–18.22.

Radiopaque lesions such as ossifying fibroma [42, 43] and odontoma [44] can grow upward into the lumen of the maxillary sinus. The posterior sextant of the maxilla was affected in 17% of ossifying fibromas [43]. Three of the four maxillary ossifying fibromas affected the sinus, of which two obturated it [42]. Figure 11.45 displays a large case of juvenile ossifying fibroma which has substantially replaced the entire hemimaxilla.

The posterior sextant was affected in 47% of all cases with florid osseous dysplasia (FOD; Table 10.6 Figure 11.46a–d) [45], but in only 74% of cases of focal osseous dysplasia (FocOD) (Table 10.5) [46]. Although the OD lesions may achieve substantial dimensions and protrude into the maxillary sinus, as in Figure 11.46e, they are infrequently associated with symptoms.

The ossifying fibroma [42, 43] and complex odontomas (Figures 11.47–11.49) [46] are generally indistinguishable on conventional radiographs. To understand how the previously distinct ameloblastic fibro-odontoma fits into the odontoma classification, see Figure 11.49 (fully discussed in Chapter 10). The soft-tissue windows were separately reported by Piette et al. [47]. According to a synthesis of case reports on large odontomas [44], most are likely to grow and occupy the entire vertical dimension of the maxillary sinus. The tooth it prevented from erupting is frequently reported as being displaced upward to the floor of the orbit (Figure 11.48).

11.5.2.3 Miscellaneous Rare Lesions Affecting the Maxillary Sinus

Radiopacities, such as Figure 11.50, associated with the floor of the sinus that may convincingly look like pathology, may be iatrogenic; they are sinus-floor elevation grafts (see also Figures 11.6 and 20.9). Figure 11.51 displays periapical sclerosis at the apices of an endodontically treated molar. These and dense bone islands are unusual in the maxilla, particularly the posterior sextant [48]. Figure 11.52 is an endostosis, which may be mistaken for an antrolith, which, according to Drumond et al.'s [13] large study, is very rare. Therefore, upon reflection, diagnosis of antroliths which have not changed in shape and position over a period of time, such as that in Figure 11.51, may ultimately be confirmed by CBCT. Using this modality, a clear fusion within the sinus wall, as in Figure 11.52, would mean an endostosis that requires no treatment, in comparison to a nonfusion meaning an antrolith, which may require surgery in the face of an otherwise intractable sinusitis.

A rare, but important phenomenon is SSS, which presents with painless spontaneous enophthalmos, hypoglobus (downward displacement of the eye into the sinus), and facial deformities (Figure 11.53) [49]. These occur secondarily to chronic maxillary sinus atelectasis. Gaudino et al. produced a very good pictorial essay on CT and MRI investigations of SSS [50].

References

1. MacDonald, D.S. (2015). Maxillofacial fibro-osseous lesions. *Clin. Radiol.* 70: 25–36.
2. MacDonald, D.S. (2016). Lesions of the jaws presenting as radiolucencies on cone-beam computed tomography. *Clin. Radiol.* 71: 972–985.
3. MacDonald, D., Li, T., Leung, S.F. et al. (2017). Non-Hodgkin lymphoma arising within the alveolus of the maxilla. *Oral Surg. Oral Med. Oral Pathol. Oral Radiol.* 124: e233–e238. https://doi.org/10.1016/j.oooo.2017.04.015.
4. Eggesbø, H.B. (2006). Radiological imaging of inflammatory lesions in the nasal cavity and paranasal sinuses. *Eur. Radiol.* 16: 872–888.
5. MacDonald-Jankowski, D.S. (2004). Fibro-osseous lesions of the face and jaws. *Clin. Radiol.* 59: 11–25.
6. Kim, H.Y., Kim, M.B., Dhong, H.J. et al. (2008). Changes of maxillary sinus volume and bony thickness of the paranasal sinuses in longstanding pediatric chronic rhinosinusitis. *Int. J. Pediatr. Otorhinolaryngol.* 72: 103–108.
7. Adekeye, E.O. and Cornah, J. (1985). Osteomyelitis of the jaws: a review of 141 cases. *Br. J. Oral Maxillofac. Surg.* 23: 24–35.
8. Bornstein, M.M., Seiffert, C., Maestre-Ferrín, L. et al. (2016). An analysis of frequency, morphology, and locations of maxillary sinus septa using cone beam computed tomography. *Int. J. Oral Maxillofac. Implants* 31: 280–287.
9. Sakhdari, S., Panjnoush, M., Eyvazlou, A., and Niktash, A. (2016). Determination of the prevalence, height, and location of the maxillary sinus septa using cone beam computed tomography. *Implant Dent.* 25: 335–340.
10. Kato, H., Kanematsu, M., Watanabe, H. et al. (2015). Differentiation of extranodal non-Hodgkins lymphoma from squamous cell carcinoma of the maxillary sinus: a multimodality imaging approach. *SpringerPlus* 4: 228. https://doi.org/10.1186/s40064-015-0974-y.
11. Morita, T., Yamashiro, M., Kayamori, K. et al. (2016). Primary intraosseous squamous cell carcinoma derived from a maxillary cyst: a case report and literature review. *Mol. Clin. Oncol.* 4: 553–558.
12. MacDonald, D. and Lim, S. Extranodal lymphoma arising within the maxillary alveolus; a systematic review. *Oral Radiol.* 34: 185. https://doi.org/10.1007/s11282-018-0312-5.
13. Drumond, J.P., Allegro, B.B., Novo, N.F. et al. (2017). Evaluation of the prevalence of maxillary sinuses abnormalities through spiral computed tomography (CT). *Int. Arch. Otorhinolaryngol.* 21: 126–133.
14. Bomeli, S.R., Branstetter, B.F. 4th, and Ferguson, B.J. (2009). Frequency of a dental source for acute maxillary sinusitis. *Laryngoscope* 119: 580–584.
15. Costan, V.V., Popescu, E., and Stratulat, S.I. (2013). A new approach to aesthetic maxillofacial surgery: surgical treatment of unilateral exophthalmos due to maxillary sinus mucocele. *J. Craniofac. Surg.* 24: 914–916.
16. Li, T.K. and MacDonald-Jankowski, D.S. (1991). An unusual presentation of a high-grade, non-Hodgkin's lymphoma in the maxilla. *Dentomaxillofac. Radiol.* 20: 224–226.
17. Ghosh, A., Pal, S., Srivastava, A., and Saha, S. (2015). Modification of endoscopic medial maxillectomy: a novel approach for inverted papilloma of the maxillary sinus. *J. Laryngol. Otol.* 129: 159–163.
18. Mendenhall, W.M., Hinerman, R.W., Malyapa, R.S. et al. (2007). Inverted papilloma of the nasal cavity and paranasal sinuses. *Am. J. Clin. Oncol.* 30: 560–563.
19. D'Anza, B., Langford, C.A., and Sindwani, R. (2017). Sinonasal imaging findings in granulomatosis with polyangiitis (Wegener granulomatosis): a systematic review. *Am. J. Rhinol. Allergy* 31: 16–21.
20. Pakalniskis, M.G., Berg, A.D., Policeni, B.A. et al. (2015). The many faces of granulomatosis with polyangiitis: a review of the head and neck imaging manifestations. *AJR Am. J. Roentgenol.* 205: W619–W629.
21. Berden, A., Göçeroglu, A., Jayne, D. et al. (2012). Diagnosis and management of ANCA associated vasculitis. *BMJ* 344: e26.
22. MacDonald-Jankowski, D.S. (1992). The involvement of the maxillary sinus by odontogenic keratocysts. *Clin. Radiol.* 45: 31–33.
23. MacDonald-Jankowski, D.S. (2010). Orthokeratinized odontogenic cyst; a systematic review. *Dentomaxillofac. Radiol.* 39: 455–467.

24. Macdonald-Jankowski, D.S. (2010). Glandular odontogenic cyst: systematic review. *Dentomaxillofac. Radiol.* 39: 127–139.
25. MacDonald-Jankowski, D.S., Yeung, R., Lee, K.M., and Li, T.K. (2004). Ameloblastoma in the Hong Kong Chinese. Part 1: systematic review and clinical presentation. *Dentomaxillofac. Radiol.* 33: 71–82.
26. MacDonald-Jankowski, D.S., Yeung, R., Lee, K.M., and Li, T.K. (2004). Ameloblastoma in the Hong Kong Chinese. Part 2: systematic review and radiological presentation. *Dentomaxillofac. Radiol.* 33: 141–151.
27. Luo, H.Y. and Li, T.J. (2009). Odontogenic tumors: a study of 1309 cases in a Chinese population. *Oral Oncol.* 45: 706–711.
28. Nastri, A.L., Wiesenfeld, D., Radden, B.G. et al. (1995). Maxillary ameloblastoma: a retrospective study of 13 cases. *Br. J. Oral Maxillofac. Surg.* 33: 28–32.
29. MacDonald-Jankowski, D.S. and Li, T.K.L. (2010). Keratocystic odontogenic tumour in a Hong Kong community; the clinical and radiological presentations and the outcomes of treatment and follow-up. *Dentomaxillofac. Radiol.* 39: 167–175.
30. MacDonald, D., Gu, Y., Zhang, L., and Poh, C. (2013). Can clinical and radiological features predict recurrence in solitary keratocystic odontogenic tumors? *Oral Surg. Oral Med. Oral Pathol. Oral Radiol.* 115: 263–271.
31. MacDonald, D.S., Li, T.K., and Goto, T.K. (2015). A consecutive case series of nevoid basal cell carcinoma syndrome affecting the Hong Kong Chinese. *Oral Surg. Oral Med. Oral Pathol. Oral Radiol.* 120: 408–415.
32. MacDonald-Jankowski, D.S. (2011). Keratocystic odontogenic tumour; a systematic review. *Dentomaxillofac. Radiol.* 40: 1–23.
33. MacDonald-Jankowski, D.S., Yeung, R., Lee, K.M., and Li, T.K. (2002). Odontogenic myxomas in the Hong Kong Chinese: clinicoradiological presentation and systematic review. *Dentomaxillofac. Radiol.* 31: 71–83.
34. MacDonald-Jankowski, D.S., Yeung, R., Lee, K.M., and Li, T.K. (2004). Computed tomography of odontogenic myxoma. *Clin. Radiol.* 59: 281–287.
35. MacDonald-Jankowski, D.S. (1993). Mucosal antral cysts in a Chinese population. *Dentomaxillofac. Radiol.* 22: 208–210.
36. MacDonald-Jankowski, D.S. (1994). Mucosal antral cysts observed within a London innercity population. *Clin. Radiol.* 49: 195–198.
37. Choudhury, N., Hariri, A., and Saleh, H. (2015). Endoscopic management of antrochoanal polyps: a single UK centre's experience. *Eur. Arch. Otorhinolaryngol.* 272: 2305–2311.
38. Lee, D.H., Yoon, T.M., Lee, J.K., and Lim, S.C. (2016). Difference of antrochoanal polyp between children and adults. *Int. J. Pediatr. Otorhinolaryngol.* 84: 143–146.
39. MacDonald-Jankowski, D.S. (2009). Fibrous dysplasia: a systematic review. *Dentomaxillofac. Radiol.* 38: 198–215.
40. Macdonald-Jankowski, D.S. and Li, T.K. (2009). Fibrous dysplasia in a Hong Kong community: the clinical and radiological features and outcomes of treatment. *Dentomaxillofac. Radiol.* 38: 63–72.
41. MacDonald-Jankowski, D.S., Yeung, R., Lee, K.M., and Li, T.K. (2004). Computed tomography of fibrous dysplasia. *Dentomaxillofac. Radiol.* 33: 114–118.
42. Macdonald-Jankowski, D.S. (2009). Ossifying fibroma: systematic review. *Dentomaxillofac. Radiol.* 38: 495–513.
43. Macdonald-Jankowski, D.S. and Li, T.K. (2009). Ossifying fibroma in a Hong Kong community: the clinical and radiological features and outcomes of treatment. *Dentomaxillofac. Radiol.* 38: 514–523.
44. MacDonald-Jankowski, D.S. (1996). Odontomas in a Chinese population. *Dentomaxillofac. Radiol.* 25: 186–192.
45. MacDonald-Jankowski, D.S. (2003). Florid cemento-osseous dysplasia: a systematic review. *Dentomaxillofac. Radiol.* 32: 141–149.
46. MacDonald-Jankowski, D.S. (2008). Focal cemento–osseous dysplasia: a systematic review. *Dentomaxillofac. Radiol.* 37: 350–360.
47. Piette, E.M., Tideman, H., and Wu, P.C. (1990). Massive maxillary ameloblastic fibro-odontoma; case report with surgical management. *J. Oral Maxillofac. Surg.* 48: 526–530.

48. MacDonald-Jankowski, D.S. (1999). Idiopathic osteosclerosis in the jaws of Britons and of the Hong Kong Chinese: radiology and systematic review. *Dentomaxillofac. Radiol.* 28: 357–363.
49. Martínez-Capoccioni, G., Varela-Martínez, E., and Martín-Martín, C. (2016). Silent sinus syndrome an acquired condition and the essential role of otorhinolaryngologist consultation: a retrospective study. *Eur. Arch. Otorhinolaryngol.* 273: 3183–3188.
50. Gaudino, S., Di Lella, G.M., Piludu, F. et al. (2013). CT and MRI diagnosis of silent sinus syndrome. *Radiol. Med.* 118: 265–275.

Chapter 12

Lesions within the soft tissues

12.1 Introduction

This chapter addresses the diagnosis of calcifications occurring within the soft tissues of the face and neck. These calcification/s present as a radiopacity, which, as already described in Chapter 10, appears as a white area on a conventional radiograph, most usually a panoramic radiograph or lateral cephalogram; the latter is generally taken for orthodontic purposes. In addition to conventional radiography, advanced imaging modalities such as *computed tomography* (CT) and *magnetic resonance imaging* (MRI) are frequently used to investigate jaw lesions. Although calcified lesions and structures are still white on images made by either CT (see Chapter 4) or *cone-beam computed tomography* (CBCT; see Chapter 5), they appear black on MRI, as do air-filled spaces and blood vessels (see Chapter 6).

Although there are a number of entities that can appear as radiopacities in the soft tissues of the face and jaws (Figure 12.1), the clinically most important are *calcified carotid artery atheroma* (CCAA), salivary calculi, calcified lymphoid tissue, tonsilloliths, the stylohyoid complex, and the triticeous cartilage (also called triticeal cartilage or cartilago triticea). Figure 12.2 provides a diagnostic algorithm based on panoramic imaging presentation which can be applied to assist in distinguishing CCAA from other entities.

Although the majority of these calcifications occur in specific sites (the most frequent and/or important are set out in Figures 12.1 and 12.2) and as a result are readily identifiable, some are not, such as acne scars. An extraoral clinical examination will result in diagnosis of the latter in most cases. Calcification of the musculature, particularly adjacent to its insertion, may occur in rare cases. The main cause is myositis ossificans. This exists in two forms: *myositis ossifican progressive* (MOP, also called fibrodysplasia ossificans progressiva) [1, 2] and *myositis ossifican traumatica* (MOT) [1, 3]. When it affects the muscles of mastication, it causes severe trismus [1]. A history of trauma is present in 75% of cases [4]. Due to the superimposition of the mandible, the calcifications are best observed in cross-sectional imaging: CT [1, 3, 4], MRI [1], and CBCT [2].

Outside the jaw bones, radiopacities within the soft tissues of the lateral neck, in addition to normal structures such as the stylohyoid complex (including the hyoid bone), also affect the aging thyroid cartilage and several laryngeal cartilages such as the triticeous cartilage. These calcifications may reflect two different

Oral and Maxillofacial Radiology: A Diagnostic Approach, Second Edition. Edited by David MacDonald.
© 2020 John Wiley & Sons, Inc. Published 2020 by John Wiley & Sons, Inc.

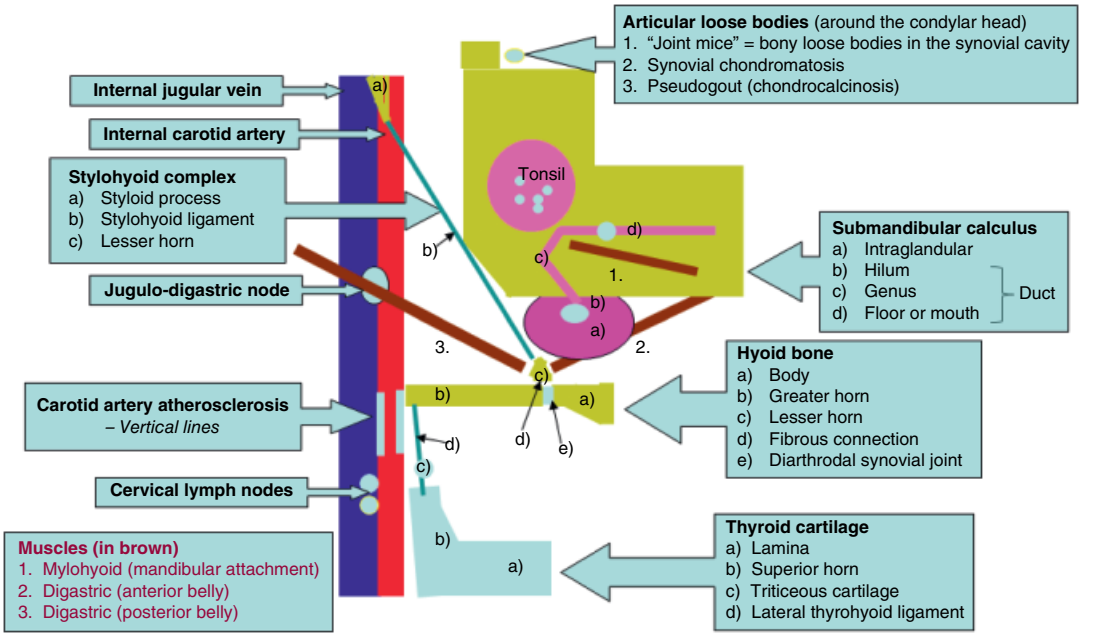


Figure 12.1 Calcifications that may be observable on a panoramic radiograph (and also on a lateral cephalogram, generally taken for orthodontic purposes) in and around the soft tissues of the anterior neck. The internal jugular vein is in blue and the common carotid artery, continuing superiorly above the hyoid bone as the internal carotid artery, is in red. Note: The lateral thyrohyoid ligament is a round elastic cord, which forms the posterior border of the thyrohyoid membrane and passes between the tip of the superior cornu of the thyroid cartilage and the distal extremity of the greater cornu of the hyoid bone.

processes of deposition, either by bone cells or by nonbone cells. The latter process is by dystrophic calcification, usually in chronic inflammatory lesions or those with multiple episodes of inflammation. Dystrophic calcification is commonly observed in the soft tissues of the jaws as calcification of the tonsils (now usually secondary to tonsillitis), of the cervical lymph nodes (Figure 12.3), or of atherosclerotic plaques in the carotid arteries.

Although this classically pertains to panoramic radiographs and lateral cephalograms, it now includes CBCT. As these generally occur as incidental findings, their detection requires that the clinician routinely reviews the entire image and/or dataset, in addition to monitoring the specific purpose for which the image was prescribed. Although the causes, set out in Table 10.1, of radiopacities presenting within the face and jaws are wide and varied, ranging from artifacts in image production and variations in normal anatomy to manifestations of disease processes (Figure 12.1), the most important cause/s are those for CCAA. Before we address CCAAs, we will first consider tonsilloliths and the variants of normal anatomy.

Tonsilloliths represent dystrophic calcification within the tonsillar or adenoid crypts. Although these cases may or may not have a history of tonsillitis, the literature suggests that tonsilloliths are a major source of halitosis [5]. Palatine tonsilloliths

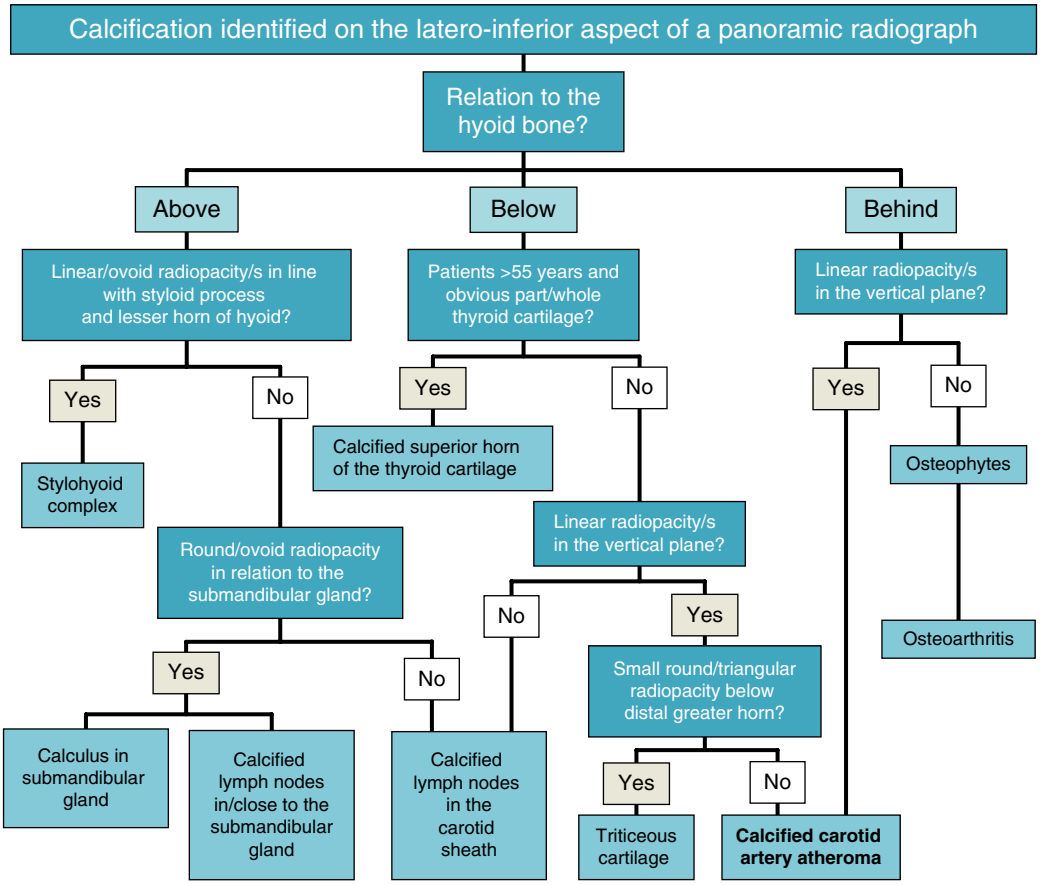


Figure 12.2 Flowchart to characterize the appearance of calcifications in the soft tissues of the neck on the latero-inferior aspect of a panoramic radiograph. Initial decisions involve determining the location of the calcification relative to the hyoid bone and further characterization relative to other structures or appearance. Calcifications in the neck can range from variants of normal anatomy, such as the stylohyoid complex or triticeous cartilage, and calcifications of the thyroid cartilage (in older patients) to abnormal calcification in the salivary glands and ducts and in arteries secondary to pathological processes. Source: Adapted from MacDonald D., Chan A., Harris A., Vertinsky T., Farman A.G., Scarfe W.C. (2012). Diagnosis and management of calcified carotid artery atheroma: dental perspectives. *Oral Surg Oral Med Oral Pathol Oral Radiol*. 114: 533–47.

are most obvious on panoramic radiographs and cephalograms, but are also readily displayed by CBCT (Figure 12.4). Although mainly "superimposed over the ramus of the mandible at the level coincident with and inferior to the soft palate," they were also observed in the soft tissue posterior to the ramus, posterio-inferior to the angle and inferior to the body of the mandible. Their prevalence was 13% in Japanese [6], 8% in American [5], and 5% in Iranian panoramic radiographs [7]. Takahashi et al. note: "In both communities the prevalence increases with age. A significant correlation was observed between the detectability on panoramic radiographs and the size of tonsilloliths as revealed by CT images" [6].



Figure 12.3 Part of a panoramic radiograph displaying large calcified lymph nodes, tonsilloliths, and an elongated styloid process. Most of the calcified lymph nodes lie in a vertical chain coincident with the internal jugular vein and carotid artery. The tonsilloliths are frequently superimposed on the mandibular foramen. L, left. Source: Juan, Y.H., Hsuan, H.F., Ng, K.K., et al. (2015). Chain of rings: a radiographic sign of papillary thyroid cancer. *Acta Clin. Belg.* 70: 124–126. Reproduced with permission of Taylor & Francis.

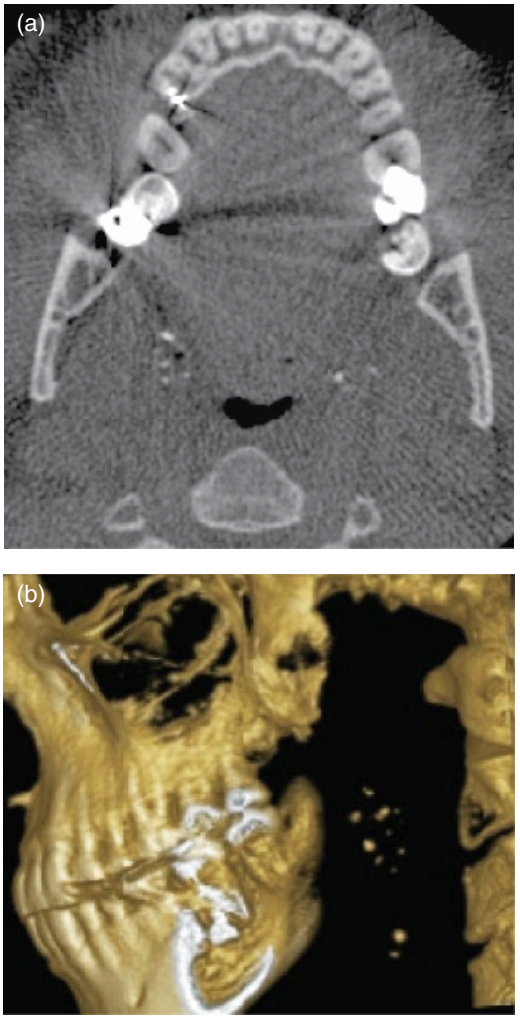


Figure 12.4 Cone-beam computed tomography (CBCT) of tonsilloliths. (a) Axial CBCT showing tonsilloliths adjacent to the oropharynx just medial to the mandibular foramen. (b) Three-dimensional reconstruction, cutting away the posterior body and vertical ramus of the mandible to display the tonsilloliths. Source: Courtesy of Dr. Alexandre Khairallah, University of Lebanon.

12.2 Radiopacities Outside the Bony Jaws

12.2.1 CALCIFICATIONS OF THE STYLOHYOID COMPLEX

The 12 most common patterns of "calcification of the stylohyoid complex" are set out in Figure 12.5 [8]. These are based on the four developmental regions of this complex: tympanohyal (skull base), stylohyal (the majority of the styloid process), ceratohyal (contributes to the elongated styloid process and stylohyoid ligament), and hypohyal (the lesser horn of hyoid component of the stylohyoid ligament). This system of patterns was introduced for clinical use because traditional

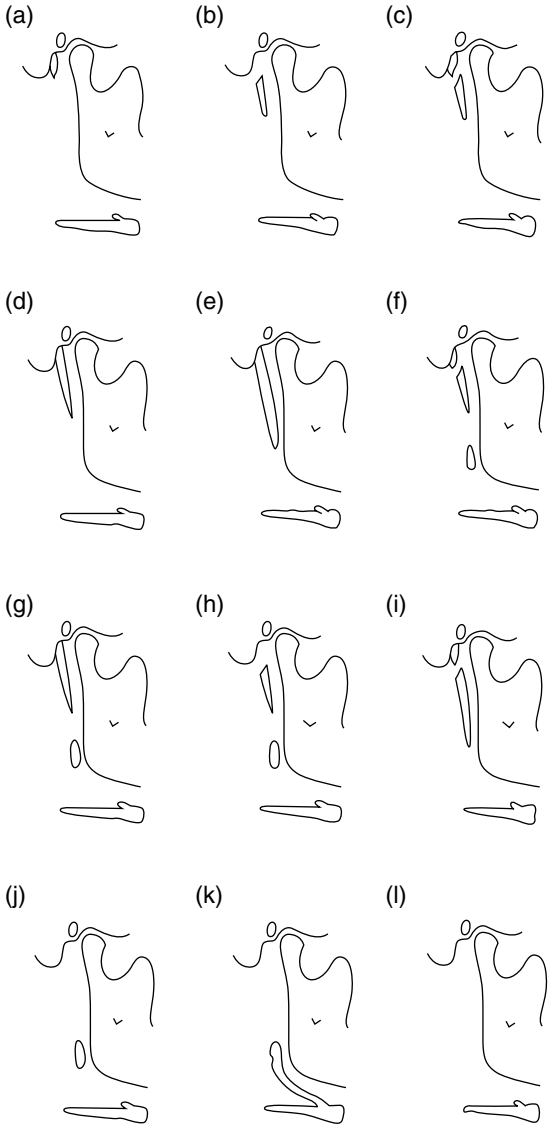


Figure 12.5 The 12 patterns of calcification of the stylohyoid complex used by MacDonald-Jankowski [8]. Pattern: (a) Region 1 = tympanohyal alone; (b) Region 2 = stylohyal alone; (c) Regions 1 and 2, separate; (d) Regions 1 and 2, continuous; (e) Regions 1, 2, and 3, continuous; (f) Regions 1, 2, and 3, separate; (g) Regions 1 and 2, continuous but separate from 3; (h) Regions 2 and 3, separate; (i) Regions 2 and 3, continuous but separate from 1; (j) Region 3 alone; (k) Regions 3 and 4, continuous (may include calcification in one other region); (l) No styloid process visible. Note 1: Regions 1, 2, 3, and 4 coincide with the four centers of ossification of the stylohyoid complex: tympanohyal, stylohyal, ceratohyal, and hypohyal. Note 2: Patterns (a–d) are normal styloid processes, pattern (e) is an elongated styloid process, and patterns (f–k) are calcified stylohyoid ligaments. Source: MacDonald-Jankowski, D.S. (1990). The synchondrosis between the greater horn and the body of the hyoid bone: a radiological assessment. *Dentomaxillofac. Radiol.* 19: 171–172.

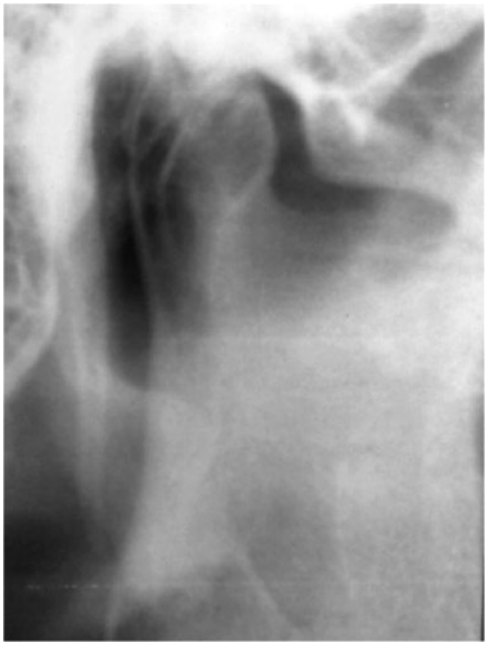


Figure 12.6 Panoramic radiograph displaying a normal styloid process, which can extend as inferior as the middle of the mandibular foramen. This example is of continuous bone and comprises the tympanohyal and stylohyal components (pattern d).

measurement from panoramic radiographs is subject to substantial magnification and distortion, especially in the region posterior to the alveolar processes [8]. A more effective and clinical parameter for assessing an elongated styloid process on a panoramic radiograph is when its tip is lower than the midpoint of the mandibular foramen (Figure 12.6). 'Calcifications of the stylohyoid complex' are also obvious on CBCT (Figure 12.7) and on CT (Figures 12.8a–e and 12.9).

The following paragraphs summarize the different prevalences of the more common patterns in two world communities, Hong Kong and London. The percentages are cited in that order. A normal styloid process (patterns a–d; 84% vs. 73%) and pattern d on its own (67% vs. 40%) were

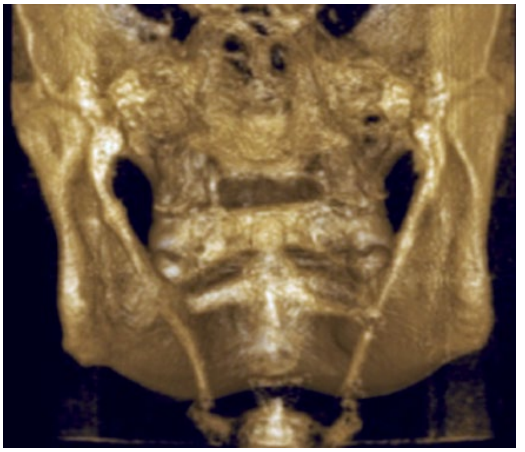


Figure 12.7 Three-dimensional reconstruction of cone-beam computed tomography of a completely calcified stylohyoid ligament from the base of the skull to the hyoid bone. Source: Courtesy of Dr. Alexandre Khairallah, University of Lebanon.

significantly more prevalent in the Hong Kong Chinese (Figures 12.6 and 12.8a and b), whereas a calcified stylohyoid ligament (patterns f–k) was significantly more frequent in Londoners (4% vs. 16%; Figure 12.7). Segmentation (Figure 12.9) was significantly more frequent in Londoners (6% vs. 23%). Bilateral symmetry, with regard to pattern, was significantly more frequent in the Chinese (100% vs. 93%; Figures 12.7 and 12.8a and b). There was no significant difference between Hong Kong and London for an elongated styloid process (pattern e; 9% and 8%, respectively; Figures 12.7, 12.8c–e and 12.9).

Okabe et al. [9] observed similarity in pattern distribution between their 80-year-old Japanese and the Hong Kong Chinese just discussed. They suggested that this was perhaps due to similarities in East Asian genotypes and phenotypes. The major difference was that their sample displayed a substantially greater proportion of pattern e (35%). As the Okabe et al. [9] study was exclusively among 80-year-olds, this difference was considered

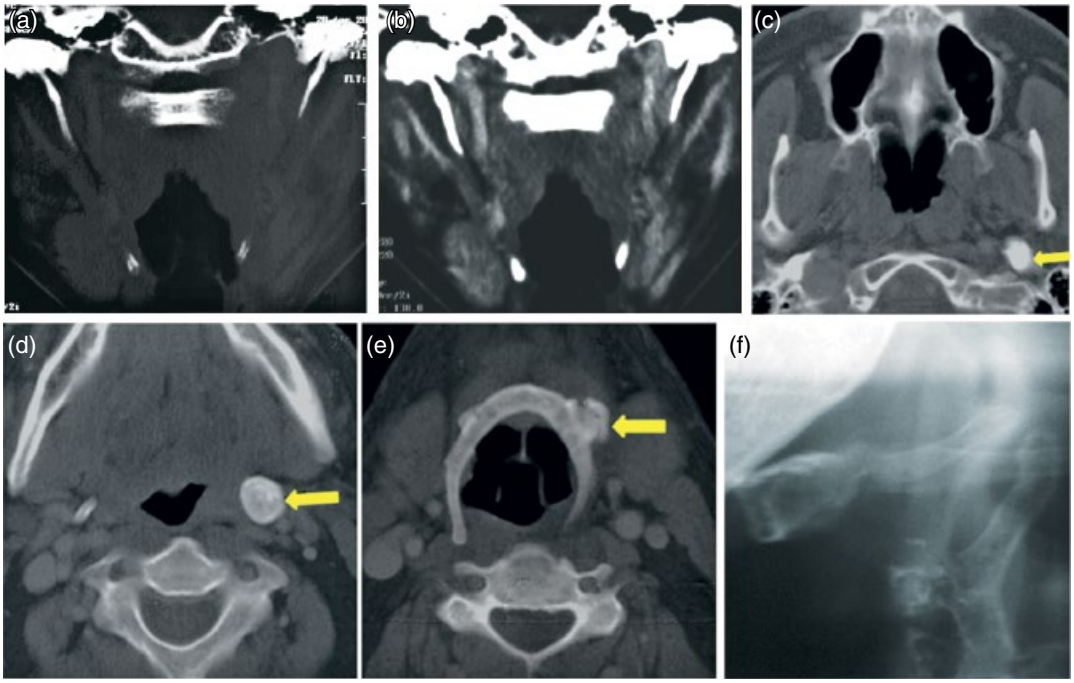


Figure 12.8 Coronal reconstruction of computed tomography (CT) displays the styloid process within the bone (a) and soft-tissue (b) windows. The coronal section is at the level of the anterior arch of C1. The styloid processes on these coronal sections are angled medially, running almost straight (in part tracing out the stylohyoid ligament) toward the junction between the body and the greater horn of the hyoid bone. The greater horns on each side are observed in cross-section. (c), (d) and (e) are adapted and reprinted with permission; Murtagh RD, Caracciolo JT, Fernandez G. CT findings associated with Eagle syndrome. *AJNR Am J Neuroradiol* 2001;22:1401–1402. They are axial reconstructions displaying an elongated styloid process close to its origin at the base of the skull (c), its maximal thickness at the level of the angle of the mandible and its insertion into the hyoid bone. NOTE: styloid process in all images of both cases are bone; a cortex and an internal trabecular pattern are observable in (c) to (e). The calcified component of the contralateral sylohyoid complex displays the same osseous elements in (d). (f) Panoramic radiograph displays the hyoid bone immediately below the angle of the mandible. Below the hyoid bone is the superior horn and partially calcified lateral lamina of the thyroid cartilage. In reality, in contrast to its traditional display in many anatomical texts, the hyoid bone infrequently exists as a complete unified bone, except in the oldest patients. The various parts are more frequently observed radiologically as separate bones joined by radiolucent spaces, representing the diarthrodial synovial joints. In this figure the anterior rectangular bone represents the body of the hyoid, whereas the small round bone superimposed and or in contact with its superiodistal margin is the lesser horn. Immediately distal to the above joint is a horizontal V whose upper limb represents the image of the ipsilateral greater horn. The lower, longer, almost horizontal image represents the contralateral greater horn. Calcification of the thyroid cartilage is encountered increasingly in the older patient. Nevertheless, as is obvious here, it can coexist with a hyoid bone displaying all of its components as still separate bony entities.

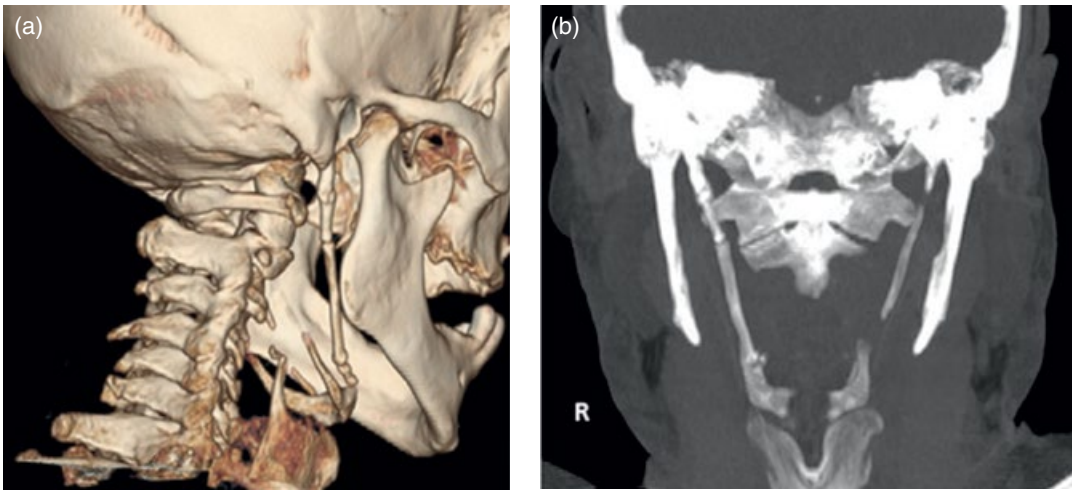


Figure 12.9 (a) The three-dimensional computed tomographic (CT) reconstruction reveals that the ossification of the right stylohyoid ligament from the base of the skull to the body of the hyoid bone. (b) The coronal CT reveals joint spaces within the otherwise completely ossified right stylohyoid ligament. Key: R, Right. Note: the superior horn and the laminae of the thyroid cartilage is also ossified. In this 65-year old male. Source: Reprinted with permission; Ata-Ali J., Ata-Ali F., Melo M., Andrés-Teruel J.C., Soto-Sarrion C. (2017). Eagle syndrome compared with stylohyoid syndrome: complete ossification of the stylohyoid ligament and joint. *Br J Oral Maxillofac Surg*. 55: 218–219.

to be a phenomenon of aging. That was supported by a Brazilian report measuring directly from panoramic radiographs [10]. Okabe et al. [9] also reported that the elongated styloid process (Figures 12.7, 12.8c–e and 12.9) correlated significantly with increased serum calcium concentration and heel bone density, as well as with the patient's height and weight. Therefore, these findings "may provide potentially life-saving information about elderly people" [9].

The styloid process also runs in an anterior and medial direction to the hyoid bone (Figure 12.7, Figures 12.8a and b, and Figure 12.9 respectively); the inferior horn and upper half of the body of the hyoid bone form the caudal component of the stylohyoid complex.

The upper half of the hyoid bone is derived in common with the cranial components of the stylohyoid complex from the second pharyngeal arch or Reichert's cartilage. The rest of the hyoid is derived from the third pharyngeal arch. The hyoid bone arises from six centers of ossification, two for the body and one for each horn [11]. The lesser horn may not fuse with the body (see Figure 1.32b), but it is attached by fibrous tissue to the greater horn, which in turn articulates with the body by a diarthrodial synovial joint (Figure 12.8f). This last feature is important, because it is clearly observed on panoramic and lateral cephalometric radiographs, particularly in children. It should not be mistaken for a hyoid bone fracture [12].

The stylohyoid complex infrequently causes difficulty in its recognition, except perhaps pattern j, in which no other landmarks of the stylohyoid complex are available. This could be mistaken for CCAA. Occasionally, a long styloid

process may cause Eagle's syndrome, which among other features may cause atypical pain [13].

12.2.2 CALCIFICATION OF THE THYROID CARTILAGE

Figures 12.8f and 12.9 and the later Figure 12.13 display calcification of the thyroid cartilage. The thyroid cartilage calcifies from a posteriolateral to anteriomedial direction [14]. Based on Hounsfield units (HU), "the thyroid cartilage is not consistently denser than soft tissue until greater than 40 years of age, which would make laryngeal ultrasound feasible for this population" [14].

Although most calcifications are readily identifiable, some, particularly the triticeous cartilage, are not. This cartilage occurs midway on the posterior margin of the posterior thyrohyoid ligament, which places it in a similar position to a CCAA when viewed on a panoramic radiograph or lateral cephalogram. Ahmad et al. reported that most triticeous cartilages are round, whereas most CCAAs appear as curvilinear radiopacities [15].

12.2.3 CALCIFIED CAROTID ARTERY ATHEROMA

The presence of calcifications in the lateral soft tissues of the neck on maxillofacial images has received increasing attention in dentistry since CCAA was first reported to be visible on panoramic radiographs in 1981 [16]. Much of the text from this point onward has been derived or adapted from earlier publications by the present author in conjunction with his co-authors [17–20]. CCAA occurs secondary to mature atheromatous plaque formation and represents an increased risk of a stroke, also known as a *cerebrovascular accident* (CVA) [21]. The presence of CCAA has been reported in many global communities [22].

CVA is a complex disease process with regard to its classification, etiology, diagnosis, prevention, and treatment. There are two causes of stroke: ischemic and hemorrhagic [23]. Strokes caused by the rupture of a blood vessel in the brain are called hemorrhagic strokes. These account for 13% of all CVAs, yet are responsible for more than 30% of all stroke deaths [23]. Hemorrhagic strokes are subdivided into subarachnoid and intracerebral hemorrhage, depending on the location of the intracranial bleed. Ischemic strokes are caused by thrombotic occlusion of feeder arteries in the brain or by emboli, most of which arise from pre-existing thrombi. About 87% of all strokes are ischemic [23] and are the second leading cause of mortality in most developed countries. Therefore, factors associated with this disease are important to identify. Emboli may arise from the heart (referred to as cardioembolic) and are considered either high risk (e.g. associated with atrial fibrillation, rheumatic disease of the mitral or aortic valve, artificial heart valves) or low risk (e.g. due to calcification of the annulus or ring of the mitral valve, patent foramen ovale). However, atheroma-related formations of thrombi and emboli in the carotid artery are the most frequent cause of stroke [24]. In the neck, CCAA can occur either in the *common carotid artery* (CCA) at the junction (bifurcation) of the *internal carotid artery* (ICA) and the *external carotid artery* (ECA) located lateral and inferior to the hyoid bone, or in the ICA. Atheroma forms in the artery's tunica intima, resulting in atherosclerosis and reduction or occlusion of the lumen, referred to as stenosis. Atherosclerotic lesions are frequently stenotic or ulcerated and are considered especially unstable, forming intraluminal thrombi.

The prevalence of CCAA on panoramic images of asymptomatic middle age (greater than 50 years) to elderly adults ranges from 2 to 4.5% [22]. The prevalence of CCAA is substantially higher (22–37%) in populations with systemic medical risk factors, including dilated cardiomyopathy [25]. Other risk factors identified in the literature, mainly co-authored by Friedlander, were recently summarized: these are type 2 diabetes, obstructive sleep apnea syndrome, renal disease and metabolic syndrome, patients receiving radiation therapy to the neck, and being a postmenopausal woman [17].

Figure 12.10 is an overview of the clinical diagnostic and management algorithms for dental practitioners when CCAA are identified radiologically, and describes and illustrates current appropriate radiographic modalities and medical management strategies used to confirm and assess stenosis associated with CCAA.

Current literature suggests that the risk of stroke should not be estimated solely on the incidental finding of CCAA on panoramic images. Other risk factors such as age, smoking history, total cholesterol level, and hypertension should also be part of the overall risk assessment [22]. In particular, increased *blood pressure* (BP) is one of the most important elements in atheroma formation and is of significant importance in patients with CCAA. In patients with identified CCAA, BP assessment at least once during a course of treatment can help identify at-risk patients and result in appropriate referral for further medical evaluation (Figure 12.10) [26]. Raised BP is not only implicated in an increased risk of ischemic stroke, but also of hemorrhagic stroke. Routine monitoring of the dental patient's BP has a greater positive impact on the patient's health than relying solely on recognition of CCAA as an incidental finding on panoramic radiographic images. A panoramic radiograph should never be taken primarily to detect CCAAs. This would offend against current good practice, as embodied by the Federal Drug Administration's (FDA) guidelines directed to reducing unnecessary irradiation of the patient [27, 28]. Additionally, CCAAs usually present on panoramic radiographs as curvilinear, irregular parallel radiopacities about 1.5–2.5 cm inferior-posterior to the angle of the mandible adjacent to the cervical spine, at or below the third and fourth cervical vertebrae, and inferior and lateral to the hyoid bone, posterior to the oropharyngeal airway space [17]. In order to avoid sending false positives to the patient's primary care physicians, the dentist should seek advice first from a radiologist (oral and maxillofacial radiologist, if available). Alternately, or in addition, a raised chin *posterio-anterior* (PA) projection of the mandible should be taken on a panoramic radiographic unit with a lateral-cephalometric attachment. PA is preferred to anterio-posterior (AP) so as to reduce the radiation dose to the eyes, and thereby reduce cataract formation [29]. True positives are seen when the CCAA is observed lateral to the third to fifth cervical vertebrae (Figure 12.11). This distinguishes CCAA from other causes of calcifications in the posteriolateral part of the neck, as already revealed in Figures 12.1 and 12.2. On these images, calcifications within the carotid arteries will appear lateral to the spine, whereas calcifications in the thyroid gland, thyroid cartilage, triticeous cartilage, vertebral column, or epiglottis will be in the midline, superimposed over the spine (Figure 12.11) [17]. This readily reduces the number of false positives (Figure 12.12). It is emphasized again that while every panoramic radiograph (or every image or dataset, for that matter) should be scrutinized for incidental findings, a panoramic radiograph

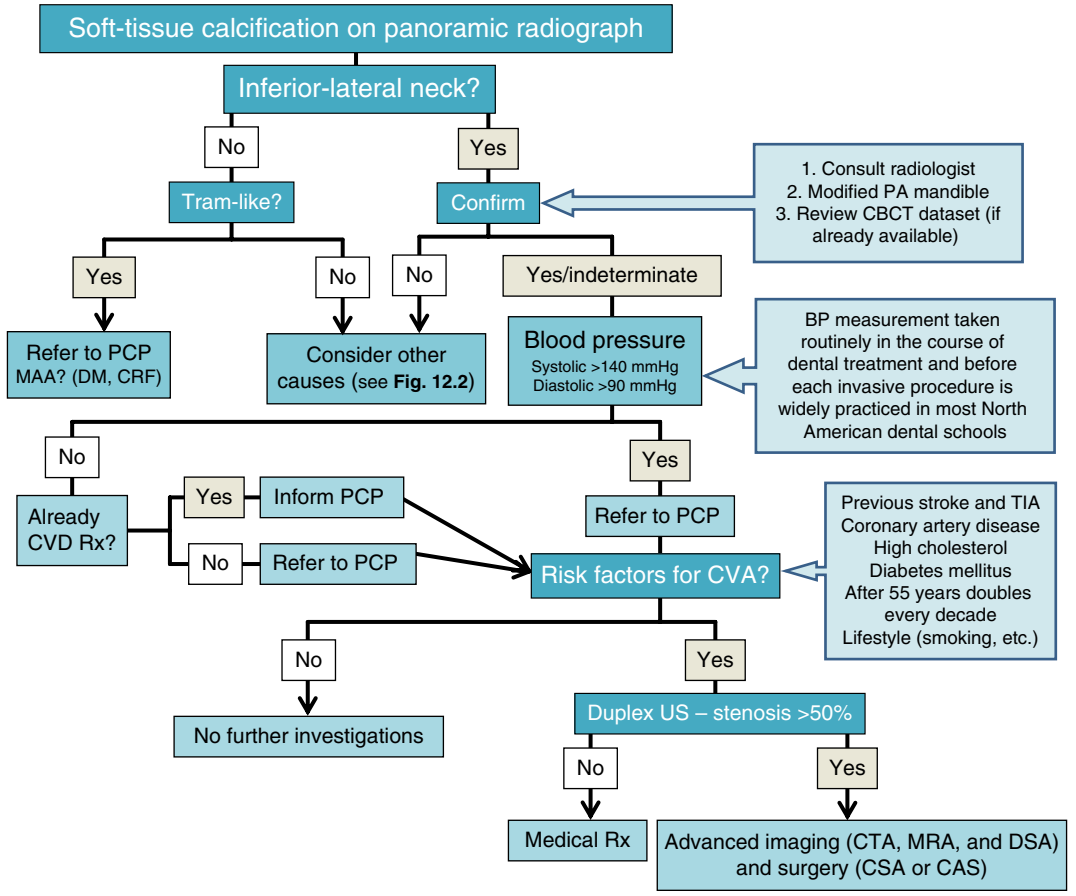


Figure 12.10 Flowchart providing a management algorithm for referral of patients with suspected calcified carotid artery atheroma (CCAA) on panoramic images. Initial decisions involve establishing the location of the calcification to the lateral neck. Secondary considerations involve establishing patient risk based on clinical history. BP, blood pressure; CAS, carotid artery stenting; CBCT, cone-beam computed tomography; CEA, carotid endarterectomy; CRF, chronic renal failure; CSA, carotid surgical stent; CTA, computed tomography angiography; CVA, cerebrovascular accident; CVD, cardiovascular disease; DM, diabetes mellitus; DSA, digital subtraction angiography; MAA, medial artery atherosclerosis; MRA, magnetic resonance imaging angiography; PA, posterio-anterior (extraoral image of the mandible); PCP, primary-care physician; Rx, treatment; TIA, transient ischemic attack; US, ultrasonography. Source: Adapted from MacDonald D., Chan A., Harris A., Vertinsky T., Farman A.G., Scarfe W.C. (2012). Diagnosis and management of calcified carotid artery atheroma: dental perspectives. *Oral Surg Oral Med Oral Pathol Oral Radiol*. 114: 533–47.

should never be prescribed solely for the detection of CCAA. Furthermore, not only do medical facilities have more appropriate imaging modalities (see later in the chapter), but the perceived absence of a CCAA on a panoramic radiograph may be a false negative. False negatives associated with the detection of CCAA on panoramic radiographs can occur since the CCAA may be inferior to the area covered by the panoramic radiograph, or, if within this area, may not be visible because the degree of calcification is inadequate for display [30].

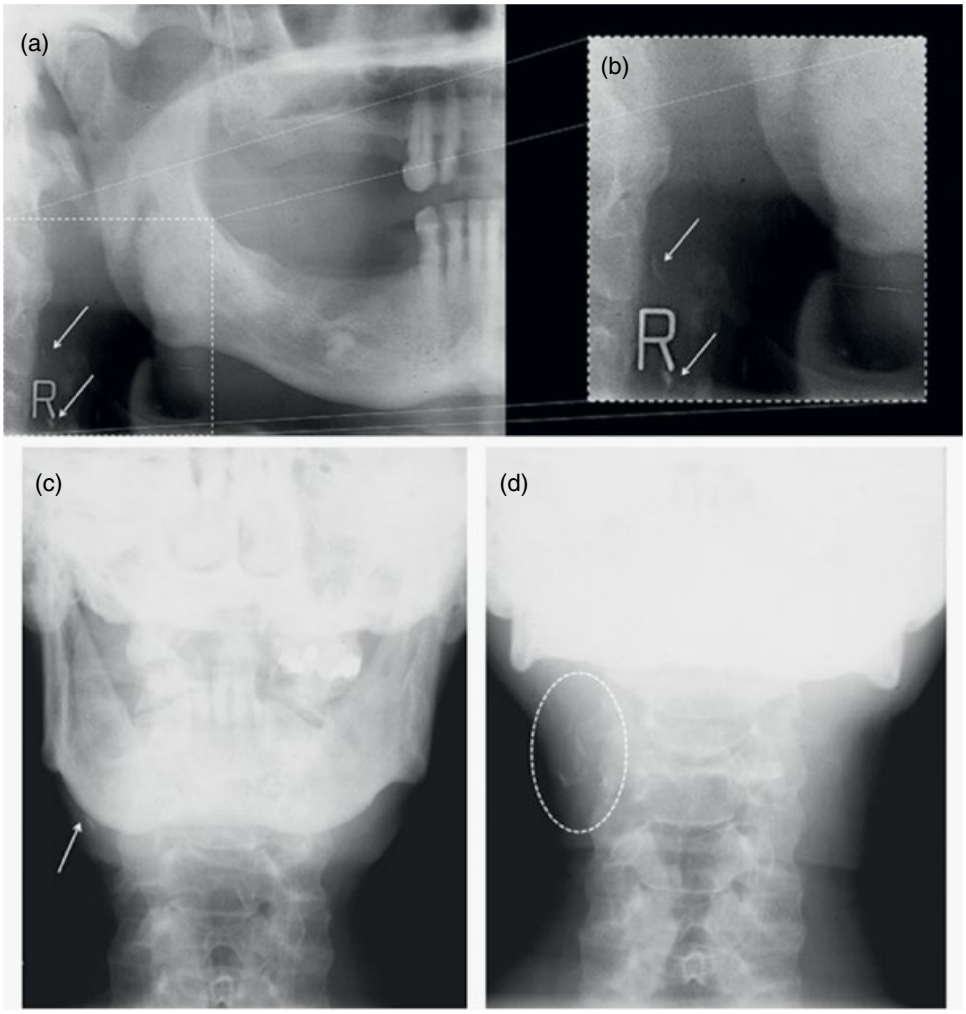


Figure 12.11 Cropped (a) and magnified (b) right panoramic images demonstrating multiple curvilinear dystrophic calcifications anterior to the third and fourth cervical vertebrae and posterior to the orthopharyngeal airway space, suggestive of calcified carotid artery atheroma (CCAA; arrows). (c) Conventional posterio-anterior (PA) and (d) modified PA (head tilted up with reduced kVP exposure) images clearly demonstrate the presence of multiple clustered curvilinear dystrophic calcifications in the right lateral neck, consistent with a working diagnosis of CCAA. R, right. Source: Reproduced with permission from MacDonald, D., Chan, A., Harris, A., Vertinsky, T., Farman, A.G., Scarfe, W.C. (2012). Diagnosis and management of calcified carotid artery atheroma: dental perspectives. *Oral Surg. Oral Med. Oral Pathol. Oral Radiol.* 114: 533–547.

12.3 The Significance of Arterial Calcifications

Atherosclerosis is a fatty deposition within the tunica intima of large and elastic arteries. These deposits, known as atheromatous plaques, can produce ischemic incidents – *transient ischemic attacks* (TIA), heart attacks, and CVAs – either by reducing local blood flow by stenosis or by giving rise to emboli, which may eventually occlude a cerebral end artery. These emboli account for the majority of strokes. Almost all emboli are noncalcified and are not visible on conventional radiography; only one case of a calcified embolus, which arose from a CCAA, appears to have been reported [31]. This is most likely because calcification usually occurs in the more mature and deeper parts of atheromatous plaque. The definitive treatment for a symptomatic patient (TIA, transient monocular blindness, or a nondisabling stroke) with grade high to moderate (50% as demonstrated by catheter angiography) or high (70% as demonstrated by noninvasive imaging) stenosis of the internal carotid artery is *carotid endarterectomy* (CEA) [32–34]. CEA carries an overall perioperative stroke or mortality risk of slightly less than 6% [32, 34, 35]. Although *carotid artery stenting* (CAS) is becoming an increasingly popular therapeutic alternative for patients at high risk for CEA [36], the results of the International Carotid Stenting Study (ICSS) observed that the number of fatal or disabling strokes and the cumulative five-year risk did not differ significantly between these two procedures [37]. Although more nondisabling strokes were found for CAS procedures, this was weighed favorably against the increased risk of procedural myocardial infarction, cranial nerve palsy, and access-site hematoma associated with CEA [37]. For asymptomatic patients with stenosis of less than 50%, the primary therapies include a combination of antihypertensive treatment (to maintain BP below 140/90 mmHg), tobacco cessation, statin antihyperlipidemia medication (to reduce low-density lipoprotein cholesterol to below 100 mg/dl), and aspirin antithrombolytic therapy [36]. Secondary therapies involve the management of contributing conditions such as diabetes mellitus and hyperhomocysteinemia [36].

The dystrophic calcification of the tunica intima resulting in CCAA can be distinguished radiographically from another calcified form of arteriosclerosis, *medial artery arteriosclerosis* (MAA) or Mönckeberg's medial calcific sclerosis. The mechanism of calcification in MAA is generalized rather than localized, as it affects the tunica media of medium and smaller muscular arteries rather than the tunica intima as found in CCAA. The radiological presentation of MAA is distinctive and readily identified on plain film. Calcifications are typically diffuse, multiple, and circumferential along the wall of the arterial vessel. MAA appears as either a "rail track" on planar images (Figure 12.13a) or a "pipe stem" in volumetric renderings (Figure 12.13b). MAA is generally observed in the limbs and rarely reported in the head and neck [38]. Unlike CCAA, MAA does not cause luminal narrowing. However, MAA may be an indicator of peripheral artery disease, including diabetes mellitus or chronic kidney disease. MacDonald et al. recently reported a case in which both CCAA and MAA (Figure 12.13) were observed, conditions with separate calcific mechanisms [39]. This particular patient had a complex and longstanding medical history arising from chronic renal failure, which later provoked tertiary parathyroidism (Figure 9.20).

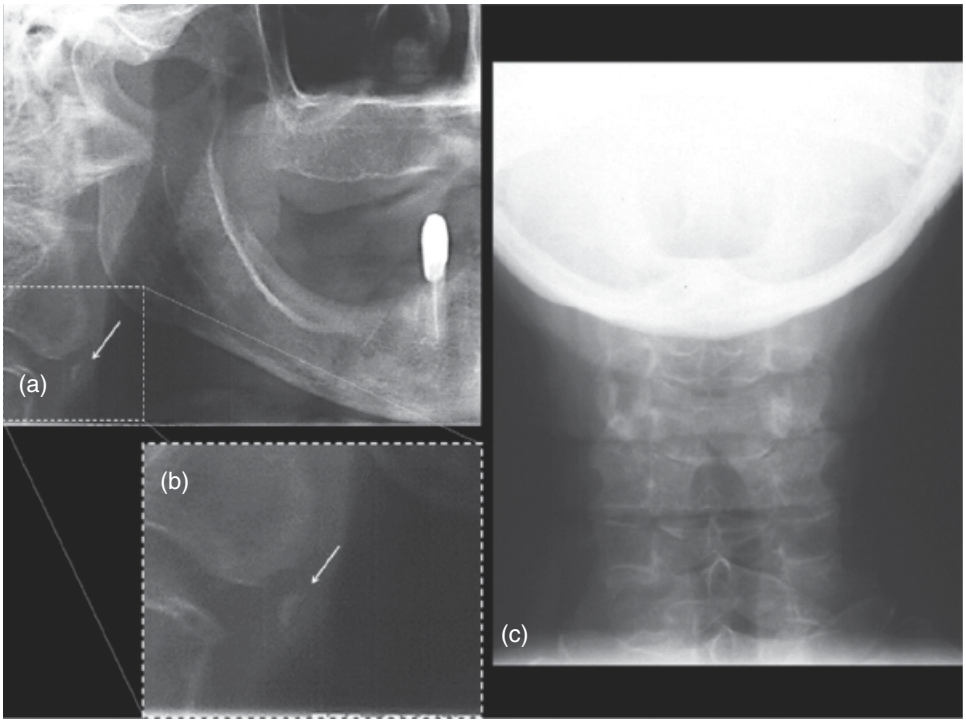


Figure 12.12 Representative images depicting a false-positive calcified carotid artery atheroma (CCAA). Suspicious dystrophic lateral neck calcification identified in the right inferior-lateral portion of a panoramic image (a), with imaging features consistent with a working diagnosis of CCAA (arrow). Cropped and magnified area of interest (b). Modified (chin-elevated) posterior–anterior image of the neck at a reduced exposure (c), clearly depicting the lateral soft tissues without presence of calcifications. These imaging features are ambiguous for the presence of CCAA and suggest a false-positive appearance on the panoramic image. Source: Reproduced with permission from MacDonald, D., Chan, A., Harris, A., Vertinsky, T., Farman, A.G., Scarfe, W.C. (2012). Diagnosis and management of calcified carotid artery atheroma: dental perspectives. *Oral Surg. Oral Med. Oral Pathol. Oral Radiol.* 114: 533–547.

Although current opinion is divided as to whether MAA is actually distinct from atherosclerosis [38], more recently the same authority stated that "the lesion we call Mönckeberg's medial sclerosis is not purely a medial lesion, and apparently is not the lesion described by Mönckeberg" [40]. Therefore, prudence would direct that cases of MAA should also be evaluated for atherosclerosis.

CBCT imaging is being increasingly applied to clinical dentistry. On this form of imaging, recognition of the salient features of CCAA, while depending on the plane viewed, is extremely useful in differentiating between this and other neck calcifications [41]. On axial sections, most CCAA presented as single or multiple "rice grains," or linear or curvilinear homogeneous opacifications (Figure 12.14). They are most commonly located in the soft tissue approximately 0–10 mm anteriolaterally to the anterior tubercle of the transverse process, lateral or more often laterio-posterior to the greater cornu of the hyoid bone. They are always posteriolateral to the pharyngeal airway space. In coronal sections, CCAA are lateral to the anterior tubercle of

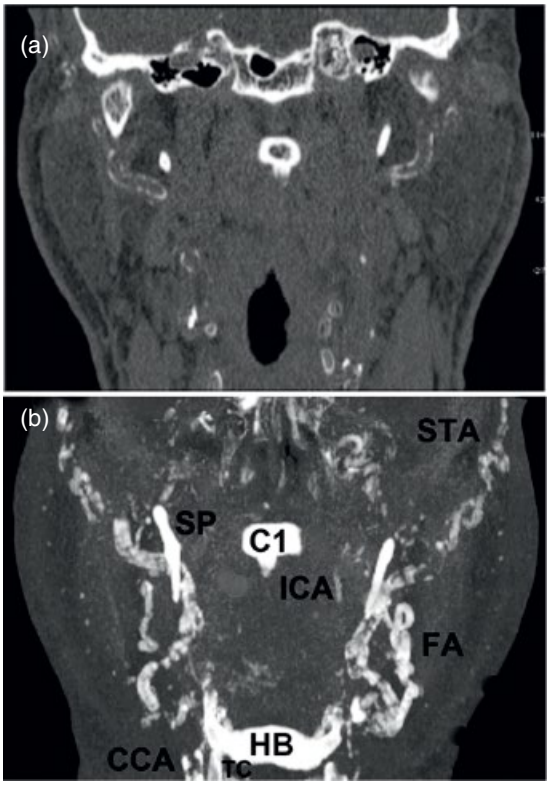


Figure 12.13 Coronal computed tomography images of a patient demonstrating two forms of atherosclerosis: medial artery arteriosclerosis (MAA) or Mönckeberg's medial calcific sclerosis; and calcified carotid artery atheroma (CCAA). (a) Medium-slice maximum-intensity projection. Note the "rail-track" opaque calcification associated with MAA outlining the external carotid artery and its branches, and the "plaque-like" calcification in the region of the bifurcation of the internal and external carotid arteries associated with CCAA. (b) Three-dimensional reconstruction displaying the MAA, as "pipe-stem," in the facial artery (FA) and the superficial temporal artery (STA), branches of the external carotid. Plaque-like radiopacities are observed in the common carotid artery (CCA) below the hyoid bone (HB) and in the left internal carotid artery (ICA). C1, anterior arch of the first cervical vertebra; SP, styloid process; TC, calcified lamina of the superior cornu of the thyroid cartilage. Source: Reproduced with permission from MacDonald, D., Chan, A., Harris, A., Vertinsky, T., Farman, A.G., Scarfe, W.C. (2012). Diagnosis and management of calcified carotid artery atheroma: dental perspectives. *Oral Surg. Oral Med. Oral Pathol. Oral Radiol.* 114: 533–547.

the cervical vertebrae (Figure 12.15). On sagittal sections, CCAA are medial and inferior to the angle of the mandible, and lateral and mostly anterior to the cervical tubercle, with a vertical position varying from C3 to C5 (Figure 12.16) [17].

When the presence of CCAA is suspected, the patient should be informed of the dental imaging findings, particularly in relation to the course of the ICA and the role of CCAA in the etiology of stroke. The patient should then be informed that while the identification of CCAA on panoramic radiography provides reasonable accuracy (up to 80%) in the detection of stenosis, the false-positive rate is 20% [42].

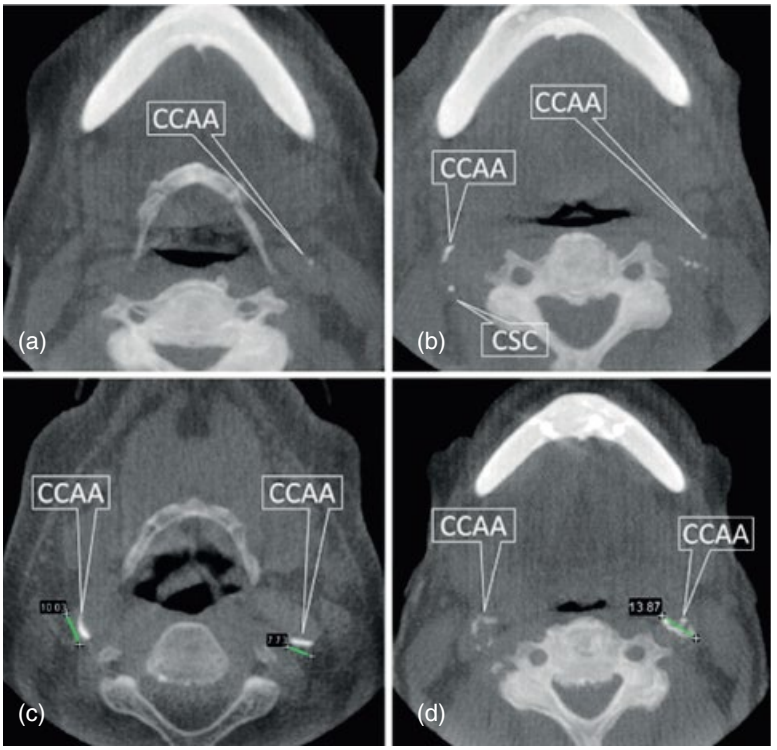


Figure 12.14 Axial reconstructions of cone-beam computed tomographic datasets demonstrating calcified carotid artery atheroma (CCAA) as a single rice grain (a), multiple "rice grains" (b right), linear (b left; c right), and curvilinear (c left; d left) homogeneous opacifications. As the size of the CCAA increases, the number of ipsilateral opacifications also tends to increase (d left), forming larger coalescing masses (d right). The proximity to the calcified stylohyoid chain (CSC) is clearly evident. Source: Reproduced with permission from MacDonald, D., Chan, A., Harris, A., Vertinsky, T., Farman, A.G., Scarfe, W.C. (2012). Diagnosis and management of calcified carotid artery atheroma: dental perspectives. *Oral Surg. Oral Med. Oral Pathol. Oral Radiol.* 114: 533–547.

Next, referral to an appropriate medical physician should be considered, with particular attention to the patient's age, presenting medical history, and current condition. Of patients who present with CCAA on panoramic imaging, 80–86% demonstrate low-grade (0–29%) stenosis which is not hemodynamically significant [42, 43]. So it is probable that if all patients who demonstrate CCAA are referred for medical assessment, diagnostic medical imaging tests (see later in the chapter) will be performed, many of which would be unnecessary. Therefore, dental practitioners should be prudent in referring patients with suspected CCAA.

This in no way suggests that the dentist's vigilance is unimportant, but instead cautions that the mere presence of a calcification does not categorically mean that it is a CCAA. Nevertheless, a referral of a CCAA to medical services is not without cost, particularly in countries where radiological services are already overloaded [18]. It simply requires dentists to be more discriminating in their referrals, which should only be made after the dentist has distinguished true positives from false positives.

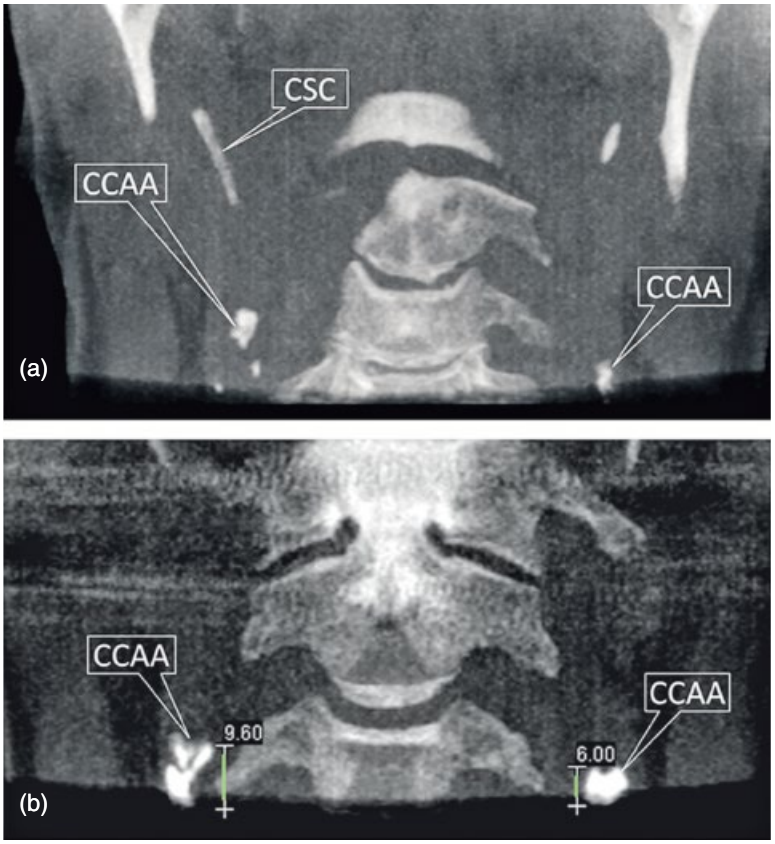


Figure 12.15 Coronal maximum-intensity reconstructions demonstrating calcified carotid artery atheroma (CCAA) lateral to the cervical vertebrae and presenting as linear globular (a) or globular calcifications (b). Relationship to the calcified stylohyoid chain (CSC) is evident. Source: Reproduced with permission from MacDonald, D., Chan, A., Harris, A., Vertinsky, T., Farman, A.G., Scarfe, W.C. (2012). Diagnosis and management of calcified carotid artery atheroma: dental perspectives. *Oral Surg. Oral Med. Oral Pathol. Oral Radiol.* 114: 533–547.

Initially, the location of the calcification should be confirmed to be in the lateral neck (e.g. modified PA or by correlation to available CBCT imaging). Patients who report no medical history should be referred immediately for a cardiovascular consultation. A written consultation referral together with copies of the dental images should be sent to the patient's primary-care physician. However, referral of patients who report a history of current therapy for cardiovascular disease should be carefully considered. In this circumstance, it would be more appropriate to contact the physician directly to discuss the significance of the radiological findings. Nevertheless, patients with current cardiovascular disease who present with sustained in-office hypertension (>140 mmHg systolic, >90 mmHg diastolic) should be referred immediately [17].

Figure 12.10 provides an algorithm for the management of suspected arterial calcifications identified on maxillofacial imaging, taking into consideration a patient's BP status. It clearly defines the role of the dental practitioner.

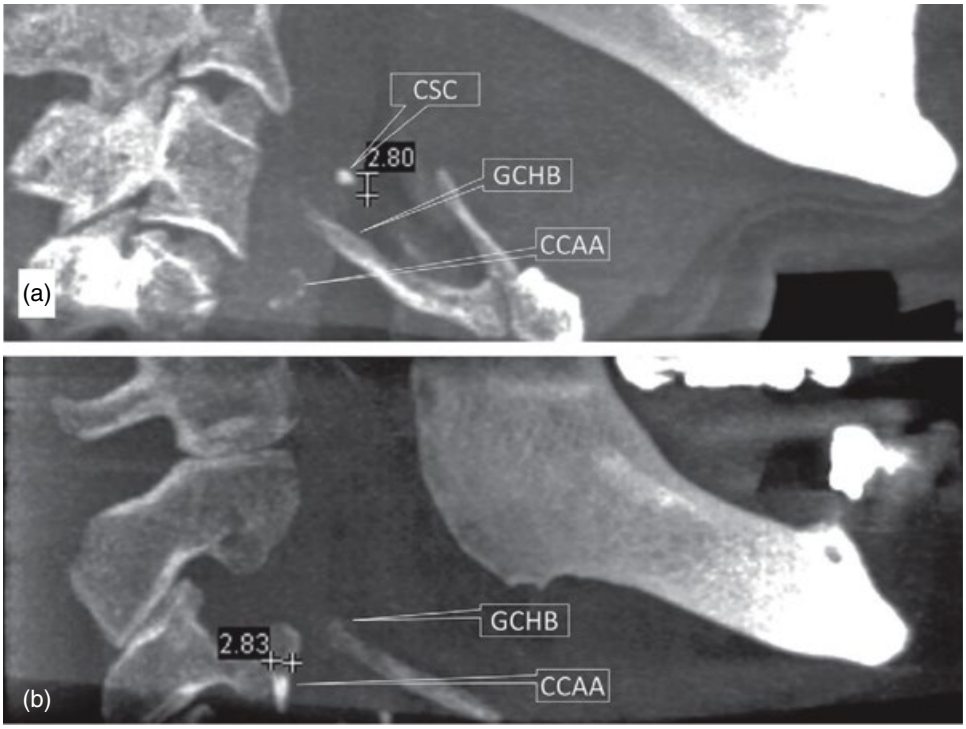


Figure 12.16 Sagittal maximum-intensity reconstructions demonstrating the location of calcified carotid artery atheroma (CCAA) of two different cases (a and b) in relation to the hyoid bone at the level of the greater cornu of the hyoid bone (GCHB). An isolated calcified stylohyoid chain (CSC) is shown. Source: Reproduced with permission from MacDonald, D., Chan, A., Harris, A., Vertinsky, T., Farman, A.G., Scarfe, W.C. (2012). Diagnosis and management of calcified carotid artery atheroma: dental perspectives. *Oral Surg. Oral Med. Oral Pathol. Oral Radiol.* 114:533–547.

12.4 Medical Imaging of CCAA

12.4.1 PRINCIPLES OF MEDICAL IMAGING

Knowledge of the medical imaging of CCAA is essential in understanding the medical diagnostic phase [44, 45]. The purpose of carotid bifurcation imaging in medicine is to detect stroke-prone carotid bifurcation plaque and identify a high-risk patient likely to benefit from therapy to reduce stroke risk. Stroke risk for patients with suspected carotid bifurcation disease is dependent on many factors, most importantly a history of neurological symptoms, the degree of stenosis, and, to a lesser extent, plaque characteristics such as ulcerations, intraplaque hemorrhage, and lipid content. For neurologically symptomatic individuals, evaluation of the carotid bifurcation is recommended for every patient [44]. Evaluation and treatment of patients who are neurologically asymptomatic are much more controversial. Therefore, management of a patient with suspected CCAA who is referred to a physician from a dental practitioner based on either panoramic and/or modified PA or CBCT imaging is not straightforward. In this population, further imaging investigation is recommended only for

1. patients with symptoms of carotid artery ischemia; and
2. patients who present with high-risk factors (e.g. high BP, known coronary artery disease, diabetes, smoking, or hypercholesterolemia), especially in the presence of a carotid bruit [44, 45].

12.4.2 IMAGING STRATEGIES

The imaging modalities most often used to evaluate patients for cervical carotid artery stenosis are *carotid duplex ultrasound imaging* (CDUS), *computed tomography angiography* (CTA), MRI, *magnetic resonance angiography* (MRA), and *digital subtraction angiography* (DSA).

Ultrasonography (US) is generally the first modality used to investigate a patient who presents with symptoms, or an asymptomatic patient with a carotid bruit or suspected CCAA. US produces two types of images, both providing different information. Grayscale US is used to determine the composition and structure of atheromatous plaque (echogenicity) using grayscale median values, which predict the stroke risk of a particular plaque [46]. Grayscale imaging of the CCA, its bifurcation, and both the ICA and ECA are usually performed in longitudinal and transverse planes. Imaging of the ICA and CCA is performed with caudad angulation of the transducer in the supraclavicular area and cephalad angulation at the level of the mandible. A plaque with a substantial fatty or fatty-fibrous component has a greater risk of embolizing, particularly more so when ulceration of its luminal surface or undermining of its periphery is observed. Calcification can be observed on US by a hyperechogenic interface and a "back shadow" or "posterior shadow" (Figure 12.17). This shadow is distant to the transducer and represents maximal reflection of the US at the soft tissue/calcified tissue interface back to the transducer.

Doppler US (Figure 12.18) is used to determine the velocity of the blood flow of the CCA and ICA (Figure 12.19). Determining the degree of carotid artery stenosis using this technique is indirect, based on an analysis of the *peak systolic velocity* (PSV) or the *end-diastolic velocity* (EDV), or both, of the ICA artery. The severity of stenosis is based on PSV flow velocity in the ICA as follows [46]: normal to less than 50% stenosis (<125 cm/s); 50–70% stenosis (125–230 cm/s); and ≥70% stenosis (>230 cm/s). The ratio of blood flow velocities in the ICA to those in the CCA (V_{ICA}/V_{CCA}) in normal individuals is about 1. It is constant for women throughout life, but is 0.8 for men at 20 years and rises gradually to 1.0 at 60 years [47]. The categorization of stenosis using the V_{ICA}/V_{CCA} ratio mirrors the PSV values [46]: normal to less than 50% stenosis (<2.0); 50–70% stenosis (2.0–4.0); and ≥70% stenosis (>4; Figure 12.19).

Both grayscale and Doppler images are displayed on the same monitor; hence this mode of US imaging for CCAA is called CDUS. Although US is noninvasive, a universal carotid artery screening program for all (especially for those in middle age and older) using duplex Doppler US would be ideal; because of limited resources, however, it is restricted to the two classes of patients mentioned at the end of the previous section, namely those with symptoms of carotid artery ischemia and those with high-risk factors. The reliability of US results is highly dependent on clinical technical skill [48]. In addition, there are limitations in visualization of the proximal carotid artery and intracranial portions. Furthermore, the results of US may be unreliable in the presence of heavily calcified atherosclerotic plaque. Once a hemodynamically significant stenosis is confirmed by CDUS, the patient is usually referred for additional radiological

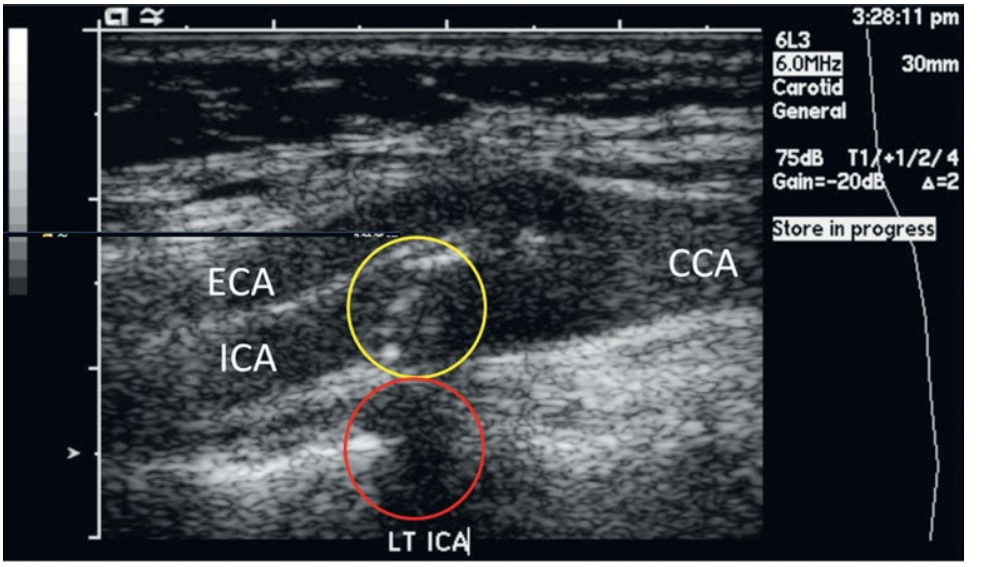


Figure 12.17 Grayscale ultrasound image of patient with suspected left cervical carotid artery stenosis. The vasculature is shown as linear hypoechogenic (dark) outlines oriented horizontally rather than vertically, and includes the common carotid artery (CCA), and the internal carotid artery (ICA) and external carotid artery (ECA). The image shows a hyperechogenic focus (bright, within a yellow circle) in the ICA slightly above the carotid bifurcation, representing an atheromatous plaque with posterior shadowing (within a red circle), consistent with calcified atherosclerotic plaque. LT, left. Source: Reproduced with permission from MacDonald, D., Chan, A., Harris, A., Vertinsky, T., Farman, A.G., Scarfe, W.C. (2012). Diagnosis and management of calcified carotid artery atheroma: dental perspectives. *Oral Surg. Oral Med. Oral Pathol. Oral Radiol.* 114: 533–547.

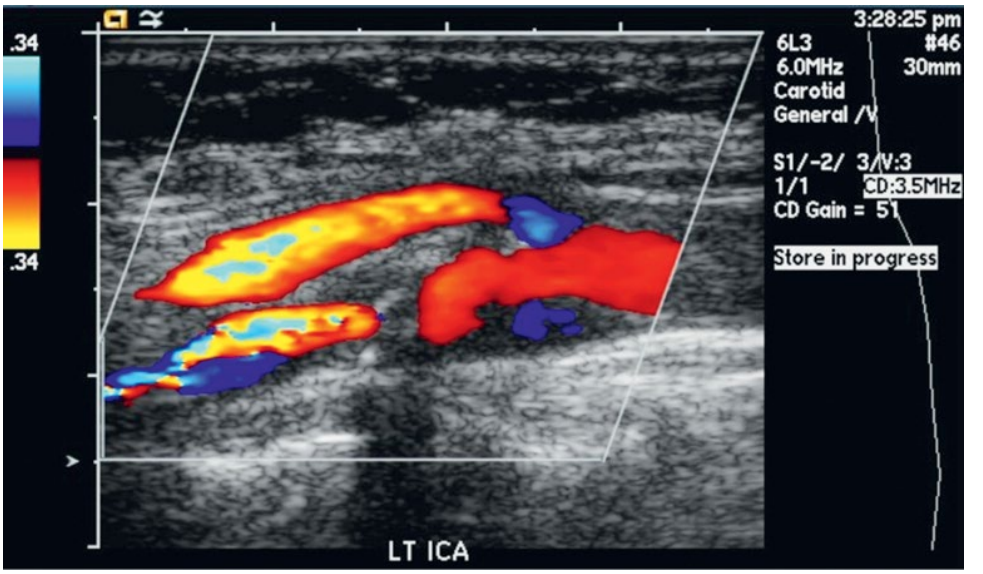


Figure 12.18 Color Doppler ultrasound of the same patient and vessel (left internal carotid artery or LT ICA) as in Figure 12.17. The image demonstrates the lack of color in the region of the calcified atheromatous plaque, with turbulent flow and color aliasing distal (to the left) of the stenosis. Source: Reproduced with permission from MacDonald, D., Chan, A., Harris, A., Vertinsky, T., Farman, A.G., Scarfe, W.C. (2012). Diagnosis and management of calcified carotid artery atheroma: dental perspectives. *Oral Surg. Oral Med. Oral Pathol. Oral Radiol.* 114: 533–547.

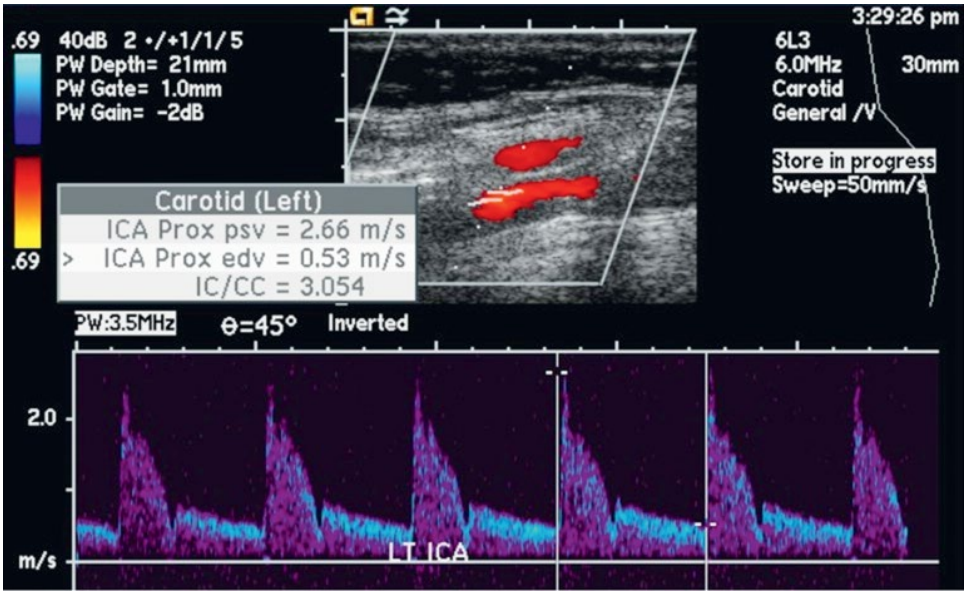


Figure 12.19 Spectral sampling display of the same patient and vessel (left internal carotid artery or LT ICA) as in Figure 12.17. Analysis reveals an elevated peak systolic velocity (PSV) of 266 cm/s and a V_{ICA}/V_{CCA} PSV value ratio of 3.054, confirming the presence of a significant stenosis. EDV, end-diastolic velocity. CC, common carotid artery; IC, internal carotid artery. Source: Reproduced with permission from MacDonald, D., Chan, A., Harris, A., Vertinsky, T., Farman, A.G., Scarfe, W.C. (2012). Diagnosis and management of calcified carotid artery atheroma: dental perspectives. *Oral Surg. Oral Med. Oral Pathol. Oral Radiol.* 114: 533–547.

investigations supervised by a neuroradiologist, head and neck radiologist, vascular surgeon, or cardiologist, and reported by a radiologist.

CTA is performed by multiplanar reconstruction from *multidetector computed tomography* (MDCT) after intravenous administration of radiographic contrast material (Figure 12.20) [44]. CTA provides anatomical imaging from the aortic arch through the circle of Willis. Unlike CDUS, CTA provides direct imaging of the arterial lumen suitable for direct evaluation of stenosis. CTA is generally considered the gold standard imaging modality prior to surgical intervention, except when calcification is present, when MRA could be a better modality (see next paragraph). Although not yet a standard, a further technical development in conjunction with MDCT is *dual-source computed tomography* (DSCT), which employs two sources using peak kilovolts (kVps) 120 and 80 simultaneously [48]. This gives superior display of the noncalcified structure of the carotid artery.

MRA is noninvasive and the radiofrequency signal characteristics of flowing blood are sufficiently distinct from surrounding soft tissue to allow imaging of the arterial lumen [49]. The two techniques of MRA used in carotid artery imaging included contrast-enhanced MRA and time-of-flight MRA. Contrast-enhanced MRA, which requires the intravenous injection of a gadolinium-based contrast agent, accurately displays stenosis and allows characterization of the plaque morphology. The last includes the structure of the atherosclerotic plaque (Figure 12.21). Time-of-flight MRA

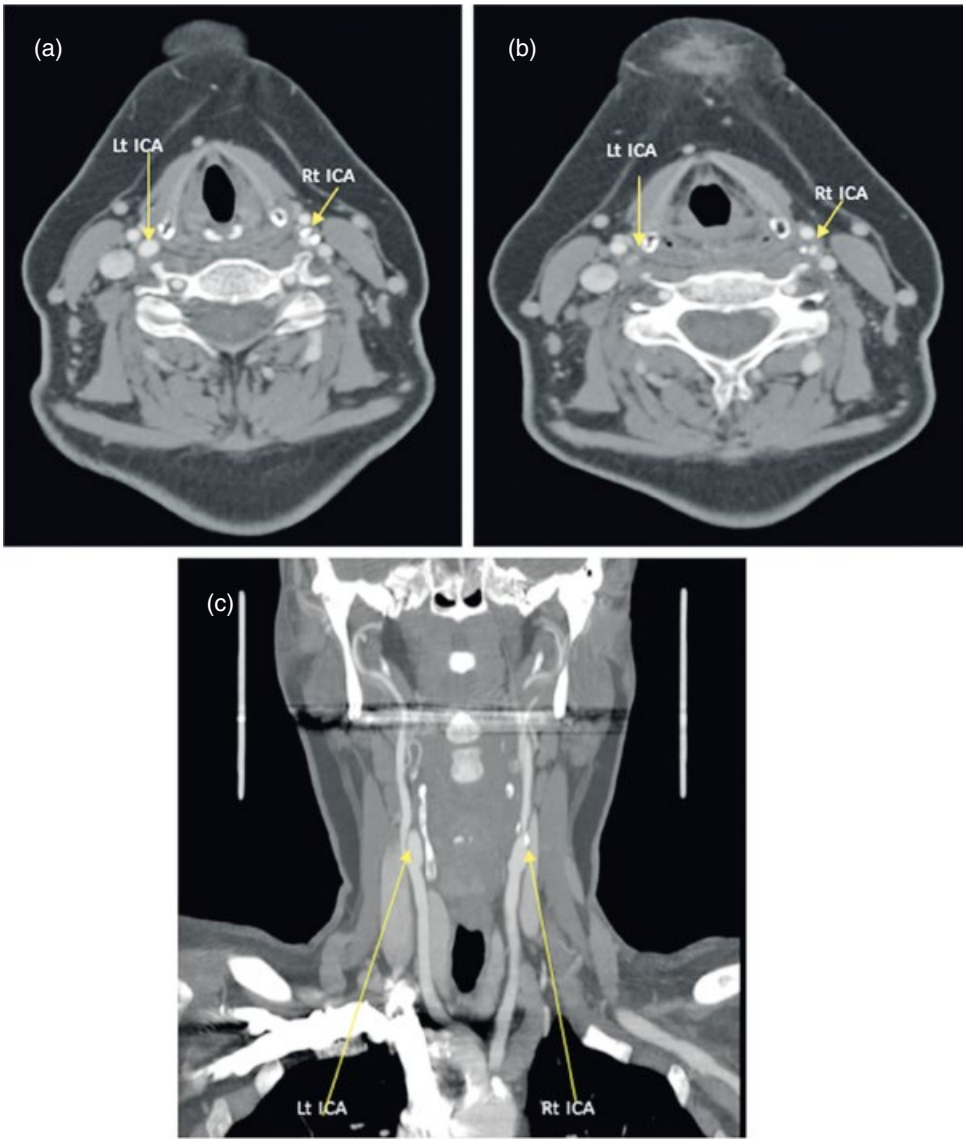


Figure 12.20 Axial (a and b) and coronal (c) computed tomographic angiographic images demonstrating a "high-grade stenosis" (>70%) of the left internal carotid artery (Lt ICA) and almost complete stenosis of the right ICA (Rt ICA). Source: Reproduced with permission from MacDonald, D., Chan, A., Harris, A., Vertinsky, T., Farman, A.G., Scarfe, W.C. (2012). Diagnosis and management of calcified carotid artery atheroma: dental perspectives. *Oral Surg. Oral Med. Oral Pathol. Oral Radiol.* 114: 533–547.

spares the patient a gadolinium injection, but tends to overestimate the degree of carotid stenosis [49]. The recent introduction of three Tesla units has enhanced MRA; however, these examinations are expensive and availability is limited.

Catheter-based DSA (Figure 12.22) is still considered to be the gold standard for the evaluation of carotid artery stenosis [44, 50]. DSA provides high-quality imaging that is accurate, rendering images from which lesions from the aortic arch to the

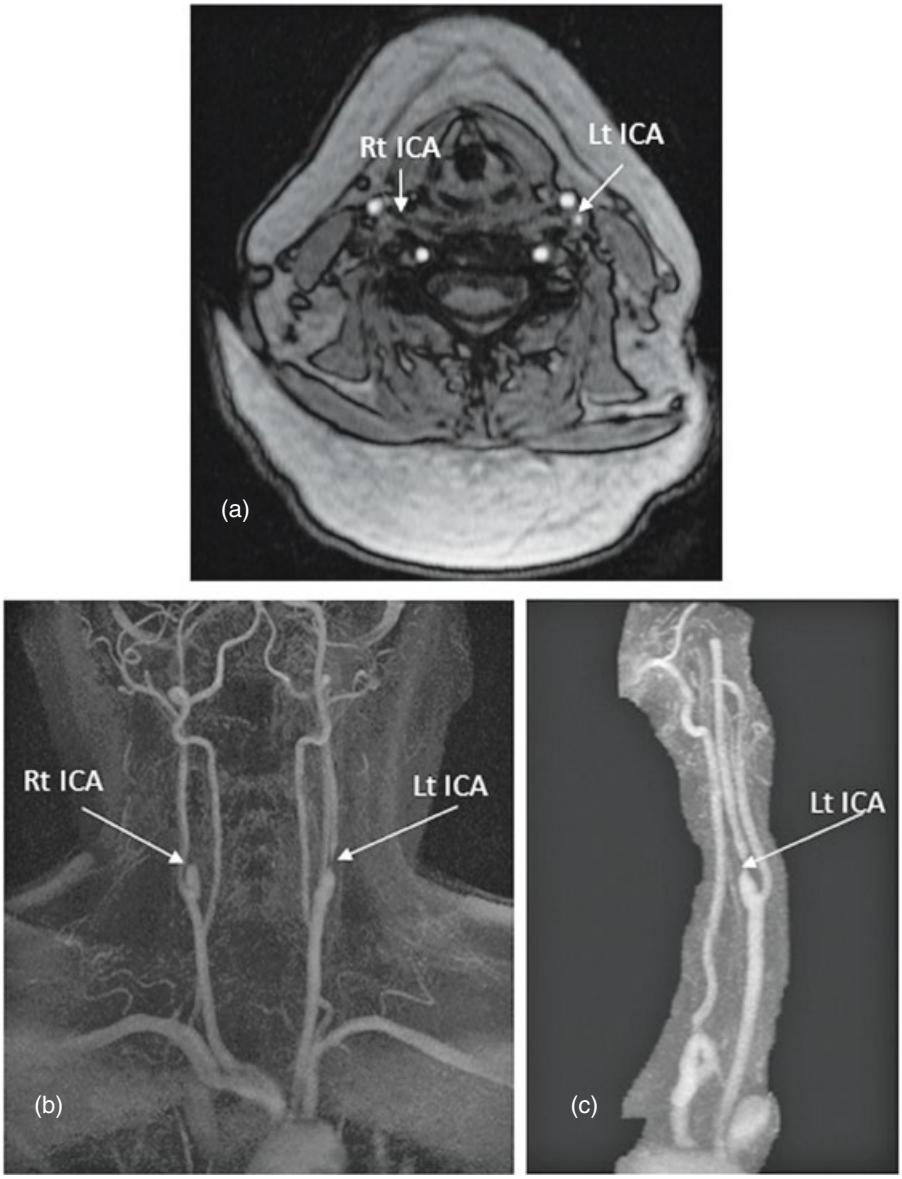


Figure 12.21 Coronal (a) and three-dimensional reconstruction (b) magnetic resonance angiography (MRA) images demonstrating "high-grade" stenosis (>70%) in the left internal carotid artery (Lt ICA) and complete occlusion of the right ICA (Rt ICA), with no flow seen distally. (b) Three-dimensional reconstruction of MRA. (c) "High-grade stenosis" of the left ICA. Source: Reproduced with permission from MacDonald, D., Chan, A., Harris, A., Vertinsky, T., Farman, A.G., Scarfe, W.C. (2012). Diagnosis and management of calcified carotid artery atheroma: dental perspectives. *Oral Surg. Oral Med. Oral Pathol. Oral Radiol.* 114: 533–547.

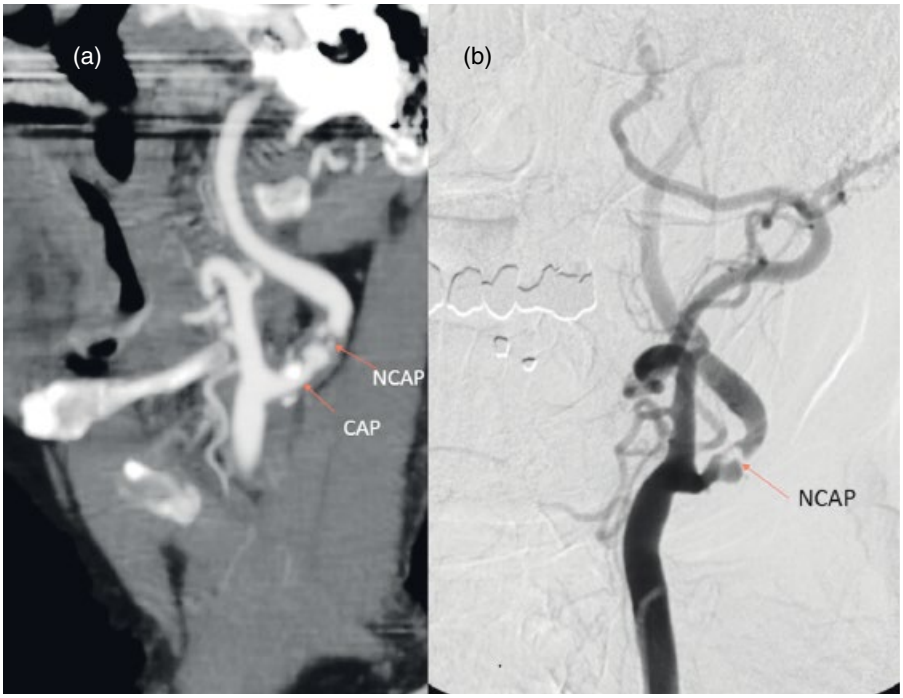


Figure 12.22 (a) Sagittal computed tomographic angiographic image reconstruction displaying a mixed calcified atherosclerotic plaque (CAP) and noncalcified atherosclerotic plaque (NCAP) and ICA stenosis on the same level as the hyoid bone. (b) Lateral digital subtraction angiogram of the same patient. Source: Reproduced with permission from MacDonald, D., Chan, A., Harris, A., Vertinsky, T., Farman, A.G., Scarfe, W.C. (2012). Diagnosis and management of calcified carotid artery atheroma: dental perspectives. *Oral Surg. Oral Med. Oral Pathol. Oral Radiol.* 114: 533–547.

intracranial vessels can be easily interpreted. Because of cost and associated risks, specifically stroke, the procedure is generally reserved for patients with equivocal CDUS or CTA before CEA or CAS.

Determination of the *lipid-rich necrotic cores* (LRNC) may further improve patient outcomes [51].

12.5 Concluding Remarks

The calcification of CCAA represents the maturation of localized atherosclerotic plaque in a region that has been associated with a high risk of cerebral emboli. The presence of calcification at this location does not, however, infer the presence of a hemodynamically significant stenosis (>50%) related to a risk of stroke. High BP is an important contributing factor for ischemic (and also hemorrhagic) strokes. Therefore, patients with an elevated BP, particularly in the presence of CCAA, should be referred for immediate medical consultation by written referral. Not all patients who are referred to medical practitioners with suspected CCAA identified will undergo imaging. Medical imaging protocols have been established depending on the assessment of risk factors and patient symptoms. The most common imaging modality used to evaluate patients for cervical carotid artery stenosis is CDUS imaging.

This is being used with increasing frequency as a screening tool for individuals in middle age or beyond. Advanced imaging (CTA, MRA, DSA) is reserved for situations where initial findings are equivocal or when surgery (CEA/CAS) is anticipated.

The following guidance can be concluded:

1. The dental practitioner is responsible for identification of calcifications that occur incidentally on images that are used for dental diagnosis. The practitioner should make every effort to differentiate the presence of CCAA from these incidental calcifications (e.g. imaging consultation, modified PA).
2. The significance of CCAA observed incidentally on dental images depends on patient history (e.g. previous stroke, current cardiovascular therapy, smoking status) and current BP status.
3. Medical consultations should be requested for all patients who present with CCAA on dental images. These may be informal (e.g. by telephone) for patients with controlled BP and who are on current cardiovascular therapy, or formal (e.g. written referral) for patients with sustained elevated BP and no cardiovascular history. In addition to the risk of a stroke, CCAA may also indicate other important medical conditions, such as metabolic syndrome (insulin-resistance syndrome), a potentially lethal disease [46].

References

1. Jayade, B., Adirajaiah, S., Vadera, H. et al. (2013). Myositis ossificans in medial, lateral pterygoid, and contralateral temporalis muscles: a rare case report. *Oral Surg. Oral Med. Oral Pathol. Oral Radiol.* 116: e261–e266.
2. Orhan, K., Uyanik, L.O., Erkmen, E., and Kilinc, Y. (2012). Unusually severe limitation of the jaw attributable to fibrodysplasia ossificans progressiva: a case report with cone-beam computed tomography findings. *Oral Surg. Oral Med. Oral Pathol. Oral Radiol.* 113: 404–409.
3. Thangavelu, A., Vaidhyanathan, A., and Narendar, R. (2011). Myositis ossificans traumatica of the medial pterygoid. *Int. J. Oral Maxillofac. Surg.* 40: 545–549.
4. Schiff, M.J. and Meara, D.J. (2013). Myositis ossificans of the temporalis muscle: case report and review of the literature. *J. Oral Maxillofac. Surg.* 71: 1893–1898.
5. Bamgbose, B.O., Ruprecht, A., Hellstein, J. et al. (2014). The prevalence of tonsilloliths and other soft tissue calcifications in patients attending oral and maxillofacial radiology clinic of the University of Iowa. *ISRN Dent.* 2014: 839635. https://doi.org/10.1155/2014/839635.
6. Takahashi, A., Sugawara, C., Kudoh, T. et al. (2017). Prevalence and imaging characteristics of palatine tonsilloliths evaluated on 2244 pairs of panoramic radiographs and CT images. *Clin. Oral Investig.* 21: 85–91. https://doi.org/10.1007/s00784-016-1752-0.
7. Ghabanchi, J., Haghnegahdar, A., Khojastehpour, L., and Ebrahimi, A. (2015). Frequency of tonsilloliths in panoramic views of a selected population in southern Iran. *J. Dent. (Shiraz)* 16: 75–80.
8. MacDonald-Jankowski, D.S. (2001). Calcification of the stylohyoid complex in Londoners and Hong Kong Chinese. *Dentomaxillofac. Radiol.* 30: 35–39.
9. Okabe, S., Morimoto, Y., Ansai, T. et al. (2006). Clinical significance and variation of the advanced calcified stylohyoid complex detected by panoramic radiographs among 80-year-old subjects. *Dentomaxillofac. Radiol.* 35: 191–199.
10. Rizzatti-Barbosa, C.M., Ribeiro, M.C., Silva-Concilio, L.R. et al. (2005). Is an elongated stylohyoid process prevalent in the elderly? A radiographic study in a Brazilian population. *Gerodontology* 22: 112–115.

11. Sperber, G.H. (2001). *Craniofacial Development*, 55–59. Hamilton, Canada: BC Decker.
12. MacDonald-Jankowski, D.S. (1990). The synchondrosis between the greater horn and the body of the hyoid bone: a radiological assessment. *Dentomaxillofac. Radiol.* 19: 171–172.
13. Hernández, J.L. and Velasco, J. (2008). Neurological picture. Elongated styloid process (Eagle's syndrome) as a cause of atypical craniocervical pain. *J. Neurol. Neurosurg. Psychiatry* 79: 43.
14. Wenaas, A.E., Tran, B., and Ongkasuwan, J. (2016). The progression of thyroid cartilage calcification as it relates to the utilization of laryngeal ultrasound. *Laryngoscope* 126: 913–917.
15. Ahmad, M., Madden, R., and Perez, L. (2005). Triticeous cartilage: prevalence on panoramic radiographs and diagnostic criteria. *Oral Surg. Oral Med. Oral Pathol. Oral Radiol. Endod.* 99: 225–230.
16. Friedlander, A.H. and Lande, A. (1981). Panoramic radiographic identification of carotid arterial plaques. *Oral Surg. Oral Med. Oral Pathol.* 52: 102–104.
17. MacDonald, D., Chan, A., Harris, A., Vertinsky, T., Farman, A.G., Scarfe, W.C. (2012). Diagnosis and management of calcified carotid artery atheroma: dental perspectives. *Oral Surg. Oral Med. Oral Pathol. Oral Radiol.* 114: 533–547.
18. MacDonald, D., Chan, A., Harris, A., Vertinsky, T., Farman, A.G., Scarfe, W.C. (2013). In reply. *Oral Surg. Oral Med. Oral Pathol. Oral Radiol.* 115: 700–701.
19. MacDonald, D. (2013). How should dentists recognise calcified carotid artery atheromas? *Gerodontology* 30: 169–170.
20. MacDonald, D.S., Zhang, L., and Gu, Y. (2012). Calcification of the external carotid arteries and their branches. *Dentomaxillofac. Radiol.* 41: 615–618.
21. Hollander, M., Bots, M.L., Del Sol, A.I. et al. (2002). Carotid plaques increase the risk of stroke and subtypes of cerebral infarction in asymptomatic elderly: the Rotterdam study. *Circulation* 105: 2872–2877.
22. Mupparapu, M. and Kim, I.H. (2007). Calcified carotid artery atheroma and stroke: a systematic review. *J. Am. Dent. Assoc.* 138: 483–492.
23. National Stroke Association. Understand stroke: what is stroke? 2016. http://www.stroke.org/site/PageServer?pagename = type Accessed November 27, 2016.
24. Roger, V.L., Go, A.S., Lloyd-Jones, D.M. et al. (2012). Heart disease and stroke statistics – 2012 update: a report from the American Heart Association. *Circulation* 125: e2–e220.
25. Sung, E.C., Friedlander, A.H., and Kobashigawa, J.A. (2004). The prevalence of calcified carotid atheromas on the panoramic radiographs of patients with dilated cardiomyopathy. *Oral Surg. Oral Med. Oral Pathol. Oral Radiol. Endod.* 97: 404–407.
26. Herman, W.W., Konzelman, J.L. Jr., Prisant, L.M., and Joint National Committee on Prevention, Detection, Evaluation, and Treatment of High Blood Pressure (2004). New national guidelines on hypertension: a summary for dentistry. *J. Am. Dent. Assoc.* 135: 576–584.
27. International Atomic Energy Agency (IAEA). ICRP issues statement lowering threshold for eyelens Vienna, Austria. https://rpop.iaea.org/RPOP/RPoP/Content/News/ICRP-statement-threshold-eye-lens.htm (Accessed December 28, 2016.)
28. Kratz, R.J., Walton, J.N., MacEntee, M.I., and Nguyen, C.T. (2017). Panoramic radiographs made before complete removable dental prostheses fabrication: a retrospective study of clinical significance. *J. Pros. Dent.* 118: 26–30.
29. US Food and Drug Administration. Dental radiographic examinations: recommendations for patient selection and limiting radiation exposure. 2012. http://www.fda.gov/downloads/Radiation-EmittingProducts/RadiationEmittingProductsandProcedures/MedicalImaging/MedicalX-Rays/UCM329746.pdf (Accessed December 1, 2016)
30. Friedlander, A.H. (2009). Odd practice. *Br. Dent. J.* 207: 464–465.
31. Tardy, J., Da Silva, N., Glock, Y., and Larrue, V. (2008). Neurological pictures. Stroke with calcium emboli related to a calcified stenosis of internal carotid artery. *J. Neurol. Neurosurg. Psychiatry* 79: 1273–1274.
32. Barnett, H.J., Taylor, D.W., Eliasziw, M. et al. (1999). The North American symptomatic

carotid endarterectomy trial: surgical results in 1415 patients. *Stroke* 30: 1751–1758.
33. Markus, H.S., King, A., Shipley, M. et al. (2010). Asymptomatic embolisation for prediction of stroke in the Asymptomatic Carotid Emboli Study (ACES): a prospective observational study. *Lancet Neurol.* 9: 663–671.
34. Wennberg, D.E., Lucas, F.L., Birkmeyer, J.D. et al. (1998). Variation in carotid endarterectomy mortality in the Medicare population: trial hospitals, volume, and patient characteristics. *JAMA* 279: 1278–1281.
35. Goodney, P.P., Lucas, F.L., Travis, L.L. et al. (2008). Changes in the use of carotid revascularization among the Medicare population. *Arch. Surg.* 143: 170–173. (Correction in Arch. Surg. 2009; 144: 769.).
36. Brott, T.G., Halperin, J.L., Abbara, S. et al. (2011). 2011 ASA/ACCF/AHA/AANN/AANS/ACR/ASNR/CNS/SAIP/SCAI/SIR/SNIS/SVM/SVS Guideline on the Management of Patients with Extracranial Carotid and Vertebral Artery Disease. A Report of the American College of Cardiology Foundation/American Heart Association Task Force on Practice Guidelines, and the American Stroke Association, American Association of Neuroscience Nurses, American Association of Neurological Surgeons, American College of Radiology, American Society of Neuroradiology, Congress of Neurological Surgeons, Society of Atherosclerosis Imaging and Prevention, Society for Cardiovascular Angiography and Interventions, Society of Interventional Radiology, Society of NeuroInterventional Surgery, Society for Vascular Medicine, and Society for Vascular Surgery. Developed in Collaboration with the American Academy of Neurology and Society of Cardiovascular Computed Tomography. *J. Am. Coll. Cardiol.* 57: e16–e94. Erratum in *J Am Coll Cardiol* 2011;57:2379.
37. Bonati, L.H., Dobson, J., Featherstone, R.L. et al. (2015). Long-term outcomes after stenting versus endarterectomy for treatment of symptomatic carotid stenosis: the International Carotid Stenting Study (ICSS) randomised trial. *Lancet* 385: 529–538.
38. MacDonald, D. (2011). *Oral and Maxillofacial Radiology: A Diagnostic Approach*, 151–159. Ames, IA: Wiley-Blackwell.
39. Fishbein, G.A. and Fishbein, M.C. (2009). Arteriosclerosis: rethinking the current classification. *Arch. Pathol. Lab. Med.* 133: 1309–1316.
40. Fishbein, M.C. and Fishbein, G.A. (2015). Arteriosclerosis: facts and fancy. *Cardiovasc. Pathol.* 24: 335–342. Erratum in *Oral Surg. Oral Med. Oral Pathol. Oral Radiol. Endod.* 2005; 99: 225–30.
41. Scarfe, W.C. and Farman, A.G. (2008). Soft tissue calcifications in the neck: maxillofacial CBCT presentation and significance. *Australasian Dent. Practice* 19 (Jul/Aug): 102–108.
42. Ertas, E.T. and Sisman, Y. (2011). Detection of incidental carotid artery calcifications during dental examinations: panoramic radiography as an important aid in dentistry. *Oral Surg. Oral Med. Oral Pathol. Oral Radiol. Endod.* 112: e11–e17.
43. Friedlander, A.H., Garrett, N.R., Chin, E.E., and Baker, J.D. (2005). Ultrasonographic confirmation of carotid artery atheromas diagnosed via panoramic radiography. *J. Am. Dent. Assoc.* 136: 635–640.
44. Ricotta, J.J., Aburahma, A., Ascher, E. et al. (2011). Updated Society for Vascular Surgery guidelines for management of extracranial carotid disease. *J. Vasc. Surg.* 54: e1–e31. Erratum in *J. Vasc. Surg.* 2012; 55: 894.
45. Goldstein, L.B., Adams, R., Alberts, M.J. et al. (2006). Primary prevention of ischemic stroke: a guideline from the American Heart Association/American Stroke Association Stroke Council: cosponsored by the Atherosclerotic Peripheral Vascular Disease Interdisciplinary Working Group; Cardiovascular Nursing Council; Clinical Cardiology Council; Nutrition, Physical Activity, and Metabolism Council; and the Quality of Care and Outcomes Research Interdisciplinary Working Group: the American Academy of Neurology affirms the value of this guideline. *Stroke* 37: 1583–1633.
46. Grant, E.G., Benson, C.B., Moneta, G.L. et al. (2003). Carotid artery stenosis: gray-scale and Doppler US diagnosis – Society of Radiologists in Ultrasound Consensus Conference. *Radiology* 229: 340–346.
47. Kochanowicz, J., Turek, G., Rutkowski, R. et al. (2009). Normal reference values of

ratios of blood flow velocities in internal carotid artery to those in common carotid artery using Doppler sonography. *J. Clin. Ultrasound* 37: 208–211.
48. Das, M., Braunschweig, T., Mühlenbruch, G. et al. (2009). Carotid plaque analysis: comparison of dual-source computed tomography (CT) findings and histopathological correlation. *Eur. J. Vasc. Endovasc. Surg.* 38: 14–19.
49. DeMarco, J.K., Huston, J. III, and Bernstein, M.A. (2004). Evaluation of classic 2D time-of-flight MR angiography in the depiction of severe carotid stenosis. *AJR Am. J. Roentgenol.* 183: 787–793.
50. Mühlenbruch, G., Das, M., Mommertz, G. et al. (2010). Comparison of dual-source CT angiography and MR angiography in preoperative evaluation of intra- and extracranial vessels: a pilot study. *Eur. Radiol.* 20: 469–476.
51. Brinjikji, W., Huston, J. 3rd, Rabinstein, A.A. et al. (2016). Contemporary carotid imaging: from degree of stenosis to plaque vulnerability. *J. Neurosurg.* 124: 27–42.

Chapter 13

Imaging of the salivary glands

13.1 Introduction

There are three pairs of major salivary glands: the parotid, submandibular, and sublingual glands. These are exocrine glands and are sited adjacent to the oral cavity, whereas the many thousands of minor salivary glands are sited within the oral mucosa.

The parotid gland is the largest. It is sited behind the ramus of the mandible and is a serous-secreting gland. It includes lymph nodes, which are incorporated during its embryological development. It has an accessory lobe which extends anteriorly, alongside the parotid duct, on the surface of the masseter muscle. The duct passes medially approximately 1 cm below the zygomatic arch, pierces the buccinator muscle, and enters the oral cavity opposite to the second maxillary molar. The gland is divided into superficial and deep components, defined by the plane of the facial nerve which runs through and divides within the gland.

The submandibular gland is a walnut-sized gland which lies inferiomedial to the body of the mandible and wraps around the posterior free margin of the mylohyoid muscle. It is a mixed mucous- and serous-secreting gland. The secretory duct runs from the hilum upward, bends around the posterior of the mylohyoid muscle at the genu, and runs just under the mucosa of the floor of the mouth, to emerge anteriorly at the sublingual papilla.

The sublingual gland is an almond-sized gland which is almost wholly mucous, lies in the floor of the mouth above the mylohyoid muscle, and drains by several ducts into the floor of the mouth. The minor salivary glands are generally mucous, except the *von Ebner's* glands of the dorsum of the tongue, which are serous.

The normal function of the salivary glands is essential for a healthy oral cavity, which in turn is essential for a healthy body, and not only because it is the organ for the ingress of food and drink, facilitating swallowing and nutrition, speech and taste. Absence of saliva may lead to dysphagia, dysphonia, and dysgeusia. A "dry mouth" (xerostomia) may not only make speaking and swallowing difficult, but promote mucosal infections and dental caries. Over the last decade, the biomarkers in saliva have been extensively studied in order to determine which may become a potential diagnostic tool for a range of diseases from caries through to diseases with more serious outcomes, such as autoimmune and cardiovascular diseases, diabetes mellitus, and oral cancer [1].

Diseases of salivary glands can affect one or more glands. Affected glands generally appear swollen or enlarged. This may be accompanied by pain, particularly if the disease is of acute onset, and sometimes by a reduced saliva flow rate. Obstructive

Oral and Maxillofacial Radiology: A Diagnostic Approach, Second Edition. Edited by David MacDonald.
© 2020 John Wiley & Sons, Inc. Published 2020 by John Wiley & Sons, Inc.

disease or neoplasia most frequently affects one gland, whereas systemic disease affects more than one, and frequently presents bilaterally. It is usually swelling of the larger parotid and submandibular glands that is most clinically obvious.

Imaging of the salivary glands includes almost the entire range of imaging modalities, from conventional plain film and fluoroscopic imaging, including sialography, through *computed tomography* (CT), *magnetic resonance imaging* (MRI), *salivary gland ultrasound* (SGUS), scintigraphy, and *positron emission tomography* (PET) [2]. Figure 13.1 overviews the main glandular lesions. Ultrasound is the first-line

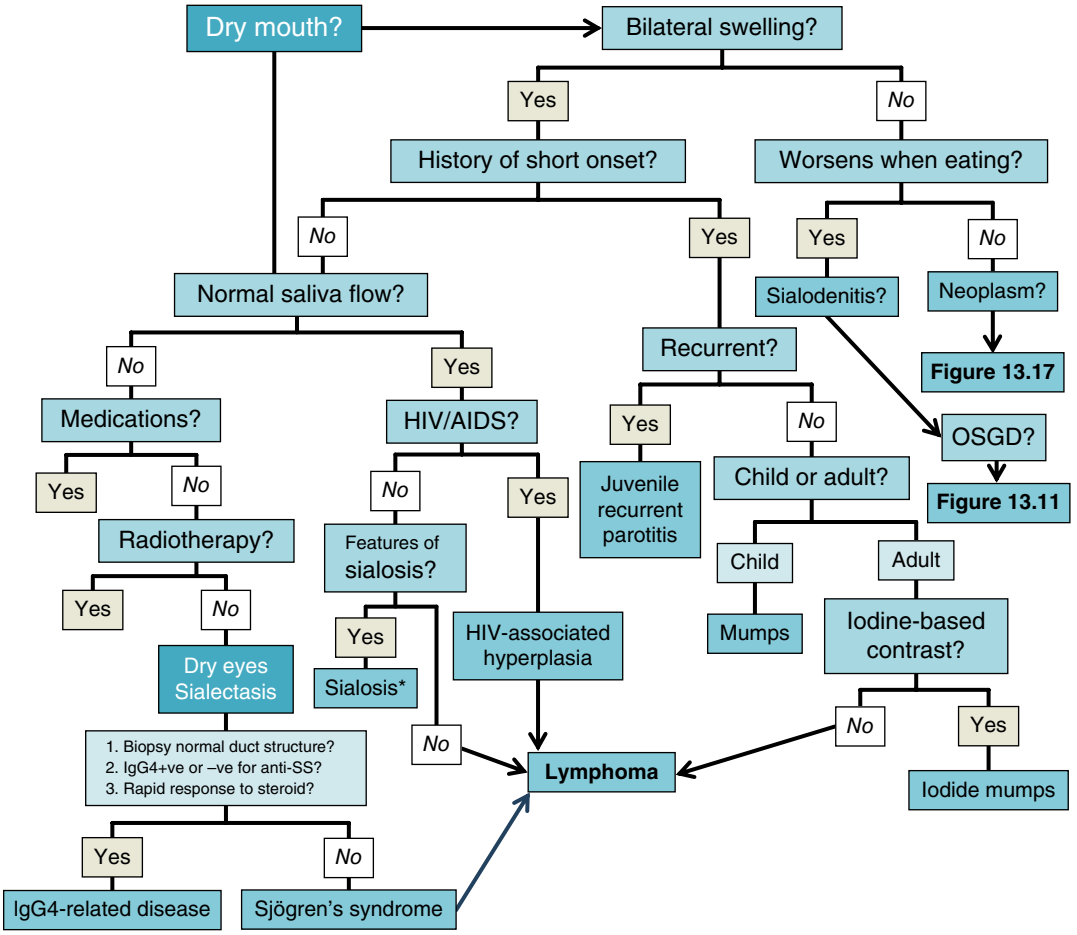


Figure 13.1 Overview of the main categories of glandular lesions, with a particular focus on those causing dry mouth and/or bilateral swelling. Note 1: Some HIV/AIDS cases may also exhibit dry mouth. Note 2: Sialosis (asterisk) classically presents as bilateral painless swellings, which may also be the initial presentation of sarcoidosis. Therefore, in absence of a history suggestive of sialosis, consider sarcoidosis, particularly if facial nerve paralysis and uveitis are also present. Presence of bilateral hilar lymphadenopathy on thoracic radiography is diagnostic for sarcoidosis. Bilateral swelling of lower poles of the parotids in absence of all the above, consider Warthin's tumor. +ve, positive; -ve, negative; HIV/AIDS, human immunodeficiency virus/acquired immune deficiency syndrome; OSGD, obstructive salivary gland disease.

investigation. The classical imaging technique for salivary gland disease is sialography (Figure 13.2). Although it temporarily slipped into abeyance, it has experienced a renaissance due to its central role in interventional sialography, a therapeutic modality for the conservative (or minimal surgical) treatment of *obstructive salivary gland disease* (OSGD). This treatment is frequently mediated by fluoroscopy (see Figure 13.2b). This conservative treatment can also be achieved under ultrasound guidance and may include salivary-stone lithotripsy. The basic principles of SGUS were introduced in Chapter 8. The later Figure 13.4 will familiarize the nonradiologist reader with SGUS images. It sets out the greyscale images both of the normal parotid gland and of the normal submandibular gland, drawing attention also to adjacent anatomical landmarks as they would be observed in the axial plane. These are readily observable in the SGUS of lesions in the later Figures 13.5–13.8, 13.10, and 13.13.

The nonradiologist reader should be aware that fluoroscopy (Figures 13.2b, 13.13b, and 13.14) presents the radiodensities in reverse greyscale to that presented on conventional radiography. Fluoroscopy is a common vehicle for interventional procedures in radiology, such as in angiography (Figures 12.22b, 14.5a, b, 14.6, and 14.7d, c).

A general reduction in function is likely to be due to a systemic cause, such as Sjögren's syndrome, diabetes mellitus, or radiotherapy, and a wide range of medications, including methamphetamine, a recreational drug which causes "meth mouth." Infections also affect one or more

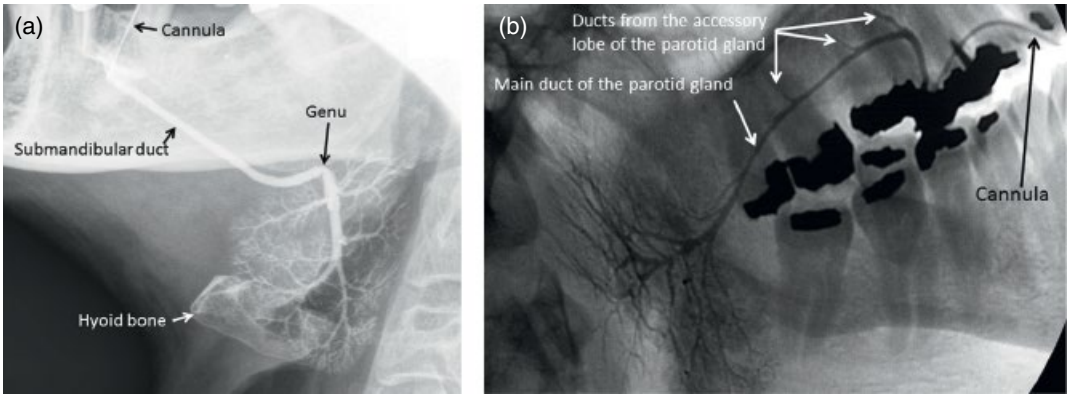


Figure 13.2 Sialography of normal submandibular and parotid glands. (a) Conventional sialographic image of the left submandibular gland. The submandibular duct runs over the mylohyoid muscle to its posterior margin, then bends sharply down over it (genu = knee) to enter the hilum of the submandibular gland. The "blush" around the ducts represents the contrast media getting down as far as the acini. This should not be mistaken for sialectasis, displayed in Figure 13.3. (b) Fluoroscopic image of a right parotid gland. The main duct receives the ducts from the accessory lobe of the parotid gland, then drains into the oral cavity through the parotid papilla, which is usually found opposite to the second maxillary molar. Both show a normal "tree in winter" appearance of a slim uniform trunk of the main extraglandular duct and finely branching primary and secondary ducts. Source: Courtesy of Dr. Jackie Brown, Senior Lecturer in Dental & Maxillofacial Radiology at King's College London, London, United Kingdom.

salivary glands; the most frequent cause of sialadenitis is obstruction. Individual major salivary glands can be affected by OSGD or by neoplasms. Although the latter still necessitates the affected gland's removal, until recently the former frequently did so too.

This chapter will address the most frequent and/or important diseases affecting the major salivary glands. These are mainly of inflammatory or neoplastic origin. It will not discuss rare diseases such as *necrotizing sialometaplasia* [3] or vascular anomalies [4], which are considered elsewhere. The reader should also be aware of other lesions that may occur within the submandibular space or immediately adjacent to it, which are not glandular in origin. These occur particularly in children and are the second branchial cleft cyst, the thyroglossal duct cyst, the foregut duplication cyst, and the dermoid and epidermoid cysts [5].

13.2 Dry Mouth

The dry mouth referred to here is not physiological, such as after exercise or a failure to hydrate adequately, but is a persistent complaint, perhaps accompanied by dysphagia, dysphonia, and dysgeusia, and confirmed by clinical examination. Although the clinical details for that examination are addressed elsewhere, some of these will be absence of pooling of saliva in the floor of the mouth, dry mucosa, oral infection, poor oral hygiene, and rampant caries in what may have been a previously well-maintained and restored dentition. The clinical examination will include inspection and palpation of the major salivary glands to determine swelling and whether it affects the whole gland, particularly the parotids, or just part of it. It should be noted that certainly in Europe and North America, this examination should be routinely performed by the dentist at review/check-up appointments. The clinical history will include a drug history, including recreational drugs, and any prior radiation treatment. A detailed review on the causes, diagnosis, and treatment of salivary hypofunction has been recently published [6]. Because of this, it should be appreciated that "bilateral swellings," although presented as a subordinate heading to "dry mouth" in Figure 13.1, should be considered, in the absence of a dry mouth, a main heading in its own right; hence its prominent position in the flowchart (Figure 13.1).

13.2.1 SJÖGREN'S SYNDROME

Sjögren's syndrome is an autoimmune disease that may be confined to the salivary and lacrimal glands – sometimes described as *primary Sjögren's syndrome* (pSS) or the "sicca complex" – whereas *secondary Sjögren's syndrome* (sSS) has been used when it presents with other systemic connective tissue or organ-specific autoimmune diseases, such as systemic lupus erythematosus or rheumatoid arthritis. According to Theander and Jacobsson, the causative mechanism "for the simultaneous or sequential development of multiple autoimmune diseases in one individual is not well understood" [7]. They suggest that "common genetic backgrounds and additional immunogenetic, environmental, or hormonal factors may be responsible for the formation of subsets of autoimmune disease clustering." A more simplified diagnostic tool for the diagnosis of Sjögren's syndrome than the multistep American European Consensus Criteria (AECG) was recently proposed [8]. Sjögren's syndrome is considered to be present when two out of three criteria are satisfied; these include a positive labial salivary gland biopsy, altered tear-breakup

time in an eye test, and presence of anti-Ro and/or anti-La antibodies [8].

Three-quarters of cases are in females in the fourth to seventh decades. The parotid is affected in 90%. Although bilateral disease is typical, one side may be more severely affected. The recurring progressive swelling can be accompanied occasionally by discomfort or even pain. Although the lobar architecture is preserved, the progressive parenchymal damage eventually results in the typical sialectasis obvious on sialography (Figure 13.3) and parenchymal echotexture changes on SGUS. It should be noted that sialectasis is not pathognomonic for Sjögren's syndrome because it can be secondary to chronic infection of the salivary glands.

Poul et al. reported that high-spatial-resolution SGUS is more sensitive than sialography for the investigation of Sjögren's syndrome (Figure 13.5). Furthermore, they reported that accuracy is increased when SGUS is carried out in conjunction with sialography [9]. Nevertheless, a recent systematic review that included only 31 studies out of the 167 already published agreed that ultrasound was effective for the assessment of major salivary gland pathology, but found considerable variation in the definitions of ultrasound anomalies, and concluded that further studies were required to validate and standardize the SGUS anomalies of pSS [10]. One of the authors of the systematic review, Baldini [11], has attempted this and has recommended SGUS for the noninvasive and early diagnosis of pSS. Nevertheless, Fox [12], who pronounced the systematic review "excellent," declared that while SGUS can be used to examine the large salivary glands, minor salivary gland biopsy remained the diagnostic "gold standard."

Although neoplasms of the salivary glands have long been displayed by MRI (see also Kinoshita et al.'s pictorial essay [13]),

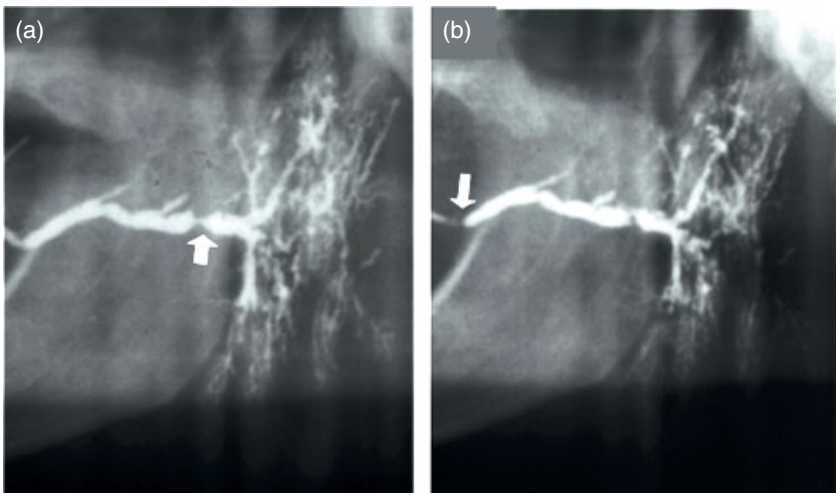


Figure 13.3 Panoramic radiographs exhibiting sialectasis secondary to Sjögren's syndrome. (a) Sialographic image displaying optimal filling of the duct structure with the cannula still in place, and exhibiting irregular ducts and sialectasis or dilations within the substance of the parotid gland. There are two constrictions (strictures) of the main duct. The more distal stricture is just mesial to the hilum of the main parotid lobe (white arrow in a) and the other just distal to the parotid papilla (white arrow in b). (b) Emptying film (the cannula has been removed) demonstrating no emptying, meaning that the two constrictions of the main duct are preventing drainage.

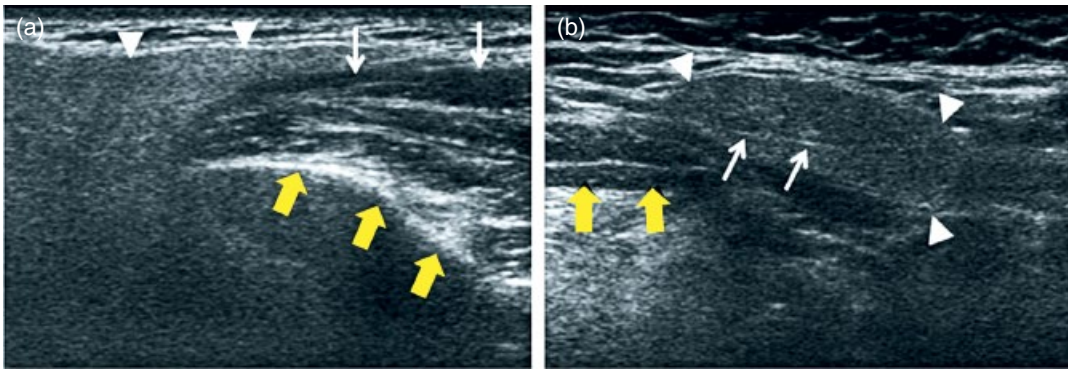


Figure 13.4 Ultrasound images of normal parotid (a) and submandibular (b) glands. Both images are made at about the axial plane. The skin and subcutaneous tissues are at the top of each image, where the transducer is positioned. Therefore, as you proceed downward you are going deeper into the patient. (a) The white arrowheads denote the surface of the normal parotid gland, which is almost uniformly homogeneous throughout. The white arrows denote the surface of the masseter and the yellow arrows the hyperechogenic (white) surface of the bone of the vertical ramus. The latter is due to reflection of a substantial proportion of the ultrasound waves back to the transducer. Much of the masseter is hypoechogenic (black), which is normal. (b) The whole normal submandibular gland is delineated by the three white arrowheads. The yellow arrows denote the mylohyoid muscle, which is hypoechogenic (black). The white arrows indicate an intraglandular duct. Source: Adapted and reproduced with permission from Cheng, S.C., Wu, V.W., Kwong, D.L., and Ying, M.T. 2011. Assessment of post-radiotherapy salivary glands. *Br. J. Radiol.* 84: 393–402.

preliminary work by a Japanese team presents MRI sialography as an alternative to conventional sialography [14–16]. They compared normal and Sjögren's syndrome patients with stimulated [15] and unstimulated salivary flow [16].

Over a decade ago, Morgen et al. observed severe *central nervous system* (CNS) manifestations on MRI reminiscent of *multiple sclerosis* in pSS patients [17]. They suggested that future controlled studies will be necessary to more precisely estimate the prevalence of CNS lesions in pSS, specifically of discrete white-matter abnormalities. Ding et al. reported that small *region-of-interest* (ROI) diffusion-weighted MRI revealed differences between cases of Sjögren's syndrome and others, whereas larger ROIs did not [18]. No other publications addressing these or other applications of MRI with regard to Sjögren's syndrome have appeared.

In addition to dry mouth, Sjögren's syndrome can cause dry eyes, which "can lead to corneal abrasions, infection, ulceration, chronic scarring and, in severe cases, perforation" [19]. Of 616 Chinese patients with pSS, 7% had *neuromyelitis optica spectrum disorder* (NMOSD) [20], an idiopathic, severe, demyelinating disease preferentially affecting the optic nerve and spinal cord. On the other hand, those pSS patients without NMOSD had significantly more interstitial lung disease and renal tubular acidosis [20].

The lymphoepithelial element of Sjögren's syndrome represents an autoimmune process characterized by a benign lymphocytic epitheliotropism in the salivary glands. Due in part to the presence of this lymphoid tissue, patients are 44 times more at risk of developing a secondary lymphoma [21].

13.2.2 IGG4-RELATED DISEASE

Painless swelling of the major salivary and lacrimal glands, which formerly were diagnosed as *Mikulicz disease* and, in some cases, multiple glands affected by chronic sclerosing sialadenitis (*Kuettner tumor*), are now considered elements of *IgG4-related disease* (IgG4-RD) [22]. This is a multisystemic disease which was first recognized in 2003 [22, 23]. It has a prevalence of 2.2 cases per 100 000 Japanese [23]. Although no familial element has yet been identified, this will require more studies from a variety of ethnicities to be certain [23]. Histopathologically it exhibits diffuse organ infiltration by plasma cells expressing IgG4 [24], irregular fibrosis, and obstructive vasculitis [22]. The last feature partially or wholly obturates small veins (obliterative phlebitis) [23]. Its response to immunosuppressive therapy reinforces the suspicion of an autoimmune disease of chronic inflammatory response etiology [25].

IgG4-RD causes persistent painless swelling of the large salivary (sialadenitis) and lacrimal (dacryodenitis) glands, usually bilaterally. The differential diagnosis includes Sjögren's syndrome, from which IgG4-RD should be distinguished as it rapidly responds to corticosteroid therapy, whereas Sjögren's syndrome does not, and sarcoid. The other head and neck structures which may be affected are the thyroid glands, lymph nodes (71% of 42 cases) [26], and sinonasal cavities. Although IgG4-RD may exhibit mild dry mouth (flow rate was lower than normal, resting lower in 81%, and stimulated lower in 36% of 42 cases) [26] and/or eyes, it is negative for Sjögren's syndrome (anti-Ro and anti-La) antibodies and minor labial gland biopsy displays normal duct structure. It was set against a background of lymphocytic infiltration and lymphoid follicle and immunostain for IgG4-positive plasma cells. Finally it most frequently affects the submandibular rather than the parotid glands [22, 23] and middle-aged or older men rather than women [25]; women predominated in the Chinese case series [26]. It is distinguished by a characteristic elevation of serum IgG4 levels and histopathology.

Because IgG4-RD is a multisystemic disease, consideration of whole-body cross-sectional imaging is recommended in the diagnostic work-up of a suspected case [22]. *Fluorodeoxyglucose positron emission tomography/CT* (FDG PET/CT) will not only advance the diagnosis by mapping the sites of inflammation, and define the extent of the disease, but also guide biopsy both in decision-making and in the institution of the appropriate therapy.

The imaging of salivary glands alone is not sufficiently pathognomic. Bilateral lesions need to be distinguished from lymphoma, sarcoid, and Sjögren's syndrome, and unilateral lesions need to be distinguished from malignant tumors by other means, such as the characteristic "capsule-like rim" surrounding the parotid lesions which are almost pathognomic for IgG4-RD. The earlier Mikulicz disease presented as painless swelling of the major salivary glands and lacrimal gland. These appear on T2-weighted MRI as hypointense and on postcontrast T1-weighted MRI as diffuse homogeneous enhanced bilateral swellings [22]. The earlier Kuettner tumor, a hard swelling of the submandibular glands, appears as isointense on both T1- and T2-weighted MRI [22].

SGUS was found to have superior sensitivity, specificity, and accuracy than CT, MRI, or FDG PET/CT [27]. The IgG4-RD adenitis has five patterns, largely

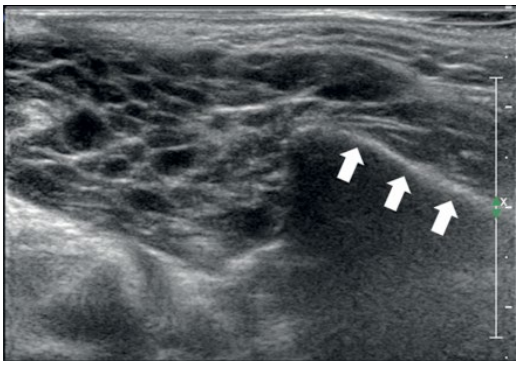


Figure 13.5 Ultrasound image of the parotid gland in a patient with primary Sjogren's syndrome. The parenchyma shows a typical "honeycomb" pattern. The top of the image is the skin and subcutaneous tissue, where the transducer is positioned. The hyperechoic line (white) that the white arrows indicate is the surface of the vertical ramus. The almost homogeneous area deeper to the hyperechoic line is the "acoustic shadow." Together, the hyperechoic line and the acoustic shadow suggest bone or other calcified tissues, such as a calcified carotid artery atheroma (see Figure 12.17). Source: Courtesy of Dr. Jackie Brown, Senior Lecturer in Dental & Maxillofacial Radiology at King's College London, London, United Kingdom.

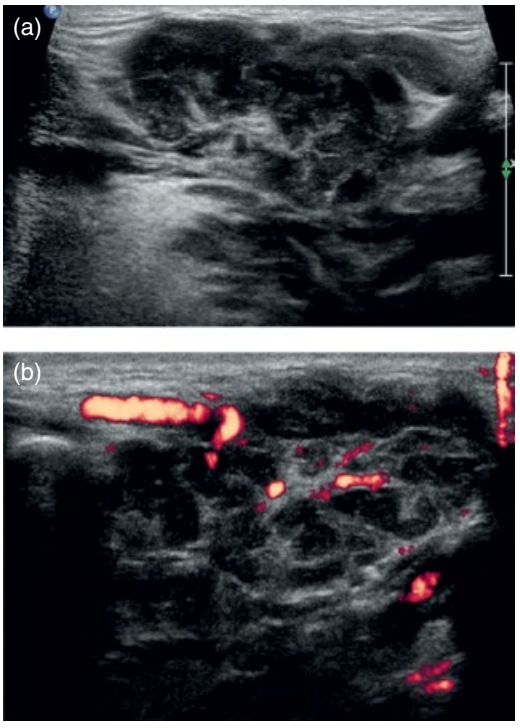


Figure 13.6 Ultrasound images (a) without and (b) with color Doppler of the submandibular gland in a patient with IgG4-related disease. Note the multifocal hypoechoic foci creating a heterogeneous appearance to the gland parenchyma. Source: Courtesy of Dr. Jackie Brown, Senior Lecturer in Dental & Maxillofacial Radiology at King's College London Dental Institute of Guy's, King's College & St Thomas' Hospitals, London, United Kingdom.

hypoechoic, on SGUS (Figure 13.6). After corticosteroid therapy, the glands decrease in size significantly and on ultrasound become more homogeneous. The superficial hypoechoic pattern, more prevalent in the submandibular gland, becomes less marked or disappears completely. This early diagnosis can facilitate early and effective treatment by corticosteroids, avoiding unnecessary examinations and surgical intervention; a significant proportion of submandibular and parotid glands in a Chinese case series had already been removed [26].

13.2.3 RADIOTHERAPY-INDUCED SALIVARY DYSFUNCTION

Radiotherapy-induced salivary dysfunction is produced by two therapeutic vehicles: external beam radiation or intravenous delivery of radioactive iodine [3]. Radiotherapy-induced salivary dysfunction can be induced by direct exposure of the salivary glands to the radiation beam when they have been included in the radiotherapy field, because of their proximity to the primary cancer and/

or lymph nodes [28]. Similar damage can be inflicted indirectly by way of the blood by the deposition of radioactive iodine (^{131}I), a critical treatment modality for thyroid disease, particularly well-differentiated thyroid cancer [3, 29] such as papillary and follicular thyroid carcinomas [30].

The initial and acute response of the salivary gland to radiation-induced damage is pain and swelling [3]. A decrease in saliva is noted during the first weeks of radiotherapy and may persist, rendering these patients susceptible to an increase in caries, a painful burning mouth, dysphagia, dysphonia, and dysgeusia [28].

The reported incidence ranges from 10 to 60% depending on cumulative dose and number of treatments [3]. The average time to late-stage symptoms is four to eight months [3]. The extent of ^{131}I injury can be determined by scintigraphy, which reveals "abnormalities in uptake and secretory ability in asymmetric combinations of the major salivary glands" [30].

Wu et al. observed that clinically swelling was present in almost every one of 12 cases and that sialendoscopically, stenosis was the most frequently observed feature [29]. At the time of sialendoscopy, stenoses were dilated and the duct system irrigated, although there was little mucous plugging. Furthermore, this sialendoscopy itself improved salivary gland function in comparison to that prior to the sialendoscopy. The function of the parotid glands was more severely affected than that of the submandibular glands. This was put down to the serous glands of the parotid being more radio-sensitive than the mucous glands. It should be noted that this study was not controlled and was dependent on performing sialendoscopy before stenosis became too severe to navigate the ducts.

SGUS displays radiation-induced sialadenitis of the parotid and submandibular glands of a patient treated by ^{131}I for a thyroid carcinoma (Figure 13.7). Choi et al.'s small report on MR sialography revealed that it was useful in showing the extent of severity of radioactive iodine–induced sialadenitis. The authors introduced a grading system on the basis of this work, which they suggested could also describe the resultant salivary gland dysfunction [31].

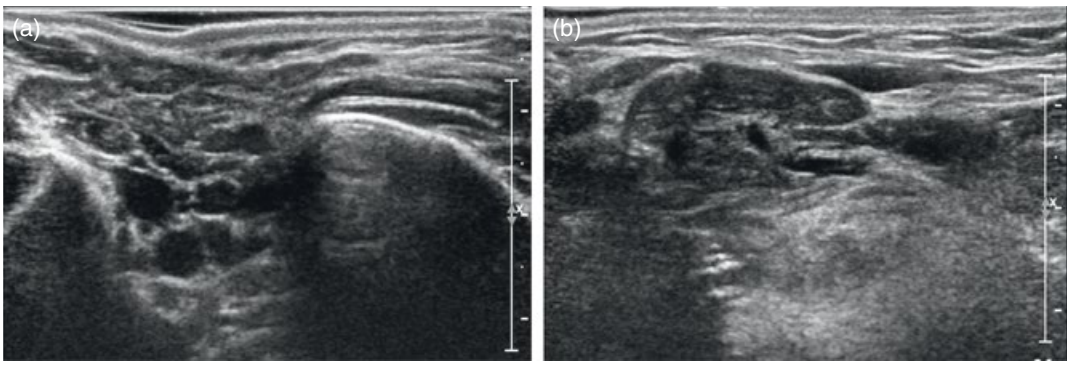


Figure 13.7 Images of (a) the parotid gland and (b) the submandibular gland in a patient suffering from radiation-induced sialadenitis following radioiodine ablation of a papillary thyroid carcinoma. Source: Courtesy of Dr. Jackie Brown, Senior Lecturer in Dental & Maxillofacial Radiology at King's College London, London, United Kingdom.

13.3 Bilateral Swelling

Bilateral swelling of the salivary gland can be of rapid onset or it can be chronic (Figure 13.1). The most frequent cause of rapid onset of swelling and pain is mumps, whereas the chronic swellings are features of Sjögren's syndrome and *human immunodeficiency virus* (HIV) infection. Although these are associated with dry mouth, there are other lesions which, though painless, are markers of potentially serious lesions. These swellings could be *sialosis* or the rarer *sarcoidosis*.

13.3.1 SIALOSIS

Sialosis, also called sialadenosis, is a non-inflammatory, non-neoplastic phenomenon, which manifests as recurrent and occasionally tender, usually bilateral, swelling, principally of the parotid glands. SGUS displays homogeneous, uniformly hyperechoic parotid glands, and on CT the major salivary glands will appear homogeneous and may be uniformly hypodense due to fatty infiltration. Sialosis is associated with endocrine and deficiency diseases. It also is associated with alcoholism, malnutrition, diabetes mellitus, diabetes insipidus, acromegaly, hypoparathyroidism, uremia, and liver disease (including cirrhosis). Malnutrition, including kwashiorkor, also encompasses vitamin deficiencies (Vitamins A, B1, and B3), eating disorders (10–50% of all cases of *bulimia nervosa*), and gastrointestinal diseases. Some drugs such as guanethidine, thioridazine, or isoprenaline will cause sialosis. Sialosis frequently precedes the onset of diabetes mellitus, which should be considered in cases where the cause of sialosis is not obvious or is unknown. The pathogenesis of sialosis is not well known [3].

13.3.2 SARCOIDOSIS

Sarcoidosis is a systemic disease with an idiopathic etiology [4]. As painless swelling of the parotid glands is a well-recognized feature of sarcoidosis, they should be examined in such cases. The parotids can be affected in up to 30% of cases and may be the initial presentation of sarcoidosis. When symmetric bilateral hilar adenopathy is already present on thoracic radiography, then this and the clinical examination alone are sufficient for the diagnosis of sarcoidosis. If this is absent, then a biopsy may only be required to display the diagnostic noncaseating granuloma. Treatment is normally effected by oral steroids [32]. The swellings, like sialosis, are bilateral and may be painless. If accompanied by facial nerve paralysis and uveitis, then *Heerfordt syndrome* should be considered [4]. The swellings' presentation on CT may be as multiple noncavitating masses, which in MRI and SGUS are multiple homogeneous nodules (see Bag et al.'s Figure 11 [4]). Sarcoidosis may also give rise to cervical lymphadenopathy and frequently demonstrates enlarged intraparotid nodes. Because uveitis is a serious risk to vision, a prompt referral of the patient to an ophthalmologist is recommended [33].

13.3.3 HIV-ASSOCIATED SALIVARY GLAND DISEASE

The incidence of HIV/AIDS in the United States is 19 per 100 000 annually, especially in men and those of sub-Saharan African origin of between 25 and 35 years of age [34]. Nevertheless, any age group, even neonates, can prove HIV positive [21]. The most frequent oral findings suggestive of HIV infection in adults are candidiasis, hairy leukoplakia, non-Hodgkin lymphoma, and necrotizing ulcerative gingivitis/periodontitis. The last is easily observed

on oral examination and conventional dental radiography. This can also determine the destruction caused by related *Kaposi's sarcoma*, which if large can be further imaged by CT or MRI if necessary, or even by PET FDG, which will reveal the Kaposi's sarcoma to be very avid foci [34]. Ultimately, positive serology for HIV will confirm the diagnosis.

Although unilateral or bilateral swelling of the parotid glands and dry mouth are infrequent manifestations of HIV infection [34], a clinical examination to identify the most frequent manifestations should be instituted whenever thought appropriate [21]. Patton notes that "Parotid enlargement in HIV-seropositive patients may represent several conditions including HIV-associated lymphoepithelial lesions, hyperplastic reactive lymphadenopathy, benign *lymphoepithelial cysts* (LEC), lymphoma… and *diffuse infiltrative lymphocytosis syndrome* (DILS)" and recommends that SGUS offers a simple and rapid diagnosis of the HIV salivary gland disease. SGUS identifies one of four main presentations: lymphocytic aggregations, lymphoepithelial cysts, fatty infiltration, and lymphadenopathy only [34].

LECs are the most common cause of parotid enlargement in HIV-positive patients [21, 35] and may be an early indicator of HIV infection or emergence of AIDS in those born with HIV [35]. LECs are usually slow growing and painless [21]. These swellings are generally bilateral, unlike the more infrequent sporadic non-HIV-positive cases, which are unilateral [21]. LECs generally appear on SGUS as round, deeply hypoechoic, cystic areas with well-defined margins and posterior acoustic enhancement (Figure 13.8). They range from 0.5 to 5 cm in diameter. They also may display internal septae [35]. DILS needs to be distinguished from Sjögren's syndrome and has more extraglandular involvement, larger cystic foci, and cystic involvement of lymph nodes both within and outside the parotid gland [35].

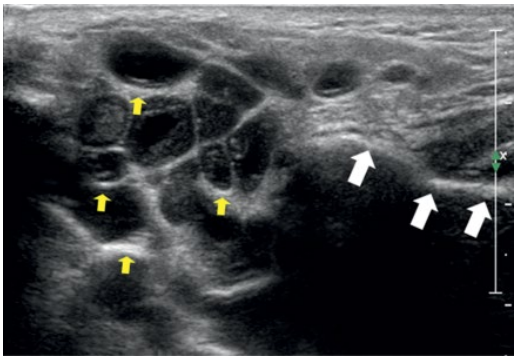


Figure 13.8 Ultrasound image of the parotid gland in a patient with HIV-associated benign lymphoepithelial cysts. These present as round, deeply hypoechoic, cystic areas with well-defined margins and posterior acoustic enhancement (yellow arrows). Note: This is different to the acoustic shadow (black area) deep to the hyperechogenic lateral surface of the vertical ramus (white arrows), as also displayed on Figure 13.5. Source: Courtesy of Dr. Jackie Brown, Senior Lecturer in Dental & Maxillofacial Radiology at King's College London, London, United Kingdom.

Lipodystrophy syndrome, a triad of significant body fat redistribution, dyslipidemia, and insulin resistance, is a side effect of the *highly active antiretroviral therapy* (HAART) used to reduce the replication rate of HIV [30]. In addition to a "buffalo hump," neck thickening, and breast and waist hypertrophy, paraparotid fat depositions may occur, causing parotid gland enlargement (see Mandel's Figure 8 [30]).

13.3.4 MUMPS

Hitherto acute sialadenitis, such as in mumps, was generally readily diagnosed by its classical presentation and was so quickly self-resolving that there was little role for radiology, particularly when

mumps presents within an epidemic and affects young patients. The mumps virus, a *ribonucleic acid* (RNA) virus of the *Paramyxoviridae* family [36], has since the Second World War been the subject of a very successful worldwide vaccination campaign as part of the *measles-mumps-rubella* (MMR) vaccine. This began to change as epidemics were reported not only in well-vaccinated child populations, but also in universities and colleges in North America and Europe. Furthermore, the diagnosis of mumps in well-vaccinated populations is challenging, not only because the classical presentation of parotitis is less obvious in such populations, but also because the laboratory tests are less sensitive [37]. The clinical symptoms and signs of over 4000 boys and young men "included: swelling of one or more salivary glands (94%), fever (55%), malaise (29%), headache (15%), abdominal pain (7%), nausea (7%), vomiting (5%), orchitis (4% of males aged >12 years), meningoencephalitis (0.5%) and pancreatitis (0.03%)" [38]. There is no single explanation for these epidemics: in some situations it is attributed to reduction in herd immunity due to a failure to be vaccinated or to complete a vaccination program; in others the epidemics occur in well-vaccinated populations, where over 90% are vaccinated. This is believed to reflect a decline in the mumps' seropositivity, which was observed in Korea among young teenagers, particularly males [37]. Furthermore, this predilection for males in part may reflect their high face-to-face interaction rates [38, 39], but also in part their lower mumps antibody titers [40]. Nevertheless, presentation in the older patient may require appropriate imaging, such as SGUS. Zamir et al. reported that 8% of the 4000 males who got mumps in their study were over 30 years of age [38].

Iodide mumps is a rare side-effect of iodine-based contrast media. Zhang et al. synthesized the literature of three dozen cases occurring over the last six decades, and reported that although in almost all cases the iodide was delivered intravascularly, four patients developed iodide mumps after taking an oral preparation [41]. The mean age was 60 years and the age range was 8–78 years. The iodide mumps presented bilaterally in 86% of cases; the submandibular glands alone in over half of cases; and both the submandibular and parotid glands in a third. Onset of iodide mumps varied from a few minutes to 5 days and persisted from 12 hours to 11 days. Although so far there have not been any long-term consequences of iodide mumps, clinicians have to be alive to the possibility that they may be observing an allergic response to the contrast medium, particularly if the onset is immediate and is accompanied by the common clinical signs of allergy, such as urticaria, bronchospasms, and angioneurotic edema [30]. Another form of iatrogenic mumps is *anesthetic mumps* due to the displacement of air/anesthetic gases into the parotid glands, particular when the gas is developed by a face mask rather than by intubation [41].

Although SGUS contributes little to the diagnosis of mumps in an epidemic affecting young patients, it may be helpful in ruling out other common causes of gland swelling, such as obstruction, particularly if the disease manifests unilaterally. On SGUS, the mumps-affected parotid gland is hypoechoic, heterogeneous, and hyperemic, and shows a rounded shape "with a convex lateral surface and a hypoechogenic structure" [42]. Such a case is displayed in Figure 13.9. This was a middle-aged male, who presented with a rapid onset of bilateral swelling of the submandibular and parotid glands. Early

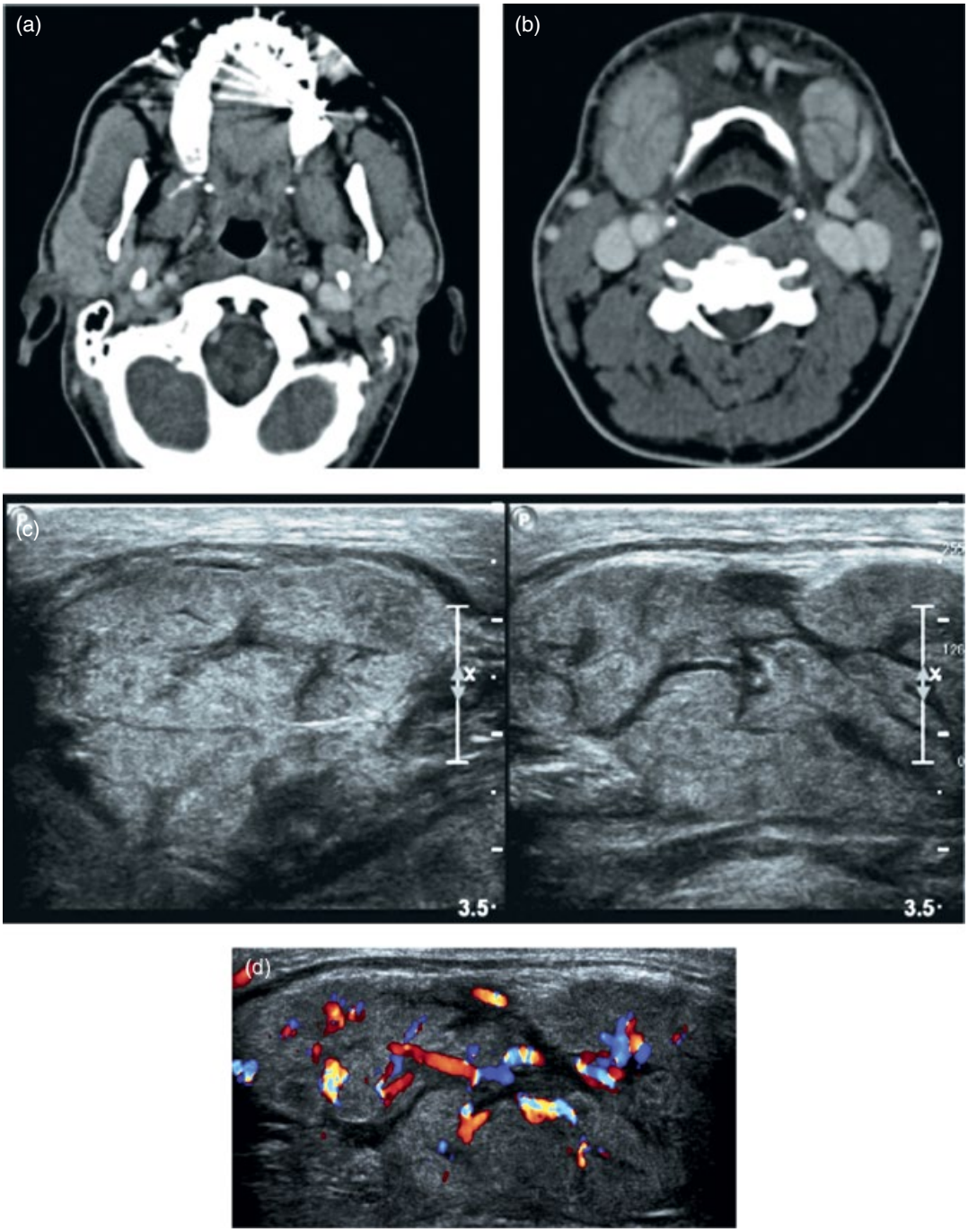


Figure 13.9 Adult mumps. (a) Contrast-enhanced soft-tissue window axial computed tomography (CT) at the level of the first cervical vertebra. Bilateral swollen parotid glands are displayed. The accessory lobe and the duct of the right parotid gland are displayed. (b) Contrast-enhanced soft-tissue window axial CT at the level of the third cervical vertebra. Bilateral swollen submandibular glands are displayed. The facial vein is observed running on the lateral surface of the left submandibular gland. (c) Grayscale ultrasound displays diffuse, almost symmetrical swelling of both submandibular glands. The parenchyma has a diffuse heterogeneous hypoechoic presentation, which is consistent with an acute sialadenitis. There are no hyperechoic foci suggestive of sepsis. (d) Color Doppler ultrasound reveals hyperemia, which is consistent with acute sialadenitis. Source: Courtesy of Dr. Eli Whitney, Program Director, Oral Medicine-Oral Pathology Residency, University of British Columbia.

diagnosis and intravenous immunotherapy may minimize complications of mumps [43] such as orchitis, which affected 3.8% and 7% of males over 12 years of age in Zamir et al.'s [38] and Barskey et al.'s [39] reports, respectively. Therefore, to effect an early diagnosis of mumps in an adult male in order to minimize the onset of orchitis, an SGUS should be indicated in the first instance.

13.3.5 JUVENILE RECURRENT PAROTITIS

Juvenile recurrent parotitis (JRP) is an idiopathic inflammatory disease of the salivary glands that occurs in all main ethnic groups [44, 45]. It is the most common inflammatory salivary gland disorder in children in the United States and is second after mumps globally [46]. It presents between infancy and the onset of puberty by 15 years of age. Males are more frequently affected [47]. B-mode ultrasonography is the diagnostic imaging modality of choice as it is noninvasive [45, 47] and is well tolerated in children; this may show multiple hypoechoic foci, ranging from 0.5 to 4 mm in diameter, scattered randomly throughout the affected gland, against a background of hypoechoic change within the parenchyma (Figure 13.10). This may affect one or both parotid glands.

Serum amylase is raised during a JRP episode (as it is in mumps), a marker of inflammation of the salivary gland [45]. Xie et al. revealed that unilateral cases differed significantly from bilateral cases; the salivary function was poorer in the latter. Although the etiology is still uncertain, there is a trend toward considering a multifactorial etiology. Nevertheless, an idiopathic etiology means that since the pathenogenesis is unknown, steps cannot be effectively taken to both treat JRP and prevent it [45]. On sialendoscopy, the most common finding was a blanched mucosa (no blood vessels were visible). Other findings were stenosis and dilations of the ducts with mucous plugs and intraductal debris [46]. Nevertheless, Schneider et al. stated that the advantages of sialendoscopy were that it did not just confirm the diagnosis of JRP, but also "provided therapeutic intervention" [47]. The most common complication of sialendoscopy was a transient swelling of the salivary gland [46].

13.3.6 OBSTRUCTIVE SALIVARY GLAND DISEASE

OSGD is caused either by obturation of the lumen of a main duct, by a "stone" (sialolithiasis) by constriction, (or a narrowing) of the duct (stenosis), or by both together [48]. Although it affects a substantial proportion of the population, producing symptoms in 0.45% of the general population [49], post-mortem studies revealed sialolithiasis in 1.2% [50]. Furthermore, according to Iro et al. about 60 cases of OSGD occur per million of population annually [51]. Nevertheless, most patients will experience only a single episode of OSGD throughout their lives [49]. Although it affects individuals most frequently from the fourth up to the seventh decades [49], it presented most commonly in the fourth decade for both parotid and submandibular calculi in five independently performed studies for symptomatic salivary calculi [51]. Figure 13.11 reveals three diagnostic features found in OSGD: lithiasis, stenosis, and dilation, as published under the auspices of the European Salivary Gland Society [52]. The first two, lithiasis (Figure 13.12) and stenosis (Figure 13.13), require treatment to clear the obstruction and will be the focus here. While dilation may indicate damage to the duct system,



Figure 13.10 Ultrasound image of the parotid gland in a patient with juvenile parotitis. Note the small hypoechoic sialectatic foci scattered throughout the gland parenchyma. Source: Courtesy of Dr. Jackie Brown, Senior Lecturer in Dental & Maxillofacial Radiology at King's College London, London, United Kingdom.

particularly as sialectasis (Figure 13.14), there is up to now no specific intervention or need to address this.

The "stone," frequently referred to as a calculus, may be sufficiently calcified to present as a radiopacity on plane film radiography. It is also observable by SGUS by virtue of the hyperechoic surface and acoustic shadow. The obturation may also be noncalcified. Both this and stenosis may require the introduction of contrast media into the duct system (sialography) to be visible as filling defects in the former and a band of stenosis in the latter, enabling optimal diagnosis of the nature of the obstruction and the details of duct anatomy should a minimally invasive approach be planned. It goes without saying that any suspected case of OSGD should be preceded by a clinical examination. Extraglandular factors, such as carcinoma arising from the floor of the mouth, can rarely obstruct the submandibular duct. This can present on CT or MRI as a dilation of one or both ducts. If obstructed, a major clinical complaint is pain and swelling from the affected gland at meal times. The clinical examination may reveal a stone within the duct as it runs forward under the floor-of-mouth mucosa. When anteriorly placed, these can be readily "released" by a small incision.

A problem of OSGDs is that the stasis they produce can be the basis of infection. Such infections are bacterial and if left untreated may develop into abscesses (see Bag et al.'s Figures 8 and 9 [4]). Unless the patient is extremely unwell and dehydrated, when more than one major gland may be affected by ascending infection, such as ascending parotitis, this bacterial infection generally affects only the gland with the obstruction. When the infection becomes chronic, the patient experience repeated painful episodes. This chronicity is reflected in changes to the gland and ducts, with destruction of the acini, reduction in saliva production, dilated irregular ducts, further stone formation in ducts or in the parenchyma, duct strictures, and ultimately fibrosis and gland atrophy (Figure 13.12).

Chronic sialadenitis affecting the parotid gland is common and manifests as recurrent, often painful swellings with pus-tinged thick mucous discharge [53]. Chronic sialadenitis manifests on sialography as dilated irregular ducts (Figure 13.14) and loss of normal saliva production (manifest by reduced or no emptying following removal of the cannula; Figure 13.15). Choi et al. [54] reported a correlation between the grades of inflammation of the sialographic images and the amount of retention of the contrast medium, and between those and the degree of salivation.

According to Ngu et al. [55], many of the 36% of patients reporting the symptoms of OSGD suffered only a single episode. As a result, they do not display any

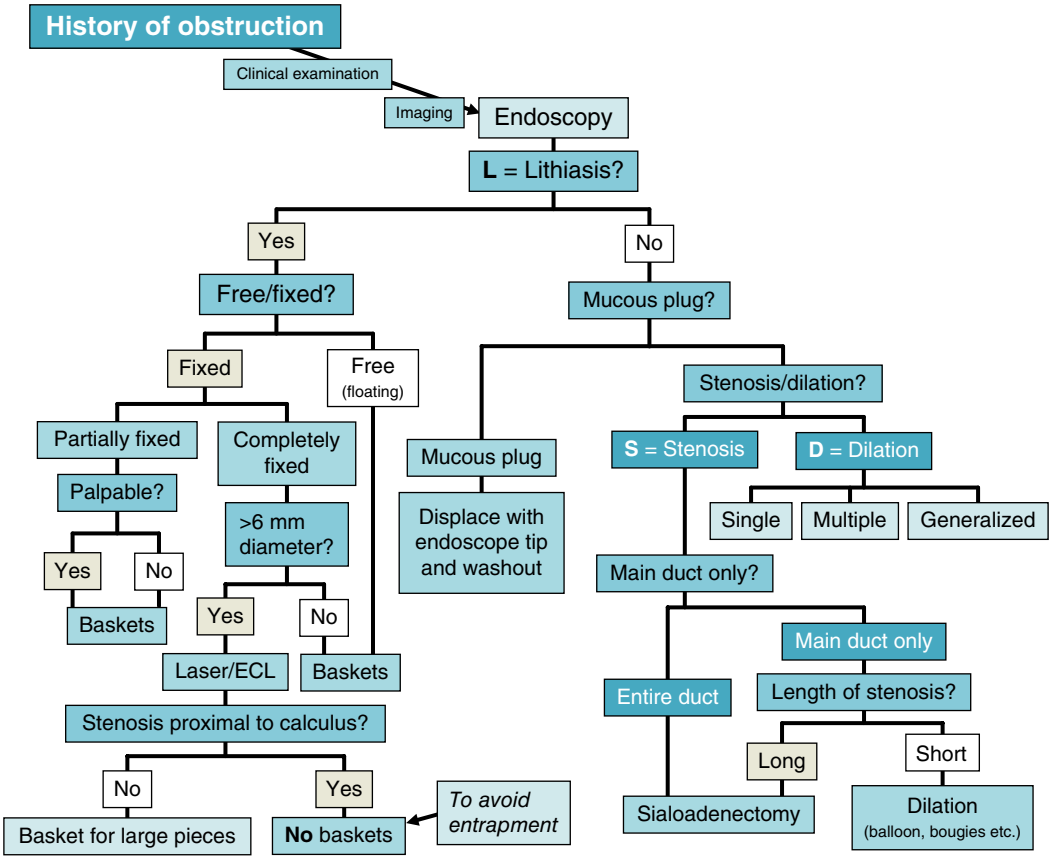


Figure 13.11 Overview of obstructive salivary gland disease – LSD, namely lithiasis, stenosis, and dilation. ECL, external cavity laser. Source: Classification inspired by Marchal, F., Chossegros, C., Faure F. et al. (2008). Salivary stones and stenosis. A comprehensive classification. *Rev. Stomatol. Chir. Maxillofac.* 109: 233–236.

abnormality on sialography, Therefore, Ngu et al. recommend that such cases should be initially investigated by ultrasound in order to avoid unnecessary irradiation [55].

Sialolithiasis accounts for half of the cases of major salivary gland disease. According to Iro et al. [51], it accounts for 60 cases per million of population per year. Its peak occurs early in the fourth decade.

Although calculi are most frequently calcified and visible on conventional radiology and on CT, approximately 40% of calculi in the parotid gland are noncalcified and therefore translucent. They may be visualized only by ultrasound or by sialography as a filling defect (see Figure 13.15).

According to McGurk et al. [56], the submandibular gland is most vulnerable to sialolithiasis. It accounts for 63–94% of calculi, in contrast to the parotid's 6–21%. The sublingual gland is infrequently affected (Table 13.1).

McGurk et al. also report that the average size of submandibular calculi is about 8.5 mm in diameter, in contrast to



Figure 13.12 Parotid sialogram performed with fluoroscopy showing a diffuse stricture of the mid third of the left parotid duct and associated proximal duct dilation, extending into the hilum and several primary intraglandular ducts. There are also sialectatic cavities in the mid and inferior poles of the gland. A filling defect in the dilated duct represents a mucous plug (arrow shows rectangular area between accessory ducts). Source: Courtesy of Dr. Jackie Brown, Senior Lecturer in Dental & Maxillofacial Radiology at King's College London Dental Institute of Guy's, King's College & St Thomas' Hospitals, London, United Kingdom.

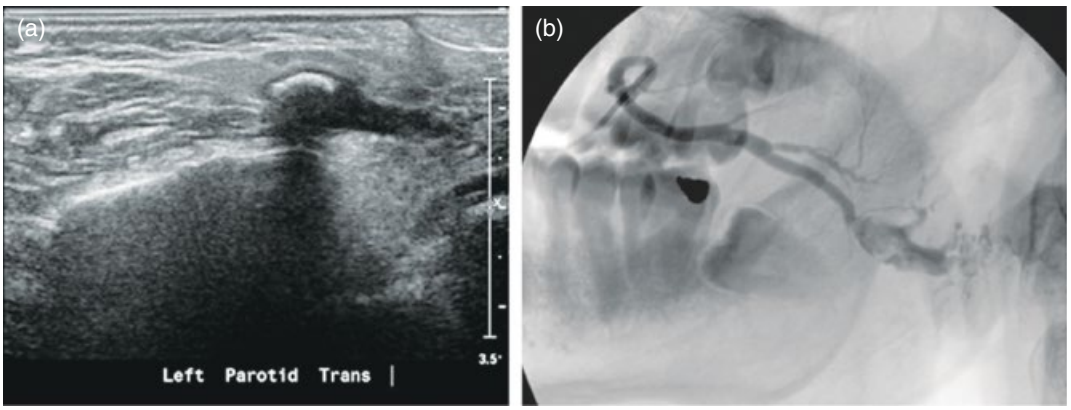


Figure 13.13 (a) Salivary gland ultrasound (SGUS) and (b) sialogram (fluoroscopic) images of a large stone in the hilum of the left parotid gland. Note: The SGUS demonstrates the hyperechoic (white semilunar feature in the superior half of the SGUS) surface of the calculus above the acoustic shadow it cast (the black band below it). A limitation of the SGUS is that although it illustrates the dilated duct (coming from the gland) to the stone (the well-defined horizontal black band), it fails to show the details of the duct extending from the stone to the duct orifice. The sialogram, on the other hand, displays the latter. Source: Courtesy of Dr. Jackie Brown, Senior Lecturer in Dental & Maxillofacial Radiology at King's College London, London, United Kingdom.

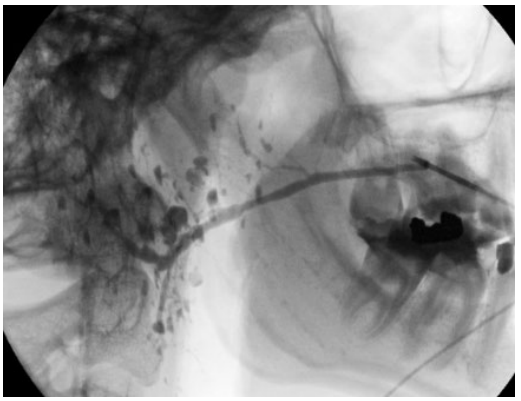


Figure 13.14 Fluoroscopic image of a right parotid gland exhibiting sialectasis secondary to sialadenitis. Source: Courtesy of Dr. Jackie Brown, Consultant in Dental & Maxillofacial Radiology at Guy's & St Thomas' Hospitals Foundation Trust, and Senior Lecturer in Maxillofacial Radiology at King's College London, London, United Kingdom.

6.6 mm for the parotid [56]. They affirm that size influences management. Smaller calculi are more easily eradicated by both lithotripsy and, if mobile, basket extraction.

Traditionally, submandibular calculi lying anteriorly in the duct within the floor of the mouth have, as already mentioned, been released by a simple incision, whereas those more posteriorly placed have frequently necessitated adenectomy (removal of the gland), with its attendant morbidity. The most important cosmetic complications are postsurgical scarring and also trauma to the cervical branch of the VII nerve and its attendant paralysis of the platysma.

Current developments in technology and techniques in minimal invasive management of calculi and stenoses have afforded oral and maxillofacial radiologists a unique opportunity to move from their traditional diagnostic role into direct patient treatment. This was made possible by interventional sialography using wire baskets (Figure 13.16). This has since been joined by sialendoscopy (and microforceps) and lithotripsy. Retrieval of calculi by basket or microforceps, or lithotripsy, is the treatment of choice for those calculi with a diameter of less than 7 mm [50].

A European multicenter report on minimally invasive management of salivary calculi of 4691 patients over 14 years has confirmed its reliability in calculi elimination; 80% of the calculi had been successfully removed, leaving a functionally normal salivary gland [50]. It should be noted that this recovery of function was not to its original level. Nevertheless, only 3% of the gland ultimately had to be removed. Although the remaining 17% of patients retained fragments of calculi, they were free of symptoms. Lithotripsy of the parotid rendered 60% calculus free and relieved a further 30% of their symptoms, even although they still retained fragments.

Two recent systematic reviews [57, 58] which included reports of sialendoscopy alone and reports of sialendoscopy and surgery revealed that sialendoscopy is effective and safe for the diagnosis and treatment of patients with OSGD; the later study [58] was much the larger. Approving of this later systematic review's conclusions, the authoritative European Sialoendoscopy Training Centre (ESTC) commented on the heterogeneity and variation between the many reports of sialendoscopy, which make accurate systematic reviews difficult [59]. It is noteworthy that the ESTC had a few years earlier cautioned that SGUS's limited sensitivity and negative predictive value cannot reliably exclude small calculi [60].

Strictures of the salivary gland, according to Ngu et al. [55], are perhaps more common and more important than

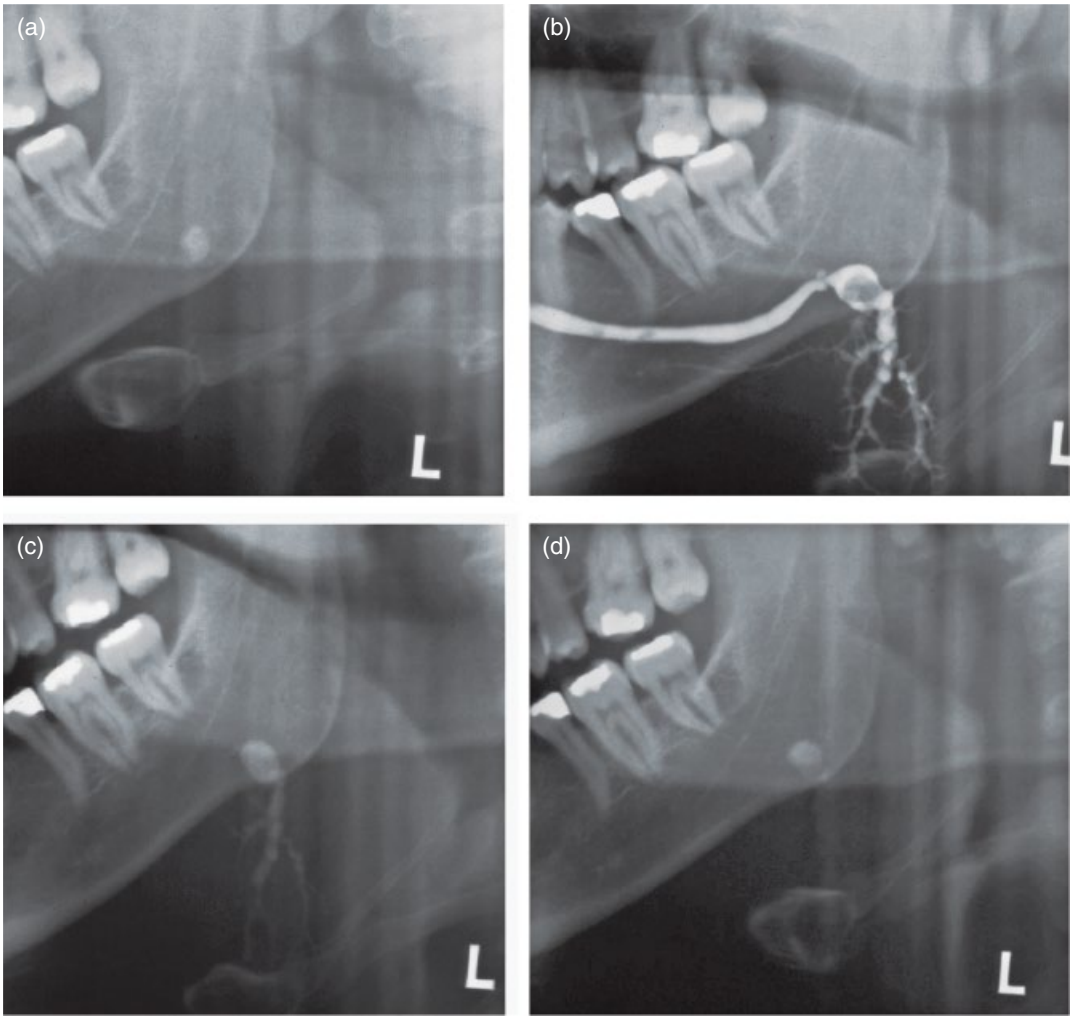


Figure 13.15 Sialogram exhibiting a dilated intraglandular duct system with delayed emptying. (a) Pre-sialogram image displaying a calculus. (b) Sialogram displaying a dilated intraglandular duct system. There is also a dilation within the extraglandular duct, just at the genu at the posterior margin of the myelohyoid muscle. Although the position of this dilation is consistent with the position of the calculus, the central lucency within the dilation suggests that only part of the calculus is calcified. The sialogram also shows a constriction proximal to the dilation. (c) Immediate emptying shows incomplete emptying. (d) Emptying five minutes later shows complete emptying, returning the image to its precontrast state observed in (a). Note 1: This case demonstrates the importance of taking a precontrast image. Note 2: The positions of the hyoid bone, soft palate, and tongue vary markedly between the panoramic radiographs taken on four separate occasions. L, left.

previously perceived. This has also been observed by those using microendoscopy [55]. The reason could be that it can be difficult to distinguish between strictures and calculi on the basis of clinical presentation, though they frequently present with early-morning swellings and bilateral parotid involvement. This phenomenon is

Table 13.1 Percentages of calculi according the gland (submandibular and parotid) and particular site within each gland.[a]

Gland	Percentages	Site	Percentages
Submandibular	85.1	Hilum	48.5
		Duct	29.0
		Gland	7.6
Parotid	15.0	Hilum	1.8
		Duct	3.6
		Gland	9.6
Total	100.1		100.1

[a]Derived from reference, Iro, H., Zenk, J., Escudier, M.P. et al. (2009). Outcome of minimally invasive management of salivary calculi in 4,691 patients. *Laryngoscope* 119: 263–268.

best appreciated by sialography, because it will "simulate the meal-time scenario where copious saliva is produced rapidly." This is not possible with other imaging modalities such as ultrasound, CT, and MRI. Once the stricture has been identified, it can then be dilated by balloons [61].

13.4 Neoplasms

The WHO's 2017 edition of the classification of salivary gland neoplasms identified 11 different benign tumors and 22 malignant tumors which arise from salivary gland epithelium [62]. A few more new malignant salivary gland tumors have been added since the 2005 edition [63] and between 75% and 85% are benign [64]. Salivary gland carcinomas account for 0.5% of all cancers and 6% of those of the head and neck [64]. Most remain symptom free until they achieve substantial dimensions that are clinically noticeable or affect nerves or muscles [65]. It follows that the more common, superficially sited neoplasms will be more clinically obvious. Although the central role of needle biopsy in the definitive differentiation between malignant and benign neoplasms is almost unanimously proclaimed by the literature [65, 66], there are clear supporting roles for advanced imaging modalities. These have been identified in Figure 13.17.

Palpation and MRI were superior to SGUS for prediction of a tumor's location, according to de Ru et al. [66]. It is important to note that the quality of SGUS and its interpretation are very dependent upon the excellence of the equipment and the technical and interpretative abilities of the operator. Furthermore, the use of ultrasound-guided needle biopsies by radiologists with or without input from surgeons is likely to continue to grow, because it is more likely to be more readily available than an MRI, which at best gives predictions as to whether a lesion is benign or malignant [67].

Needle biopsies include *fine needle aspiration biopsy* (FNAB) and *core needle biopsy* (CNB); the former provides a specimen for cytology, whereas the latter delivers a fine core of tissue for histopathological evaluation. Recent reports have advocated in favor of the core needle method [68]. Pratap et al. [68] preferred US-guided CNB because it is very safe (only one case with complications, a subclinical hematoma)

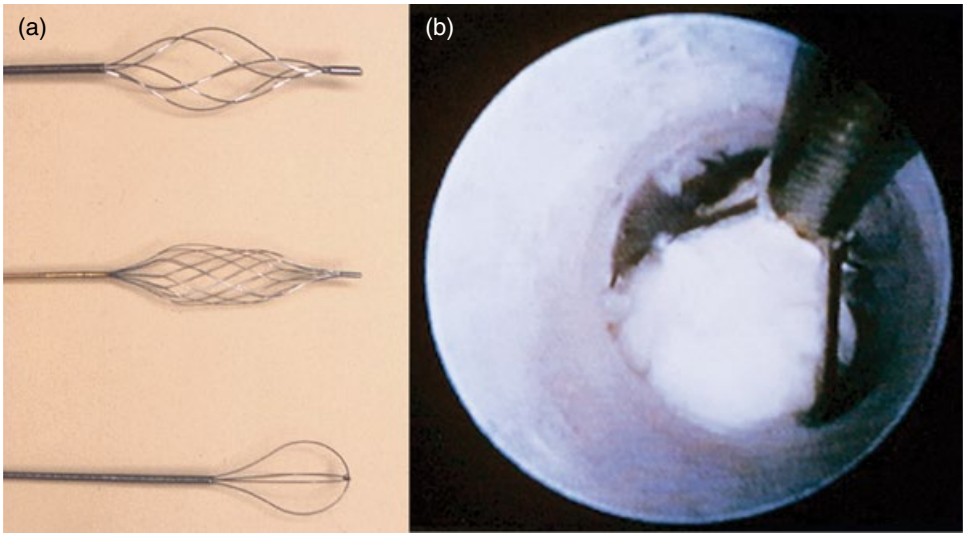


Figure 13.16 Baskets for delivery of calculi from within the salivary gland ducts and sialendoscopy. (a) Three differing styles of Dormia baskets for salivary stone extraction. At the top a 5-wire basket suitable for capturing larger stones; in the middle a finer, 12-wire basket suitable for smaller stones; at the bottom a tipless basket suitable for impacted stones. (b) Image seen down a sialendoscope while capturing a stone in a basket. Source: Reproduced with permission from Brown, J.E. (2006). Interventional sialography and minimally invasive techniques in benign salivary gland obstruction. *Semin. Ultrasound CT MR* 27: 465–475.

and less dependent on cytopathological expertise. They found that only 4% of CNBs were not diagnostic, in contrast to 26% for FNAB cytology. Although Pfeiffer et al. pronounced CNB "a safe and reliable technique in the majority of cases, its risks in the head and neck are not negligible" [69]. This is "due to the proximity of major neurovascular structures and airways" [69]. They "recommend special attention after neck surgery and radiotherapy and when the target is not clearly circumscribed and is close to major vessels" [69].

Breeze et al., using CNB acquired under US guidance [70], cautioned that this is selective sampling and, because the samples are usually taken from the center of the lesion, the capsule is normally absent. This may lead to a wrong diagnosis, because infiltration of the capsule in an otherwise histopathologically benign lesion would have been missed.

Although Naz et al. reportedly found a good concordance between FNAB and histology, *pleomorphic adenoma*, if inadequately aspirated, led to diagnostic difficulty requiring repeat aspiration [71]. They reported that while pleomorphic adenoma (also called pleomorphic salivary adenoma) was the most common benign neoplasm, non-Hodgkin lymphoma was the most frequent malignant neoplasm affecting the salivary glands, rather than the aforementioned tumors of glandular epithelial origin.

The literature is mixed in its reporting of the relative effectiveness of FNAB and MRI. Generally, both are similarly predictive of benign and malignant lesions. Paris et al. reported that both used together reduced false negatives [72]. Nevertheless, recently Kikuchi et al., albeit based on a small sample, advised that diffusion-weighted MRI should be performed first so

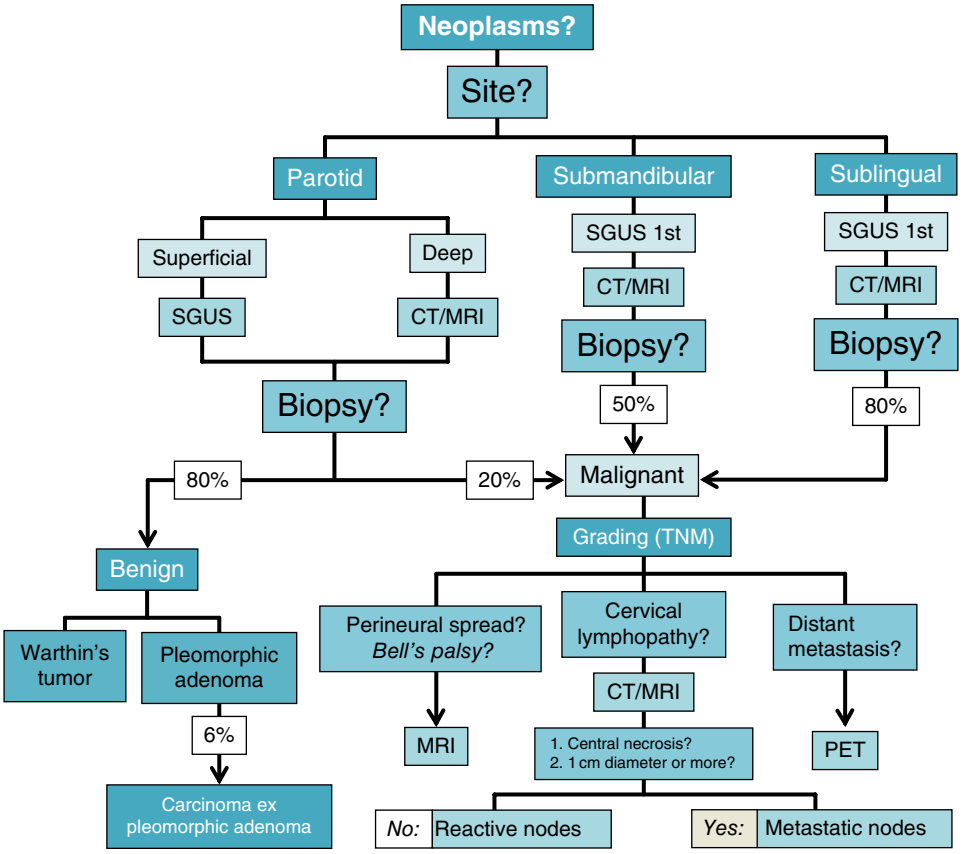


Figure 13.17 Overview of the principal glandular neoplasms and their imaging strategies. CT, computed tomography; MRI, magnetic resonance imaging; PET, positron emission tomography; SGUS, salivary gland ultrasonography. Note: Although several recent authorities advocate the use of diffusion-weighted MRI in addition to the clinical examination to determine between pleomorphic adenoma or Warthin's tumor prior to biopsy, the more widespread availability of SGUS makes it most likely be the advanced imaging modality to be used first.

that the more frequent benign tumors are diagnosed prior to biopsy [73]. Their reasoning was that although CNB has superior sensitivity and a lower rate of sampling error than FNAB, it imparts a higher risk of injury to the structures it transverses, such as the facial nerve [73]. Their rationale is that highly cellular tissues/lesions produce low *apparent diffusion coefficient* (ADC), whereas the myxoid component of the most common salivary gland tumor, the pleomorphic adenoma, is water-molecule rich and has a high ADC [73].

The two most frequent salivary gland neoplasms are the pleomorphic adenoma and the *Warthin tumor*. Another benign neoplasm, the *oncocytoma*, though rare at 4 out of 171 benign parotid tumors, is increasingly being recognized [74]. Before we discuss these three benign tumors, we will briefly overview the malignant tumors of the salivary glands, the most important of which will be addressed in Chapter 19, which is dedicated to malignancies of the head and neck.

Malignant neoplasms of the salivary glands, as stated earlier, account for 25% or less of all salivary gland neoplasms. They are proportionally more frequent in the smaller glands, particularly the minor salivary glands sited in the oral mucosa, and are therefore obvious and accessible to an intraoral approach. Nevertheless, radiology, as set out in Figure 13.16, is required to stage them correctly. Of the 24 malignant salivary gland tumors determined by the WHO over a decade ago, the most frequent is the *mucoepidermoid carcinoma* [63]. Since then other new malignant salivary gland neoplasms have been discovered, such as *mammary analogue secretory carcinoma* [63].

13.4.1 PLEOMORPHIC ADENOMA (ICD-O 8940/0)

Pleomorphic adenoma is the most common salivary gland neoplasm [75]. Bell et al. defined it as "a benign tumour with variable cytomorphological and architectural manifestations. The identification of epithelial and myoepithelial components is essential for the diagnosis." Karyotypical abnormalities are present in 70% of pleomorphic adenomas [75]. Although the mean age is 46 years, the age of first presentation ranges from the first to the tenth decades [75]. Bell et al. note that "Recurrence is low. Complete resection ensures the lowest rate" [75] and that "Multiple recurrences, deep parotid lobe location, male sex and older patient age are associated with increased malignancy" [75].

Formerly, large pleomorphic adenomas were detected as space-occupying lesion defects in sialograms. In modern practice, it may be best to evaluate first by SGUS (Figure 13.18), if available, and more definitively by MRI (see Figures 6.2, 6.4 and 6.5). Although the superficial parotid and other salivary glands are readily accessible to investigation by SGUS and needle biopsy, this is less true for the deep extension into the parotid gland.

Pleomorphic adenomas occur at a rate of 80% in the parotid gland [75], with the remaining 20% distributed through the other major and minor salivary glands of the oral and nasal cavities. While 80% of pleomorphic adenomas develop in the superficial lobe of the parotid gland, they have even been found in upper respiratory and alimentary tracts [75]. Pleomorphic adenomas generally present as a heterogeneously hypoechoic mass on SGUS. The outline is frequently lobulated, and small daughter lesions may be visible and should be identified to the surgeon. Vascularity is described as a "basket-weave" pattern of peripheral vessels, with occasional small internal vessels visible. SGUS has a role in localizing the tumor in relation to the plane of the facial nerve, and in guiding FNAB sampling of accessible lesions. On MRI, a well-circumscribed enhancing intraparotid mass can be seen that is hypointense on T1-weighted images and isointense to hyperintense on T2-weighted images. Tartaglione et al. reported that pleomorphic adenomas are more hyperintense in T2-weighted images and exhibit a lobulated shape. On both CT and MRI, smaller lesions are more homogeneous, with mild to moderate enhancement; the larger lesions are more heterogeneous, with areas of internal cystic change/necrosis (Figure 13.19) [76]. Attyé et al. revealed that "diffusion imaging is an efficient method for highlighting the intraparotid facial nerve" [77]. Nevertheless, Liu et al. warned of transient signal loss on some diffusion weighted imaging of the parotid gland [78]. This, and an overestimation of ADC, could be partially offset by increasing the number of excitations.

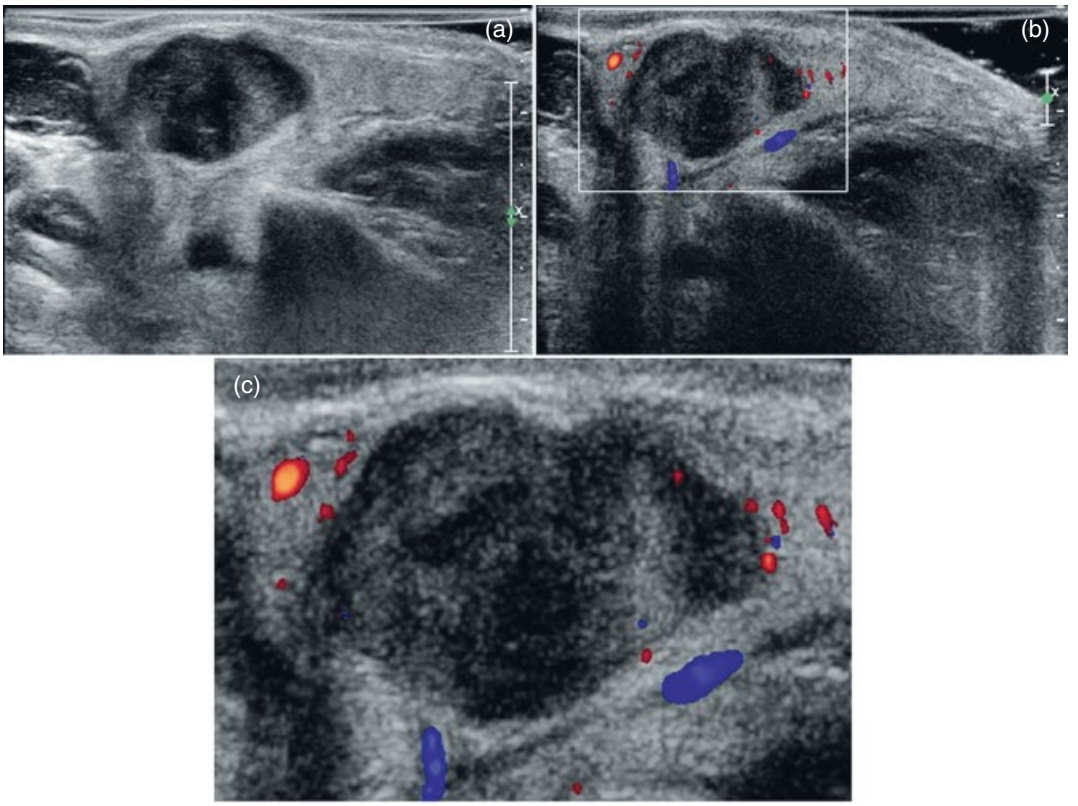


Figure 13.18 (a) Grayscale and (b) color Doppler ultrasound images showing the ultrasound appearances of a pleomorphic adenoma in the superficial parotid gland. (a) Reveals the heterogeneous internal structure of this well-defined lesion. (c) A blow-up of the box in (b) reveals the distribution of blood vessels at the periphery of the tumor. Source: Courtesy of Dr. Jackie Brown. Senior Lecturer in Dental & Maxillofacial Radiology at King's College London, London, United Kingdom.

Features associated with a recurrent pleomorphic adenoma include a multilobular outline, a much younger age of first presentation (namely a mean age of 33–35 years in comparison to 45–50 years), and a tendency to occur in females. The most important cause of recurrence is enucleation, with rupture and incomplete tumor excision at operation. Furthermore, an incomplete pseudocapsule, tumor extension, or the presence of islands of pleomorphic adenoma beyond the capsule is linked to recurrence. MRI is the imaging study of choice for recurrent pleomorphic adenomas. Although Witt et al. state that MRI is the optimal modality for imaging recurrent pleomorphic adenomas, MRI frequently misses many lobules of the initial multilobular pleomorphic adenoma [79].

Williams et al. defined *carcinoma ex pleomorphic adenoma* (Ca-ex-PA; ICD-O 8941/3) as "an epithelial and/or myoepithelial malignancy developing from primary or recurrent pleomorphic adenoma. The carcinoma component can be either purely epithelial or myoepithelial in presentation with infiltration into the surrounding glandular tissue and extraglandular tissue" [80]. It accounts for 3.6% of all salivary gland tumors [80].

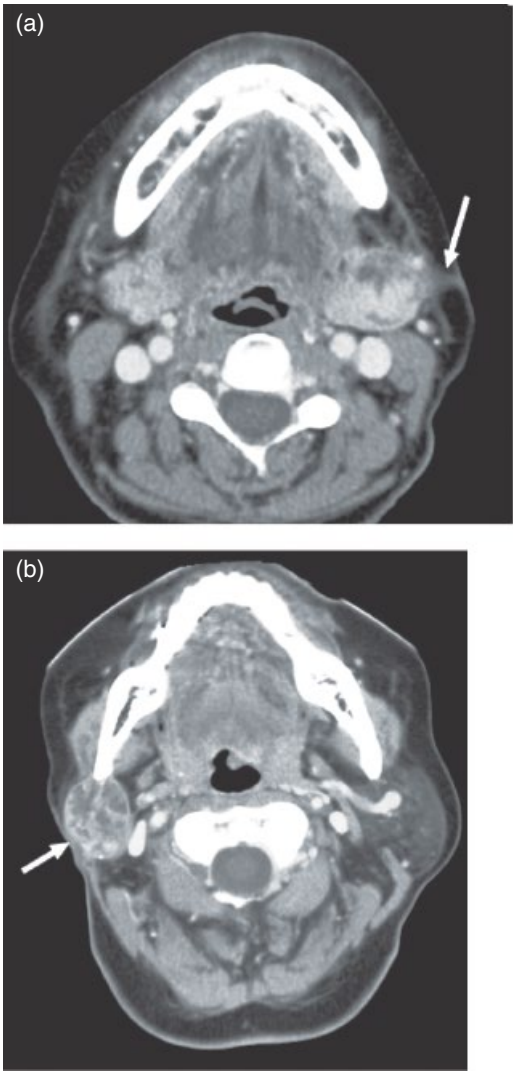


Figure 13.19 Computed tomography (CT) of parotid pleomorphic adenoma. (a) Axial postgadolinium CT showing a pleomorphic adenoma arising in the left submandibular gland. The tumor is well circumscribed with a heterogeneous internal appearance. Note the biopsy tract (arrow). (b) Axial postgadolinium CT showing recurrent pleomorphic adenoma arising in a post right parotidectomy surgical bed. Note the similar internal architecture to (a) (arrow).

Be aware of rapidly growing swelling, particularly when associated with a preexisting swelling. Although generally pain free, pain may accompany this growth. The ca-ex-PA is an aggressive malignancy, with local or distant metastasis occurring in as many as 70% of cases [81]. Five-year survival ranges from 25% to 65% of cases. The best survival is associated with purely intraglandular or minimal-invasion cases [81].

In addition to Ca-ex-PA, there is another related malignant lesion, the *metastasizing pleomorphic adenoma* (MPA; ICD-O 8940/1) [75], which is histologically a benign pleomorphic adenoma. It has been suggested that multiple recurrences and surgical procedures may seed pleomorphic adenoma cells into the venous circulation, with subsequent metastasis. Bell et al. reported that "The most common distant site is bone, followed by head and neck and lung" [75]. Although MPAs generally occur 15 years after the initial presentation and are associated with multiple recurrences, a few have presented at the same time as the first pleomorphic adenoma [81]. Although the mean age is 50 years, some can first present in the early teens. According to Bell et al., "The prognosis of most histologically benign tumors is generally good" [75].

Pleomorphic adenomas on MRI generally present as a well-circumscribed enhancing intraparotid mass that is hypointense on T1-weighted images and isointense to hyperintense on T2-weighted images.

13.4.2 WARTHIN TUMOR (ICD-O 8561/0)

The WHO's 2017 edition's definition is: "Warthin tumour is a benign salivary gland tumour composed of oncocystic epithelial cell lining ductal, papillary and cystic structures in a lymphoid stroma." A slowly growing tumor that usually presents as a painless mass just above the

angle of the mandible, it is the second most common tumor of the parotid gland after pleomorphic adenomas. It is a benign epithelial tumor composed of glandular and cystic elements. Its stroma has lymphoid tissue with germinal centers [82]. This lesion is also called *papillary cystadenoma lymphomatosum*. Unlike the pleomorphic adenoma, it exhibits no tendency for malignant transformation.

The most recent case series of Warthin tumor in a New Zealand community [83], since 2000, reported that of the 41 cases, 31%, 25%, and 20% occurred in those of European, Polynesian, and East Asian origin, respectively. Although these percentages did not differ for other benign parotid tumors in the same study, it would appear that Polynesians and East Asians in this community are more at risk of acquiring a Warthin tumor. Furthermore, three recent East Asian case series reveal that Warthin tumor, though still the second most prevalent benign parotid tumor, is marginally only in second place to pleomorphic adenomas [84, 85]; only Li et al.'s report placed Warthin tumor in its usual clear second position [86], where it accounted for 23% of all benign parotid tumors. Proportionally, Warthin's tumor in sub-Saharan Africans may be as infrequent as 1 in every 40 pleomorphic adenomas [87]. Historically, Warthin tumor patients have a history of smoking; 78% of recent patients were smokers [88]. Although Patel et al.'s more recent report found a reduced 70% association between Warthin's tumor patents and smoking, this was still significantly higher than the 37% of smokers for the other benign parotid tumors [83]. The peak incidence lies between the fifth and sixth decades of life; the mean is 57 years [88]. Warthin tumor presented significantly older, with a 60 years mean age, in comparison to other benign parotid tumors' 48 years mean age [83].

Although the traditional view that Warthin tumor is the most common salivary tumor to present bilaterally has been recently upheld by Patel et al.'s 27% in New Zealanders [83], the rarer oncocytoma may actually present more frequently bilaterally and multifocally in at least one case series [89].

Warthin tumors are found significantly more in the inferior pole of the parotid gland 86% [83]. They can grow by on average 8% per year [90], doubling every nine years. Nevertheless, they have been known to fluctuate in size and even shrink.

On CT or MRI, these lesions are well encapsulated and mildly enhanced using standard contrast injection protocols. The average size at clinical discovery was 4 cm [89]. The smallest lesions are predominantly solid; as they enlarge they become inhomogeneous and cystic, due to epithelial-lined spaces that contain numerous papillary fronds (Figure 13.18) [91]. On MRI, these lesions exhibit hypointense T1-weighted and heterogeneous hyperintense T2-weighted signals. The lesions are unicystic, hypoechoic, can appear septated on ultrasound, and frequently demonstrate strong internal vascularity. Ultrasound-guided FNAB again plays an important role in definitive diagnosis. The ultrasound, MRI, and CT images of one case are compared in Figure 13.20.

The incidence rate of *autoimmune thyroiditis* in Orabona et al.'s series (9.5%) was significantly greater than that of the general population (0.58%; $p < 0.001$) [92]. Analysis of their series and their review of the literature suggests that the Warthin tumor arises from an autoimmune reaction. The authors suggest that further studies are needed to confirm this hypothesis [92].

Bell et al. stated that "malignant transformation in Warthin tumor is extremely rare; however, there are a few reported examples in both the epithelial and lymphoid component" [75].

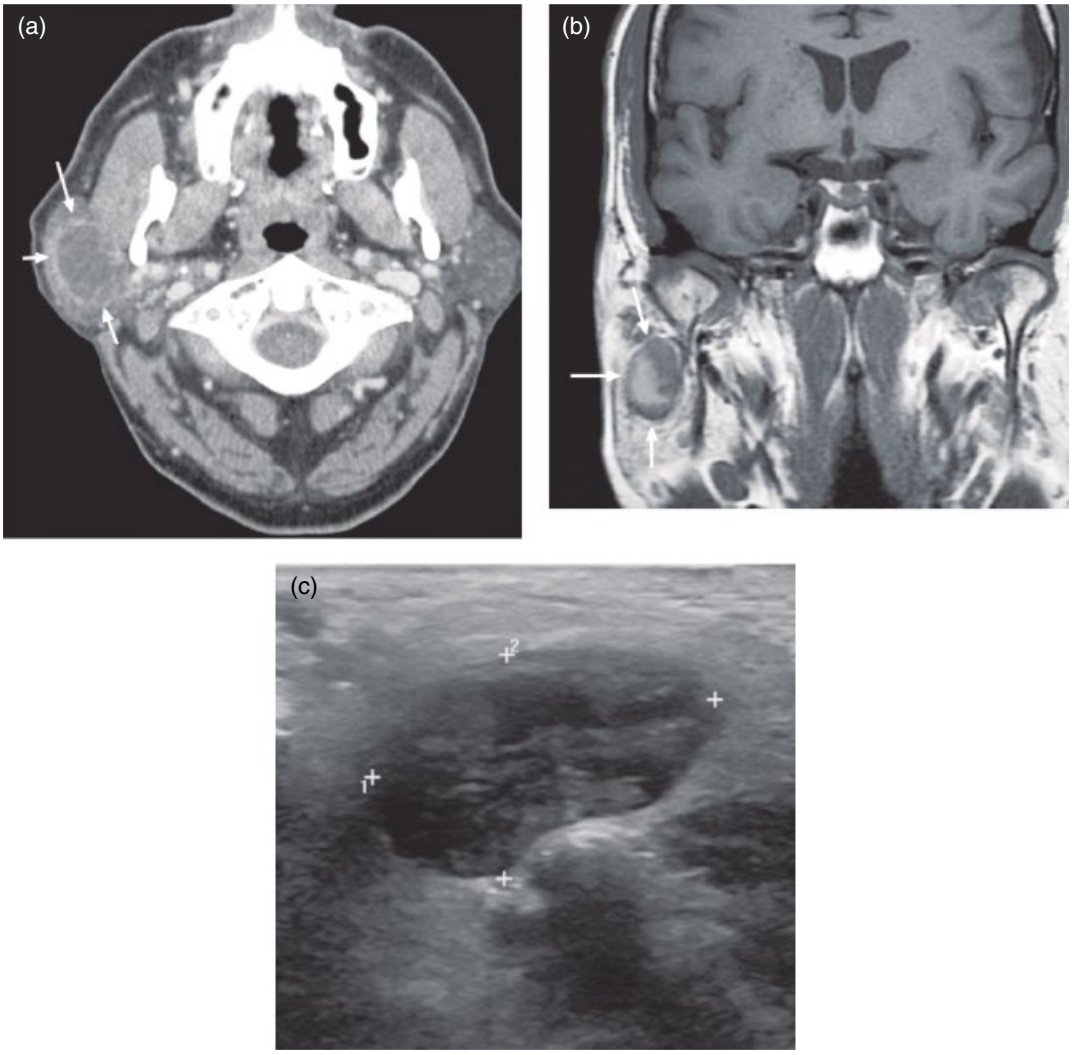


Figure 13.20 Computed tomography (CT), magnetic resonance imaging (MRI), and ultrasound of Warthin's tumor. (a) Axial postgadolinium T1-weighted CT of Warthin's tumor in the right parotid gland (arrows). This is an intermediate-size Warthin's tumor and already exhibits moderate internal low density compatible with cystic change. (b) Coronal postgadolinium T1-weighted MRI of the same patient showing a heterogeneous, well-circumscribed right parotid mass (arrows), consistent with the pathologically proven diagnosis of Warthin's tumor. (c) Ultrasound image of the same tumor. The hypoechoic (dark) areas are consistent with cystic change within the otherwise solid tumor. Source: Courtesy of Dr. Sven Aippersbach and Dr. Montgomery Martin, Vancouver.

13.4.3 ONCOCYTOMA (ICD-O 8290/0)

The WHO's 2017 edition defined that "oncocytoma is a benign salivary gland tumour composed predominantly of oncocytes, which are large epithelial cells with eosinophilic granular cytoplasm resulting from the accumulation of mitochondria" [93]. It accounted for 2% of all salivary gland tumors [93]. A small case series revealed a relative period prevalence of

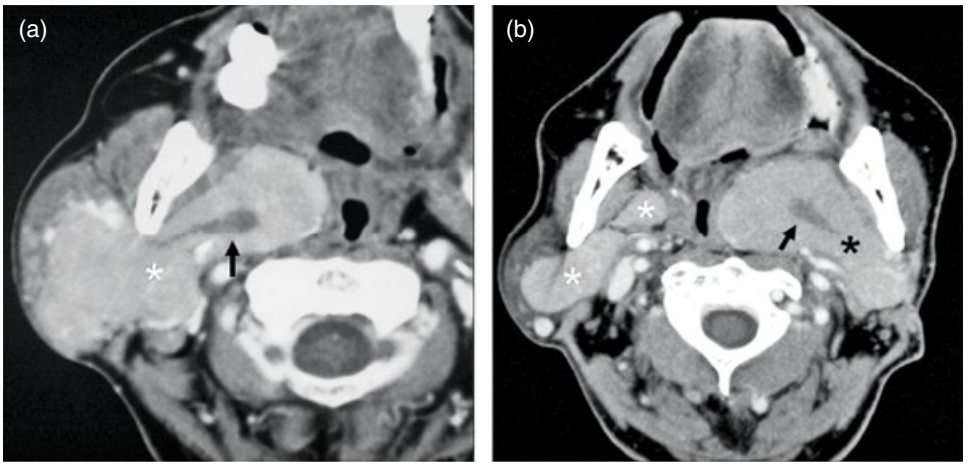


Figure 13.21 Contrast-enhanced computed tomography of two cases of oncocytomas in the parotid glands of elderly patients. Each displays a nonenhancing curvilinear cleft (arrow). (a) The large tumor (asterisk) extends medially through the right stylomandibular gap into the parapharyngeal space. (b) The white asterisks demonstrate synchronous bilateral parotid oncocytomas in the right parotid gland. They exhibit homogeneous enhancement. The black asterisk indicates a large left parotid tumor. Source: Reproduced with permission from Tan, T.J. and Tan, T.Y. (2010). CT features of parotid gland oncocytomas: a study of 10 cases and literature review. *AJNR Am. J. Neuroradiol.* 31: 1413–1417.

0.5 lesions a year for an East Asian institution. It was twice as frequent in females and has a mean age of 61 years [89]. Half of the lesions were both bilateral and multifocal and affected both superficial and deep lobes. The unilateral and solitary cases were confined to the superficial lobe.

The principal CT feature of parotid gland oncocytomas is a well-defined margin [89]. The contour was either smooth or lobulated and the enhancement homogeneous or heterogeneous. More than half of Tan and Tan's case series included a nonenhancing curvilinear cleft (see Figure 13.21) or a cystic component [89]. SGUS agrees with this, demonstrating heterogeneous appearances within a well-defined hypoechoic, unicystic mass.

Katabi and Assaad stated that though true recurrence after excision is rare, additional oncocytomas may arise within the residual parotid gland [93].

References

1. Javaid, M.A., Ahmed, A.S., Durand, R., and Tran, S.D. (2016). Saliva as a diagnostic tool for oral and systemic diseases. *J. Oral Biol. Craniofac. Res.* 6: 66–75.
2. Afzelius, P., Nielsen, M.Y., Ewertsen, C., and Bloch, K.P. (2016). Imaging of the major salivary glands. *Clin. Physiol. Funct. Imaging* 36: 1–10.
3. Sanan, A. and Cognetti, D.M. (2016). Rare parotid gland diseases. *Otolaryngol. Clin. N. Am.* 49: 489–500.
4. Bag, A.K., Curé, J.K., Chapman, P.R. et al. (2015). Practical imaging of the parotid gland. *Curr. Probl. Diagn. Radiol.* 44: 167–192.
5. Kelly, T.G., Faulkes, S.V., Pierre, S.K. et al. (2015). Imaging submandibular pathology in the paediatric patient. *Clin. Radiol.* 70: 774–786.
6. Saleh, J., Figueiredo, M.A., Cherubini, K., and Salum, F.G. (2015). Salivary hypofunction: an update on aetiology, diagnosis and therapeutics. *Arch. Oral Biol.* 60: 242–255.

7. Theander, E. and Jacobsson, L.T. (2008). Relationship of Sjögren's syndrome to other connective tissue and autoimmune disorders. *Rheum. Dis. Clin. N. Am.* 34: 935–947.
8. Rasmussen, A., Ice, J.A., Li, H. et al. (2014). Comparison of the American-European consensus group Sjogren's syndrome classification criteria to newly proposed American College of Rheumatology criteria in a large, carefully characterised sicca cohort. *Ann. Rheum. Dis.* 73: 31–38.
9. Poul, J.H., Brown, J.E., and Davies, J. (2008). Retrospective study of the effectiveness of high resolution ultrasound compared with sialography in the diagnosis of Sjogren's syndrome. *Dentomaxillofac. Radiol.* 37: 392–397.
10. Jousse-Joulin, S., Milic, V., Jonsson, M.V. et al. (2016). Is salivary gland ultrasonography a useful tool in Sjögren's syndrome? A systematic review. *Rheumatology (Oxford)* 55: 789–800.
11. Baldini, C., Luciano, N., Tarantini, G. et al. (2015). Salivary gland ultrasonography: a highly specific tool for the early diagnosis of primary Sjögren's syndrome. *Arthritis Res. Ther.* 28: 146.
12. Fox, R.I. (2016). Is salivary gland ultrasonography a useful tool in Sjogren's syndrome? *Rheumatology (Oxford)* 55: 773–774.
13. Kinoshita, T., Ishii, K., Naganuma, H., and Okitsu, T. (2004). MR imaging findings of parotid tumors with pathologic diagnostic clues: a pictorial essay. *Clin. Imaging* 28: 93–101.
14. Morimoto, Y., Habu, M., Tomoyose, T. et al. (2006). Dynamic magnetic resonance sialography as a new diagnostic technique for patients with Sjogren's syndrome. *Oral Dis.* 12: 408–414.
15. Morimoto, Y., Ono, K., Tanaka, T. et al. (2005). The functional evaluation of salivary glands using dynamic MR sialography following citric acid stimulation: a preliminary study. *Oral Surg. Oral Med. Oral Pathol. Oral Radiol. Endod.* 100: 357–364.
16. Ono, K., Morimoto, Y., Inoue, H. et al. (2006). Relationship of the unstimulated whole saliva flow rate and salivary gland size estimated by magnetic resonance image in healthy young humans. *Arch. Oral Biol.* 51: 345–349.
17. Morgen, K., McFarland, H.F., and Pillemer, S.R. (2004). Central nervous system disease in primary Sjogrens syndrome: the role of magnetic resonance imaging. *Semin. Arthritis Rheum.* 34: 623–630.
18. Ding, C., Xing, X., Guo, Q. et al. (2016). Diffusion-weighted MRI findings in Sjögren's syndrome: a preliminary study. *Acta Radiol.* 57: 691–700.
19. Ciurtin, C., Ostas, A., Cojocaru, V.M. et al. (2015). Advances in the treatment of ocular dryness associated with Sjögren's syndrome. *Semin. Arthritis Rheum.* 45: 321–327.
20. Qiao, L., Wang, Q., Fei, Y. et al. (2015). The clinical characteristics of primary Sjogren's syndrome with neuromyelitis optica spectrum disorder in China: a STROBE-compliant article. *Medicine (Baltimore)* 94: e1145. https://doi.org/10.1097/MD.0000000000001145.
21. Greaves, W.O. and Wang, S.A. (2011). Selected topics on lymphoid lesions in the head and neck regions. *Head Neck Pathol.* 5: 41–50.
22. Fujita, A., Sakai, O., Chapman, M.N., and Sugimoto, H. (2012). IgG4-related disease of the head and neck: CT and MR imaging manifestations. *Radiographics* 32: 1945–1958.
23. Kamisawa, T., Zen, Y., Pillai, S., and Stone, J.H. (2015). IgG4-related disease. *Lancet* 385: 1460–1471.
24. Ghably, J.G., Borthwick, T., O'Neil, T.J. et al. (2015). IgG4-related disease: a primer on diagnosis and management. *Ann. Allergy Asthma Immunol.* 114: 447–454.
25. Vasaitis, L. (2016). IgG4-related disease: a relatively new concept for clinicians. *Eur. J. Intern. Med.* 27: 1–9.
26. Li, W., Chen, Y., Sun, Z.P. et al. (2015). Clinicopathological characteristics of immunoglobulin G4-related sialadenitis. *Arthritis Res. Ther.* 17: 186. https://doi.org/10.1186/s13075-015-0698-y.
27. Shimizu, M., Okamura, K., Kise, Y. et al. (2015). Effectiveness of imaging modalities for screening IgG4-related dacryoadenitis and sialadenitis (Mikulicz's disease) and for differentiating it from Sjögren's syndrome (SS), with an emphasis on sonography. *Arthritis Res. Ther.* 17: 223.
28. Acauan, M.D., Figueiredo, M.A., Cherubini, K. et al. (2015). Radiotherapy-induced salivary dysfunction: structural changes, pathogenetic

mechanisms and therapies. *Arch. Oral Biol.* 60: 1802–1810.
29. Wu, C.B., Xi, H., Zhou, Q., and Zhang, L.M. (2015). Sialendoscopy-assisted treatment for radioiodine-induced sialadenitis. *J. Oral Maxillofac. Surg.* 73: 475–481.
30. Mandel, L. (2014). Salivary gland disorders. *Med. Clin. North Am.* 98: 1407–1449.
31. Choi, J.S., Lim, H.G., Kim, Y.M. et al. (2015). Usefulness of magnetic resonance sialography for the evaluation of radioactive iodine-induced sialadenitis. *Ann. Surg. Oncol.* 22 (Suppl 3): 1007–1013.
32. Ungprasert, P., Crowson, C.S., and Matteson, E.L. (2016). Clinical characteristics of parotid gland sarcoidosis: a population-based study. *JAMA Otolaryngol. Head Neck Surg.* 142: 503–504.
33. Lowe, J., Whatley, B., Kashani, S., and Howlett, D. (2015). A 22 year old woman with bilateral panuveitis and parotid swelling. *BMJ* 351: h4178. https://doi.org/10.1136/bmj.h4178.
34. Patton, L.L. (2013). Oral lesions associated with human immunodeficiency virus disease. *Dent. Clin. N. Am.* 57: 673–698.
35. Sujatha, D., Babitha, K., Prasad, R.S., and Pai, A. (2013). Parotid lymphoepithelial cysts in human immunodeficiency virus: a review. *J. Laryngol. Otol.* 127: 1046–1049.
36. Sabbe, M. and Vandermeulen, C. (2016). The resurgence of mumps and pertussis. *Hum Vaccin Immunother* 12: 955–959.
37. Park, S.H. (2015). Resurgence of mumps in Korea. *Infect Chemother.* 47: 1–11.
38. Zamir, C.S., Schroeder, H., Shoob, H. et al. (2015). Characteristics of large mumps outbreak: clinical severity, complications and association with vaccination status of mumps outbreak cases. *Hum. Vaccin. Immunother.* 11: 1413–1417.
39. Barskey, A.E., Schulte, C., Rosen, J.B. et al. (2012). Mumps outbreak in Orthodox Jewish communities in the United States. *N. Engl. J. Med.* 367: 1704–1713.
40. Kenny, L., O'Kelly, E., Connell, J. et al. (2016). Mumps outbreaks in a highly vaccinated population: investigation of a neutralization titre against the current circulating wildtype genotype G5 mumps virus. *J. Clin. Virol.* 74: 8–12.
41. Zhang, G., Li, Y., Zhang, R. et al. (2015). Acute submandibular swelling complicating arteriography with iodide contrast: a case report and literature review. *Medicine (Baltimore)* 94: e1380.
42. Gritzmann, N., Rettenbacher, T., Hollerweger, A. et al. (2003). Sonography of the salivary glands. *Eur. Radiol.* 13: 964–975.
43. Senanayake, S.N. (2008). Mumps: a resurgent disease with protean manifestations. *Med. J. Aust.* 189: 456–459.
44. Roby, B.B., Mattingly, J., Jensen, E.L. et al. (2015). Treatment of juvenile recurrent parotitis of childhood: an analysis of effectiveness. *JAMA Otolaryngol. Head Neck Surg.* 141: 126–129.
45. Xie, L.S., Pu, Y.P., Zheng, L.Y. et al. (2016). Function of the parotid gland in juvenile recurrent parotitis: a case series. *Br. J. Oral Maxillofac. Surg.* 54: 270–274.
46. Ramakrishna, J., Strychowsky, J., Gupta, M., and Sommer, D.D. (2015). Sialendoscopy for the management of juvenile recurrent parotitis: a systematic review and meta-analysis. *Laryngoscope* 125: 1472–1479.
47. Schneider, H., Koch, M., Künzel, J. et al. (2014). Juvenile recurrent parotitis: a retrospective comparison of sialendoscopy versus conservative therapy. *Laryngoscope* 124: 451–455.
48. Brown, J.E. (2006). Interventional sialography and minimally invasive techniques in benign salivary gland obstruction. *Semin. Ultrasound CT MR* 27: 465–475.
49. Capaccio, P., Torretta, S., Ottavian, F. et al. (2007). Modern management of obstructive salivary diseases. *Acta Otorhinolaryngol. Ital.* 27: 161–172.
50. Drage, N.A., Brown, J.E., Escudier, M.P., and McGurk, M. (2000). Interventional radiology in the removal of salivary calculi. *Radiology* 214: 139–142.
51. Iro, H., Zenk, J., Escudier, M.P. et al. (2009). Outcome of minimally invasive management of salivary calculi in 4,691 patients. *Laryngoscope* 119: 263–268.
52. Marchal, F., Chossegros, C., Faure, F. et al. (2008). Salivary stones and stenosis. A comprehensive classification. *Rev. Stomatol. Chir. Maxillofac.* 109: 233–236.
53. Wang, S., Marchal, F., Zou, Z. et al. (2009). Classification and management of chronic sialadenitis of the parotid gland. *J. Oral Rehabil.* 36: 2–8.
54. Choi, J.W., Lee, S.S., Huh, K.H. et al. (2009). The relationship between sialographic

images and clinical symptoms of inflammatory parotid gland diseases. *Oral Surg. Oral Med. Oral Pathol. Oral Radiol. Endod.* 107: e49–e56.
55. Ngu, R.K., Brown, J.E., Whaites, E.J. et al. (2007). Salivary duct strictures: nature and incidence in benign salivary obstruction. *Dentomaxillofac. Radiol.* 36: 63–67.
56. McGurk, M., Escudier, M.P., Thomas, B.L., and Brown, J.E. (2006). A revolution in the management of obstructive salivary gland disease. *Dent. Update* 33: 28–30. 33–36. Erratum in *Dent Update* 2006;33:83.
57. Strychowsky, J.E., Sommer, D.D., Gupta, M.K. et al. (2012). Sialendoscopy for the management of obstructive salivary gland disease: a systematic review and meta-analysis. *Arch. Otolaryngol. Head Neck Surg.* 138: 541–547.
58. Atienza, G. and López-Cedrún, J.L. (2015). Management of obstructive salivary disorders by sialendoscopy: a systematic review. *Br. J. Oral Maxillofac. Surg.* 53: 507–519.
59. Pezier, T.F., Prasad, S., and Marchal, F. (2016). Towards an international database of benign salivary disease: RE: management of obstructive salivary disorders by sialendoscopy: a systematic review. *Br. J. Oral Maxillofac. Surg.* 54: 968–969.
60. Terraz, S., Poletti, P.A., Dulguerov, P. et al. (2013). How reliable is sonography in the assessment of sialolithiasis? *AJR Am. J. Roentgenol.* 201: W104–W109.
61. Drage, N.A., Brown, J.E., Escudier, M.P. et al. (2002). Balloon dilatation of salivary duct strictures: report on 36 treated glands. *Cardiovasc. Intervent. Radiol.* 25: 356–359.
62. El-Naggar, A.K., JKC, C., Grandis, J.R. et al. (eds.) (2017). *WHO Classification of Head and Neck Tumours*, 159–202. Lyon: International Agency for Research on Cancer (IARC).
63. Yin, L.X. and Ha, P.K. (2016). Genetic alterations in salivary gland cancers. *Cancer* 122: 1822–1831.
64. Seethala, R.R. (2017). Salivary gland tumors: current concepts and controversies. *Surg. Pathol. Clin.* 10: 155–176.
65. Liu, Y., Li, J., Tan, Y.R. et al. (2015). Accuracy of diagnosis of salivary gland tumors with the use of ultrasonography, computed tomography, and magnetic resonance imaging: a meta-analysis. *Oral Surg. Oral Med. Oral Pathol. Oral Radiol.* 119: 238–245. e2.
66. de Ru, J.A., van Leeuwen, M.S., van Benthem, P.P. et al. (2007). Do magnetic resonance imaging and ultrasound add anything to the preoperative workup of parotid gland tumors? *J. Oral Maxillofac. Surg.* 65: 945–952.
67. Inohara, H., Akahani, S., Yamamoto, Y. et al. (2008). The role of fine-needle aspiration cytology and magnetic resonance imaging in the management of parotid mass lesions. *Acta Otolaryngol.* 128: 1152–1158.
68. Pratap, R., Qayyum, A., Ahmed, N. et al. (2008). Ultrasound-guided core needle biopsy of parotid gland swellings. *J. Laryngol. Otol.* 122: 1–4.
69. Pfeiffer, J. and Ridder, G.J. (2010). How safe is the use of ultrasound-guided cutting needle biopsy in the head and neck? *Eur. Radiol.* 20: 2933–2938.
70. Breeze, J., Andi, A., Williams, M.D., and Howlett, D.C. (2009). The use of fine needle core biopsy under ultrasound guidance in the diagnosis of a parotid mass. *Br. J. Oral Maxillofac. Surg.* 47: 78–79.
71. Naz, S., Hashmi, A.A., Khurshid, A. et al. (2015). Diagnostic role of fine needle aspiration cytology (FNAC) in the evaluation of salivary gland swelling: an institutional experience. *BMC Res. Notes* 8: 101. https://doi.org/10.1186/s13104-015-1048-5.
72. Paris, J., Facon, F., Pascal, T. et al. (2005). Preoperative diagnostic values of fine-needle cytology and MRI in parotid gland tumors. *Eur. Arch. Otorhinolaryngol.* 262: 27–31.
73. Kikuchi, M., Koyasu, S., Shinohara, S. et al. (2016). Preoperative diagnostic strategy for parotid gland tumors using diffusion-weighted MRI and technetium-99m pertechnetate scintigraphy: a prospective study. *PLoS ONE* 11 (2): e0148973.
74. Wu, S., Liu, G., Chen, R., and Guan, Y. (2012). Role of ultrasound in the assessment of benignity and malignancy of parotid masses. *Dentomaxillofac. Radiol.* 41: 131–135.
75. Bell, D., Bullerdiek, J., Gnepp, D.R. et al. (2017). Pleomorphic adenoma. In: *WHO Classification of Head and Neck Tumours* (ed. A.K. El-Naggar, C. JKC, J.R. Grandis, et al.), 159–202. Lyon: International Agency for Research on Cancer (IARC).

76. Tartaglione, T., Botto, A., Sciandra, M. et al. (2015). Differential diagnosis of parotid gland tumours: which magnetic resonance findings should be taken in account? *Acta Otorhinolaryngol. Ital.* 35: 314–320.
77. Attyé, A., Karkas, A., Troprès, I. et al. (2016). Parotid gland tumours: MR tractography to assess contact with the facial nerve. *Eur. Radiol.* 26: 2233–2241.
78. Liu, Y.J., Lee, Y.H., Chang, H.C. et al. (2015). A potential risk of overestimating apparent diffusion coefficient in parotid glands. *PLoS One* 10: e0124118.
79. Witt, R.L., Eisele, D.W., Morton, R.P. et al. (2015). Etiology and management of recurrent parotid pleomorphic adenoma. *Laryngoscope* 125: 888–893.
80. Williams, M.D., Ihrier, S., and Seethala, R. (2017). Carcinoma expleomorphic adenoma. In: *WHO Classification of Head and Neck Tumours* (ed. A.K. El-Naggar, C. JKC, J.R. Grandis, et al.), 175–176. Lyon: International Agency for Research on Cancer (IARC).
81. Knight, J. and Ratnasingham, K. (2015). Metastasising pleomorphic adenoma: systematic review. *Int. J. Surg.* 19: 137–145.
82. Nagao, T., Gnepp, D.R., RHW, S., and Vielh, P. (2017). Warthin tumour. In: *WHO Classification of Head and Neck Tumours* (ed. A.K. El-Naggar, C. JKC, J.R. Grandis, et al.), 188–189. Lyon: International Agency for Research on Cancer (IARC).
83. Patel, D.K. and Morton, R.P. (2016). Demographics of benign parotid tumours: Warthin's tumour versus other benign salivary tumours. *Acta Otolaryngol.* 136: 83–86.
84. Rong, X., Zhu, Q., Ji, H. et al. (2014). Differentiation of pleomorphic adenoma and Warthin's tumor of the parotid gland: ultrasonographic features. *Acta Radiol.* 55: 1203–1209.
85. Miao, L.Y., Xue, H., Ge, H.Y. et al. (2015). Differentiation of pleomorphic adenoma and Warthin's tumour of the salivary gland: is long-to-short diameter ratio a useful parameter? *Clin. Radiol.* 70: 1212–1219.
86. Li, J.J., Zhang, G.H., Liu, X. et al. (2013). Retrospective review of 190 patients treated for parotid tumors: a single institute experience. *Chin. Med. J.* 126 (5): 988–990.
87. Somefun, O.A., Oyeneyin, J.O., Abdulkarrem, F.B. et al. (2007). Surgery of parotid gland tumours in lagos: a 12 year review. *Niger. Postgrad. Med. J.* 14: 72–75.
88. Chedid, H.M., Rapoport, A., Aikawa, K.F. et al. (2011). Warthin's tumor of the parotid gland: study of 70 cases. *Rev. Col. Bras. Cir.* 38: 90–94. (English, Portuguese).
89. Tan, T.J. and Tan, T.Y. (2010). CT features of parotid gland oncocytomas: a study of 10 cases and literature review. *AJNR Am. J. Neuroradiol.* 31: 1413–1417.
90. Schwalje, A.T., Uzelac, A., and Ryan, W.R. (2015). Growth rate characteristics of Warthin's tumours of the parotid gland. *Int. J. Oral Maxillofac. Surg.* 44: 1474–1479.
91. Minami, M., Tanioka, H., Oyama, K. et al. (1993). Warthin tumor of the parotid gland: MR-pathologic correlation. *AJNR Am. J. Neuroradiol.* 14: 209–214.
92. Orabona, G.D., Abbate, V., Piombino, P. et al. (2015). Warthin's tumour: Aetiopathogenesis dilemma, ten years of our experience. *J. Craniomaxillofac. Surg.* 43: 427–431.
93. Katabi, N. and Assaad, A. (2017). Oncocytoma. In: *WHO Classification of Head and Neck Tumours* (ed. A.K. El-Naggar, C. JKC, J.R. Grandis, et al.), 189–190. Lyon: International Agency for Research on Cancer (IARC).

Chapter 14

Oral and maxillofacial vascular lesions

14.1 Introduction

Vascular lesions of the face and jaw are important to the clinician, because they require a clear diagnosis prior to the treatment planning of any other anomaly. If they are not recognized, or are misdiagnosed, procedures may result in significant morbidity or mortality, through bleeding or obstruction of the airway. Some, because of their size, may cause cardiac failure, while others are associated with well-defined conditions. Although the number of vascular lesions as set out in Table 14.1 is extensive, this chapter will focus on the most common vascular lesions that affect the *oral and maxillofacial* (OMF) region, as shown in Figure 14.1.

Vascular lesions of the face and jaw can be categorized into two broad categories: vascular tumors (most commonly hemangiomas) and vascular malformations. This distinction is often apparent on the basis of the clinical examination, supplemented by appropriate radiological and genetic [1] investigations. Hemangiomas generally present as a "birthmark," appearing shortly after birth. Most will involute spontaneously within the first decade. Vascular malformations present at birth and continue to grow with the individual. They do not involute spontaneously.

Vascular malformations can be further subdivided into high- or low-flow lesions, since hemodynamic characteristics are critical to the definition, understanding, and treatment of these lesions.

Cutaneous or mucosal vascular lesions of the OMF region are by far the most frequent. One small case series (n = 115) reported that approximately 71% of lesions affected the superficial structures, while approximately 10% affected glandular tissue, and 10% demonstrated osseous involvement, with the maxilla being the most common site [2].

Although most vascular lesions will be apparent on clinical examination, some may also be identified as incidental findings on standard conventional radiography prescribed for other clinical reasons. These can present as phleboliths within the soft tissues by virtue of their calcified content or as a radiolucency within the jaw bones, as exemplified in Figure 14.2. While conventional radiography, particularly the panoramic radiograph, will be prescribed on the occasion of a vascular lesion being detected on clinical examination, the vast majority of such cases will be noncalcified and not visible on such images. Indeed, some intraosseous vascular lesions may also have considerable soft-tissue involvement (Figure 14.3), Therefore, introductions of those modalities which assess soft tissues is now indicated. These are *ultrasound* (US), *computed tomography* (CT), and *magnetic resonance imaging* (MRI). Grayscale US

Oral and Maxillofacial Radiology: A Diagnostic Approach, Second Edition. Edited by David MacDonald.
© 2020 John Wiley & Sons, Inc. Published 2020 by John Wiley & Sons, Inc.

Table 14.1 International Society for the Study of Vascular Anomalies (ISSVA) classification.

Vascular (or vasoproliferative) neoplasms	Vascular malformations
Infantile hemangioma	Slow-flow vascular malformations
Congenital hemangioma	*Capillary malformation*
Rapidly involuting congenital hemangioma (RICH)	*Venous malformation*
Noninvoluting congenital hemangioma (NICH)	*Lymphatic malformation*
Kaposiform hemangioendothelioma (KHE) and tufted angiomas (with/without Kasabach–Merritt syndrome)	Fast-flow vascular malformations
Spindle cell hemangioendothelioma	*Arterial malformation*
Epithelioid hemangioendothelioma	*Arteriovenous malformation*
Other rare hemangioendotheliomas (i.e. composite, retiform, and others)	*Arteriovenous fistula*
Angiosarcoma	Combined vascular malformations (various combinations of the above)
Dermatology acquired vascular tumors (i.e. pyogenic granuloma)	

(Figure 14.4c) can be useful to identify the lesion within its local soft tissues, particularly if the lesion is not deep. Doppler US (Figure 14.4d) allows both vascularity and flow rate (high flow versus low flow) to be determined. With the advent of *cone-beam computed tomography* (CBCT) and its increasing utilization in dental offices, more asymptomatic maxillofacial vascular lesions are likely to be identified [3, 4], and knowledge of their radiological appearance is crucial to ensure appropriate diagnostic work-up and management.

In order to definitively diagnose vascular lesions, CT and MRI are performed, invariably with iodine-based or gadolinium-based intravenous contrast media, respectively (Figures 14.3–14.8). From these, *three-dimensional* (3D) reconstructions can be created for CT (Figure 14.4b) and MRI (Figure 14.4j). Prior to surgery, catheter angiography (transfemoral, transradial, or direct puncture approach) is frequently beneficial for full characterization of high-flow lesions (Figures 14.5a–b and 14.6c–f).

MRI of vascular anomalies provides excellent noninvasive assessment of lesion characteristics, including their flow and enhancement characteristics, as well as permitting volumetric imaging and subsequent 3D reconstructions. These 3D reconstructions can be very useful in preoperative planning. In addition, MRI lacks ionizing radiation, which, similar to US, is of particular importance in the pediatric population. MRI can also be utilized to monitor serially treated lesions for degree of response to therapy. The major disadvantages of MRI include access limitations, high cost, and the need for cooperative patients. The last is necessary since motion artifact, longer scan times, and/or patient claustrophobia severely

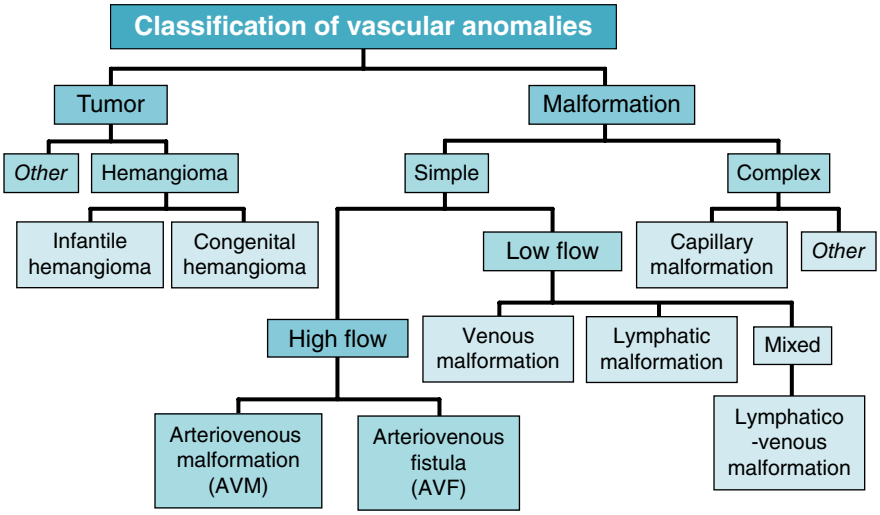


Figure 14.1 Simplified flowchart of the classification of vascular anomalies by lesion type and flow characteristics, if applicable.

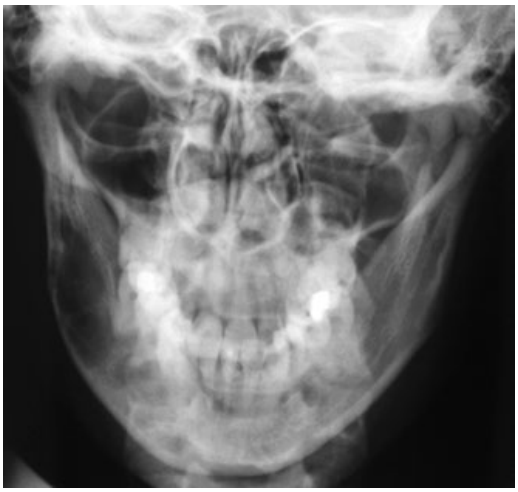


Figure 14.2 Anterioposterior projection of the mandible displaying a lucency affecting the buccal half of the posterior body of the right mandible. It is well defined with minimal buccolingual displacement. The only hint of its presence on the accompanying panoramic radiograph was that the trabeculae, but not the teeth, appeared out of focus. This was an incidental finding on a female student in her late teens. It was treated by sclerotherapy.

degrade image quality. MRI protocols vary from institution to institution. Spin-echo or fast spin-echo T1-weighted sequences provide excellent anatomical detail, allowing for evaluation of lesion morphology, tissue planes, and flow voids, as well as delineation of anatomical relationships with adjacent structures and neurovascular bundles. Although the anatomical detail is typically limited in peri- or intraosseous lesions, it is nevertheless superior to conventional radiographs and US. Fat-saturated T2-weighted sequences are crucial, as they often best define the lesion's borders, given the fat normally found within the subcutaneous and deeper soft tissues, and can be helpful in assessing fatty stroma within the lesion. Gradient-echo T2-weighted sequences are valuable in assessing for intralesional hemosiderin or phleboliths/dystrophic calcification. Pre- and postgadolinium-enhanced fat-saturated T1-weighted images should be routinely performed in the evaluation of vascular lesions, since these can provide

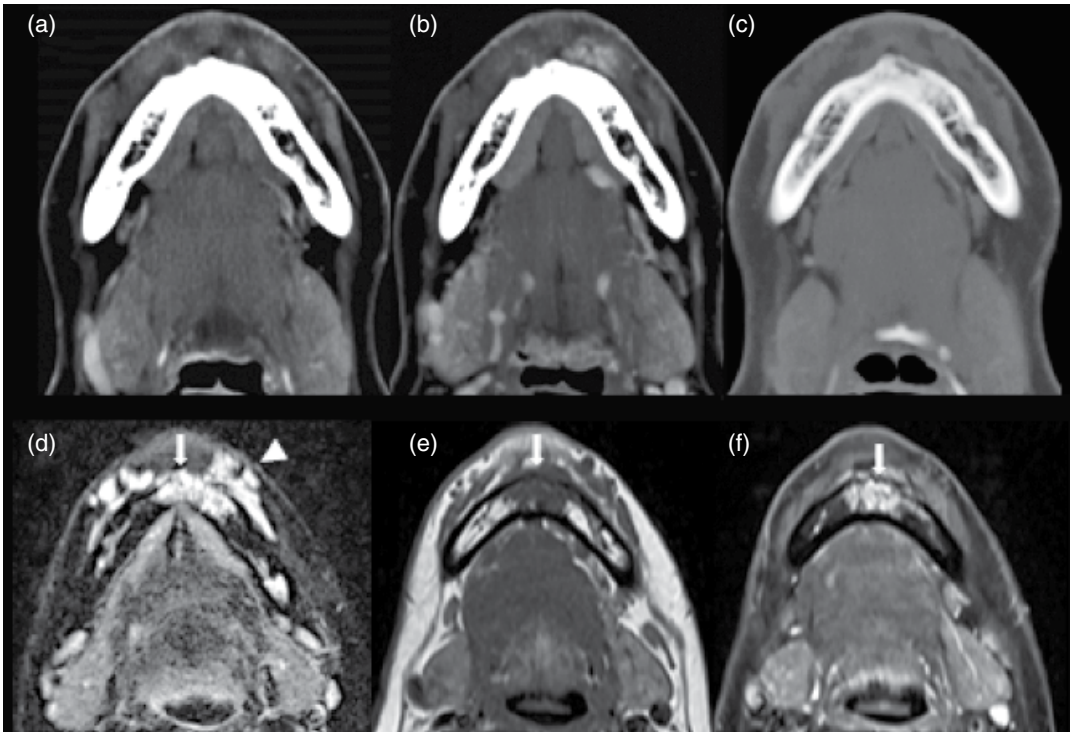


Figure 14.3 Hemangioma with intra- and extraosseous components centered on the mandible. Contrast-enhanced computed tomography at the level of the mandible demonstrates no apparent soft-tissue abnormality in the soft tissues anterior to the mandible during non-Valsalva imaging (a), and venous distension of a vascular malformation in the left paramedian soft tissues anterior to the mandible (b), with (c) associated subtle lytic change of the mandible on the left involving the roots of the left central and lateral incisors. (d) T2 fat-saturated turbo spin-echo sequence demonstrates abnormal increased signal involving the mental protuberance of the mandible (arrow), with extraosseous soft tissue anterior to the left mandible (arrowhead). (e) Pre-contrast T1-weighted sequences demonstrate low signal in the mental protuberance, in keeping with marrow replacement by the hemangioma (arrow). (f) There is marked enhancement of the lesion following administration of intravenous gadolinium (arrow).

very useful information regarding the pattern and extent of lesion enhancement, as well as assessment of response to treatment (such as sclerotherapy) [5, 6].

Assessment of vascular anomalies often utilizes multiple imaging modalities. A brief overview of the various radiological techniques can be found in Table 14.2, with specific imaging characteristics of these lesions described in detail in this chapter.

14.2 Classification System

The International Society for the study of Vascular Anomalies' (ISSVA) classification of vascular anomalies, which expanded upon Mulliken and Glowaki's basic classification system of vascular tumors and malformations [7], was initially adopted in 1996, in an attempt to provide a common language in the assessment of vascular lesions. This revised classification was based on

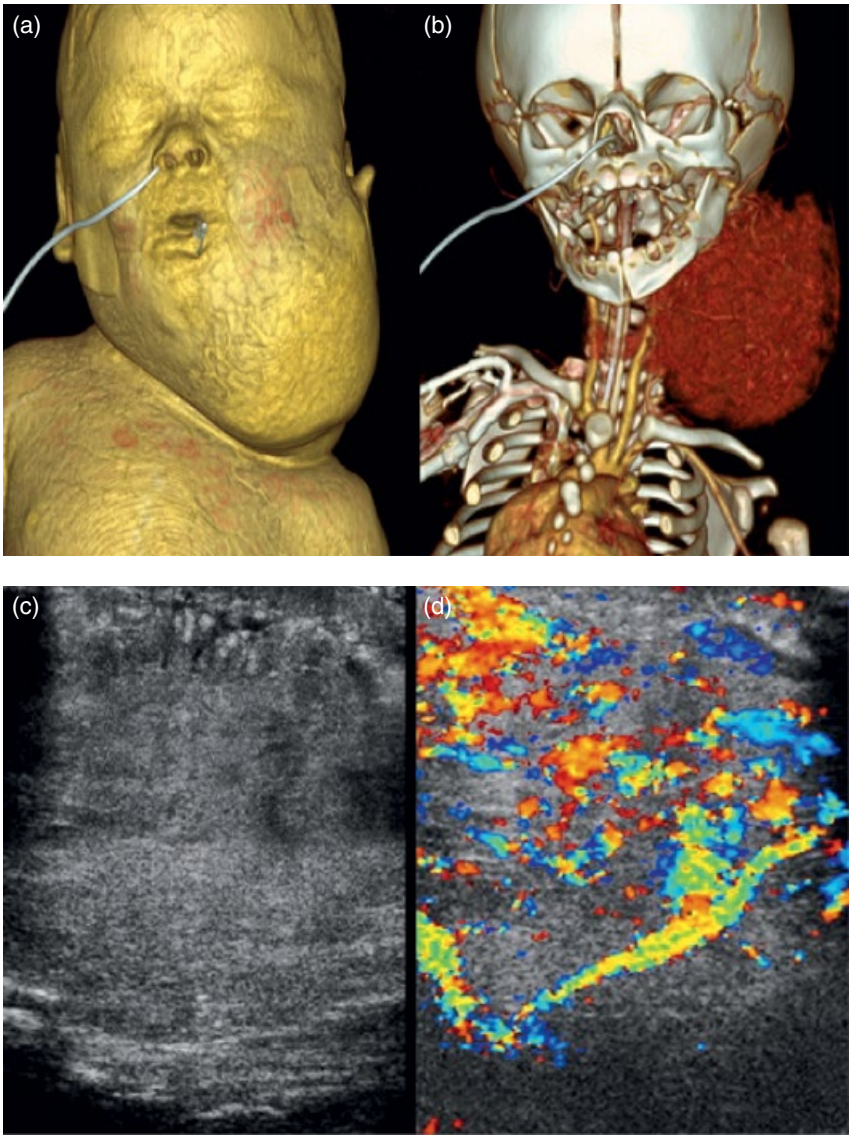
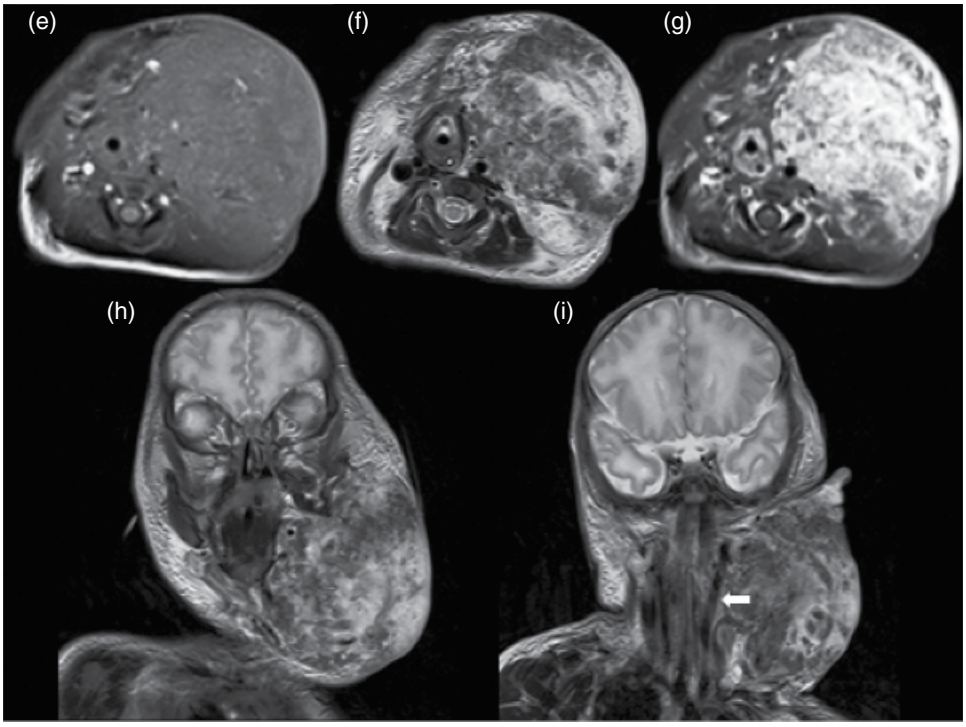


Figure 14.4 Pediatric submandibular kaposiform hemangioendothelioma. (a) Contrast-enhanced coronal computed tomography demonstrating surface rendering of the large submandibular extraosseous tumor (b) and three-dimensional reconstruction demonstrating relation to adjacent vasculature and osseous structures. (c) Grayscale ultrasound (US) revealing a heterogeneous mass with nonspecific features. (d) Doppler US displaying significant vascularity. Axial MR imaging centered at the level of the left submandibular lesion demonstrating it to be heterogeneously hyperintense to musculature on T2-weighted sequences (e), and isointense to adjacent musculature on nonenhanced T1-weighted sequence (f). (g) Displaying marked heterogeneous enhancement following administration of intravenous gadolinium contrast agent. (h and i) T2-weighted coronal slices demonstrating the heterogeneous lesion resulting in minimal medial deviation of the left internal carotid artery. (j) Magnetic resonance angiography allowing for assessment of major inflow and outflow vessels, demonstrating reduced signal within the mass relative to the central circulation and adjacent left carotid artery.



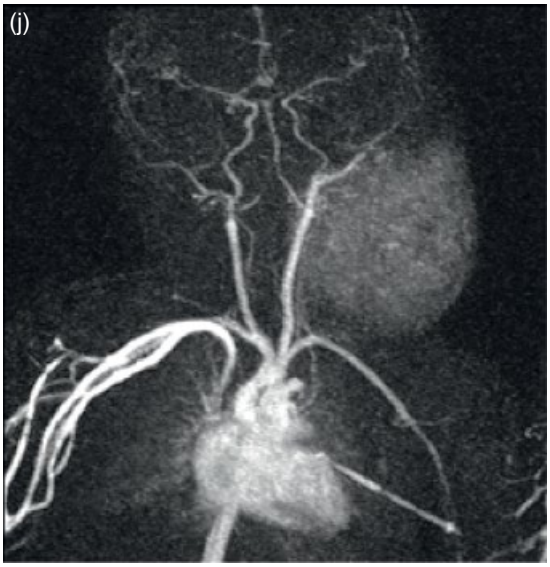


Figure 14.4 (Continued)

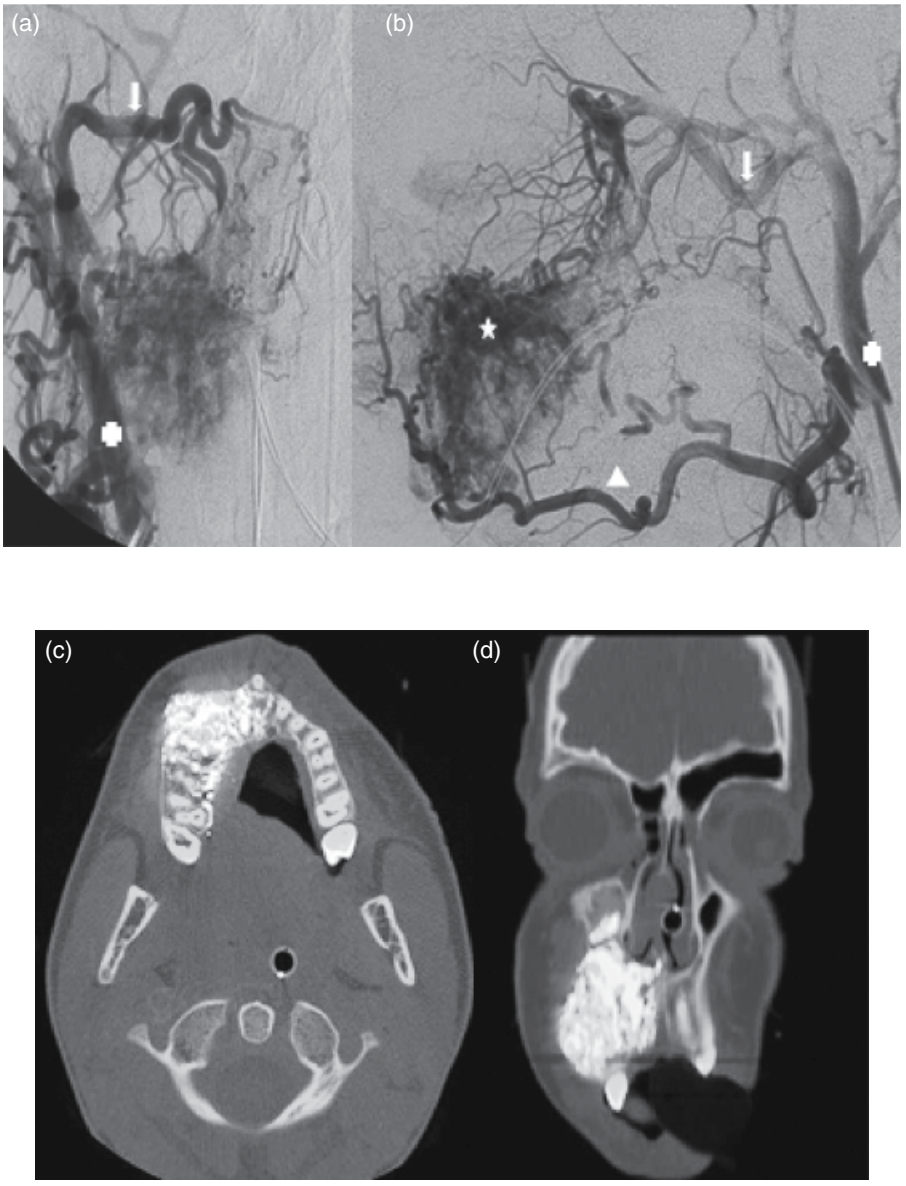


Figure 14.5 Right maxillary arteriovenous malformation (AVM). (a and b) Catheterization and angiogram of the right external carotid artery (cross) demonstrating arteriovenous shunting, with the nidus of the AVM centered in the right maxilla, with multiple inflow vessels, originating from the right internal maxillary artery (a and b, arrow) and the right facial artery (b, arrowhead). Note the distinct tangle of vessels centrally in the vascular lesion (b, asterisk), which represents the characteristic nidus seen in AVMs. Given its intraosseous location, preoperative embolization using n-butyl cyanoacrylate (nBCA) via percutaneous access was performed, followed by uneventful surgical excision. Postembolization non-contrast CT (c and d) demonstrates the high-attenuation embolic agent in the right maxilla.

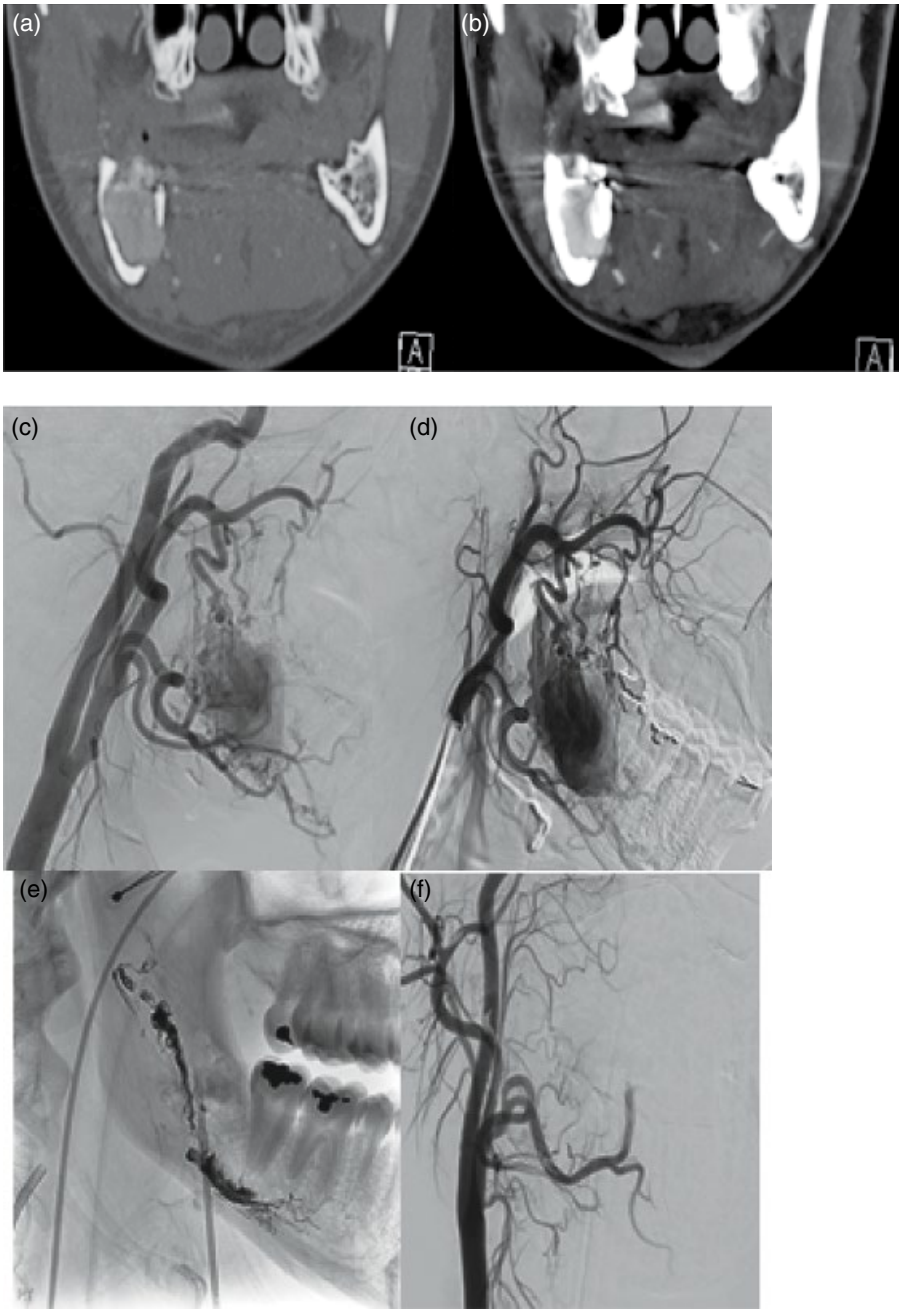


Figure 14.6 Iatrogenic right mandibular arteriovenous fistula (AVF) following wisdom tooth extraction. Computed tomography angiogram (a) windowed for assessment of the neck and facial osseous structures and (b) for vascular assessment demonstrates a right mandibular high-flow vascular lesion with a large well-defined intraosseous venous varix located within the right mandibular ramus posterior to the right second molar. Catheter angiography (c and d) demonstrates multiple branches from the inferior alveolar artery communicating with a large intraosseous venous sac (c), with venous drainage to the pterygoid venous plexus and to the external jugular vein (c). Embolization of this fistula was achieved using a combination of transarterial and percutaneous intraosseous transvenous embolic technique, with post-treatment angiography demonstrating obliteration of the AVF (d). A, viewed from anterior perspective.

Table 14.2 Summary of characteristics of advanced imaging modalities of hemangiomas.

Ultrasound (US)	**Infantile hemangiomas** typically lack macroscopic vessels and are confined to subcutaneous tissues **Congenital hemangiomas** with visible vessels and variable depth
	Increased color Doppler flow, with arterial and venous waveforms
	Two criteria reported to aid in distinguishing hemangioma from other soft-tissue masses: High Doppler shift (>2 kHz) High vessel density (>5 vessels/cm^2)
Computed tomography (CT)	Limited utility relative to US and MRI Discrete, lobulated mass which is also displayed on US and MRI, *but* with prominent draining veins and trabeculations
	Intraosseous hemangiomas may demonstrate serpiginous vascular channels *and* may have low-attenuation fatty stroma
Magnetic resonance imaging (MRI)	**T2-weighted** images → Hyperintense **T1-weighted** images → if low fatty component → Isointense *but* if prominent fatty component → Hyperintense
	Prominent draining veins seen as both central and peripheral vascular structures
	Marked and progressive enhancement with gadolinium
	Involuting hemangiomas may demonstrate components of fat signal and absent flow voids. Note: Flow voids commonly present on gradient-echo sequences.

hemodynamic features, with emphasis on the flow rate of vascular malformations. The ISSVA classification system was subsequently updated and expanded in 2014 to reflect the pathological basis of disease, in lieu of lesion hemodynamics [8].

The ISSVA classification (Table 14.1) is often used as a framework to understand vascular malformations of the face and jaw, because current management strategies for high- and low-flow vascular malformations require an understanding of the pathogenesis, classification, and, most importantly, hemodynamics of these lesions. A simplified flowchart and approach to the classification of vascular anomalies are found in Figure 14.1.

Hemangiomas constitute the most common vascular tumor of the head and neck region, and can be further classified into infantile and congenital. Arterial lesions are typically high flow, with *arteriovenous malformations* (AVM) being the classical lesions (Figure 14.5). Although congenital *arteriovenous fistulas* (AVF) in the maxillofacial region are rare, iatrogenic AVFs do occur (Figure 14.6). Low-flow lesions include *venous malformations* (VM), lymphatic malformations, and combined lymphaticovenous malformations

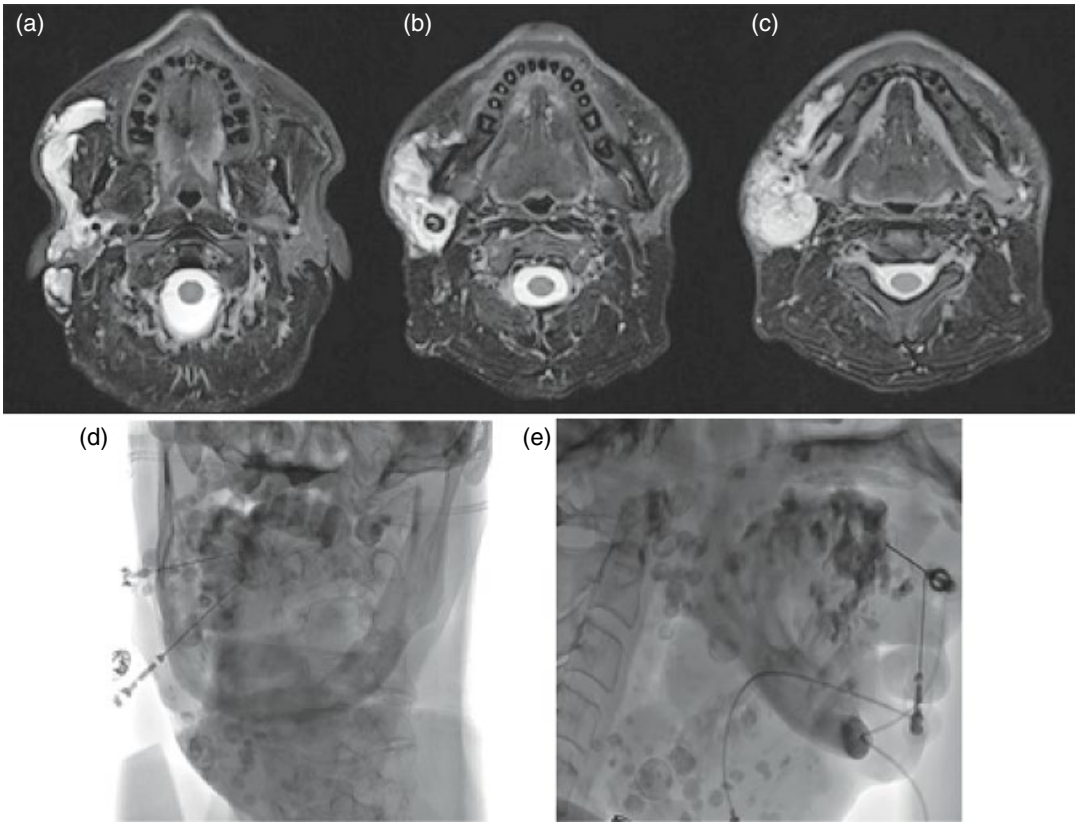


Figure 14.7 Large right facial and submandibular venous malformation (VM). (a–c) Limited slices of T2-weighted axial magnetic resonance imaging (MRI) of the neck demonstrating well-circumscribed abnormal hyperintensity involving the right facial, parotid, and submandibular regions representing the VM. (d and e) Spot fluoroscopic images during the course of percutaneous sclerotherapy, demonstrating multiple rounded opacities projected in the soft tissues anterior to the cervical spine and projected over the mandible, in keeping with phleboliths, a characteristic finding of VM.

(Figure 14.7). Low-flow malformations with a venous component include distensible and nondistensible lesions (Figure 14.8). Pure lymphatic malformations are beyond the scope of this chapter.

Accurate diagnosis and hemodynamic characterization are summarized in Figure 14.1 and are critical in determining the most appropriate treatment strategy: low-flow malformations are typically amenable to sclerotherapy, whereas embolization is often required for high-flow lesions, with or without surgical resection.

14.3 Hemangiomas

Hemangiomas typically present as a single lesion. Multiple cutaneous lesions can be associated with additional non-cutaneous lesions, and warrant further work-up [9]. Infantile and congenital

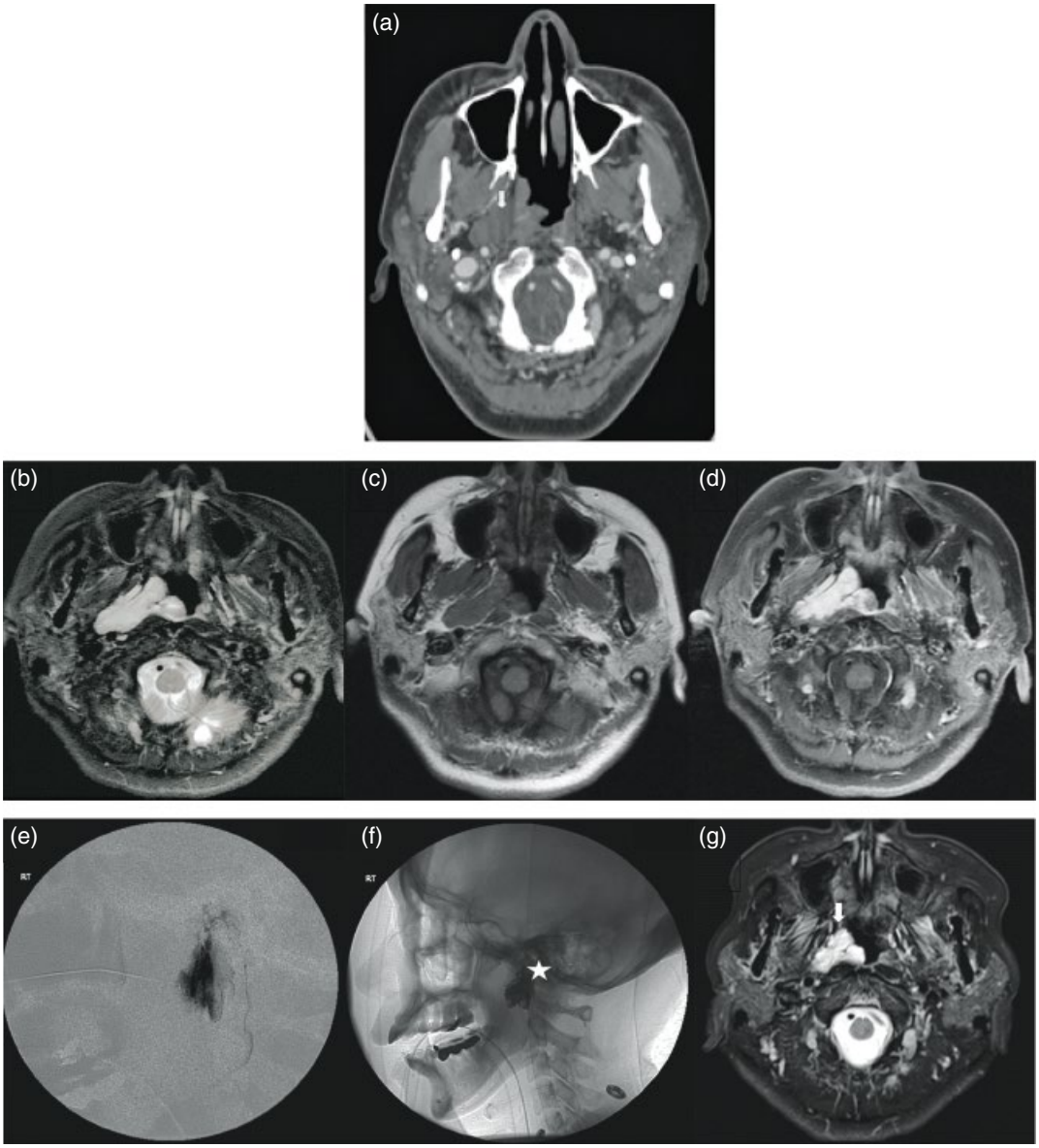


Figure 14.8 Combined lymphaticovenous malformation of the nasopharynx in a 48-year-old female with a history of "pulsatile" nasopharyngeal mass. (a) Computed tomography angiogram of the neck demonstrates a large well-defined, nonenhancing mass in the region of the right fossa of Rosenmuller (arrow). (b) T2-weighted magnetic resonance imaging (MRI) clearly demonstrates the lesion to be a well-circumscribed hyperintense mass, (c) with it isointense on T1, and (d) demonstrating intense, progressive enhancement following administration of intravenous contrast medium. Percutaneous transnasal sclerotherapy (e and f) with bleomycin and Lipiodol (asterisk). Follow-up MRI six weeks post-sclerotherapy (g) demonstrates a decrease in size of the right nasopharyngeal lymphaticovenous malformation (arrow).

hemangiomas have different clinical and radiological appearances, natural history, and treatment approaches. Maxillofacial hemangiomas are the most common tumor in Caucasian infants, with an estimated incidence of approximately 10–12% of all infant tumors, and representing approximately 60% of all head and neck tumors [10, 11]. Infantile hemangiomas are characterized by a proliferative phase between two weeks and two months of life, with completion of proliferation typically during the first year of life, and an involution phase occurring during the next decade [10, 12]. Congenital hemangiomas are fully formed at birth and are reported to account for approximately 30% of hemangiomas in the pediatric population [5, 10, 11].

Histologically, hemangiomas represent focal hyperplasia of the endothelial cells, which line the inner surface of vessels [13, 14]. As hemangiomas mature, blood-filled vascular spaces and channels develop, leading to their characteristic clinical and radiological appearance. There is significant histological variation depending on the stage of the lesion. In the early proliferative phase, endothelial hyperplasia predominates, resulting in narrow or absent vascular channels with little to no flow. In later stages, during involution, endothelial flattening occurs, permitting vascular filling with blood components, ultimately being predominantly replaced by fibrofatty tissue [15].

Hemangioma development is poorly understood and numerous developmental hypotheses exist, including placental origin, estrogen signaling, hypoxemia, genetic, and growth factor theories [15, 16]. An example of a hemangioma affecting the midline mandible is demonstrated in Figure 14.3.

14.4 Infantile Hemangiomas

Infantile hemangiomas, traditionally and erroneously called capillary malformations, have been reported to occur in approximately 10% of infants during the first 12 months of life, with a 3–5 : 1 female predominance [17]. The majority of infantile hemangiomas are superficial, and primarily manifest as localized skin thickening or as a cutaneous lesion of variable shape and color, with or without a telangiectatic patch. The proliferative phase is characterized by rapid growth during the first 12 months of life. During this stage, the lesion is typically composed of a cellular mass with poor vascular architecture. On average, 80% of infantile hemangiomas have been reported to reach their final size by 3.2 months of life [18], and virtually all reach maximal proliferation after 5 months of age. The involution phase typically occurs at 12–18 months in most cases, and continues for an average of 3–5 years [17]. It has been reported that involution typically occurs at a rate of 10% per year, such that 50% involute by 5 years and 90% have involuted by 9 years [19]. Involuted infantile hemangiomas are very unlikely to regrow.

14.5 Congenital Hemangiomas

Congenital hemangiomas are fully developed lesions at birth, and seldom demonstrate significant postnatal growth. On occasion, antenatal diagnosis is possible during routine detailed sonographic assessment of fetal anatomy at 18–20 weeks' gestation, which most women receive as part of standard prenatal care [20]. The 2006 ISSVA classification further classifies these lesions as *rapidly involuting congenital hemangiomas* (RICH) and *noninvoluting congenital hemangiomas* (NICH) [8].

RICH are characteristically present at birth as a protuberant tumor, with an average diameter of 5 cm, and classically having a central scar [10]. The involution phase is rapid, with complete or near complete regression by 12–18 months of life [18]. Postinvolution clinical appearance is highly variable, ranging from no vestigial evidence to focal skin redundancy [18].

NICH are histologically similar to RICH; however, there is proportionate lesional growth with the child, and absence of spontaneous involution. Both lesions are typically high flow, and present as a single lesion with an average diameter of 5 cm. Shape and coloration of the lesions are variable [21].

A rare vascular tumor is *kaposiform hemangioendothelioma* (KHE), which typically presents during infancy and is often initially diagnosed as an infantile hemangioma due to the similar age of presentation and cutaneous findings [22]. An example of this rare vascular tumor can be seen in Figure 14.4, and shares many of the imaging findings of hemangiomas. However, this rare vascular tumor can be distinguished from infantile hemangiomas on the basis of its tissue infiltration, endothelial spindling, microthrombi, hemosiderin, and lymphatic abnormalities, as well as expression of D2-40, a cell surface marker not typically expressed by other vascular tumors [23]. Moreover, KHE can demonstrate high-flow features, as well as Kasabach–Merritt phenomenon, a consumptive coagulopathy, with associated thrombocytopenia. In general, other than infantile hemangiomas, these other vascular neoplasms are rare entities.

14.6 Imaging Techniques

Diagnosis of a hemangioma is predominantly clinical, particularly for cases with superficial involvement. Radiological assessment is typically reserved for deep lesions, and a multimodality approach is often required for adequate evaluation in terms of the margins, which are typically well defined. Sometimes these have nodular extensions that are best seen with contrast imaging [6].

Although conventional radiography (including panoramic radiographs) can be helpful in evaluating intraosseous hemangiomas, or hemangiomas with sufficient mass effect to cause adjacent bony distortion or remodeling, its use is extremely limited due to poor soft-tissue contrast resolution, as well as superimposition of adjacent and contralateral structures. Intraosseous hemangiomas can have a multicystic (or multilocular on conventional and CT radiography), also known described as "soap bubble," appearance, and can result in cortical thinning and demineralization [24, 25].

Sonographic evaluation often constitutes the initial imaging modality, yielding information regarding the structure of the lesion, as well as its hemodynamic characteristics. Duplex US, which combines gray-scale US with Doppler US, has the added benefits of being relatively easy to access, low cost, and noninvasive, and does not use ionizing radiation. This lack of ionizing radiation is particularly relevant given the young population typically affected by hemangiomas. The disadvantages of US include its low spatial resolution and its inability to evaluate deep, peri-, or intraosseous lesions. Optimal imaging techniques utilize high-frequency linear transducers, typically 5–10 MHz [26]; Duplex US can also be utilized to differentiate between high-flow lesions (such as AVMs) and low-flow lesions, as well as to identify prominent arterial supply or draining veins. Hemangiomas are typically heterogeneous structures, with predominantly hypoechoic stroma in up to 80% of cases [27]. Tubular

anechoic structures representing vascular channels can also be detected in a few cases. On occasion, infantile hemangiomas may appear as isoechoic focal skin thickening without an appreciable mass lesion or vascular component. Doppler interrogation is particularly helpful in differentiating hemangiomas from other vascular lesions. Hemangiomas are characteristically hypervascular lesions with both arterial and venous waveforms, with characteristic high vessel density (>5 vessels/cm^2) and high Doppler shift (>2 kHz) [5].

CT assessment of hemangiomas is of limited utility. On noncontrast examinations, hemangiomas are typically hypoattenuating masses, albeit appearances can be highly variable. Infantile hemangiomas, in particular, are often occult on CT; however, this modality is useful in the evaluation of associated dystrophic calcifications. The main strength of CT consists in providing high-resolution anatomical information between the hemangioma and adjacent osseous structures. In particular, CT is crucial in evaluating intraosseous hemangiomas. Intravenous contrast administration increases the conspicuity of the lesion, often with diffuse and marked enhancement. CT angiography provides excellent spatial resolution of vascular structures, and multiphasic assessment can be useful in delineating arterial from venous components, as well as potentially better characterizing the filling pattern [5].

MRI assessment of hemangiomas yields superior soft-tissue detail, allowing improved characterization of the lesion and its relation to adjacent structures. T1-weighted appearances are variable. Although the lesion is classically isointense to adjacent musculature, it can have regions of high intensity if there is intralesional adipose tissue, as seen during the involution phase. Signal nulling on fat-saturated T1-weighted images is useful to confirm presence of an adipose component, as well as to delineate the level of vascularity. Pre- and postgadolinium T1-weighted sequences demonstrate enhancement, reflective of the vascular nature of these lesions. Hemangiomas are high intensity on T2-weighted imaging. Gradient-echo sequences will demonstrate hypointensity where there is intralesional calcification, phleboliths, or degrading blood products. Conventional time-of-flight and phase-contrast MR angiography techniques, although useful in high-flow lesions, have limited utility in hemangiomas. Improvements in dynamic contrast-enhanced MRI techniques now provide high temporal resolution and moderate spatial resolution.

Conventional angiography is of limited utility, but is invaluable in troubleshooting complex cases and is typically only performed if embolization or other neuroradiological interventional approaches are being considered. The characteristic US, CT, and MRI imaging findings of hemangiomas are summarized in Table 14.2.

14.7 Treatment

Management of infantile and congenital hemangiomas of the maxillofacial region is largely dependent on patient age, clinical symptoms, lesion size and location, expected natural progression, and functional compromise. Large lesions prone to ulceration or hemorrhage, or those that result in a reduction in function, typically require treatment, whereas small superficial infantile hemangiomas can be monitored clinically in many instances. Lip and philtrum hemangiomas, on the other hand, are often frequently subject to prompt treatment, given cosmetic concerns and increased risk of ulceration. It is important to emphasize that most infantile hemangiomas regress spontaneously, and observation is generally appropriate.

14.7.1 MEDICAL THERAPY

Conservative therapy of hemangiomas typically consists of clinical observation. An estimated 80% of infantile hemangiomas will involute spontaneously, without any need for intervention. Propranolol, a nonselective beta-blocker, is considered first-line medical therapy for treatment of infantile hemangiomas [28]. Its use in their treatment was initially documented in 2008 in a child who demonstrated regression of a facial hemangioma while being treated with systemic propranolol for obstructive hypertrophic cardiomyopathy [29]. Propranolol is typically administered via the oral route with a dosing regimen of 1 mg/kg/day. Although its mechanism of action in the treatment of infantile hemangiomas is not well understood, proposed hypotheses include vasoconstriction; decreased renin production; and inhibition of angiogenesis [28]. Due to its systemic effects and negative chronotropic and inotropic effects on the heart, patients should be screened prior to initiating treatment for cardiovascular, pulmonary, and metabolic abnormalities, and monitored for hypotension, bradycardia, respiratory distress, hypoglycemia, and hyperkalemia for the duration of therapy [28]. Propranolol has not demonstrated this same benefit in the management of congenital hemangiomas.

Corticosteroids are a second-line medical therapy, and their application can be local or systemic. However, utilization in pediatric populations is generally a risk-versus-benefit decision, given the associated systemic risks of long-term steroid utilization. Prednisone has been utilized in the treatment of cutaneous infantile hemangiomas, at doses in the 2–4 mg/kg range [30]. Parotid hemangiomas are resistant to corticosteroid therapy [31]. The exact mechanism of corticosteroids in the treatment of hemangiomas is unclear; some researchers propose inhibition of *vascular endothelial growth factor A* (VEGF-A) expression, which leads to inhibition of vasculogenesis in vivo [32].

Use of interferon ALFA-2a and ALFA 2b [31], imiquimod [33], and bleomycin [34] has been documented, with varying levels of success reported in the literature.

14.7.2 INTERVENTIONAL AND SURGICAL TREATMENT

Laser therapy has become an important modality in the management of hemangiomas. Argon and carbon dioxide lasers have been utilized in the treatment of infantile and congenital hemangiomas. Newer *neodymium-doped yttrium aluminum garnet* (Nd:YAG) lasers are also becoming increasingly popular in the treatment of most hemangiomas, in particular large superficial ones, with appreciable reductions in size [35, 36]. The proposed mechanism of action of laser therapy involves intralesional coagulation, followed by fibrofatty replacement.

Surgical excision remains an option for the treatment of lesions not amenable to observation, medical therapy, or interventional techniques. Lenticular and circular surgical excision techniques are the mainstay in the resection of hemangiomas [37, 38]. Lenticular excision can result in larger scarring at the surgical site relative to the initial lesion size [39]. Circular excision is the preferred surgical technique, as it has been associated with decreased scarring [37]. Historical, albeit currently seldom utilized, approaches include intratumoral ligation, resulting in the interruption of blood flow, subsequently promoting fibrofatty replacement [40]. Similarly, in cases of highly vascular hemangiomas of the maxillofacial region, ligation of the external carotid

artery, or selective external carotid branch ligation, has been performed to reduce blood supply, but has been met with limited success. This is rarely done now, and is largely replaced by newer and less invasive techniques. *Interventional radiological* (IR) techniques may include endovascular and percutaneous intralesional therapies, and are often performed when medical therapies have failed. IR may be used to aid planned surgery by performing preoperative embolization, or can, in selected cases, be used to manage high-flow-related complications, such as heart failure.

Thermal ablation techniques, such as cryotherapy, can also be utilized in the treatment of infantile and superficial congenital hemangiomas, but are ineffective in the treatment of deep hemangiomas [41].

14.8 High-flow Vascular Lesions

14.8.1 ARTERIAL MALFORMATIONS

14.8.1.1 Aneurysms

Congenital arterial aneurysms of the OMF region are rare. These are usually asymptomatic, but may require intervention. Pseudoaneuryms are more common, and typically are a result of trauma or surgery [42]. Most aneurysms and pseudoaneurysms can be treated using endovascular interventional techniques, such as coil embolization or endovascular injection of liquid embolic agents [42]. Percutaneous image-guided management may also be appropriate in selected cases. Very uncommonly, there may be a need for combined endovascular and surgical management, or exclusively surgical management.

14.8.1.2 Arteriovenous Malformations

AVMs occur when embryonic vascular networks fail to differentiate, and thus bypass the high vascular resistance capillary bed. Approximately 60% of AVMs exist at birth or present clinically during early childhood, with approximately 10% manifesting during late childhood, 10% in adolescence, and 20% in adulthood, corroborating the proposed hypothesis of progesterone receptors accounting for their expansion during puberty [43, 44]. In the OMF region, an AVM may manifest clinically with discomfort or pain at rest, visible pulsation, acute swelling due to thrombosis, or hemorrhage [5]. AVMs gradually enlarge with time as they recruit more arterial feeders. AVM-related altered flow patterns can lead to venous stenosis, thrombosis, and/or hemorrhage. An example of an AVM is demonstrated in Figure 14.5.

AVMs are characterized by rapid arterial flow through a nidus into the draining venous circulation (i.e. arteriovenous shunting) [45]. They can occur virtually anywhere in the OMF region, and represent a progressive benign disease process. Recognition of these vascular lesions is important due to their potentially life-threatening complications, including massive hemorrhage and airway compromise. In addition, there may be significant morbidity, including cosmetic and functional impact. Hemorrhage can occur spontaneously or due to trauma and other iatrogenic causes, such as dental extraction, tooth eruption, or biopsy [46]. AVMs commonly occur as isolated lesions; however, they can also occur as manifestations of multisystem disorders, such as Bonnet–Dechaume–Blanc syndrome, a rare and nonheritable syndrome which affects the brain, retina, skin, bones, kidneys, muscles, and gastrointestinal tract [47].

The Schobinger staging system [44] has been devised to assess the clinical features of high-flow AVMs. Quiescence occurs during Stage I, and can progress to local pulse and thrill in Stage II lesions. Stage III lesions are characterized by regional destruction (dystrophic skin changes, ulceration, and/or bleeding) with pain, ischemia, and necrosis, and Stage IV can lead to high-output cardiac failure in a minority of cases.

14.8.1.2.1 Imaging Technique

Similar to other vascular malformations, imaging is crucial to adequately characterize the AVM and its involvement with surrounding structures, and for treatment planning. On US, AVMs demonstrate elevated systolic and diastolic flow. Arteriovenous shunting typically results in intralesional arterial waveforms, as well as in the outflow venous circulation [48]. Contrast-enhanced CT scan can show diffuse enhancement, because the contrast study is usually acquired in a steady state of contrast circulation with the lesion enhancing uniformly. However, bolus contrast-enhanced CT angiographic imaging is much better at demonstrating a distinct tangle of vessels, representing the nidus, as well as the inflow and outflow vascular anatomy. MRI findings include a network of dilated arteries and veins, with flow voids on both T1- and T2-weighted spin-echo sequences [48]. Magnetic resonance angiography (MRA) can be performed with or without contrast administration, and can employ time-resolved techniques. These techniques allow for better depiction of the nidus, associated inflow and outflow vessels, as well as providing data for the calculation of shunt volume/fraction [49]. However, *computed tomographic angiography* (CTA) is superior to MRA for vascular assessment, due to its higher spatial resolution, as well as superior ability to assess associated osseous changes.

Catheter angiography remains the gold standard for characterizing an AVM, including nidal arteries and draining veins, and associated arteriovenous shunting. It may be required for accurate diagnosis, especially when considering optimal methods of treatment [50]. The dynamic nature of angiography allows for better characterization of lesion flow dynamics, as well as of the nidus.

14.8.1.2.2 Treatment Strategies

AVM treatment is challenging given the high rate of recurrence [51]. Current indications for treatment of AVMs in the OMF region include recurrent hemorrhage, pain, ulceration, progressive enlargement, and mass effect resulting in functional limitations (such as issues with mastication), speech impairment (especially if lesions involve the tongue), and, rarely, high-output cardiac failure [51]. The goal of therapy should be elimination of the nidus; however, this may not be possible without significant morbidity, local tissue damage, or functional implications. Understanding the hemodynamics of AVMs allows for choosing the most appropriate management strategy. Although clinical observation may be considered, the nidus tends to enlarge and recruit additional nidal supply over time, and may become symptomatic due to local mass effect or following thrombosis and/or hemorrhage. AVMs can also demonstrate high-flow arteriopathy of the inflow (nidal) arteries, with potential flow-related aneurysms, or with similar changes occurring on the venous side [46, 52].

Although AVMs may be excised surgically, the margins of the nidus can be relatively poorly defined in the soft tissues, making complete excision challenging. The nidus, and associated arteries and veins,

may be difficult to identify at the time of surgery, with increased risk of significant bleeding and other morbidity during resection. It is imperative to discuss and inform patients of the potential morbidity associated with surgical intervention and to balance this with the potential for cure. Catheter angiography with embolization may offer definitive therapy, or can be followed by surgical resection of the nidus. However, failure to completely treat (usually by resection) the nidus represents a major and common failure of surgery, resulting in AVM recurrence. One large study found that rates of recurrence of extracranial AVMs were 81% in patients treated with resection (with or without embolization) and 98% in patients treated with embolization alone [53]. Management of patient expectations is an important aspect of AVM treatment, given the risks of recurrence and morbidity associated with treatment, including cosmetic impact. Agents such as medical-grade alcohol, *n-butyl cyanoacrylate* (nBCA), and Onyx can all be used for embolization of AVMs [11]. Transarterial techniques may also be combined with percutaneous intralesional treatment, or transvenous approaches. The use of Onyx as a preoperative liquid embolic agent may offer advantages to other agents as it has improved visualization at the time of surgery, appearing "black" in the embolized vessels. It is important to remember that bipolar cautery must be used when resecting AVMs that have been embolized with Onyx, as this embolic agent is flammable and at increased risk of electrocautery-induced ignition with monopolar cautery systems.

14.8.1.3 Arteriovenous Fistulae

AVF are abnormal direct communications between an artery and a vein, and can be classified as either simple or complex. Simple AVFs contain a single inflow artery, whereas complex AVFs have multiple inflow arteries. Both types can be associated with dilatation of the inflow/outflow circulation, as well as aneurysm formation. AVFs are distinguished from AVMs by the absence of a vascular nidus. The most common AVF of the head and neck region pertain to the orbits and the intracranial dural venous sinuses, and is beyond the scope of this book. However, these are important entities to consider, as severe maxillofacial injury can result in the development of post-traumatic orbital and intracranial AVFs. AVFs of the OMF region are rare, and often iatrogenic. They are frequently associated with mandible or zygomatic fractures. An example of an AVF secondary to wisdom tooth extraction is demonstrated in Figure 14.6. True congenital AVFs are exceedingly rare, with only a few case reports in the literature [54]. When AVFs occur in the maxillofacial region, the facial artery is frequently involved due to its anatomical location, and the paucity of adjacent soft tissue to act as a barrier to trauma [55].

14.8.1.3.1 Imaging Technique

AVFs share many of the same features as AVMs, and include identification of a direct arterial–venous communication, with arterialization of flow in the draining vein(s) on Doppler interrogation. Turbulent and high flow at the AV communication is often seen [56].

CTA and MRA, as well as conventional angiography, demonstrate a direct arterial–venous communication, with characteristic early filling of the involved outflow venous system, which is often enlarged, possibly aneurysmal or ectatic (i.e. mildly dilated, not meeting size criteria of aneurysmal dilation). In addition, enlargement of the feeder arteries can be seen, especially in longstanding AVFs [56].

Overall, the work-up of AVF is very similar to that for AVM.

14.8.1.3.2 Treatment

Treatment options include both surgical and interventional approaches. Classically, surgical ligation of the fistula and associated vascular branches was performed, with high success but potentially requiring complex surgical exposures. Endovascular techniques have become the preferred management strategy, having a high success rate, ranging from 80% to 100%, with the added benefit of a lower complication rate and reduced morbidity compared to surgery [5, 57]. Embolization is often performed using a transarterial approach, and may involve the use of liquid embolics, such as nBCA or Onyx, sclerosant agents, such as medical-grade alcohol, or vascular coils. Larger fistulae may require additional endovascular techniques, such as vascular occluder devices (for instance, Amplatzer plugs), covered stents, or a combination of a variety of different endovascular options [5]. Transvenous embolization of AVF may also be appropriate, depending on the angio architecture of the lesion. Careful pretreatment planning is paramount to determine if selective embolization is possible, or if large vessel sacrifice is required.

14.9 Low-flow Vascular Lesions

14.9.1 VENOUS MALFORMATIONS (VM)

VM have been reported to occur with an incidence of approximately 1 in 5000, with approximately 40% of these lesions occurring in the head and neck region. Within the OMF region, the oral cavity, tongue, pharynx, and musculature of the facial expression and of mastication are the most commonly affected areas [58, 59]. However, lesions involving the orbit are also frequent. VM are referred to as low-flow vascular lesions, and differ histologically from infantile hemangiomas. GLUT1 (Glucose transporter 1) is not expressed in VMs but is in infantile hemangiomas, and this immunohistochemical marker can be utilized to differentiate between the two entities [60]. VM are postcapillary lesions, with no direct arterial–venous shunting. They demonstrate variable intralesional venous ectasia, which is their characteristic feature. Intralesional stasis is common, with dystrophic calcification occurring following spontaneous focal thrombosis, resulting in characteristic "phleboliths," as seen in Figure 14.7. VMs classically demonstrate synchronized and proportional growth with the body, and do not involute spontaneously. The pathogenesis of VMs is poorly understood [58, 60].

The clinical presentation of VMs is largely dependent on size and location. Small lesions are typically asymptomatic, aside from possible cosmetic concerns. Large lesions can result in significant symptomatology due to local mass effect, and significant swelling in the setting of venous engorgement secondary to either stasis, Valsalva maneuvers, head position, or activity [5, 61]. VMs can be superficial or deep. Superficial lesions often spare the overlaying cutaneous or mucosal surfaces; however, in some patients alterations in skin color can occur, with a blue or purple appearance, as the lesion is situated closer to (or involves) the dermis, mucosa, or subcutaneous tissues. Superficial lesions, especially those present in the skin or mucosal surfaces, are at increased risk of trauma and, consequently, bleeding [62]. Intramuscular VMs can also result in motor dysfunction, pain with mastication or other oral movements, and contracture.

A classical intramuscular location is the masseter [62, 63]. Large VMs can cause significant pain, and those involving the tongue and oral cavity can also affect speech, swallowing, and breathing.

Although the clinical appearance of VMs is usually classical, they may be difficult to distinguish from other vascular malformations; thus, radiological diagnosis is important in helping reach an accurate diagnosis, permitting full characterization of extent and location of involvement, and for treatment planning.

14.9.1.1 Combined Lymphaticovenous Malformations

Low-flow malformations can be composed of a combination of both venous and lymphatic components. The lymphatic component of combined lymphaticovenous lesions often contains dilated lymph vessels distended with serous fluid. Combined lymphaticovenous malformations are complex, and beyond the scope of the current chapter. For illustrative purposes, an example of a combined lymphaticovenous malformation can be seen in Figure 14.8.

14.9.1.1.1 Imaging Technique

The sonographic appearance of VM consists of a lesion of heterogeneous echogenicity, with "cystic"-appearing regions, often containing echogenic foci with posterior acoustic shadowing representing intralesional phleboliths. Internal vascular channels can be detected in many cases. Reasonable-sized lesions are typically compressible. Lesions with small vascular channels are more echogenic and less compressible. Doppler interrogation is variable, but always lacks arterial flow. Monophasic venous flow can be detected in a minority of lesions, but can be seen in those with larger associated draining veins, and can be augmented by manual compression. VMs can demonstrate variable distension upon Valsalva maneuvers. However, lesions with smaller vascular channels may have no detectable flow pattern [56, 64].

CT findings typically include the presence of a lobulated soft-tissue mass, usually isoattenuating to adjacent muscle. Phleboliths are easily identified as calcific foci of variable size within the VM. The low-flow nature of these lesions often results in variable and progressive enhancement upon intravenous contrast administration. Those with a finer intralesional network of venous channels typically demonstrate patchy or delayed enhancement, as do larger VMs. Adjacent fatty hypertrophy is common. A prominent draining vein (or veins) can sometimes be seen, depending on the subtype of low-flow malformation [5]. An important pertinent negative finding is the absence of a large feeder artery on vascular imaging [56, 62, 64].

MRI findings are also variable. T1-weighted sequences demonstrate a multilobulated lesion with variable signal intensity, often isointense to adjacent musculature. As with CT, adjacent fatty hypertrophy is present. T2-weighted sequences classically demonstrate high signal intensity. Phleboliths often result in rounded areas of low signal intensity on T2-weighted images. Vascular flow voids are not observed, given their low-flow nature. Gadolinium enhancement is variable, reflecting the heterogeneous vascular channel sizes. This can result in patchy enhancement for lesions with small channels, and more brisk enhancement for lesions with larger channels [5, 25, 56, 62, 65]. VMs are also characterized by progressive contrast enhancement, typically best recognized on sequential postcontrast enhanced T1-weighted sequences (i.e. axial, sagittal, and coronal scans). It should be

noted that since low-flow malformations occur as part of the abnormal development of the venous and lymphatic system of the head and neck region, they can be associated with intracranial developmental venous anomalies, which are usually incidental findings and carry little clinical significance. They can, however, especially the larger facial lesions, be associated with cavernous malformations of the brain, which have a low risk of hemorrhage, but should be ruled out with dedicated MRI.

Conventional angiography is essentially of no value, unless there is concern of a high-flow component. Most lesions are occult or may demonstrate subtle blush on angiography, classically occurring in the venous phase. Dual-phase CTA, consisting of a dynamic nonaugmented arterial phase and Valsalva-augmented venous phase, can be useful in characterizing these venous lesions, as well as in demonstrating the distensible venous components of VM and combined lymphaticovenous malformations [61].

14.9.1.1.2 Treatment Strategies

Intervention is typically reserved for those with significant pain, swelling, or clinical dysfunction. Indications for treatment have been devised by numerous authors. Lee [64] developed a set of absolute and relative indications for treatment of general vascular malformations, which expanded on previous recommendations by Tan et al. [66] and Dubois and Garel [48] (Table 14.3). However, for cases requiring intervention, therapeutic options are broad, and can be divided into medical, interventional, and surgical approaches.

VMs of the maxillofacial region can often be followed clinically. Indications for intervention include persistent, intractable pain; functional deficits, including swallowing or speech impediments; airway compromise; acute thrombosis with pain; cosmetic concerns; and hemorrhage. Some lesions, if superficial, can be managed surgically, through clipping, cautery, and excision.

Sclerotherapy is an important technique utilized in the treatment of low-flow vascular malformations. Sclerotherapy is a technique whereby sclerosing agents are administered into the VM, promoting inflammation, thrombosis, and subsequent lesion involution and fibrofatty replacement. Technical success is largely dependent on lesion characteristics and size. In general, smaller lesions, and lesions with restricted venous drainage, such as Type I and Type II Dubois category VMs (i.e. isolated malformations without venous drainage, or with drainage into normal veins, respectively), are associated with a better response to therapy, with a greater reduction in size [5]. It is important to note that these reported responses to therapy are not specific to the head and neck region, and rates may vary.

Percutaneous sclerotherapy is considered first-line treatment given its minimally invasive nature [5]. Typically, it can be performed using fluoroscopic and US guidance. Utilization of an angiography suite is ideal, allowing for direct percutaneous intralesional phlebography. Treatment of most lesions can be performed with intravenous sedation. Treatment of smaller lesions may be performed on an outpatient basis. Larger lesions, or high-risk lesions, may require overnight observation for analgesic concerns and assessment for possible sclerotherapy-related complications. Sclerotherapy using medical-grade alcohol (ethanol) as the sclerosant is exceptionally painful, and general anesthesia is typically required when this sclerosing agent is selected. Similarly, treatment of complex lesions may also be better done using general anesthesia.

Table 14.3 Guidelines and indication for intervention in venous malformations.

Author	Absolute indications	Relative indications
Lee [64]	Hemorrhage	Progressive disabling pain or discomfort
	Secondary complications of venous hypertensions	Functional disability or impairment affecting daily activity and quality of life
	Lesion located at life- or limb-threatening region (e.g. proximity to the airway)	Cosmetically severe deformity accompanying physical or psychological disability and negative impact on quality of life
	Lesions threatening vital functions (e.g. vision, hearing, eating, or breathing)	Vascular bone syndrome with rapid progress of long bone growth discrepancy accompanied by significant pelvic tilt or compensatory scoliosis
		Lesions located at a region with a high risk of complication (e.g. hemarthrosis, deep venous thrombosis)
		Lesions with recurrent infection or sepsis
Tan [66]	Hemorrhage	Nonsevere cosmetic deformity
	Disabling pain necessitating the use of oral analgesia	
	Functional impairment secondary to swelling or pain	
	Tissue loss or ulceration	
	Severe cosmetic deformity	
Dubois [48]	Pain	
	Functional problems	
	Esthetic problems	

In general, treatment of superficial lesions using conventional sclerosants (i.e. medical-grade alcohol) is discouraged due to the high risk of skin/mucosal injury. Associated complications include erythema, scarring, necrosis, hyperpigmentation, hemoglobinuria, thrombophlebitis, and, rarely, thromboembolism [5, 67].

Choice of sclerosing agent is largely dependent on lesion characteristics and size, although operator preference and experience are important considerations. Ethanol and *sodium tetradecyl sulfate* (STS) are both routinely used sclerosants. STS has the added benefit of being able to be foamed, permitting easy visualization under US, as well as improved sclerosant contact with lesion endothelium. Additional sclerosing agents include doxycycline, bleomycin, ethanolamine oleate, polidocanol,

alcoholic solution of Zein, and sodium Morrhuate [5]. Bleomycin has demonstrated advantages over the other sclerosants; in particular, reduction in treatment-related swelling, minimal risk of nerve injury, and reduced risk of cutaneous injury. It has become the agent of choice for many VMs previously felt too risky to treat with conventional sclerosants, and is extremely useful for treatment of lesions involving the tongue, lips, oral/buccal mucosa, and where facial, lingual, or marginal mandibular nerve injury is a concern. Extremely rare complications of intravascular ethanol administration include pulmonary arterial vasospasm, cardiac arrest, hyperthermia, intoxication, and bronchospasm, and patients treated with this sclerosant should be monitored for a minimum of three to six hours [5].

Sclerotherapy can also be utilized as an adjunct to surgery with the aim of decreasing lesion size, and decreasing the risk of hemorrhage during surgery. Mucosal and superficial VMs may also be amenable to Nd:YAG laser therapy [68].

VMs are diaphanous, thin walled, and often more extensive than anticipated, therefore the rupture risk is elevated and can result in unanticipated hemorrhage intraoperatively.

Intralesional phlebography allows characterization of the extent and structure of the malformation and associated venous outflow. Glue or coil embolization can be performed at the same time, with the occasional requirement for compression of the outflow venous circulation in order to ensure optimal embolization. Ideally, the entire lesion can be filled in this manner, including the outflow venous channels, which may be difficult to manage surgically [5, 11, 62].

Superficial lesions are more amenable to percutaneous sclerotherapy than deep lesions. Sclerosants should be utilized with caution in the tongue, oral cavity, and pharynx due to the risk of post-treatment inflammatory reaction and swelling, which risk airway compromise if severe [5, 11, 62].

Preoperative planning is essential and should include careful consideration of the size and location of the incision or incisions, and plans for adequate marginotomy when necessary for removal of the malformation [62, 69]. It is important to prepare for potential bleeding by having hemostatic agents readily available. The choice of hemostatic agents varies greatly by institution, practitioner, and procedure. The use of intraoperative angiography is rarely required. These lesions may be percutaneously cannulated when superficial, or exposed intraoperatively and then cannulated under direct visualization, especially if deep or complex. After lesions have been successfully cannulated and embolized, the risk of hemorrhage during conventional surgical resection is decreased.

14.10 Concluding Remarks

Vascular anomalies of the OMF region are not infrequent, and many are apparent on clinical examination. Clinical appearance and age of presentation are often useful parameters in determining the etiology of lesions. However, failure to identify asymptomatic lesions on panoramic dental radiographs or CBCT can result in the risk of hemorrhage if dental instrumentation occurs, as such recognition is crucial. Definitive diagnosis is performed typically with the aid of multiple radiological modalities, and treatment options vary tremendously depending on the lesion. Diagnostic and interventional neuroradiology referral is suggested for most suspected lesions.

References

1. Blei, F. (2013). Medical and genetic aspects of vascular anomalies. *Tech. Vasc. Interv. Radiol.* 16: 2–11.
2. Nair, S.C., Spencer, N.J., Nayak, K.P., and Balasubramaniam, K. (2011). Surgical management of vascular lesions of the head and neck: a review of 115 cases. *Int. J. Oral Maxillofac. Surg.* 40: 577–783.
3. MacDonald, D. (2016). Lesions of the jaws presenting as radiolucencies on cone-beam CT. *Clin. Radiol.* 71: 972–995.
4. MacDonald, D. (2017). Cone-beam computed tomography and the dentist. *J. Investig. Clin. Dent.* 8: https://doi.org/10.1111/jicd.12178.
5. Legiehn, G.M. and Heran, M.K. (2006). Classification, diagnosis, and interventional radiologic management of vascular malformations. *Orthoped Clin. Nor. Am.* 37: 435–474. vii–viii.
6. Vilanova, J.C., Barcelo, J., Smirniotopoulos, J.G. et al. (2004). Hemangioma from head to toe: MR imaging with pathologic correlation. *Radiographics* 24: 367–385.
7. Mulliken, J.B. and Glowacki, J. (1982). Hemangiomas and vascular malformations in infants and children: a classification based on endothelial characteristics. *Plast. Reconstr. Surg.* 69: 412–422.
8. Dasgupta, R. and Fishman, S.J. (2014). ISSVA classification. *Semin. Pediatr. Surg.* 23: 158–161.
9. Waner, M., North, P.E., Scherer, K.A. et al. (2003). The nonrandom distribution of facial hemangiomas. *Arch. Dermatol.* 139: 869–875.
10. Berenguer, B., Mulliken, J.B., Enjolras, O. et al. (2003). Rapidly involuting congenital hemangioma: clinical and histopathologic features. *Pediatr. Dev. Pathol.* 6: 495–510.
11. Heran, M.K. and Burrill, J. (2012). Vascular pediatric interventional radiology. *Can. Assoc. Radiol. J.* 63 (3 Suppl): S59–S73.
12. Garzon, M.C., Huang, J.T., Enjolras, O., and Frieden, I.J. (2007). Vascular malformations: Part I. *J. Am. Acad. Dermatol.* 56: 353–370. quiz 71–74.
13. Cohen, M.M. Jr. (2002). Vasculogenesis, angiogenesis, hemangiomas, and vascular malformations. *Am. J. Med. Genet.* 108 (4): 265–274.
14. Boye, E., Yu, Y., Paranya, G. et al. (2001). Clonality and altered behavior of endothelial cells from hemangiomas. *J. Clin. Invest.* 107: 745–752.
15. Lo, K., Mihm, M., and Fay, A. (2009). Current theories on the pathogenesis of infantile hemangioma. *Semin. Ophthalmol.* 24: 172–177.
16. Boscolo, E. and Bischoff, J. (2009). Vasculogenesis in infantile hemangioma. *Angiogenesis* 12: 197–207.
17. Gorincour, G., Kokta, V., Rypens, F. et al. (2005). Imaging characteristics of two subtypes of congenital hemangiomas: rapidly involuting congenital hemangiomas and noninvoluting congenital hemangiomas. *Pediatr. Radiol.* 35: 1178–1185.
18. Browning, J.C. and Metry, D.W. (2008). Rapidly involuting congenital hemangioma: case report and review of the literature. *Dermatology* 14: 11.
19. Chang, L.C., Haggstrom, A.N., Drolet, B.A. et al. (2008). Growth characteristics of infantile hemangiomas: implications for management. *Pediatrics* 122 (2): 360–367.
20. Cabrita, S.V., Goncalves, S., Rodrigues, H. et al. (2009). Antenatal diagnosis of congenital hepatic hemangioma: a case report. *Cases J.* 2: 6829.
21. Enjolras, O., Mulliken, J.B., Boon, L.M. et al. (2001). Noninvoluting congenital hemangioma: a rare cutaneous vascular anomaly. *Plast. Reconstr. Surg.* 107: 1647–1654.
22. Garcia-Monaco, R.D. and Giachetti, A. (2014). Infantile hemangioma or kaposiform hemangioendothelioma? *J. Vasc. Interv. Radiol.* 25: 810.
23. Navarro, O.M., Laffan, E.E., and Ngan, B.Y. (2009). Pediatric soft-tissue tumors and pseudo-tumors: MR imaging features with pathologic correlation: part 1. Imaging approach, pseudotumors, vascular lesions, and adipocytic tumors. *Radiographics* 29: 887–906.
24. Kakimoto, N., Tanimoto, K., Nishiyama, H. et al. (2005). CT and MR imaging features of oral and maxillofacial hemangioma and vascular malformation. *Eur. J. Radiol.* 55: 108–112.
25. Gelbert, F., Riche, M.C., Reizine, D. et al. (1991). MR imaging of head and neck vascular malformations. *JMRI* 1: 579–584.

26. Dubois, J., Soulez, G., Oliva, V.L. et al. (2001). Soft-tissue venous malformations in adult patients: imaging and therapeutic issues. *Radiographics* 21: 1519–1531.
27. Trop, I., Dubois, J., Guibaud, L. et al. (1999). Soft-tissue venous malformations in pediatric and young adult patients: diagnosis with Doppler US. *Radiology* 212: 841–845.
28. Drolet, B.A., Frommelt, P.C., Chamlin, S.L. et al. (2013). Initiation and use of propranolol for infantile hemangioma: report of a consensus conference. *Pediatrics* 131: 128–140.
29. Leaute-Labreze, C., Dumas de la Roque, E., Hubiche, T. et al. (2008). Propranolol for severe hemangiomas of infancy. *N. Engl. J. Med.* 358: 2649–2651.
30. Sadan, N. and Wolach, B. (1996). Treatment of hemangiomas of infants with high doses of prednisone. *J. Pediatr.* 128: 141–146.
31. Blei, F., Isakoff, M., and Deb, G. (1997). The response of parotid hemangiomas to the use of systemic interferon alfa-2a or corticosteroids. *Arch. Otolaryngol.* 123: 841–844.
32. Greenberger, S., Boscolo, E., Adini, I. et al. (2010). Corticosteroid suppression of VEGF-A in infantile hemangioma-derived stem cells. *N. Engl. J. Med.* 362: 1005–1013.
33. Ho, N.T., Lansang, P., and Pope, E. (2007). Topical imiquimod in the treatment of infantile hemangiomas: a retrospective study. *J. Am. Acad. Dermatol.* 56: 63–68.
34. Luo, Q.F. and Zhao, F.Y. (2011). The effects of Bleomycin A5 on infantile maxillofacial haemangioma. *Head Face Med.* 7: 11.
35. Vesnaver, A. and Dovsak, D.A. (2006). Treatment of vascular lesions in the head and neck using Nd:YAG laser. *J. Craniomaxillofac. Surg.* 34: 17–24.
36. Vesnaver, A. and Dovsak, D.A. (2009). Treatment of large vascular lesions in the orofacial region with the Nd:YAG laser. *J. Craniomaxillofac. Surg.* 37: 191–195.
37. Mulliken, J.B., Rogers, G.F., and Marler, J.J. (2002). Circular excision of hemangioma and purse-string closure: the smallest possible scar. *Plast. Reconstr. Surg.* 109: 1544–1554. discussion 55.
38. Vlahovic, A., Simic, R., and Kravljanac, D. (2007). Circular excision and purse-string suture technique in the management of facial hemangiomas. *Int. J. Pediatr. Otorhinolaryngol.* 71: 1311–1315.
39. Wu, J.K. and Rohde, C.H. (2009). Purse-string closure of hemangiomas: early results of a follow-up study. *Ann. Plast. Surg.* 62: 581–585.
40. Popescu, V. (1985). Intratumoral ligation in the management of orofacial cavernous haemangiomas. *J. Maxillofac. Surg.* 13: 99–107.
41. Li, Z.P. (1992). Therapeutic coagulation induced in cavernous hemangioma by use of percutaneous copper needles. *Plast. Reconstr. Surg.* 89: 613–622.
42. Barbalho, J.C., Santos, E.S., Menezes, J.M. Jr. et al. (2010). Treatment of pseudoaneurysm of internal maxillary artery: a case report. *Craniomaxillofac Trauma Reconstr.* 3: 87–89.
43. Duyka, L.J., Fan, C.Y., Coviello-Malle, J.M. et al. (2009). Progesterone receptors identified in vascular malformations of the head and neck. *Otolaryngol. Head Neck Surg.* 141: 491–495.
44. Kohout, M.P., Hansen, M., Pribaz, J.J., and Mulliken, J.B. (1998). Arteriovenous malformations of the head and neck: natural history and management. *Plast. Reconstr. Surg.* 102: 643–654.
45. International Society for the Study of Vascular Anomalies. ISSVA Classification of Vascular Anomalies. 2018. http://www.issva.org/classification. (Accessed May 10, 2018.)
46. Marler, J.J. and Mulliken, J.B. (2005). Current management of hemangiomas and vascular malformations. *Clin. Plast. Surg.* 32: 99–116. ix.
47. Garzon, M.C., Huang, J.T., Enjolras, O., and Frieden, I.J. (2007). Vascular malformations. Part II: associated syndromes. *J. Am. Acad. Dermatol.* 56: 541–564.
48. Dubois, J. and Garel, L. (1999). Imaging and therapeutic approach of hemangiomas and vascular malformations in the pediatric age group. *Pediatr. Radiol.* 29: 879–893.
49. Reinacher, P.C., Stracke, P., Reinges, M.H. et al. (2007). Contrast-enhanced time-resolved 3-D MRA: applications in neurosurgery and interventional neuroradiology. *Neuroradiology* 49 (Suppl 1): S3–S13.
50. Ernemann, U., Kramer, U., Miller, S. et al. (2010). Current concepts in the classification, diagnosis and treatment of vascular anomalies. *Eur. J. Radiol.* 75: 2–11.
51. Noreau, G., Landry, P.P., and Morais, D. (2001). Arteriovenous malformation of the

mandible: review of literature and case history. *J. Can. Dent. Assoc.* 67: 646–651.
52. Ethunandan, M. and Mellor, T.K. (2006). Haemangiomas and vascular malformations of the maxillofacial region – a review. *Br. J. Oral Maxillofac. Surg.* 44: 263–272.
53. Liu, A.S., Mulliken, J.B., Zurakowski, D. et al. (2010). Extracranial arteriovenous malformations: natural progression and recurrence after treatment. *Plast Recontr. Surg.* 125: 1185–1194.
54. Rappaport, I. and Rappaport, J. (1977). Congenital arteriovenous fistula of the maxillofacial region. *Am. J. Surg.* 134: 39–48.
55. Lutcavage, G.J. (1992). Traumatic facial artery aneurysm and arteriovenous fistula: case report. *J. Oral Maxillofac. Surg.* 50: 402–405.
56. Lowe, L.H., Marchant, T.C., Rivard, D.C., and Scherbel, A.J. (2012). Vascular malformations: classification and terminology the radiologist needs to know. *Semin. Roentgenol.* 47: 106–117.
57. Saini, A. and Jackson, J.E. (2008). Arteriovenous fistulas of the facial artery after mandibular surgery: treatment by embolization. *AJR* 190: W35–W40.
58. Buckmiller, L.M., Richter, G.T., and Suen, J.Y. (2010). Diagnosis and management of hemangiomas and vascular malformations of the head and neck. *Oral Dis.* 16: 405–418.
59. Glade, R.S., Richter, G.T., James, C.A. et al. (2010). Diagnosis and management of pediatric cervicofacial venous malformations: retrospective review from a vascular anomalies center. *Laryngoscope* 120: 229–235.
60. Leon-Villapalos, J., Wolfe, K., and Kangesu, L. (2005). GLUT-1: an extra diagnostic tool to differentiate between haemangiomas and vascular malformations. *Br. J. Plast. Surg.* 58: 348–352.
61. Heran, M.K., Rootman, J., Sangha, B.S., and Yeo, J.M. (2014). Dynamic arterial and valsalva-augmented venous phase multidetector CT for orbital vascular lesions: a pictorial review. *Ophthamol Plast. Reconstr. Surg.* 30: 180–185.
62. Zheng, J.W., Mai, H.M., Zhang, L. et al. (2013). Guidelines for the treatment of head and neck venous malformations. *Int. J. Clin. Exp. Med.* 6: 377–389.
63. Rosbe, K.W., Hess, C.P., Dowd, C.F., and Frieden, I.J. (2010). Masseteric venous malformations: diagnosis, treatment, and outcomes. *Otolaryngol. Head Neck Surg.* 143: 779–783.
64. Lee, B.B. (2005). New approaches to the treatment of congenital vascular malformations (CVMs) – a single centre experience. *Eur. J. Vasc. Endovasc. Surg.* 30: 184–197.
65. Flors, L., Leiva-Salinas, C., Maged, I.M. et al. (2011). MR imaging of soft-tissue vascular malformations: diagnosis, classification, and therapy follow-up. *Radiographics* 31: 1321–1340. discussion 40–41.
66. Tan, K.T., Kirby, J., Rajan, D.K. et al. (2007). Percutaneous sodium tetradecyl sulfate sclerotherapy for peripheral venous vascular malformations: a single-center experience. *J. Vasc. Interv. Radiol.* 18: 343–351.
67. Cahill, A.M. and Nijs, E.L. (2011). Pediatric vascular malformations: pathophysiology, diagnosis, and the role of interventional radiology. *Cardiovasc. Interv. Radiol.* 34: 691–704.
68. Rebeiz, E., April, M.M., Bohigian, R.K., and Shapshay, S.M. (1991). Nd-YAG laser treatment of venous malformations of the head and neck: an update. *J. Am. Acad. Otolaryngol.* 105: 655–661.
69. Noel, A.A., Gloviczki, P., Cherry, K.J. Jr. et al. (2000). Surgical treatment of venous malformations in Klippel-Trenaunay syndrome. *J. Vasc. Surg.* 32: 840–847.

Chapter 15

Fractures of the face and jaws

15.1 Introduction

Fractures of the facial skeleton are common and account for 4% of emergency room (ER) attendance [1]. These fractures arise due either to blunt-force trauma or to penetrating-force trauma; the former occur particularly in a civilian context, whereas the latter occur as a result of bullet or blast injury in a military context [2]. Blunt-force trauma generally causes a fracture/s of the bone; if the ends are displaced they first need to be brought together (reduction) and held there (fixation) until adequate healing has occurred. Penetrating-force trauma generally results not only in disruption of the soft and hard tissues, but also in their loss. This chapter will focus only on those fractures caused by blunt-force trauma, arising from physical assaults [3], traffic accidents [4], and sporting accidents [5]. The last have become increasingly important, primarily due to the increased popularity of skiing and snowboarding [5]. Although snowboarding injury cases are twice as likely to produce facial fractures than those caused by skiing, skiing is more likely to result in more than one facial fracture [5]. There is a direct relationship between the severity of the facial injury and patients reporting work disabilities [6].

Figure 15.1 offers an overview of this chapter. Although brain and eye injuries are outside its remit, circumstances where they may occur are indicated in the text. Nevertheless, whenever the reader otherwise suspects such an injury, appropriate and prompt referral is recommended. Prior to the advent of cross-sectional imaging, conventional imaging was the norm. The main conventional imaging projections are set out in Table 15.1. These projections are still performed to investigate facial trauma when the clinical examination has revealed where the suspected fracture is, and that it is likely to be amenable to standard treatment without the need to expose the patient, particularly if young, to the high radiation dose of *computed tomography* (CT). After review of these conventional radiographs, a prescription for a CT may be necessary. The CT studies in this chapter indicate the circumstances when this modality may be appropriate.

Figure 15.2 displays the percentage of fracture sites of the mandible and the middle face. The latter is composed of the maxilla, zygomatic or malar, palatine, and ethmoid bones. The mandible is in effect a bent or U-shaped long bone with a joint at each end (Figure 15.3). Fractures of the mandible tend to fracture at particular points of weakness. These are the condylar neck (Figure 1.12), the angle, especially if a third molar is present, and the parasymphyseal area at the canine site. The long roots of the last point penetrate

Oral and Maxillofacial Radiology: A Diagnostic Approach, Second Edition. Edited by David MacDonald.
© 2020 John Wiley & Sons, Inc. Published 2020 by John Wiley & Sons, Inc.

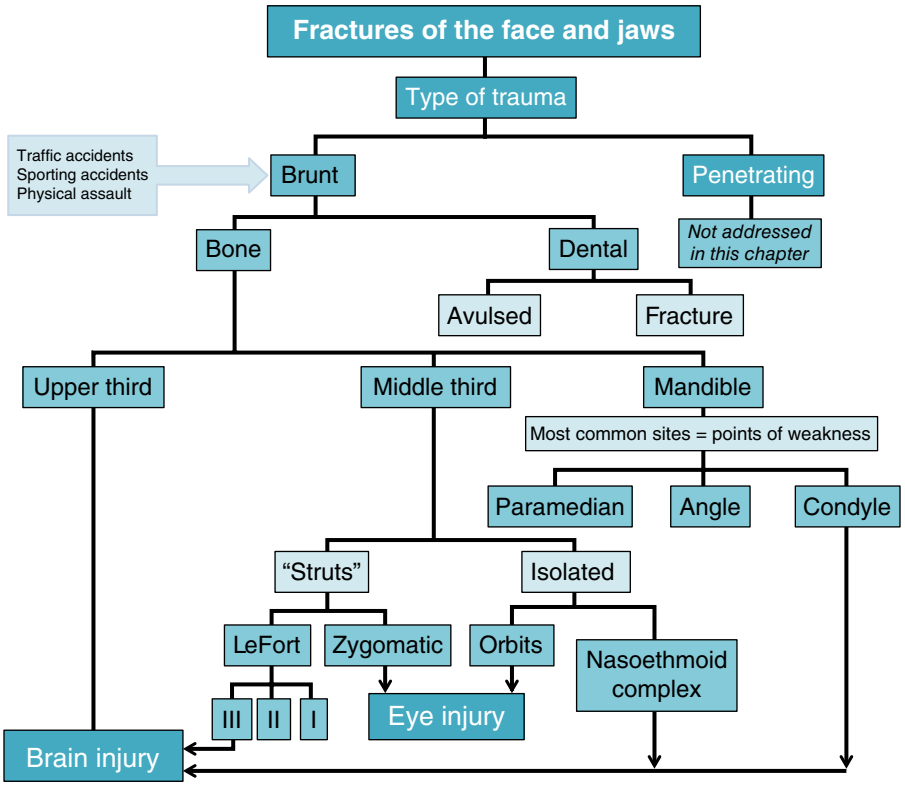


Figure 15.1 Flowchart giving an overview of trauma to the face and jaws. It focuses solely on trauma sustained in a civilian context (blunt-force trauma). Although fractures to the upper third of the face and damage to the brain should be considered, they are outside the remit of this chapter; points at which they should be considered are raised in the text. The "struts" are identified in Figure 15.2.

through much of the thickness of the mandible and thus weaken it (Figure 15.4). On the other hand, the middle third of the face, which is constructed of a series of buttresses [7] or struts (Figure 15.2), fractures more like a "crumple zone," as in modern car safety design, allowing dissipation of the traumatizing energy in order to protect the brain. Fractures of the middle third of the face occur along planes of weakness almost perpendicular to these struts; these are the LeFort (Figure 15.5) and zygomatic/malar (Figure 15.6) fractures.

Although the LeFort classification, based on low-velocity blunt trauma of a century ago, is still relevant with regard to physical assault and sports, it is not with regard to the high-velocity trauma of a traffic accident (Figure 15.7). Nevertheless, retention of the LeFort classification is still valuable, as it permits clinicians to communicate with each other concisely because it is so widely known [8].

Trauma to the face and particularly the jaws will also disrupt the dentition, which has been addressed fully elsewhere [9]. The avulsed tooth or fractured or displaced dental restoration (amalgam, crown, bridge, or other dental prosthesis) may be displaced into the pharynx (Figure 15.8) and subsequently to the lungs (Figure 15.9), where it may provoke respiratory distress [10]. In addition to ensuring that the mouth and throat are clear of teeth and debris prior

Table 15.1 Basic conventional radiography for investigation of fractures of the face and jaws.

Fracture site	Basic conventional radiographic projection/s
Mandible–body–posterior	Panoramic radiograph
	Occlusal (intraoral–central beam true to the occlusal plane)
Mandible–body–midline	Panoramic radiograph
	Occlusal (intraoral–central beam true to the occlusal plane)
	Standard anterior occlusal (intraoral = large periapical image)
Mandible–angle and ramus	Panoramic radiograph
	Posterioanterior projection of the mandible
Midface/LeFort fracture	Occipito-mental (Waters') projection
Malar/zygomatic fracture	Occipito-mental (Waters') projection
	Submento-vertex (requires lateral neck projection first to exclude facture of the cervical vertebra)
Orbital blowout fracture	Occipito-mental (Waters') projection

Note: Some institutions include other projections in their protocols. The technical details of these projections are addressed in standard radiographic texts. Note: The above protocols are increasingly augmented or even replaced in a hospital situation by the availability of cross-sectional imaging (mainly computed tomography (CT) as revealed in the text).

to endotracheal intubation [11], a *chest X-ray* (CXR; Figure 15.9) should be prescribed, particularly of the unconscious patient [12]. In cases of severe trauma, the initial clinical investigation by the *oral and maxillofacial* (OMF) or dental clinician may be permitted during any brief interlude in the considerable activity to preserve the patient's life and limb (including sight and brain integrity). The OMF clinician should determine whether teeth or dental restorations were inhaled, and promote the prescription of a CXR or the review of one or the CT dataset if either has already been made.

Although the incidence of life-threatening hemorrhage of facial fractures is low (0.33%), when it does occur the risk of death is high [13]; nearly a quarter of 19 cases in one study died after receiving a mean of 9.5 units of red blood cells. Although other injuries contributed to most of the other deaths, no deaths were reported in the cases treated by arterial ligation [13]. Nevertheless, due to ligation's higher morbidity, the use of radiological embolization (by angiography) is a better alternative [13]. Dean et al.'s protocol (their Figure 10) clearly indicates that radiologists should perform this [13]. A *transarterial embolism* (TAE) was performed on a life-threatening hemorrhage arising from a comminuted LeFort I fracture [14].

All these together indicate that although the majority of facial fractures are relatively easy to diagnose and treat by experienced surgeons, there is an important minority of cases that require a more careful evaluation, which includes the participation of the radiologist. Much of the following discussion will address particular areas of difficulty and appropriate cross-sectional imaging.

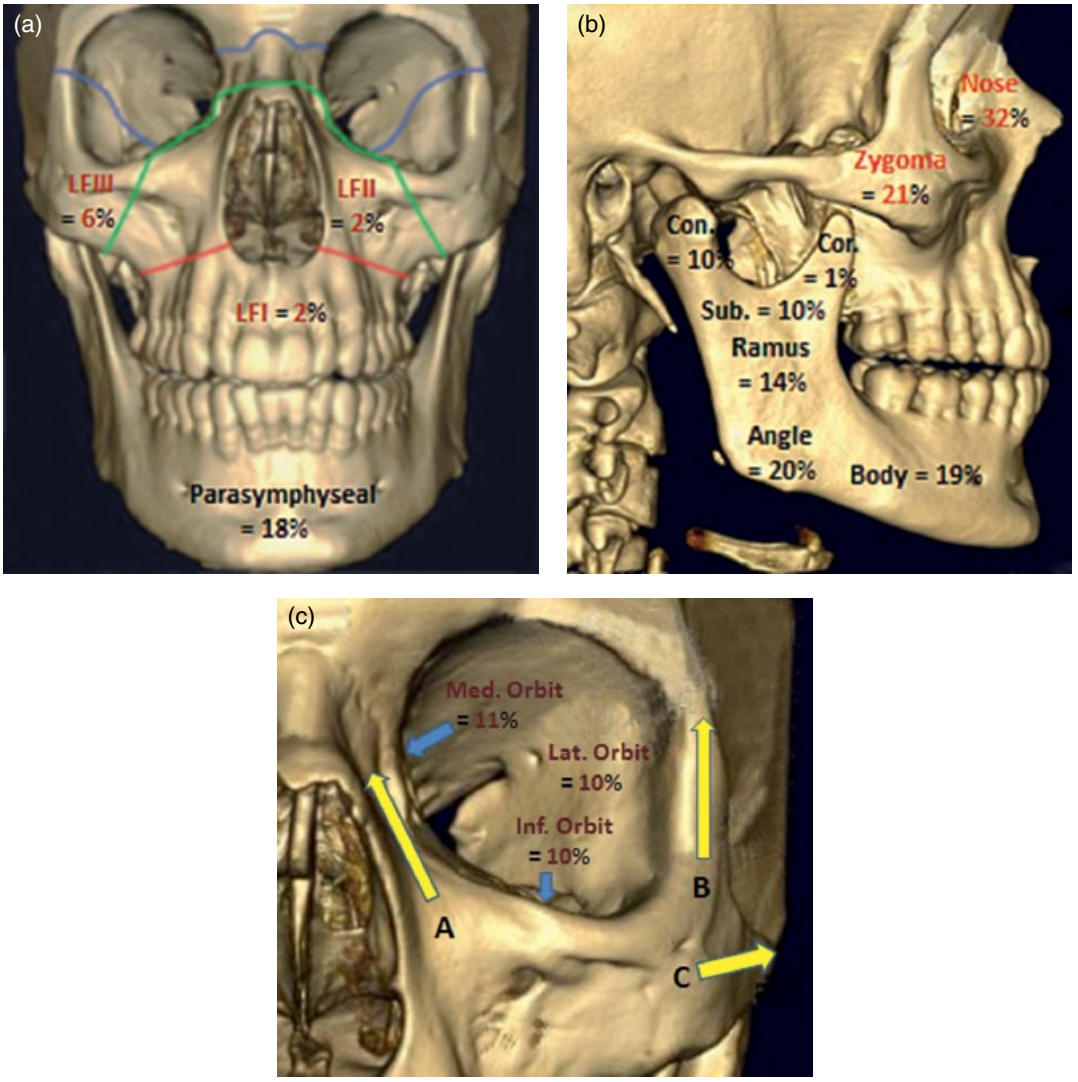


Figure 15.2 Three-dimensional reconstructions from a computed tomographic dataset of the head: (a) from an anterior perspective and (b) from a lateral perspective. Percentages of blunt-mechanism facial fractures according to site reported by Mundinger et al. They reported 8127 fractures in 4398 patients (62% White and 31% Black Americans, with 39% and 26% sustaining injury due a traffic accident or physical assault, respectively), of which 5704 and 1507 occurred in the maxilla and mandible, respectively. Those of the mandible are in black, whereas those of the maxilla are in red. (c) Percentages of fractures of the walls of the orbit are in dark red. As it can be assumed that these orbital fractures occurred separately from the other fractures, they were blowout fractures. The yellow arrows represent the struts and the direction of the occlusal forces to the skull base: A = maxilla-frontal process; B = zygomatico-frontal process; and C = zygomatico-temporal process. The blue arrows indicate the medial wall and the inferior wall (floor) of the orbit. Con, Condyle; Cor, Coronoid process; Inf., inferior; Lat, lateral; LF, LeFort; Med, medial or nasal; Sub, subcondylar. Source: Information from Mundinger GS, Dorafshar AH, Gilson MM, Mithani SK, Kelamis JA, Christy MR, Manson PN, Rodriguez ED. Analysis of radiographically confirmed blunt-mechanism facial fractures. *J. Craniofac. Surg.* 2014;25:321–7.



Figure 15.3 Skull base with the mandible and hyoid bone superimposed upon it. As the mouth is closed and the teeth are in articulation, the condylar of the mandible is within the glenoid fossa, which is separated from the middle cranial fossa and temporal lobe of the brain by a thin cortex. The mandible is displayed as a U-shaped, bent long bone with a joint at either end.

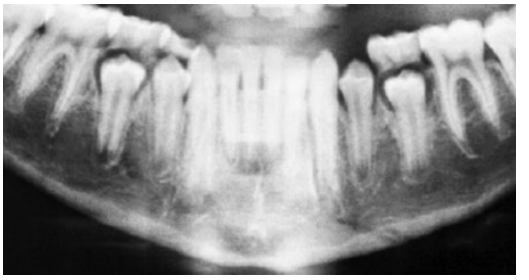


Figure 15.4 Panoramic radiograph displaying an undisplaced fracture through the paramedian (parasymphyseal) mandible of this 12-year-old. The two fracture lines indicate fracture of the buccal and lingual cortex rather than comminution. The long root of the lower left canine has contributed to the fracture occurring at this site. This panoramic radiograph is exceptionally good for one taken under suboptimal conditions, as normally it requires optimal technique and cooperation from the patient, who has to stand vertical and perfectly still throughout the exposure time of at least 15 seconds, to get the lower anterior sextant so well positioned in the narrow anterior focal trough and without movement artifacts.

15.2 Change in Pattern of Fractures According to Age

In general, 46% of all facial fractures in an urban population are caused by traffic accidents, despite regulations compelling the use of seat belts, helmets, and child seats [4]. When specific age groups such as children and juveniles, and the elderly, are studied separately, different pictures emerge. Children are particularly susceptible to fractures because of their greater ratio of cranial to body mass [15]. The majority, which are caused by falls (between 64% [16] and 71% [17]), are confined to the skull vault and are associated with cerebral concussion [16]. Mandibular fractures in children in half of cases have an injury elsewhere: 32% have a skull fracture, 27% a middle face fracture, and 8% a cervical spine fracture [18].

Patients 60 years of age and above were admitted with facial fractures after a fall in half of cases. Although treated conservatively in 95% of cases, they had a higher inpatient mortality in comparison to the younger patient [19]. Furthermore, although only 5% had a concomitant fracture of the skull base, 63% had a brain injury [19]. A further 31% had a thoracic injury, 15% an abdominal injury, and 5% a cervical spine injury; the rest of the spine was injured in 21% [19]. As populations age their increasing frailty [20] presents the clinicians with challenges in diagnosis and management of fractures, which have to take account of

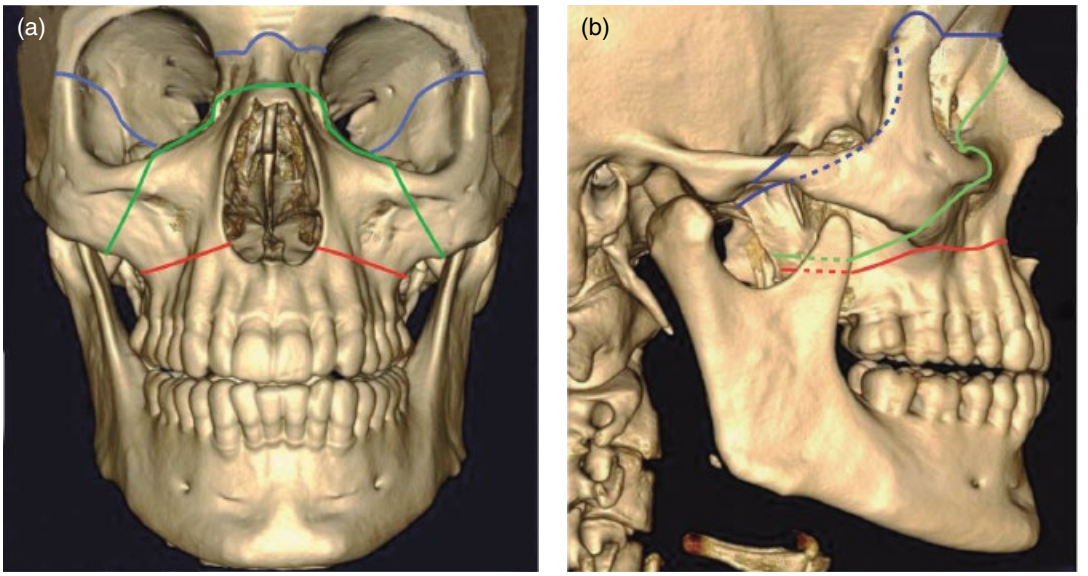


Figure 15.5 Three-dimensional reconstructions from a computed tomographic dataset of the head: (a) from an anterior perspective and (b) from a lateral perspective. LeFort fractures of the midface. Red – LeFort I; green – LeFort II; blue – LeFort III (fracture through the base of the skull and therefore a neurosurgical referral). Note 1. All LeFort fractures are transmitted through to the pterygoid plates. Note 2. LeFort I and II fractures both fracture the medial wall of the maxillary sinus/lateral wall of the nose. Note 3. A bilateral LeFort I fracture will separate the nasal cartilage and nasal bone from the floor of the nose/nasal surface of the hard palate. Source: Courtesy of Bruce McCaughey, Senior Photography/ Audio-Visual Technician, Faculty of Dentistry, University of British Columbia.

the declining function of a quarter of the injured patient six months after their admission for trauma [21].

15.3 Major Initial Considerations of the Patient Presenting with a Face and/or Jaw Fracture

Fractures of the skull base are frequently associated with maxillofacial trauma. Due to the more extensive trauma inflicted by high-velocity incidents, it is important for the OMF practitioner to bear in mind the possibility of factures of the skull base. Figure 15.10 considers the sites and some of the most important clinical features and complications of skull base fractures (discussed by Bobinski et al.) [22]. Therefore, early in the clinical examination, the patient should be inspected for signs suggestive of base-of-skull fracture. Periorbital ecchymosis ("raccoon eyes" or "panda eyes"), particularly if bilateral, is suggestive of a fracture of the anterior cranial fossa (Figures 15.11 and 15.12). In the absence of a fracture, this should prompt consideration of neuroblastoma or multiple myeloma. Battle's sign (mastoid ecchymosis) prompts consideration of a fracture in the posterior cranial fossa. *Cerebrospinal fluid* (CSF) rhinorrhea or otorrhea is a very strong indicator of skull base fracture [23]. Any suspected CSF leak should be confirmed by β2-transferin and followed

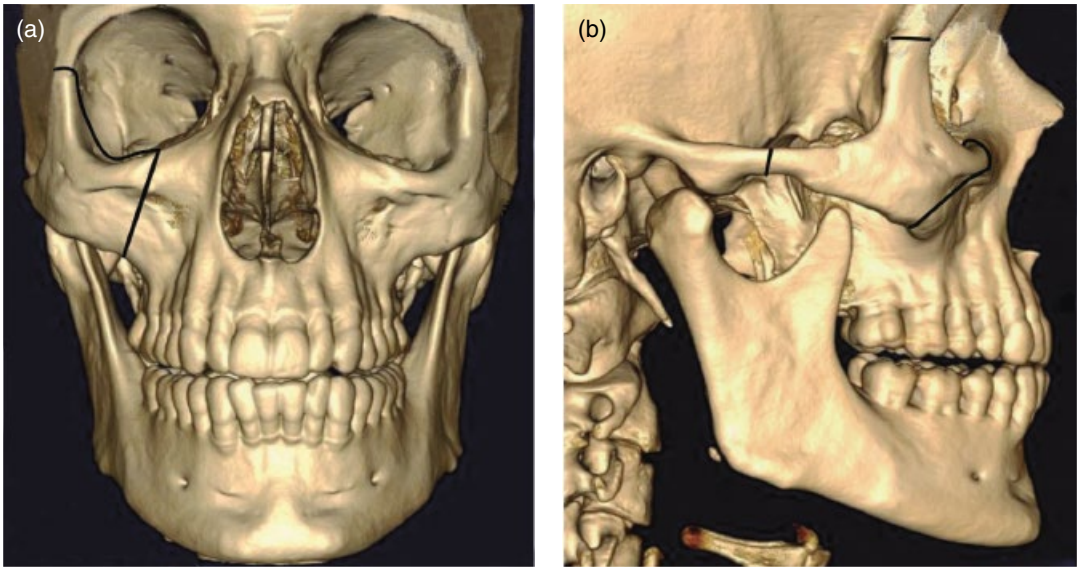


Figure 15.6 Three-dimensional reconstructions from a computed tomographic dataset of the head: (a) from an anterior perspective and (b) from a lateral perspective. Zygomatic fracture, also called malar fracture. The five fracture lines of the zygomatic fracture are the anterior maxilla, the zygomatico-frontal process (or distraction of the zygomatic-frontal suture), the zygomatic arch, the floor of the orbit, and the lateral/buccal surface of the maxillary sinus. Source: Courtesy of Bruce McCaughey, Senior Photography/Audio-Visual Technician, Faculty of Dentistry, University of British Columbia.

up by high-spatial-resolution CT [24]. Reddy and Baugnon have other protocols for suspected CSF leak cases [24]. Bleeding from the ear, also an important sign [25], will be discussed later in relation to fractures of the mandibular condyles.

The association between facial fractures, particularly of the upper face, and occult intracranial injury and death requires that clinicians attending to facial fractures due to blunt trauma be aware that that any involvement of the upper facial skeleton is highly associated with underlying occult intracranial injury, even in a fully alert patient [26]. In addition to this, the same group of authors reported that patients with complex fractures of the middle third of the face had a 57% increased risk of death; unexpectedly, it was the LeFort II that had the 94% increased risk of death, whereas the LeFort III had no significant association with death [27].

LeFort fractures routinely do also fracture the pterygoid plates (Figures 15.5 and 15.13), part of the skull base. Because of pneumatization of the superior aspect of the pterygoid process by the sphenoid sinus, fractures through this area include the sphenoid sinus floor [28]. An et al. reassuringly advised that this phenomenon was not only unlikely to be injurious to the patient overall, but rather allowed dissipation of the traumatic energy before it could be transmitted to the brain [28].

15.4 Initial Imaging Considerations

Imaging will depend on whether the OMF clinician is the first to examine the patient, as would most likely be the case for a simple fracture following a physical assault, or somewhat later in the case of

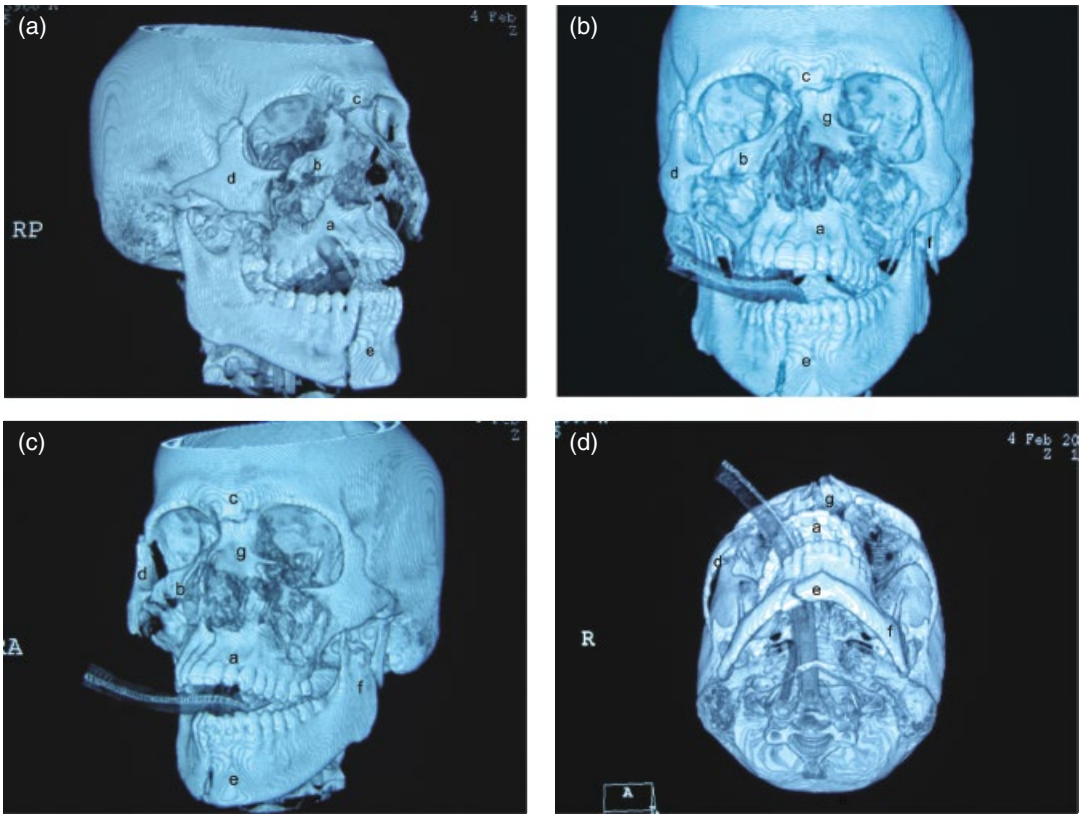


Figure 15.7 A three-dimensional reconstruction from a computed tomographic dataset of a case featuring multiple facial fractures: (a) from an anterior right oblique perspective; (b) from an anterior perspective; (c) from an anterior left oblique perspective; and (d) from an inferior perspective. The letters appearing on the figures denote particular fractures: a, LeFort I; b, LeFort II; c, LeFort III; d, zygomatic fracture; e, fractured mandible – midline; f, fractured mandible – condyle; g, nasal complex fracture. Note: Left zygomatic bone articulations with adjacent frontal and temporal bones are still intact. A, anterior; R, right. Source: Courtesy of Dr. Ian Matthew; Faculty of Dentistry; University of British Columbia. (c) Reproduced with permission from MacDonald-Jankowski, D.S. and Li, T.K. (2006). Computed tomography for oral and maxillofacial Surgeons. Part 1: spiral computed tomography. *Asian J. Oral Maxillofac. Surg.* 18: 68–77.

a major traumatic event such as a road traffic accident with multiple injuries. In the case of the former a simple CT of the face and head extending down into the neck would suffice, whereas in the latter instance more extensive investigations will have already been performed, increasing using *whole-body CT for trauma* (WBCTT; Figure 15.14) [29]. Nevertheless, if a head-only CT has been performed, it will have adequately included the face and jaws in 85% of cases [30]; it should also include the cervical spine. This will be explained later in this chapter.

Although panoramic radiographs (Figure 15.4) were considered the "unofficial gold standard" for mandibular frac-

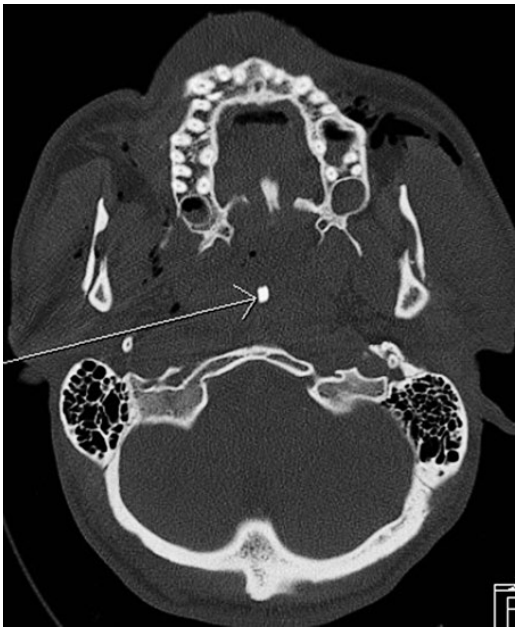


Figure 15.8 Axial computed tomography bone window displaying a tooth fragment in nasopharynx (arrow). Other injuries are bilateral condylar fractures, with extensive overlapping of the fractured ends. See also Figure 1.19. This is due to the general unfavorability of fractures through the condylar neck, which permits the attached musculature to pull the fractured ends over each other. There are also fractures through the right maxillary alveolus and emphysema particularly in the left soft tissue, but seen also in the right. Note: tooth-like radiopacity in the midline of the posterior hard palate is a torus palatinus – a frequently observed normal variant.

tures [31] of the conscious and ambulant patient two decades ago, these have been displaced by cross-sectional imaging. CT identifies more fractures, particularly those of the angle, ramus, and condylar neck, than panoramic images [32], in addition to intracapsular fractures of the condyle and comminuted fractures of the body (Figure 15.15). Furthermore, many patients with complex maxillofacial fractures benefit from the CT's short scan time [33]. Cross-sectional imaging by CT [7] is required for fractures of the skeleton of the middle third of the face, as these fractures are generally complex (Figures 15.7, 15.11, and 15.12), reflecting the midface's complex anatomy, which encloses cavities for the eyes, the nose, and the maxillary sinus. The classical fracture patterns of fractures of the middle third of the face are LeFort I, II, and III (Figure 15.5) and the zygomatic (also called malar) fractures (Figure 15.6).

Mundinger et al. reported that although bilateral fractures occurred in only 19% of cases in their study, cases with bilateral fractures have significantly more total areas fractured that those cases with only unilateral fractures. Two-thirds of these bilateral fractures were LeFort fractures [34].

15.5 Expected Radiological Findings of Fractures of the Face and Jaws

The distribution of radiographically confirmed blunt-mechanism facial fractures in percentages is displayed in Figure 15.2.

15.6 Fractures of the Mandible

Although the clinical examination will reveal most if not all information with regard to the site/s degree and the favorability (the ability of fractured bone ends to remain in their normal pre-extraction position after reduction without substantial fixation) of the fracture, substantial swelling, which can quickly follow severe facial trauma, makes clinical evaluation of the patient difficult (Figure 15.7 and 15.15). The clinical examination was

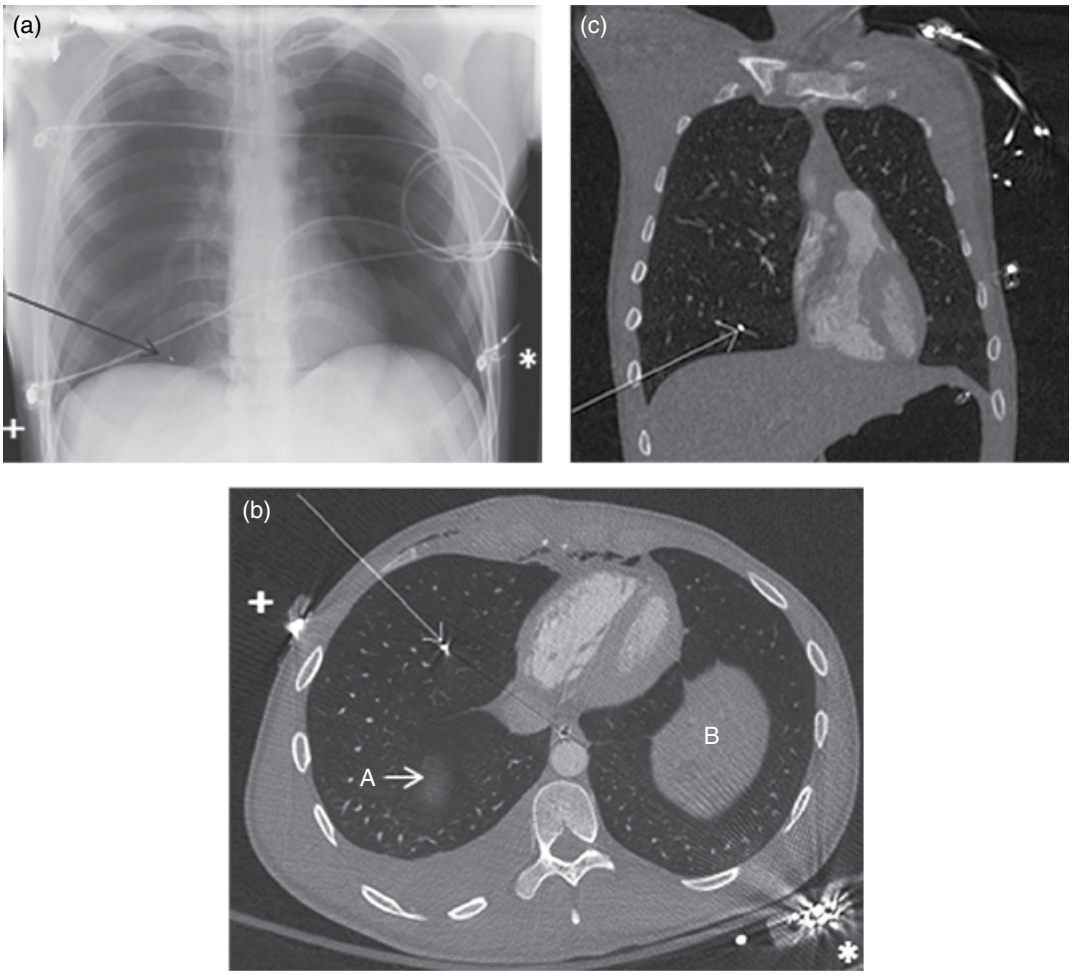


Figure 15.9 Amalgam in lung in (a) supine anterio-posterior (AP) chest X-ray (CXR) and (b and c) computed tomography. (a) The arrow indicates the amalgam fragment in the lower lobe of the right lung. The electrodynograph (EDG) leads are also obvious (asterisk and plus sign). (b) Axial reconstruction at the level of the apex of the right dome of the diaphragm (A; the left dome of the diaphragm is B). The amalgam fragment is anterior to A (arrow). The asterisk and the plus sign are the leads on the chest wall, also displayed in (a). The image in (c) presents a coronal reconstruction through the right sterno-clavicular joint. Note: It should be appreciated that the CXR was made when the patient is supine and is therefore anterioposterior, thus differing from the usual CXR, which is a posterioanterior projection made when the patient is vertical.

accurate in only two-thirds of mandibular fractures [35], thus emphasizing the importance of radiology to the assessment of the fractured mandible. As revealed in Figure 15.15, the fracture/s may be so complex that really only cross-sectional images will reveal the true extent of damage.

Although the mandible articulates with the skull base, which separates the temporal fossa and lobe from the joint by an often paper-thin bone of the glenoid

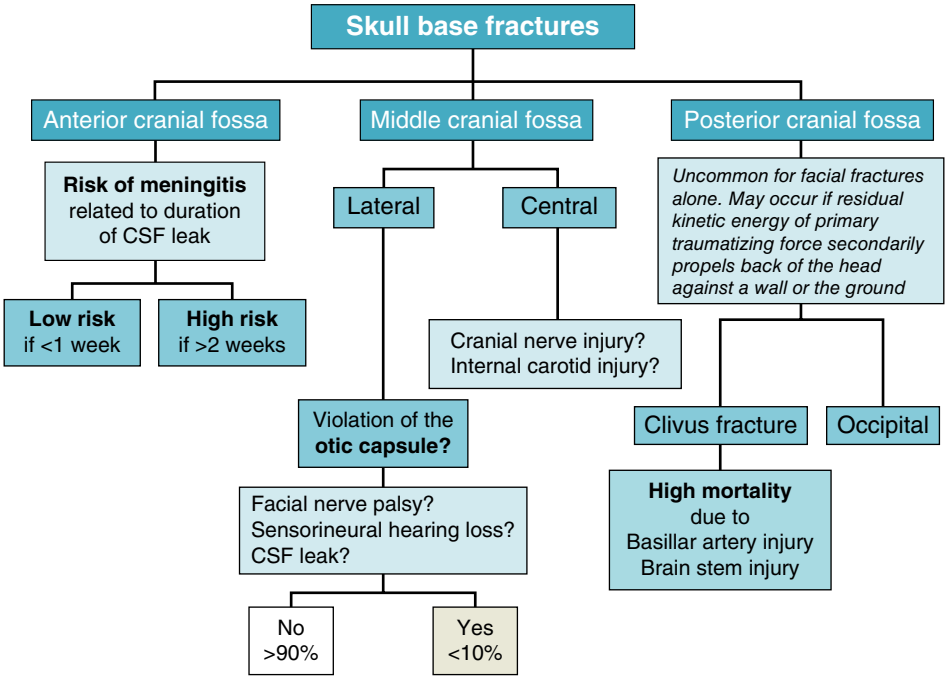


Figure 15.10 Sites, clinical features and complications of fractures through the skull base. CSF, cerebrospinal fluid.

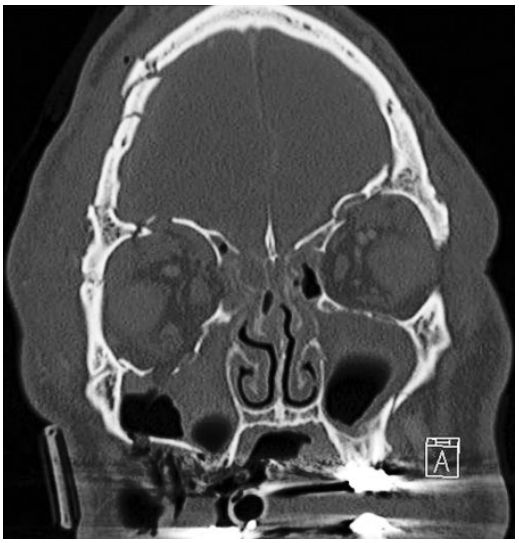


Figure 15.11 Coronal bone-window computed tomography displaying a LeFort III with fracturing of the anterior cranial fossa. The fracture of the right zygoma is also comminuted, which includes the floor of the orbit and the adjacent skull vault. A, anterior.

fossa (Figure 15.16), it is very uncommon that this bone is fractured or is penetrated by the condyle (Figure 15.17). Nevertheless, fractures of the glenoid fossa do occur in 3% of mandibular-only fractures and in 19% of those with multiple fractures (Figure 15.18) [36].

A phenomenon affecting the mandible that may enhance the risk of fracture are impacted (unerupted teeth with completely formed roots) third molar teeth. Their presence increases the risk of a fracture through the angle, but their absence enhances the risk of a condylar fracture [37].

Although *external auditory canal bleeding* (EACB) is very suggestive of a base-of-skull fracture, its most common cause, it has also been associated with mandibular condyles, which have been displaced back against the external auditory canal, fracturing it (Figure 15.16). EACB was associated with 15% of base-of-skull

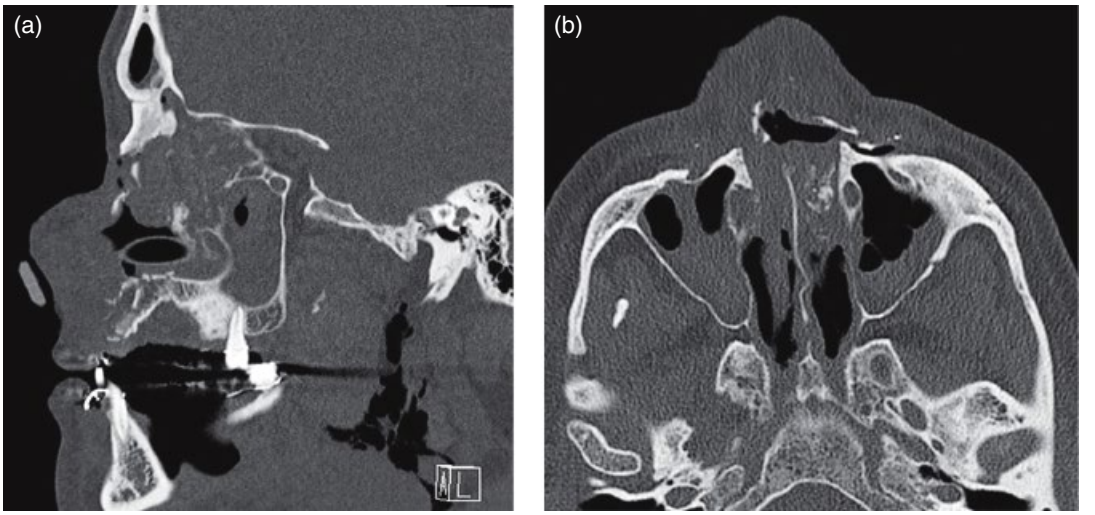


Figure 15.12 Sagittal (a) and axial (b) bone-window computed tomography displaying fractures of the ethmoids and the cribiform plate. The nasal bones and the anterior nasal spine are fractured and the bridge of the nose flattened. (b) Displays buckling of the nasal septum. A, anterior; L, lateral.

fractures and 13% of mandibular fractures, of which 92% were intracapsular [25].

In 7% of mandibular fractures, there was association with a fracture of the posterior maxilla and/or the pterygoid plates by the secondary transmission of the traumatizing force to them via the displacement of the ramus or the coronoid process into them by the primary traumatizing force (Figure 15.13) [38].

15.7 Fractures of the Middle Third of the Face

Most fractures of the middle third of the face occur when the traumatizing force impacts the face perpendicular to the struts (Figure 15.2) and disrupts them, resulting in an alteration in the external facial skeleton and thereby the facial contour. There is another group of fractures of the middle third of the face which occur when the traumatizing force directly strikes the front of the eyeball (also called the globe) and displaces it back into the orbital cavity (also called the orbit), causing it in turn to fracture the wall/s of the orbital cavity. This is a blowout fracture (Figures 15.19 and 15.20). The external facial skeleton remains intact, but the eyeball on the traumatized side may be found deeper in its socket, in comparison to its unaffected fellow. This is enophthalamos, which will be discussed later in this chapter.

Although fractures of the pterygoid plates are commonly associated with LeFort fractures, Garg et al. reported that a third do not. Other causes are base-of-skull fracture and severely displaced zygomaticomaxillary and mandibular fractures [39].

15.8 Fracture of the External Facial Skeleton

These fractures are divided into medial and lateral areas. LeFort fractures (Figures 15.7 and 15.11) constitute the bulk of the former and zygomatic/malar

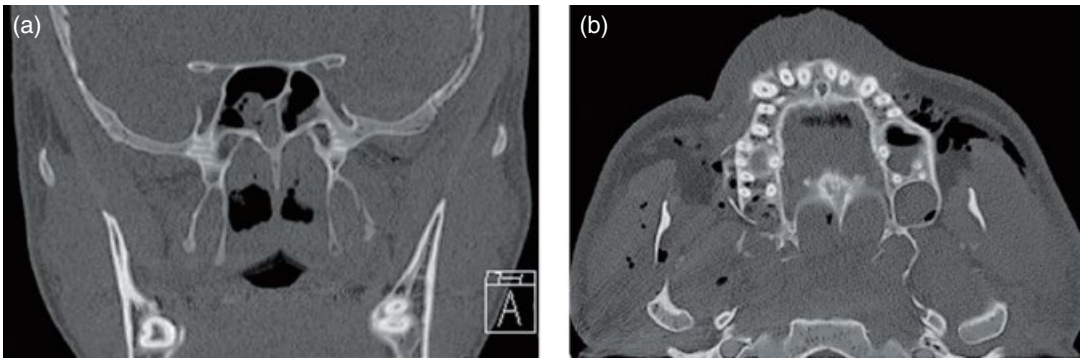


Figure 15.13 Coronal (a) and axial (b) bone-window computed tomography displaying fractures of the pterygoid plates; (b) is from the same case as in Figure 15.8. A, anterior.

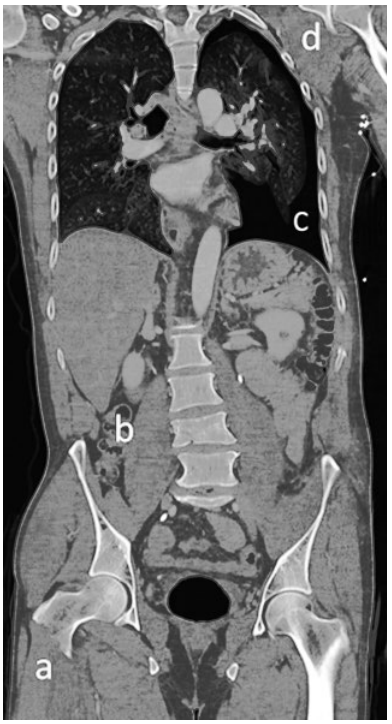


Figure 15.14 Coronal reconstruction of whole-body computed tomography for trauma, displaying a fractured femur (a), a compression (wedge-shaped) fracture of a lumbar vertebra (b), pneumothorax of the left lung (c), and (d) emphysema in the soft tissue adjacent to the ribcage on the left side.

fracture (Figures 15.7, 15.21, and 15.22) the latter. As the LeFort III fracture involves the skull base (Figure 15.11) frequently with CSF rhinorrhea, it is considered a cranial fracture. There is another important group, the nasal and increasingly nasoethmoid complex of fractures (Figure 15.12), ranging from a simple fracture of the nasal bones of the external nose to more severe fractures extending into the ethmoid air cells and even to the cribiform plate, and thereby to the floor of the anterior cranial fossa (Figure 15.12).

Displacement of a zygomatic/malar fracture into the orbit can cause proptosis (exophthalamos), with forward displacement of the eyeball (Figure 15.22).

15.9 Orbital Blowouts

Although orbital blowout fractures were more often complicated by ocular injuries compared with other facial fracture patterns, high-impact zygomatic fractures were most commonly associated with blindness [40]. Therefore, an ophthalmic examination should be undertaken preoperatively of all zygomaticomaxillary fractures, because



Figure 15.15 Computed tomography of a bilateral comminuted fracture of the mandible. This fracture is accompanied by significant facial and neck swelling. The black areas within the soft tissue represent emphysema. Source: Courtesy of Dr. Martin Aidelbaum, Faculty of Dentistry, University of British Columbia.



Figure 15.17 Condylar head fractured through the glenoid fossa into the middle cranial fossa (arrow). The medial maxilla displays a LeFort II fracture. There is some emphysema lateral to the right maxillary sinus and anterior to the left maxillary sinus.

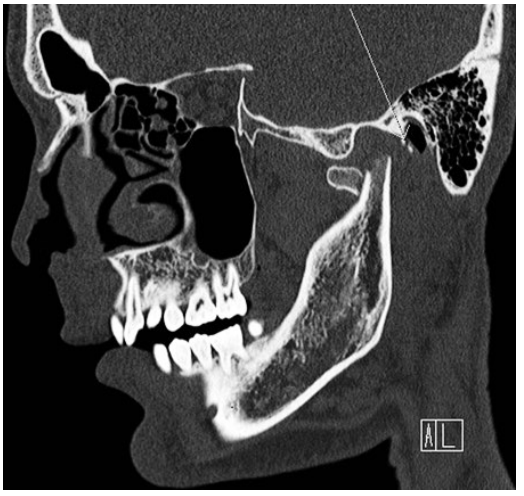


Figure 15.16 Sagittal bone-window computed tomography revealing a fracture through the condylar neck and accompanying fracture of the external acoustic meatus. The condylar head is displaced anteriorly. Note the thinness of the bone between the glenoid and middle cranial fossae. A, anterior; L, lateral.

10% of these fractures are associated with major or blinding injuries to the eyeball itself and a further 6% with traumatic optic neuropathy [41]. It also follows that as the blowout fracture is achieved by the secondary displacement of the globe/eyeball back into the orbital cavity by the primary traumatizing force directly impacting on it, the eyeball has sustained trauma. Therefore, it would be prudent that all such cases are referred to an ophthalmic specialist at the earliest opportunity.

Fractures of the orbital floor (Figures 15.19 and 15.20) and medial wall (Figures 15.19 and 15.20) each accounted for a third of all orbital fractures [41], which is also confirmed by Mundinger et al. [34]. Blowout fractures in East Asians are more likely to involve the medial wall, in contrast to those in Caucasians, which more frequently affect the floor [42]. Although the most frequent

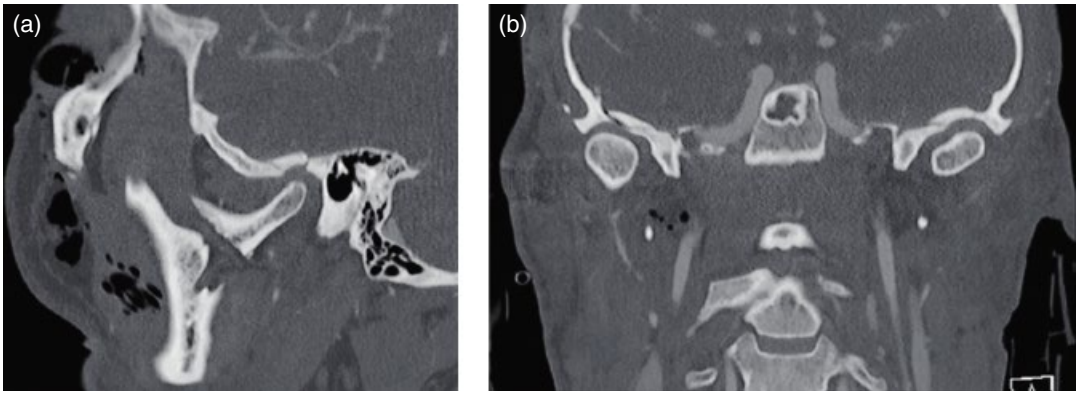


Figure 15.18 Sagittal (a) and coronal (b) bone-window computed tomography displaying a fracture through the sigmoid notch separating the condyle and its neck from the rest of the ramus. The condylar head on both sides has fractures through the roof of the glenoid fossa into the middle cranial fossa. Note the extra- and intracranial internal carotid arteries in (b).

complication of a blowout fracture is diplopia (28%), followed by limitation in extraocular movement (13%) and then by enophthalamus (3%) [43], enophthalmos is indicative of a severe orbital blowout [44]. CT permits better appreciation of injury to the optic nerve at its passage through the optic canal at the time of first presentation [41]. A retro-orbital hemorrhage is an important complication to detect (Figure 15.23).

Early use of CT in the diagnosis of nasoethmoid orbital fractures will optimize the success of the outcome, minimizing later postoperative deformities [45].

15.10 Other Important Considerations Relating to Fractures of the Face and Jaws

Emphysema or air entrapment in the soft tissues after fractures through the walls of the sinuses and nasal cavity (Figures 15.8, 15.13, 15.15, 15.18, and 15.20), though not common, is not unexpected of fractures of the middle third of the face [46]. Nevertheless, a substantial comminuted fracture of the body of the mandible in Figure 15.15 reveals extensive emphysema in the soft tissues immediately adjacent to the fractures and the suprahyoid neck. Emphysema from a facial fracture can spread to the mediastinum by way of the deep spaces of the neck (see Table 17.2) [47, 48].

Cervical spine fractures accompany 6.7% of all maxillofacial fractures in the United States [49]. Elahi et al. reported that the sixth and seventh cervical vertebrae were affected in 41% of their cases of cervical spine injury [50]. Mundinger et al. reported that although 6.6% of facial fracture patients had at least one fracture of the cervical spine, 1.2% had multiple fractures [34]. Those with frontal, LeFort III, and panfacial fractures (Figures 15.7 and 15.11) had significantly more cervical spine fractures than others [34]. Therefore, all seven cervical vertebrae should be included in any imaging protocol of facial fractures. Fractures of the upper face are associated with injury to the middle and lower cervical spine (Figure 15.24), and unilateral mandibular

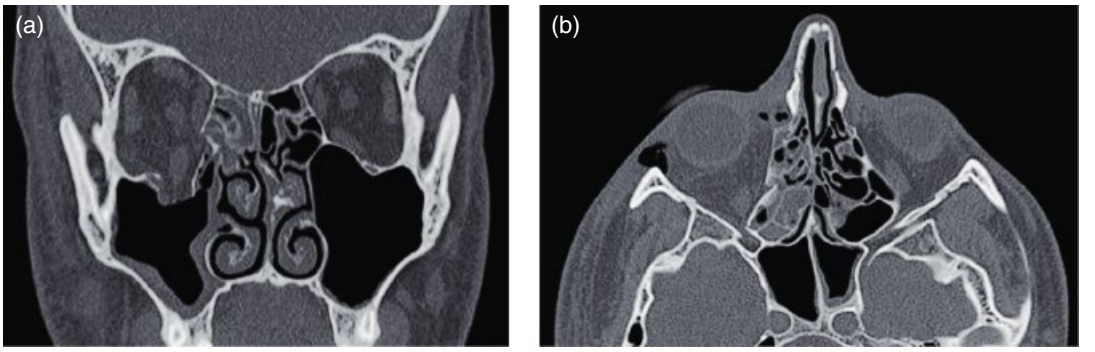


Figure 15.19 Coronal (a) and axial (b) bone window computed tomography displaying a blowout fracture into the right maxillary sinus. (a) Trapdoor fracture of the floor of the orbit with accompanying prolapse of some of the orbital contents. (b) There is also a fracture of the right lamina papyracea (also called the orbital lamina). The lumens of the right ethmoid air cells are opacified.

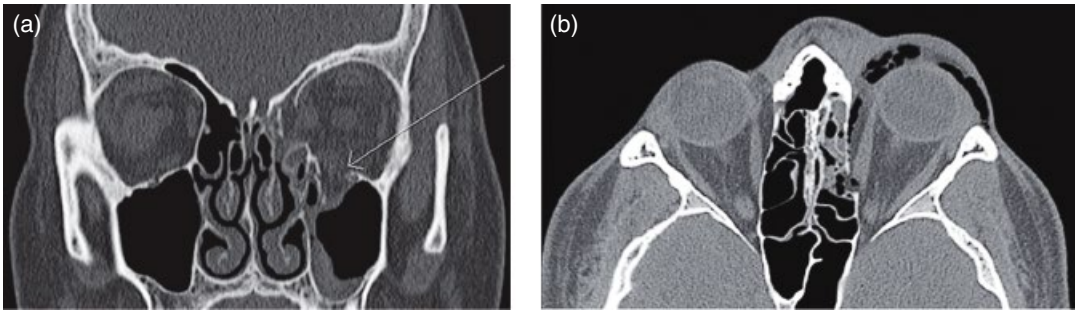


Figure 15.20 Coronal (a) and axial (b) bone-window computed tomography revealing a blowout fracture of the left orbit. (a) Trapdoor through the medial orbital floor. (b) Fracture of the lamina papyracea, opacification of the ethmoid air cells, and orbital emphysema in the left lower eyelids.

fractures are associated with injury to the upper cervical spine (Figure 15.25) [51]. Although the literature has made a case for inclusion of the cervical spine in a prescription for CT, already indicated for the further investigation of facial trauma by the clinical examination and any conventional radiographs, cervical spine CT should not otherwise be undertaken lightly. Such prescription should follow the guidelines of either the National Emergency X-Radiography Utilization Study (NEXUS) [52] or the Canadian Cervical Spine Rule for Radiography (CCR) [53].

15.10.1 RECENT DEVELOPMENTS IN TRAUMA RADIOLOGY DETECTION AND DIAGNOSIS OF FRACTURES OF THE FACE AND JAWS

In addition to WBCTT (Figure 15.14) becoming a standardized CT examination of trauma patients [29], cone-beam computed tomography (CBCT) technology has been successfully applied (see Chapter 5) in the operating room or theater by incorporation of a C-arm [50]. Two-thirds of the 177 patients imaged with such a unit had fractures of the face and jaws [54].



Figure 15.21 Axial bone-window computed tomography displaying a comminuted fracture of the left zygoma, including the zygomatic arch. The left ramus is fractured and the anterior portion displaced laterally.



Figure 15.22 Axial bone-window computed tomography displaying a fractured zygoma. It has been displaced medially into the right orbit, which exhibits proptosis.

Postoperatively, this technology allowed immediate revision of the surgery. Stuck et al. reported that intraoperative CBCT was successfully performed for 46 consecutive patients with facial fractures and had immediate revision of 26% of reductions [55]. The three-dimensional reconstruction of the CBCT dataset was particularly valuable [55], as is obvious in the three-dimensional reconstruction of the very complex facial trauma case displayed in Figure 15.7. The treatment plan

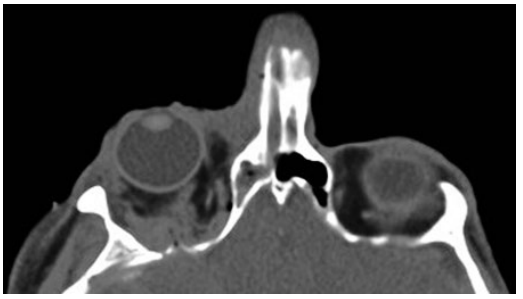


Figure 15.23 Axial soft-tissue computed tomography displaying proptosis of the right eye. This due to a retro-orbital hemorrhage.

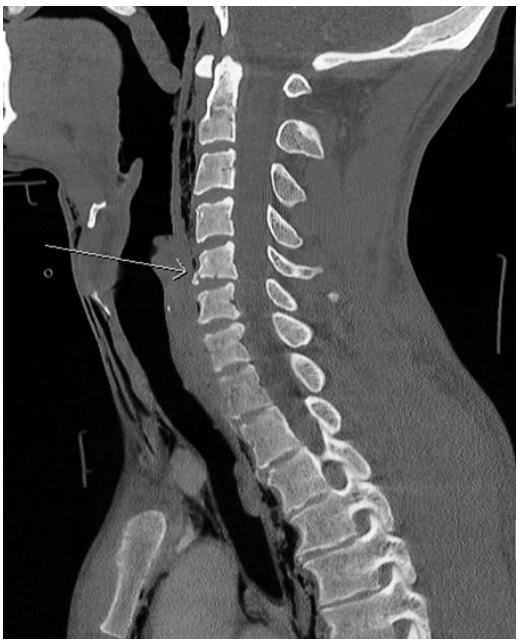


Figure 15.24 Sagittal bone-window computed tomography revealing a "teardrop" fracture of the body of the fifth cervical vertebra (C5, arrow). There is also emphysema in both the danger and prevertebral spaces extending into the mediastinum.

of nearly 10% of 164 patients who had equivocal clinical and conventional radiographic findings was changed after a CBCT investigation [56]. The current

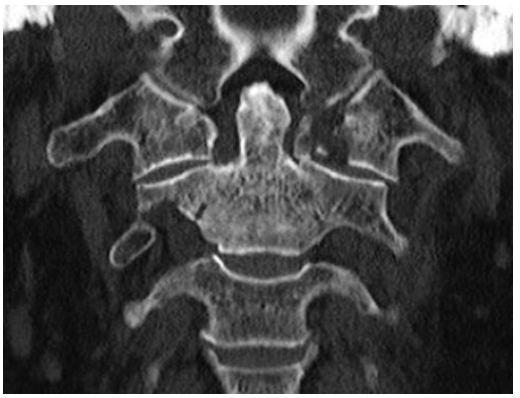


Figure 15.25 Coronal bone-window computed tomography of a fracture through the left lateral body of the first cervical vertebra (C1).

standard CBCT unit used in many dental offices has a limited role in the radiological diagnosis and assessment of fractures. Almost all units use a panoramic radiographic gantry, which requires the patient to stand perfectly vertical and to maintain an optimal posture and be motionless during the exposure, requirements that are unlikely to be achieved in a real-life ER situation, where it is less likely to find such patients who are fully conscious, sober, and cooperative. Although recently a small case series reported on the use of CBCT for orbital fractures, despite CBCT's much lower radiation dose, multidetector computed tomography (MDCT) is preferred, particularly for the detection of retro-orbital (retrobulbar) hemorrhage (Figure 15.23) [57].

References

1. Rashid, A., Eyeson, J., Haider, D. et al. (2013). Incidence and patterns of mandibular fractures during a 5-year period in a London teaching hospital. *Br. J. Oral Maxillofac. Surg.* 51: 794–798.
2. Powers, D.B. and Delo, R.I. (2013). Characteristics of ballistic and blast injuries. *Atlas Oral Maxillofac. Surg. Clin. North Am.* 21: 15–24.
3. Salonen, E.M., Koivikko, M.P., and Koskinen, S.K. (2010). Violence-related facial trauma: analysis of multidetector computed tomography findings of 727 patients. *Dentomaxillofac. Radiol.* 39: 107–113.
4. Leles, J.L., dos Santos, E.J., Jorge, F.D. et al. (2010). Risk factors for maxillofacial injuries in a Brazilian emergency hospital sample. *J. Appl. Oral Sci.* 18: 23–29.
5. Tuli, T., Haechl, O., Berger, N. et al. (2010). Facial trauma: how dangerous are skiing and snowboarding? *J. Oral Maxillofac. Surg.* 68: 293–299.
6. Girotto, J.A., MacKenzie, E., Fowler, C. et al. (2001). Long-term physical impairment and functional outcomes after complex facial fractures. *Plast. Reconstr. Surg.* 108: 312–327.
7. Winegar, B.A., Murillo, H., and Tantiwongkosi, B. (2013). Spectrum of critical imaging findings in complex facial skeletal trauma. *Radiographics* 33: 3–19.
8. Fraioli, R.E., Branstetter, B.F. 4th, and Deleyiannis, F.W. (2008). Facial fractures: beyond Le Fort. *Otolaryngol. Clin. N. Am.* 41: 51–76. vi.
9. Andreasen, J.O., Bakland, L.K., Flores, M.T. et al. (2011). *Traumatic Dental Injuries: A Manual*, 3e. Wiley-Blackwell.
10. Madan, K., Aggarwal, A.N., Bhagat, H., and Singh, N. (2013). Acute respiratory failure following traumatic tooth aspiration. *BMJ Case Rep.* 2013: bcr2012008393. https://doi.org/10.1136/bcr-2012-008393.
11. Casap, N., Alterman, M., Lieberman, S., and Zeltser, R. (2011). Enigma of missing teeth in maxillofacial trauma. *J. Oral Maxillofac. Surg.* 69: 1421–1429.
12. DeAngelis, A.F., Barrowman, R.A., Harrod, R., and Nastri, A.L. (2014). Review article: maxillofacial emergencies: maxillofacial trauma. *Emerg. Med. Australas* 26: 530–537.
13. Dean, N.R., Ledgard, J.P., and Katsaros, J. (2009). Massive hemorrhage in facial fracture patients: definition, incidence, and management. *Plast. Reconstr. Surg.* 123: 680–690.
14. Imai, T., Michizawa, M., Yamamoto, N. et al. (2014). Life-threatening oronasal hemorrhage managed by transcatheter embolization of bilateral maxillary arteries in an elderly patient with

comminuted LeFort I fracture. *Oral Surg. Oral Med. Oral Pathol. Oral Radiol.* 118: e6–e11.
15. Haug, R.H. and Foss, J. (2000). Maxillofacial injuries in the pediatric patient. *Oral Surg. Oral Med. Oral Pathol. Oral Radiol. Endod.* 90 (2): 126–134.
16. Eggensperger Wymann, N.M., Hölzle, A., Zachariou, Z., and Iizuka, T. (2008). Pediatric craniofacial trauma. *J. Oral Maxillofac. Surg.* 66: 58–64.
17. Gassner, R., Tuli, T., Hächl, O. et al. (2003). Cranio-maxillofacial trauma: a ear review of 9,543 cases with 21,067 injuries. *J. Craniomaxillofac. Surg.* 31: 51–61.
18. Swanson, E.W., Susarla, S.M., Ghasemzadeh, A. et al. (2015). Application of the mandible injury severity score to pediatric mandibular fractures. *J. Oral Maxillofac. Surg.* 73: 1341–1349.
19. Zelken, J.A., Khalifian, S., Mundinger, G.S. et al. (2014). Defining predictable patterns of craniomaxillofacial injury in the elderly: analysis of 1,047 patients. *J. Oral Maxillofac. Surg.* 72: 352–361.
20. Boers, M. and Cruz Jentoft, A.J. (2015). A new concept of health can improve the definition of frailty. *Calcif. Tissue Int.* 97: 429–431.
21. Provencher, V., Sirois, M.J., Ouellet, M.C. et al. (2015). Decline in activities of daily living after a visit to a Canadian emergency department for minor injuries in independent older adults: are frail older adults with cognitive impairment at greater risk? *J. Am. Geriatr. Soc.* 63: 860–868.
22. Bobinski, M., Shen, P.Y., and Dublin, A.B. (2016). Basic imaging of skull base trauma. *J. Neurol. Surg. B Skull. Base.* 77: 381–387.
23. Severson, M.A. 3rd, Bell, R.S., and Armonda, R.A. (2013). Triage and management of cranial injuries. *Atlas Oral Maxillofac. Surg. Clin. North Am.* 21: 105–115.
24. Reddy, M. and Baugnon, K. (2017). Imaging of cerebrospinal fluid rhinorrhea and otorrhea. *Radiol. Clin. N. Am.* 55: 167–187.
25. Lu, C., He, D., and Yang, C. (2014). Which craniofacial fractures are associated with external auditory canal bleeding? *J. Oral Maxillofac. Surg.* 72: 121–126.
26. Bellamy, J.L., Mundinger, G.S., Flores, J.M. et al. (2013). Facial fractures of the upper craniofacial skeleton predict mortality and occult intracranial injury after blunt trauma: an analysis. *J. Craniofac. Surg.* 24: 1922–1926.
27. Bellamy, J.L., Mundinger, G.S., Reddy, S.K. et al. (2013). Le Fort II fractures are associated with death: a comparison of simple and complex midface fractures. *J. Oral Maxillofac. Surg.* 71: 1556–1562.
28. An, J., Dai, F., Sun, Z., and Zhang, Y. (2014). Classification and characteristics of pterygoid process fracture associated with maxillary transverse fracture. *Oral Surg. Oral Med. Oral Pathol. Oral Radiol.* 117: 243–252.
29. Wiklund, E., Koskinen, S.K., Linder, F. et al. (2015). Whole body computed tomography for trauma patients in the Nordic countries 2014: survey shows significant differences and a need for common guidelines. *Acta Radiol.* 57: 750–757.
30. Holmgren, E.P., Dierks, E.J., Homer, L.D., and Potter, B.E. (2004). Facial computed tomography use in trauma patients who require a head computed tomogram. *J. Oral Maxillofac. Surg.* 62: 913–918.
31. Wilson, I.F., Lokeh, A., Benjamin, C.I. et al. (2001). Prospective comparison of panoramic tomography (zonography) and helical computed tomography in the diagnosis and operative management of mandibular fractures. *Plast. Reconstr. Surg.* 107: 1369–1375.
32. Roth, F.S., Kokoska, M.S., Awwad, E.E. et al. (2005). The identification of mandible fractures by helical computed tomography and panorex tomography. *J. Craniofac. Surg.* 16: 394–399.
33. Preda, L., La Fianza, A., Di Maggio, E.M. et al. (1998). Complex maxillofacial trauma: diagnostic contribution of multiplanar and tridimensional spiral CT imaging. *Radiol Med (Torino)* 96: 178–184. (Italian).
34. Mundinger, G.S., Dorafshar, A.H., Gilson, M.M. et al. (2014). Analysis of radiographically confirmed blunt-mechanism facial fractures. *J. Craniofac. Surg.* 25: 321–327.
35. Thai, K.N., Hummel, R.P. III, Kitzmiller, W.J., and Luchette, F.A. (1997). The role of computed tomographic scanning in the management of facial trauma. *J. Trauma* 43: 214–217. discussion 217–218.
36. Ogura, I., Kaneda, T., Sasaki, Y. et al. (2015). Prevalence of temporal bone fractures in patients with mandibular fractures using multidetector-row CT. *Clin. Neuroradiol.* 25: 137–141.

37. Naghipur, S., Shah, A., and Elgazzar, R.F. (2014). Does the presence or position of lower third molars alter the risk of mandibular angle or condylar fractures? *J. Oral Maxillofac. Surg.* 72: 1766–1772.
38. Imai, T., Sukegawa, S., Kanno, T. et al. (2014). Mandibular fracture patterns consistent with posterior maxillary fractures involving the posterior maxillary sinus, pterygoid plate or both: CT characteristics. *Dentomaxillofac. Radiol.* 43: 20130355.
39. Garg, R.K., Alsheik, N.H., Afifi, A.M., and Gentry, L.R. (2015). Pterygoid plate fractures: not limited to Le Fort fractures. *J. Craniofac. Surg.* 26: 1823–1825.
40. Magarakis, M., Mundinger, G.S., Kelamis, J.A. et al. (2012). Ocular injury, visual impairment, and blindness associated with facial fractures: a systematic literature review. *Plast. Reconstr. Surg.* 129: 227–233.
41. Lee, H.J., Jilani, M., Frohman, L., and Baker, S. (2004). CT of orbital trauma. *Emerg. Radiol.* 10: 168–172.
42. Sun, M.T., Wu, W., Watanabe, A. et al. (2015). Orbital blowout fracture location in Japanese and Chinese patients. *Jpn. J. Ophthalmol.* 59: 65–69.
43. Shin, J.W., Lim, J.S., Yoo, G., and Byeon, J.H. (2013). An analysis of pure blowout fractures and associated ocular symptoms. *J. Craniofac. Surg.* 24: 703–707.
44. Kelley, P., Hopper, R., and Gruss, J. (2007). Evaluation and treatment of zygomatic fractures. *Plast. Reconstr. Surg.* 120: 5S–15S.
45. Sargent, L.A. (2007). Nasoethmoid orbital fractures: diagnosis and treatment. *Plast. Reconstr. Surg.* 120: 16S–31S.
46. Brasileiro, B.F., Cortez, A.L., Asprino, L. et al. (2005). Traumatic subcutaneous emphysema of the face associated with paranasal sinus fractures: a prospective study. *J. Oral Maxillofac. Surg.* 63: 1080–1087.
47. Patel, N., Lazow, S.K., and Berger, J. (2010). Cervicofacial subcutaneous emphysema: case report and review of literature. *J. Oral Maxillofac. Surg.* 68: 1976–1982.
48. Makrides, H. and Lawton, L.D. (2017). Don't blow it! Extensive subcutaneous emphysema of the neck caused by isolated facial injuries: a case report and review of the literature. *J. Emerg. Med.* 52: e57–e59. https://doi.org/10.1016/j.jemermed.2015.12.025.
49. Roccia, F., Cassarino, E., Boccaletti, R., and Stura, G. (2007). Cervical spine fractures associated with maxillofacial trauma: an 11-year review. *J. Craniofac. Surg.* 18: 1259–1263.
50. Elahi, M.M., Brar, M.S., Ahmed, N. et al. (2008). Cervical spine injury in association with craniomaxillofacial fractures. *Plast. Reconstr. Surg.* 121: 201–208.
51. Mithani, S.K., St-Hilaire, H., Brooke, B.S. et al. (2009). Predictable patterns of intracranial and cervical spine injury in craniomaxillofacial trauma: analysis of 4786 patients. *Plast. Reconstr. Surg.* 123: 1293–1301.
52. Hoffman, J.R., Wolfson, A.B., Todd, K., and Mower, W.R. (1998). Selective cervical spine radiography in blunt trauma: methodology of the National Emergency X-Radiography Utilization Study (NEXUS). *Ann. Emerg. Med.* 32: 461–469.
53. Stiell, I.G., Wells, G.A., Vandemheen, K.L. et al. (2001). The Canadian C-spine rule for radiography in alert and stable trauma patients. *JAMA* 286: 1841–1848.
54. Pohlenz, P., Blessmann, M., Blake, F. et al. (2007). Clinical indications and perspectives for intraoperative cone-beam computed tomography in oral and maxillofacial surgery. *Oral Surg. Oral Med. Oral Pathol. Oral Radiol. Endod.* 103: 412–417.
55. Stuck, B.A., Hülse, R., and Barth, T.J. (2012). Intraoperative cone beam computed tomography in the management of facial fractures. *Int. J. Oral Maxillofac. Surg.* 41: 1171–1175.
56. Kaeppler, G., Cornelius, C.P., Ehrenfeld, M., and Mast, G. (2013). Diagnostic efficacy of cone-beam computed tomography for mandibular fractures. *Oral Surg. Oral Med. Oral Pathol. Oral Radiol.* 116: 98–104.
57. Brisco, J., Fuller, K., Lee, N., and Andrew, D. (2014). Cone beam computed tomography for imaging orbital trauma—image quality and radiation dose compared with conventional multislice computed tomography. *Br. J. Oral Maxillofac. Surg.* 52: 76–80.

Chapter 16

Temporomandibular joint diseases

16.1 Introduction

The purpose of this chapter is to direct the reader to the appropriate imaging and its interpretation, so as to enhance effective treatment planning of a particular patient's *temporomandibular joint* (TMJ) disease. Although *temporomandibular joint disorders* (TMDs), the most frequent clinical phenomenon affecting the TMJ, are a major source of human misery, provoking the spilling of much academic ink over the last five decades, we will first consider the anatomy, the basics of TMJ imaging, and other pathology that may affect the TMJ.

The TMJ exists between the mandible and the temporal bone of the skull (Figure 16.1). Although among the smallest, it is one of the most important joints in the body as being part of the masticatory apparatus it is necessary for nutrition. The TMJ also has the most complicated motion of all joints [1], combining rotation and gliding, which is facilitated by two separate synovial cavities separated by a meniscus (Figure 16.2). Not only is the movement of these bilateral joints linked, they are also affected by the patient's dental occlusion. Although the dental occlusion has been fully addressed elsewhere and will therefore not be discussed further in this chapter, the importance of having the jaws closed with the teeth in maximum intercuspation to optimize imaging is emphasized.

An overview of the lesions affecting the TMJ is set out in the flowcharts in Figures 16.3 and 16.4.

16.2 Overview of the Anatomy of the Temporomandibular Joint and Some Clinical Implications

The TMJ has three basic components: the condylar head, the joint space (bisected by an articular disc/meniscus to form two synovial cavities), and the glenoid fossa and articular eminence of the temporal bone (Figure 16.2). This complex is contained within a fibrous capsule. The glenoid fossa is divided into two parts by a narrow slit, the petrotympanic fissure, which calcifies as the patient ages [2]. Although the bone (the *roof of the glenoid fossa*, RGF) separating the TMJ from the middle cranial fossa is very thin, about 1 mm [3], it is only infrequently penetrated traumatically by the condylar head or by TMJ lesions, such as chondromatosis (Figure 16.5). Chronic TMD may by way of osteoarthritis provoke thickening of the RGF [4]. The joint space is visualized as a radiolucent structure (Figure 16.6) by virtue of its wholly soft-tissue content on conventional radiography (including panoramic radiography), conventional tomography, bone-window *multidetector*

Oral and Maxillofacial Radiology: A Diagnostic Approach, Second Edition. Edited by David MacDonald.
© 2020 John Wiley & Sons, Inc. Published 2020 by John Wiley & Sons, Inc.

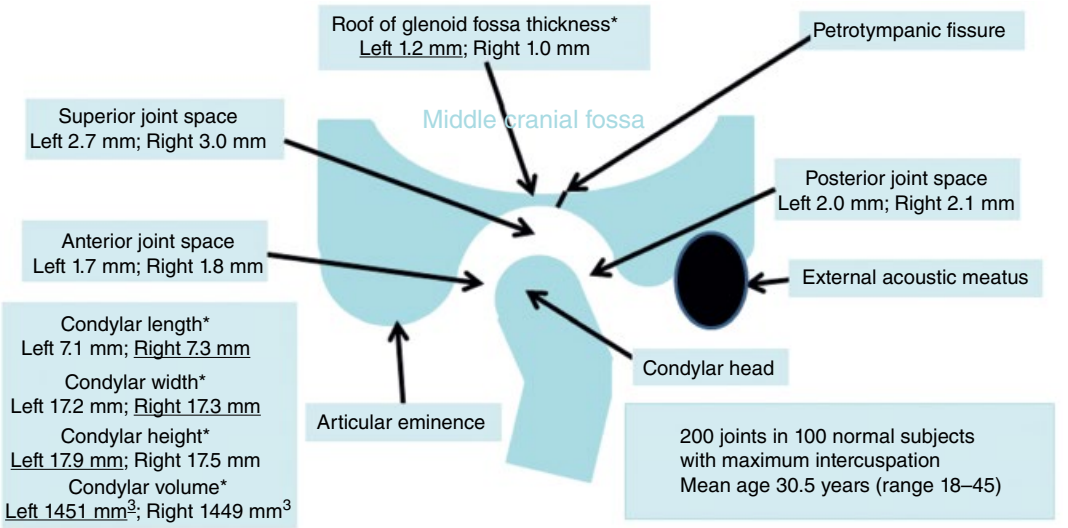


Figure 16.1 Schematic diagram in a sagittal plane displaying the main skeletal components of the temporomandibular joint and their relations, as observable on cone-beam computed tomography (CBCT). Note: Only the condyle and base of the skull will be displayed on CBCT. Both the superior and inferior joint cavities and the intervening meniscus cannot be displayed by CBCT as separate entities. Asterisk indicates significant difference. Underlining indicates the longer side for that value. Source: Measurements in millimeters (reduced to one decimal point) derived from Al-koshab, M., Nambiar, P., and John, J. (2015). Assessment of condyle and glenoid fossa morphology using CBCT in South-East Asians. *PLoS One*. 10: e0121682.

computed tomography (MDCT), and *cone-beam computed tomography* (CBCT). The only radiopacities that may be observed occasionally within this space by these modalities are *articular loose bodies*. These radiopacities represent "joint mice" (isolated bone fragments from the condyle or temporal bone), *synovial chondromatosis* [5], and *pseudogout* (*chondrocalcinosis*; Figure 16.5) [6]. The last two diseases can erode through the skull base [7, 8]. Yokota et al. included *chondrosarcoma* and *osteosarcoma* in the differential diagnosis of a case of synovial chondromatosis [9].

The condylar head in the axial (horizontal) plane is not only bean or almond shaped medially-laterally, but the medial pole is more posteriorly positioned relative to the lateral pole. Therefore, rather than the long axis of the condylar head being directed laterally-medially perpendicular to the sagittal plane, it is angled backward by an average of 20° from that perpendicular (Figure 15.3). Therefore, any reconstructions of the TMJ in the sagittal or coronal plane will transect the condylar head tangentially rather than orthoradially. As a result, some oral and maxillofacial radiologists will use an axial reconstruction from an existing MDCT or CBCT dataset of the head or a *submentovertex* (SMV) projection to determine this posterior angulation of the condylar head, prior to performing a small *field-of-view* (FOV) high-spatial-resolution CBCT of that joint.

The normal shape of the condylar head in the sagittal plane is rounded. The size and shape of the normal condyles are broadly symmetrical bilaterally. The *bifid mandibular condyle* (BMC) is a normal

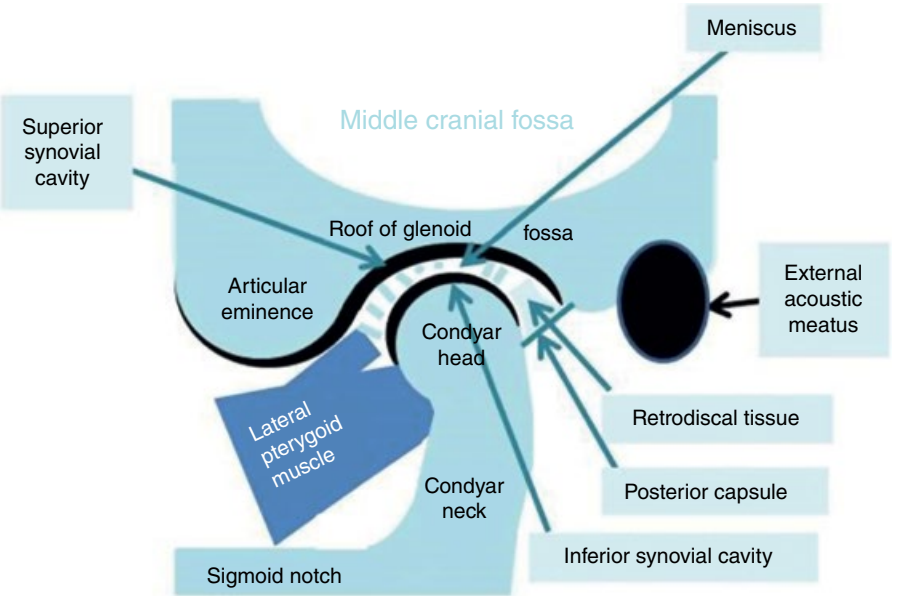


Figure 16.2 Schematic diagram displaying the main anatomical features of the soft-tissue component of the temporomandibular joint (TMJ) in a sagittal plane, as observable on magnetic resonance imaging. The C-shaped inferior synovial cavity caps the condylar head and permits rotational movement, whereas the sigmoid-shaped superior synovial cavity lies between the meniscus and the glenoid fossa and the articular eminence, permitting gliding movement of the condylar head and the meniscus together. The forward-gliding movement of the meniscus and the mandible on mouth opening is effected by the lateral pterygoid, which is inserted into both the pterygoid pit in the neck of the condyle and the anterior margin of the meniscus. Inserted into the posterior margin of the meniscus is the elastin- and collagen-rich retrodiscal tissue, which assists in retraction of the meniscus on closing. This tissue also has a rich venous plexus and therefore features prominently when the TMJ is inflamed. The posterior capsule prevents dislocation posteriorly.

variant (Figure 16.7) and should be identified as such and not mistaken for pathology. To complicate this identification, the BMC is three times more likely to present on panoramic radiographs and CBCTs unilaterally [10]. Nikolova et al.'s summary of the literature reported that BMC's incidence on panoramic radiographs ranges from 0.02% in Brazilians and 0.5% in Turks to 3.5% in Iranians. BMC's incidence on CBCTs in Koreans was 0.5% [10].

Although the condylar head in the adult has a cortex, this cortex does not begin to appear until the early teens [11]. This normal reason for the absence of a cortex should be considered when reviewing images of children and adolescents.

The final major component of the TMJ is the articular disc or meniscus (Figure 16.6), which features prominently in the majority of symptomatic TMJs. It is a fibrous structure which is attached directly to the capsule laterally and medially, and indirectly posteriorly by the retrodiscal tissue. Anteriorly it is attached to the lateral pterygoid muscle, which pulls it forward in conjunction with the condylar head, to which the lateral pterygoid is also attached (into the pterygoid pit in the anterior condylar neck).

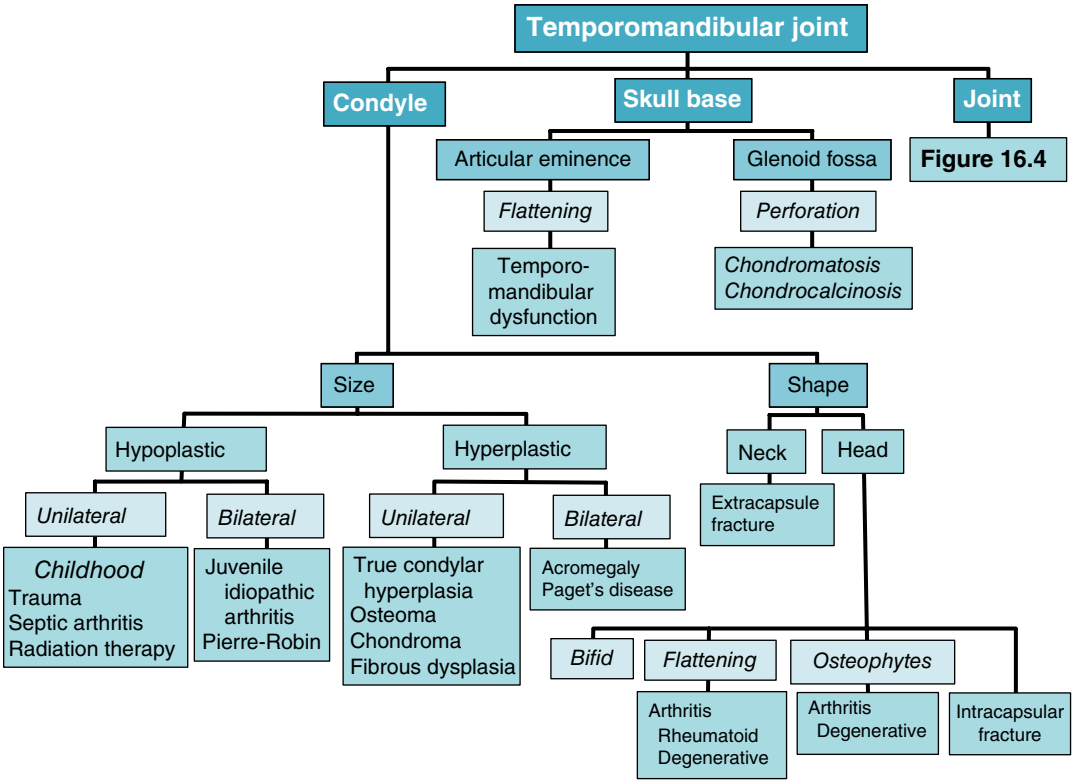


Figure 16.3 Temporomandibular joint – condyle and skull base.

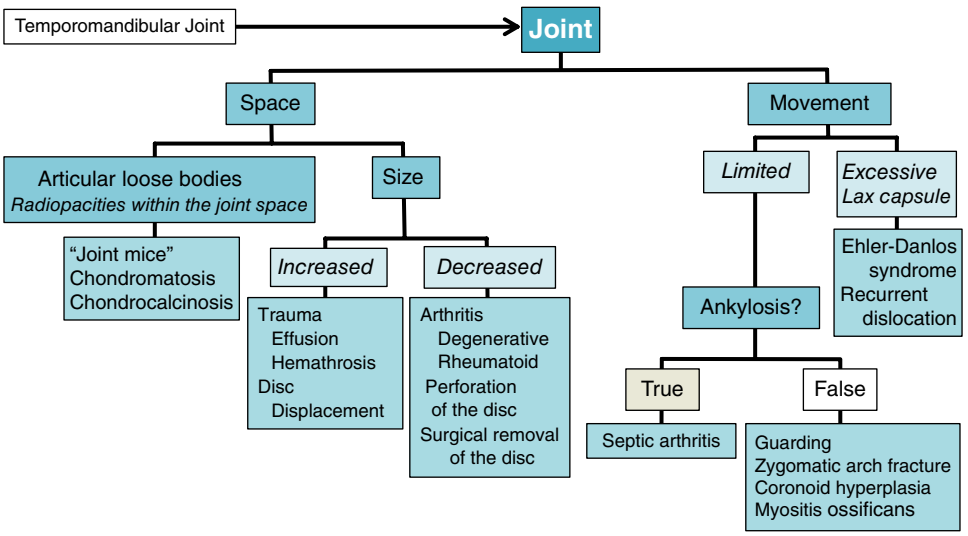


Figure 16.4 Temporomandibular joint – joint.

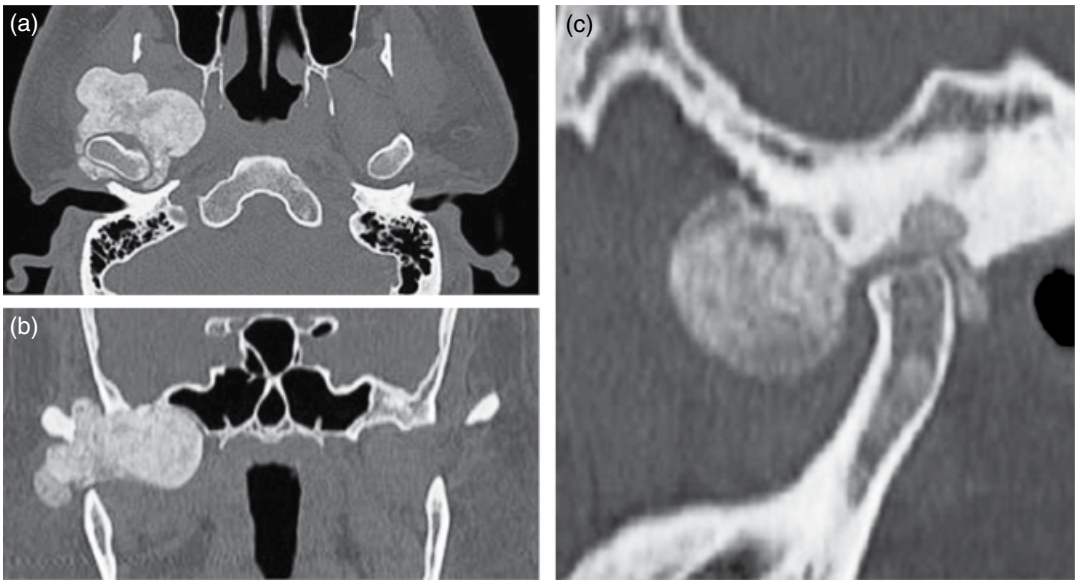


Figure 16.5 Cone-beam computed tomography of pseudogout (chondrocalcinosis) affecting the right condyle: (a) axial, (b) coronal, and (c) sagittal reconstructions. Source: Reproduced with permission from Kudoh, K., Kudoh, T., Tsuru, K., and Miyamoto, Y. (2017). A case of tophaceous pseudogout of the temporomandibular joint extending to the base of the skull. *Int. J. Oral Maxillofac. Surg.* 46:355–359.

16.3 Imaging of the Temporomandibular Joint

Historically, modalities using ionization radiation, namely conventional radiography and then computed tomography (Figure 16.6), have been used for TMJ disease. Today the only conventional radiography technique that still has a role in TMJ imaging is the panoramic radiograph, as it gives an overview of the condyle and adjacent osseous structures (Figure 16.8). Other conventional tomographic techniques such as transcranial and transpharyngeal projections are redundant. Although panoramic radiography is the most accessable modality, it is the least reliable, both due to superimposition (of the zygomatic arch, base of the skull, and the secondary image of the other side) and due to distortion [10], particularly in the posterior sextant, including the TMJ [12]. TMJ arthography, once a widely used diagnostic technique, is today employed as a therapeutic vehicle [13, 14]. Although the soft-tissue window of MDCT can display the disc in most patients, it is inferior to *magnetic resonance imaging* (MRI) (see Figure 16.6b and c) in displaying the entire soft-tissue component of the TMJ. In addition, the application of ultrasound to the TMJ is occasionally reported [15, 16]. Kirkhus et al. note that "Ultrasonography may be a valuable tool in the initial assessment of TMJ inflammation" [16]. Ultrasound of joints elsewhere in the body can be used to diagnose *juvenile idiopathic arthritis* (JIA) [17], which will be addressed later in this chapter. This is particularly important since involvement of the TMJ may only become noticeable clinically and on conventional radiography once substantial and irreparable damage has been done.

The advent of CBCT, with its better bone detail and a lower radiation dose, is

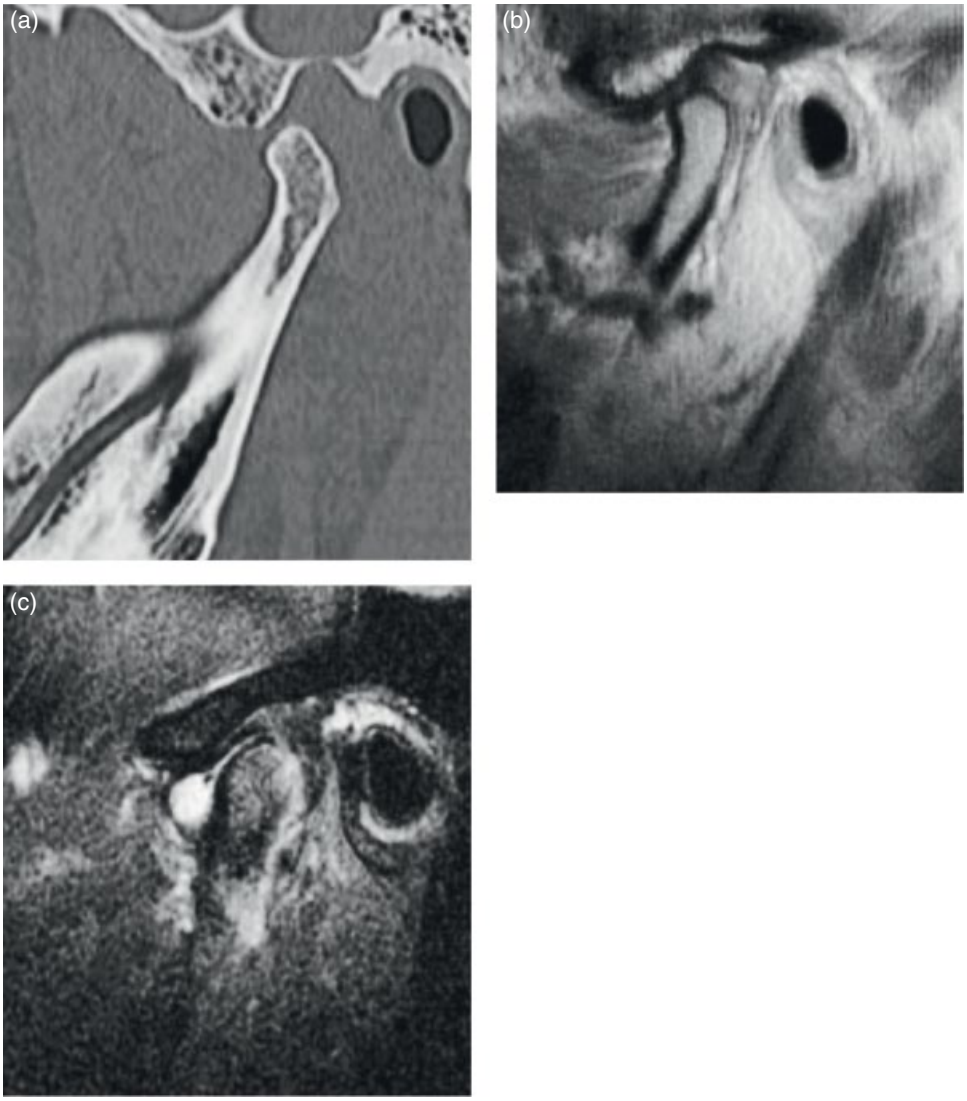


Figure 16.6 Bone-window computed tomography (a) and magnetic resonance images (MRI) – T1 weighted (b) and fat saturated T2 weighted (c) – are of the same patient investigated for a painful joint after trauma. (a) This displays exquisite bone detail. The soft tissue in this bone window is a uniform gray, punctuated only by the air-filled external acoustic meatus. (b) The hypointensity of the cortices of the condyle and glenoid fossa is similar to that of the air-filled external acoustic meatus. The T1-weighted MRI displays the soft-tissue anatomy in great detail. The isointense (gray) muscle fasiculae of the lateral pterygoid muscle is clearly obvious inserting into the pterygoid fossa. The interarticular disc appears as a hypointense (dark) structure in a normal relationship to the condylar head. (c) The hyperintense (bright white) area represents an effusion into the joint space and is indicative of ongoing inflammation. The hyperintense condylar marrow, which appeared relatively hyperintense in (b), is now hypointense in the fat-saturated (fat-suppression) T2-weighted image. Source: Reproduced with permission from MacDonald-Jankowski, D.S., Li, T.K., and Matthew, I. (2006). Magnetic resonance imaging for oral and maxillofacial Surgeons. Part 2: clinical applications. *Asian J. Oral Maxillofac. Surg.* 18:236–247.



Figure 16.7 Cropped panoramic radiograph of a 31-year-old male showing a bifid right condyle.

displacing MDCT for display of the osseous component and its changes [18].

The first image usually taken of a patient presenting with symptoms or signs indicating a TMJ problem is the panoramic radiograph. This provides the clinician with a lateral view of the condylar head and neck. Although the width of the focal plane of the panoramic radiograph is likely to include the whole width of the condylar head, the shape of the head can vary between patients. Nevertheless, if the condyles are symmetrical in shape and size, it is reasonable to assume they are normal, particularly in the absence of symptoms. However, beware that systemic diseases such as acromegaly, Paget's, and JIA frequently manifest bilaterally. Therefore, consideration of their other salient features is necessary. Those of acromegaly and Paget's are fully addressed in standard texts. Pierre-Robin is characterized by cleft palate, retrognathia, and glossoptosis. Although the significance of flattened condyles, erosions, and osteophytes to a diagnosis of TMD is considered later (Figure 16.14), an important systematic cause of TMJ erosion is scleroderma. This occurs in 6.3% of scleroderma patients in comparison to 1.8% in a control group [19] presenting with mechanical joint problems matched for gender and age; this difference was significant [19, 20].

Any difference in size between a patient's condylar heads can be assessed first by ensuring that the patient has been properly positioned within the panoramic radiographic unit prior to exposure. This may be readily assessed by comparing the width of the vertical rami and the molar teeth of both sides (Figure 16.8). Any difference should then be compared to the patient. If clinical re-examination of the patient confirms that there is no difference between the sides, then the image has been distorted due to incorrect positioning.

After it has been determined that one side is indeed larger, the clinician needs to determine which side is abnormal, because the other, smaller side could be hypoplastic. This can be appreciated by an abnormally shaped vertical ramus and an obtuse gonial angle (the angle formed by the lower border of the mandible and the posterior margin of the vertical ramus; see Figure 10.31). Hypoplasia of one side can result from a developmental accident such as hemorrhage of the stapedial artery in utero, with disruption of adjacent tissues including the condylar growth center. It can also occur in infancy due to radiotherapy. The midline of the mandible is skewed toward the hypoplastic side. An increase in size could be due to hyperplasia, neoplasia, or dysplasia results in the midline being skewed away from the hyperplastic side (Figure 16.9).

Lesions affecting the condyle may arise either primarily within it, such as osteoma (Figure 16.9) and chondrosarcoma, or elsewhere in the mandible and subsequently involve it, such as osteogenic sarcoma (Figure 16.10) and fibrous dysplasia (FD; Figure 16.11).



Figure 16.8 Upper half of a panoramic radiograph of a scleroderma patient. The right condyle is substantially shorter in comparision to the normal left condyle; compare the size of the brackets. The condylar height of each is defined by the superior point of the condylar head and the inferior point of the sigmoid notch. The distal-most maxillary molar on each side has been identified according to its international dental notation (see Figure 1.21) Note: The widths of the vertical rami and the maxillary molar teeth are similar, suggesting that the patient was properly placed within the panoramic radiograph prior to exposure. R, right. Source: Courtesy of Dr. Mervyn Gronitzky, Jewish General Hospital, Montreal.

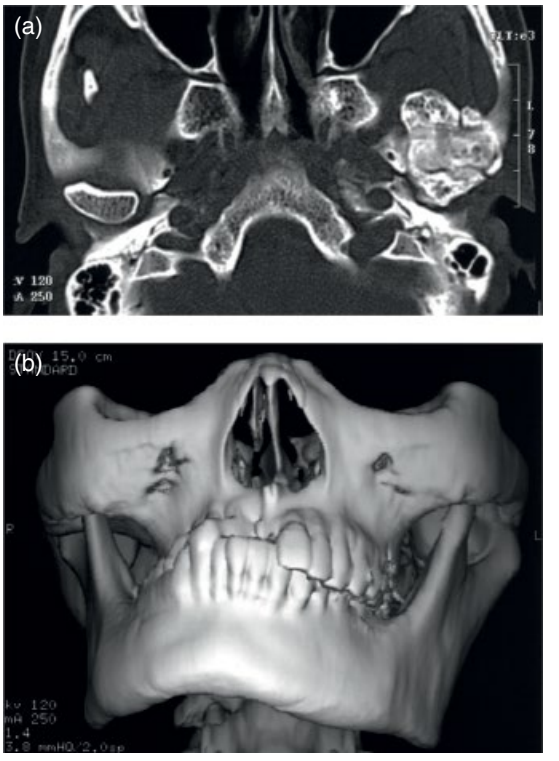


Figure 16.9 Computed tomography of an osteoma affecting the left condylar head. (a) Axial computed tomography (bone window) displaying the osteoma. In comparison with the normal ovoid-shaped contralateral right condylar head, the affected left condyle has substantially expanded in all directions. It has substantially reduced the joint space. (b) Three-dimensional reconstruction of the osteoma, displaying it as an expansion mainly of the medial pole of the condylar head. There is a midline shift to the unaffected right side (away from the hyperplastic or larger left side) and marked facial asymmetry.

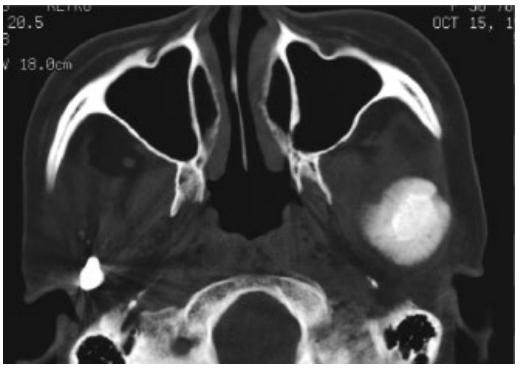


Figure 16.10 Axial computed tomography (bone window) of osteosarcoma affecting the condylar head. The primary site in the body of the mandible recurred twice after wide resections (see Figure 10.4). It has now spread to the condyle. The axial section displays an outline of a normal-sized and -shaped condylar head surrounded by a sunburst halo.

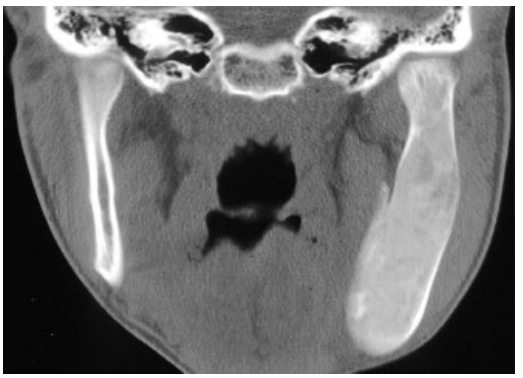


Figure 16.11 Coronal computed tomography (bone window) displaying fibrous dysplasia affecting the mandible and involving the condyle. The superior or articular portion of the condyle appears sclerotic and the neck is wider. Note the lingula.

One East Asian report on FD revealed that 6 of the 12 cases affecting the mandibular posterior sextant including the ramus also affected the condyle [20]. This high proportion of condylar involvement was not observed for most other lesions with a predilection for the posterior mandible affecting the same community. Of the 31 cases out of 36 ameloblastomas affecting the posterior sextant of the mandible, 2 involved the condyle [21]. Both were of the unicystic variant. One of these cases is featured in Figure 1.42. It has not replaced entirely the normal trabeculae of the condyle. The condyle was involved by only 1 of the 13 mandibular *keratocystic odontogenic tumors* (KCOTs) which affected the posterior sextant [22]. Only 1 of 6 mandibular cases of odontogenic myxoma approached the condyle [23]. These results would suggest that odontogenic neoplasms are unlikely to reach the condyle, even though the majority arise within the posterior sextant of the mandible.

Although the TMJ may be spared in most odontogenic neoplasms, certainly in the Southern Chinese community from which the above reports [20–23] were derived, nevertheless it is likely to be challenged by the change in jaw dynamics occasioned by these large lesions and their subsequent management.

16.4 Ankylosis

Ankylosis of the TMJ is the complete or partial fusion of the mandibular condyle to the temporal bone. Trauma is the cause in most cases. Traumatic TMJ ankylosis has been classified into two types, which are displayed in Figure 16.12.

Ankylosis of the TMJ results in restricted mouth opening, thereby interfering with speech and mastication. The destruction of the condylar cartilage, in the child, results in disturbances in the growth of the mandible, which may also contribute to airway problems [24]. Although associated with histories of trauma and infection, both local and systemic [24], its precise etiology and

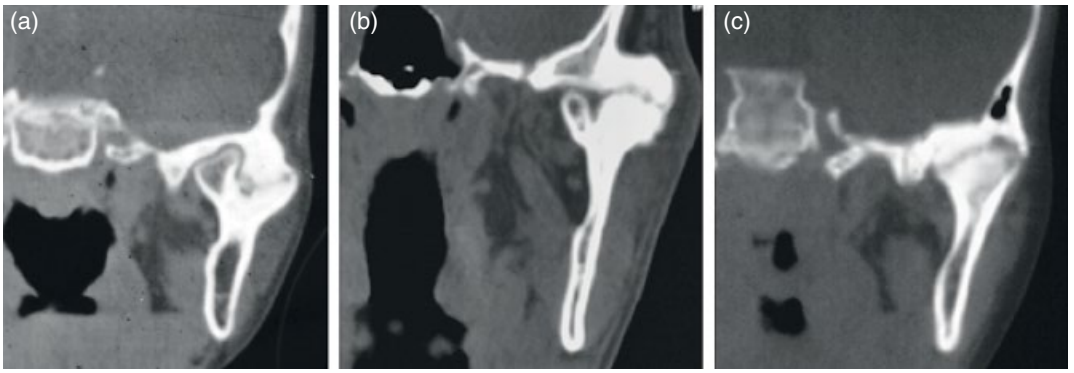


Figure 16.12 Classification of temporomandibular joint ankylosis derived from 130 Chinese cases. Type A1 is fibrous ankylosis without bony fusion of the joint (not displayed); Type A2 (a) is ankylosis with bony fusion on the lateral side of the joint, while the residual condyle fragment is bigger than half of the condylar head in the medial side; Type A3 (b) is similar to A2, but the residual condylar fragment is smaller than 0.5 of the condylar head; Type A4 (c) is ankylosis with complete bony fusion of the joint. Source: He, D., Yang, C., Chen, M., Zhang, X., Qiu, Y., Yang, X., Li, L., and Fang, B. (2011). Traumatic temporomandibular joint ankylosis: our classification and treatment experience. *J. Oral Maxillofac. Surg.* 69: 1600–1607. Reproduced with permission of Elsevier.

pathenogenesis are still not understood [25]. Due to its infrequent occurrence and difficulty in obtaining an entire surgical specimen including the temporal bone (understandably to minimize damage to the superjacent temporal lobe), a considered histopathological evaluation is not possible. Nevertheless, a study of 14 specimens reveals that both osteoarthritis and enthesopathy (the insertions of the tendons into the bone) occurred in TMJ ankylosis. These are suggestive of mechanical stress on the joint [25]. Nevertheless, ankylosis was discovered as a late complication in six out of nine cases of otogenic *septic arthritis of the temporomandibular joint* (SATMJ) in a case series; five cases required surgery [26].

SATMJ is extremely rare, affecting 2–10 out of every 100 000 individuals [27]. Its clinical presentation includes preauricular pain and trismus [27]. In order to prevent complications such as osteoarthritis, osteomyelitis bone erosions, ankylosis, sepsis, and brain abcesses, early diagnosis and prompt treatment are necessary [27]. Although the TMJ is near to the auditory apparatus, which experiences a high global prevalence of otitis media, common in childhood [28], a minuscule number of otogenic infections result in SATMJ. Nevertheless, early diagnosis and treatment are necessary [14]. Although 78 cases in the English literature (of which 40 are Chinese [29]) arise from infections contiguous to the TMJ, less than half arise from dental infection, whereas all continuous infections from the Japanese literature arise from dental infections [30]. Most of the remainder were due to hematogeous spread [30]. MRI performed for four of the seven cases of SATMJ revealed increased joint effusions (Figure 16.13) [31].

16.5 Temporomandibular Joint Disorder

In the population at large, it is not uncommon for individuals to experience pain and stiffness within one or both TMJs at least once in their life. These are the

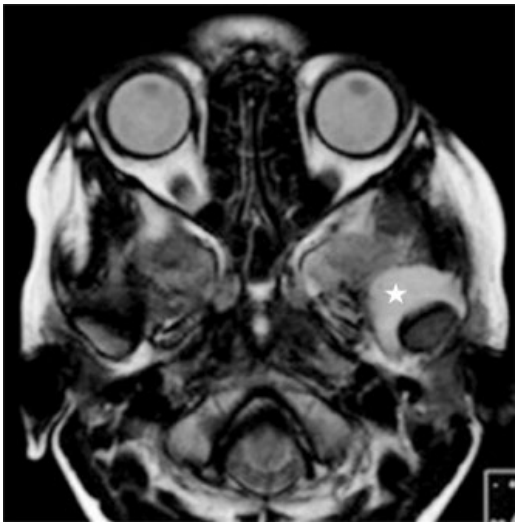


Figure 16.13 Axial T2-weighted magnetic resonance images showing significant effusion (asterisk) of the left temporomandibular joint associated with septic arthritis of the temporomandibular joint (SATMJ). Reproduced with permission from Bast, F., Collier, S., Chadha, P., and Collier, J. (2015). Septic arthritis of the temporomandibular joint as a complication of acute otitis media in a child: a rare case and the importance of real-time PCR for diagnosis. *Int. J. Pediatr. Otorhinolaryngol.* 79:1942–1945.

clinical hallmarks of the most common TMJ disease, TMD.

TMDs are, after chronic low back pain, the most important musculoskeletal disorder. They may affect a tenth of the population each year, manifesting as joint and/or facial pain, or dysfunctions such as problems with mastication. TMDs have a propensity to affect adult females during the menarche [32]. This suggests that female sex hormones may play a role.

There are two main TMDs: disc displacement (also called "internal derangement"), which is the more common, and osteoarthritis. Disc displacement occurs either with reduction or with no reduction on opening. It predominantly occurs anteriorly and is frequently referred to as *anterior disc displacement* (ADD), and occasionally as anterior disc displacement with reduction (ADDwR; Figure 16.14) or anterior disc displacement without reduction (ADDwoR; Figure 16.15) [33]. The patient frequently experiences a "click" or "pop" with ADDwR, when the disc returns (reduces) to its normal relationship to the condylar head. ADDwoR is often associated with a limitation in mouth opening from an average of 3.5 cm (normal) to 2 cm [33]. Hu et al. additionally adduced evidence that ADDwoR in a juvenile, during the pubertal growth spurt, may lead to mandibular growth disturbance, resulting in a shorter condylar head [34].

The three most common arthritides affecting the body are osteoarthritis (also called osteoarthrosis and degenerative joint disease), *rheumatoid arthritis* (RA), and gout (also called calcium pyrophosphate disease). Although gout affecting the TMJ is rare, cases of pseudo-gout (Figure 16.5) do occur. Osteoarthritis is the most common and generally affects the elder patient [35]. Loesser et al. noted that "ageing promotes the development of osteoarthritis in conjunction with other risk factors" [35]. These other risk factors, particularly for osteoarthritis of the knee, are gender, prior injury, and genetic predisposition [35]. Primary osteoarthritis of the TMJ arises from chronic overloading due to habits such as gum chewing, or unilateral chewing, which may be caused by a poorly maintained dental occlusion or it may arise from parafunction, such as bruxism and jaw clenching [36]. Osteoarthritis generally exhibits low inflammation, whereas autoimmune disease such as rheumatoid and psoriatic arthritis exhibits high inflammation [36]. These last diseases in addition affect other joints in the same patient.

The diagnostic process of TMD begins with the patient's complaint and the subsequent clinical examination, as it does for all disease. The most important and frequent clinical presentation is pain

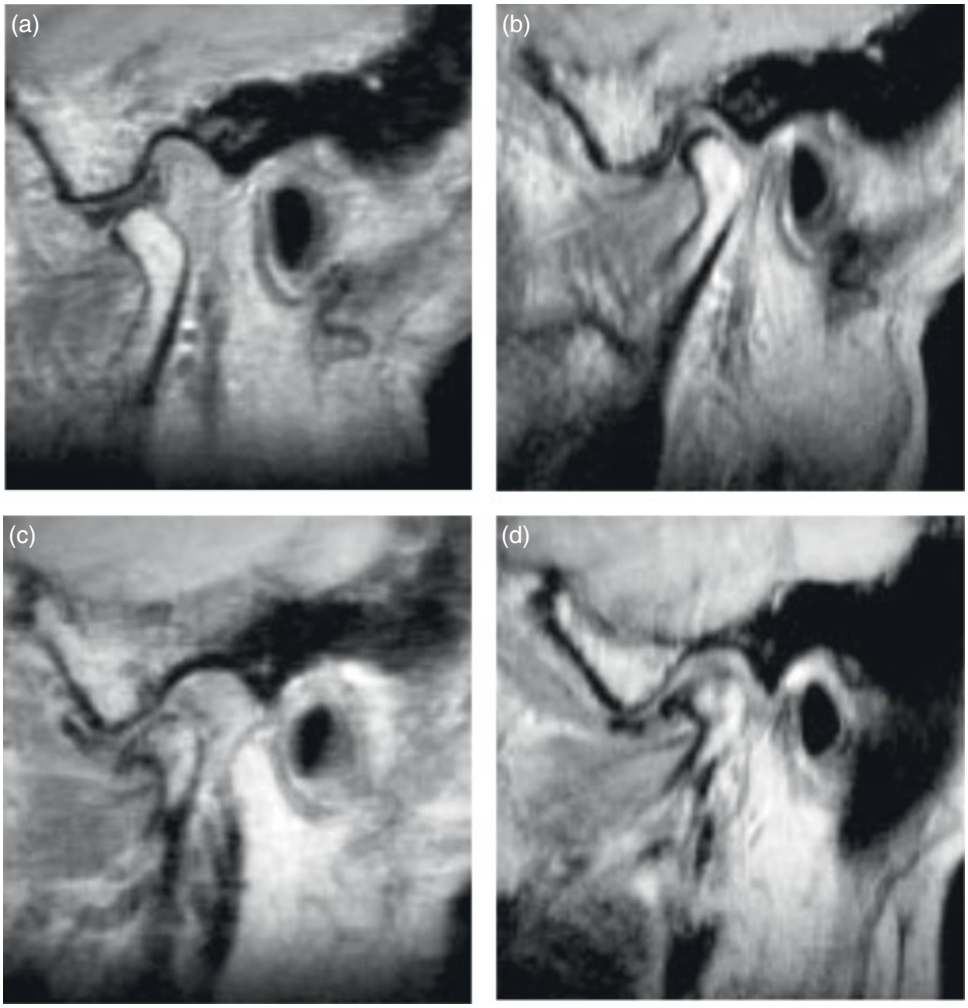


Figure 16.14 T1-weighted magnetic resonance images (MRI) exhibiting the side displaying partial disc displacement now in the normal disc position when in the open mouth position (a) and anterior disc displacement (ADD) in the closed mouth position (b), whereas the side displaying complete disc displacement showed ADD both in the open (c) and closed (d) mouth positions. This is an example of an anterior disc displacement without reduction (ADDwoR). The marrow of the condyle is normally fat filled and is hyperintense on T1-weighted MRI. The abnormal side exhibits an osteophyte, which gives the abnormal condyle the appearance of a bird's head. The normal side displays the meniscus (hypointense disc) properly interposed between the condyle and articular surface in both open and closed positions. The abnormal side displays ADD. Source: Reproduced with permission from MacDonald-Jankowski, D.S., Li, T.K., and Matthew, I. (2006). Magnetic resonance imaging for oral and maxillofacial Surgeons. Part 2: clinical applications. *Asian J. Oral Maxillofac. Surg.* 18:236–247.

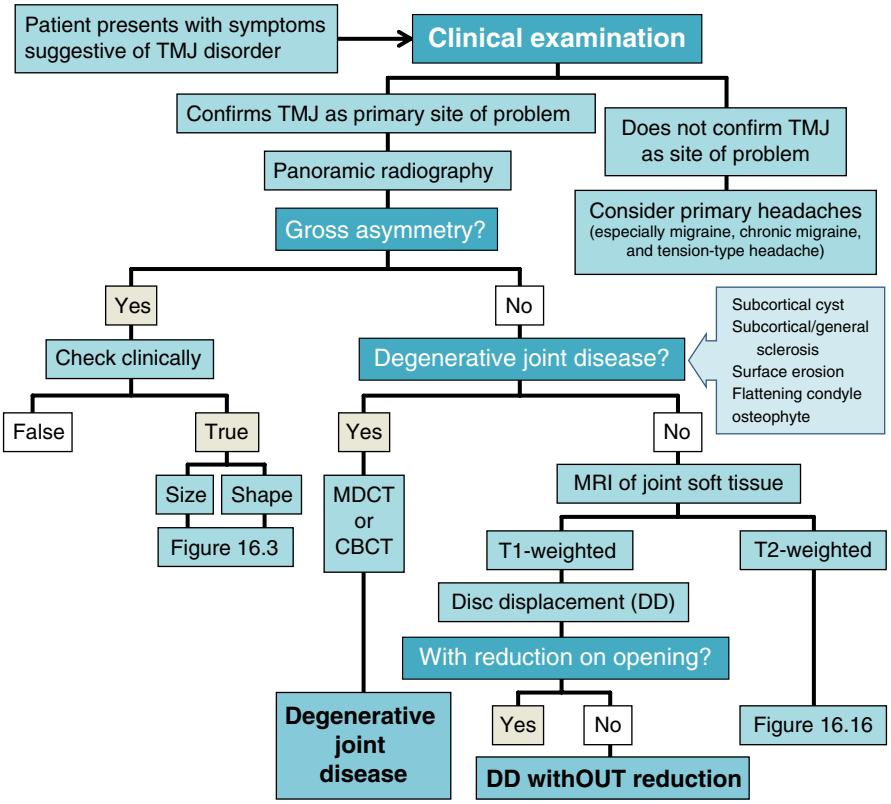


Figure 16.15 Flowchart displaying a process for the investigation of a case presenting with symptoms suggestive of a temporomandibular joint (TMJ) disorder. True asymmetry is suggestive of a systemic cause. Such causes are set out in the preceding flowcharts. Recent research suggests that magnetic resonance images (MRI) and cone-beam computed tomography (CBCT) together may optimize the evaluation of a clinical apparent temporomandibular disorder (TMD). In addition to degenerative joint disease, T1-weighted MRI can allow confirmation of disc displacement with/without reduction. The presense of an effusion within the joint space or within the bone marrow is suggestive of an ongoing inflammatory process.

in the TMJ and/or in the masticatory musculature. Other causes of pain around the jaws are primary headaches (such migraine, chronic migraine, and tension-type headache), which are often co-morbities of painful TMJs [37].

In Table 16.1, a synthesis of three American reports [38], a definite minority of cases present without pain, particularly those with disc displacement with reduction on mouth opening. This is significantly less than for disc displacement without reduction on opening and when degenerative joint disease is radiologically apparent (see Table 16.1), although many cases display bilateral joint involvement (this was significantly the greatest for disc displacement with reduction; see Table 16.1). Chantaracherd et al.'s report [38] substantially confirmed the general findings of Larheim's work carried out over a decade earlier. In addition to patients, Larheim included healthy symptom-free volunteers [39]. He found that

Table 16.1 Temporomandibular disorder; Synthesis of three American case series.

Temporomandibular disorder stage or step	Number of cases	Number of cases with pain (%)	% of cases with bilateral disease
Normal	N/A	N/A	N/A
Disc displacement with reduction	217	154 (71%)	69%
Disc displacement WithOUT reduction	77	63 (82%)	28%
Degenerative joint disease	241	202 (84%)	42%

Note: Cases with disc displacement with reduction on jaw opening present significantly less frequently with pain than those with disc displacement without reduction on jaw opening (FET = 0.04), and even less frequently in comparison with those with degenerative joint disease (FET = 0.007). Bilateral disease is significantly more present in cases of disc displacement with reduction than in those without reduction (FET 1.76×10^{-10}) and those with degenerative joint disease (FET = 4.9×10^{-9}).
N/A, information not available.
Source: Adapted from Chantaracherd, P., John, M.T., Hodges, J.S., and Schiffman, E.L. (2015). Temporomandibular joint disorders' impact on pain, function, and disability. *J. Dent. Res.* 94 (3 Suppl): 79S–86S.

Table 16.2 Definitions of changes observed in the condylar head on panoramic radiographs, magnetic resonance images, and computed tomography, and those selected for cone-beam computed tomography.

Term	Definition
Osteophyte	Marginal hypertrophy with sclerotic borders and exophytic angular formation off osseous tissue arising from the surface
Subcortical sclerosis	Any increased thickness of corticsal plate in load-bearing areas relative to adjacent non-load-bearing areas
Subcortical cyst	A cavity below the articular surface that deviates from normal marrow pattern
Surface erosion	Loss of continuity of articular cortex
Articular surface flattening	A loss of the rounded contour of the surface
General sclerosis	No clear trabecular orientation with no delineation between the cortical layer and the trabecular bone that extends throughout the condylar head

Source: Adapted from Ahmad, M., Hollender, L., Anderson, Q, et al. (2009). Research diagnostic criteria for temporomandibular disorders (RDC/TMD): development of image analysis criteria and examiner reliability for image analysis. *Oral Surg. Oral Med. Oral Pathol. Oral Radiol. Endod.* 10: 844–860 and Larheim, T.A., Abrahamsson, A.K., Kristensen, M., et al. (2015). Temporomandibular joint diagnostics using CBCT. *Dentomaxillofac. Radiol.* 44: 20140235.

disc displacement without reduction and degenerative joint disease occurred more in TMJ patients than in healthy nonsymptomatic volunteers, thus indicating that these two phenomena require diagnosis and treatment. Although disc displacement was bilateral, pain, joint effusion, and marrow changes were generally unilateral. Furthermore, Larheim found that TMJ pain was positively dependent on TMJ effusion and condylar marrow abnormalities, but negatively dependent on cortical bone abnormalities. This means that more emphasis needs to be placed on T2-weighted MRI that displays the effusions, rather than simply reviewing MDCT or CBCT of the condyle. This is important, as the availability of CBCT may lead to its unnecessary overuse.

Although Suenaga et al. agreed that the clinical examination is necessary, it is the imaging that may better reveal the cause of the pain [40]. The six most important causes of pain are disc displacement (or internal joint derangement), joint effusion, bone marrow effusion, osteoarthritis, and myositis, or muscle pain. Ultrasonography has a role in the evaluation of of muscle pain [40]. Nevertheless, the disadvantage of imaging that does not relate back to the clinical findings is that radiological findings that are suggestive of abnormality in the absence of clinical findings may prompt unnecessary treatment. It is well understood that treatments in general can produce unwanted side effects in the patient, thus there is the risk of creating problems for that patient that did not previously exist. A recent example of this pertaining to the TMJ is Al-Moriassi et al.'s systematic review on orthognathic surgery (to address jaw discrepancies) on young adults. Although this surgery resulted in a decrease of TMD symptoms in many of those who were symptomatic before surgery, it created symptoms in a smaller group of patients who were symptom free prior to surgery [41]. Finally, Bakke et al. [42] advised that "radiographic findings should be used with care and only as a supplement to clinical assessment."

Ahmad et al. [43] developed and defined the image analysis criteria for Dworkin and LeResche's Research Diagnostic Criteria for Temporomandibular Disorders (RDC/TMD) [44], a widely used diagnostic system for TMD since 1992. Larheim et al. [45] reduced the number of criteria pertaining to the condylar head to those in Table 16.2.

Table 16.1 sets out Chantaracherd et al.'s distribution of their American cases among the three disease stages and their association with pain and bilaterality [38]. These authors made it clear that the presumption that normal TMJs when diseased progress first to soft-tissue changes – namely disc displacement with reduction, then without reduction, and then onto osseous change, that is degenerative joint disease – was not yet proven. In a more recent follow-up of the cases in Table 16.1, Schiffman et al. [46] reported that it was clear that this presumption did not apply to the majority of the cases followed up. Instead, they found that three-quarters remained stable. Although some of cases showed progression, others regressed to a less severe stage. Also, degenerative joint disease in some cases preceded soft-tissue changes. Furthermore, these authors were unable to predict which cases would progress. They finally suggested that "clinical practice should focus on symptom management rather than structural intervention for the TMJ" [46]. My statistical analysis of their results in Table 16.1 with regard to pain would indicate that disc displacement with reduction is significantly less troublesome to the patient in relation to this symptom. An interesting aspect of Schiffman et al.'s

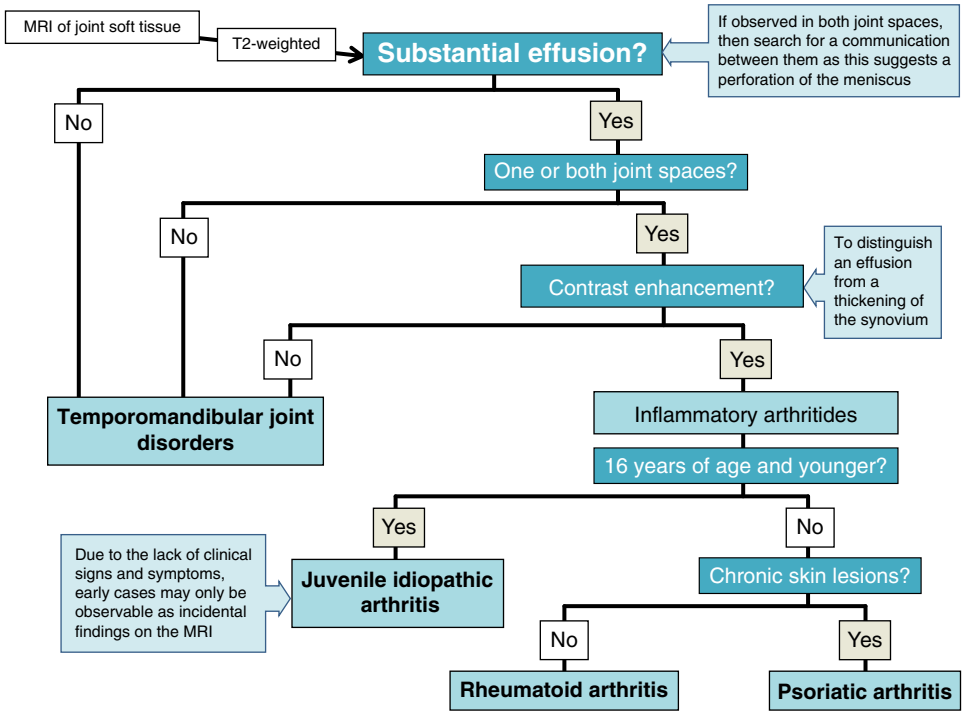


Figure 16.16 Flowchart continuing Figure 16.15 with an emphasis on effusion and contrast enhancement. There is an urgent need to diagnose juvenile idiopathic arthritis (JIA) as early as possible to prevent further damage to the joints, even although the patient may be symptom free and displaying no clinically observable signs. To this end, the temporomandibular joint (TMJ) and other joints observable on magnetic resonance images (MRI) taken of a child for other reasons should be reviewed for JIA. Although 80% of cases of rheumatoid arthritis (RA) are positive for rheumatoid factor, the presence of skin lesions typical of psoriasis will distinguish between RA and psoriatic arthritis.

report was that they replaced MDCT with CBCT for follow-up [46].

An imaging protocol is outlined in Figures 16.15 and 16.16, beginning with the patient's complaint suggestive of TMD and a subsequent clinical examination which confirms it. The panoramic radiograph's display of the entire gnathic bony apparatus, including the teeth, may reveal one or more causes of TMJ disease which are not primarily TMD. These have been already addressed in Figures 16.3 and 16.4. Any gross asymmetry should be confirmed by clinical examination. If the radiographic technique is at fault, a decision should be taken as to whether it is necessary to re-expose the patient, particular if young. The appearance of the osseous changes of flattening of the condylar head and small osteophytes (Figure 16.14), but associated with a smooth cortical outline, should be interpreted not as osteoarthritis but as remodeling [39]. Some flattening of the condyle has been reported in 35% of symptom-free patients [47]. No erosions or osteophytes were observed in such patients [47].

Although disc displacement is significantly more prevalent in TMD patients than in symptom-free volunteers, it can also appear in the latter group. Because it does not occur in preschool children, it can be surmised that disc displacement

is an acquired phenomenon that may develop early in life. Disc displacement on its own is only part of the TMD story. The presence of joint effusions and marrow abnormalities, optimally displayed by MRI, suggest a subset of cases which have more severe joint pathology. Joint effusion is displayed in 15% of TMD patients and bone marrow abnormalities in 30% [39].

T1-weighted MRI will display disc displacement and whether it reduces on opening. T2-weighted MRI, usually with fat saturation, reveals effusion in the joint. Although the presence of effusion suggests inflammation, some effusion has also been observed in healthy volunteers.

Fluid in the synovial spaces is displayed as a hyperintense signal on T2-weighted MRI (see Figure 16.6c). It has been observed in half of symptom-free volunteers, ranging from just dots or a line to a "moderate" amount. The amount of fluid within the joint space must be a "marked" accumulation, such as is evident in Figure 16.6c, to be described as an effusion. Larheim reported that this effusion in two-thirds of cases was found exclusively or predominantly in the upper compartment of the anteriolateral recess. Although the discs of both joints of most patients were displaced, effusion was predominantly unilateral. The amount of effusion varied over time and correlated well with the severity of pain [39].

If an effusion is observed in both joint spaces, a search should be undertaken for a communication between them as a result of a perforation. Furthermore, if the effusion is substantial, it may be difficult to distinguish it from synovial proliferation. If the latter is suspected, then a contrast-enhanced MRI may be indicated, as the synovium would be enhanced. The presence of marked synovial enhancement should prompt consideration of RA, psoriatic arthritis, and ankylosing spondylitis in an adult [32], and JIA in a child or juvenile (this will be discussed later in this chapter). Both the soft and bony tissues are affected by the RA's pannus. This and the enlarged synovium allow RA to be distinguished from osteoarthritis. Nevertheless, because the assessment is subjective, Resnick et al. [48] reported that the "calculation of a ratio of pixel intensity between TMJ synovium and the longus capitus muscle is a reliable way to quantify synovial enhancement."

The bone marrow appears normally as a homogeneous bright signal on proton density images and a homogeneous intermediate signal on T2-weighted images. Edema of the marrow presents as a reduced signal on proton density and an increased signal on T2-weighted images [39].

Kuroda et al. reported that the *signal intensity ratios* (SIR) of *fluid-attenuated inversion recovery* (FLAIR) T1-weighted MRI of the retrodiscal tissue were significantly higher in painful TMJs than in painless TMJs [49].

The most reliable presentation of osteonecrosis on MRI is the appearance of edema and sclerosis of the marrow. Although the designation of osteonecrosis has been awarded to this presentation as it is observed with regard to osteonecrosis of the hip, the condition in the TMJ appears to be less aggressive. Currently there is no published evidence to suggest that patients presenting with this phenomenon should be treated differently [39].

A major problem of MRI as the purported "gold standard" for TMDs in particular is in both access and cost. Its ability to investigate a patient without imparting an ionizing radiation dose to that patient, particularly the more vulnerable child patient, is only shared by

ultrasonography [17]. This becomes a major issue when addressing JIA, which first presents in children and adolescents.

16.6 Juvenile Idiopathic Arthritis

JIA, formerly called juvenile rheumatoid arthritis, is the most common autoimmune connective-tissue disease affecting developing individuals [50]. Globally it occurs in 1 in 1000 children and juveniles before 16 years of age and with a duration of at least 6 weeks [51]. JIA is a clinically diverse and genetically complex disease; the International League of Association for Rheumatology (ILAR) [52] has defined seven categories based on distinct clinical and laboratory features (Table 16.3) [53–55]. Although the TMJ is affected by JIA in 17–83% of cases depending on category, diagnostic criteria, and ethnicity [51], Frid et al. reported that 12% of their over 3000 JIA cases had TMJ involvement [53]. They also reported that those with TMJ involvement had more polyarticular disease, more disability, and a lower *health-related quality of life* (HRQOL) [53]. Bilateral TMJ involvement ranges from 53% to 83% [51]. Although Table 16.3 displays two categories which have clear genetic and/or familial elements, JIA-associated *single nucleotide polymorphisms* (SNPs) are rarely functioning variants and are therefore unhelpful in determining its pathenogenesis and effective therapy [56]. Most categories of JIA are associated with a uveitis which is insidious in onset and is potentially blinding [54, 57]. Furthermore, the systemic arthritis category is associated with the potentially lethal *macrophage activation syndrome* (MAS).

A major problem of JIA is that due to its insidious and asymptomatic progress, it is frequently not detected and diagnosed until symptoms present, after much damage has already been done. JIA is not only common, but is generally not well understood by the health professions, save by rheumatologists and by medical and dental pediatric specialists. Therefore, in the absence of awareness of already diagnosed JIA cases and a family history, such as that pertinent to *enthesitis-related arthritis* (ERA) and to psoriatic arthritis, such cases will be missed. Nevertheless, all imaging prescribed for other clinical reasons should be reviewed and any feature suggestive of TMJ promptly and appropriately referred.

Although conventional radiology is the primary diagnostic modality to identify those features that rule out other lesions, such as neoplasms, developmental lesions, and other arthritides [50], it is unhelpful in the diagnosis of JIA. Contrast-enhanced MRI is currently the imaging modality of choice [58]. Although it is frequently described as the gold standard for JIA, there is considerable overlap between the normal range and that of JIA, even with time-intensity curves. Von Kalle et al. suggested that thickening of the joint space was the earliest sign to indicate JIA reliably [59].

Ultrasonography continues to make inroads into many clinical fields, and joint imaging has become one of the latest. In cases of myalgia in relation to TMD, MRI and ultrasonography of the masticatory musculature have assisted in the diagnosis and monitoring of outcomes of treatment [60]. The European Society of Musculoskeletal Radiology's (ESSR) Arthritis Subcommittee on the use of ultrasonography in rheumatic disease has revealed those features of the disease that US can display; these are the proliferation of synovium and tenosynovitis [61]. A contributor to that report, Sudoł-Szopińska, has revealed the use of US for JIAs [17].

Table 16.3 Seven categories of juvenile idiopathic arthritis (JIA) defined by the International League of Association for Rheumatology (ILAR).

ILAR Category	TMJ	Uveitis	Other important features
Oligoarticular JIA *(4 or fewer joints during the first 6 months)* (50%)	N/A	Frequent	Onset in infancy Large joints (knees and ankles)
Persistent	5%		
Extended (5 or more joints after the first 6 months)	20%	Frequent	
Polyarticular JIA *(5 or more joints during the first 6 months)* (40%)	24%		
RF negative (15–25%)	N/A	Frequent	
RF positive (5–10%)	11%		Similar to adult rheumatoid arthritis
Systemic-onset JIA (5–10%)	51%	Rare	Onset in infancy Generalized rash and lymphadenopathy Hepatomegaly and/or splenomegaly Mimics many other diseases at onset 5–8% MAS – a life-threatening disease
Enthesitis-related arthritis (ERA) (5–10%)	N/A	7–15%	Males over 6 years of age HLA-B27 positive Sacroiliac joint tenderness ERA, AS, AAU in first-degree relative
Psoriatic arthritis (5–10%)	N/A	10–20%	Dactylitis, nail pitting, or onycholysis Psoriasis in first-degree relative
Undifferentiated (10%)	N/A	10–21%	

Source: Adapted from Carrasco, R. (2015). Juvenile idiopathic arthritis overview and involvement of the temporomandibular joint: prevalence, systemic therapy. *Oral Maxillofac. Surg. Clin. North Am.* 27: 1–10., El Assar de la Fuente, S., Angenete, O., Jellestad, S. et al. (2016). Juvenile idiopathic arthritis and the temporomandibular joint: a comprehensive review. *J. Craniomaxillofac. Surg.* 44 (5): 597–607.; Tugal-Tutkun, I., Quartier, P., and Bodaghi, B. (2014). Disease of the year: juvenile idiopathic arthritis-associated uveitis--classification and diagnostic approach. *Ocul. Immunol. Inflamm.* 22: 56–63. and Frid, P., Nordal, E., Bovis, F., et al. (2017). Temporomandibular joint involvement in association with quality of life, disability, and high disease activity in juvenile idiopathic arthritis. *Arthritis Care Res. (Hoboken)* 69: 677–686.
AAU, acute anterior uveitis; AS, ankylosing spondylitis; MAS, macrophage activation syndrome; N/A, no information available; RA, rheumatoid arthritis; RF, rheumatoid factor; TMJ, temporomandibular junction.

This has focused on other accessible joints of the body, but not TMJs.

Although originally called juvenile rheumatoid arthritis, the manifestation in children is very different from that in adults. The hand, limb, and spinal deformities in RA do not develop in JIA, except in those cases in which JIA had not been diagnosed early enough and appropriately treated [58]. Nevertheless, affected TMJs infrequently produce symptoms until substantial damage has been done [58]. Abramowicz et al. stated that TMJ pain is unreliable to screen for JIA [58].

Furthermore, in a minority of cases uveitis precedes symptoms suggestive of JIA. As uveitis constitutes an ophthalmic emergency, it should not only be recognized certainly by all those who attend to children, but also prompted in radiology reports when evidence of JIA presents to the radiologist. The early detection of JIA is also necessary for early treatment to avoid facial deformity and functional impairment of late-treated cases. The most frequent deformity was microstomia, an outcome of those cases which were diagnosed and treated when they were already advanced, which is now seen infrequently.

The craniofacial growth disturbances related to TMJ abnormality in Norwegian JIA patients were followed up for 27 years [62]. TMJ involvement was 40% of JIA cases, similar to that in other Scandinavian communities. Microstomia occurred with bilateral TMJ involvement only in 27% of the entire series of patients. Nevertheless, "growth disturbances did not always follow TMJ involvement, not even when affected early" [62].

Simard et al.'s Swedish study, based on five registries, found a significantly higher risk of malignancy, particularly lymphoproliferative, among those JIA patients diagnosed in the last two decades in comparison to the general population [63]. A large German cohort did not find an overall increased cancer risk. Nevertheless, the results suggested an increased risk of melanoma in female JIA patients [64].

16.7 Concluding Remarks

1. Although there are many TMJ diseases, TMDs are the most common. Bifid condyles are also common, and since they are normal anatomical variants they should be distinguished from disease.
2. The most useful current imaging modalities for TMJ disease are MRI and CBCT. These have displaced almost every other formerly used modality. Arthography is still used, but now mainly as a therapeutic vehicle. Ultrasonography, used for diagnosis of lesions affecting other joints, has been tentatively used for TMJ disease.
3. The CBCT is displacing MDCT not only because of its ease of access and lower radiation dose, especially if a small FOV is used, but also because of its high spatial resolution.
4. MRI best displays the soft-tissue component of the joint. It can display effusion and with contrast enhancement also distinguish an effusion from synovial proliferation indicative of an RA and JIA.
5. TMDs present as disc displacements with or without reduction and osteoarthritis. Recent research suggests that the process from normal through disc displacement with and then without reduction to osteoarthritis is not linear. TMD cases can resolve.
6. An incidental finding of features suggestive of TMDs in TMJ symptom-free adult individuals should prompt careful reflection before any decision to treat. Some of these features may also represent resolved cases. Incidental findings in TMJ symptom-free children should prompt consideration of JIA.
7. JIAs are not uncommon. They only present with symptoms once much irreparable damage has been done. Fortunately, due to the awareness of JIAs by key specialties, deformities such as microstomia are less common today. Nevertheless, better and more accessible diagnostic methods are necessary to diagnose JIA early.

While a family history assists in some cases, contrast-enhanced MRI imaging, necessarily performed in a medical facility, is both expensive and invasive and is therefore unsuitable for JIA screening. High-resolution ultrasonography has the potential to be used in the community by appropriately skilled practitioners. Currently this has been applied to other joints in suspected JIA cases.

8. JIA is a group of systemic diseases. Some have had potentially lethal outcomes in some cases and others blinding uveitis. Suspected cases should be reviewed by rheumatologists and ophthalmologists.

References

1. Wang, X.D., Zhang, J.N., Gan, Y.H., and Zhou, Y.H. (2015). Current understanding of pathogenesis and treatment of TMJ osteoarthritis. *J. Dent. Res.* 94: 666–673.
2. Monteiro, J.C., Ennes, J.P., and Zorzatto, J.R. (2011). Ossification of the petrotympanic fissure: morphological analysis and clinical implications. *Cranio* 29: 284–290.
3. Al-koshab, M., Nambiar, P., and John, J. (2015). Assessment of condyle and glenoid fossa morphology using CBCT in South-East Asians. *PLoS One* 24 (10): e0121682.
4. Ejima, K., Schulze, D., Stippig, A. et al. (2013). Relationship between the thickness of the roof of glenoid fossa, condyle morphology and remaining teeth in asymptomatic European patients based on cone beam CT data sets. *Dentomaxillofac. Radiol.* 42: 90929410.
5. Yu, Q., Yang, J., Wang, P. et al. (2004). CT features of synovial chondromatosis in the temporomandibular joint. *Oral Surg. Oral Med. Oral Pathol. Oral Radiol. Endod.* 97: 524–528.
6. Barthelemy, I., Karanas, Y., Sannajust, J.P. et al. (2001). Gout of the temporomandibular joint: pitfalls in diagnosis. *J. Craniomaxillofac. Surg.* 29: 307–310.
7. Kudoh, K., Kudoh, T., Tsuru, K., and Miyamoto, Y. (2017). A case of tophaceous pseudogout of the temporomandibular joint extending to the base of the skull. *Int. J. Oral Maxillofac. Surg.* 46: 355–359.
8. Yoshitake, H., Kayamori, K., Wake, S. et al. (2016). Synovial chondromatosis of the right side temporomandibular joint extending to the middle cranial fossa: a case report with 7-year postoperative follow up and expression of a biomarker of cell proliferative activity. *Int. J. Surg. Case Rep.* 20: 133–137.
9. Yokota, N., Inenaga, C., Tokuyama, T. et al. (2008). Synovial chondromatosis of the temporomandibular joint with intracranial extension. *Neurol. Med. Chir. (Tokyo)* 48: 266–270.
10. Nikolova, S.Y., Toneva, D.H., and Lazarov, N.E. (2016). Incidence of a Bifid mandibular condyle in dry mandibles. *J. Craniofac. Surg.* 28: 2168–2173.
11. Lei, J., Liu, M.Q., Yap, A.U., and Fu, K.Y. (2013). Condylar subchondral formation of cortical bone in adolescents and young adults. *Br. J. Oral Maxillofac. Surg.* 51: 63–68.
12. Langland, O.E., Langlais, R.P., McDavid, W.D., and DelBalso, A.M. (1989). *Panoramic Radiology*, 2e, 51–57. Philadelphia: Lea & Febiger.
13. Cai, X.Y., Yang, C., Chen, M.J. et al. (2012). Arthroscopic management for synovial chondromatosis of the temporomandibular joint: a retrospective review of 33 cases. *J. Oral Maxillofac. Surg.* 70: 2106–2113.
14. Bast, F., Collier, S., Chadha, P., and Collier, J. (2015). Septic arthritis of the temporomandibular joint as a complication of acute otitis media in a child: a rare case and the importance of real-time PCR for diagnosis. *Int. J. Pediatr. Otorhinolaryngol.* 79: 1942–1945.
15. Katzberg, R.W., Conway, W.F., Ackerman, S.J. et al. (2017). Pilot study to show the feasibility of high-resolution sagittal ultrasound imaging of the temporomandibular joint. *J. Oral Maxillofac. Surg.* 75: 1151–1162.
16. Kirkhus, E., Gunderson, R.B., Smith, H.J. et al. (2016). Temporomandibular joint involvement in childhood arthritis: comparison of ultrasonography-assessed capsular width and MRI-assessed synovitis. *Dentomaxillofac. Radiol.* 45: 20160195.

17. Sudoł-Szopińska, I., Grochowska, E., Gietka, P. et al. (2016). Imaging of juvenile idiopathic arthritis. Part II: ultrasonography and MRI. *J. Ultrason.* 16: 23.
18. Dagenais, M., MacDonald, D., Baron, M. et al. (2015). The Canadian Systemic Sclerosis Oral Health Study IV: oral radiographic manifestations in systemic sclerosis compared with the general population. *Oral Surg. Oral Med. Oral Pathol. Oral Radiol.* 120: 104–111.
19. Baron, M., Hudson, M., Dagenais, M. et al. (2016). Relationship between disease characteristics and oral radiologic findings in systemic sclerosis: results from a Canadian oral health study. *Arthritis Care Res. (Hoboken).* 68: 673–680.
20. MacDonald-Jankowski, D.S. and Li, T.K. (2009). Fibrous dysplasia in a Hong Kong community: the clinical and radiological features and outcomes of treatment. *Dentomaxillofac. Radiol.* 38: 63–72.
21. MacDonald-Jankowski, D.S., Yeung, R., Lee, K.M., and Li, T.K. (2004). Ameloblastoma in the Hong Kong Chinese. Part 2: systematic review and radiological presentation. *Dentomaxillofac. Radiol.* 33: 141–151.
22. MacDonald-Jankowski, D.S. and Li, T.K. Keratocystic odontogenic tumor in a Hong Kong community: the clinical and radiological presentations and the outcomes of treatment and follow-up. *Dentomaxillofac. Radiol.* 39: 167–175.
23. MacDonald-Jankowski, D.S., Yeung, R., Lee, K.M., and Li, T.K. (2002). Odontogenic myxomas in the Hong Kong Chinese: clinicoradiological presentation and systematic review. *Dentomaxillofac. Radiol.* 31: 71–83.
24. Chidzonga, M.M. (1999). Temporomandibular joint ankylosis: review of thirty-two cases. *Br. J. Oral Maxillofac. Surg.* 37: 123–126.
25. Duan, D., Li, J., Xiao, E. et al. (2015). Histopathological features of hypertrophic bone mass of temporomandibular joint ankylosis (TMJA): an explanation of pathogenesis of TMJA. *J. Craniomaxillofac. Surg.* 43: 926–933.
26. Burgess, A., Celerier, C., Breton, S. et al. (2017). Otogenic temporomandibular arthritis in children. *JAMA Otolaryngol. Head Neck Surg.* 143: 466–471. https://doi.org/10.1001/jamaoto.2016.3977.
27. Lohiya, S. and Dillon, J. (2016). Septic Arthritis of the temporomandibular joint – unusual presentations. *J. Oral Maxillofac. Surg.* 74: 87–94.
28. Homøe, P., Kværner, K., Casey, J.R. et al. (2017). Panel 1: epidemiology and diagnosis. *Otolaryngol. Head Neck Surg.* 156 (4_suppl): S1–S21.
29. Cai, X.Y., Yang, C., Zhang, Z.Y. et al. (2010). Septic arthritis of the temporomandibular joint: a retrospective review of 40 cases. *J. Oral Maxillofac. Surg.* 68: 731–738.
30. Ishikawa, S., Watanabe, T., and Iino, M. (2017). Acute septic arthritis of the temporomandibular joint derived from otitis media: a report and review of the English and Japanese literature. *Oral Maxillofac. Surg.* 21: 83–85.
31. Cai, X.Y., Yang, C., Chen, M.J. et al. (2010). Arthroscopic management of septic arthritis of temporomandibular joint. *Oral Surg. Oral Med. Oral Pathol. Oral Radiol. Endod.* 109: 24–30.
32. Morales, H. and Cornelius, R. (2016). Imaging approach to temporomandibular joint disorders. *Clin. Neuroradiol.* 26: 5–22.
33. Hu, Y.K., Yang, C., and Xie, Q.Y. (2016). Changes in disc status in the reducing and nonreducing anterior disc displacement of temporomandibular joint: a longitudinal retrospective study. *Sci. Rep.* 6: 34253. https://doi.org/10.1038/srep34253.
34. Hu, Y.K., Yang, C., Cai, X.Y., and Xie, Q.Y. (2016). Does condylar height decrease more in temporomandibular joint nonreducing disc displacement than reducing disc displacement? A magnetic resonance imaging retrospective study. *Medicine (Baltimore).* 95: e4715. https://doi.org/10.1097/MD.0000000000004715.
35. Loeser, R.F., Goldring, S.R., Scanzello, C.R., and Goldring, M.B. (2012). Osteoarthritis: a disease of the joint as an organ. *Arthritis Rheum.* 64: 1697–1707.
36. Mercuri, L.G. (2008). Osteoarthritis, osteoarthrosis, and idiopathic condylar resorption. *Oral Maxillofac. Surg. Clin. North Am.* 20: 169–183.
37. Speciali, J.G. and Dach, F. (2015). Temporomandibular dysfunction and headache disorder. *Headache.* 55 (Suppl 1): 72–83.

38. Chantaracherd, P., John, M.T., Hodges, J.S., and Schiffman, E.L. (2015). Temporomandibular joint disorders' impact on pain, function, and disability. *J. Dent. Res.* 94 (3 Suppl): 79S–86S.
39. Larheim, T.A. (2005). Role of magnetic resonance imaging in the clinical diagnosis of the temporomandibular joint. *Cells Tissues Organs* 180: 6–21.
40. Suenaga, S., Nagayama, K., Nagasawa, T. et al. (2016). The usefulness of diagnostic imaging for the assessment of pain symptoms in temporomandibular disorders. *Jpn. Dent. Sci. Rev.* 52: 93–106.
41. Al-Moraissi, E.A., Wolford, L.M., Perez, D. et al. (2017). Does orthognathic surgery cause or cure temporomandibular disorders? A systematic review and meta-analysis. *J. Oral Maxillofac. Surg.* 75: 1835–1847. https://doi.org/10.1016/j.joms.2017.03.029.
42. Bakke, M., Petersson, A., Wiesel, M. et al. (2014). Bony deviations revealed by cone beam computed tomography of the temporomandibular joint in subjects without ongoing pain. *J. Oral Facial Pain Headache.* 28: 331–337.
43. Ahmad, M., Hollender, L., Anderson, Q. et al. (2009). Research diagnostic criteria for temporomandibular disorders (RDC/TMD): development of image analysis criteria and examiner reliability for image analysis. *Oral Surg. Oral Med. Oral Pathol. Oral Radiol. Endod.* 10: 844–860.
44. Dworkin, S.F. and LeResche, L. (1992). Research diagnostic criteria for temporomandibular disorders: review, criteria, examinations and specifications, critique. *J. Craniomandib. Disord.* 6: 301–355.
45. Larheim, T.A., Abrahamsson, A.K., Kristensen, M., and Arvidsson, L.Z. (2015). Temporomandibular joint diagnostics using CBCT. *Dentomaxillofac. Radiol.* 44: 20140235.
46. Schiffman, E.L., Ahmad, M., Hollender, L. et al. (2017). Longitudinal stability of common TMJ structural disorders. *J. Dent. Res.* 96: 270–276.
47. Brooks, S.L., Westesson, P.L., Eriksson, L. et al. (1992). Prevalence of osseous changes in the temporomandibular joint of asymptomatic persons without internal derangement. *Oral Surg. Oral Med. Oral Pathol.* 73: 118–122.
48. Resnick, C.M., Vakilian, P.M., Breen, M. et al. (2016). Quantifying temporomandibular joint synovitis in children with juvenile idiopathic arthritis. *Arthritis Care Res. (Hoboken)* 68: 1795–1802.
49. Kuroda, M., Otonari-Yamamoto, M., Sano, T. et al. (2015). Diagnosis of retrodiscal tissue in painful temporomandibular joint (TMJ) by fluid-attenuated inversion recovery (FLAIR) signal intensity. *Cranio* 33: 271–275.
50. Sudoł-Szopińska, I., Matuszewska, G., Gietka, P. et al. (2016). Imaging of juvenile idiopathic arthritis. Part I: clinical classifications and radiographs. *J. Ultrason.* 16: 225–236.
51. El Assar de la Fuente, S., Angenete, O., Jellestad, S. et al. (2016). Juvenile idiopathic arthritis and the temporomandibular joint: a comprehensive review. *J. Craniomaxillofac. Surg.* 44: 597–607.
52. Hersh, A.O. and Prahalad, S. (2015). Immunogenetics of juvenile idiopathic arthritis: a comprehensive review. *J. Autoimmun.* 64: 113–124.
53. Frid, P., Nordal, E., Bovis, F. et al. (2017). Temporomandibular joint involvement in association with quality of life, disability, and high disease activity in juvenile idiopathic arthritis. *Arthritis Care Res. (Hoboken)* 69: 677–686.
54. Tugal-Tutkun, I., Quartier, P., and Bodaghi, B. (2014). Disease of the year: juvenile idiopathic arthritis-associated uveitis – classification and diagnostic approach. *Ocul. Immunol. Inflamm.* 22: 56–63.
55. Carrasco, R. (2015). Juvenile idiopathic arthritis overview and involvement of the temporomandibular joint: prevalence, systemic therapy. *Oral Maxillofac. Surg. Clin. North Am.* 27: 1–10.
56. Donn, R., DeLeonibus, C., Meyer, S., and Stevens, A. (2016). Network analysis and juvenile idiopathic arthritis (JIA): a new horizon for the understanding of disease pathogenesis and therapeutic target identification. *Pediatr. Rheumatol. Online J.* 14: 40.
57. Oray, M. and Tuğal-Tutkun, İ. (2016). Treatment of juvenile Idiopathic arthritis-associated uveitis. *Turk. J. Ophthalmol.* 46: 77–82.
58. Abramowicz, S., Kim, S., Prahalad, S. et al. (2016). Juvenile arthritis: current concepts in terminology, etiopathogenesis, diagnosis,

and management. *Int. J. Oral Maxillofac. Surg.* 45: 801–812.
59. von Kalle, T., Stuber, T., Winkler, P. et al. (2015). Early detection of temporomandibular joint arthritis in children with juvenile idiopathic arthritis the role of contrast-enhanced MRI. *Pediatr. Radiol.* 45: 402–410.
60. Ariji, Y. and Ariji, E. (2017). Magnetic resonance and sonographic imagings of masticatory muscle myalgia in temporomandibular disorder patients. *Jpn. Dent. Sci. Rev.* 53: 11–17.
61. Plagou, A., Teh, J., Grainger, A.J. et al. (2016). Recommendations of the ESSR Arthritis Subcommittee on ultrasonography in inflammatory joint disease. *Semin. Musculoskelet. Radiol.* 20: 496–506.
62. Arvidsson, L.Z., Fjeld, M.G., Smith, H.J. et al. (2010). Craniofacial growth disturbance is related to temporomandibular joint abnormality in patients with juvenile idiopathic arthritis, but normal facial profile was also found at the 27-year follow-up. *Scand. J. Rheumatol.* 39: 373–379.
63. Simard, J.F., Neovius, M., Hagelberg, S., and Askling, J. (2010). Juvenile idiopathic arthritis and risk of cancer: a nationwide cohort study. *Arthritis Rheum.* 62: 3776–3782.
64. Barth, S., Schlichtiger, J., Hartmann, B. et al. (2017). Incidence of malignancies in patients with juvenile idiopathic arthritis: a retrospective single-center cohort study in Germany. *Mod. Rheumatol.* 27: 60–65.

Part 4
Extragnathic lesions



Chapter 17

Introduction to extragnathic lesions

17.1 Introduction

This chapter introduces some important anatomical and technical aspects of the radiology of those lesions that present outside the maxillofacial regions. The extragnathic head and neck will be considered as two separate anatomical regions, the skull base and the neck. The benign and malignant lesions affecting either or both of these regions are addressed in Chapters 18 and 19, respectively.

17.2 The Skull

This section places particular emphasis on the base of the skull, which appears increasingly within large *fields of view* (FOVs) in *cone-beam computed tomography* (CBCT) (Figure 17.1). Although it is generally held that this area is properly the purview of the medically trained head and neck radiologist or neuroradiologist, it is important that the *oral and maxillofacial* (OMF) practitioner prescribing and interpreting these images be aware of some of the important lesions that may incidentally present (Figure 17.2). Knowledge of such lesions enables those practitioners to recognize the abnormality and refer it promptly and appropriately. It is expected that datasets of large FOVs would be reported by a radiologist (see Chapter 5).

17.2.1 BASIC ANATOMY OF THE SKULL BASE

The anatomy of the skull base is both complex and subject to much variation, such as asymmetrical pneumatization and the appearance of the foramina, which can present as pseudolesions [1]. The base of the skull is divided into three fossae: *anterior cranial fossa* (ACF), *middle cranial fossa* (MCF), and *posterior cranial fossa* (PCF) [2]. The boundary between the ACF and the MCF is the posterior margin of the lesser wing of the sphenoid. The boundary between the MCF and the PCF is delimited by the posterior superior margin of the petrous temporal bone and the posterior clinoid process of the body of the sphenoid. The emphasis of this chapter is on the MCF and the PCF, because they are most likely to appear on large FOV CBCT images. Of these, the portions of the base of the skull that are most likely to be captured are the clivus and petrous temporal bone (Figure 17.3). Some important lesions that may affect the orbit have been considered, because the orbit is just as likely to be captured as the MCF and the PCF.

The *sella turcica* (ST), sometimes called the *pituitary fossa*, is a salient point in cephalometry essential for the diagnosis and treatment planning of craniofacial abnormalities. Although significant differences in skeletal class of the face and jaws

Oral and Maxillofacial Radiology: A Diagnostic Approach, Second Edition. Edited by David MacDonald.
© 2020 John Wiley & Sons, Inc. Published 2020 by John Wiley & Sons, Inc.

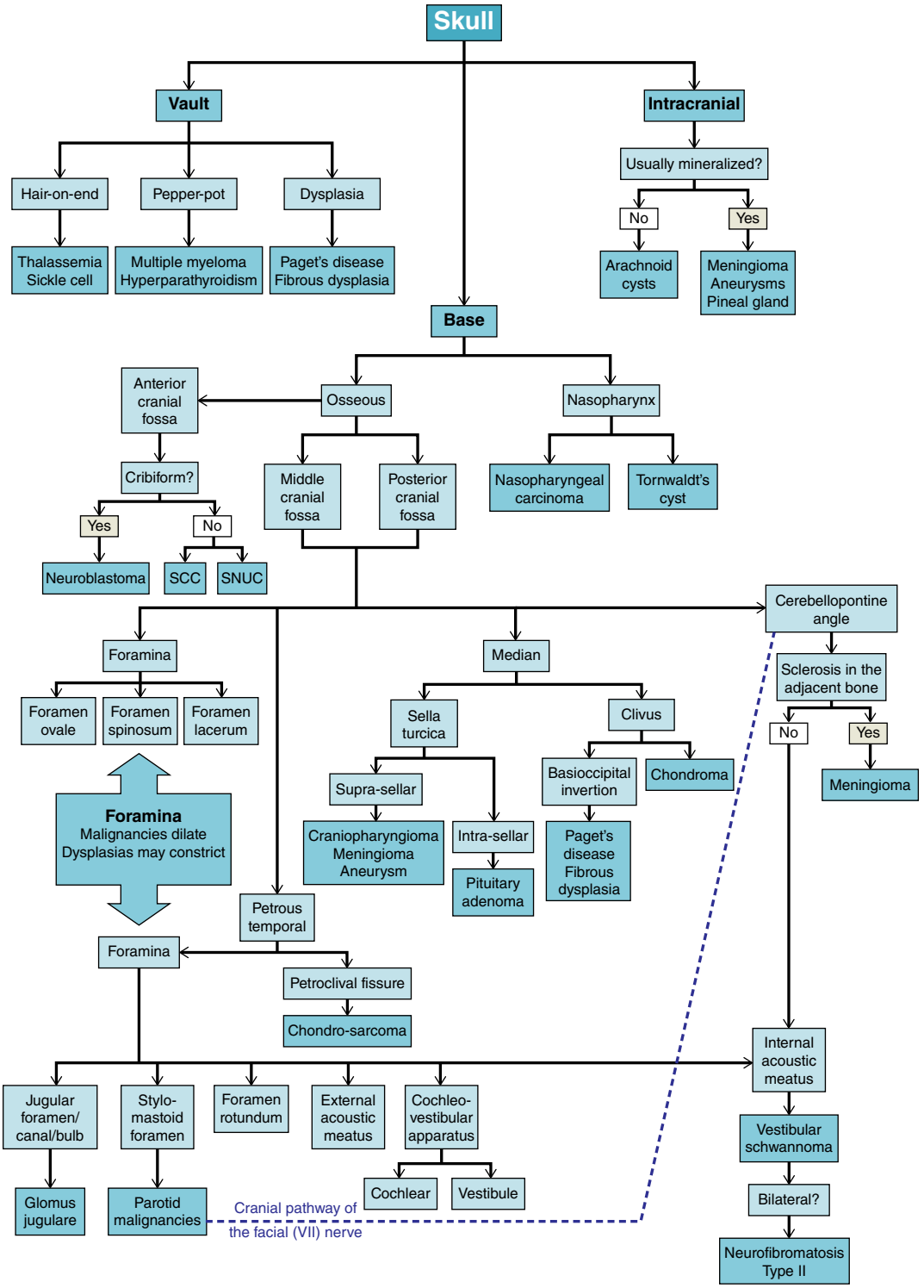


Figure 17.1 Flowchart of the important and/or more frequently occurring lesions affecting the skull. SCC, squamous cell carcinoma; SNUC, sino-nasal undifferentiated carcinoma.

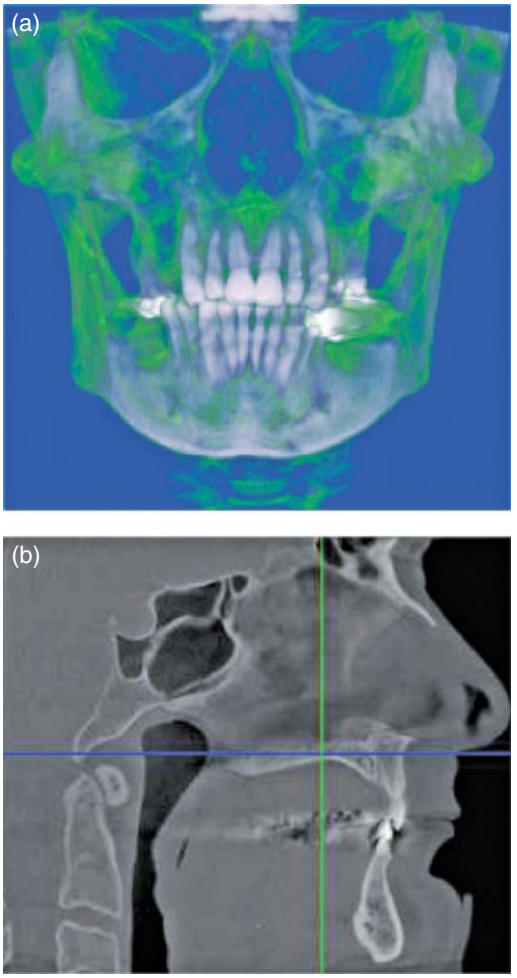


Figure 17.2 Cone-beam computed tomography (CBCT) as part of the assessment of a patient being considered for osseointegrated implants in both jaws. This was made on an i-CAT type of CBCT unit with its large field of view. (a) A three-dimensional reconstruction of the dataset seen from an anterior or frontal perspective. It can be seen that the base of the skull has been captured in (b). Source: Courtesy of Dr. Babak Chehroudi, Faculty of Dentistry, University of British Columbia.

were found only between skeletal Classes II and III (the former has smaller ST diameters, the latter larger diameters) [3], this opportunity should also be used for assessment of the size and shape of the ST that may arise from other causes. The dimensions of a normal ST are set out in Table 17.1 [4]. The dimensions of the ST are larger in the older patient [4].

17.2.2 CROSS-SECTIONAL IMAGING OF THE SKULL BASE: MAGNETIC RESONANCE IMAGING AND COMPUTED TOMOGRAPHY

Current imaging of the skull base relies heavily on *computed tomography* (CT) and *magnetic resonance imaging* (MRI). CT, particularly *multidetector computed tomography* (MDCT), is superior to MRI for evaluating bone erosion and destruction, particularly if the unit used has a high spatial resolution. A rudimentary knowledge of skull base structures and foramina is required for both interpreting the spread of cancer through the skull base and searching for certain neurogenic tumors (such as schwannomas). Some cases occur within foramina. In particular, the pterygopalatine fossa, sphenopalatine foramen, foramen rotundum, inferior orbital fissure, carotid canal, and jugular/hypoglossal foramina should be studied (see Figure 17.3).

MRI is introduced in Chapter 6. It is excellent for visualizing soft-tissue involvement, including the bone marrow. For the head and neck, precontrast MRI images are usually first acquired in axial/sagittal planes with T1 weighting. T1-weighted images show anatomy well, with good contrast between muscles and intervening fat planes (Figure 17.4). This is because on T1-weighted images muscles are relatively dark (isointense) and fatty tissue is bright, or more accurately of high signal intensity (hyperintense). In adults, bone marrow is normally bright due to fatty infiltration. When tumor,

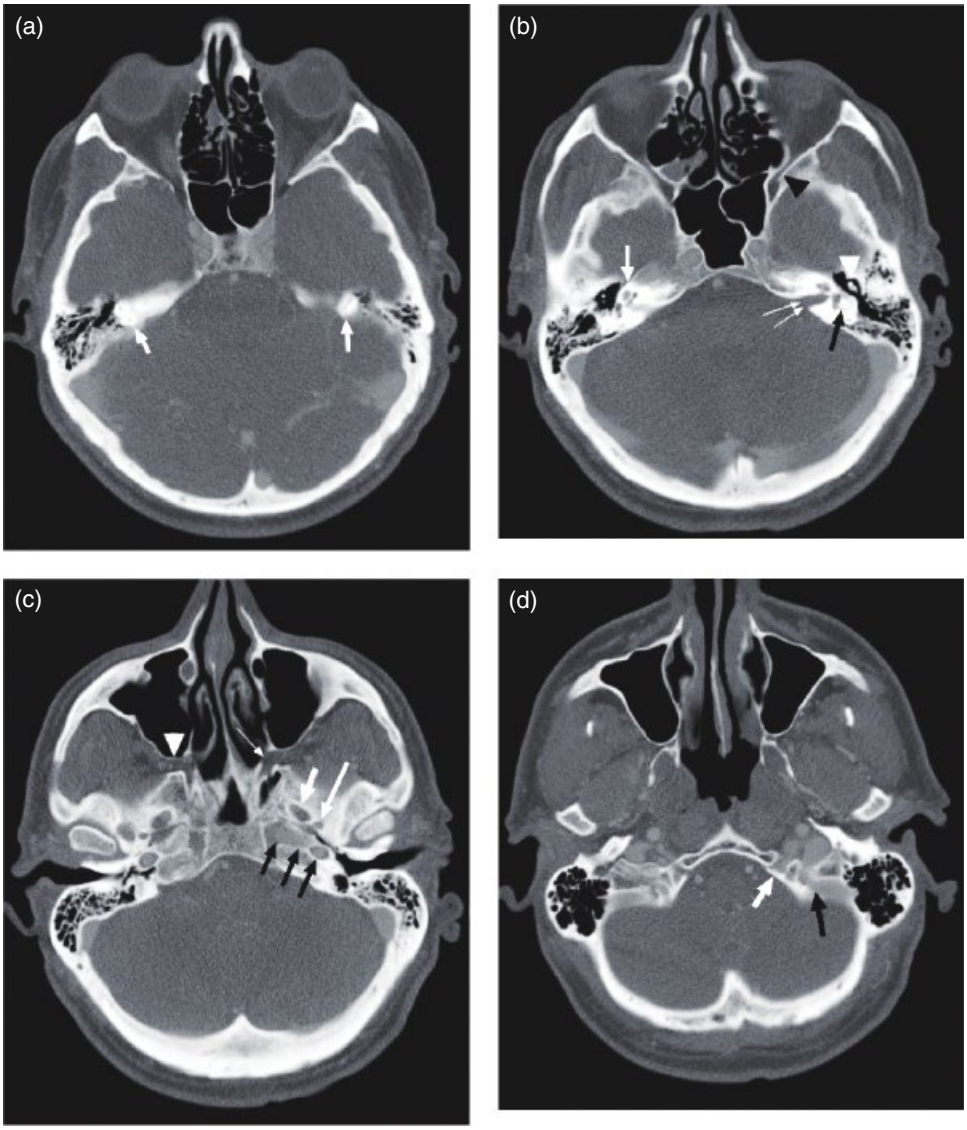


Figure 17.3 Computed tomography, normal axial sections (bone windows). (a) At the level of the base of the sella turcica, showing ethmoid and superior mastoid air cells. The vertical semicircular canals of the inner ear are visible within the petrous temporal bone (arrows). (b) At the level of the left internal auditory canal (double arrows). The cochlea of the inner ear is visible (single white arrow) and the "signet ring" shape of the left horizontal semicircular canal is seen (black arrow). The ossicles of the middle ears are visible, more so on the left (white arrowhead). The left inferior orbital fissure is marked with a black arrowhead. The ethmoid, sphenoid, and mastoid air cells are visible. (c) At the level of the condylar head. The foramen ovale (short white arrow) and spinosum (long white arrow) are visible. The left carotid canal is seen ending medially at the foramen lacerum (black arrows). The pterygopalatine fossa is shown (white arrowhead) and the sphenopalatine foramen (thin white arrow). The conchae (turbinates) are partially visualized in the nasal cavity. (d) At midmaxillary sinus level. The nasal cavity and posterior nasopharynx are visible. The hypoglossal canal (white arrow) and jugular foramen (black arrow) are visible on the left. The mastoid air cells are extensively pneumatized. Note: When viewing axial reconstructions, consider that you are viewing them from below.

Table 17.1 Dimensions of the sella turcica in 6-year-olds and 21-year-olds of both sexes.

Years	Dimension	Males			Females		
6 years of age	Length	8.8	SD	1.5	8.5	SD	1.3
	Depth	6.3	SD	0.8	6.6	SD	0.7
	Diameter	10.0	SD	1.3	9.0	SD	1.3
21 years of age	Length	8.9	SD	0.9	8.4	SD	1.6
	Depth	7.3	SD	1.1	7.2	SD	1.2
	Diameter	11.3	SD	1.1	11.7	SD	1.1

SD, standard deviation.
Source: Derived from Axelsson S, Storhaug K, Kjaer I. Post-natal size and morphology of the sella turcica. Longitudinal cephalometric standards for Norwegians between 6 and 21 years of age. *Eur. J. Orthod.* 2004;26:597–604.

infection, or inflammation displaces fatty marrow, it becomes "dark" on T1-weighted images, making MRI exquisitely sensitive for detecting these pathologies. Be aware that in younger people the bone marrow is not yet fatty and may be normally dark on T1-weighted images. Fatty marrow replacement occurs at different times in different bones; in the mandible it generally happens between 10 and 15 years of age. T1-weighted scans are also called "anatomy scans" or "fat scans" (see Chapter 6).

MRI images are then acquired with T2 weighting (Figure 17.4). On these images, structures containing a high percentage of water are bright or hyperintense. Hence tissues that are neoplastic, edematous, or inflamed tend to be bright on T2-weighted images. T2-weighted images are also called "pathology scans" or "water scans" (see Chapter 6).

By definition, muscles and brain tissue are considered isointense on T1- and T2-weighted images – their signal intensities are used as a reference to label other structures as hyper- or hypointense. T2-weighted images are always acquired before giving MRI contrast. MRI contrast has a significant effect on T1-weighted images.

After intravenous administration of gadolinium contrast, some normally T1-weighted isointense structures will become hyperintense or bright. The nasal mucosa will vividly enhance; looking at the nasal septum and turbinates on T1-weighted images is a good way of determining whether MRI contrast has been administered (compare Figures 17.4a and b). Many inflammatory, infectious, and neoplastic lesions will also enhance with contrast. In order to see these optimally, a technique called "fat saturation" is usually used in the head and neck. This decreases the signal from normal fat, making it dark and allowing pathological enhancement to stand out (Figure 17.4b). Postcontrast fat-saturated T1-weighted images are excellent for detecting malignant lesions (see Figures 19.3e and f, 19.6c, 19.7b and c, 19.8c, 19.9, 19.11, 19.12c, 19.15a–c, 19.16, 19.17, 19.18b, 19.23b and d, 19.26b and c, 19.33, and 19.34b and c) as well as many benign pathologies affecting the skull base (Figures 18.2b, 18.5a and b, 18.6, 18.9b, 18.10b and c, 18.12, 18.13b, 18.14c, and 18.15). MRI is contraindicated in certain cases – for example patients with either a pacemaker or an intraocular metallic foreign body (see Chapter 6). In these patients CT imaging will be done.

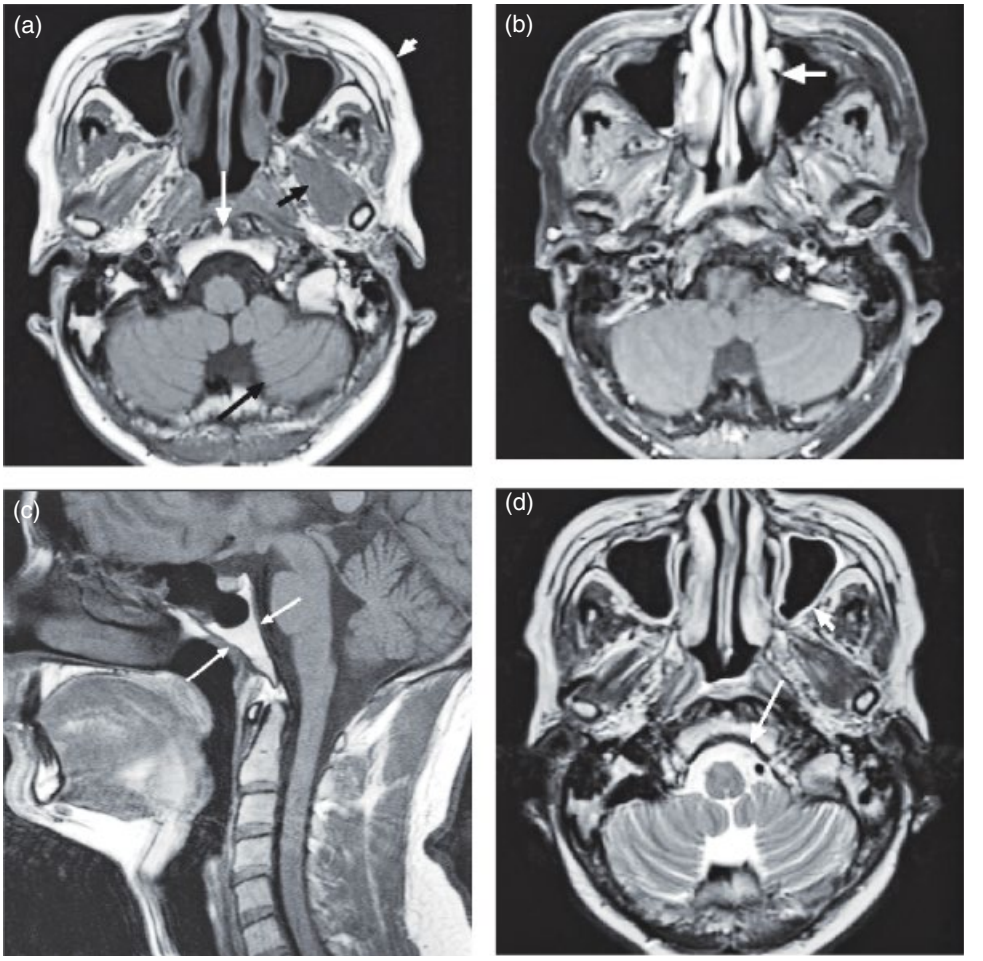


Figure 17.4 Normal magnetic resonance imaging (MRI) soft-tissue contrast pre- and postcontrast. (a) Axial non-contrast T1-weighted MRI. Note the bright subcutaneous fat (short white arrow) and the fatty marrow in the clivus (long white arrow). The lateral pterygoid muscle (short black arrow) and cerebellar hemisphere (long black arrow) both exhibit isointense T1-weighted signals. (b) Axial postgadolinium fat-saturated T1-weighted MRI. Compare this to the noncontrast T1-weighted image (a) and see how brightly normal nasal mucosa (arrow) enhances. Compare the subcutaneous fat signal with that from (a); it is now dark due to the fat saturation. (c) Sagittal noncontrast T1-weighted MRI. Note the high signal in the clivus corresponding to fatty marrow (arrows). (d) Axial noncontrast T2-weighted MRI. Note the normally bright cerebrospinal fluid surrounding the medulla (long arrow). The thin layer of inflamed mucosa in the left maxillary sinus also displays a hyperintense T2-weighted signal (short arrow).

17.3 Swellings of the Neck

17.3.1 RELEVANT ANATOMY AND CLASSIFICATIONS

Imaging of swellings of the neck, in particularly those of the suprahyoid, form an important part of OMF practice. The clinician classically divides the neck into its anatomical triangles and locates the lesion in question accordingly (Figure 17.5). The OMF clinician should be aware that head and neck radiologists commonly consider lesions according to alternate compartments and spaces (Table 17.2). Such awareness will enhance the quality of OMF clinicians' communication with their radiologists so as to optimize patient care.

Since there are these and other different ways to classify head and neck anatomy, it is important to know something about each classification and how they differ before using them as a template to study pathology.

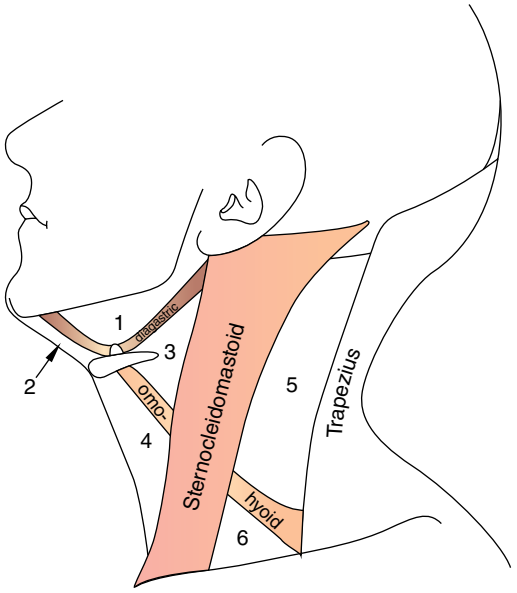


Figure 17.5 Classical triangles of the neck. 1 = submaxillary or diagastric or submandibular triangle; 2 = submental or suprahyoid triangle; 3 = superior carotid triangle; 4 = inferior carotid triangle; 5 = occipital triangle; 6 = subclavian triangle. Collectively, 1+2+3+4 = anterior triangle and 5+6 = posterior triangle.

Table 17.2 Deep spaces of the suprahyoid neck.

Primarily contains	Name of space	Major contents and comments
Muscles	Masticator[a]	Muscles of mastication
	Prevertebral	Prevertebral and paraspinal muscles
Vessels and nerves	Carotid[a]	Carotid artery, internal jugular vein, cranial nerves IX–XII, and internal jugular lymph nodes
Salivary glands	Parotid	Parotid gland and lymph nodes
	Submandibular	Submandibular gland and lymph nodes
	Sublingual	Sublingual gland
Lymphoid tissue and mucosa	Pharyngeal mucosal[a]	Tonsils and pharyngeal mucosa
Potential spaces	Parapharyngeal[a]	Fat, vessels, and nerves
	Danger	A pathway for prevertebral abscess enlargement tracks to mediastinum
	Retropharyngeal	Fat and lymph nodes

[a] Spaces which directly abut the pharyngeal mucosal space.

Classical anatomists divided the neck into simple triangles based on superficial muscular landmarks that could be easily appreciated via surface anatomy or superficial dissection [5]. This schema is useful for clinical examination and planning surgical approaches to the neck. After the advent of cross-sectional imaging techniques, a new system became popular based on cervical fascial planes that divide the neck into compartments [6]. This system is clinically relevant, because these planes can limit and guide the spread of disease occurring within a compartment. Because lymph nodes occur in multiple compartments and are interconnected by lymphatics, nodal classification by fascial planes is less relevant. Different systems of cervical lymph node classification have evolved. Therefore, there are separate systems in use, each with its advantages and disadvantages.

17.3.2 CLASSICAL TRIANGLES OF THE NECK

The neck is divided initially into two triangles, anterior and posterior, by the midplane of the sternocleidomastoid muscle. The anterior triangle is further divided by the omohyoid and diagastric muscles into the submental triangle (also termed suprahyoid), submaxillary triangle (also termed diagastric or submandibular), and superior/inferior carotid triangles. The posterior triangle is split by the omohyoid muscle into a large occipital triangle and a smaller subclavian (also called the supraclavicular or omoclavicular) triangle (Figure 17.5).

17.3.2.1 Submandibular Triangle

The submandibular triangle is particularly relevant to oral pathology. Primary lesions are generally observed on clinical inspection, ideally while still small and symptom free. On occasion the symptoms may not immediately suggest a malignancy; a floor-of-the-mouth *squamous cell carcinoma* (SCC) causing an obstruction of the submandibular duct may produce symptoms suggestive of a submandibular duct calculus. The need for imaging at this stage may not be immediately obvious. Nevertheless, advanced imaging such as MRI can reveal the degree of invasion (see Figure 19.23). Those SCCs, which appear more posteriorly in the oral cavity, are larger and/or already have invaded bone, so advanced imaging is now indicated. This emphasizes the importance of early and appropriate imaging – the SCC can be detected, diagnosed, and treated early so as to improve the prognosis.

Cysts such as ranulas and dermoid cysts are not life threatening unless they achieve substantial dimensions to threaten the airway. Figure 6.10 shows a sublingual dermoid cyst.

17.3.2.2 Anterior Triangle

The principal organs are the thyroid and parathyroid glands and the larynx. Laryngeal SCC is the most common malignancy of the throat [7]. Figure 19.27 displays such a case. Figure 19.5 demonstrates a case of chondrosarcoma affecting the larynx. The pathology of those lesions causing swelling of the thyroid varies and will not be considered.

17.3.2.3 Posterior Triangle

The posterior triangle contains numerous lymph nodes that can become enlarged from metastatic, infectious, or inflammatory disease. This is its main relevance to the OMF clinician.

17.3.3 FASCIAL COMPARTMENTS OF THE NECK

The fascial planes of the neck form the boundaries of a compartmental anatomical classification scheme that is often used by head and neck radiologists. The fascia are initially divided into two layers: superficial and deep. The superficial cervical fascial compartment lies beneath the skin, containing subcutaneous fat, the platysma muscle, and vessels and nerves. The deep cervical fascia divides the remainder of the neck into multiple anatomical compartments or "spaces" and defines the aerodigestive tract; a description of these is set out in Table 17.2. These spaces are most often used when describing pathology occurring above the hyoid bone. Because the suprahyoid region is generally most relevant to OMF pathology, the infrahyoid region, except for some laryngeal cancers, is not covered here.

17.3.4 PHARYNGEAL MUCOSAL SPACE

This contains the pharyngeal mucosa and the tonsils. *Nasopharyngeal carcinoma* (NPC) arises from squamous mucosa in this space and is an important lesion, particularly among those of East Asian origin. The incidence of NPC has declined in Chinese immigrant populations compared with native populations in China [8]. Figure 19.15 exhibits an NPC that occupied the entire posterior pharyngeal wall and has spread to retropharyngeal nodes and the chain of lymph nodes under the cover of the sternocleidomastoid muscle.

17.3.5 PAROTID, SUBMANDIBULAR, AND SUBLINGUAL SPACES

The parotid submandibular and sublingual glands are encased in their own individual spaces. Though the parotid is the largest of the salivary glands, it tends to have a higher proportion of benign to malignant neoplasms than the submandibular, sublingual, and minor salivary glands. Examples of MRI of *pleomorphic salivary adenoma* (PSA) are seen in Figures 6.2, 6.4, 6.5, 13.18, and 13.19. Malignant neoplasms arising in this gland are displayed in Figures 19.12–19.14.

17.3.6 MASTICATOR SPACE

The masticator space contains the muscles of mastication, i.e. the pterygoids, temporalis, and masseter muscles, as well as the inferior alveolar nerve. Intrinsic lesions are uncommon; this space is most often invaded by pathology from outside its borders, such as SCC (see Figure 19.16).

17.3.7 CAROTID SPACE

The carotid space contains the carotid artery, jugular vein, and vagus nerve. Carotid body tumors are relatively rare tumors arising from neuroendocrine cells at the carotid bifurcation – hence, within the carotid space. These are also called *paragangliomas* and are described later in Chapter 18. Many of the deeper and larger lymph nodes lie adjacent to this space.

17.3.8 PREVERTEBRAL, DANGER, RETROPHARYNGEAL, AND PARAPHARYNGEAL SPACES

The prevertebral, danger, and retropharyngeal spaces are normally very thin,

approximating collapsed tubes lying immediately anterior to the vertebral column. The prevertebral space is immediately anterior to the vertebral bodies and extends from the skull base to the coccyx. The danger space lies anterior to the prevertebral space and stops inferiorly at the diaphragm. If an abscess forms in this space, the infection can easily spread inferiorly into the chest – hence, the "danger." The retropharyngeal space lies between the danger and premucosal spaces. It contains lymph nodes that often become involved with metastatic disease in head and neck cancers. The parapharyngeal space resides between the masticator, carotid, and pharyngeal mucosal spaces and contains mainly fat. When tumors are nearby, the pattern of displacement of this space is useful for determining where the tumor originated.

There are more named fascial spaces than those listed in this chapter. The reader who wants to become more familiar with all the spaces is referred to excellent books by Harnsberger [9] and Som and Curtin [10].

The new level-based systems, designed to be used with cross-sectional imaging, are discussed in Chapter 19 (see Figure 19.36 and Table 19.2).

References

1. Schmalfuss, I.M. and Camp, M. (2008). Skull base: pseudolesion or true lesion? *Eur. Radiol.* 18: 1232–1243.
2. Pierot, L., Boulin, A., Guillaume, A., and Pombourcq, F. (2002). Imaging of skull base tumours in adults. *J. Radiol.* 83: 1719–1734. French.
3. Alkofide, E.A. (2007). The shape and size of the sella turcica in skeletal Class I, Class II, and Class III Saudi subjects. *Eur. J. Orthod.* 29: 457–463.
4. Axelsson, S., Storhaug, K., and Kjaer, I. (2004). Post-natal size and morphology of the sella turcica. Longitudinal cephalometric standards for Norwegians between 6 and 21 years of age. *Eur. J. Orthod.* 26: 597–604.
5. Drake, R.L., Pawlina, W., Carmichael, S.W., and Albertine, K.H. (2008). Anatomical sciences education, clinical anatomy, and the anatomical record: take your pick. *Anat. Sci. Educ.* 1: 2.
6. Harnsberger, H.R. (1995). *Handbook of Head and Neck Imaging*, 2e. St. Louis: Mosby.
7. Li, X.Y., Guo, X., Feng, S. et al. (2009). Relationship between a family history of malignancy and the incidence of laryngeal carcinoma in the Liaoning province of China. *Clin. Otolaryngol.* 34: 127–131.
8. Yu, W.M. and Hussain, S.S. (2009). Incidence of nasopharyngeal carcinoma in Chinese immigrants, compared with Chinese in China and South East Asia: review. *J. Laryngol. Otol.* 2: 1–8.
9. Harnsberger, H.R. (2011). *Diagnostic Imaging. Head and Neck*, 2e. Salt Lake City: Amirsys.
10. Som, P.M. and Curtin, H.D. (2011). *Head and Neck Imaging*, 5e. St. Louis: Mosby.

Chapter 18
Benign lesions

18.1 Introduction

This chapter discusses some common (and not so common) benign swellings affecting the skull base and suprahyoid region. As most of these arise in specific anatomical sites within the base of the skull, reference should be made to Figure 17.1. Although most of these lesions will be observed by radiologists in the course of normal practice, most of them are likely only to come to the attention of the majority of oral and dental practitioners as incidental findings upon routine review of the entire dataset of large *field-of-view* (FOV) *cone-beam computed tomography* (CBCT) by themselves (if formally trained for this) or by radiologists to whom they have referred the datasets. This has already been discussed in Chapter 5. That also includes the differential diagnoses of many of these lesions, which may include malignant lesions, which are addressed separately in Chapter 19. The imaging modalities commonly used are *computed tomography* (CT) and *magnetic resonance imaging* (MRI). As noted earlier in this textbook, destructive bony pathology is usually better seen on CT.

18.2 Pituitary Adenoma

Pituitary adenomas (Figure 18.1) are benign tumors that arise from the adenohypophysis, or anterior lobe of the pituitary gland. They may be endocrinologically active and secrete the same hormones that the pituitary normally produces, only in excess amounts. The most common "functioning" pituitary tumor is a prolactinoma [1]; the excess prolactin may produce amenorrhea and galactorrhea in women and impotence in men. Both prolactinomas and "nonfunctioning" adenomas occur at approximately the same frequency: 25% of the total. Nonfunctioning tumors may present with decreased visual acuity when the tumor begins to compress the adjacent optic chiasm (Figure 18.2). Other lesions that may resemble pituitary adenomas include aneurysms, meningiomas, and schwannomas. Craniopharyngiomas and Rathke's pouch cysts also occur in the sella, but are predominantly cystic instead of solid.

18.3 Craniopharyngioma (ICD-O 9350/1)

Kalabi et al. defined the craniopharyngioma, previously known as the pituitary adamantinoma, as "a benign epithelial tumour thought to derive from the Rathke cleft" [2]. Craniopharyngiomas comprise 6–13% of all pediatric brain tumors and have a bimodal age distribution, peaking between 5 and 14 years and after 65 years of age [3, 4]. Three-quarters of these tumors are suprasellar, with most of the

Oral and Maxillofacial Radiology: A Diagnostic Approach, Second Edition. Edited by David MacDonald.
© 2020 John Wiley & Sons, Inc. Published 2020 by John Wiley & Sons, Inc.

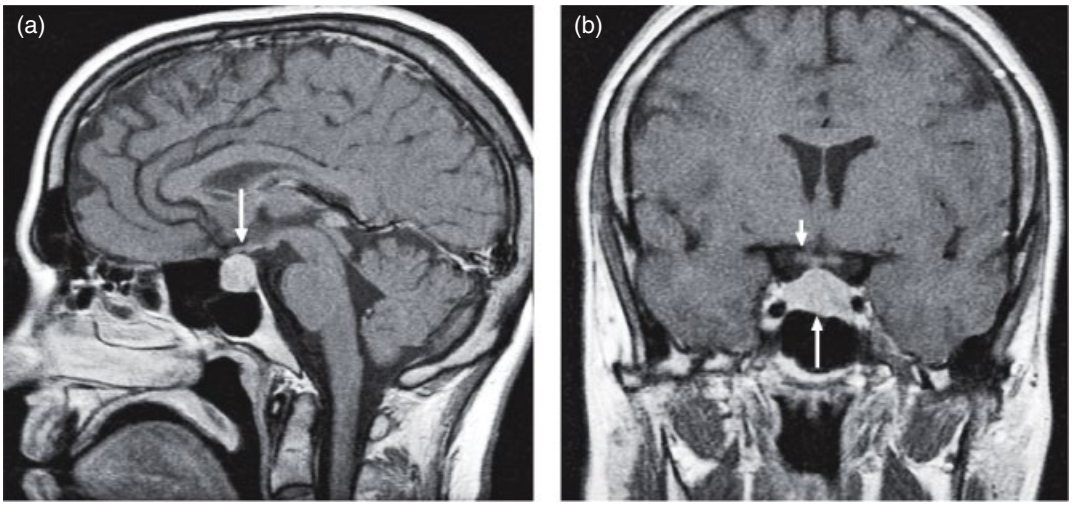


Figure 18.1 Postgadolinium T1-weighted magnetic resonance imaging of a pituitary adenoma. (a) Sagittal plane displays a round, enhancing adenoma of intermediate–high signal intensity (arrow). Note the air-filled sphenoid sinus below it and anterior to the slightly more hyperintense and homogeneous marrow-filled clivus. (b) Coronal plane displays the adenoma (long arrow). Its well-defined lateral margins touch the medial surface of the cavernous sinus bilaterally. The optic chiasma is seen immediately above as an isointense horizontal bar (short arrow pointing to right side of chiasm). The lateral pterygoid muscles are just inserting into the pterygoid pit of the condylar neck.

remaining lesions combined sellar–suprasellar. Rarely are they completely intrasellar [3, 4]. They can occur also outside the skull in the nasopharynx [2]. The craniopharyngioma usually presents as a small enhancing solid nodule within or adjacent to a lobulated cystic lesion with enhancing walls [3, 4]. This cystic component contains a brown, so-called machine oil, fluid [2]. The cystic part is often divided into multiple compartments, each with a slightly different though homogeneous T1- and T2-weighted MRI signal intensity. When they become large enough, craniopharyngiomas can produce obstructive hydrocephalus by blocking the foramen of Monroe (Figure 18.3). Craniopharyngiomas may be treated surgically, perhaps also with adjuvant radiotherapy. They "may be associated with long-term morbity and recurrence" [2].

Rathke cleft cysts can sometimes mimic craniopharyngiomas [5]. These lesions also arise from the Rathke cleft and are seen in the same location. Unlike craniopharyngiomas they are generally purely cystic (no solid component), rarely calcify, and minimally enhance with intravenous (IV) contrast [6, 7]. They also rarely produce symptoms [8].

18.4 Intracranial Aneurysms

Intracranial aneurysms are focal dilations of cerebral blood vessel walls with various shapes – some saccular, others fusiform. Arterial aneurysms are commonly caused by injury to the blood vessel walls from atherosclerosis and/or focal hemodynamic pressure. These aneurysms usually occur at vessel bifurcations, most often affecting the middle cerebral, supraclinoid

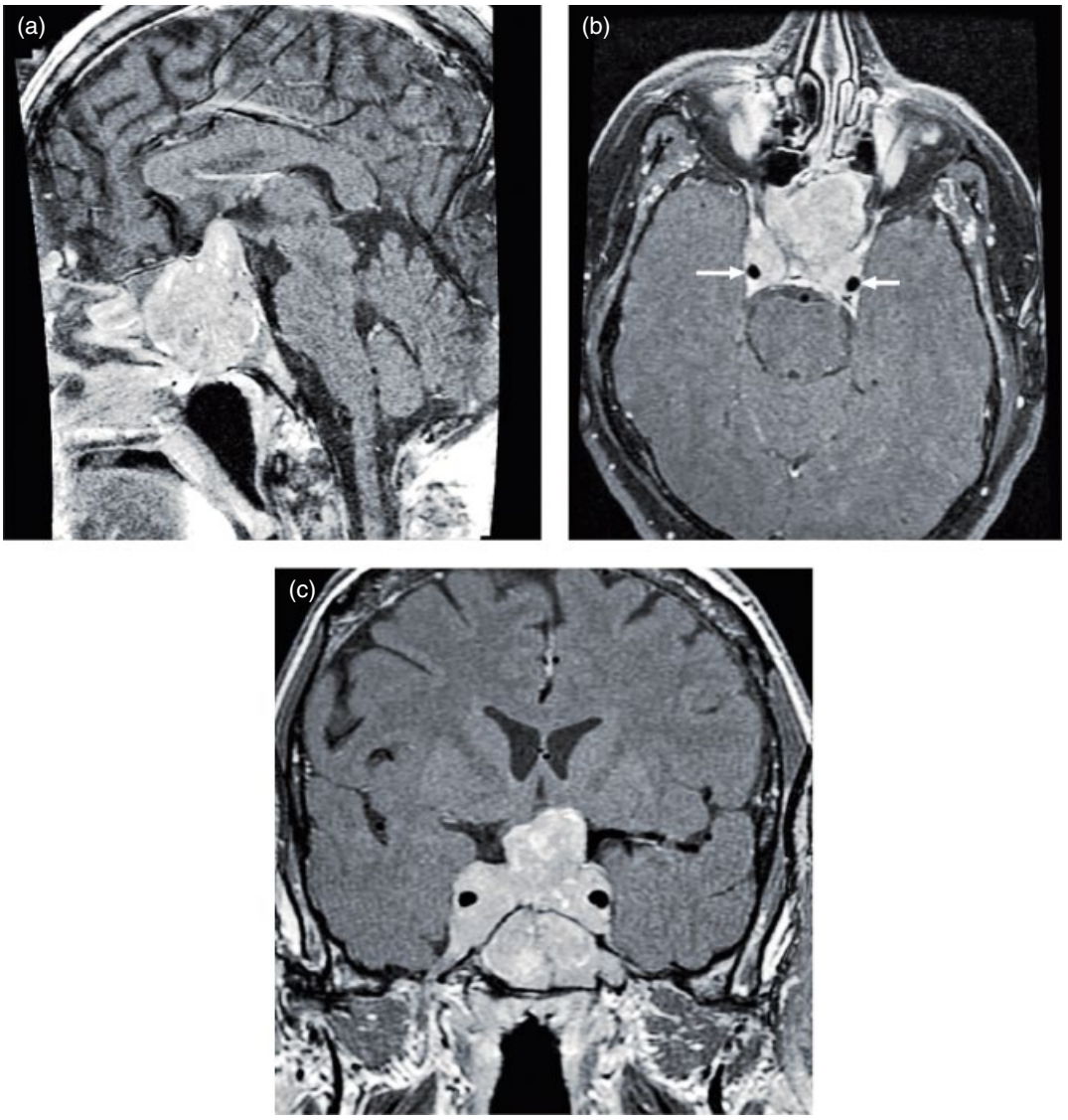


Figure 18.2 Postgadolinium T1-weighted magnetic resonance imaging (MRI) of a considerably larger pituitary adenoma than that displayed in Figure 18.1. It now encases the cavernous portion of the carotid arteries and markedly compresses the optic chiasm, displacing it superiorly. (a) Sagittal plane displaying a lobular enhancing adenoma of intermediate–high signal intensity with heterogeneous enhancement. Note that the tumor has traversed the sellar floor to completely fill and expand the adjacent sphenoid sinus. The tumor has also eroded and remodeled the marrow-filled clivus, pushing the superior clival border inferiorly. (b) Axial postgadolinium fat-saturated T1-weighted MRI at the level of the superior surface of the orbit; the superior rectus muscles are displayed. The encased carotid arteries are observed as signal voids (arrows), as is the basilar artery on the anterior aspect of the midbrain. (c) Coronal plane displaying the same adenoma. It completely encases the cavernous portion of the carotid arteries. Inferiorly, it fills the sphenoid sinus. The roof of the nasal cavity has been displaced slightly downward. The superior expansion has compressed the optic chiasm and brought the adenoma into broad contact with the hypothalamus. The lateral pterygoid muscles are just inserting into the pterygoid pit of the condylar neck.

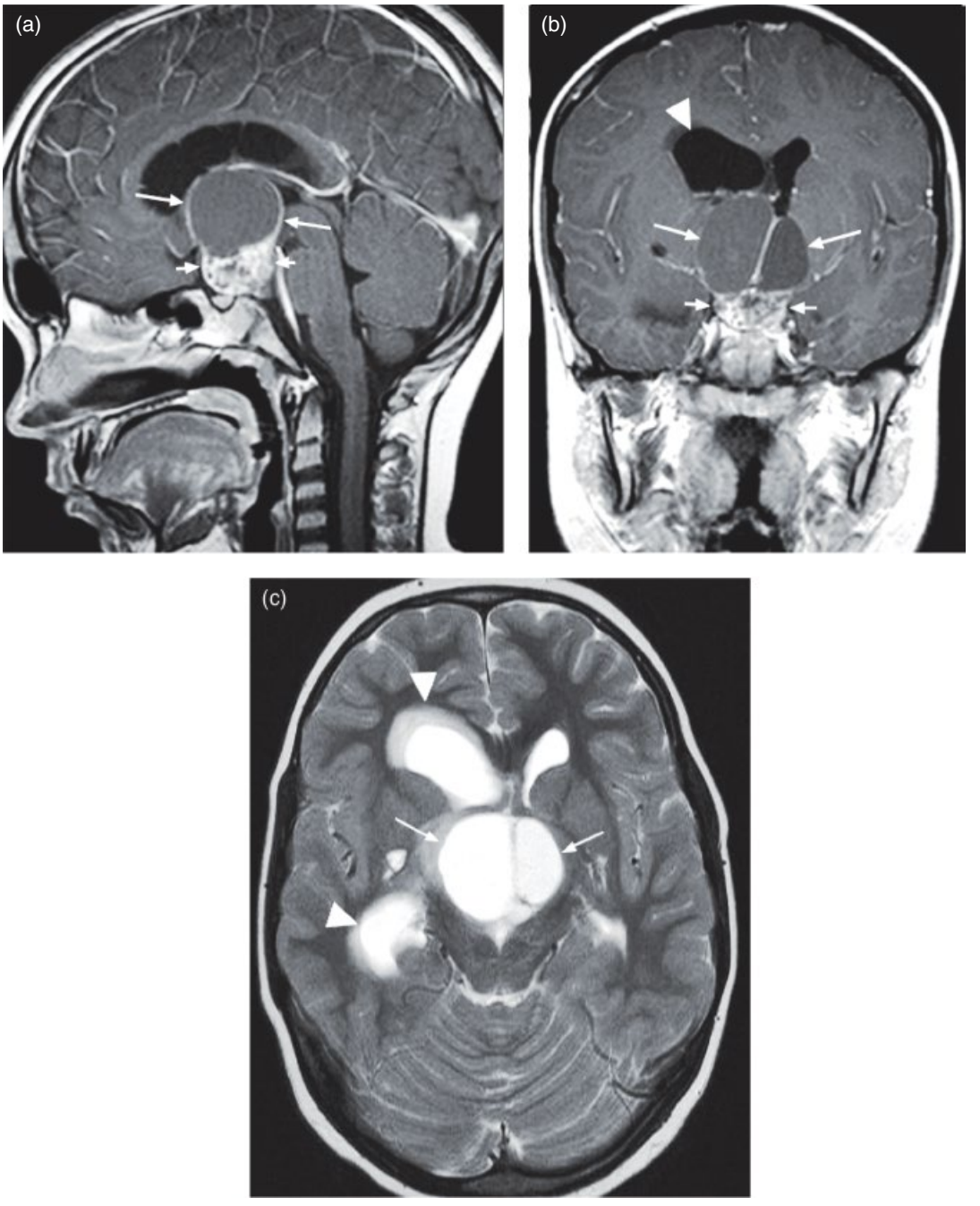


Figure 18.3 Magnetic resonance imaging (MRI) of a craniopharyngioma producing unilateral intraventricular hydrocephalus. (a) Sagittal postcontrast T1-weighted MRI showing a large complex cystic suprasellar craniopharyngioma. Note the characteristic heterogeneous solid enhancing portion (short arrows) and the large associated cyst with enhancing walls (long arrows). (b) Coronal postcontrast T1-weighted image from the same patient. The solid (short arrows) and cystic (long arrows) parts of the lesion are displayed. The left cyst compartment has a higher signal than its fellow; different cyst MRI signal levels are a common feature of this tumor. The mass is obstructing the right side of the foramen of Monroe, producing unilateral right intraventricular obstructive hydrocephalus. Note the dilated right lateral ventricle (arrowhead). (c) Axial T2-weighted image from the same patient. The cystic portion of the tumor is well seen (arrows). Note the dilated right frontal and temporal ventricular horns: hydrocephalus caused by the tumor (arrow heads).

internal carotid, posterior communicating, cavernous carotid, anterior communicating, and vertebrobasilar arteries, in descending order of frequency [9]. The prevalence of *unruptured intracranial aneurysms* (UIA) is estimated to range between 0.4 and 6%, depending on the study design [10]. There is a 4% increased risk of having a UIA if a first-degree relative has a cerebral aneurysm [11]. Over the course of a lifetime, the risk of an aneurysm rupturing is substantial, estimated from 20% to 50% [12]; risk increases with the size of the aneurysm. In a 1998 systematic review, Rinkel et al. [10] found that in aneurysms under 1 cm, the risk is 0.7% per year, and for over 1 cm 4% per year, with an overall annual risk of 1.9% [9, 10, 13]. Posterior circulation aneurysms, symptomatic aneurysms, and female sex carry a higher risk of rupture. Incidental aneurysms less than 0.5 mm carry a low risk and conservative management is recommended [14]. An increased incidence of cerebral aneurysm is seen in patients with autosomal dominant polycystic kidney disease, fibromuscular dysplasia, Marfan's and Ehlers-Danos syndromes, and cerebral arteriovenous malformations [15].

Since the consequences of intracranial aneurysm rupture can be devastating, imagers must keep a careful eye out for these lesions on routine exams. Larger aneurysms are easily seen on postcontrast CT as well-circumscribed, brightly enhancing structures related to cerebral vessels (Figure 18.4). Occasionally, an aneurysm wall will calcify, making it easy to see on a noncontrast CT. The appearance of aneurysms on MRI varies depending on the way imaging data was acquired. On T2-weighted images, the aneurysm will appear as a dark, hypointense, well-circumscribed structure (Figure 18.4). The inside of the aneurysm is dark rather than bright on T2-weighted images due to the presence of flowing blood. On postcontrast T1-weighted images, aneurysms have a heterogeneous internal appearance due to a combination of flow artifact and contrast effect (Figure 18.4). Smaller aneurysms can be detected with special magnetic resonance techniques (magnetic resonance arteriography) or conventional catheter angiography.

18.5 Paraganglioma (ICD-O 8693/3)

Kimura et al. define the *paraganglioma* as "neuroendocrine neoplasm arising from paraganglia in the vagal trunk near its exit from the brain stem. Paragangliomas associated with peripheral nerve branches are usually defined for their anatomical site (e.g. laryngeal paraganglioma" [16]. It is also called the glomus vagale tumor. The middle ear paraganglioma arises in the adventitia of the jugular bulb or on the medial promontory wall of the middle ear [16]. This is also called the glomus jugulare tumor. Other paragangliomas are the *carotid body tumor* and the *glomus tympanicum* (the tympanic cavity), and along the extracranial course of the vagus nerve (glomus vagale). Above the shoulders 99% of paragangliomas arise in these spots, with just over half at the carotid bifurcation [17]. Women predominate, ranging from 67% in a European community [18] to 96% in a Latin American study [19]. Malignant transformation is rare [20]. Most paragangliomas are discovered incidentally during radiological examination for another lesion. These are very vascular tumors and enhance brightly with IV contrast (Figures 18.5 and 18.6). The prognosis of a paraganglioma is site, size, and genotype dependent [16]. The main treatment modalities are radiotherapy and

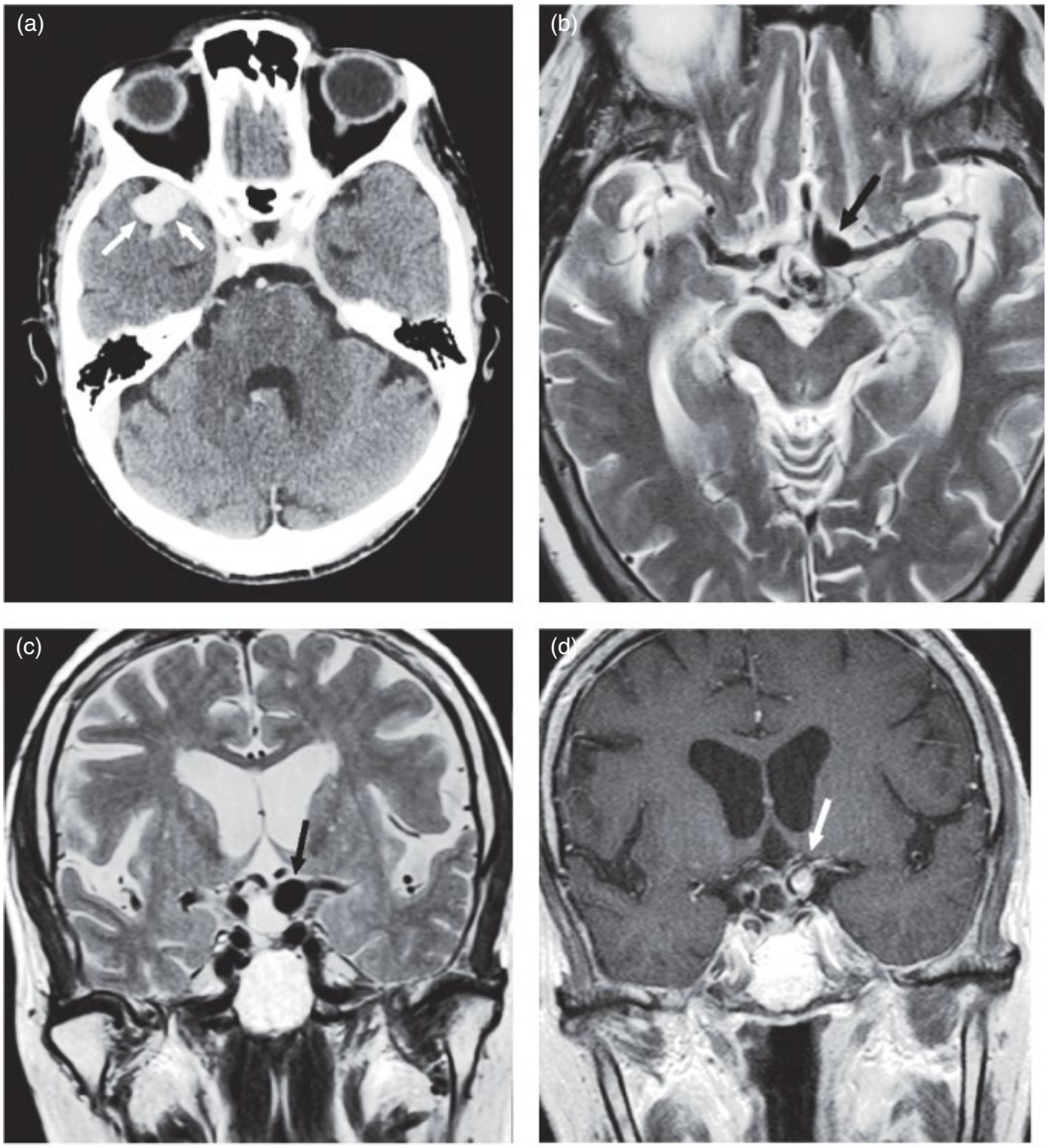


Figure 18.4 Computed tomography (CT) and magnetic resonance imaging (MRI) of intracranial aneurysms. (a) Axial postcontrast CT of a distal right middle cerebral artery aneurysm (arrows). Cerebral aneurysms are usually homogeneously bright on postcontrast CT, unless they have internal thrombus; then they will have heterogeneous internal density. (b) Axial T2-weighted MRI of a terminal internal carotid artery aneurysm (arrow). Note the low signal within the aneurysm due to the presence of flowing blood. The reader will notice a mixed signal oval structure just posterior and medial to the aneurysm. This is a small craniopharyngioma. (c) Coronal T2-weighted MRI from the same patient as (b). Again, the aneurysm is seen as a well-circumscribed hypodense structure. The cystic craniopharyngioma just medial to it is bright. (d) Coronal postcontrast T1-weighted MRI from the same patient as (b). Note the mixed signal within the aneurysm due to a combination of flow artifact and intravascular contrast (arrow). Most aneurysms are better defined on T2-weighted sections.

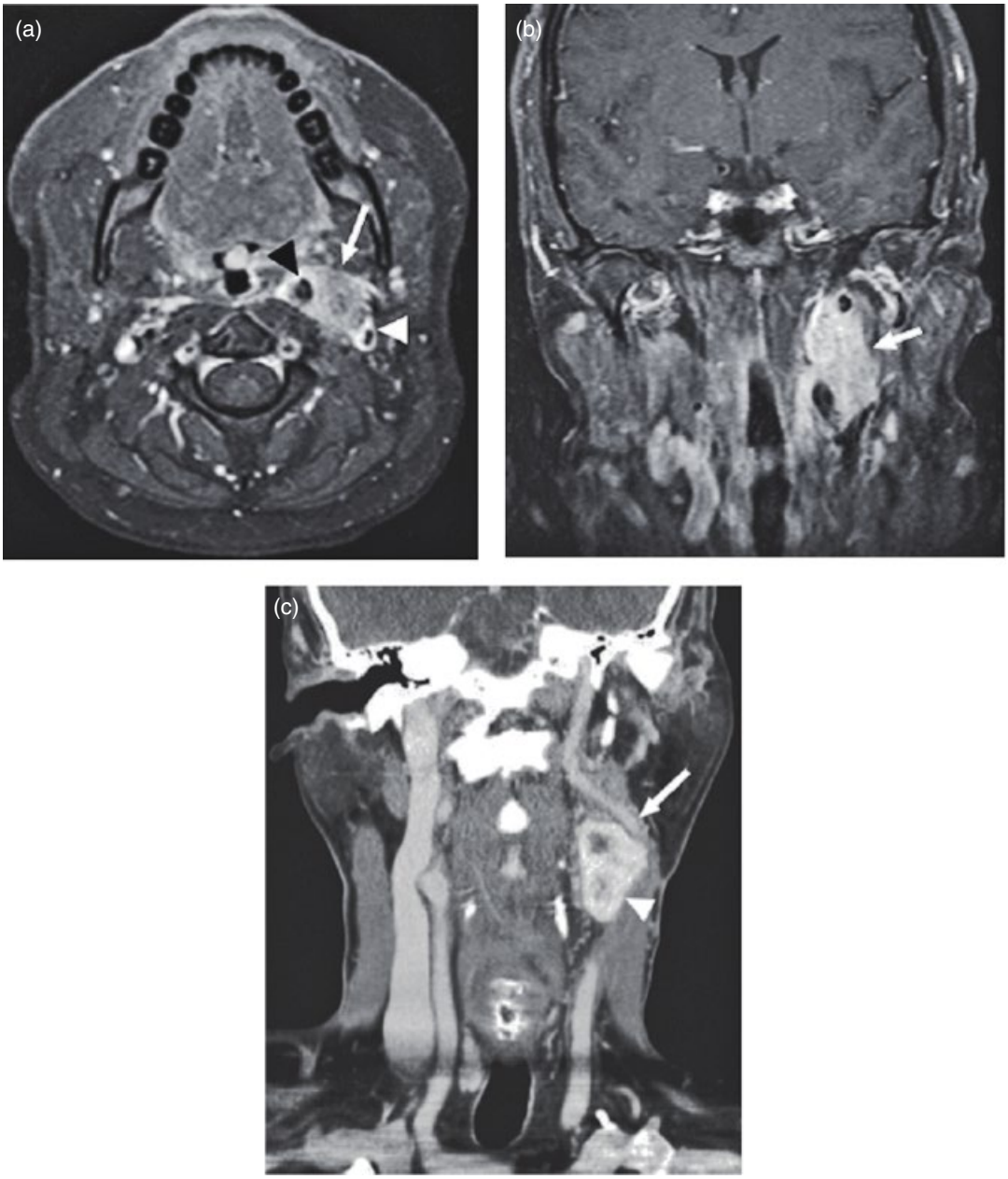


Figure 18.5 Magnetic resonance imaging (MRI) and computed tomography (CT) of carotid paragangliomas. (a) Axial postgadolinium fat-saturated T1-weighted MRI of a left carotid paraganglioma (arrow). Note how the internal carotid artery (black arrowhead) and external carotid artery (white arrowhead) are splayed just above the carotid bifurcation. This is a consistent feature of this tumor. (b) Coronal postgadolinium fat-saturated T1-weighted MRI from the same patient showing the longitudinal extent of the paraganglioma in (a) (arrow). (c) Coronal enhanced CT of a different patient. Note how the internal carotid artery has been displaced laterally (arrow). The tumor enhances brightly (arrowhead).

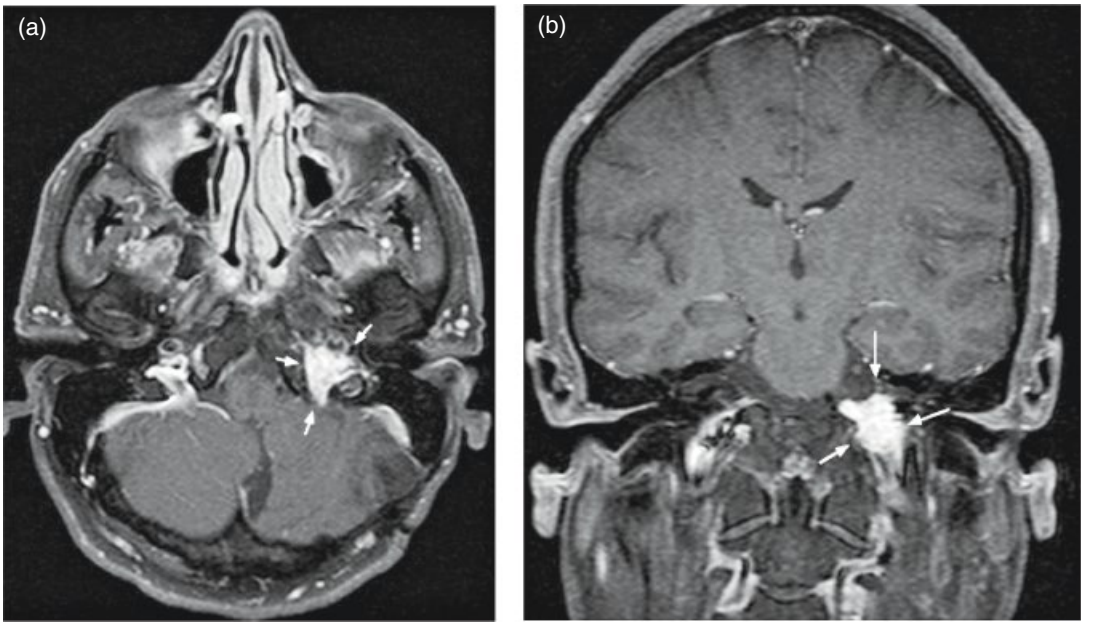


Figure 18.6 Magnetic resonance imaging (MRI) of a jugular paraganglioma (also called a glomus jugulare). (a) Axial postgadolinium fat-saturated T1-weighted MRI of a left glomus jugulare tumor (arrows). Note the resemblance to the jugular schwannoma in Figure 18.10. Glomus tumors tend to be slightly more irregular in shape than schwannomas. Unlike schwannomas, on T2-weighted imaging they have a "salt and pepper" internal appearance; the dark "pepper" spots are flow voids from numerous internal vessels (not shown). (b) Coronal postgadolinium fat-saturated T1-weighted MRI from the same patient showing a glomus jugulare (arrows).

stereotactic surgery to effect a cure rate of over 90%. On the other hand, nearly two-thirds develop neurological defects, usually of the vagus, but also of other cranial nerves [16]. If left untreated, these lesions can remain stable for a long period or grow only very slowly [16].

18.6 Schwannoma (ICD-O 9560/0)

Thompson et al. define the schwannoma as "a benign tumour of Schwann-cell phenotype" [21]. Schwannomas are nerve sheath tumors that arise from cells that produce layered myelin covering peripheral nerve axons. They can occur in any peripheral nerve and the majority are benign. In the head and neck, schwannomas are found mostly in cranial nerves, but also in nerves arising from cervical roots. They tend to present late because they are slow growing. Most schwannomas occur sporadically, except in *neurofibromatosis type 2* (NF2), a rare autosomal dominant disorder that is characterized by multiple inherited schwannomas, meningiomas, and ependymomas (also called *MISME syndrome*) [22]. One of the key diagnostic features of NF2 is the presence of bilateral vestibular schwannomas (Figure 18.7).

The most common site for schwannomas in the head and neck is the vestibular division of the eighth cranial nerve, hence the vestibular schwannoma. The vestibular schwannoma has also been called *acoustic neuroma*, which is a

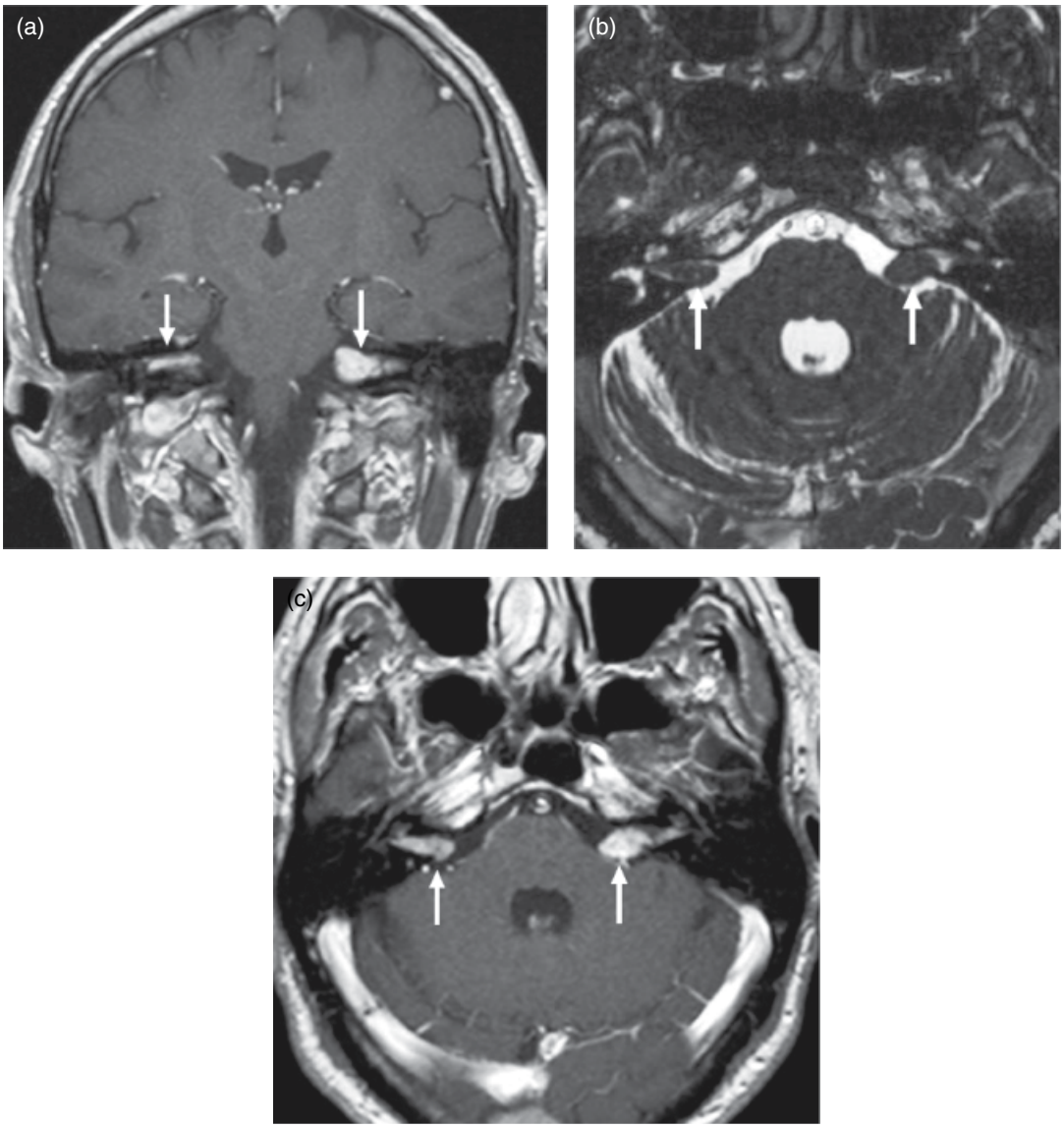


Figure 18.7 Magnetic resonance imaging (MRI) of small bilateral vestibular schwannomas in neurofibromatosis Type 2. (a) Coronal postgadolinium T1-weighted MRI shows enhancement of bilateral vestibular schwannomas (arrows). (b) Axial balanced steady-state free precession (CISS) MRI shows the left tumor protruding into the perimesencephalic cistern, whereas the right lesion is mostly intracanalicular (arrows). (c) Axial postgadolinium T1-weighted MRI; both schwannomas enhance (arrows).

misnomer because it occurs very rarely in the acoustic (cochlear) branch of this nerve. Unilateral hearing loss from compression of the adjacent acoustic branch of the eighth nerve is the most common presenting symptom. Small vestibular schwannomas can be completely intracannalicular – i.e. residing within the internal auditory canal (see the right-sided tumor in Figure 18.7). As they get larger

they expand the bony canal and travel medially, compressing the brain stem (Figures 18.8 and 18.9).

The next most common cranial nerve schwannomas arise in the trigeminal, facial, glossopharyngeal, vagus, and spinal accessory nerves, in descending order of frequency. These can occur both intracranially and extracranially. A jugular foramen schwannoma can resemble a glomus jugulare tumor

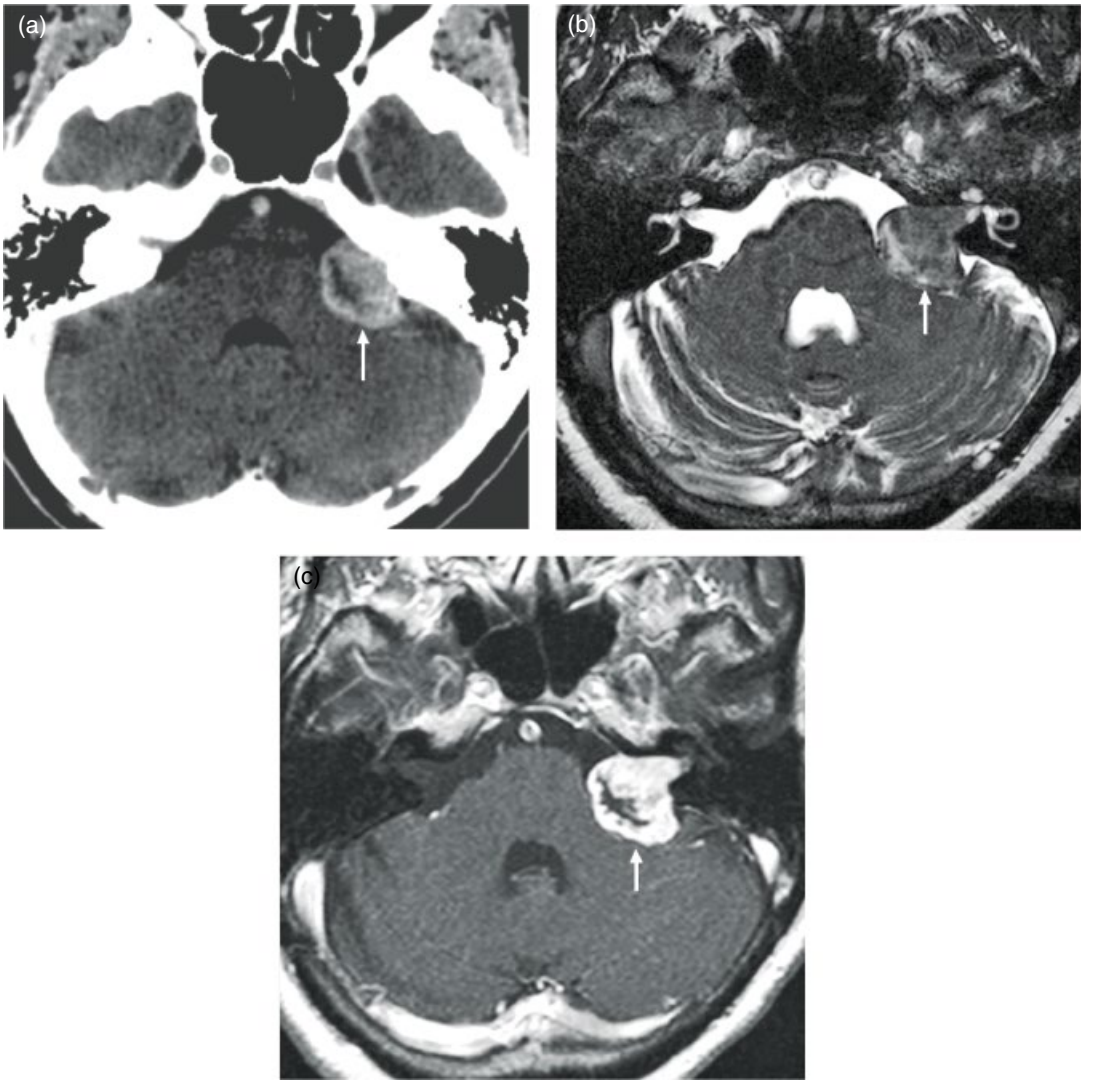


Figure 18.8 Computed tomography (CT) and magnetic resonance imaging (MRI) of a typical vestibular schwannoma (arrows). (a) Axial postcontrast CT showing an enhancing left cerebellopontine angle vestibular schwannoma (soft-tissue window). (b) Axial balanced steady-state free precession (CISS) MRI shows the common ice-cream-cone shape; the handle of the "cone" is formed by a tumor within the internal auditory canal, whereas the "ice-cream ball" is produced by a tumor in the perimesencephalic cistern. This lesion is indenting the middle cerebellar peduncle (brachium pontis). (c) Axial postgadolinium T1-weighted MRI shows the usual bright enhancement with often-seen internal cystic change and/or necrosis.

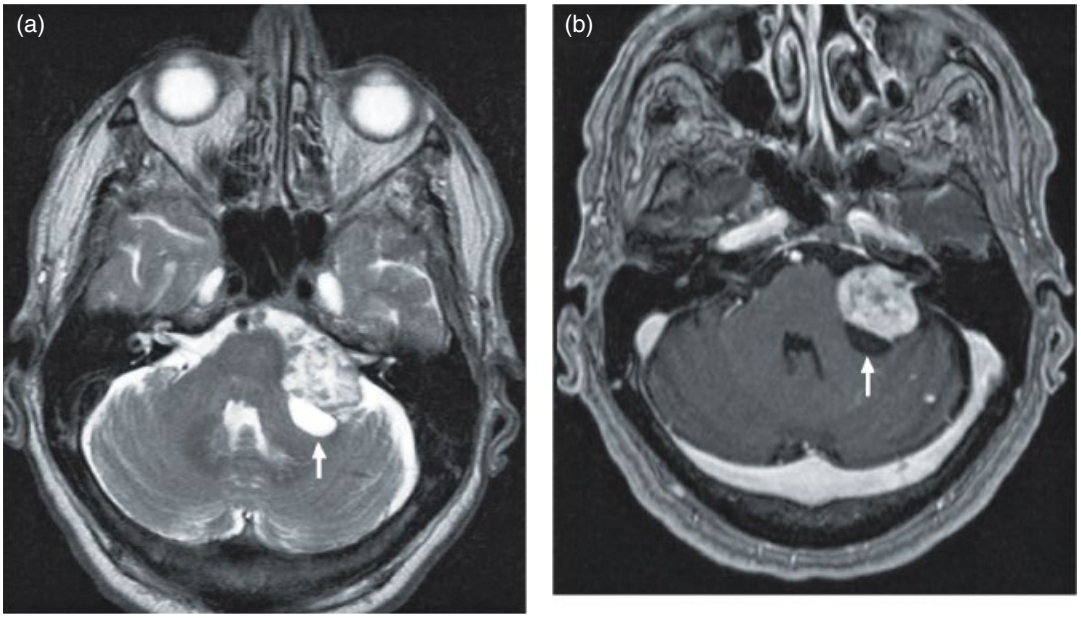


Figure 18.9 Magnetic resonance imaging (MRI) of a variant vestibular schwannoma. (a) Axial T2-weighted MRI displaying a left cerebellopontine angle mass. This lesion does not exhibit the characteristic ice-cream-cone shape, because it is predominantly extracanalicular. Note the tumor-associated cyst adjacent to the posterior edge of the lesion (arrow); these occur in a minority of cases. The cyst is the same signal intensity as cerebrospinal fluid (CSF). (b) Axial postgadolinium fat-saturated T1-weighted MRI showing characteristic bright enhancement of the vestibular schwannoma. Note how the tumor-associated cyst's signal intensity tracks that of the CSF (arrow).

on postcontrast CT and MRI images; compare Figures 18.5 and 18.10.

Schwannomas have a very low potential to recur and their malignant transformation is very rare [21].

18.7 Meningioma (ICD-O 9530/0)

Ro et al. defined the meningioma as neoplasm composed of meningothelial cells [23]. These arise from the leptomeningeal coverings of the brain. They are the most common primary intracranial tumor and are almost always benign. Meningiomas occur in different intracranial locations but have a uniform imaging appearance: homogeneous bright postcontrast enhancement with smooth, well-circumscribed borders (Figures 18.11–18.14). They are usually globular in shape, but can occur as plaques (called "en plaque"; see Figure 18.13). When meningiomas occur next to bone, they often induce sclerosis (Figures 18.11b and 18.13); this is one way in which they can be differentiated from paragangliomas and schwannomas arising in skull base foramina. Meningiomas are slow growing and, when large enough, will cause symptoms from the mass effect on local structures. They can sometimes occur extracranially, e.g. in the optic nerve sheath (Figure 18.14), and rarely within the cerebral ventricles.

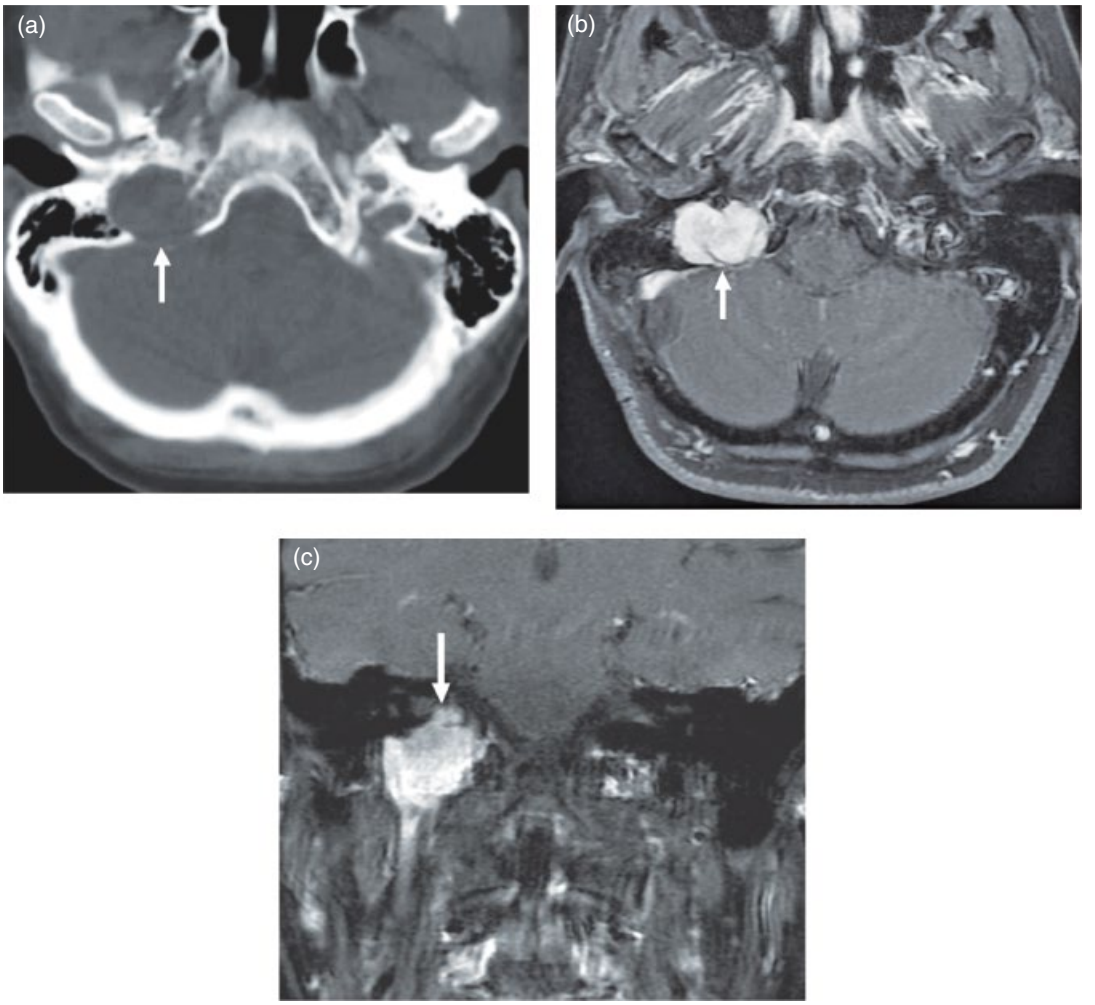


Figure 18.10 Computed tomography (CT) and magnetic resonance imaging (MRI) of a schwannoma enlarging the right jugular foramen (arrows). (a) An axial CT (bone window), at the level of the condylar heads, displaying a well-defined radiolucency produced by a schwannoma in the right jugular bulb, eroding into the mastoid air cells laterally and the clivus medially. The sharp zone of transition between tumor and bone is characteristic of benign lesions. (b) Axial postgadolinium fat-saturated T1-weighted MRI showing the usual bright enhancement seen in schwannomas. (c) Coronal postgadolinium fat-saturated T1-weighted MRI revealing the schwannoma as a well-defined isointense structure compressing the right internal jugular vein.

18.8 Orbital Venous Malformation (formerly the Orbital Hemangioma)

This tumor is mentioned here because it is the most common orbital tumor in adults; hence, it is most likely to be seen by the oral and maxillofacial practitioner. Like schwannomas, meningiomas, and paragangliomas, they present as a well-circumscribed, brightly enhancing mass (Figure 18.15). Intraorbital schwannomas and paragangliomas are very rare.

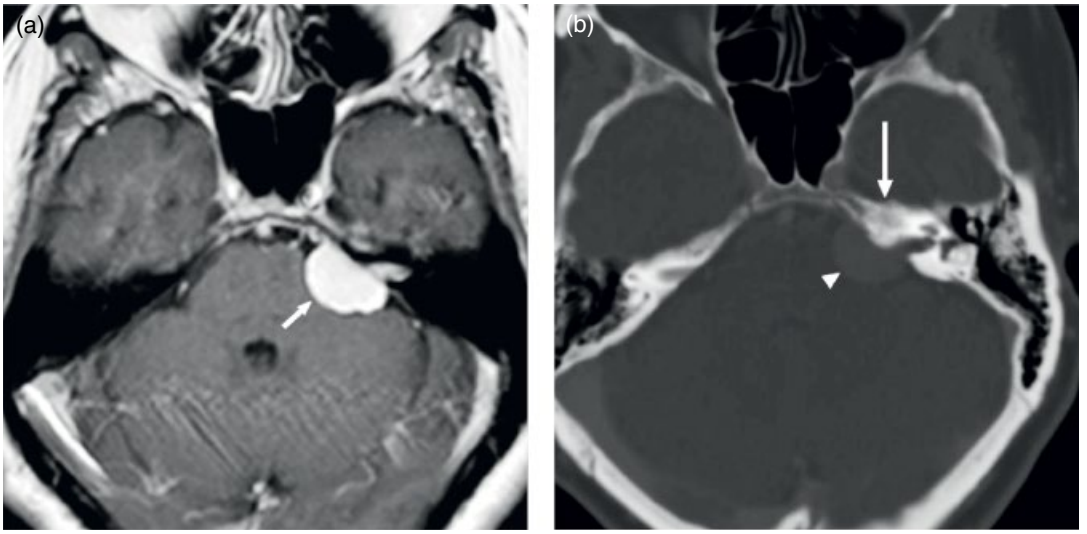


Figure 18.11 Magnetic resonance imaging (MRI) and computed tomography (CT) of a cerebellopontine angle (CPA) meningioma mimicking a vestibular schwannoma. (a) Axial postgadolinium T1-weighted MRI showing an enhancing hemisphere-shaped left CPA meningioma (arrow). This is similar in appearance to the variant vestibular schwannoma seen in Figure 18.9. Occasionally CPA meningiomas will spread out onto adjacent dura, forming a "dural tail"; this feature is not seen with vestibular schwannomas. (b) Axial CT showing subtle bone sclerosis induced by the meningioma in the apex of the right petrous temporal bone (long arrow). The meningioma is barely visible on this bone window (arrowhead). A vestibular schwannoma will not induce sclerosis and, unlike a CPA meningioma, often produces widening of the internal auditory canal.

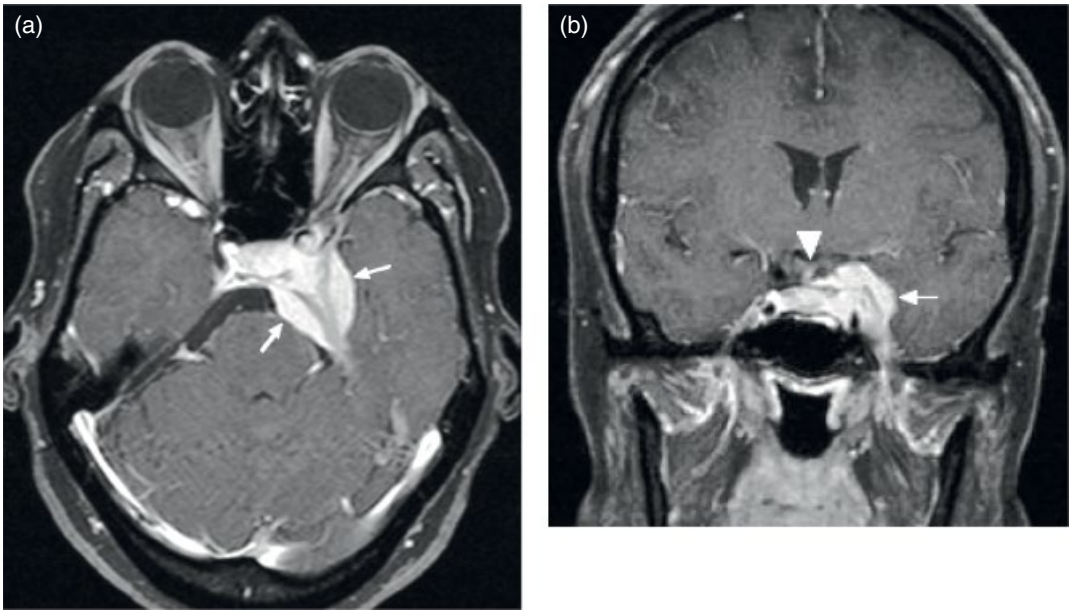


Figure 18.12 Magnetic resonance imaging (MRI) of a left cavernous sinus meningioma. (a) Axial postgadolinium fat-saturated T1-weighted image of a left cavernous sinus meningioma extending posterolaterally onto the petrous temporal bone (arrows). (b) Coronal postgadolinium fat-saturated T1-weighted MRI showing the same meningioma as in (a). The tumor is encasing the left cavernous sinus (arrow) and extending medially into the sella, where it is mildly displacing the pituitary stalk to the right (arrowhead).

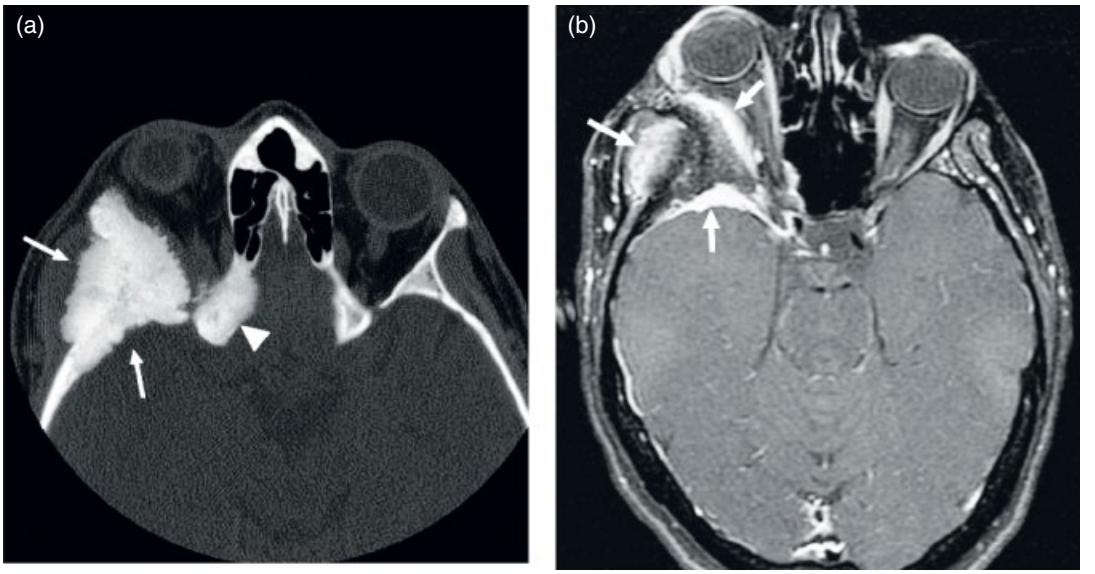


Figure 18.13 Computed tomography (CT) and magnetic resonance imaging (MRI) of a meningioma encasing the right greater sphenoid wing, producing marked hyperostosis. (a) Axial computed tomography (bone window) of a right greater sphenoid wing meningioma producing marked hyperostosis (long arrows). Note how the hyperostosis has extended medially to involve the right anterior clinoid process (arrowhead). (b) Axial postgadolinium fat-saturated T1-weighted MRI showing the same tumor as (a). The central hyperostotic bone is dark. The tumor surrounding the bone enhances brightly and has a layered "en plaque" morphology rather than the usual globular shape (arrows). Note how the intraorbital component of the meningioma is producing proptosis.

18.9 Arachnoid Cysts

Arachnoid cysts are benign, incidental intracranial lesions that are not uncommon. They occur in the arachnoid membrane in characteristic locations; most commonly the middle cranial fossa (Figure 18.16a and b). Arachnoid cysts may enlarge very slowly over time, producing mild scalloped pressure erosion along the adjacent inner table (Figure 18.16c). They are almost always asymptomatic.

18.10 Benign Salivary Gland Tumors

These have been addressed in Chapter 13. Pleomorphic adenoma are shown in Figures 13.18 and 13.19, the Warthin tumor in Figure 13.20, and oncocytoma in Figure 13.21.

18.11 Inverted Papilloma (ICD-O 8121/1)

Hunt et al. defined the inverted papilloma as a "surface mucosa lesion of the sinonasal tract that usually shows inverted growth and has multilayered epithelium with mucocytes and transmigrating neutrophils" [24]. The inverted papillomas are uncommon, slow-growing, predominantly unilateral benign tumors of the nasal mucosal surface [25, 26]. These most often occur in the lateral nasal wall near the middle meatus. This tumor is presented here to illustrate that even benign tumors can be quite locally destructive; so much so that they can resemble malignant lesions radiologically: compare Figure 11.17 with an example of squamous cell carcinoma (SCC) in Figure 11.13.

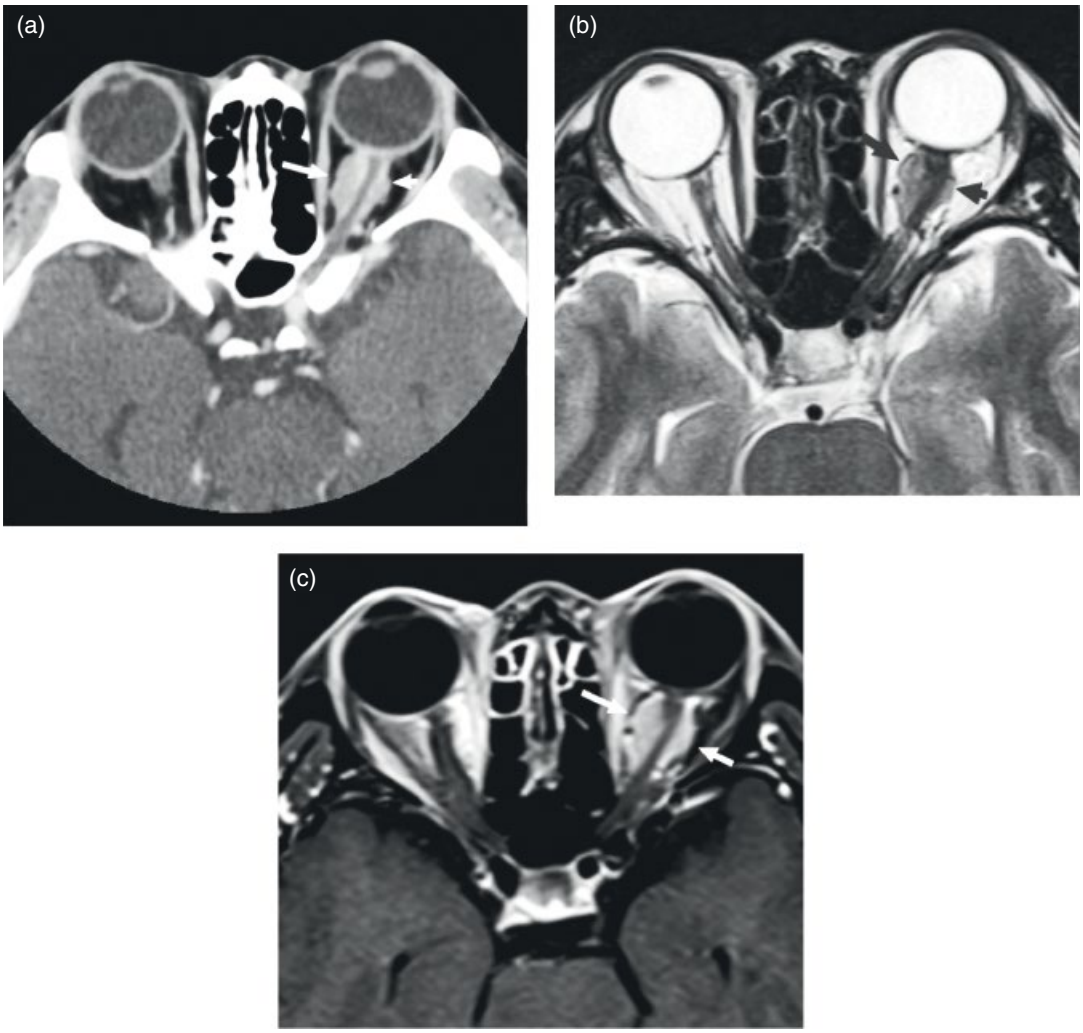


Figure 18.14 Computed tomography (CT) and magnetic resonance imaging (MRI) of a left optic nerve sheath meningioma. (a) Axial postcontrast CT showing a meningioma arising from the left optic nerve sheath (arrows). (b) Axial T2-weighted MRI displays the same meningioma as isointense to brain. (c) Axial postgadolinium fat-saturated T1-weighted MRI showing characteristic bright enhancement through the meningioma.

Secondary malignancy, usually SCC, will arise in 5% of these lesions [27].

18.12 Tornwaldt Cyst

Tornwaldt (also known as "Thornwaldt") cysts are small, solitary congenital cysts that are located in the high posterior nasopharynx between the longus coli muscles (Figure 18.17). They arise from small foci of primitive pharyngeal mucosa that were dragged superiorly from their original location by the ascending notochord on its way to meet the skull base. Most Tornwaldt cysts range from 0.2 to 1.0 cm in size, although they can be up to 3 cm. Because they contain mucus they are bright on T2-weighted MRIs and isointense to muscle on T1-weighted MRI and CT [28].

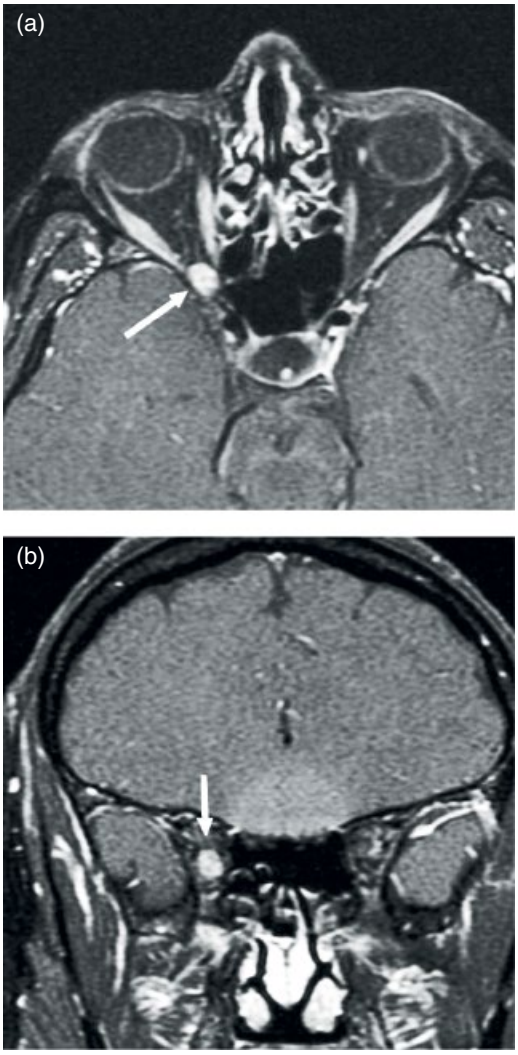


Figure 18.15 Magnetic resonance imaging (MRI) of a venous malformation within the orbital apex. (a) Axial postgadolinium fat-saturated T1-weighted MRI displays characteristic bright enhancement of a hemangioma in the right orbital apex (arrow). (b) Coronal postgadolinium fat-saturated T1-weighted MRI showing the same venous malformation (arrow).

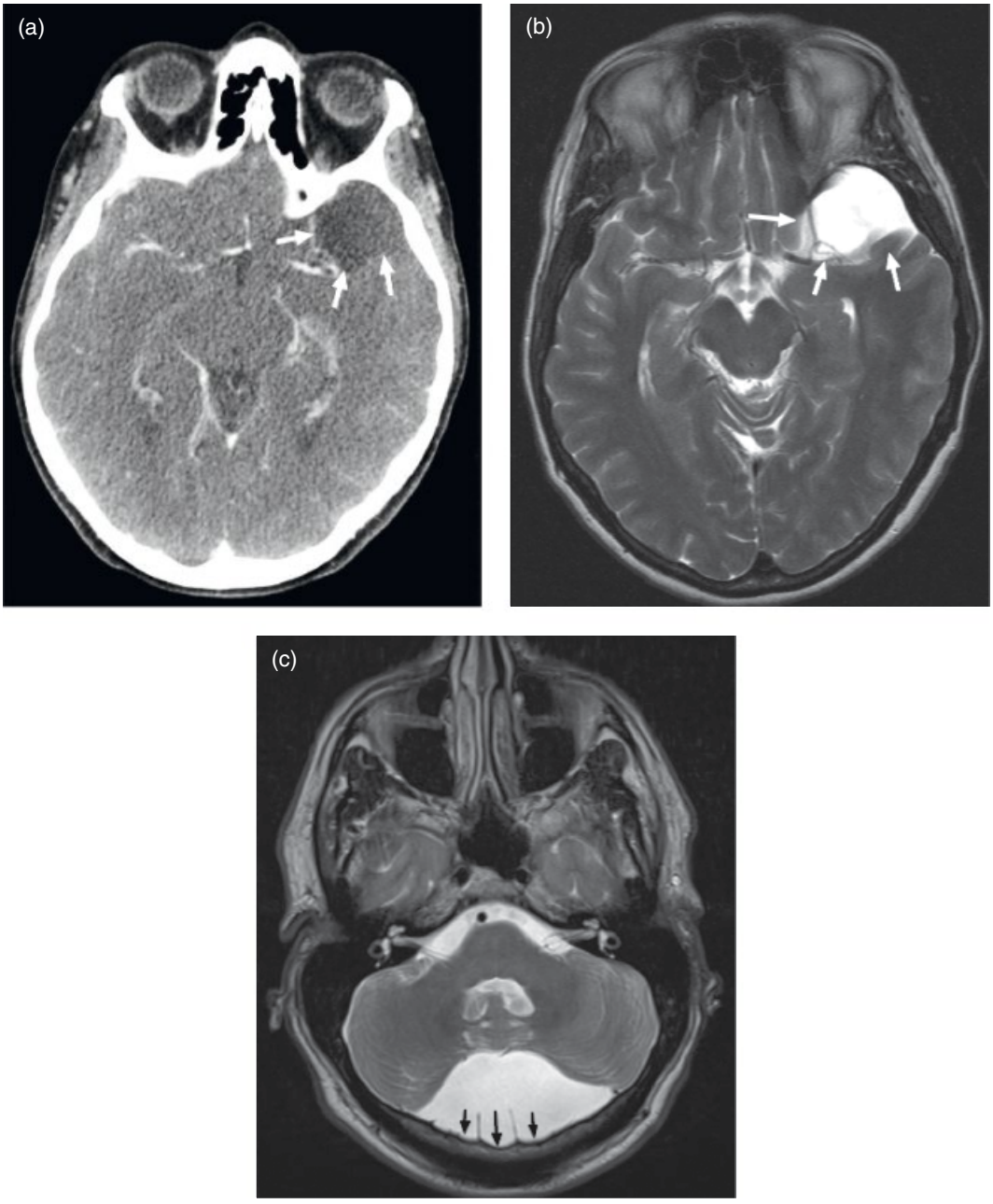


Figure 18.16 Computed tomography (CT) and magnetic resonance imaging (MRI) of intracranial arachnoid cysts (white arrows). (a) Axial postcontrast CT of a left anterior temporal arachnoid cyst. This is a very common location for this benign lesion. (b) Axial T2-weighted MRI of the same cyst. Since the cyst contains cerebrospinal fluid (CSF), the cyst signal is identical to that of CSF elsewhere surrounding the brain. (c) Axial T2-weighted MRI showing a posterior fossa arachnoid cyst. Scalloping of the adjacent inner table of the skull is a characteristic feature of arachnoid cysts (black arrows). A benign developmental variant called a mega cisterna magna is found in the same location and can look almost identical, though lacking inner table scalloping.

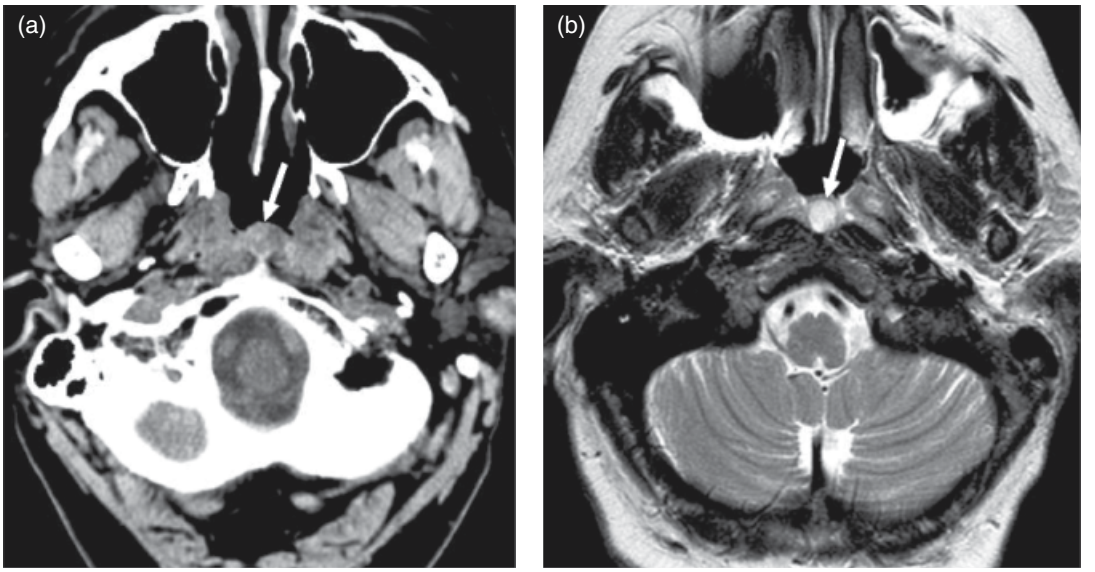


Figure 18.17 Computed tomography (CT) and magnetic resonance imaging (MRI) of a patient with a Tornwaldt's cyst (arrow). (a) Axial noncontrast CT (soft-tissue window) at the level of the insertion of the lateral pterygoid into the pterygoid pit of the condyle, revealing a round, well-defined cystic lesion on the high midline posterior nasopharyngeal wall (arrow). (b) Axial T2-weighted MRI of the same patient showing hyperintense signal within the cyst – the same as cerebrospinal fluid surrounding the brain stem. These cysts are benign and always occur in this location.

The rim may slightly enhance with either CT or MRI contrast. These lesions are benign and usually discovered incidentally. The incidence at autopsy is 4% [29].

18.13 Osteoma (ICD-O 9180/0)

Toner et al. defined the osteoma as "a benign neoplasm composed of mature bone, limited almost exclusively to the craniofacial bones" [30]. In the head and neck these are usually quite dense, with imaging characteristics similar to cortical bone (Figures 10.35 and 18.18). Osteomas can be found in the mandible, maxilla [31], paranasal sinuses, calvarium [32], and adjacent to the external auditory canal. They can be sessile or pedunculated. These lesions usually occur sporadically, but are also seen in Gardner's syndrome, a rare, autosomal dominant inherited condition associated with malignant colonic polyps [33].

18.14 Thalassemia

Thalassemia (See also 9.5.1) is an uncommon group of inherited defects in the hemoglobin molecule that can lead to severe anemia, most prominently in the homozygous beta thalassemia subtype. The anemia triggers extensive red marrow proliferation in the medullary bony cavity; this produces coarse thickened trabeculae, widening of the medullary cavity, and cortical thinning. In the skull, new bone forms beneath the periosteum in response to the expanding marrow, causing a typical hair-on-end appearance (Figure 18.19) [28, 34]. Other hematopoetic conditions that can

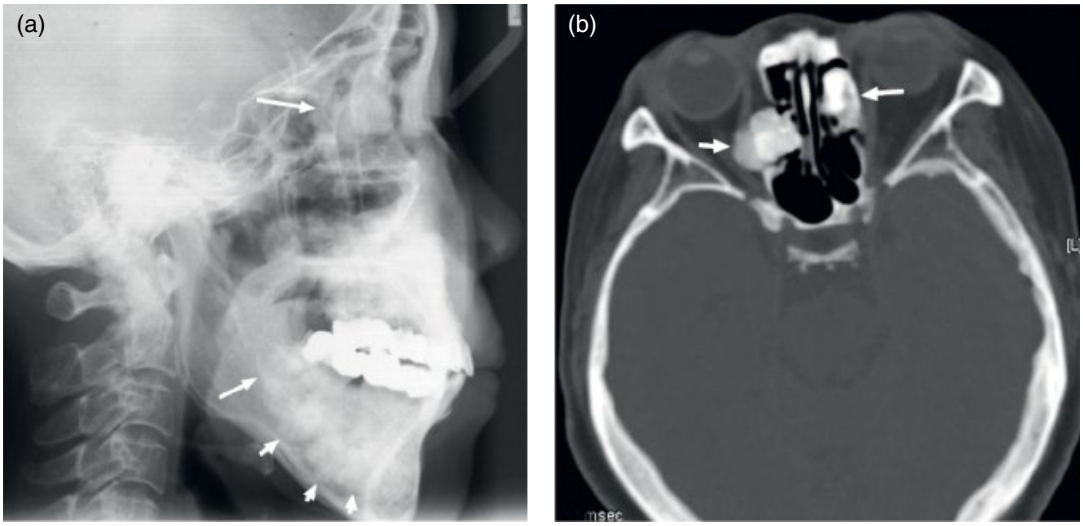


Figure 18.18 Computed tomography (CT) of osteomas affecting the medial orbital walls and jaws. (a) Lateral radiograph of the skull in a patient with Gardner's syndrome, showing dense lesions superimposed on the anterior orbit and multiple radiopacities in the jaws (arrows). Figure 10.3 displays the panoramic radiograph of this case. (b) Axial CT of the same patient showing osteomas arising from the medial wall of both orbits (arrows). On the right the lesion is displacing the medial rectus muscle laterally and slightly indenting the right optic nerve, producing mild proptosis. This lesion is separated from the adjacent bone by a radiolucent zone. Source: Reproduced with permission fromLee, B.D., Lee, W., Oh, S.H., Min, S.K., and Kim, E.C. (2009). A case report of Gardner syndrome with hereditary widespread osteomatous jaw lesions. *Oral Surg. Oral Med. Oral Pathol. Oral Radiol. Endod.* 107: e68–e72.

affect the skull in a similar manner include sickle-cell disease, polycythemia rubra vera, and hereditary spherocytosis. Other figures of the same case are Figures 9.14 and 11.10.

18.15 Fibrous Dysplasia

The presentations of *fibrous dysplasia* (FD) is discussed in Chapter 10. FD is a sporadic disorder of osteoblastic differentiation and maturation causing medullary bone to be replaced with fibrous tissue. The fibrous tissue produces expansion, leading to deformity of the involved bone. The radiographic appearance of the medullary cavity changes markedly, since it is now filled with dysplastic bone. Typically this has been described as having a ground-glass appearance on plain films [35]. In addition to this, other descriptors have been used for CT, including "peau d'orange," "whorled," "pagetoid," and "smokey" [36] (Figures 18.20 and 18.21). FD is a nonhereditary condition, although it can be associated with genetic mutation, i.e. in McCune-Albright syndrome [37] (Figure 18.22).

18.16 Paget's Disease

Paget's disease (historically called *osteitis deformans*) is a disorder of bone remodeling characterized by increased and disorganized bone turnover [38]. This produces bony expansion and deformity, not unlike FD. Both conditions evolve very slowly and in the skull can produce lion-like facies termed leontiasis ossea (see Chapter 10). Unlike FD, Paget's goes

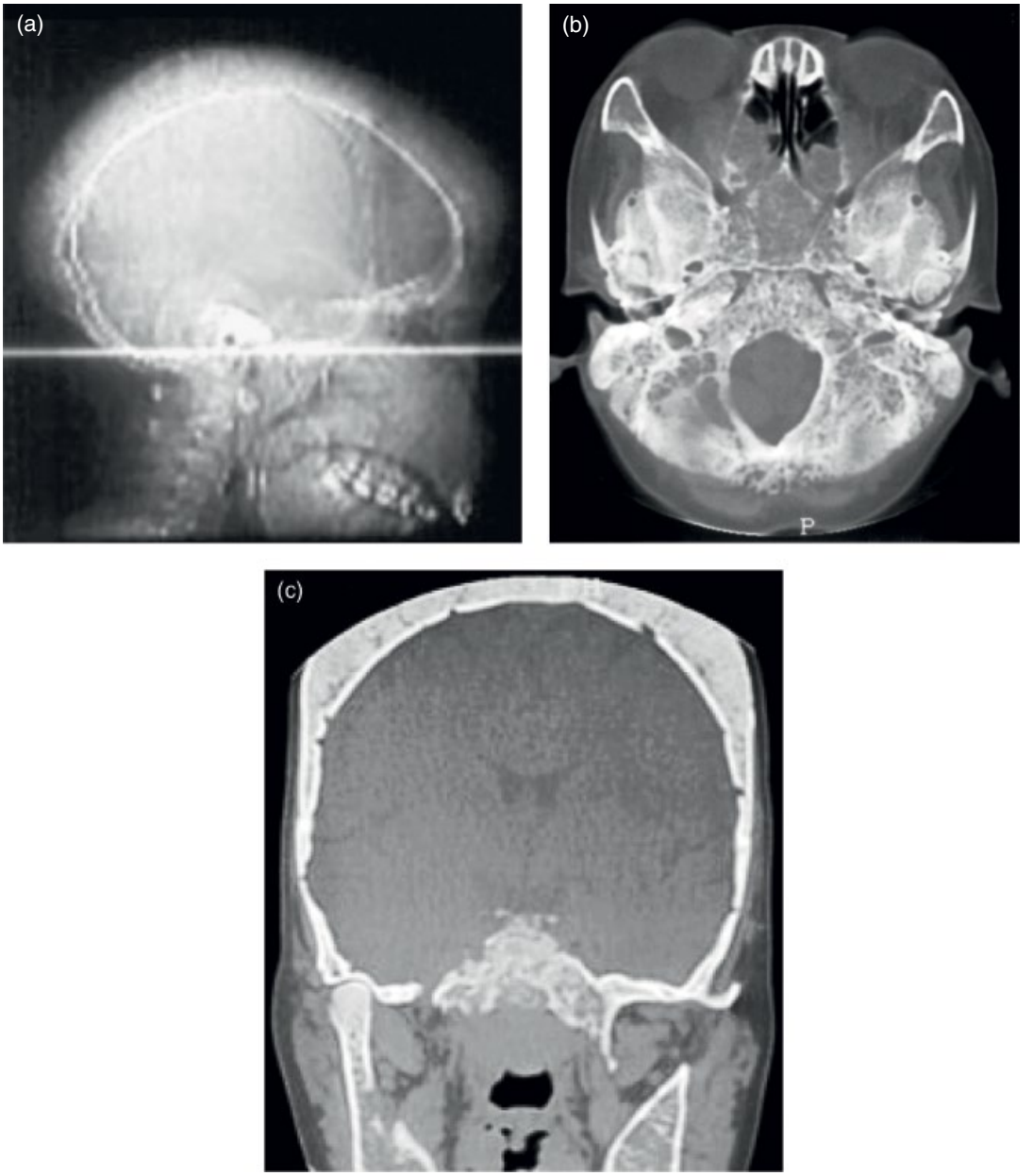


Figure 18.19 Computed tomography (CT) of thalassemia. (a) The scout view displaying the characteristic hair-on-end trabecular pattern involving the entire calvarium. The maxillary antrums have been completely obliterated due to the expanding bone (See Figure 11.10). (b) Axial CT section (bone window) displaying complete obliteration of the sphenoid sinus and most of the ethmoid air cells. The overall presentation is that of thick coarse trabeculae. The cortex in places is partially replaced. This is particularly obvious in the medial orbital walls. (c) Coronal section (bone window) through the anterior clinoid process displaying complete obliteration of the sphenoid sinus and complete replacement of normal bone almost everywhere with thickened coarse trabeculae.

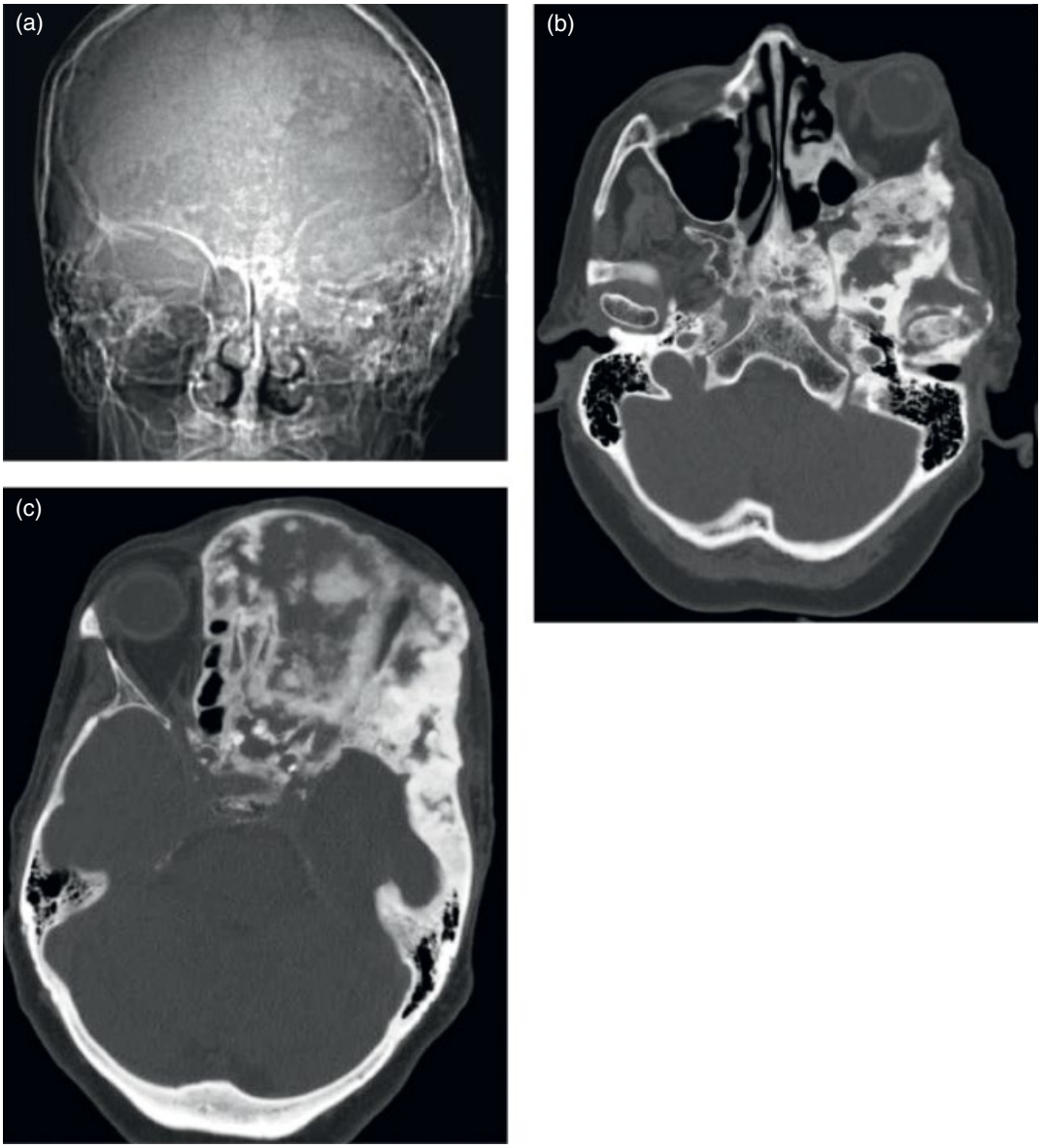


Figure 18.20 Computed tomography (CT) of fibrous dysplasia affecting the base of the skull and frontal bone. (a) A posterioanterior conventional radiograph of the skull, displaying a mixed-density expansile lesion with associated loss of the left orbital roof. (b) Axial CT (bone window) displaying a dysplastic lesion replacing the body of the left sphenoid, pterygoid, and maxilla. The appearance of the bone is peau d'orange with radiolucent areas. The dysplastic lesion has expanded into the orbit, producing proptosis (exophthalmos) of the left eye. (c) Axial CT (bone window) at the level of the roof on the nose and right orbit. The dysplastic bone is partially radiolucent with interspersed radiopacities, as observed in (a).

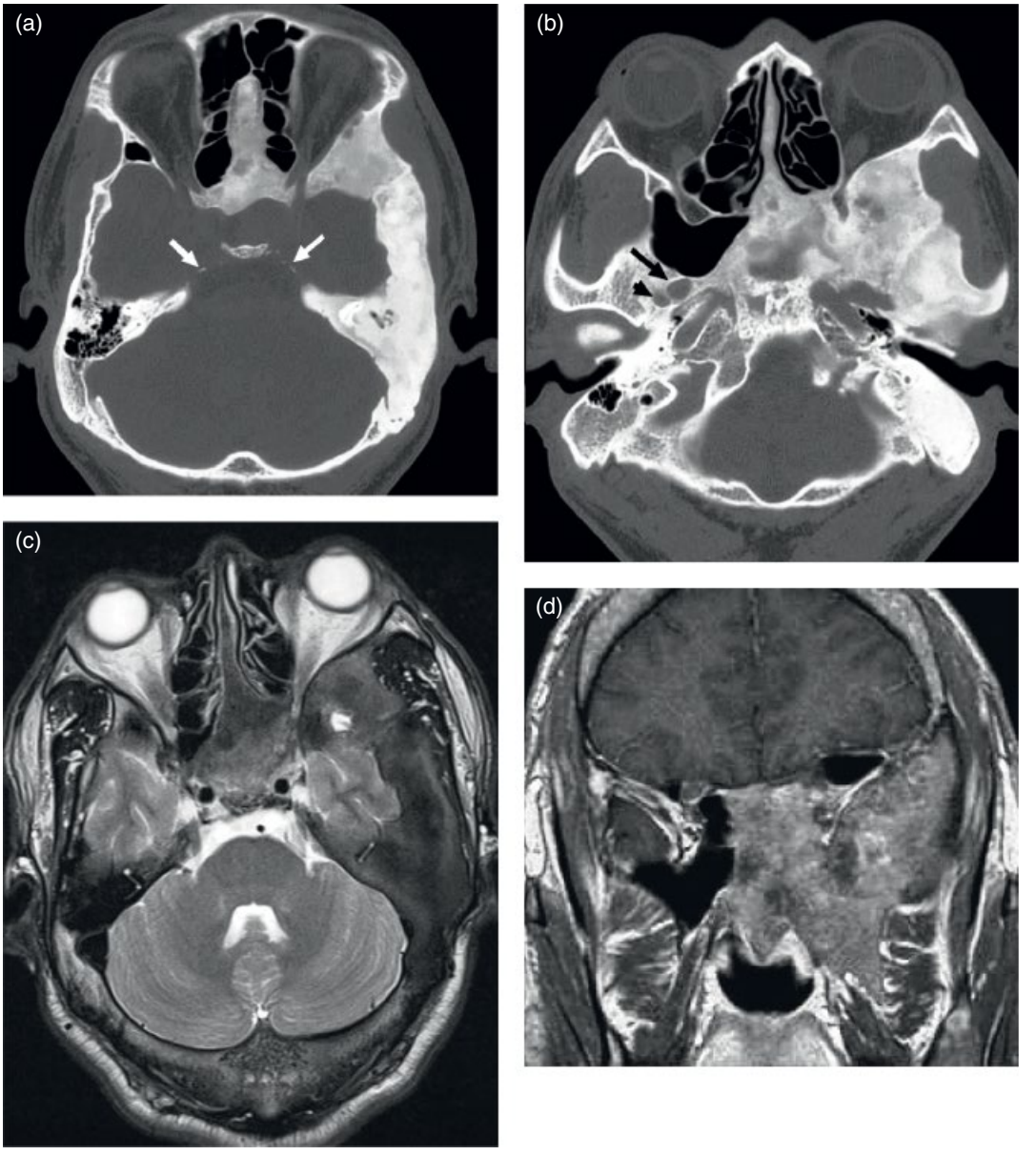


Figure 18.21 Computed tomography (CT) (bone windows) and magnetic resonance imaging (MRI) of fibrous dysplasia (FD). (a) Axial CT at the level of optic canal and clinoid processes. Calcification of the petroclinoid ligaments is apparent (white arrows). FD affects the left sphenoid, ethmoid, and temporal bones. The dysplastic bony process barely crosses the left temporo-occipital suture to affect the occipital bone. The left petrous temporal bone is completely affected. The adjacent mastoid air cells are almost completely absent. The left vertical semicircular canal is apparent and the sclerosis bordering it is similar to the unaffected side. The dysplastic bone exhibits a ground-glass appearance. (b) Axial CT at the level of the globe (eyeball) and right condylar head. The body and greater wing of the left sphenoid bone are affected. The right foramina ovale (long black arrow) and spinosum (short black arrow) are clearly visible just posterior to extensive lateral right sphenoid sinus pneumatization. (c) Axial of T2-weighted MRI, at the level of the globe (eyeball). The dysplastic bone is mostly hypointense, although some parts exhibit slightly higher signal intensity in inverse proportion to the amount of dense bone in different parts of the lesion. (d) Coronal postgadolinium T1-weighted MRI displaying increased signal in the dysplastic bone, now isointense to hyperintense.

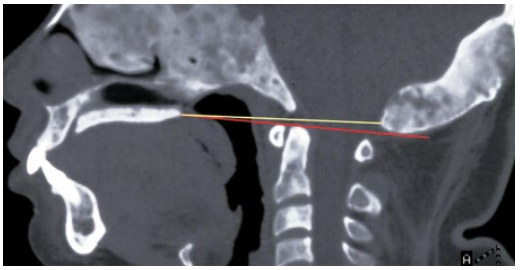


Figure 18.22 Sagittal computed tomography of McCune-Albright's syndrome. Fibrous dysplasia (FD) has affected the sphenoid bone, clivus, and occipital bone in addition to the hard palate, maxilla, and mandible. This case does not display basilar invagination (BI; also called basilar impression). Note 1: FD affecting the base of the skull may be affected by BI, which is determined by observing the relation of the dens to either McGregor's or Chamberlain's line. Note 2: McGregor's line (red) joins the posterior margin of the hard palate with the under surface of the occipital bone. The tip of the odontoid should *not* be more than 7 mm above this line. Note 3: Chamberlain's line (yellow) joins the posterior margin of the hard palate with the opisthion (posterior margin of foramen magnum) of the squamous occipital bone. The tip of the odontoid should *not* be more than 5 mm above this line.

through three stages: an early lytic phase, also called *osteoporosis circumscripta*, in which bone resorption predominates; a "mixed" phase; and a sclerotic phase in which the bones become dense. The imaging findings between the two conditions still overlap; the interested reader is referred to an article by Tehranzadeh et al. [39].

References

1. Oruckaptan, H.H., Senmevsim, O., Ozcan, O.E., and Ozgen, T. (2000). Pituitary adenomas: results of 684 surgically treated patients and review of the literature. *Surg. Neurol.* 53: 211–219.
2. Kalabi, N., Hunt, J.L., Thompson, L.D.R., and Wenig, B.M. (2017). Craniopharyngioma. In: *WHO Classification of Head and Neck Tumours* (ed. A.K. El-Naggar, J.K.C. Chan, J.R. Grandis, et al.), 73. Lyon: International Agency for Research on Cancer (IARC).
3. Garre, M.L. and Cama, A. (2007). Craniopharyngioma: modern concepts in pathogenesis and treatment. *Curr. Opin. Pediatr.* 19: 471–479.
4. Haupt, R., Magnani, C., Pavanello, M. et al. (2006). Epidemiological aspects of craniopharyngioma. *J. Pediatr. Endocrinol.* 19 (Suppl 1): 289–293.
5. Shin, J.L., Asa, S.L., Woodhouse, L.J. et al. (1999). Cystic lesions of the pituitary: clinicopathological features distinguishing craniopharyngioma, Rathke's cleft cyst, and arachnoid cyst. *J. Clin. Endocrinol. Metab.* 84: 3972–3982.
6. Nakasu, Y., Isozumi, T., Nakasu, S., and Handa, J. (1990). Rathke's cleft cyst: computed tomographic scan and magnetic resonance imaging. *Acta Neurochir.* 103: 99–104.
7. Kucharczyk, W., Peck, W.W., Kelly, W.M. et al. (1987). Rathke cleft cysts: CT, MR imaging, and pathologic features. *Radiology* 165: 491–495.
8. Ross, D.A., Norman, D., and Wilson, C.B. (1992). Radiologic characteristics and results of surgical management of Rathke's cysts in 43 patients. *Neurosurgery* 30: 173–178; discussion 178–179.
9. Wiebers, D.O., Whisnant, J.P., Huston, J. III et al. (2003). Unruptured intracranial aneurysms: natural history, clinical outcome, and risks of surgical and endovascular treatment. *Lancet* 362: 103–110.
10. Rinkel, G.J., Djibuti, M., Algra, A., and van Gijn, J. (1998). Prevalence and risk of rupture of intracranial aneurysms: a systematic review. *Stroke* 29: 251–256.
11. The International Study of Unruptured Intracranial Aneurysms Investigators, Magnetic Resonance Angiography in Relatives of Patients with Subarachnoid Hemorrhage Study Group (1999). Risks and benefits of screening for intracranial aneurysms in first-degree relatives of patients with sporadic subarachnoid hemorrhage. *N. Engl. J. Med.* 341: 1344–1350.
12. Le Roux, P.D., Winn, H.R., and Newell, D.W. (2004). *Management of Cerebral Aneurysms*. Philadelphia: Saunders.

13. The Magnetic Resonance Angiography in Relatives of Patients with Subarachnoid Hemorrhage Study Group, International Study of Unruptured Intracranial Aneurysms Investigators (1998). Unruptured intracranial aneurysms – risk of rupture and risks of surgical intervention. *N. Engl. J. Med.* 339: 1725–1733.
14. Komotar, R.J., Mocco, J., and Solomon, R.A. (2008). Guidelines for the surgical treatment of unruptured intracranial aneurysms: the first annual J. Lawrence pool memorial research symposium – controversies in the management of cerebral aneurysms. *Neurosurgery* 62: 183–193; discussion 193–194.
15. Brisman, J.L., Song, J.K., and Newell, D.W. (2006). Cerebral aneurysms. *N. Engl. J. Med.* 355: 928–939.
16. Kimura, N., Capella, C., Gill, A. et al. (2017). Laryngeal, middle ear and vagal paragangliomas. In: *WHO Classification of Head and Neck Tumours* (ed. A.K. El-Naggar, J.K.C. Chan, J.R. Grandis, et al.), 281–284. Lyon: International Agency for Research on Cancer (IARC).
17. Erickson, D., Kudva, Y.C., Ebersold, M.J. et al. (2001). Benign paragangliomas: clinical presentation and treatment outcomes in 236 patients. *J. Clin. Endocrinol. Metab.* 86: 5210–5218.
18. Makeieff, M., Raingeard, I., Alric, P. et al. (2008). Surgical management of carotid body tumours. *Ann. Surg. Oncol.* 15: 2180–2186.
19. Luna-Ortiz, K., Rascon-Ortiz, M., Villavicencio-Valencia, V. et al. (2005). Carotid body tumours: review of a 20-year experience. *Oral Oncol.* 41: 56–61.
20. Bomanji, J.B., Hyder, S.W., Gaze, M.N. et al. (2001). Functional imaging as an aid to decision-making in metastatic paraganglioma. *Br. J. Radiol.* 74: 266–269.
21. Thompson, L.D.R., Bullerdiek, J., Flucke, U., and Franchi, A. (2017). Schwannoma. In: *WHO Classification of Head and Neck Tumours* (ed. A.K. El-Naggar, J.K.C. Chan, J.R. Grandis, et al.), 48–49. Lyon: International Agency for Research on Cancer (IARC).
22. Neff, B.A. and Welling, D.B. (2005). Current concepts in the evaluation and treatment of neurofibromatosis type II. *Otolaryngol. Clin. N. Am.* 38: 671–684.
23. Ro, J.U., Beil, D., Nicolai, P., and Thompson, L.D.R. (2017). Meningioma. In: *WHO Classification of Head and Neck Tumours* (ed. A.K. El-Naggar, J.K.C. Chan, J.R. Grandis, et al.), 50–51. Lyon: International Agency for Research on Cancer (IARC).
24. Hunt, J.L., Bell, D., and Sarioglu, S. (2017). Sinonasal papilloma, inverted type. In: *WHO Classification of Head and Neck Tumours* (ed. A.K. El-Naggar, J.K.C. Chan, J.R. Grandis, et al.), 28–29. Lyon: International Agency for Research on Cancer (IARC).
25. Lawson, W., Le Benger, J., Som, P. et al. (1989). Inverted papilloma: an analysis of 87 cases. *Laryngoscope* 99: 1117–1124.
26. Vrabec, D.P. (1994). The inverted Schneiderian papilloma: A 25-year study. *Laryngoscope* 104: 582–605.
27. Mendenhall, W.M., Hinerman, R.W., Malyapa, R.S. et al. (2007). Inverted papilloma of the nasal cavity and paranasal sinuses. *Am. J. Clin. Oncol.* 30: 560–563.
28. Tyler, P.A., Madani, G., Chaudhuri, R. et al. (2006). The radiological appearances of thalassaemia. *Clin. Radiol.* 61: 40–52.
29. Magliulo, G., Fusconi, M., D'Amico, R., and de Vincentiis, M. (2001). Tornwaldt's cyst and magnetic resonance imaging. *Ann. Otol. Rhinol. Laryngol.* 110: 895–896.
30. Toner, M., Allen, C.M., and Castle, J. (2017). Osteoma. In: *WHO Classification of Head and Neck Tumours* (ed. A.K. El-Naggar, J.K.C. Chan, J.R. Grandis, et al.), 246. Lyon: International Agency for Research on Cancer (IARC).
31. Johann, A.C., de Freitas, J.B., de Aguiar, M.C. et al. (2005). Peripheral osteoma of the mandible: case report and review of the literature. *J. Craniomaxillofac. Surg.* 33: 276–281.
32. Sayan, N.B., Ucok, C., Karasu, H.A., and Gunhan, O. (2002). Peripheral osteoma of the oral and maxillofacial region: a study of 35 new cases. *J. Oral Maxillofac. Surg.* 60: 1299–1301.
33. Buch, B., Noffke, C., and de Kock, S. (2001). Gardner's syndrome – the importance of early diagnosis: a case report and a review. *SADJ* 56: 242–245.
34. Tunaci, M., Tunaci, A., Engin, G. et al. (1999). Imaging features of thalassemia. *Eur. Radiol.* 9: 1804–1809.

35. Lisle, D.A., Monsour, P.A., and Maskiell, C.D. (2008). Imaging of craniofacial fibrous dysplasia. *J. Med. Imaging Radiat. Oncol.* 52: 325–332.
36. MacDonald-Jankowski, D. (2009). Fibrous dysplasia: a systematic review. *Dentomaxillofac. Radiol.* 38: 196–215.
37. Defilippi, C., Chiappetta, D., Marzari, D. et al. (2006). Image diagnosis in McCune-Albright syndrome. *J. Pediatr. Endocrinol.* 19: 561–570.
38. Ralston, S.H. (2008). Pathogenesis of Paget's disease of bone. *Bone* 43: 819–825.
39. Tehranzadeh, J., Fung, Y., Donohue, M. et al. (1998). Computed tomography of Paget disease of the skull versus fibrous dysplasia. *Skelet. Radiol.* 27: 664–672.

Chapter 19
Malignant lesions

In the United States every year, about 10 000 deaths are attributed to *head and neck cancer* (HNC) [1]. Between 90% and 95% of all HNCs are *squamous cell carcinomas* (SCC). SCC of the head and neck arises from the oral cavity, oropharynx and larynx, and less frequently from the nasopharynx and nasal cavity [1]. Before addressing SCC, those malignant lesions affecting the bones of the skull base and the salivary glands will be considered. Although the malignancies affecting the base of the skull, and of course also the extragnathic benign lesions considered in Chapter 18, are of exquisite interest to the radiologist, oral and dental practitioners should also be aware of them, since the recent advent of *cone-beam computed tomography* (CBCT), particularly its large *field of view* (FOV), will capture bone-resorbing lesions within the anterior and middle cranial fossae. As these structures are outside the clinical remit of the dental and the oral specialist in most jurisdictions, the datasets of such investigations' images should be referred to a radiologist in the first instance, and diagnosis of a malignancy or suspected malignancy referred onward to an appropriate head and neck specialist or specialist *head and neck tumor* (HNT) center.

The reader should note that recently two publications have made a number of major changes to the diagnosis of the malignancies of the head and neck [2, 3] and their staging [3]. The WHO's 2017 edition updates head and neck malignancies, whereas the American Joint Committee on Cancer's (AJCC) eighth edition, effective from 2018, wrought some important changes (see Table 19.1 later). These updates and changes have been integrated throughout this chapter.

19.1 Introduction to Management of a Patient with Head and Neck Cancer

As the management of cancer is tailored to each patient, there is no rigid template. The management of a particular patient takes account of the site, size, and type of cancer, including the degree of differentiation, its staging, the presence of co-morbidities that may affect (invariably adversely) treatment or its outcome, and the patient's support system (family or society).

Generally, HNT groups treat all cancers of the head and neck except those affecting the brain and thyroid, but HNT groups such as that of the British Columbia Cancer Agency (BCCA) include thyroid cancers in their purview. Other HNCs are lymphomas and melanomas. Lymphomas, particularly extranodal cases arising within

Oral and Maxillofacial Radiology: A Diagnostic Approach, Second Edition. Edited by David MacDonald.
© 2020 John Wiley & Sons, Inc. Published 2020 by John Wiley & Sons, Inc.

the jaws, have already been fully addressed in Chapters 9 and 11.

Cancers of the oral cavity and oropharynx often present with loco-regional symptoms including pain, bleeding, non-healing ulcers, hoarseness, otalgia, and/or a palpable neck mass. Suspicious lesions may also be discovered by the patient's dentist or family physician. This is followed by referral to an otolaryngologist or head and neck specialist, who will perform a thorough head and neck examination, including the cervical neck, oral cavity, oropharynx, and endoscopic nasopharyngoscopy of the nasopharynx, base of the tongue, larynx, and hypopharynx. Any suspicious lesions should be biopsied.

Upon confirmation of malignancy, patients will then be referred to a head and neck oncologist, and ideally reviewed by a multidisciplinary team; this may include a surgical oncologist, otolaryngologist, radiation oncologist, and/or medical oncologist. The initial consultation includes a thorough physical examination of the head and neck region, followed by staging investigations to determine the extent of the disease. This may include blood tests, chest radiograph, panoramic radiographs, neck ultrasound, *computed tomography* (CT), *magnetic resonance imaging* (MRI), and/or *positron emission tomography* (PET) (Figure 19.1). Management options would then be reviewed with the patient, and may be influenced by many factors, including the patient's performance status, extent of disease, treatment intent (curative versus palliative), potential response to therapy, and the patient's preference.

At the BCCA, the Head and Neck Tumour Group is a provincial interdisciplinary team that includes surgical oncologists, radiation oncologists, medical oncologists, pathologists, diagnostic radiologists, nuclear medicine physicians, dentists, speech/swallowing pathologists (therapists), dieticians, and nurses. Cases are reviewed at a weekly tumor conference that is video-linked to all regional cancer centers, as well as participating community hospitals. Case presentations include a review of diagnostic images and pathological specimens, followed by a discussion regarding optimal management, treatment planning, and post-treatment response assessment. The patient is then seen by the appropriate clinicians to discuss the treatment options, potential side effects, and anticipated treatment outcomes. Treatment preparation begins after the patient has understood and consented to a management plan.

19.2 Overview of Imaging Modalities Used in Diagnosis and Assessment of Malignant Lesions

Figure 19.1 displays the main imaging modalities. Although each has been addressed in detail elsewhere in this textbook, a number of essential points will now be discussed. The clinical examination of a lesion of the face and jaws will invariably include conventional radiography, particularly if the lesion is adjacent to the jaw bones, to determine whether there is gross erosion (Figures 1.38, 9.16 and 9.18). Periapical radiographs are best because of their best spatial resolution (Figure 9.22). SCC spread into the bone and thereby the bone marrow requires jaw-bone resection and subsequent reconstruction. Lymphoma is the next most frequent malignancy of the face and jaws and is generally treated by chemotherapy [4].

CTs and/or MRIs are generally prescribed in accordance with established protocols. The basics of these modalities has already been addressed in Chapters 4

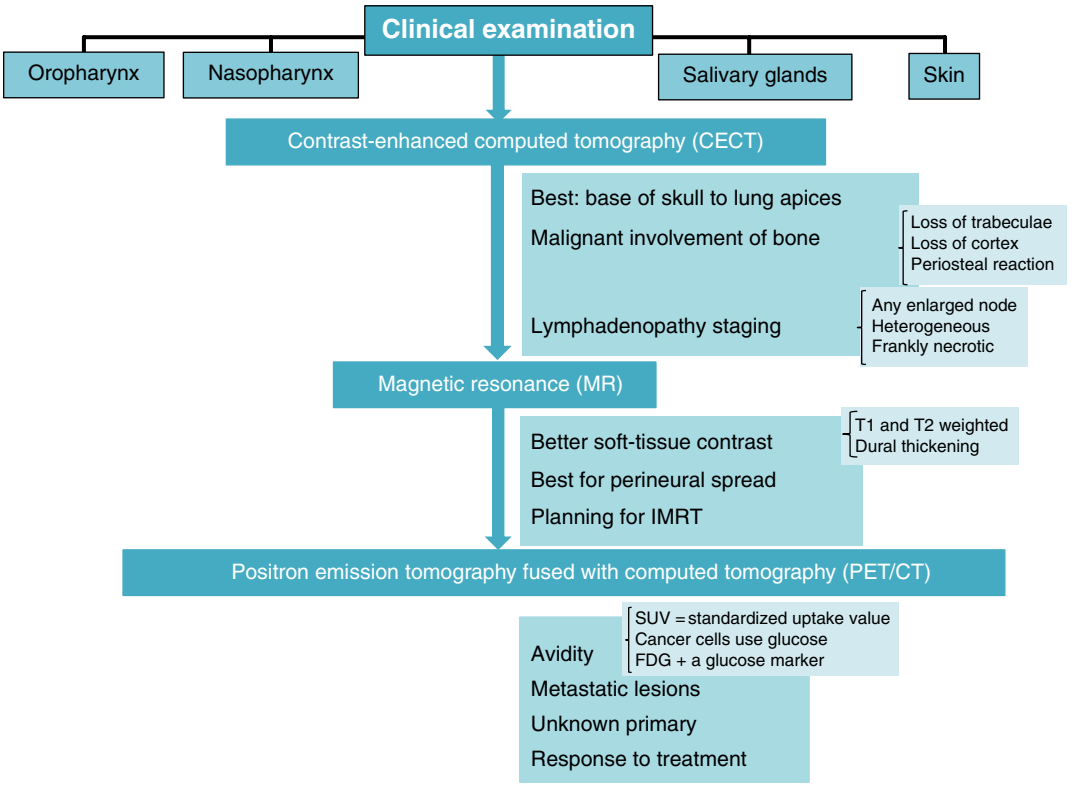


Figure 19.1 Imaging of clinically malignant lesions of the face and jaws. FDG, fluorine-18 fluorodeoxyglucose; IMRT, intensity-modulated radiotherapy.

and 6. In the first instance the patient will be imaged at least as far down as the thoracic inlet. Contrast will be used. In the case of CT, both precontrast and postcontrast exposures using *contrast-enhanced computed tomography* (CECT) will be taken in order to determine whether enhancement of the blood vessels in and around the lesion has taken place. Enhancement also assists with staging; for example, enhancement of the dura adjacent to a suspected malignancy indicates that the brain may be at least in danger of being invaded, and it may increase the sensitivity to detect malignant lymphadenopathy. In addition, the bone windows will be scrutinized to determine whether there is bone erosion. MRI is preferred for imaging of the soft tissues. If clinicians are concerned that the lesion has metastasized, PET may then be prescribed. PET has already been addressed in Chapter 7. Many PET units today are most likely fused with CT (PET/CT). Although, as discussed in Chapter 7, the main nuclear tracer for oncology is *fluorine-18 fluorodeoxyglucose* (F-18 FDG), the use of F-18 incorporated into *sodium fluoride* (F-18 NaF) can allow PET to be used for bone scans. Traditional bone scanning by gamma camera with *technetium-99m* (TC-99m, a metastable nuclear isomer of technetium-99) is still performed.

Although the functional imaging of PET/CT complements CT and MRI investigations by disclosure of the lesion's degree of uptake of the radioactive-labeled tracer (avidity), usually FDG, measured as

standardized uptake values (SUV), it is subject to false positives. These are infections, recent muscular activity (chewing gum), recent biopsies, and treatment (surgical and/or radiotherapy). Upon exclusion of these, PET/CT can be used to confirm an uncertain diagnosis by CT and/or MRI of a primary tumor, to discover *cancers of unknown primary* (CUPs), and to determine the extent of malignant disease beyond the primary site, particularly into the cervical lymph nodes and/or its metastasis to other sites elsewhere in the patient. This information is important for staging and treatment planning. Upon completion of primary treatment, subsequent PET/CT can be used to determine the success of the primary treatment.

The malignant lesions of the head and neck addressed in this chapter are divided in those affecting bones of the skull base, salivary gland malignancies, and SCC of the aerodigestive tract.

19.3 Malignant Lesions Affecting the Bones of the Skull Base

Most of these lesions occur at specific sites. The relationships of lesions to the anatomy of the skull base and to each other in a differential diagnosis are set out in Figure 17.1.

19.3.1 MULTIPLE MYELOMA

Multiple myeloma, introduced in Chapter 9, is a malignancy of plasma cells found in bone marrow and lymphatics. It occurs in older people and accounts for 3–10 cases per 100 000 annually. In North America, it is approximately twice as common in African-Americans as in Caucasians. Although this disease most commonly has a widespread distribution through the bone-marrow cavities, occasionally it presents as a solitary lesion (solitary plasmacytoma). It is the most common primary bone tumor affecting the cranial vault. Multiple myeloma in the calvarium will cause punched-out lucent lesions. These, in advanced cases, lead to a salt-and-pepper appearance (Figure 19.2a). On CT there will be loss of the trabecular pattern in the marrow space (Figure 19.2b) [5].

19.3.2 CHORDOMA (ICD-O 9370/3)

Baumhoer et al. defined the chordoma as a "malignant tumour with notochordal differentiation. Chordomas are rare, slowly expansile malignant neoplasms thought to arise from embryonic notochord remnants" [6]. The chordoma most commonly involves the clivus. The nasopharynx and nasal cavity are affected by local extension [6]. The average age at diagnosis is approximately 50 years. Chordomas rarely metastasize and are locally aggressive, producing symptoms from cranial nerve compression and destruction of local skull base structures [7]. As such, these patients often present with diplopia due to third and sixth nerve involvement [8]. On CT, chordomas are seen as lobulated midline mass lesions, often with flecks of internal calcification (Figure 19.3a and b). On MRI, they are hyperintense on T2-weighted images (Figure 19.3c), with heterogeneous enhancement on postgadolinium sections (Figure 19.3d) [9]. The 3-, 5-, and 10-year survival rates after resection are 81%, 74%, and 59%, respectively [6].

19.3.3 CHONDROSARCOMA (ICD-O 9222/1 (LOW GRADE – GRADE 1) AND ICD-O 9220/3 (HIGH GRADE – GRADE 2 OR 3)

Chondrosarcoma (introduced in Chapter 10) is the second most frequent malignant tumor of bone, after osteosarcoma. Baumhoer et al. define the

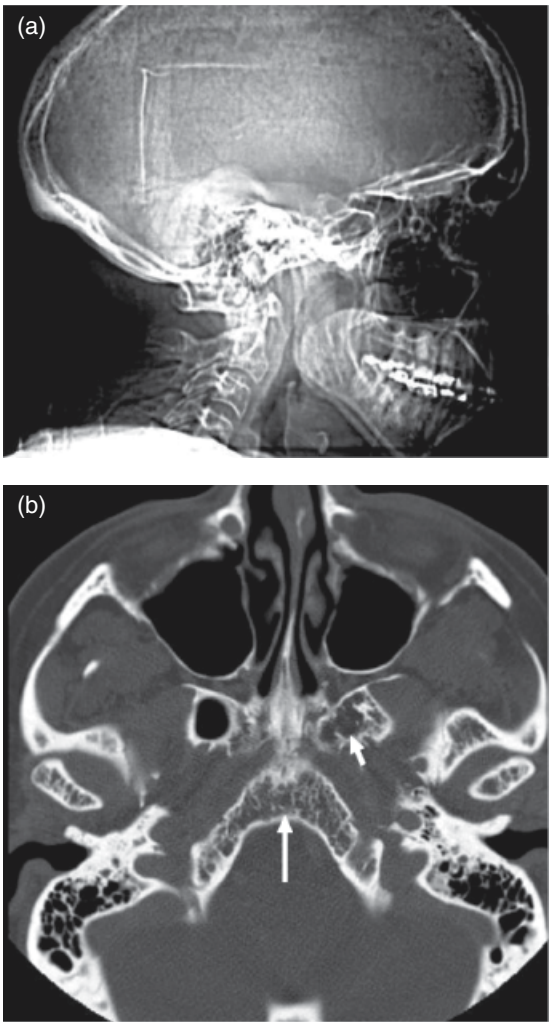


Figure 19.2 Multiple myeloma affecting the skull. (a) Lateral projection of the skull. Note the salt-and-pepper appearance of the cranial vault produced by numerous myelomatous deposits. (b) Axial computed tomography (bone window). Note the focal loss of bony trabeculae within the clivus (long arrow) and the left basal pterygoid plate (short arrow).

chondrosarcoma as "a malignant bone tumour [that] produces cartilaginous matrix" [10]. Those affecting the face and jaws account for 4% of all chondrosarcomas. Chondrosarcomas of the skull base most often arise in a paramedian position (Figure 19.4) in contrast to chordomas that occur in the midline (Figure 19.3). Lower-grade lesions expand locally, producing cranial nerve deficits much like those caused by chordomas. The higher-grade lesions rarely metastasize, but if they do, it is usually to the lungs. Chondrosarcomas can also occur in the cavernous sinus, superior midline nasal septum, and laryngeal cartilage (Figure 19.5) [11–13]. They are composed of chondroid matrix; hence on CT they often contain an irregular lattice of internal calcification. Chondrosarcomas are well-circumscribed, lobulated tumors that exhibit low to isointense T1-weighted signals, hyperintense

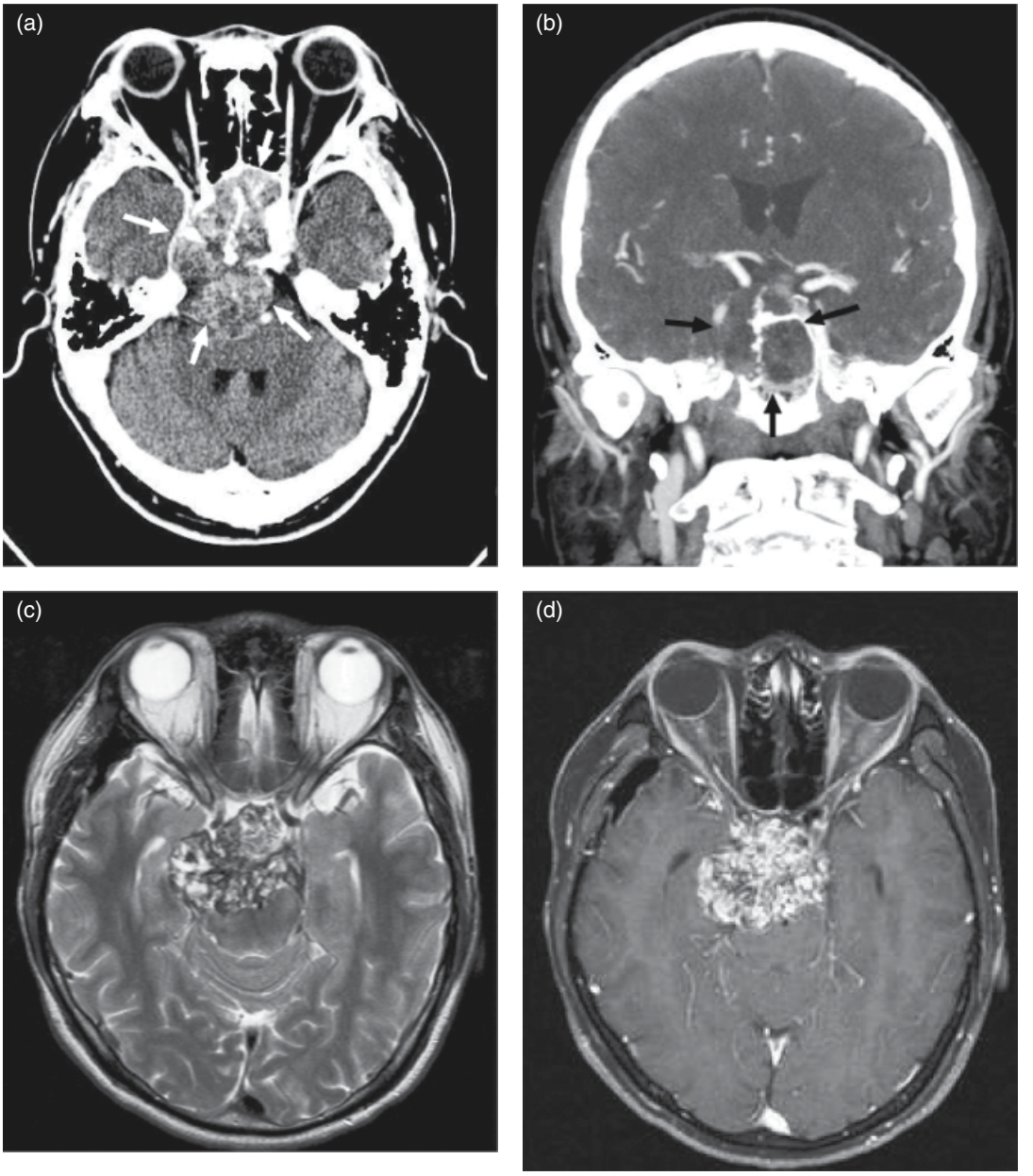


Figure 19.3 Computed tomography (CT) and magnetic resonance imaging (MRI) of chordoma. (a) Axial postcontrast CT (soft-tissue window) of a well-defined chordoma destroying the clivus and extending anteriorly to fill the sphenoid sinus and abut the posterior ethmoid air cells. Posteriorly the lesion grossly indents the brain stem and displaces the basilar artery to the left. (b) Coronal postcontrast CT (soft-tissue window) of the same lesion expanding the sphenoid sinus and destroying the right lateral wall. The arteries exhibit greater enhancement than the right jugular vein. (c) Axial T2-weighted MRI at the level of the optic nerve traversing the optic canal, displaying a heterogeneous, well-defined chordoma centered in the dorsum sellae. It is expanding into the left temporal lobe and the midbrain. The optic chiasm is not seen since it is displaced superiorly. (d) Axial postgadolinium fat-saturated T1-weighted MRI at a level near (c).

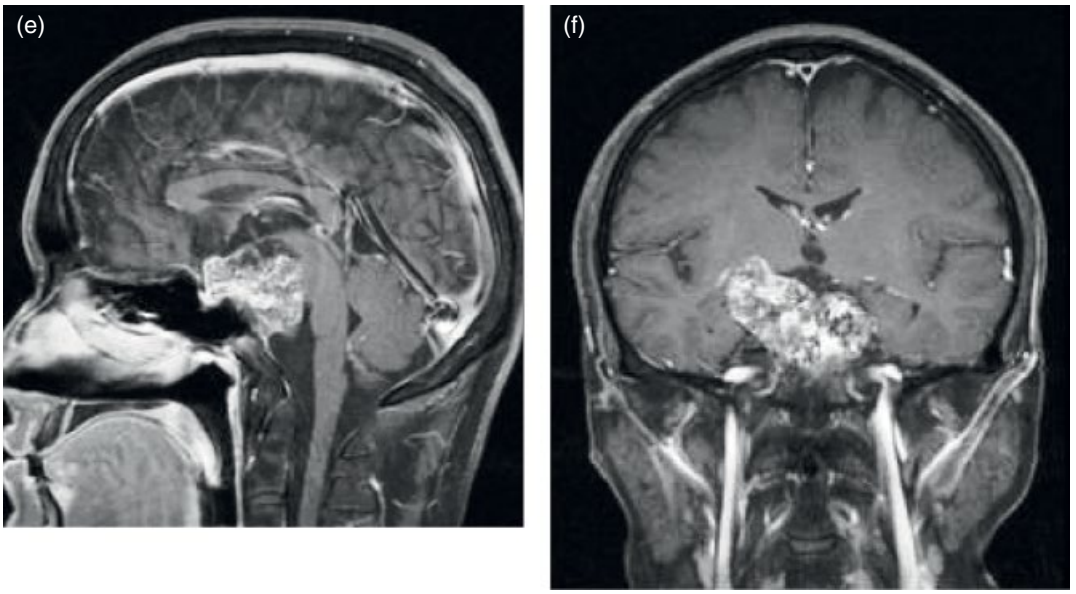


Figure 19.3 (Continued) (e) Sagittal postgadolinium T1-weighted fat-saturated MRI showing a well-defined lobulated lesion destroying the clivus and extending anteriorly over the dorsum sellae into the pituitary fossa. It has also expanded posteriorly against the midbrain and pons. (f) Coronal fat-saturated T1-weighted MRI of the same lesion.

T2-weighted signals, and heterogeneous enhancement on MRI.

19.3.4 OLFACTORY NEUROBLASTOMA (OCD-O 9522/3)

Olfactory neuroblastoma (ONB), also called esthesioneuroblastoma, is defined by Bell et al. as "a malignant neuroectodermal neoplasm with neuroblastic differentiation, most often localized to the superior nasal cavity" [14]. Although there is no consistent genetic pattern of gains, deletions, and aberrations, Bell et al. reported one study revealing that a specific deletion on chromosome 11 and a gain on chromosome 1p were associated with metastasis and a worse prognosis [14]. Although ONB can include the superior turbinate and the superior half of the nasal septum, it must involve the cribriform plate to be diagnosed as a ONB [14]. It is an uncommon lesion, comprising 3% of all sinonasal tumors. Its wide age range (2–90 years) of first presentation peaks in the fifth and sixth decades [14]. It most often presents with symptoms of unilateral nasal obstruction, with or without epistaxis. Due to the initial lack of severe symptomatology, these tumors present late and are often large at the time of diagnosis. Radiologically these lesions will traverse the cribriform plate, forming an intracranial component [15]. On CT and MRI they vividly enhance, filling one or both sides of the nasal cavity. Bell et al. note that "MRI better delineates sinonasal, intraorbital, or intracerebral extension" [14]. CT displays better any erosion of the cribriform plate, lamina papyracea, and fovea ethmoidalis [14]. ONBs are locally invasive (Figures 19.6 and 19.7) and will rarely metastasize to retropharyngeal nodes [16]. High-grade ONBs are associated with

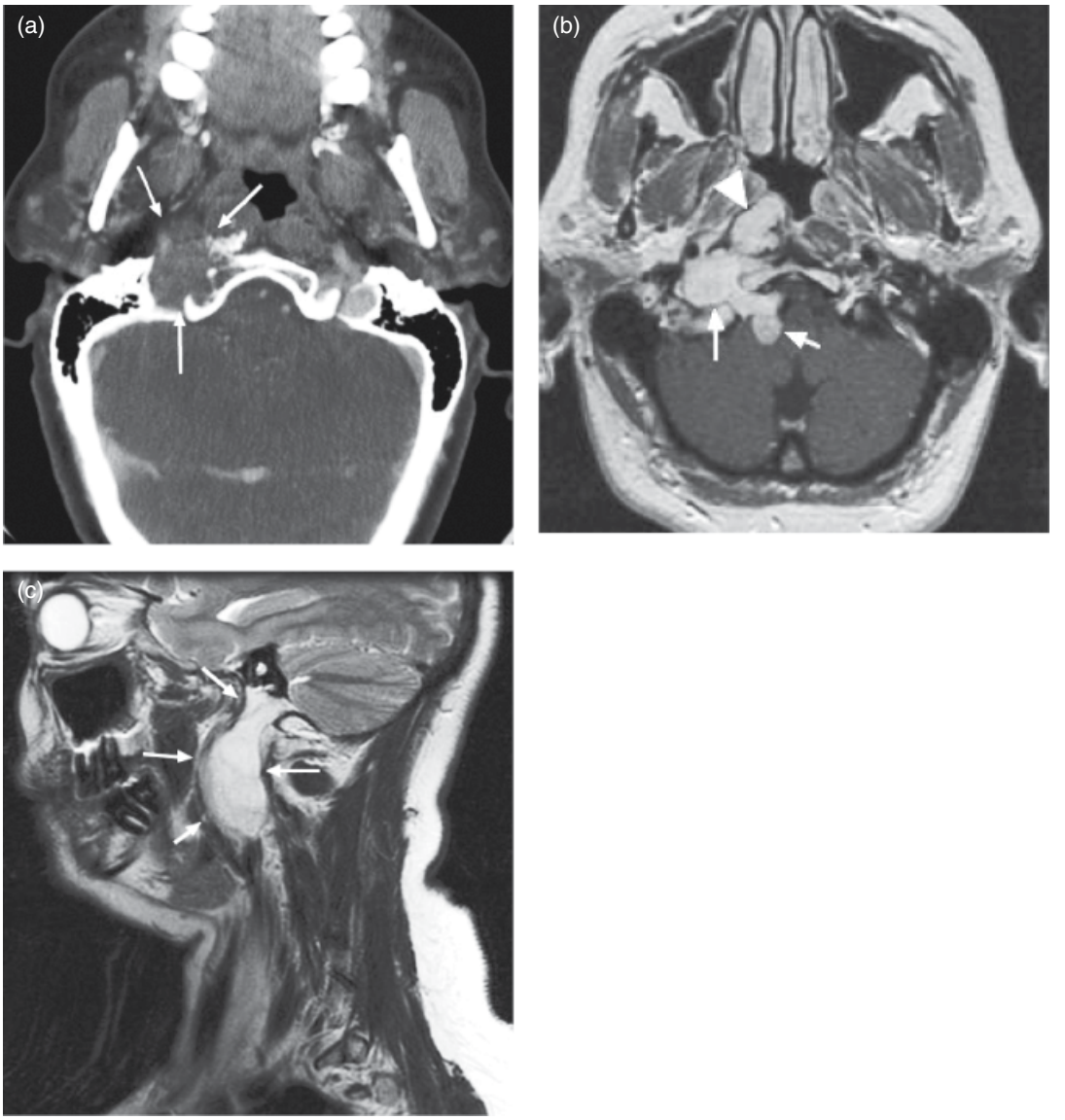


Figure 19.4 Computed tomography (CT) and magnetic resonance imaging (MRI) of a right petroclival fissure chondrosarcoma. (a) Axial postcontrast CT (soft-tissue window) displaying a well-defined chondrosarcoma (arrow) centered in the right petroclival fissure, eroding into the right inferolateral clivus, and expanding laterally into the jugular foramen. This is a typical location for this tumor. (b) Axial T1-weighted MRI of the same patient. The lesion (white arrows) has traveled posteriorly through the right jugular foramen into the posterior cranial fossa and has extended anteromedially into the right fossa of Rosenmuller (white arrowhead). (c) Sagittal T1-weighted MRI displaying inferior extension of the lesion through the jugular foramen and down the jugular sheath.



Figure 19.5 Axial postcontrast computed tomography (soft-tissue window) of low-grade chondrosarcoma involving the right thyroid cartilage of the larynx (arrow). The lesion does not enhance, but has a hypodense center, suggestive of necrosis.

more aggressive disease and "significantly worse survival particularly if it has already metastasized" [14].

19.3.5 NASAL LYMPHOMA

Primary nasal lymphoma is more frequent in East Asians, being quite rare in Caucasians. The most common subtype is diffuse large B-cell lymphoma (Figure 11.15), followed by the *T-cell natural killer* (T/NK) [17]. In a recent Chinese report, sinonasal lymphomas accounted for 22% of all sinonasal malignancies over the same period [18]. Furthermore, nasal lymphomas occurred four times more frequently than sinus lymphomas. The main symptoms were a "snuffle," epistaxis, purulent nasal discharge, and fever [18]. This is mentioned here to point out that lymphoma can mimic many different types of tumors in different parts of the body, and the nasal cavity is no exception. Note the similarity to both olfactory neuroblastoma (see Figures 19.6 and 19.7) and sinonasal undifferentiated carcinoma (Figure 19.8). This tumor can also mimic the far more common SCC, which also has a high prevalence in East Asians. A Brazilian case series of T/NK nasal lymphomas (predominantly middle-aged males) reported that in advanced stages the addition of chemotherapy does not appear to improve survival compared to radiotherapy alone [19].

19.3.6 SINONASAL UNDIFFERENTIATED CARCINOMA (ICD-O 8020/3)

Lewis et al. defined *sinonasal undifferentiated carcinoma* (SNUC) as "an undifferentiated carcinoma of the sinonasal tract without glandular or squamous features and not otherwise classifiable" [20]. This extremely malignant neoplasm grows rapidly and metastasizes early (Figure 19.8). It has a poor prognosis despite aggressive multimodality therapy [21,22]. Histologically

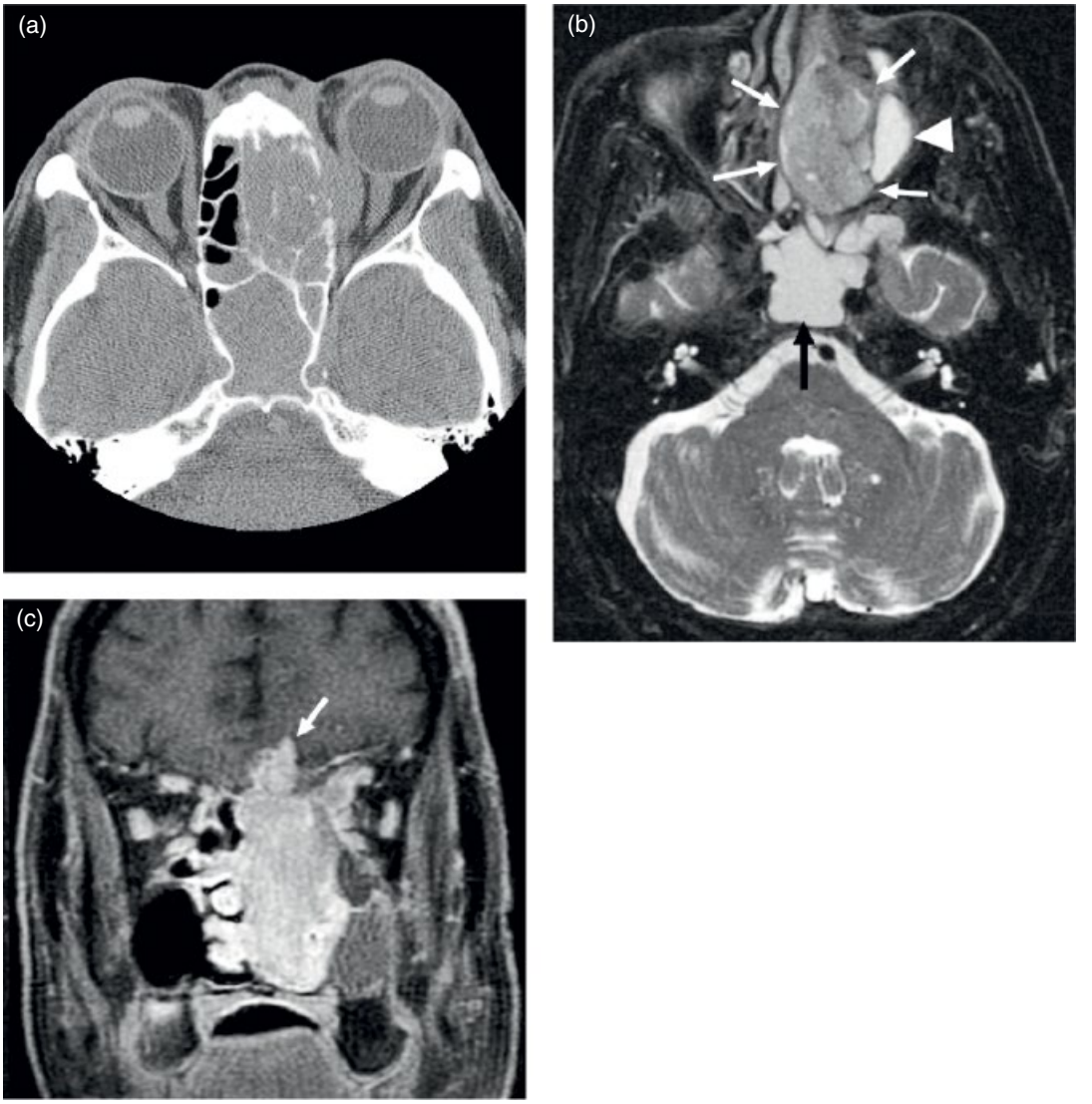


Figure 19.6 Computed tomography (CT) and magnetic resonance imaging (MRI) of an olfactory neuroblastoma involving the left nasal cavity, ethmoid air cells, and orbit. (a) Axial CT (bone window) at mid orbital level showing opacification of the left ethmoid air cells. The bony left ethmoid sinus is partially destroyed. The tumor has extended through the medial wall of the left orbit to elevate the left medial rectus muscle and produce mild proptosis. (b) Axial T2-weighted MRI at the level of the superior orbital cavity displaying a well-defined, mildly lobulated isointense lesion centered in the left nasal cavity (white arrows). Just posterior to the mass is a fluid-filled sphenoid sinus showing high T2 signal (black arrow). Another small fluid collection is seen lateral to the mass (white arrowhead). (c) Coronal post-gadolinium fat-saturated T1-weighted MRI displaying a lobulated enhancing mass filling the left nasal cavity and ethmoid air cells. It is expanding laterally into the orbit and maxillary sinus. The tumor is extending through the cribriform plate to indent the olfactory gyrus of the left frontal lobe (arrow).

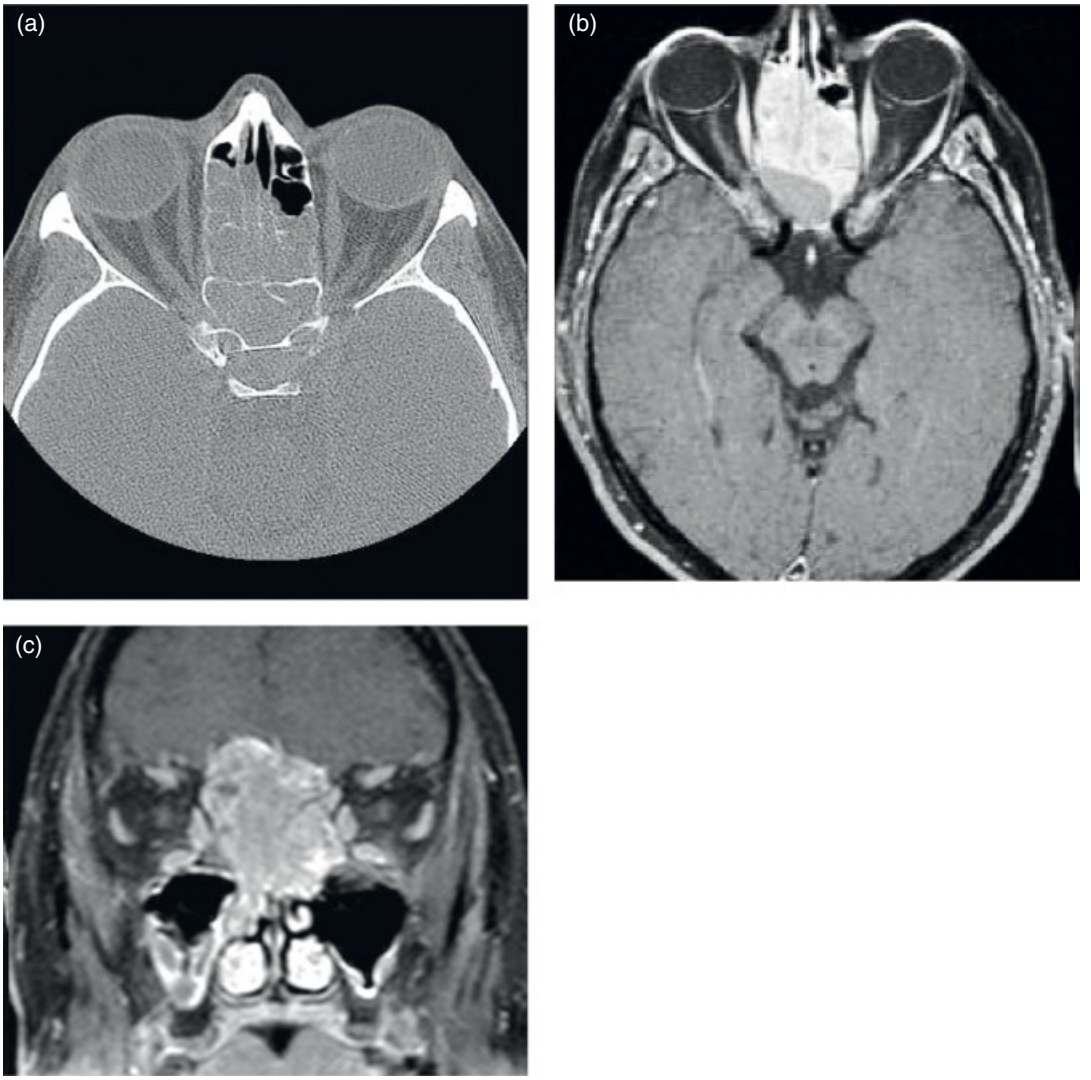


Figure 19.7 Computed tomography (CT) and magnetic resonance imaging (MRI) of an olfactory neuroblastoma centered in the nasal cavity and extending upward through the floor of the anterior cranial fossa. (a) Axial CT (bone window) showing involvement of the ethmoid air cells. (b) Axial postgadolinium fat-saturated T1-weighted MRI showing enhancement of the neuroblastoma. The nonenhancing posterior part consists of proteinaceous fluid. (c) Coronal postgadolinium fat-saturated T1-weighted MRI showing the neuroblastoma. Note that the mucosa of both maxillary sinus floors and of the inferior concha are thickened and hyperintense, suggesting that they are inflamed.

it is a neuroendocrine carcinoma, belonging to the same group as olfactory neuroblastoma. SNUC accounts for approximately 3% of upper aerodigestive tumors and most often occurs in the nasal cavity. As such, it often exhibits intracranial and orbital invasion when diagnosed [20, 23]. The symptoms it produces at presentation are common to other sinonasal diseases (nasal obstruction, unilateral pain, epistaxis).

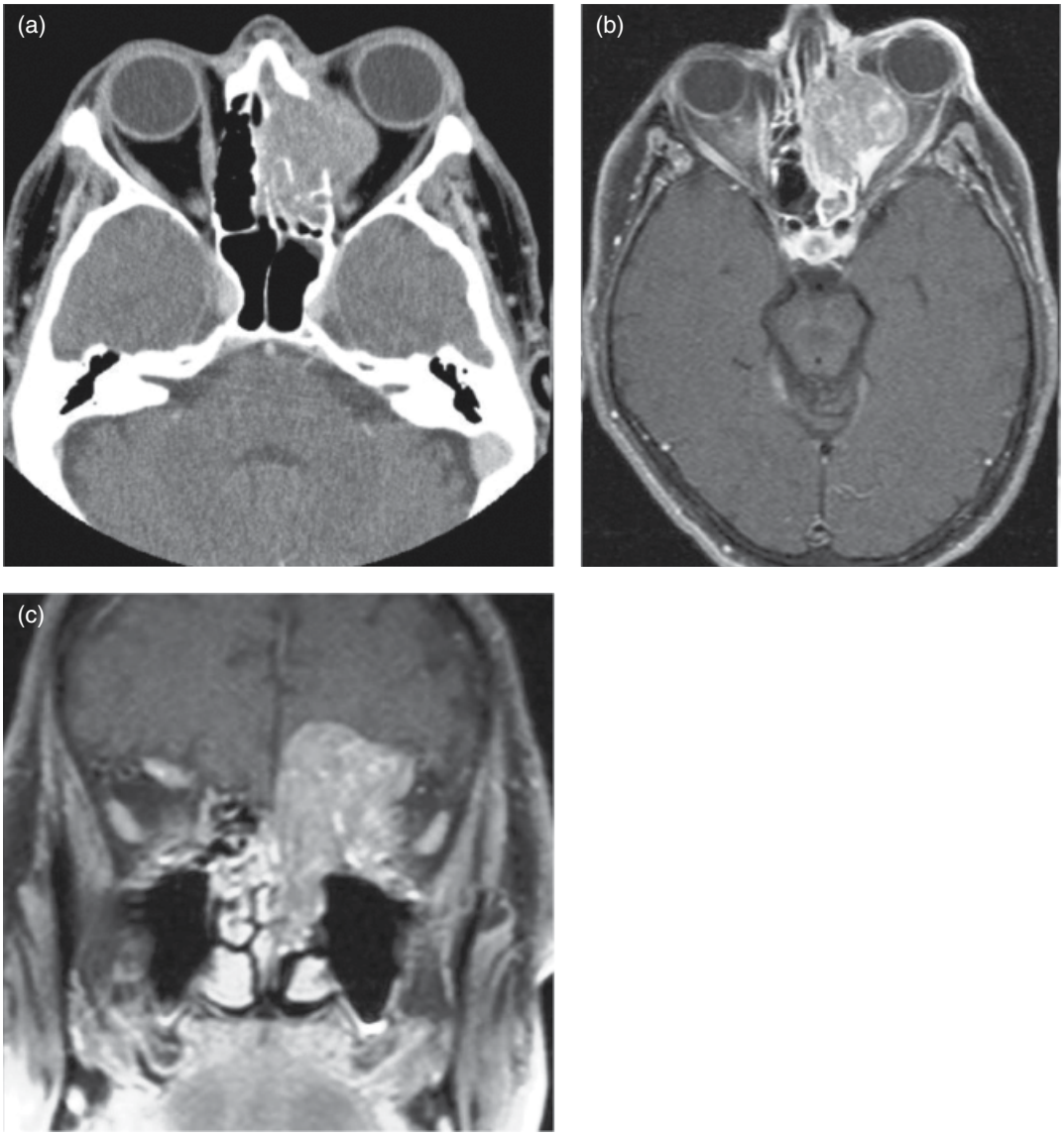


Figure 19.8 Computed tomography (CT) and magnetic resonance imaging (MRI) of a sinonasal undifferentiated carcinoma (SNUC) invading the base of the skull. (a) Axial CT (soft-tissue window) showing a soft-tissue mass obliterating the right ethmoid air cells. The SNUC has destroyed much of the lateral wall of the nose and invaded the medial aspect of the orbital cavity. The left eye now exhibits proptosis. (b) Axial postgadolinium T1-weighted MRI revealing mildly heterogeneous enhancement though the SNUC. The involvement of the orbital cavity is more marked and the eye displays more proptosis. (c) Coronal postgadolinium T1-weighted MRI revealing enhancement throughout the SNUC. Extensive invasion of the left orbit is obvious, with encasement of the medial orbital muscles and destruction of the floor of the anterior cranial fossa. The tumor is compressing the inferior part of the left frontal lobe.

On CT and MRI, these tumors look similar to SCC, an enhancing locally destructive mass. SNUC is an aggressive lesion and has a poor prognosis, although this has improved recently due to trimodality therapy [20]. Nevertheless, primary resection significantly enhances patient survival [20].

19.4 Malignant Salivary Gland Neoplasms

Salivary gland tumors are rare, accounting for fewer that 15 cases per 100 000 per year, of which a quarter are malignant [24]. Malignant salivary gland neoplasms can be divided into epithelial and nonepithelial tumors. The epithelial neoplasms can be further subdivided into carcinomas that differentiate toward acinar, ductal, myoepithelial, or mixed-cell types; adenocarcinomas; and carcinomas arising from benign mixed tumors (malignant mixed tumors). The mucoepidermoid carcinoma is the most common epithelial salivary carcinoma, followed by adenoid cystic carcinoma [25]. Other common types of salivary gland carcinomas include acinic cell carcinoma and polymorphous low-grade adenocarcinoma. There are a host of other rare carcinomas, including basal cell clear cell, cystadenocarcinoma, oncocytic, mucinous, salivary duct, sebaceous, squamous, adenocarcinoma *not otherwise specified* (NOS), myoepithelial, epimyoepithelial, and small- and large-cell undifferentiated tumors (see later in this chapter). Malignant mixed tumors include carcinoma ex pleomorphic adenoma and carcinosarcoma.

This classification scheme substantially follows that put forth by Ellis and Auclair at the US Armed Forces Institute of Pathology (AFIP) [26]. The reader should be aware that there is some variation in the literature regarding the nomenclature and classification of salivary gland tumors. For instance, many adenocarcinomas will also commonly be called carcinomas. Adenocarcinoma NOS is a catch-all classification for those salivary malignancies that show ductal or glandular differentiation, but cannot be easily placed in a specific category; the WHO's 2017 edition upheld this definition [24]. The most common tumors will be described here. In general, the relative incidence of salivary gland malignancy is inversely proportional to the size of the gland, with the highest frequency of malignancy (80%) found in the minor glands, whereas only 20% of parotid tumors are malignant.

19.4.1 MUCOEPIDERMOID CARCINOMA (ICD-O 8430/3)

Brandwein-Gensler et al. defined *mucoepidermoid carcinomas* (MEC) as "a distinctive salivary gland malignancy composed of mucinous, intermediate (clear-cell) and squamous tumour cells forming cystic and solid patterns" [27]. Although it has a wide age distribution, it is "the most common salivary gland malignancy in children and young adults" [27]. In the major salivary glands, MEC most commonly occurs in the parotid [28]. In the minor salivary glands, this tumor vies with adenoid cystic carcinoma for the most frequent malignant neoplasm [29]. MEC occurs spontaneously, but is also associated with prior exposure to therapeutic ionizing radiation [30]. The mucin-secreting cell type accounts for its inhomogeneous enhancement on CT and MRI. Low-grade tumors present as a well-defined heterogeneous mass with sharp margins, low T1-weighted and low T2-weighted signals. Higher-grade – i.e. more malignant – MECs exhibit less well-defined borders with greater enhancement (Figure 19.9). Low- and intermediate-grade MECs are less aggressive and completely

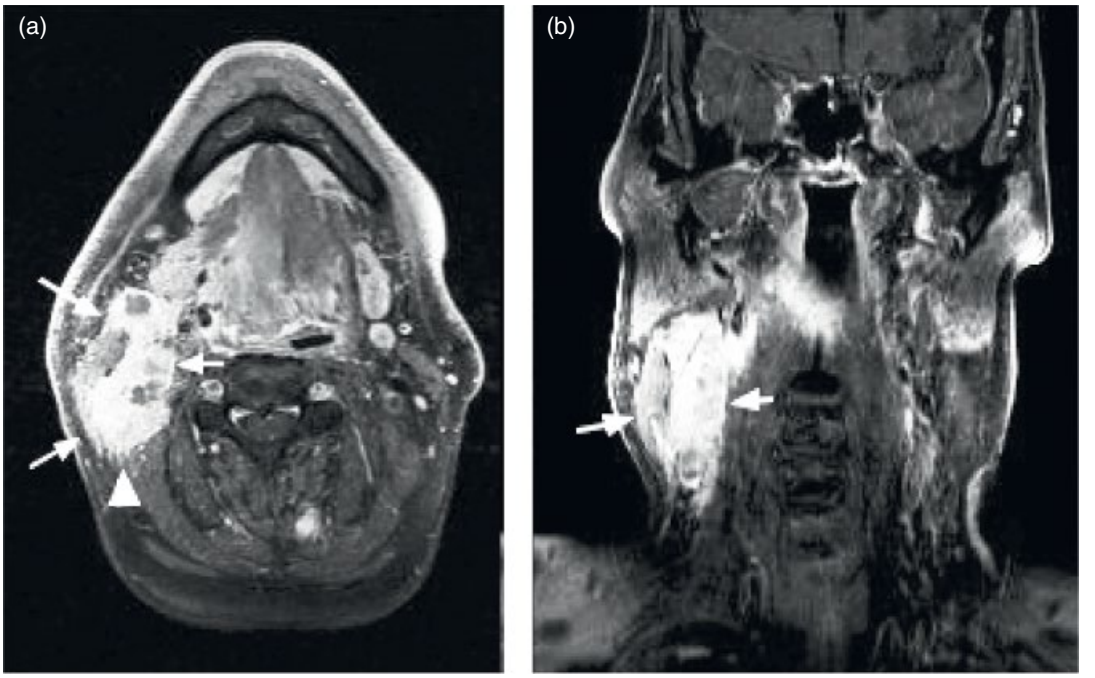


Figure 19.9 Magnetic resonance imaging (MRI) of high-grade mucoepidermoid carcinoma (MEC) of the right parotid gland. (a) Axial postgadolinium fat-saturated T1-weighted MRI showing a right parotid MEC (arrows). Note how the posterior border is less well defined, suggestive of a high-grade lesion (arrowhead). (b) Coronal postgadolinium fat-saturated T1-weighted MRI of the same patient.

curable by excision. Brandwein-Gensler et al. noted that "The 10-year survival for low-, intermediate- and high-grade MECs are approximately 90%, 70% and 25% respectively" [27].

19.4.2 ADENOID CYSTIC CARCINOMA (ICD-O 8200/3)

Stenman et al. defined *adenoid cystic carcinoma* (ACC) as "a slow-growing and relentless salivary gland malignancy composed of epithelial and myoepithelial neoplastic cells that form various patterns, including tubular, cribriform and solid forms" [31]. On CT it presents as an enhancing mass, sometimes with adjacent bone erosion (Figure 19.10). On MRI the tumor is usually seen as a T1-weighted hypointense, mildly T2-weighted hyperintense lesion that moderately enhances (see Figure 19.11). These characteristics are not specific and are also seen in other head and neck neoplasms. Lower-grade tumors are often well circumscribed and high-grade lesions tend to have a poorly defined border. The mean age of ACC at diagnosis is 50 years and, like MEC, there is a wide age range (13–89 years) [31].

One particularly bad feature of ACC is perineural spread; this is seen in 69% of cases and is associated with increased treatment failures [31, 32]. Perineural spread is diagnosed on CT via widening of associated neural foramina (Figure 19.10) and on MRI as postgadolinium enhancement within foramina (Figures 19.11 and 19.12) [33]. These findings are often

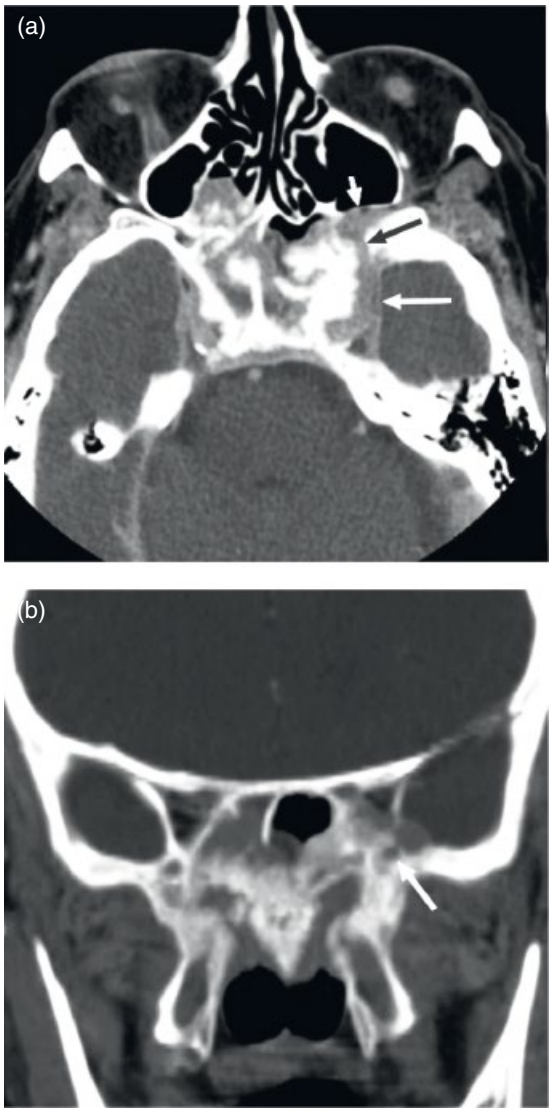


Figure 19.10 Computed tomography (CT) of adenoid cystic carcinoma arising within the sphenoid sinus, producing neural foraminal widening and a permeative bone pattern. (a) Axial postcontrast CT through the roof of the orbit, showing obliteration of the sphenoid sinus with bone destruction and invasion of adjacent structures (long white arrow). The tumor is seen traveling through the foramen rotundum (black arrow) and the left cavernous sinus (short white arrow), dilating the former structure. (b) Coronal CT bone window, at the level of the pterygoid plates, showing extensive pterygoid and midsphenoid permeative infiltration with tumor. The white arrow points to a mildly enlarged left foramen rotundum; its fellow is also enlarged.

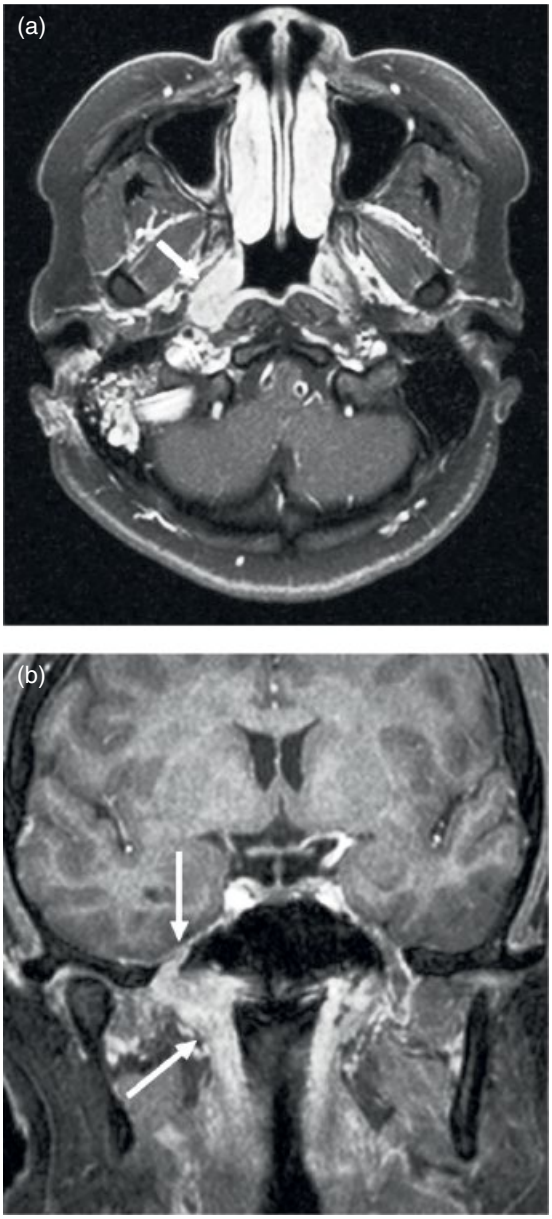


Figure 19.11 Postgadolinium fat-saturated T1-weighted magnetic resonance imaging of adenoid cystic carcinoma arising in the right fossa of Rosenmuller. (a) Adenoid cystic carcinoma producing a right fossa of Rosenmuller mass (arrow). The lesion is compressing the Eustachian tube, causing the right mastoid air cells to fill with fluid and become inflamed. (b) Coronal section from the same patient. The tumor is extending superiorly from the right fossa of Rosenmuller (oblique arrow) through the foramen ovale (vertical arrow).

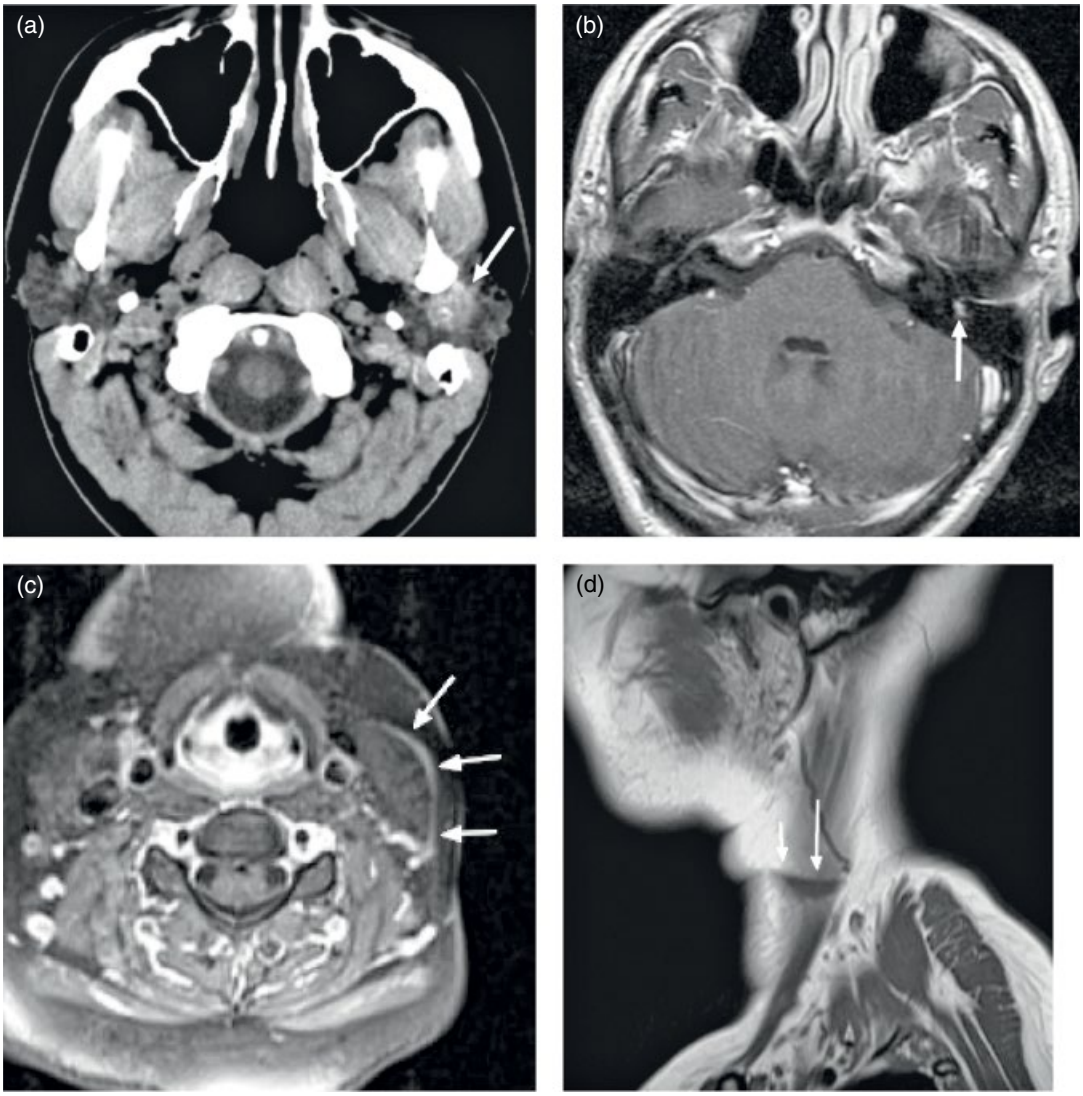


Figure 19.12 Computed tomography (CT) and magnetic resonance imaging (MRI) of adenoid cystic carcinoma showing perineural spread. (a) Axial CT (soft-tissue window) showing an adenoid cystic carcinoma arising in the left parotid gland (arrow). (b) Axial postgadolinium T1-weighted MRI of the same patient. Abnormal enhancement is present in the geniculate ganglion of the left facial nerve (arrow) due to retrograde perineural spread from a tumor invading the facial nerve within the left parotid gland. (c) Axial postgadolinium fat-saturated T1-weighted MRI of a different patient, showing perineural spread of adenoid cystic carcinoma along the left lateral cutaneous nerve (arrows). The original lesion was in the left submandibular gland; this was excised and the tumor recurred in the latter nerve. (d) Sagittal noncontrast T1-weighted MRI showing a thickened lateral cutaneous nerve (arrows) from adenoid cystic carcinoma perineural spread.

subtle and, due to a high pretest probability, a pathological diagnosis of ACC should prompt careful radiological examination of all neural foramina associated with cranial nerves that pass through or nearby the lesion. MRI is currently the best modality for this, reaching a sensitivity of 95% [34]. Imaging detection of perineural spread is important, because 30–45% of perineural invasion is clinically asymptomatic [35], and the presence of perineural spread correlates with a decreased five-year survival rate [36]. Singh et al. reveal some imaging pitfalls of perineural spread: non-neoplastic enhancement mimicking perineural tumor spread secondary to inflammation, and tumor foci below the spatial resolution of the MRI scan [37]. Radiation oncologists will also try to include visible regions of perineural spread in their treatment plan. Perineural spread is also seen with SCC and occurs much less frequently with other head and neck neoplasms.

19.4.3 ACINIC CELL CARCINOMA (ICD-O 8550/3)

Simpson et al. defined *acinic cell carcinoma* as "a malignant salivary gland neoplasm composed of cancer cells with acinar features. A subset of this entity has been reclassified as secretory carcinoma" [38]. These are unusually slow-growing neoplasms containing clusters of cells with serous acinar differentiation. The mean age at diagnosis is 52 years [37]. The majority occur in the parotid gland (86%) [39], and acinic cell carcinoma is the most common malignant salivary neoplasm to present bilaterally (3% of cases) [40]. On CT and MRI, the appearance is nonspecific, similar to other small benign (and some malignant) salivary gland tumors (Figure 19.13). Diagnosis is usually obtained by fine-needle aspiration biopsy. Although this cancer is not aggressive, neck nodes and the lung may be involved. As many as one-third may recur. The 20-year survival is 90%.

19.4.4 OTHER RARE MALIGNANT SALIVARY NEOPLASMS

A sample of rare salivary gland neoplasms is presented in Figure 19.14. The appearance of these lesions correlates with their degree of biological aggressiveness; for example, the mucinous adenocarcinoma in Figure 19.14c is destroying bone, so it is more likely a high-grade lesion. Otherwise the appearance is generally nonspecific with regard to the histological subtype, and diagnosis is made by biopsy or excision rather than by imaging. Figures 19.14a–d are epithelial neoplasms. Figure 19.14e is a nonepithelial tumor: diffuse large B-cell lymphoma.

19.5 Squamous Cell Carcinomas of the Aerodigestive Tract

SCC arises from the epithelial layer of the nasopharynx, oral cavity, and larynx and is the most frequent primary malignancy observed in dental practice. In North America, an estimated 58 000 new cases of oral cancer occurred in 2012. The *age-standardized incidence rates* (ASR) per 10 000 000 in 2012 were 3.3 for lip, whereas oral cavity, nasopharyngeal, other pharyngeal, and laryngeal sites were 5.1, 2.4, 2.5, and 0.5 cases per 100 000, respectively [41]. The median age at diagnosis is 60 years, with a five-year combined survival of approximately 60% [42]. The most important associated risk factors for oral cancer are tobacco and alcohol, with a subset of oropharyngeal SCC with *human*



Figure 19.13 Axial postcontrast computed tomography (soft-tissue window), showing acinic cell carcinoma of the left parotid gland. Note the mild rim enhancement (arrow).

papilloma virus (HPV). HPV in conjunction with inherited genetic factors may predispose the patient to cancer [41]. Epstein–Barr virus has also been associated with aerodigestive SCCs, particularly in *nasopharyngeal carcinoma* (NPC: SCC of the nasopharynx), though it is so ubiquitous that it has been hard to prove a causal role [43–45]. For NPC there is a significantly higher incidence in East Asians. Nevertheless, it is in "virtually all poorly and undifferentiated nonkeratinized NPC" [41]. The worldwide age distribution for NPC is bimodal, with peaks between 15 and 24 years and 65 and 79 years [46].

In the aerodigestive tract, SCC will typically present a surface abnormality (e.g. erythroplakia, leukoplakia) or a palpable mass. SCC tends to occur in characteristic locations; in the nasopharynx, the fossa of Rosenmuller is a common site (Figures 19.15–19.17).

19.5.1 NASOPHARYNGEAL CARCINOMA

Posteriorly sited NPCs initially produce mild, nonspecific symptoms – i.e. Eustachian tube obstruction leading to chronic otitis media, referred pain to the ear, or epistaxis. This makes them challenging to discover at an early stage. As the tumor advances, it will characteristically begin to invade adjacent cranial foramina, most commonly traveling superiorly through the foramen ovale into "Meckel's cave" (the cave of dura mater which contains the trigeminal ganglion) to produce trigeminal nerve symptoms [47]. From here the tumor can extend into the cavernous sinus, occasionally affecting the intracavernous portion of the abducens (sixth cranial) nerve to produce lateral rectus muscle palsy and hence diplopia [48]. Once in the cavernous sinus, the tumor

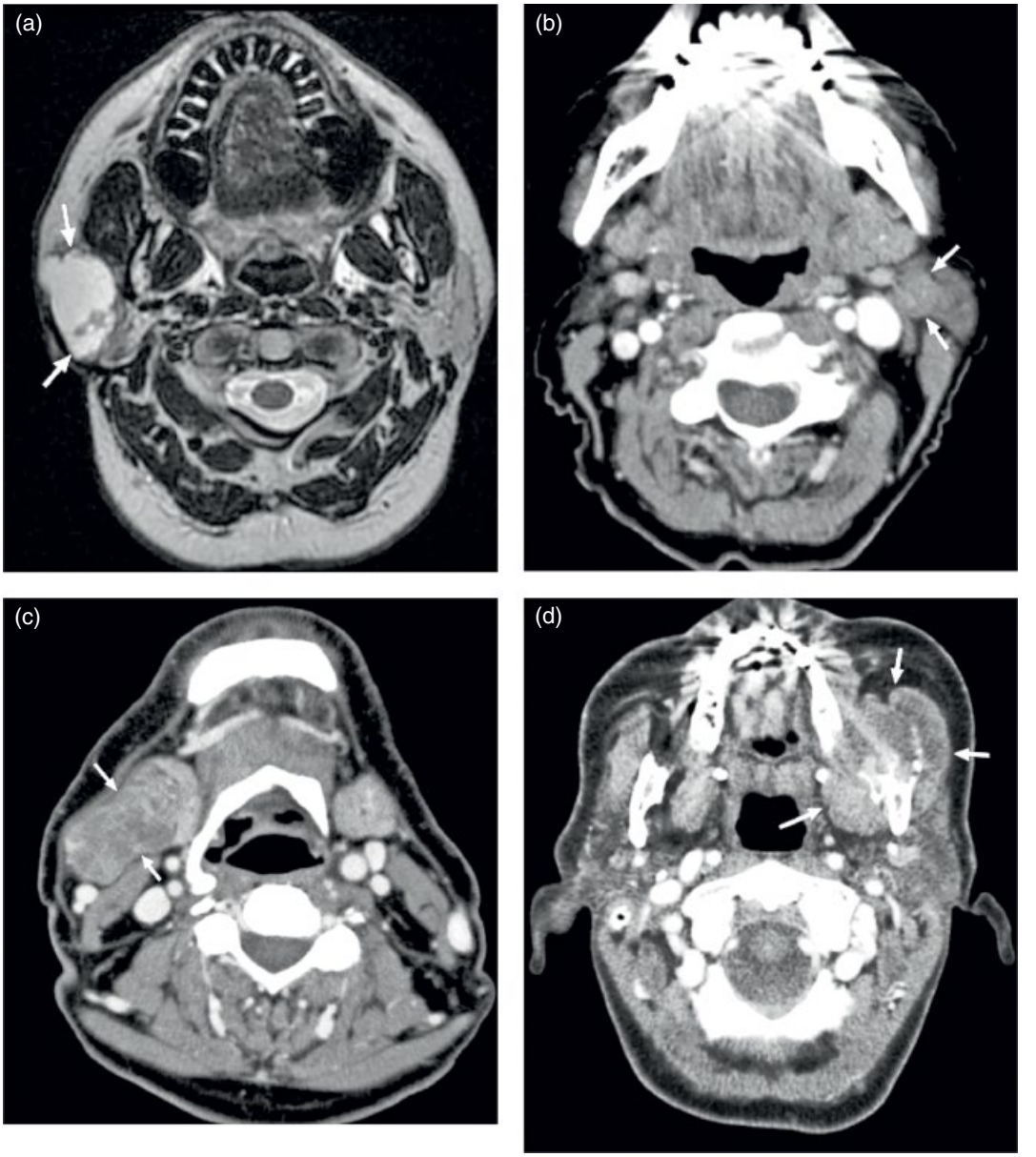


Figure 19.14 Rare malignant salivary gland neoplasms. (a) Axial T2-weighted magnetic resonance imaging (MRI) of a carcinoma ex pleomorphic adenoma of the right parotid gland (arrow). (b) Axial postcontrast computed tomography (CT) of a myoepithelial carcinoma of the left parotid gland (arrow). (c) Axial postcontrast CT of a carcinosarcoma of the right submandibular gland (arrow). (d) Axial postcontrast CT of a mucinous adenocarcinoma destroying the left mandible (arrow). Not only has it substantially destroyed the vertical ramus, it has displaced the remnant buccally, as defined by a broken line of dots just under the masseter muscle. Note the metallic spray artifact anteriorly. (e) Axial postcontrast CT of diffuse large B-cell lymphoma involving both parotid glands.



Figure 19.14 (Continued)

can travel anteriorly to reach the superior orbital fissure and immediately below this extend through the foramen rotundum (Figure 19.16d) into the pterygopalatine fossa. The fossa of Rosenmuller tumor can also travel anteriorly to wrap around the lateral pterygoid plate into the infratemporal fossa. From here, cancer can extend medially to enter the pterygopalatine fossa (Figure 19.16a), sometimes connecting to its fellow that has traveled to the same location through the cavernous sinus and foramen rotundum. A tumor in the pterygopalatine fossa can pass medially through the sphenopalatine foramen into the nasal cavity (Figure 19.16a). There are other locations where NPC can enter the skull; sometimes tumor will travel superiorly through the carotid canal, petroclival fissure (Figure 19.16a and c), and/or hypoglossal canal. The latter course will cause hypoglossal nerve dysfunction, leading to unilateral tongue atrophy (Figure 19.17a and b). Once inside the skull, the tumor can elevate the dura (Figure 19.16a), occasionally forming a mass large enough to compress the brain (Figure 19.16c). From here, the tumor will rarely cross the dura to invade cerebral tissue.

NPC will also directly invade bone of the skull base; this is the next most frequent route to intracranial invasion after foramen ovale [47]. Clival invasion occurs frequently too. MRI is much more sensitive than CT for detecting early clival invasion; the earliest sign of bone invasion is loss of high T1 fatty marrow signals. This can occur before any bone loss is evident on CT, although CT has the upper hand when it comes to evaluating the severity and extent of bone destruction. Early to moderate bone invasion by aggressive carcinoma will produce a permeative or moth-eaten pattern on CT, where the overall bone density decreases and the bone markings become indistinct (Figure 19.18; see also Figure 19.10 for the same pattern produced by ACC). Without treatment the bone involvement will progress, producing complete destruction or a lytic pattern

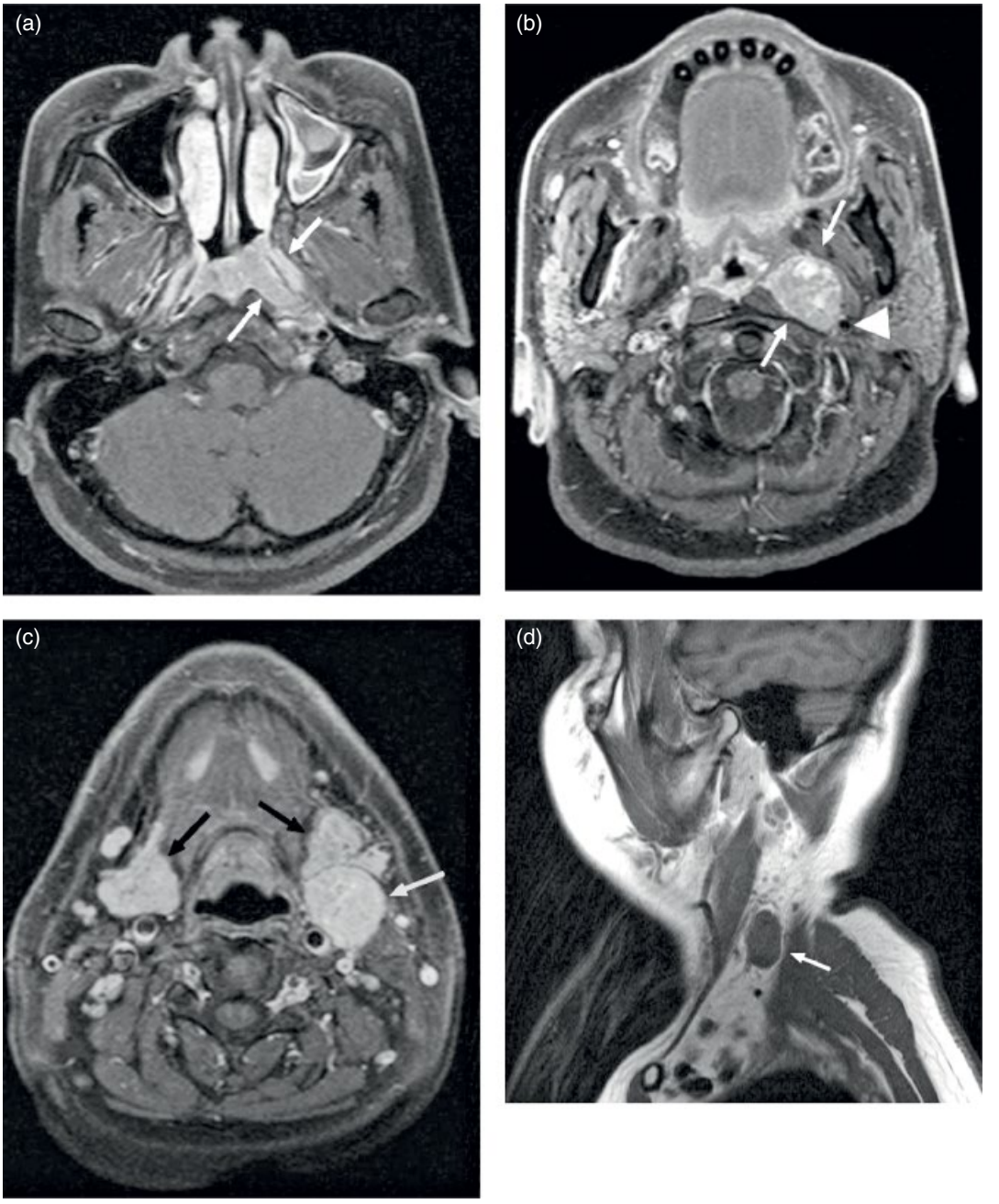


Figure 19.15 "Classical" nasopharyngeal carcinoma of the fossa of Rosenmuller with nodal metastases. (a) Axial postgadolinium fat-saturated T1-weighted magnetic resonance imaging (MRI) through the superior nasopharynx showing squamous cell carcinoma in the left fossa of Rosenmuller (arrows). This is a common location. (b) Axial postgadolinium fat-saturated T1-weighted MRI at the level of the maxillary alveolar ridge, where a large metastatic left retropharyngeal node is seen (arrows). This is also termed a node of Rouvière. These nodes are by definition located medial to the internal carotid artery (arrowhead). There is also a tiny right node of Rouvière present. (c) Axial postgadolinium fat-saturated T1-weighted MRI at a level through the floor of the mouth. An enlarged metastatic left internal jugular chain node is seen (white arrow). The submandibular glands exhibit more enhancement than usual due to recent radiotherapy (black arrow). (d) Sagittal T1-weighted image showing an enlarged posterior cervical triangle chain node (arrow). Note the difference fat saturation makes. Whereas (a), (b), and (c) use fat saturation to make the cutaneous fat "dark," that in (d), which does not use fat saturation, is "bright."

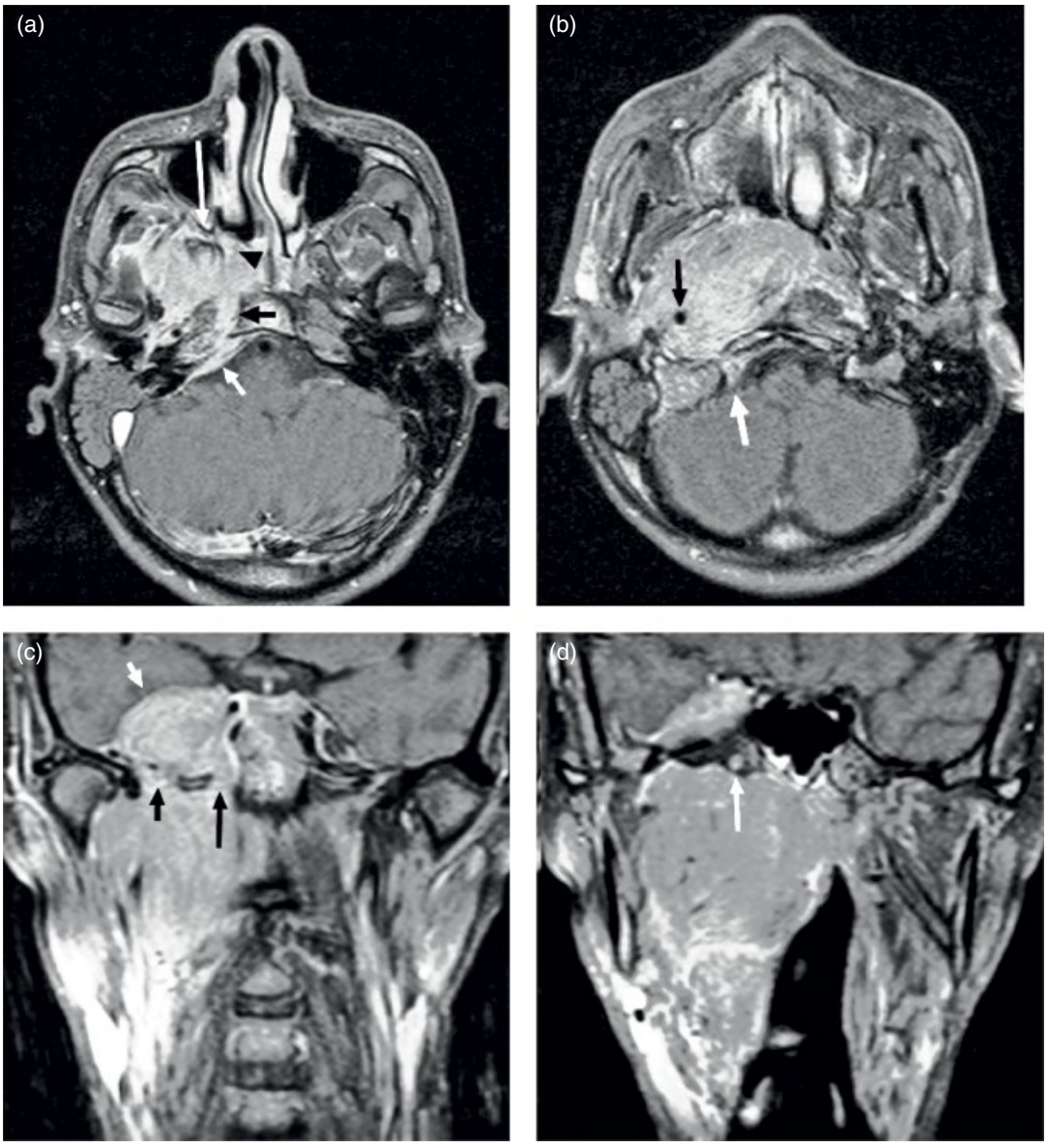


Figure 19.16 Postgadolinium fat-saturated T1-weighted magnetic resonance imaging (MRI) of a large right fossa of Rosenmuller nasopharyngeal carcinoma (NPC) with invasion of multiple skull base foramina. (a) Axial MRI through the level of the petrous temporal bones, showing a large right fossa of Rosenmuller NPC. The tumor is extending anterolaterally through the sphenopalatine foramen (black arrowhead) into the pterygopalatine fossa (long white arrow). Carcinoma is also extending posteriorly through the right petroclival fissure (black arrow) to form a mound on the posterior surface of the petrous temporal bone (short white arrow). The tumor has extensively invaded the right paravertebral, danger, retropharyngeal, and masticator spaces. The right pterygoid muscles are almost completely encased. (b) Axial MRI through the level of the hard palate. The tumor is encasing the right internal carotid artery (black arrow) and traveling through the right hypoglossal foramen (white arrow). (c) Coronal MRI showing a tumor extending superiorly from the right infratemporal fossa through the foramen ovale (short black arrow) and the petroclival fissure (long black arrow). A tumor mass is seen in the medial right middle cranial fossa (white arrow). (d) Coronal MRI anterior to (c) showing a tumor within the right foramen rotundum (arrow).

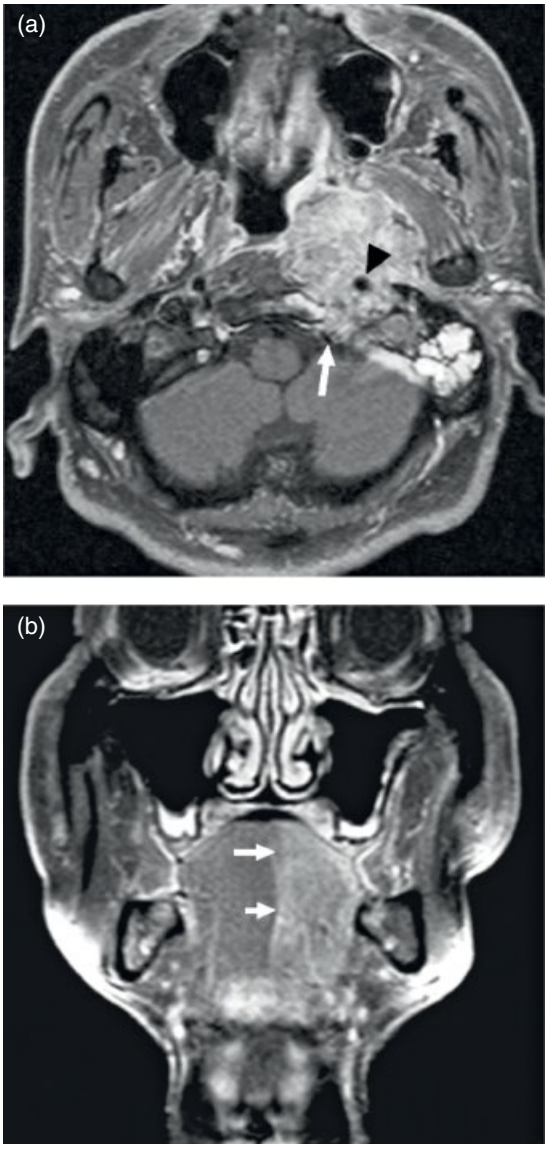


Figure 19.17 Left fossa of Rosenmuller nasopharyngeal carcinoma invading the left hypoglossal foramen, causing left tongue atrophy. (a) Axial postgadolinium fat-saturated T1-weighted magnetic resonance imaging (MRI) showing large left fossa of Rosenmuller cancer invading through the hypoglossal foramen (white arrow), encasing the left hypoglossal nerve en route. The left internal carotid artery (black arrowhead) and left medial pterygoids muscle are also encased. (b) Coronal postgadolinium fat-saturation T1-weighted MRI showing the effect of left hypoglossal nerve encasement. The left side of the tongue exhibits mild fatty atrophy (arrows).

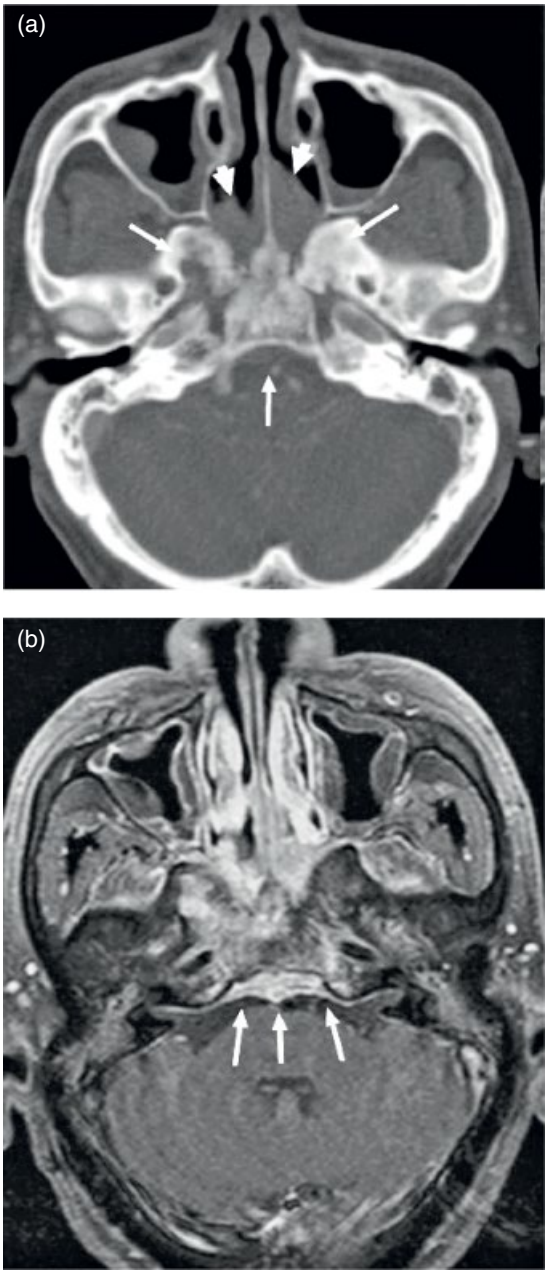


Figure 19.18 Nasopharyngeal carcinoma invading the clivus, producing a "permeative" bone pattern. (a) Axial bone-window computed tomography showing extensive permeation of the clivus, medial temporal, and medial sphenoid bones (long arrows). Note that the bone is not grossly destroyed, though the bony density is moderately decreased. A small posterior nasopharyngeal mass is present (short arrows). (b) Axial postgadolinium fat-saturated T1-weighted magnetic resonance imaging showing enhancing tumor extending from the posterior nasopharynx through the same bones. The tumor is accumulating between the bony clivus and overlying dura, pushing the dura away (arrows).

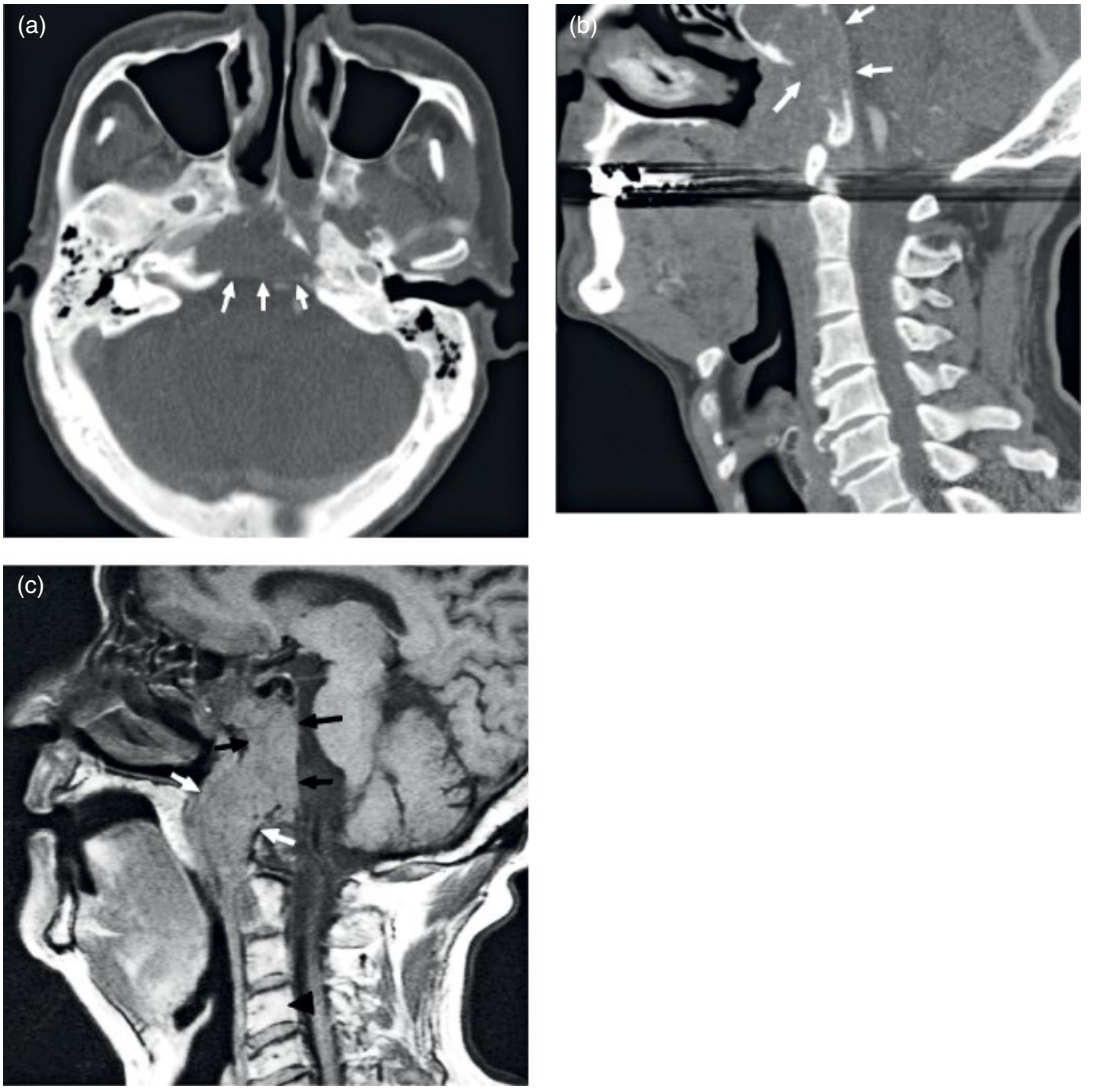


Figure 19.19 Nasopharyngeal carcinoma (NPC) invading the clivus, producing a lytic bone pattern. (a) Axial computed tomography (CT) displaying NPC invading the skull base with lysis of the clivus (arrows). (b) Sagittal CT showing near complete destruction of the clivus (arrows) and posterior sphenoid. The spray artifact caused by dental metal restoration does not affect the area of interest. (c) Sagittal T1-weighted magnetic resonance imaging shows a substantial soft-tissue mass occupying the posterior nasopharynx, abutting the posterior palate, and extending down into the superior oropharynx (white arrows). From here the tumor has traveled posteriorly to invade and completely replace the marrow of the clivus (black arrows). If the clivus was normal, it should have a high T1-weighted marrow signal, similar to the C4 vertebral body (black arrowhead).



Figure 19.20 Computed tomography (CT) revealing subtle bone invasion (arrow) by a retromolar squamous cell carcinoma (SCC) of the anterior aspect of the vertical ramus and internal oblique line of the edentulous posterior body of the mandible. (a) Axial CT (bone window) with intravenous contrast, at the level of the mandibular foramen, displaying erosion of the medial aspect of the vertical ramus by the SCC. (b) Coronal CT (bone window) with intravenous contrast displaying erosion of the internal oblique line of the edentulous posterior body of the mandible. Note how the bony defect is more easily seen in the coronal plane.

(Figure 19.19). When the bone is completely destroyed, the dark cortical margin will disappear on MRI (Figure 19.19c).

Due to an extensive lattice of retropharyngeal lymphatics and relatively innocuous initial symptoms, approximately half of patients with NPC will initially present to their clinical attendants with palpable, often bilateral metastatic cervical adenopathy. The lymphatic drainage of the nasopharynx is such that enlarged retropharyngeal nodes are frequently seen [49]; by definition these nodes lie medial to the internal carotid

arteries. They are also named the nodes of Rouvière (Figure 19.15b and Figure 19.33). Metastatic internal jugular and posterior cervical triangle chain adenopathy is also commonly seen with NPC.

19.5.2 ORAL CANCER

Oral cancer can arise from two organs: from the skin of the lips and from the mucosa of the mouth and of the pharynx. Although SCC of the oral cavity should be more visible than that of the pharynx, it may pass unnoticed until it provokes symptoms, by which time it may have not only achieved substantial dimensions, but metastasized to loco-regional lymph nodes or beyond. Therefore, the early diagnosis of cancer of the oral cavity is dependent upon the vigilance of the patient's regular dentist and/or dental hygienist in routinely examining the mouth for lesions. This examination should extend back into the tonsils and base of the tongue, as oropharyngeal cancers are increasing in incidence [50], particularly those associated with HPV [51]. Table 19.1 tabulates the most important changes the eighth edition of the manual of the AJCC [3] (effective 2018) made to the seventh edition of 2010 that would impact radiological practice. It includes consideration of the role of the HPV in SCCs and the responsiveness of these HPV positive SCCs to treatment [52]. The eighth edition of the AJCC manual [3] came into effect in 2018 with a number of important changes to the seventh, 2010 edition. The more important of these are set out in Table 19.1.

According to the eighth edition of the AJCC manual, the lips, the most frequent site of SCC occurrence (related to sun exposure), have been transferred to the "Cutaneous Carcinoma of the Head and Neck" chapter. Therefore, the oral cavity now only includes the buccal mucosa, both alveolar ridges, the anterior two-thirds of the tongue, the retromolar trigones, the floor of the mouth, and the palate [3]. In this region, the tongue and floor of the mouth are the most frequent sites for cancer. SCC arises less frequently in the retromolar trigone, buccal, and gingival mucosa.

The following text serves as a brief overview of the imaging of oral cancer as it occurs in different sites.

SCC of the retromolar trigone, though uncommon, spreads early, and carries a poor prognosis [53]. The presence of bony invasion (Figure 19.20) is an important piece of information for establishing prognosis and guiding therapy for these and other oral cancers. CT is the most often-used modality for assessing cortical bony invasion, for which it is effective [54]. For this location it is important to reconstruct additional images in the coronal plane for best sensitivity. This is because any bony defects associated with retromolar trigone tumors will lie nearly parallel to the axial plane. In order to optimally detect such defects an imaging plane perpendicular to the axis of the lesion should be selected (Figure 19.20b). MRI can also be used for evaluation of bone involvement [55].

SCCs arising from the lateral and superior surfaces of the tongue are usually first discovered by the patient's oral or dental practitioner due to observable ulceration and/or a palpable mass. Although these tumors are easily seen by direct observation, they can be challenging to detect on CT studies due to bone-hardening artifact from the adjacent mandible.

Floor-of-mouth SCCs can be difficult to detect on CT, since their enhancement can be masked by similar enhancement from normal adjacent sublingual salivary glands. Such carcinomas are more easily seen on MRI. Anterior floor-of-mouth carcinomas will occasionally obstruct the submandibular (Wharton's) duct at its ostium, causing duct dilation. Such dilation is a valuable clue to the presence of a small occult anterior floor-of-mouth carcinoma (Figure 19.21).

Table 19.1 American Joint Committee of Cancer and Union of International Cancer Control's Cancer Staging Manual, changes in the eighth edition that may affect the radiologist.

Changes	Comment
"Lip and Oral Cavity" chapter has been separated out so that it is the "Oral Cavity" alone.	Lip goes into the "Cutaneous Carcinoma of the Head and Neck" chapter.
"T" for oral lesions now considers the depth of invasion in staging. It is determined historically and is measured from the basement membrane. Note that it is not synonymous with tumor thickness.	Although this is precisely determined by the pathologist, the radiologist is able to contribute usefully by determining infiltration into the tongue or the soft tissues of the oral cavity, as this assists in preoperative planning.
Human papilloma virus (HPV) P16-positive (P16+ve) carcinomas have a better prognosis and have different imaging and managing protocols.	My comment on this is that clearly, unless the HPV P16 status is available to the radiologist when reporting, obviously the carcinoma should be reported as if it were P16 -ve (negative) and the report qualified with a statement that the P16 status was not known at the time.
Different staging for oropharyngeal squamous cell carcinoma (OPSSC) and nasopharyngeal carcinoma (NPC) according to their HPV P16 or Epstein Barr virus (EBV) status, respectively.	But if the OPSSC is P16+ve or the NPC is EBV+ve (the majority of NPCs), then they will be considered to have better prognoses than the P16 -ve and EBV -ve cases
Cancer of unknown primary.	Recorded as "TO." Note that if the node is EBV+ve, then the primary is in the nasopharynx.
The radiologist is in the prime position to report on the presence of extranodal extension (ENE), except for EBV+ve NPC and P16+ve cancers.	Therefore the radiologist should report ENE in addition to the node's size (particularly if over 10 mm in short axis), shape, necrosis, and cystic change.

Source: Adapted from Glastonbury, C.M., Mukherji, S.K., O'Sullivan, B., and Lydiatt, W.M. (2017). Setting the stage for 2018: how the changes in the American Joint Committee on Cancer/Union for International Cancer Control Cancer Staging Manual eighth edition impact radiologists. *AJNR Am. J. Neuroradiol.* 38: 2231–2237.

Occasionally these tumors will erode into the adjacent mandible; this is best detected on CT and also is important.

19.6 Information for Presurgical Planning

The oropharynx lies posterior to the oral cavity and includes the posterior third of the tongue, bounded by the circumvallate papillae, the posterior pharyngeal wall, the soft palate and uvula, and the palatine tonsils. It ends superiorly at the junction of the hard and soft palate, inferiorly at the hyoid bone/valleculae, and anteriorly at the palatoglossal arch, i.e. the anterior tonsillar pillars. The posterior pharyngeal wall abuts the second and third cervical vertebrae.

Oropharyngeal soft-palate SCCs will eventually destroy the hard palate and

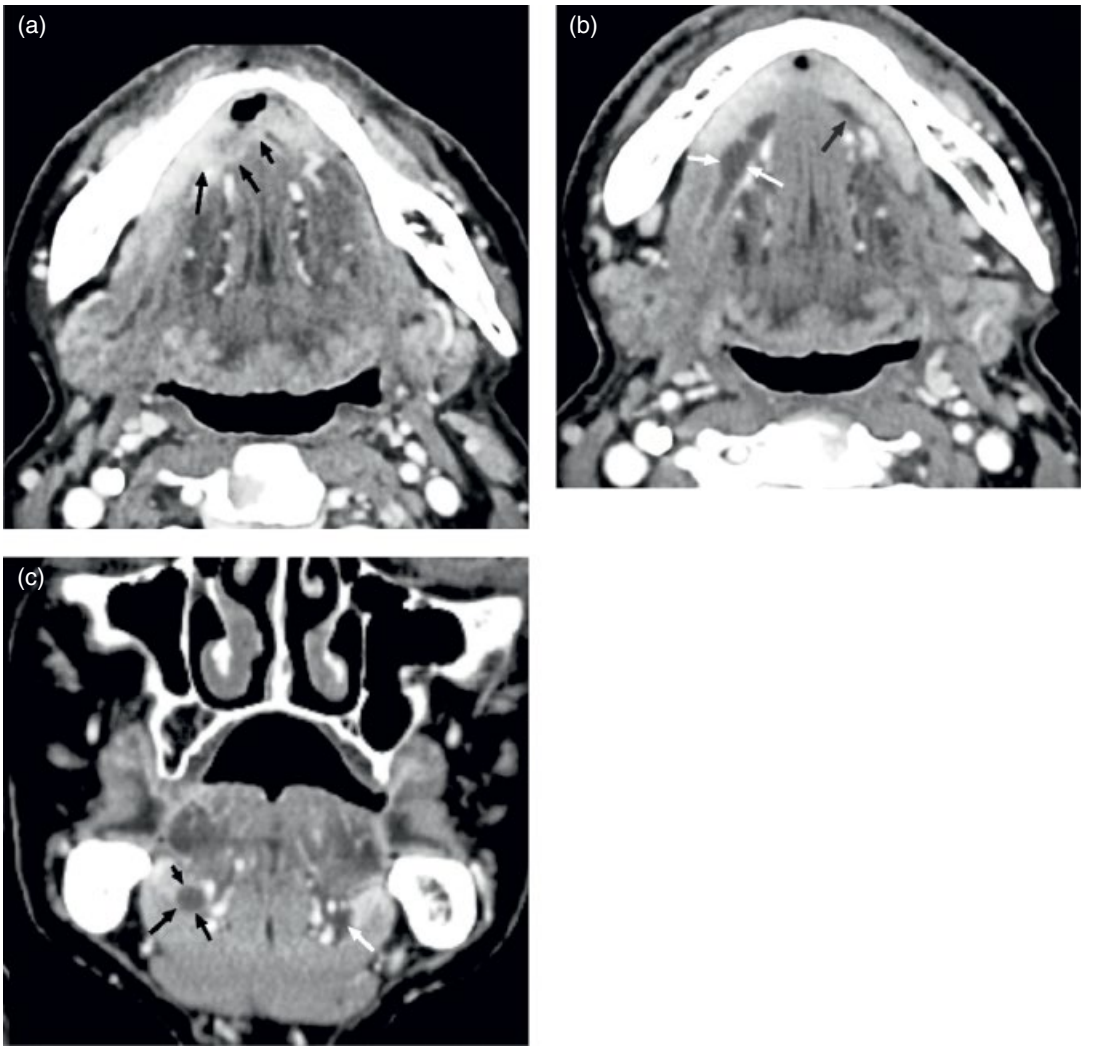


Figure 19.21 Magnetic resonance imaging and computed tomography (CT) of a squamous cell carcinoma (SCC) affecting the floor of the mouth and causing dilation of the submandibular ducts. (a) Axial postcontrast CT showing an SCC (arrows) in the anterior floor of the mouth. The lesion is difficult to detect, since the adjacent sublingual salivary glands also enhance, masking the presence of cancer. (b) Axial postcontrast CT showing dilation of both submandibular ducts (arrows) due to compression by the tumor. The left duct is more dilated than the right. (c) Coronal postcontrast CT showing dilation of both submandibular ducts (arrows).

spread onto the tonsillar pillars. This tumor can involve the palatine branches of the maxillary nerves en route to exhibiting perineural tumor spread [56]. Such behavior is more common with ACC, but is also seen with SCC.

In the palatine tonsil, almost all SCCs arise in the anterior pillar. Smaller lesions are sometimes challenging to detect here via cross-sectional imaging and are best seen on clinical examination. As the tumor enlarges, it will first extend superiorly and

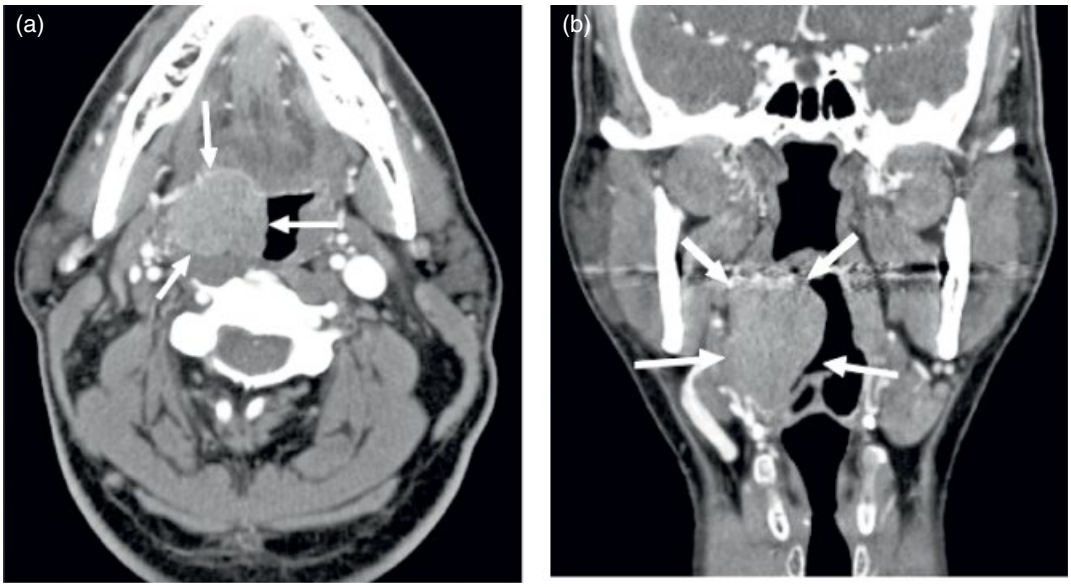


Figure 19.22 Computed tomography (CT) of a squamous cell carcinoma of the right palatine tonsil. (a) Axial postcontrast CT at the level of the basal process of the mandible, showing a large enhancing right tonsillar mass (arrows). It has well-defined margins and is invading the adjacent dorsum of the tongue. (b) Coronal postcontrast CT in a plane just anterior to the insertion of the lateral pterygoid muscle into the pterygoid pit, showing an enhancing right tonsillar mass with well-defined margins. It is invading the soft palate and displacing the lateral lamina of the thyroid cartilage and the right vallecula. It extends into the right half of the oropharynx.

inferiorly, invading the tongue base and soft palate (Figure 19.22). Highly aggressive lesions will travel laterally, traversing the boundaries of multiple fascial compartments to reach subcutaneous fat (Figure 19.23). Tonsillar and soft-palate cancers commonly metastasize to retropharyngeal, internal jugular, and posterior cervical triangle chain nodes (Figure 19.23c and d). An important radiological clue to the detection of palatine tonsil SCCs is the asymmetry of the oropharynx in the axial plane. This can be very obvious, as in Figure 19.24, or subtle, as in Figure 19.25. In the latter there was only a slight enhancement of the SCC. In both cases, PET/CT displayed their hyperavidity, which confirmed a radiological diagnosis of SCC of the tonsil, reinforced by the clinical findings suggestive of an SCC.

SCCs of the tongue base are often initially silent and, when discovered, tend to be larger and more advanced. From an imaging perspective, these SCCs are difficult to detect on contrast-enhanced CT, because they are nearly isointense to surrounding normal-enhancing glossal lymphatic tissue (i.e. the lingual tonsil). Radiologically, the tongue base is a major "blind spot" where tumors can hide; hence, this area should be carefully evaluated whenever the oral and maxillofacial practitioner is confronted with metastatic adenopathy with no obvious primary cancer. MRI is much more sensitive than CT vis à vis the tongue base, and is the primary modality used for assessment here (Figure 19.26); PET/CT is even more sensitive than MRI.

SCCs of the anterior tongue and floor of the mouth will metastasize to

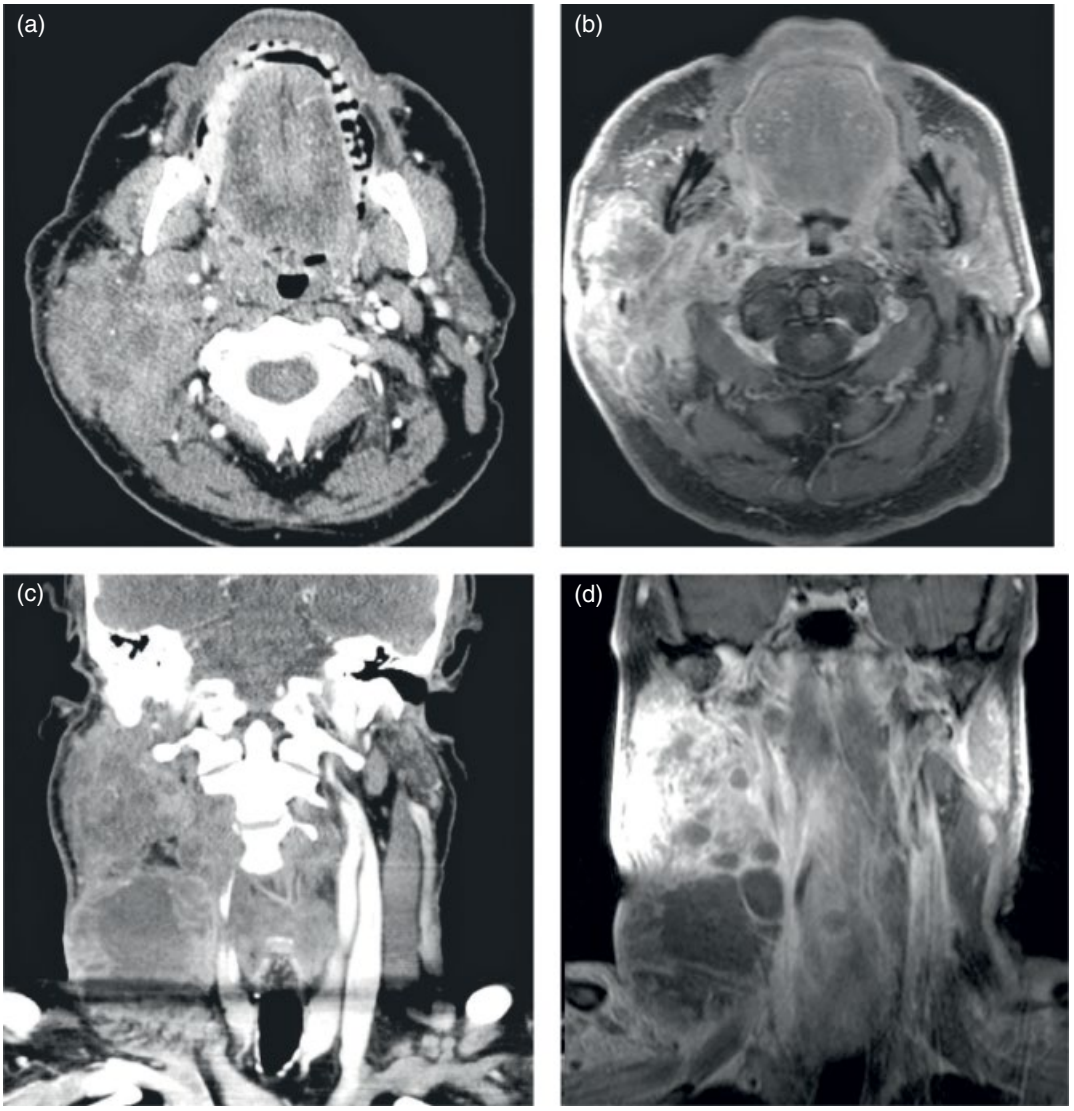


Figure 19.23 Computed tomography (CT) and magnetic resonance imaging (MRI) of a huge aggressive squamous cell carcinoma (SCC) arising in the right palatine tonsil. It is associated with substantial lymphadenopathy. (a) Axial postcontrast CT (soft-tissue window) at the level of the occlusal plane. The affected tonsil mildly enhances and mildly effaces the right side of the oropharynx. The tumor has spread laterally, encasing the carotid sheath en route to intersecting a large nodal metastasis beneath the sternocleidomastoid muscle. This type of spread is unusually aggressive, crossing multiple fascial planes. (b) Axial postgadolinium fat-saturated T1-weighted MRI showing enhancement of the same tumor. (c) Coronal postcontrast CT at the level of the odontoid peg of the second cervical vertebra. The left main jugular and carotid vessels are observed throughout most of their cervical course. The right neck is almost completely occupied by a confluent nodal mass. The central hypodense regions within the latter mass are suggestive of necrosis, characteristic of metastatic SCC. (d) Coronal postgadolinium fat-saturated T1-weighted MRI showing the same mass AS in (c). Central necrosis is particularly obvious in the inferior nodes.

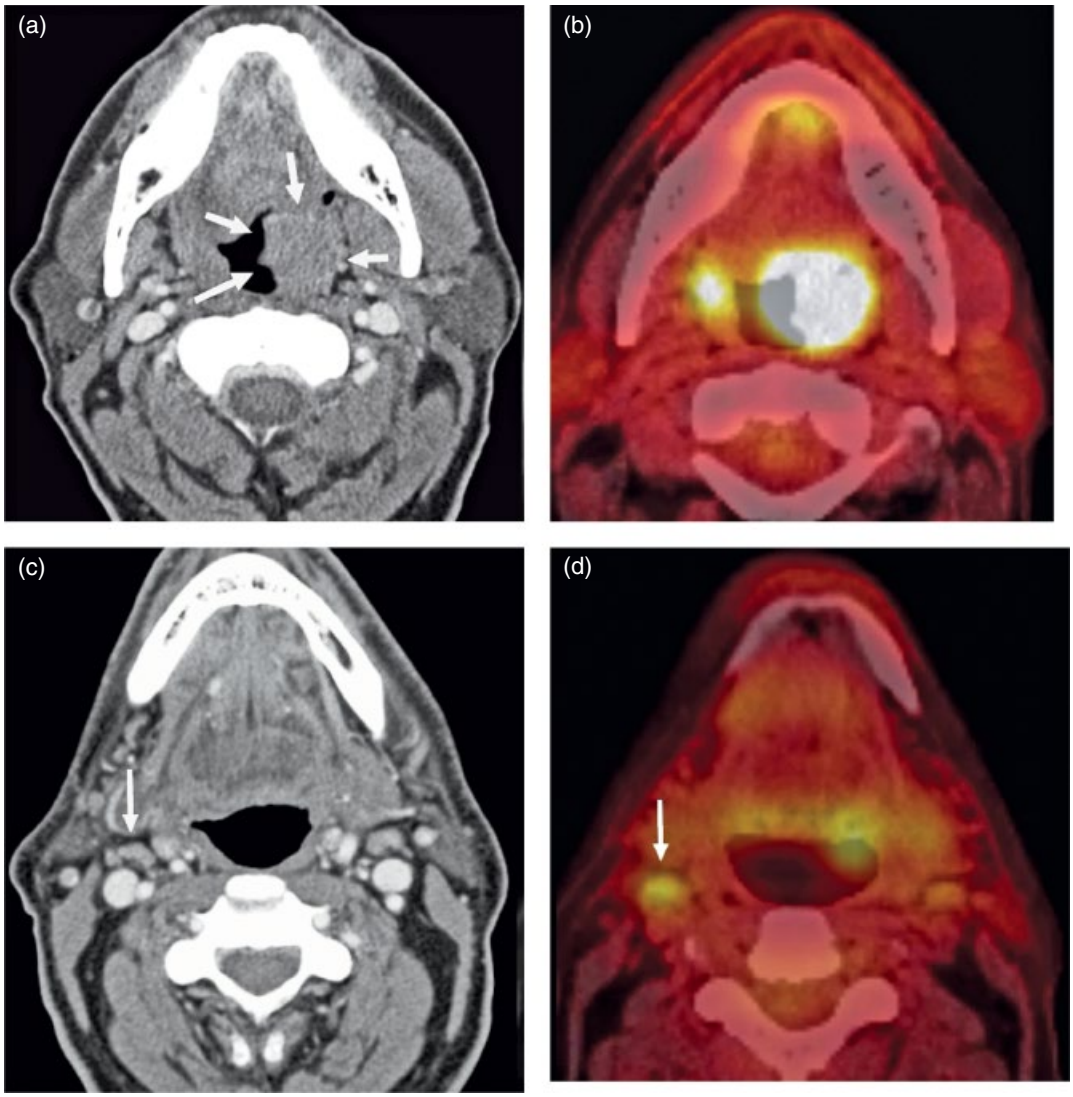


Figure 19.24 Computed tomography (CT) and positron emission tomography (PET) fused with CT (PET/CT) of left tonsillar squamous cell carcinoma (SCC) with nodal metastasis. (a) Axial enhanced (postcontrast) CT showing a left tonsillar mass expanding into the oropharynx (arrows). (b) Corresponding PET/CT image showing fluorodeoxyglucose (FDG) uptake in the mass; hence the lesion is hypermetabolic – consistent with cancer. The left tonsillar SCC is large enough to easily detect on CT. (c) Enhanced (postcontrast) axial CT at a level through the mandible demonstrating a tiny right jugulodiagastric node (arrow). By CT size criteria (i.e. short axis nodal diameter < 1 cm), this node would be considered benign. Hence, the PET/CT can detect metastatic tumor within lymph nodes much earlier than plain CT. (d) Axial PET/CT at the same level showing FDG uptake in the jugulodiagastric node (arrow), suspicious for metastatic disease. This node would be called negative by CT or magnetic resonance imaging size criteria.

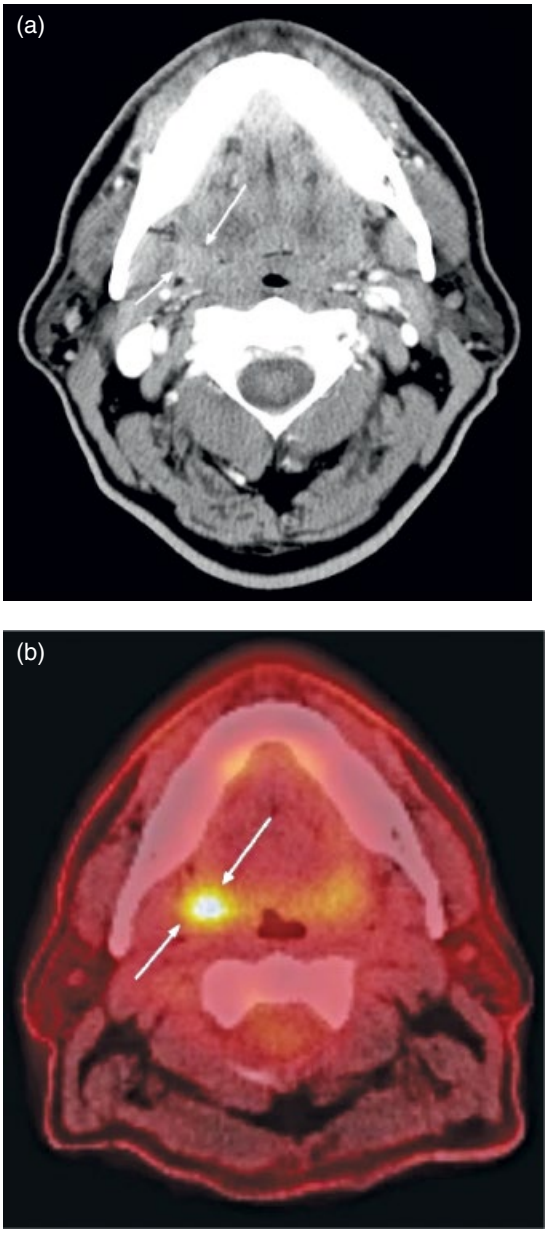


Figure 19.25 Computed tomography (CT) and positron emission tomography (PET) fused with CT (PET/CT) of squamous cell carcinoma (SCC) of the right tonsil. (a) Axial postcontrast CT showing barely visible enhancement of a right tonsillar SCC (arrows). (b) Axial PET/CT showing increased fluorodeoxyglucose uptake in the tumor (arrows). The SCC is much easier to see and the increased uptake makes the diagnosis of malignancy much more likely.

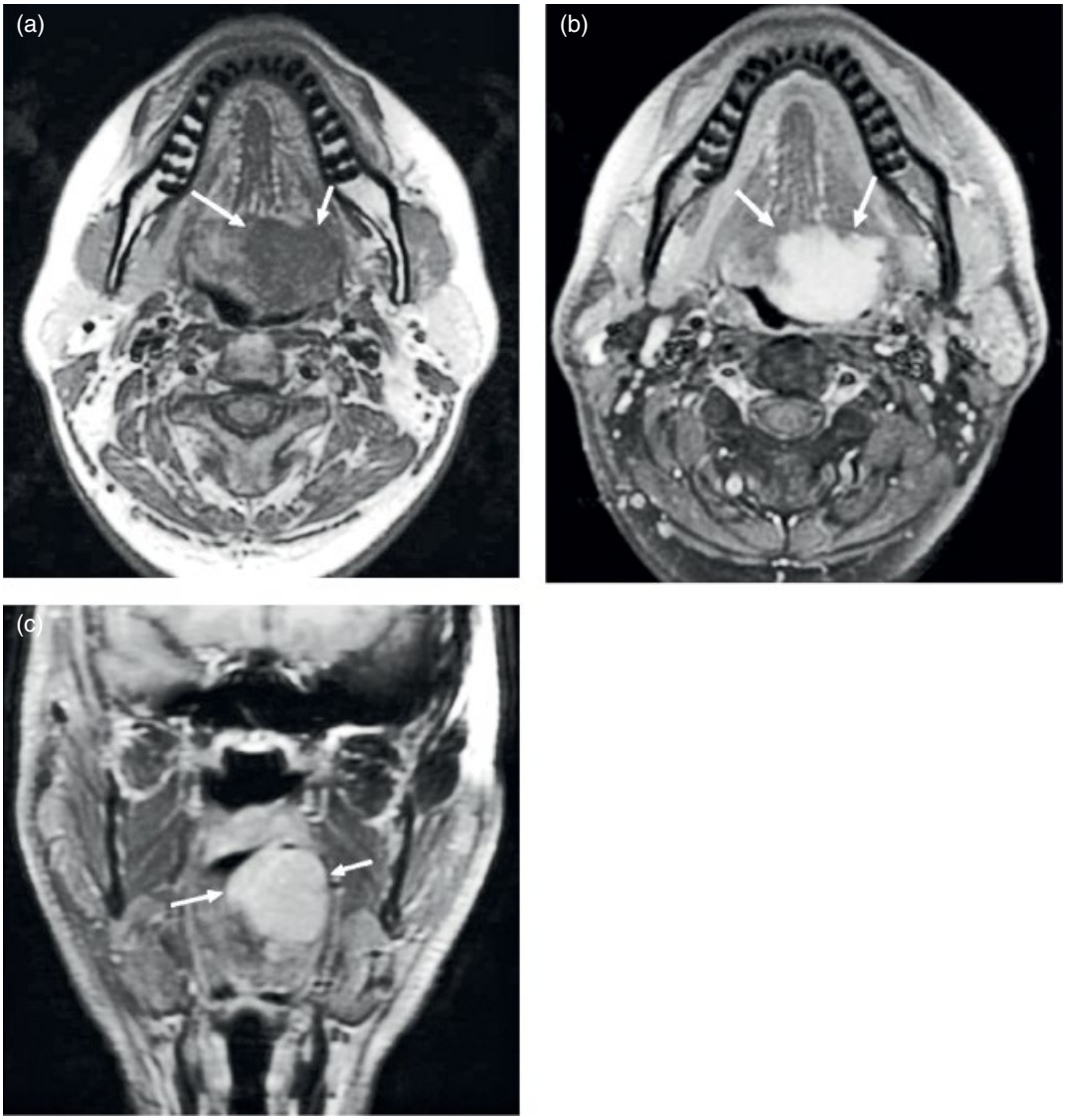


Figure 19.26 Magnetic resonance imaging (MRI) of a squamous cell carcinoma (SCC) arising on the left side of the dorsum of the tongue. (a) Axial noncontrast T1-weighted MRI showing the SCC as a well-defined hypointensity infiltrating isointense lingual musculature (arrows). (b) Axial postgadolinium fat-saturated T1-weighted MRI shows enhancement of the SCC (arrows), which has deeply invaded the tongue. The neoplasm also extends posteriorly into the oropharynx. (c) Coronal postgadolinium fat-saturated T1-weighted MRI with enhancement of the SCC, which has deeply invaded the tongue (arrows). Note the difference fat saturation makes. Whereas (b) and (c) use fat saturation to make the cutaneous fat "dark," in (a), which does not use fat saturation, it is "bright."

submental, submandibular, and jugular chain nodes, often bilaterally. SCCs of the posterior tongue will more often metastasize to internal jugular and posterior cervical triangle chain nodes.

Hypopharyngeal cancers are uncommon, accounting for less than 1% of all new cases in Canada. The hypopharynx lies posterior to the aryepiglottic folds and extends between the hyoid bone and the cricopharyngeus muscle (approximately the lower edge of the cricoid cartilage). Below the cricopharyngeus, the hypopharynx continues on as the cervical esophagus. In North America, the majority of hypopharyngeal SCCs (65–85%) arise in the pyriform sinus. This is important, because the pyriform sinus is another "blind spot" where tumors are difficult to detect on postcontrast CT; 10–20% of hypopharyngeal SCCs are found on the posterior wall and 5–15% in the postcricoid area [57].

Laryngeal cancer is the most common upper aerodigestive tract SCC [41]. An estimated 13 474 new cases occurred in the United States in 2012 [41]. The larynx lies anterior to the hypopharynx and extends between the glosso/pharyngoepiglottic folds and cricoid cartilage. It can be divided into supraglottic, glottic, and infraglottic portions; the glottis comprises the true vocal cords. Although the majority of laryngeal SCCs occur in the glottis (Figure 19.27), metastatic adenopathy occurs much more frequently with supraglottic tumors, due to the relatively rich supply of lymphatics in this location (Figure 19.28).

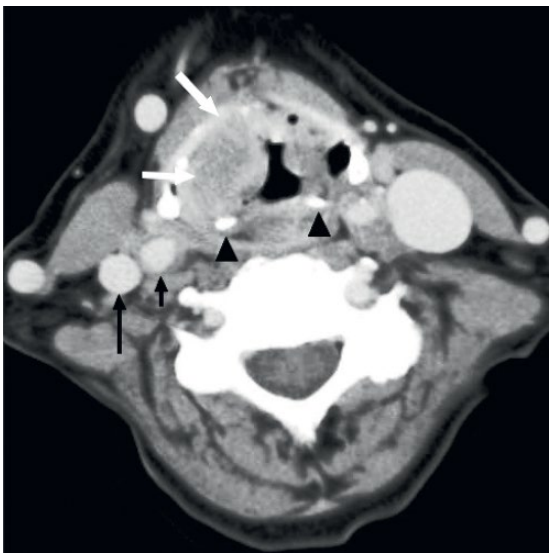


Figure 19.27 Axial postcontrast computed tomography of squamous cell carcinoma of the larynx expanding into the glottic aperture. The squamous cancer is seen as a lobulated mass (white arrows) immediately medial to the right thyroid cartilage. The left glottic tissue is mildly swollen, likely from a combination of edema and tumor. The arytenoid cartilages are well seen (black arrowheads). The right internal jugular vein (long black arrow) and internal carotid artery (short black arrow) are almost the same size. Normally the internal jugular vein is larger than the carotid artery; this is somewhat exaggerated on the left.

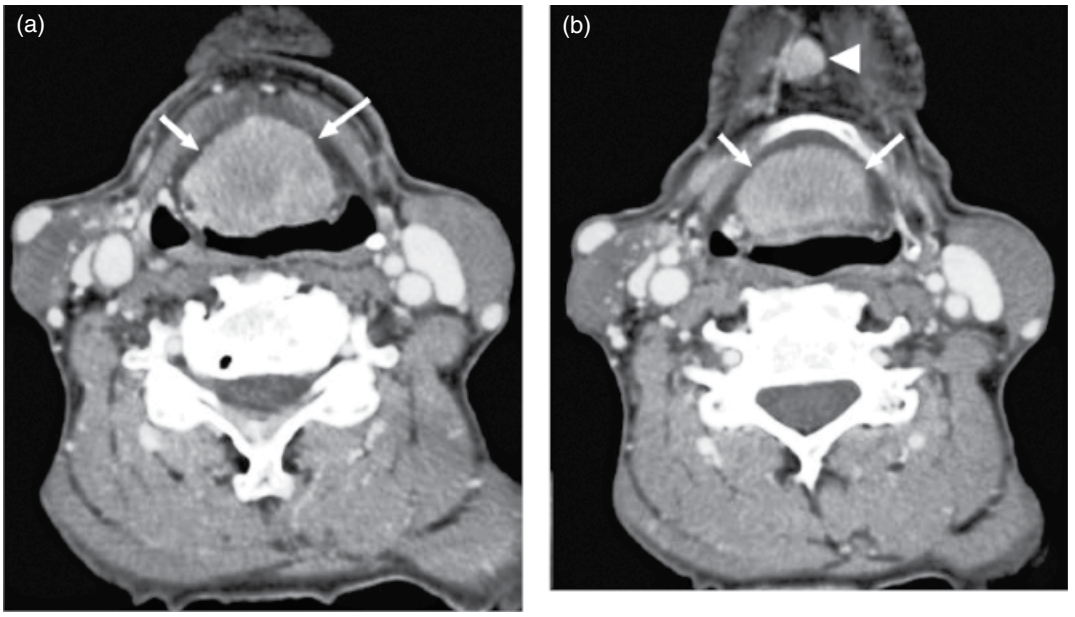


Figure 19.28 Computed tomography (CT) of supraglottic squamous cell carcinoma (SCC). (a) Axial postcontrast CT showing a large enhancing supraglottic SCC (white arrows). (b) At a level slightly above (a), showing the mass and a mildly enlarged metastatic submental node (arrowhead).

19.7 Radiology of Cervical Lymphadenopathy

The detection of metastatic lymph nodes is important in staging the tumor. A single ipsilateral metastatic node reduces overall survival by 50% [58]. Cervical metastatic lymphadenopathy may be discovered by the patient or upon a routine physical examination, or it may be searched for upon detection and/or diagnosis of the primary tumor. The flowchart in Figure 19.29 indicates a process that can be undertaken upon discovery of an enlarged lymph node in the neck, which in turn may lead to discovery of the primary tumor and to its subsequent "staging." The clinical (physical) examination of the neck is associated with about 30% false positives and about 20% false negatives [58]. Therefore, cross-sectional imaging, mainly CT or MRI, is required (ultrasound can also play a role) before further management is considered. Since these images are only able to detect metastatic nodal disease indirectly, based on anatomical and functional distortions produced by tumor inside the node, false positives and false negatives are also present. Therefore, histopathology remains the "gold standard," now supplemented by molecular techniques [59]. Unfortunately, histopathology can only be performed on surgical specimens or needle biopsies, which are dependent upon the surgeon's high confidence in the radiological examinations performed and interpreted by the radiologist.

Figure 19.30 identifies the main radiological features, such as size, shape, and central necrosis (Figure 19.31), or the cystic formation that may be looked for to determine whether the nodes may be affected by metastatic disease. The absence of a fatty hilum at the periphery of an enlarged node may indicate a

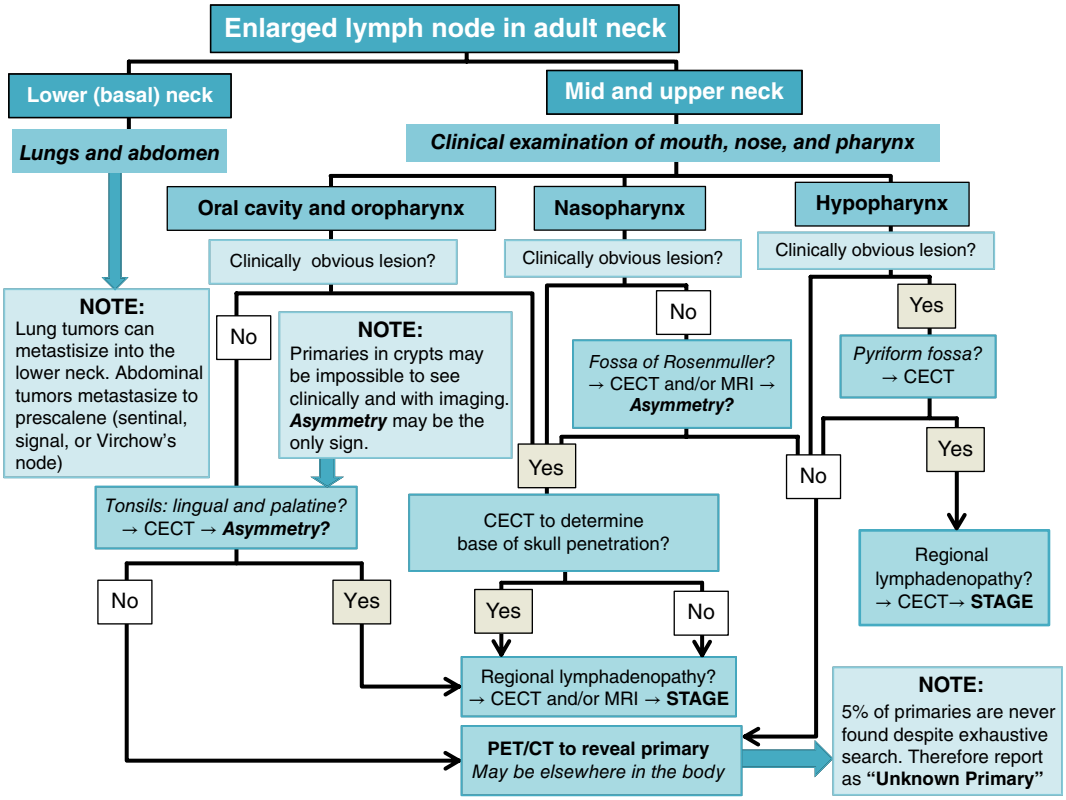


Figure 19.29 Enlarged lymph node in the adult neck. CECT, contrast-enhanced computed tomography; MRI, magnetic resonance imaging; PET/CT, positron emission tomography fused with computed tomography.

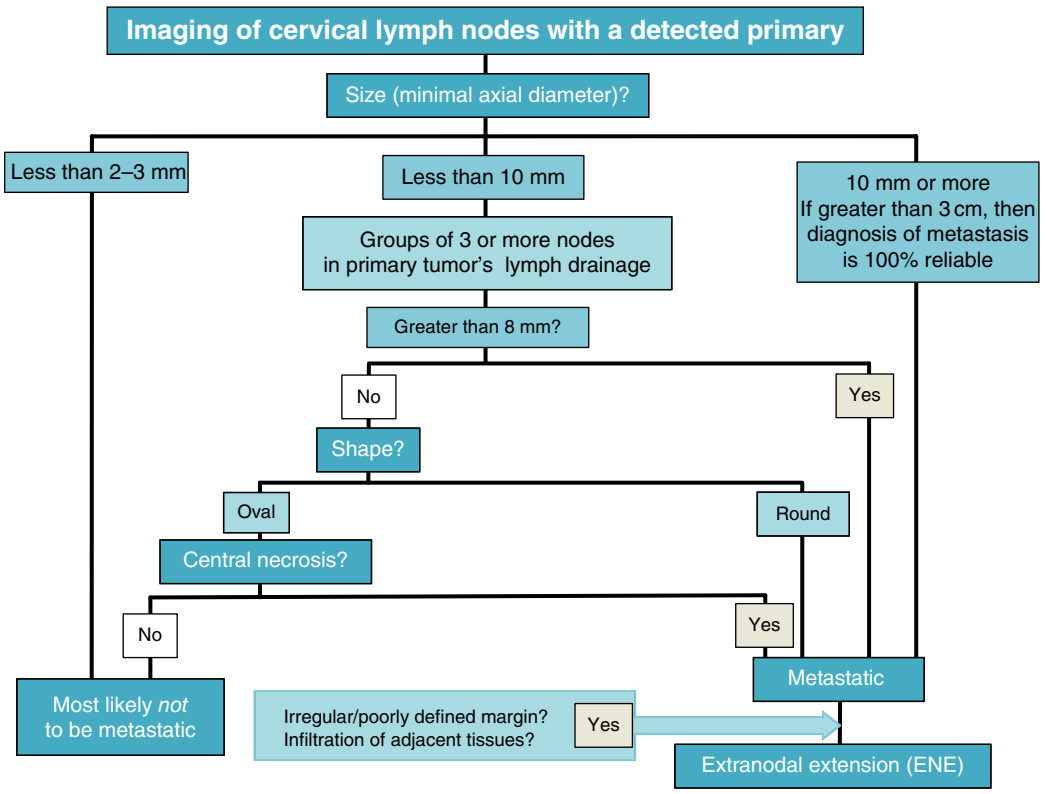


Figure 19.30 Main radiological features of a cervical lymph node, particularly sought after detection and diagnosis of a primary tumor of the head and neck.

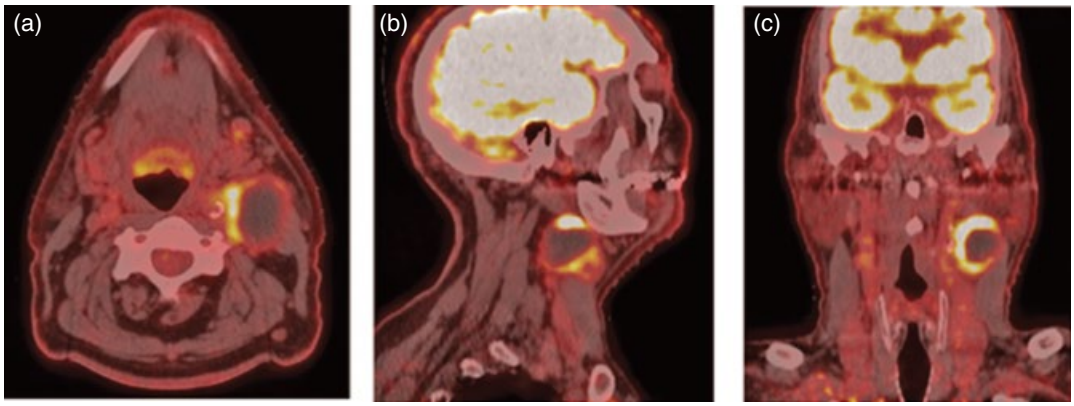


Figure 19.31 Large lymph node (jugulodiagastric) displaying central necrosis from left to right on (a) axial, (b) sagittal, and (c) coronal reconstructions of positron emission tomography fused with computed tomography. There was no observable primary, therefore the diagnosis of "unknown primary" was made.

metastatic node rather than a reactive node, which became enlarged secondary to inflammation alone. This impression of benignity is enhanced if the node preserves its normal oval or kidney-bean shape. A general rule of thumb is that if a patient has a known primary upper aerodigestive tract malignancy and a cervical lymph node is found with a short-axis diameter greater than 1 cm, that node is considered suspicious for metastatic disease [60]. How suspicious? The 1 cm criterion was chosen by pathologically examining many nodes in patients with head and neck cancer and choosing a nodal size cutoff point where the majority of nodes are positive for metastatic disease. This cutoff gives high specificity, i.e. a high ability to detect metastatic disease. Unfortunately, it also produces lower sensitivity; i.e. a significant number of nodes below 1 cm will also have tumor in them [61]. The short-axis measurement should be used, because it has been found to be the most reliable. Van den Brekel et al. reported sensitivity and specificity of 42% and 99%, respectively, for a 1 cm threshold [62]. Published size criteria vary and have been finessed; some authors have shown that different criteria apply to different node locations and shapes [63]. Mancuso et al. demonstrated that the cutoff point for retropharyngeal nodes is lower [64], and Kelly and Curtin set these at greater than 0.5 cm [58].

Nodes that are round instead of oval and clustered nodes in the lymphatic drainage path of a tumor are more suspicious. The presence of central necrosis in an enhancing node is highly suggestive of metastatic disease [63]; this is often seen in advanced SCC metastases (e.g. Figures 19.23 and 19.32). Figures 19.15, 19.23, 19.24c and d, 19.28b, and 19.31–19.34 show metastatic nodes in the neck. Although Kelly and Curtin distinguish between nodes displaying central necrosis and a cystic appearance on the basis of the mechanisms involved [58], it makes no difference to the fact that both indicate metastasis of the affected node/s.

PET/CT in Figure 19.24c and d displays an avid lymph node which is smaller than the 1 cm threshold for diagnosis by CT or MRI. After having considered the causes for false positives on PET/CT and excluding them, then this node should be considered radiologically positive for metastasis.

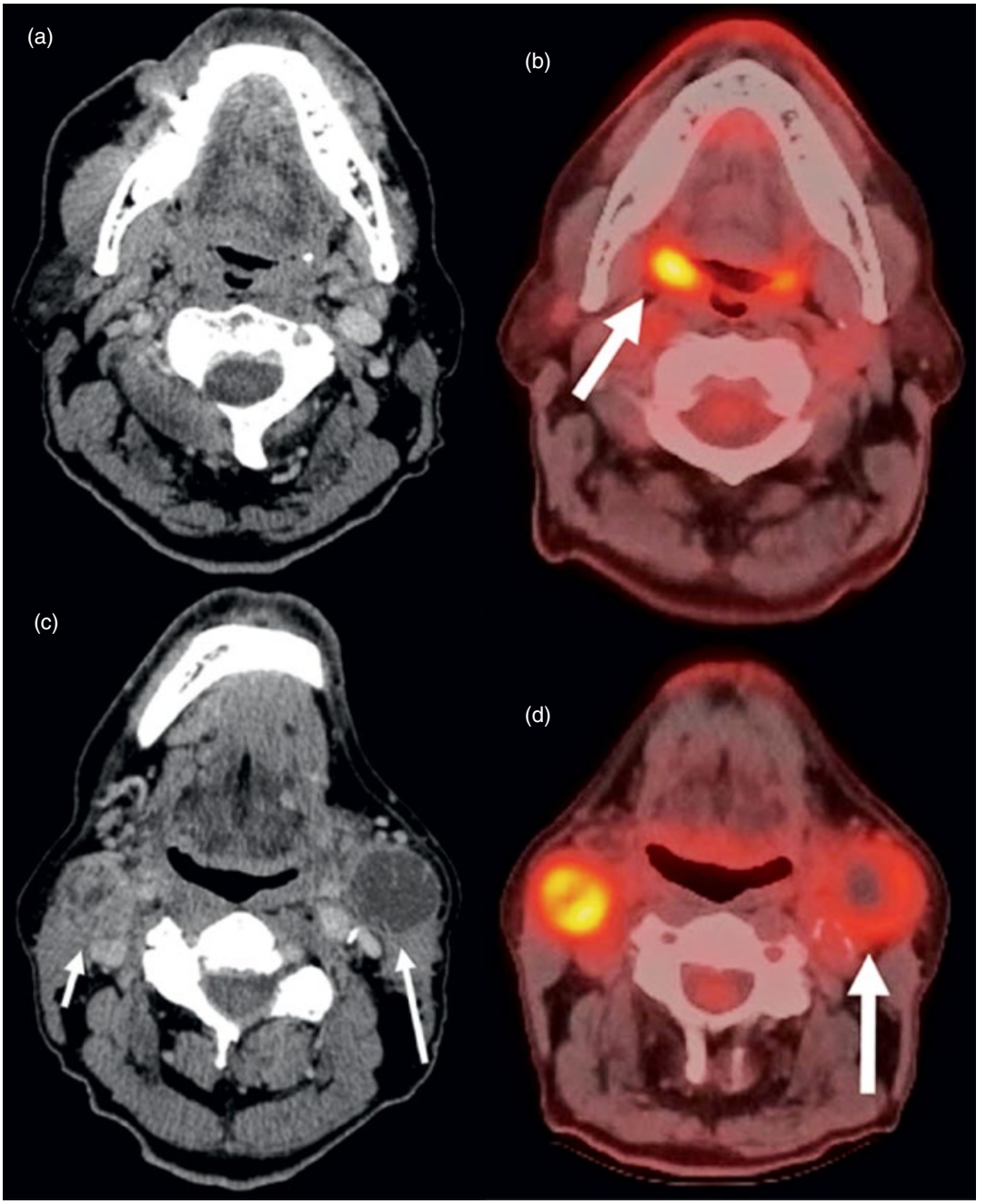


Figure 19.32 Squamous cell carcinoma, biopsy taken from cervical lymph node, primary unknown. (a) Staging axial computed tomography (CT) scan of the neck did not reveal an obvious primary lesion. (b) Staging positron emission tomography fused with computed tomography (PET/CT) scan of the same patient confirms a primary lesion arising from the right tonsillar fossa (arrow). (c) Axial CT scan revealing bilateral cervical lymphadenopathy. Note the solid nature of the right cervical lymph node (short arrow), versus the cystic appearance of the left lymph node (long arrow). (d) PET/CT images of the same lymph nodes. Note the lack of fluorodeoxyglucose accumulation within the cystic lymph node (arrow).

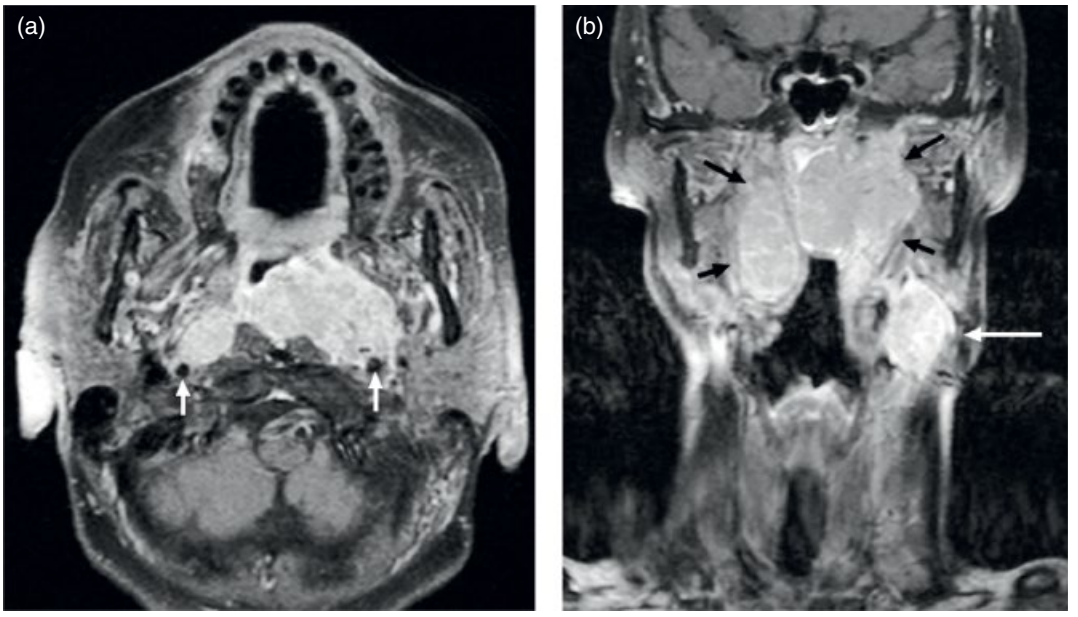


Figure 19.33 Postgadolinium T1-weighted fat-saturated magnetic resonance imaging (MRI) displaying confluent metastatic retropharyngeal adenopathy (nodes of Rouvière). (a) Axial MRI at the level of the occlusal plane. Note that the majority of adenopathy is medial to the internal carotid arteries (arrows). This is a defining characteristic of retropharyngeal nodes. (b) Coronal MRI showing the retropharyngeal nodal mass (black arrows) as well as a metastatic internal jugular node (white arrow). Note that all observed nodes are larger than 1 cm on the short axis, hence likely metastatic.

The AJCC's eighth edition enacted a significant innovation in comparison to the seventh edition by recognizing *extranodal extension* (ENE) as an important diagnostic and prognostic feature [65]. An ENE may be defined as the spread or metastasis of malignant cells from within a lymph node through its capsule into adjacent tissues. It is also called extracapsular spread. An example of ENE is displayed in Figure 19.35.

19.8 Cervical Lymph Node Classification and Staging

The clinician should be aware from the outset that there are a number of ways to name and classify cervical lymph nodes. Some nodes have specific names, derived from the anatomist who first identified them, e.g. Rouvière's (Figures 19.15b and 19.33) or Virchow's [66, 67] nodes, which are still used by many head and neck clinicians, including radiologists; or from their precise anatomical position, e.g. jugulodigastric (Figures 19.24c and d, 19.31). Many clinicians simply describe nodes in relation to the classical anatomical triangles described in Chapter 17 (see Figure 17.5) and relevant surface anatomy structures; for example, submental, submandibular, retropharyngeal, internal jugular, and posterior cervical triangle nodes (Figures 19.31–19.34). This scheme is derived from a more elaborate system of classification published by the French anatomist Rouvière in 1938, based on connected nodal chains [68].

Since then, new "level-based" systems have been described that are

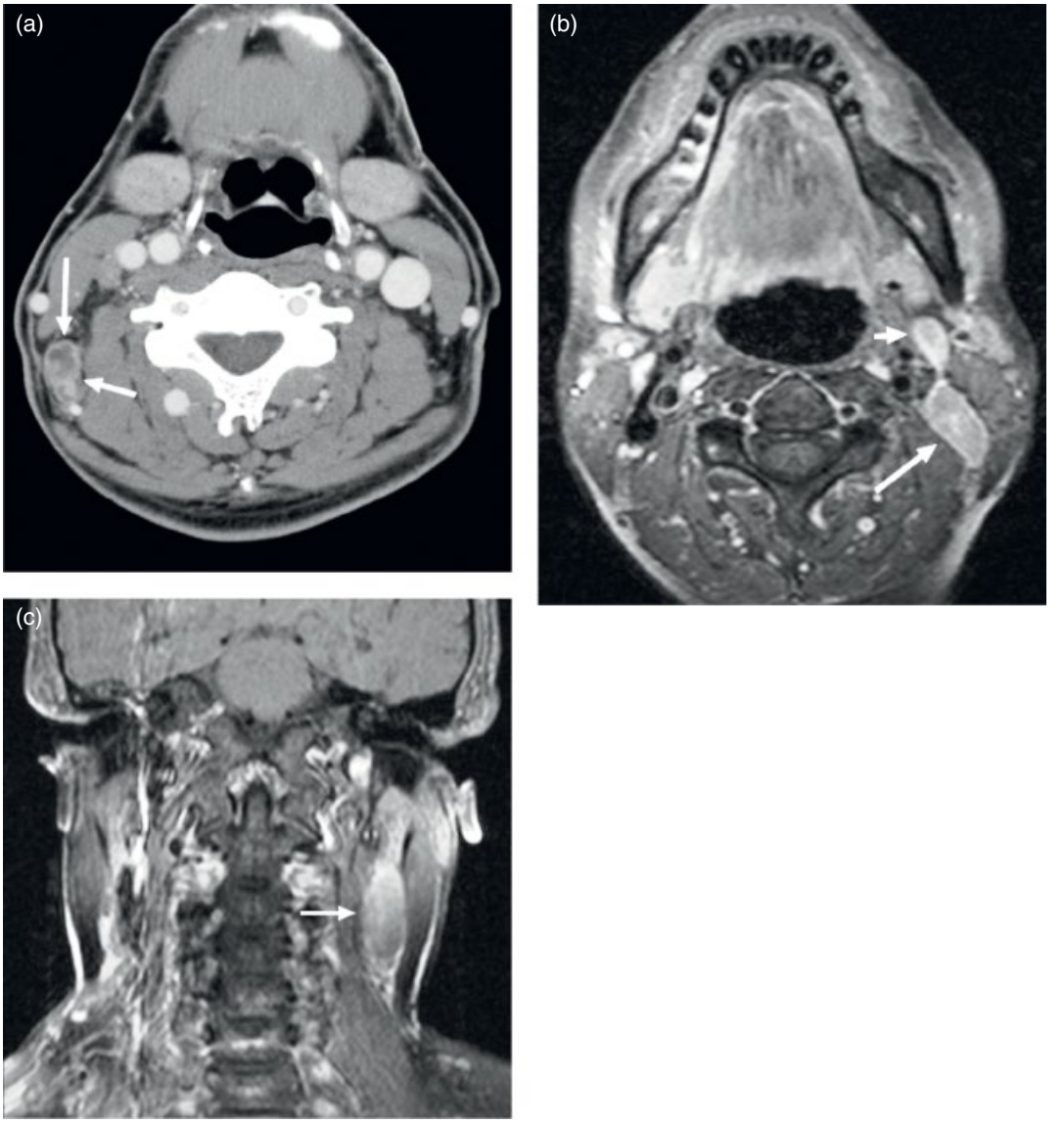


Figure 19.34 Metastatic posterior cervical triangle and internal jugular chain nodes. (a) Axial postcontrast computed tomography showing a metastatic right posterior cervical triangle chain node (arrow). The low density in the center of the node suggests necrosis; this is often seen with metastatic squamous cell carcinoma. (b) Axial postgadolinium fat-saturated T1-weighted MRI through the level of the mandibular alveolar ridge, showing metastatic left internal jugular (short arrow) and posterior cervical triangle (long arrow) nodes. (c) Coronal postgadolinium fat-saturated T1-weighted MRI through the level of the odontoid process, showing the same posterior cervical triangle node as in (b) (arrow).

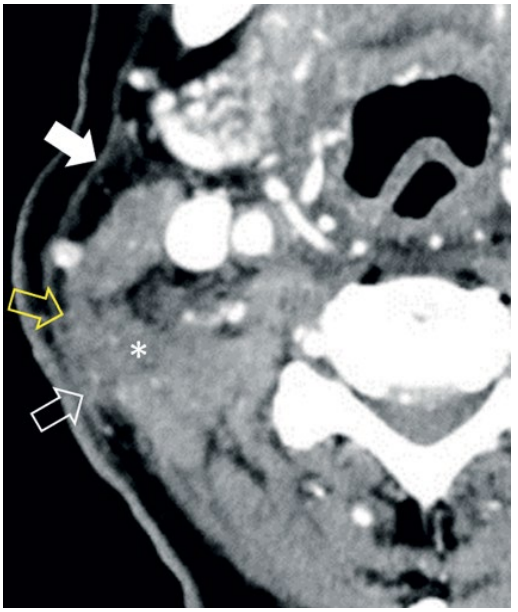


Figure 19.35 Extranodal extension (ENE). Axial reconstruction of contrast-enhanced computed tomography at the level of the basal process of the mandible and vallecula, displaying ENE in a node in the right neck. The asterisk denotes the center of the node. The yellow-outlined arrow indicates the fuzzy irregular border of the ENE as it extends well outside its lymph-node capsule. The solid white arrow identifies the normal deep cervical fascia, whereas the white-outlined arrows indicates infiltration of the fascia by the ENE.

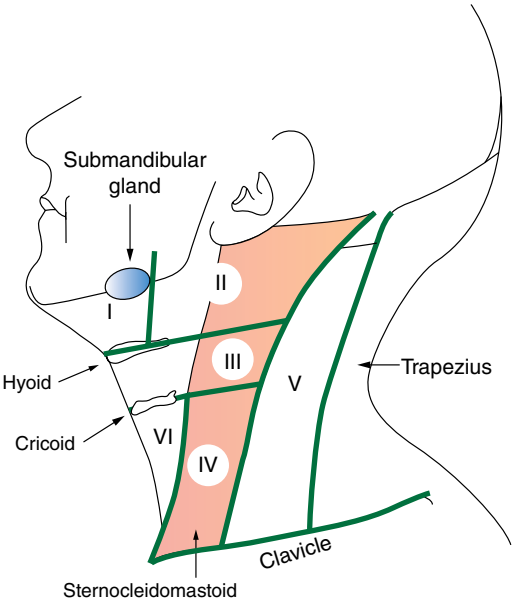


Figure 19.36 Level system of lymph node classification (see Table 19.2 for explanation).

designed to be used with cross-sectional imaging. The three most widely used are the AJCC system, the 1998 modification of the American Academy of Otolaryngology Head and Neck Surgery system, and Som et al.'s imaging-based system [68] (Figure 19.36 and Table 19.2). All three use similar major landmarks to define six or seven different cervical levels (I–VII); see Som et al. [69–71]. These level systems resolve most of the ambiguity that occurs when attempts are made to apply Rouvière's system to cross-sectional imaging. The boundaries of the level systems are also aligned with lymphatic drainage pathways. Precise literature is available describing which levels specific head and neck anatomical structures drain into [65].

SCCs of the neck are staged via the "TNM" or tumor, node, metastasis system. The primary tumor is first given a T grade from 1 to 4 based on the size of the tumor and the presence and degree of invasion of surrounding structures. The N grade from 0 to 3 is determined by the number, size, and distribution of lymph node metastases. The M grade is scored from 0 to 1 on the presence or absence of distant metastases. Hence, the reader may encounter tumor staging nomenclature such as "T1N2M0" in reference to SCC. For a complete description of the TNM system, see the AJCC staging manual [72]. TNM staging is extremely important, because it determines the patient's prognosis and optimum treatment.

Table 19.2 Som's level system of cervical lymph node classification for use with cross-sectional imaging in the transverse (axial) plane.

Level	Location	Contains
I	Above hyoid bone Below mylohyoid muscle Anterior to posterior border of submandibular gland	Submandibular and submental nodes
II	Between hyoid bone and skull base Anteriorly bounded by back of submandibular gland Posteriorly by back of sternocleidomastoid	Jugulodigastric and upper internal jugular chain nodes
III	Between hyoid bone and cricoid cartilage Anterior to back of sternocleidomastoid Lateral to carotid artery	Mid internal jugular chain nodes
IV	Between cricoid cartilage and clavicle Anterior to line connecting posterior margins of sternocleidomastoid/scalenus anterior	Lower internal jugular chain nodes
V	Posterior cervical triangle nodes Between posterior to line connecting posterior margins of sternocleidomastoid/scalenus anterior and anterior edge of trapezius	Posterior cervical triangle chain nodes
VI	Between hyoid bone and manubrium Medial to carotid arteries	
VII	Behind manubrium	Level VII nodes
Other levels	Medial to carotid arteries Within 2 cm of skull base	Retropharyngeal nodes
	Below clavicle Lateral to internal carotid arteries	Supraclavicular nodes

Source: Som PM, Curtin HD, Mancuso AA. Imaging-based nodal classification for evaluation of neck metastatic adenopathy. *Am. J. Roentgenol.* 2000;174:837–844.

19.9 Radiological Reporting of Head and Neck Tumors

Although the radiologist (including the functional imaging physician) will describe HNTs according to the TNM system, the clinician should be aware of the impact of the AJCC's eighth edition on the radiological reporting of HNTs [3]. Glastonbury et al. have noted a number of important changes since the seventh edition that may affect how the radiologist reports such cancer [73]. These are tabulated in Table 19.1.

In addition to the three groups of HNTs which have already been addressed, namely base of the skull, salivary gland malignancies, and aerodigestive malignancies (SCCs and lymphomas), the radiologist will be alive to other very rare HNTs (such as melanomas) and malignancies

which arise elsewhere in the body, including the brain. The radiologist and/or functional imaging physician may, besides other imaging modalities, suggest other tests that may be performed by other specialists. The latter is a product of the increasing breakdown of the "specialist silo" due to the current interdisciplinary approach to residency training and to interdisciplinary case conferences, such as the weekly HNT case conference at BCCA and many other similar institutions. The BCCA HNT group conference is further enhanced by telemedicine links with other BCCA centers providing cancer care in more remote communities. This allows the clinicians caring for such remotely treated patients access to comment and advice from the wider specialist community. Needless to say, in order to preserve patient confidentiality, access to such conferences is confined to approved personnel. Similar centers in the USA include the National Institutes of Health's (NIH) National Cancer Institute (NCI) designated cancer centers.

19.9.1 "CANCER OF UNKNOWN PRIMARY"

When a patient presents with predominantly cervical adenopathy and no clinically obvious primary tumor, then it is termed a *cancer of unknown primary* (CUP) as mentioned earlier. Such a case is displayed in Figure 19.31. The search for the primary evaded CECT (Figure 19.32a), but was obvious as avidity in the right palatine tonsil (Figure 19.32b). Although the CECT revealed bilateral cervical adenopathy, the PET/CT revealed that while the right side was avid, the large necrotic or cystic node in the neck was not. The latter did give rise to a slight annular avidity. The area of hypoavidity in the former node indicated a necrotic area. Central necrosis is typical of metastatic nodes. An intensive search is undertaken as indicated by Figure 19.29, which involves CT investigations of the thorax (lungs), and abdomen (including pelvis). Lung tumors can metastasize to the basal cervical region and tumors in the abdomen can travel up paraspinal lymphatics to lodge in the "left prescalene" or Virchow's node, near the thoracic duct. The latter node is called a *sentinel* or *signal node* because of its ability to signal the presence of tumor in the abdomen [66, 73]. According to Lydiatt et al., the eighth edition of the AJCC created "T0" for CUP cases [74].

The precise annual incidence of CUPs cannot be known, because when the primary of some cancers initially designated as CUPs is later found, the CUP designation may disappear from the subsequent statistics. Nevertheless, the American Cancer Society (ACS) estimates that about 33 770 cases of CUP will have been diagnosed by December 2018 in the United States, representing about 2% of all cancers [75].

When metastatic nodal disease is found, predominantly in the mid and upper neck, a search for an upper aerodigestive tract carcinoma should be initiated; 70–90% of these cases are SCC [76]. Postcontrast CT and/or MRI is performed and if a primary tumor is not found, multiple biopsies are taken, initially from suspicious regions and then from a grid layout. If these investigations are negative, an FDG PET/CT is indicated. FDG PET/CT will detect the primary tumor in about 30% of cases where CT and MRI have failed [77, 78]. Although still superior to CT and MRI, PET/CT is least sensitive toward detecting primary tumors in the tongue base and tonsils [79]. If the PET/CT is negative, and a primary tumor is not found,

a diagnosis of CUP is made. Since the primary of the CUP displayed in Figure 19.32a and b was eventually discovered, this case can no longer be referred to as a CUP. Kelly and Curtain suggested that a cervical node with a cystic appearance should prompt consideration of "primary SCC arising in the lymphoid tissue of the palatine tonsil or tongue base [58]. Figure 19.32a and b reveals such a case. In 5% of these cases the primary tumor will never be found, despite intensive work-up [80].

19.9.2 OTHER CAUSES OF MALIGNANT CERVICAL NODE ENLARGEMENT

There are other malignant causes of cervical adenopathy, including metastatic disease from elsewhere in the body, lymphoma, and leukemia. These can present as multiple discrete enlarged nodes (e.g. chronic lymphocytic leukemia, Figure 19.37a and b) and/or confluent masses (diffuse large B-cell lymphoma, Figure 19.37c and d). In addition, there are numerous non-neoplastic conditions that cause enlarged cervical nodes; a discussion of these is beyond the scope of this book. The interested reader is referred to review articles by Ferrer [81] and Kaji et al. [82].

19.10 Radiation Therapy and the Role of the Radiation Oncologist

After their initial diagnosis, most patients are seen by a surgical oncologist or otolaryngologist, as well as a *radiation oncologist* (RO). An RO is a medical specialist doctor with training in the use of radiation therapy to treat or reduce the symptoms of cancer. The RO will review the patient's history, perform a physical examination, and complete the necessary staging investigations to assist in developing the optimal treatment options for the patient. If the regimen includes radiation therapy, and the patient consents to the potential side effects and goals of treatment, the patient will then be seen by an oncology dentist, nurse, dietician, and speech/swallowing therapist. An immobilization shell will be constructed so that the patient's treatment set-up can be accurately reproduced on a daily basis for each treatment. A contrast-enhanced CT scan is obtained with the patient in the treatment shell; these images are then imported into a software system to plan the course of radiation.

The construction of a radiotherapy plan is an interdisciplinary process. It begins with the acquisition of CT images with the patient in the treatment position. The RO is responsible for contouring targets to treat (i.e. tumors, lymph nodes, and high-risk regions) and organs to avoid (i.e. spinal cord, brain stem, mandible, salivary glands) on the CT images. Some tumors and normal structures are more accurately identified on MRI or PET images; these images can be superimposed on top of the CT images for optimal tumor and organ localization (Figure 19.38). Local tumor extent may also be influenced by the physical examination. Radiation dose calculations are based on the electron density information in CT images. Using CT images and radiotherapy planning software, a radiation dosimetrist and medical physicist then construct and calculate a radiation plan based on the contours (Figure 19.38d). Head and neck cancer regimens at modern radiotherapy centers are usually treated with either *three-dimensional conformal radiotherapy* (3DCRT) or *intensity-modulated radiotherapy* (IMRT).

Typical curative radiotherapy regimens range between 25 and 35 treatments,

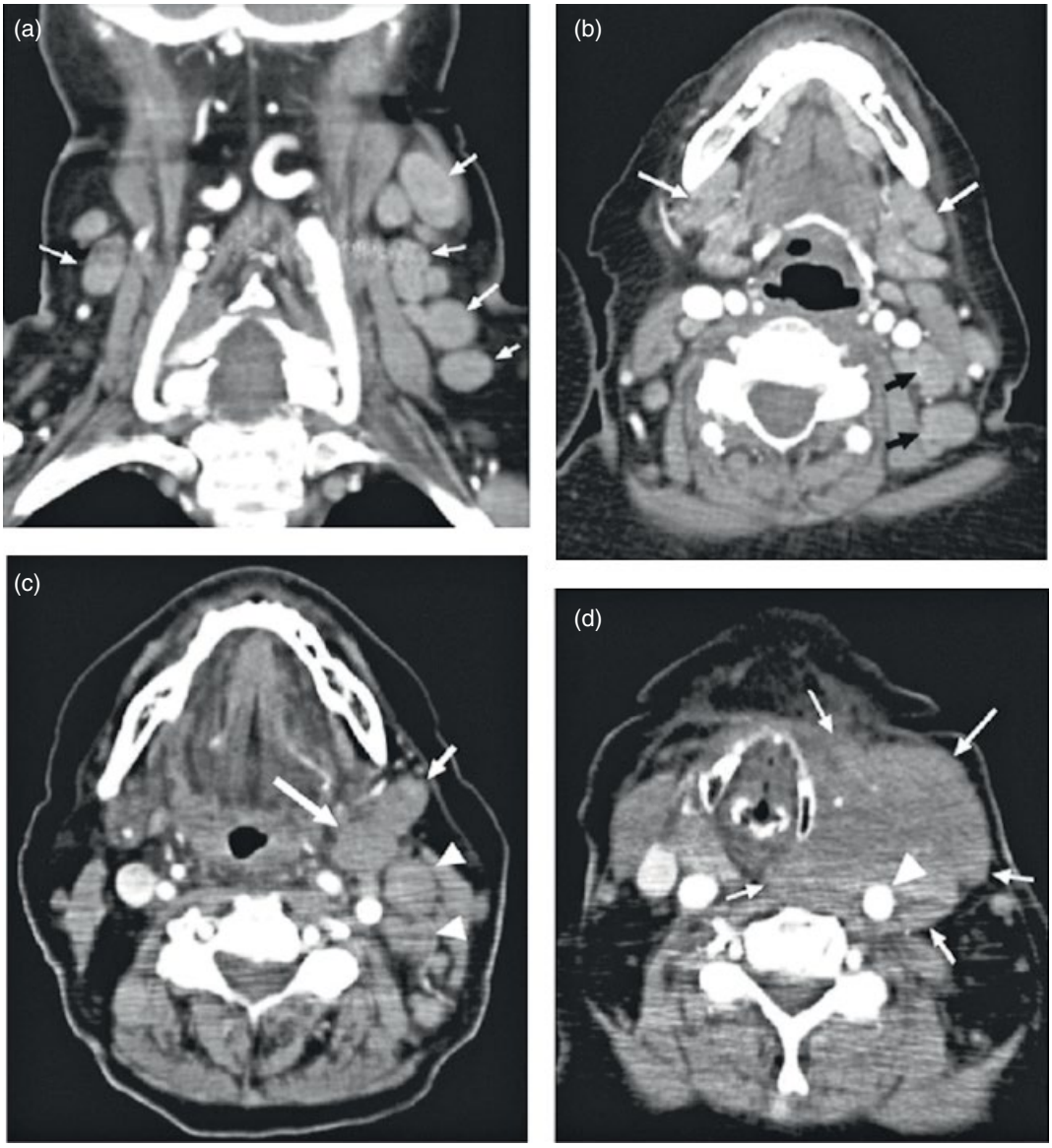


Figure 19.37 Systemic causes of malignant cervical adenopathy. (a) Coronal postcontrast computed tomography (CT) showing moderate bilateral cervical adenopathy (arrows) from chronic lymphocytic leukemia. (b) Axial postcontrast CT of the same patient showing bilateral submandibular adenopathy (white arrows) and left posterior cervical triangle chain nodes (black arrows). (c) Axial postcontrast CT from a patient with diffuse large B-cell lymphoma. Note the left submandibular (short arrow) and internal jugular chain (long arrow) nodes. The two enlarged nodes (arrowheads) medial to the left sternocleidomastoid muscle are challenging to classify using older nomenclature. Is the more anterior node an internal jugular chain node or a posterior cervical triangle chain node? This ambiguity is resolved using newer level systems of nodal classification (see Table 19.2). (d) The same patient as in (c) at a more inferior level. The adenopathy has coalesced into a huge mass (arrows) that is encasing the left internal carotid artery (arrowhead) and markedly displacing the larynx to the right. (e) Coronal postcontrast CT of the same patient as in (c). Note the large confluent nodal mass encasing the left internal carotid artery (arrowheads).

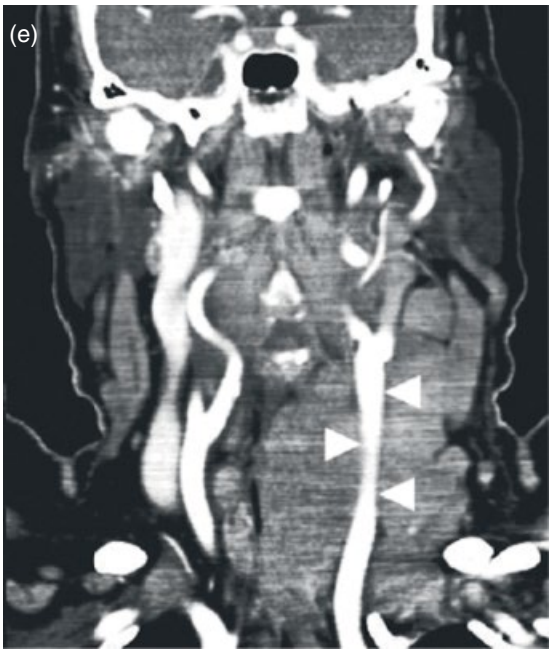


Figure 19.37 (Continued)

usually once a day, five days a week; palliative regimens range between 5 and 20 treatments. Treatments are delivered on a daily basis by *radiation therapists* (RT). Routine checks are conducted by the RT and RO to ensure that the patient's position and treatments are reliably reproduced. During the course of therapy, the RO and nurses will manage the patient's acute side effects.

19.10.1 IMPORTANCE OF COLLABORATION BETWEEN DIAGNOSTIC RADIOLOGY AND RADIATION THERAPY

The diagnostic radiologist and nuclear medicine physician have important roles in patient care, and may begin at the pre-diagnosis stage, where they are involved with image-guided biopsies. Once a malignant diagnosis has been established, they interpret staging investigations including plain radiographs, bone scans, CT, MRI, and PET scans. At the BCCA, they are also active participants in the weekly interdisciplinary tumor conferences, where they will review appropriate images related to cases being discussed.

By the accurate identification of the primary tumor and involved lymph nodes, CT, MRI, and FDG PET/CT contribute to the delineation of the radiation therapy portal, as the *gross tumor volume* (GTV) is important in determination of the contour volume [3].

In addition, the diagnostic radiologist also plays an important role during the radiotherapy planning process. Modern head and neck radiotherapy techniques are heavily dependent on imaging modalities; radiation tumors and avoidance structures must be identified and drawn on each CT

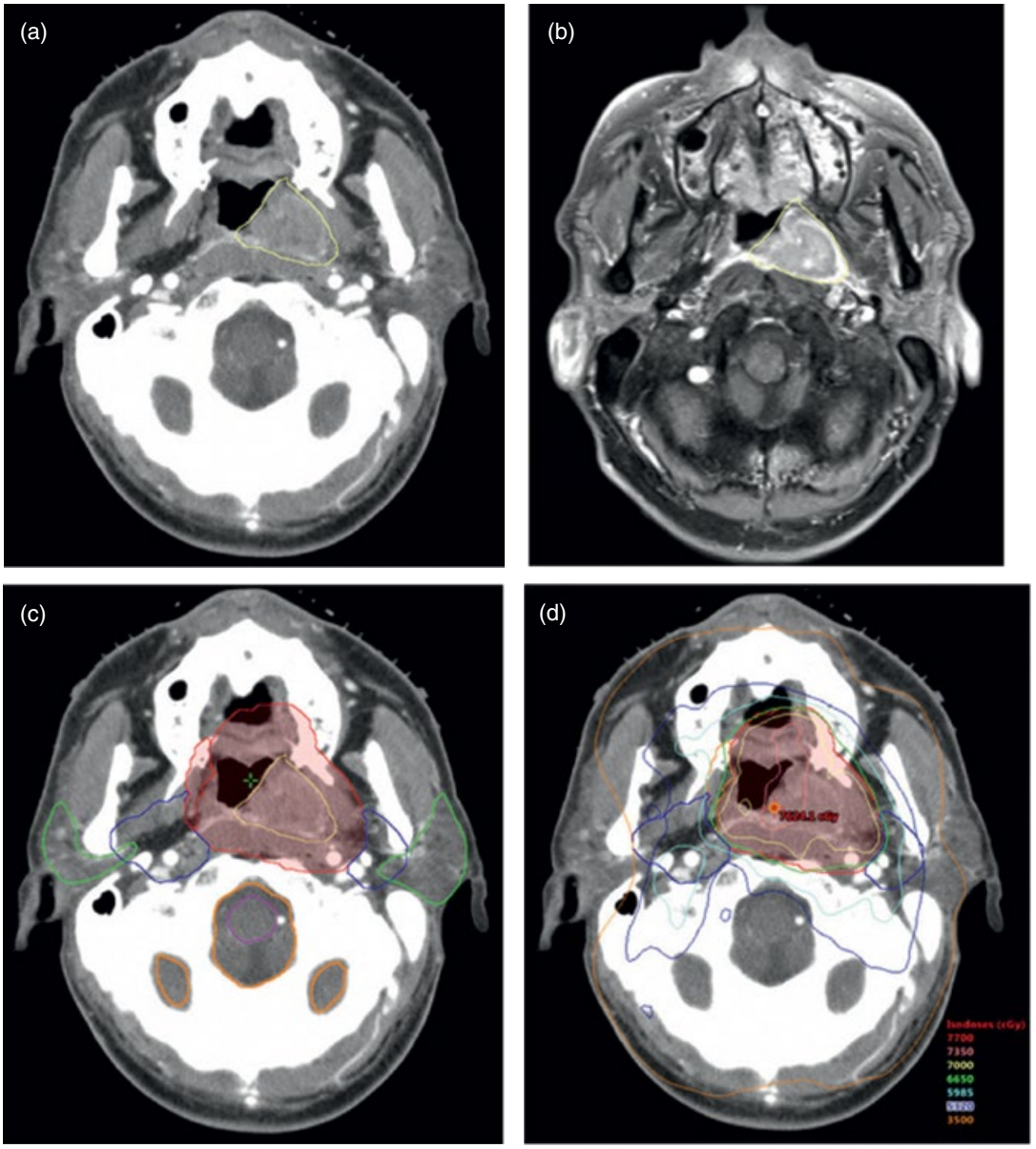


Figure 19.38 Radiotherapy contours and radiation plan for a nasopharyngeal carcinoma. (a) Identifying the nasopharyngeal carcinoma (yellow contour) on a computed tomography (CT) image. (b) The same contour is identified on the corresponding magnetic resonance image. Note the improved soft-tissue differentiation compared to the CT image. (c) Additional contours, including the high-risk volume surrounding the gross tumor (red), and a lower-risk volume encompassing the adjacent lymph node regions (blue). Organ-sparing regions are also contoured, including the parotid glands (green), spinal cord (magenta), and brain (orange). (d) The calculated radiation plan and isodose lines.

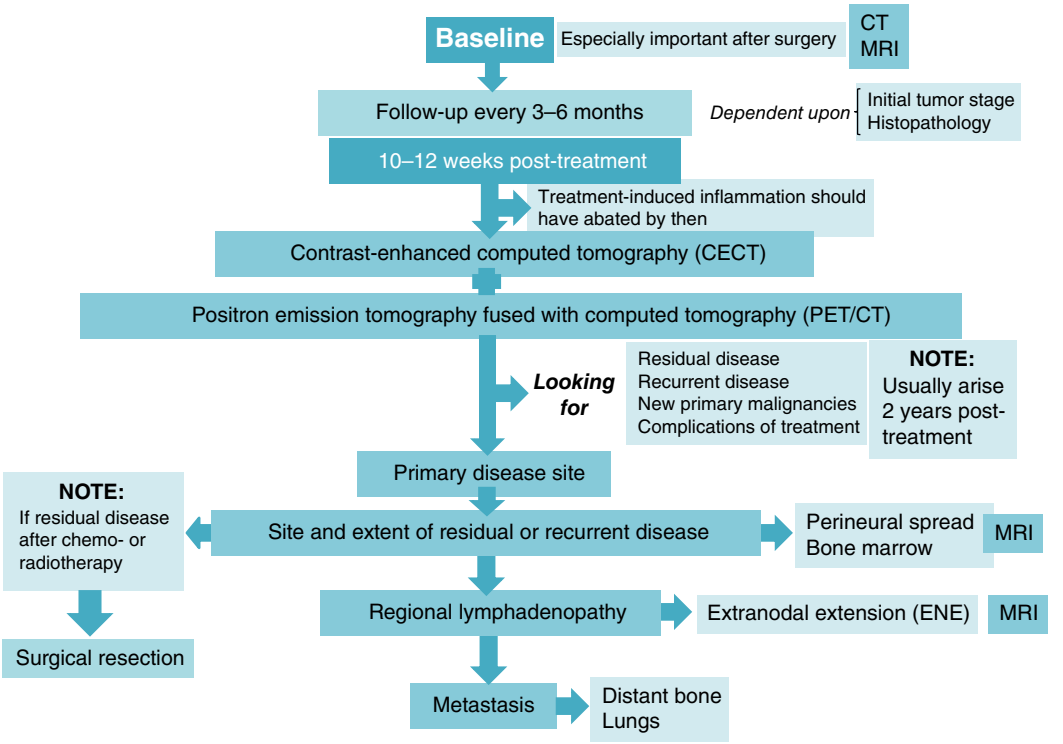


Figure 19.39 Flowchart revealing the essential stages with the most appropriate imaging modalities for follow-up after primary treatment of a malignancy affecting the head and neck.

slice in order to construct and calculate an appropriate radiotherapy plan. Failure to adequately identify structures may lead to underdosing of tumors or overdosing of critical organs. It is occasionally difficult to identify the local extent of disease, particularly cases involving the base of skull, perineural invasion, or equivocal cervical lymphadenopathy. For these cases, it is important to have a strong collaborative relationship between the RO and diagnostic radiologist to accurately delineate radiation targets and avoidance structures. At the BCCA, there are treatment planning (contouring) workstations in the diagnostic imaging department to facilitate interdisciplinary consultation and contouring of challenging cases. Thus, the diagnostic radiologist and nuclear medicine physician are integral members of the interdisciplinary head and neck team.

19.10.2 AFTER A COURSE OF RADIATION THERAPY

After completion of radiotherapy, the patient's response to therapy, including long-term side effects, will be monitored by the RO, dentist, dietician, speech/language therapist, and other clinicians every two to six months, for up to five years or longer. CT, MRI, and PET/CT will be undertaken as required, as indicated in Figure 19.39.

19.10.3 IMAGING OF THE POST-TREATMENT MANAGEMENT OF CANCER OF THE HEAD AND NECK

After diagnosis, treatment planning, and treatment of the cancer, generally in line with protocols but tailored as necessary

for that particular patient, the patient is still subject to management of the primary lesion. This entails follow-up and any retreatment as necessary. Again, these are performed in accordance with protocols and invariably involve cross-sectional radiology.

CECT and MRI are performed after treatment, particularly after surgery, to establish a baseline. At or just prior to the third month following primary treatment, a PET/CT is performed, by which time the treatment-induced inflammation should have abated. Therefore, any avid areas will represent residual disease. If there is none, then it is reasonable to surmise, in the absence of any other adverse features, that primary treatment has so far been successful. Some imaging may indicate a complication. If subsequent follow-up visits indicate the possibility of a recurrence, then CECT, MRI, PET/CT are indicated. If this happens, it is generally about two years after the primary treatment. Again, a biopsy and staging are required. Recently, imaging of the cervical lymph nodes has been performed to determine not simply whether an enlarged lymph node is neoplastic or reactive, but whether there is extracapsular spread of the metastatic deposit from the lymph node out into the adjacent tissues, in other words an ENE, as discussed earlier.

References

1. Chen, Y.J., Rath, T., and Mohan, S. (2018). PET-computed tomography in head and neck cancer: current evidence and future directions. *Magn. Reson. Imaging Clin. N. Am.* 26: 37–49.
2. El-Naggar, A.K., JKC, C., Grandis, J.R. et al. (eds.) (2017). *WHO Classification of Head and Neck Tumours*, 1–184. Lyon: International Agency for Research on Cancer (IARC).
3. Amin, M.B., Edge, S., Greene, F. et al. (eds.) (2017). *AJCC Cancer Staging Manual*. Springer International.
4. MacDonald, D., Li, T., Leung, S.F. et al. (2017). Extranodal lymphoma arising within the maxillary alveolus: a case report. *Oral Surg. Oral Med. Oral Pathol. Oral Radiol.* 124: e233–e238.
5. Angtuaco, E.J., Fassas, A.B., Walker, R. et al. (2004). Multiple myeloma: clinical review and diagnostic imaging. *Radiology* 231: 11–23.
6. Baumhoer, D., Bullerdiek, J., Chordoma, N.P. et al. (eds.) (2017). *WHO Classification of Head and Neck Tumours*, 76. Lyon: International Agency for Research on Cancer (IARC).
7. Doucet, V., Peretti-Viton, P., Figarella-Branger, D. et al. (1997). MRI of intracranial chordomas. Extent of tumour and contrast enhancement: criteria for differential diagnosis. *Neuroradiology* 39: 571–576.
8. Mendenhall, W.M., Mendenhall, C.M., Lewis, S.B. et al. (2005). Skull base chordoma. *Head Neck* 27: 159–165.
9. Erdem, E., Angtuaco, E.C., Van Hemert, R. et al. (2003). Comprehensive review of intracranial chordoma. *Radiographics* 23: 995–1009.
10. Baumhoer, D., Casiraghi, O., Coleman, H. et al. (2017). Chondrosarcoma. In: *WHO Classification of Head and Neck Tumours* (ed. A.K. El-Naggar, C. JKC, J.R. Grandis, et al.), 243–244. Lyon: International Agency for Research on Cancer (IARC).
11. Hong, P., Taylor, S.M., Trites, J.R. et al. (2009). Chondrosarcoma of the head and neck: report of 11 cases and literature review. *J. Otolaryngol. Head Neck Surg.* 38: 279–285.
12. Koch, B.B., Karnell, L.H., Hoffman, H.T. et al. (2000). National cancer database report on chondrosarcoma of the head and neck. *Head Neck* 22: 408–425.
13. Mark, R.J., Tran, L.M., Sercarz, J. et al. (1993). Chondrosarcoma of the head and neck. The UCLA experience, 1955–1988. *Am. J. Clin. Oncol.* 16: 232–237.
14. Bell, D., Franchi, A., Gillison, M. et al. (2017). Olefactory neuroblastoma. In: *WHO Classification of Head and Neck Tumours* (ed. A.K. El-Naggar, C. JKC, J.R. Grandis, et al.), 57–59. Lyon: International Agency for Research on Cancer (IARC).
15. Bradley, P.J., Jones, N.S., and Robertson, I. (2003). Diagnosis and management of esthesioneuroblastoma. *Curr. Opin. Otolaryngol. Head Neck Surg.* 11: 112–118.

16. Zollinger, L.V., Wiggins, R.H. 3rd, Cornelius, R.S., and Phillips, C.D. (2008). Retropharyngeal lymph node metastasis from esthesioneuroblastoma: a review of the therapeutic and prognostic implications. *Am. J. Neuroradiol.* 29: 1561–1563.
17. Cuadra-Garcia, I., Proulx, G.M., Wu, C.L. et al. (1999). Sinonasal lymphoma: a clinicopathologic analysis of 58 cases from the Massachusetts General Hospital. *Am. J. Surg. Pathol.* 23: 1356–1369.
18. Zhu, L., Fang, P., Liu, Y., and Tong, B. (2015). Clinical and diagnosis analysis of malignant lymphoma in nasal cavity and paranasal sinus. *Lin Chung Er Bi Yan Hou Tou Jing Wai Ke Za Zhi (J. Clin. Otorhinolaryngol. Head Neck Surg.)* 29: 255–257. (Chinese).
19. Tababi, S., Kharrat, S., Sellami, M. et al. (2012). Extranodal NK/T-cell lymphoma, nasal type: report of 15 cases. *Eur. Ann. Otorhinolaryngol. Head Neck Dis.* 129: 141–147.
20. Lewis, J.S., Bishop, J.A., Gillison, M. et al. (2017). Sinonasla undifferentiated carcinoma. In: *WHO Classification of Head and Neck Tumours* (ed. A.K. El-Naggar, C. JKC, J.R. Grandis, et al.), 18–20. Lyon: International Agency for Research on Cancer (IARC).
21. Mendenhall, W.M., Mendenhall, C.M., Riggs, C.E. Jr. et al. (2006). Sinonasal undifferentiated carcinoma. *Am. J. Clin. Oncol.* 29: 27–31.
22. Kim, B.S., Vongtama, R., and Juillard, G. (2004). Sinonasal undifferentiated carcinoma: case series and literature review. *Am. J. Otolaryngol.* 25: 162–166.
23. Musy, P.Y., Reibel, J.F., and Levine, P.A. (2002). Sinonasal undifferentiated carcinoma: the search for a better outcome. *Laryngoscope* 112: 1450–1455.
24. Seethala, R.R. (2017). Salivary gland tumors: current concepts and controversies. *Surg. Pathol. Clin.* 10: 155–176.
25. El-Naggar, A.K., Chan, J.K.C., Grandis, J.R. et al. (eds.) (2017). *WHO Classification of Head and Neck Tumours*, 163–184. Lyon: International Agency for Research on Cancer (IARC).
26. Ellis, G.L., Auclair, P.L., Armed Forces Institute of Pathology, and Universities Associated for Research and Education in Pathology (1996). *Tumours of the Salivary Glands*. Washington, DC: Armed Forces Institute of Pathology, under the auspices of Universities Associated for Research and Education in Pathology.
27. Brandwein-Gensler, M., Bell, D., Inagaki, H. et al. (2017). Mucoepidermoid carcinoma. In: *WHO Classification of Head and Neck Tumours* (ed. A.K. El-Naggar, C. JKC, J.R. Grandis, et al.), 163–164. Lyon: International Agency for Research on Cancer (IARC).
28. Boahene, D.K., Olsen, K.D., Lewis, J.E. et al. (2004). Mucoepidermoid carcinoma of the parotid gland: the Mayo Clinic experience. *Arch. Otolaryngol. Head Neck Surg.* 130: 849–856.
29. Hyam, D.M., Veness, M.J., and Morgan, G.J. (2004). Minor salivary gland carcinoma involving the oral cavity or oropharynx. *Aust. Dent. J.* 49: 16–19.
30. Henze, M. and Hittel, J.P. (2001). Mucoepidermoid carcinoma of the salivary glands after high dosage radiotherapy. *Laryngo-Rhino-Otologie* 80: 253–256.
31. Stenman, G., Licitra, L., said-Al-Naief, N. et al. (2017). Adenoid cystic carcinoma. In: *WHO Classification of Head and Neck Tumours* (ed. A.K. El-Naggar, C. JKC, J.R. Grandis, et al.), 164–165. Lyon: International Agency for Research on Cancer (IARC).
32. Garden, A.S., Weber, R.S., Morrison, W.H. et al. (1995). The influence of positive margins and nerve invasion in adenoid cystic carcinoma of the head and neck treated with surgery and radiation. *Int. J. Radiat. Oncol. Biol. Phys.* 32: 619–626.
33. Saremi, F., Helmy, M., Farzin, S. et al. (2005). MRI of cranial nerve enhancement. *Am. J. Roentgenol.* 185: 1487–1497.
34. Nemzek, W.R., Hecht, S., Gandour-Edwards, R. et al. (1998). Perineural spread of head and neck tumours: how accurate is MR imaging? *Am. J. Neuroradiol.* 19: 701–706.
35. Catalano, P.J., Sen, C., and Biller, H.F. (1995). Cranial neuropathy secondary to perineural spread of cutaneous malignancies. *Am. J. Otolaryngol.* 16: 772–777.
36. Vrielinck, L.J., Ostyn, F., van Damme, B. et al. (1988). The significance of perineural spread in adenoid cystic carcinoma of the major and minor salivary glands. *Int. J. Oral Maxillofac. Surg.* 17: 190–193.
37. Singh, F.M., Mak, S.Y., and Bonington, S.C. (2015). Patterns of spread of head and neck

adenoid cystic carcinoma. *Clin. Radiol.* 70: 644–653.
38. Simpson, R.H.W., Chiosea, S., Katabi, N. et al. (2017). Acinic cell carcinoma. In: *WHO Classification of Head and Neck Tumours* (ed. A.K. El-Naggar, C. JKC, J.R. Grandis, et al.), 166–167. Lyon: International Agency for Research on Cancer (IARC).
39. Al-Zaher, N., Obeid, A., Al-Salam, S., and Al-Kayyalic, B.S. (2009). Acinic cell carcinoma of the salivary glands: a literature review. *Hematol. Oncol. Stem Cel Ther.* 2: 259.
40. Kim, S.A. and Mathog, R.H. (2005). Acinic cell carcinoma of the parotid gland: a 15-year review limited to a single surgeon at a single institution. *Ear Nose Throat J.* 84: 597–602.
41. Pezzuto, F., Buonaguro, L., Caponigro, F. et al. (2015). Update on head and neck cancer: current knowledge on epidemiology, risk factors, molecular features and novel therapies. *Oncology* 89: 125–136.
42. D'Souza, G., Kreimer, A.R., Viscidi, R. et al. (2007). Case-control study of human papilloma virus and oropharyngeal cancer. *N. Engl. J. Med.* 356: 1944–1956.
43. Chien, Y.C., Chen, J.Y., Liu, M.Y. et al. (2001). Serologic markers of Epstein-Barr virus infection and nasopharyngeal carcinoma in Taiwanese men. *N. Engl. J. Med.* 345: 1877–1882.
44. Raab-Traub, N. (2002). Epstein-Barr virus in the pathogenesis of NPC. *Semin. Cancer Biol.* 12: 431–441.
45. Cruz, I., Van Den Brule, A.J., Brink, A.A. et al. (2000). No direct role for Epstein-Barr virus in oral carcinogenesis: a study at the DNA, RNA and protein levels. *Int. J. Cancer* 86: 356–361.
46. Bray, F., Haugen, M., Moger, T.A. et al. (2008). Age-incidence curves of nasopharyngeal carcinoma worldwide: bimodality in low-risk populations and aetiologic implications. *Cancer Epidemiol. Biomark. Prev.* 17: 2356–2365.
47. Chong, V.F., Fan, Y.F., and Khoo, J.B. (1996). Nasopharyngeal carcinoma with intracranial spread: CT and MR characteristics. *J. Comput. Assist. Tomogr.* 20: 563–569.
48. Ilhan, O., Sener, E.C., and Ozyar, E. (2002). Outcome of abducens nerve paralysis in patients with nasopharyngeal carcinoma. *Eur. J. Ophthalmol.* 12: 55–59.
49. Marur, S. and Forastiere, A.A. (2008). Head and neck cancer: changing epidemiology, diagnosis, and treatment. *Mayo Clin. Proc.* 83: 489–501. Erratum in *Mayo Clin. Proc.* 2008; 83:604.
50. Auluck, A., Walker, B.B., Hislop, G. et al. (2014). Population-based incidence trends of oropharyngeal and oral cavity cancers by sex among the poorest and underprivileged populations. *BMC Cancer* 14: 316.
51. Auluck, A., Hislop, G., Bajdik, C. et al. (2010). Trends in oropharyngeal and oral cavity cancer incidence of human papillomavirus (HPV)-related and HPV-unrelated sites in a multicultural population: the British Columbia experience. *Cancer* 116: 2635–2644.
52. Mehanna, H., Evans, M., Beasley, M. et al. (2016). Oropharyngeal cancer: United Kingdom National Multidisciplinary Guidelines. *J. Laryngol. Otol.* 130: S90–S96.
53. Binahmed, A., Nason, R.W., Abdoh, A.A., and Sandor, G.K. (2007). Population-based study of treatment outcomes in squamous cell carcinoma of the retromolar trigone. *Oral Surg. Oral Med. Oral Pathol. Oral Radiol. Endod.* 104: 662–665.
54. Lane, A.P., Buckmire, R.A., Mukherji, S.K. et al. (2000). Use of computed tomography in the assessment of mandibular invasion in carcinoma of the retromolar trigone. *Otolaryngol. Head Neck Surg.* 122: 673–677.
55. Crecco, M., Vidiri, A., Angelone, M.L. et al. (1999). Retromolar trigone tumours: evaluation by magnetic resonance imaging and correlation with pathological data. *Eur. J. Radiol.* 32: 182–188.
56. Ginsberg, L.E. and DeMonte, F. (1998). Imaging of perineural tumour spread from palatal carcinoma. *Am. J. Neuroradiol.* 19: 1417–1422.
57. Helliwell, T.R. (2003). Best practice no 169: evidence based pathology: squamous carcinoma of the hypopharynx. *J. Clin. Pathol.* 56: 81–85.
58. Kelly, H.R. and Curtin, H.D. (2017). Chapter 2 squamous cell carcinoma of the head and neck-imaging evaluation of regional lymph nodes and implications for management. *Semin. Ultrasound CT MR* 38: 466–478.

59. Elsheikh, M.N., Rinaldo, A., Hamakawa, H. et al. (2006). Importance of molecular analysis in detecting cervical lymph node metastasis in head and neck squamous cell carcinoma. *Head Neck* 28: 842–849.
60. Friedman, M., Roberts, N., Kirshenbaum, G.L., and Colombo, J. (1993). Nodal size of metastatic squamous cell carcinoma of the neck. *Laryngoscope* 103: 854–856.
61. Don, D.M., Anzai, Y., Lufkin, R.B. et al. (1995). Evaluation of cervical lymph node metastases in squamous cell carcinoma of the head and neck. *Laryngoscope* 105: 669–674.
62. van den Brekel, M.W., Stel, H.V., Castelijns, J.A. et al. (1990). Cervical lymph node metastasis: assessment of radiologic criteria. *Radiology* 177: 379–384.
63. van den Brekel, M.W., Castelijns, J.A., and Snow, G.B. (1998). The size of lymph nodes in the neck on sonograms as a radiologic criterion for metastasis: how reliable is it? *Am. J. Neuroradiol.* 19: 695–700.
64. Mancuso, A.A., Harnsberger, H.R., Muraki, A.S., and Stevens, M.H. (1983). Computed tomography of cervical and retropharyngeal lymph nodes: normal anatomy, variants of normal, and applications in staging head and neck cancer. Part II: pathology. *Radiology* 148: 715–723.
65. Cervin, J.R., Silverman, J.F., Loggie, B.W., and Geisinger, K.R. (1995). Virchow's node revisited. Analysis with clinicopathologic correlation of 152 fine-needle aspiration biopsies of supraclavicular lymph nodes. *Arch. Pathol. Lab. Med.* 119: 727–730.
66. Loh, K.Y. and Yushak, A.W. (2007). Images in clinical medicine. Virchow's node (Troisier's sign). *N. Engl. J. Med.* 357: 282.
67. Rouvière, H. (1938). *Anatomy of the Human Lymphatic System, a Compendium Translated from the Original. Anatomie des Lymphatiques de l'Homme* (trans. M. J. Tobias). Ann Arbor, MI: Edwards Bros.
68. Som, P.M., Curtin, H.D., and Mancuso, A.A. (2000). Imaging-based nodal classification for evaluation of neck metastatic adenopathy. *Am. J. Roentgenol.* 174: 837–844.
69. Som, P.M., Curtin, H.D., and Mancuso, A.A. (1999). An imaging-based classification for the cervical nodes designed as an adjunct to recent clinically based nodal classifications. *Arch Otolaryngol. Head Neck Surg.* 125: 388–396.
70. Som, P.M. and Curtin, H.D. (2003). *Head and Neck Imaging*, 4e. Mosby, St.: Louis.
71. Som, P.M. (1992). Detection of metastasis in cervical lymph nodes: CT and MR criteria and differential diagnosis. *Am. J. Roentgenol.* 158: 961–969.
72. Huang, S.H. and O'Sullivan, B. (2017). Overview of the 8th edition TNM classification for head and neck cancer. *Curr. Treat. Options in Oncol.* 18: 40. https://doi.org/10.1007/s11864-017-0484-y.
73. Glastonbury, C.M., Mukherji, S.K., O'Sullivan, B., and Lydiatt, W.M. (2017). Setting the stage for 2018: how the changes in the American Joint Committee on Cancer/Union for International Cancer Control Cancer Staging Manual eighth edition impact radiologists. *AJNR Am. J. Neuroradiol.* 38: 2231–2237.
74. Lydiatt, W.M., Patel, S.G., O'Sullivan, B. et al. (2017). Head and neck cancers—major changes in the American Joint Committee on Cancer eighth edition Cancer Staging Manual. *CA Cancer J. Clin.* 67: 122–137.
75. American Cancer Society. Key Statistics for Cancers of Unknown Primary. https://www.cancer.org/cancer/cancer-unknown-primary/about/key-statistics.html (Accessed December 30, 2017)
76. Donta, T.S. and Smoker, W.R. (2007). Head and neck cancer: carcinoma of unknown primary. *Topics Magnet. Reson. Imag.* 18: 281–292.
77. Jereczek-Fossa, B.A., Jassem, J., and Orecchia, R. (2004). Cervical lymph node metastases of squamous cell carcinoma from an unknown primary. *Cancer Treat. Rev.* 30: 153–164.
78. Johansen, J., Buus, S., Loft, A. et al. (2008). Prospective study of 18FDG-PET in the detection and management of patients with lymph node metastases to the neck from an unknown primary tumour. Results from the DAHANCA-13 study. *Head Neck* 30: 471–478.
79. Dong, M.J., Zhao, K., Lin, X.T. et al. (2008). Role of fluorodeoxyglucose-PET versus fluorodeoxyglucose-PET/computed tomography

in detection of unknown primary tumour: a meta-analysis of the literature. *Nucl. Med. Commun.* 29: 791–802.
80. Schmalbach, C.E. and Miller, F.R. (2007). Occult primary head and neck carcinoma. *Curr. Oncol. Rep.* 9: 139–146.
81. Ferrer, R. (1998). Lymphadenopathy: differential diagnosis and evaluation. *Am. Fam. Physician* 58: 1313–1320.
82. Kaji, A.V., Mohuchy, T., and Swartz, J.D. (1997). Imaging of cervical lymphadenopathy. *Semin. Ultrasound CT MR* 18: 220–249.

Part 5
Osseointegrated implants



Chapter 20

Osseointegrated implants

20.1 Introduction

Osseointegrated implants, simply referred to as "implants," were first developed by Brånemark and his team half a century ago [1]. Since then they have completely transformed prosthodontics. The osseointegrated implant has become the treatment of choice for replacement of one or more missing teeth. In addition to excellent technical skills, careful assessment of the patient is necessary to ensure that the implant/s and subsequent restoration have the best chance of success. Although osseointegrated implants have achieved considerable long-term success, as evidenced by a recent American Academy of Osseointegration (AAO) systematic review [2] (the results of which are summarized in Table 20.1), prior to the advent of *cone-beam computed tomography* (CBCT), cross-sectional imaging of some sort has generally come to be viewed as essential for successful implants. Table 20.1 reveals that the success of retention of those implants placed in the mandible is greater than that of those implanted in the maxilla [2]. The reduction in alveolar bone height (compare Figures 20.1 and 20.2) that can occur in a longstanding edentulous saddle (Figure 20.2) is addressed by a number of approaches, as set out in Figure 20.3 [3]. Javed and Romanos' systematic review revealed that the critical factors for the long-term survival of dental implants in the reduced maxillary alveolar height of the posterior sextant were "a well-designed surgical protocol, achievement of sufficient primary stability at the time of implant placement, and pre- and postsurgical oral hygiene maintenance visits" [4].

Success of the dental implant depends largely on a thorough preoperative assessment of the patient's medical [5] and oral condition, as well as assessment of the alveolar bed on and around the prospective implant. The anatomy, quantity, and quality of alveolar bone determine the suitability for implant placement and the appropriate size, length, and position of the implant. All implant planning is made with some form of radiographic investigation. Although conventional dental radiography such as periapical radiography and panoramic radiography still plays a major role in the initial examination and evaluation of the prospective patient, they can provide only anatomical information in the two-dimensional mesiodistal plane. Nevertheless, this is important, as it will reveal hitherto unknown lesions and anatomical features, which may not only impact subsequent treatment planning, but may indicate that the proposed implants are not feasible, thus contraindicating CBCT. Although such lesions, like dense bone islands (idiopathic osteosclerosis) and osseous dysplasia (see Chapter 10), pose no threat to the

Oral and Maxillofacial Radiology: A Diagnostic Approach, Second Edition. Edited by David MacDonald.
© 2020 John Wiley & Sons, Inc. Published 2020 by John Wiley & Sons, Inc.

Table 20.1 Summary of survival of implants from a systematic review of implants in completely edentulous arches.

Jaw	Mandible		Maxilla	
Prosthesis	Fixed	Removable	Fixed	Removable
5-year survival	97%	96%	88%	
10-year survival	91%	95%	81%	
15-year survival	82%		70%	

Source: Bryant, S.R., MacDonald-Jankowski, D., and Kim, K. (2007). Does the type of implant prosthesis affect outcomes for the completely edentulous arch? *Int. J. Oral Maxillofac. Implants* 22: 117–139. Erratum in *Int. J. Oral Maxillofac. Implants* 2008; 23: 56.

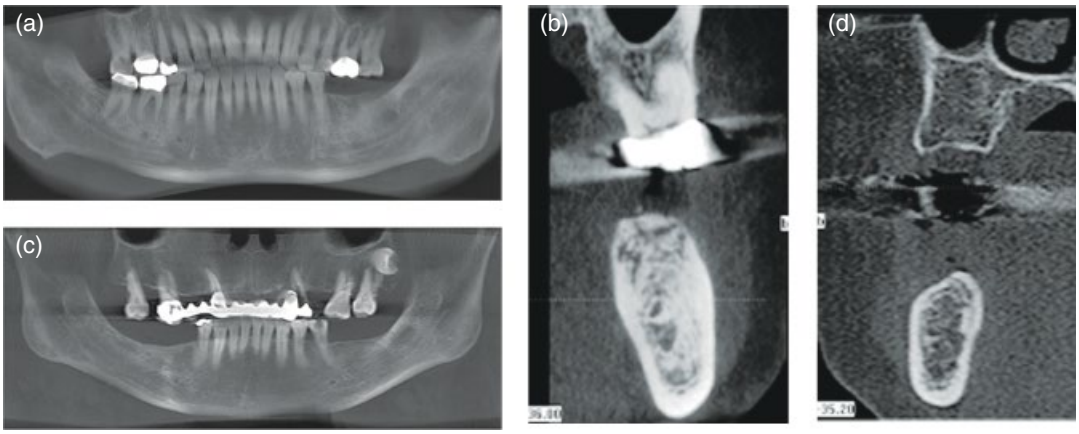


Figure 20.1 Panoramic and cross-sectional reconstructions of cone-beam computed tomography of two cases (a–d) displaying edentulous alveolar processes with good bone height and quality for both jaws. Source: Courtesy of Dr. Thomas Li, oral and maxillofacial radiologist.

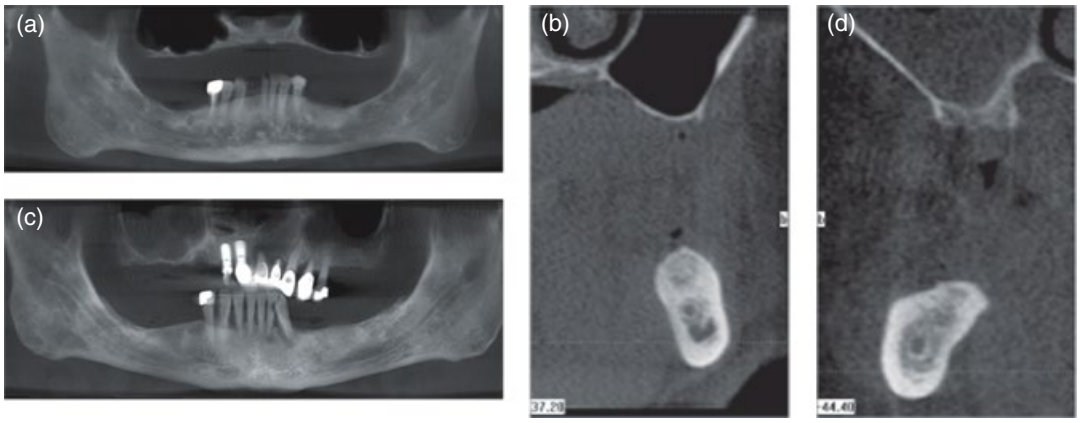


Figure 20.2 Panoramic and cross-sectional reconstructions of cone-beam computed tomography of two cases (a–d) displaying edentulous alveolar processes with reduced bone height and quality for both jaws. Note that for both cases the floor of the maxillary antrum is separated from the oral mucosa by only a cortex. This is particularly apparent in (b). Source: Courtesy of Dr. Thomas Li, oral and maxillofacial radiologist.

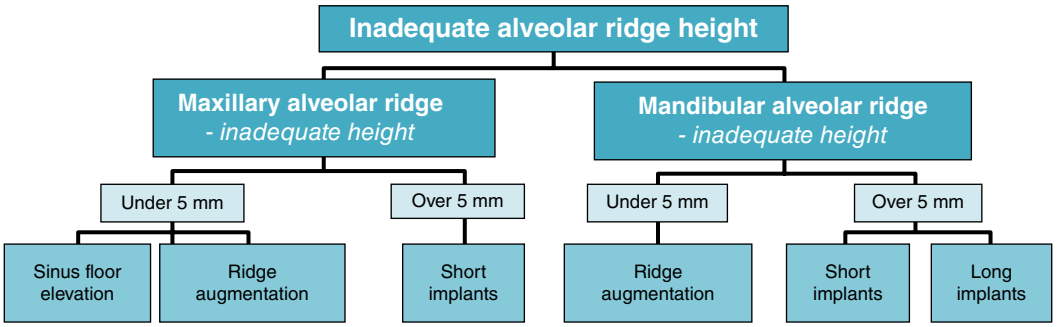


Figure 20.3 General approaches to treatment of an inadequate alveolar ridge height.

patient's general well-being when undisturbed, their presence contraindicates the placing of an implant in that site/s. Although such use of the panoramic radiograph may be condemned by some colleagues as "scanning," this is not the same as panoramic radiographic scanning prior to design of *complete removable prostheses* (CRP), which was yet again recently shown to be without clinical merit [6]. Unlike CRPs, the placing of implants is an invasive process, which is accompanied by a risk of complication and failure that could leave the patient worse off.

Having taken the value of the panoramic radiograph and any supplemental periapical radiographs into account, the clinician needs some form of tomographic or *three-dimensional* (3D) imaging to demonstrate the anatomy of the proposed implant's alveolar bed in the buccolingual plane. To maximize the chance for successful osseointegration, implants have to be placed accurately in the alveolar bed in a 3D space. The objective is to have an adequate area of contact between the implant and sound alveolar bone, while avoiding anatomical hazards such as the mandibular canal, the incisive canal, the lingual foramina, the maxillary antrum, and the submandibular fossa.

In 2000, the American Academy of Oral and Maxillofacial Radiology (AAOMR) recommended that preimplant planning should include cross-sectional imaging [7]. Initially this was provided by linear then complex motion tomography, and then medical facility–based *computed tomography* (CT). Since the advent of CBCT in the early 2000s all these have become redundant. The exceptions to the preference of CBCT over CT are perhaps when facial reconstruction is required in a hospital setting, such as after cancer ablation or severe facial trauma, and where intravenous contrast is required. Other imaging methods such as *magnetic resonance imaging* (MRI) and *ultrasonography* (US) have been explored with limited success and will not be considered further. A comparison of the main features of four imaging modalities that can be used in preimplant planning is set out in Table 20.2.

20.2 How CBCT Assists the Optimal Placing of Implants

CBCT assists dentists or prosthodontists and their surgeons to place the implant not only in sites which allow optimum alveolar ridge augmentation, osseointegration, and subsequent restoration (Figure 20.4), but also in those at risk of a complication. Wanner et al. reported in

Table 20.2 Comparison of the main features of four imaging modalities that can be employed in preimplant planning.

Imaging Modality	Convenience Footprint and price	Cross-section (Yes/no)	Spatial resolution	Magnification and distortion	Patient positioning	Software (Yes/no)	Dental EPR (Yes/no)
Intraoral radiography	**Excellent**	No	**Excellent**	None if paralleling technique is used	**Upright**	No	**Yes**
Panoramic radiography	**Excellent**	No	Very good	This is a major problem	**Upright**	No	**Yes**
Computed tomography (CT)	Poor	Yes	Adequate	**Clinically insignificant**	Supine[a]	Yes	Possible
Cone-beam computed tomography (CBCT)	Considerable improvement in all the above over last decade	Yes	Adequate	**Clinically insignificant**	**Upright**	Yes	**Yes**

Note: All the features which confer an advantage to the clinician have been rendered in bold. EPR, electronic patient record.
[a] There may be a difficulty with some software in aligning the CT's dataset to the occlusal plane. The position of the tongue will also differ in comparison to its position when imaged in the upright or vertical position.

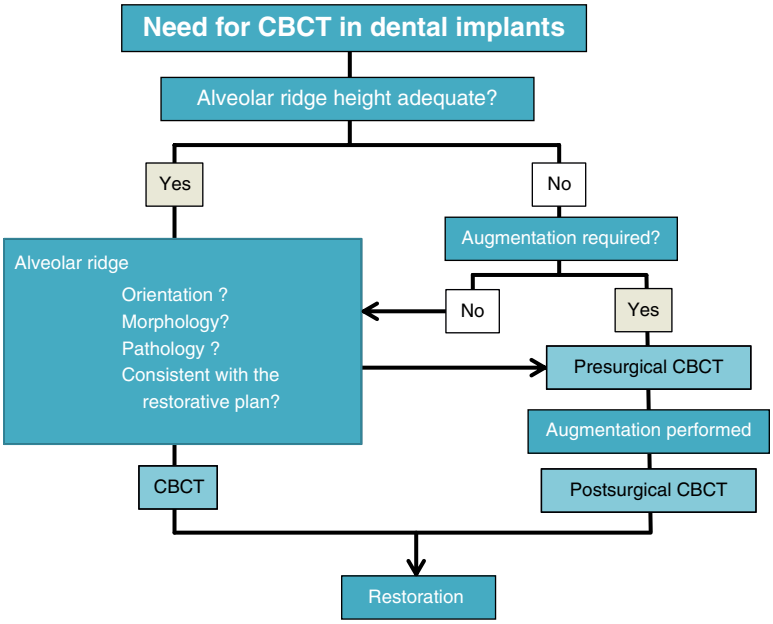


Figure 20.4 Roles of cone-beam computed tomography (CBCT) in dental implantology. After giving consideration to all the elements in the Alveolar ridge box an earlier dismissed of augmentation may need to be revisited.

their systematic review that the five most frequent complications were permanent nerve injury, damage to teeth adjacent to the implant, excessive bleeding in the floor of the mouth, mandibular fracture, and displacement of implants into the maxillary sinus [8]. Inadvertent injury to the mandibular canal and its neurovascular contents is minimized by CBCT, which allows accurate measurement to determine the safe depth of the implant [7].

20.3 Selection of Field of View and Other Preimaging Planning

Figure 5.7 sets out the *fields of view* (FOVs) available for preimplant planning. The basic principle is to use the smallest FOV that would adequately cover the region of interest. Therefore, a single site will need only a small FOV, unless there is a compelling reason to use a medium FOV as set out in Figure 5.7. Generally, the FOV should include the mandibular canal for a mandibular implant or the sinus floor for a maxillary implant. If a stent is available, it should be inserted prior to imaging.

The spatial resolution for preimplant planning is usually about 0.3 mm voxel size, which is still better than the best *multidetector computed tomography* (MDCT) spatial resolution of 0.35 mm voxel size. So far there is no evidence to show that this spatial resolution is inadequate.

Nevertheless, the provision of stents by the dentist or prosthodontist prior to CBCT exposure ensures that the implants are placed precisely where they are required. This correct placement of the implant also minimizes the chance of complications arising from misplaced implants (Figure 20.5).



Figure 20.5 Cone-beam computed tomography displaying perforation (indeed, replacement) of the labial cortex by the implant. This implant has failed. Source: Courtesy of Dr. Thomas Li, oral and maxillofacial radiologist.

20.4 Computer-aided Planning

After scanning, the dataset is stored as a series of axial slices. Depending on the resolution and slice thickness, the number of axial slices can range from 30 to 300. These are then reconstructed into a 3D dataset and further reconstructed into multiplanar images. The standard, indeed default, CBCT multiplanar display of a dataset is displayed in Figure 5.1. This is not the best way to demonstrate anatomy of the dentomaxillofacial complex, particularly when implants are being considered. Therefore, the "curved" program analogous to the MDCT's Dentoscan program is better (Figures 5.2, 20.1, 20.2, 20.6–20.9). This is displayed as a panoramic-like image, but without the superimpositions, secondary images, and distortions of the conventional panoramic radiograph. This panoramic-like image, also called a synthetic, reformatted, reconstructed panoramic image, follows the line of the arch chosen by the reviewing clinician, who also chooses the thickness of this reformation. The transaxial reconstructions are reformatted perpendicular to the panoramic image, allowing the reviewing clinician to review the cross-sectional anatomy of the intended implant site/s. Figure 20.9 displays a case in which panoramic and transaxial reconstructions were used to review a site for *sinus floor elevation* (SFE), again after the augmentation of the alveolus was performed, and yet again after the implant had osseointegrated.

Prior to discussing failure, mainly due in the incorrect placement of implants, Figure 20.7 raises the issue of the need to evaluate the ridge carefully for pre-existing pathology prior to placement of implants. While these do not always contraindicate implant placement, additional steps may need to be taken, as explained in Chapter 10 with regard to osseous dysplasia. The band of sclerosing osteitis in the right side of the mandible in Figure 20.7 will require careful review to ensure that the inflammatory cause for its persistence is no longer present, and that the subsequent surgical procedure that is performed takes this dense bone into account.

Currently there is a wide range of software programs available to the restorative dentist and implantologist. Most of these are set out in Vercruyssen et al.'s Table 1 [9]. They identified both the static (surgical guide) and dynamic (navigational) systems (Figure 20.10). The former use stereolithography or laboratory-fabricated surgical guides (stents), whereas the second is based on optical tracking technology, analogous to an automobile's *global positioning system* (GPS). Almost all software programs in Vercruyssen et al.'s Table 1 permit virtual implant planning [9]. These have

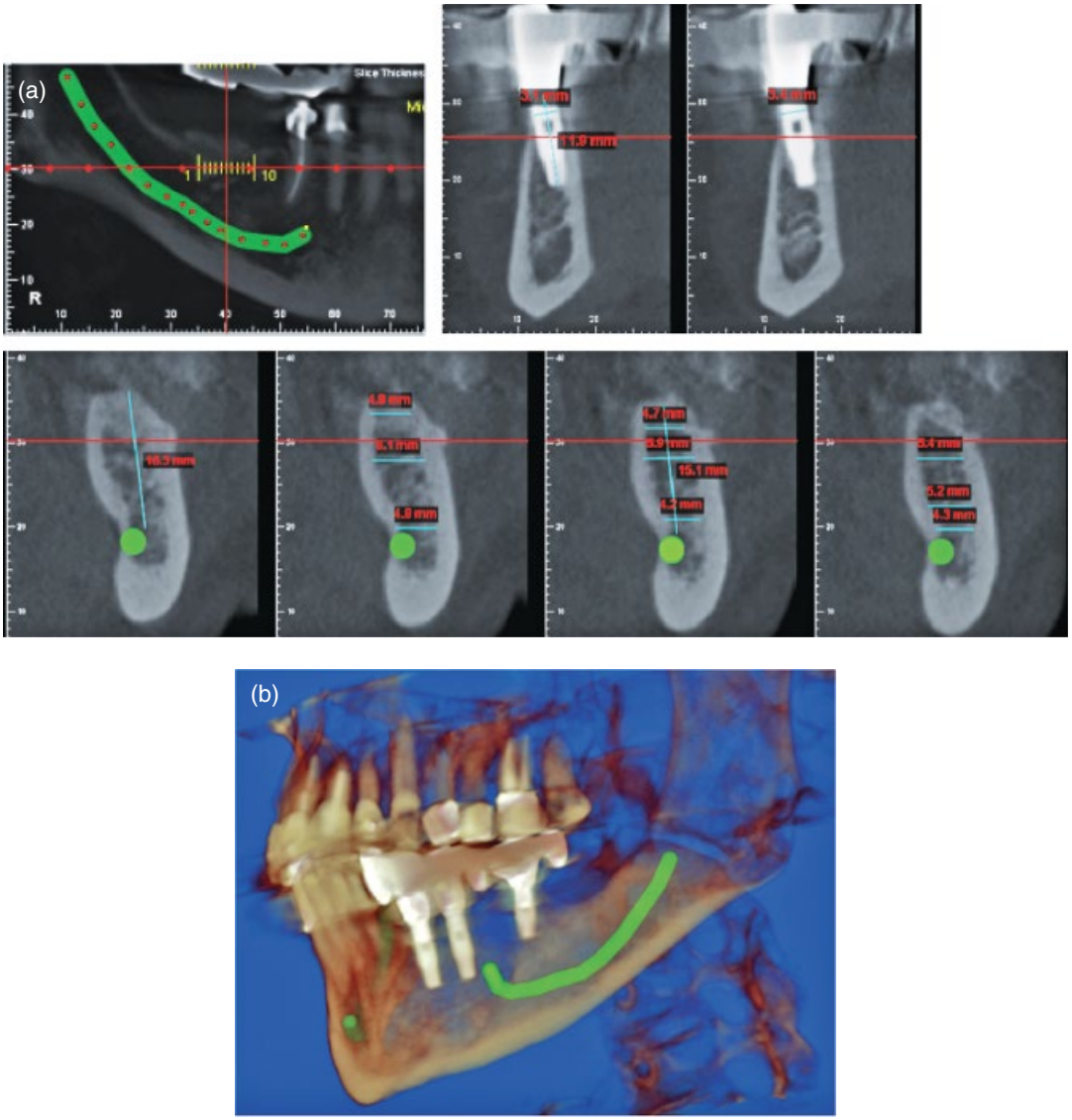


Figure 20.6 (a) Sections showing measurements (Dolphin Implanner; Dolphin Imaging and Management Solutions, Chatsworth, LA, USA) made on data from an iCAT scan. (b) Three-dimensional reconstruction of the mandible, with the mandibular canal indicated by a green line. Source: Courtesy of Dr. Babak Chehroudi, Faculty of Dentistry, University of British Columbia.

been especially developed to assist dental practitioners in performing preoperative planning. They contain the size and shape of commonly available implants for the clinician to select and place in the patient's alveolar bed as captured by CBCT.

The ideal features of a radiographic stent are that in addition to being comfortable and stable when placed in the patient, it should be sufficiently radiopaque to indicate the intended tooth position without inducing scatter. It should also be

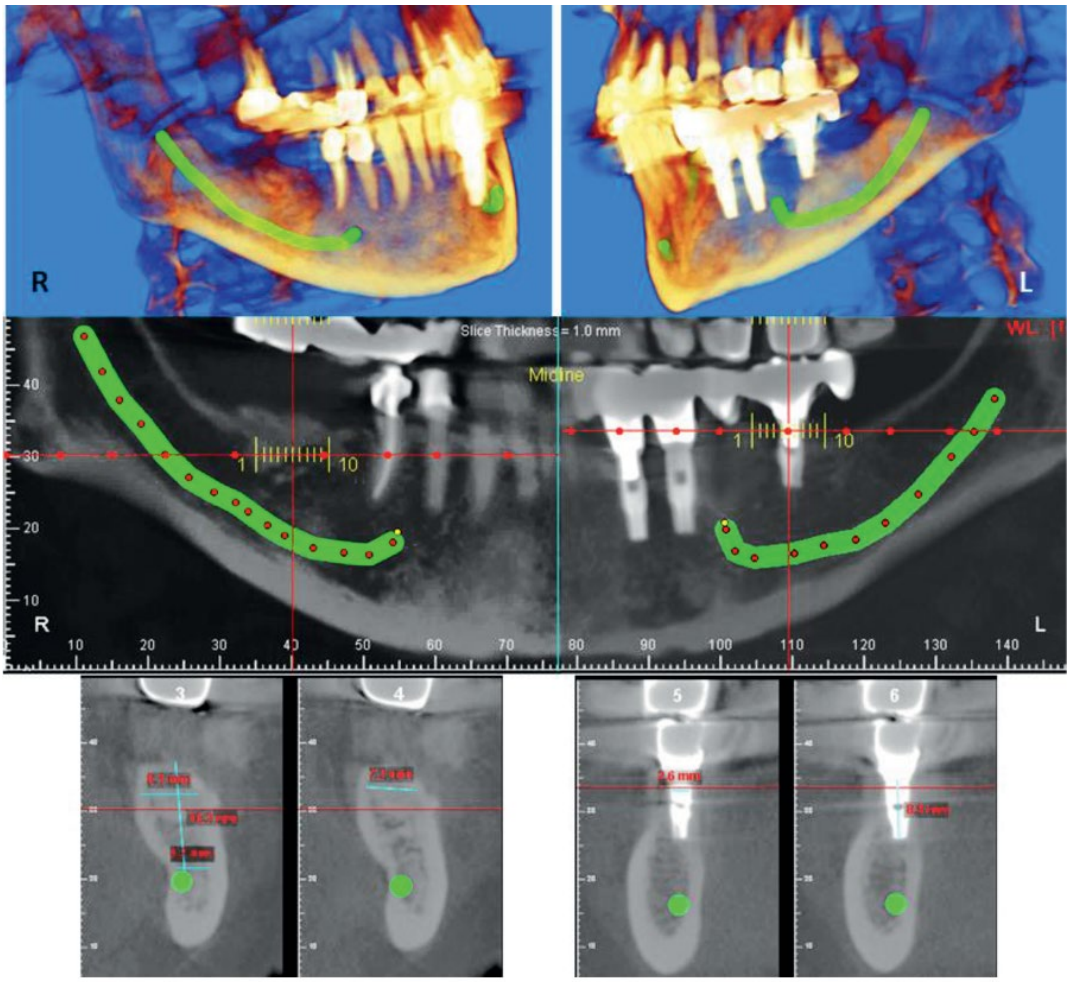


Figure 20.7 Cone-beam computed tomography (CBCT) of review of an implant on the left mandible and potential implant site on the right mandible, made from Dolphin Implanner software. (a) Three-dimensional reconstructions display the positioning of the mandibular canal (in green). Note the spray artifact associated with the fixed bridge in comparison to the minimal effect produced by the titanium implant. (See Chapter 5 for a full discussion of the effect of different metals on CBCT). (b) The midline of the reconstructed panoramic radiograph is denoted by a light blue vertical line. The 1–10 mm scale on the right encompasses most of the radiopaque region that denotes sclerosing osteitis (see Chapter 10) and that on the left encompasses the short implant in the first molar site. The less radiodense titanium component called the "fixture" is directly fused (osseointegrated) to the bone; the more radiodense component inserted into the coronal part of the fixture is the "abutment" upon which the restoration (a crown or bridge) is constructed. (c) Four transaxial reconstructed images, two from each side, directly correspond to the sites gradated 1 to 10 in the panoramic reconstruction in (b). The transaxial reconstructions (at 3 and 4 mm on the scale, viewed from behind) indicate the radiodensity and extent of the sclerosing osteitis, which needs careful consideration prior to implant placement, and the poor positioning of the implant (at 5 and 6 mm). The last is substantially positioned against the lingual cortex instead of directly in the cancellous bone. Note: It is very likely that this implant has been placed prior to the advent of CBCT and therefore did not benefit from the cross-sectional imaging that could have recommended that a longer implant be used in additionally to being optimally positioned. L, left; R, right. Source: Courtesy of Dr. Babak Chehroudi, Faculty of Dentistry, University of British Columbia.

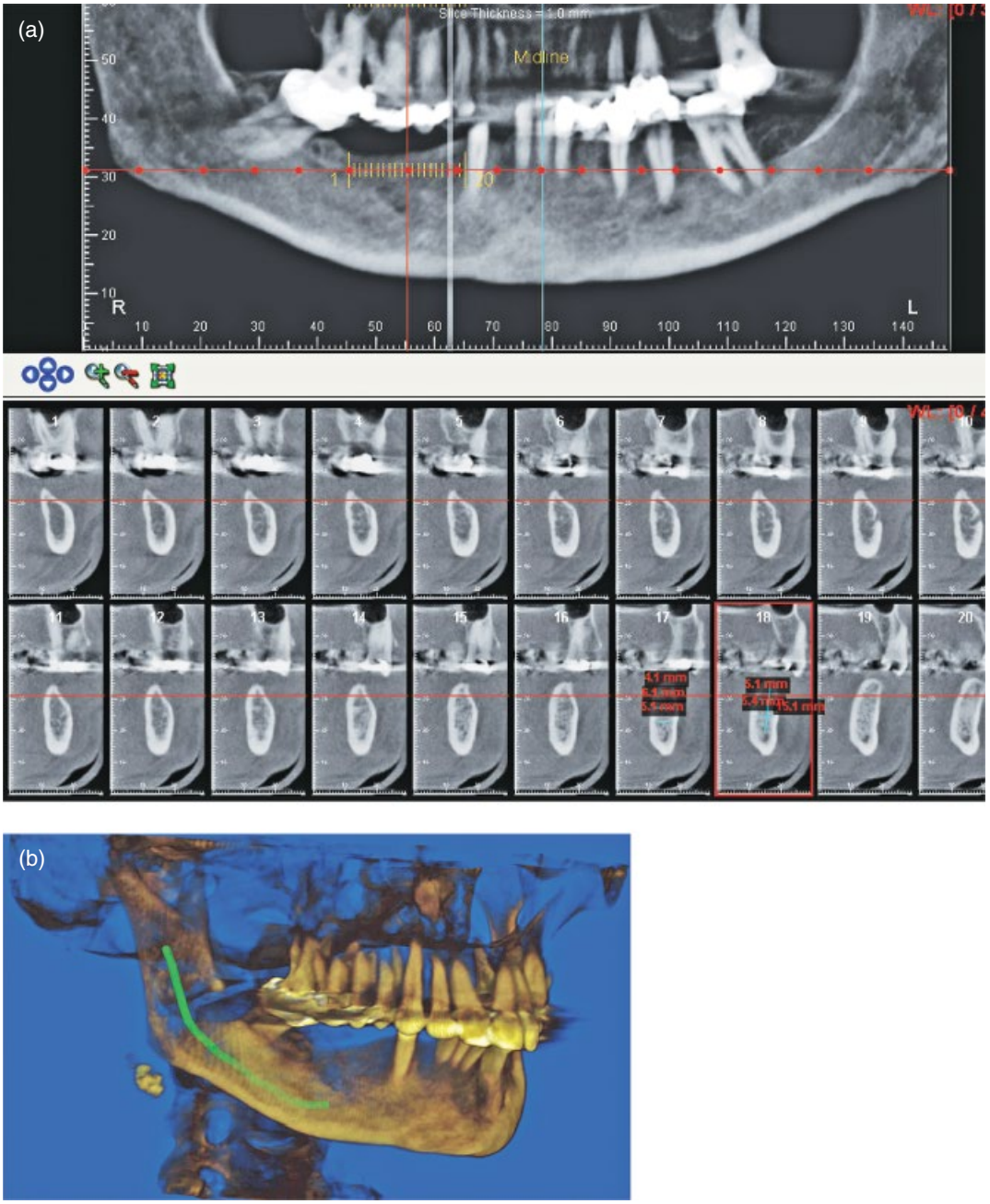


Figure 20.8 (a) Sections showing measurements (Dolphin Implanner) made on data from an iCAT scan. (b) Three-dimensional reconstruction of the mandible, with the mandibular canal indicated by a green line. Note the incidental finding of a radiopaque structure just below the angle of the mandible. This position is consistent with calcification within a lymph node. L, left; R, right. Source: Courtesy of Dr. Babak Chehroudi, Faculty of Dentistry, University of British Columbia.

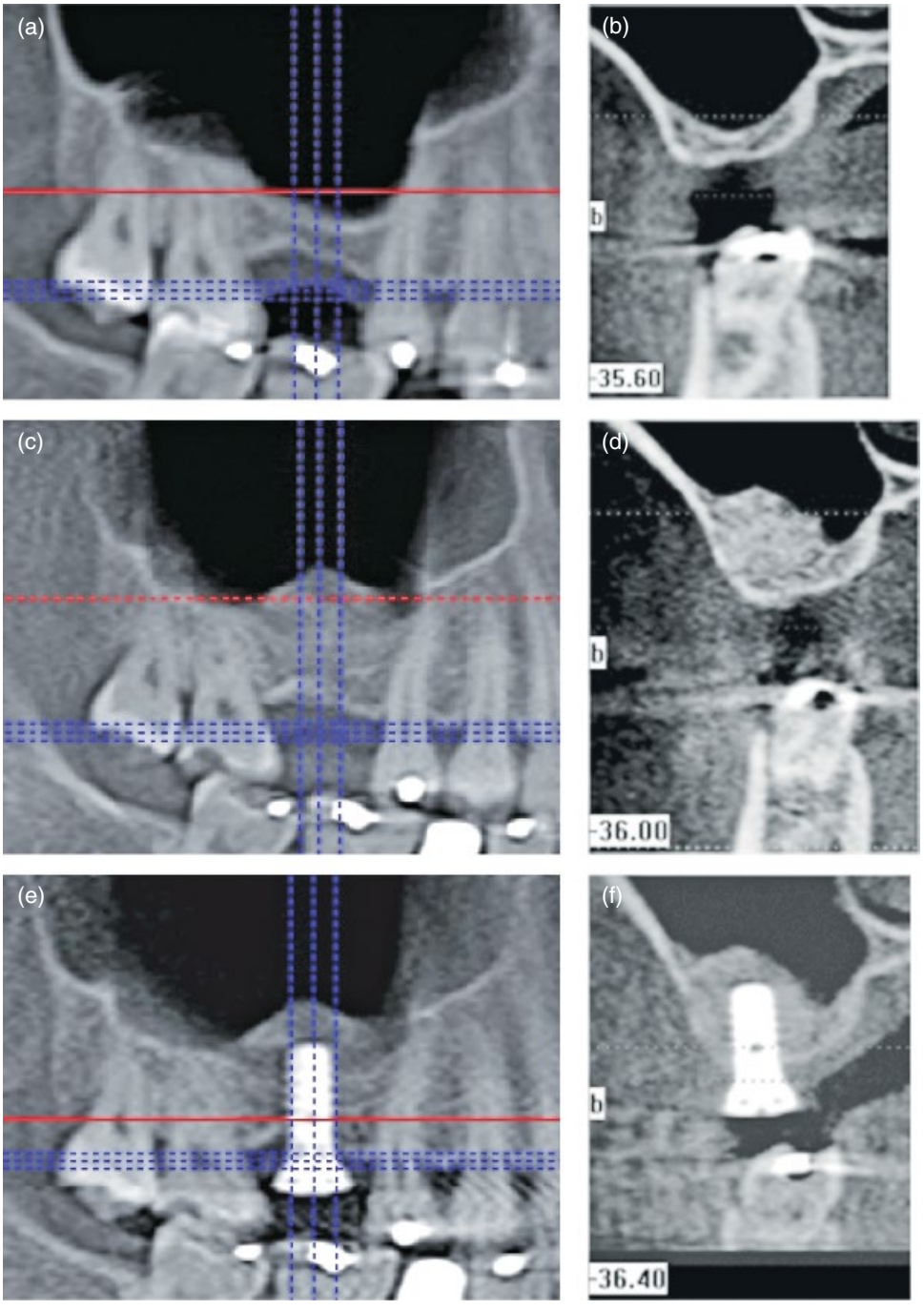


Figure 20.9 Cone-beam computed tomography of a case that has had a maxillary sinus floor elevation. (a and b) Reduced height of the maxillary alveolus. (c and d) Increased height after maxillary sinus floor elevation. (e and f) Implant has osseointegrated. Note: Figure 11.50 displays bilateral maxillary sinus floor elevation lifts. Although there is good osseointegration between the implant and the bone, it is deficient on the implant's distal aspect. Source: Courtesy of Dr. Thomas Li, oral and maxillofacial radiologist.

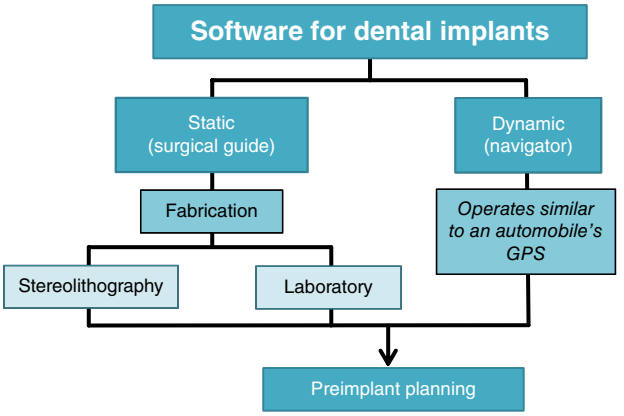


Figure 20.10 Types of software available for preimplant planning. GPS, global positioning system.

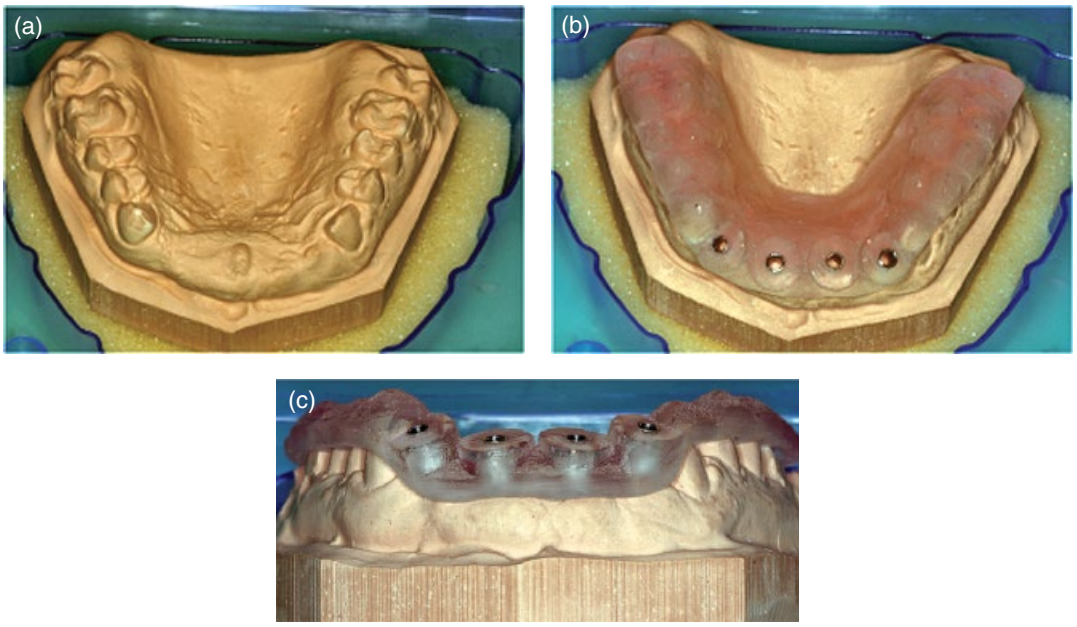


Figure 20.11 (a) Stone model of upper jaw exhibiting the edentulous anterior site that will receive implants. (b and c) Surgical stent made of acrylic with metal-lined holes to guide the drill. Source: Courtesy of Dr. Thomas Li, oral and maxillofacial radiologist.

sterilizable if it is to be used as a surgical guide [10].

The rigid surgical guide stent with bur holes can be used to guide drilling and implant placement to a high degree of precision. Figures 20.11 and 20.12 display two different stents. Both have metal-lined holes to facilitate the precise placement of drilled holes.

20.5 Implant Failure

Failure to osseointegrate is perhaps the most important reason for failure (Figure 20.13). Other causes of failure are the placement of an implant into the mandibular canal (Figure 20.14) and maxillary antral cavity, the accessory mental foramen, mandibular

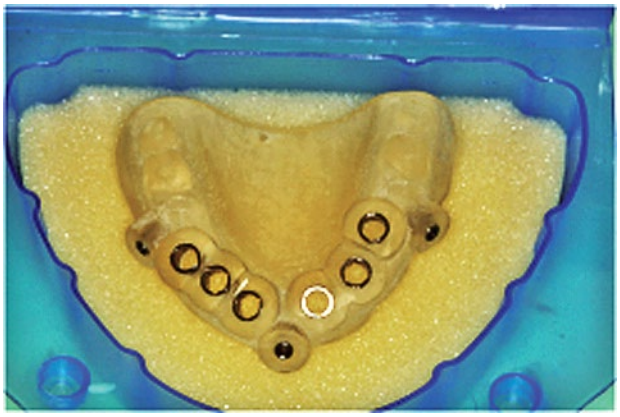


Figure 20.12 Surgical stent made of acrylic with metal-lined holes to guide the drill. This stent differs from that in Figure 20.11 because it has additional holes so that the stent may be stabilized by screwing it into the alveolus prior to drilling the holes for the implants. Source: Courtesy of Dr. Thomas Li, oral and maxillofacial radiologist.

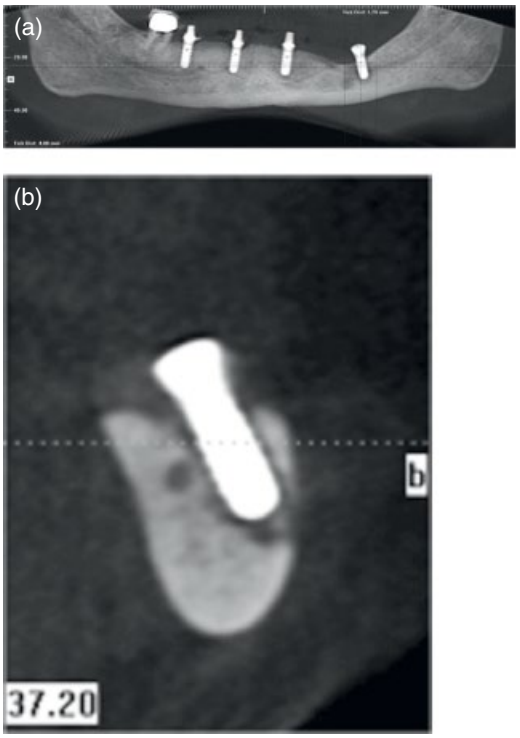


Figure 20.13 Cone-beam computed tomography (a and b) showing failure of osseointegration. The implant is completely surrounded by a radiolucent space. Source: Courtesy of Dr. Thomas Li, oral and maxillofacial radiologist.

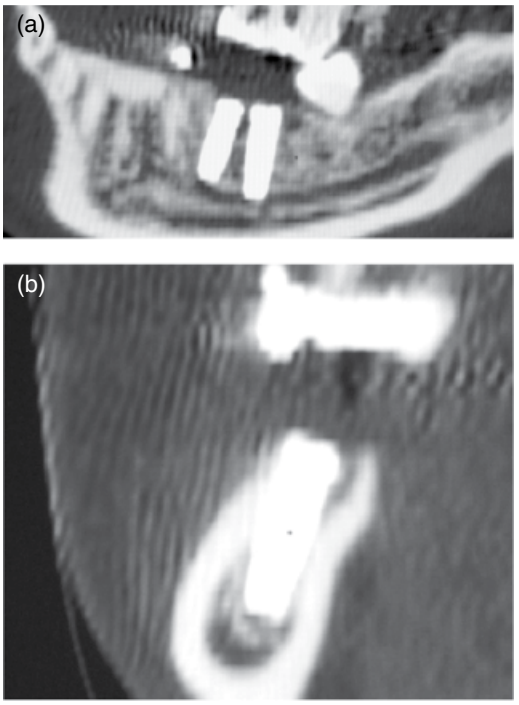


Figure 20.14 Helical computed tomography (a and b) displaying an implant inserted into the mandibular canal. Source: Courtesy of Dr. Thomas Li, oral and maxillofacial radiologist.

incisive canal, lingual foramen, floor of the mouth, submandibular fossa, nasopalatine (incisive) foramen, buccal concavity of the maxilla, and thin and/or inclined alveolar ridges.

20.5.1 ACCESSORY MENTAL FORAMEN

Accessory mental foramina have been reported in 7% of CBCTs in one study [11]. Of the 15 cases observed, 9 ran distoinferiorly from the anterior loop of the intraosseous mental nerve. Naitoh et al.'s Figure 6b displays a case course obliquely through the buccal cortex to reach the foramen [11].

20.5.2 MANDIBULAR INCISIVE CANAL

Makris et al. reviewed 100 CBCTs [12]. They reported the mandibular incisive canal to be 1.5 cm from the mental foramen to the symphysis. The entire canal was visible in only 18% of cases. It displayed a marked tendency to be closer to the buccal cortex at the mental foramen (85% buccal to 10% lingual). As the mandibular incisive canal migrated distomesially, it showed an increased tendency to approach the lingual cortex at the symphysis (60% buccal to 35% lingual) [12].

20.5.3 LINGUAL FORAMEN

The blood supply of the anterior sextant of the mandible is substantially supplied by branches of the sublingual arteries, which penetrate the bone by way of the lingual foramina [13]. Although sublingual arteries are a major contributor of this blood, due to extensive anastomosis with the submental branch of the facial artery, up to 50% of this blood is by way of the latter [14]. Furthermore, the close proximity of the sublingual arteries to the lingual cortex, particularly at the symphysis, makes them vulnerable to damage if that cortex is perforated [13]. Figure 20.15 shows five examples of lingual foramina and intraosseous canals. The fact that they convey blood vessels raises the possibility of uncontrolled bleeding into the floor of the mouth if damaged. This may produce swelling, which through obstruction of the upper airways may cause respiratory distress [15]. According to Dubois et al., although in almost every case the bleeding begins during surgery, the effect of the vasoconstrictive agent in the local anesthesia combined with an injury of the lingual arteriovenous plexus can result in delayed swelling [16]. Balaguer-Martí et al. reported that at least a half of cases in their systematic review of 17 cases occur in the anterior sextant of the mandible and were due to long implants (15 mm or more) that perforated the lingual plate [15]. Balaguer-Martí et al. remarked that when the worldwide use of implants is considered, such a phenomenon must be under-reported [15]. Both angulation and the size of the implant need to be carefully considered to avoid perforation of the lingual wall [17].

20.5.4 SUBMANDIBULAR FOSSA

The submandibular fossa can be difficult to examine clinically. This lingual concavity of the posterior body of the mandible can be very deep and markedly limit the height of alveolar bone available for the implant; then the implant may need to be inserted at an angle. Parnia et al. classified the degree of concavity of the submandibular fossa into three groups: Type I (less than 2 mm, 20%), Type II (2–3 mm, 52%), and Type III (more than 3 mm, 28%) [18]. Although such a perforation into the very vascular floor of the mouth may cause a

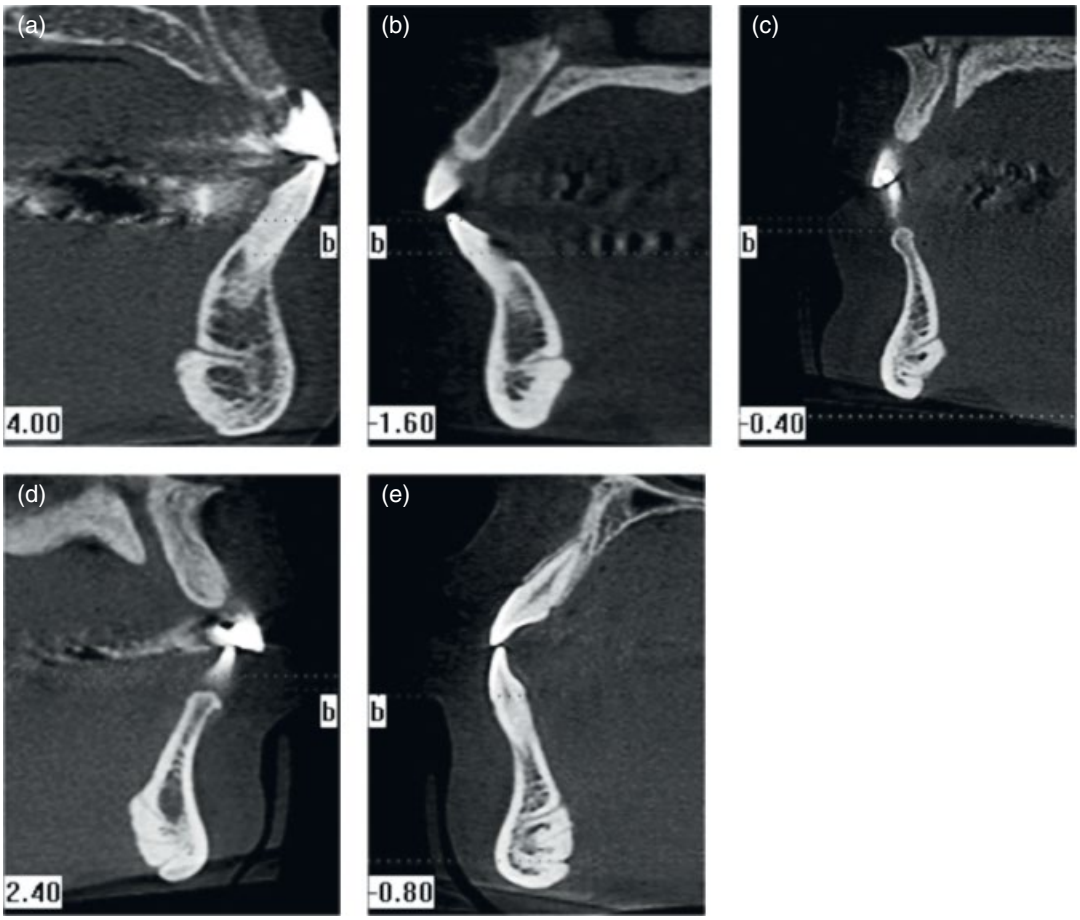


Figure 20.15 Lingual canals observed on cone-beam computed tomographic images. (a) One lingual canal and a narrow maxillary ridge. (b) One lingual canal and a narrow maxillary ridge. (c) Two lingual canals and a narrow ridge in both jaws. (d) Three lingual canals and a narrow mandibular ridge. (e) Three lingual canals and a narrow ridge in both jaws. Note also the normal incisive (nasopalatine) canals. Source: Courtesy of Dr. Thomas Li, oral and maxillofacial radiologist.

life-threatening hemorrhage, injury to salivary glands – although infrequently reported – has happened [19]. Furthermore, such injury may result in plunging ranulae [20, 21].

While inserting an implant into the posterior sextant of the mandible without the use of cross-sectional imaging or a surgical guide, a dentist inadvertently inserted an implant into the submandibular fossa. It migrated into the neck and was removed under general anesthetic (Figure 20.16) [22].

20.5.5 VARIATION IN NASOPALATINE (INCISIVE) CANAL

The anterior sextant of the maxillary ridge is a necessary platform upon which a restored dentition can be built in order to achieve acceptable esthetic phonation and a good functional outcome [23]. The nasopalatine canal in the maxilla has a highly variable diameter, path, and morphology. The diameter of the narrowest part of the canal can range from 3 to 8 mm. Figure 20.15 displays

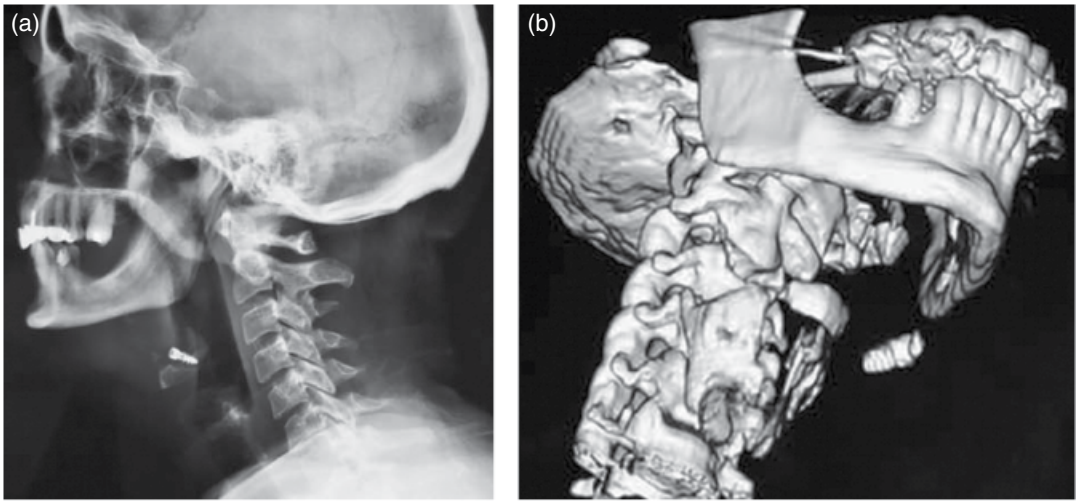


Figure 20.16 Displacement of an implant into the submandibular fossa and its subsequently migration down into the neck. (a) Lateral cephalogram. (b) Three-dimensional reconstruction of computed tomography. Source: Reprinted with permission of Giudice, A., Colangeli, W., Barca, I. et al. (2015). Accidental displacement and migration of an endosseous implant into submandibular fossa. *J. Oral Implantol* 41: 323–325.

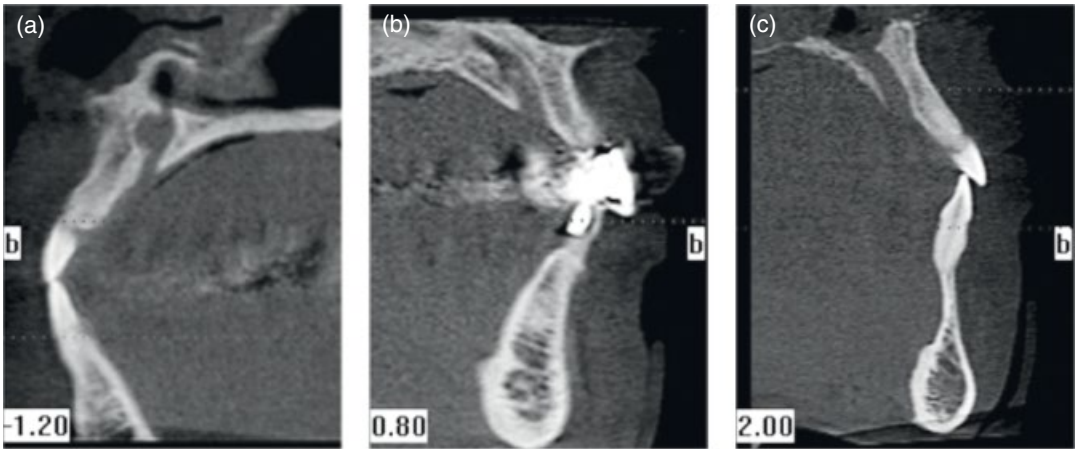


Figure 20.17 Variety in shape of incisive (nasopalatine) canals (a–c) observed on cone-beam computed tomographic images: (a) displays an early nasopalatine duct cyst. Source: Courtesy of Dr. Thomas Li, oral and maxillofacial radiologist.

a range of normal nasopalatine canals. The diameter is often not uniform throughout the canal's course. Because its position may not be exactly in the midline, it is important before any implant is placed in the maxillary central incisal region that CBCT is performed to examine this anatomy. An implant placed into the nasopalatine canal can lead to a failure in osseointegration. Furthermore, nasopalatine nerve damage will cause numbness of the incisive papilla. Figure 20.17 show examples of nasopalatine canals unusual to the point of abnormal, including an early nasopalatine duct cyst (see Chapter 9) that should be recognized and treated at this stage.

Due to the significant challenge of marked alveolar ridge atrophy, subsequent long-term edentulism, or its loss secondary to trauma, the nasopalatine canal may need to be utilized for implants. There are two principal strategies: incisive canal deflation, which requires the complete removal of the neurovascular bundle and grafting so that an implant can be placed there; and neurovascular bundle lateralization, which replaces the neurovascular bundle in a more posterior position. Both have been associated with either hyperesthesia or hypoesthesia, in spite of the extensive anastomoses that exist between the incisive neurovascular bundle and the greater palatine nerve and artery [23]. Although de Mello et al.'s systematic review revealed a high degree of success, they advise caution because of the low level of evidence in these studies [23]. Furthermore, they were unable to identify factors that predict sensory disturbance.

20.5.6 BUCCAL CONCAVITY IN THE MAXILLA

It is common to have a concavity on the cortex buccal to an extraction site. The degree of this concavity would affect the position of the implant. Buccal fenestration can easily occur if no detailed preoperative radiographic assessment has been made (Figure 20.5). Failure to assess the buccal concavity can lead to fenestration of the alveolar bone, recession of the gingival margin, and exposure of the implant's thread.

20.5.7 THIN AND INCLINED ALVEOLAR RIDGE

The alveolar ridge in the incisal region of both jaws can be very thin (Figures 20.15 and 20.17). If the narrowest part of the ridge is less than 3 mm, implants are contraindicated, unless bone grafting has been successfully performed. Furthermore, the vertical angulation of this narrow alveolar ridge can form an acute angle to the standing teeth. This phenomenon is more common in the maxillary canine and premolar region. Implant planning in this region could consider inserting the implant at an acute angle to the suprastructure. An angled abutment may be needed.

20.6 Postimplant Follow-up Radiography

Follow-up is generally performed by conventional radiography, namely periapical radiographs. These reveal both the degree of osseous intergration and the alveolar bone height in relation to the osseointegrated implant. Some clinicians use CBCT for at least a few cases, but, as indicated by Schulze et al. (see Chapter 5), these are rendered unreliable due to the metal artifact, mainly beam hardening in the case of the titanium implant and, furthermore, by any mathematically unsophisticated *metal-artifact reduction* (MAR) algorithms [24]. Although Figure 20.7 displays a pre-existing titanium implant fixture causing minimal artifact in contrast to the metal of the bridge and the abutment, the reader should be aware that the *peak kilovoltage* (kVp) of the CBCT unit is important. The unit used in Figure 20.7 was an iCAT, which has a higher kVp than most current units. This resulted in reduced artifacts from titanium implants.

20.7 Concluding Remarks

The recent introduction of CBCT has completely revolutionized oral and maxillofacial radiology and implantology. In spite of

the substantial body of literature that has emerged, only very little of it so far has approximated to the highest standard of clinical evidence. Therefore, the use of CBCT, as with any other radiological investigation, needs to be clearly indicated for that particular patient. Nevertheless, there is a duty of care that all clinicians bear: to ensure that each potential implant patient has been properly evaluated, so that each implant can be safely placed within the patient with the greatest chance of success. Due to an overall reduction in radiation dose, increased availability, the facility of simulation, and an understanding of the risks of implant placement, it is becoming more difficult to justify not using cross-sectional imaging as part of preimplant planning.

As already stated in Chapter 5, dentists are responsible for the interpretation of the entire dataset, whether by themselves or by a radiologist. This is necessary to identify hitherto unknown findings that may also require treatment. An example is the calcification within the soft tissue in Figure 20.8. This and other calcifications in the soft tissues are comprehensively discussed in Chapter 12.

References

1. Brånemark, P.I., Hansson, B.O., Adell, R. et al. (1977). Osseointegrated implants in the treatment of the edentulous jaw. Experience from a 10-year period. *Scand J. Plast Reconstr Surg. Suppl.* 16: 1–132.
2. Bryant, S.R., MacDonald-Jankowski, D., and Kim, K. (2007). Does the type of implant prosthesis affect outcomes for the completely edentulous arch? *Int. J. Oral Maxillofac. Implants* 22: 117–139. Erratum in *Int J Oral Maxillofac Implants* 2008;23:56.
3. Sanz, M., Donos, N., Alcoforado, G. et al. (2015). Therapeutic concepts and methods for improving dental implant outcomes. Summary and consensus statements. The 4th EAO Consensus Conference 2015. *Clin. Oral Implants Res.* 26 (Suppl 11): 202–206. https://doi.org/10.1111/clr.12674.
4. Javed, F. and Romanos, G.E. (2015). Role of implant diameter on long-term survival of dental implants placed in posterior maxilla: a systematic review. *Clin. Oral Investig.* 19: 1–10.
5. Donos, N. and Calciolari, E. (2014). Dental implants in patients affected by systemic diseases. *Br. Dent. J.* 217: 425–430.
6. Kratz, R., Walton, J.N., MacEntee, M.I. et al. (2017). Panoramic radiographs made before complete removable dental prostheses fabrication: a retrospective study of clinical significance. *J. Prosthet. Dent.* 118: 26–30.
7. Tyndall, D.A. and Brooks, S.L. (2000). Selection criteria for dental implant site imaging: a position paper of the American Academy of Oral and Maxillofacial Radiology. *Oral Surg. Oral Med. Oral Pathol. Oral Radiol. Endod.* 89: 630–637.
8. Wanner, L., Manegold-Brauer, G., and Brauer, H.U. (2013). Review of unusual intraoperative and postoperative complications associated with endosseous implant placement. *Quintessence Int.* 44: 773–781.
9. Vercruyssen, M., Fortin, T., Widmann, G. et al. (2014). Different techniques of static/dynamic guided implant surgery: modalities and indications. *Periodontol.* 66: 214–227.
10. De Kok, I.J., Thalji, G., Bryington, M., and Cooper, L.F. (2014). Radiographic stents: integrating treatment planning and implant placement. *Dent. Clin. N. Am.* 58: 181–192.
11. Naitoh, M., Hiraiwa, Y., Aimiya, H. et al. (2009). Accessory mental foramen assessment using conebeam computed tomography. *Oral Surg. Oral Med. Oral Pathol. Oral Radiol. Endod.* 107: 289–994.
12. Makris, N., Stamatakis, H., Syriopoulos, K. et al. (2010). Evaluation of the visibility and the course of the mandibular incisive canal and the lingual foramen using cone-beam computed tomography. *Clin. Oral Implants Res.* 21: 766–771.
13. Rosano, G., Taschieri, S., Gaudy, J.F. et al. (2009). Anatomic assessment of the anterior mandible and relative hemorrhage risk in implant dentistry: a cadaveric study. *Clin. Oral Implants Res.* 20: 791–795.

14. He, P., Truong, M.K., Adeeb, N. et al. (2017). Clinical anatomy and surgical significance of the lingual foramina and their canals. *Clin. Anat.* 30: 194–204.
15. Balaguer-Martí, J.C., Peñarrocha-Oltra, D., Balaguer-Martínez, J., and Peñarrocha-Diago, M. (2015). Immediate bleeding complications in dental implants: a systematic review. *Med. Oral Patol. Oral Cir. Bucal.* 20: e231–e238.
16. Dubois, L., de Lange, J., Baas, E., and Van Ingen, J. (2010). Excessive bleeding in the floor of the mouth after endosseus implant placement: a report of two cases. *Int. J. Oral Maxillofac. Surg.* 39: 412–415.
17. Pigadas, N., Simoes, P., and Tuffin, J.R. (2009). Massive sublingual haematoma following osseo-integrated implant placement in the anterior mandible. *Br. Dent. J.* 206: 67–68.
18. Parnia, F., Fard, E.M., Mahboub, F. et al. (2010). Tomographic volume evaluation of submandibular fossa in patients requiring dental implants. *Oral Surg. Oral Med. Oral Pathol. Oral Radiol. Endod.* 109: e32–e36.
19. Nahlieli, O., Droma, E.B., Eliav, E. et al. (2008). Salivary gland injury subsequent to implant surgery. *Int. J. Oral Maxillofac. Implants* 23: 556–560.
20. Loney, W.W. Jr., Termini, S., and Sisto, J. (2006). Plunging ranula formation as a complication of dental implant surgery: a case report. *J. Oral Maxillofac. Surg.* 64: 1204–1208.
21. Mandel, L. (2008). Plunging ranula following placement of mandibular implants: case report. *J. Oral Maxillofac. Surg.* 66: 1743–1747.
22. Giudice, A., Colangeli, W., Barca, I. et al. (2015). Accidental displacement and migration of an endosseous implant into submandibular fossa. *J. Oral Implantol* 41: 323–325.
23. de Mello, J.S., Faot, F., Correa, G., and Chagas Júnior, O.L. (2017). Success rate and complications ass*ociated with dental implants in the incisive canal region: a systematic review*. *Int. J. Oral Maxillofac. Surg.* 46: 1584–1591. https://doi.org/10.1016/j.ijom.2017.05.002.
24. Schulze, R.K., Berndt, D., and d'Hoedt, B. (2010). On cone-beam computed tomography artifacts induced by titanium implants. *Clin. Oral Implants Res.* 21: 100–107.

Index

AAPM TG18 (American Association of Physicists) in Medicine Task Group 18, 51
Accessory mental foramen, 623, 625
Achondroplasia, 9
Acinic cell carcinoma, 567, 572, 573
Acne, 19, 129, 283, 387
Acne scar, 19, 129, 387
Acoustic impedance (Z), 152
Acoustic neuroma. *See* Vestibular schwannoma
Acoustic noise, 121, 122
Acromegaly, 424, 499
Actinomyces, 125
Active matrix light crystal display (AMLCD), 50
Adenocarcinoma, 70, 139, 278, 567, 572, 574
Adenocarcinoma not otherwise specified (NOS), 567
Adenoid cystic carcinoma (ACC), 15, 567–572, 575, 584
Adenomatoid odontogenic tumor (AOT), 15, 325
Adverse drug reaction (ADR), 86
AIDS (Acquired immunodeficiency syndrome), 424, 425
Ambient lighting, 47, 49, 52, 54–55, 58, 105
Ambiguous Figures. *See* Reversible figures
Ameloblastic carcinoma, 15, 192, 206, 209
Ameloblastic fibroma, 15, 246–247
Ameloblastic fibro-odontoma (AFO), 15, 324, 375
Ameloblastoma, 15, 17, 27, 28, 31, 34, 35, 37, 107, 166, 191, 192, 194, 196, 201, 203, 206–220, 223, 225–228, 230, 232, 235–237, 240, 243, 260, 303, 325, 326, 328, 347, 349, 359, 360, 379, 501
Amelogenesis imperfecta, 12, 13
American Board of radiology (ABR), 52, 64
American Joint Committee on Cancer (AJCC), 67, 555, 582, 583, 597, 599
Anatomy scan (T1-weighted MRI), 116, 523
Aneurysmal bone cyst (ABC), 15, 244, 249–252, 299
Aneurysms, 126, 277, 462, 463, 529–534
Ankylosis, 501–502
Annihilation radiation, 135, 137
Anodontia, 9, 13
Anterior cranial fossa (ACF), 360, 478, 483, 485, 519, 565, 566
Anterior disc displacement (ADD), 503
Antrochoanal polyp (ACP), 347, 367, 380
Antrolith, 19, 353, 382
Apert syndrome, 9, 10
Apparent diffusion coefficient (ADC), 131, 371, 436, 437
Arachnoid cyst, 542, 545
Arteriovenous fistula (AVF), 448, 454, 455, 464–465
Arteriovenous malformation (AVM), 86, 448, 453, 455, 462–465, 533
Articular loose bodies, 494
Artifacts, 4, 6, 10, 17, 57, 58, 80–85, 87, 100, 103–104, 111, 117–119, 124, 143, 147, 155–156, 161, 162, 169, 171, 274, 343, 344, 388, 448, 477, 533, 534, 574, 582, 620, 628. *See also* Metal artifacts
ASR (age-standardised incidence rates), 572
Atherosclerosis. *See* Calcified carotid artery atheroma (CCAA)
Atherosclerotic plaque, 273, 388, 405–407, 410
Attenuation coefficient, 77, 85, 94, 95, 146, 147
AUC (Area under the curve), 131
Avalanche photodiodes (APD), 146
Avascular necrosis, 180

Bandwidth (BW), 115
Basioccipital invertion, 520
Baskets, 151, 153, 154, 432, 435, 437
Battle's sign, 478
B-cell lymphoma, 144, 186, 352, 563, 572, 574, 600, 601
Benign lymphoepithelial lesions, 425
Blood pressure (BP), 396, 397
BMD (Bone mineral density), 187, 189, 190
BMI (Body mass index), 190
BOB CAT, 67
Botryoid odontogenic cyst, 200
Brain injury, 477
BRCA1/2 genes, 69
Bremsstrahlung, 80
Brightness, 49, 51–55, 153
British Columbia Cancer Agency (BCCA), 64, 82, 117, 118, 138, 142, 183, 285, 286, 310, 317, 350, 352, 354, 360, 555, 556, 599, 602, 604
Bruits, 405
Buccal bifurcation cyst (BBC). *See* Paradental cyst

Calcifications of stylohyoid complex, 274
Calcified atherosclerotic plaque (CAP), 405, 406, 410
Calcified carotid artery atheroma (CCAA), 5, 36, 108, 153, 156, 187, 387–389, 394–411, 422
Calcifying cystic odontogenic tumor (CCOT), 16, 201, 202, 221, 230, 325, 328
Calcifying epithelial odontogenic tumor (CEOT), 15, 201, 325–328

Oral and Maxillofacial Radiology: A Diagnostic Approach, Second Edition. Edited by David MacDonald.

© 2020 John Wiley & Sons, Inc. Published 2020 by John Wiley & Sons, Inc.

Calcifying odontogenic cyst (COC), 15, 16, 221, 230, 325, 328
Calculus (Salivary), 153, 274, 429, 431–433, 526
Capillary malformation, 448, 458
Carcinoma ex pleomorphic adenoma, 438, 567, 574
Cardiac implantable electronic device (CIED), 119, 120, 121
Carnoy's solution, 15, 207, 213, 215, 216, 220, 228
Carotid artery atherosclerosis. *See* Calcified carotid artery atheroma
Carotid artery stenting (CAS), 397, 399, 410, 411
Carotid body tumor. *See* Carotid paraganglioma
Carotid endarterectomy (CEA), 397, 399, 410, 411
Carotid paraganglioma, 535
Carotid space, 525, 527
Cathode ray tube (CRT), 51, 53
CCR (Canadian Cervical Spine Rule for Radiography), 488
Cementoblastoma, 6, 15, 312, 317–322
Cemento-osseous dysplasia. *See* Osseous dysplasia
Cemento-ossifying fibroma. *See* Ossifying fibroma
Central giant cell granuloma (CGCG), 37, 243, 245, 246
Central giant cell lesion, 171
Central necrosis, 86, 123, 125, 128, 129, 195, 351, 586, 591, 593, 599
Central nervous system (CNS), 378, 420
Cerebellopontine angle (CPA), 538, 539, 541
Cerebral vascular accident (CVA), 395
Cerebrospinal fluid (CSF), 478, 479, 483, 485, 524, 539, 545, 546
Cervical lymph nodes, 141–144, 155, 180, 273, 388, 526, 558, 592–598, 605
Cervical spine fracture, 477, 487
Chamberlain's line, 551
Cherubism, 15, 166, 171–175, 244, 294
Childhood illness, 12, 13
Chondrocalcinosis, 494, 497
Chondrosarcoma, 15, 279–281, 494, 499, 526, 558–563
Chronic kidney disease (CKD), 86, 399
Claustrophobia, 122, 146, 448
Cleft lip and palate, 8, 9, 95, 177
Cleidocranial dysostosis, 37
Clivus, 519, 524, 530, 531, 540, 551, 558–562, 579, 580
CNR (Contrast-to-noise ratio), 115
Cochleovestibular apparatus, 520
Coincidence, 135, 136
Color-coded 3D reformatting, 75
Common carotid Artery (CCA), 143, 388, 395, 401, 405–407
Complete removable prosthesis (CRP), 8, 615
Complex motion tomography, 615
Complex regional pain syndrome (CRPS), 127
Compression of images, 55–56
Computed tomography angiography (CTA), 397, 405, 407, 410, 411, 463, 464, 467
Computer-aided planning, 618–623
Condensing osteitis, 4, 317, 329–331
Condylar hyperplasia, 9, 496
Cone-beam computed tomography (CBCT), 10, 11, 19, 47, 59, 63, 75, 84, 89–108, 161, 167, 169, 174, 178, 185, 197, 198, 202, 205, 208, 217–219, 239, 250, 255, 260, 273, 286, 295, 301, 308–310, 312–314, 319, 330, 341–344, 346, 349, 362, 367, 370, 373, 376, 387, 390, 392, 397, 402, 448, 488, 494, 497, 505, 506, 514, 519, 521, 529, 555, 614, 616–618, 620, 622, 624, 626, 627
Congenital hemangioma, 448, 455, 458–462
Congenital syphilis, 13
Contrast index, 218
Contrast induced nephropathy (CIN), 86
Contrast medium (CM), 84, 86, 236, 426, 429, 457
Conventional radiography (CR), 3, 4, 6–16, 35, 36, 47, 48, 50, 51, 53, 63, 75, 94, 95, 127, 142, 161, 167, 169, 172, 173, 175, 181, 183, 185, 187, 191, 193, 195, 205, 210, 212, 214–216, 220, 232, 234, 235, 246–248, 252, 253, 257, 259, 273, 274, 282, 288, 289, 293–295, 299, 300, 303–305, 307, 316, 356, 358, 364, 365, 370, 381, 382, 387, 399, 417, 447, 449, 459, 473, 475, 488, 489, 493, 497, 549, 556, 628
Core needle biopsy (CNB), 434–436
Coronoid hyperplasia, 496
COTS (Commercial off-the-shelf) monitors, 51, 52, 54
Craniopharyngioma, 529–530, 532, 534
CRI (Chronic renal insufficiency), 191
Cribiform plate, 484, 485
Crouzon syndrome, 9
CRT (Cathode ray tube), 51, 53
Cuberilles, 85, 93–95
CUP (Carcinoma of unknown primary), 141, 145, 599, 600
Cyst type (Lingual bone defect), 256

Danger space, 525, 528
Degenerative Joint Disease (DJD), 503, 505–507
Dense bone island (DBI), 4, 15, 18, 19, 59, 324, 329–331, 382, 613
Dens-in-dente, 13
Dental computed tomography (DCT). *See* Cone-beam computed tomography
Dental notation, 22, 23, 164, 500
Dentigerous cyst, 4, 15, 27, 33, 37, 39, 69, 166, 201–206, 325, 326, 347, 357, 358, 361, 379, 380
Dentinogenesis imperfect, 12, 13
Dentinogenic ghost cell tumor (DGCT), 15, 325, 328
Dermoid cyst, 124, 153, 418, 526
Detectors, 47, 48, 55, 76, 77, 80, 82, 94, 135, 136, 162, 307
Diabetes mellitus (DM), 397, 399, 415, 417, 424
Diamagnetic, 125
DICOM, 51, 254
Diffuse infiltrative lymphocytosis syndrome (DILS), 425
Diffusion-weighted (DWI) MRI, 127, 128, 130, 131, 145, 182, 371, 420, 436, 437
Digital subtraction angiography (DSA), 397, 405, 408, 411
Dilaceration, 13
Disc displacement (Temporomandibular joint disease/dysfunction), 493–513
Doppler ultrasound, 406, 427, 438
DOR (Diagnostic odds ratio), 131
Double-strand breaks (DSB), 86
Down's syndrome, 13
Dry eyes, 420
Dry mouth, 415, 416, 418–425

Dual energy computed tomography (DECT), 76, 80–81, 84, 85
Dual energy X-ray absorptiometry. *See* DXA (Dual-energy X-ray absorptiometry)
Duplex ultrasound, 153
DXA (Dual-energy X-ray absorptiometry), 187, 189, 190
Dynamic contrast enhanced (DCE) MRI, 127, 131, 182, 249, 460

Echo time (TE), 113
Ectodermal dysplasia, 13
Ehler-Danlos syndrome, 496
Embolism, 475
Emphysema, 481, 485–489
Enophthalmos, 377, 382, 487
Enthesitis-related arthritis (ERA), 510, 511
Ependymomas, 536
Epidermolysis bullosa, 13
Epiglottis, 163, 286, 396
Evidence-based practice (EBP), 63
Ewing's sarcoma, 279, 281
EWS-FL11 fusion gene, 281
Exostosis, 377
Expanding osseous dysplasia (EOD), 289, 306, 315–316
External acoustic meatus (EAM), 11, 486, 498
External auditory canal bleeding (EACB), 483
External carotid Artery (ECA), 395, 401, 405, 406, 453, 535
Extracorpreal shock wave lithopripsy (ESWL), 154
Extramedullary hematopoiesis (EMH), 178
Extranodal extension (ENE), 70, 129, 583, 595, 597, 605
Eye injury, 473

Facial clefting, 9
Facial filters, 129
Facial pain, 127
Familial adenomatous polyposis (FAP), 278, 317
Familial fibrous dysplasia (Cherubism), 15, 166, 171–175, 244, 294
Familial gigantiform cementoma. *See* Expanding osseous dysplasia
Fat scan (T1-weighted MRI), 116, 523
Fast (or turbo) spin echo(FSE), 117
Fat suppression, 114, 116, 117, 123–125, 128, 129, 498
FDG (Fluorodeoxyglucose), 136–139, 141, 142, 144, 145, 181, 285, 318, 421, 425, 557, 587, 588, 594, 599, 602
Fibro-osseous lesion (FOL), 7, 18, 23, 30, 212, 279, 286–289, 293–295, 299, 301, 303–305, 308–313, 316–317, 347, 363, 364, 370, 373, 374
Fibrosarcoma, 15
Fibrous dysplasia, 4, 6, 7, 14, 15, 17, 18, 27–30, 32, 34, 37, 40, 94, 172, 226, 232, 252, 274, 287, 289–293, 295, 296, 299, 353, 368–373, 381, 382, 499, 501, 547, 549–551
Field of view (FOV), 10, 11, 36, 66, 84, 90–102, 104, 105, 107, 126, 127, 147, 185, 199, 294, 295, 308, 330, 342–344, 346, 494, 512, 519, 521, 529, 555, 617–618
Fine-needle aspiration biopsy (FNAB), 434–437, 440, 572
Fine-needle aspiration cytology (FNAC), 131
FISP (Fast imaging with steady state precession), 117
FLASH (Fast low angle shot), 117
Flat panel detector (FPD), 92, 95
Flat panel display, 50
Flattening the condyle, 508
Floor of the mouth, 97, 118, 124, 415, 418, 429, 432, 526, 576, 582, 584, 585, 617, 625
Florid cemento-osseous dysplasia. *See* Florid osseous dysplasia
Florid osseous dysplasia (FOD), 6, 18, 37, 41, 57, 167, 176, 278, 306–311, 314–316, 374, 382
18-Fluorodeoxyglucose (FDG), 136–139, 141, 142, 144, 145, 181, 285, 318, 421, 425, 557, 587, 588, 594, 599, 602
Fluoroscopy, 417, 431
Fluorosis, 12
FNAB. *See* Fine-needle aspiration biopsy
FNAC. *See* Fine-needle aspiration cytology
Focal Cemento-osseous dysplasia. *See* Focal osseous dysplasia
Focal osseous dysplasia (FocOD), 37, 42, 305, 306, 310–314, 316, 329, 382
Foramen lacerum, 522
Foramen of Monroe, 530, 532
Foramen ovale, 373, 395, 522, 550, 570, 573, 575, 577
Foramen rotundum, 521, 569, 575, 577
Foramina (F.) for the base of the skull, 521
Foramina spinosum, 522, 550
Forceps delivery, 9
Fossa of Rosenmuller, 457, 562, 570, 573, 575–578
Fovea ethmoidalis, 561
Fractures and hemorrhage, 475
Fractures and vision, 489
Fractures of the base-of-the-skull, 477, 478
Fractures of the cervical spine, 487
Fractures of the face: current causes, 473–490
Fractures of the mandible, 190, 473, 481–484
Fractures of the maxilla, 473, 476, 478, 481, 484, 486
Free induction density (FID), 114
FSE (Fast (or turbo) spin echo), 117
FS or FatSat (Fat saturation), 117, 123, 124, 126, 130, 147, 182, 509, 523, 524, 576, 578, 589

Gadolinium, 123–126, 128, 129, 167, 169, 249, 305, 407, 408, 448, 451, 455, 466, 523
Gardner's syndrome, 274, 275, 278–279, 546, 547
GBCAs (Gadolinium-based contrast agents), 125, 126
Giant cell granuloma. *See* Central giant cell lesion
Giant cell tumor of bone, 245
Gigantiform cementoma. *See* Expanding osseous dysplasia
Gigantism, 13
Glandular odontogenic cyst (GOC), 15, 37, 40, 166, 168, 206, 218, 234, 236–239, 379
Global groups, 37–44, 66, 161, 203, 210, 212, 225–228, 230, 232, 235–237, 240, 291, 293, 298, 301, 303–306, 311, 313, 323, 325
Glomus tumors, 536. *See also* Paragangliomas
GLUT1 (Glucose transporter 1), 465

GNAS (Guanine nucleotide-binding protein), 288, 289
Gorham's disease, 161, 165, 171
Gorlin-Goltz Syndrome. *See* Nevoid basal cell carcinoma syndrome
Granuloma, 4, 37, 166, 194, 197, 198, 200, 243–246, 349, 355, 375, 378, 424, 448
Granulomatosis and polyangiitis (GPA), 355, 378
Grayscale standard display function (GSDF), 51, 53
GTV (Gross tumor volume), 602

HAART (Highly active antiretroviral therapy), 425
Helical computed tomography (HCT), 75, 78–80, 624
Hemangioma, 447–450, 455–462, 465, 540–542, 544
Hemarthrosis, 468
Hemifacial hyperplasia, 9
Hemifacial hypoplasia, 9
Hemifacial microstomia, 9
Hemorrhagic stroke, 395, 396, 410
Hereditary gingival hyperplasia, 173
Hereditary persistence of fetal hemoglobin (HPFH), 176
H3F3A, 245
High Doppler shift, 455, 460
High vessel density, 455, 460
HIV (Human immunodeficiency virus), 424, 425
HIV-associated hyperplasia, 416
HIV-associated salivary gland disease, 424–425
Hodgkin lymphoma, 141, 181
Hounsfield unit (HU), 79, 84, 103, 146, 195, 215, 216, 308, 369, 395
Human-contrast sensitivity (HCS), 53
Human genome project, 64, 67
Human papilloma virus (HPV), 70, 573, 582, 583
Hydrocephalus, 177, 530, 532
Hyoid bone, 18, 20, 21, 29, 33, 163, 191, 273, 387–389, 391–396, 400, 404, 410, 433, 477, 527, 583, 590, 598
Hypertelorism, 177
Hyperthyroidism, 86
Hypoparathyroidism, 424
Hypopharyngeal cancer, 590
Hypopharynx, 556, 590
Hypopituitism, 13
Hypothyroidism, 86

Iatrogenic, radiopacities, 274. *See also* Metal artifacts
Idiopathic osteosclerosis, 4, 15, 18, 19, 37, 42, 259, 317, 324, 329–331, 613
IgG4-related disease (IgG4-RD), 421–422
Illuminance. *See* Ambient lighting
Image enhancement, 49, 55
IMPROVE, 67
IMRT (intensity-modulated radiotherapy), 557, 600
Infantile hemangioma, 448, 455, 458–461, 465
Informationist, 67
Interarticular disc, 498
Interferon ALFA, 461
Internal acoustic meatus, 520
Internal carotid artery (ICA), 191, 388, 395, 399, 401, 405–410, 451, 534, 535, 576–578, 590, 601
International classification of diseases for oncology (ICD-O), 16, 192–194, 206–220, 230–236, 240–242, 246–247, 249–252, 299–305, 317–328, 437–442, 529–530, 533–540, 542–543, 546, 558–572
International Myeloma Working Group (IMWG), 182
Interventional sialography, 153–154, 417, 432, 435
Intracranial aneurysm, 530–534
Inverted papilloma, 138, 347, 354, 375, 378, 542–543
Involuting hemangioma, 455
Iodide mumps, 426
Iodine allergy, 87
iPad, 52
Ischemic stroke, 180, 395, 396
ISSVA (International Society for the Study of Vascular Anomalies), 448, 450, 455, 458

Joint effusion, 502, 507, 509
Joint mice, 494
JPEG (Joint photographic experts group), 56
Jugular foramen, 522, 538, 540, 562
Jugular glomus (glomus jugulare), 533, 536, 538. *See also* Jugular paraganglioma
Jugular paraganglioma, 536
Jugulo-digastric node, 388
Juvenile idiopathic arthritis (JIA), 497, 499, 508, 510–513
Juvenile (aggressive) ossifying fibroma. *See* Ossifying fibroma
Juvenile psammomatoid ossifying fibroma. *See* Ossifying fibroma
Juvenile recurrent parotitis (JRP), 428
Juvenile trabecular ossifying fibroma. *See* Ossifying fibroma

Kaposiform hemangioendothelioma (KHE), 448, 451, 459
Kaposi's sarcoma, 425
K-edge, 80
Keratocyst. *See* Keratocystic odontogenic tumor; Odontogenic keratocyst
Keratocystic odontogenic tumor (KCOT), 15, 16, 26–28, 30, 37, 38, 64, 68–70, 166, 171, 176–178, 200, 201, 203, 206, 209, 218, 220–230, 235, 237, 239, 240, 248, 259, 304, 328, 347, 349, 360–362, 379, 380, 501
Kuettner tumor. *See* IgG4-related disease

LAC (Linear attenuation coefficient), 147
Lamina papyracea (fracture), 355, 488, 561
Langerhan's cell histiocytosis, 171, 186–188
Laryngeal cancer, 527, 590
Laryngeal cartilage, 148, 274, 280, 387, 559
Lateral cephalograms, 11, 20–22, 35, 36, 49, 387, 388, 395, 627
Lateral periodontal cyst, 26, 200, 228, 234
Lateral radicular cyst, 228
Law, 6
Lax temporomandibular capsule, 496
LCD (Liquid crystal display), 51, 53
LED (Light emission diode), 52–54, 98–100, 295
LeFort fracture, 475, 478, 479, 481, 484
Leontiasis ossea, 190, 275, 276, 547
LILACS, 37, 66
Lingual bone defect (LBD), 15, 36, 253–261
Lingual foramen, 625

Lipodystrophy syndrome, 425
Lithotripsy, 151, 154, 156, 417, 432
LOXL4 (Lysyl oxidase-like 4), 70
Luminance. *See* Brightness
LUT (Look-up table), 51, 54
Lymphatic malformation, 448, 455, 456
Lymphatico-venous malformation, 455, 457, 466–469
Lymph nodes, 19, 20, 75, 86, 108, 128–129, 141–144, 152, 154, 155, 180, 182, 194, 273, 274, 388, 390, 415, 421, 423, 425, 525–528, 558, 582, 587, 591–598, 600, 602, 603, 605
Lymphocytic leukemia, 181, 600, 601
Lymphoepithelial cysts (LEC), 425

Mach band effect, 19–21, 23, 25, 57–59, 321, 329, 381
Magnetic field strength (T), 112, 119, 128
Magnetic resonance angiography (MRA), 397, 405, 407–409, 411, 451, 463, 464
Magnetic resonance imaging (MRI)
  accidents, 119
  compatible, 112, 120
  safety, 119, 120, 145
  suite, 112, 120
Malignant ameloblastoma. *See* Metastasizing ameloblastoma
Malocclusion, 180, 297
Mandibular incisive canal, 625
MAPK (Mitogen-activated protein kinase), 175, 208, 245
Mastermind-like protein 2 (MAML2), 237
Masticator space, 525, 527, 577
McCune-Albright syndrome (MAS), 275, 290, 291, 299, 510, 511, 547
Mcgregor's line, 551
Measles-mumpsrubella (MMR) vaccine, 426
Meckel's cartilage, 281
Meckel's cave, 573
Medial artery arteriosclerosis (MAA), 397, 399–401
Medical-grade diagnostic monitors (MGD), 51–54
Medicinal-related osteonecrosis of the jaws (MRONJ), 190, 283–286, 298
Meningioma, 529, 536, 539–543
Meningoencephalitis, 426
MeSH (Medical Subject Heading), 65
Metal artifacts, 10, 80, 82–84, 103–104, 118, 628
Metal artifact reduction (MAR), 80, 83–85, 104, 118, 628
Metastasizing ameloblastoma, 206, 209
MGUS (Monoclonal gammopathy of undetermined significance), 182
MI (Mechanical Index), 156
Microvascular decompression (MVD), 69, 127
Middle cranial fossa, 295, 354, 477, 486, 487, 493, 519, 542, 555, 577
Mikulicz disease. *See* IgG4-related disease
MISME syndrome, 536
Moebius syndrome, 9
Monckeberg's medial artery arteriosclerosis. *See* Medial artery arteriosclerosis
MPA (microPascals), 439
MRONJ. *See* Medicinal-related osteonecrosis of the jaws (MRONJ)
MTV (Metabolic tumor volume), 139
Mucocele, 343, 353
Mucoepidermoid carcinoma (MEC), 15, 125, 193, 236, 237, 437, 567–568
Mucosal antral (pseudo) cyst, 23, 92, 347, 364, 365, 380–381
Mucous plug, 423, 428, 431
Multidetector Computed tomography (MDCT), 8, 10, 75–77, 80, 87, 90, 91, 93–96, 99, 103, 107, 117, 118, 136, 138, 141, 167, 169, 173, 181, 185, 218, 219, 351, 407, 490, 494, 495, 497, 499, 505, 507, 508, 512, 521, 617, 618
Multiplanar reformation (MPR), 89, 90, 139
Multiple myeloma, 181–183, 283, 478, 558, 559
Mumps, 153, 424–428
Myositis ossificans, 387
Myxofibroma. *See* Odontogenic myxoma

Nasal lymphoma, 563
Nasoethmoid complex, 485
Nasopalatine Canal, 185, 214, 254, 626–628
Nasopalatine duct cyst (NPC), 15, 166, 199, 252, 253, 255, 527, 573, 575, 577, 581–583, 627
Nasopharyngeal carcinoma, 142, 527, 573–583, 603
Nasopharynx, 36, 367, 380, 457, 481, 522, 530, 543, 555, 556, 558, 572, 573, 576, 579–581, 583
nBCA (n-butyl cyanoacrylate), 453, 464, 465
Nd-YAG (Neodymium-doped yttrium aluminium garnet) laser, 461, 469
Negative Predictive Value (NPV), 14, 65, 69, 432
Nephrogenic systemic fibrosis (NSF), 126
Neuro-cardio-facial-cutaneous (NCFC) syndrome, 244
Neurofibroma, 9, 13
Neurofibromatosis type II (NF2), 536
Neuroma, 536
Neuromyelitis optica spectrum disorder (NMOSD), 420
Nevoid basal cell carcinoma syndrome (NBCCS), 9, 37, 43, 68, 69, 166, 167, 171, 176–178, 220, 223, 360, 380
NEXUS (National Emergency X-radiography Utilization Study), 488
NHS (National Health Service, UK), 67
NICE (National Institute for Health and Care Excellence, UK), 67
N/m^2 (Newton per square meter), 154
Node of Rouvière, 576
Non-Hodgkin's lymphoma, 345
Non-involuting congenital hemangioma (NICH), 448, 458, 459
Non-transfusion-dependent thalassemia (NTDT), 179, 180
Noonan syndrome (NS), 175, 244
NOS (Not otherwise specified), 567
Notebook, 53

Obstructive salivary gland disease (OSGD), 416–418, 428–434
Odontogenic keratocyst (OKC), 14, 166, 202, 220, 221, 223, 230, 239, 240, 328, 360. *See also* Keratocystic odontogenic tumor

Odontogenic myxoma, 6, 7, 14, 15, 27–29, 37, 38, 107, 165, 166, 168, 201, 206, 218, 226, 228, 230–236, 347, 363, 364, 379, 380, 501
Odontoma, 6, 15, 22, 203, 223, 230, 246, 278, 317, 322–324, 328, 353, 374, 375, 382
Olfactory neuroblastoma (ONB), 561–565
Oncocytoma, 138, 436, 440–442, 542
Onyx, 464, 465
Ophthalmic referral, 486
Orbit (fracture), 476, 486, 487, 490
Orbital blowout, 475, 485–487
Orbital venous malformation, 540
Orchitis, 426, 428
Oropharyngeal squamous cell carcinoma (OPSCC), 70, 583
Oropharynx, 36, 123, 192, 390, 555, 556, 580, 583, 585–587, 589
Orthokeratinized odontogenic cyst (OOC), 15, 35, 37, 39, 166, 213, 226–230, 239–243, 347, 358, 379
Orthokeratotic variant (of the former odontogenic keratocyst), 239, 240
Osseointegrated implants, 66, 96, 119, 297, 312, 316, 342, 521, 613–629
Osseous dysplasia (OD), 6, 15, 18, 22, 24, 25, 37, 41, 42, 57, 92, 167, 176, 194, 247–249, 278, 286, 289, 305–317, 353, 374, 382, 613, 618
Ossifying fibroma (OF), 14, 15, 18, 37, 41, 252, 286, 287, 299–305, 353, 373, 382
Osteitis, 4, 15, 276, 283, 317, 321, 324, 329–331, 547, 618, 620
Osteoarthritis, 493, 502, 503, 507–509, 512
Osteoblastoma, 15, 317–319, 321
Osteochondroma, 305
Osteofibroma. *See* Ossifying fibroma
Osteoid osteoma, 15, 318, 321
Osteoma, 15, 274, 278, 279, 317, 318, 321, 499, 500, 546, 547
Osteomyelitis, 4, 12, 59, 142, 281–283, 321, 344, 347, 502
Osteonecrosis, 190, 283–286, 298, 509
Osteopenia, 171, 181, 187, 190
Osteophyte, 499, 504, 506, 508
Osteoporosis, 81, 91, 181, 187–190, 276, 277, 283–285, 551
Osteosarcoma, 15, 278–281, 283, 299, 318, 331, 347, 353, 371, 494, 501, 558
Osteosclerosis, 4, 15, 18, 19, 37, 42, 181, 190, 259, 284, 317, 321, 324, 329–331, 355, 613
Otitis media, 502, 503, 573

Paget's disease of bone (PDB), 276–278, 280, 283
Panda eyes, 478
Papillary cystadenoma lymphomatosum. *See* Warthin's (Warthin) tumor
Paradental cyst, 199
Paragangliomas, 527, 533–536, 539, 540
Parakeratotic variant (of the former odontogenic keratocyst), 14
Paramagnetic, 125
Parapharyngeal space, 116, 442, 525, 527–528
Parotid space, 525, 527
Pathology scan (T2-weighted MRI), 116, 523
Periapical cemental dysplasia. *See* Periapical osseous dysplasia
Periapical cyst. *See* Radicular cyst
Periapical osseous dysplasia (POD), 131
Periapical radiolucency of inflammatory origin (PRIO), 15, 26, 100, 181, 194, 197–200, 206, 253, 349
Pericoronal radiolucencies, 200–201
Perimesencephalic cistern, 537, 538
PET (Positron emission tomography), 16, 50, 52, 76, 131, 135–148, 167, 181, 285, 416, 421, 436, 556, 557, 587, 588, 594
PET/CT (fused Positron emission tomography and computed tomography), 135–146, 148, 181, 246, 318, 421, 557, 558, 585, 587, 588, 593, 594, 599, 604, 605
PET/MRI (fused Positron emission tomography and magnetic resonance imaging), 131, 146–148
Petroclival fissure, 562, 575, 577
Petrous temporal bone, 356, 519, 522, 541, 550, 577
Pfeiffer syndrome, 9
Pharyngeal mucosal space, 525, 527, 528
Phlebolith, 86, 447, 449, 456, 460, 465, 466
Photoelectric effect (PEE), 80
Photomultiplier tube (PMT), 146
Pierre-Robin syndrome, 9
Piezoelectric crystal, 152
Pindborg's tumor. *See* Calcifying epithelial odontogenic tumor (CEOT)
Pineal gland, 520
'Pipe stem,' 399, 401
Pituitary adenoma, 529–531
Pixelation, 51
Pixel-to-pixel, 51
Pleomorphic (salivary) adenoma (PSA), 15, 114, 116, 125, 435, 527
Polyps, 278, 279, 347, 365–367, 380–381, 546
Positive predictive value (PPV), 14, 65, 69
Positron emission tomography (PET), 16, 50, 52, 76, 131, 135–148, 167, 181, 285, 416, 421, 436, 556, 557, 587, 588, 594
Posterior cranial fossa, 478, 519, 562
Posterior (acoustic) shadowing, 406
Prevertebral space, 148, 489, 525, 528
Primary intraosseous squamous cell carcinoma (PIOSCC), 192, 194, 347
Primordial odontogenic tumor (POT), 15, 242–244
PRIO. *See* Periapical radiolucency of inflammatory origin
Propranolol, 461
Proptosis, 298, 316, 368, 381, 382, 485, 489, 542, 547, 549, 564, 566. *See also* Enophthalmos
Proton density, 114, 147, 509
Pseudogout. *See* Chondrocalcinosis
Psoriatic arthritis, 503, 508–511
PTCH1 (protein patched homolog1), 64, 68–70, 176, 177, 221, 223, 230
Pterygoid plates, 217, 363, 371, 381, 478, 479, 484, 485, 559, 569, 575
PubMed, 37, 65, 66, 98
Pulse sequence, 113, 117
Pustulosis, 283

Pyrexia of unknown origin (PUO), 145
Pyriform fossa, 592

QI (Quality improvement), 67

Raccoon eyes, 478
Radiation oncologist (RO), 64, 104, 556, 572, 600–602, 604
Radiation therapist (RT), 602
Radicular cyst, 26, 166, 194, 197–200, 203, 228, 347, 349, 356, 379
Radiofrequency (RF) coils, 112–115
Radiology, definitions, 65
Radiotherapy, 141, 209, 280, 417, 420, 422–423, 435, 499, 530, 533, 557, 558, 563, 576, 600, 602–604
Radiotherapy-induced salivary dysfunction, 422–423
'Rail track,' 399, 401
Rapidly involuting congenital hemangioma (RICH), 448, 458, 459
RAS/MAPK pathway. *See* MAPK
Raster, 51
Rathke's pouch cyst, 529
RDC/TMD (Research Diagnostic Criteria for TMD), 506, 507
Recurrent dislocation, 496
Relative period prevalence (RPP), 14, 162, 166, 172, 175, 201, 220, 325, 441
Relaxation, 114, 115, 147
Renal insufficiency, 126, 191
Renal osteodystrophy (ROD), 191, 192
Repetition time (TR), 113, 114, 116, 117
Retropharyngeal space, 154, 525, 527, 528
Reversible figures, 57
Rheumatoid arthritis, 139, 190, 418, 503, 508, 510, 511
'Rice grains,' 400, 402
ROD. *See* Renal osteodystrophy
Root resorption, 12, 17, 25, 27, 33, 59, 167, 169, 173, 175, 180, 186, 187, 193, 199, 201, 203–207, 209, 211–213, 222, 224, 226–229, 231, 235, 237–239, 241, 243, 246, 248, 249, 251, 252, 275, 292, 297, 302–304, 311–313, 318, 321, 322, 325–328, 331, 358
Routine radiographic screening, 8

Salivary gland ultrasound (SGUS), 416, 417, 419, 421–426, 428, 429, 431, 432, 434, 436, 437, 442
SAPHO syndrome, 283
Sarcoidosis, 416, 424
SATMJ (septic arthritis of the temporomandibular joint), 502, 503
Schwannomas, 521, 529, 536–541
Scleroderma (systemic sclerosis), 163, 164, 170, 499, 500
Sclerotherapy, 449, 450, 456, 457, 467, 469
SE (Spin echo), 117, 449, 450
Sella turcica, 519, 522, 523
Sensitivity, 14, 53, 65, 68, 69, 75, 131, 141, 148, 154, 181, 221, 421, 432, 436, 557, 572, 582, 593
Sentinel Node, 599
Sequential computed tomography, 78
Serum amylase, 428
Shimming, 124
Shimming coils, 124
Sialadenitis, 130, 153, 418, 421, 423, 425, 427, 429, 432
Sialectasis, 417, 419, 429, 432
Sialography, 153–154, 416, 417, 419, 420, 423, 429, 430, 432, 434, 435
Sialolithiasis, 428, 430
Sialoliths. *See* Calculus; Salivary
Sialosis, 416, 424
Sicca complex, 418
Sickle cell anemia (SCA), 180
Sickle cell disease (SCD), 171, 176, 178, 180, 547
Sickle cell trait (SCT), 180
Signal Node. *See* Sentinel Node
Silent sinus syndrome (SSS), 353, 377, 382
Silicon photomultipliers (SiPM), 146
Simple bone cyst (SBC), 15, 22, 24, 25, 164, 166, 218, 226, 235, 247–250, 255
Sinus floor-lift grafts, 376
Sinusitis, 183, 341, 343, 344, 346, 347, 353–366, 382
Sjogren's syndrome, 416–422, 424, 425
SNR (Signal-to-noise ratio), 95, 102, 112, 115, 119, 124, 136, 141
SNUC (Sino-nasal undifferentiated carcinoma), 520, 563, 565–567
Soft tissue filler (STF), 129
Solitary osseous plasmacytoma (SOP), 181
Sonic hedgehog (SHH), 68
SPAIR (Spectral attenuated inversion recovery), 124
SPAMM (Spatial modulation of magnetization), 118
Specificity, 14, 65, 68, 69, 128, 131, 141, 142, 148, 154, 176, 221, 421, 593
SPECT (Single photon emission computed tomography), 50
Spin-lattice, 115. *See also* T1 weighted MRI
Spin-spin, 115. *See also* T2 weighted MRI
Squamous cell carcinoma (SCC), 12, 15, 31, 70, 81, 118, 123, 125, 127–129, 136, 138, 142, 161, 166, 192, 217, 219, 345–347, 350, 360, 378, 526, 542, 555, 572–591, 594, 596
Squamous odontogenic tumor, 15, 240–242
SRC homology 3 domain-binding protein 2 (SR3BP), 172
Stafne's cyst. *See* Lingual bone defect
Stafne's type (lingual bone defect), 36, 253–261
Stenosis, 108, 155, 278, 395, 396, 399, 401, 404–410, 423, 428–430, 462
Stereolithography, 618
Stickler syndrome, 9
STIR (Short T1 inversion recovery), 124
Storage of images, 56
Stricture (salivary), 151, 419, 429, 431–434
Stroke risk, 404, 405
Stylohyoid complex, 20, 273, 274, 387, 389–395
Stylomastoid foramen, 520
Sublingual space, 525, 527
Submandibular calculus, 388
Submandibular fossa, 246, 250, 253, 615, 625–627
Submandibular space, 123, 418, 525, 527
Submentovertex (SMV), 494
Supernumerary teeth, 278, 358, 379
Superparamagnetic, 125

SUV (standard uptake value), 139–140, 143–145, 371, 558
Synovial chondromatosis, 494
Synovitis, 283
Systematic review (SR), 14, 65, 96, 126, 139, 164, 290, 378, 419, 507, 533, 613
Systemic sclerosis (scleroderma), 26, 161, 163, 164, 170–171, 499, 500

Tablet, 52, 53
Taurodontism, 8, 179
TE (Echo time), 113, 114, 116, 117
Technetium-99 (TC-99m), 142, 181, 283, 557
Temporomandibular joint disorder (TMD), 493, 499, 502–510, 512
TFT (Thin film transistor), 53
Thalassemia, 171, 176, 178–180, 344, 347, 348, 375, 546–548
Thyroid cartilage, 81, 387–389, 393–396, 401, 563, 585, 590
TI (Thermal index), 156
TIC (Time intensity curve), 131, 510
TIFF (Tagged image file format), 56
Time of flight (TOF), 126–127, 136, 140–141, 407, 460
Timing value, 113
TLG (Total lesion glycolysis), 139
TNM (Tumor, node, metastasis system), 597, 598
Tonsillolith, 274, 387–390
Tornwaldt's cyst, 546
Torus palatinus, 197, 343, 481
Transarterial embolism (TAE), 475
Transducer, 152–154, 405, 420
Transient ischemic attack (TIA), 397, 399
Traumatic bone cyst. *See* Simple bone cyst
Traumatic optic neuropathy, 486
Treacher-Collins syndrome, 9
Trigeminal neuralgia, 127
Triticeous cartilage, 387, 389, 395, 396
Tuberculosis (TB), 20, 274
Turner's tooth, 13
T1 weighted MRI, 116, 125, 126, 182, 183, 236, 248, 350, 354, 360, 421, 441, 498, 504, 505, 509, 524, 532, 535–544, 550, 560–562, 564–566, 568, 571, 576, 578, 586, 589, 596, 5321
T2 weighted MRI, 116–117, 182, 183, 236, 305, 421, 507, 509, 524, 530, 534, 539, 543, 545, 546, 550, 564

UIA (Unruptured intracranial aneurysms), 533
Ultrasonography (US), 87, 151, 154–157, 397, 405, 428, 436, 497, 507, 510, 512, 513, 615
Ultrasound, 16, 52, 63, 64, 131, 151–157, 198, 395, 405, 406, 416, 417, 419, 420, 422, 425, 429–431, 434, 435, 437, 438, 440, 441, 447, 451, 455, 497, 556, 591
Ultrasound-guided fine needle aspiration (UG-FNA), 154
Upper respiratory tract infection (URTI), 349, 353

Vascular anomaly, 3, 86, 418, 448–450, 455, 469
VEGF-A (Vascular endothelial growth factor), 461
Venous malformation, 448, 455, 456, 540–542, 544
Verrucous carcinoma, 15
Vestibular schwannoma, 536–539, 541
Viewing angle, 53
Virchow's Node. *See* Sentinal Node
Virtual monochromatic image (VIM), 81
Volume acquisition computed tomography. *See* Helical computed tomography (HCT)
Volumetric computed tomography (VCT), 89. *See also* Cone-beam computed tomography
Volumetric renderings, 399

Warthin's (Warthin) tumor, 15, 153, 416, 436, 439–441, 542
Water scan (T2-weighted MRI), 182, 183, 236, 305, 421, 507, 509, 523, 524, 530, 534, 539, 543, 545, 546, 550, 564
Wegener's granulomatosis. *See* Granulomatosis and polyangiitis
Weighted average (WA), 81
Whole-body CT for trauma (WBCTT), 480, 488

Young's modulus, 154

Zygomatic (fracture), 464, 475, 479, 480, 485